The Pathophysiologic Basis of Nuclear Medicine

Abdelhamid H. Elgazzar
Editor

Fourth Edition

Springer

The Pathophysiologic Basis of Nuclear Medicine

Abdelhamid H. Elgazzar
Editor

The Pathophysiologic Basis of Nuclear Medicine

Fourth Edition

Springer

Editor
Abdelhamid H. Elgazzar
Department of Nuclear Medicine
Kuwait University
Safat, Kuwait

ISBN 978-3-030-96251-7 ISBN 978-3-030-96252-4 (eBook)
https://doi.org/10.1007/978-3-030-96252-4

This Springer imprint is published by the registered company Springer Nature Switzerland AG
The registered company address is: Gewerbestrasse 11, 6330 Cham, Switzerland

To the Poor Around the Globe who Need More Justified Care and Attention

Foreword to the Fourth Edition

Understanding the basic pathophysiology of the disease processes is the core of diagnostic images interpretation, and it is of utmost importance that nuclear medicine physicians have this knowledge. Professor Abdelhamid H. Elgazzar is an internationally recognized nuclear medicine specialist, researcher, and highly productive author, whose analytic, incisive, and inquisitive mind gave early promise of an outstanding career. Prof Elgazzar and his international colleagues have provided us with 13 chapters that are coherent in the systemic presentation of the pathophysiology in relation to disease processes and the impact on scintigraphic patterns. These chapters discuss cell structure and function, radiopharmaceutical localization, biologic effects of ionizing radiation, and radionuclide therapy and provide very useful information alongside the clinical presentations.

The context of this extraordinary book is much needed for nuclear medicine residents, physicians as well as researchers. These chapters contain a wealth of information that is clinically relevant. Since Professor Elgazzar is one of the pioneers in this field, he has now assured us that his knowledge has been passed down to the next generation of nuclear medicine physicians. He is generous enough to share his accumulated experience as a consultant to ensure that we have well-rounded molecular imaging specialists. His shared knowledge in this book is priceless.

We are most grateful to Prof. Elgazzar and his coauthors for updating this outstanding textbook and providing us with the latest diagnostic skills.

Abass Alavi
Department of Radiology
University of Pennsylvania, School of Medicine,
Philadelphia, PA, USA

Foreword to the First Edition

Diagnostic imaging studies may be interpreted in one of two ways. The initial approach is that of the "imager," dealing solely with pattern recognition. In this respect, the experienced observer will surely outperform the younger physician who possesses a more limited fund of such knowledge in his or her memory bank. The other means of interpreting images draws basic pathophysiology and clinical knowledge of a disease entity into the interpretive process. Functional nuclear medicine imaging studies are exquisitely sensitive but notoriously nonspecific. For this reason, nuclear medicine is most often used as a screening tool or as a monitor of changes in function when therapeutic interventions are performed.

The nonspecificity of radionuclide imaging studies makes it particularly important that nuclear medicine physicians have a broad, in-depth understanding of the basic pathophysiology of the disease processes which they are being asked to study. It is in this area that Dr. Abdelhamid H. Elgazzar and his many colleagues have excelled. In the following 22 chapters, they provide us with a lucid, systemic presentation of the pathophysiology associated with various disease processes and how this knowledge impacts on scintigraphic interpretations. In addition to the clinical presentations, chapters dealing with cell structure and function, radiopharmaceutical localization, biologic effects of ionizing radiation, and radionuclide therapy provide very useful information. The format employed by this gifted international panel of authors provides us with an extraordinary text which differs from some of the other fine publications in our field. It remains true to the very essence of functional imaging which characterizes the field of nuclear medicine and distinguishes it from the more morphologically based radiologic imaging procedures.

Both residents and active practitioners of nuclear medicine will profit from the enormous amount of clinically relevant information provided herein. This volume will surely enhance our role as well-rounded nuclear medicine physicians, as opposed to being more limited "imagers." It is only in this manner that we can fulfill our obligation as true consultants and play a pivotal role in assisting patient management decisions.

We are most indebted to Dr. Elgazzar and his coauthors for enhancing our diagnostic skills with this extraordinary textbook.

New York, NY, USA — Leonard M. Freeman

Preface to the Fourth Edition

The fact that the understanding of the different clinical and basic features of diseases is crucial for all physicians practicing imaging cannot be overemphasized. Awareness of these basic features including anatomy, physiology, and pathophysiology of diseases to be diagnosed or treated by nuclear medicine is of particular importance for those practicing nuclear medicine to increase diagnostic accuracy and to ensure optimal imaging, with the ultimate goal of timely and appropriate intervention. This was behind the idea of this book which is now in its fourth edition.

The correlation of these basic disease aspects with the scintigraphic features of various conditions is further emphasized in this updated edition. The imaging specialist must appreciate the patient's clinical problem and the pathophysiologic changes to fully utilize nuclear images. Working from this clinical context, the specialist can then apply his/her understanding of the pathophysiologic basis of disease and the knowledge of how such pathology may translate into various imaging patterns. The difference between film reading dealing solely with pattern recognition and proper interpretation of a clinical scintigraphic image in the holistic approach integrating clinical, laboratory, and pathophysiologic understanding should be appreciated to achieve proper clinical impact. My original interest in this concept came many years ago since I am trained in pathology and laboratory medicine in addition to nuclear medicine. I enjoyed trying to explain the scintigraphic features and the radiotracers behavior within normal and abnormal tissues.

The developments in the field of nuclear medicine and its expansion continue to occur at a rapid pace. Additionally unraveling new facts on the pathophysiology of diseases is also continuing. To continue the efforts to accommodate these continuing developments and be in line with the future direction of nuclear medicine and molecular imaging, the fourth edition of *The Pathophysiologic Basis of Nuclear Medicine* was developed.

This edition reflects the significant new developments in the area of molecular imaging with more emphasis given to the basis and application of PET/CT.

Based on the readers' feedback and reviews, the chapters of this book have been changed and consolidated into 13 chapters. The edition starts with a chapter on the principles of pathophysiology followed by biologic effects of ionizing radiation and the relevant cell biology and basis of radiopharmaceutical distribution and mechanisms of uptake. The following chapters are on pathophysiologic basis and correlated applications on inflammation, musculoskel-

etal, endocrine, genitourinary, respiratory, circulatory including cardiovascular and lymphatic, and central nervous systems. The chapter on tumor scintigraphy starts with basic tumor features and then clinical utilization. This chapter details PET/CT management of individual tumors. Furthermore the radiopharmaceuticals for PET imaging have been updated with more details and correlation with pathophysiologic changes such as hypoxia, angiogenesis, and proliferation. The last chapter is devoted to the basis of the use of radionuclides in the therapy treatment and is updated to accommodate recent advances including prostate cancer treatment. Additional information about clinical and imaging correlation makes this text a very useful companion to those who are being trained in nuclear medicine technology and clinical nuclear medicine and radiology.

This updated volume should hopefully help medical professionals to further understand what nuclear medicine technology can offer for the diagnosis and treatment of disease. Further in-depth understanding of the scientific and clinical basis of the new directions in medical imaging will certainly lead to further improvements in effective utilization and interpretation. The new edition is more simplified and easier to read although it includes the most up-to-date essential information needed for an in-depth understanding of the field.

Kuwait City, Kuwait Abdelhamid H. Elgazzar

Preface to the Third Edition

Awareness of the impact of pathophysiology in particular on imaging studies is critical to the proper practice of nuclear medicine. The correlation of these basic aspects with the scintigraphic features of various diseases is further emphasized in this edition. The imaging specialist must appreciate the patient's clinical problem and the pathophysiologic changes to fully utilize nuclear images. Working from this clinical context, the specialist can then apply his/her understanding of the pathophysiologic basis of disease and the knowledge of how such pathology may translate into various imaging patterns. The difference between film reading dealing solely with pattern recognition and proper interpretation of a clinical scintigraphic image in the holistic approach integrating clinical, laboratory, and pathophysiologic understanding should be appreciated to achieve proper clinical impact. New developments in molecular biology, radiopharmaceuticals, and hybrid imaging have continued to contribute to the rapid change in the field of nuclear medicine and molecular imaging. To continue the efforts to accommodate these changes and be in line with the future direction of nuclear medicine and molecular imaging, the third edition of *The Pathophysiologic Basis of Nuclear Medicine* was developed.

This edition reflects new developments in the area of molecular imaging with more emphasis given to the basis and application of PET/CT. The chapter on tumor scintigraphy details PET/CT management of individual tumors. Furthermore the radiopharmaceuticals for PET imaging have been updated with more details and correlation with pathophysiologic changes such as hypoxia, angiogenesis, and proliferation. The additional information about clinical and imaging correlation makes this text a very useful companion to those who are being trained in nuclear medicine technology and clinical nuclear medicine.

It is my hope that this book will help medical professionals to further understand what nuclear medicine technology can offer for the diagnosis and treatment of disease. Deep understanding of the scientific and clinical basis of the new directions in medical imaging will certainly lead to further improvements and innovations in this important field of medicine. This updated edition will hopefully help in the understanding of the field of nuclear medicine in depth and further advance and improve current diagnostic and therapeutic modalities in the treatment of disease.

Kuwait City, Kuwait — Abdelhamid H. Elgazzar

Preface to the Second Edition

The field of nuclear medicine is continuing to grow rapidly and incorporating advances in molecular biology, molecular imaging, and pathophysiology. In an effort to accommodate these changes and be in line with the future direction of nuclear medicine, we have updated the first edition of *The Pathophysiologic Basis of Nuclear Medicine*, building on its strengths and making modifications to remedy any weak areas.

To reflect new developments in the area of molecular imaging, a separate chapter on the basis of positron emission tomography has been included, more information about therapy using radionuclides has been added, and the chapters on the cell, radiopharmaceutical uptake, inflammation, bone, respiratory and neurology have been expanded. Furthermore, the clinical aspects of the role of molecular imaging in nuclear imaging are emphasized, since an imaging specialist must appreciate the patient's clinical problem for a full utilization of nuclear images. For instance, the difference between superficial film reading and proper interpretation of a clinical scintigraphic image by a holistic approach has been highlighted. Working from this clinical context, the specialist can then apply his/her understanding of the pathophysiologic basis of disease and the knowledge of how such pathology may translate into various imaging patterns. Awareness of the impact of pathophysiology on imaging studies is critical to the proper practice of nuclear medicine. The additional information about clinical and imaging correlation makes this text an invaluable companion to those who are being trained in nuclear medicine technology and clinical nuclear medicine.

We extend our appreciation to reviewers of several journals as well as members of the nuclear medicine community from around the world for their helpful and motivating feedback, both published and private. It is my sincere hope that this book will help medical professionals to further understand what nuclear medicine technology can offer in the diagnosis and treatment of disease. A deeper understanding of the scientific and clinical basis of new directions in medical imaging will certainly lead to further modifications and new innovations. I also hope that this revised text will help to advance knowledge in the field of nuclear medicine and improve currently available diagnostic and therapeutic tools in the treatment of patients with various diseases.

Kuwait City, Kuwait — Abdelhamid H. Elgazzar

Preface to the First Edition

There is a great difference between superficial reading of a film and proper interpretation of a clinical scintigraphic image by an imaging specialist. Fully utilizing the clinical image, the imaging specialist evaluates both the anatomical and the physiological structure of the human body. First the specialist must appreciate the patient's clinical problem. Working from this clinical context, he then applies his understanding of the pathophysiological basis of disease and his knowledge of how such pathology may translate into various imaging patterns. This awareness of the impact of pathophysiology on imaging studies is critical to the proper practice of nuclear medicine.

Nuclear medicine is a unique and growing medical specialty that contributes most significantly to our understanding of the functional changes which accompany disease. In this way, nuclear medicine helps to advance scientific understanding. Both the diagnostic and the therapeutic aspects of nuclear medicine rely for their efficacy on the physiological changes produced by disease. Clearly, a detailed understanding of both normal and morbid pathophysiology is prerequisite to a successful career in this growing field of medicine.

Today nuclear medicine is one of the medical specialties with great opportunities for innovation and creative thinking. We are fortunate to be practicing nuclear medicine at a time of rapid scientific progress and significant growth in our contributions to patient care and well-being. The resources devoted to nuclear medicine, however, will be most profitably used when both researchers and practicing physicians have taken the time to understand the pathophysiological basis of scintigraphy and radionuclide therapy.

As a practicing nuclear medicine physician and teacher, I know that beginning students and physicians in both radiology and nuclear medicine have in the past lacked a concise textbook which focuses on the pathophysiological basis of nuclear medicine. I feel that the contributing authors to this book have collectively fulfilled this need. In addition, I hope that this book will serve as a practical reference for practicing radiologists and nuclear medicine physicians. Given the rapid pace of research in the field of nuclear medicine, keeping up to date after the completion of formal training is a challenge for all of us.

Along with the contributing authors, I hope that this book will help to spread medical knowledge and enhance patient care within the field of nuclear medicine.

Kuwait City, Kuwait — Abdelhamid H. Elgazzar

Acknowledgement

My thanks and appreciation go to Dr. Abdelmonem Omar, Dr. Shaimaa Alfarsi, Mrs. Heba Essam, Dr. Israa Alkasaby, Aseel Alkandari, and Mrs. Jehan Ghoneim, who sincerely supported to make this edition a reality.

Contents

Contributors

Saud A. Alenezi, MD, ABNM, FRCPC Department of Nuclear Medicine, Faculty of Medicine, Kuwait University, Kuwait City, Kuwait

Naheel Alnafisi, MD Department of Nuclear Medicine, Faculty of Medicine, Kuwait University, Kuwait City, Kuwait

Maryam Al-Qabandi, PhD Department of Nuclear Medicine, Faculty of Medicine, Kuwait University, Kuwait City, Kuwait

Jehan Alshammary, PhD Department of Nuclear Medicine, Faculty of Medicine, Kuwait University, Kuwait City, Kuwait

Shorouk Dannoon, PhD Department of Nuclear Medicine, Faculty of Medicine, Kuwait University, Kuwait City, Kuwait

Mohamed A. Elfawal, MD, MSc, PhD Department of Pathology, Faculty of Medicine, Kuwait University, Kuwait City, Kuwait

Abdelhamid H. Elgazzar, MD, FCAP Department of Nuclear Medicine, Faculty of Medicine, Kuwait University, Kuwait City, Kuwait

Department of Nuclear Medicine, Kuwait University, Kuwait City, Kuwait

Mohammad Ghanem, MD, FRCPC Department of Nuclear Medicine, Faculty of Medicine, Kuwait University, Kuwait City, Kuwait

Ahmed M. Mohammed, MSc, MHPE Department of Nuclear Medicine, Faculty of Medicine, Kuwait University, Kuwait City, Kuwait

James M. Mountz, MD, PhD Division of Nuclear Medicine, Department of Radiology, The University of Pittsburgh Medical Center, Pittsburgh, PA, USA

Razi Muzaffar, DO Division of Nuclear Medicine, Department of Radiology, Saint Louis University, St. Louis, MO, USA

Medhat M. Osman, MD, ScM, PhD Division of Nuclear Medicine, Department of Radiology, Saint Louis University, St. Louis, MO, USA

Ismet Sarikaya, MD Department of Nuclear Medicine, Faculty of Medicine, Kuwait University, Kuwait City, Kuwait

Pathophysiology: General Principles

1

Abdelhamid H. Elgazzar

1.1 Introduction

Understanding pathophysiology of the disease is essential for all who study and work in any field of medicine. Since nuclear medicine deals with functional and molecular changes, it becomes crucial to understand the pathophysiologic changes of relevant diseases and disease-like conditions to properly study and practice the field.

Pathophysiology has been changing and expanding with added new knowledge. Since the late 1970s, tremendous developments in molecular biology and genetics have provided medical science with an unprecedented chance to understand the molecular basis of disease. The disease can now be defined based on abnormal deviation from normal regional biochemistry. Since pathophysiology is a bridge between pathology and physiology, it is imperative to understand the principles of both disciplines.

1.2 Pathology

Pathology is concerned with studying the nature of the disease, including its causes, development, and consequences, with emphasis on the structural changes of diseases. Specifically, pathology describes the origin of disease, its etiologies, se, and how it progresses and manifests clinically in individuals to determine its treatment. Thus, pathology plays a vital role across all facets of medicine throughout life, and currently, it extends to the examination of molecules within organs, tissues, or body fluids.

1.3 Definition of Disease

The precise definition of disease is as complex as an exact definition of life. It may be relatively easier to define disease at a cellular and molecular level than at l individual level. Throughout the history of medicine, two main concepts of the disease have predominated: ontological and physiological [1].

The ontological concept views disease as an independent and self-sufficient entity and runs a regular course with a natural history of its own. The physiological concept, on the other hand, defines disease as a deviation from normal physiology or biochemistry; the disease is a statistically defined deviation of one or more functions from those of healthy people under the circumstances as close as possible to those of a person of the same sex and age of the patient. Most diseases begin with cell injury, which occurs if the cell is unable to maintain homeostasis.

A. H. Elgazzar (✉)
Department of Nuclear Medicine, Faculty of Medicine, Kuwait University, Kuwait City, Kuwait

A. H. Elgazzar (ed.), *The Pathophysiologic Basis of Nuclear Medicine*,
https://doi.org/10.1007/978-3-030-96252-4_1

1.3.1 Homeostasis

The term homeostasis is used by physiologists to mean maintenance of static, or constant, conditions in the internal environment by means of positive and negative feedback of information. About 56% of the adult human body is fluid. Most of the fluid is intracellular, and about one-third is the extracellular fluid that is in constant motion throughout the body and contains the ions (sodium, chloride, and bicarbonate) and nutrients (oxygen, glucose, fatty acids, and amino acids) needed by the cells to maintain life. Extracellular fluid was described as the internal environment of the body and hypothesized that the same biological processes that make life possible are also involved in disease [1]. As long as all the organs and tissues of the body perform functions that help to maintain homeostasis, the cells of the body continue to live and function properly [1].

1.3.2 The Genome

At birth, molecular blueprints collectively make up a person's genome or genotype that will be translated into cellular structure and function. A single gene defect can lead to biochemical abnormalities that produce many different clinical manifestations of disease or phenotypes, a process called pleiotropism. Many different gene abnormalities can result in the same clinical manifestations of the disease—a process called genetic heterogeneity. Thus, diseases can be defined as abnormal processes as well as abnormalities in molecular concentrations of different biological markers, signaling molecules, and receptors.

1.4 Physiology

Physiology is the study of normal, healthy bodily function. It is concerned with the science of the mechanical, physical, bioelectrical, and biochemical functions of humans in good health, their organs, and the cells of which they are composed. It is a broad science which aims to understand the mechanisms of living, from the molecular basis of cell function to the integrated behavior of the whole body.

1.5 Cell Biology

Cell biology is a field that focuses on the study of cell structure and function, on how cells are formed and divide, and how they differentiate and specialize. This field defines both the general properties, common to most cell types, and also details the unique features of specialized cells, which allow them to perform different specialized functions [2]

1.6 Pathophysiology

Pathophysiology is a convergence of pathology and physiology. It deals with the disruption of normal mechanical, physical, and biochemical functions, either caused by a disease or resulting from a disease or abnormal syndrome or condition that may not qualify to be called a disease, and now includes the molecular mechanisms of disease. In 1839, Theodor Schwann discovered that all living organisms are made up of discrete cells [2]. In 1858, Rudolph Virchow observed that disease could not be understood unless it was realized that the ultimate abnormality must lie in the cell. He correlated disease with cellular abnormalities as revealed by chemical stains, thereby founding the field of cellular pathology. He defined pathology as physiology with obstacles [3].

Since the time of Virchow, gross pathology and histopathology have been the foundation of the diagnostic process and the classification of disease. Traditionally, the four aspects of a disease process that form the core of pathology are etiology, pathogenesis, morphological changes, and clinical significance [4]. The altered cellular and tissue biology and all forms of loss of function of tissues and organs s result from cell injury and cell death. Therefore, knowledge of the structural and functional reactions of cells and

tissues to injurious agents, including genetic defects, is the key to understanding the disease process. Currently, diseases are defined and interpreted in molecular terms and not just as general descriptions of altered structure. Accordingly, pathology is evolving into a bridging discipline that involves both basic science and clinical practice and is devoted to studying the structural and functional changes in cells, tissues, and organs that underlie disease [4]. The use of molecular, genetic, microbiological, immunological, and morphological techniques is helping us to understand both ontological and physiological causes of disease.

1.7 Basic Major Principles of Pathophysiology

1.7.1 Cell Injury

The cellular injury occurs if the cell is unable to maintain homeostasis. The causes of cellular injury may be hypoxia (oxygen deprivation), infection, or exposure to toxic chemicals (Table 1.1). In addition, immunological reactions, genetic derangements, and nutritional imbalances may also cause cellular injury. For example, in hypoxia, glycolytic energy production may continue, but ischemia (loss of blood supply) compromises the availability of metabolic substrates and may injure tissues faster than hypoxia. Various types of cellular injury are summarized in Table 1.2, Fig. 1.1.

1.7.1.1 Biochemical Cell Injury

Regardless of the nature of injurious agents, there are several common biochemical themes or mechanisms responsible for cell injury [5]:

Table 1.1 Mechanisms of cellular injury

Hypoxic: most common
Chemical
Structural trauma
Immunological/inflammatory Infectious
Genetic derangement
Nutritional imbalance

Table 1.2 Main general responses to injury

Cellular adaptation
Atrophy
Hypertrophy
Hyperplasia
Metaplasia
Dysplasia
Cell death
Apoptosis
Necrosis

1. ATP depletion: Depletion of ATP is one of the most common consequences of ischemic and toxic injury. ATP depletion induces cell swelling, decreases protein synthesis, decreases membrane transport, and increases membrane permeability.
2. Oxygen and oxygen-derived free radicals: Ischemia causes cell injury by reducing blood supply and cellular oxygen. Radiation, chemicals, and inflammation generate oxygen-free radicals that destroy the cell membrane and cell structure.
3. Loss of calcium homeostasis: Most intracellular calcium is in the mitochondria and endoplasmic reticulum. Ischemia and certain toxins increase the concentration of Ca^{2+} in the cytoplasm, which activates a number of enzymes and causes intracellular damage, and increases membrane permeability.
4. Mitochondrial dysfunction: A variety of stimuli (free Ca^{2+} levels in cytosol, oxidative stress) cause mitochondrial permeability transition (MPT) in the inner mitochondrial membrane, resulting in the leakage of cytochrome *c* into the cytoplasm.
5. Defects in membrane permeability: All forms of cell injury and many bacterial toxins and viral proteins damage the plasma membrane. The result is an early loss of selective membrane permeability.

1.7.1.2 Intracellular Accumulations

Normal cells generally accumulate certain substances such as electrolytes, lipids, glycogen, proteins, calcium, uric acid, and bilirubin that are involved in normal metabolic processes. As a manifestation of injury and metabolic derangements in

cells, abnormal amounts of various substances, either normal cellular constituents or exogenous substances, may accumulate within the cytoplasm or nucleus, either transiently or permanently. One of the major consequences of failure of transport mechanisms is cell swelling due to excess intracellular fluid. Abnormal accumulations of organic substances such as triglycerides, cholesterol and cholesterol esters, glycogen, proteins, pigments, and melanin may be caused by disorders in which the cellular capacity exceeds the synthesis or catabolism of these substances. Dystrophic calcification occurs mainly in injured or dead cells, while metastatic calcification may occur in normal tissues due to hypercalcemia that may be a consequence of increased parathyroid hormone, destruction of bone tissue, renal failure, and vitamin D-related disorders.

All these accumulations harm cells by "crowding" the organelles and by causing excessive and harmful metabolites that may be retained within the cell or expelled into the extracellular fluid and circulation.

1.7.2 Cell and Tissue Response to Injury

The normal cell is able to handle normal physiological and functional demands, the so-called normal homeostasis. However, physiological and morphological cellular adaptations normally occur in response to excessive physiological conditions or some adverse or pathological stimuli [4]. The cells adapt in order to escape and protect themselves from injury. An adapted cell is neither normal nor injured but has an altered steady-state, and its viability is preserved. If a cell cannot adapt to severe stress or pathological stimuli, the consequence may be cellular injury (Fig. 1.1) that disrupts cell structures or deprives the cell of oxygen and nutrients. Cell injury is reversible up to a certain point, but irreversible (lethal) cell injury ultimately leads to cell death, generally known as necrosis. By contrast, an internally controlled suicide program, resulting in cell death, is called apoptosis.

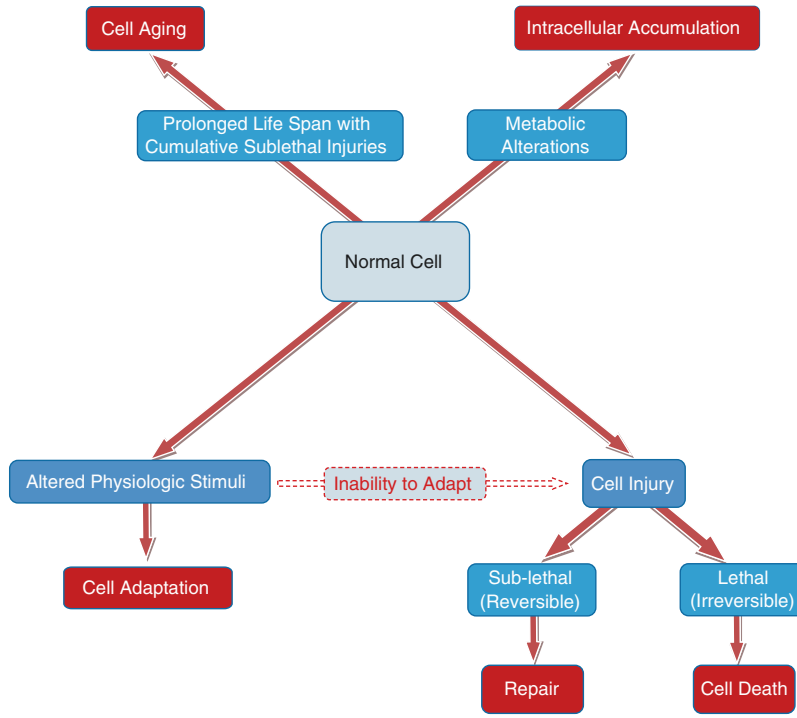

Fig. 1.1 Cell responses to stress and injury

1.7.2.1 Cell Adaptation

Some of the most significant physiological and pathological adaptations of cells involve changes in cellular size, growth, or differentiation [4, 5]. These include (a) atrophy, a decrease in size and function of the cell (Fig. 1.2); (b) hypertrophy, an increase in cell size (Fig. 1.3); (c) hyperplasia, an increase in cell number (Fig. 1.4); (d) metaplasia, an alteration of cell differentiation (Fig. 1.5); and (e) dysplasia, an abnormal growth or development of cells (Fig. 1.6). The adaptive response may also include the intracellular accumulation of normal endogenous substances (lipids, protein, glycogen, bilirubin, and pigments) or abnormal exogenous products. Cellular adaptations are a common and central part of many disease states. The molecular mechanisms leading to cellular adaptation may involve a wide variety of stimuli and various steps in cellular metabolism. Increased production of cell signaling molecules, alterations in the expression of cell surface receptors, and overexpression of intracellular proteins are typical examples.

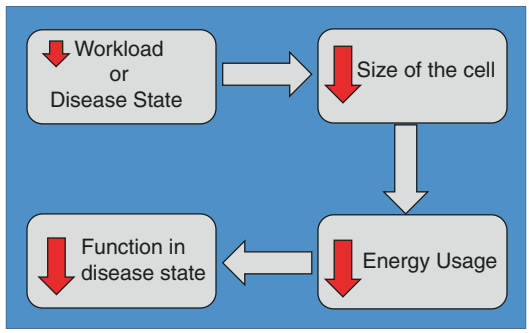

Fig. 1.2 Atrophy

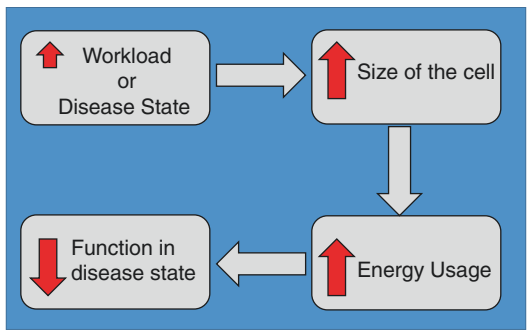

Fig. 1.3 Hypertrophy

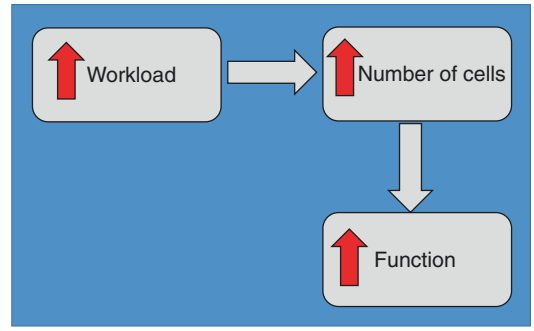

Fig. 1.4 Hyperplasia

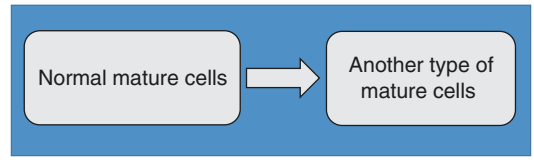

Fig. 1.5 Metaplasia

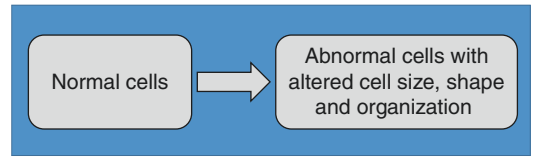

Fig. 1.6 Dysplasia

Atrophy

Atrophy is a decrease in the size of cells which may lead to a decrease in the size of a body part, organ, or tissue that was normal in size for the individual, considering age and circumstance, prior to the diminution. Examples include muscle atrophy from lack of use (most common) or disease.

Hypertrophy
Hypertrophy is a non-tumorous enlargement of a tissue or organ due to an increase in the size rather than the number of constituent cells. Examples include myocardial muscle hypertrophy due to prolonged strain secondary to hypertension.

Hyperplasia
Hyperplasia is the abnormal multiplication or increase in the number of normal cells in a normal arrangement in an organ or a tissue. Typical hyperplasia is a physiological response to a specific stimulus, and the cells of a hyperplastic growth remain subject to normal regulatory control mechanisms. Examples include endometrial hyperplasia resulting from high levels of estrogen.

Metaplasia
Metaplasia is the transformation of one mature differentiated cell type into another mature differentiated cell type as an adaptive response to some insult or injury. By this change in differentiation (and hence patterns of gene expression), the cells should be more resistant to the effects of the insult. It is usually a reversible phenomenon. Examples include a transformation of columnar epithelial cells of salivary gland ducts to squamous epithelial cells when stones are present. The development of glandular epithelium (glandular metaplasia) in the esophagus in patients with gastric acid reflux is another example (Barrett's esophagus).

Dysplasia
Dysplasia refers to the abnormality of the growth or development resulting in alteration in size, shape, and organization of adult cells or organs. It is characterized by the decreased amount of mature cells and an increased amount of immature cells, leading to an abnormal tissue arrangement. Such cells could return to the proper formation, but in some cases, the cells worsen and become carcinogens. In dysplasia, cell maturation and differentiation are delayed, in contrast to metaplasia, in which cells of one mature, differentiated type are replaced by cells of another mature cell [6].

1.7.2.2 Cell Death

Cell death is extremely important in the maintenance of tissue homeostasis, embryonic development, immune self-tolerance, and regulation of cell viability by hormones and growth factors.

Necrosis (Non-regulated, Inflammatory, Accidental Cell Death)
Necrosis is cellular death resulting from the progressive derivative action of enzymes on the lethally injured cells, ultimately leading to cellular swelling, dissolution, and rupture. Cell membranes swell and become permeable. Lytic enzymes destroy the cellular contents, which then leak out into the intercellular space, leading to the mounting of an inflammatory response (Fig. 1.7a). The morphological appearance of necrosis results from the denaturation of proteins and enzymatic digestion (autolysis or heterolysis) of the cell. Different types of necrosis occur in different organs or tissues. The most common type is coagulative necrosis, resulting from hypoxia and ischemia. It is characterized by denaturation of cytoplasmic proteins, breakdown of organelles, and cell swelling (Fig. 1.8), and it occurs primarily in the kidneys, heart, and adrenal glands. Liquefactive necrosis may result from ischemia or bacterial infections. The cells are digested by hydrolases, and the tissue becomes soft and liquefies. As a result of ischemia, the brain tissue liquefies and forms cysts. In infected tissue, hydrolases are released from the lysosomes of neutrophils; they kill bacterial cells and the surrounding tissue cells, resulting in the accumulation of pus. Caseous necrosis, present in the foci of tuberculous infection, is a combination of coagulative and liquefactive necrosis. In fat necrosis, the lipase enzymes break down triglycerides and form opaque, chalky necrotic tissue as a result of the saponification of free fatty acids with alkali metal ions. The necrotic tissue and the debris usually disappear by a combined process of enzymatic digestion and fragmentation, or they become calcified.

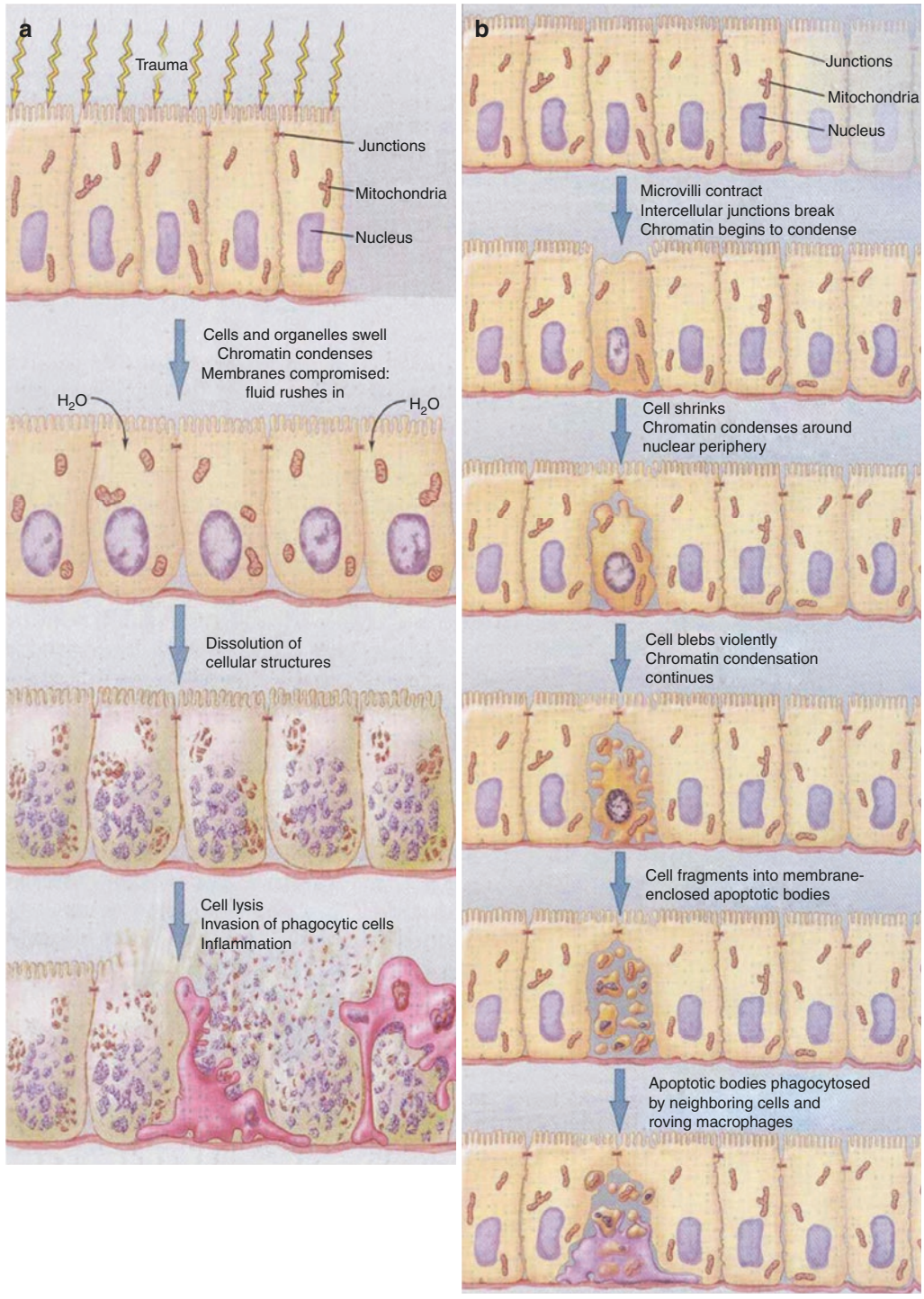

Fig. 1.7 (**a**, **b**) Diagram illustrating cell death. Accidental cell death (**a**) where necrosis occurs as a result of injury to cells. Typically, groups of cells are affected. In most cases, necrotic cell death leads to an inflammatory response (red "angry" macrophages). (**b**) Illustrates apoptosis or active cell suicide, which typically affects single cells. Neighboring cells remain healthy. Apoptotic cell death does not lead to an inflammatory response (From [7], with permission)

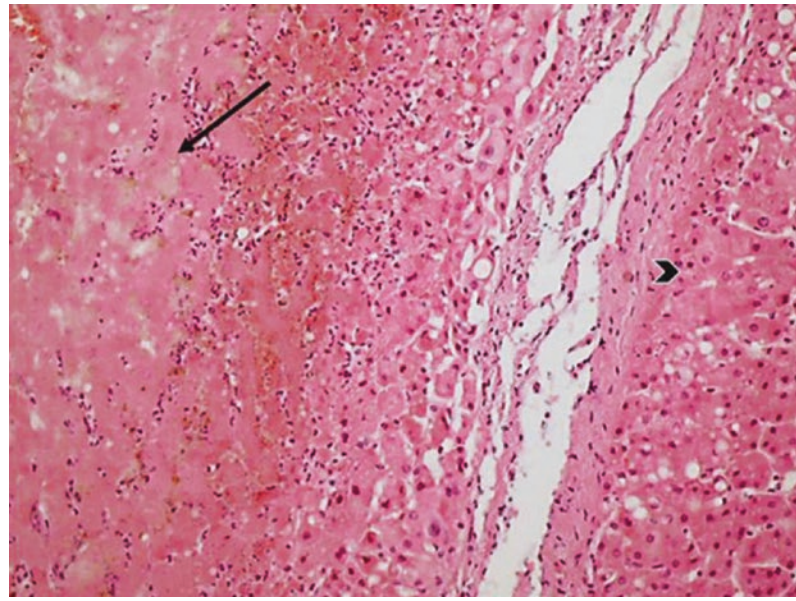

Fig. 1.8 Coagulative necrosis in a case of myocardial infarction. Note the necrotic area on the left side (*arrow*) with no cellular details and loss of nuclei compared to normal myocardial cells on the right side (*arrowheads*) (Courtesy of Professor Magda Elmonayeri with thanks)

Apoptosis (Regulated, Non-inflammatory Cell Death)

Apoptosis, a type of cell death implicated in both normal and pathological tissue, is designed to eliminate unwanted host cells in an active process of cellular self-destruction effected by a dedicated set of gene products. Apoptosis occurs during normal embryonic development and is a homeostatic mechanism to maintain cell populations in tissues. It also occurs as a defense mechanism in immune reactions and during cell damage by disease or noxious agents. Various kinds of stimuli may activate apoptosis. These include injurious agents (radiation, toxins, free radicals), specific death signals (TNF and Fas ligands), and withdrawal of growth factors and hormones. Within the cytoplasm, a number of protein regulators (Bcl-2 family of proteins) either promote or inhibit cell death. In the final phase, the execution caspases activate the proteolytic cascade that eventually leads to intracellular degradation, fragmentation of nuclear chromatin, and breakdown of the cytoskeleton.

The most important morphological characteristics are cell shrinkage, chromatin condensation, and the formation of cytoplasmic blebs and apoptotic bodies (Fig. 1.9) that are subsequently phagocytosed by adjacent healthy cells and macrophages. Unlike necrosis, apoptosis is nuclear and cytoplasmic shrinkage and affects scattered single cells. Two major apoptotic pathways have been defined in mammalian cells: the death receptor pathway and the mitochondrial pathway.

Cells undergo programmed death in response to both internal surveillance mechanisms and signals sent by other cells (Fig. 1.7b). Thus, some cells effectively volunteer to die, whereas other cells are nominated for death by others. Table 1.3 summarizes the cell responses to cell injuries [6].

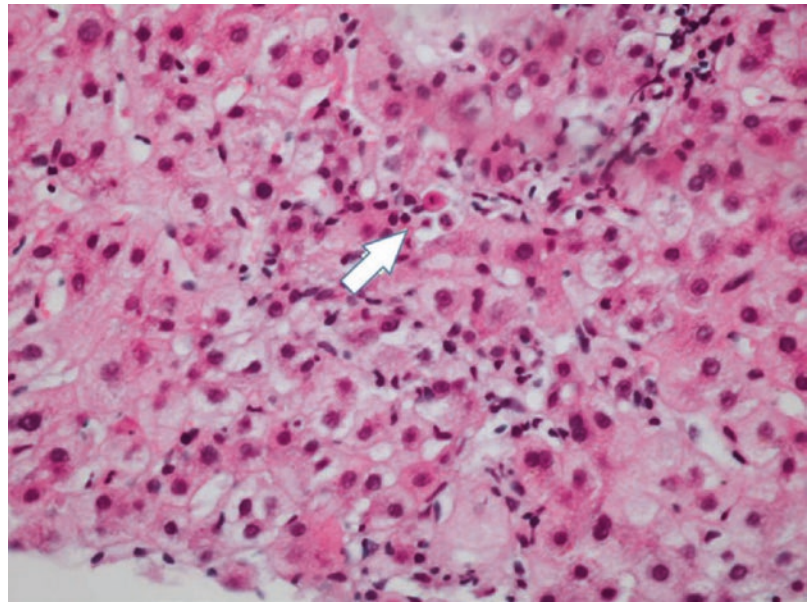

Fig. 1.9 A photomicrograph of a liver biopsy from a patient with hepatitis C and cirrhosis owing an apoptotic body (*arrow*)

Table 1.3 Responses to various cell injuries

Type	Responses
Adaptation	Atrophy, hypertrophy, hyperplasia, metaplasia
Active cell injury	Immediate response of "entire cell"
Reversible	Loss of ATP, cellular swelling, detachment of ribosomes, autophagy of lysosomes
Irreversible	"Point of no return" structurally when vacuolization of the mitochondria occurs, and calcium moves into the cell
Necrosis	Common type of cell death with severe cell swelling and breakdown of organelles
Apoptosis	Cellular self-destruction to eliminate unwanted cell population
Chronic cell injury (subcellular alterations)	Persistent stimuli response may involve only specific organelles or cytoskeleton, e.g., phagocytosis of bacteria
Accumulations or infiltrations	Water, pigments, lipids, glycogen, proteins
Pathological calcification	Dystrophic and metastatic calcification

adopted From Virchow [4]

References

1. McCormick F (2010) The molecular pathology of cancer. Nat Rev Clin Oncol 7:251–265
2. Pentimalli A, Giordano A. Cell biology and genetics. Life Sci. 2017. https://doi.org/10.1016/B978-0-12-809633-8.12390-8
3. Wagner HN (1995) Nuclear medicine: what it is and what it does. In: Wagner HN, Szabo Z, Buchanan JW (eds) Principles of nuclear medicine. Saunders, Philadelphia, pp 1–8
4. Virchow R (1958) Disease, life, and man. Stanford University Press, Stanford
5. McCance KL, Huether SE (2005) Pathophysiology. The biologic basis for disease in adults and children, 4th edn. Mosby, St. Louis
6. Cotran RS, Kumar V, Collins T (2010) Robbins pathologic basis of disease, 8th edn. Saunders, Philadelphia
7. Pollard TD, Earnshaw WC (2002) Cell biology. Saunders, Philadelphia

2 Ionizing Radiation: Biologic Effects and Essential Cell Biology

Maryam Al-Qabandi and Jehan Alshammary

2.1 Introduction

Ionizing radiation can ionize matter directly or indirectly when its quantum energy exceeds the ionization potential of atoms, thus introducing a reactive and potentially damaging ion into the environment of the irradiated medium. Examples of ionizing radiations are X-rays, γ-rays, energetic neutrons, electrons, protons, and heavier particles (such as α-particles). Radiation used in diagnostic imaging and treatment of diseases like cancer consists mainly of high energy photons such as X-rays and γ-rays. Biologic effects of radiation result principally from damage to deoxyribonucleic acid (DNA). DNA damage is considered the principal target in cells (Fig. 2.1). DNA double-strand break (DSB) constitutes the leading and most dangerous type of DNA damage by radiation. In response, three intimately related cellular processes intervene DNA repair, recombination, and replication. Alternatively, inaccurately repaired or unrepaired DNA lesions can lead to mutagenesis and cell death (Fig. 2.1). The biological effects of IR depend on several factors, such as the received dose and the area of the body exposed, making them variable and inconsistent. These effects can be early or delayed, somatic or hereditary, and stochastic or deterministic. Stochastic effects refer to random and unpredictable effects usually following chronic exposure to low-dose radiation. Genetic effects and carcinogenesis following diagnostic imaging are examples of stochastic effects. Deterministic (non-stochastic) effects are non-random effects and have a highly predictable response to radiation. Some of the known deterministic effects are radiation-induced lung fibrosis and cataract. Thus, radiation users need to be familiar with its biological effects and their pathophysiological basis.

2.2 Overview of the Genetic Material

To understand how ionizing radiation can affect cells in in the body, overview the structure of the Genetic material is presented.

2.2.1 DNA and Gene Expression

The ability of cells to maintain a high degree of order depends on the hereditary information that is stored in the genetic material, the DNA. The total genetic information stored in the chromosomes of an organism is said to constitute its genome. The human genome consists of 23 pairs of chromosomes. A chromosome is formed from a single, enormously long DNA molecule that

M. Al-Qabandi (✉) · J. Alshammary
Department of Nuclear Medicine, Faculty of Medicine, Kuwait University, Kuwait City, Kuwait
e-mail: maryam.alqabandi@ku.edu.kw

A. H. Elgazzar (ed.), *The Pathophysiologic Basis of Nuclear Medicine*,
https://doi.org/10.1007/978-3-030-96252-4_2

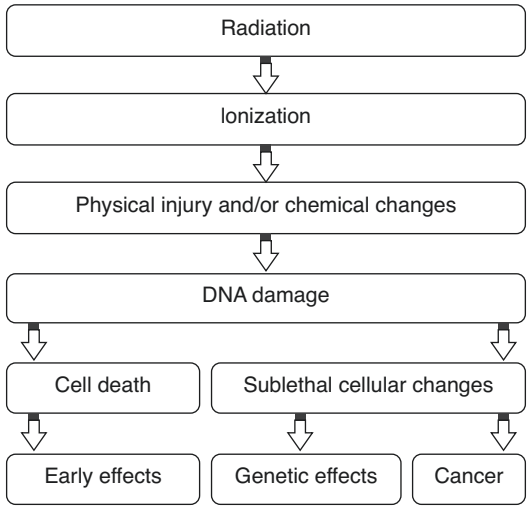

Fig. 2.1 Effects of ionizing radiation

consists of many small subsets called genes; these represent a specific combination of DNA sequence designed for a specific cellular function. There are approximately 100,000 genes per human genome, and only 15% of the genome is actively expressed in any specific cell type. The genetic information is transcribed into ribonucleic acid (RNA), which subsequently is translated into a specific protein on the ribosome. The three most important events in the existence of a DNA molecule are replication, repair, and expression.

2.2.2 DNA Structure

The most widespread DNA structure, discovered by Watson and Crick in 1953, represents DNA as a double helix containing two polynucleotide strands that are antiparallel and following an intrinsic directionality (5′–3′ direction) (Fig. 2.2). The "backbone" of the DNA molecule is composed of the deoxyribose sugars joined by phosphodiester bonds to a phosphate group, while the bases are linked in the middle of the molecule by hydrogen bonds. Two of the bases, thymine (T) and cytosine (C), are called pyrimidines, while the other two, adenine (A) and guanine (G), are called purines (Fig. 2.2). These bases link together through weak hydrogen bonds, and form base pairs. Adenine always pairs with thymine, A and T. Cytosine with guanine, C and G.

2.2.3 DNA Replication and Transcription

To serve as the primary genetic material, all the nuclei chromosomes duplicate their DNA before every cell division. The principle of complementary base pairing dictates that the process of replication proceeds by a mechanism in which a new DNA strand is synthesized that matches each of the original strands serving as a template [2]. Replication is semiconservative, in the sense that at the end of each round of replication, one of the parental strands is maintained intact, and it combines with one newly synthesized complementary strand (Fig. 2.2). At the end of replication, a repair process known as DNA proofreading is catalyzed by DNA ligase and DNA polymerase enzymes, which cut out the inappropriate or mismatched nucleotides from the new strand and replace these with the appropriate complementary nucleotides (Fig. 2.2). The replication process is almost errorless, and the DNA sequences are maintained with very high fidelity. The essence of heredity is the ability of the cell to use the information in its DNA to control and direct the synthesis of all proteins in the body.

2.2.4 DNA Repair, Recombination and Replication

For each type of DNA damage, the cell has evolved a specific method of repairing the damage or eliminating the damaging compound [3–6]. Genetic lesions include DNA base damage or base misincorporation, DNA crosslinks, and DNA strand breaks. These are repaired by (1) direct reversal, (2) base excision repair (BER), (3) nucleotide excision repair, (4) mismatch repair, (5) homologous recombination (HR), (6) nonhomologous end-joining (NHEJ) and (7) translesion DNA synthesis.

DNA single strand breaks (SSBs) are of little biologic consequence as far as cell killing is con-

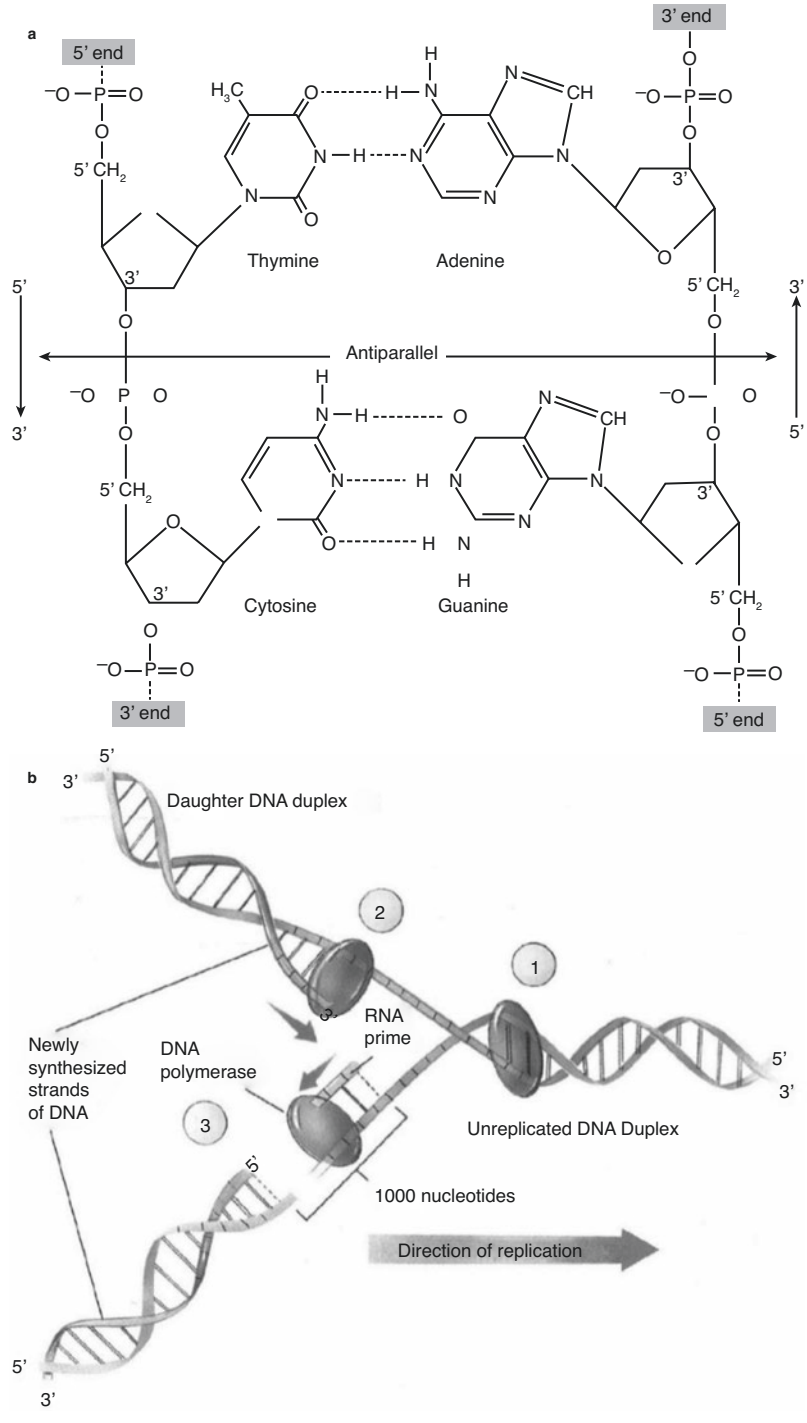

Fig. 2.2 DNA structure and replication. (**a**) The double-stranded DNA molecule consists of four bases (thymine, cytosine, adenine, and guanine), deoxyribose sugar, and phosphate. The antiparallel nature of DNA strands shows the opposite direction of the two strands of a double helix. Note the hydrogen bonds between the two strands of DNA molecules (Reprinted with permission from Devin). (**b**) DNA replication fork. Replication occurs in three stages: special proteins separate and stabilize the strands of the double helix, creating a fork (*1*). During continuous synthesis of a new DNA strand, DNA polymerase adds nucleotides to the 3′ end of a leading strand (*2*). In discontinuous synthesis, a short RNA primer is added 1000 nucleotides ahead of the end of lagging strand. DNA polymerase then adds nucleotides to the primer until the gap is filled (*3*) [1]

cerned because they are repaired readily using the excision repair mechanism. The damaged DNA polynucleotide chain is cleaved by enzymes on either side of the damage. The short segment resulting gap is then filled by a DNA polymerase using the opposite (complementary) undamaged strand as a template to guide the repair process. If just one nucleotide is damaged, it can be fixed by

a process called base excision repair. Here, the damaged base is snipped out and replaced with a new one.

In contrast, DNA double-strand breaks (DSBs) are much more difficult to repair and also much more dangerous. They represent the principal lesion that, if not adequately repaired, can lead to cell death via the generation of lethal chromosomal aberrations or the direct induction of apoptosis [7]. Alternatively, an inaccurately repaired or unrepaired DSB may result in mutations or genomic rearrangements in a surviving cell, which in turn can lead to genomic instability and subsequently result in malignant cell transformation. The cell can repair and/or restart replication forks by multiple mechanisms. For DSBs, there are two principal recombinational repair pathways: the homologous recombination (HR) and the nonhomologous end-joining (NHEJ) that employ entirely separate protein complexes [4, 8, 9].

HR reparation pathway requires an undamaged template molecule that contains a homologous DNA sequence at the time of the radiation damage. This repair by homologous recombination utilizes sequence homology with an identical or highly similar copy of the broken region. It typically operates on the sister chromatid in the late S and G_2 phases of the cell cycle. Undamaged DNA from both strands is used as a template to repair the break. This process is accurate, considered error-free and does not usually cause mutations. However, mutations in genes acting in HR can lead to both impaired DNA replication and increased radiation sensitivity [8, 10].

On the other hand, NHEJ repair pathway of the two double-stranded DNA ends, does not require an undamaged template and does not rely on extensive homologies between the recombinant ends and can possibly occur in all cell-cycle phases. NHEJ is suggested to be the dominant DSB repair pathway. This repairing process involves the repair proteins recognizing lesion termini, cleaning up the broken ends of the DNA molecule, and the final ligation of the broken ends. The process is inherently error-prone and mutagenic because it does not rely on sequence homology and can introduce sequence changes during repair with the loss or addition of nucleotides at the break site [11]. And, mutations in NHEJ genes lead to greater radiation hypersensitivity than mutations in HR genes, suggesting that NHEJ is the dominant pathway for the removal of IR-induced DSBs [8].

2.2.5 Outcomes for DNA Damage Repair

There are essentially four possible outcomes for DNA damage repair. One option is that the cell is able to completely repair the damage, function normally and survive. Another possible option, is that the DNA damage is severe enough and cannot be replaced, and this unfortunately leads to the apoptosis or self-destruction of the cell. It is also possible that the unrepaired mutation prior to mitosis, is passed to the daughter cells with three possible resulting responses:

1. Critical life-sustaining components are missing; the daughter cell may become apoptotic. Sufficient DNA damage may trigger an apoptotic signaling cascade, forcing the cell into programmed cell death.
2. The daughter cell survives the permanent genetic mutation to pass on its damaged DNA and may become senescent, i.e., irreversibly dormant. A gene mutation is any inherited change in the genetic material involving irreversible alterations in the sequence of DNA nucleotides. It may be classified into two categories: base substitutions and frameshift mutations. These mutations may be phenotypically silent (hidden) or expressed (visible). Research show that radiation increases the rate of mutation [12].
3. The daughter cell survives the mutation and may become malignant. If enough mutated cells survive, they can undergo rapid cell division and form a new growth called a neoplasm or a new growth called a tumor. Tumors are an abnormal mass of tissue. Sometimes these neoplasms can be benign, in other words, not harmful to our health. But in other times, they can be malignant, what we call cancerous [13].

2.2.6 Tumor Suppressor Genes

Many genes are activated in our body's repair pathway. Tumor suppressor genes, for instance, is a class of genes that encode proteins to control cell division and block cancerous cells from proliferating. However, if a tumor suppressor gene is lost or mutated with loss of its activity, uncontrollable mitosis is initiated, leading to cancer development. So the inactivation of tumor suppressor genes is one type of genetic alteration that contributes to tumor genesis. There are many different cancer suppressor genes, but an essential one is the p53 gene. Mutations of the gene p53 could play a role in up to 50% of all cancers, including leukemia, brain tumors, breast and colon, and lung carcinomas.

Mutations of tumour suppressor genes can also be inherited. BRCA1 and BRCA2 are two cancer suppressor genes associated with inherited or familial breast cancer. All cells contain two copies of BRCA1 and BRCA2 genes. Some individuals are born with a specific mutation or different mutations in these genes, and they develop an increased incidence of breast cancer. Individuals who inherit mutations have usually one copy of the gene that is not working. If the other copy is lost, DNA repair is not possible. Moreover, when the cell replicates its DNA during cell division, more mistakes enter into that replicate. Those mistakes make it more likely that the cell will become cancerous.

2.3 Basic Cell and Tissue Biology

The human body contains trillions of cells generated by repeated division from a single precursor cell. They constitute clones. With proliferation, some cells become specialized with a different structure, chemistry, and function.

More than 200 distinct cell types assemble into various tissue types such as epithelial, connective tissue, muscle, and nervous tissue. Different cells assemble to form each organ in the body. Although these cells often differ markedly, they all have similar essential characteristics.

2.3.1 Cell Types

The human body contains approximately 200 different cell types that represent, for the most part, discrete and distinctly different categories based on histological and morphological characteristics and cellular function. Recent subtler techniques involving immuno-histology and mRNA expression reveal new subdivisions of cell types within the traditional classification. Different cell types, such as neurons and lymphocytes, have the same genome, but the structural and functional differences are so extreme that it is difficult to imagine coming from the same cell. Different cell types synthesize different sets of proteins.

Differentiated cells have unique proteins with specific functions absent in other cells. The genome of a cell contains the essential information to produce thousands of different proteins and RNA molecules in its DNA sequence. A cell typically expresses a fraction of these genes, and the different types of cells in a human body arise from the expression of different sets of genes. Moreover, cells can change the genes they express in response to signals from other cells or the environment.

Different cells perform different functions. The most important cellular functions are movement, conductivity, metabolic absorption, secretion, excretion, respiration, and reproduction.

2.3.2 Tissue Types

In the human body, specialized cells of one or more types organize into cooperative assemblies, the tissues that perform unique functions. Different types of tissue compose organs, and organs, in turn, are integrated to perform complex functions.

The four major tissue types are epithelial, muscle, connective, and nervous. Some tissues do not exist as isolated units but rather in association with one another and variable proportions, forming different organs and systems in the body such as blood and lymphoid tissues. Such tissue cells are in contact with a network of extracellular

macromolecules known as the extracellular matrix, which holds cells and tissues together, that provides an organized latticework within which cells can migrate and interact with one another.

All tissues are further divided into many subtypes (Table 2.1).

2.3.3 Normal and Neoplastic Growth of Cells

Cellular reproduction is usually a tightly controlled process. Social control genes regulate cell division, proliferation, and differentiation under normal conditions. Certain stimuli and growth factors, both physiological and pathological, can influence a cell's reproduction rate. An uncontrolled cellular division that serves no purpose is called neoplasia. The uncontrolled growth of an abnormal cell that serves no purpose will give rise to a tumor or neoplasm that can be benign or malignant. Transformation is the process by which a normal cell becomes a cancer cell.

The common characteristics of cancerous tissue include a local increase in the cell population, loss of typical arrangement of cells, variation of cell shape and size, increase in nuclear size and density of staining, increase in mitotic activity, and abnormal mitoses and chromosomes.

Cancer cells produce many substances referred to as tumor cell markers. These can be hormones, enzymes, gene products, or antigens found on tumor cell plasma membrane or in the blood, spinal fluid, or urine. Regarding the tissue origin of cancer, in children up to 10 years of age, most tumors develop from hematopoietic organs, nerve tissues, connective tissues, and epithelial tissues (in decreasing order). This proportion gradually changes with age so that after 45 years of age, more than 90% of all tumors are of epithelial origin.

2.3.4 Cell Death

Cell death is essential in maintaining tissue homeostasis, embryonic development, immune self-tolerance, killing by immune effector cells, and regulation of cell viability by hormones and growth factors [14, 15].

Deregulation of cell death, however, is a feature of disease including cancer, myocardial infarction, cerebral stroke, and autoimmunity [14].

Based on the new recommendations of the nomenclature committee for cell death, it can be regulated and nonregulated. The regulated type is represented predominantly by apoptosis but also includes other types (Table 2.2).

2.4 Sources, Types, and Effects of Ionizing Radiation

2.4.1 Sources of Ionizing Radiation

Our bodies are exposed to radiation in two different ways depending on the location of the radiation-emitting source. For "external exposure," radiation comes from a radiation-emitting source present outside the body, such as radioactive materials existing on the ground, suspended in the air, or attached to clothes or the body's surface. Conversely, for internal exposure to radiation, radioactive material is present inside our bodies. Internal exposure to ionizing radiation can come from sources (1) ingested from food or drink; (2) inhaled from the air; (3) absorbed through the skin (percutaneous absorption); (4) from wound contamination, and (5) administered of radiopharmaceuticals for medical diagnostic imaging or therapeutic purposes. Once radioactive materials enter the body, the body will continuously be exposed to radiation until the radioactive materials are excreted biologically in the urine or feces (biological half-life) or as the radioactivity weakens over time. The difference between internal and external exposure lies in whether the radiation source is inside or outside the body. The body is equally exposed to radiation in both cases.

Exposure to ionizing radiation comes from several natural and man-made sources (Table 2.3). Whether the radiation source is natural or artificial, and independently of the dose of radiation, there will be some biological effects. The nuclear medicine professional should provide informa-

Table 2.1 Tissue types

Tissue	Tissue type	Location	Function
Epithelial	Simple squamous	Lines major organs	Absorption, filtration, secretion
	Simple cuboidal	Lines tubules and ducts of glands	Absorption and secretion
	Simple columnar	Lines GI tract	Secretion and absorption
	Stratified squamous	Lines interior of mouth, tongue, vagina	Protection
	Transitional	Lines urinary bladder	Permits stretching
Connective	Loose connective	Deep layers of skin, blood vessels, organs	Support, elasticity
	Dense connective	Tendons, ligaments	Attaches structures together, provides strength
	Elastic connective	Lungs, arteries, trachea, vocal cards	Provides elasticity
	Reticular connective	Spleen, liver, lymph nodes	Provides internal scaffold for soft organs
	Cartilage	Ends of long bones, trachea, tip of nose	Provides flexibility and support
	Bone	Bones	Protection, support, muscle attachment
	Vascular connective tissue	Within blood vessels	Transport of gases, blood clotting
	Adipose tissue	Deep layers of skin, surrounds heart, kidney	Support, protection, heat conservation
Muscle	Smooth muscle	GI tract, uterus, blood vessels, and bladder	Propulsion of materials
	Cardiac muscle	Heart	Contraction
	Skeletal muscle	Attached to bones	Movement
Neural	Different types of neurons	Brain and spinal cord	Conduction of electrical impulse, neurotransmission

Table 2.2 Cell death classification

1. Regulated (programmed, noninflammatory)
Apoptosis
Autophagy
Necroptosis
Mitotic catastrophe
Lysosomal-mediated programmed cell death
2. Nonregulated (inflammatory, accidental)
Necrosis

Table 2.3 Sources of ionizing radiation

Natural sources	Man-made sources
External radiation	Medical
Cosmic rays	Occupational
Terrestrial radiation	Nuclear power
Internal radiation	Nuclear explosions
Inhalation (radon gas)	Nuclear accidents
Ingestion	

tion to the patient and the public about the radiation risks from these sources and compare exposure from medical procedures to natural sources.

2.4.2 Types of Ionizing Radiation

Incident electromagnetic radiation (X-rays and γ-rays) or charged particulate radiation (α-particles, β-particles, and neutrons) interact with orbital electrons within the cellular atoms and molecules to cause their excitation or ionization. α-particles are helium nuclei made of two protons and two neutrons ejected at high speed, while β-particles are electrons ejected from a nucleus. Particle beams also include neutron beams and proton beams. γ-ray photons are types of electromagnetic waves. While α-particles, β-particles, and γ-ray photons originate within the nucleus, X-ray photons are generated outside the nucleus. X-ray photons include Bremsstrahlung (braking) X-rays and characteristic X-rays. Exciting radiations involve raising a bound electron to a higher energy state. A low-energy particle transfers sufficient energy to bump an electron from the atom's inner to the outer shell without removing it from its orbit.

The atom is in a higher energy state and is thus, called excited. The displaced electron promptly returns to the lower-energy shell, releasing its recently acquired energy as characteristic X-ray in a process called de-excitation. Ionizing radiations can create an ion pair following the electron ejection process. Ionization occurs when the radiation has sufficient energy to overcome the electron's binding energy and completely eject it from its orbit. The ejected electron may be sufficiently energetic to cause secondary ionizations on its own. Such an electron is called a delta γ-ray. The vacancy or positive electric charge in the host atom makes it very reactive. It will be easily attracted and interact with atoms having an excess negative charge. The irradiation of cellular material with such ionizing radiation gives rise to a flux of energetic secondary particles (electrons). These unbound secondary electrons migrate away from their production site and perturb the surrounding medium by giving up their energy through a series of interactions with other atoms and molecules.

Charged particles have high kinetic energy and can ionize matter directly. They deposit energy in the medium through direct Coulomb interactions with the orbital electrons of atoms in the absorber. In particular, α-particles have a high ionization density, causing ionization at a density hundred times as high as that of β-particles.

Indirectly ionizing radiation consists of uncharged, neutral particles such as X-ray or γ-ray photons which ionize matter indirectly using secondary electrons generated through their interaction with the substances. They deposit energy in the absorber through a two-step process. The neutral particle releases a charged particle in the absorber. Furthermore, the produced particle deposits partially or completely its kinetic energy in the absorber through Coulomb interactions with the orbital electrons. Energy transfer from the primary radiation beam to biological targets is constantly via the flux of secondary electrons produced, irrespectively of the nature of the primary radiation (charged particles and electromagnetic waves). These unbound and energetic secondary electrons can migrate away

from their production site and perturb the surrounding medium by giving up their energy through a series of interactions with other atoms and molecules. This energy absorption process gives rise to free highly reactive and unstable radicals, and it is the subsequent chemical interaction involving these are the true causative of radiation damage.

The energy from ionizing radiations is not deposited uniformly in the absorbing medium. When α- and β-particles or X- and γ-rays interact with matter, they transfer their energy heterogeneously and generate thus, clusters of ionization within a few nanometers diameter range, i.e., high-density ionization [16]. For energy deposition below 100 eV, spurs are produced. They involve, on average, three ion pairs within a diameter of about 4 nm. For an energy level ranging between 100 to 500 eV, blobs with 12 ion pairs within a diameter of about 7 nm are produced. Blobs are groups of overlapping spurs. For X-rays and γ-rays, 95% of the energy deposition events are spurs, whereas blobs remain less frequent [16]. These ionization clusters have dimensions similar to the DNA double helix diameter (about 2.5 nm) and can cause multiple radical attacks if they overlap the DNA helix. Thus, these locally multiplied damage sites could lead to considerable local damage, including DSBs, SSBs, and base damage.

External exposure to α-particles does not cause harmful effects on the body. α-particles cannot penetrate the skin layer because their penetrating distance is about several tens of micrometers. However, internal exposure to radioactive material that emits α-particles causes large amounts of ionization clusters within tissues, providing concentrated energy.

Ionization clusters can significantly damage DNA and have strong biological effects. β-particles cause direct ionization, but because of their low ionization density, their biological effects are less catastrophic than those of α-particles. β-particles have a penetrating distance of about several millimeters and could affect the skin and subcutaneous tissues. β-particles can cause burn-like symptoms when doses are very high, but they do not reach deep into the body. γ-rays and X-rays reach deep organs and tissues because of their high penetrating power. Nevertheless, because of their low ionization density, their biological effects are similar to those of β-particles.

On the other hand, in the case of internal exposure, all radioactive materials emitting α-particles, β-particles, or γ-rays could strongly affect cells within the body. Given the distance α-particles travel, their effects are visible on tissues containing the radioactive materials. However, due to their significant biological effects, caution is required with internal exposure.

2.4.3 Biochemical Effects of Exposure to Ionizing Radiation

Biological damage occurs due to chemical changes caused by ionization at the cellular level. Cell materials can be affected by ionizing radiation either directly or indirectly [16] (Fig. 2.3).

The two mechanisms of ionizing radiation effects on DNA: the direct, or target, mechanism and the indirect, through the production of free radicals that consequently cause damage.

2.4.3.1 Direct Effect

Direct effects of ionizing radiation occur when radiation ionizes atoms in DNA molecules or some other parts of the cell critical to its survival. The direct effect of ionizing radiation acts by direct collisions with target atoms. All atoms or molecules within the cells, such as enzymatic and structural proteins and RNA, are vulnerable to ionizing radiation injury. DNA, however, is the principal target [16]. If enough atoms are affected such that the chromosomes do not replicate properly, or if there is a significant alteration in the information carried by the DNA molecule, then the cell may be destroyed by "direct" interference with its life-sustaining system.

Charged particles with sufficient energy, e.g., electrons, interact directly with cellular components (atoms, molecules) without an intermedi-

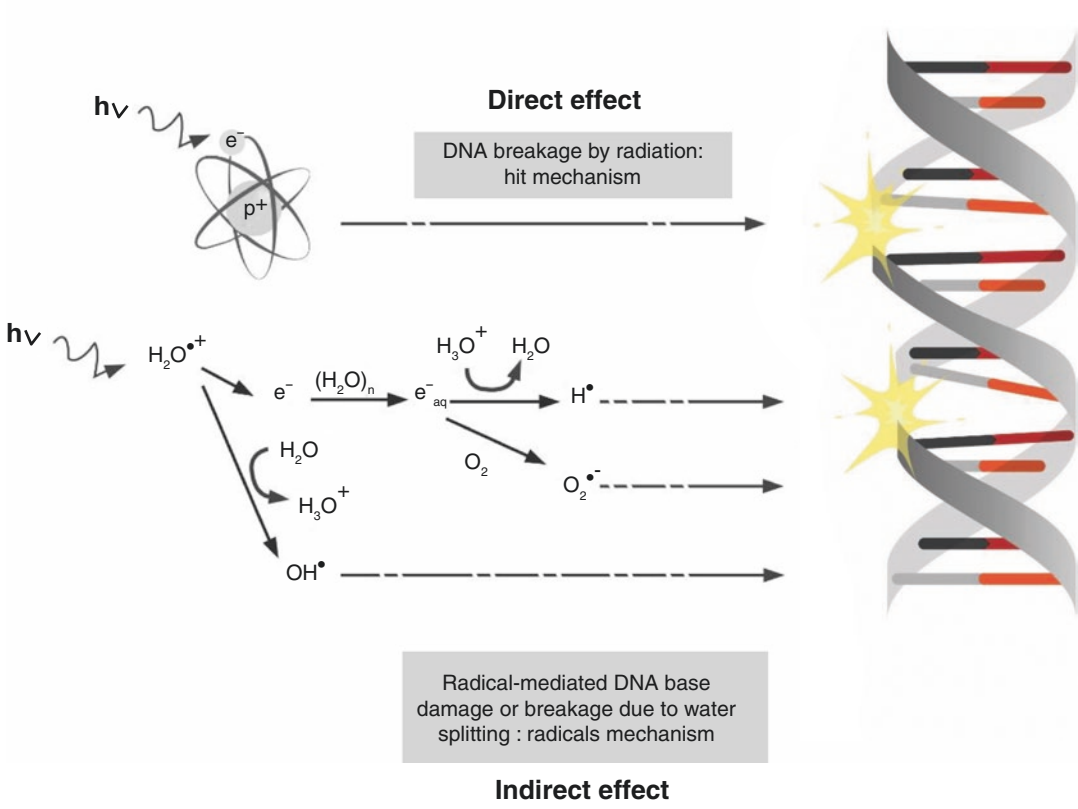

Fig. 2.3 Direct and indirect effects of radiation on DNA

ary step. The charged particle can continue interacting with other cellular atoms or molecules until all its kinetic energy is lost. Such interaction may ionize or excite the atoms and initiate a chain of events leading to a biological change and affecting the ability of the cell to reproduce and, thus, survive. The recoil electron directly ionizes the target molecule by creating ions that can physically break either the sugar–phosphate backbone of the DNA or its base pairs, thus affecting the ability of the cell to reproduce and ultimately survive. Luckily, ionizing radiation rarely interacts directly with DNA molecules as they occupy only a tiny fraction of the cell. In typically oxygenated cells, the direct effect of ionizing radiation accounts for about one-third of the damage for low LET radiations (such as electrons and photons).

2.4.3.2 Indirect Effect

Indirect effects of ionizing radiation are more frequent to occur. The indirect effect remains the leading cause of radiation damage, with about two-thirds of the biological damage. It is predominant with low linear energy transfer (LET) radiation, e.g., X-rays and γ-rays. At the same time, direct action is dominant with high LET radiation, e.g., charged particles (α- and β-particles) and neutrons. Indirect action of ionizing radiation involves radiation effects on atoms or molecules which are not constituent parts of the biological target. The probability of radiation interaction with DNA is minimal since it only represents a small cell fraction. As water is the main component of cells, there is a much higher probability that the recoil electron will interact with the water molecules.

The indirect effect of ionizing radiation occurs when an uncharged particle, e.g., photons, forms a free radical through water radiolysis of the cellular water molecule. When ionizing radiation interacts with a water molecule, the energy absorbed by the water molecule results in the breakage of the bonds holding the molecule together and in the formation of ion pairs such as hydrogen (H) and reactive oxygen metabolites such as hydroxyl radicals (OH) (Fig. 2.3). If oxygen atoms are present in the medium, other more aggressive free radicals such as hydroperoxyl and hydrogen peroxide can form. Free radicals are uncharged molecules carrying an unpaired valence electron in the outer shell. This state is associated with a high degree of chemical instability and makes them highly chemically reactive. Free radicals may recombine or interact with other fragments or ions to form compounds, such as water, without harming the cell. Free radicals would also quickly bond to other atoms or molecules, creating toxic substances like hydrogen peroxide (H_2O_2), contributing to apoptosis. Free radicals can also diffuse far enough to reach the critical target and produce chemical modifications and harmful effects. For the indirect action of X-rays, for example, the chain of events, from the absorption of the incident X-ray photon to the final observed biologic effect, may be described as follows:

1. When X-ray photons interact with water, two types of free radicals can be formed:

$$H^{\cdot} \rightarrow H^{\cdot}\left(\text{hydrogen}\right) + OH^{\cdot}\left(\text{hydroxy}\right).$$

2. The presence of an excess of oxygen during cells irradiation allows the formation of additional free radicals and increase biological damage:

$$R^{\cdot} + O_2 \rightarrow RO_2^{\cdot}\left(\text{highly toxic}\right).$$

$$H^{\cdot} + O_2 \rightarrow HO_2^{\cdot}\left(\text{hydroxyperoxy free radicals}\right).$$

$$HO_2^{\cdot} + HO_2^{\cdot} = H_2O_2\left(\text{highly toxic}\right) + O_2.$$

It is worth noting that antioxidants block hydroxyl-peroxy free radical combination into the highly unstable hydrogen peroxide.

3. Those highly toxic free radicals will induce chemical changes in the DNA structure from breaking its bonds, leading to severe biologic damages.

2.5 Cellular Effects of Exposure to Ionizing Radiation

To understand the biological effects of radiation exposure, it is thus essential, to begin with, a description of the different cellular lesions such as DNA damages (i.e., breaks) (Fig. 2.4) which will lead to cellular injury if not repaired as well as genomic instability and cancer.

2.5.1 Radiation-Induced DNA Strand Breaks

Ionizing radiation induces many DNA lesions, most of which are repaired successfully by the cell. Ionizing radiation can cause DNA lesions directly (the recoil electron directly ionizes the target molecule) or indirectly (the recoil electron interacts with water to produce an OH. free radical, which diffuses and interacts with the target molecule, here DNA). A dose of radiation causing one lethal event per cell (on average) leaves 37% of irradiated cells still viable; this is called the D0 dose. For mammalian cells, the X-ray D0 dose usually lies between 1 and 2 Gy. The number of DNA lesions per cell detected immediately after exposure to 1 mGy of X-rays (the equivalent of 1 mSv) is on average equal to 1 single-strand break at one location per cell. Double-strand breaks occur less frequently, at 0.04 locations per cell, which means that if 100 cells are evenly exposed to 1 mGy of X-rays, double-strand breaks occur in four cells (Table 2.4) [17].

Irradiated cells with a modest dose of X-rays, many breaks of a single-strand occur. By contrast, if the breaks in the two strands are opposite

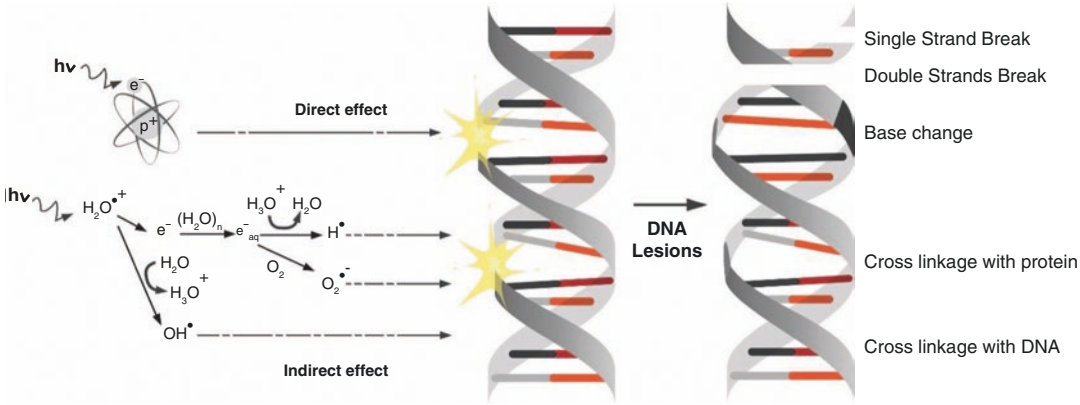

Fig. 2.4 DNA lesions: DNA strand breaks and base loss

Table 2.4 Radiation-induced DNA damages

Damage per 1 mGy of X-rays (per cell)	Averaged number of DNA lesions
Base damage	2.5
Single-strand breaks	1.0
Double-strand breaks	0.04
DNA–DNA crosslinks	0.03

one another or separated by only a few base pairs, this may lead to a DSB (double-strand break), resulting in chromatin cleavage into two pieces. DSBs are believed to be the principal lesions produced in chromosomes by radiation [18].

The interaction of two DSBs can cause cell killing, carcinogenesis, mutations, or genetic effects. There are many kinds of DSBs. They vary in the distance between the breaks on the two DNA strands and the types of end groups formed. The DSB yield in irradiated cells is about 0.04 times that of SSBs, and they are induced linearly with dose, indicating that single tracks of ionizing radiation form them. And, if breaks from both free radicals and direct ionizations occur in both directly opposed strands or separated by only a few base pairs, this could induce a double-strand break in which the chromatin snaps into pieces.

While the number of DNA lesions generated by irradiation is large, there are several mechanisms for DNA damage repairing or eliminating the damaging compound. As a result of cells tremendous ability to repair the damage, not all radiation effects are irreversible, and the percentage of lesions evolving into cell apoptosis is low. Multiple enzymatic mechanisms for detecting and repairing radiation-induced DNA lesions are triggered. They play an essential role in the recovery of cells from radiation and other damaging agents. SSBs have little biologic consequence as far as cell killing is concerned because they are repaired readily using the excision repair mechanism.

On the other hand, DSBs are much more difficult to repair and also much more dangerous. They represent the principal lesion that, if not adequately repaired, can generate lethal chromosomal aberration and lead to cell death. The homologous recombination (HR) and the nonhomologous end-joining (NHEJ) are the two primary repair pathways for DSBs [4, 8, 9].

Alternatively, inaccurately repaired DSB may result in mutations or genomic rearrangements in a surviving cell. In turn, it can lead to genomic instability and subsequently result in malignant cell transformation [19].

2.5.2 Radiation Induced Cell Injury

In general, an injury with a high chance of repair is sublethal, repaired with treatment is potentially lethal, and permanent is considered lethal. The nucleus is relatively more radiosensitive than the

cytoplasmic structures. Nuclear changes after radiation include swelling of the nuclear membrane and disruption of chromatin materials. Cytoplasmic changes include swelling, vacuolization, mitochondria disintegration and endoplasmic reticulum disintegration, and reduction in the number of polysomes [20, 21].

Depending on the radiation dose and the subcellular changes, along with the previously described factors, the potential effects on the cell may vary [20] (Table 2.5). Radiation dose is expressed as the absorbed energy by the irradiated tissue. After exposure to ionizing, cellular injury occurs in one of the following forms [22]:

1. Division delay: After exposure to 0.5–3 Gy of radiation, delayed mitosis is observed; however, near-normal restoration of mitotic activity is achieved following several generations.
2. Reproductive failure: The failed mitotic activity is permanent, and eventually, cell death follows. This is observed linearly after exposure to more than 1.5 Gy. Below this level, the reproductive failure is random in nature and nonlinear.
3. Interphase death: Apoptosis, or programmed cell death, is defined as a particular set of microscopic changes associated with cell death. Radiation-induced apoptosis is highly related to the type of involved cell. Lymphocytes, for example, are highly susceptible to radiation by this mechanism.

Table 2.5 Types of cellular damage in relation to approximate radiation dose

Dose grays (rads)	Type of damage	Comments
0.01–0.05 (10–50)	Mutation (chromosomal aberration, gene damage)	Irreversible chromosome breaks, may repair
1 (100)	Mitotic delay, impaired cell function	Reversible
3 (300)	Permanent mitotic inhibition, impaired cell function, activation and deactivation of cellular genes and oncogenes	Certain functions may repair; one or more divisions may occur
>4–10 (>400–1000)	Interphase death	No division
500 (50,000)	Instant death	No division
		Proteins coagulate

2.5.3 The Bystander Effect and Genomic Instability

Radiation effects have been observed to an extent beyond that explained by effects exerted on directly irradiated cells. Cells in temporal or spatial distance from the initial radiation insult have been shown to have delayed effects of radiation. Two phenomena are described: The Bystander Effect and the Genomic Instability.

The Bystander effect refers to the radiation damage induced in cells within an organ or the whole body that have not been directly exposed to radiation. In other words, a cell that a charged particle has not traversed is damaged as a result of radiation interactions occurring in neighboring cells [23–25]. A possible explanation is that, through cell-to-cell interaction, the directly irradiated cells communicate with adjacent cells (local level), which may elicit a response from the latter and spread the effect of radiation to a more significant number of cells and distant organs (long-range abscopal level). The mechanism is not clearly understood, and the overall relevance is currently difficult to gauge; however, gap junctional intercellular communication [26] or release of soluble factors (such as cytokines) [27] from irradiated cells is presented.

The Bystander effect has been mainly described for densely ionizing radiation such as charged α-particles [28, 29]. However, it has also been observed in low LET radiation (such as X-rays or γ-rays). Low LET radiation amplifies the overall radiation effect, making the overall radiation risk higher than expected from considerations of the gross response exhibited by those cells that have been directly irradiated. Bystander (nontargeted) and directly irradiated cells show a similar type of DNA damage, mutation and carcinogenesis [24].

Maximal radiation-induced genetic damage is formed shortly (minutes to hours) after radiation exposure. Nevertheless, it has been observed that the irradiated cells and descendants may show delayed effects. Cells that sustain nonlethal DNA damage show an increased mutation rate in descendants several generations after the initial exposure [30]. Delayed effects include delayed reproductive death up to six generations following the primary insult [31].

2.6 Factors Affecting Radiation Hazards

2.6.1 Factors Related to Ionizing Radiation

Radiation injury is a function of the ionizing radiation type and the target tissue. Specific factors related to radiation itself determine the various effects of the same radiation dose on biological organs.

1. Type of Radiation
   Electromagnetic and particulate (charged and uncharged) ionizing radiation have different ionizing properties. They differ in penetrability based on their LET, which expresses energy loss per unit distance traveled (kilo electron volts per micrometer). The linear energy transfer (LET) is high for α-particles, lower for β-particles, and less for γ-rays and X-rays. α-particles are the least penetrating but induce severe cellular damage. β-particles travel a longer distance, and γ-rays are the most penetrating type of ionizing radiation.
2. Mode of Administration
   The radiation dose is an essential factor. In addition, a single dose of radiation causes more damage than the same dose being divided (fractionated). Collectively these two factors are expressed as dose per fraction.
3. Dose Rate
   Dose rate expresses the time for which dose is administered. If the same total dose is administered over a more extended period, the cellular repair is improved, and cellular damage becomes negligible.

2.6.2 Factors Related to Biological Target

Certain properties of tissues and cells can significantly modify the biological effects of ionizing radiation.

2.6.2.1 Cell-Cycle Phase

Normal cells are cycled through five physiological phases: the pre-DNA synthetic phase (G1), the DNA synthetic phase (S), the post-DNA synthetic phase (G2), mitosis (M), and the more recently identified phase of no growth (G0), corresponding to the time after mitosis to the start of the G1 phase [32].

- The G0 phase is a latent phase. Cells are prepared to be recruited into the reproductive cycle, the G1 phase.
- The G1 phase is the first active phase of the reproductive cycle. In this phase, the cells synthesize RNA, enzymes, and proteins in anticipation of entering subsequent phases of the reproductive cycle.
- The S phase follows the G1 phase. The predominant event in this phase is the synthesis of DNA. At the end of the S phase, the cells contain twice the original amount of DNA.
- The G2 phase follows the S phase. During the G2 phase, the mitotic spindle essential for cell division is created. In the mitotic phase, the M phase, cell division takes place.

Ionizing radiation can affect all phases of the cell cycle with different radiosensitivity. Cells are most radiosensitive in the G1, G2, and M phases, respectively. They are most radioresistant in the S phase. Irradiation during the G2 phase retards the onset of cytokinesis. Irradiation during mitosis induces chromosomal aberrations. For a given cell cycle, radiation injury also differs from one cell type to another by altering radiation injury. For example, the reproductive cells have higher radiation sensitivity during the M phase, whereas

DNA synthesis and chromosome lesions occur during the G2 phase.

Recovery from sublethal injury happens in all phases of the cell cycle. However, this is more important in the S phase, which is also the most radioresistant phase. Exposed cells to radiation in the G0\G1 phase of the cell cycle tend to cease their progression into the G2\M phase. G2 synchronization produces a cluster of radiosensitive cells. A second hit within a time frame of 5–12 h leads to a higher proportion of deleterious effects [33]. The latter happens for radioisotopes with sequential α or β decay as in 90Sr\90Y [33].

2.6.2.2 Cell Radiosensitivity

The degree of cell sensitivity is directly related to the reproductive capacity of cells and tissues, thus stem cells (germ cells are more radiosensitive than mature differentiated cells. In 1906, one of radiology's most important discoveries was made: the law of Bergonié and Tribondeau, which states that "the Radiosensitivity of a tissue is directly proportional to its reproductive capacity and inversely proportional to its degree of differentiation" [34]. Although all cells can be affected by ionizing radiation, normal cells and their tumors vary in their sensitivity to radiation.

Radiosensitivity varies in function of the mitosis rate and cellular maturity. Rapidly dividing cells are more radiosensitive than cells that do not divide. And, undifferentiated cells are more radiosensitive than the mature cells that have specialized in function (Fig. 2.5). For example, undifferentiated hematopoietic cells in bone marrow proliferating from stem cells and differentiating into various blood cells are susceptible to radiation. They die after exposure to a small

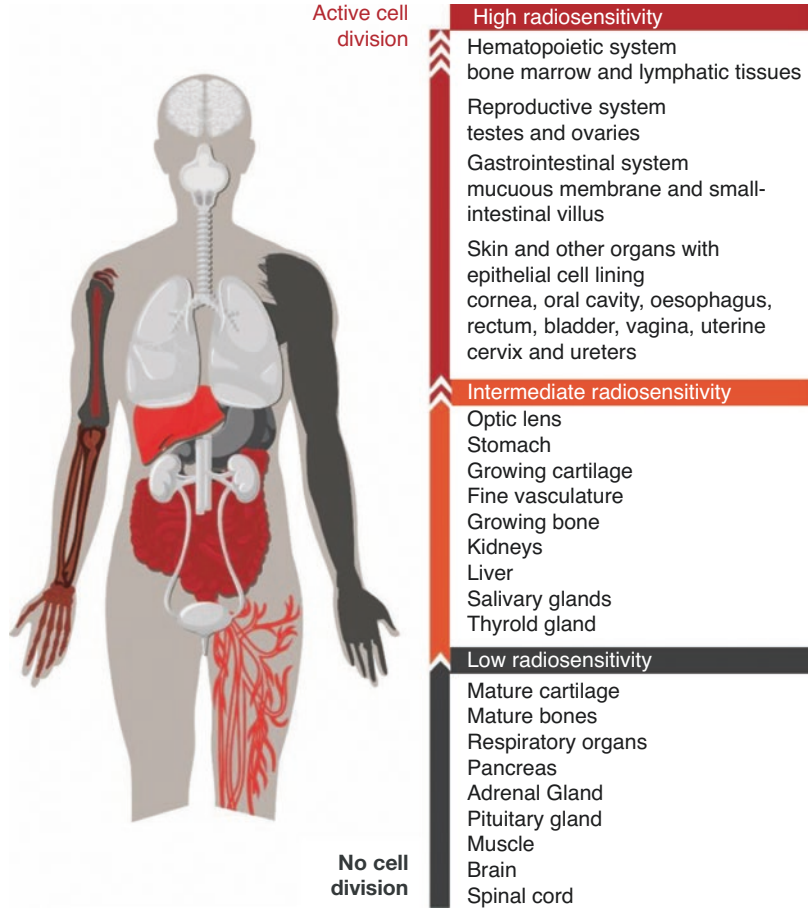

Fig. 2.5 Organs and tissues radiosensitivity

amount of radiation. As a result, the supply of blood cells is suspended, and the number of various types of cells in the blood decreases. In addition, the epithelium of the digestive tract is constantly metabolized and is also highly sensitive to radiation. On the other hand, nerve tissues, muscle tissues, and parathyroid cells are highly radioresistant. They no longer undergo cell division at the adult stage and are known to be resistant to radiation (Fig. 2.5).

2.6.2.3 Effect of Radiation Dose on Cell Dynamics

Exposure of highly dividing cells to high dose radiation would severely delay cell division activity. The mitotic rate is affected for an extended period before going back to normal. Exposure of highly dividing cells to moderate doses of radiation would delay mitotic activity on average for an intermediate period. Subsequently, the mitotic activity is moderately increased shortly before returning to normal. Moreover, exposure of highly dividing cells to low dose radiation would lead initially to a mild delay in cells mitotic activity followed by a short period of increased mitosis before the mitotic rate returns to normal.

2.6.2.4 Repair Capacity of Cells

Some cells have a higher capacity than others to repair the damage caused by ionizing radiation. Thus, the biological effects of the same radiation dose differ from one cell to the other. A significant repair occurs quickly, within 3 h. However, malignant cells have a decreased capacity to repair radiation damage.

2.6.2.5 Degree of Tissue Oxygenation

Molecular oxygen potentiates radiation response; this is called the oxygen effect. The amount of present molecular oxygen rather than the rate of oxygen utilization by the cells is the most critical factor to increase cellular radiation sensitivity. The probable mechanism is the allowance of additional free radicals, which enhance the damage of cells [21]. The free radicals produced due to direct or indirect effects of ionizing radiation are highly reactive will interact with other molecules to share electrons. Molecular oxygen (O_2) has two unpaired electrons and can thus directly interact with free radicals, leading to DNA damage by the indirect chain of reactions.

2.7 Biological Effects of Exposure to Ionizing Radiation

The effects of ionizing radiation on the human body depend on several factors, such as the nature of the effect and the timing after exposure. Biological effects due to exposure to ionizing radiation are variable and inconsistent. They can appear early (short term) or delayed (long term), be somatic or hereditary, and stochastic or deterministic types of effects (Fig. 2.6). Effects symptoms that appear within several weeks are acute (early) effects, while effects that develop after a relatively long time are called late effects. In particular, it takes several years to decades until a person develops cancer. Radiation effects can also be classified in the difference in mechanisms of how radiation effects appear, i.e., deterministic effects and stochastic effects.

Deterministic effects manifest themselves with a severity that is dose-related. They do not appear unless exposed to radiation exceeding a certain level of radiation dose after which the response is dose-related: a threshold value. Most of the deterministic effects represent acute disorders whose symptoms appear within several weeks after exposure. And, mostly known deterministic effects are radiation-induced lung fibrosis and cataract.

On the other hand, stochastic effects refer to random and unpredictable effects usually following chronic exposure to low-dose radiation. Their incidence cannot be denied entirely, even with low-dose exposure. Stochastic effects are dose-related, but the severity of the resultant condition is not related to the received dose. Thus, their management is generally on the safe side under

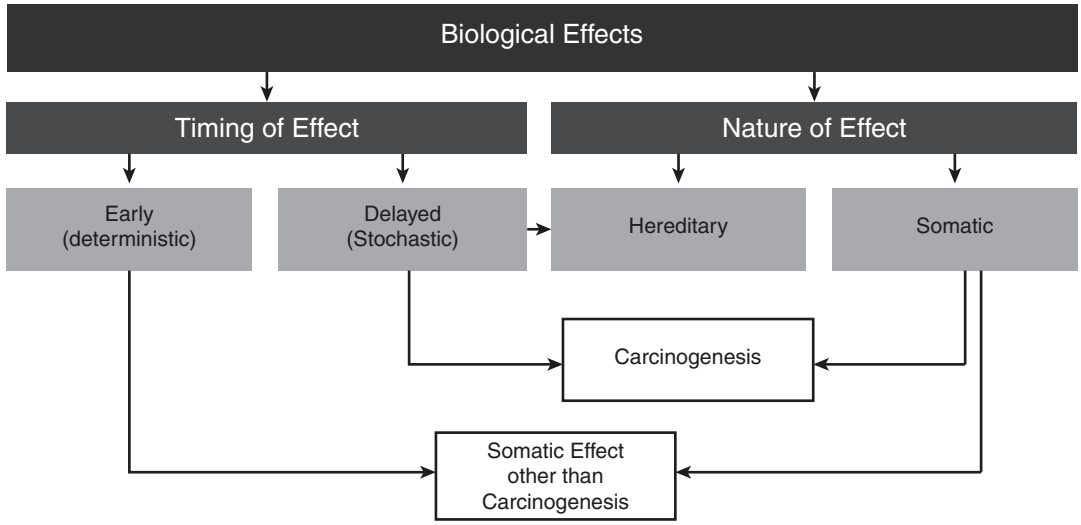

Fig. 2.6 The various biological effects of ionizing radiation

the assumption that there is no threshold value. Genetic effects and carcinogenesis following diagnostic imaging are stochastic.

Effects can be classified into early or deterministic, which have a threshold, and delayed or stochastic, with no threshold. Effects are also classified into somatic and hereditary. The somatic include early and delayed effects (cancer).

Table 2.6 The timescales of radiation effects

Action	Approximative timescale
Initial ionizing event	10^{-18} s
Transit of secondary electrons	10^{-15} s
Production of ion radicals	10^{-10} s
Production of free radicals	10^{-9} s
Chemical changes	10^{-5} s
Individual cell death	Hours–months
Gross, biological effects	Hours–years

2.7.1 Timescales of Radiation Effects

At the cellular scale, the initial ionization events are the precursors to a chain of subsequent events that may eventually lead to the biological and clinical, at the macroscopic scale, manifestation of radiation damage. Although the chemical changes may appear to operate over a short time, about 10^{-5} s, this period is a factor of 10^{-18} longer than the time taken for the original particle to traverse the cell nucleus. Thus, there is a relatively long period during which chemical damage is inflicted (Table 2.6). Cell death in individual lethally damaged cells takes place later, within an hour to 1 day, usually at the point when the cell subsequent attempts to enter mitosis. Clinically observable radiation effects result from the wholesale functional impairment that follows from lethal damage being inflicted on many cells or critical substructures. It takes some time until the reaction occurring at the cellular level develops into clinical symptoms at an individual level, and the timescale of the whole process may extend to months or years. This period is called the incubation period. Thus, in clinical studies, any deleterious health effects of a radiation procedure may not be seen until long after the diagnostic test or treatment has been completed (Table 2.6) [35].

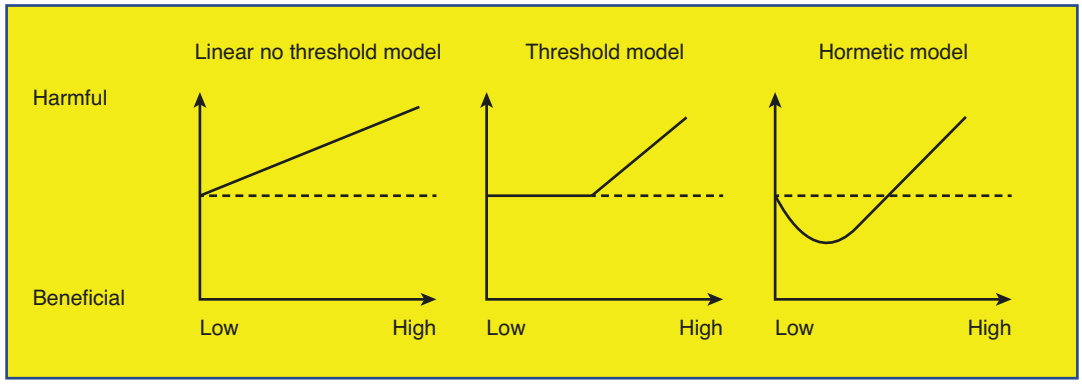

Fig. 2.7 Comparison between three different dose–response models. The *dashed line* represents health effects in the absence of radiation. *Y*- and *X*-axes represent health effects and radiation dose, respectively. (Reproduced from Ernst et al. [36] with permission)

2.7.2 Dose–Response Models

Many models predict relationships between the radiation dose and the effect of radiation exposure to a biological target. However, these models differ due to different underlying assumptions. Figure 2.7 illustrates three models describing the response of a biological system to various radiation doses.

1. Linear No-Threshold Model
   This model assumes that any level of radiation is harmful and that the risk increases linearly with increments of dose. It is applied for radiation protection purposes to limit the risk to workers in radiation fields.
2. Threshold Model
   This model assumes that radiation risk is linearly related to the dose; however, this occurs if the received dose is above the threshold level. There is no risk expected below the threshold level. The theory behind the threshold level is that some degree of cellular damage should accumulate and produce cell damage.
3. Hormesis Model
   In this model, there is a bimodal effect of radiation. Below a certain threshold level, radiation is protective. Harmful effects happen only when above the threshold dose level. The rationale is that radiation at low levels induces protective cellular mechanisms which prevent DNA damage from occurring spontaneously or due to other stresses [37, 38]. Figure 2.8 presents the scheme of the dose–response function (Reproduced with permission from Feinendegen [39]).

2.7.2.1 Deterministic Radiation Effects

Deterministic effects are nonrandom and have a highly predictable response to radiation. Even if some cells die due to exposure to a small amount of radiation, clinical symptoms do not appear if tissues and organs can fully function with the remaining cells. When the radiation increases and more cells die, relevant tissues and organs suffer temporary dysfunction, and some clinical symptoms may appear. However, such symptoms improve when normal cells proliferate and increase in number.

When cells in tissues or organs are damaged severely due to a large amount of radiation, this may lead to permanent cell damage or morphological defects. In this manner, there is a specific exposure dose above which symptoms appear and under which no symptoms appear for deterministic effects due to cell deaths. Such dose is called the threshold dose.

Acute Disorders

Clinically observed radiation effects in whole tissues or organs reflect the damage inflicted to

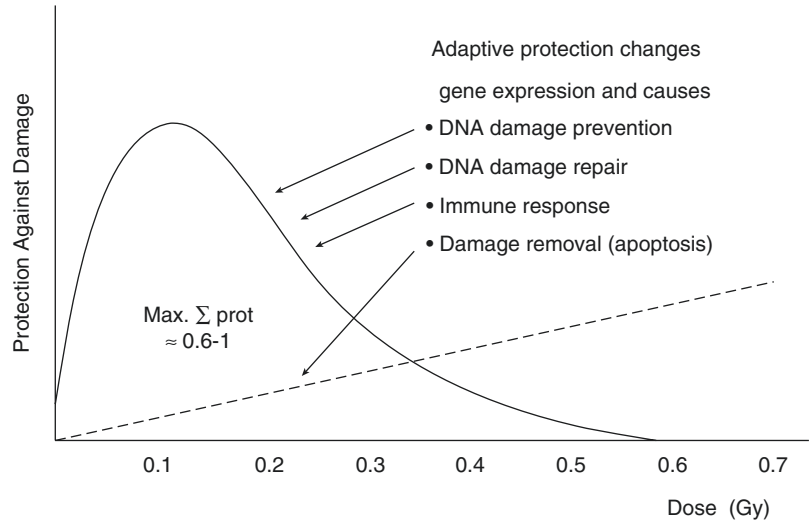

Fig. 2.8 Low-dose (low LET)-induced adaptive protection changes

large numbers of constituent cells and, thus, appear on a timescale which is mainly governed by the underlying proliferation rates of those cells. Early (or acute) effects appear within days, weeks or months of irradiation. They are associated with fast-proliferating, i.e., undifferentiated cells of irradiated tissues or organs. They are acute with transient disruption of the integrity and function of affected tissues or organs. If the doses are relatively low, the stems cells will be able to differentiate shortly after exposure. Damaged tissues and organs will heal with a re-established function at least partially.

Local Exposure Effects

When enough radiation is delivered locally to a particular tissue or organ, as in the case of radiation therapy, which focuses on a specific field, acute effects can appear in the exposed area. Examples include skin erythema and gastrointestinal edema, and ulceration.

Whole-Body Exposure Effects

Following exposure to a large, single, short-term whole-body dose of ionizing radiation, the resulting injury is a rapid whole-body response called the Acute Radiation Syndrome (ARS) and is expressed as a series of clinical symptoms. Radiation exposure at levels exceeding 1 Gy at one time may cause effects on the human body due to cell deaths. Organs susceptible to radiation are more likely to be affected by a small amount of radiation. This series of disorders in organs is called Acute Radiation Syndrome (ARS). The sequence of events can be generally divided into four clinical periods (Fig. 2.9).

1. The prodromal period: symptoms appear within 48 h after the exposure. Exposure to radiation exceeding 1 Gy may cause loss of appetite, nausea and vomiting, and exposure to radiation exceeding 4 Gy may cause headaches. When exposure doses exceed 6 Gy, such symptoms as diarrhea and fever may appear.
2. The incubation period, from 48 h to 2–3 weeks after exposure, when the patient becomes asymptomatic.
3. The manifest or onset phase, from week 6 to week 8 after exposure, when variable symptoms appear based on the radiation dose. Disorders appear in the hematopoietic organ, gastrointestinal tract, and nerves and blood vessels, in this order, as doses increase. Disorders mainly appear in organs and tissues susceptible to radiation. In general, the larger the exposure dose, the shorter the incubation phase.
4. The recovery period: If the patient survives, recovery occurs from 6 weeks to several months after exposure.

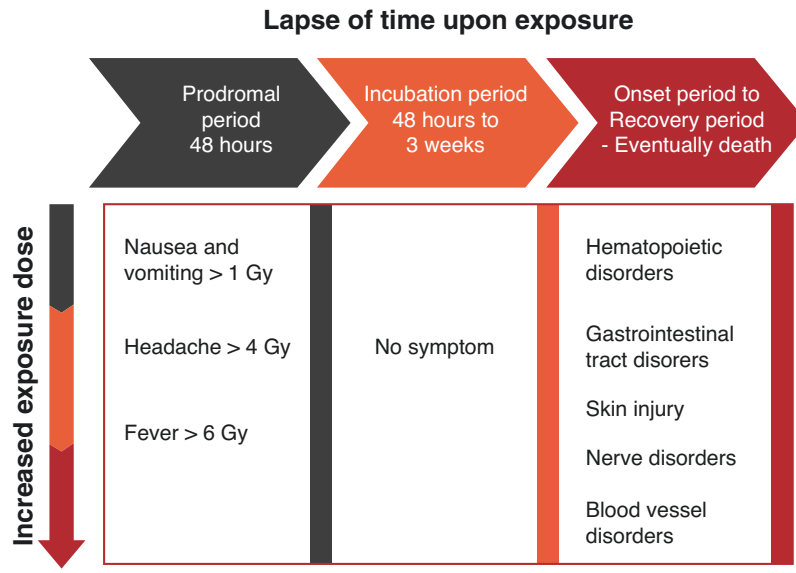

Fig. 2.9 Acute radiation syndrome effects upon exposure to radiation

The presentation of these periods and their duration depend on the amount of radiation exposure. In general, about half of those who receive doses of 2 Gy suffer vomiting within 3 h, and symptoms are rare after doses below 1 Gy. With a sufficiently high radiation dose, acute radiation sickness may result. Additional symptoms related to specific organ injury may occur, based on the dose, and are divided according to the known acute radiation syndromes:

1. Radiation Sickness

   The symptoms can be mild, such as loss of appetite and mild fatigue, or evident only on laboratory tests with mild lymphopenia (subclinical), or maybe severe, appearing as early as 5 min after exposure to very high doses of 10 Gy or more and also include fatigue, sweating, fever, apathy, and low blood pressure. Lower doses delay the onset of symptoms and produce less severe symptoms or a subclinical syndrome that can occur with doses of less than 2 Gy to the whole body, and recovery is complete with 100% survival.
2. Hematopoietic (Bone Marrow) Syndrome

   A blood cells number decrease due to deterioration of hematopoietic capacity may occur at higher doses of more than 1.5–2 Gy to the whole body. With doses up to 4 Gy, a radiation prodrome is seen, followed by a latent period of up to 3 weeks. The clinical effects are not seen for several weeks after the radiation dose when anemia, petechiae, increased blood pressure, fatigue, ulceration in the mouth, epilation, purpura, or infection appear. At doses on the order of 4–8 Gy, a modified bone marrow syndrome occurs. The latest period is shortened, and the manifest illness is aggravated. Death is possible due to bleeding with exposure in this dose range.
3. Gastrointestinal Syndrome

   This syndrome occurs with still higher doses of 6–10 Gy, which can cause manifestations related to the gastrointestinal tract in addition to those of the bone marrow syndrome. Initially, loss of appetite, apathy, nausea, and vomiting occur for 2–8 h. These effects may subside rapidly. Malaise, anorexia, nausea, vomiting, high fever, persistent diarrhea, abdominal distention, and infections appear several days later. During the second week of irradiation, severe dehydration, hemoconcentration, and circulatory collapse may be seen, eventually leading to death.
4. Central Nervous System Syndrome

   The central nervous system is generally resistant to radiation effects. A dose higher than 10 Gy is required to cause substantial

effects on the brain and the nervous system. Symptoms include intractable nausea and vomiting, confusion, convulsions, coma, and absent lymphocytes. The prognosis is poor, with death in a few days.

In most types of radiotherapy, the late effects are considered to be most critical and generally limit the total dose that may be delivered to the tumor. If the radiation tolerance of the late-responding tissues is exceeded, then the subsequent reactions, depending on the tissues in which they arise, may seriously affect mobility and quality of life and may even be life-threatening. Such problems arise long after the completion of treatment and are, thus, impossible to correct. Although they may be unpleasant, acute reactions in radiotherapy are usually transient and easier to control by adjusting the treatment dose delivery pattern and simple medication. In radionuclide therapies, it is possible to circumvent acute radiation toxicities once they begin to occur, such as by accelerating clearance of the radiopharmaceutical.

Delayed Effects

Fetal Disorders

Deterministic effects include fetal effects with a shallow threshold dose. Radiation exposure during pregnancy passes through the womb to the unborn child, who may also be exposed. The embryonic stage is one of the most radiosensitive stages in the life of any organism, and the incidence of effects has time specificity.

The classical triad of effects of radiation on the embryo is growth retardation, embryonic, fetal, or neonatal death, and congenital malformation. The probability of finding one or more of these effects depends upon radiation dose, the dose rate, and the stage of gestation at exposure. The stage of development is critical since the differentiated organ will be most vulnerable; this determines the type of abnormality or malformation observed. The effect of exposure to radiation exceeding 0.1 Gy during the germinal stage or pre-implantation period, first 2 weeks of conception, is an all-or-none effect leading to embryo abortion. Following this period and up to 8 weeks, the possibility of miscarriage decreases, but the embryo is very vulnerable to dysplasia (malformations). Radiation exposure above 0.1 Gy during the embryonic period (or organogenesis period) when the cerebrum is actively growing (early fetal period) poses risks of mental retardation, congenital malformation, as well as organ-specific effects. For example, radioactive iodine administered to a pregnant mother who passed 10–13 weeks of gestation will cross the placenta and accumulate in the already formed fetal thyroid. A summary of the possible effects of irradiation at various stages of gestation is shown in Table 2.7. The development of cancer at an early age is controversial. Risks of stochastic effects such as cancer or hereditary disorders also increase depending on exposure dose levels. Studies have suggested an increased risk of hematopoietic and solid tumors at an early age [40].

Table 2.7 Effects of radiation on the unborn child

Stage of gestation (days)	Possible effects
1–9	Death of embryo is most likely, with little chance of malformation
10–12	Reduced lethal effect with still little chance of malformation
13–56	Production of congenital malformation and retarded growth
57–112	Extreme mental retardation (time of most severe effect on CNS)
113–175	Less frequent effect on CNS
After 175	Very low frequency of CNS effects (no reported case of severe retardation)

However, a comparison between individuals whose parents were exposed to radiation during the atomic bombing of Hiroshima and Nagasaki and those whose parents were not showed any significant differences in a large number of variables, including congenital effects, stillbirths, and cancer at an early age.

Leukemia and Cancer

Cancer is an essential concern of radiation. It has been recognized for more than 90 years that ionizing radiation causes cancers. Highly proliferating

tissues are more prone to radiation tumor induction. Cancer becomes evident only long after the first damage is done, following a period of latency. First leukemia appearance is at least 2–5 years after exposure, while solid tumors appear after at least 10 years, often several decades. The tumors associated with radiation include leukemia, multiple myeloma, and cancers of the breast, colon, thyroid, ovary, lung, urinary bladder, stomach, CNS (other than the brain), and esophagus.

There is no clear evidence that low-level radiation causes cancer. Khamwan et al. [41] studied 6000 patients given a diagnostic dose of I-131. There was no increase in the incidence of thyroid cancer in this population, including a subset of 2000 children [41]. Brix et al. [42] also studied 2000 patients treated with I-131 in doses of up to several hundreds of MBq with 20 years' follow-up. The incidences of thyroid cancer and leukemia were identical to those among patients treated surgically for the same conditions. To complicate the issue further, recently acquired data minimize the effects of low-level radiation in the induction of cancer and even suggest that such levels of radiation exposure may be helpful [43]. DNA mutations unrelated to radiation appear continuously. Each day the intrinsic human metabolism produces on average 240,000 DNA mutations in each body cell [44]. During youth, in general, cancer infrequently occurs thanks to mutations repair. With old age, the capability to repair may decrease, and cancer appears more frequently. A high dose of 2 Gy adds 4000 (20 mutations/cGy) to the daily 240,000 mutations. Ward [21] determined that a low radiation dose of 0.2 Gy stimulates repair by 50–100% and adds only 400 mutations to the intrinsic 240,000 mutations. Our repair mechanism's reduced ability to correct the very high background of intrinsic mutations increases the risk of developing cancer. Genetic impairment of DNA repair capacity results in death from cancer at an early age. Loss of DNA repair capacity with age increases the risk of cancer. Exposure to high doses of radiation similarly reduces the repair capacity of cellular DNA and increases the risk of cancer [45, 46].

Genetic Effects

Genetic effects may include changes in the number and structure of chromosomes and gene mutations, dominant or recessive. They depend on the following factors:

1. The stage of germ cell development

   Immature germ cells appear to be capable of repair, while in mature germ cells, there is little or no repair (Table 2.1).
2. The dose rate

   The repair process starts simultaneously with radiation damage. The damage with a high dose rate is corresponding; lower dose rates produce minor mutations. At a low-intermediate dose rate, time is an essential factor in the outcome of radiation injuries. However, this does not hold in the case of a high radiation rate, where the repair process is minimal due to the direct action of injury.
3. The dose fractionation

   The time interval between fractions is significant for the frequency of mutations. Dose fractionation reduces the number of translocations; however, the incidence of mutations will not be affected by increasing the time interval between fractions.
4. The interval between exposure and conception

   The mutation frequency is shallow if conception occurs after 7 weeks, but it is high when radiation exposure and conception interval is 7 weeks or less.

Other Late-Onset Somatic Disorders

1. Cataract

   Chronic and acute exposure to the eyes can lead to cataracts secondary to inducing lens fiber disorganization. Not all radiation is equally effective in producing cataracts; neutrons are much more efficient than other types of radiation. In man, the cataractogenic threshold is estimated at 2–5 Gy as a single dose or 10 Gy as a fractionated dose. The period between exposure and the appearance of the lens opacities averages 2–3 years, ranging from 10 months to more than 30 years.

2. Hypothyroidism

   The thyroid gland is exposed to radiation during radiation therapy of malignant head and neck tumors or treating hyperthyroidism with I-131. Patients who received doses 10–40 Gy to the thyroid to treat other malignant diseases developed hypothyroidism a few months to years following exposure. A lower moderate dose of (10–20 Gy) can result in hypothyroidism, while 500 Gy or more is required to eradicate the thyroid.

3. Aplastic Anemia

   Human radiation exposure can cause aplastic anemia, depending upon the dose and fractionation. Death may be the result of aplastic anemia. Permanent anemia could result from the reduced capability of cellular proliferation due to the accumulation of residual injury in stem cells. It is essential to realize that when part of the body is irradiated, the bone marrow that survives unimpaired will replace what is damaged. If only 10% of active bone marrow escapes irradiation, mortality can be decreased from 50% to zero, based on animal studies.

Psychological and Psychiatric Effects of Ionizing Radiation Exposure

In addition to noticeable CNS effects discussed earlier, exposure to radiation has other vital side effects that cannot be ignored; the psychological effects. Exposure to ionizing radiation whether due to environmental contamination such as radiation accidents, radiotherapy and diagnostics, occupational roles and space travel is a possible risk-factor for cognitive dysfunction [47]. Which can be early or late effect. This effect is not only due to high level exposure but also low levels [48]. Molecular studies described the various inflammatory and signaling mechanisms involved in cellular damage and repair which consequently drive physiological alterations that may lead to functional alterations [49].

Studies researched these topics decades ago till the present. Perceptions and memories were explored in atomic veterans and patients treated for brain tumors. Findings suggest that side effects involve emotional and cognitive processing of a new perspective that contradicts prior beliefs, trouble with memories and memory loss [50]. Cognitive deficits are related to certain factors that must be considered, including the human life span, as effects might differ with age at exposure and outcome assessment. Family members' health conditions, which may exacerbate distress, is another factor to be considered.

A case study of men who were exposed to non-background ionizing radiation while participating in atmospheric nuclear tests showed that the subjects has developed a virtually identical complex of debilitating psychiatric symptoms resulted from almost entirely focused upon the health effects of the radiation to which the subjects were exposed to. This symptom complex appears to comprise a syndrome [51].

Another recent study recently published, researched the potential psychological issues faced by British nuclear weapons testing program veterans. The study assessed the prevalence of clinically relevant anxiety and aimed to explore experiences of worry and the broader potential psychological impact and effects. The results of this qualitative study showed the following: More than third (33.7%) of the participants met the criteria for clinically relevant anxiety, the interviewers generated from (21.3%) of the participants three interconnected themes giving a rich description of the verbal data in relation to the psychological impact, namely "worry, responsibility, and guilt" and "change across the life course." Frustration and anger toward authorities resulting from perceived negligence and deception were also there. In addition; the participants showed some instances of worry regarding their family members' health [49]. Data suggest that guilt toward family members' health must be considered in potentially exposed individuals and transparency from authorities of medical personnel when dealing with any radiological exposure are of importance to reduce potential distress and anxiety [49].

Needless to say that the psychological and psychiatric effects of ionizing radiation exposure area need more research to develop some clearer interventions to deal with it.

2.7.2.2 Stochastic Radiation Effects

The effects of low-level radiation are considerably in debate. At one end, several theories and reports describe the harmful effects of low-level radiation and how underestimated the risks are. There are theories and reports of harmless and even potentially valuable effects of exposure to such radiation levels at the other extreme.

The theories describing the effects of low-level radiation and the projected risk estimates of cancer development or genetic effects in humans are purely mathematical and not actual observations. The data from populations exposed to high-level radiation were extrapolated to determine the likelihood of these events at low-level radiation exposure. Such events occur at meager rates in any given population and further complicate the issue after long latency periods. Therefore, reliable epidemiological data are challenging to obtain.

2.8 Exposure from Medical Procedures

For medical radiation, the chest X-ray delivers 0.1 mSv to the chest wall (Table 2.8). The average nuclear medicine procedure delivers 3 mSv to the whole body. The absorbed dose from the C-14 urea breath test is equivalent to that received during a 1 h flight. These values compared with those of natural sources of radiation, particularly cosmic rays, which deliver an average of 3.6 mSv per year in the United States and are higher in certain areas, the actual magnitude of the low level of radiation can be appreciated.

These levels of exposure from diagnostic medical procedures have no detectable biological effects. Less than 0.006% of those undergoing nuclear medicine procedures in the United States might be affected annually. PET studies deliver higher doses to the patient to compensate for the short half-life of positron-emitting radioisotopes. Because these radioisotopes are of high energy and prepared in high initial dosing to account for the rapid decay, PET technologist, radio pharmacists, and workers at cyclotrons are usually exposed to higher doses than other workers in the nuclear medicine field.

Therapeutic applications of radioisotopes involve not only malignant but also benign conditions, such as hyperthyroidism and arthroplasty, and are widely expanding. In the treatment of thyroid cancer, large doses of I-131 may cause depression of the bone marrow. It is essential to mention that the level of exposure from medical exposure has globally increased according to recent surveys [52]. The global exposure per capita has increased from 0.4 mSv in 2000 to 0.62 mSv in 2008 (Table 2.9).

Although globally the exposure of medical exposure is still around 20% of the total exposure per caput since the exposure from natural sources contributes to slightly less than 80%, the exposure from medical exposure in certain groups of countries with high physician-to-population ratios has dramatically increased to be almost equal to the dose from natural exposure as illustrated in the United States. This increase has been attributed mainly to the increase in the utilization of CT scans.

Positive health effects are observed from low-dose radiation exposure, i.e., decreased mortality and decreased cancer rates, in human populations exposed to low-level radiation and reported in extensive studies [43]. Several studies compared areas of high background to those with low radiation.

Lower cancer incidence or mortality rates in the former were the findings in many such studies in China [44], India [45], Iran [46], and the United States [53]. However, this epidemiological study does not compare an individual's radiation exposure to cancer rate; therefore, a strong conclusion cannot be solely based on such studies. On the other hand, none of these studies had shown a higher cancer incidence in high background radiation zones. An epidemiological study [43] comparing cancer mortality in Canada's nuclear industry workers to non-radiation workers has found similar favorable effects for low radiation exposure. The former group of workers had cancer mortality of 58% of the national average compared to 97 % of that in

Table 2.8 Radiation dose from common natural and medical sources

Diagnostic X-ray procedures	Effective dose per scan Based dose based on ICRP 103 (mSv)
X-ray CT of the head and neck	1.2
X-ray CT of the chest	6.2
Panoramic dental radiography	0.026
Intravenous urography (IVU)	3
Barium enema (lower GI X-ray)	6
Chest X-ray	0.1
Mammography	0.36

Diagnostic nuclear medicine (+A10:C20 procedures)	Effective dose per scan Based dose based on ICRP 103 (mSv)
Tc-99m-MAA lung perfusion study	0.017 (mSv/MBq)
Tc-99m-DTPA lung ventilation study (ventilation can be evaluated with the ^{99m}Tc-labeled aerosols, DTPA and Technegas)	0.015 (mSv/MBq)
Tc-99m-MDP bone scan (20 mCi)	4
Effective doses from CT component of PET/CT (diagnostic)	2.60–21.45
Effective doses from FDG-PET/CT (total)	8–26.85
Effective doses from FDG-PET (5–15 mCi)	3.515–10.545
CT component of PET/CT (attenuation only)	0.5–1.0
One-day Tl-201 stress (3.5 mCi)/redistribution protocol	15.3
Tl-201 stress (3.0 mCi) / redistribution with optional additional imaging protocols (re-injection of Tl-201 (1.5 mCi) after redistribution imaging)	19.7

Exposure from "Natural Radiation"	Effective dose per scan Based dose based on ICRP 103 (mSv)
2-h flight at altitude of approximately 6100 m	0.004
World Health Organization recommended reference level per year for intake of radionuclides in water (IAEA 2001)	0.1
Ingestion (food and drinking-water)	0.3
Terrestrial sources	0.5
Inhalation of natural gas at home (mainly radon)	1.2
Cosmic radiation (at sea level)	0.4
Total background radiation level	2.4

Table 2.9 Changes in exposure from medical sources

Year	Annual per caput dose (mSv)
1988	0.35
1993	0.30
2000	0.40
2008	0.62

UNSCEAR 2008 Report [52]

the latter. Cohen [43] studied the relationship between lung cancer death rates and residential radon gas in the United States. He found that lung cancer decreased for increments in radon levels. These findings were consistent even after reanalysis and correcting for confounding factors such as smoking. To date, there is considerable debate regarding this study.

2.9 Summary

Several biological effects can result from ionizing radiation. These can be due to direct or indirect mechanisms, and they can be acute or delayed. Acute effects occur with exposure to

high-level radiation. Delayed effects may appear after a long time and include cancer, genetic effects, effects on the unborn child, and others such as cataracts and hypothyroidism. Based on our current knowledge, no level of radiation exposure is considered safe, and no level is uniformly dangerous. Radiation doses have to reach a certain level to produce acute injury but not cause cancer or genetic damage. Absorbed doses from nuclear medicine procedures are very low, and no biological effects in individuals due to ionizing radiation were seen. Fears of radiation must not be permitted to undermine the great value of radiation in clinical practice. However, safe handling of all levels of radiation is vital to prevent or minimize possible biological effects.

References

1. Raven PH, Johnson GB (1992) Biology, 3rd edn. Mosby-Year Book, St. Louis
2. Alberts B (2003) DNA replication and recombination. Nature 421(6921):431–435
3. Friedberg EC (2001) How nucleotide excision repair protects against cancer. Nat Rev Cancer 1:22–33
4. Khanna KK, Jackson SP (2001) DNA double-strand breaks: signaling, repair and the cancer connection. Nat Genet 27(3):247–254
5. Sancar A, Lindsey-Boltz L, Unsal-Kaçmaz K, Linn S (2004) Molecular mechanisms of mammalian DNA repair and the DNA damage checkpoints. Annu Rev Biochem 73:39–85
6. Lieberman HB (2008) DNA damage repair and response proteins as targets for cancer therapy. Curr Med Chem 15(4):360–367
7. Vilenchik MM, Knudson AG (2003) Endogenous DNA double-strand breaks: production, fidelity of repair, and induction of cancer. Proc Natl Acad Sci 100(22):12871–12876
8. Thompson LH, Schild D (2001) Homologous recombinational repair of DNA ensures mammalian chromosome stability. Mutat Res 477(1–2):131–153
9. Jackson SP (2002) Sensing and repairing DNA double-strand breaks. Carcinogenesis 23(5):687–696
10. Powell SN, Kachnic LA (2003) Roles of BRCA1 and BRCA2 in homologous recombination, DNA replication fidelity and the cellular response to ionizing radiation. Oncogene 22(37):5784–5791
11. Rothkamm K, Krüger I, Thompson LH, Löbrich M (2003) Pathways of DNA double-strand break repair during the mammalian cell cycle. Mol Cell Biol 23(16):5706–5715
12. Shibai A, Takahashi Y, Ishizawa Y, Motooka D, Nakamura S et al (2017) Mutation accumulation under UV radiation in Escherichia coli. Sci Rep 7(1):14531
13. Harper JW, Elledge SJ (2007) The DNA damage response: ten years after. Mol Cell 28(5):739–745
14. Galluzzi L, Vitale I, Abrams JM, Alnemri ES, Baehrecke EH et al (2012) Molecular definitions of cell death subroutines: recommendations of the nomenclature committee on cell death 2012. Cell Death Differ 19(1):107–120
15. Neves AA, Brindle KM (2014) Imaging cell death. J Nucl Med 55(1):1–4
16. Steel GG (1996) From targets to genes: a brief history of radiosensitivity. Phys Med Biol 41(2):205–222
17. Morgan WF (2008) 44th Annual meeting of the National Committee on radiation protection and measurements. NCRP, Bethesda, MD
18. Pierce AJ, Stark JM, Araujo FD, Moynahan ME, Berwick M et al (2001) Double-strand breaks and tumorigenesis. Trends Cell Biol 11(11):S52–S59
19. Willers H, Dahm-Daphi J, Powell SN (2004) Repair of radiation damage to DNA. Br J Cancer 90(7):1297–1301
20. Da Costa PE (1990) Robbins' pathologic basis of disease. R. S. Cotran, V. Kumar and S. L. Robbins. W. B. Saunders, Philadelphia, 1989. J Pathol 160(1):89–89
21. Ward JF (1988) DNA damage produced by ionizing radiation in mammalian cells: identities, mechanisms of formation, and reparability. In: Cohn WE, Moldave K (eds) Progress in nucleic acid research and molecular biology. Academic Press, San Diego, CA, pp 95–125
22. Bolus NE (2001) Basic review of radiation biology and terminology. J Nucl Med Technol 29(2):67–73. test 76-7
23. Murphy JB, Liu JH, Sturm E (1922) Studies on x-ray effects: ix. The action of serum from x-rayed animals on lymphoid cells in vitro. J Exp Med 35(3):373–384
24. Baskar R (2010) Emerging role of radiation induced bystander effects: cell communications and carcinogenesis. Genome Integr 1(1):13
25. Prise KM, O'Sullivan JM (2009) Radiation-induced bystander signalling in cancer therapy. Nat Rev Cancer 9(5):351–360
26. Azzam EI, de Toledo SM, Little JB (2001) Direct evidence for the participation of gap junction-mediated intercellular communication in the transmission of damage signals from alpha-particle irradiated to non-irradiated cells. Proc Natl Acad Sci U S A 98:473–478
27. Ramesh R, Marrogi AJ, Munshi A, Abboud CN, Freeman SM (1996) In vivo analysis of the 'bystander effect': a cytokine cascade. Exp Hematol 24(7):829–838
28. Iyer R, Lehnert BE, Svensson R (2000) Factors underlying the cell growth-related bystander responses to α particles. Cancer Res 60:1290–1298
29. Hall EJ, Hei TK (2003) Genomic instability and bystander effects induced by high-LET radiation. Oncogene 22(45):7034–7042
30. Morgan WF (2003) Non-targeted and delayed effects of exposure to ionizing radiation: II. Radiation-

induced genomic instability and bystander effects in vivo, clastogenic factors and transgenerational effects. Radiat Res 159(5):581–596
31. Suzuki K, Ojima M, Kodama S, Watanabe M (2003) Radiation-induced DNA damage and delayed induced genomic instability. Oncogene 22:6988–6993
32. Huber MA, Terezhalmy GT (2003) The head and neck radiation oncology patient. Quintessence Int 34:693–717
33. Kendall GM (2000) Second-event theory reviewed. J Radiol Prot 20:79–80
34. Bergonié J, Tribondeau L (2003) Interpretation of some results from radiotherapy and an attempt to determine a rational treatment technique. 1906. Yale J Biol Med 76:181–182
35. Dale RG, Wondergem J (2014) Nuclear medicine physics: a handbook for teachers and students. IAEA, Vienna. (ISBN 92-0-107304-6)
36. Ernst M, Freed ME, Zametkin AJ (1998) Health hazards of radiation exposure in the context of brain imaging research: special consideration for children. J Nucl Med 39(4):689–698
37. Johansson L (2003) Hormesis: an update of the present position. Eur J Nucl Med Mol Imaging 30(6):921–933
38. Vaiserman A, Koliada A, Zabuga O, Socol Y (2018) Health impacts of low-dose ionizing radiation: current scientific debates and regulatory issues. Dose Response 16(3):1559325818796331
39. Feinendegen LE (2005) Evidence for beneficial low level radiation effects and radiation hormesis. Br J Radiol 78(925):3–7
40. Kneale GW, Stewart AM (1976) Mantel-Haenszel analysis of Oxford data. II. Independent effects of fetal irradiation subfactors. J Natl Cancer Inst 57(5):1009–1014
41. Khamwan K, Krisanachinda A, Pasawang P (2010) The determination of patient dose from (18)F-FDG PET/CT examination. Radiat Prot Dosimetry 141(1):50–55
42. Brix G, Lechel U, Glatting G, Ziegler SL, Münzing W et al (2005) Radiation exposure of patients undergoing whole-body dual-modality 18F-FDG PET/CT examinations. J Nucl Med 46(4):608–613
43. Cohen BL (1995) Test of the linear-no threshold theory of radiation carcinogenesis for inhaled radon decay products. Health Phys 68(2):157–174
44. High Background Radiation Research Group, China (1980) Health survey in high background radiation areas in China. Science 209(4459):877–880
45. Nambi KS, Soman SD (1980) Environmental radiation and cancer in India. Health Phys 52(5):653–657
46. Ghiassi-nejad M, Mortazavi SMJ, Cameron JR, Niroomand-rad A, Karam PA (2002) Very high background radiation areas of Ramsar, Iran: preliminary biological studies. Health Phys 82(1):87–93
47. Narasimhamurthy RK, Mumbrekar KD, Rao BSS (2022) Effects of low dose ionizing radiation on the brain—a functional, cellular, and molecular perspective. Toxicology 465:153030
48. Pasqual E, Boussin F, Bazyka D, Nordenskjold A, Yamada M et al (2021) Cognitive effects of low dose of ionizing radiation—lessons learned and research gaps from epidemiological and biological studies. Environ Int 147:106295
49. Collett G, Young WR, Martin W, Anderson RM (2021) Exposure worry: the psychological impact of perceived ionizing radiation exposure in British nuclear test veterans. Int J Environ Res Public Health 18:12188
50. Garcia B (1994) Social-psychological dilemmas and coping of atomic veterans. Am J Orthopsychiatry 64:651–655
51. Vyner HM (1983) The psychological effects of ionizing radiation. Cult Med Psychiatry 7:241–261
52. UNSCEAR (2010) 2008 Report. Sources and effects of ionizing radiation. United Nations Scientific Committee on the Effects of Atomic Radiation, New York
53. Jagger J (1998) Natural background radiation and cancer death in Rocky Mountain states and Gulf Coast states. Health Phys 75(4):428–430

3 Basis of Radiopharmaceutical Localization

Shorouk Dannoon

3.1 Radiopharmaceuticals Overview

Nuclear medicine is noninvasive imaging at the cellular and molecular levels based on pathological processes. Radiopharmaceuticals (radiotracers) are given to the patient for imaging purposes. Radiopharmaceuticals are chemical compounds or biological moieties that contain radioactive element within their structures for either diagnosis or treatment. They are considered radioactive drugs. Trace amounts is administered to the patient, and the mass is extremely small. This amount is not enough to produce a pharmacologic effect and chemical toxicity is not as great of a concern as with standard pharmaceuticals.

All radionuclides used in radiopharmaceutical preparations are artificially produced. In general, the production involves a stable nuclide (target) that is bombarded with high-energy particles (neutrons or positively charged particles) to yield the radioactive nuclide of interest. The nuclear medicine radionuclides are usually obtained from a reactor, cyclotron, or generator [1]. The nuclear reactor utilizes the fast neutrons emitted from fission reaction of enriched Uranium-235 (^{235}U) [1, 2]. Enriched ^{235}U in uranium fuel rods are placed into a tank of heavy water (D_2O), which is used as a moderator for controlling fission released neutron energy. The fast neutrons are slowed down to thermal energy by their interaction with D_2O. The thermal neutrons are easily captured by other Uranium atoms to initiate additional fission reactions and this chain reaction maintains the flux of neutrons. The rate of nuclear fission is controlled by the position of control rods. The control rods are made of Cadmium or Boron that have a high cross-section for absorbing neutrons. The production of neutron activated radionuclide is achieved by introducing the target material (stable nuclides) through ports into the neutron flux in the D_2O tank. To insure the safety of the surroundings, the whole reactor is shielded with concrete [1, 2].

As for cyclotrons, they are a type of particle accelerator invented by Ernest O. Lawrence in 1932 in which charged particles accelerate outward from the center along a spiral path. The particles (protons) are held in a spiral path by a static magnetic field and accelerated by a rapidly varying electric field. Stable, nonradioactive isotopes are placed inside the cyclotron, then the accelerated charged particles (protons) bombard the stable isotopes creating radioactive isotopes for nuclear medicine and other purposes [1, 3].

On the other hand, generators are more convenient method of obtaining medical radionuclides with short half-lives [1, 4]. They consist of a longer lived parent radionuclide that is loaded onto a column that decays to the daughter radionuclide.

S. Dannoon (✉)
Department of Nuclear Medicine, Faculty of Medicine, Kuwait University, Kuwait City, Kuwait
e-mail: shorouk.dannoon@ku.edu.kw

A. H. Elgazzar (ed.), *The Pathophysiologic Basis of Nuclear Medicine*,
https://doi.org/10.1007/978-3-030-96252-4_3

The parent and daughter radionuclides are chemically different that the daughter is removed from the column by elution with a solvent while the parent stays absorbed to the column. Upon elution of the daughter radionuclide, the parent radionuclide decays to build up more daughter radionuclide until the parent activity is depleted [1, 4]. The column is shielded in lead. To date are useful medical radionuclide generators which are: ^{99}Mo/^{99m}Tc, ^{68}Ge/^{68}Ga, ^{82}Sr/^{82}Rb,^{90}Sr/^{90}Y and ^{188}W/^{188}Re.

Radionuclide can be introduced into a drug in different approaches. Isotopic labeling involves the substitution of a stable nuclide with its radioactive isotope creating a radioactive analogue [5]. The radioactive analogue has similar chemical and biological properties to the stable parent compound. Therefore, the radioactive analogue will be a physiological tracer. However, the nonisotopic labeling approach involves incorporating a radioactive nuclide that was not previously present in the parent compound [5]. The majority of the radiopharmaceutical in clinical practice today are the nonisotopic labeled compounds. The nonisotopic labeled radiopharmaceuticals split into two different categories: essential and tagged radionuclide. The essential is also referred to as integrated radionuclide. In this labeling method, the radionuclide is an important component in the overall structure of the drug, without it the drug will not have the same biodistribution. The chelation of the radionuclide to the ligand results in the desired complex. The majority of the earlier radiopharmaceuticals were the integrated ones. More recently, the work has been toward production of target-specific radiopharmaceuticals to minimize the unnecessary radiation exposure to the body during imaging or radiotherapy. The most convenient approach is to incorporate radiometals to receptor-specific molecules such peptides, antibodies, and antigens. The radionuclide is attached to the biological molecule via a bifunctional chelate (BFC), which can hold the radiometal tightly and at the same time form a stable conjugation with the active groups of the biological molecule. In this method, the radionuclide is being tagged along till the biological molecule reaches its target.

Radiopharmaceuticals have been used in diagnostic and radiotherapeutic agents. There are two types of diagnostic radiopharmaceutical. Single photon emission computed tomography (SPECT) radiopharmaceuticals that contain gamma emitting radioisotopes. Positron emission tomography (PET) radiopharmaceuticals that contain positron emitting radioisotope. While therapeutic radiopharmaceuticals contain auger electrons, β^- or α particles that are known to be highly ionizing as they are non-penetrating radiation, so they deliver cytotoxic doses to diseased sites, resulting in the death of the cells.

3.2 Mechanisms of Radiopharmaceuticals Localization

The uptake and retention of radiopharmaceuticals by different tissues and organs involve many different mechanisms, as summarized in Table 3.1. The pharmacokinetics, biodistribution, and metabolism of the radiopharmaceutical are very important to understanding the mechanisms of radiopharmaceutical localization in the organ or tissue of interest. Injury to a cell or tissue significantly alters the morphology and molecular biology compared with that of normal tissue or organs.

3.2.1 Compartmentalized Localization

Compartmentalized localization is when molecules of interest are spread in an enclosed volume or space.

- Uniform distribution within a compartment.

  The model example of uniform dispersion within a compartment is the blood pool. The quantitative determination of blood volume can be done using the tracer dilution method. Radioiodinated human serum albumin with I-125 (I-125 HSA) is used to determine plasma volume because it is a radiopharmaceutical that diffuses in the

Table 3.1 Mechanisms of radiopharmaceuticals' localization

Localization mechanism	Radiopharmaceuticals
Compartmentalized localization	^{125}I-HAS, ^{125}Cr-RBC, ^{99m}Tc-RBC, Xe-133, ^{111}In-DTPA, ^{99m}Tc-DTPA, ^{99m}Tc-Sulfur-colloid
Passive diffusion	^{99m}Tc-DTPA (brain), ^{99m}Tc-HMPAO, ^{99m}Tc-ECD, ^{99m}Tc-sestamibi, ^{99m}Tc-tetrofosmin, [^{13}N]NH_3,^{67}Ga-citrate, [^{18}F]FDOPA, [^{18}F]FMISO
Facilitated diffusion	[^{18}F]FDG, ^{99m} Tc-disofenin and mebrofenin, ^{99m}Tc (V) DMSA (MTC)
Active transport	$^{123}I^-$ and $^{131}I^-$, $^{99m}TcO_4^-$(Thyroid), $^{201}Tl^+$, $^{82}Rb^+$, ^{123}I-MIBG, ^{99m}Tc (III) DMSA (Renal), [^{18}F]FACBC, [^{18}F]FLT, [^{18}F]FET, [^{18}F]Choline and [^{11}C]Choline
Filtration	^{99m}Tc-DTPA (renal), ^{99m}Tc-MAG_3, ^{125}I-iothalamate, and ^{51}Cr-EDTA
Secretion	$^{99m}TcO_4^-$(stomach), ^{99m}Tc-MAG_3
Phagocytosis	^{99m}Tc-sulfur colloid
Cell sequestration	Denatured ^{99m}Tc-RBC
Capillary blockade	^{99m}Tc-MAA
Ion exchange	$^{89}Sr^{2+}$, $^{18}F^-$
Chemisorption	^{99m}Tc-MDP, ^{99m}Tc-HDP, ^{153}Sm-EDTMP
Cellular migration	^{111}In-oxine-WBC, ^{99m}Tc-HMPAO-WBC
Receptor binding	^{68}Ga-DOTA-PSMA, ^{18}F-PSMA, ^{131}I-tositumomab and ^{111}In/^{90}Y-ibritumomab tiuxetan, ^{111}In-octreoscan, ^{68}Ga-DOTA-octreotide, ^{64}Cu-DOTA-tyr^3-octreotate, [^{18}F] Florbetapir, [^{18}F]Florbetapir, [^{18}F]flutemetamol, [^{18}F]FES, [^{123}I]ioflupane (DaTscan)

plasma [6, 7]. Red blood cells (RBC) radiolabeled with Cr-51 is a radiopharmaceutical that diffuses within the cellular content of blood, so it is used to determine red cell volume/mass [7, 8]. Tc-99m labeled RBCs are dispersed in the blood and used in gated blood pool imaging of left ventricular wall motion and determination of left ventricular ejection fraction [9].

- Nonuniformities within a compartment.

  In certain incidents, radiopharmaceuticals may have nonuniform distribution within the compartment due to pathological condition. For example, a localized area of increased ^{99m}Tc-RBCs activity can be caused by increased blood volume in a hemangioma [10, 11].

  In other situations, areas of decreased radiopharmaceutical concentration are usually the result of an obstruction in a compartmental space. In a complete obstruction in the lung airways demonstrated by Xe-133 ventilation, then there will be absence of Xe-133 in the area beyond the site of airway obstruction [12, 13]. If partial obstruction (common in COPD), then there will be absence of Xe-133 in the affected area upon initial inhalation and breath-hold, but Xe-133 gas will pass through the site(s) of partial obstruction over time during equilibrium rebreathing [14].

  As for In-111-pentetate (DTPA), it can diffuse freely in the extracellular fluid and can accumulate in lesions with defects in Blood Brain Barrier (BBB). Obstructions can also occur in the CSF space. Both ^{99m}Tc-DTPA andIn-111-DTPAcan be used for the assessment of BBB disruption as it localizes in areas within the cranium that had been disrupted by infection, neoplasms, trauma, or stroke [15, 16]. ^{99m}Tc-DTPA is a nondiffusible tracer for evaluation of BBB permeability, similar to ^{99m}Tc-pertechnetate and ^{99m}Tc glucoheptonate. ^{99m}Tc-DTPA brain scintigraphy has been used in the past to detect brain infarcts as well as brain metastases [15, 16].

  An obstruction in the cystic duct of the biliary tract will be visualized due to decrease of radiopharmaceutical in the gallbladder, and if the common bile duct is obstructed, there will be decrease of radiopharmaceutical in the small intestine. Tc-99m hepatobiliary radiopharmaceuticals, disofenin (DISIDA), and mebrofenin (BRIDA), are excreted from the liver into the bile and flow through the biliary tract with normal flow into the gallbladder and into the intestine [17].

- Leakage from the compartment.

  In some pathological conditions there could be an abnormal leakage from the compartment, and radiopharmaceuticals can detect and identify the location of this leakage. For example, gastrointestinal hemorrhage (GI bleeding), blood leaks from the vasculature and accumulates in the GI tract and Tc-99m RBCs can be used to detect the site of the GI bleeding [18, 19].
- Movement/flow within a compartment.

  In some pathological conditions, there may be a change in the direction, rate and extent of flow within a compartment. Tc-99m sulfur colloid is the preferred radiopharmaceutical for determining the rate of emptying of gastric contents into the intestine because it is not absorbed by the GI tract. Tc-99m sulfur colloid bound in scrambled eggs can be used to evaluate gastric empting of food solids while Tc-99m sulfur colloid mixed in water or other liquid such as juice that can be used to evaluate gastric emptying of liquids [20, 21]. Individual patient gastric emptying is compared to normal values.

3.2.2 Passive Diffusion

Passive diffusion is the movement of molecules from high to low concentration to achieve even concentration (chemical equilibrium). In biological systems, passive diffusion usually involves the ability of molecules to cross the phospholipid membrane so these molecules should be highly lipid soluble and be in a neutral state not charged under physiological pH conditions. Also, their molecular size should be small enough to pass through the small pores of the membrane. The molecule movement across the membrane is simply a molecular motion and does not require additional energy, transporters, carriers, or receptors. The passive diffusion is nonselective, noncompetitive, and not subjected to saturation.

A classic example of passive diffusion in nuclear medicine is ^{99m}Tc-DTPA brain imaging. ^{99m}Tc-DTPA cannot normally penetrate the blood–brain barrier (BBB) that is made of endothelial cells of the cerebral vessels form a continuous layer without gap junctions preventing the diffusion of hydrophilic (water-soluble) molecules. So normally, ^{99m}Tc-DTPA remains in the blood pool until cleared by the kidneys. In conditions that result in disruption of the BBB, such as tumor, stroke, and infection, the ^{99m}Tc-DTPA can diffuse across the disrupted BBB and accumulate in that affected area of the brain [15, 16].

Intact BBB allows the transport of small molecules across the plasma membrane of the neuron by facilitated diffusion. However, diffusion is not a unidirectional process, and there is a need for accumulation and retention of radiopharmaceuticals at the site of interest in order to take a meaningful image. The localization of the cerebral perfusion radiopharmaceuticals ^{99m}Tc-exametazime (HMPAO) and ^{99m}Tc-bicisate (ECD) which are lipophilic radiotracers, involve the delivery via cerebral arterial blood flow, diffusion into the brain and retention in the brain due to conversion to a more stable hydrophilic molecule and enzymatic metabolism, respectively [22, 23] (Fig. 3.1).

^{99m}Tc-myocardial perfusion agents involve the delivery by blood flow through the coronary arteries, diffusion into myocardial cells and retention in those cells [24, 25]. Both ^{99m}Tc-sestamibi and ^{99m}Tc-tetrofosmin cross the cell membranes by lipophilic diffusion and then are retained by electrostatic binding to negative electrical charges on the mitochondrial membranes in normal cells when Ca^{2+} are significantly low [26]. In cases of irreversible ischemia when extracellular levels of Ca^{2+} enters the cell and binds to the mitochondria, Tc-myocardial perfusion agents are blocked from binding to the mitochondria.

$[^{13}N]NH_3$, as a nonionic form, is freely permeable to all cell membranes. It diffuses across the myocardial cell capillary membrane, then is converted to N-13 glutamine by glutamine synthetase, and subsequently is trapped within tissues by incorporation in the cellular pool of amino acids [27, 28]. Myocardial uptake is proportional to coronary blood flow. The linear relationship between distribution of $[^{13}N]NH_3$ and the regional blood perfusion allows for the imaging and measurement of cerebral and myocardial blood flows [27, 28].

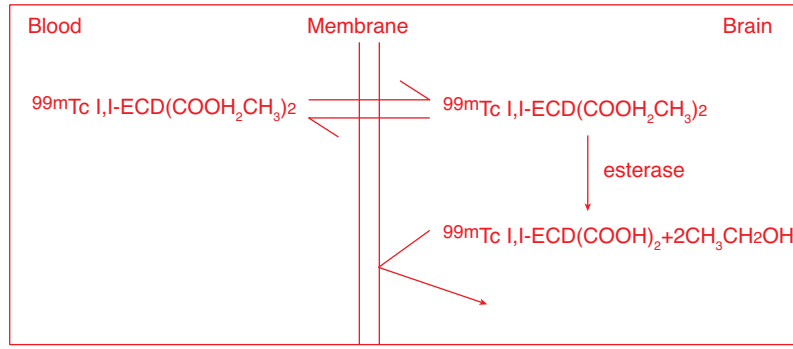

Fig. 3.1 ^{99m}Tc-ECD is a neutral, lipophilic complex that can cross the BBB via passive diffusion. It is retained in the brain after undergoing enzymatic hydrolysis of one of the ester functions to become an ionized metabolite by esterase enzyme

^{67}Ga-citrate is known to localize in tumors and inflammatory lesions. It is speculated based on in vivo studies, that free and unbound ^{67}Ga-citrate diffuse into the cells and once within the cells, ^{67}Ga binds to iron-binding proteins such as lactoferrin and ferritin preventing back-diffusion of free ^{67}Ga [29, 30].

[^{18}F]Fluorodopa ([^{18}F]FDOPA) is neutral and capable of crossing the BBB. Up on crossing the BBB, [^{18}F]FDOPA is decarboxylated by cellular aromatic amino acid decarboxylase (AAAD) to form fluorodopamine (FDA) which remains within the neuron. [^{18}F]FDOPA selectively localize within the basal ganglia of the brain in the area that controls movement. [^{18}F]FDOPA targets the presynaptic dopaminergic function in the brain. In degenerative diseases such as Parkinson's disease, there is loss of dopaminergic neurons, so there will be less accumulation of [^{18}F]FDOPA in the basal ganglia than a healthy, age-matched control. [^{18}F]FDOPA has other applications, it can accumulate in vivo within tumors and in evaluation of pheochromocytoma and thyroid carcinoma due to the increase utilization of amino acid by the cancerous lesions [31–33].

^{18}F-Fluoromisonidazole ([^{18}F]FMISO) diffuses freely into all cells. However, it accumulates in viable hypoxic cells, diffuses out of normoxic cells and is not retained in necrotic cells. Upon entering a viable cell, ^{18}F-MISO is in an environment where electron transport is taking place, the NO_2 substituent (which has a high electron affinity) takes on an electron to form the radical anion reduction product. If O_2 is also present, that electron is rapidly transferred to oxygen and ^{18}F-MISO changes back to its original structure and can leave the cell [34, 35]. However, in the absence of O_2 in hypoxic cell, a second electron reacts with the nitroimidazole (radical anion reduction product) to form a 2-electron reduction product then the reduced [^{18}F]FMISO reacts nondiscriminately with peptides and RNA within the cell and gets trapped. Therefore, the retention of [^{18}F]FMISO is inversely related to the intracellular partial pressure of O_2 [34, 35].

3.2.3 Facilitated Diffusion

Facilitated diffusion requires a carrier to transport a molecule across the membrane. Carriers are selective and only specific molecules fit into them. Therefore, there is competition with similar molecules that fit into this carrier and due to limited number of carriers, it is possible to reach saturation. However, facilitated diffusion utilizes carriers that are passive, so it does not require external energy but needs a concentration gradient to operate. This mechanism allows the transport of molecules in either direction through the membrane based on the concentration of gradient. The most commonly used PET radiotracer, F-18 flurodeoxyglucose ([^{18}F]FDG), is transferred into the cell through facilitated diffusion mechanism. [^{18}F]FDG, is a radiolabeled analogue of D-glucose (Fig. 3.2), so it enters the cell via transmembrane protein transporters [GLUT] similar to glucose. Cellular uptake of [^{18}F]FDG reflects the glucose metabolism so glucose and [^{18}F]FDG are competing for the same GLUT transporters, and elevated

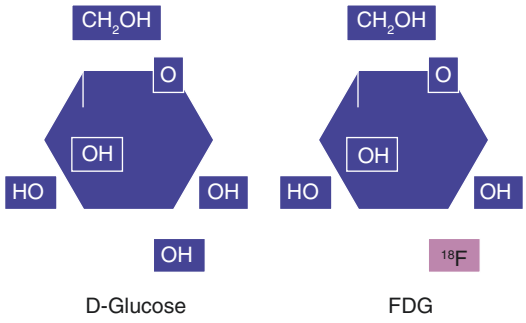

Fig. 3.2 [^{18}F]FDG is an analogue of D-glucose. The hydroxyl group at the second position in D-glucose is replaced by F-18 in [^{18}F]FDG

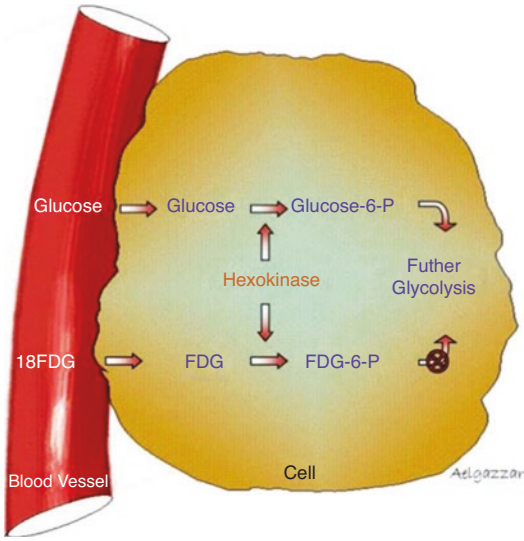

Fig. 3.3 Both of glucose and [^{18}F]FDG are transported into the cell via Glut transporters. Upon entering the cell, both undergo phosphorylation at the 6 position by hexokinase. Phosphorylated-glucose will undergo additional enzymatic steps, however, phosphorylated-[^{18}F]FDG at the 6 position does not and becomes trapped inside the cell.

blood levels of glucose will decrease cellular uptake of [^{18}F]FDG. Once inside the cell, both glucose and [^{18}F]FDG are phosphorylated by hexokinase resulting in Glucose-6-phosphate and [^{18}F]FDG-6-phosphate, respectively (Fig. 3.3). Glucose-6-phosphate enters the glycolytic pathway but [^{18}F]FDG-6-phosphate is blocked and is retained in the cell as it does not fit in the GLUT to diffuse out, and this is referred to as metabolic trapping. [^{18}F]FDG-6-phosphate may be converted back to [^{18}F]FDG, however the enzyme responsible for such a conversion is present in very low concentration or not present all in cancer tissue allowing for better images of oncological patients. [^{18}F]FDG accumulated in granulomatous tissue and macrophages so it has been used to image infection and inflammation as well [36–39].

On the other hand, the hepatocytes in the liver extract substances from the blood and secrete them into the bile. ^{99m}Tc labeled tracers like disofenin and mebrofenin diffuse through pores in the endothelial lining of the sinusoids, bind to the anionic membrane-bound carriers on the hepatocyte and secreted into the bile similar to bilirubin [40].

At alkaline pH (pH 8–9), ^{99m}Tc forms a pentavalent complex with DMSA (^{99m}Tc (V) DMSA). This complex mimics phosphate ion and is rapidly excreted in the urine. It localizes in a number of tumors such as medullary thyroid carcinoma (MTC), bone metastases and other bone lesions. Its uptake is dependent on extracellular Na^+ concentration, indicating the importance of sodium-dependent transporter in ^{99m}Tc (V) DMSA uptake [15].

3.2.4 Active Transport

Active transport utilizes carriers to transport molecules across membranes but unlike facilitated diffusion it requires energy such as ATP. By using energy to transport molecules across the membrane, molecules can be transported against a concentration gradient. Since a carrier is used, it is selective and only specific molecules that fit the carrier will be transported across the membrane. Therefore, there is competition with similar molecules that fit into this carrier and due to limited number of carriers, it is possible to reach saturation.

One of the first active transport radiotracers in Nuclear Medicine is the concentration of iodide in the thyroid gland. Radioisotopes of iodine such as $^{123}I^-$ and $^{131}I^-$ are useful radiopharmaceuticals to evaluate thyroid function. Iodide ions are transported into thyroid cells via the Na^+/I^- symporter. In the thyroid, iodide is oxidized to iodine and

becomes bound to tyrosine which is transformed to the thyroid hormones [41–44]. In addition, Tc-99m-pertechnetate ($^{99m}TcO_4^-$) accumulates in the thyroid similar to iodide since it has a negative charge and similar ionic size [44]. Presence of iodide in the blood from iodine containing medications or iodine contrast agents will compete with these radiopharmaceuticals for thyroid uptake resulting in poor image quality.

Another well-known example of active transport is the Na^+/K^+ pump, especially of importance in the heart muscle. Thallous chloride ($^{201}Tl^+$) has been used for myocardial perfusion scans. $^{201}Tl^+$ is a radiometal so it is not an analogue of K^+ but it has a similar ionic radius, a single positive charge and fits in the Na^+/K^+ pump [45–47]. Uptake in heart muscle demonstrates viability. The delivery to the myocardial cells is by blood flow through the coronary arteries so the heart muscle uptake reflects coronary perfusion. It has been also used for tumors such as brain tumors, osteosarcomas low-grade lymphomas, Kaposi sarcomas, and parathyroid tumors [45, 46]. This accumulation is a function of blood flow and active transport system of Na^+/K^+ pump within cell membrane. The uptake can be inhibited by blocking the Na^+/K^+ pump with ouabain, digitalis and furosemide [48, 49]. A PET myocardial perfusion radiotracer is rubidium chloride ($^{82}Rb^+$). $^{82}Rb^+$ is a chemical analog of potassium as it falls immediately below it on the periodic table. $^{82}Rb^+$ fits in the Na^+/K^+ pump and its uptake is similar to $^{201}Tl^+$ [48].

I-123-metaiodobenzylguanidine (^{123}I-MIBG) is an analog of noradrenaline. It fits in the prenorepinephrine transporter (adrenergic presynaptic neurons) in adrenergic nerve terminals. Norepinephrine transporter is a transmembrane carrier that transports monoamine neurotransmitters into neurons where they are accumulated in storage vesicles. These transporters are over expressed on certain neoplasms such as neuroblastoma, pheochromocytoma, medullary thyroid carcinoma, retinoblastoma, melanoma and bronchial carcinoma [49, 50].

At acidic pH (pH 2–3), ^{99m}Tc forms a trivalent complex with DMSA (^{99m}Tc (III) DMSA). ^{99m}Tc-DMSA accumulates in proximal tubular cells of kidneys and thereby used for renal cortical imaging. ^{99m}Tc-DMSA is filtered as bound to α1-microglobulin and accumulates in the kidneys by megalin/cubilin-mediated endocytosis of the ^{99m}Tc-DMSA protein complex. Renal accumulation of ^{99m}Tc-DMSA is dependent on megalin/cubilin receptor function and therefore is a marker of proximal tubule endocytic activity [51–53].

Fluciclovine, anti-1-amino-3-^{18}F-fluorocyclobutane-1-carboxylic acid ([^{18}F]FACBC). [^{18}F]FACBC is for men with suspected prostate cancer recurrence based on their elevated prostate specific antigen (PSA) levels. [^{18}F]FACBC takes advantage of the increased amino acid transport in prostate cancer cells, and it is taken up by the L-amino acid transporter and alanine-serine-cysteine transporter systems. These transporters are unregulated in prostate cancer and are associated with more aggressive disease. Once inside the cell, [^{18}F]FACBC does not undergo metabolism and the amino acid transporters mediate influx and efflux of amino acids, so [^{18}F]FACBC washout occurs over time [54–57]. Therefore, early imaging is recommended to maximize lesion uptake.

^{18}F-Fluorothymidine ([^{18}F]FLT) is utilized to measure cellular proliferation as the concentration of [^{18}F]FLT in cells is proportional to cellular proliferation. It is transported from the blood into cells by active transport. Once in the cell, [^{18}F]FLT is a substrate for thymidine kinase I (TK1) and is phosphorylated but not incorporated into DNA (Fig. 3.4). Phosphorylated FLT cannot exit

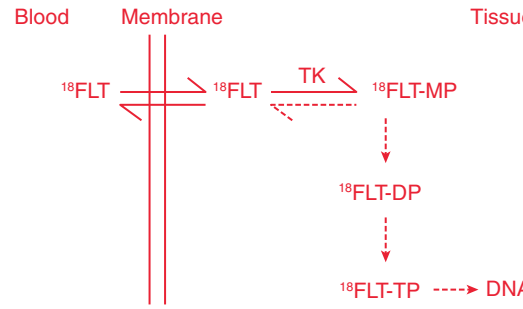

Fig. 3.4 Upon entering the cell via an active transport mechanism, [^{18}F]FLT undergoes phosphorylation by TK1. Phosphorylated-[^{18}F]FLT does not exit the cells and its concentration in cells is proportional to cellular proliferation

the cell. One advantage of [^{18}F]FLT is that it is only a substrate for TK1 and not for mitochondrial TK2 and so it is a more specific tracer compared with other fluorinated tracers for cellular proliferation [58, 59].

^{18}F-Fluoro-Ethyl-Tyrosine ([^{18}F]FET), is an amino acid analog and it reflects the increased amino acid transport of tumor cells. It is a neuro-oncologic PET radiotracer. It is actively taken up in tumor cells via amino acid transport system L. It is neither incorporated into proteins nor readily degraded, resulting in high intracellular concentrations [60]. Radiolabelled amino acid-based agents are useful in PET brain tumor imaging because [^{18}F]FDG is somewhat insensitive for detecting tumors and lesions in the brain due the high levels of glycolytic metabolism in the normal cortex and white matter [61].

[^{18}F]Choline and [^{11}C]Choline target the cellular membrane phospholipids. They enter the cell through choline transporters with accumulation in tumors due to malignancy-induced overexpression of choline kinase (CK) that catalyzes the phosphorylation of choline to form phosphorylcholine followed by generation of phosphatidylcholine in the tumor cell membrane [62–65]. They have been approved for recurrent prostate cancer detection.

3.2.5 Filtration

Filtration is a passing of molecules through pores or channels due to hydrostatic or osmotic pressure gradient. The molecular size vs. pore size and availability are the most important factors in filtration. In addition, filtration requires a force or pressure gradient, it does not require external energy or carriers. Filtration is not competitive so it is not subjected to saturation. Glomerular filtration by the kidney is the prime example of filtration to estimate the function of the renal tissue. Only small hydrophilic molecules (i.e., molecular weight of <5000) can pass through the glomerular pores, and only the ones that are free in plasma (not bound to proteins) are available to be filtered, and these molecules should not be able to be secreted or reabsorbed by tubule. Blood pressure is the pressure gradient for glomerular filtration. Even though many radiopharmaceuticals are excreted by glomerular filtration, ^{99m}Tc-DTPA, ^{99m}Tc-MAG$_3$, ^{125}I-iothalamate, and ^{51}Cr-EDTA are the radiopharmaceuticals that are mainly used for glomerular function renal imaging studies [66–69].

3.2.6 Secretion

Secretion is active transport of substances out of glands and other tissues. For example, the secretion of hydrochloric acid (HCl) by the stomach, secretion of H^+, K^+, NH_3, urea, creatinine or histamine by the kidney tubular cells into the urine, and secretion of bilirubin by the liver into the bile. In Meckel's Diverticulum, a patch of ectopic stomach tissue is usually found in the intestine, so it may secrete hydrochloric acid (HCl) that erodes the intestinal wall, which leads to bleeding. Tc-99m-pertechnetate (TcO_4^-) is negatively charged and of similar size as chloride (Cl^-), so it is secreted as pertechnic acid ($H^+TcO_4^-$) by both normal stomach tissue and Meckel's Diverticula [70, 71].

As for the kidneys, the tubular cells secrete some waste products into the urinary collecting system. ^{99m}Tc-mertiatide (^{99m}Tc-MAG3) is cleared from the blood by this mechanism, resulting in much higher urinary concentrations and better contrast compared to radiopharmaceuticals eliminated by glomerular filtration [66–69].

3.2.7 Phagocytosis

Phagocytosis is a Greek word for cell eating. It is a process of the cell engulfing a particle and internalizing it. Reticuloendothelial system (RES) cells, such as Kupffer cells in the liver and reticular cells in the spleen, capture and engulf colloidal particles such as Tc-99m sulfur colloid (^{99m}Tc-SC) of particle size range between 0.1–1.0 μm [72, 73]. Focal areas that does not have Kupffer cells, such a tumor, cyst, abscess, or hemangioma, will not have an uptake of ^{99m}Tc-sulfur colloid (cold region) [74].

Also, colloidal particles smaller than 0.1 μm show rapid clearance from the interstitial space

into lymphatic vessels and significant retention in lymph nodes when injected into the interstitial fluid [75]. Cancerous nodes replaced by tumor tissues will not sequester the colloids so no uptake of radioactivity will be visualized (cold region). ^{99m}Tc-antimony sulfide colloid (0.002–0.015 μm), ^{99m}Tc-human serum albumin (0.01–0.02 μm) or ^{99m}Tc-nanocolloid are ideal for lymphoscintigraphic studies [76]. However, these radiotracers are not available in the USA, so passing ^{99m}Tc-SC through 0.2 μm filter is being used for lymphoscintigraphic [76].

3.2.8 Cell Sequestration

Cell sequestration is the process of removal of old or damaged red blood cells from circulation which is mainly associated with the spleen. RBC are labeled with Tc-99m using the commercially available kit, then they are carefully denatured by heating at 49–50 °C for 15 min. Heating RBCs changes their shape from tough biconcave disks to spherocytes with knobby projections and a fragile cell membrane. When they squeeze through the 3 μm pores in the cords of the red pulp they get lysed, releasing their radioactive contents within the spleen. Splenic removal of RBCs is a more selective process than removal by the liver and other RES tissue. This imaging procedure is especially useful for localizing and/or identifying ectopic accessory spleens [77, 78].

3.2.9 Capillary Blockade

Capillary blockade is the physical trapping of particles in capillaries and pre-capillary arterioles (microembolization). The diameter of capillaries and pre-capillary arterioles are about 10 microns and 20–30 microns, respectively, so the radiotracer particles should be a little bigger in size between 15 and 50 microns. The delivery to the capillary is through the blood flow so when the radiolabelled particles are injected intravenously, the lungs are the first capillary encountered. Tc-99m radiolabeled macroaggregated albumin (Tc-99m-MAA) have been used for perfusion lung imaging. The localization in each of the lungs is an indicator for the relative blood flow to each of the two lungs. Therefore, ^{99m}Tc-MAA perfusion lung imaging can also be used to assess blood flow through the pulmonary arteries [79, 80]. If ^{99m}Tc-MAA is injected through a catheter positioned in the hepatic artery, then the hepatic blood flow will deliver it to the capillaries in the liver to evaluate blood flow within the liver [81].

3.2.10 Ion Exchange

Ion exchange is the exchange of ionic chemical analogs. Current radiopharmaceuticals that localize by this mechanism are strontium chloride ($^{89}Sr^{2+}$), a beta-emitter used to treat painful bone metastases, and sodium fluoride ($^{18}F^{-}$), a PET agent used for bone scans [82, 83]. In the hydroxyapaptite of the bone matrix,$^{89}Sr^{+2}$ replaces Ca^{+2} while $^{18}F^{-}$ replaces OH^{-}. Fluoride ions diffuse from the blood compartment and exchange with hydroxyl groups in hydroxyapatite crystal to form fluoroapatite. Uptake of fluoride ion into bone may be due to primary and metastatic tumors as well as bone turnover (metabolism) [82, 83].

3.2.11 Chemisorption

Chemisorption is the binding of phosphate-type compounds onto the surface of the bone. The strength of this binding is intermediate between chemical covalent bonding and hydrogen bonding (adsorption). Radiolabeled diphosponates compounds, ^{99m}Tc-MDP and ^{99m}Tc-HDP are used for bone imaging while ^{153}Sm-EDTMP is used for the treatment of painful bone metastases. Localization is on the surface, therefore, uptake is proportional to the surface area [84, 85]. The larger the surface area of increased bone metabolism, the higher the uptake in that areas such as fracture, infection, and tumor. In addition to chemisorption on the surface of bone, there can also be chemisorption onto calcium phosphate crystals that precipitate in certain soft tissues as a consequence of severe hyperparathyroidism, hypercalcemia, and myocardial infarction.

3.2.12 Cellular Migration

Cellular migration is the directed movement of cells due to stimuli such as the chemotaxis of white blood cells to the site of infection and inflammation. Radiolabeled autologous leukocytes with ^{111}In-oxine or ^{99m}Tc-exametazime (^{99m}Tc-HMPAO) can be used to localize sites of infection similar to the circulating leukocytes due to the attraction of released chemotactic factors [86, 87].

3.2.13 Receptor Binding

Receptor binding is similar to the "lock-and-key" concept. It is the binding of a biological molecule to a specific receptor such as the binding of an antibody or antibody fragment to an antigen and peptides, hormones or neurotransmitter binding to their receptors. Receptor and antigen bindings are very selective and specific; therefore, competition from similar molecules for these receptors and antigens binding is a concern with the possibility saturation. Many tumor cells express antigens or receptors that are expressed in small amounts in normal cells. But tumor cells have higher expression of these antigens and receptors. The localization of radiolabeled antibodies, proteins, hormones, and peptides depend on the blood clearance, tumor blood flow, tumor mass and tumor cell viability. The radionuclide of use should match the pharmacokinetics of the biological molecule. For example, antibodies should be labeled with long half-life radionuclides such as ^{111}In and ^{131}I, while peptides can be labeled with shorter lived radionuclides such as ^{99m}Tc, ^{18}F, or ^{123}I for imaging studies. Iodine-131 is the most used radionuclide for both diagnostic and therapeutic studies. Radioiodide can be labeled on tyrosine residue in the antibody or peptide. However, the other radionuclides are indirectly labeled in which they are coordinated to a chelate such as DTPA or DOTA that is covalently attached to the biological molecule (bifunctional chelating approach).

Antibodies (Ab) are also known as immunoglobulins (Ig) which are a group of glycoprotein molecules produced by B-lymphocytes in response to antigenic stimulation. Ab binds to a specific site of the antigen in which an antigen can have multiple binding sites for different Ab. Although much research has been conducted with radiolabeled antibodies, few are currently marketed. In-111 capromab pendetide (ProstaScint), a monoclonal murine IgG antibody directed to prostate specific membrane antigen (PSMA), is used for staging and follow-up of prostate cancer [88–90]. PSMA is a membrane protein that is expressed in prostate tissue and overexpressed on prostate carcinoma. PSMA has a unique structure consisting of three sections: internal cellular, transmembrane and extracellular portions. ProstaScint was later found to bind to the intracellular epitope of PSMA. Therefore, it was discontinued by the manufacturing company in 2018 after the FDA approved smaller urea-based molecules targeting the extracellular epitope of PSMA. ^{68}Ga-DOTA-PSMA and [^{18}F]PSMA, are the urea-based, low molecular weight inhibitors of PSMA that have replaced ProstaScint [88–90].

^{131}I-tositumomab and ^{111}In/^{90}Y-ibritumomab tiuxetan, are monoclonal murine IgG that bind to CD20 receptors on B-cells and non-Hodgkin's lymphoma tumor cells. These labeled antibodies are used for diagnostic, monitoring, and treatment of non-Hodgkin's lymphoma [91, 92].

Many neuroendocrine tumors have an over expression of somatostatin receptors (SSTR) and there are 5 SSTR subtypes. The two naturally occurring SST peptides, 14 and 28 amino acids long, which are known to have short biological half-life due to enzymatic degradation. A number of biologically stable SST analogues were synthesized. Octreotide analogue is an 8 amino acid long analogue that has a high affinity to 2 and 5 SSTR subtypes. ^{111}In-pentetreotide (Octreoscan), a radiolabeled form of octreotide, is used to detect, localize and evaluate such somatostatin-expressing tumors by binding to these receptors [93]. When octreotide is labeled with ^{90}Y or ^{177}Lu, then it is used for therapeutic purposes. Recently ^{68}Ga-DOTA-octreotide has been approved for PET studies of neuroendocrine tumors [94, 95]. In addition, ^{64}Cu-DOTA-tyr^3-octreotate has been approved as a PET diagnostic agent for neuroen-

docrine tumors but Cu-64 emits β^- so it can be used for therapeutic purposes as well [96].

[^{18}F]Florbetapir (Amyvid, Eli Lilly/Avid Radiopharmaceuticals), [^{18}F]florbetaben (Neuraceq, Piramal Imaging) and [^{18}F]flutemetamol (GE Healthcare. VizamylTM) are radiopharmaceuticals used for patients who are being evaluated for Alzheimer's disease (AD) and other causes of cognitive impairment in the cortical regions and hippocampus. After injection, the tracers diffuse through the blood-brain barrier and binds with high affinity and specificity to β-amyloid neuritic plaques (Aβ aggregates) in the brain of adult patients with cognitive impairment. They rapidly enter the brain and quickly washes out from the brain if not bound to β-amyloid neuritic plaques [97, 98]. These radiotracers share a common imaging target and similar imaging characteristics (Aβ tracers). They can differ in their tracer kinetics, specific binding ratios and optimal imaging parameters therefore, they will have different recommended injected doses, time to initiate imaging post-injection, and scan duration [97, 98].

[^{18}F]Fluoroestradiol ([^{18}F]FES) is an analog of estrogen and is used to detect estrogen receptor-positive breast cancer lesions. It has a high overall sensitivity and specificity in assessing the ER status in breast cancers. [^{18}F]FES uptake has been approved to guide in therapy selection and to predict endocrine treatment response [99].

[^{123}I]ioflupane (DaTscan) is a chemical derivative of cocaine. It binds to presynaptic dopamine transporters, which are primarily located in the striatum. Loss of dopamine transporter density, as occurs in Parkinson's disease, results in reduced uptake of the radiopharmaceutical. The radiotracer localizes to the dopamine transporters in the basal ganglia [100].

3.3 Altered Biodistributions Due to Radiochemical Impurities from Improper Radiopharmaceutical Preparations

Improper preparation can lead to the presence of radiochemical impurities in the final radiopharmaceutical dose. Radiochemical impurities have different pharmacokinetics and biodistributions from the radiopharmaceutical product of interest, and hence these impurities can reduce the image quality while exposing the patients to unnecessary radioactive dose. Therefore it is very important to recognize common radiochemical impurities and their localizations. Table 3.2 lists the main possible radiochemical impurities along with localization site [101].

Table 3.2 Radiopharmaceuticals' predominant radiochemical preparation impurity

Radiopharmaceutical	Predominant radiochemical impurity	Possible localization
^{99m}Tc-radiopharmaceuticals	TcO_4^-	Salivary glands, thyroid, stomach, GI tract, and urine/bladder
	TcO_2 Colloids (particles)	Phagocytized by the liver
^{111}In-radiophamraceuticals	$In(OH)_3$ Colloids (particles)	Phagocytized by liver and spleen
	$^{111}In^{+3}$	Binds to plasma transferrin, and has prolonged blood pool retention
^{123}I/^{131}I-radiopharmaceuticals	$^{123}I/^{131}I^-$	Thyroid
^{18}F-radiopharmaceuticals	$^{18}F^-$	Bone
^{68}Ga-radiophamraceuticals	$^{68}Ga(OH)_3$ Colloids (particles)	Phagocytized by liver and spleen
	$^{68}Ga^{+3}$	Binds to plasma transferrin, and has prolonged blood pool retention

References

1. Kowalsky RJ, Falen SW (2011) Radionuclide production. Radiopharmaceuticals in nuclear pharmacy and nuclear medicine. American Pharmacists Association, pp 31–46
2. Mausner LF, Mirzadeh S (2003) Reactor production of radionuclides. In: Welch M, Redvanly C (eds) Handbook of radiopharmaceuticals radiochemistry and applications. Wiley, pp 87–117
3. Ruth TJ (2003) Accelerators available for isotope production. In: Welch M, Redvanly C (eds) Handbook of radiopharmaceuticals radiochemistry and applications. Wiley, pp 71–85
4. Mahmood A, Jones AG (2003) Technetium radiopharmaceuticals. In: Welch M, Redvanly C (eds) Handbook of radiopharmaceuticals radiochemistry and applications. Wiley, pp 323–325
5. Evans EA (1981) Synthesis of radiolabelled compounds. J Radioanal Chem 64:9–32
6. Bonfils P, Damgaard M, Stokholm KH, Nielsen SL (2012) Tc-99m-albumin can replace I-125-albumin to determine plasma volume repeatedly. Scand J Clin Lab Invest 72:447–451
7. Fairbanks VF, Klee GG, Wiseman GA, Hoyer JD, Tefferi A et al (1996) Measurement of blood volume and red cell mass: re-examination of ^{51}Cr and ^{125}I methods. Blood Cells Mol Dis 22:169–186
8. Berman I, Carr R, Malone E (1964) Determination of total blood volume from measurements of total red blood cell mass and plasma volume, using simultaneously injected isotopes. Nature 202:1013–1015
9. Hambÿe AS, Verbeke KA, Vandermeiren RP, Joosens EJ, Verbruggen AM et al (1997) Comparison of modified technetium-99m albumin and technetium-99m red blood cells for equilibrium ventriculography. J Nucl Med 38:1521–1528
10. Sheakley ML, Gordon L (1984) Evaluation of hepatic hemangioma with Tc-99m labeled red blood cells. J Nucl Med Technol 17:119–121
11. Dong H, Zhang Z, Guo Y, Zhang H, Xu W (2017) The application of technetium-99m-red blood cell scintigraphy in the diagnosis of orbital cavernous hemangioma. Nucl Med Commun 38:744–747
12. Wagner HN, Lopez-Majano V, Langan JK, Joshi RC (1968) Radioactive xenon in the differential diagnosis of pulmonary embolism. Radiology 91:1168–1174
13. Mishkin FS, Brashear RE, Reese IC (1970) Evaluation of regional perfusion and ventilation using xenon 133 and the scintillation camera. Am J Roentgenol 108:60–70
14. Alderson PO, Lee H, Summer WA, Motazedi A, Wagner HN (1979) Comparison of Xe-133 washout and single-breath imaging for the detection of ventilation abnormalities. J Nucl Med 20:917–922
15. Barth A, Haldemann AR, Reubi JC, Rösier H, Kinser JA et al (1996) Noninvasive differentiation of meningiomas from other brain tumours using combined ^{111}indium-octreotide/^{99m}technetium-DTPA brain scintigraphy. Acta Neurochir 138:1179–1185
16. Inoue Y, Momose T, Machida K, Honda N, Mamiya T et al (1993) Delayed imaging of Tc-99m-DTPA-HSA SPECT in subacute cerebral infarction. Radiat Med 11:214–216
17. Balon HR, Fink-Bennett DM, Brill DR, Fig LM, Freitas JE et al (1997) Procedure guideline for hepatobiliary scintigraphy. J Nucl Med 38:1654–1657
18. Rantis PC, Harford FJ, Wagner RH, Henkin RE (1995) Technetium-labelled red blood cell scintigraphy: is it useful in acute lower gastrointestinal bleeding? Int J Colorect Dis 10:210–215
19. Dam HQ, Brandon DC, Grantham VV, Hilson AJ, Howarth DM et al (2014) The SNMMI procedure standard/EANM practice guideline for gastrointestinal bleeding scintigraphy 2.0. J Nucl Med Technol 42:308–317
20. Jian R, Ducrot F, Piedeloup C, Mary JY, Najean Y, Bernier JJ (1985) Measurement of gastric emptying in dyspeptic patients: effect of a new gastrokinetic agent (cisapride). Gut 26:352–358
21. Ertay T, Doğan AS, Ülker Ö, Durak H (2014) In vitro evaluation of Tc-99m radiopharmaceuticals for gastric emptying studies. Mol Imaging Radionucl Ther 23:21–24
22. Nakamura K, Tukatani Y, Kubo A, Hashimoto S, Terayama Y et al (1989) The behavior of ^{99m}Tc-hexamethylpropyleneamineoxime (^{99m}Tc-HMPAO) in blood and brain. Eur J Nucl Med 15:100–107
23. Vanbilloen HP, Cleynhens BJ, Verbruggen AM (1998) Importance of the two ester functions for the brain retention of ^{99m}Tc-labelled ethylene dicysteine diethyl ester (^{99m}Tc-ECD). Nucl Med Biol 25:569–575
24. Berman DS, Kiat H, Maddahi J (1991) The new ^{99m}Tc myocardial perfusion imaging agents: 99mTc-sestamibi and 99mTc-teboroxime. Circulation 84(3 Suppl):I7–I21
25. Braat SH (1991) ^{99m}Tc myocardial perfusion imaging. Curr Opin Radiol 3:810–816
26. Nakamura K, Sammiya T, Hashimoto J, Ishibashi R, Matsumoto K et al (1996) Comparison of cationic myocardial perfusion agents: characteristics of accumulation in cultured smooth muscle cells. Ann Nucl Med 10:375–381
27. Kitsiou NK, Bacharach SL, Bartlett ML, Srinivasan G, Summers RM et al (1999) ^{13}N-ammonia myocardial blood flow and uptake: relation to functional outcome of asynergic regions after revascularization. J Am Coll Cardiol 33:678–686
28. Ziessman H, O'Malley J (2014) Cardiac system. In: Thrall J (ed) Nuclear medicine: the requisites. Elsevier, pp 378–423
29. Hoffer P (1980) Gallium: mechanisms. J Nucl Med 21:282–285
30. Muranaka A, Ito Y, Hashimoto M, Namba M, Nishitani K et al (1980) Uptake and excretion of 67Ga-citrate in malignant tumors and normal cells. Eur J Nucl Med 5:31–37

31. Plathow C, Weber WA (2008) Tumor cell metabolism imaging. J Nucl Med 49(suppl):43S–63S
32. Koopmans KP, Neels ON, Kema IP, Elsinga PH, Links TP et al (2009) Molecular imaging in neuroendocrine tumors: molecular uptake mechanisms and clinical results. Crit Rev Oncol Hematol 71:199–213
33. Neels OC, Koopmans KP, Jager PL, Vercauteren L, van Waarde A et al (2008) Manipulation of [^{11}C]-5-hydroxytryptophan and 6-[^{18}F]fluoro-3,4-dihydroxy-l-phenylalanine accumulation in neuroendocrine tumor cells. Cancer Res 68:7183–7190
34. Masaki Y, Shimizu Y, Yoshioka T, Nishijima K, Zhao S et al (2017) FMISO accumulation in tumor is dependent on glutathione conjugation capacity in addition to hypoxic state. Ann Nucl Med 31:596–604
35. Li F, Joergensen JT, Hansen AE, Kjaer A (2014) Kinetic modeling in PET imaging of hypoxia. Am J Nucl Med Mol Imaging 4:490–506
36. Reske SN, Grillenberger KG, Glatting G, Port M, Hildebrandt M et al (1997) Overexpression of glucose transporter 1 and increased FDG uptake in pancreatic carcinoma. J Nucl Med 38:1344–1348
37. Brown RS, Wahl RL (1993) Overexpression of Glut-1 glucose transporter in human breast cancer: an immunohistochemical study. Cancer 72:2979–2985
38. Rempel A, Mathupala SP, Griffin CA, Hawkins AL, Pedersen PL (1996) Glucose catabolism in cancer cells: amplification of the gene encoding type II hexokinase. Cancer Res 56:2468–2471
39. Caraco C, Aloj L, Chen LY, Chou JY, Eckelman WC (2000) Cellular release of [^{18}F]2-fluoro-2-deoxyglucose as a function of the glucose-6-phosphatase enzyme system. J Biol Chem 275:18489–18494
40. Lan JA, Chervu LR, Johansen KL, Wolkoff AW (1988) Uptake of technetium 99m hepatobiliary imaging agents by cultured rat hepatocytes. Gastroenterology 95:1625–1631
41. Chung JK (2002) Sodium iodide symporter: its role in nuclear medicine. J Nucl Med 43:1188–1200
42. Bizhanova A, Kopp P (2009) Minireview: the sodium-iodide symporter NIS and pendrin in iodide homeostasis of the thyroid. Endocrinology 150:1084–1090
43. Robbins RJ, Schlumberger MJ (2005) The evolving role of 131I for the treatment of differentiated thyroid carcinoma. J Nucl Med 46:28S–37S
44. Drew H, LaFrance N, Chen J (1987) Thyroid imaging studies. J Nucl Med Technol 15:79–87
45. McCall D, Zimmer LJ, Katz AM (1985) Kinetics of thallium exchange in cultured rat myocardial cells. Circ Res 56:370–376
46. Arbab AS, Koizumi K, Toyama K, Arai T, Araki T (1997) Ion transport systems in the uptake of 99Tcm-tetrofosmin, ^{99m}Tc-MIBI and ^{201}Tl in a tumour cell line. Nucl Med Commun 18:235–240
47. Askari A (2019) The sodium pump and digitalis drugs: dogmas and fallacies. Pharmacol Res Perspect 7:e00505
48. Glynn IM, Richards DE (1982) Occlusion of rubidium ions by the sodium-potassium pump: its implications for the mechanism of potassium transport. J Physiol 330:17–43
49. Pandit-Taskar N, Modak S (2017) Norepinephrine transporter as a target for imaging and therapy. J Nucl Med 58:39S–53S
50. Zhang H, Huang R, Cheung NK, Guo H, Zanzonico PB et al (2014) Imaging the norepinephrine transporter in neuroblastoma: a comparison of [^{18}F]-MFBG and 123I-MIBG. Clin Cancer Res 20:2182–2191
51. Weyer K, Nielsen R, Petersen SV, Christensen EI, Rehling M et al (2013) Renal uptake of 99mTc-dimercaptosuccinic acid is dependent on normal proximal tubule receptor-mediated endocytosis. J Nucl Med 54:159–165
52. Willis KW, Martinez DA, Hedley-Whyte ET, Davis MA, Judy PF et al (1977) Renal localization of 99mTc-stannous glucophetonate and 99mTc-stannous dimercaptosuccinate in the rat by frozen section autoradiography: the efficiency and resolution of technetium-99m. Radiat Res 69:475–488
53. Peters AM, Jones DH, Evans K, Gordon I (1988) Two routes for 99mTc-DMSA uptake into the renal cortical tubular cell. Eur J Nucl Med 14:555–561
54. Okudaira H, Shikano N, Nishii R, Miyagi T, Yoshimoto M et al (2011) Putative transport mechanism and intracellular fate of trans-1-amino-3-18F--fluorocyclobutanecarboxylic acid in human prostate cancer. J Nucl Med 52:822–829
55. Ren J, Yuan L, Wen G, Yang J (2016) The value of anti-1-amino-3-18F-fluorocyclobutane-1-carboxylic acid PET/CT in the diagnosis of recurrent prostate carcinoma: a meta-analysis. Acta Radiol 57:487–493
56. Odewole OA, Tade FI, Nieh PT, Savir-Baruch B, Jani AB et al (2016) Recurrent prostate cancer detection with anti-3-[^{18}F]FACBC PET/CT: comparison with CT. Eur J Nucl Med Mol Imaging 43:1773–1783
57. Oka S, Okudaira H, Ono M, Schuster DM, Goodman MM et al (2014) Differences in transport mechanisms of trans-1-amino3-[^{18}F]fluorocyclobutanecarboxylic acid in inflammation, prostate cancer, and glioma cells: comparison with L-[methyl^{11}C] methionine and 2-deoxy-2-[^{18}F]fluoro-D-glucose. Mol Imaging Biol 16:322–329
58. Peck M, Pollack HA, Friesen A, Muzi M, Shoner SC et al (2015) Applications of PET imaging with the proliferation marker [^{18}F]-FLT. Q J Nucl Med Mol Imaging 59:95–104
59. Been LB, Suurmeijer AJ, Cobben DC, Jager PL, Hoekstra HJ et al (2004) [^{18}F]FLT-PET in oncology: current status and opportunities. Eur J Nucl Med Mol Imaging 31:1659–1672
60. Langen KJ, Hamacher K, Weckesser M, Floeth F, Stoffels G et al (2006) O-(2-[^{18}F]fluoroethyl)-L-tyrosine: uptake mechanisms and clinical applications. Nucl Med Biol 33:287–294
61. Pauleit D, Stoffels G, Bachofner A, Floeth FW, Sabel M et al (2009) Comparison of (^{18})F-FET and

(^{18})F-FDG PET in brain tumors. Nucl Med Biol 36:779–787
62. Kennedy EP, Weiss SB (1956) The function of cytidine coenzymes in the biosynthesis of phospholipides. J Biol Chem 222:193–214
63. Kent C (1990) Regulation of phosphatidylcholine biosynthesis. Prog Lipid Res 29:87–105
64. Hara T, Kosaka N, Kishi H (1998) PET imaging of prostate cancer using carbon-11-choline. J Nucl Med 39:990–995
65. DeGrado TR, Baldwin SW, Wang S, Orr MD, Liao RP et al (2001) Synthesis and evaluation of (18) F-labeled choline analogs as oncologic PET tracers. J Nucl Med 42:1805–1814
66. Blaufox MD, Aurell M, Bubeck B, Fommei E, Piepsz A et al (1996) Report of the radionuclides in nephrourology committee on renal clearance. J Nucl Med 37:1883–1890
67. Eshima D, Taylor A (1992) Technetium-99m (^{99m}Tc) mercaptoacetyltriglycine: update on the new ^{99m}Tc renal tubular function agent. Semin Nucl Med 22:61–73
68. Bubeck B, Brandau W, Weber E, Kälble T, Parekh N et al (1990) Pharmacokinetics of technetium-99m-MAG3 in humans. J Nucl Med 31:1285–1293
69. Schaap GH, Alferink TH, de Jong RB, Oe PL, Roos JC et al (1988) ^{99m}Tc-MAG3: dynamic studies in patients with renal disease. Eur J Nucl Med 14:28–31
70. Williams JC (1983) Pertechnetate and the stomach—a continuing controversy. J Nucl Med 24:633–636
71. Chaudhuri TK (1975) Cellular site of secretion of $^{99m}TcO_4$ in the stomach. A controversial point. J Nucl Med 16:1204–1205
72. Higgins CB, Taketa RM, Taylor A, Halpern SE, Ashburn WL (1974) Renal uptake of ^{99m}Tc-sulfur colloid. J Nucl Med 15:564–566
73. Klingensmith WC III, Ryerson TW (1973) Lung uptake of ^{99m}Tc-sulfur colloid. J Nucl Med 14:201–204
74. Prakash R, Gupta RK, Narayanan RV, Chakravarty SK (1989) Technetium-99m radiocolloid scintigraphy, planar and SPECT red blood cell imaging and ultrasonography in diagnosis of hepatic hemangioma. Australas Radiol 33:237–244
75. Oussoren C, Velinova M, Scherphof G, van der Want J, van Rooijen N et al (1998) Lymphatic uptake and biodistribution of liposomes after subcutaneous injection: IV. Fate of liposomes in regional lymph nodes. Biochim Biophys Acta 1370:259–272
76. Hung JC, Wiseman GA, Wahner HW, Mullan BP, Taggart TR et al (1995) Filtered technetium-99m-sulfur colloid evaluated for lymphoscintigraphy. J Nucl Med 36:1895–1901
77. Armas RR (1985) Clinical studies with spleen-specific radiolabeled agents. Semin Nucl Med 15:260–275
78. Atkins HL, Eckelman WC, Hauser W, Klopper JF, Richards P (1972) Splenic sequestration of ^{99m}Tc-labeled red blood cells. J Nucl Med 13:811–814
79. Levine G (1980) Tc-99m MAA: a model for administering the desired number of particles for pulmonary perfusion studies. J Nucl Med Technol 8:33–36
80. Bolstad DM, Valley TB, Wilson ME, Hung JC (1992) An improved technique for reducing the number of particles in a technetium-99m macroaggregated albumin injection. J Nucl Med Technol 20:220–223
81. Ziessman HA, Wahl RL, Juni JE, Gyves JE, Ensminger WD et al (1985) The utility of SPECT for 99mTc-MAA hepatic arterial perfusion scintigraphy. AJR Am J Roentgenol 145:747–751
82. Fukushi Y, Ozawa T, Wakui M, Nishiyama A (1995) Sr^{2+} can pass through Ca^{2+} entry pathway activated by Ca2+ depletion, but can be hardly taken up by the Ca^{2+} stores in the rat salivary acinar cells. Tohoku J Exp Med 176:83–97
83. Czernin J, Satyamurthy N, Schiepers C (2010) Molecular mechanisms of bone 18F-NaF deposition. J Nucl Med 51:1826–1829
84. Subramanian G, McAfee JG, Blair RJ, Kallfelz FA, Thomas FD (1975) Technetium-99m-methylene diphosphonate—a superior agent for skeletal imaging: comparison with other technetium complexes. J Nucl Med 16:744–755
85. Sartor O, Hoskin P, Bruland ØS (2013) Targeted radio-nuclide therapy of skeletal metastases. Cancer Treat Rev 39:18–26
86. Roca M, de Vries EF, Jamar F, Israel O, Signore A (2010) Guidelines for the labelling of leucocytes with (111)In-oxine. Inflammation/infection taskgroup of the European Association of Nuclear Medicine. Eur J Nucl Med Mol Imaging 37:835–841
87. Allan RA, Sladen GE, Bassingham SC, Lazarus SEM, Clarke I et al (1993) Comparison of simultaneous 99mTc-HMPAO and 111In oxine labelled white cell scans in the assessment of inflammatory bowel disease. Eur J Nucl Med 20:195–200
88. Wester HJ, Schottelius M (2019) PSMA-targeted radiopharmaceuticals for imaging and therapy. Semin Nucl Med 49:302–312
89. Lin M, Ta RT, Kairemo K, Le DB, Ravizzini GC (2021) Prostate-Specific Membrane Antigen-Targeted Radiopharmaceuticals in Diagnosis and Therapy of Prostate Cancer: Current Status and Future Perspectives. Cancer Biother Radiopharm 36(3):237–251. https://doi.org/10.1089/cbr.2020.3603. Epub 2020 Jun 23. PMID: 32589458.
90. Okarvi SM (2019) Recent developments of prostate-specific membrane antigen (PSMA)-specific radiopharmaceuticals for precise imaging and therapy of prostate cancer: an overview. Clin Transl Imaging 7:189–208
91. Davies A (2007) Radioimmunotherapy for B-cell lymphoma: Y^{90} ibritumomab tiuxetan and I^{131} tositumomab. Oncogene 26:3614–3628
92. Jacene HA, Filice R, Kasecamp W, Wahl RL (2007) Comparison of ^{90}Y-Ibritumomab Tiuxetan and ^{131}I-Tositumomab in clinical practice. J Nucl Med 48:1767–1776

93. Leners N, Jamar F, Fiasse R, Ferrant A, Pauwels S (1996) Indium- 111-pentetreotide uptake in endocrine tumors and lymphoma. J Nucl Med 37:916–922
94. Deppen SA, Blume J, Bobbey AJ, Shah C, Graham MM, Lee P, Delbeke D, Walker RC (2016) 68Ga-DOTATATE compared with 111In-DTPA-octreotide and conventional imaging for pulmonary and gastroenteropancreatic neuroendocrine tumors: a systematic review and meta-analysis. J Nucl Med 57:872–878
95. Yang J, Kan Y, Ge BH, Yuan L, Li C et al (2014) Diagnostic role of Gallium-68 DOTATOC and Gallium-68 DOTATATE PET in patients with neuroendocrine tumors: a meta-analysis. Acta Radiol 55:389–398
96. Ullrich M, Bergmann R, Peitzsch M, Zenker EF, Cartellieri M et al (2016) Multimodal somatostatin receptor theranostics using [(64)Cu]Cu−/[(177)Lu]Lu-DOTA-(Tyr(3))octreotate and AN-238 in a mouse pheochromocytoma model. Theranostics 6:650–665
97. Yeo JM, Waddell B, Khan Z, Pal S (2015) A systematic review and meta-analysis of (18)F-labeled amyloid imaging in Alzheimer's disease. Alzheimers Dement 1:5–13
98. Auvity S, Tonietto M, Caillé F et al (2020) Repurposing radiotracers for myelin imaging: a study comparing 18F-florbetaben, 18F-florbetapir, 18F-flutemetamol,11C-MeDAS, and 11C-PiB. Eur J Nucl Med Mol Imaging 47:490–501
99. Liao GJ, Clark AS, Schubert EK, Mankoff DA (2016) J Nucl Med 57:1269–1275
100. Roussakis AA, Piccini P, Politis M (2013) Clinical utility of DaTscan™ (123I-Ioflupane Injection) in the diagnosis of Parkinsonian syndromes. Degen Neurol Neuromusc Dis 3:33–39
101. Vallabhajosula S, Killeen RP, Osborne JR (2010) Altered biodistribution of radiopharmaceuticals: role of radiochemical/pharmaceutical purity, physiological, and pharmacologic factors. Semin Nucl Med 40:220–241

Inflammation

4

Abdelhamid H. Elgazzar
and Ahmed M. Mohammed

4.1 Introduction

Inflammation was described as early as 3000 BC in an Egyptian papyrus [1] and is still a common problem despite continuous advancements in prevention and treatment methods. The recent outbreak of the new viral infection Covid-19 [2] is an evidence of how infection is still a common problem and new types can emerge. Infection can be serious and life threatening. It can cost more than other diseases such as cancer and dibetes. The proper and timely diagnosis, knowledge of comorbidities and delineation of the site and extent of inflammation are crucial to the clinical management of infection and for monitoring the response to therapy [3].

This issue is relevant to nuclear medicine, since physiological along with morphological imaging has an important role in achieving this goal.

Inflammation is a complex tissue reaction to injury. Injury may be caused not only by living microbes, i.e., bacteria, viruses, or fungi, leading to infection, but also by injurious chemical, physical, immunological, or radiation agents (Fig. 4.1).

Inflammation is fundamentally a protective reaction against the cause of cell injury as well as the consequence of such injury. However, inflammation is potentially harmful and may even be life threatening. Since most of the essential components of the inflammatory process are found in the circulation, inflammation occurs only in vascularized tissue. Inflammation is generally considered a nonspecific response, because it happens in the same way regardless of the stimulus and the number of exposures to the stimulus [3, 4]. This is different from the immune system, which has memory, and the antigens are specific and induce a specific response. If infection is the initial event causing tissue injury, the challenge for the host is to react as quickly as possible to terminate the spread of infection, even at the cost of further tissue damage [5].

4.2 Classification of Inflammation

Inflammation may be classified as acute or chronic. Acute inflammation is the immediate or early response to injury and is of relatively short duration. It lasts for minutes, hours, or at most a few days. Chronic inflammation, on the other hand, is of longer duration and may last from weeks to years [6]. The distinction between acute and chronic inflammation, however, depends not only on the duration of the process but also on other pathological and clinical features.

A. H. Elgazzar (✉) · A. M. Mohammed
Department of Nuclear Medicine, Faculty of Medicine, Kuwait University, Kuwait City, Kuwait

A. H. Elgazzar (ed.), *The Pathophysiologic Basis of Nuclear Medicine*,
https://doi.org/10.1007/978-3-030-96252-4_4

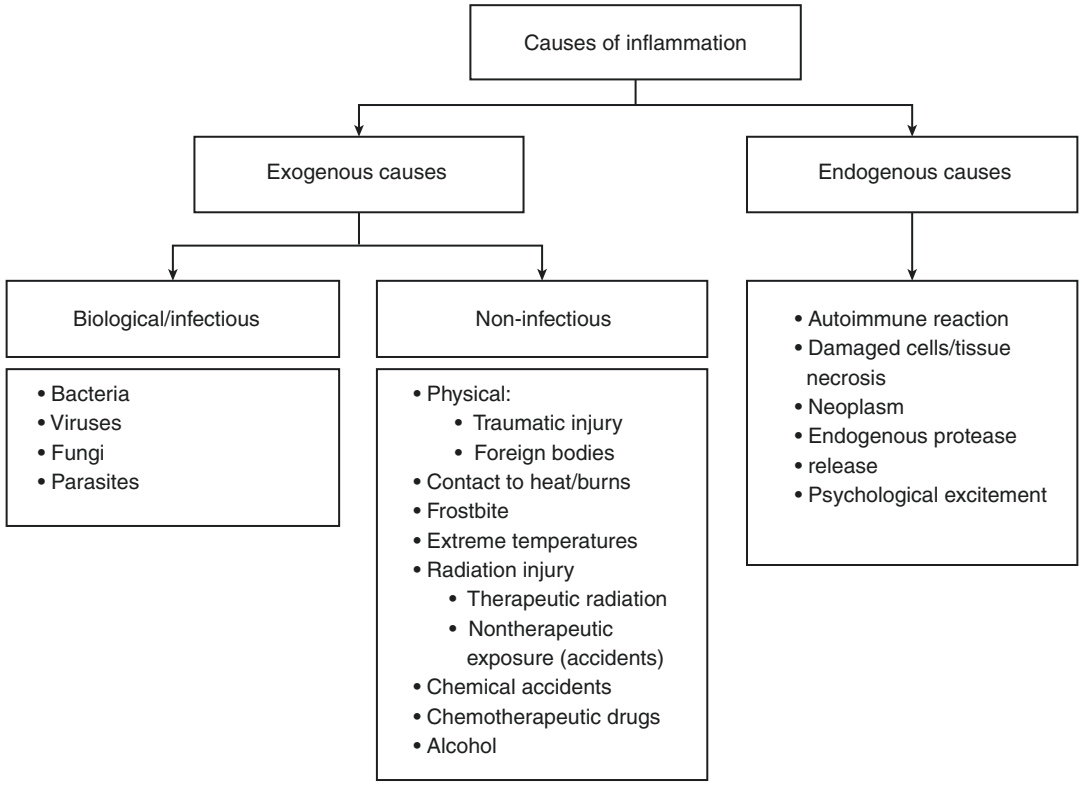

Fig. 4.1 Summary of causes of inflammation

4.3 General Pathophysiological Changes of Inflammation

There are certain pathophysiologic changes accompanying inflammation and some are common in all types. These may occur at the region of the inflammation (Local) or may also be systemic (Fig. 4.2).

4.3.1 Local Pathophysiological Changes of Inflammation

4.3.1.1 Acute Inflammation Associated Changes

Acute inflammation continues only until the threat to the host has been eliminated, which usually takes 8–10 days, although this is variable. Inflammation is generally considered to be chronic when it persists for longer than 2 weeks [2]. Many regional and systemic changes accompany acute inflammation and are mediated by certain chemicals produced endogenously called chemical mediators and are behind the spread of the acute inflammatory response following injury to a small area of tissue into uninjured sites. These chemical mediators include mediators released from cells such as histamine and prostaglandins and others in plasma which are released by some systems contained in the plasma which are the four enzymatic cascade systems: the complement, the kinins, the coagulation factors, and the fibrinolytic system which produce several inflammatory mediators [4–7]. Cytokines are also important mediator and play a roe in FDG uptake in inflammtory foci [8]. Table 4.1 summarizes the main chemical mediators of inflammation.

Acute inflammation is characterized by the following major regional components:

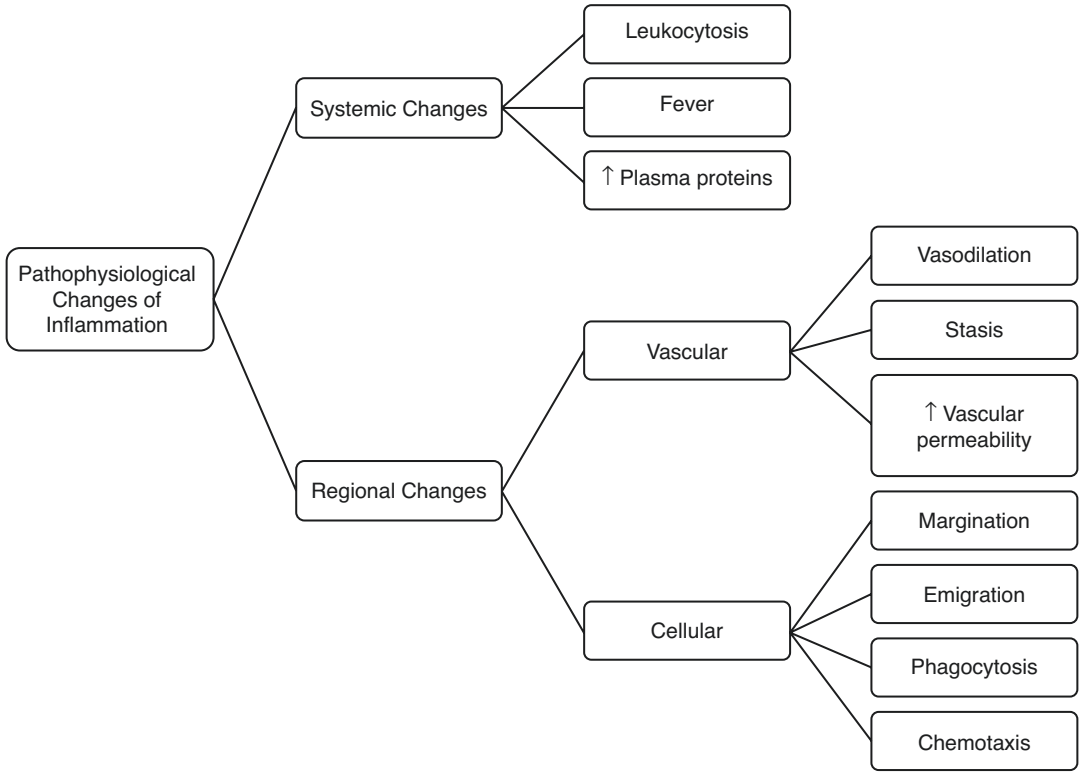

Fig. 4.2 Summary of general pathophysiologic changes accompanying inflammation

Local Vascular Changes

1. Vasodilation following transient vasoconstriction is one of the most important changes that accompany acute inflammation, and it persists until the end of the process. It involves first the arterioles and then results in the opening of new capillary beds in the area.
2. Increased vascular permeability due to:
   (a) Contraction of endothelial cells with widening of intercellular gaps.
   (b) Direct endothelial injury, resulting in endothelial cell necrosis and detachment.
   (c) Leukocyte-mediated endothelial injury: Leukocytes adhere to the endothelium, which becomes activated, thereby releasing toxic oxygen species and proteolytic enzymes and causing endothelial injury.
   (d) Angiogenesis: With inflammation, endothelial cells may proliferate and form new capillaries and venular beds (angiogenesis). These capillary sprouts remain leaky until endothelial cells differentiate.
3. Stasis (slowing of circulation): Increased permeability with extravasation of fluid into the extravascular spaces results in concentration of red blood cells in the small vessels and increased viscosity of the blood, with slowing of circulation in the local vessels. Figures 4.3 and 4.4 illustrate the main vascular changes.

Formation of Exudate

Increased permeability of the microvasculature, along with the other changes described, leads to leakage with formation of "exudate," an inflammatory extravascular fluid with a high protein content, much cellular debris, and a specific gravity above 1.020. This is the hallmark of acute inflammation, which may also be called exudative inflammation. It indicates significant alteration in the normal permeability of the small blood vessels in the region of injury.

The two components of exudate, fluid and protein, serve good purposes. Fluid increase helps to dilute the toxins. Protein increase

Table 4.1 Chemical mediators of inflammation

Mediator	Characteristics and role in inflammation
A. *Cell factors*	
Histamine	Stored in mast cells, basophil and eosinophil leukocytes, and platelets
Release from sites of storage is stimulated by complement components C3a and C5a and by lysosomal proteins released from neutrophils	
Responsible for vasodilation and the immediate phase of increased vascular permeability	
Lysosomal compound	Released from neutrophils and includes cationic proteins, which may increase vascular permeability, and neutral proteases, which may activate complement
Prostaglandins	Long-chain fatty acids derived from arachidonic acid and synthesized by many cell types. Some prostaglandins potentiate the increase in vascular permeability caused by other compounds
Leukotrienes	Synthesized from arachidonic acid, especially in neutrophils, and have vasoactive properties
5-Hydroxytryptamine (serotonin)	A potent vasoconstrictor present in high concentrations in mast cells and platelets
Lymphokines	Released by lymphocytes and may have vasoactive or chemotactic effects
B. *Plasma factors*	
Products of complement activation	
C5a	Chemotactic for neutrophils, increases vascular permeability, releases histamine from mast cells
C3a	Similar to but less active than C5a
C567	Chemotactic for neutrophils
C56789	Cytolytic activity
C4b, 2a, 3b	Facilitates phagocytosis of bacteria by macrophages (opsonization of bacteria)
Kinin system	Bradykinin included in the system is the most important vascular permeability factor, also a mediator for pain which is a major feature of acute inflammation
Coagulation factors	Responsible for the conversion of soluble fibrinogen into fibrin, a major component of the acute inflammatory exudate
Fibrinolytic system	Plasmin included in the fibrinolytic system is responsible for the lysis of fibrin into fibrin degradation products, which have a local effect on vascular permeability

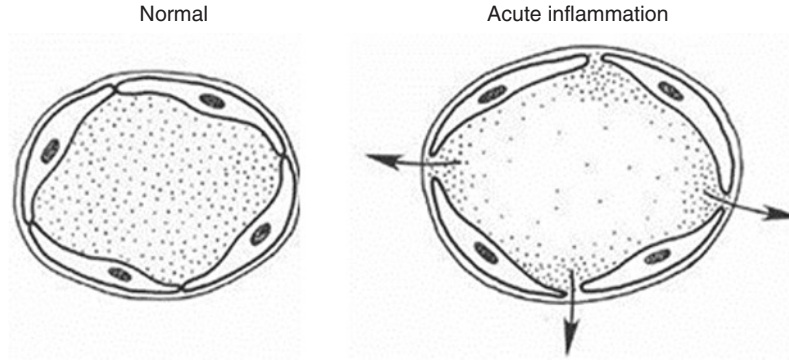

Fig. 4.3 Vasodilation of vessels and opening of the intercellular gaps in inflammation

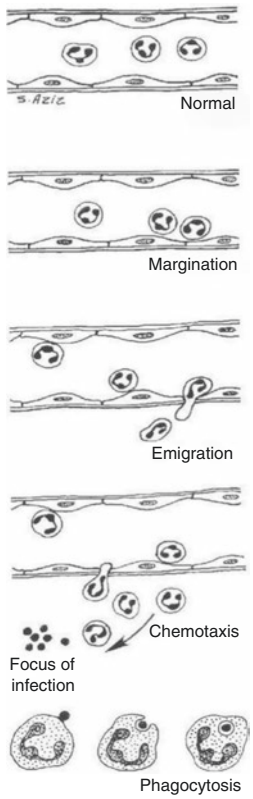

Fig. 4.4 Sequence of cellular changes that accompany inflammation (redraw)

includes globulins that provide protective antibodies, while fibrin helps to limit the spread of bacteria and promotes healing. Exudate varies in composition. In early or mild inflammation, it may be watery (serous exudate) with low plasma protein content and few leukocytes. In more advanced inflammation, the exudate becomes thick and clotted (fibrinous exudate). When large numbers of leukocytes accumulate (Fig. 4.5), the exudate consists of pus and is called suppurative, while if it contains erythrocytes due to bleeding, it is referred to as hemorrhagic. Pus, accordingly, is a variant of exudate that is particularly rich in leukocytes, mostly neutrophils and parenchymal cell debris.

Exudate should be differentiated from "transudate," which is a fluid with low protein concentration and a specific gravity of less than 1.012. Transudation is associated with normal endothelial permeability [8, 9].

Local Cellular Events

1. Margination.

   After stasis develops, leukocytes will be peripherally oriented along the vascular endothelium, a process called leukocytic margination (Fig. 4.3).
2. Diapedesis (emigration).

   Leukocytes emigrate from the microcirculation and accumulate at the site of injury.
3. Chemotaxis.

   Once outside the blood vessel, the cells migrate at varying rates of speed in interstitial tissue toward a chemotactic stimulus in the inflammatory focus. Through chemoreceptors at multiple locations on their plasma membranes, the cells are able to detect where the highest concentrations of chemotactic factors are and to migrate in their direction. Granulocytes, including the eosinophils, basophils, and some lymphocytes, respond to such stimuli and aggregate at the site of inflammation. The primary chemotactic factors include bacterial products, complement components C5a and C3a, kallikrein and plasminogen activators, products of fibrin degradation, prostaglandins, and fibrinopeptides. Histamine is not a chemotactic factor but facilitates the process. Some bacterial toxins, particularly from gram-negative bacteria and streptococcal streptolysins, inhibit neutrophil chemotaxis [3, 6, 9].
4. Phagocytosis.

   This defense mechanism is particularly important in bacterial infections. The polymorphonuclear leukocytes and macrophages ingest debris and foreign particles.

4.3.1.2 Local Sequelae of Acute Inflammation

Acute inflammation has several possible local sequelae. These include resolution, suppuration (formation of pus), organization, and progression to chronic inflammation. Resolution means complete restoration of tissues to normal. Organization

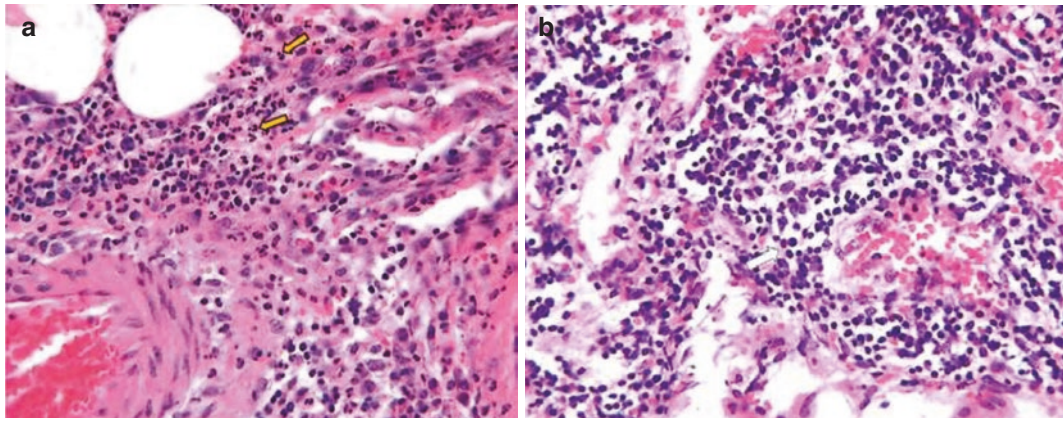

Fig. 4.5 Microphotograph of acute inflammation showing numerous inflammatory cells particularly polymorphonuclear leukocytes, which are identified better (*arrows*) on higher power

of tissues refers to their replacement by granulation tissue with formation of large amounts of fibrin, growth of new capillaries into fibrin, migration of macrophages into the zone, and proliferation of fibroblasts resulting in fibrosis and consequently exudate becoming organized.

4.3.1.3 Chronic Inflammation Associated Changes

Acute inflammation may progress to a chronic form characterized by reduction of the number of polymorphonuclear leukocytes but proliferation of fibroblasts with collagen production. Commonly, chronic inflammation may be primary with no preceding acute inflammatory reaction. Chronic inflammation, whether following acute inflammation or not, is characterized by a proliferative (fibroblastic) rather than an exudative response with predominantly mononuclear cell infiltration (macrophages, lymphocytes, and plasma cells) (Fig. 4.6). Vascular permeability is also abnormal, but to a lesser extent than in acute inflammation with formation of new capillaries.

4.3.1.4 Abscess Formation

Abscess is defined as a collection of pus in tissues, organs, or confined spaces, usually caused by bacterial infection. The first phase of abscess formation is cellulitis, characterized by hyperemia, leukocytosis, and edema, without cellular necrosis or suppuration. This stage is also called phlegmon. It may be followed in some organisms by necrosis and liquefaction and walling off of the pus, which results in abscess formation that can be present with both acute and chronic inflammation.

4.3.2 Systemic Pathophysiological Changes of Inflammation

Three major systemic changes are associated with inflammation: leukocytosis, fever, and an increase in plasma proteins. Leukocytosis is an increased production of leukocytes due to stimulation by several products of inflammation such as complement component C3a and colony-stimulating factors. A febrile response is due to

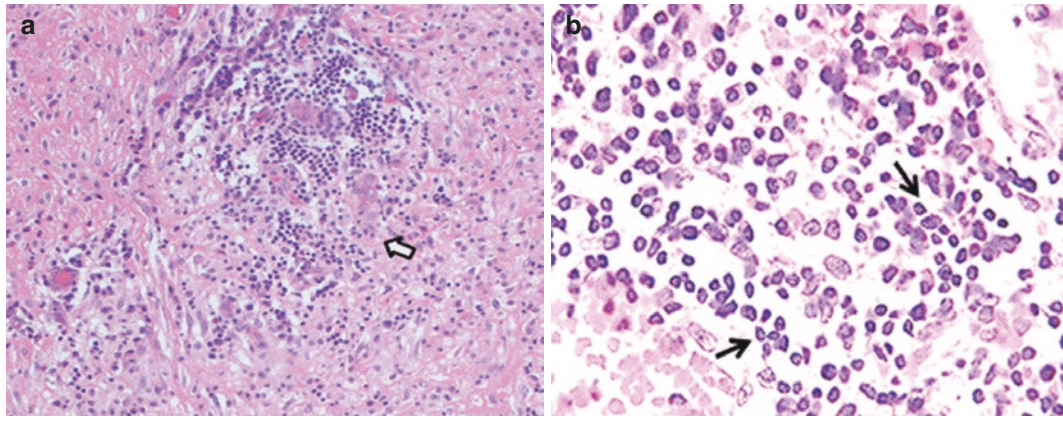

Fig. 4.6 (**a**) Microphotograph illustrating chronic inflammation. The predominant cells are lymphocytes (arrow). (**b**) Higher power of a microphotograph of chronic inflammation clearly showing the mononuclear cells (arrows)

the pyrogens. The increase in plasma proteins is due to the stimulation of the liver by some products of inflammation, leading to increased synthesis of certain proteins referred to as acute-phase reactants which include C-reactive protein, fibrinogen, and haptoglobin and are anti-inflammatory [3].

4.3.3 Pathophysiological Changes of Healing

Healing of tissue after injury is closely linked to inflammation since it starts by acute inflammation. Healing may lead to restoration of normal structure and function of the injured tissue (resolution) or to the formation of a scar consisting of collagen (repair) when resolution cannot be achieved because the tissue is severely injured or cannot regenerate.

In either case, acute inflammation occurs first and for this reason is considered the defensive phase of healing. Healing (resolution and repair) occurs in two overlapping phases, reconstruction and maturation, and may take as long as 2 years. The reconstructive phase starts 3–4 days after injury, continues for approximately 2 weeks, and is characterized by fibroblasts followed by collagen synthesis. The maturation phase is characterized by cell differentiation, scar formation, and remodeling of the scar; it begins several weeks after injury and may take up to 2 years to complete.

4.4 Pathophysiology of Major Soft Tissue Inflammation

4.4.1 Abdominal Inflammation

An abdominal abscess may be formed in an abdominal organ or within the abdomen outside the organs. There are several types of abdominal infection: abscess; cellulitis (phlegmon), i.e., early inflammation of the soft tissue prior to or without formation of an abscess. Abscesses fall into three categories (Fig. 4.7):

The organisms causing abscesses may reach the tissue by direct implantation such as penetrating trauma, may spread from contiguous infection, through hematogenous or lymphatic routes from a distant site, or through migration of resistant flora into an adjacent, normally sterile area such as in perforation of an abdominal viscus.

Factors predisposing to abscess formation include impaired host defense mechanisms; trauma/surgery; obstruction of urinary, biliary, or respiratory passages; foreign bodies; chemical or immunological irritation; and ischemia. Abdominal surgery (particularly of the colon, appendix, and biliary tree) and trauma are the most common; less common are appendicitis,

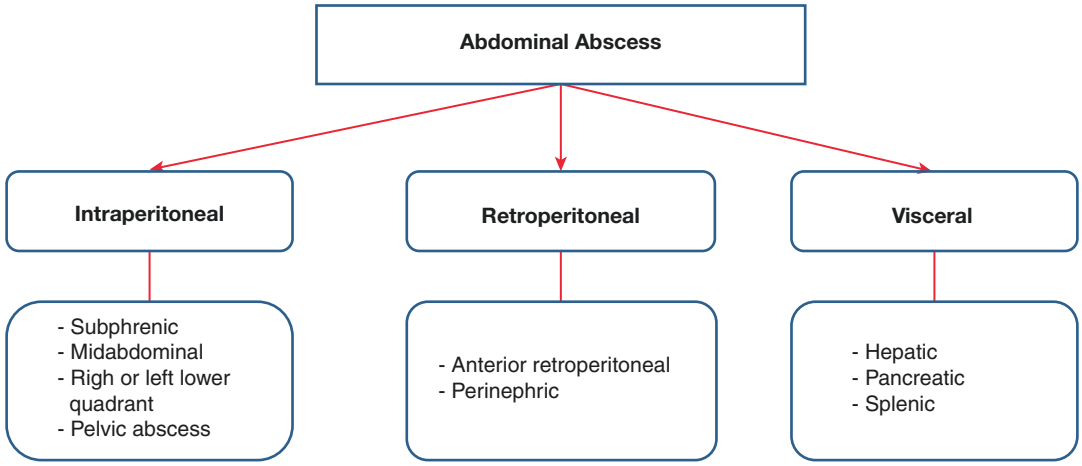

Fig. 4.7 Categories of abdominal abscess

diverticulitis, and pelvic inflammatory disease. The formation of fibrin in the abdominal cavity is a common pathophysiological pathway for abdominal abscess formation due to diminished fibrin degradation. Hyaluronan-based agents were found to reduce adhesion formation after surgery and reduce abscess formation in experimental peritonitis. Possible mechanisms of action of hyaluronan include modulation of the inflammatory response and enhanced fibrinolysis [10]. Low pH, large bacterial inocula, poor perfusion, the presence of hemoglobin, and large amounts of fibrin (which impedes antibiotic penetration) make the abscess a cloistered environment that is penetrated poorly by many antimicrobial therapies [11, 12]. Therefore, management of these infections requires prompt recognition, early localization, and effective drainage, as well as appropriate antimicrobial use. Once the diagnosis is made and the abscess is localized, treatment should begin promptly. Percutaneous or open surgical drainage should be used. Broad-spectrum antibiotics should be given until culture and sensitivity data are obtained. Localization is crucial since, for example, percutaneous drainage is inappropriate for abscesses in certain locations such as the posterior subphrenic space or in the porta hepatis. In the liver, abscesses occur in the right lobe in approximately 95% of the cases, and in 70% of cases, the liver abscesses are solitary [13].

Accumulation of leukocytes in the abscess is the pathophysiological basis for using labeled white blood cells for abscess imaging. In the acute phase, migration of leukocytes is vigorous. Later, the migration rate slows, and the cell type changes from predominantly neutrophils to mononuclear cells (lymphocytes, plasma cells, and macrophages). This pathophysiological change associated with the chronic state explains the better diagnostic accuracy of labeled leukocyte scans in acute as opposed to chronic abscesses.

Inflammatory bowel disease (IBD) is an idiopathic disease, probably involving an immune reaction of the body to its own intestinal tract. The two major types of IBD are ulcerative colitis (UC) and Crohn's disease (CD). Crohn's disease is also referred to as regional enteritis, terminal ileitis, or granulomatous ileocolitis. IBD is a disease of industrialized nations and observed most commonly in Northern Europe and North America. Incidence among whites is approximately four times that of other races, slightly greater in females and higher in Ashkenazi Jews (those who have immigrated from Northern Europe) than in other groups. The risk of developing UC is higher in nonsmokers and former

smokers than in current smokers. Incidence peaks in the second and third decades of life. A second smaller peak occurs in patients aged 55–65 years. CD and UC can occur in childhood, although the incidence is much lower in children younger than 15 years with some differences in presentation and more negative effect on quality of life in younger age group [14].

The etiology of IBD is unsettled. Suspected factors include environmental, infectious, genetic, autoimmune, and host factors. A great deal of research has been performed to discover potential genes linked to IBD. One of the early linkages discovered was on chromosome 16 (*IBD1* gene), which led to the identification of the *NOD2* gene (now called *CARD15*) as the first gene clearly associated with IBD (as a susceptibility gene for Crohn's disease). Studies have also provided strong support for IBD susceptibility genes on chromosomes 5 (5q31) and 6 (6p21 and 19p). None of these mechanisms have been implicated as the primary cause, but they are postulated as potential causes. The lymphocyte population in persons with IBD is polyclonal, making the search for a single precipitating cause difficult. The trigger for the activation of the immune response has not been defined. However, possible triggers include a pathogenic organism (unidentified yet), an immune response to an intraluminal antigen (e.g., cow's milk protein), or an autoimmune process with immune response to an intraluminal antigen and a similar antigen present on intestinal epithelial cells. In any case, activation of the immune system leads to inflammation of the intestinal tract, both acute and chronic [15–22].

The pathophysiology of IBD is still incompletely understood and is under active investigation, but the common end pathway is inflammation of the mucosal lining of the intestinal tract, causing ulceration, edema, bleeding, and fluid and electrolyte loss. The inflammation of the intestinal mucosa includes both acute inflammation with neutrophilic infiltration and chronic with mononuclear cell infiltration (lymphocytic and histiocytic) [23].

In UC, inflammation always begins in the rectum, extends proximally a certain distance, and then abruptly stops. A clear demarcation exists between involved and uninvolved mucosa. The rectum is always involved in UC, and no "skip areas" are present. UC primarily involves the mucosa and the submucosa, with formation of crypt abscesses and mucosal ulceration. The mucosa typically appears granular and friable. In more severe cases, pseudopolyps form, consisting of areas of hyperplastic growth with swollen mucosa surrounded by inflamed mucosa with shallow ulcers. In severe UC, inflammation and necrosis can in rare cases extend below the lamina propria to involve the submucosa and the circular and longitudinal muscles.

UC remains confined to the rectum in approximately 25% of cases. In the remainder of cases, UC spreads proximally and contiguously. Pancolitis occurs in 10% of patients. The small intestine is essentially not involved, except when the distal terminal ileum is inflamed in a superficial manner, referred to as backwash ileitis. Even with less than total colonic involvement, the disease is strikingly and uniformly continuous. As the disease becomes chronic, the colon becomes a rigid foreshortened tube that lacks its usual haustral markings, leading to the lead pipe appearance observed on barium enema. The skip areas (normal areas of the bowel interspersed with diseased areas) observed in CD of the colon do not occur in UC.

CD, on the other hand, consists of segmental involvement by a nonspecific granulomatous inflammatory process. The most important pathological feature is the involvement of all layers of the bowel, not just the mucosa and the submucosa, as is characteristic of UC.

Furthermore, CD is discontinuous, with skip areas interspersed between one or more involved areas. Late in the disease, the mucosa develops a cobblestone appearance, which results from deep longitudinal ulcerations interlaced with intervening normal mucosa. The three major patterns of involvement in CD are (1) disease in the ileum and cecum, occurring in 40% of patients; (2)

disease confined to the small intestine, occurring in 30% of patients; and (3) disease confined to the colon, occurring in 25% of patients. Rectal sparing is a typical but not constant feature of CD. However, anorectal complications (e.g., fistulas, abscesses) are common. Much less commonly, CD involves the more proximal parts of the GI tract, including the mouth, tongue, esophagus, stomach, and duodenum. CD causes three patterns of involvement: (1) inflammatory disease, (2) strictures, and (3) fistulas.

The incidence of gallstones and kidney stones is increased in CD because of malabsorption of fat and bile salts. Gallstones are formed because of increased cholesterol concentration in the bile, caused by a reduced bile salt pool. Patients who have CD with ileal disease or resection also are likely to form calcium oxalate kidney stones. With the fat malabsorption, unabsorbed long-chain fatty acids bind calcium in the lumen. Oxalate in the lumen normally is bound to calcium. Calcium oxalate is poorly soluble and poorly absorbed; however, if calcium is bound to malabsorbed fatty acids, oxalate combines with sodium to form sodium oxalate, which is soluble and is absorbed in the colon (enteric hyperoxaluria). The development of calcium oxalate stones in CD requires an intact colon to absorb oxalate. Patients with ileostomies do not develop calcium oxalate stones. Extraintestinal manifestations of IBD include iritis, episcleritis, arthritis, and skin involvement, as well as pericholangitis and sclerosing cholangitis.

The most common causes of death in IBD are peritonitis with sepsis, malignancy, thromboembolic disease, and complications of surgery. Malnutrition and chronic anemia are observed in long-standing CD. Children with CD or UC can exhibit growth retardation.

Patients with UC most commonly present with bloody diarrhea, whereas patients with CD usually present with non-bloody diarrhea. Abdominal pain and cramping, fever, and weight loss occur in more severe cases. The presentation of CD is generally more insidious than that of UC. UC and CD are generally diagnosed using clinical, endoscopic, and histologic criteria. However, no single finding is absolutely diagnostic for one disease or the other. Furthermore, approximately 20% of patients have a clinical picture that falls between CD and UC; they are said to have indeterminate colitis. Accordingly, imaging may be needed for the detection and for evaluation of the disease activity during its course.

4.4.2 Chest Inflammation

The chest is a common site of various types of infection, acute and chronic. Such infections are frequent in the elderly and in immunosuppressed patients, including cancer patients. Common inflammatory conditions relevant to nuclear medicine include pneumonia, sarcoidosis, diffuse interstitial fibrosis, and *Pneumocystis* (*jirovecii*) *carinii* pneumonia (see also Chap. 8).

4.4.2.1 Sarcoidosis (See also Chap. 8)

Sarcoidosis is an inflammatory condition of uncertain etiology characterized by the presence of noncaseating granulomas involving multiple organs. The disease is recognized as a member of a large family of granulomatous disorders and has been reported from all parts of the world. Current evidence points to genetic predisposition and exposure to yet unknown transmissible agent(s) and/or environmental factors as etiological agents [24]. Recently it has been recognized to be a Th1-mediated disease as it is dominated by gene signatures associated with IFNȳ signaling [25].

The lung is most commonly and usually the first site of involvement, and the inflammatory processes extend through the lymphatics to the hilar and mediastinal nodes. The lung is involved in more than 90% of cases. Pulmonary sarcoidosis starts as diffuse interstitial alveolitis, followed by the characteristic granulomas. Granulomas are present in the alveolar septa as well as in the walls of the bronchi and pulmonary arteries and veins. The center of the granuloma contains epithelioid cells derived from mononuclear phagocytes, multinucleated giant cells, and macrophages. Lymphocytes, macrophages, monocytes, and fibroblasts are present at the

periphery of the granuloma [26]. Sarcoidosis represents a challenge to clinical investigation because of its unpredictable course, uncertain response to therapy, and diversity of potential organ involvement and clinical presentations [27]. The diagnosis is based on a compatible clinical and/or radiological picture, histopathological evidence of noncaseating granulomas in tissue biopsy specimens, and exclusion of other diseases capable of producing similar clinical or histopathological appearances. Even microscopically, the noncaseating granulomas are not specific [24]. Infection by mycobacterial species other than *Mycobacterium tuberculosis* frequently leads to the production of noncaseating granulomas [28]. The condition is underdiagnosed in some areas. However, owing to the increasing awareness, it is being diagnosed more frequently than a few decades ago [26].

The disease runs a benign course with spontaneous remission of the activity though some degree of residual pulmonary function abnormality persists. Only a minority of patients develop complicated disease that may lead to blindness, renal failure, liver failure, and heart involvement.

Advanced age, the presence of pulmonary symptoms, the presence of parenchymal lesions on chest radiograph, a previous history of treatment with corticosteroids, and the presence of extrathoracic involvements at the time of detection are possible prognostic factors in patients with sarcoidosis. The mode of onset and the extent of the disease are also related to prognosis. An acute onset with erythema nodosum or asymptomatic bilateral hilar lymphadenopathy usually heralds a self-limiting course, whereas an insidious onset, especially with multiple extrathoracic lesions, may be followed by relentless, progressive fibrosis of the lungs and other organs.

4.4.2.2 *Pneumocystis carinii* (jirovecii) Pneumonia

Pneumocystis carinii (*jirovecii*) pneumonia (PCP) is a condition that may be endemic or epidemic. It is caused by *Pneumocystis jirovecii* which is a common and potentially lethal opportunistic pneumonia-causing fungus in immunocompromised patients. *Pneumocystis jirovecii* pneumonia (PCP) is classically associated with acquired immunodeficiency syndrome (AIDS), but it also affects patients with malignancy, rheumatologic conditions, or transplantation. The condition can be common also in premature infants and debilitated children, but it is also seen in congenital immunodeficiency and in patients who are receiving chemotherapy and corticosteroids. It remains a significant cause of morbidity and mortality in human immunodeficiency virus and nonhuman immunodeficiency virus-associated immunosuppressed patients [29]. It is the most common infection in AIDS patients, and it remains an important cause of morbidity and mortality [30]. Pathophysiologically, *Pneumocystis jirovecii* adheres to the surface epithelium of type 1 alveolar cells, which stimulates cytokines, chemokines, and cellular infiltrate in the lungs to eradicate the infection. In immunocompetent hosts, this results in a mild inflammatory response with minimal damage to the lung. However, patients with a diminished immune response due to lack or incomplete function of certain immune system components develop hyperinflammatory responses that cause direct damage to the lung [31]. The introduction of highly active antiretroviral therapy in industrialized nations however has led to dramatic declines in the incidence of AIDS-associated complications, including PCP. In the developing countries, no decline has occurred [32]. Transmission is usually airborne. The pathological changes are predominantly in the lungs with an inflammatory reaction consisting of plasma cells of variable amount, monocytes, and histiocytes. The diagnosis is currently established through identification of the organisms in bronchial secretions obtained by bronchoalveolar lavage or bronchial washings [33]. Gallium-67 is an important imaging modality that helps in the diagnosis and evaluation of the activity of the disease.

4.4.2.3 Interstitial Pulmonary Fibrosis

Idiopathic pulmonary fibrosis is a rare disease characterized by chronic, progressive irreversible interstitial lung fibrosis along with inflammatory changes of unknown cause. Clinically, the condition is often diagnosed at an advanced stage and carry a poor prognosis. The median

estimated survival time from the time of diagnosis is 2–5 years. Recently several subtypes have been clearly identified with different outcomes [34, 35]. Early intervention is crucial to improve the prognosis. The pathologic changes of parenchymal inflammation and interstitial fibrosis start with alveolitis followed by derangement of the alveolar-capillary units, leading progressively to the end stage of fibrosis. There is a correlation between the inflammatory activity and the amount of gallium-67 activity in the lungs [36] and is recommended as useful for monitoring the results of therapy [37].

4.4.2.4 Coronavirus Disease 2019 Pneumonia

The coronavirus disease 2019 is caused by SARS-CoV-2. The virus causes respiratory, gastrointestinal, and neurological diseases and may lead to severe acute respiratory syndrome. It is transmitted primarily via large respiratory droplets during close face-to-face contact. Infection can spread by asymptomatic, presymptomatic, and symptomatic carriers. The average time from exposure to the onset of symptoms is 5 days, and 97.5% of patients who develop symptoms do so within an average of 11.5 days [38]. When the virus is transmitted, it directly infects cells of the upper and lower respiratory tract, especially nasal ciliated and alveolar epithelial cells [38]. Coronaviruses are large, enveloped single-stranded RNA viruses that can be found in humans and other mammals, such as dogs, cats, chickens, cattle, pigs, and birds. The virus causes respiratory, gastrointestinal, and neurological diseases.

The virus causes respiratory, gastrointestinal, and neurological diseases. Clinically, it presents with a variety of signs and symptoms and may also be asymptomatic. When symptomatic, the presentation includes fever, dry cough, shortness of breath, fatigue, myalgias, nausea and/or vomiting or diarrhea, headache, weakness, loss of taste, and rhinorrhea. Diagnosis is made by detection of SARS-CoV-2 via reverse transcription polymerase chain reaction (PCR) testing, although false-negative test results occur.

4.4.3 Renal Inflammation

Urinary tract infection (UTI) is among the most common infections which can occur in either an uncomplicated host setting with no underlying structural or functional abnormality of the genitourinary tract; or complicated, where there is. For complicated situations, common predisposing factors are the presence of a foreign body, including urinary catheter, or disruption of normal urinary flow by obstruction or retention [39]. The presence of a urinary catheter, or other urine drainage device, provides a ready scaffold for organisms to develop a biofilm, which in turn shields organisms from being eradicated successfully. Similarly the presence of renal calculi similarly can be linked to biofilm production [39].

Urinary tract infection is common particularly in children. There are two main varieties of acute renal infection: pyelitis, which is confined to the renal pelvis, and pyelonephritis, where the renal parenchyma is also involved. It is not always possible to differentiate between the two conditions on clinical grounds. The pathology of acute pyelitis is not very well understood. The importance of the condition, however, lies in the fact that recurrent subclinical attacks are believed to be significant in the pathogenesis of chronic pyelonephritis.

The number of patients with chronic kidney disease and consequent end-stage renal disease is rising worldwide [40]. End-stage kidney disease, defined as that requiring dialysis or receipt of a transplant or that which may lead to death from chronic kidney failure, generally affects less than 1% of the population [37]. Among today's challenges is to identify those at greatest risk for end-stage renal disease and intervene effectively to prevent progression of early chronic kidney disease and conditions leading to chronic disease [41].

Rarely, uncomplicated acute pyelonephritis causes suppuration and renal scarring. However, urinary infections in patients with renal calculi, obstructed urinary tract, neurogenic bladder, or diabetes are frequently much more destructive and have ongoing sequelae [42].

4.4.3.1 Acute Pyelonephritis

Acute pyelonephritis is a common medical problem. The diagnosis and management of this condition is complex. Patients initially diagnosed with pyelonephritis typically exhibit symptoms and laboratory evidence suggesting infected urine, with signs referable to upper urinary tract infection. However, no consistent set of signs and symptoms are sensitive and specific for this diagnosis. Symptoms of acute pyelonephritis generally develop rapidly over a few hours or a day. Symptoms of lower UTI may or may not be present. These include dysuria; urinary frequency, hesitancy, and urgency; gross hematuria; and suprapubic discomfort, heaviness, pain, or pressure. Additionally, flank pain and tenderness, unilateral or sometimes bilateral, are present. Fever is not always present. When present, it is not unusual for the temperature to exceed 103 °F (39.4 °C). Rigor, chills, malaise, and weakness may be present. Anorexia, nausea, vomiting, and diarrhea may also be present. Most patients have significant leukocytosis, pyuria with leukocyte casts in the urine, and bacteria on a gram stain of unspun urine.

Many conditions and clinical situations are associated with an increased risk of pyelonephritis. Table 4.2 lists common risk factors.

Table 4.2 Common risk factors for pyelonephritis

Mechanical factors
• Obstruction
• Prostatic infection
• Calculi
• Urinary diversion procedure
• Infected cysts
• External drainage with urinary catheters or nephrostomy tubes
• Stents
• Vesicoureteral reflux
• Neurogenic bladder
• Bladder or renal abscesses
• Fistulas
• Recent urinary tract instrumentation
Metabolic and hormonal factors
• Diabetes mellitus
• Pregnancy
• Renal impairment
• Malakoplakia
• Primary biliary cirrhosis
Immune factors
• Transplant recipients
• Neutropenia
• Congenital or acquired immunodeficiency syndromes
Infectious factors (unusual pathogens)
• Yeasts and fungi
• *Mycoplasma* species
• Resistant bacteria, including *P. aeruginosa*
• Calculi-predisposing bacteria, including *Proteus* species and *Corynebacterium urealyticum*
Other factors
• Uncircumcised penis
• Old age
• Recent antimicrobial use

Adopted from [43, 44]

Pyelonephritis is significantly more common in females (higher in white than in black) compared to males. Approximately 10–30% of women develop a symptomatic UTI at some point in their lives.

Acute pyelonephritis is a bacterial infection of the kidney with acute inflammation of the pyelocaliceal lining and renal parenchyma centrifugally along medullary rays. This can occur by more than one way. Most often it occurs because of ascending infection from the lower urinary tract (Fig. 4.8). The initial colonization of the walls of the ureter is in areas of turbulent flow which leads to paralysis of peristalsis. Dilation and functional obstruction result in subsequent pyelonephritis. Another way is by direct reflux of bacteria. Hematogenous spread to the kidney by gram-positive and less likely by gram-negative organisms is the third way that can occur. This has become less prevalent since the advent of rapid use of antibiotics. Little or no evidence supports lymphatic spread.

Grossly, the kidney is enlarged and edematous. The cut surface may show small abscesses in the cortex, and more often there are wedge-shaped purulent areas streaking upward from the medulla, with normal areas of the kidney tissue intervening in between infected zones (Fig. 4.9).

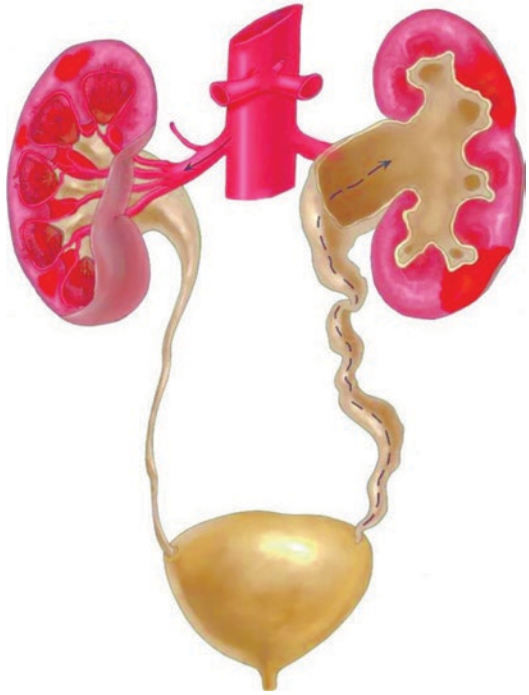

Fig. 4.8 Diagram illustrating the routes of inducing urinary tract infection. The *left-hand side* represents the hematogenous route, while the *right-hand side* represents the retrograde route such as with vesicoureteral reflux

Frequently, the pelvis and calyces are inflamed and dilated. In severe infection, renal papillary necrosis may be present.

Microscopically, there is intense inflammation, with infiltration of polymorphonuclear leukocytes throughout the interstitial tissue and abscess formation. There is destruction of the tubules, but the glomeruli and blood vessels are often unaffected. The disease remains essentially focal in character, with areas of normal tissue. Following treatment and removal of predisposing factors such as obstruction, healing may occur, leaving coarse scars which stretch from the medulla to the capsule of the kidney.

4.4.3.2 Chronic Pyelonephritis

Chronic pyelonephritis is a chronic condition affecting the pelvis and parenchyma and resulting from recurrent or persistent renal infection. It occurs almost exclusively in patients with major anatomic anomalies, including urinary tract obstruction, struvite calculi, renal dysplasia, or, most commonly, vesicoureteral reflux (VUR) in young children. Grossly, the kidney shows normal areas alternating with zones of scarring.

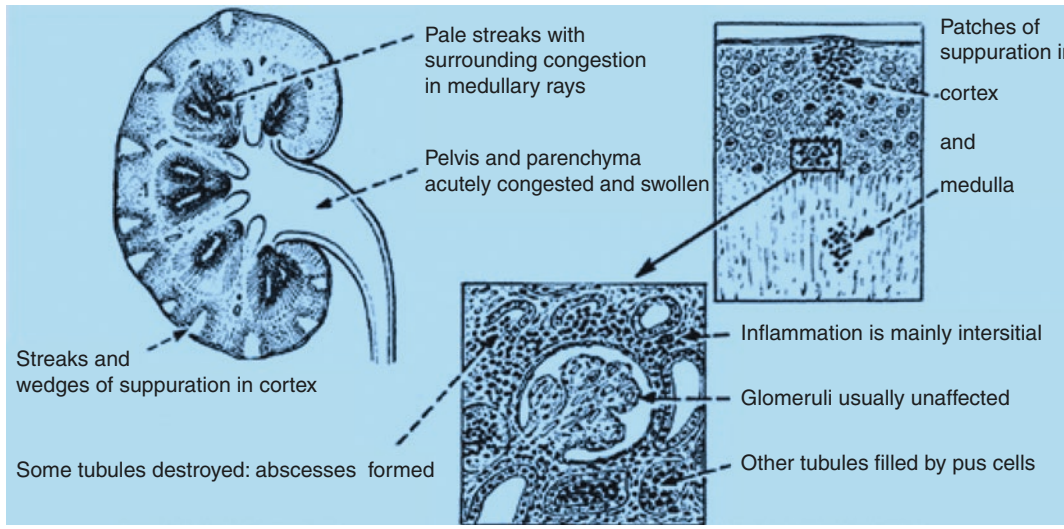

Fig. 4.9 Acute pyelonephritic changes (modified from [45] with permission)

Wedge-shaped scars can be seen on the subcapsular surface of the kidney. The appearance differs, depending on the presence or absence of obstruction. Chronic pyelonephritis in the presence of intra- or extrarenal obstruction shows dilation of the pelvocalyceal system and sometimes peripelvic fibrosis. If no obstruction is present, the pelvic change is in the form of peripelvic fibrosis rather than dilation (Fig. 4.10).

Microscopically, the scarred areas show changes in the interstitium and tubules. The interstitial tissue shows infiltration by predominantly lymphocytes and plasma cells. The tubules become atrophic and may collapse (Fig. 4.11). The glomeruli may be normal in some cases, while in others periglomerular fibrosis is present.

4.4.3.3 Scrotal Inflammation (See Chap. 7)

Inflammation of the epididymis (epididymis) is common, and sometimes it involves testicles (epididymoorchitis). The condition may be infectious or noninfectious. Noninfectious may follow urinary obstruction or can be drug-induced. It can affect children and adults. Bacterial ascent through the urogenital tract is the most common etiology in acute infectious epididymitis [46].

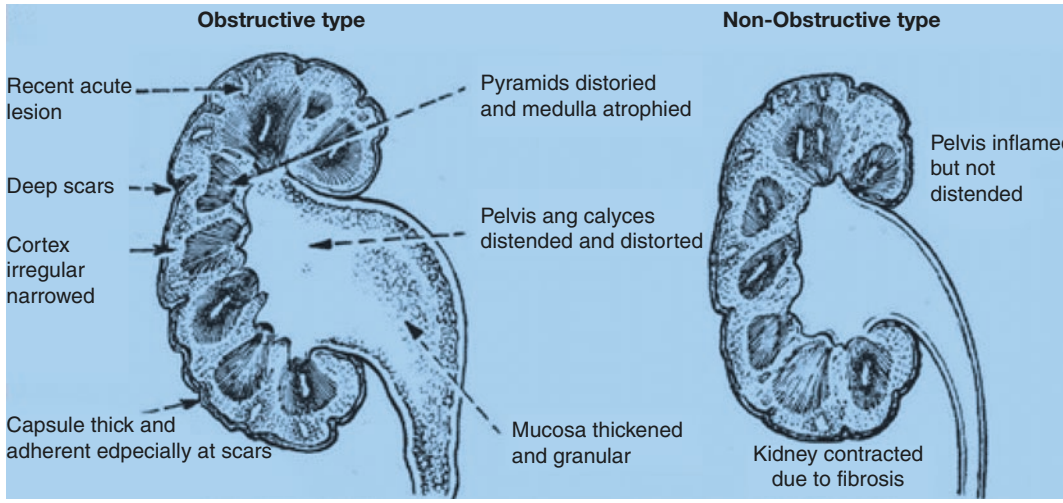

Fig. 4.10 Types of pyelonephritic changes based on whether obstruction is present (from [5] with permission)

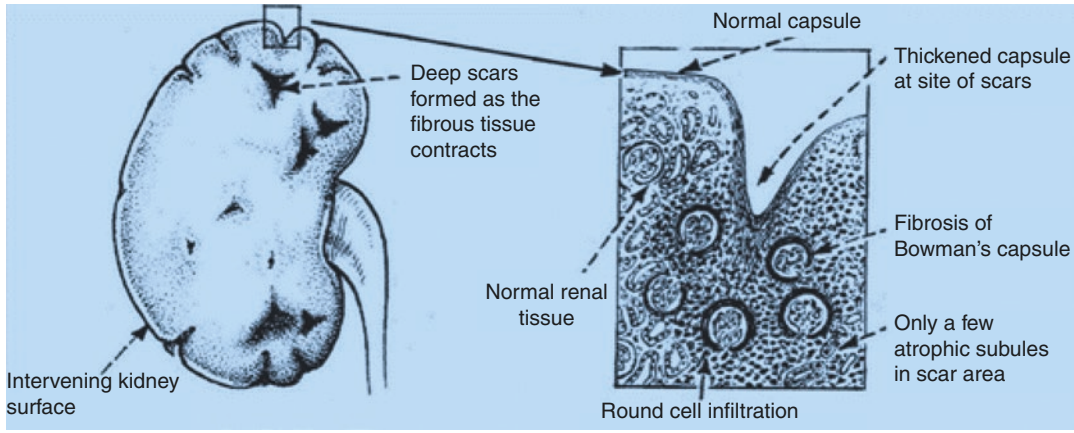

Fig. 4.11 Main pathological changes of chronic pyelonephritis (modified from [45] with permission)

4.4.4 Pathophysiology of Cellulitis

Cellulitis describes infection of the dermis and subcutaneous tissues which lead to pain, erythema, edema, and warmth. It results from disruption of the skin and invasion by microorganisms. Peripheral vascular disease and diabetes increase susceptibility to this form of infection because minor injuries to the skin in the feet or toes can serve as entry points for infection. Other patients susceptible to cellulitis include those with foreign bodies penetrating the skin, such as intravenous catheters and orthopedic hardware [47]. There is a risk for rapid spread of infection in patients with diabetes, immunodeficiency, impaired peripheral circulation, or a history of lymphadenectomy with cellulitis.

4.4.5 Pathophysiology of Endocarditis

Endocarditis is the inflammation of endocardium, which may be infective or non-infective. Infective endocarditis is usually caused by bacteria, commonly, streptococci or staphylococci, or fungi. It may present with fever, heart murmurs, embolic phenomena, petechiae, anemia, and endocardial vegetations. Vegetations may lead to valvular incompetence or narrowing, myocardial abscess, or mycotic aneurysm. Noninfecive endocarditis on the other hand is characterized by accumulation of sterile platelet and fibrin thrombi on cardiac valves and adjacent endocardium. Noninfective endocarditis may sometimes lead to infective endocarditis. Both conditions can result in embolization and impaired cardiac function. Pathophysiologically, the condition develops in three stages; Bacteremia, adhesion (microorganisms adhere to the surface of abnormal or damaged endothelium), and colonization with proliferation of the microorganism leading to inflammation and formation of vegetations. The disease may lead to local and systemic sequalae. Local sequalae include myocardial abscesses, valvular regurgitation which if severe may lead to heart failure and death. Aortitis may also occur due to local spread of infection. Prosthetic valve infections are particularly associated with local consequences. Systemic complications are predominantly due to embolization from vegetations on valvular surfaces. Pulmonary infarction, pneumonia, or empyema may follow right sided lesions while left sided lesions may lead to emboli of kidneys, spleen, central nervous system, skin, and retina [48].

4.4.6 Pathophysiology of Thyroid Gland Inflammation (See also Chap. 6)

Thyroiditis is a group of inflammatory thyroid diseases. It may affect the gland diffusely or focally and can be due to infection by microorganisms or noninfectious. There are many classifications and terminologies for the condition based on clinical, histopathologic, etiology, and other factors. Simply it can be classified into acute, subacute, and chronic [49].

Acute thyroiditis is a rare but serious form secondary to bacteria. Subacute thyroiditis is a painful, inflammatory disease of viral origin. Hashimoto's thyroiditis is chronic thyroiditis due to autoimmune pathogenesis, and patients may be euthyroid, develop hypothyroidism, or thyrotoxicosis that is usually transient. Silent and postpartum thyroiditis is also of autoimmune origin, occurring either sporadically or postpartum and clinically present with transient thyrotoxicosis. Riedel's thyroiditis is a rare chronic inflammatory disorder of uncertain etiology, characterized by dense thyroid fibrosis [50, 51].

4.5 Pathophysiology of Major Skeletal Inflammations

Osteomyelitis indicates an infection involving the cortical bone as well as the marrow (see Chap. 5). It is classified into many types based on several pathological and clinical factors [52–60] including route of infection, patient age, etiology, and onset. Hematogenous osteomyelitis most commonly affects children, and the metaphyses of long bones are the most common sites.

Nonhematogenous osteomyelitis, on the other hand, occurs as a result of penetrating trauma, spread of a contiguous soft tissue infection, or inoculation, as in drug addicts [59–65]. Many organisms have been encountered in the pathogenesis of osteomyelitis, particularly gram-positive organisms, the most common being *Staphylococcus aureus* [65–67]. Like many other pathological conditions of bone, infections cause reactive new bone formation which—among other factors, particularly increased blood flow—is the principle reason for the accumulation of bone-seeking radiopharmaceuticals at the site of skeletal infections.

It is difficult to draw the line between acute and chronic osteomyelitis. Chronic osteomyelitis has been defined as a skeletal infection with a duration as short as 5 days or as long as 6 weeks. It is characterized by less marked inflammatory cell infiltrates than acute infection and may exhibit a variable amount of necrotic tissue. Acute septic arthritis is a medical emergency, since it may result in destruction of the articular cartilage and permanent disability if treatment is delayed [66]. See Chap. 5 for more details on skeletal inflammations.

4.6 Fever and Inflammation of Unknown Origin

Fever of unknown origin (FUO) describes an illness of several episodes of fever exceeding 38.3 °C or at least 3-week duration, with no diagnosis after an appropriate inpatient or outpatient evaluation. There are many causes of fever of unknown origin. Infection accounts for only about 25% of these causes. Neoplasms are responsible for approximately 15–25%. Other etiologies include collagen vascular disease, granulomatous diseases, pulmonary emboli, cerebrovascular accidents, and drug fever.

There are many causes of fever of unknown origin. The causes of FUO include infectious diseases, neoplasms, and noninfectious inflammatory diseases. Many cases (25%) remain undiagnosed after workup. Inflammation, neoplasia, and other causes such as pulmonary emboli, cerebrovascular accidents, and drugs are responsible for FUO [68]. Inflammation of unknown origin (IUO) has a similar definition to the fever of unknown origin but with a temperature not exceeding 38.3 °C and raised inflammatory markers (C-reactive protein [CRP] >30 mg/L and/or increased erythrocyte sedimentation rate on >3 occasions. Both FUO and IUO have similar causes, and the workup is identical for both conditions [69].

FUO can be categorized into four subgroups; (1) classical FUO, (2) nosocomial (health care-associated), (3) neutropenic (immune-deficient), and (4) HIV-related. As with other patients, among immune-compromised patients FUO can be due to infectious and noninfectious causes. The majority of infections included respiratory tract infections (28.8%), secondary bacteremia due to gram-negative bacilli (15.7%), genitourinary tract infections (12.9%), skin and soft tissue infections (11.3%), and primary bacteremia (11.0%). One hundred nine (23%) cases were due to noninfectious conditions such as malignant neoplasm, metastatic disease, and drug-induced fever. Although noninfectious neoplastic-related fever was more common (41%) among non-neutropenic patients, noninfectious drug-induced fever was more common among neutropenic patients (13%). In 47 (10%) cases, the cause of the fever could not be determined [70].

Most cases of FUO in HIV-infected patients are the result of opportunistic infections. In a study using F-18-FDG-PET/CT, the etiology of the FUO was identified in 17 of 20 (85%) patients. The causes of FUO in the patients for whom the etiology was determined included tuberculosis ($n = 8$), lymphoma ($n = 3$), nontuberculous mycobacteria ($n = 3$), pneumococcal infection ($n = 1$), visceral disseminated leishmaniasis ($n = 1$), and dental infection ($n = 1$). The remaining three patients had drug-induced or HIV-related fever. This study also confirms the value of FDG/PET in fever FUO in HIV positive patients similar to non-HIV patients [71].

Since no localizing signs are evident, functional modalities, particularly FDG-PET/CT, are of utmost importance in the workup of patients with FUO. FDG-PET/CT is a sensitive diagnos-

tic technique for evaluating FUO by facilitating anatomical localization of focally increased FDG uptake, thereby guiding further diagnostic tests to achieve a final diagnosis. FDG-PET/CT should become a routine procedure in the workup of FUO when diagnostic clues are absent. FDG-PET/CT appears to be a cost-effective routine imaging technique in FUO by avoiding unnecessary investigations and reducing the duration of hospitalization [71, 72].

4.7 Radiopharmaceuticals for Inflammation Imaging

Many radioisotopes have been used to detect and localize infection (see Table 4.3). Several mechanisms explain the uptake of these radiotracers at the site of infection:

1. Increased vascular permeability.
   (a) ^{111}In and ^{99m}Tc human polyclonal IgG
   (b) ^{111}In monoclonal IgM antibody
   (c) ^{111}In and ^{99m}Tc liposomes
   (d) ^{111}In biotin and streptavidin
   (e) ^{99m}Tc nanocolloids56
   (f) ^{111}In chloride
   (g) ^{67}Ga citrate.
2. Migration of WBCs to the site of infection.
   (a) ^{111}In- and ^{99m}Tc-labeled leukocytes
   (b) ^{99m}Tc anti-WBC antibodies.
3. Binding to proteins at the site of infection, i.e., ^{67}Ga citrate (lactoferrin and other iron-containing proteins).
4. Binding to WBCs at the site of infection.
   (a) Chemotactic peptides.
   (b) Interleukins.
5. Binding to bacteria.
   (a) ^{99m}Tc-labeled ciprofloxacin antibiotic
   (b) ^{67}Ga citrate.
6. Metabolic trapping, i.e., F-18 fluorodeoxyglucose.

Since there are limitations to the radiopharmaceuticals available for imaging infection, the search continues for better agents with ideal properties. They should:

1. Be easy to prepare.
2. Have low cost and wide availability.
3. Ensure rapid detection and localization of infections (<3 h).
4. Have low toxicity and produce no immune response.
5. Clear rapidly from the blood with no significant uptake in the liver, spleen, GI tract, bone, kidneys, bone marrow, or muscle.
6. Clear rapidly from the background.
7. Have high specificity and sensitivity and be able to differentiate infection from other causes of inflammation and tumors.
8. Be able to differentiate acute from chronic infection.

Table 4.3 Radiopharmaceuticals for imaging infection [66, 73–80]

Gallium-67 citrate
Gallium-68 citrate, Gallium-68 transferrin
Labeled WBCs using ^{111}In-oxine or ^{99m}Tc-HMPAO (^{99m}Tc-hexamethylpropyleneamine oxime)
Labeled particles
Nanocolloid
Liposomes
Labeled large protein
Nonspecific immunoglobulins
Specific immunoglobulins: polyclonal and monoclonal
Antigranulocyte monoclonal antibodies
Anti-E-selectin antibodies
Labeled receptor-specific small proteins and peptides
Chemotactic peptides
Interleukins
Labeled antibiotics: ciprofloxacin
^{18}F-FDG
Labeled Vitamin B
In-111 Biotin

Gallium-67 has been used for many years to detect inflammation. The multiple mechanisms of uptake of gallium by inflammatory tissue include the following:

1. Increased vascular permeability.
2. Gallium-67-binding substances at the site of inflammation.
   (a) Transferrin (due to leakage of plasma proteins).
   (b) Lactoferrin (secreted with lysosomal contents of stimulated or dead neutrophils).
   (c) Siderophores produced by bacteria.
3. Leukocytes: direct uptake.
4. Bacteria: direct uptake.

Sfakianakis et al. [74] found that ^{111}In leukocyte imaging accuracy was best for relatively acute infections (less than 2 weeks) but yielded a 27% false-negative rate among patients with prolonged infections. In a recent meta-analysis which included 6649 articles on prospective and retrospective diagnostic studies performed on patients with diabetes in whom there was a clinical suspicion of osteomyelitis of the foot ^{99m}Tc-HMPAO-labeled WBC scintigraphy and ^{8}F-FDG-PET offer the highest specificity [85]. On the other hand, ^{67}Ga imaging had its highest sensitivity in long-standing processes, with false-negative results of 19% in relatively acute infections of less than 1-week duration [62].

An earlier systematic review of the published studies in humans cited in PubMed written in English, French, German, Italian, and Spanish, it was again found that labeled leukocyte is a sensitive method to localize abdominal abscesses and can guide dedicated US and CT investigations to improve their diagnostic potential [76].

Table 4.4 lists the main advantages and disadvantages of the major radiopharmaceuticals used for inflammation imaging.

Several monoclonal antibodies are used to detect infections. These antibodies are mainly directed against receptors on inflammatory cells.

Labeled antigranulocyte agents most commonly used are intact murine immunoglobulin G (IgG) antibodies against normal cross-reactive antigen-95 (anti-NCA-95, ^{99m}Tc-BW250/183, ^{99m}Tc-besilesomab [Scintimun®]) and the murine Fab fragment of the IgG antibody directed against the glycoprotein cross-reactive antigen-90 (anti-NCA-90, ^{99m}Tc-sulesomab, LeukoScan®). The 99mTc anti-NCA-90 Fab fragments can recognize a specific cross-reacting antigen (NCA-90) (the surface antigenic glycoprotein) on granulocytes, promyelocytes, and myelocytes [77–79]. LeukoScan uptake at the site of infection is explained partly by the migration of circulating antibody-labeled granulocytes to the site of infection. Uptake is also explained by the fact that the greater proportion of the labeled antibody fragment is in a free soluble form which can easily cross capillary membranes, binding to the leukocyte once in situ. This mechanism is favored by the increased capillary permeability at the site of infection. An important advantage of LeukoScan is the 5 min preparation time compared with the 2 h 30 min required by a specialized team for labeling leukocytes. Despite the fact that LeukoScan involves the i.v. injection of mouse proteins, no anaphylactic or other hypersensitivity reactions were observed.

^{99m}Tc ciprofloxacin (*Infecton*) is also being used to image infection. Ciprofloxacin is a broad-spectrum fluoroquinolone antibiotic that inhibits DNA gyrase and/or topoisomerase IV of bacteria. Patients receive ^{99m}Tc ciprofloxacin 10 mCi, and images are obtained at 1, at 3–4, and, occasionally, at 24 h postinjection. ^{99m}Tc ciprofloxacin may be useful in distinguishing infection from inflammation. Early images of noninfectious rheumatologic inflammatory conditions were positive, but activity decreased with time.

^{111}In- and ^{99m}Tc-labeled chemotactic peptide analogs have been used for detecting and localizing infections. Imaging can be performed at less than 3 h postinjection, which compares favorably with the 18–24 h or more for most other agents [65].

Labeled liposomes have been used for scintigraphic imaging of infection and inflammation [79]. Boerman et al. [81] used ^{111}In-labeled sterically stabilized liposomes (long circulating) in rats and showed that the clearance of this agent is similar to that of ^{111}In IgG. The uptake in abscess was twice as high as that of IgG and the abscess was visualized as early as 1 h postinjection. ^{99m}Tc nanocolloid has also been tried but has not gained wide acceptance.

F-18 fluorodeoxyglucose (FDG-PET) is now an important diagnostic agent for infectious and noninfectious soft tissue and skeletal inflammations including inflammatory bowel disease, fevers of unknown origin, rheumatologic disorders, tuberculosis infection, fungal infection, pneumonia, abscess, postarthroplasty infections, chronic and vertebral osteomyelitis, sarcoidosis, and chemotherapy-induced pneumonitis [82–84]. Inflammatory conditions show high FDG uptake which is related to increased glucose metabolism that is produced by stimulated inflammatory cells, macrophage

Table 4.4 Advantages and disadvantages of the main available radiopharmaceuticals for inflammation

	Gallium-67 citrate	^{111}In WBC	^{99m}Tc-WBC	FDG-PET/CT
Advantages	Whole-body imaging	Whole-body imaging	Whole-body imaging/ Earlier diagnosis (2–4 h) Better physical characteristics of technetium than ^{67}Ga and ^{111}In	Whole-body imaging Early results
Disadvantages	Results after 24 h or more Physiological liver, spleen, and bowel activity Uptake in tumors	Tedious procedure Results at 24 h Physiological liver and spleen activity	Tedious procedure Physiological bowel activity by 2 h	High radiation dose

proliferation, and healing [86]. Additionally, the circulating cytokines associated with inflammation as mediators increase the affinity of the glucose transporters for FDG [87]. While uptake of FDG continues to increase at malignant sites for several hours, as can be shown by an incremental increase of the standardized uptake values (SUV), inflammatory lesions peak at approximately 60 min, and their SUV either stabilize or decline thereafter. This difference in the behavior of FDG in malignant versus inflammatory cells can be explained best by the varying levels of enzymes that degrade deoxyglucose-6-phosphate in the respective cells. Glucose-6-phosphatase dephosphorylates intracellular FDG-6-phosphate, allowing it to leave the cell. It has been shown that most tumor cells have low levels of this enzyme, while its expression is high in the mononuclear cells [86–89]. For this reason, imaging at two time points after administration of FDG may prove to be important in differentiating between these two common disorders.

Recent reports described Ga-68-Citrate and Ga-68-transferrin as possible agents for PET-imaging of infection. Ga-68 has half-life of 68 min compared to 78.3 h for Ga-67.

The short half-life of Ga-68 (68 min) helps in lower dosimetry to the patient. Ga-68 compared to FDG is that it is positive only in cases of infection. Preliminary reports suggest Ga-68-Citrate PET/CT is useful in the diagnosis of suspected bone infections with reliable accuracy. Ga-68-Citrate or Ga-68-transferrin was able to detect infected lesions in rats and patients as focal uptake within 30 min [90].

4.8 Infection Imaging

Diagnosis and localization of infection by clinical and laboratory methods is often difficult. The results frequently are nonspecific and imaging may be needed. Imaging of infection may be achieved by either nuclear medicine or other strictly morphological methods. Several nuclear medicine modalities are used to diagnose and localize soft tissue and skeletal infections. These include ^{111}In-labeled white blood cells, ^{67}Ga citrate, IgG polyclonal antibodies labeled with ^{111}In or ^{99m}Tc, monoclonal antibodies such as antigranulocyte antibodies, ^{99m}Tc HMPAO-labeled white blood cells, ^{99m}Tc nanocolloid, ^{99m}Tc-DMSA, ^{99m}Tc-glucoheptonate, ^{99m}Tc-MDP multiphase bone scan, ^{111}In-labeled chemotactic peptide analogs, and F-18-FDG. X-ray, CT, MRI, and ultrasonography are other modalities useful in the diagnosis and localization of both soft tissue and skeletal inflammations. These studies are complementary to the physiological modalities of nuclear medicine.

4.8.1 Imaging of Soft Tissue Infections

The strategy for imaging soft tissue infections depends on the pathophysiological and clinical features, including whether localizing signs and

symptoms are present and the location and duration of the suspected infection.

4.8.2 Imaging When Localizing Signs Present

When there are localizing signs, morphologic modalities such as X-ray, US, CT, and MRI are first used. The advantages of these modalities are numerous, but most importantly, they provide quick results and adequate anatomic details. These studies can be used to guide needle aspiration and abscess drainage. Ultrasound can be used portably for critically ill patients. One of the major limitations of these modalities is the inability to differentiate infected from noninfected tissue abnormalities, particularly in early stages of infection (phlegmon) before formation of abscesses.

The diagnostic accuracy of these morphological modalities may be compromised in cancer patients, and the evaluation of studies that use these techniques may be difficult. This is because the interpretation of these modalities depends on the presence of normal anatomical markers, which may be altered or obliterated by either the cancer treatment or the cancer itself [99]. For example, both CT and MRI are often of little value in distinguishing posttreatment scarring from recurrent tumor.

When the results of the morphological modalities are inconclusive, nuclear medicine techniques may be used to detect abdominal infections. The ability to image the entire body is the major advantage of nuclear medicine modalities (Fig. 4.12). Hence, radionuclide techniques are often used in cases with no localizing signs. In one study, 16% of patients suspected of having abdominal infection in fact had extra-abdominal infections as seen on ^{111}In leukocyte scans [100]. Accordingly, negative morphological modalities, when used first, may be followed by whole-body nuclear imaging. Labeled WBC studies are the most specific for acute infections (Figs. 4.13 and 4.14). Ga-67 is more suitable for infection of longer duration (Fig. 4.15). ^{99m}Tc HMPAO-labeled WBCs frequently are used in critically ill patients [43] after US and/or CT have yielded inconclusive results. It is worthy of note that ^{99m}Tc HMPAO-labeled WBCs provide quicker results than ^{67}Ga- or ^{111}In-labeled WBCs. Minoja et al. [101] reported a sensitivity of 95%, a specificity of 91%, and an accuracy of 94% for ^{99m}Tc-labeled WBC scanning in intensive care unit patients with occult infections. Gallium-67 scan has been reported to have better diagnostic specificity than the C-reactive protein test for abdominal infections [102].

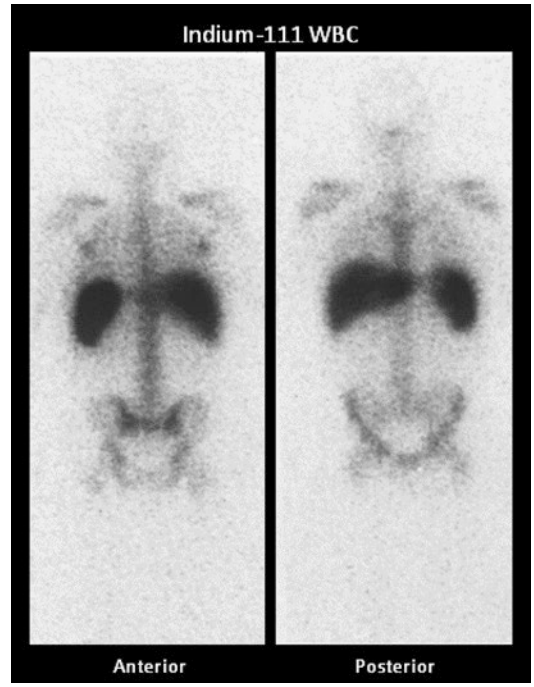

Fig. 4.12 Whole-body 24 h ^{111}In-labeled leukocyte scan obtained in a patient with a 10-day history of fever and no localizing signs. Anterior and posterior images reveal physiological uptake in the bone marrow, liver, and spleen with no abnormal accumulation of labeled cells

4.8.2.1 Imaging Abdominal Infections

Abdominal Abscess

Rapid and accurate diagnosis of an abdominal abscess is crucial. The mortality from untreated abscesses approaches 40% and may reach 100% in some series. The mortality among patients treated reaches 11% [91–98]. Delayed diagnosis is associated with higher mortality in spite of treatment. If localizing signs suggest abdominal infection, morphological modalities, predomi-

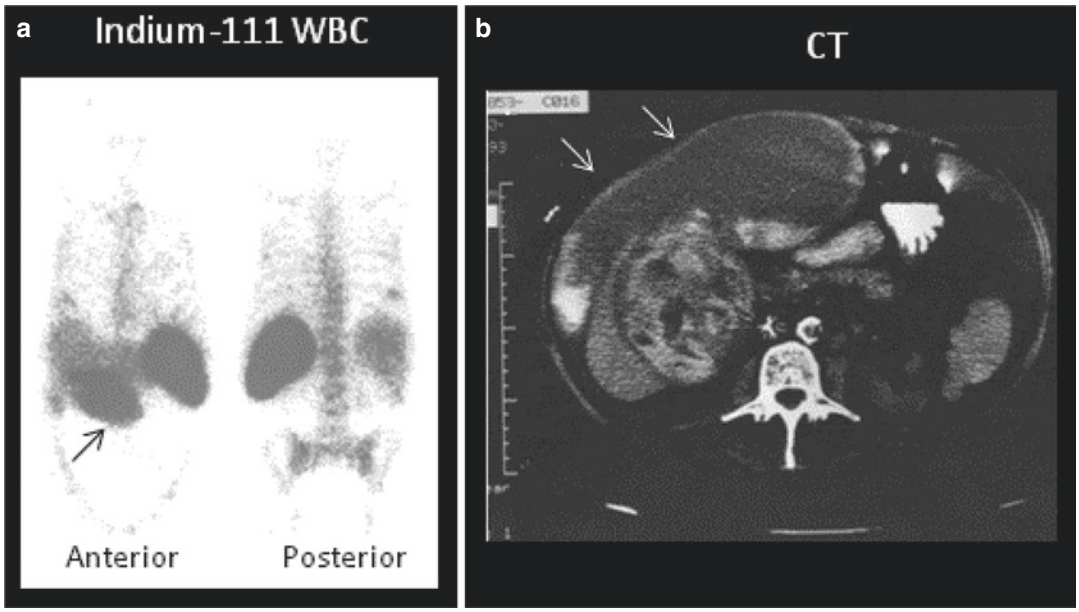

Fig. 4.13 (**a**, **b**) ^{111}In-labeled leukocyte study (**a**) shows a large acute abdominal abscess (*arrow*) corresponding to the finding (*arrows*) on CT (**b**)

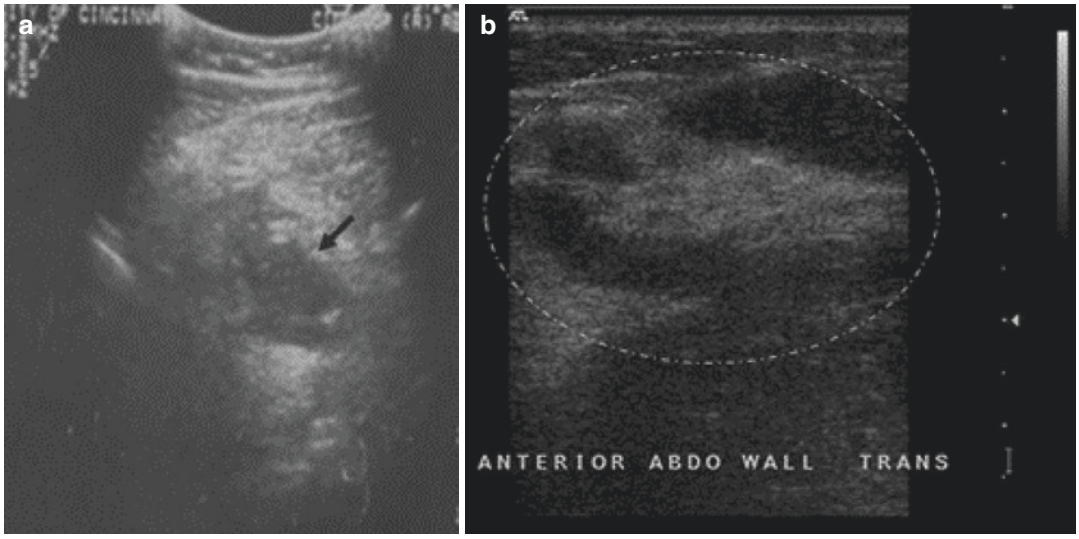

Fig. 4.14 (**a**) Ultrasonographic study of a patient with abdominal pain and malaise. The study helped make the diagnosis of abdominal abscess (*arrow*) and provided accurate localization. (**b**) Ultrasonography of the abdomen revealing infected hydatid liver cyst (circle)

nantly ultrasound (Fig. 4.14) and CT (Fig. 4.15), may be used first, depending on the location of suspected infection in the abdomen. Standard radiographs have low sensitivity, although when seen, findings are specific.

The advantages of these modalities are numerous. Most importantly they provide quick results and adequate anatomical details. These studies can be used to guide needle aspiration and abscess drainage. Ultrasound can be used porta-

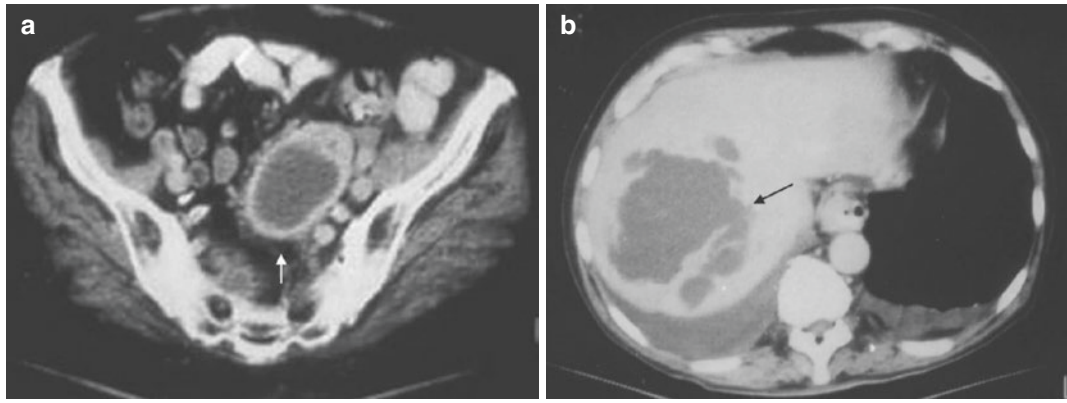

Fig. 4.15 Representative images of CT scans of the abdomen illustrating (**a**) periappendicular abscess (*arrow*) and (**b**) hepatic abscess (*arrow*)

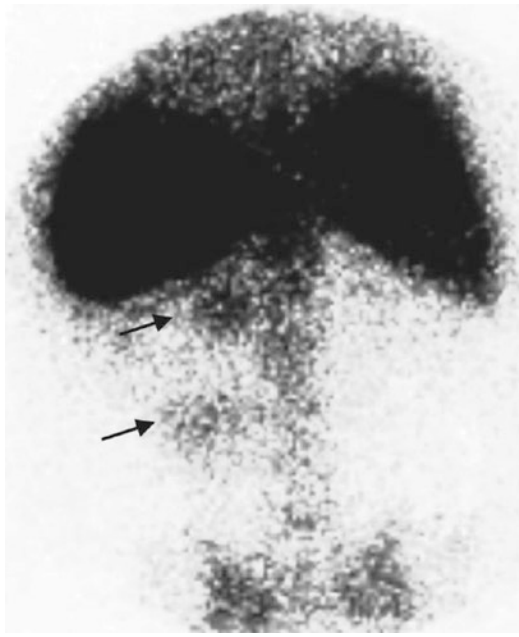

Fig. 4.16 ^{111}In-labeled leukocyte scan posterior projection of the abdomen demonstrating two foci (*arrows*) of abnormal accumulation of labeled cells at the ends of a vascular graft indication infection of the graft

bly for critically ill patients. One of the major limitations of these modalities is the inability to differentiate infected from noninfected tissue abnormalities, particularly in early stages of infection (phlegmon) before the formation of abscesses.

When the results of the morphological modalities are inconclusive, nuclear medicine techniques are used to detect abdominal infections. The ability to image the entire body is the major advantage of nuclear medicine modalities. Hence, radionuclide techniques are often used in cases with no localizing signs. In one study, 16 % of patients suspected of having abdominal infection were shown to have extra-abdominal infections as seen on ^{111}In leukocyte scans [103]. Accordingly, negative morphological modalities, when used first, may be followed by whole-body nuclear imaging. Labeled WBC studies are the most specific for acute infections (Fig. 4.16). ^{67}Ga is more suitable for infection of longer duration (Fig. 4.17). ^{99m}Tc-HMPAO-labeled WBCs frequently used in critically ill patients after US and/or CT have yielded inconclusive results.

Inflammatory Bowel Disease

Upright chest radiography and abdominal series, barium enema, and upper GI CT scanning, MRI, and ultrasonography are the main imaging modalities used for the diagnosis. CT scanning and ultrasonography are best for demonstrating complications such as intra-abdominal abscesses and fistulas. Evaluation of the extent of the disease and disease activity is often difficult. A wide variety of approaches depicting the different stages of the inflammatory response have

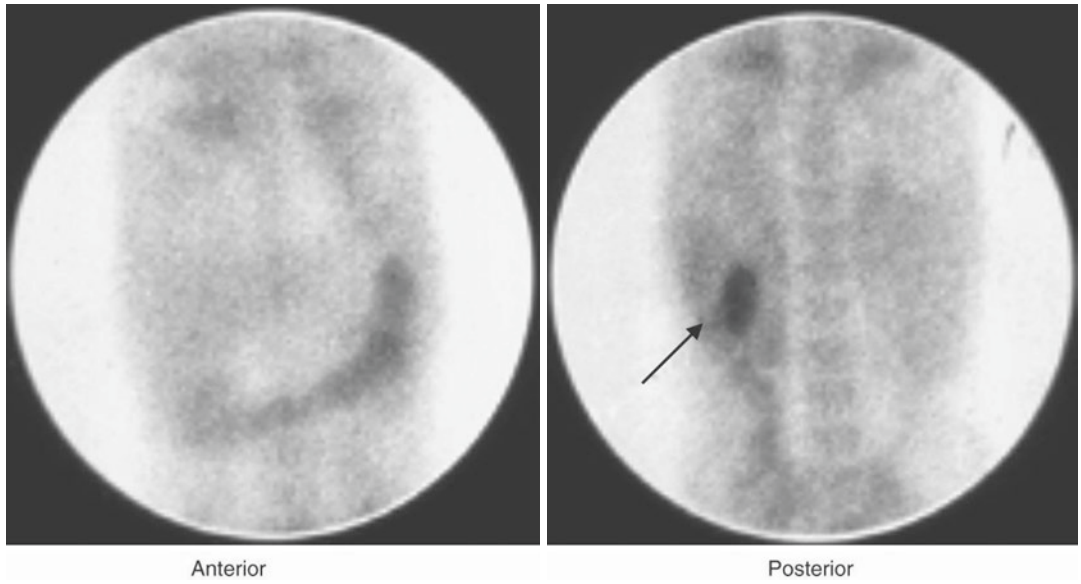

Fig. 4.17 A 72 h gallium-67 image of abdomen anterior and posterior projections for a 21-year-old female with a 6-week history of intermittent fever. No localizing signs were reported. The images demonstrate increased accumulation of gallium-67 in a perirenal abscess (*arrow*) seen in posterior view

been developed. Nonspecific radiolabeled compounds, such as 67Ga citrate and radiolabeled polyclonal human immunoglobulin, accumulate in inflammatory foci mainly due to enhanced vascular permeability [104]. Specific accumulation of radiolabeled compounds in inflammatory lesions results from binding to activated endothelium (e.g., radiolabeled anti-E-selectin), the enhanced influx of leukocytes (e.g., radiolabeled autologous leukocytes, antigranulocyte antibodies, or cytokines), the enhanced glucose uptake by activated leukocytes (18F-fluorodeoxyglucose), or direct binding to microorganisms (e.g., radiolabeled ciprofloxacin or antimicrobial peptides). Scintigraphy using autologous leukocytes, labeled with ^{111}In or ^{99m}Tc, is still considered the "gold standard" nuclear medicine technique for the imaging of infection and inflammation, but the range of radiolabeled compounds available for this indication is still expanding. Positron emission tomography with 18F-fluorodeoxyglucose has been shown to delineate various infectious and inflammatory disorders with high sensitivity. In a study [104], gallium, magnetic resonance imaging (MRI), and PET-FDG were compared for their ability to detect disease activity. PET-FDG showed more than twice as many lesions in the abdomen of patients with Crohn's disease as did gallium. Not all lesions on MRI were FDG positive, suggesting they might represent areas of prior inflammation.

4.8.2.2 Imaging Chest Infections

The role of the chest X-ray cannot be overemphasized. The chest X-ray should be used as the initial imaging modality for most chest pathologies. In many instances, however, an additional modality is needed to evaluate certain chest conditions including infections.

Although CT often clearly depicts chest pathology including infections, ^{67}Ga is still used in such cases particularly if PET is not available. ^{111}In leukocytes have limited utility for chest infections. Siemon et al. [104] studied ^{67}Ga imaging in a variety of pulmonary disorders and has excellent sensitivity and specificity (Table 4.5). Gallium-67 has also been widely

used in AIDS patients to detect PCP (Fig. 4.18). It is highly sensitive and correlates with the response to therapy. In a study comparing ^{67}Ga, bronchial washing, and transbronchial biopsy in 19 patients with PCP and AIDS, ^{67}Ga and bronchial washing were 100% sensitive compared with 81% for transbronchial biopsy [106]. ^{67}Ga is also valuable in idiopathic pulmonary fibrosis, sarcoidosis, and amiodarone toxicity [107, 108]. It is also useful in monitoring response to therapy of other infections including tuberculosis (Fig. 4.19).

Table 4.5 ^{67}Ga findings in patients with lung pathologies including infections

Pathology	Patients (*n*)	Ga negative (%)	Ga positive (%)
Normal	100	100	–
Active tuberculosis	197	3	97
Inactive tuberculosis	32	100	–
Pulmonary abscess	18	–	100
Asbestosis	12	–	100
Cancer	264	10	90

From [105]

^{111}In WBC imaging is less helpful, as the specificity of abnormal pulmonary uptake (either focal or diffuse) is very low. Noninfectious problems that cause abnormal uptake include congestive heart failure, atelectasis, pulmonary embolism, ARDS, and idiopathic conditions [109]. FDG-PET has been currently used for infections including some chest infectious diseases including sarcoidosis (Fig. 4.20) and Pneumocystis jirovecii Pneumonia and interstitial lung disease (Fig. 4.21). More recently, F-18 FDG has been used for Covid-19 disease (Fig. 4.22).

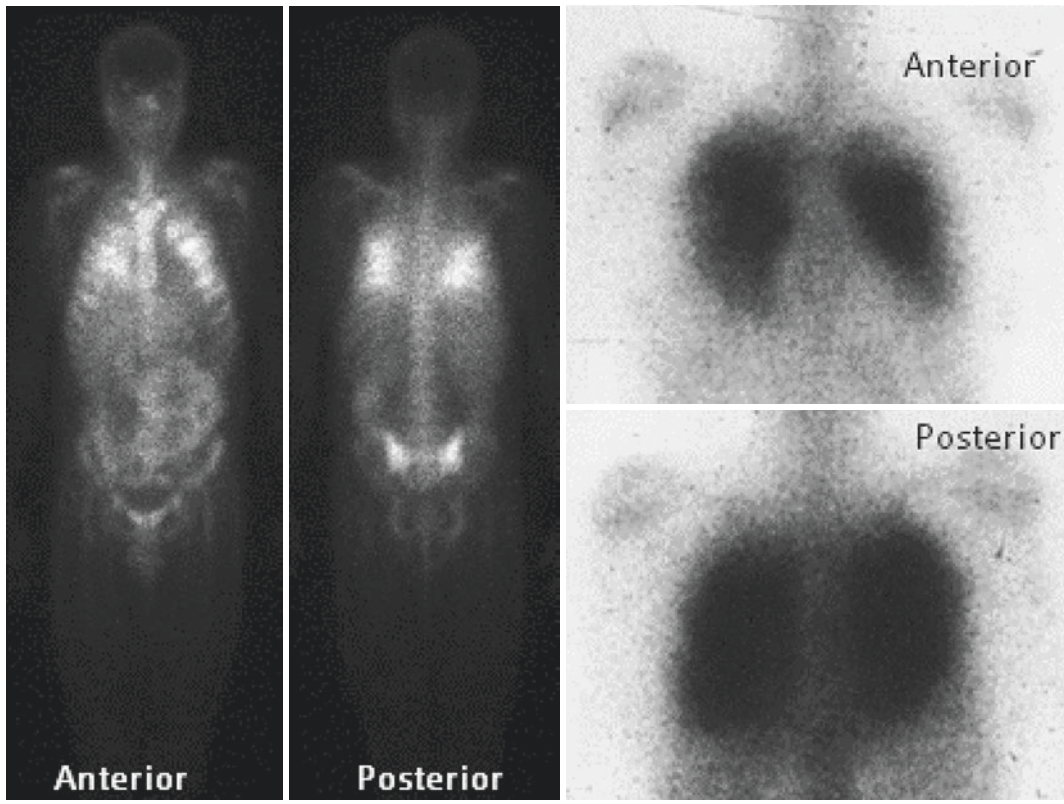

Fig. 4.18 Whole-body and spot chest Gallium-67 images of an AIDS patient with a 5-week history of fever. Images show diffuse uptake in both lungs illustrating the typical pattern of gallium-67 in PCP

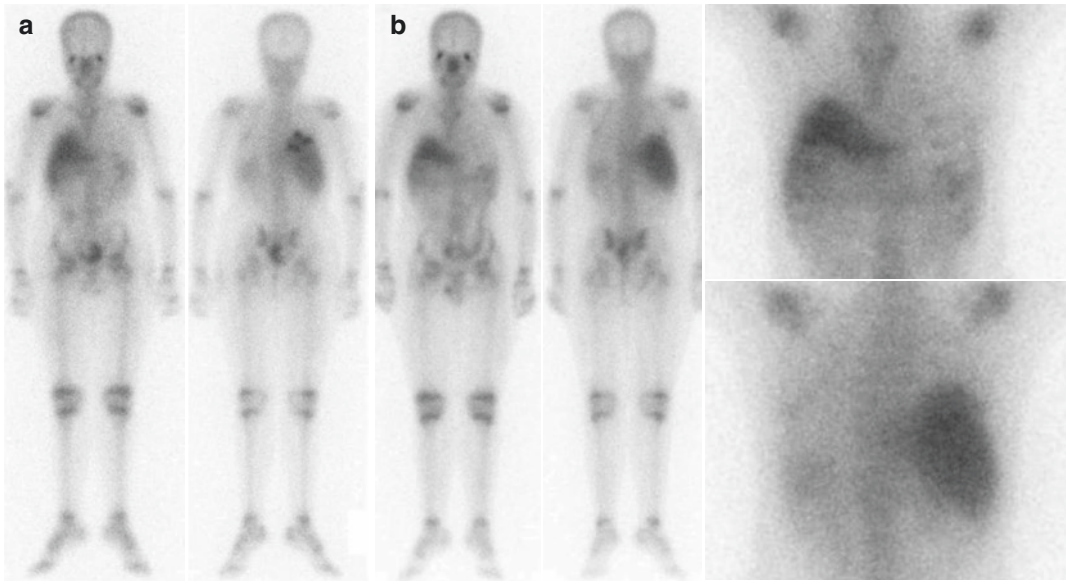

Fig. 4.19 (**a**, **b**) Gallium-67 studies of a patient with tuberculosis. Initial study (**a**) showing abnormal uptake of the right lung (*arrows*) which disappeared on follow-up study (**b**) 3 months after starting therapy, indicating excellent response to treatment

4.8.2.3 Imaging Renal Infections

The CT scan has good sensitivity and specificity in the diagnosis of renal infections. Ultrasound has been used frequently to evaluate the kidneys with suspected infections, even though it is not sensitive. It is used primarily to screen for obstruction or abscess when resolution of UTI is slower than expected with treatment. The sensitivity of US has been shown to be less than 60% [110] and is significantly inferior to that of cortical scintigraphy (sensitivity of 86% and specificity of 81% using ^{99m}Tc-glucoheptonate). Positive ultrasonography can obviate the need for DMSA; however, because of a large number of false-negative results with reported sensitivities of 42–58% and underestimation of the pyelonephritis lesions, ultrasonography cannot replace ^{99m}Tc-DMSA [111]. To date ^{99m}Tc-DMSA is considered the most sensitive method for the detection of acute pyelonephritis in children (Fig. 4.23). It also permits the photopenic area to be calculated as the inflammatory volume which correlates with the severity of infection and the possibility of scar formation even though some of the defects detected might be too small to be clinically significant. Currently US is recommended as the initial imaging modalities by the American Academy of Pediatrics and the National Institute for Health and Clinical Excellence (NICE) in atypical and recurrent UTI in pediatric age group [112, 113]. The pathophysiological basis of the ability of Doppler sonography in detecting acute pyelonephritis is the fact that in the acute phase of pyelonephritis the focal decrease of renal perfusion due to edema causes vascular compression, intravascular granulocyte aggregation, or both, leading to capillary and arteriolar occlusion facilitating the detection of these hypovascular areas [114].

4.8.2.4 Imaging of Skeletal Infection

Several imaging techniques are being utilized for the detection of osteomyelitis including the standard radiograph, computerized tomography, magnetic resonance imaging, and several nuclear medicine modalities. The choice of modality depends on the clinical presentation, particularly its duration, the site of suspected infection, and whether the site of suspected infection has been affected by previous pathology. The pathophysiology of skeletal inflammations and relevant scintigraphic considerations are discussed in detail in Chap. 5, on the musculoskeletal system.

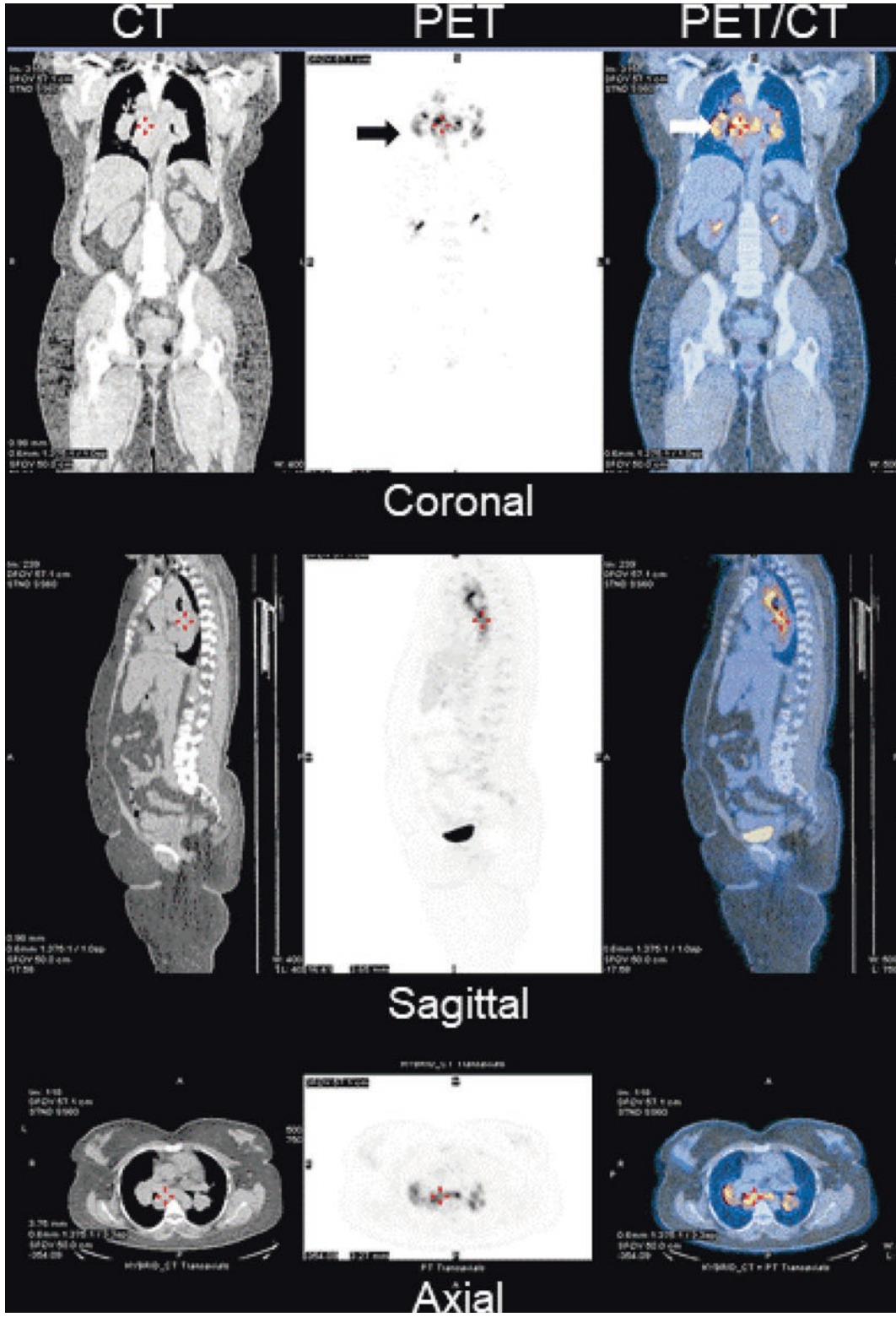

Fig. 4.20 F-18 FDG in a case of pulmonary sarcoidosis illustrating uptake in bilateral hilar adenopathy (arrow)

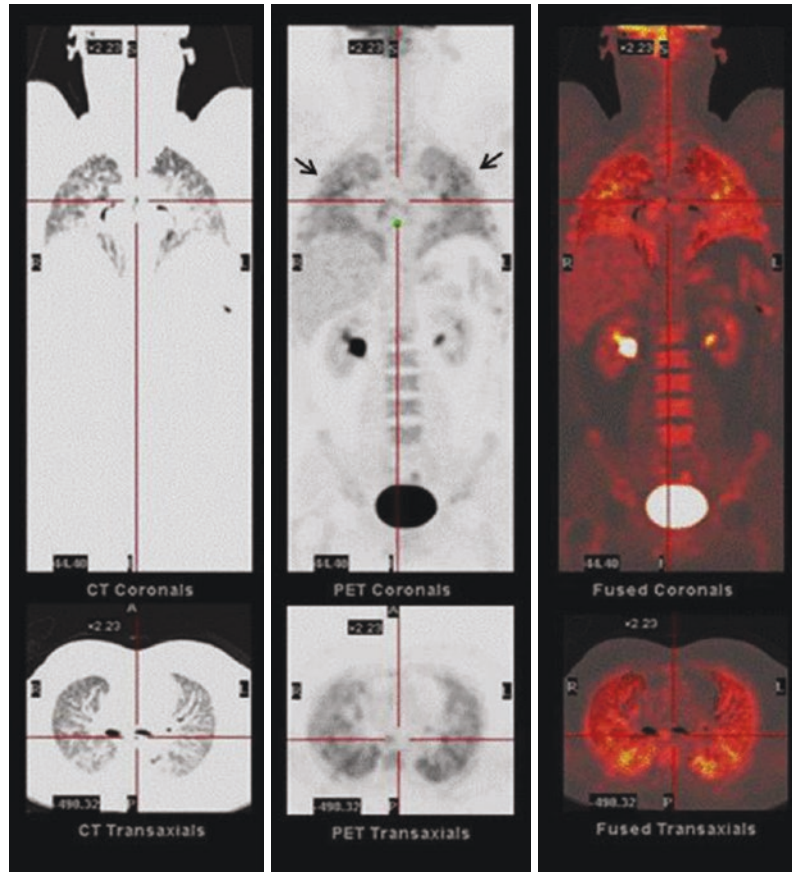

Fig. 4.21 F-18 FDG-PET/CT representative images illustrating the pattern of diffuse interstitial fibrosis with diffuse hypermetabolic activity in both lungs (arrows)

4.8.3 Imaging When No Localizing Signs Present

When no localizing clinical signs are present, which is common in cancer and immunosuppressed patients, nuclear medicine procedures are often the imaging modalities chosen. The ability to screen the entire body is particularly important for many such cases.

The optimal choice of radiotracer again depends on the duration of infection. ^{111}In-labeled white blood cells are the most specific for acute infections, but false-positive results have been reported with some tumors, swallowed infected sputum, GI bleeding, and sterile inflammation. False-negative results have been reported in infections present for more than 2 weeks. More rarely, such false-negative results occur for infections present for only 1 week. Gallium-67 is less specific than labeled WBCs, as it is taken up by many tumors and by sterile inflammation. Several radiolabeled antibody preparations and a radiolabeled antibacterial agent have been introduced and evaluated, but none of these have been used widely. Labeled antibody scintigraphy uses antigranulocyte agents, most commonly intact murine immunoglobulin G (IgG) antibodies against normal cross-reactive antigen-95 (anti-NCA-95, ^{99m}Tc-BW250/183, ^{99m}Tc-besilesomab [Scintimun®]) and the murine Fab fragment of the IgG antibody directed against the glycoprotein cross-reactive antigen-90 (anti-NCA-90, ^{99m}Tc-sulesomab, LeukoScan®). ^{99m}Tc-IgG scintigraphy is a highly sensitive technique for the recognition of infection but has a low specificity. PET-FDG has now largely taken the place occupied by citrate of Gallium-67. Visualization of inflammatory lesions does not just rely on the

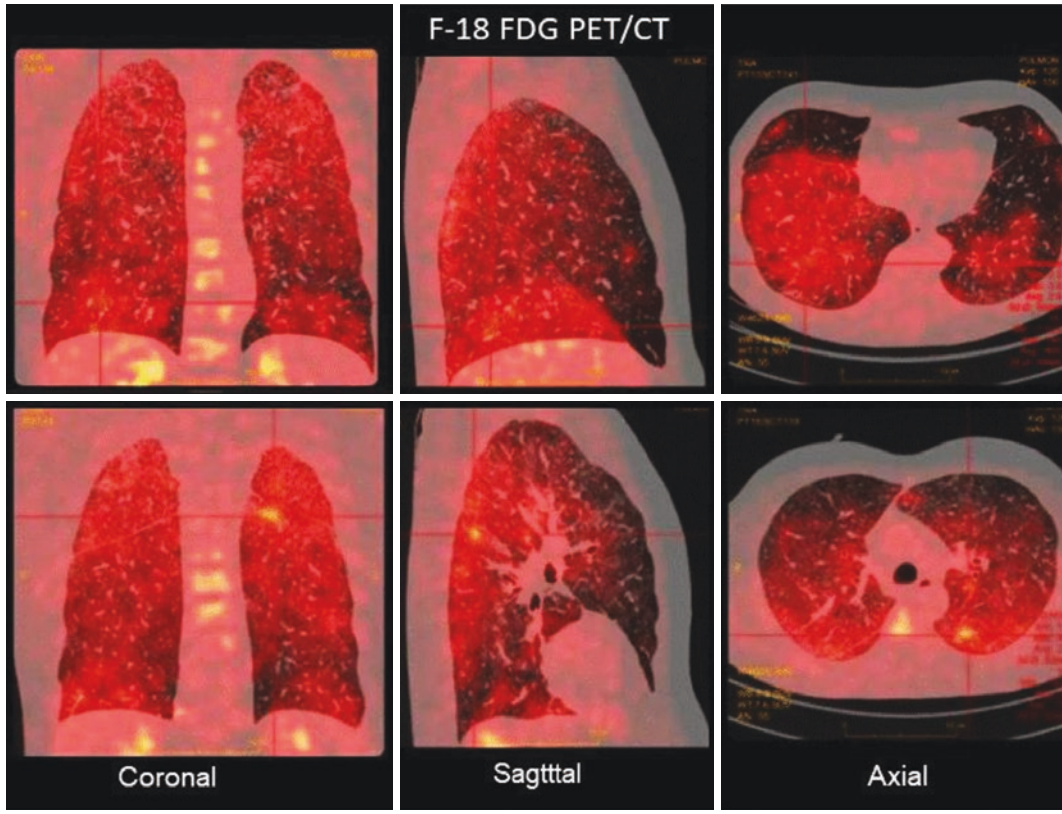

Fig. 4.22 70-year-old man who had interim FDG-PET/CT for his known lymphoma. No diagnosis of Covid-19 on arrival. Selected coronal sagittal and axial cuts show multiple peripheral predominantly basal infiltrates in both lungs consistent with Covid 19 which was later confirmed

presence of immune cells, but uptake requires the activation of these immune cells. FDG-PET reveals infectious and noninfectious inflammatory diseases as well as malignant diseases; all are causes of fever of unknown origin. Recent studies support the use of FDG-PET (Fig. 4.24) in the patient with FUO [8, 115]. FDG is sensitive and its short half-life does not delay the performance of any additional radionuclide studies that might be needed.

Various chronic infectious diseases that are frequent clinical challenges are better diagnosed with the use of PET, particularly when this imaging is combined with CT. For noninfectious inflammatory diseases, FDG-PET has proved particularly helpful for the diagnosis and management of large vessels arteritis and inflammatory bowel disease [85, 116, 117].

Correlation with morphological modalities after successful radionuclide localization of infection can be of great help. For example, this correlation provides anatomical information prior to surgical interventions. Morphological modalities are useful in the management of inflammatory diseases particularly if localizing signs are present. They have the very important advantages of better spatial resolution than nuclear medicine modalities. X-rays, CT, MRI, and US usually yield fast results but unfortunately may not distinguish infected from noninfected tissue. Figure 4.25 illustrates suggested algorithms for the diagnosis of soft tissue infections.

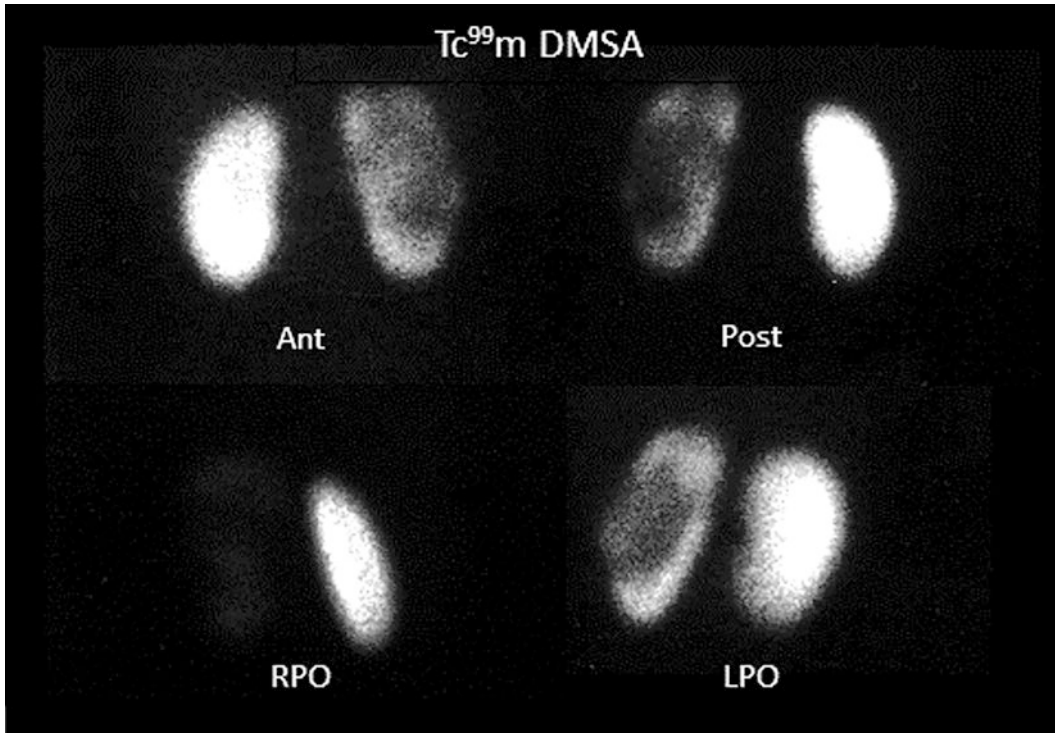

Fig. 4.23 ^{99m}Tc-DMSA study in a patient with chronic pyelonephritis and significant urine outflow obstruction. Note the irregularly thinned cortex and the dilated pelvocalyceal system on the left affected kidney

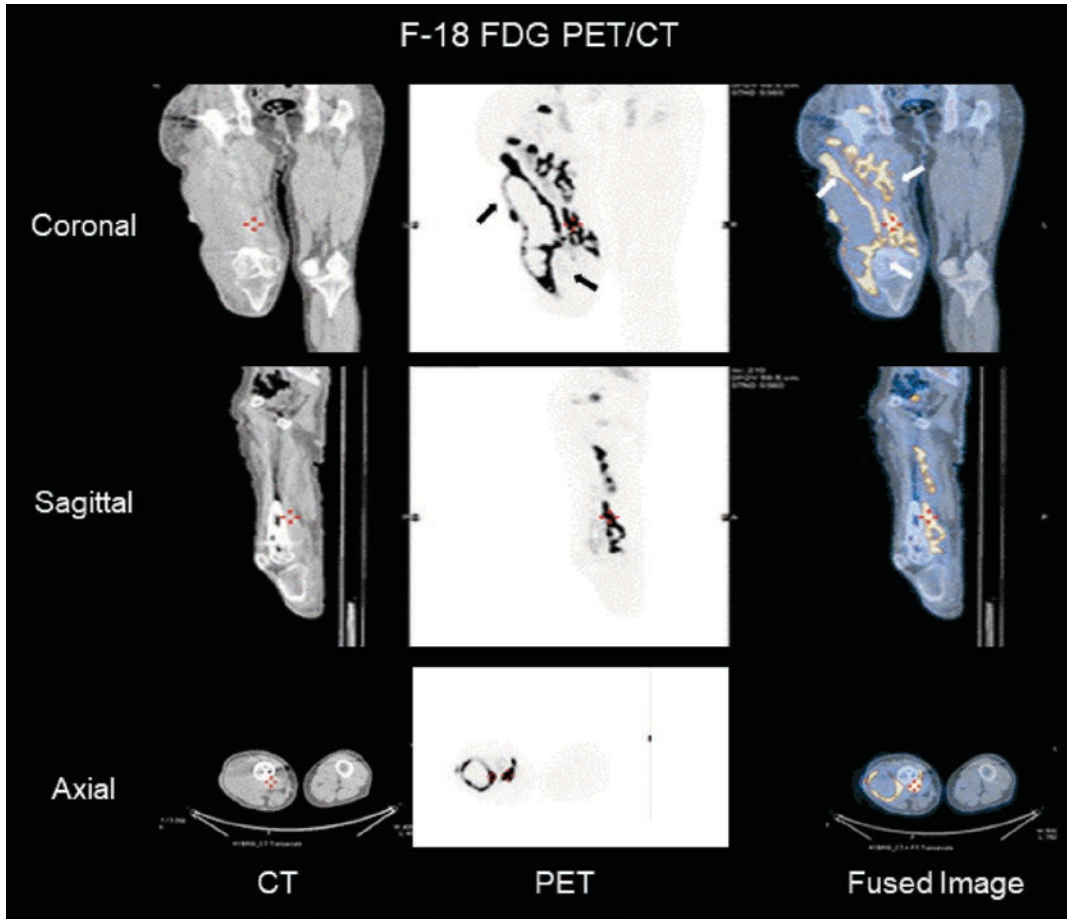

Fig. 4.24 FDG-PET study illustrating soft tissue infection with extensive uptake of the right lower extremity (arrows) of a patient with a history of traffic accident and amputation presented with fever for 3 weeks

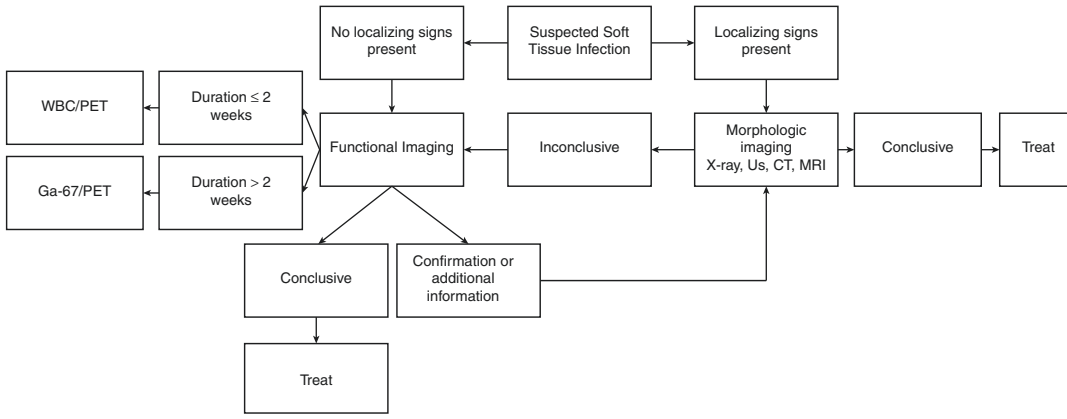

Fig. 4.25 A diagram illustrating a recommended strategy for imaging soft tissue infections. Note that in case of suspected renal infection, ^{99m}Tc-DMSA scan is preferred; in infections of relatively long duration, labeled WBC may be used, but if negative, 67Ga or other labeled antibodies should follow before excluding chronic active infection due to possible false-negative results with labeled WBC

4.9 Summary

Inflammation is a complex nonspecific tissue reaction to injury which can be due to trauma, microorganisms, ischemia, chemicals, radiation, or autoimmune injury. It is nonspecific, because it happens in the same way regardless of the type of injury and the number of exposures to that stimulus. When inflammation is due to microorganisms, it is infection which has been known since the time of Pharos more than 3000 years ago.

Many morphological and functional imaging modalities are available to help diagnose and localize inflammation of the soft tissue and bone. It is clear that no single technique is ideal in all situations. The choice depends on several factors, including whether localizing signs are present, the site of possible infection, whether anatomy is normal or altered by surgery or trauma, the duration of symptoms and signs, and the presence of other underlying diseases such as cancer. For physicians, understanding the pathophysiological changes is crucial for deciding on an appropriate diagnostic strategy. Understanding pathophysiological changes also helps the nuclear physician to recognize and explain the scintigraphic patterns of inflammatory conditions (Table 4.6 summarizes common examples). Further evaluation of PET in diagnosis, localizing, and follow-up of inflammations is a current interest. The discovery of new radiopharmaceuticals that will be ideal for more specific imaging of inflammation is an important topic for future research.

Table 4.6 Correlation of pathophysiological features and scintigraphic findings of infection

Pathological change at the site of infection	Scintigraphic pattern
Hyperemia	Locally increased accumulation of several radiotracers, increased flow and blood pool activity on bone scan; hyperemic pattern on delayed bone images may be present with soft tissue infection
Increased vascular permeability	Increased migration of WBCs, increased accumulation of ^{67}Ga, increased uptake of radiolabeled antibodies
Increased migration of WBCs and chemotaxis	Increased accumulation of labeled WBCs
Increased secretion of iron-containing globulin by injured and stimulated WBCs	Increased accumulation of ^{67}Ga
Localized areas of renal parenchymal damage in pyelonephritis	Areas of reduced or absent DMSA uptake
Dilation of PC system in pyelonephritis	Prominent pelvocalyceal system on DMSA images
Formation of woven bone	Increased uptake of ^{99m}Tc-MDP with prolonged accumulation of radiotracer
Increased expression of glucose transporters on cell surface	Increased uptake of ^{18}F-FDG

References

1. Granger DN, Senchenkova E (2010) Inflammation and the microcirculation. Morgan & Claypool Life Sciences, San Rafael
2. Ciotti M, Ciccozzi M, Terrinoni A, Jiang WC, Wang CB, Bernardini S (2020) The COVID-19 pandemic. Critical reviews in clinical laboratory sciences, 57(6):365–388
3. McCane KL, Huether SE (2019) Innate immunity: inflammation. In: McCance KL, Huether SE (eds) (2019) Pathophysiology: The biologic basis for disease in adults and children, 8th edn. Elsevier, St. Louis, MO
4. Signore A (2013) About inflammation and infection. Signore EJNMMI Res 3:8–9
5. Nathan C (2002) Points of control in inflammation. Nature 420:846–852
6. Kumar V, Abbas A, Aster JC (2020) Robbins and Cotzan, pathologic basis of disease, 10th edn. Saunders, Philadelphia
7. Rankin JA (2004) Biological mediators of acute inflammation. Clin Issues 15:3–17
8. Botting RM, Botting JH (2000) Pathogenesis and mechanisms of inflammation and pain: an overview. Clin Drug Investig 19(suppl 2):1–7
9. Hernandez-Pando R, Bornstein QL, Aguilar LD, Orozo EH, Madrigal VK, Martinez CE (2000) Inflammatory cytokine production by immunological and foreign body multinucleated giant cells. Immunology 100:352–358
10. Reijnen MM, Bleichrodt RP, van Goor H (2003) Pathophysiology of intra-abdominal adhesion and abscess formation, and the effect of hyaluronan. Br J Surg 90:533–541
11. Mazuski JE, Solomkin JS (2009) Intra-abdominal infections. Surg Clin North Am 89:421–437
12. Hasper D, Schefold JC, Baumgart DC (2009) Management of severe abdominal infections. Recent Pat Antiinfect Drug Discov 4:57–65
13. Zibari GB, Maguire S, Aultman DF, McMillan RW, McDonald JC (2000) Pyogenic liver abscess. Surg Infect 1:15–21
14. Greth J, Torok HP, Koenig A, Folwaczny C (2004) Comparison of inflammatory bowel disease at younger and older age. Eur J Med Res 9:552–554
15. Inoue S, Nakase H, Chiba T (2005) Etiopathogenesis and aggravating factors of ulcerative colitis. Nippon Rinsho 63:757–762
16. Baron S, Turck D, Leplat C, Merle V, Gower-Rousseau C, Marti R, Yzet T, Lerebours E, Dupas JL, Debeugny S, Salomez JL, Cortot A, Colombel JF (2005) Environmental risk factors in paediatric inflammatory bowel diseases: a population based case control study. Gut 54:357–363
17. Kolls JK, Zhang Z (2005) Anti-interleukin-12 antibody for active Crohn's disease. N Engl J Med 352:627–628
18. Kolls JK, Zhang Z (2004) Anti-interleukin-12 antibody for active Crohn's disease. N Engl J Med 351:2069–2079
19. Shanahan F (2005) Physiological basis for novel drug therapies used to treat the inflammatory bowel diseases I. Pathophysiological basis and prospects for probiotic therapy in inflammatory bowel disease. Am J Physiol Gastrointest Liver Physiol 288:G417–G421
20. Sakamoto N, Kono S, Wakai K, Fukuda Y, Satomi M, Shimoyama T, Inaba Y, Miyake Y, Sasaki S, Okamoto K, Kobashi G, Washio M, Yokoyama T, Date C, Tanaka H, Epidemiology Group of the Research Committee on Inflammatory Bowel Disease in Japan (2004) Dietary risk factors for inflammatory bowel disease: a multicenter case–control study in Japan. Inflamm Bowel Dis 11:154–163
21. Regueiro M, Kip KE, Cheung O, Hegazi RA, Plevy S (2005) Cigarette smoking and age at diagnosis of inflammatory bowel disease. Inflamm Bowel Dis 11:42–47
22. Pierik M, Yang H, Barmada MM, Cavanaugh JA, Annese V, Brant SR, Cho JH, Duerr RH, Hugot JP, DP MG, Paavola-Sakki P, Radford-Smith GL, Pavli P, Silverberg MS, Schreiber S, Taylor KD, Vlietinck R, IBD International Genetics Consortium (2005) The IBD international genetics consortium provides further evidence for linkage to IBD4 and shows gene-environment interaction. Inflamm Bowel Dis 11:1–7
23. Hatoum OA, Binion DG (2005) The vasculature and inflammatory bowel disease: contribution to pathogenesis and clinical pathology. Inflamm Bowel Dis 11:304–313
24. Zumla A, James DG (1996) Granulomatous infections: etiology and classification. Clin Infect Dis 23:146–158
25. Culver DA, Valeyre D (2016) Emerging ideas about sarcoidosis pathophysiology. Curr Opin Pulm Med 22:466–468
26. Fink CW, Cimaz R (1997) Early onset sarcoidosis: not a benign disease. J Rheumatol 24:174–177
27. Center D, McFadden R (1985) Pulmonary defense mechanisms. In: Sodeman W, Sodeman T (eds) Pathologic physiology, mechanisms of disease. Saunders, Philadelphia, pp 460–481
28. Mandel J, Weinberger SE (2001) Clinical insights and basic science correlates in sarcoidosis. Am J Med Sci 321:99–107
29. Medical Section of the American Lung Association (1997) Diagnosis and treatment of disease caused by nontuberculous mycobacteria. Am J Respir Crit Care Med 156:S1–S25
30. Sharma SK, Mohan A (2002) Sarcoidosis: global scenario & Indian perspective. Indian J Med Res 116:221–247
31. Avino LJ, Naylor SM, Roecker AM (2016) Pneumocystis jirovecii Pneumonia in the Non-HIV-infected population. Ann Pharmacother 50:673–679

32. Nagai S, Shigematsu M, Hamada K, Izumi T (1999) Clinical courses and prognoses of pulmonary sarcoidosis. Curr Opin Pulm Med 5:293–298
33. Wazir JF, Ansari NA (2004) Pneumocystis carinii infection. Update and review. Arch Pathol Lab Med 128:1023–1027
34. Raghu G, Collard HR, Egan JJ, Martinez FJ, Behr J et al (2011) An official ATS/ERS/JRS/ALAT statement: idiopathic pulmonary fibrosis: evidence-based guidelines for diagnosis and management. Am J Respir Crit Care Med 183:788–824
35. Travis WD, Costabel U, Hansell DM, King TE Jr, Lynch DA et al (2013) An official American Thoracic Society/European Respiratory Society statement: update of the international multidisciplinary classification of the idiopathic interstitial pneumonias. Am J Respir Crit Care Med 188:733–748
36. Pinlaor S, Mootsikapun P, Pinlaor P, Phunmanee A, Pipitgool V, Sithithaworn P, Chumpia W, Sithithaworn J (2004) PCR diagnosis of Pneumocystis carinii on sputum and bronchoalveolar lavage samples in immunocompromised patients. Parasitol Res 94:213–218
37. Chisholm A, Collard HR, Flaherty KR, Myers J, Raghu G et al (2017) The diagnosis of idiopathic pulmonary fibrosis: current and future approaches. Lancet 5:61–71
38. Wiersinga WJ, Rhodes A, Cheng AC, Peacock SJ, Prescott HC (2020) Pathophysiology, transmission, diagnosis, and treatment of coronavirus disease 2019 (COVID-19): a review. JAMA 324:782–793. https://doi.org/10.1001/jama.2020.12839
39. Walsh C, Collyns T (2020) Pathophysiology of urinary tract infections. Surgery 38:191–196
40. Kasseh (1966) Pathogenesis of pyelonephritis in the kidney. In: Mostafi FK, Smith DE (eds) The kidney. Williams & Wilkins, Baltimore, pp 204–212
41. Meguid El Nahas A, Bello Aminu K (2005) Chronic kidney disease: the global challenge. Lancet 365:331–340
42. White SL, Cass A, Atkins RC, Chadban SJ (2005) Chronic kidney disease in the general population. Adv Chronic Kidney Dis 12:5–13
43. Hooton TM, Stamm WE (1997) Diagnosis and treatment of uncomplicated urinary tract infection. Infect Dis Clin N Am 11:551–581
44. Ronald AR, Harding GKM (1997) Complicated urinary tract infections. Infect Dis Clin N Am 11:583–592
45. Govan A, Macfarlane P, Callander R (1988) Pathology illustrated, 2nd edn. Churchill Livingstone, Edinburgh
46. Çek M, Sturdza L, Pilatz A (2017) Acute and chronic epididymitis. Eur Urol Suppl 16: 124–131
47. Baddour LM (2000) Cellulitis syndromes: an update. Int J Antimicrob Agents 14:113–116
48. Keynan Y, Rubinstein E (2013) Pathophysiology of infective endocarditis. Curr Infect Dis Rep 15:342–346
49. Fabrizio Monaco F (2003) Classification of thyroid diseases: suggestions for a revision. J Clin Endocrinol Metabol 88:1428–1432
50. Vehling D, Neurath M, Siessmeier T, Schunk K, Bartenstein P (2000) FDG-PET, anti-granulocyte-scintigraphy and hydro-MRI in the determination of bowel wall inflammation in Crohn's disease. J Nucl Med 41:11P
51. Pavlidis ET, Pavlidis TE (2019) A review of primary thyroid lymphoma: Molecular factors, diagnosis and management J Invest Surg; 32:137–142
52. Calhoun JH, Manring MM, Shirtliff M (2009) Osteomyelitis of the long bones. Semin Plast Surg 23:59–72
53. Haas DW, McAndrew M (1996) Bacterial osteomyelitis in adults: evolving considerations in diagnosis and treatment. Am J Med 101:550–561
54. Cierny G, Mader JT, Pennick H (1985) A clinical staging system of adult osteomyelitis. Contemp Orthop 10:17–37
55. Mandell GA (1996) Imaging in the diagnosis of musculoskeletal infections in children. Curr Probl Pediatr 26:218–237
56. Mader JT, Dhraminder M, Calhoun J (1997) A practical guide to the diagnosis and management of bone and joint infections. Drugs 54:253–264
57. Bonakdar-pour A, Gaines VD (1983) The radiology of osteomyelitis. Orthop Clin North Am 14:21–37
58. Trueta J (1959) The three types of acute hematogenous osteomyelitis: a clinical and vascular study. J Bone Joint Surg 41B:671–680
59. Elgazzar AH, Abdel-Dayem HM (1999) Imaging skeletal infections: evolving considerations. In: Feeman LM (ed) Nuclear medicine annual. Lippincott Williams & Wilkins, Philadelphia, pp 157–191
60. Elgazzar AH, Abdel-Dayem HM, Clark J, Maxon HR (1995) Multimodality imaging of osteomyelitis. Eur J Nucl Med 22:1043–1063
61. Torda AJ, Gottlieb T, Bradbury R (1995) Pyogenic vertebral osteomyelitis: analysis of 20 cases and review. Clin Infect Dis 20:320–328
62. Song KS, Ogden JA, Ganey T, Guidera KT (1997) Contiguous discitis and osteomyelitis in children. J Pediatr Orthop 17:470–477
63. Ring D, Wenger DR, Johnson C (1994) Infectious spondylitis in children. The convergence of discitis and vertebral osteomyelitis. Orthop Trans 18:97–98
64. Bauer TM, Pipperet H, Zimmerli W (1997) Vertebral osteomyelitis caused by group B streptococci [streptococcus agalactiae] secondary to urinary tract infection. Eur J Microb Infect Dis 16:244–246
65. Perrone C, Saba J, Behloul Z, Salmon-Ceron D, Leport C, Vilde JL, Kahn MF (1994) Pyogenic and tuberculous spondylodiskitis [vertebral osteomyelitis] in 80 adult patients. Clin Infect Dis 19:746–750
66. Sundberg SB, Savage JP, Foster BK (1989) Technetium phosphate bone scan in the diagnosis of septic arthritis in childhood. J Pediatr Orthop 9:579–585

67. Love C, Palestro CJ (2004) Radionuclide imaging of infection. J Nucl Med Tech 32:47–57
68. Arnon-Sheleg E, Israel O, Keidar Z (2020) PET/CT imaging in soft tissue infection and inflammation—an update. Semin Nucl Med 50:35–49
69. Kouijzer IJE, Mulders-Manders CM, Bleeker-Rovers CP, Oyen WJG (2018) Fever of unknown origin: the value of FDG-PET/CT. Semin Nucl Med 48:100–107
70. Toussaint E, Bahel-Ball E, Vekemans M, Georgala A, Al-Hakak L, Paesmans M, Aoun M (2006) Causes of fever in cancer patients (prospective study over 477 episodes). Support Care Cancer 14:763–769
71. Schönau V, Vogel K, Englbrecht M et al (2018) The value of ^{18}F-FDG-PET/CT in identifying the cause of fever of unknown origin (FUO) and inflammation of unknown origin (IUO): data from a prospective study. Ann Rheum Dis 77:70–77
72. Martin C, Castaigne C, Tondeur M, Flamen P, De Wit S (2013) Role and interpretation of fluorodeoxyglucose-positron emission tomography/computed tomography in HIV-infected patients with fever of unknown origin: a prospective study. HIV Med 14(8):455–462. https://doi.org/10.1111/hiv.12030. Epub 2013 Mar 20. PMID: 23517190
73. Lazzeri E, Erba P, Perri M, Doria R, Tescini C et al (2010) Clinical impact of SPECT/CT with In-111 biotin on the management of patients with suspected spine infection. Clin Nucl Med 35:12–17
74. Sfakianakis GN, Al-Sheikh W, Heal A et al (1982) Comparison of scintigraphy with In-111 leukocytes and Ga-67 in the diagnosis of occult sepsis. J Nucl Med 23:618–626
75. Liberatore M, Calandri E, Ciccariello G, Fioravanti M, Megna V, Rampin L, Marzola MC, Zerizer I, Al-Nahhas A, Rubello D (2010) The labeled-leukocyte scan in the study of abdominal abscesses. Mol Imaging Biol 12:563–569
76. Blazeski A, Kozloff KM, Scott PJ (2010) Besilesomab for imaging inflammation and infection in peripheral bone in adults with suspected osteomyelitis. Rep Med Imaging 3:1–11
77. Gratz S, Reize P, Pfestroff A, Höffken H (2012) Intact versus fragmented ^{99m}Tc-monoclonal antibody imaging of infection in patients with septically loosened total knee arthroplasty. J Int Med Res 40:1335–1342
78. Goldsmith SJ, Vallabhajosula S (2009) Clinically proven radiopharmaceuticals for infection imaging: mechanisms and applications. Semin Nucl Med 39:2–10
79. Sierra JM, Rodriguez-Puig D, Soriano A et al (2008) Accumulation of ^{99m}Tc-Ciprofloxacin in *Staphylococcus aureus* and *Pseudomonas aeruginosa*. Antimicrob Agents Chemother 52:2691–2692
80. O'Sullivan MM, Powell N, French AP, Williams KE, Morgan JR, Williams BD (1988) Inflammatory joint disease: a comparison of liposome scanning, bone scanning and radiography. Ann Rheum Dis 47:485–491
81. Boerman OC, Storm G, Oyen WJG, van Bloois L, van der Meer JWM (1995) Sterically stabilized liposomes labeled with In-111 to image focal infection. J Nucl Med 36:1639–1644
82. Blockmans D, Knockaert D, Maes A et al (2001) Clinical value of [18F]fluorodeoxyglucose positron emission tomography for patients with fever of unknown origin. Clin Infect Dis 32:191–196
83. Meller J, Altenvoerde G, Munzel U et al (2000) Fever of unknown origin: prospective comparison of [18F]FDG imaging with a double-head coincidence camera and gallium-67 citrate SPET. Eur J Nucl Med 27:1617–1625
84. Bleeker-Rovers CP, de Kleijn EMHA, Corstens FHM et al (2004) Clinical value of FDG PET in patients with fever of unknown origin and patients suspected of focal infection or inflammation. Eur J Nucl Med Mol Imaging 31:29–37
85. Lauri C, Tamminga M, Glaudemans AWJM, Orozco JLE, Erba PA et al (2017) Detection of osteomyelitis in the diabetic foot by imaging techniques: a systematic review and meta-analysis comparing MRI, white blood cell scintigraphy, and FDG-PET. Diabetes Care 40:1111–1120
86. Chacko TK, Zhuang HM, Alavi A (2002) FDG-PET is an effective alternative to WBC imaging in diagnosing and excluding orthopedic infections. J Nucl Med 43:126P
87. Matsui T, Nakata N, Nagai S, Nakatani A, Takahashi M et al (2009) Inflammatory cytokines and hypoxia contribute to ^{18}F-FDG uptake by cells involved in pannus formation in rheumatoid arthritis. J Nucl Med 50:920–926
88. Chacko TK, Moussavian B, Zhuang HM, Woods K, Alavi A (2002) Critical role of FDG-PET imaging in the management of patients with suspected infection in diverse settings. J Nucl Med 43:126P
89. El-Zeftawy H, LaBombardi V, Dakhel M, Heiba S, Adbel Dayem H (2002) Evaluation of 18F-FDG PET imaging in diagnosis of disseminated mycobacterium avium complex (DMAC) in AIDS patients. J Nucl Med 43:127P
90. Kumar V, Boddieti DK (2013) (68) Ga-radiopharmaceuticals for PET imaging of infection and inflammation. Recent Results Cancer Res 194:189
91. Emmi V, Sganga G (2008) Diagnosis of intra-abdominal infections: clinical findings and imaging. Infez Med 16(Suppl 1):19–30
92. Chen SC, Yen CH, Lai KC, Tsao SM, Cheng KS, Chen CC, Lee MC, Chou MC (2005) Pyogenic liver abscesses with Escherichia coli: etiology, clinical course, outcome, and prognostic factors. Wien Klin Wochenschr 117(23–24):809–815
93. Bulger EM, McMahon K, Jurkovich GJ (2003) The morbidity of penetrating colon injury. Injury 34:41–46
94. Capitan Manjon C, Tejido Sanchez A, Piedra Lara JD, Martinez Silva V, Cruceyra Betriu G, Rosino Sanchez A, Garcia Penalver C, LeivaGalvis O (2003)

Retroperitoneal abscesses—analysis of a series of 66 cases. Scand J Urol Nephrol 37:139–144
95. Haraldsen P, Andersson R (2003) Quality of life, morbidity, and mortality after surgical intensive care: a follow-up study of patients treated for abdominal sepsis in the surgical intensive care unit. Eur J Surg Suppl 588:23–27
96. Kaplan GG, Gregson DB, Laupland KB (2004) Population-based study of the epidemiology of and the risk factors for pyogenic liver abscess. Clin Gastroenterol Hepatol 2:1032–1038
97. Tunuguntla A, Raza R, Hudgins L (2004) Diagnostic and therapeutic difficulties in retroperitoneal abscess. South Med J 97:1107–1109
98. Men S, Akhan O, Koroglu M (2002) Percutaneous drainage of abdominal abscess. Eur J Radiol 43:204–218
99. Morales CH, Villegas MI, Villavicencio R, Gonzalez G, Perez LF, Pena AM, Vanegas LE (2004) Intra-abdominal infection in patients with abdominal trauma. Arch Surg 139:1278–1285
100. Rubin RH, Fischman AJ (1996) Radionuclide imaging of infection in the immunocompromised host. Clin Infect Dis 22:414–422
101. Datz FL (1996) Abdominal abscess detection: gallium, In-111 and Tc-99m labeled leukocytes and polyclonal and monoclonal antibodies. Semin Nucl Med 26:51–64
102. Minoja G, Chiaranda M, Fachinetti A, Raso M, Dominioni L, Torre D, De Palma D (1996) The clinical use of Tc-99m labeled WBC scintigraphy in clinically ill surgical and trauma patients with occult sepsis. Intensive Care Med 22:867–871
103. Yang MD, Jeng LB, Kao A, Lin CC, Lee CC (2003) C-reactive protein and gallium scintigraphy in patients after abdominal surgery. Hepato-Gastroenterology 50:354–356
104. Vehling D, Neurath M, Siessmeier T, Schunk K, Bartenstein P (2000) FDG-PET, anti-granulocyte-scintigraphy and hydro-MRI in the determination of bowel wall inflammation in Crohn's disease. In J Nucl Med 41:11P.
105. Siemon JK, Siegfried GF, Waxman AD (1978) The use of Ga-67 in pulmonary disorders. Semin Nucl Med 3:235–249
106. Gotthardt M, Bleeker-Rovers CP, Boerman OC, Oyen WJG (2010) Imaging of inflammation by PET. Conventional scintigraphy and other imaging techniques. J Nucl Med 51:1937–1949
107. Woolfenden JM, Corrasquillo JA, Larson SA, Simmons TJ, Masur H, Smith PD, Shelhamer JH, Ognibene FP (1987) Acquired immunodeficiency syndrome: Ga-67 citrate imaging. Radiology 162:383–387
108. Tuazon CU, Delaney MD, Simon GL, Witorsch P, Varma PM (1985) Utility of gallium-67 scintigraphy and bronchial washings in the diagnosis and treatment of Pneumocystis carinii pneumonia deficiency syndrome. Am Rev Resp Dis 132:1087–1092
109. Moinuddin M, Rackett J (1986) Gallium scintigraphy in the detection of amiodarone lung toxicity. Am J Radiol 147:607–609
110. Coak PS, Datz FL, Disbro MA, Alazaraki N, Taylor A (1984) Pulmonary uptake in indium-111 leukocyte imaging: clinical significance in patients with suspected occult infections. Radiology 150:557–561
111. Conway JJ (1988) Role of scintigraphy in urinary tract infection. Semin Nucl Med 18:308–319
112. Mackenzie JR (1996) A review of renal scarring in children. Nucl Med Comm 17:176–190
113. El Hajjar M, Launay S, Hossein-Foucher C, Foulard M, Robert Y (2002) Power Doppler sonography and acute pyelonephritis in children: comparison with Tc-99m DMSA scintigraphy. Arch Pediatr 9:21–25
114. The American Academy of Pediatrics, Subcommittee on Urinary Tract Infection, Steering Committee on Quality Improvement and Management (2011) Urinary tract infection: clinical practice guideline for the diagnosis and management of the initial UTI in febrile infants and children 2 to 24 months. Pediatrics 128:572–575, 112
115. La Scola C et al (2013) Different guidelines for imaging after first UTI in febrile infants: yield, cost, and radiation. Pediatrics 131:e665–e671
116. Federici L, Blondet C, Imperiale A et al (2010) Value of 18F-FDG-PET/CT in patients with fever of unknown origin and unexplained prolonged inflammatory syndrome: a single centre analysis experience. Int J Clin Pract 64(55–60):118
117. Spier BJ, Perlman SB, Jaskowiak CJ, Reichelderfer M (2010) PET/CT in the evaluation of inflammatory bowel disease: studies in patients before and after treatment. Mol Imaging Biol 12:85–88

Musculoskeletal System

5

Abdelhamid H. Elgazzar and Saud A. Alenezi

5.1 Introduction

Bone is a rigid connective tissue which provides support and protection for the organs and tissue of the body. Certain bones such as the skull, vertebrae, and ribs, marrow cavities serve as sites of blood formation. Bone also has an important function in mineral homeostasis. Scintigraphy plays a crucial role in the diagnosis and management of various skeletal diseases. The expanding use of this imaging modality in the area of benign bone disorders is particularly notable.

5.2 Anatomical and Physiological Considerations

5.2.1 Bone Structure

Structure of normal adult bone can be summarized in four categories:

1. *Gross level*
   The skeleton consists of two major parts: axial skeleton and appendicular skeleton (Fig. 5.1). The axial skeleton includes the skull, spine, and rib cage (ribs and sternum), while the appendicular skeleton involves the bones of the extremities, pelvic girdle, and pectoral girdle (clavicles and scapulae).
2. *Tissue level*
   Bone is divided into two types of tissues forming the skeleton: compact or cortical and cancellous, trabecular, or spongy bone. The spongy bone has a turnover rate of approximately eight times greater than the case of cortical bones and hosts hematopoietic cells and many blood cells. In mature bone, compact bone forms an outer layer (cortex) which surrounds an inner one of loose trabecular, cancellous, or spongy bone in the medulla. The architecture is arranged in the Haversian system. The spongy portion contains hematopoietic cells, which produce blood cells, fat, and blood vessels. The compact bone constitutes 80% of the skeletal mass and contains 99% of the total body calcium and 90% of its phosphorus.

   The appendicular skeleton is composed predominantly of cortical bone. The cortical bone is thicker in the diaphysis than in the metaphysis and epiphysis of long bones. The blood supply to the metaphysis is also different since it is rich and consists of large sinusoids which make the flow of blood slower, a feature that predisposes to bacterial proliferation. The spine, however, is composed predominantly of cancellous bone in the body of the vertebra and compact bone in the endplates and posterior elements.

A. H. Elgazzar (✉) · S. A. Alenezi
Department of Nuclear Medicine, Faculty of Medicine, Kuwait University, Kuwait City, Kuwait

A. H. Elgazzar (ed.), *The Pathophysiologic Basis of Nuclear Medicine*,
https://doi.org/10.1007/978-3-030-96252-4_5

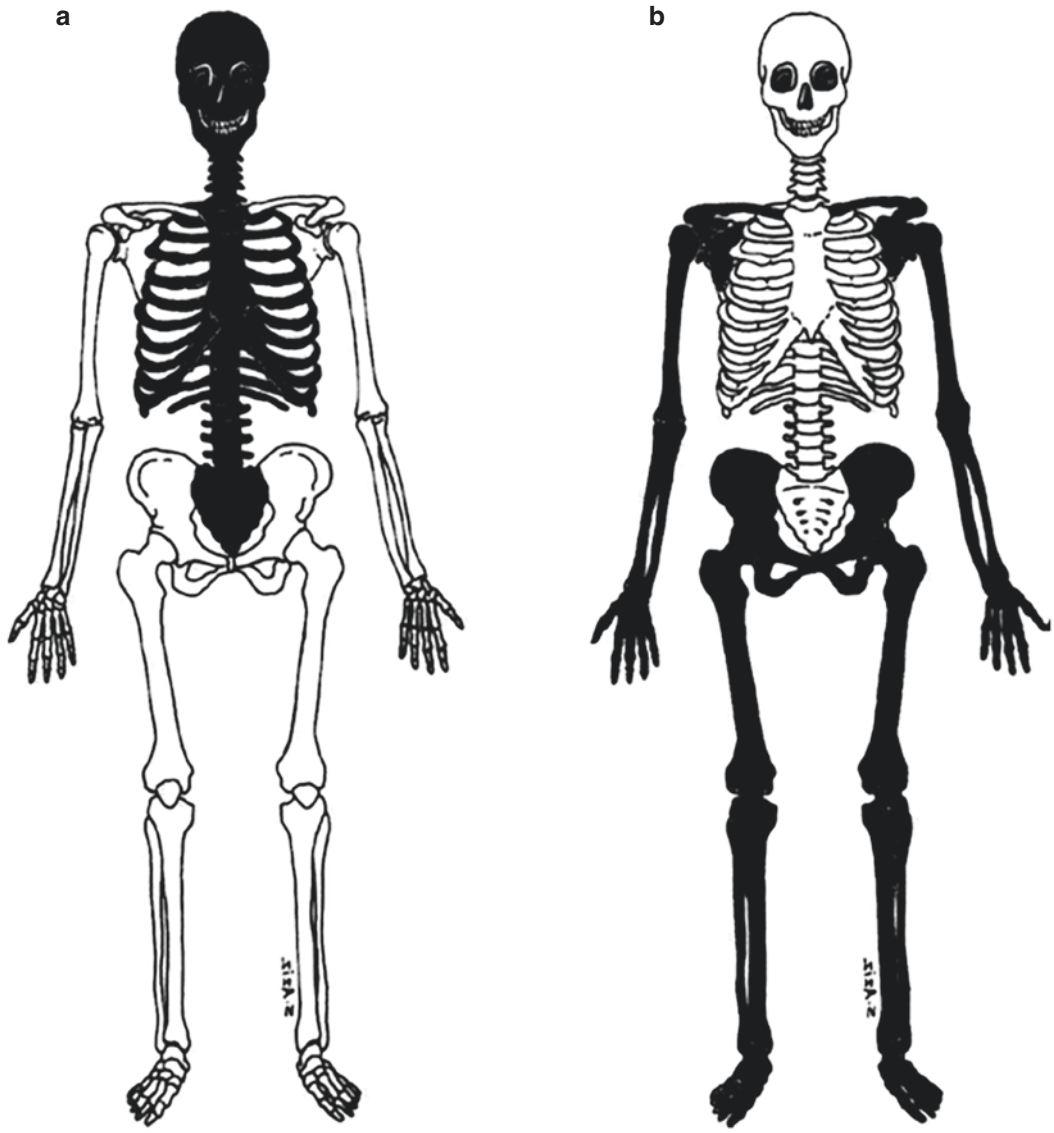

Fig. 5.1 Axial (**a**) and appendicular (**b**) skeletons

3. *Cellular level*

Three types of cells are seen in bone: (1) osteoblasts that produce the organic bone matrix, (2) osteocyte that produces the inorganic matrix, and (3) osteoclasts which are active in bone resorption [1]. Osteoclasts are derived from the hematopoietic system in contrast to the mesenchymal origin of osteoblasts. Osteocytes are derived from osteoblasts that have secreted bone around themselves [2].

4. *Molecular level*

At the molecular level, bone matrix is composed primarily of organic matrix (approximately 35%) including collagen and glycoproteins and inorganic matrix (approximately 65%), which includes hydroxyapatite, cations (calcium, magnesium, sodium, potassium, and strontium), and anions (fluoride, phosphorus, and chloride [3]. There is now strong evidence that the gut microbiome regulates bone homeostasis in health and disease,

Table 5.1 Bone structures and their functions

Major structural elements	Function
Bone cells	
Osteoblasts	Synthesize collagen and proteoglycans, stimulate osteoclast resorptive activity
Osteocytes	Maintain bone matrix
Osteoclasts	Resorb bone, assist with mineral homeostasis
Bone matrix	
Organic matrix	
Collagen fibers	Provide support and tensile strength
Proteoglycans	Control transport of ionized materials through matrix
Sialoprotein	Promotes calcification
Osteocalcin	Inhibits calcium/phosphate precipitation, promotes bone resorption
Laminin	Stabilizes basement membranes in bone
Osteonectin	Binds calcium to bones
Albumin	Transports essential elements to matrix
Inorganic matrix	
Calcium	Crystallizes to provide rigidity and compressive strength
Phosphate	Regulates vitamin D and thereby promotes mineralization

Modified from [1]

and that prebiotic and probiotics protect against bone loss [4, 5]. Table 5.1 summarizes the major constituents of bone and their function.

5.2.2 Blood Supply

Bones are richly supplied by blood and receive about 10–15% of the cardiac output [6]. The pattern of the skeletal blood supply varies with the age group. In children epiphyseal, metaphyseal, and diaphyseal vessels are present. In adults, all vessels communicate together. Nutrient and periosteal arteries feed a rich network of vessels to supply the cortex and medulla (Fig. 5.2). This vasculature takes the form of interconnecting capillaries, sinusoids, and veins. It is estimated that blood flow to cancellous bone containing marrow is 5–13 times higher than in cortical bone [7].

5.2.3 Bone Remodeling

Within all bones, a balance between osteogenesis and bone resorption continuously occurs, even in normal nonviolated bone. Remodeling occurs throughout life, with removal and replacement of bone at different rates in different parts of the skeleton. Bone remodeling is regulated by parathyroid hormone, vitamin D, and numerous other factors. It is estimated that 18% of the skeleton is replaced yearly in adults, indicating that the entire skeleton is replaced every 5 years. The process is more active in cancellous bone, with a yearly replacement rate of approximately 25% compared with 2% for compact bone [8]. Turnover varies and is affected by many factors including drugs (Table 5.2) and disease. Most bone diseases are the result of bone remodeling abnormalities [9]. Certain diseases are characterized by increase in the rate of remodeling, and therefore known as high-turnover disorders, and may affect the entire skeleton or a single bone. In this group, both osteoblastic and osteoclastic activities are increased, but the amount of bone formed is usually less than the bone removed resulting in osteopenia. An exception is Paget's disease which, in later stages of its course, osteoblastic exceeds osteoclastic activity. The stress fracture is not as thought due to repeated traumatic microfractures. It is a focal area of increased bone turnover secondary to the repeated stress.

5.2.4 Bone Marrow

Bone marrow is a soft tissue that is found at the inner aspect of the bones and has multiple important functions [10]. It is a hematopoietic organ involved in the production of new blood cells. Also, it has a mechanical function as it contains bone marrow mesenchymal stem cells that contribute to building the bone. In addition, bone marrow has an immune function as the

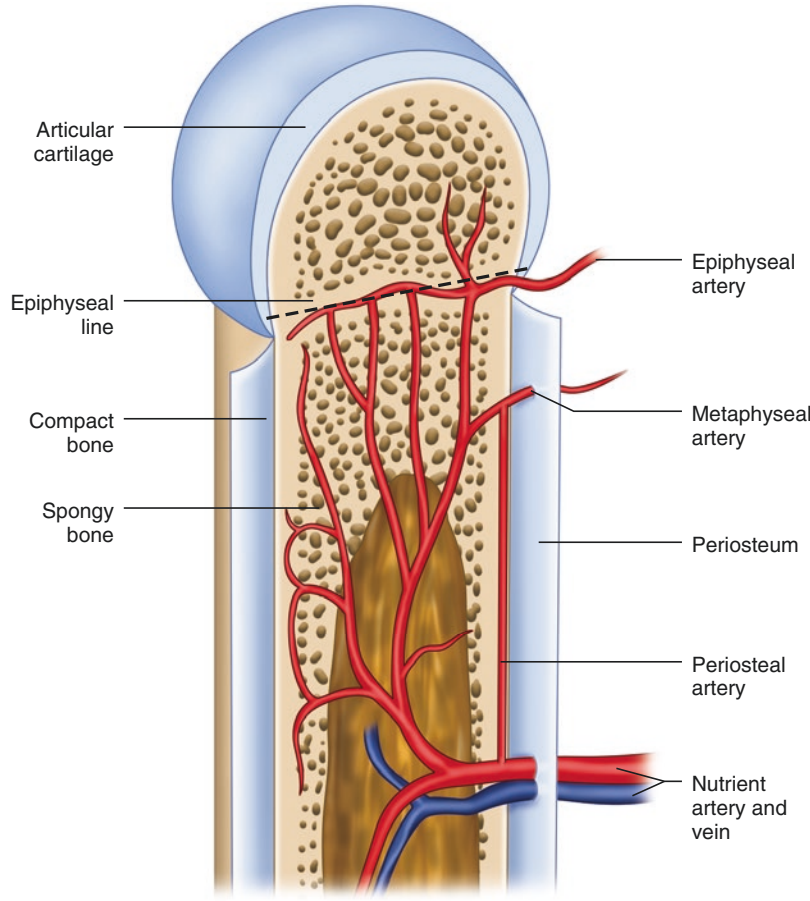

Fig. 5.2 Diagram illustrating blood supply to a long bone

hematopoietic stem cells produce multiple types of immune cells [11]. Bone marrow adipose tissue may also have a beneficial impact on skeletal health [12].

Normally, almost the entire fetal marrow space is occupied by red (hematopoietic) marrow at birth. Conversion from red to yellow, non-hematopoietically active marrow, starts in the immediate postnatal period. This process begins in the extremities and progresses in general from the peripheral to the central skeleton and from diaphyseal to metaphyseal regions in individual long bones. By approximately the age of 25 years, marrow conversion to the adult pattern is complete (Fig. 5.3). In adults, hematopoietic bone marrow usually is confined to the skull, vertebrae, ribs, sternum, pelvis, and proximal portions of the humerus and femur. Fatty marrow in other bones may contain islands of hematopoietic tissue, however, and for this reason, variations on the normal adult pattern of hematopoietic bone marrow are frequently encountered. Acquired alterations in the distribution of hematopoietic bone marrow may be due to surgery, trauma, infection, and other destructive processes. Furthermore, with increasing demand for red cells, reconversion of yellow-to-red marrow may take place. This process follows the reverse order of the initial red-to-

yellow marrow conversion. Accordingly, it starts in the axial skeleton, followed by the extremities from proximal to distal [13–15].

Table 5.2 Inhibitors and stimulators of bone turnover

Bone turnover inhibitors
Estrogens
Estrogen receptor antagonists
Tamoxifen
Raloxifene
Calcitonin
Vitamin D derivatives
Calciferol
Calcitriol
Bisphosphonates
Etidronate
Pamidronate
Alendronate
Zoledronic acid
Tiludronate
Clodronate
Thiazide diuretics
Bone turnover stimulators
Anabolic steroids
Parathyroid hormone and peptides
Fluoride

5.2.5 Bone Response to Injury

The principle response of bone to injury and disease is reactive bone formation. This reactive bone goes through stages. It is disorganized early but later may remodel to normal bone. This new disorganized bone is termed woven bone (Fig. 5.4) and is active with no lamellar arrangement.

Technetium99m diphosphonates are the radiopharmaceuticals most commonly used for skeletal scintigraphy. These agents concentrate predominantly in the mineral phase of bone, which consists of crystalline hydroxyapatite and amorphous calcium phosphate. Using an in vitro assay, Francis et al. [16] showed that the competitive adsorption of ^{99m}Tc diphosphonates to pure inorganic hydroxyapatite was 40 times than pure organic bone matrix. These radiopharmaceuticals do not localize to a significant degree in osteoblasts or in osteoid.

While several factors affect the uptake of diphosphonates in the skeleton, blood flow and extraction efficiency are the most important. Increased flow of blood produces increased

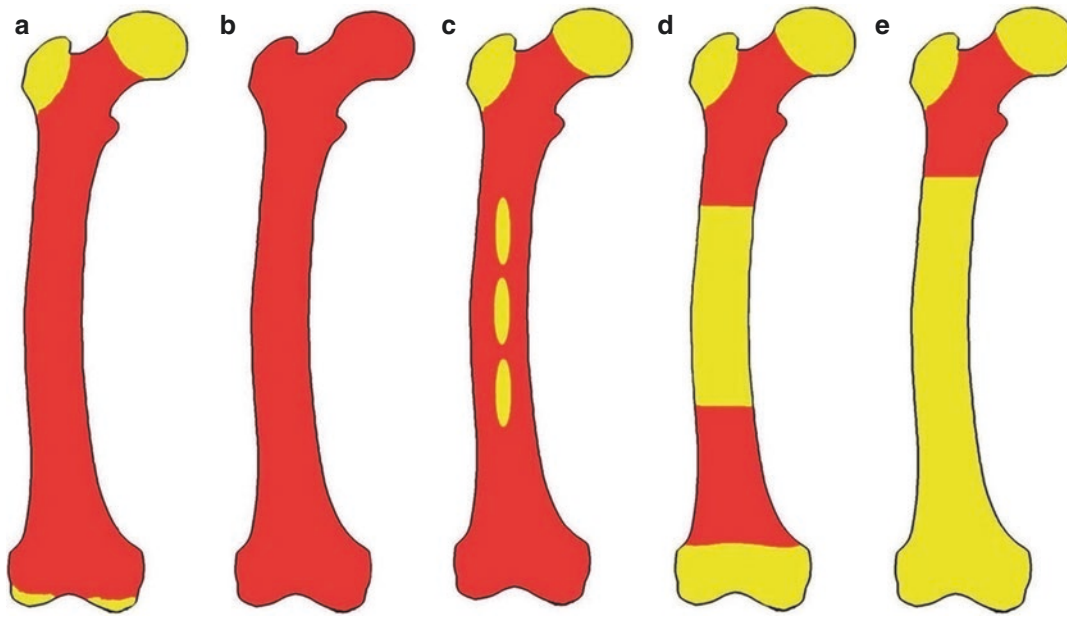

Fig. 5.3 Bone marrow distribution in a long bone illustrating changes during development over the years till the adult pattern is reached by about 25 years of age: (**a**) birth; (**b**) 7-year-old; (**c**) 14-year-old; (**d**) 18-year-old; (**e**) 25-year-old

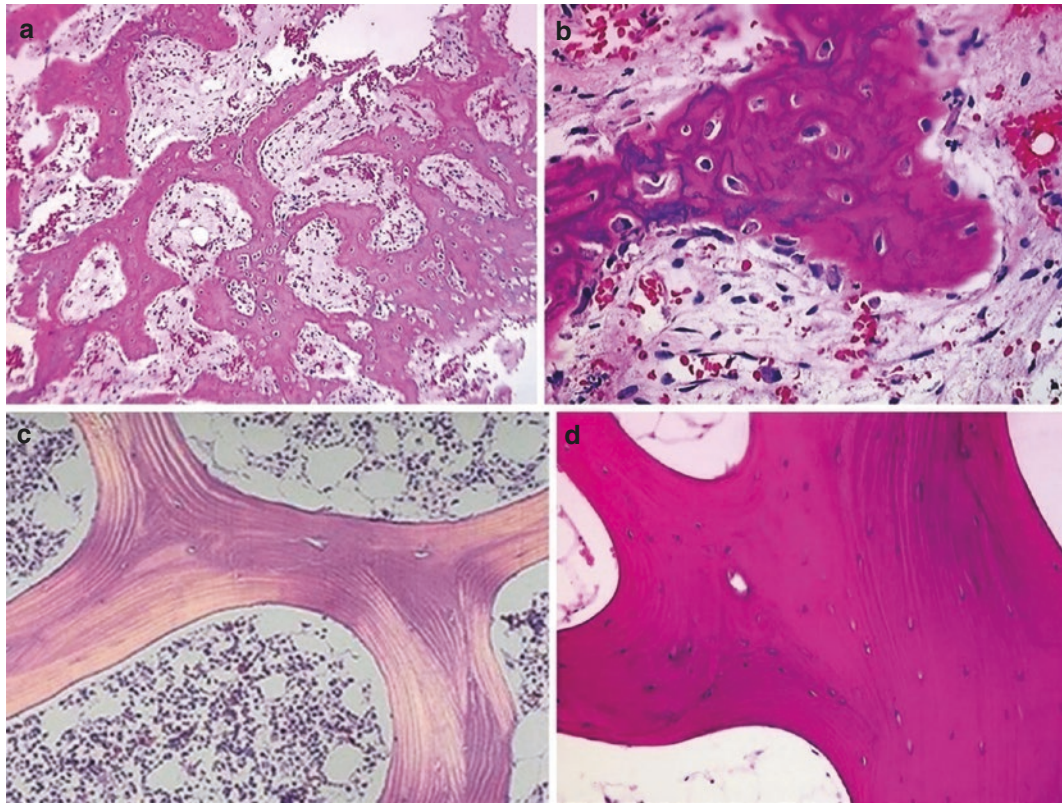

Fig. 5.4 (**a**–**d**) Photomicrographs illustrating the difference between woven and lamellar bone. The irregular and disorganized nature of woven bone at different microscopic magnification levels (**a** ×10; **b** ×40) is easily seen compared to lamellar bone depicted in **c** (×10) and **d** (×40). The bony spicules in lamellar structure are even, with occasional lacunae containing osteocytes. Cellular marrow is seen between the spicules of bone

uptake. Pathological foci containing woven bone show increased uptake due to higher extraction efficiency. Other factors also influence diphosphonate uptake:

1. Blood flow
2. Extraction efficiency
3. Vitamin D
4. Parathyroid hormone
5. Corticosteroids
6. Intraosseous tissue pressure
7. Capillary permeability
8. Acid–base balance
9. Sympathetic tone

Accordingly, in children prominent uptake of the radiopharmaceutical is seen at the costochondral junctions, at the metaphyseal ends of the normal long bones, and in the facial bones. When the skeleton has matured, this prominent uptake at the costochondral junctions and metaphyseal ends of long bones disappears. Overall, the skeletal accumulation of diphosphonates decreases with age, particularly in the extremities [17].

Bone scintigraphy shows many patterns, some specific, in a variety of benign and malignant bone diseases. Many of these patterns are better understood once the underlying pathophysiological changes are appreciated.

5.3 Nonneoplastic Bone Diseases

5.3.1 Inflammatory Bone Diseases

5.3.1.1 Skeletal Infections

Definitions

The term osteomyelitis optimally indicates inflammation mainly due to infection involving the cortical bone as well as the bone marrow and can progress to osteonecrosis, bone destruction, and septic arthritis. Osteomyelitis has a bimodal age distribution with peak incidences in children under 5 and adults over 50 years of age [18]. Recent studies indicate an increase in the incidence and severity of acute osteomyelitis in children, linked to the increasing prevalence of methicillin-resistant Staphylococcus Aureus (MRSA) [19, 20].

When infection starts in the periosteum, such as in cases of direct extension of bone infection, it produces periostitis. At this stage, infection may not yet involve the cortex or marrow, and the condition is called infectious periostitis. When infection involves the cortex, the term infectious osteitis is used. When the bone marrow is involved as well, the term osteomyelitis is applied (Fig. 5.5).

Classification of Osteomyelitis

The pathophysiology, imaging, and classification of osteomyelitis are challenging, varying with the age of the patient, the chronicity of infection, the route of infection, and the immune and vascular status of the patient and the affected region of the skeleton. Osteomyelitis may be classified as hematogenous and nonhematogenous [21–23] (Table 5.3). In hematogenous osteomyelitis, the metaphyses of long bones are the most common site. Nonhematogenous osteomyelitis occurs as a result of penetrating trauma, spread of a contiguous soft tissue infection, or inoculation (as in drug addicts). Hematogenous spread is the predominant route of infection in children aged less than 16 years and usually causes long bone osteomyelitis [18, 24]. Hematogenous spread is less common in adults and when it occurs usually leads to vertebral osteomyelitis. Adult osteomyelitis is most commonly caused by contiguous spread from soft tissue infections or direct inoculation [25]. Infantile osteomyelitis refers to that occurring prior to 1 year of age; the juvenile type occurs between 1 year and the age at closure of the physes; adult type occurs after closure of the physes. While gram-positive bacteria such as *Staphylococcus aureus* are the most frequent cause, many different organisms have been encountered in osteomyelitis [26–29] (Table 5.4). The pathogens responsible for osteoarticular infections in children have changed in recent years with alterations in immunization practices, emergence of resistant bacteria, and changes in patterns of immune-modulating diseases and medications in children [30].

Pathophysiological Changes

Acute hematogenous osteomyelitis occurs most commonly in children, affecting males approximately twice as often as females. It has a

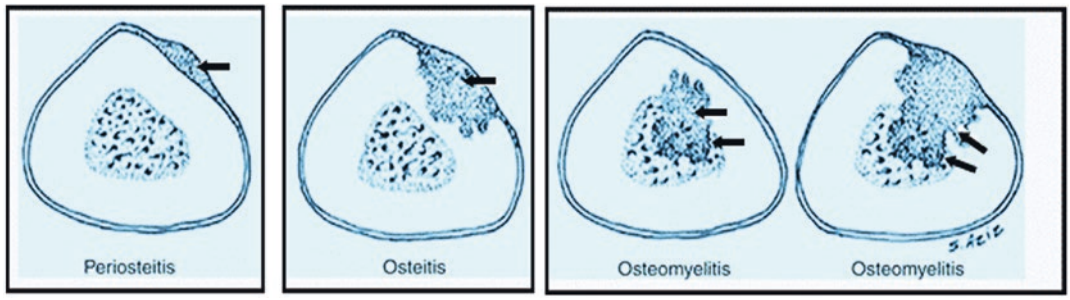

Fig. 5.5 A comparison of the extent of infection in osteomyelitis compared with the extent of infection in periostitis and in ostei

Table 5.3 Classifications and staging of osteomyelitis

Basis of classification	Types
Presentation	(I) Acute, (II) subacute, (III) chronic
Route of infection	(I) Hematogenous, (II) direct extension (nonhematogenous)
Age	(I) Infantile (including neonatal), (II) juvenile, (III) adult
Causative organism	(I) Pyogenic, (II) nonpyogenic
Location	(I) Appendicular skeleton osteomyelitis: metaphyseal, epiphyseal, diaphyseal
	(II) Axial skeleton osteomyelitis (examples: vertebral and bony pelvis osteomyelitis)
Multifactorial (Waldvogel classification):	(I) Hematogenous osteomyelitis
	(II) Osteomyelitis secondary to contiguous infection
	(III) Osteomyelitis associated with vascular insufficiency
Anatomy of disease and host physiology (Cierny-Mader classification of adult type)	Anatomical types: (I) medullary, (II) superficial, (III) localized, (IV) diffuse
	Physiological class:
	A. Normal host
	B. Compromised host
	Systemic compromise
	Local compromise
	Local and systemic compromise
	C. Prohibitive: treatment worse than disease
Prior pathology at the site of interest	(I) Violated bone (complicated) osteomyelitis, (II) nonviolated bone osteomyelitis

Table 5.4 Organisms associated with osteomyelitis in different clinical settings

Clinical situation	Most likely associated microorganisms causing bone infection
All types of osteomyelitis	*Staphylococcus aureus*
Infantile osteomyelitis	*S. aureus* and group B streptococci
Vertebral osteomyelitis	*S. aureus*, *Pseudomonas aeruginosa*, *Escherichia coli*, streptococci
Diabetic foot osteomyelitis	*S. aureus*, enterococcus, enterobacteria
Intravenous drug abusers	*P. aeruginosa*, *Klebsiella*
Immunosuppressed patients	*Salmonella*, *Aspergillus*, *Mycobacterium avium* complex, *Candida albicans*
Sickle cell disease	*Salmonella*, *S. aureus*
Hospital-acquired infections	*P. aeruginosa*, *Klebsiella*
Drinking raw milk in brucella-endemic areas	*Brucellosis*
Cat and human bites	*Pasteurella multocida*, *Eikenella corrodens*
Sharp object passing deep into foot tissue	*P. aeruginosa*
Contamination of open wound by soil	*Clostridia*, *Nocardia*
Infected catheter-related bone infections	*E. coli*, *C. albicans*

predilection for the metaphyses of long bones, where blood flow is rich and relatively sluggish and bone is relatively porous in comparison to the diaphysis (Fig. 5.6). Here the blood flows through large intramedullary venous sinusoids, a fertile site for bacterial lodgment and proliferation [22]. The process starts by implantation of organisms in the bone marrow. As infection becomes established in the marrow, it provokes acute suppurative neutrophilic infiltrates and edema with local ischemia, vasospasm, and thrombosis. Infection subsequently may spread from metaphyseal focus into the epiphysis, the joint space, the subperiosteal space, the shaft of the bone, and the surrounding soft tissues (Fig. 5.7). The disease has increased in frequency, virulence, and degree of soft tissue involvement in recent years [30].

In children between 1 and approximately 16 years of age, the blood supply to the medullary space of bone enters through the nutrient artery and then passes through smaller vessels toward the growth plate. Once these vessels reach the metaphyseal side of the growth plates, they turn back upon themselves in loops to empty into large sinusoidal veins, where the blood flow is slower. The epiphyseal plate separating the

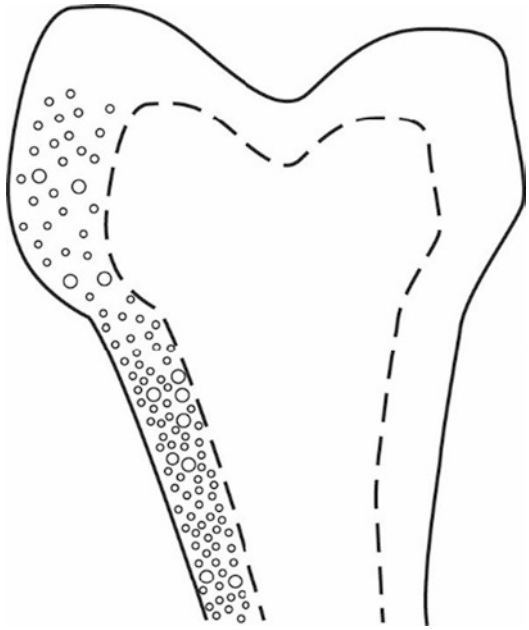

Fig. 5.6 Diagram of part of a long bone illustrating the more porous nature of the metaphysis, the most frequently affected site by hematogenous skeletal infections

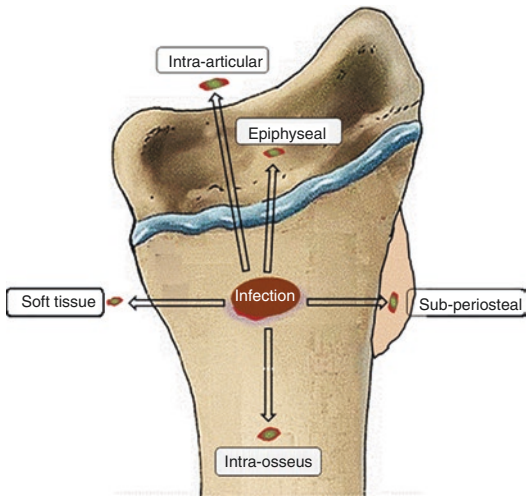

Fig. 5.7 Spread of hematogenous osteomyelitis

epiphyseal and metaphyseal blood supplies acts as a barrier to the spread of infection (Fig. 5.8), making joint involvement less common in this age group. In this situation, infection must first break through the bone to produce joint infection (Fig. 5.8). This occurs in the locations where the metaphysis is within the joint capsule (proximal femur in the hip joint, distal tibia in the ankle joint, proximal humerus in the shoulder joint, and rarely proximal radius in the elbow joint). Conversely, in infants and adults, the terminal branches of the nutrient artery extend into the epiphysis, as there is no growth plate barrier. This vascular communication between epiphyses and metaphyses facilitates the spread of infection to adjacent joints (Fig. 5.8). In flat bones, acute hematogenous osteomyelitis is found mainly at locations with vascular anatomy similar to that of the long bone metaphyses, such as the bony pelvis, vertebrae, and calcaneus [31].

When infection lifts the periosteum, the blood supply may be impaired, causing necrosis of bone or sequestrum (Fig. 5.9). In some cases, infection may stimulate osteoblastic activity, particularly from the periosteum, forming new subperiosteal bone that may envelop the infectious focus (involucrum). This osteogenesis may occasionally continue long enough to give rise to a densely sclerotic pattern of osteomyelitis that is referred to as sclerosing osteomyelitis. The infection can spread through the periosteum as the rise in intramedullary pressure may lead to rupture of the bony cortex, producing a cortical track known as a cloaca (Fig. 5.9). This causes elevation of the periosteum and disrupts the periosteal blood supply to the bone [32] Delayed complications from acute osteomyelitis include growth arrest, fracture, soft tissue infection, and chronic osteomyelitis [33].

It is difficult to draw the line between acute and chronic osteomyelitis. However, it should be noted that cases of clear chronic osteomyelitis need special handling in diagnosis and management. Chronic osteomyelitis has variously been defined as symptomatic osteomyelitis with a duration ranging from 5 days to 6 weeks [34].

Since the pathology of osteomyelitis varies with age, microorganisms, prior therapy, underlying diseases, and other factors, it is somewhat inappropriate to depend only on duration of the disease to define chronicity. Chronic osteomyelitis has less marked inflammatory cell reactions and may occur without preceding acute inflammation. Microscopically, chronic osteomyelitis shows predominantly lymphocytes and plasma cells rather than polymorphonuclears (Fig. 5.10).

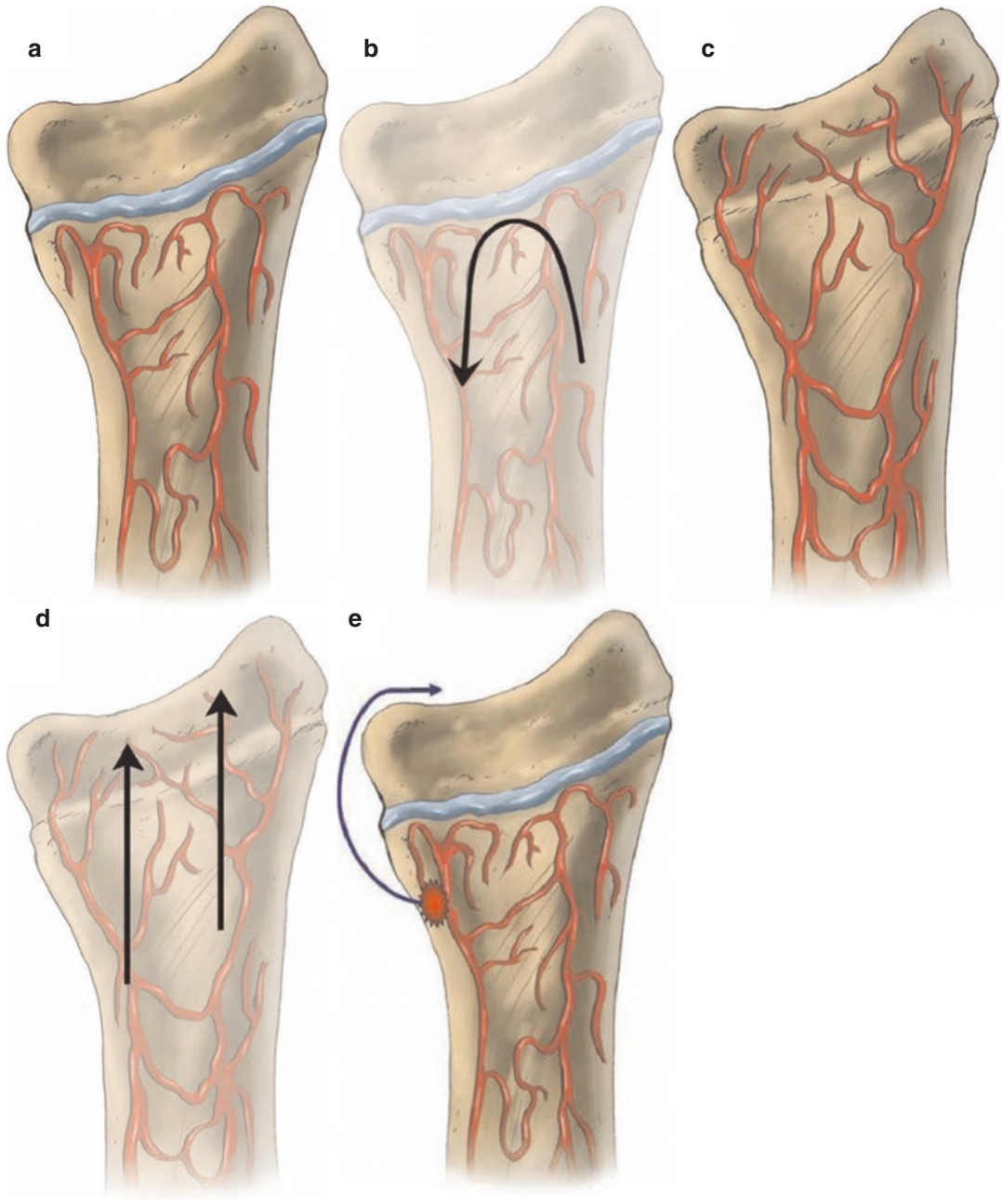

Fig. 5.8 (**a**–**e**) Diagram illustrating the vascular communication between the metaphysis and epiphysis of long bones. When the growth plate (**a**) is present, it acts as a barrier, and vessels turn on themselves forming loops. This acts to prevent infection that is most commonly present in the metaphysis from extending to epiphysis and adjacent joint (**b**). Conversely, in neonates after the closure of the growth plate (**c**), infection extends more easily (**d**) to the joint since there is free vascular communication between metaphysis and epiphysis. (**e**) illustrates the path of severe infection which is able to involve the joint, when the growth plate is present, by breaking through the bone

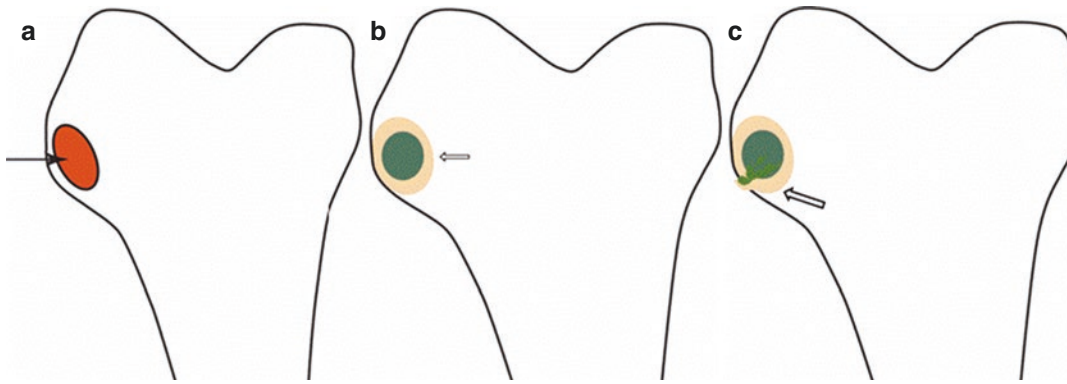

Fig. 5.9 (**a–c**) Diagrammatic representation of the sequestrum (**a**) showing the necrotic segment of bone (*arrow*) and involucrum (**b**), which has a layer of new bone formation (*arrow*) surrounding the focal infection. (**c**) illustrates cloaca with the sinus track (*arrow*)

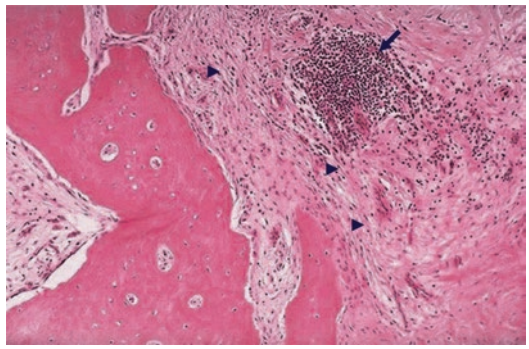

Fig. 5.10 Chronic osteomyelitis. A photomicrograph of a specimen of bone from a patient with long-standing chronic osteomyelitis. Note the presence of numerous lymphocytes (*arrow*) as well as fibrosis (*arrowheads*) within the marrow space

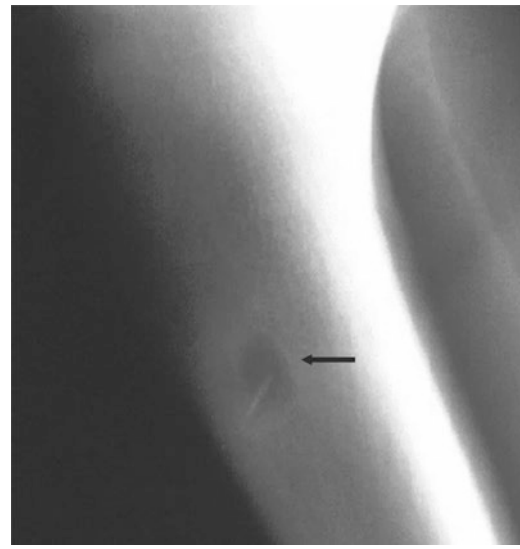

Fig. 5.11 Radiograph showing Brodie's abscess (*arrow*)

There is also fibrosis and a variable amount of necrotic tissue, and sequestra may form in some cases. The presence of necrotic tissue may also lead to draining sinuses or organization in the medullary cavity, forming a cystic cavity (Brodie's abscess) (Fig. 5.11). Because these abscesses are avascular, levels of antibiotics sufficient to eradicate the bacteria may not be achieved during treatment. Accordingly, bacteria may remain indolent for a long time (inactive disease). Reactivation of the disease may occur later, even years after the initial episode (active disease). It was recently suggested that bacterial biofilm formation and bacterial invasion within the osteocyte are contributing factors to the formation of chronic and recurrent osteomyelitis [24]. It is important to evaluate patients for possible chronic disease and to either exclude or confirm the presence of chronic active infection. The continuation of intravenous antibiotic therapy and/or surgical intervention to eradicate infection will depend on that determination [35].

Vertebral osteomyelitis (spondylodiskitis) is a specific form of osteomyelitis that has some unique features. It accounts for 3–5% of cases of osteomyelitis [36]. Sixty-nine percent of the patients had lumbar involvement [37] followed

by the thoracic and cervical spine. Several factors predispose to vertebral osteomyelitis:

1. Diabetes mellitus
2. Drug addiction
3. Old age
4. Oral steroid therapy
5. Dialysis
6. Urinary tract infection
7. Genitourinary instrumentation
8. Prior back surgery
9. Bacteremia secondary to intravenous cannulation
10. Spinal trauma

The disease occurs most frequently in adults with a mean age of 60–70 years, although it also occurs at all other ages, including in children. The pyogenic form most often is caused by *Staphylococcus aureus*, but streptococci and gram-negative bacteria are also involved [26–28]. Infection usually originates at a distant site with hematogenous extension to contiguous vertebral bodies [38] and the intervening space via the ascending and descending branches of the posterior spinal artery. Also, the venous supply of the spine allows backflow from the pelvic venous plexus due to the lack of valves [39]. Extension to the posterior elements (pedicles, transverse processes, posterior spinous processes, and laminae) has been noted in 3–12% of cases. However, involvement of posterior elements only is exceedingly rare, with only 15 cases reported to date. Other causes include extension of infection from adjacent structures and complications from spinal surgery and trauma.

In adults, the causative organism generally settles in the richly vascularized subchondral vertebral endplates with eventual progression of infection into the adjacent intervertebral disk, which is relatively avascular. In childhood, infection often starts at the disks, which are nourished by small perforating vessels. In either case, local spread of infection eventually occurs and causes endplate destruction, disk space narrowing, and collapse. Figure 5.12 illustrates possible ways of development of vertebral osteomyelitis. These changes may take weeks to be seen on radiographs [24, 35]. Since the disk is almost invariably involved in vertebral infections, the term spondylodiskitis is preferred [26, 27].

Diabetic foot osteomyelitis is a unique clinical and pathological problem. It is a common complication of diabetes, particularly when angiopathy is present. It occurs in 15% of adult diabetic patients and, without prompt diagnosis and treatment, may lead to amputation. Diabetic foot infections typically begin in a wound, most often a neuropathic ulceration. Ulceration of the foot is 50 times more common in diabetics, and the incidence of amputation of the lower extremities is 25 times greater than among the general population. More than 90% of osteomyelitis of the foot of diabetic patients occurs as a result of the spread of infection from adjacent foot ulcers [29, 40].

Early diagnosis is difficult, both clinically and radiologically, because of superimposed disease processes, such as neuroarthropathy, chronic soft tissue infection, and edema. There is particular difficulty in differentiating osteomyelitis from

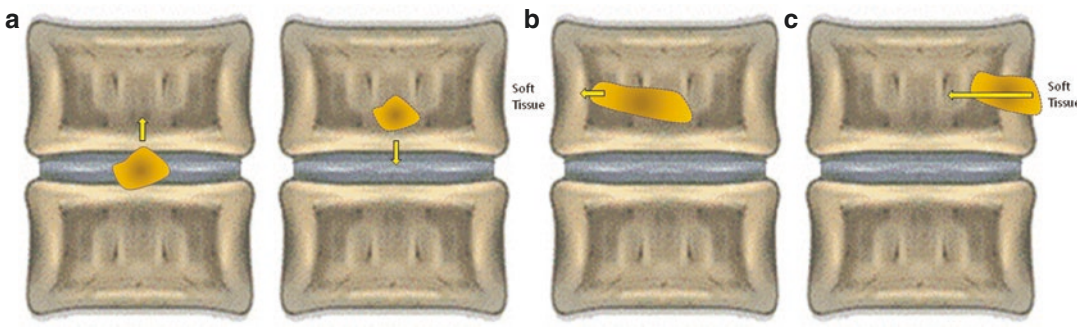

Fig. 5.12 (**a**–**c**) The possible ways of development and extension of infection in hematogenous vertebral osteomyelitis

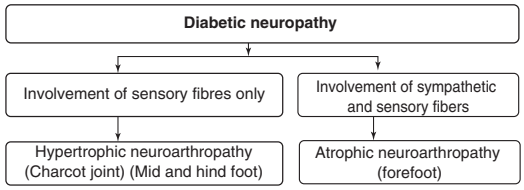

Fig. 5.13 Types of diabetic neuropathy. (From [19], with permission)

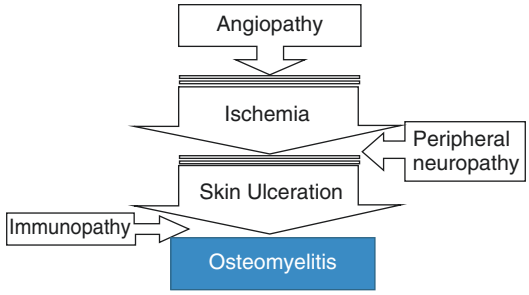

Fig. 5.14 Changes leading to skeletal infections in diabetics. (Modified from [19], with permission)

neuroarthropathy as the two conditions have similar clinical presentations. Neuroarthropathy has a better prognosis than osteomyelitis and is managed differently. Thus, it is critical to make the correct diagnosis.

Neuroarthropathy is characterized by destructive joint changes. A combination of factors is involved (Fig. 5.13). Loss of protective pain and proprioceptive sensation along with hyperemia secondary to loss of vasoconstrictive neural impulses is thought to result in atrophic neuropathy, occurring most frequently in the forefoot [41].

Conversely, absence of sympathetic fibers in the presence of sensory fiber involvement tends to result in hypertrophic neuroarthropathy, which occurs most frequently in the mid- and hindfoot. Since the patient continues to walk and traumatize the foot, disuse osteoporosis is usually absent. Unrelenting trauma may also result in rapidly progressive destruction, sometimes with disintegration of one or more tarsal bones within a period of only a few weeks. This is a rapidly progressive form of neuroarthropathy which has more inflammatory reaction than otherwise. A long history of diabetes mellitus with a combination of angiopathy, neuropathy, and immunopathy predisposes to pedal osteomyelitis (Fig. 5.14). Metatarsal bones and the proximal phalanges are the most commonly involved sites [42, 43].

The severity of diabetic foot ulcers at presentation is greater than previously reported, as one-third had both peripheral arterial disease and infection. The majority of ulcers (52%) were located on the non-plantar surface of the foot [44]. Diabetic foot osteomyelitis can affect any bone but most frequently the forefoot (90%), followed by the midfoot (5%) and the hindfoot (5%) [45]. Forefoot has a better prognosis than midfoot and hindfoot osteomyelitis. The risk of above ankle amputation is significantly higher for hindfoot (50%) than midfoot (18.5%) and forefoot (0.33%) [44].

In osteomyelitis associated with sickle cell disease, erythrocytes become viscous and sickle abruptly when exposed to hypoxia, since hemoglobin S is sensitive to hypoxemia. This may compromise the microvascular flow and may cause infarction, the most common skeletal complication of sickle cell disease. For symptomatic sickle cell patients, distinguishing infarction from osteomyelitis is critical. Although less common than infarctions, osteomyelitis is the second most frequent bacterial infection in children with sickle cell disease after pneumonia [46].

Osteomyelitis may occur as a primary event or may be superimposed on infarcts as the necrotic bone is a fertile site for such secondary infections. *S. aureus* and *Salmonella* are frequent causative organisms.

Periprosthetic Infections: Hip and knee arthroplasties are two of the most frequent orthopedic procedures, exceeding 600,000 per year in the USA alone [47–49].

Between 10 and 25% of patients experience discomfort within 5 years after hip or knee replacement [50]. This can be due to loosening with or without infection. Loosening is the most common complication after hip replacements, occurring in up to 50% of femoral components and in 15% of acetabular components by 10 years after surgery.

Periprosthetic infections are a clinically important complication after joint replacement. Although the incidence of infection was reported previously to be as high as 4% after the primary

surgery and 32% after revision of hip arthroplasty, the currently reported incidence of infections after total hip or knee arthroplasties is only 0.5–2% and is less than 3% following revision surgery and occurs mostly within 4 months of operation [51, 52].

The cementless porous-coated prosthesis depends on bone ingrowth for fixation and induces more reactive bone formation than the cemented prosthesis. Differences between cemented and porous-coated hip prostheses largely explain the scintigraphic patterns noted after hip arthroplasty. Prominent although still "normal" activity may remain present for years, depending on the location of the finding and type of prosthesis. After knee replacement, however, the most common complications are fracture, dislocation, and avascular necrosis followed by loosening of the tibial component, with infection occurring less frequently [52].

The incidence of loosening associated with infection is high and is found in up to 80% of infected prostheses [53].

Heterotopic bone formation following arthroplasties is not uncommon and is present in about 50–55% of hip prostheses and 10% of knee prostheses [49, 54].

Infectious (septic) arthritis refers to the invasion of synovial space by microbes. The synovial space contains synovial fluid, which is produced by a rich capillary network of the synovial membrane. This is a viscous fluid that serves to lubricate, nourish, and cushion the avascular joint cartilage. When the synovial space is infected, bacterial hyaluronidase decreases the viscosity of the synovial fluid. Pain is then felt with stress on the joint capsule.

Acute septic arthritis is usually caused by bacteria, while fungal and mycobacterial pathogens are seen more commonly in chronic arthritis. Acute septic arthritis is a medical emergency. Delay in the diagnosis and treatment may result in destruction of the articular cartilage and permanent disability. The lytic enzymes in the purulent articular fluid destroy the articular and epiphyseal cartilage. Additionally, pus in the joint space increases the intracapsular pressure with epiphyseal ischemia. Concomitant osteomyelitis is not uncommon and is potentially severe [55]. A recent study reported 36% of patients with septic arthritis having concomitant bone infection which is called osteoarticular infection [56]. Other sequelae include dislocation, deformity, and destruction of the femoral head and neck. Hence, drainage and antibiotic therapy must be considered without delay [34, 57].

Microorganisms usually reach the joint by a hematogenous route, contagiously from an adjacent osseous infection, or through traumatic/surgical inoculation. Cetratin factors and disease conditions increases the risk for infectious arthritis in adults and children (Table 5.5).

The joints most commonly involved in children are the hip (35%), knee (35%), and ankle (10%). When the synovium becomes hyperemic in septic arthritis, flow to adjacent extra-articular bone will also increase via anastomoses from the synovial vascular network to juxtaepiphyseal and epiphyseal vessels supplying the epiphysis and metaphysis. Accordingly, increased uptake of bone-seeking radiopharmaceutical typically is seen in and around affected joints [57, 59].

Chronic nonbacterial osteomyelitis is an autoinflammatory bone disorder, covering a clinical spectrum with asymptomatic inflammation of single bones at one end and chronic recurrent multifocal osteomyelitis (CRMO) at the other

Table 5.5 Risk factors for infectious arthritis [55–58]

Route of infection	Risk factors
Hematogenous	Human immunodeficiency virus infection
	Immunosuppressive medication
	Immunosuppressive medication
	Intravenous drug abuse
	Diabetes mellitus
	Osteoarthritis
	Rheumatoid arthritis
	Sexual activity (gonococcal)
Contiguous	Osteomyelitis in an adjacent bone
	Skin infection
	Infected skin ulcers
Direct inoculation	Prior intraarticular injection
	Post prosthetic joint replacement
	Recent joint surgery

end. Recently, significant dysregulation of cytokine responses was demonstrated in CRMO.

Chronic nonbacterial osteomyelitis primarily affects children and adolescents, but can occur in all age groups. Peak onset of the disease is between 7 and 12 years of age with a slight female predominance. The clinical presentation is variable, with relatively benign, self-limiting episodes of monofocal bone lesions to its most severe form, CRMO. The exact molecular pathophysiology of chronic nonbacterial osteomyelitis remains largely unknown. Provided familial clusters and the association with inflammatory disorders of the skin and intestine suggest a genetic predisposition. The molecular pathophysiology of autoinflammatory bone disorders is complex and incompletely understood. Current knowledge indicates that bone inflammation is the net result of impaired immune responses with disbalanced cytokine expression, osteoclast differentiation and activation, osteolysis, and bone remodeling [60].

Multimodality Imaging of Skeletal Infections

In many clinical practices, skeletal infections are frequently encountered. For example, such infections are commonly seen in cancer patients and in immunosuppressed individuals. Particularly when comorbidity is present, the clinical presentation may be confusing, and the laboratory findings often are not specific. Several imaging modalities are now being utilized for detection of osteomyelitis, including standard radiography, computerized tomography (CT), magnetic resonance imaging (MRI), and nuclear medicine techniques. The choice of modality depends on clinical presentation, duration of symptoms, site of suspected infection, previously known underlying pathology (such as fracture or tumor), and other factors but importantly a good understanding of the pathophysiology [34].

Acute Osteomyelitis Imaging

Standard radiographs are not sensitive for early detection of osteomyelitis, as the changes (Fig. 5.15) are evident only after 10–21 days from the time of infection [61]. The initial imaging modality in childhood osteomyelitis is conventional imaging. Normal conventional imaging does not exclude osteomyelitis [59].

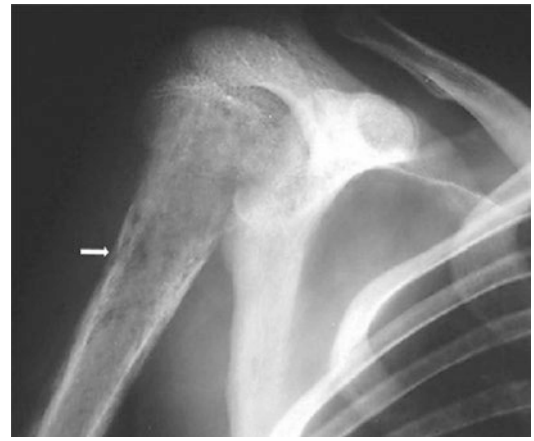

Fig. 5.15 A radiograph of an adult patient with osteomyelitis showing the typical radiographic changes of bone demineralization, bone lysis, and cortical lucency (*arrow*)

Ultrasound is useful in detecting osteomyelitis early, particularly in infants and children. Since osteomyelitis in this age group affects predominantly the end regions of long bones, ultrasound can detect characteristic findings associated with the pathological changes in these areas. Deep soft tissue fluid collection around the bone, periosteal thickening or elevation with subperiosteal fluid collection and increased vascularity within or around the periosteum are common characteristic features [62].

MRI has an important role in the diagnosis of osteomyelitis. In adults, MRI is reported to have a high diagnostic accuracy (95.6% sensitivity, 80.7% specificity) with similar performance to PET (85% sensitivity, 92.8% specificity). However studies for accuracy in children are limited to draw conclusion [63]. The average overall accuracy of MRI is similar to that of multiphase bone scans. In the last decade MRI has become an important modality for the diagnosis of acute osteomyelitis in children [30, 56]. Since it is both sensitive for the detection of early osteomyelitis and also shows accurately the extent of disease with any associated soft-tissue extension without the risks associated with radiation exposure [64]. Accordingly the current recommendation is to

start with plain X-ray followed by MRI for the diagnosis of acute osteomyelitis [65].

Bone scintigraphy is very sensitive in the early diagnosis of osteomyelitis [66, 67] and can show the abnormality as early as 24 h after infection [68].

Typically, there is focally increased flow, blood pool activity, and delayed uptake (Fig. 5.16). When the bone has not been previously affected by other pathological conditions (nonviolated), the bone scan has high accuracy and is a cost-effective modality for diagnosis of osteomyelitis with both sensitivity and specificity of 90–95% [35].

However, there have been some reports of proven early acute osteomyelitis demonstrating either reduced or normal accumulation of the radiopharmaceutical, particularly in neonates. These reports were based on the use of earlier gamma instrumentation. With the use of modern technology, the more recent reports show high accuracy of bone scan (Fig. 5.17) in the diagnosis of neonatal osteomyelitis [69–71].

Tuson et al. [70] found that the positive predictive value of reduced uptake (a "cold" scan) in a selected group of patients was higher (100%) than that of a typical "hot" scan (82%), confirming an earlier report [72] that a "cold" scan indicates more virulent disease. Cold lesions had an average shorter history (4 days) than did hot lesions (7 days) [72]. A more recent report on seven cases with cold scan osteomyelitis also confirmed the prior data regarding the more aggressive nature of this infection that was also associated with elevated ESR, significantly elevated temperature and resting pulse, longer hospital stay, and higher rate of surgical interventions [73]. Cold foci on bone scan in cases of osteomyelitis are thought to be secondary to increased intraosseous and subperiosteal pressure.

SPECT/CT had added value in the detection of osteomyelitis. In a study on 85 children suspected of having osteomyelitis, bone scan with SPECT/CTSPECT/CT was significantly superior to planar scan and changed the diagnosis and treatment planning in 14/85 (16.5%) patients. It increases the accuracy of the diagnosis in the evaluation of osteomyelitis compared to planar three-phase bone scintigraphy/SPECT. Planar bone scan/SPECT predicted the correct diagnosis in 82% of patients with proven osteomyelitis, while SPECT/CT predicted the correct diagnosis in 98% patients. Additionally, SPECT/CT was statistically more successful in detection of chronic osteomyelitis and useful in differentiating chronic from acute osteomyelitis (kappa value of 0.541 for planar scan/SPECT and 0.944 for SPECT/CT) [33].

If bone has been affected by a previous pathology (violated), particularly after orthopedic surgical procedures, which can be common in cancer patients especially with orthopedic tumors, the bone scan will still be highly sensitive, but the average specificity is only approximately 34% [35]. In such situations, unless the bone scan is unequivocally negative, an additional modality should be used, particularly scanning with leukocytes labeled with ^{111}In-oxine or ^{99m}Tc-hexamethyl propylene amine oxime (HMPAO). Overall, ^{111}In-leukocyte studies have a sensitivity of approximately 88% and a specificity of 84% for osteomyelitis [34]. This modality is particularly useful for excluding infection in previously violated bone sites such as in postsurgical and posttraumatic conditions; ^{99m}Tc-HMPAO-labeled leukocytes have sensitivity and specificity similar to those labeled with ^{111}In and can be used particularly in peripheral locations such as the extremities. In a recent meta-analysis study tc99m labeled leukocyte studies showed the highest accuracy compared to PET and MRI with a sensitivity of 91% and specificity of 92% [74]. Combined labeled leukocytes and bone scans have a better accuracy than labeled leukocyte scans alone and can help to localize abnormal foci [75–77].

Since labeled leukocyte scans show uptake by active bone marrow, it may be difficult to differentiate this normal marrow uptake from abnormal uptake due to infection. Furthermore, surgical procedures may alter the bone marrow distribution significantly. Bone marrow scan using ^{99m}Tc-sulfur colloid or nanocolloid may be used to improve the specificity of such studies.

Labeled antibodies have also been used for the diagnosis of osteomyelitis: ^{111}In- or ^{99m}Tc-labeled

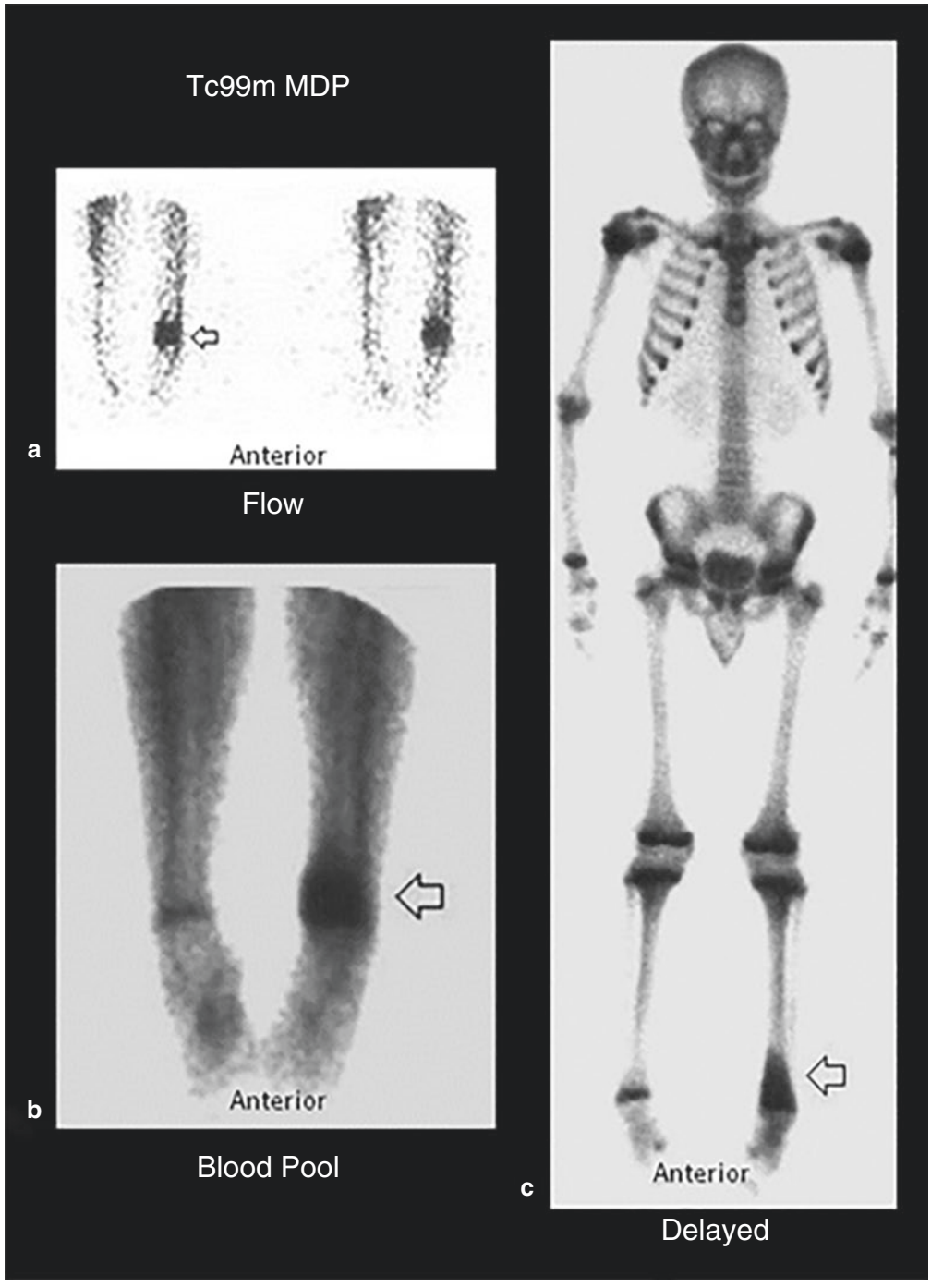

Fig. 5.16 A case of osteomyelitis in a nonviolated bone as seen on ^{99m}Tc multiphase bone scan. Regionally increased flow (**a**), blood pool activity (**b**), and delayed uptake (**c**) are noted in the left distal tibia

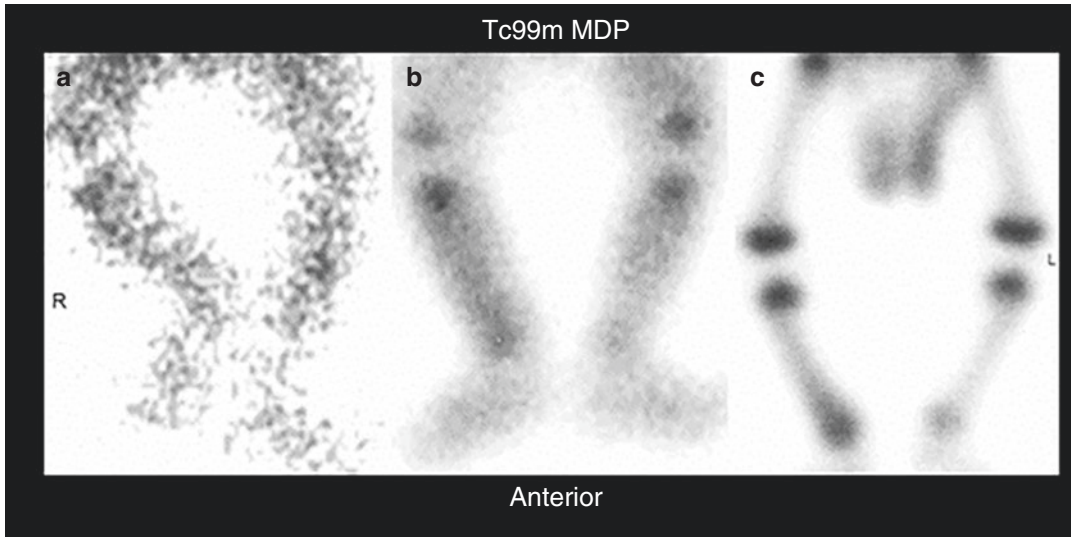

Fig. 5.17 Neonatal osteomyelitis involving right tibia. There is increased flow (**a**), increased blood pool (**b**) in the right tibia, and corresponding increased delayed activity (**c**) in the area of involved bone

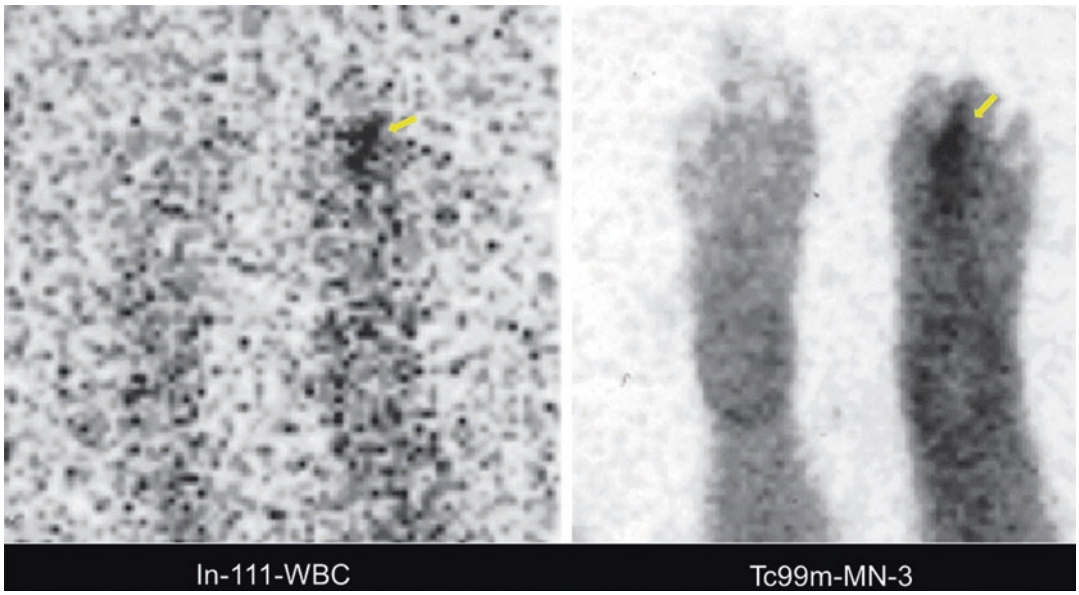

Fig. 5.18 ^{111}In-labeled leukocyte and 6-h MN3 images (plantar views) from a diabetic patient with osteomyelitis of the left second metatarsal (arrows). While both studies are positive, the superior image quality of the technetium-labeled compound can be easily appreciated. (Courtesy of Dr. Christopher Palestro, with thanks)

human nonspecific polyclonal antibodies (IgG) and monoclonal antibodies such as labeled anti-granulocyte antibodies. These agents are easier to prepare and use than labeled leukocytes. LeukoScan (anti-NCA-90) (Fig. 5.18) and fanolesomab (anti-NCA-95) were reported to have similar or better accuracy (90%) to labeled WBC scan [78].

However, more recent studies showed conflicting results and suggest that these agents do not achieve the level of accuracy that was suggested earlier and are not accurate enough to

replace labeled WBC imaging for orthopedic infection [79, 80].

In a preclinical study, Koort et al. [81] studied 16 rabbits in two groups of 8: one group was a control and the other was infected with *S. aureus* directly into the tibia. In the infected group, metaphyses were resected and replaced with a preinfected block of bone cement; in the control group, the metaphyseal defect was replaced by bone cement injected with sterile saline. Two weeks later, the bone cement in both groups was surgically removed and osteomyelitis was confirmed in the infected group. At 3 and 6 weeks, a peripheral CT and 18F-FDG positron emission tomography (PET) were performed. PET images showed not only higher 18-FDG activity in the osteomyelitic group but also continuous elevated uptake at 6 weeks. Using standardized uptake values, the control group showed a decrease from 1.9 to 1.2 at weeks 3 and 6, respectively, whereas the infected group measured a 3.1 at week 3 and 5.5 at week 6. The results showed that intact bones have low 18F-FDG uptake and normal bone healing (seen in the control group) will have a transient increase in uptake just to normalize within a 6-week period. Bone infection, however, showed a markedly higher, constant uptake. This study indicates that 18F-FDG-PET can differentiate bone healing from infection. The study also proposes that 3–6 months should be allowed following surgical or traumatic bone healing just to lower the chance of a false positive.

Reports described Ga-68-citrate and Ga-68-transferrin as possible agents for PET imaging of infection. (68)Ga has half-life of 68 min compared to 78.3 h for ^{67}Ga. Ga-68-citrate or Ga-68-transferrin was able to detect infected lesions in rats within 5–10 min postinjection, but a focal intense uptake at the lesion (SUV(max)) was visualized only at 30 min. In the patient studies, infection lesions were detected within 30 min postinjection. Blood pool and liver activities decreased during the period of study. There is no chemical difference between Ga-67-citrate and Ga-68-citrate, except for the radiolabel. Background uptake of Ga-68 and uptake by liver, cardiac blood pool activity is much lower than ^{6}Ga-67 at 60-min postinjection period. The short half-life of Ga-68 (68 min) may be advantageous from low dosimetry to the patients. The advantage of Ga-68 compared to FGD is that it is positive only in cases of infection. Preliminary reports suggest Ga-68-citrate PET/CT is useful in the diagnosis of suspected bone infections with reliable accuracy [82].

Imaging of Specific Forms of Musculoskeletal Infections

Diabetic Foot Osteomyelitis

Despite this limitation, plain X-ray has been and still the first imaging modality to consider in patients with a suspicion of diabetic foot osteomyelitis according to the Infectious Diseases Society of America /IWGDF guidelines [83]. Bone scanning is very sensitive but not specific for detecting infection in diabetics. It is usually positive in cases of neuroarthropathy as well as of infection, with a lower specificity ranging from 0 to 70% (average 27%) [34]. Accordingly, the bone scan cannot reliably distinguish infection from neuroarthropathy. The three-phase bone scan, using the parameter of arterial hyperemia only on flow studies for scan interpretation along with increased activity on blood pool and delayed images for diagnosing osteomyelitis, as stated earlier, may improve the specificity. Also, the specificity can be further improved with adding a fourth phase of imaging with acquiring a 24-h delayed image.^{67}Ga is not helpful in resolving the question of osteomyelitis in the diabetic foot, since it is also usually positive in noninfected neuroarthropathy. Indium-111 leukocyte imaging has been reported to be both sensitive and specific for diabetic foot infections. However, sensitivities range from 50 to 100% and specificities from 29 to 100% [26]. All ulcers exposing bone were found to be associated with osteomyelitis, and such patients may thus be treated without the need for imaging [84]. Patients with ulcers not exposing bone were recommended to have ^{111}In-leukocyte studies to detect osteomyelitis. False-positive results have been reported in several conditions, including rapidly progressive neuroarthropathy, and the specificity varies in the literature. The vast majority of neuroarthropa-

thies are not rapidly progressive and show no abnormal accumulation of labeled leukocytes. ^{111}In-white blood cell imaging shows significantly increased uptake. Combined bone/labeled leukocyte imaging improves the accuracy of the diagnosis of foot osteomyelitis and its differentiation from soft tissue infection. Grerand [75] reported a sensitivity of 93% and a specificity of 83% for this dual-isotope technique and concluded that it can reliably determine the site and extent of diabetic foot osteomyelitis. False-positive results however can still occur in some cases of noninfected neuroarthropathy [85]. A decreasing lesion-to-background ratio of labeled WBCs between 4 and 24 h helps to differentiate the condition from osteomyelitis, which usually does not show a decreasing ratio (Fig. 5.19). Because of the poor spatial resolution of labeled leukocyte studies, uptake in soft tissues could be incorrectly attributed to bone uptake and vice versa. Dual-isotope studies for diabetic foot allow for better localization of white blood cell activity and consequently help to increase the accuracy in differentiating osteomyelitis from cellulitis [86, 87].

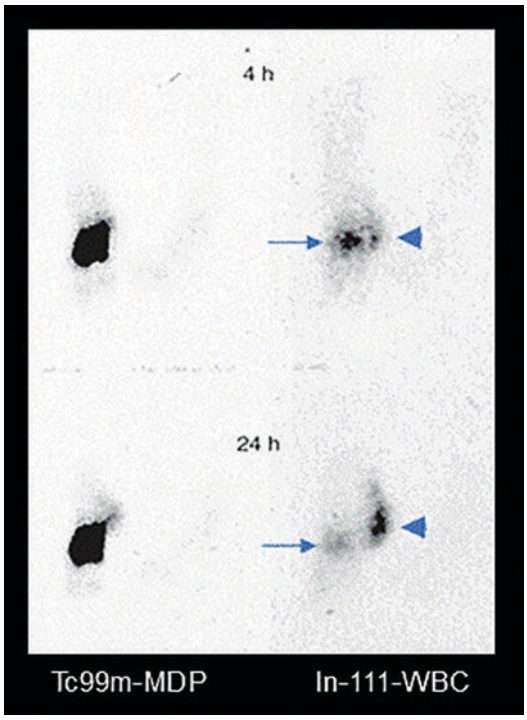

Fig. 5.19 (**a**, **b**) Simultaneous^{99m}Tc MDP and ^{111}In-labeled leukocyte bone scan illustrating the decreasing leukocyte uptake in the area of neuroarthropathy (*arrow*) and increasing uptake in the area of osteomyelitis at the region of the right heal (*arrowhead*)

Collective studies have shown an average sensitivity of 83% for both labeled leukocyte and combined bone/leukocyte scintigraphy. The average specificity, however, improved from 64% for the leukocyte scan to 80% when it was combined with bone scintigraphy [34].

SPECT/CT (Fig. 5.20) imaging for diabetic foot osteomyelitis with^{99m}Tc-MDP and In-111-labeled leukocyte scans was more accurate in diagnosing and localizing infection compared with conventional planar imaging. Additionally, it provided clear guidance and promoted many limb salvage procedures. Its use was associated also with considerably reduced length of hospitalization [67, 68]. A novel standardized hybrid image-based scoring system, Composite Severity Index (CSI), derived from Tc99m-WBC SPECT/CT images was found to have prognostic value in diabetic foot infections. In a study of 77 patients, CSI of 0 had a 92% chance of favorable outcome, which fell progressively to 25% as indices rose to ≥7 [88].

Combined ^{111}In-labeled leukocyte and ^{99m}Tc-sulfur colloid marrow scans further improve the specificity, differentiating marrow uptake of labeled leukocytes from uptake by actual bone infection. Simultaneous SPECT/CT of ^{99m}Tc-sulfur colloid (SC) and ^{111}In white blood cells (WBC) provides essentially perfect spatial registration of the tracers within anatomical sites of interest. Quantitation of this method for compensation for scatter and crosstalk was reported recently to be useful experimentally for improving quality, bias, and precision of ^{99m}Tc activity estimates in simultaneous dual-radionuclide imaging of osteomyelitis [89]. SPECT/CT with In-111-labeled leukocyte combined with bone or bone marrow scan is currently the best imaging modality for diagnosing diabetic foot osteomyelitis [90].

MRI can differentiate between soft tissue and bone infections. This is particularly important in

diabetics and has been found useful in the diagnosis of diabetic foot osteomyelitis. Several investigators found MRI to be clearly superior to the plain films and bone scintigraphy, with a sensitivity and specificity approaching 100%. These studies, however, involved mostly severe infections with significant pathological changes. Newman et al. [91] reported a sensitivity of only 29% for relatively low-grade osteomyelitis compared with 100% for labeled leukocyte

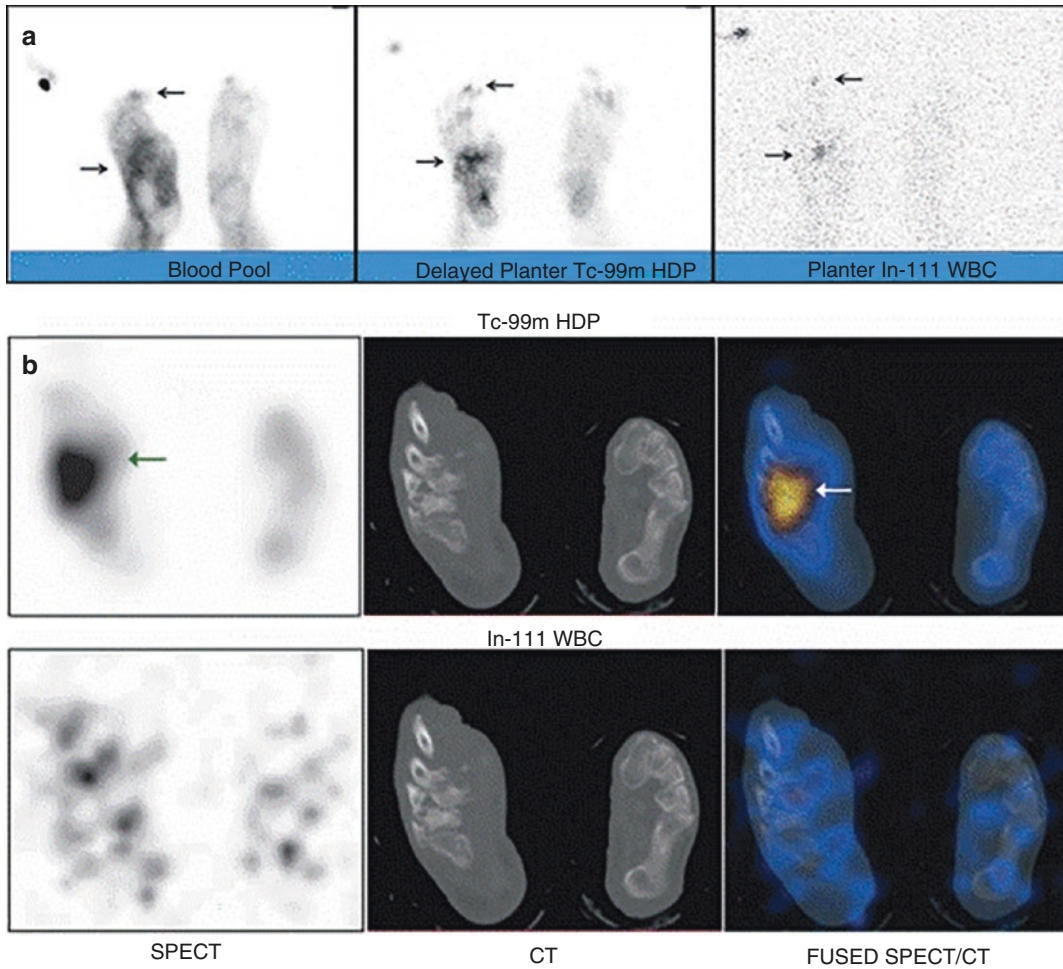

Fig. 5.20 A 59-year-old male diabetic patient S/P right great toe amputation presented with discharging ulcers on the right foot plantar surface, R/O osteomyelitis. (**a**) The blood pool image demonstrates foci of increased blood pool activity involving the probable distal third toe and mid-right foot. The delayed bone scan plantar image demonstrates foci of increased radiotracer uptake in the same regions. On the In-111 WBC plantar image, there are two foci of abnormal uptake also probably in the same areas (*black arrows*). (**b**) In the selected dual-isotope SPECT/CT transaxial slices, there is increased Tc-99m HDP uptake in the right intermediate and lateral cuneiforms and intercuneiform joint without corresponding abnormality on the simultaneously obtained In-111 WBC images (*brown arrows*). These findings are consistent with arthritic changes. (**c**) In the adjacent dual-isotope SPECT/CT transaxial slices, there is increased In-111 WBC uptake in a region of plantar ulcer without corresponding abnormal uptake on Tc-99m HDP bone scan consistent with soft tissue infection (*blue arrows*). (**d**) In another dual-isotope SPECT/CT transaxial slices, there is focal increased uptake in the right third distal phalanx on both bone scan and In-WBC scan images consistent with a small focus of osteomyelitis (*red arrows*). Based on these images, the patient was effectively treated with soft tissue debridement of the large plantar ulcer and distal right third toe partial amputation as well as antibiotics and was saved from a major foot amputation

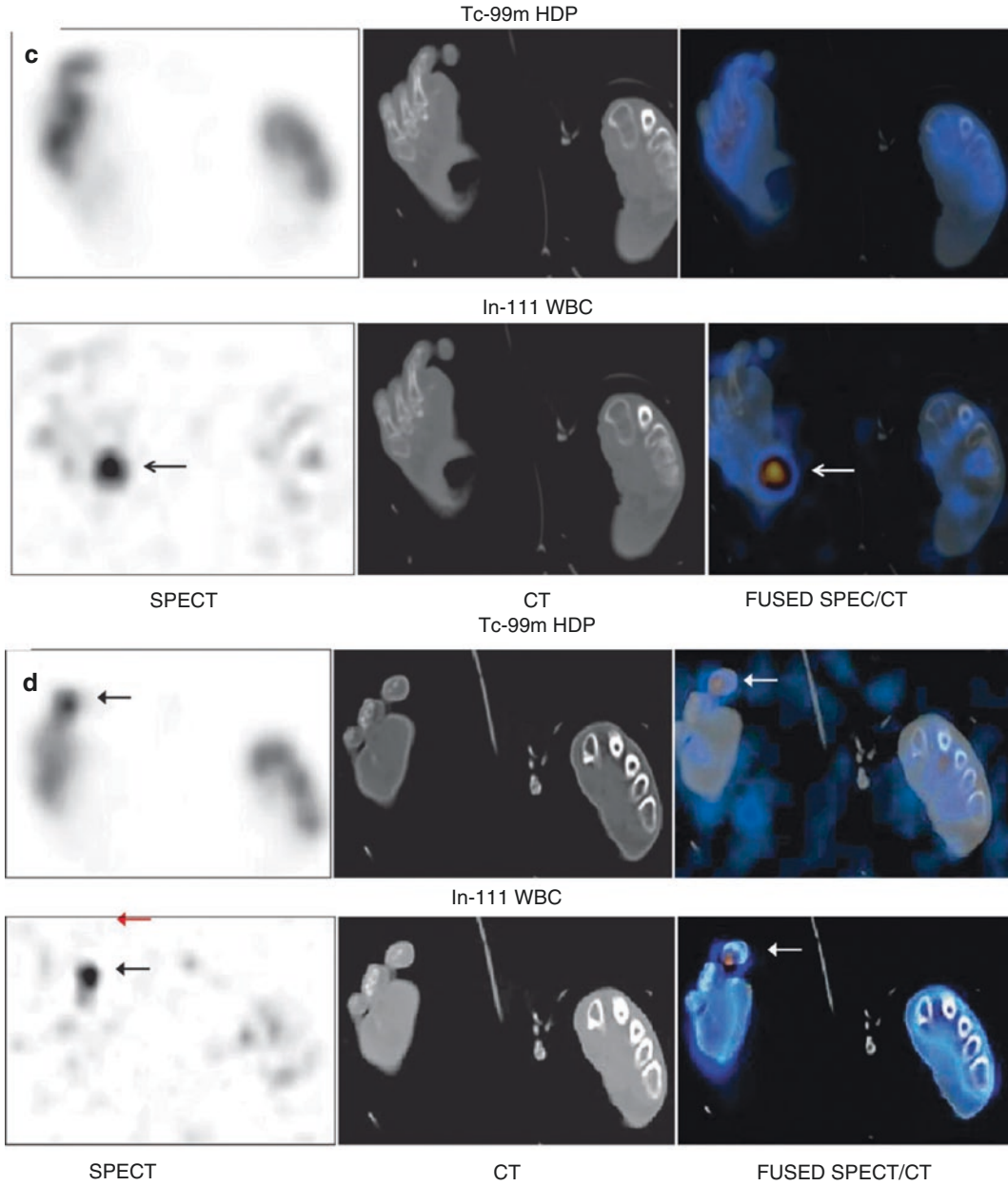

Fig. 5.20 (continued)

scanning of the same patients. The specificity was similar for both modalities. Cook et al. also reported a sensitivity of 91% and a specificity of only 69% [92].

Morrison et al. reported a lower accuracy for diabetic compared with nondiabetic cases, with sensitivity and specificity of 82 and 80%, respectively, for diabetic osteomyelitis compared with 89 and 94% for nondiabetic bone infections [93].

Beltran [94] reported the characteristic pattern of osteomyelitis as a high signal intensity from the marrow space on T_2-weighted images. However, this finding itself is not specific for

osteomyelitis and can be seen with other conditions, including rapidly progressive neuroarthropathy, and the pattern may be indistinguishable from that of osteomyelitis.

Labeled antigranulocyte antibodies are another alternative to be used for diabetic foot infection and have an advantage of earlier results and less demanding technique. The technique as mentioned earlier has been reported to be very sensitive; however, the specificity is again less than adequate with conflicting results.

PET/CT also provides faster results (typically within 2 h). A recent systemic review and meta-analysis compared MRI, labeled leukocyte scintigraphy, and FDGPET/CT for the detection of diabetic foot osteomyelitis to a reference standard of bone biopsy. Despite the comparable sensitivity of all the different imaging modalities, ranging from 89 to 93%, the specificity of ^{99m}Tc-HMPAO labeled leukocyte scintigraphy and FDGPET/CT (92%) was higher than MRI (75%) [95].

Vertebral Osteomyelitis (Spondylodiskitis)

The incidence of vertebral osteomyelitis is increasing, attributed to an ageing population with inherent co-morbidities and improved case detection [96]. Signs and symptoms of vertebral osteomyelitis are usually vague and insidious, and thus, the diagnosis and treatment may be delayed. Plain radiographs are neither sensitive nor specific for the diagnosis of vertebral infection. The bone scan may be sensitive, but it is not specific for vertebral osteomyelitis.

Computed tomography scan is quite sensitive for vertebral osteomyelitis but, like the bone scan, it is not specific. However, CT is used to guide needle biopsy.

Magnetic resonance imaging, however, is both sensitive and specific for vertebral osteomyelitis. Gadolinium-enhanced magnetic resonance imaging (MRI) is the imaging technique of choice to evaluate spinal infection [97]. It has excellent sensitivity and specificity (96% and 94%, respectively) [98, 99].

Changes of vertebral osteomyelitis have been reported to be seen on MRI as early as those on bone scan [100], although in one report, these changes were late, even later than plain film changes [101].

A recent prospective study on 32 patients using ^{18}F–FDG-PET/CT and MRI reported 100% sensitivity for both modalities and a specificity of 90.9% for ^{18}F–FDG-PET/CT and 91.7% for MRI. MRI detected more epidural/spinal abscesses[102].

Love reported on a small number of patients with vertebral osteomyelitis and found that SPECT ^{67}Ga and bone scans are more sensitive and specific than planar gallium and bone scintigraphy (91 and 92% vs. 64 and 85%, respectively). The authors found that ^{67}Ga SPECT alone has identical accuracy to combined SPECT Ga and bone and suggested the use of ^{67}Ga SPECT alone in the diagnosis of vertebral osteomyelitis since it was also sensitive and slightly more specific than MRI in their series [103]. ^{67}Ga has a sensitivity of more than 90% and a specificity of up to 100% when combined with ^{99m}Tc-MDP or alone with SPECT acquisition [104], although the authors prefer the combined approach using SPECT/CT if Gallium is to be used [105].

For planar imaging interpretation, the degree of bone uptake is compared with that of ^{67}Ga to achieve the high specificity of this combined approach (Figs. 5.21 and 5.22).

Standard radiographs are neither sensitive nor specific for the diagnosis of the relatively common spondylodiskitis. Bone scanning is also sensitive but is not specific. In cases of proven vertebral osteomyelitis, bone scan results have been negative as late as 2 weeks following the onset of symptoms [106].

Labeled leukocyte scanning using both ^{111}In and ^{99m}Tc-HMPAO is neither sensitive nor specific. This low sensitivity is due to different patterns of uptake—normal, decreased, or increased—in cases of proven vertebral osteomyelitis [107, 108]. In studying 71 patients with suspected vertebral osteomyelitis, Palestro et al. [107] found that ^{111}In-leukocyte scintigraphy demonstrated increased or decreased uptake in patients with proven osteomyelitis. Increased uptake was associated with a high specificity of 98%, but it was only 39% sensitive for the condition. The photopenic pattern was neither sensitive

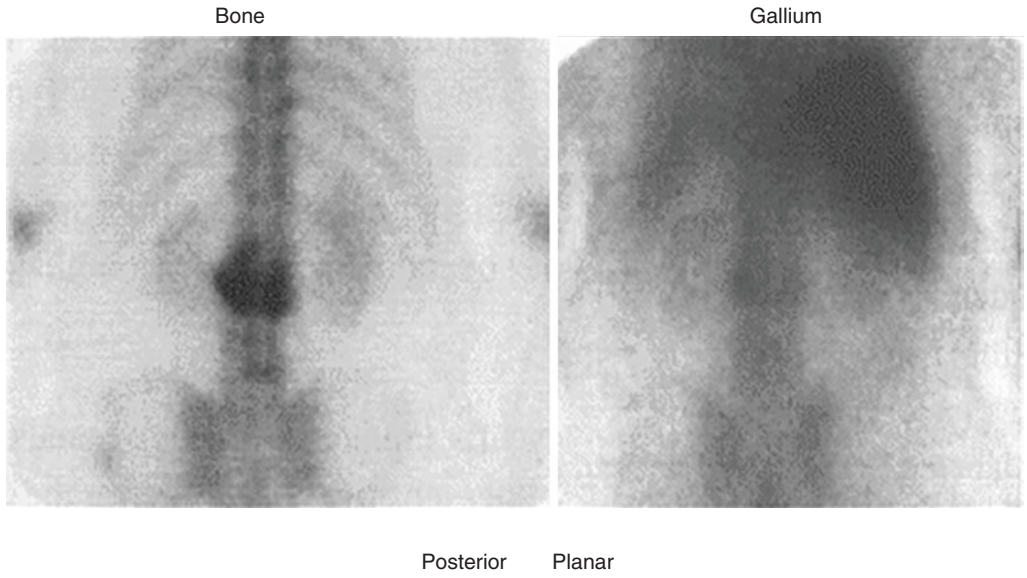

Fig. 5.21 Sequential bone/gallium scans—negative for osteomyelitis in a patient with compression fracture (gallium uptake is less than MDP uptake). (Courtesy of Dr. Christopher Palestro, with thanks)

(54%) nor specific (52%) for osteomyelitis. In a study of 91 patients with suspected vertebral osteomyelitis, Whalen et al. [108] reported a sensitivity of 17%, a specificity of 100%, and an accuracy of 31% for ^{111}In-leukocyte imaging. The authors found photon-deficient areas at the sites of proven osteomyelitis in 50% of 18 patients, and they were included in the false-negative scans. Because the diagnosis of vertebral osteomyelitis is often delayed, most infections are chronic in nature, which can explain the low sensitivity of ^{111}In leukocytes in their diagnosis. Photopenic areas on ^{111}In-leukocyte imaging in proven vertebral osteomyelitis could be secondary to secretion of antichemotactic factors by some causative organisms such as *Pseudomonas aeruginosa* and *Klebsiella pneumoniae*, which prevent enough accumulation of labeled cells at the site of infection [109, 110].

In a study performed on 30 consecutive patients, positive PET scans were found in all five cases with disc space infection. None of the patients with degenerated disc space demonstrated FDG uptake, even in the presence of substantial end-plate abnormalities, the authors suggested that FDG-PET may be useful for excluding disc space infection in equivocal MR findings [111].

FDG-PET is sensitive, has superior image quality, and is completed in a single session. The specificity of FDG-PET may also be superior to that of conventional tracers because degenerative bone disease and fractures usually do not produce intense FDG uptake [112].

Accordingly if MRI is not conclusive or there is a condraindication for its use, F-18 FDG-PET/CT is the modality of choice with Ga-67 as an alternative [113–118].

Chronic Osteomyelitis

The radiological diagnosis of chronic active osteomyelitis is neither sensitive nor specific, while bone scintigraphy is very sensitive but not specific. This low specificity is due to the chronic bone repair that is associated with increased bone metabolism and increased uptake on bone scan in the absence of active infection. It is therefore difficult to differentiate healing from chronic active disease, although increased activity on all phases of the bone scan is suggestive of chronic active disease. The bone scan, accordingly, cannot confirm the presence of active disease, but a negative scan excludes it.

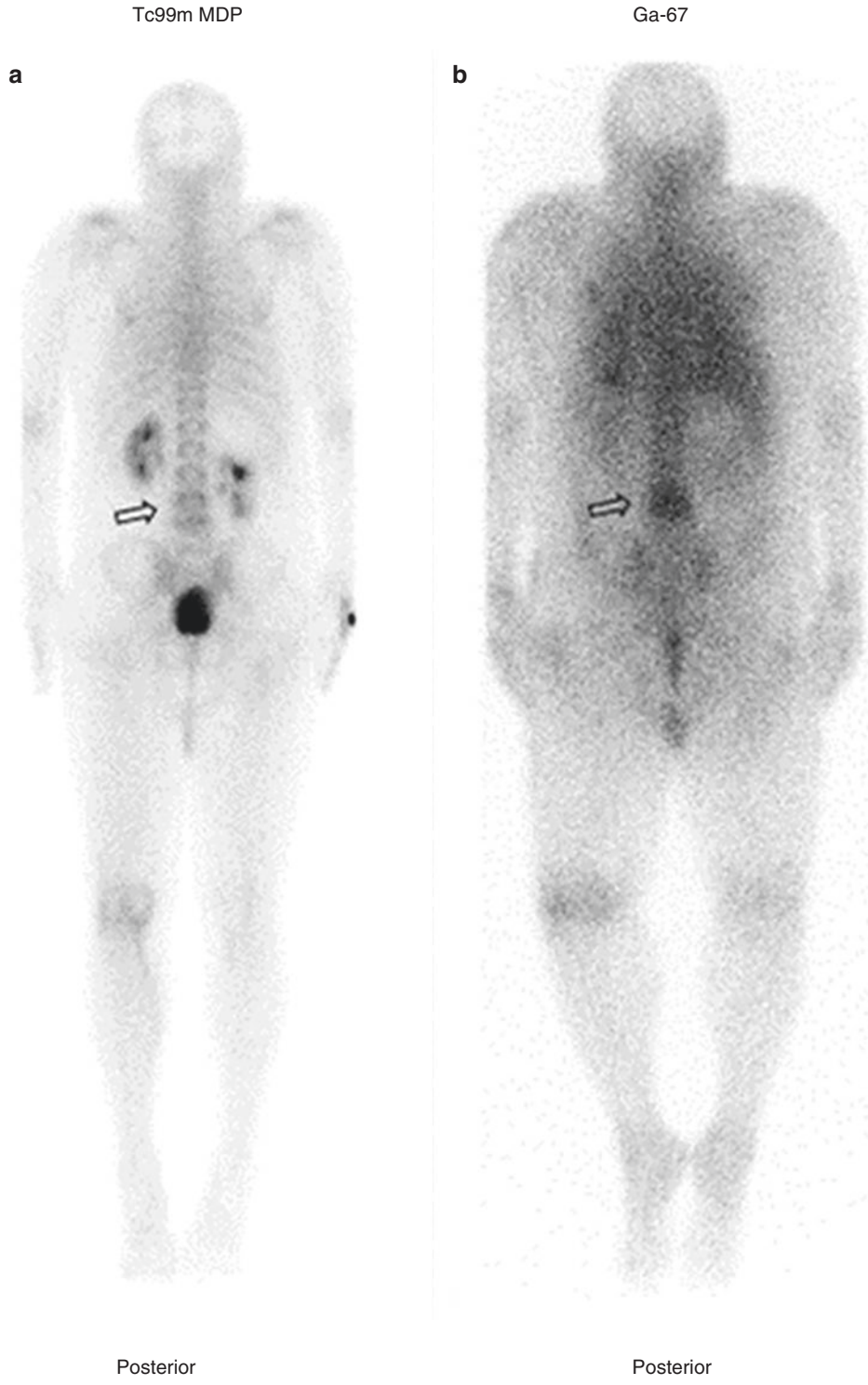

Fig. 5.22 Sequential bone/gallium scans. Posterior whole body images of bone (**a**) and Ga-67 (**b**) studies are shown, demonstrating increased uptake on both studies (arrows) at the site of L2/L-3. However, the degree of uptake is significantly higher on the Ga-67 study than bone, indicating spondylodiscitis

^{67}Ga citrate imaging is more specific than bone scanning for chronic osteomyelitis. False positives still occur in conditions such as healing fractures, tumors, and noninfected prostheses. Combined ^{99m}Tc-MDP and ^{67}Ga scans can be helpful in making the diagnosis of active disease. As Tumeh et al. [119] suggested when ^{67}Ga uptake exceeds ^{99m}Tc-MDP uptake in intensity or differs in spatial distribution, active osteomyelitis usually is present.

There is controversy regarding the role of ^{111}In-labeled leukocytes in the diagnosis of chronic osteomyelitis. Since the majority of labeled cells are polymorphonuclear cells, the test is usually normal in true chronic osteomyelitis. However, due to the difficulty in making a clinical distinction between acute and chronic active disease, results are variable and may be confusing with no advantage of ^{111}In-leukocytes over ^{67}Ga, as there was no significant difference between them in the sensitivity and specificity for both conditions [120, 121].

Determining the presence or absence of sequestra is important, as their presence may require surgical treatment. The CT scan is a sensitive modality for the detection of sequestra. MRI was found useful in detecting sequestra and was also useful in identifying the presence and sites of active chronic infection [122].A study [123] confirmed the lack of specificity of multiphase bone scans for chronic osteomyelitis and suggested a possible role for labeled IgG as a more specific agent in both central and peripheral chronic bone infections. Thus, among the commonly used modalities, combined bone and ^{67}Ga scanning is highly recommended for detecting chronic active osteomyelitis if PET is not available.

F18-FDG PET has been found valuable to assess the activity of chronic osteomyelitis by confirming the presence of metabolically active infection and guide appropriate treatment [124]. A meta-analysis study showed that FDG-PET not only is the most sensitive (96%) imaging modality for detecting chronic osteomyelitis but also has a greater specificity (91%) than radiolabeled WBC scintigraphy, bone scintigraphy, or MR [125]. Several studies reported that the overall sensitivity is 95–100% and specificity is 86–100% [124–128].

Periprosthetic Infection

- Making the distinction between mechanical failure of a prosthesis and infection is not easy. Symptoms and signs of early infection are not specific and may even be similar to those of the normal healing process. The erythrocyte sedimentation rate and leukocyte count are not sensitive, and the standard radiographic appearance of infection can mimic that of mechanical loosening. Aspiration arthrograms are relatively more accurate, but, again, the sensitivity as reported by Johnson et al. [52] is only 67%. The late stages of infection can be detected more easily on the basis of clinical findings. It is crucial, however, to initiate treatment in the early stage, as progression to a serious infection may occur rapidly [129].

In case of hip replacement, knowledge of the type of implant is important to plan a diagnostic strategy. In cemented total hip replacements, periprosthetic uptake patterns are variable during the first 12 months after joint replacement. On bone scintigraphy of the cemented hip replacement, focal uptake at the tip of the femoral component is most typical of loosening, while diffuse uptake around the shaft is most typical of infection. These patterns are not specific, however, and there are controversies regarding their value in discriminating loosening from infection. Labeled white blood cells with or without marrow scanning may be needed. In cementless, porous-coated hip arthroplasty (which depends on bony ingrowth for fixation instead of on cement), postoperative uptake on bone scintigraphy remains for 2 years or longer in asymptomatic patients [130, 131].

In knee replacement, postoperative increased uptake may also be seen on bone scintigraphy in more than 60% of femoral components and about 90% of tibial components for a long time, even when patients are asymptomatic [132].

Accordingly, for both cemented and porous-coated hip and knee replacements, a bone scan is most useful in excluding infections when it is clearly negative.

Combined bone and ^{67}Ga scans have better specificity than either scan alone (Fig. 5.23). However, ^{111}In-leukocyte imaging has proven to have better accuracy than combined ^{67}Ga/bone scan. Still, false-positive ^{111}In-leukocyte results occur as a result of physiological uptake by cellular bone marrow. Oswald et al. [131] found focal or diffuse accumulation of ^{111}In leukocytes around the prostheses for up to 2 years in 48% of uncomplicated cases. Addition of ^{99m}Tc-sulfur colloid bone marrow to ^{111}In-leukocyte scanning helps improve the specificity and is the recommended modality. The study is considered positive for infection when the ^{111}In-leukocyte uptake exceeds ^{99m}Tc colloid activity on the bone marrow scan in extent and/or focal intensity (discordant pattern). If the relative intensity and distribution of ^{111}In-labeled leukocyte localization are equal to that of ^{99m}Tc colloid (concordant pattern of normal marrow), the study is considered negative for infection [133].

Accordingly, the optimal procedure for diagnosing infection of joint replacements is combined labeled leukocyte/marrow scintigraphy (Figs. 5.24 and 5.25), which has a diagnostic accuracy of more than 90% [133].

Combined ^{111}In-WBC and ^{99m}Tc-sulfur colloid SPECT/CT are adequate tools to diagnose (prosthetic) bone and joint infections [134]. With a sensitivity of 100%, specificity of 91%, and accuracy of 95%, it seems to be significantly better than FDG-PET. ^{99m}Tc-WBC is a very sensitive tool (95%) for imaging of infection in patients with metallic implants. Specificity is also high (93–100%) with SPECT/CT, but it seems dramatically lower (53%) in case of ^{99m}Tc-WBC SPECT alone. The improvement of specificity by addition of CT to SPECT is of substantial importance, as has been shown in multiple studies [135, 136].

Antibody imaging (Fig. 5.26) has also been used to diagnose infections in patients with hip and knee prostheses with a sensitivity of 70–100% and a specificity of 83–100% for ^{99m}Tc-antigranulocyte antibodies and a sensitivity of 92% and a specificity of 88% for ^{111}In-labeled IgG [137].

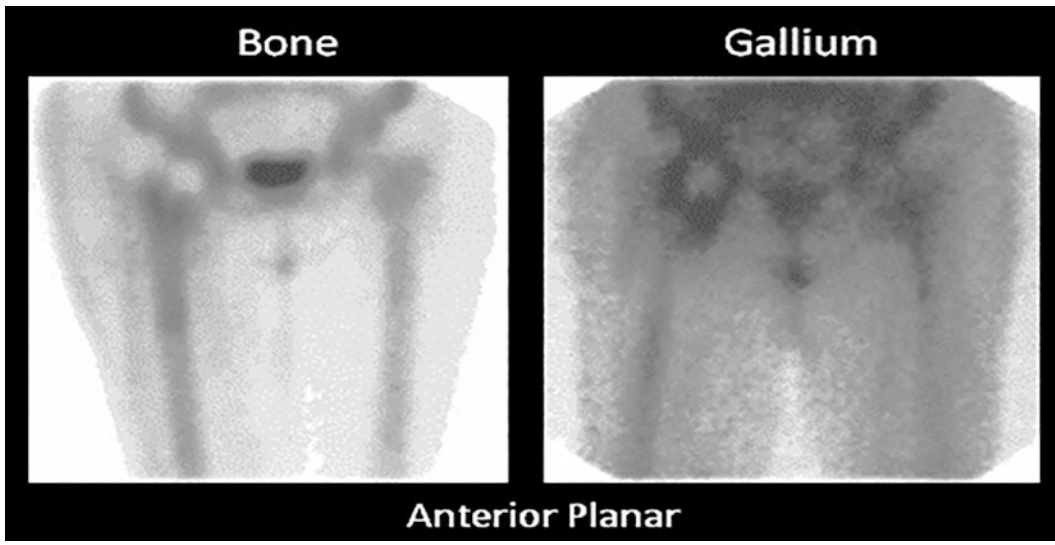

Fig. 5.23 Sequential bone/gallium scan—positive for infection of the right total hip replacement (incongruent distribution of two radiotracers). (Courtesy of Dr. Christopher Palestro, with thanks)

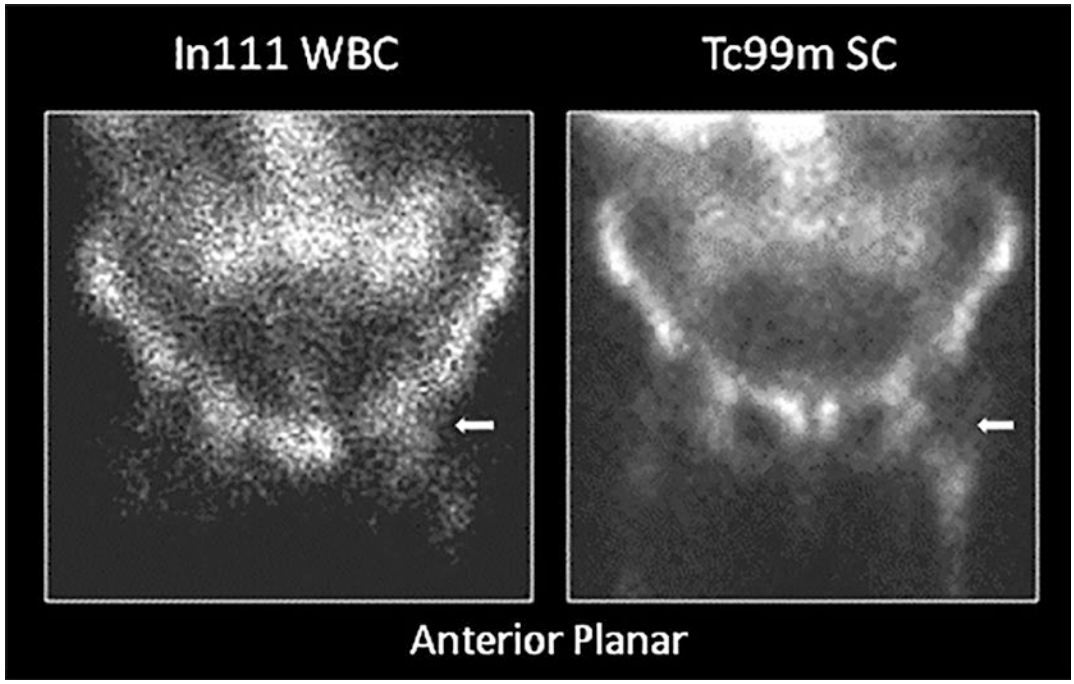

Fig. 5.24 Combined leukocyte/marrow scan with congruent uptake pattern in the left hip region (arrows) indicating no infection. (Courtesy of Dr. Christopher Palestro, with thanks)

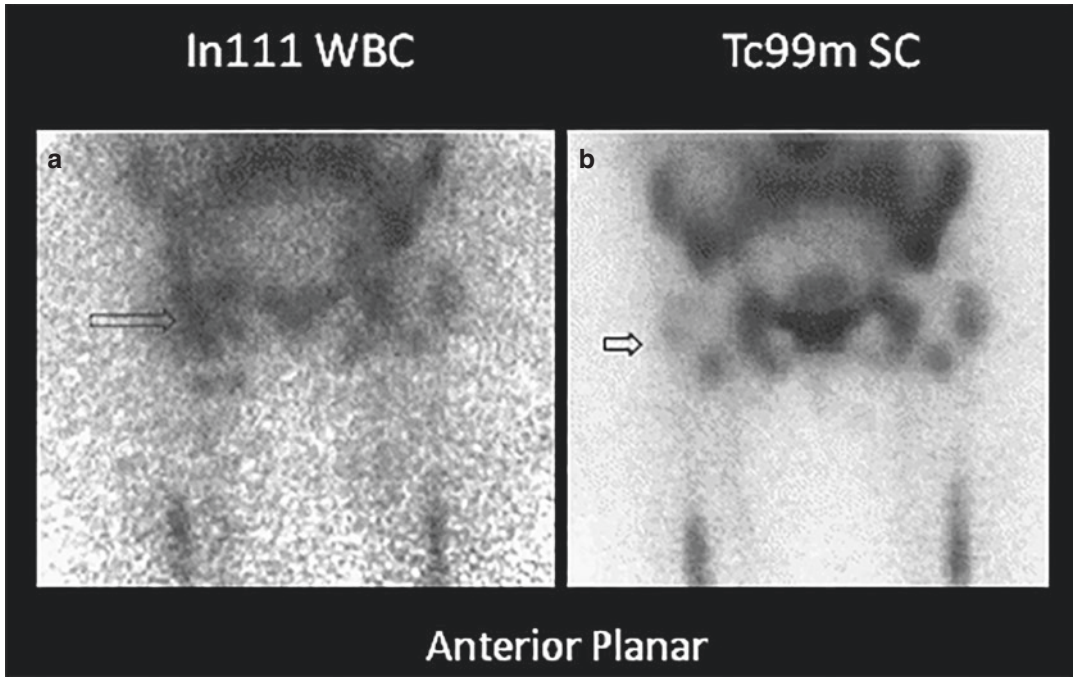

Fig. 5.25 In-111 labeled leukocyte image (**a**) for a patient with a history of bilateral hip replacements. There is accumulation of leukocytes at the right hip with no corresponding uptake on sulfur colloid bone marrow (arrows) image (**b**) indicating right periprosthetic infection showing incongruent pattern compared to the left side which shows no evidence of infection and essentially congruent leukocyte and sulfur colloid uptake pattern

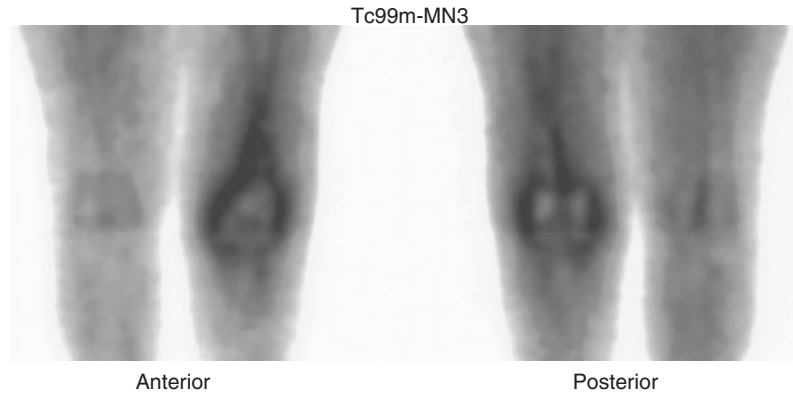

Fig. 5.26 Antigranulocyte antibody uptake indicating infected left knee prosthesis. (Courtesy of Dr. Christopher Palestro, with thanks)

Annexin-V imaging shows greater uptake with infection than with aseptic loosening and has a high negative predictive value for prosthetic infection [138] (Fig. 5.27).

FDG-PET has been shown to be useful in detecting infections and differentiate it from loosening in patients with hip and knee prostheses [139, 140]. Initial studies reported sensitivity and specificity for detecting infection of approximately 90 and 89% for hip and 90 and 72% for knee periarthroplasty infections, respectively [140]. A more recent data reported an overall sensitivity of 91–100% [135]. Specificity, however, is strongly dependent on the used criteria to report infection based on both localization and intensity of FDG uptake, ranging from 9 to 97% [137]. Specificity is generally higher in hip prostheses, compared with knee prostheses [135]. Although the intensity of FDG uptake as determined by SUV values is important in making the diagnosis of malignancy, this is not the case with periprosthetic infections. Infected prostheses often show moderate increased uptake which is not higher than that noted with aseptic loosening [139]. However, the location of the increased uptake is more important in differentiating infection from loosening since infection is characterized by uptake along the interface between bone and the prostheses, while in loosening it is around the neck and head [139]. Using this criterion, a sensitivity of 92% and a specificity of 97% have been reported [135]. This criterion however remains to be validated in a prospective study. A recent meta-analysis found that the sensitivity and specificity of FDG-PET for diagnosing lower extremity prosthetic joint infection were 87% and 82%, respectively, lower than what has been reported for combined leukocyte-marrow imaging over 30 years [141]. In a study of 34 patients ga-68 and F-18FDG PET/CT were compared and evidence that ^{68}Ga-citrate PET/CT may have a complimentary role to ^{18}F-FDG PET/CT in detecting prosthetic joint infections, since it was found to have a higher specificity (88% vs. 38%) and the ability to discriminate between an infectious condition and sterile inflammation [142].

FDG-PET/MR was reported to have sensitivity of 100% in a small series of 7 patients [143]. A more recent study confirmed the value of this technique and the superior anatomic details obtained by MRI is addition to the molicular information of PET in one single study [144].

Osteomyelitis in Patients with Sickle Cell Disease. Differentiating bone infarct from osteomyelitis clinically is difficult. Initial radiographs either are normal or show nonspecific changes. On bone scintigraphy, the findings vary. If bone scintigraphy is performed a week after the onset of symptoms, healing of the infarct may cause increased uptake rather than the typical pattern of cold defect. To add more difficulty, osteomyelitis may also cause cold defects rather than increased uptake [35, 46, 145].

Addition of ^{67}Ga or ^{99m}Tc-sulfur colloid imaging to bone scans enhances the specificity and can resolve the majority of diagnostic problems related to osteomyelitis in patients with sickle cell disease [145]. If the bone scan shows areas of increased uptake, a bone marrow scan can be added. If a marrow scan in the area of interest is

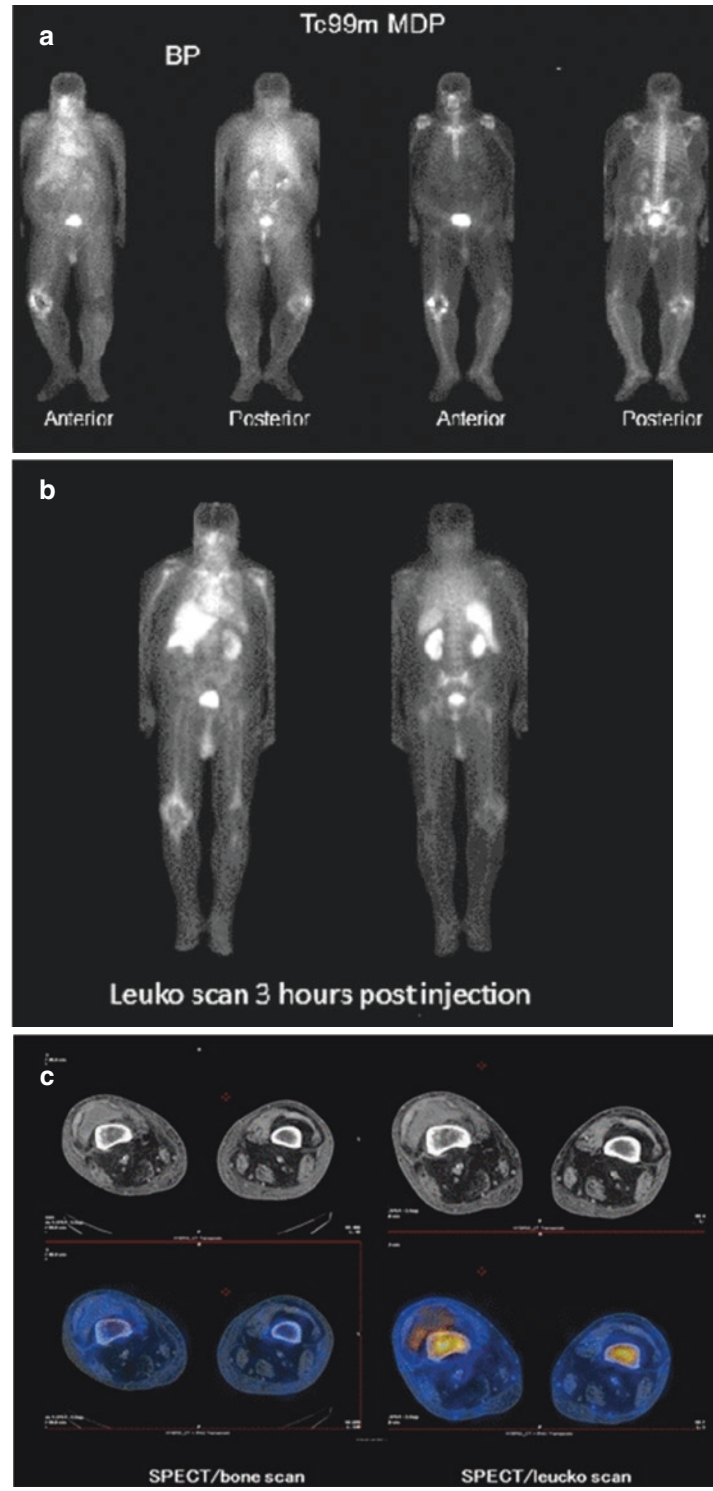

Fig. 5.27 A 68-year-old male with bilateral total knee replacement prostheses and a complaint of pain on the right side. Bone scan (**a**) showed increased blood pool and delayed activity around the right knee prosthesis (arrow). Whole-body leukoscan images (**b**) show increased accumulation around the right knee prosthesis corresponding to the bone scan findings and confirmed further by SPECT/CT of bone scan and SPECT/CT of leukoscan (**c**)

normal, it indicates osteomyelitis, while if radiocolloid photon deficiency is seen it suggests healing infarct. Conversely, if the bone scan shows a photon-deficient area, ^{67}Ga may help to differentiate osteomyelitis by showing an incongruent pattern spatially or more ^{67}Ga uptake than that on the bone scan. Infarcts will show a congruent pattern [46].

Labeled leukocytes have also been used, although we encountered technical difficulties in labeling cells of sickle cell patients with failed scans. MRI and contrast-enhanced CT scans have also been reported to be of help in patients with nondiagnostic radiographs and bone scans.

Malignant Otitis Externa

Malignant otitis externa is severe inflammation of the soft tissue of external auditory canal commonly caused by pseudomonas aeruginosa. It is an aggressive, highly morbid, and rarely life-threatening infection. Infection may spread to involve the periosteum and bone of the skull base [146]. It affects elderly patients with diabetes particularly and needs quick diagnosis and management. CT scan can help make the diagnosis. Ga-67 is highly sensitive in detecting infection but lacks the resolution to assess bone involvement. F-18 FDG PET/CT (Fig. 5.28) can be of value in assessing the infection and bone involvement and was found to have a sensitivity of 96% and a specificity of 91%, with the highest accuracy for confirming or excluding osteomyelitis compared to all other modalities [147]. It can monitor treatment response. Gallium-67 is an alternative to monitor the response to therapy.

***Infectious* (*Septic*) *Arthritis*.** Ultrasonography and also MRI are mainly used for the identifying the condition [148]. Bone scan is not routinely used and the condition can be seen when bone scan is performed for suspected osteomyelitis. However, it has been reported that identifying joint involvement and distinguishing bone from joint infection can be achieved in up to 90% of cases using bone scintigraphy [149, 150].

Bone scintigraphy, however, cannot distinguish infectious from noninfectious arthropathy. Detailed clinical information should always be an integral part of bone scan interpretation. Sundberg et al. [150] compared the interpretation of bone scans with and without knowledge of clinical information in 106 children suspected of having septic arthritis. The bone scan interpretation was correct in 13% when read without clinical history and in 70% when clinical information was

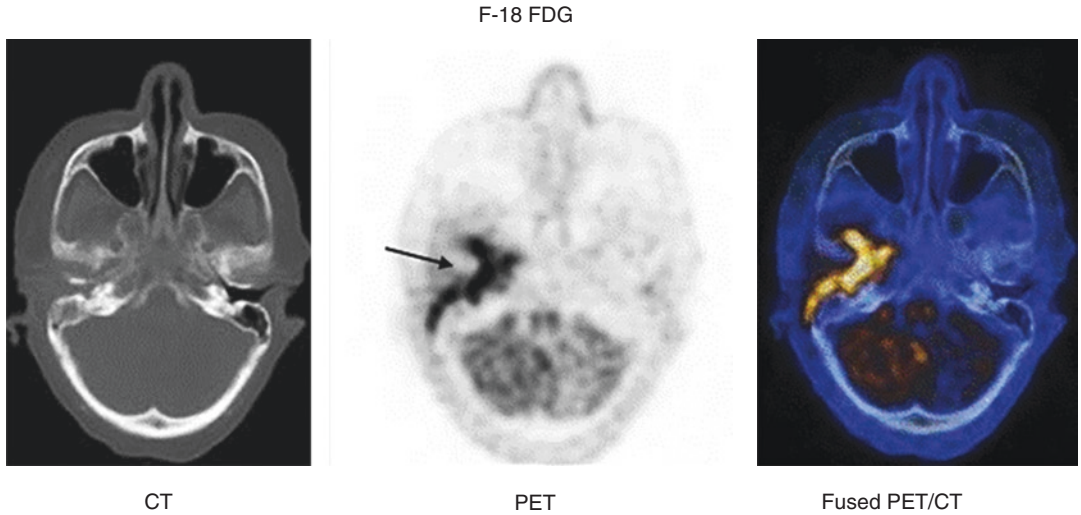

Fig. 5.28 Selected cuts of F-18 FDG study for a 73-year-old female with severe external otitis known to be due to pseudomonas aeruginosa for assessment of bone involvement. There is intense metabolic activity (arrow) along the external auditory canal with extension to the petrous bone. CT component shows total opacification of mastoid air cells, the auditory canal's soft tissue, middle ear cavity, tympanic cavity, and Eustachian tube. There is also significant rarefaction of the petrous bone

included. It is possible in the vast majority of cases to make the distinction if certain criteria are followed. Periarticular distribution of the abnormal uptake that is largely limited to the joint capsule and has a uniform pattern indicates septic arthritis. Osteomyelitis, however, shows abnormal uptake beyond the confines of the joint capsule or shows nonuniform uptake within the joint capsule [150]. To simplify the utilization of the many imaging modalities, Table 5.6 is provided to summarize the strengths and limitations of different modalities in the diagnosis of skeletal infections, Table 5.7 summarizes the correlation between scintigraphic and pathophysiological changes in skeletal infections, and Fig. 5.29 presents a suggested algorithm for the diagnosis of skeletal infection.

5.3.1.2 Noninfectious Skeletal Inflammation and Inflammatory-Like Conditions

Chronic Nonbacterial Osteomyelitis

The term chronic nonbacterial osteomyelitis describes a rare group of autoinflammatory bone diseases, including chronic recurrent multifocal osteomyelitis, synovitis, acne, pustulosis, hyperostosis, osteitis (SAPHO) syndrome, and diffuse sclerosing osteitis. The disorders are chronic in nature, but it can present with episodic flairs and periods of remission, hence the term chronic recurrent osteomyelitis. The more severe form of this group is the chronic recurrent multifocal osteomyelitis These conditions represent sterile bone lesions. This condition is primarily a childhood disorder but have an adult-onset presentation [151–153].

Chronic Recurrent Multifocal Osteomyelitis

Chronic recurrent multifocal osteomyelitis is a noninfectious inflammation of bone that has been considered as an autoinflammatory disorder of children and young adults that is characterized by nonbacterial osteomyelitis. Cultures do not show an infectious source and biopsy shows nonspecific inflammation. Antibiotics do not alter the course of the disease and symptoms are better treated with antiinflammatory medications. The disease has a relapsing and remitting course with patients typically present with bone pain in the affected sites. Common sites of involvement include the metaphyses of the long bones, clavicles, spine and pelvis. Other sites include the mandible, scapula, ribs, sternum, hands, and feet. The cause of CRMO remains uncertain, although the several studies have suggested a genetic component. Radiographs typically show lysis and sclerosis usually seen in the metaphysis of long bones and the medial clavicles. The condition is often bilateral and multifocal at presentation. Since this disease frequently involves multiple sites, some of which are asymptomatic. Whole-body MRI is recommended both to help aid in the diagnosis with multifocal involvement and document the extent of disease. During the active phase, there is bone marrow edema and often periostitis and soft tissue inflammation. Significant fluid collections, abscess, sinus tracts, and sequestra are not typical features of CRMO and are more often seen with bacterial osteomyelitis. Because of the lack of a diagnostic test, CRMO remains a diagnosis of exclusion. The most common CRMO differential diagnosis is represented by infections, malignant bone tumors, Langerhans cells histiocytosis. Although generally a self-limiting disease, CRMO can have a prolonged course and result in significant morbidity [151–155].

Bone scintigraphy shows multiple foci of increased uptake of variable intensity and on follow-up some of the preexisting foci may disappear and new one may be seen.

Osteitis Condensans Ilii

This non-specific inflammatory condition of the iliac bone affecting mainly women of childbearing age shows increased uptake in the iliac bone at the region of sacroiliac joints on the bone scan that is usually bilateral symmetric but can be asymmetrical and unilateral.

Osteitis Pubis

An inflammatory condition of the pubic bones that follows delivery, pelvic operations, and in athletes. Scintigraphically, there is intense uptake in the para articular regions of the pubic bones. MRI may show moderate to severe bone marrow edema at the pubic symphysis region.

Infantile Cortical Hyperostosis (Caffey-Silverman Disease)

This rare inflammatory condition of early infancy shows extensive periosteal new bone formation,

Table 5.6 Summary of commonly used imaging modalities for skeletal infection

Modality	Advantages	Disadvantages	Typical findings and overall accuracy
Standard radiograph	Cost-effectiveness: no additional imaging needed if positive	Low sensitivity findings take up to 2–3 weeks to appear, delaying diagnosis	Cortical destruction (very sensitive finding)
	Identify other causes of symptoms (fracture)	Low specificity to identify infection in violated bone	Soft tissue swelling with obliteration of fat planes
	Assess comorbidities such as fractures and arthritis		Endosteal scalloping; cortical tunneling
			III defined radiolucent lesions
			Osteopenia
			Sensitivity: 28–94% (average of 56%)
			Specificity: 3–92% (average of 75%)
Computed tomography	Excellent visualization of the cortex	Less resolution than plain radiography	Increased attenuation of bone marrow. Periosteal reaction and new bone formation Sequestrum
	Multiplanar and thin slice reconstruction enhance ability to evaluate infection and identify sequestra	Beam-hardening artifact	Intraosseous and/or soft tissue gas
MRI	Excellent delineation of soft tissue vs. bone infections	Bone marrow edema is nonspecific—can be seen in osteonecrosis, fractures, and metabolic bone disease	Cortical destruction
	Evaluation of bone marrow edema	Specificity is lower with small bones and in complicated cases of infection	Increased T2 signal (particularly on STIR)
	Excellent for suspected vertebral osteomyelitis		Decreased T1 signal and post-gadolinium enhancement
	Very useful in neonatal pelvic osteomyelitis to identify associated soft tissue abscesses		Sensitivity: 60–100% (average: 92%)
	No ionizing radiation		Specificity: 50–95% (average: 91%)
Multiphase bone scan	Earlier detection than plain film (24–48 h after infection)	Specificity decreases when other pathologies are present	Focal increased uptake on blood flow, blood pool, and delayed images
	Very high sensitivity for infections even in the presence of other comorbidities	Scans will stay positive for a long time after infection heals, therefore is not ideal for monitoring response to treatment	Sensitivity: 95%
	Whole-body imaging allows for detection of infection at other unsuspected sites		Specificity: nonviolated bone: 92%; violated bone 0–76% (average of 30%)
WBC scan	High specificity for infection improves bone scan specificity in the setting of violated bone	If used alone, difficult to differentiate bone vs. soft tissue infections	Focal increased uptake

(continued)

Table 5.6 (continued)

Modality	Advantages	Disadvantages	Typical findings and overall accuracy
Alone or with bone scan	Scans normalize as early as a few days and so may be used to monitor response to therapy	A tedious procedure	Dual imaging will show concordant uptake with bone scan in positive studies
			Average sensitivity: 88%
			Average specificity: 88% (91–94% when combined with bone scan)
67Ga scintigraphy	Early detection of infection	Positive findings can be nonspecific and may be positive in other settings such as tumor and inflammation	Combined scanning is considered positive when they are spatially incongruent or spatially congruent with greater gallium intensity than bone scan
Alone or with bone scan	Scans return to normal in 6 weeks with successful therapy, allowing use for monitoring treatment		Average sensitivity: 89% (better with SPECT/CT)
	Useful for chronic active and vertebral osteomyelitis		Average specificity: 70% (better with SPECT/CT)
			Particularly useful for vertebral osteomyelitis when PET is not offered
Bone marrow scan as an addition to WBC scan alone or along with bone scan	Improves specificity for infection vs. inflammation in complicated cases, such as postarthroplastic infections	Adds time and cost to the diagnostic imaging	Infection is confirmed when no bone marrow activity present corresponding to the positive area on labeled WBC scan. If activity is present, it indicates physiological bone marrow as a cause of WBC uptake
Ultrasound	Excellent for rapid and accurate detection of joint effusions	Poor modality to visualize bone	Fluid collection adjacent to the cortex of infected bone with communication to the medullary cavity
	Identify soft tissue and subperiosteal abscesses		Occasionally, superficial local defects and periosteal reactions in advanced cases of osteomyelitis
	No radiation		Absence of joint effusion will rule out septic arthritis
PET	Useful in chronic active osteomyelitis and periprosthetic infections as a single modality. Can be useful in early assessment of the response to therapy	Availability	Focally increased uptake with moderate to high SUV Sensitivity: 95–100% (chronic active osteomyelitis); 90% (preprosthetic infection)
		Expense	Specificity: 86–100% (chronic osteomyelitis); 89% hip periprosthetic infection; 72% knee periprosthetic infection

which appears on bone scans as areas of irregularly increased uptake described by Bahk as "pumpy" [156]. The standard radiograph however is the most valuable diagnostic study for this condition where it shows layers of periosteal new bone formation, with cortical thickening in variable combinations of the long bones, mandible, and clavicle. MRI, overall, adds little important additional information for the clinical evaluation of the condition, but it is useful if infection and tumor are suspected [157, 158].

Table 5.7 Correlation of imaging findings and pathophysiological features of infection

Vasodilation of blood vessels	Increased flow and blood pool activity on bone scan, increased ^{67}Ga- and ^{99m}Tc-nanocolloid accumulation
Pathological change at the site of infection	Imaging pattern
Increased permeability and chemotaxis	Increased accumulation of ^{111}In- or ^{99m}Tc-labeled WBC
Increased secretion of iron-containing globulin by injured and stimulated WBC	Increased accumulation of ^{67}Ga
Formation of woven bone	Increased uptake of ^{99m}Tc-MDP on delayed images with persistent accumulation beyond 3–4 h
Increased expression of glucose transporters	Increased accumulation of 18F-FDG on activated inflammatory cells

Sternoclavicular Hyperostosis

Bone scintigraphy shows increased uptake in the involved areas, which are usually bilateral and symmetrical, which is the typical scintigraphic feature of this chronic noninfectious inflammatory condition [156].

Osteitis Condensans of the Clavicle

This condition on bone scan shows intense unilateral focal uptake in the medial end of the clavicle and the sternoclavicular joint, which is clearly seen on pinhole imaging.

Transient Synovitis

Transient synovitis is the most common cause of acute hip pain in children and most commonly affects children between 3 and 10 years. It is a self-limited, non-specific, inflammatory joint disease of transient nature among children [159].

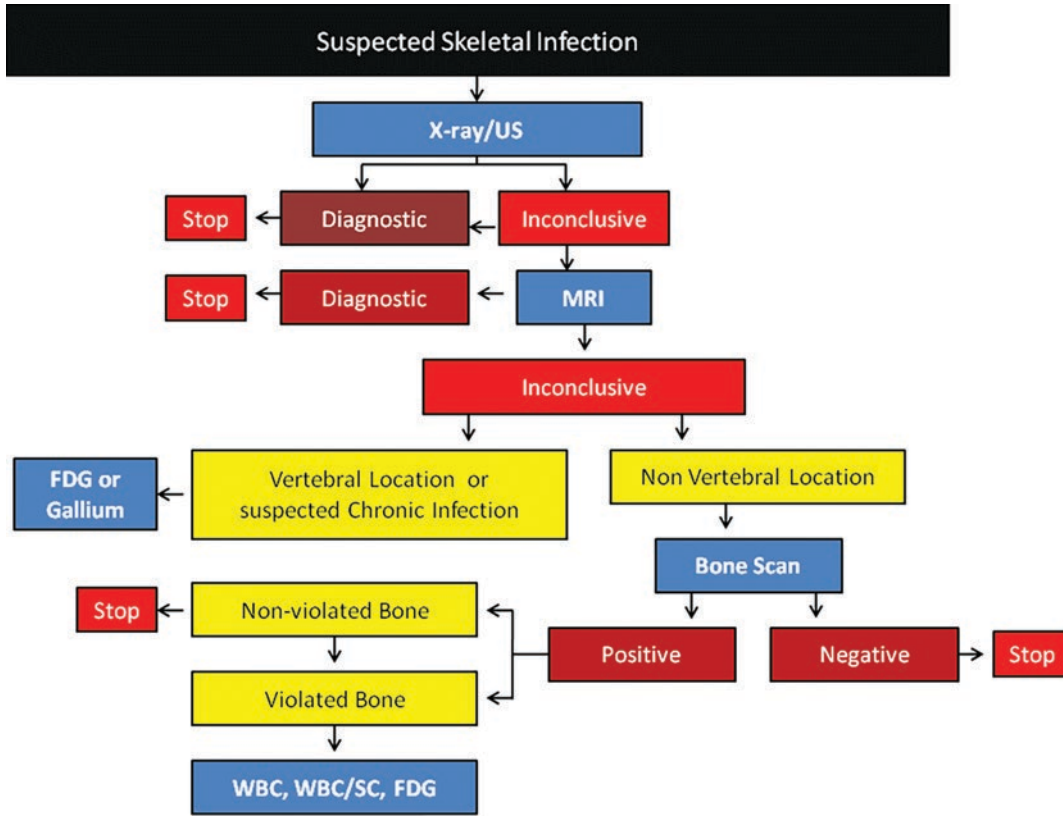

Fig. 5.29 Algorithm for the diagnosis of skeletal infection utilizing multiple modalities based on the location and probable pathophysiology of the suspected infection

Other terms for this hip condition are toxic synovitis, irritable hip syndrome, and transitory arthritis. The condition causes arthralgia and arthritis secondary to a transient inflammation of the synovium of the hip. Boys are affected much more often than girls. It preferentially affects the hip or knee and subsides without antibiotics. Resolution of symptoms generally occurs in a week and may be accelerated by NSAIDs. The etiology, full understanding of pathophysiology, and how to exclude other more serious conditions causing the same presentation are still unsettled [160]. However, the most likely mechanisms include viral infection and a hypersensitivity reaction to infection occurring elsewhere in the body.

The basic radiographic abnormality is capsular distension, and in most patients, no abnormalities are detected. It is however useful to evaluate for other etiologies of pain. Bone scan is also useful [160, 161].

On bone scan, the condition demonstrates diffusely increased joint activity on the blood flow and blood pool images. There is diffusely increased tracer uptake in the periarticular bones covered with the synovium on delayed images. The degree of uptake is minimal, barely delineating the femoral head and acetabular fossa. This may be so subtle so that it can hardly be recognized on planar images. Pinhole imaging, however, can identify subtle changes. Other patterns include normal or decreased uptake. MRI is helpful in differentiating the condition from infectious arthritis [161].

5.3.2 Avascular Necrosis (Osteonecrosis)

Avascular necrosis of bone results from imbalances between oxygen demand and supply of osseous tissues. There are many causes for osteonecrosis (Table 5.8).

In some cases, the underlying cause cannot be determined, and in this situation the term primary, idiopathic, or spontaneous osteonecrosis is used. The degree of vascular obstruction also plays a role in the development of avascular necrosis and the resulting scintigraphic and radiological changes observed.

Table 5.8 Causes of osteonecrosis

1. Trauma
2. Hemoglobinopathies
3. Exogenous or endogenous hypercortisolism
4. Renal transplantation
5. Alcoholism
6. Pancreatitis
7. Dysbaric (ex. Caisson disease)
8. Small vessel disease
9. Gaucher's disease
10. Hyperuricemia
11. Irradiation
12. Synovitis with elevation of intra-articular pressure Idiopathic (spontaneous osteonecrosis)

Table 5.9 Cell death after blood supply interruption

Cell	Time of death after interruption of blood supply
Blood-forming cells	6–12 h
Mesenchymal cells	6–12 h
Primitive osteoblasts	6–12 h
Bone cells including osteocytes and mature osteoblasts	12–48 h
Fat cells	2–5 days

Following the interruption of blood flow, the blood-forming and mesenchymal cells of the marrow as well as the primitive osteoblasts are affected first and die within 6–12 h after the interruption of the blood supply. Bone cells including osteocytes and mature osteoblasts die 12–48 h later, followed by the fat cells, which are most resistant to ischemia and die 2–5 days after the interruption of blood flow (Table 5.9). This sequence of events may explain why the bone marrow scintigraphic changes of decreased uptake appear earlier than the bone scan abnormalities. The bone marrow is affected earlier than the bone cells, which are relatively more resistant to ischemia [162, 163].

Ischemia does not directly affect the mineralized bone matrix or cartilage. The articular cartilage receives most of its nutrition by direct absorption from synovial fluid. Cartilage, how-

ever, cannot resist persistent elevation of intracapsular pressure for more than 5 days, after which degeneration begins.

The reparative process is initiated and carried out by neovascularization through the collateral circulation, advancing from the periphery of the area of necrosis or by recanalization of occluded vessels. This granulation tissue provides all the elements necessary for the formation of bone matrix and new bone deposition by young osteoblasts. This repair process may be altered. Often bone collapse results from structural weakening and external stress. Bone collapse and cartilage damage can result in significant deformity [162, 163].

When osteonecrosis occurs in growing skeleton, it is included in the group of disorders collectively called osteochondrosis. Osteochondrosis involves the epiphyses or apophyses of the growing bones. The process is due to osteonecrosis in some cases and trauma or stress in others (Table 5.10) [164]. In addition to avascular necrosis, osteochondrosis often demonstrates similar pathological features such as transchondral fractures, reactive synovitis, and cyst formation. Some common forms of osteonecrosis are described below.

Generally the common sites affected by osteonecrosis include the femoral head, humeral head, knee, femoral and tibial metadiaphysis, scaphoid, lunate, and talus [165].

Although MRI has been considered the gold-standard diagnostic modality for osteonecrosis, the disease can be diagnosed even at a very early stage using nuclear medicine imaging techniques. Available literature suggests that SPECT/CT bone scan and ^{18}F-Sodium fluoride PET/CT have similar or better results in comparison to MRI in the evaluation of osteonecrosis of the femoral head. They also provide both morphological and functional information about the diseased part and, therefore, can indicate whether the disease is active or healed [166].

Table 5.10 Osteochondroses

Involved bone	Disease
Capital femoral epiphysis	Legg-Calvé-Perthes disease
Metatarsal head	Freiberg's disease
Carpal lunate	Kienböck's disease
Tarsal navicular	Köhler's disease
Capitellum of humerus	Panner's disease
Phalanges of the hand	Thiemann's disease
Tibial tuberosity	Osgood-Schlatter disease
Proximal tibial epiphysis	Blount disease
Vertebral body	Scheuermann's disease
Patella	Sinding-Larsen-Johansson
Calcaneus	Serress disease
Ischiopubic synchondrosis	Van Neck's disease

Posttraumatic Osteonecrosis. Following a fracture, bone death of variable extent on either side of the fracture line is relatively common. Necrosis of a relatively large segment of bone following fracture or dislocation, however, is generally restricted to sites that possess a vulnerable blood supply with few arterial anastomoses. Examples include the femoral head, the body of the talus-scaphoid bone (Fig. 5.30), and the humeral head [167].

Other locations include the carpal hamate and lunate and the tarsal navicular bone. These bones are characterized by an intra-articular location and limited attachment of soft tissue, in addition to the peculiarities of their blood supply [162].

Legg-Calvé-Perthes Disease. This condition represents osteonecrosis of the femoral head in pediatric populations, especially boys 4–7 years old. The blood supply to the adult femoral heads is via the circumflex femoral branches of the profunda femoris artery. This adult pattern of femoral head vascularity usually becomes established after closure of the growth plate at approximately 18 years of age. In infancy and childhood, variable vascular patterns can be noted. The changing pattern of femoral head vascular supply with age may explain the prevalence of Legg-Calvé-Perthes disease in children between the age of 4 and 7 years and the high frequency of necrosis following femoral neck injury in this age group. Fractures of the femoral neck, more often intracapsular than extracapsular fractures, are the most common cause. Others include dislocation of the hip and slipped capital femoral epiphysis. Table 5.11 summarizes the changes that characterize the stages of the disease which vary from the sequence of changes of other types of osteonecrosis as described earlier.

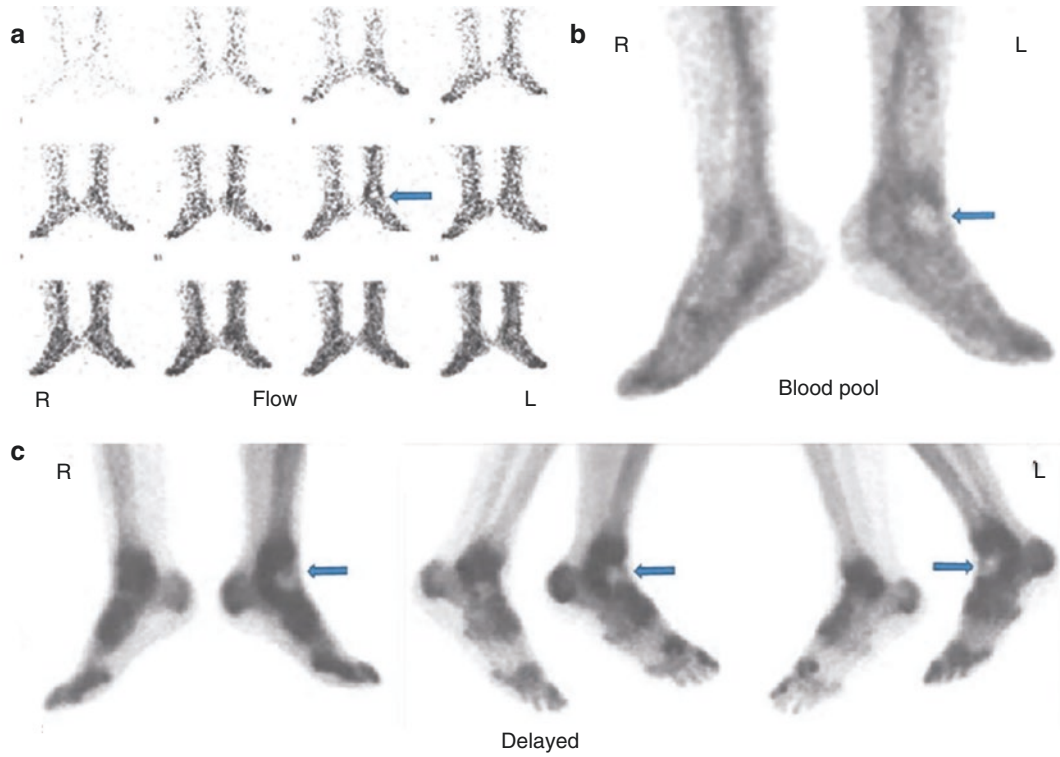

Fig. 5.30 (**a**–**c**) Posttraumatic osteonecrosis. Osteonecrosis of the talus bone in a 34-year-old male with history of foot trauma 2 months earlier. Flow images (**a**) show an ill-defined area of decreased flow in the region of the left talus, better seen on blood pool images (**b**), which also show a rim of increased blood pool activity. On delayed images (**c**), there is a photon-deficient area in the left talus surrounded by a rim of increased activity

Table 5.11 Stages of Legg-Calvé-Perthes disease

Stage	Presentation
First (incipient stage): several weeks	Edema
	Hyperemia
	Joint fluid in many cases
	Widening of joint space
	Bulging of joint capsule
Second (necrotic stage): several months to 1 year	Death of femoral head (usually starts in anterior half and may extend to other parts)
	Softening of the metaphyseal bone at the junction of the femoral neck and capital epiphyseal plate
	Cysts may be present
Third (regenerative)	Procallus formation replacing dead head
	Collapse and flattening of the femoral head
	Femoral neck may become short and wide
Fourth (residual)	Remodeling occurs
	Newly formed bone becomes organized into a line of spongy bone
	Restoration of femoral head to normal shape, more likely if only anterior portion is involved

MRI is a very useful modality in the diagnosis and predicting the course of the disease particularly later in the fragmentation stage [168, 169].

Bone scintigraphy is also useful although it is currently infrequently used as MRI is commonly used. For bone scintigraphy, pinhole imaging must be used routinely in this young age-group patients with suspected Legg-Calvé-Perthes disease rather than parallel hole. Additionally, since the anterolateral aspect of the femoral head (the principal weight-bearing region) is typically involved, but no region of the head is necessarily spared and involvement is usually not uniform, pinhole imaging using frog leg and straight anterior position is recommended for better resolving of the abnormalities in this condition. Pinhole imaging is preferred to SPECT in the diagnosis of this condition in children as it provides magnification while preserving the resolution of the images.

Bone scintigraphy is a sensitive as well as specific modality for the diagnosis of this condition showing typically a cold area with or without a rim of increased uptake (Fig. 5.31). The sensitivity and predictive value of early postoperative bone scan for detection of early avascular necrosis of the femoral head after surgical treatment of slipped capital femoral epiphysis were evaluated by Fragniere et al. [170].

The authors reviewed records of 49 patients (64 hips) operated on between 1980 and 1997

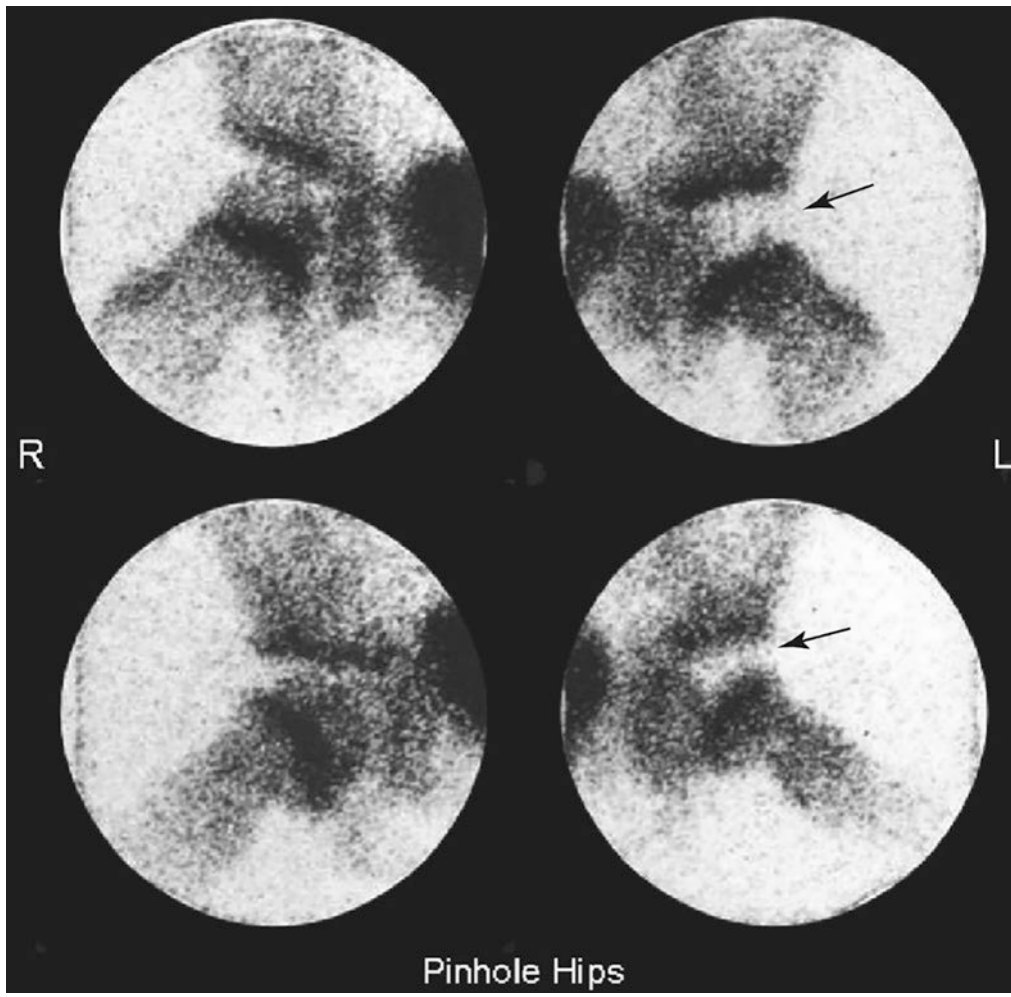

Fig. 5.31 A 6-year-old boy with left hip pain and no history of trauma. Pinhole images of the hips in anterior (*upper row*) and frog leg (*lower row*) positions. Left hip shows photon deficiency (*arrow*) indicating osteonecrosis of the left femoral head (Legg-Calvé-Perthes disease)

with a mean follow-up of 3 years. Sixty-one out of 64 hips went through an early postoperative bone scan. The three hips that developed AVN showed significant decrease in radionuclide uptake. There were neither false-positive nor false-negative cases in this series [170]. The authors concluded that bone scintigraphy has an excellent sensitivity and predictive value for detection of AVN after surgical treatment of slipped capital femoral epiphysis.

Bone scintigraphy has also been proven also to have prognostic value. Conway introduced a prognostic classification [171] of two pathways; pathway A is defined by the early appearance of a lateral column formation (before any radiological sign) in the capital femora, epiphysis indicating early and rapid revascularization. This pathway is associated with good outcome. The pathway B is defined by centrally extended scintigraphic activity from the base of the capital femoral epiphysis or by the absence of the activity in the epiphysis (lateral column formation) after 5 months. The value of scintigraphy in predicting the course of the disease was illustrated by Tsao who studied 44 consecutive patients treated for Legg-Calvé-Perthes disease who underwent serial bone scans and followed up clinically for an average period of 4.4 years. The bone scintigraphy classification characterizes pathway A by early formation of the lateral column, which is not seen in the pathway B. Pathway A included 20 hips with an average age at presentation of 6.1 years. At last follow-up, none of the patients of this group had "head-at-risk" signs or required operative treatment. Conversely, pathway B had 20 hips with an average age at presentation of 5.8 years. At last follow-up, 18 patients had head-at-risk signs with 11 patients requiring operative treatment. Bone scintigraphy classification preceded the radiographic head-at-risk signs by an average of 3 months, allowing earlier treatment and correlated with subsequent femoral head involvement [172].

The prognostic value of this classification was also more recently reconfirmed by Comte et al. [173] who showed that the presence of lateral column formation (pathway A) has a positive predictive value of 85% for good outcome. However, the pathway B with the absence of lateral column formation has a 97% positive predictive value for poor final outcome [173]. It was found that the appearance of hyperactivity of the metaphyseal growth plates is an additional prognostic information since it indicated poor outcome.

Dysbaric Osteonecrosis. This type of osteonecrosis occurs in patients subjected to a high-pressure environment, such as deep-sea divers. The exact cause of ischemia is debated. Immobilization of gas bubbles blocking the vascular channels is considered to be the major factor by many investigators. The presence of intravascular gas bubbles is seen even after ultrasound, and other techniques [174] have documented asymptomatic decompression. Shoulders, hips, knees, and ankles are commonly involved in this type.

Sickle Cell Disease Necrosis. Sickle cell disease is a relatively common hereditary hematological disorder. The disease is caused by the replacement of glutamic acid of B-chains with valine. The disease has numerous consequences; one of the most common is injury to bone. Osteonecrosis and osteomyelitis are the most common bony complications [175].

The bone manifestations occur similarly in other hemoglobinopathies and affect most commonly femora, tibiae, and humeri [176, 177]. Since sickle cell osteonecrosis most commonly involves the femoral and humeral heads although it can affect any bone of the skeleton, it is possible that the increased length of the nutrient arteries supplying the marrow in the long bones makes them more susceptible to occlusion. Necrosis of the femoral head is one of the significant skeletal disorders in sickle cell disease patients. Neonates who have sickle cell disease do not often develop osteonecrosis because of the high fetal hemoglobin level. Although the pathogenesis of the vascular occlusion leading to an infarct is not entirely clear, vaso-occlusion of the marrow is considered to be one of the main culprits in sickle cell crisis. Since hemoglobin S is sensitive to hypoxemia, erythrocytes become viscous and sickle abruptly when exposed to hypoxia. Although the exact pathophysiology of this condition in sickle cell disease patients is not entirely clear, it is proposed to be due to red cell sickling and repetitive vaso-occlusion leading to tissue hypoxia, inflam-

mation, and subsequent bone necrosis (infarct), the most common skeletal complication of sickle cell disease and subsequently results in collapse. Signs of acute infarction can include warmth, tenderness, erythema, and swelling over the site of vaso-occlusion [176]. However, these clinical signs are nonspecific and may also occur in acute osteomyelitis which may occur as a primary event or may be superimposed on infarcts as necrotic bone is a fertile site for such secondary infections [176, 177].

Thus, recognition of bone marrow infarction often relies on the use of imaging modalities. MRI is useful for determining the anatomic site and the extent of acute infarcts and contributes to differentiating acute infarcts from acute osteomyelitis [178, 179]. However it has not been found to have the specificity or sensitivity of radionuclide studies by some researchers [177].

The scintigraphic diagnosis may be straightforward using bone scan which shows photon-deficient areas in early stages. SPECT and pinhole are very valuable particularly in resolving a photon-deficient area in the middle of the increased uptake at the reparative process. In this stage, it can be difficult to differentiate osteonecrosis from osteomyelitis, and adding ^{67}Ga or bone marrow scanning may be essential. Acute chest syndrome in sickle cell patients is characterized by chest pain that can mimic several pulmonary disorders including pulmonary embolism and pneumonia [180]. This condition is believed to be a sequel of osteonecrosis of the ribs and is usually associated with pulmonary infiltrates on chest X-ray. Whole-body imaging cannot be overemphasized and should include ribs in addition to the area of interest if different (Fig. 5.32).

Idiopathic (*Primary or Spontaneous*) *Osteonecrosis*. This is a unique entity with cases presenting with no clear underlying disorders. The femoral head is the most common site involved in osteonecrosis in general [166]. It is usually bilateral and can lead to secondary osteoarthritis. It may also affects the femoral condyles, tibial plateau, wrists, and humoral heads.

Spontaneous Osteonecrosis of Femoral Head. Although no specific cause is recognized for this condition, the most popular hypothesis is an abnormality of fat metabolism, leading to marrow fatty infiltration or vascular embolization [181].

Legg-Calve-Perthes disease represents a juvenile form of idiopathic osteonecrosis of the femoral head [182].

Primary osteonecrosis of the femoral head affects adult men more frequently than women and is usually seen between the fourth and seventh decade of life. Unilateral and bilateral involvement may be detected. The reported incidence of bilateral disease has varied from 35 to 70%, influenced predominantly by the method of examination and the length of follow-up. Despite the high frequency of bilateral involvement, it usually first manifests as a unilateral symptomatic condition that can be related to osseous collapse in the more severely affected sites. The pathological findings are virtually identical to those in other varieties of osteonecrosis. To demonstrate photopenia in the femoral head, SPECT (85%) is more sensitive than planar imaging (55%) [183].

Figure 5.33 illustrates the value of SPECT in the diagnosis of the condition.

Spontaneous Osteonecrosis of the Knee (SONK). Although osteonecrosis around the knee is observed in association with steroid therapy, sickle cell anemia, other hemoglobinopathies, and renal transplantation, it may also occur in a spontaneous or idiopathic fashion. This entity occurs most characteristically in the medial femoral condyle. It can also affect the medial portion of the tibial plateau, the lateral femoral condyle, or the lateral portion of the tibial plateau alone or in combination with the medial femoral condyle. It characteristically affects older women and is characterized by abrupt onset of knee pain. Signs of localized tenderness, stiffness, effusion, and restricted motion may also be present. Unilateral involvement predominates over bilateral involvement. Initially, radiographs are normal. Weeks or months pass before changes in the weight-bearing articular surface of the medial femoral condyle can be seen. The pathogenesis of this condition is not clear. Vascular insufficiency associated with age is a proposed etiology. Traumatic microfractures in the subchondral bone with secondary disruption of the local blood supply have also been suggested. A predominant role

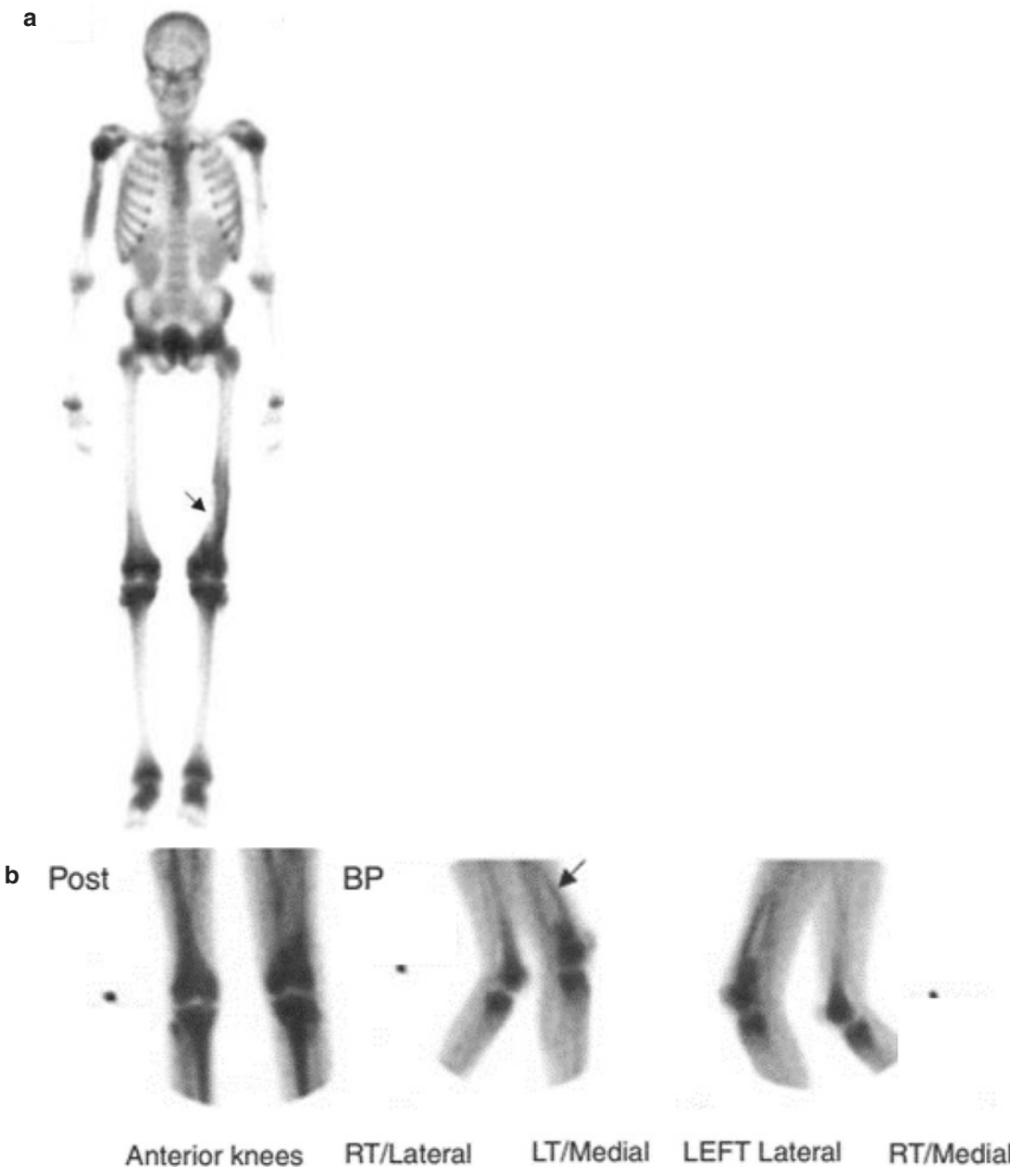

Fig. 5.32 (**a**, **b**) ^{99m}Tc-MDP whole-body (**a**) and spot images including blood pool image of the knee regions (**b**) of a 17-year-old female with sickle cell disease complaining of left thigh bony pain. Note the photon-deficient linear area in the medial aspect of the left distal femur (*arrow*) indicating acute infarction, while the multiple areas of increased uptake in the humeri and femora particularly distal left represent older infarcts in healing phase. Note also periarticular uptake throughout the skeleton representing the pattern of bone marrow expansion associated with the underlying condition of sickle cell anemia. Another associated finding of the disease is the prominent kidney uptake diffusely on the delayed images as seen in this example

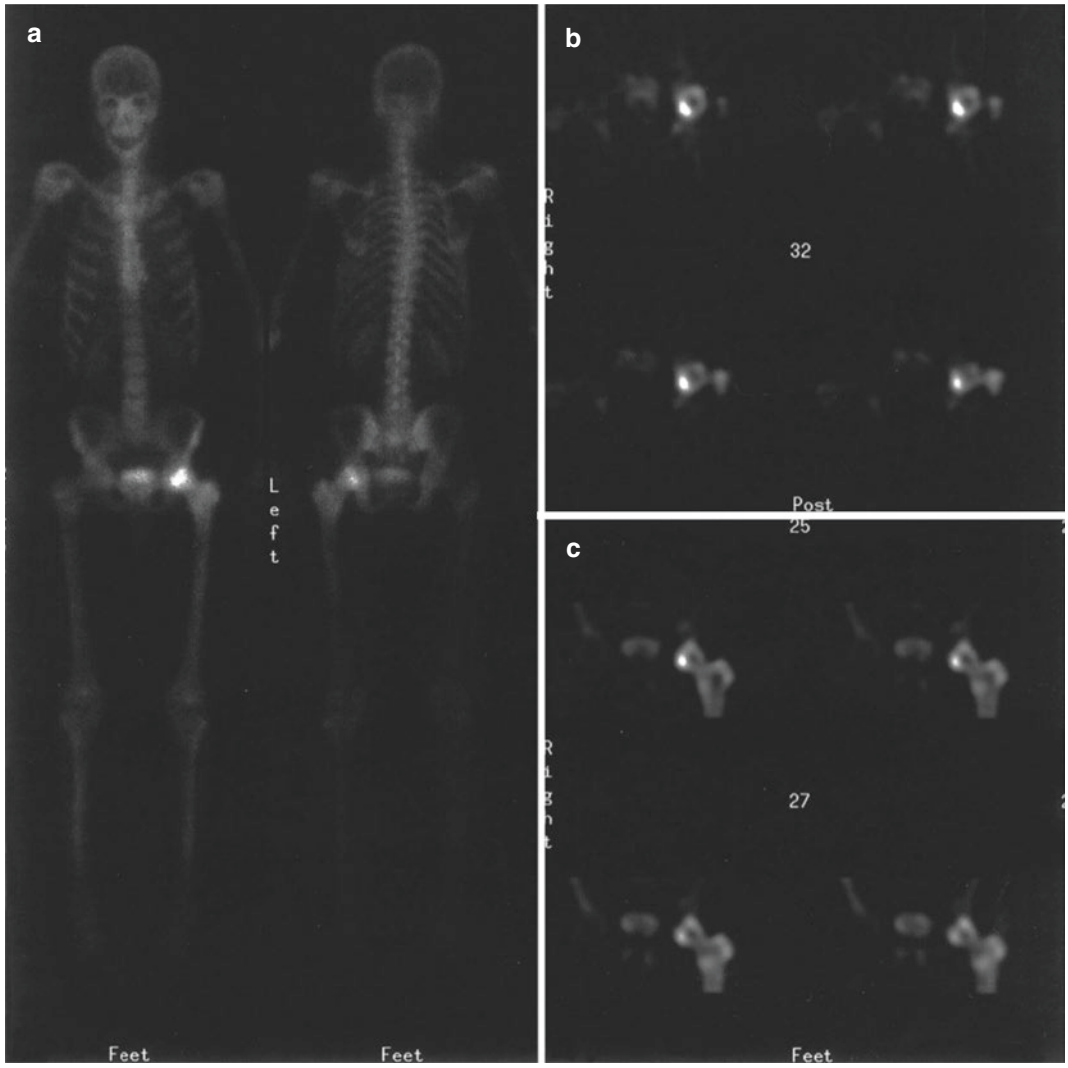

Fig. 5.33 (**a**–**c**) Bone scan from a case of osteonecrosis of the femoral head. SPECT images show a central cold area, confirming the diagnosis

of meniscus injury in the pathogenesis of spontaneous osteonecrosis has also been proposed. X-rays are usually normal at the time of presentation and may even remain so for the entire course of the disease. Bone scintigraphy is a more sensitive modality and is usually helpful in early detection. Scintigraphy may reflect the likely pathogenesis of microfractures with vascular disruption. In the first 6 months, there is increased flow, blood pool activity, and uptake on delayed images (Fig. 5.34). From 6 months to approximately 2 years, blood flow decreases as well as the blood pool activity, while delayed uptake may persist. After 2 years the bone scan tends to return to normal except in patients who develop joint collapse and secondary osteoarthritis [184].

Osteochondritis dissecans (which affects young patients and does not classically involve the weight-bearing surface of the femoral condyle) should not be confused with spontaneous osteonecrosis. Also osteoarthritis, commonly affecting the knee, is usually limited to the subchondral bone, whereas osteonecrosis tends to involve the adjacent shaft.

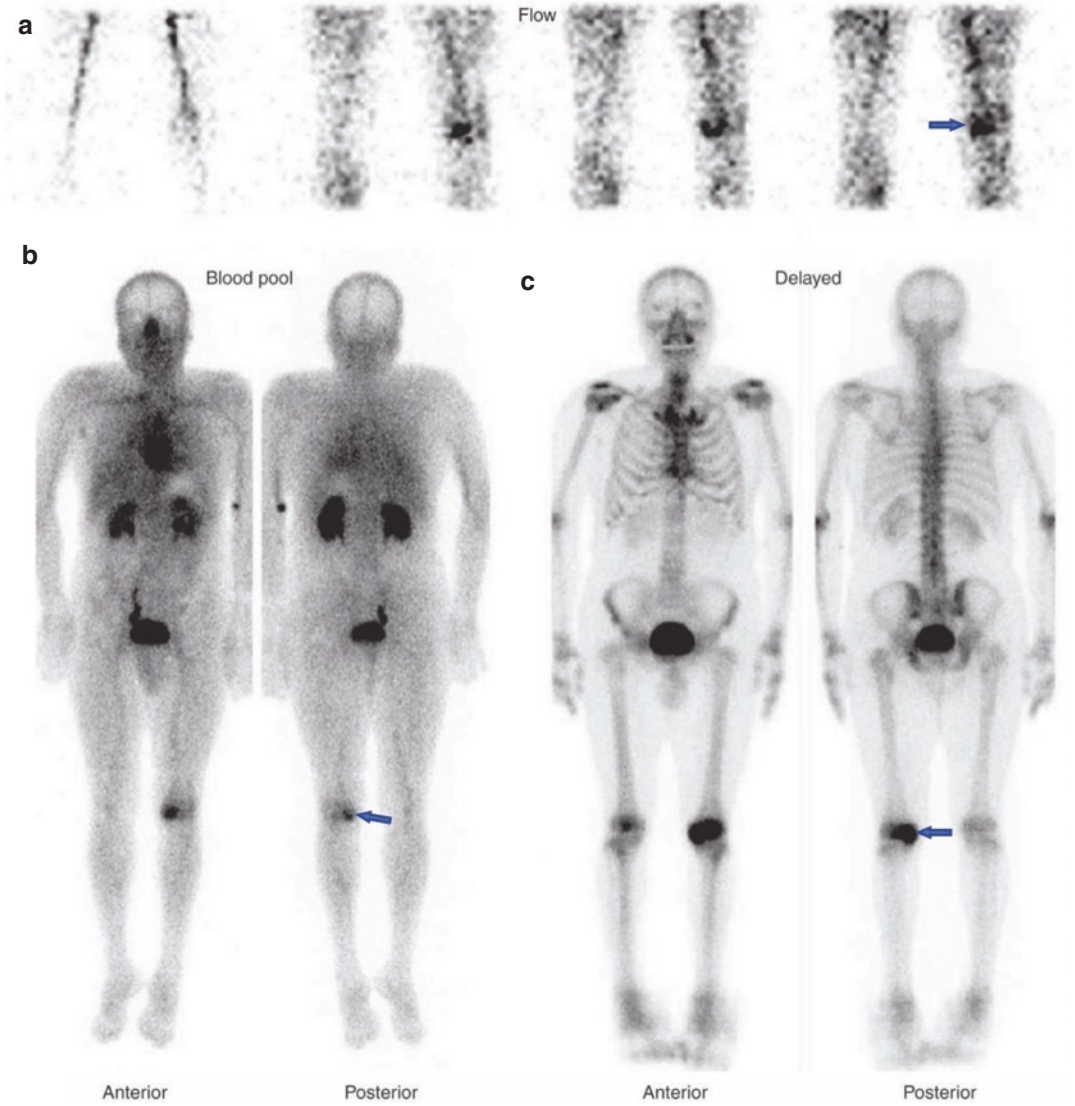

Fig. 5.34 (**a**–**c**) A case of osteonecrosis of the left knee, illustrating the typical pattern on bone scintigraphy. Note the focal increased flow and blood pool with corresponding focally increased uptake on delayed image in the region of left medial femoral epicondyle (arrow)

5.3.3 Complex Regional Pain Syndrome-1 (CRPS-1) or Reflex Sympathetic Dystrophy (RSD)

Complex Regional Pain Syndrome-1 (Reflex sympathetic dystrophy) is a clinical syndrome which has been defined according to the criteria of the International Association for the Study of Pain (IASP) as a clinical syndrome characterized by pain, allodynia, hyperalgesia, edema, abnormal vasomotor and sudomotor activity, movement disorder, joint stiffness, regional osteopenia, and dystrophic soft tissue changes [185].

The pathophysiology of CRPS-1 (RSD) is not well understood. It is believed that an imbalance between the sympathetic and neuroceptive sensory systems occurs after an event usually traumatic. Normally, afferent C and A delta fibers carry information from skin neuroceptors

to the neurons in the dorsal horn of the spinal cord. From this region, information is transferred to higher central nervous system levels and also directed through sympathetic neurons and their efferent fibers. These sympathetic fibers control the tone of distal arterioles and capillaries. It is postulated that trauma, which could be trivial, causes an alteration or imbalance of these nociceptive-sympathetic contact sites, resulting in vasomotor disturbances, pain, and dystrophic changes which form the features of this condition. It is now believed that the pathophysiology of this syndrome is, at least in part, a disease of both the central and peripheral nervous systems [185].

Synovial histopathological changes have been found in patients with CRPS-1. The most common changes are proliferation of synovial cells, subsynovial fibrosis, and vascular proliferation.

Vascular changes can be demonstrated on bone scintigraphy blood pool images, which show increased periarticular activity. A unifying pathophysiological mechanism in CRPS-1 can be proposed, related to an initial triggering injury causing an imbalance between the nociceptors and the autonomic nervous system (sympathetic and parasympathetic) to the affected area. As a result, vasomotor disturbances take place with vasodilatation as a prominent feature, leading to increased blood flow to the synovial and osseous tissues. The synovium reacts with cell proliferation and eventually secondary fibrosis. There is a lack of inflammatory cellular infiltration. The adjacent bone undergoes increased turnover locally, with some resorption. This explains the presence of radiographic and bone scintigraphic changes typical of CRPS-1, as well as the changes at the level of the synovium. The clinical course of the condition, which may be underrecognized and could vary with the location, consists of three stages: acute, dystrophic, and atrophic [186].

The first stage is characterized clinically by pain, stiffness, tenderness, and swelling of the involved joint. In stage 2, there is still pain, tenderness, and wasting of subcutaneous tissues and muscles. Thickened fascia and loss of color with cold skin are also seen. Stage 3 may last for months or becomes chronic. This stage is characterized by pronounced wasting of the muscles and subcutaneous tissue. The skin is atrophic, and smooth-appearing contractures are frequent.

Three-phase bone scintigraphy is the most sensitive modality for the diagnosis of the condition [187]. The scintigraphic pattern depends on the duration or stage of the disease [59].

In the first or acute stage (20 weeks), all three phases of bone scan typically show increased activity (Fig. 5.35). After 20 and up to 60 weeks during the dystrophic phase, the first two phases are normalized, while the delayed phase images show increased periarticular uptake. After 60 weeks (atrophic phase), the flow and blood pool images show decreased perfusion, with normal uptake on delayed images. In children with CRPS-1, decreased perfusion and uptake are the most common manifestations (Table 5.12). A unilateral decrease in the metaphyseal band of activity may be the most striking feature.

Radiopharmaceuticals other than ^{99m}Tc-MDP have also been reported to have potential use in the diagnosis. These include Tc-99m-labeled human serum albumin [188], combined N-13 ammonia and 6-[F-18] fluorodopamine [189], F-18 FDG,Tc-99m sestamibi [190], In-111 octreotides, and I-123 MIBG [191].

N-13-ammonia radioactivity has been reported to be less on the affected side than in the unaffected side, while the F-18 FDG activity is symmetrical. Accordingly FDG activity is high in the affected side [192]. I-123 MIBG, however, was found to be decreased in the affected side reflecting the impaired sympathetic dysfunction with congruent reduction in perfusion [193].

Recently, F-18 FDG PET/MRI was found to have improved sensitivity over conventional MRI in the detection of musculoskeletal changes, especially in early stages before the onset of irreversible muscle or skin atrophy [194].

Different protocols were used to treat CRPS-1 including medications orally and parenterally or sympathetic blocks, which include the tumor necrosis factor α antibody Infliximab [193], and physical therapy with varying degrees of success. The main aim of the treatment is to restore the function of the affected limb. Bone scintigraphy can be used not only to help in the diagnosis but also to monitor the disease with treatment.

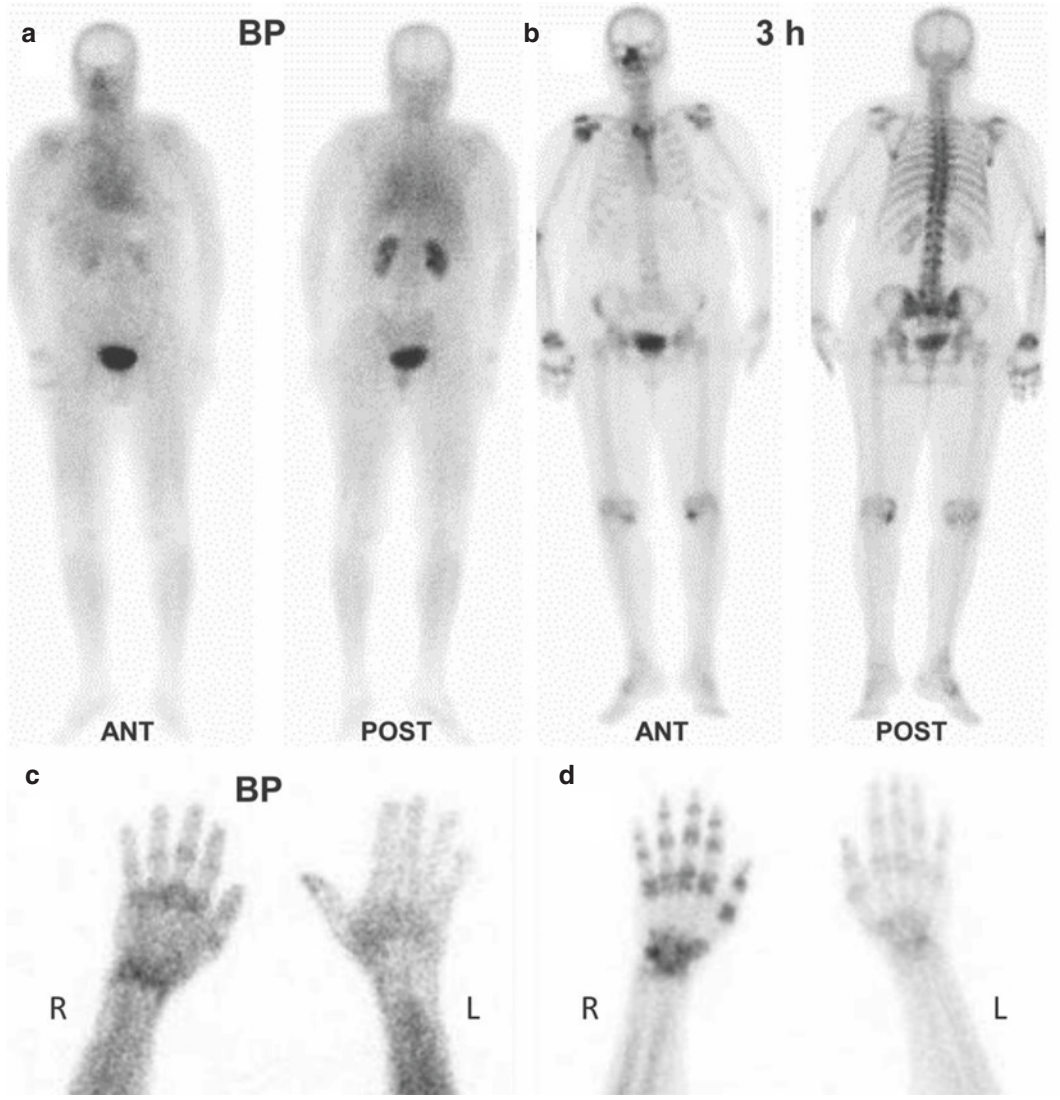

Fig. 5.35 (**a**–**d**) ^{99m}Tc-MDP whole-body and spot images of a 40-year-old male with CRPS-1 (RSD) involving the right upper extremity. Whole-body blood pool images (**a**) and blood pool spot image of the hands (**b**) show increased activity in the right shoulder wrist and hand. Delayed whole-body and spot images (**c**, **d**) show periarticular increased uptake in the right shoulder, elbow, wrist, and hand

Table 5.12 Scintigraphic patterns of CRPS-1

Pattern on bone scans	Flow on angiogram	Blood pool	Uptake in delayed images
Typical	Increased	Increased	Increased
Atypical			
CRPS-1 of children and adolescents	Decreased	Decreased	Increased
Paralysis, immobilization	Decreased	Decreased	Increased
Subacute	Normal	Normal	Increased
Late phase of CRPS-1	Normal, decreased	Normal, decreased	Variable
Persistent use of painful limb	Decreased	Decreased	Decreased

Modified from [59] with permission

5.3.4 Fibrous Dysplasia

Fibrous dysplasia is a benign, developmental, noninherited condition. It is relatively common, although the etiology is not known. The condition may involve a single bone (monostotic) or multiple bones (polyostotic) and typically results in enlargement and deformity of the involved bone. Pathologically it is characterized by slow, progressive replacement of the medullary cavity of bone by fibrocollagenous tissue containing poorly formed and randomly arranged trabeculae of woven bone, islands of cartilage, and cystic formations of varying size. The cytoplasm of osteogenic cells within the bone spicules and of the stellate and spindle-shaped cells in the stroma stains histochemically for alkaline phosphatase. A study using C-11 methionine PET in two cases of fibrous dysplasia indicated the presence of viable tumorlike cells [195].

Elevated serum alkaline phosphatase levels have been observed in about one-third of patients, usually with the polyostotic form. Alkaline phosphatase is not a sensitive indicator of the disease but correlates with its extent and severity. This finding indicates the presence of active osteoblasts with increased blood flow and blood pool activity and increased uptake of bone imaging agents [59].

The lesions are monostotic in 70–80% of patients and polyostotic in up to 30% of cases [162]. Multiphase bone scan shows intense uptake (Fig. 5.36), reflecting hyperemia as well as osteoid matrix, which is almost always asymmetrical. However, not every case has intense uptake since rarely it shows barely increased uptake probably due to concurrent bone infarct. F-18 NaF has also been found to be useful in the evaluation of the disease activity and correlates quantitatively with the clinical outcomes[196]. The condition may be associated with an endocrine abnormality (McCune-Albright syndrome), which includes precocious puberty and abnormal skin pigmentation in the form of café au lait spots [197].

5.3.5 Trauma

Trauma to the musculoskeletal system may affect bone, cartilage, muscles, and joints. To each of these structures, trauma may cause immediate damage and late changes.

5.3.5.1 Fractures

A fracture is defined as a break in the continuity of a bone. Fractures can be classified according to several features (Table 5.13). Based on the extent of the break, fractures are classified as complete or incomplete. A complete fracture breaks the bone all the way through, while with incomplete fracture, the bone is broken but stays as one piece. Fractures are also classified as open (previously called compound) if the skin is broken and closed (previously called simple) when the skin at the site of fracture is not broken [198].

The fracture pattern depends on the mechanism of injury. Compression load produces a compaction or oblique fracture. Bending load has a tendency to produce a flat transverse fracture. However, bending load on one side is associated with compression on the other side, which may affect the pattern of the fracture. Torsional force tends to produce a spiral fracture.

Other classifications are based on the number of bone pieces, the direction of the fracture line, and other factors (Table 5.13). Pathological fractures occur at the sites of preexisting abnormalities that weaken bone. A minimal force that usually would not cause the fracture of a normal bone may produce a pathological fracture. A transchondral fracture (osteochondritis dissecans) represents fragmentation and separation of portions of cartilage or cartilage and bone. This type is most prevalent in adolescents and occurs typically in the head of the femur, ankle, kneecap, elbow, and wrist [198].

The role of scintigraphy in fracture diagnosis is limited to those cases of radiologically occult fractures and fractures of the small bones of the hands and feet.

Stress Fractures. Stress fractures are due to repeated stress, each episode of which is less forceful than required to fracture the bony cortex. The stress fracture is not as thought due to repeated traumatic microfractures. It is a focal area of increased bone turnover secondary to the repeated stress. The process starts with resorption cavities before being coupled by an osteoblastic response to replace the absorbed bone.

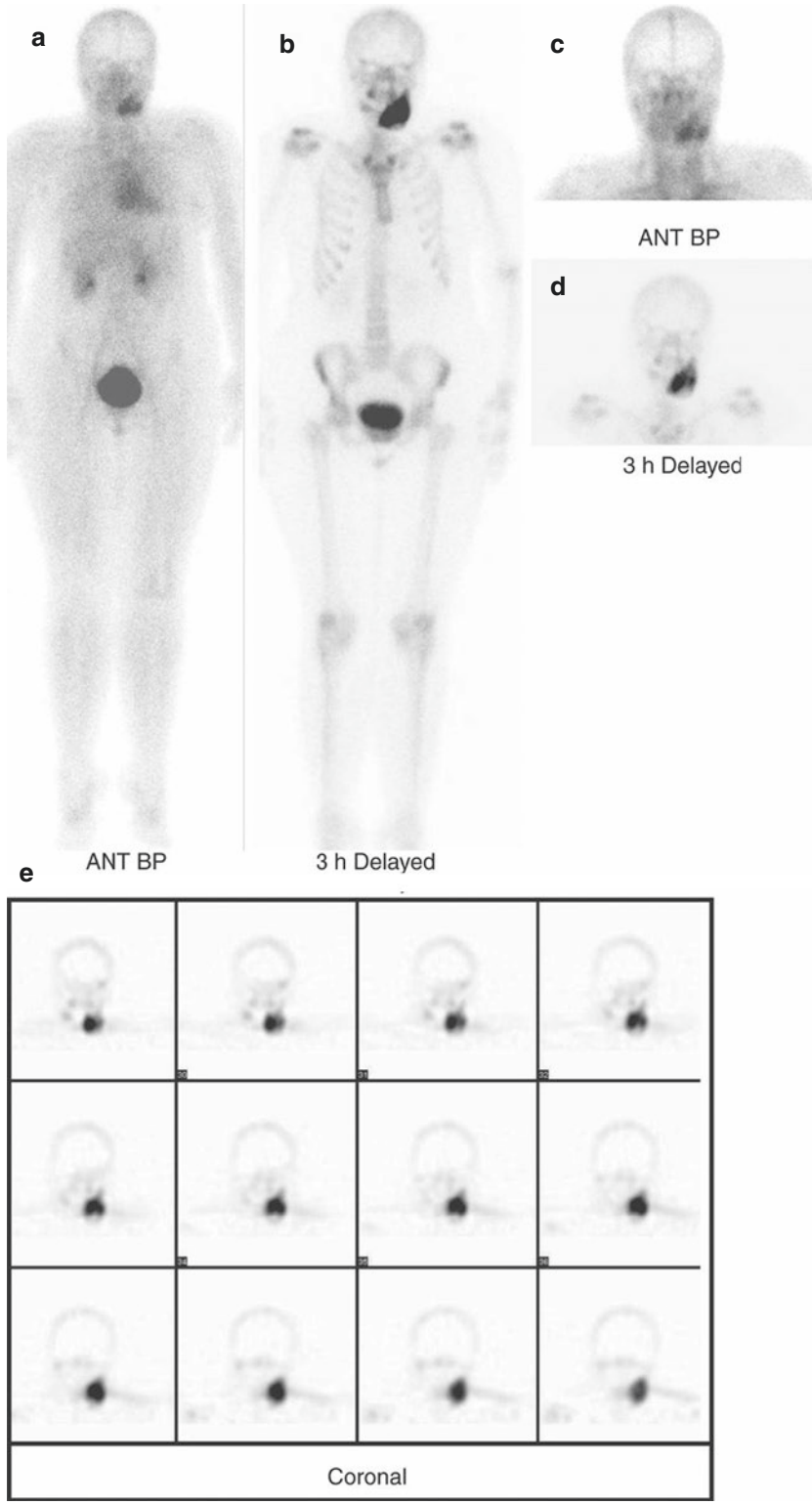

Fig. 5.36 (**a**–**e**) Whole-body blood pool and delayed images, spot blood pool and 3-h images of the head, and representative images of the SPECT study of the skull (**a**–**e**) show increased blood pool activity and intensely delayed uptake in the left mandible illustrating the scintigraphic pattern of fibrous dysplasia on multiphase bone scan

Table 5.13 Classification of fractures

Based on extent of the break:
1. Complete: bone is broken all the way through
2. Incomplete: bone is still in one piece
Based on skin condition:
1. Open: broken skin
2. Closed: intact skin
Based on resulting number of bone fragments:
1. Comminuted: multiple bone fragments
2. Noncomminuted: only two fragments
Based on direction of fracture line:
1. Linear: line is parallel to the long axis of bone
2. Oblique: line is at oblique angle to the shaft of the bone
3. Spiral: line encircles the bone
4. Transverse: line is perpendicular to the long axis of bone
Based on cause of fracture:
1. Excessive force on normal nonviolated bone: classic traumatic fracture
2. Pathological fracture: break at the site of preexisting pathology
3. Stress fractures:
Fatigue fractures: abnormal stresses applied to normal bones
Insufficiency fractures: usual stresses to abnormal bones
4. Transchondral fracture (osteochondritis dissecans)

The process of rarefaction is faster than the osteoblastic process and will progress if the individual continues stressful activity and trauma. Complete fracture through the zone of rarefaction may occur.

If this occurs in normal bones, the resulting fractures are called fatigue fractures, while if they occur on abnormal bones, as in osteoporosis, they are termed insufficiency fractures. Bone scintigraphy is much more sensitive than standard radiographs in detecting stress fractures. Fatigue fractures are common in athletes, military recruits, and dancers (Table 5.14). With repeated loading, bone loses its stiffness and strength. A fatigue fracture appears as a microfracture which causes pain but may not be detected on a plain radiograph. The progress of the process depends on the amount of further load applied to the bone. If scintigraphy is performed in the acute phase of less than 4 weeks, the flow and blood pool images show increased activity. Later, only delayed uptake will be seen. The delayed uptake is typically focal or fusiform, involving less than one-fifth of the bone (Fig. 5.37). Because bony remodeling continues for an extended time period, focal uptake on the delayed images resolves last. Uptake gradually diminishes in intensity over 3–6 months, but

Table 5.14 Location of stress fracture by activity

Location	Activity or event
Sesamoids of metatarsal bones	Prolonged standing
Metatarsal shaft	Marching; stamping on ground; prolonged standing; ballet; postoperative bunionectomy
Navicular	Stamping on ground; marching; long-distance running
Calcaneus	Jumping; parachuting; prolonged standing; recent immobilization
Tibia: mid and distal shaft	Long-distance running
Proximal shaft (children)	Running
Fibula: distal shaft	Long-distance running
Fibula: proximal shaft	Jumping; parachuting
Patella	Hurdling
Femur: shaft	Ballet; long-distance running
Femur: neck	Ballet; marching; long-distance running; gymnastics
Pelvis: obturator ring	Stooping; bowling; gymnastics
Lumbar vertebra (pars interarticularis)	Ballet; lifting heavy objects; scrubbing floors
Lower cervical, upper thoracic spinous process	Clay shoveling
Ribs	Carrying heavy pack; golf; coughing
Clavicle	Postoperative radical neck
Coracoid of scapula	Trap shooting
Humerus: distal shaft	Throwing a ball
Ulna: coronoid	Pitching a ball
Ulna: shaft	Pitchfork work; propelling wheelchair
Hook of hamate	Holding golf club, tennis racquet, baseball bat

From [185] with permission

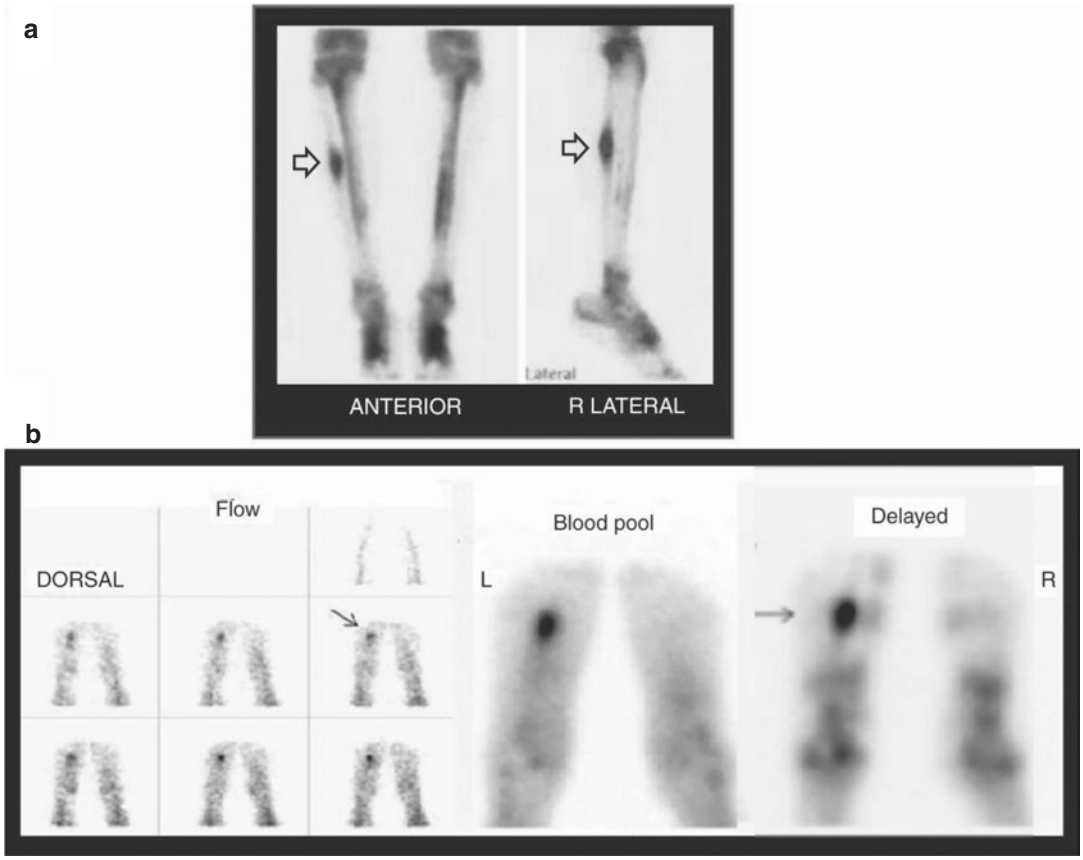

Fig. 5.37 (**a**) Representative images of a ^{99m}Tc-MDP bone scan for a 23-year-old man with an 8-week history of right shin pain. There is fusiform focus of prominent increased uptake in the shaft of the right fibula illustrating the pattern of fatigue fracture. (**b**) Another example of stress fracture in the foot with focally increased flow and blood pool with corresponding focus of increased uptake on delayed images

some increased uptake can last up to 1 year, even in uncomplicated stress fractures [199].

A grading system based on the scintigraphic appearance, classifies stress fractures into milder or more severe (Table 5.15) [201]. The minimally symptomatic grade 1 and grade 2 stress fractures typically resolve more quickly and completely. This grading system can assist in prescribing the requisite rest and rehabilitation intervals [201].

Table 5.15 Scintigraphic grading for stress fractures

Grade	Pattern
1	Small, ill-defined cortical area of mildly increased activity
2	Better-defined cortical area of moderately increased activity
3	Wide to fusiform, cortical-medullary area of highly increased activity
4	Transcortical area of intensely increased activity

The pattern of uptake of stress fractures is different from the pattern of a shin splint, which is another consequence of stress also known as Medial Tibial Stress Syndrome and occurs in the same patient population as fatigue fractures. The pain usually occurs on the anterior part of the tibia due to repetitive activity-related trauma to the tissues surrounding tibia. Pain from shin splints can be generalized across the lower two-thirds of the tibia; in contrast, pain from a stress fracture is localized (Fig. 5.37) [202]. Shin splints typically show normal flow and blood pool images, with an elongated linear pattern of increased uptake on

delayed images (Fig. 5.38). They are most commonly found in the tibiae and may coexist with fatigue fractures in the same patient. The scintigraphic pattern seen with shin splints is due to subperiosteal bone formation [203].

Spondylolysis. Spondylolysis is a condition in which there is a loss of continuity of bone of the neural arch of the vertebra due to trauma or more likely to stress. The gap or loss of continuity most commonly occurs at the junction of the lamina when the vertebra is viewed from above or between the superior and inferior articular processes (pars interarticularis or facetal joints) when viewed from the side. This condition most frequently affects the fourth and fifth lumbar vertebra, may or may not be symptomatic, and usually does not result in any neurological deficit but is a common cause of low back pain, particularly in children and young adults [204]. The diagnosis is principally radiological (CT, MRI), and scintigraphy is reserved for detection of radiologically occult stress changes and for assessing metabolic activity of the condition. Typically, a focal area of increased uptake is seen in the region of the pars interarticularis (Fig. 5.39). SPECT is much more sensitive than planar imaging in detecting the abnormality. SPECT/CT is preferred to SPECT only [205]. The treatment of this condition is usually conservative, with the use of back support, and usually corrects the problem.

Spondylolisthesis is the forward or occasionally backward movement of one vertebra over

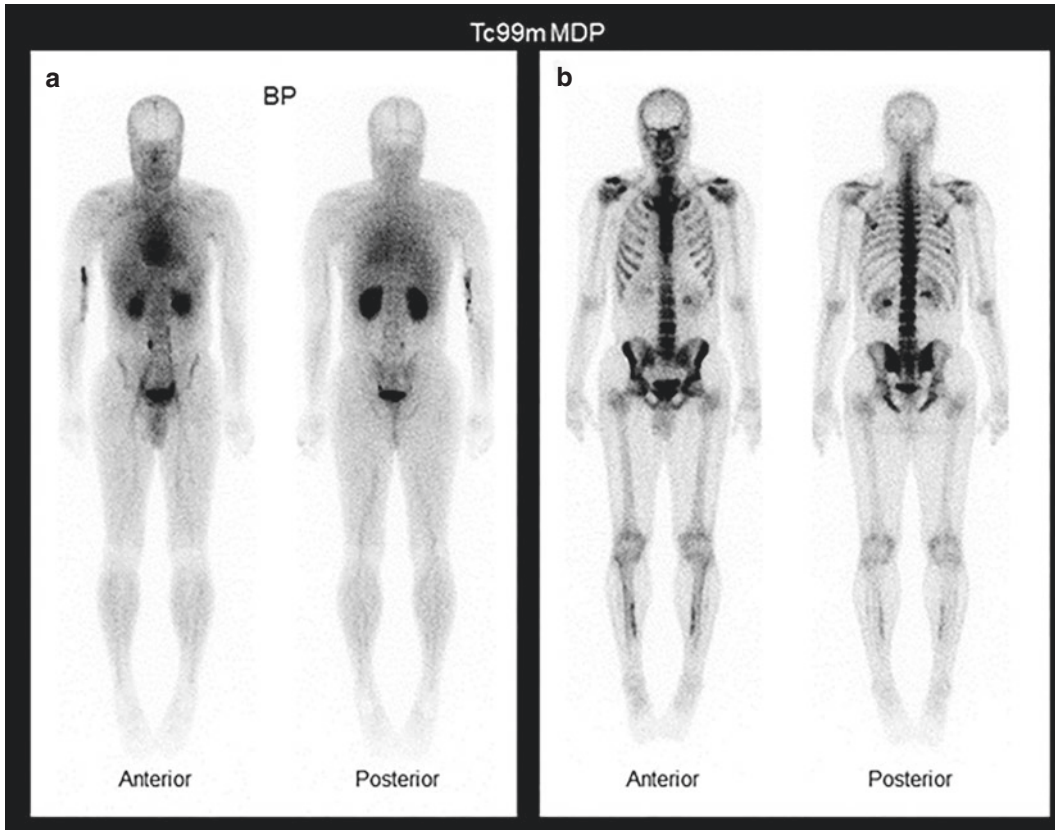

Fig. 5.38 Tc99m MDP whole-body and spot images for 33-year-old military man with history of lower back pain and bilateral leg pain more over the medial aspects for 1-year duration. Whole-body blood pool images (**a**) are unremarkable. Delayed whole-body (**b**) and spot images of the legs (**c**) and chest (**d**) demonstrate a focal area of increased uptake on the seventh rib, posteriorly, which is probably traumatic and increased linear uptake over the tibial bone bilaterally postero-medially indicating bilateral medial tibial stress syndrome (Shin splint)

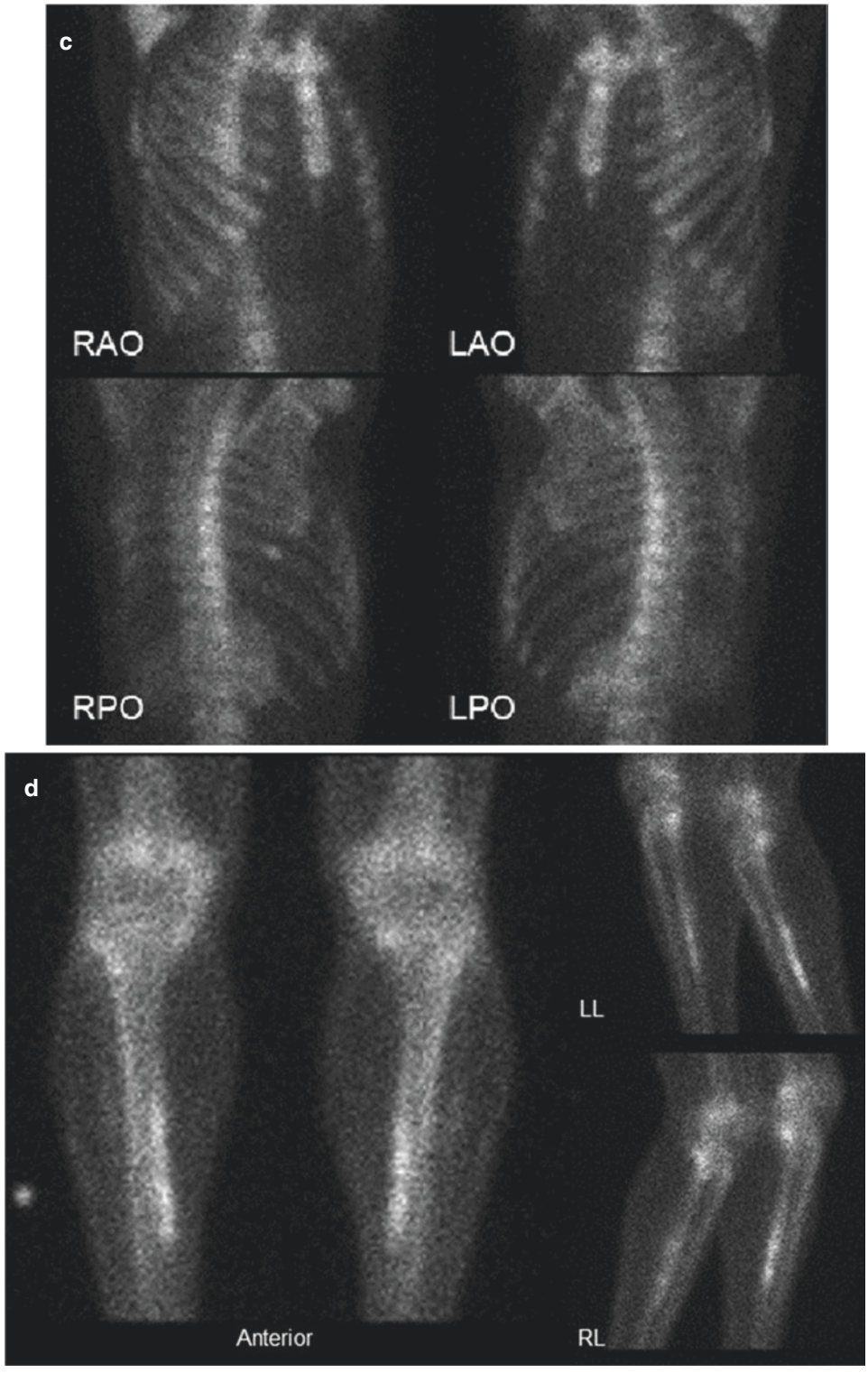

Fig. 5.38 (continued)

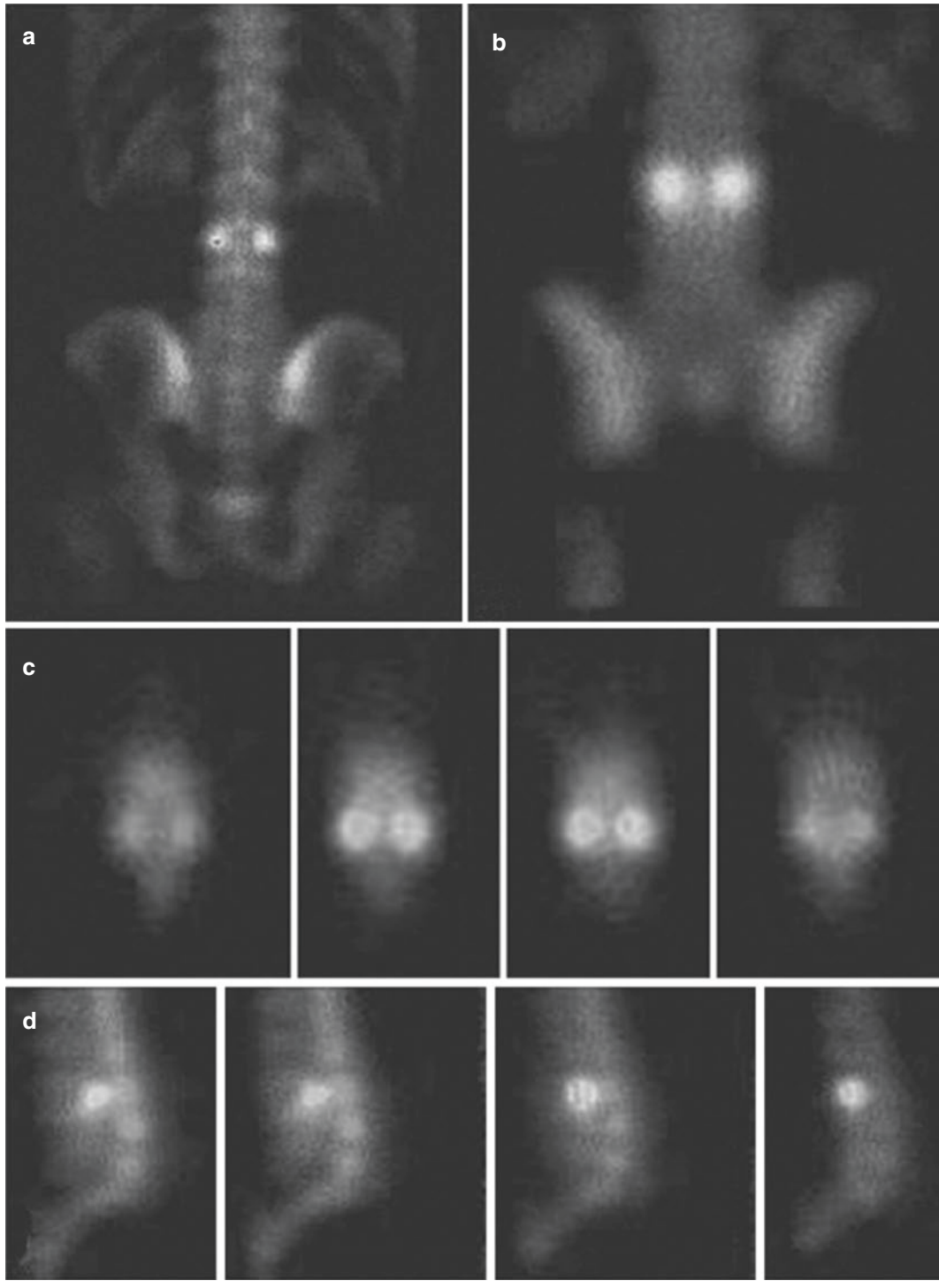

Fig. 5.39 (**a**–**d**) Planar (**a**), representative coronal cut (**b**), transaxial (**c**), and sagittal (**d**) cuts of SPECT study of a young male athlete complaining of low back pain. The study shows focally increased uptake in both sides of L-3 seen in both planar and SPECT images in a case of spondylolysis

another (Fig. 5.40a–c) as a result of fracture of the neural arch. It is again most commonly seen in the fifth lumbar vertebra, in which there is a forward shift of L-5 on the sacrum [204]. It is less commonly seen at L-4. In addition to parallel-hole high-resolution acquisition, pinhole and/or SPECT is needed, along with correlation with the plain radiographs of the lumbar spine.

5.3.5.2 Fracture Healing

Fracture union is simply defined as sufficient growth of bone across the fracture line. The healing process of a fracture is outlined as follows:

1. Formation of hematoma following the fracture event: When a fracture disrupts the periosteum and blood vessels in the cortex, marrow, and the adjacent soft tissue, bleeding occurs, and a hematoma forms between the bony fracture ends, beneath the periosteum and within the medullary cavity.
2. Invasion of granulation tissue into the hematoma: Necrosis of the bone tissue adjacent to the fracture takes place immediately. This

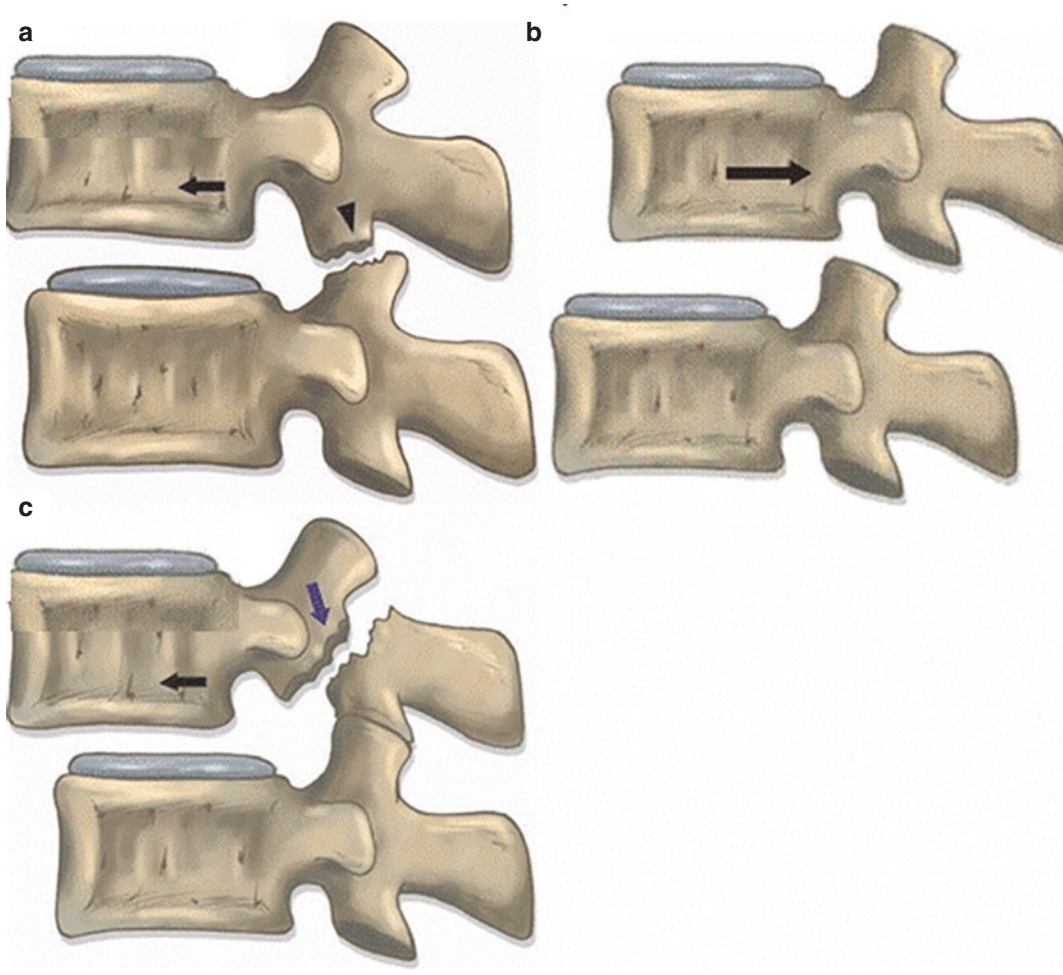

Fig. 5.40 (**a**) Spondylolisthesis without spondylolysis. Degenerative anterior spondylolisthesis. Apophyseal joint osteoarthritis allows the inferior articular processes to move anteriorly, producing forward subluxation of the superior vertebra on the inferior vertebra. (**b**) Spondylolisthesis without spondylolysis but with backward subluxation of the superior vertebra. (**c**) Spondylolisthesis with spondylolysis. The bilateral defects through the pars interarticularis allow anterior displacement of vertebral body on its neighbor, but the alignment of the apophyseal joints is normal. (Adapted from Resnick [199])

necrotic tissue along with the effect of the traumatic force induces inflammatory response with features of acute nonspecific inflammation including vasodilatation, extravasation of plasma and leukocytes, and infiltration with leukocytes. Within 48 h, blood flow to the entire bone increases with organization of the hematoma around the broken ends of bone into a fibrous network.

3. Procallus is formed along the outer surface of the shaft and over the broken ends of bone by the bone-forming cells in the periosteum, endosteum, and marrow.
4. Callus starts to form with synthesis of collagen and matrix by osteoblasts. Mineralization with calcium deposition follows to complete the formation of calluses (woven bone).
5. Remodeling: The unnecessary callus is resorbed as the process of healing continues, trabeculae are formed, and remodeling leads to alignment of the cortical bony margins and marrow cavity. Bone accordingly heals by forming new tissue rather than scar tissue.
6. Modeling: Reshaping of cortex.

Several factors affect the fracture healing, and if disturbances happen, delayed, nonunion, or malunion could result (Table 5.16). *Delayed union* indicates that union does not occur at the expected time which is difficult objectively to be determined and varies with the site of fracture, although overall it is usually 3–4 months after the fracture. *Nonunion* indicates failure of the bone ends to grow together. Instead of new bone, dense fibrous fills the gap between the broken ends and uncommonly by fibrocartilaginous tissue. Necrotic tissue is not seen unless infection is present in the area of nonunion. Delayed union and nonunion are commonly seen in tibia, fibula, and scaphoid bones. Less common sites are humerus, radius, ulna, and clavicle. Occasionally, the gap between the bone ends contains a space filled with fluid. In this case, the term false joint or *pseudoarthrosis* is applied, and persistent uptake of ^{99m}Tc-MDP continues to be seen after the usual period of healing or postoperative changes. The fracture is considered nonunited after 6 months, although in certain locations such as in case of central fracture of the femoral neck which is considered nonunited after only 3 months. Nonunion is classified predominantly according to the radiological appearance into hypervascular (hypertrophic) and avascular (atrophic) and is based on the capability of biologic reaction. Hypertrophic nonunion is rich in callus as seen on standard radiographs and has rich blood supply in the ends of the fragments with the potential to heal under the correct stable environment [206].

Table 5.16 Factors affecting fracture healing

1. Patient age: nonunion is rare in children unless there are other conditions present such as neurofibromatosis, infection, or extensive soft tissue damage
2. Weight bearing: stimulates healing of fractures
3. Fixation: stimulates union but does not accelerate repair itself
4. Nerve damage: is associated with rapid union with unknown mechanism
5. Damage of intramedullary canal and nailing: this may lead to delayed repair or to extensive reactive osteogenic activity
6. Blood supply: interrupted blood supply may cause delayed healing
7. Infection: may lead to delayed healing
8. Excessive use of steroids can cause delayed healing
9. Extent of fracture: severely displaced fractures, open fractures, loss of fragments, and extensive soft tissue damage cause delayed healing

Atrophic nonunion, however, is considered relatively avascular at the ends of the fragments, acellular, and inert, and consequently it lacks the ability to heal under the correct and stable environment [206]. This type is typically seen in tibial fractures treated by plate and screws. Both types contain fibrous tissue, hyaline cartilage, fibrocartilage, and areas of bone formation. However, the amount and type of bone formation differ between the two types. As expected, the hypertrophic type contains more areas of new bone which ossifies by both endochondral and intramembranous ossifications. Atrophic nonunion, however, has only a few areas of bone formation which forms predominantly by endochondral ossification [206]. Radiographs show most of these changes but do not reflect the biologic changes that were recently studied by Reed and associates [206] who found that hyper-

trophic nonunion shows increased apoptosis or programmed cell death (PCD) in both types. *Malunion* describes healing of a bone in a non-anatomical orientation.

Scintigraphy plays no role in the diagnosis and management of most fractures. Exceptions include occult fractures of the small bones of the hands and feet, fractures of abused children [207], and delayed union or nonunion of fractures. Bone scintigraphy often is used to detect stress fractures and can also play a role in the follow-up of these injuries, as noted above. Scintigraphy also has a role in assessing the healing of fractures and bone grafts.

5.3.5.3 Trauma to Bone Adjacent Structures

Skeletal muscle damage in variable degrees is common with fractures. The incidence of sepsis and other fracture-related complications is significantly influenced by the severity of muscle and soft tissue damage. The classical criteria for assessing skeletal muscle damage—color, consistency, bleeding, and contractility—are subjective. Research on animals and humans shows the feasibility of more accurate objective methods to assess skeletal muscle damage using radionuclide imaging techniques. Since muscle injury causes release of the muscle protein myosin from the injured cells, ^{111}In-labeled antimyosin antibodies can be used to detect and assess the extent of skeletal muscle damage [208, 209].

Tears to tendons are called sprains, while ligament tears are called strains. These injuries usually do not cause abnormal uptake on bone scintigraphy. Conversely, complete separation of tendons or ligaments from their attachments is called avulsions, and these do cause abnormal uptake on bone scans.

5.3.6 Growth Plate Injury

The physis, or growth plate, is recognized as the site of endochondral ossification and is responsible for a bone's growth in length. Although the band of increased uptake seen on scintigraphic bone images is referred to as the growth plate, it actually does not correspond to the lucent band present on a bone radiograph that is also referred to as the growth plate. The radionuclide growth plate corresponds to the dense band of bone in the metaphysis adjacent to the radiographic growth plate and is described in radiographic anatomy as the zone of provisional calcification. A key to the comparison of growth plate uptake is having both plates symmetrically positioned on the same large view. Two- or three-phase imaging is recommended in growth plate evaluation. Both flow and blood pool images show information on plate activity. They often show differences in plate function more clearly than the delayed images. The normal physis scintigraphic appearance of the growth plate changes with age. In the infant and young child, the physis has a thicker, oval-shaped appearance. With maturation, it becomes linear, and in adolescence the closing physis shows progressively decreasing activity. Growth plates in different areas of the skeleton close at different times. Skeletal maturation occurs earlier in females than in males. In addition to condition such as trauma and infection, which directly affect the physis, the plate can be influenced by mechanical stresses such as differential weight-bearing and conditions producing regional hyperemia. Rheumatoid arthritis, chronic synovitis, and lesions such as fibrous dysplasia can accelerate closure or a growth plate located in the involved region.

Physiological status of the growth plate is difficult to evaluate using morphologic imaging. Scintigraphic imaging compliments anatomical studies by reflecting the physiological status of the growth plate and has the advantage quantitation. It can also detect the abnormalities earlier than morphologic modalities and can help particularly in detecting segmental growth plate arrests that are difficult to determine by these modalities [210–212].

On scintigraphy, differences in activity and configuration of growth plates can be identified particularly on early blood pool images (Fig. 5.41) which show the differences better than on delayed images [213].

Both sides must be symmetrically positioned within the field of view. Segmental closure can

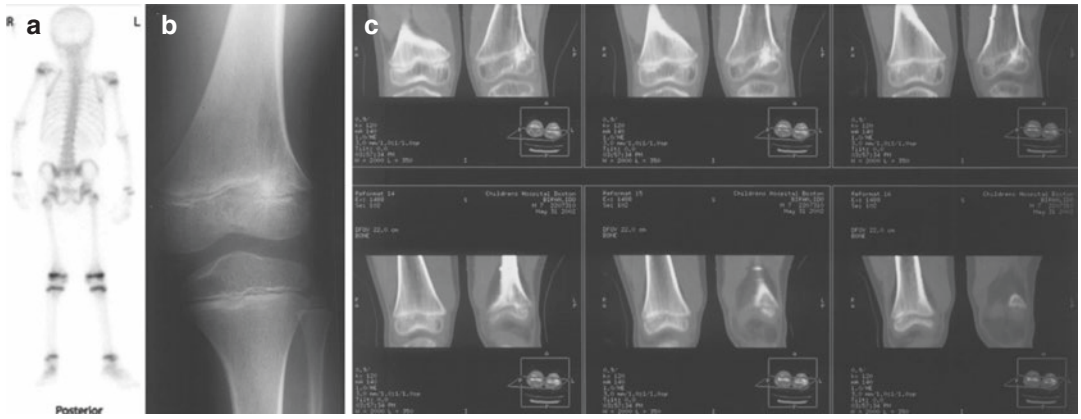

Fig. 5.41 (**a**–**c**) Growth plate injury. Whole-body anterior (**a**) and posterior bone scan of a 4-year-old boy with pain in his left knee. The scan shows increased uptake in the lateral aspect of the left distal femoral growth plate. Standard radiograph (**c**) and MRI images of the same patient illustrating the same injury

be better identified using pinhole view and quantitation [213, 214]. In addition to asymmetric and segmental differences in uptake, blurred growth plate appearance can also be seen with adjacent epiphyseal and/or metaphyseal injury [213]. These findings are not permanent as shown by Etchebehere et al. [214] who studied 18 children with uncomplicated femoral fractures by multiphase bone scintigraphy at three different time intervals (2–5, 6–12, and 18–24 months). Visual analysis of the blood flow, equilibrium, and delayed images showed increased activity in the distal femoral growth plates during the first and second time intervals, but not during the third [214].

Scintigraphy is considered the only imaging modality capable of assessing the magnitude of physeal stimulus caused by femoral fractures and to predict a favorable or unfavorable outcome of leg length by semiquantitative analysis. SPECT imaging was found useful to detect and locate decreased metabolism associated with posttraumatic closure of the physeal plate which predicts growth arrest and deformities [210, 215, 216], although pinhole magnification imaging is superior to SPECT and is the preferred method of imaging. SPECT/CT is found helpful for quantation of the osteoblastic activity in the growth plates and has the potential to improve the management of children with growth disorder [217].

Injury to the physis or growth plate in children may lead to growth arrest and/or angular deformities in the limbs. On scintigraphy, normal growth plates appear as thin well-demarcated linear activity. However, based on quantitative data in normal children, greater activity presents in the medial half of the distal femoral growth plate than the lateral half, while in the proximal tibial growth plate, the lateral half shows more activity than the medial [214]. Stress factors and mechanical loading influence the scintigraphic uptake at the growth plate. For example, when an extremity is placed at rest, as with prolonged immobilization, activity in the growth plate decreases in comparison with the contralateral weight-bearing extremity. This can occur also in ambulatory patients with a gait disturbance which results in differential weight-bearing. Conversely, increased growth plate uptake can occur on a regional basis in response to trauma, infection, and any condition that relates to increased metabolic activity in the skeleton. Systemic and metabolic diseases can result in a generalized increase in growth plate uptake throughout the skeleton. Trauma and infection may result in uniform increased activity in the plate or segmental abnormal uptake. Fractures and slipped capital femoral epiphysis result in uniformly increased plate activity at the involved location. Segmental increase and decrease in a growth plate are of particular importance, since it is associated with

the development of angular deformities. Insults such as trauma and infection directly involve the growth plate or if such injury occurs near the plate, the segmental abnormal uptake will be seen, and deformity may follow. A fracture in the metaphysis of a long bone can, for example, provoke angular deformity by stimulating an adjacent growth plate. Harcke described the increased growth plate activity with metabolic bone disease and documented a return to normal after successful treatment. Such injuries particularly fractures may cause permanent closure of segments of growth plates [218].

Partial arrest of the growth plate occurs when osseous or cartilaginous bridge forms across the plate. If this occurs laterally, the relative accelerated activity of the medial growth plate will result in valgus deformity, while if the bar is located in the medial side and normal physis continues to grow laterally, it will cause varus deformity [219].

These angular deformities could also occur secondary to contiguous chronic hyperemia of a metaphysis or epiphysis such as after a fracture to these locations which stimulates the activity of the adjacent part of the physis resulting in unequal growth with subsequent deformity [220].

Computed tomography and magnetic resonance imaging are accurate in identifying segmental closure [221].

5.3.7 Metabolic Bone Diseases

The osseous bone response to injury, regardless of the type, is characterized by increased remodeling and new bone formation in an attempt to repair the damage or to contain the noxious insult. This process is evidenced by focal increased uptake of bone-seeking agents. In contrast, in metabolic bone disease, a general imbalance of the processes of bone formation and resorption is present. The net effect resulting from these two processes determines the scintigraphic patterns observed in metabolic bone disease.

Metabolic bone disease, however, is usually linked to alterations of the calcium metabolism by one or more of a number of physiological factors. Increased rates of bone turnover are present in most metabolic bone disorders often associated with decreasing calcium content of the affected bone. This explains why most metabolic disorders result in generalized increased radiopharmaceutical uptake on bone scintigraphs, reflecting this increased bone turnover.

The regulation of calcium and bone metabolism is multifactorial and complex. Parathyroid hormone (PTH) plays an important role in these mechanisms by acting on two major target organs, bone and kidney. Its effects on the kidney are closely related to those of vitamin D. The two main actions are (1) to increase resorption of calcium and magnesium and (2) to decrease phosphate reabsorption. The effect of PTH on bone is also modulated by vitamin D and is mainly to promote efflux of calcium from bone, acting through osteoclasts [222].

In some disorders, however, abnormal bone formation has a more localized character as is the case in hypertrophic osteoarthropathy, the pathogenesis of which is still poorly understood, although neurovascular abnormalities may be present.

5.3.7.1 Paget's Disease (Osteitis Deformans)

Paget's disease of bone is common in temperate areas, where the prevalence is estimated to be 3–4% among individuals over the age of 55 years and 10% among those above 80 years of age. It is uncommon among persons under the age of 55 and in areas with warm weather such as the Middle East. The disease is asymptomatic in 90% of affected subjects.

The etiology of Paget's disease is not known; viral infection has been suggested, although direct recovery of a virus has not been made. It was proposed that a slow virus is the causative agent. It is postulated that the primary residence of the virus is the osteoblast, while the osteoclast represents a site of viral assembly. The infected osteoblasts produce excessive interleukin-6, which stimulates bone resorption and activates c-fos proto-oncogenes, which interfere with normal bone development.

The skeletal distribution of Paget's disease suggests that the disease predominates in bones containing red marrow and may be dependent on the blood supply. Normal hematopoietic bone marrow may be replaced by loose fibrous connective tissue. With time, the increased osteoblastic and osteoclastic activity ceases, marrow abnormalities return to normal, and the affected bones become sclerotic [167].

The disease simply represents a state of increased metabolic activity in bone with abnormal and excessive bone resorption and formation. The chronic acceleration of remodeling may lead to enlargement and softening of the bones affected.

Paget's disease begins with active and excessive resorption (resorption or lytic phase) which may progress rapidly and results in softening of bone. Pathological fractures frequently occur, particularly of the femur and tibia. In this phase the bone trabeculae are slender and very vascular. Giant osteoclasts are present and have been shown to take up ^{67}Ga [171]. This is followed by a mixed phase characterized by accelerated formation as well as resorption of bone. If bone formation predominates, this can be called the osteoblastic phase, and the term mixed can be reserved for those with approximately equal resorption and formation. The final phase (the sclerotic or burned-out phase) is characterized predominantly by new bone formation, more disorganized structure, thick trabeculae, and less prominent vascular sinusoids [223].

The morphology of the resorptive phase of Paget's disease is characterized by the presence of increased numbers of large multinucleated osteoclasts that may assume bizarre shapes and contain as many as 100 nuclei; normal osteoclasts have 5–10 nuclei (Fig. 5.42a, b). In the mixed phase, a profusion of osteoblasts and osteoclasts, evidence of high bone turnover, coexists in a matrix of highly vascularized fibrous tissue. This may facilitate the development of microfractures in long bones and basilar invagination when the base of the skull is diffusely involved. The late sclerotic phase is characterized by a disordered mosaic pattern of thickened lamellae containing irregular patterns of cement lines where waves of bone formation have succeeded in areas of previous bone resorption.

Although Paget's disease is diagnosed economically with standard radiographs, other modalities are needed particularly scintigraphy given the limitations of the standard radiographs. The early radiological lesions of Paget's disease reflect severe localized osteolysis. These are typically "flame-shaped" (Fig. 5.43) or inverted "V" lesions that most commonly occur proximal to the distal epiphysis of a long bone and that gradually progress to the opposite end

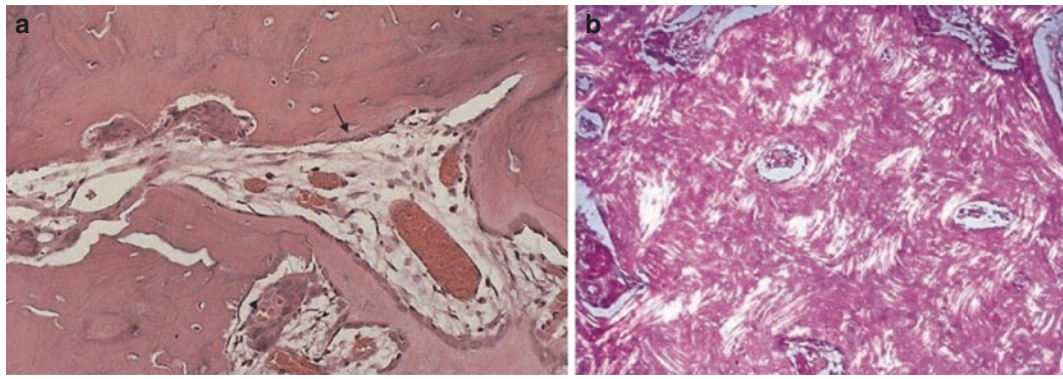

Fig. 5.42 (**a**) A microscopic picture of mixed osteoblastic-osteoclastic stage of Paget's disease. A line of osteoblasts is present at the *center right* forming new bone (*arrow*), and lacunae containing multinucleate osteoclasts is seen at the *center left* and *lower center* (*arrowhead*). The result is a patchwork mosaic of bone without an even lamellar structure. This phase is preceded by a predominantly lytic phase and is followed by a "burned-out" sclerotic phase. (**b**) Under polarized light, the irregularities of the bony lamellae are apparent

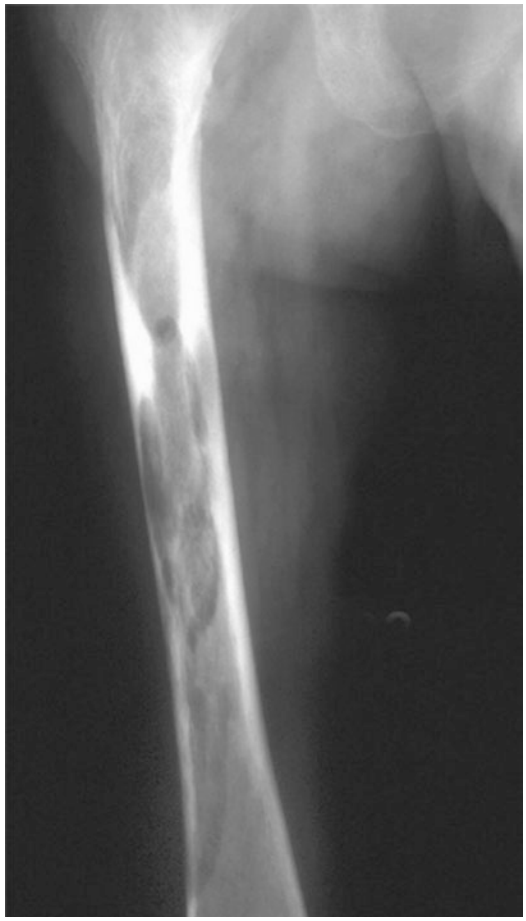

Fig. 5.43 Radiograph of a femur bone affected with Paget's disease demonstrating the typical osteolytic pattern (flame-shaped) of the disease

of the bone. Osteoporosis circumscripta is the term applied to osteolytic lesions in the skull. In the vertebrae, osteolytic lesions may simulate malignancy. As the disease evolves, the ingrowth of fibrovascular tissue "mixed stage" and a high rate of bone remodeling may lead to deformity of the skull, enlarged dense vertebral bodies, and slowly progressive deformities of weight-bearing bones. Microfractures may occur on the convex side of the femur or tibia, increasing the degree of deformity and leading to the transverse or "banana" fracture that is typical of Paget's disease. Pelvic involvement may be limited to the ilia and pubic rami, but it may involve the acetabulum or both the acetabulum and the femur. It should be noted that radiologically the pagetic process may be seen to involve subchondral bone but not to cross the joint space. In addition, Paget's patients are also susceptible to the development of inflammatory arthritis: gouty arthritis, rheumatoid arthritis, psoriatic arthritis, and ankylosing spondylitis have each been reported in association with Paget's disease. However, it is osteoarthritis that most often is the most common source of chronic joint pain and limited mobility.

MRI imaging can demonstrate the presence and extent of several characteristic disease complications, including basilar impression, spinal stenosis, and secondary neoplasm [224]. MRI can add also diagnostic value to other imaging modalities used for the diagnosis of Paget's disease, including radiographs, computed tomography, and bone scintigraphy, by demonstrating marrow changes when present and can contribute to a noninvasive diagnosis of Paget's disease in atypical presentations [225].

Although bone densitometry studies have little to do with the diagnosis of Paget's disease, the bone density pattern should be known to avoid misinterpretation of density data. Although bone density may be increased in bone that is affected by Paget's disease, density in noninvolved bones is unaffected. High DXA values may alert to the possibility of Paget's disease, especially if the value deviates from the expected normal sequence in lumbar vertebrae. Osteoporotic vertebrae may be overlooked if the average value of bone mineral density is taken in the lumbar spine without reviewing each vertebra [226]. On multiphase bone scan, dynamic flow and early static images show varying degrees of hyperemia at the sites of involvement depending on the stage of the disease, the earlier the phase, the more the hyperemia (Fig. 5.44). On delayed static images, Paget's disease appearance depends on the stage of the disease. During the active lytic phase, involvement of Paget's disease is characteristically seen as intense increased uptake which is uniformly distributed throughout the region affected (Figs. 5.44 and 5.45). An exception to this characteristic pattern of the early phase is the skull pagetic lesion which shows intense uptake at the periphery of the lesion while the center is

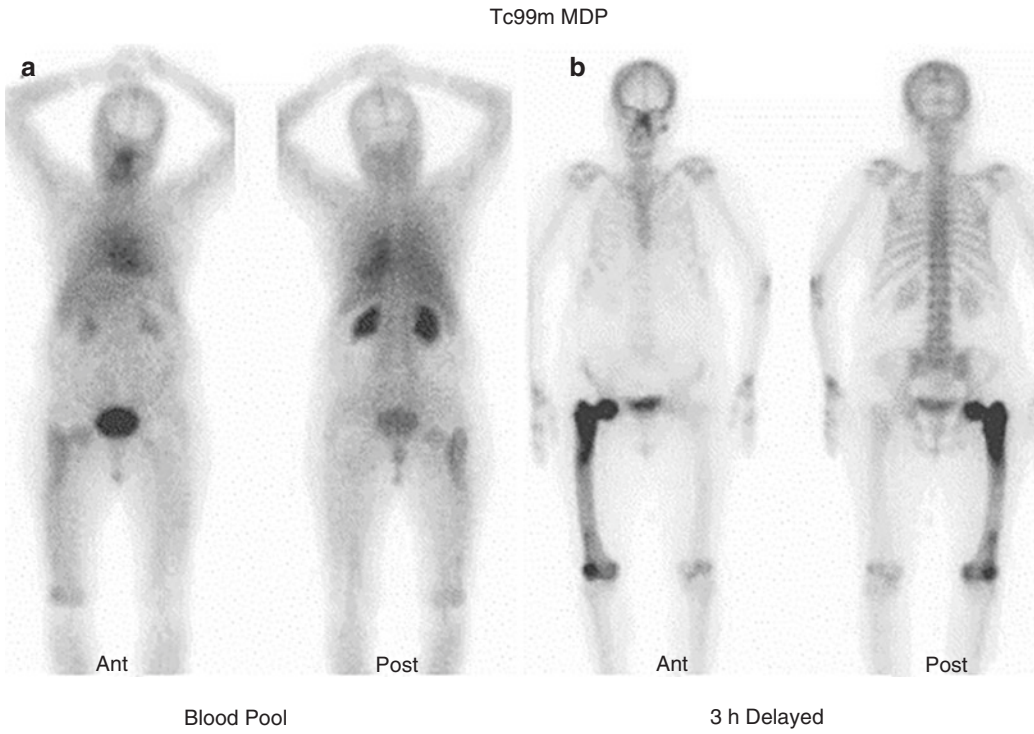

Fig. 5.44 A 76-year-old female with lytic lesion in the right tibia. Monostotic Paget's disease. Diffusely increased blood pool activity (**a**) in the right tibia is more obvious proximally with corresponding increased delayed uptake (**b**). The increased uptake involves the entire tibia but with grades of uptake from mild to intense representing uptake patterns in early active phase and later phases

cold which is referred to as osteoporosis circumscripta [227]. With time, the disease activity gradually decreases towards the sclerotic phase, and uptake of the bone imaging agents decreases as well. With time, the sclerotic phase may show practically no abnormal uptake of the radiopharmaceuticals, and hence, the disease can be detected by X-ray and missed by bone scanning. This is in contrast to the early lytic phase when bone scan is much more sensitive than radiographs. The bone scan will identify approximately 15–30% of lesions not visualized on X-rays [227, 228].

An advantage of bone scan could be contributing partly to this which is its ability to detect abnormalities in bones that are difficult to explore by radiographs such as sternum, ribs, and scapula [229].

Conversely, in about 5% of cases, the radiograph may demonstrate diffuse pagetic involvement, for example, of the pelvis, whereas the bone scan reveals little uptake of the isotope. In this circumstance, the alkaline phosphatase level may be normal or only slightly elevated, reflecting lesions that are sclerotic, relatively inactive, or "burned out." Affected bones may also appear increased in size but with preservation of the normal configuration. Characteristically, in this phase, the transition between the affected bone and adjacent normal bone is characteristically narrow during this active phase. Renier and Audran reported in a large series of 200 patients with Paget's disease, 169 (85%) with polyostotic involvement with data suggesting that the disease process spreads across a joint in some patients, even in the absence of degenerative joint disease. The authors reported several cases with extensive pagetic lesion seen on one side of a joint and a considerably smaller lesion on the other side. The study also found that Paget's disease may involve paired bones and involvement could be symmetrical [230].

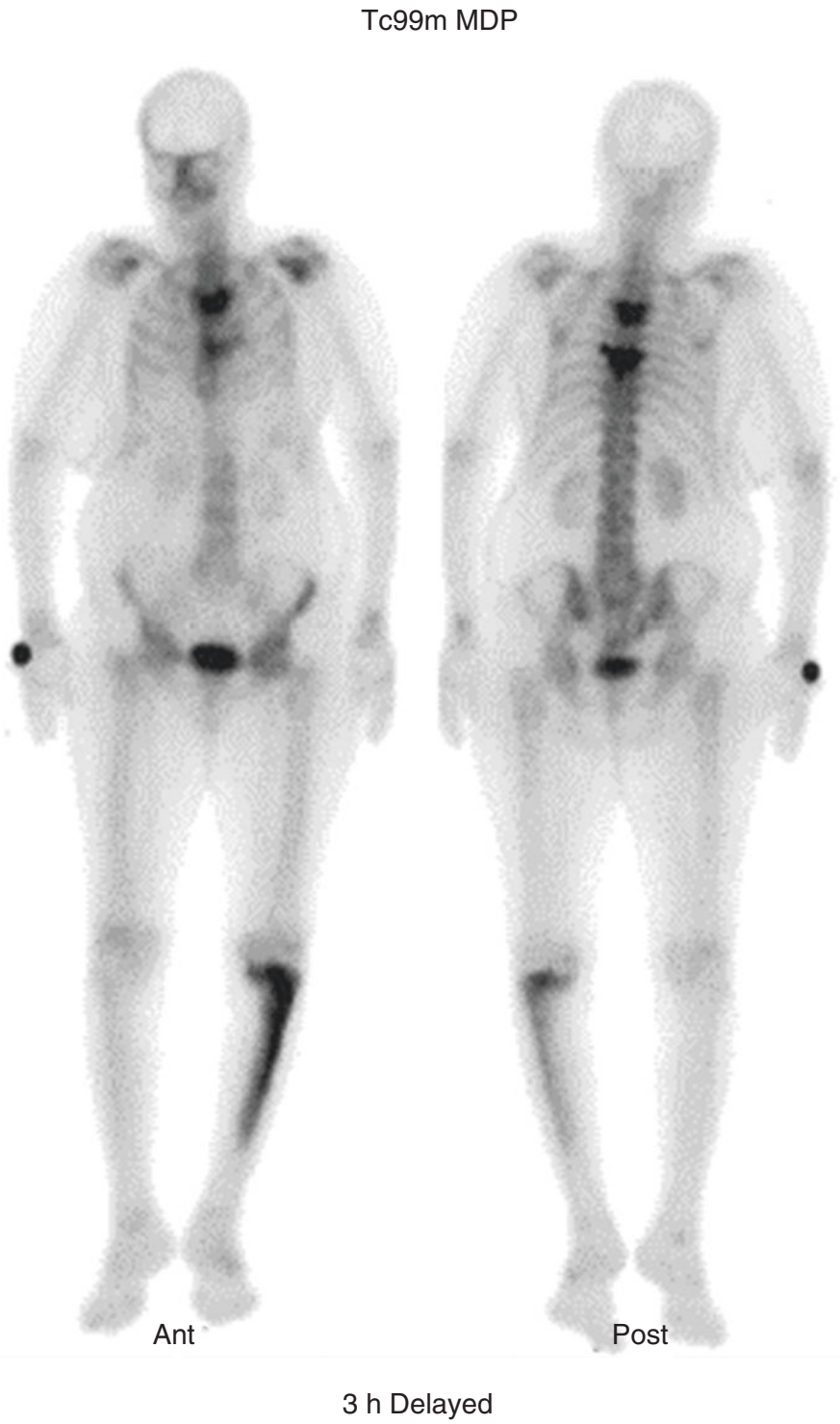

Fig. 5.45 Whole-body tc99m delayed images demonstrating a polyostotic type of the disease affecting more than one location (thoracic spine and left tibia)

The disease is often nonuniform within the skeleton. Individual-involved bones can simultaneously present more than one stage of the disease process, reflecting variations of the duration of the disease at different sites.

Paget's disease may show absent and expanded bone marrow uptake or a mixture of both. This can be explained by the presence of areas of advanced, sclerotic disease with active bone marrow and areas of earlier active disease with replaced bone marrow. Since ^{111}In-WBCs are taken up by hematopoietic bone marrow, uptake is therefore seen in areas of Paget's disease with active marrow. This can mimic the uptake in infection, particularly when it is focal [231].

5.3.7.2 Osteoporosis

Bone mass gradually increases during childhood and increases rapidly once the skeleton approaches maturity and longitudinal skeletal growth slows [232] till it reaches the peak bone mass in the second decade, although this is somewhat controversial [233].

At maturity, black men have denser skeleton than white men and black women (Fig. 5.46a), whereas white women have the least dense bones [234]. Generally, men have an average 20% greater peak bone mass than women [235]. Peak bone mass appears to be a major factor in determination of the risk of developing osteoporosis.

After reaching its peak, bone mass begins to decrease at a rate of 0.25–1% per year. Men demonstrate a gradual rate of bone loss that persists throughout the remainder of adult life. Women, however, undergo rapid rate of bone loss in the perimenopausal and postmenopausal periods [236].

Loss of trabecular bone exceeds that of compact bone. Some investigators have determined that 50% of trabecular bone and 30% of compact bone will eventually be lost [236]. Generally lifetime bone losses for men are 20–30%, while some women may lose 50% or more [234]. In postmenopausal period, women show a normal age-related annual bone loss of 1–2% in appendicular bone and about 4–6% or even 8% in the spinal trabecular bone [237, 238].

The factors related to bone loss in the perimenopausal and postmenopausal periods include age-related factors, estrogen deficiency, calcium deficiency, and other factors such as physical activity, smoking, alcohol consumption, and medications.

Remodeling has a crucial role in maintaining the integrity of normal bone and altering the bone architecture in response to stress. Trabecular bone is remodeled more rapidly than cortical bone [234]. Trabecular bone has a turnover rate approximately four to eight times as high as that of compact bone and is highly responsive to metabolic stimuli [236, 239].

This high-turnover rate in trabecular bone makes it a primary site for detecting early bone loss and for monitoring the response to interventions [240, 241].

Osteoporosis is the most common metabolic disorder of the skeletal system. It affects approximately 20 million older Americans, 90% of whom are postmenopausal [175]. Osteoporosis is "a condition in which bone tissue is reduced in amount increasing the likelihood of a fracture" [242, 243].

It results from osteoclastic bone resorption not compensated by osteoblastic bone formation. In other words, the bone is qualitatively normal but quantitatively abnormal.

Osteoporosis is characterized by abnormal reduction in bone density and hence a decrease in the amount of calcified bone mass per unit volume of skeletal tissue. The basic mechanism behind this condition is decreased bone formation (osteoid formation), even though calcium deposition may be normal. The disease develops when the process of bone resorption and formation (remodeling cycle) is disrupted, leading to an imbalance. The complete remodeling cycle that consists of activation of basic multicellular units, bone resorption, and bone formation normally takes about 4 months in adults. In patients with osteoporosis, this remodeling cycle may require up to 2 years. This can be attributed to an increase in the number of activated basic multicellular units, leading to resorption at more sites, increased rate of resorption, increased frequency

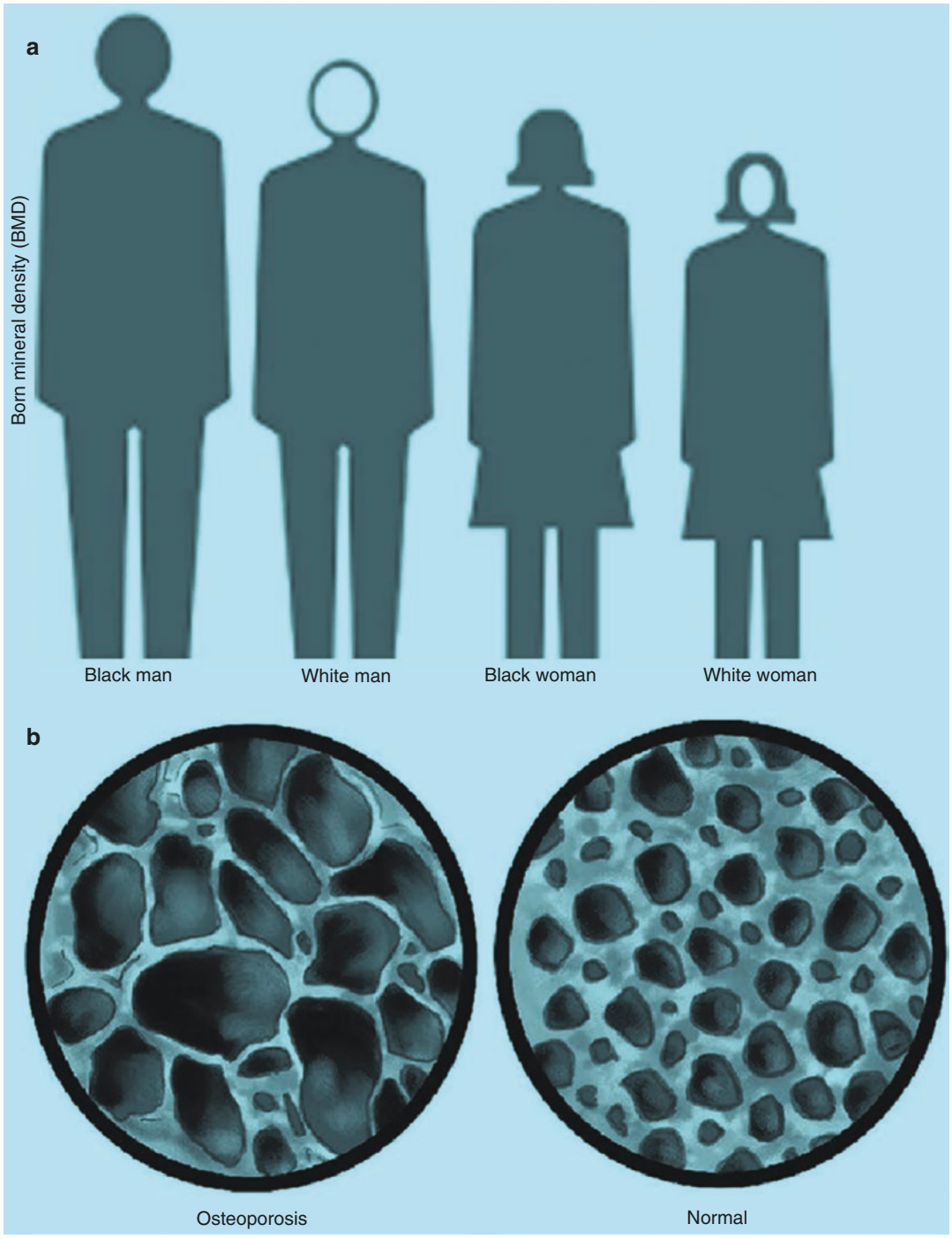

Fig. 5.46 (**a**) Histogram illustrating the peak BMD among men and women. Note that white women have the lowest value. (**b**) A diagram illustrating the bone architecture I oatoeporosis with thinner trabeculae compared to normal bone

of activation of basic multicellular units, and delay in bone formation. Osteoporosis also occurs when the numbers of osteoblasts and osteoclasts in bone are inadequate.

There are numerous causes of osteoporosis, many of which are metabolic in nature (Table 5.17). Types of osteoporosis not considered metabolic in nature include juvenile osteoporosis, which affects younger individuals and is idiopathic rather than metabolic. The disease may be generalized, involving the major portions of the axial skeleton, or regional, in one segment of the appendicular skeleton. Both compact and spongy bones are lost, but loss of spongy bone exceeds that of compact bone.

Senile osteoporosis, which is the most common type, often produces increased susceptibility to fractures in old age. Since men have greater peak bone mass than women, men are affected by senile osteoporosis later in life. It is estimated that women lose about 50% of their spongy bones, while men lose 25% when affected by the disease. Postmenopausal osteoporosis is also common; deficiency of estrogen leads to decreased bone formation. Estrogen is necessary to stimulate production of new osteoblasts, which otherwise fail to lay down sufficient bone matrix.

Table 5.17 Etiology and classification of osteoporosis

Primary
1. Involutional
Type I: postmenopausal
Type II: age related (senile)
2. Idiopathic
Juvenile
Adult
Secondary
1. Prolonged immobilization
2. Steroid therapy
3. Diabetes mellitus
4. Prolonged heparin administration
5. Sickle cell disease
6. Cushing's syndrome
7. Rheumatoid arthritis
8. Scurvy
9. Multiple myeloma
10. Osteogenesis imperfecta (brittle bone disease)
11. Disuse or immobilization of a limb (regional osteoporosis)

Prolonged use of steroids or steroid overproduction, as in Cushing's syndrome, may cause osteoporosis. This hormone increases the ability of the body to resorb bone [244].

Smoking lowers circulating estrogen levels in premenopause women and accelerates the onset of menopause, and these are risk factors for osteoporosis. Smoking is also a risk factor for osteoporosis in men. Osteoporosis has also been reported to be prevalent among patients with liver cirrhosis. In one study, the prevalence of spinal osteoporosis was 20% in cirrhotic patients compared with 10% in controls [245].

Table 5.18 summarizes risk factors of involutional osteoporosis.

Since the condition results in brittle or porous bone, patients suffer more than normal from fractures. Compression fractures of the spine, distal radius, and femoral neck are more common in the presence of osteoporosis. Repeated and multiple vertebral fractures, commonly in the thoracic spine, may lead to kyphosis and other spinal deformities [244, 246, 247].

Fractures of ribs, sternum, pelvis, and feet are also common in osteoporotic patients.

Regional and transient osteoporosis occurs in a segment of the appendicular skeleton when there is disuse or immobilization of a limb, such as would happen with paralysis or healing of a

Table 5.18 Risk factors for primary involutional osteoporosis

1. Sex (female)
2. Age, advancing
3. Positive family history
4. Race, Caucasian or Asian
5. Slender body habitus
6. Early or surgical menopause
7. Late menarche
8. Calcium deficiency
9. Alcohol, smoking, caffeine
10. Medications: steroids, heparin, thyroid hormones, anticonvulsants
11. Sedentary lifestyle
12. Hypogonadism in men
13. Anorexia nervosa
14. Hyperparathyroidism
15. Hyperthyroidism
16. Primary or secondary amenorrhea

fracture in a cast. Osteoporosis usually appears after about 8 weeks of immobilization but can develop earlier in individuals younger than 20 or older than 50 years.

Osteoporosis sometimes is obvious on plain radiographs. Quantification of bone density from plain radiographs is difficult and inaccurate. Dual-photon absorptiometry, X-ray absorptiometry, and computed tomography scans are all used to measure bone mineral density and evaluate osteoporosis. The goal of treatment is to slow down the rate of calcium and bone loss and to avoid the complications that can be disabling and life threatening.

Bone densitometers measure the radiation absorption by the skeleton to determine bone mass of the peripheral, axial, and total skeleton. Common techniques include single-photon absorptiometry (SPA) of the forearm and heel, dual-photon (DPA) and dual-energy X-ray absorptiometry (DXA) of the spine and hip, quantitative computed tomography (QCT) of the spine or forearm, and radiographic absorptiometry (RA) of the hand. Although osteoporosis sometimes is obvious on plain radiographs, quantification of bone density from plain radiographs is difficult and inaccurate. Quantitative bone densitometry is now well established in clinical practice. DXA however is the most widely used technique and is considered the gold-standard method for the measurement of bone mineral density (BMD). It has the advantages of good precision, short scan times, and stable calibration.

Bone loss measurement is performed by various methods of densitometry. Densitometry is used to (1) assess patients with a high risk for metabolic bone disease and estimate the status and severity of osteoporotic bone loss in perimenopausal women; (2) estimate fracture risk for the spine, hip, and wrist; and (3) monitor the effectiveness of treatment. The goal of the treatment is to slow down the rate of calcium and bone loss and avoid the complications that can be life threatening.

A measurement of hip BMD has been shown to be most reliable in the risk of hip fracture [248, 249], while the spine is considered the optimum site for monitoring response to therapy [250] because vertebrae are rich in the metabolically active trabecular bone. The radiation dose to the patient from a DXA scan is very low (1–10 uSv) [251] which is comparable to the average daily radiation dose of 7 uSv from natural background. For the interpretation of DXA, *T*- and to a lesser extent *Z*-score are used. Score relates the individual's density to that of young healthy adults, and *Z*-score relates to that of the same age group. *T*-score is calculated by determining the difference between a patient's measured BMD and the mean BMD of healthy young adults, matched for gender and ethnic group, and expressing the difference relative to the young adult population SD.

Based on the *T*-score values, WHO defined osteoporosis and osteopenia [252].

An individual with at *T*-score < -2.5 at the spine, hip, or forearm is classified as having osteoporosis, a *T*-score between -2.5 and -1 is classified as osteopenia, while a *T*-score > -1 is regarded as normal (Figs. 5.47 and 5.48).

Instead of comparing the patient's BMD with the young adult mean, the *Z*-score compares the bone density of the individual to the mean BMD expected for the patient's peers (age matched). Although *Z*-score is not as widely used as *T*-score, it remains a useful concept since it expresses the patient's risk of having an osteoporotic fracture relative to their peers. It is estimated that for every reduction of 1 SD in BMD, the likelihood of fracture increases by 1.5–2.5. Accordingly patients with a *Z*-score < -1 are at a substantially increased risk of fracture compared to their peers with a *Z*-score of 0. Presenting bone density result using *T*- and *Z*-score is advantageous since it avoids the confusion present when using the actual BMD values that differ among different equipment [253].

5.3.7.3 Osteomalacia and Rickets

Osteomalacia is due to abnormal mineralization of bone, predominantly as a result of vitamin D deficiency, with a decrease in bone density secondary to lack of both calcium and phosphorus. Note that in osteomalacia, the amount of osteoid (bone formation) is normal, while osteoid is

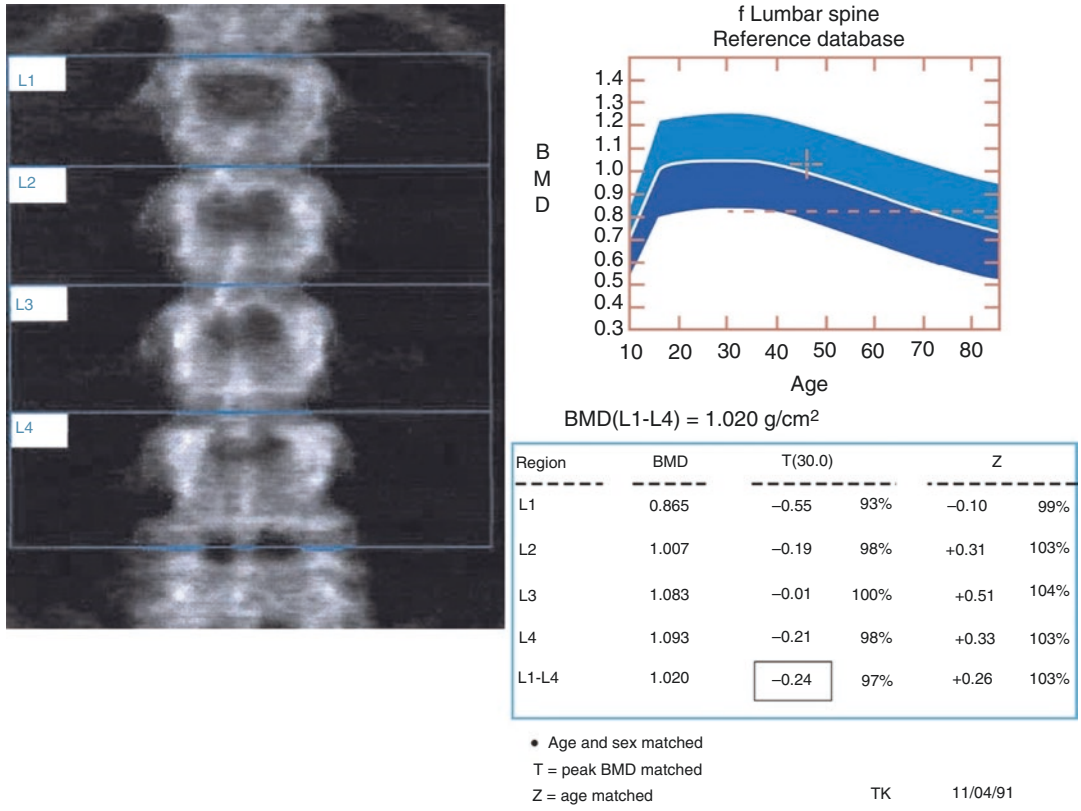

Fig. 5.47 A bone densitometry study with normal *T*-scores of ≥1 SD

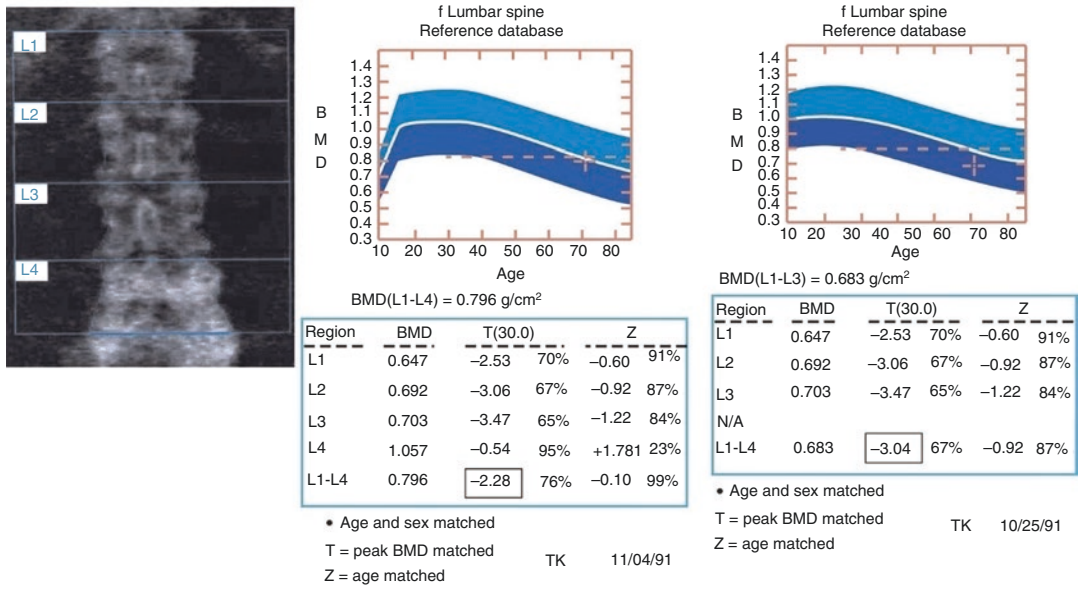

Fig. 5.48 Osteoporosis. *T*-scores are below −2.5 SD without including the—L4 vertebra with degenerative changes in analysis

decreased in osteoporosis. In other words, there is inadequate and delayed mineralization of osteoid in spongy and compact bones, which have a normal remodeling cycle as opposed to delayed cycles in osteoporosis. Simply put, in osteomalacia the osteoid tissue is normal in amount but soft since it lacks calcium, while in osteoporosis, there is a lack of osteoid tissue as a whole.

If osteomalacia occurs in growing bones prior to closure of the growth plate, it is called infantile osteomalacia, or rickets. Growing bones fail to mineralize and become soft, with resultant deformities. Growth plates and metaphysis are disorganized in patients with rickets, with a decrease in the length and width of the growth plates. Nutritional (vitamin D deficiency) rickets is now a rarity in the industrial world because of food fortification. Most cases result from hereditary inborn errors of vitamin D metabolism or end-organ unresponsiveness as is exemplified in this case of hypophosphatemic rickets.

Clinically, osteomalacia is manifested by progressive generalized bone pain, muscle weakness, hypocalcemia, pseudofractures, and, in its late stages, a waddling gait. Osteomalacia due to vitamin D depletion appears not to be suspected or diagnosed promptly in susceptible patients, probably because physicians are not sufficiently aware of this rare condition. In a study of 17 patients with osteomalacia due to vitamin D depletion, only 4 were suspected by the referring physicians, although a gastrointestinal disorder that can lead to vitamin D depletion was present in every patient [254].

Characteristic pseudofractures were seen in only seven patients. Six of the 23 patients with diffuse demineralization had an "osteoporotic-like pattern" without pseudofractures. Prominent articular manifestations were seen in seven patients, including a rheumatoid arthritis-like picture in three, osteogenic synovitis in three, and ankylosing spondylitis-like in one. Two other patients were referred to us with the diagnosis of possible metastatic bone disease attributable to polyostotic areas of increased radionuclide uptake caused by pseudofractures (Fig. 5.49). Six patients also had proximal myopathy, two elderly patients were diagnosed as having polymyalgia rheumatica, and two young patients were diagnosed as having fibromyalgia. One of the patients who presented with increased bone density was misdiagnosed as possible fluorosis. Osteomalacia is usually neglected when compared with other metabolic bone diseases and may present with a variety of clinical and radiographic manifestations mimicking other musculoskeletal disorders [255]. Eight women aged 17–72 years, six with osteomalacia and two with primary hyperparathyroidism, were studied by bone scans and Tc99m (V) DMSA scans. Many of the fracture and pseudofracture sites detected on bone scans were also visualized on 99Tcm(V)-DMSA scans which were suggested by the authors to have a potential as a screening method in patients with metabolic bone disease [256, 257].

5.3.7.4 Bone Changes of Hyperparathyroidism

Overactivity of the parathyroid gland(s) results in excess secretion of parathyroid hormone, which promotes bone resorption and consequently leads to hypercalcemia and hypophosphatemia. Primary, secondary, and tertiary hyperparathyroidism all share elevated serum calcium and parathyroid hormone but show different scintigraphic patterns.

Primary hyperparathyroidism is caused by benign adenoma in approximately 80% of cases. Hyperplasia is generally the cause in the remainder of cases, and carcinoma is a very rare cause (Fig. 5.50). Secondary hyperparathyroidism is due to compensatory hyperplasia in response to hypocalcemia. For example, this may occur in long-standing renal failure. Reduced renal production of 1,25-dihydroxyvitamin D_3 (active metabolite of vitamin D) leads to decreased intestinal absorption of calcium, resulting in hypocalcemia. Failure of the tubules to excrete phosphate results in hyperphosphatemia. Hypocalcemia is compensated for by parathyroid hyperplasia and excess production of parathyroid hormone [246, 247].

Tertiary hyperparathyroidism describes a condition of persistent parathyroid hormone over-

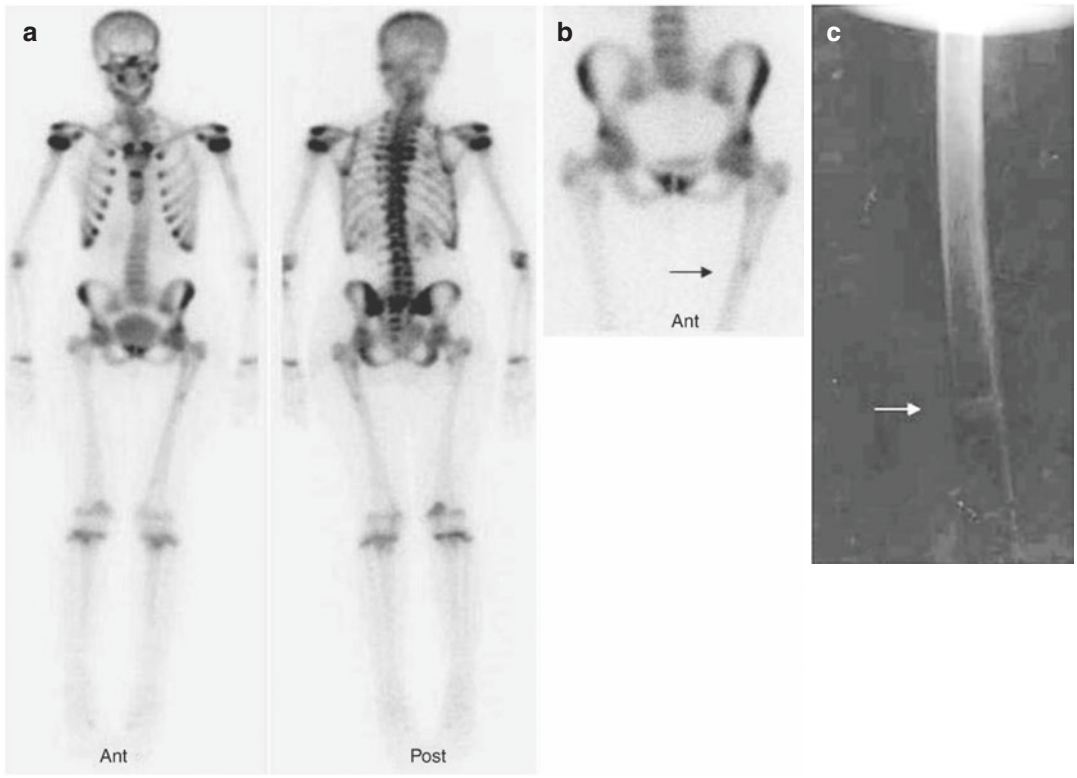

Fig. 5.49 (**a**–**c**) Osteomalacia. Whole-body bone scan of a 19-year-old patient with osteomalacia. Note the increased uptake in the costochondral junctions, spine, mandible, and the fracture of the left femur seen better on the spot image of the pelvis (**b**) and on the radiograph (**c**)

production (even after a low calcium level has been corrected) as a result of autonomous hyperplastic parathyroid tissue.

In all forms of hyperparathyroidism, there is increased bone resorption associated with increased osteoblastic activity, leading to increased uptake of bone-seeking radiopharmaceuticals. This is least prominent in primary compared with the other forms of hyperparathyroidism.

After parathyroidectomy for primary or secondary hyperparathyroidism, hypocalcemia is generally transient and normal parathyroid tissue recovers function quickly (usually within 1 week) even after long-term suppression. Severe and prolonged hypocalcemia may occur in some cases despite normal or even elevated levels of parathyroid hormone leading to hungry bone syndrome [258].

5.3.7.5 Renal Osteodystrophy

Renal osteodystrophy is a metabolic condition of bone associated with chronic renal failure. It is a frequent complication of renal insufficiency that became more prevalent recently due to the improved survival of patients with renal failure. This led to increased number of patients with the condition, changed our understanding, and defined the forms of the disease [259, 260].

The pathogenesis of renal osteodystrophy is incompletely understood. However, two mechanisms predominate: secondary hyperparathyroidism and abnormal vitamin D metabolism following reduced renal function. Renal insufficiency results in decreased excretions of phosphate leading to hyperphosphatemia which in turn causes decrease in serum calcium and consequently secondary hyperparathyroidism.

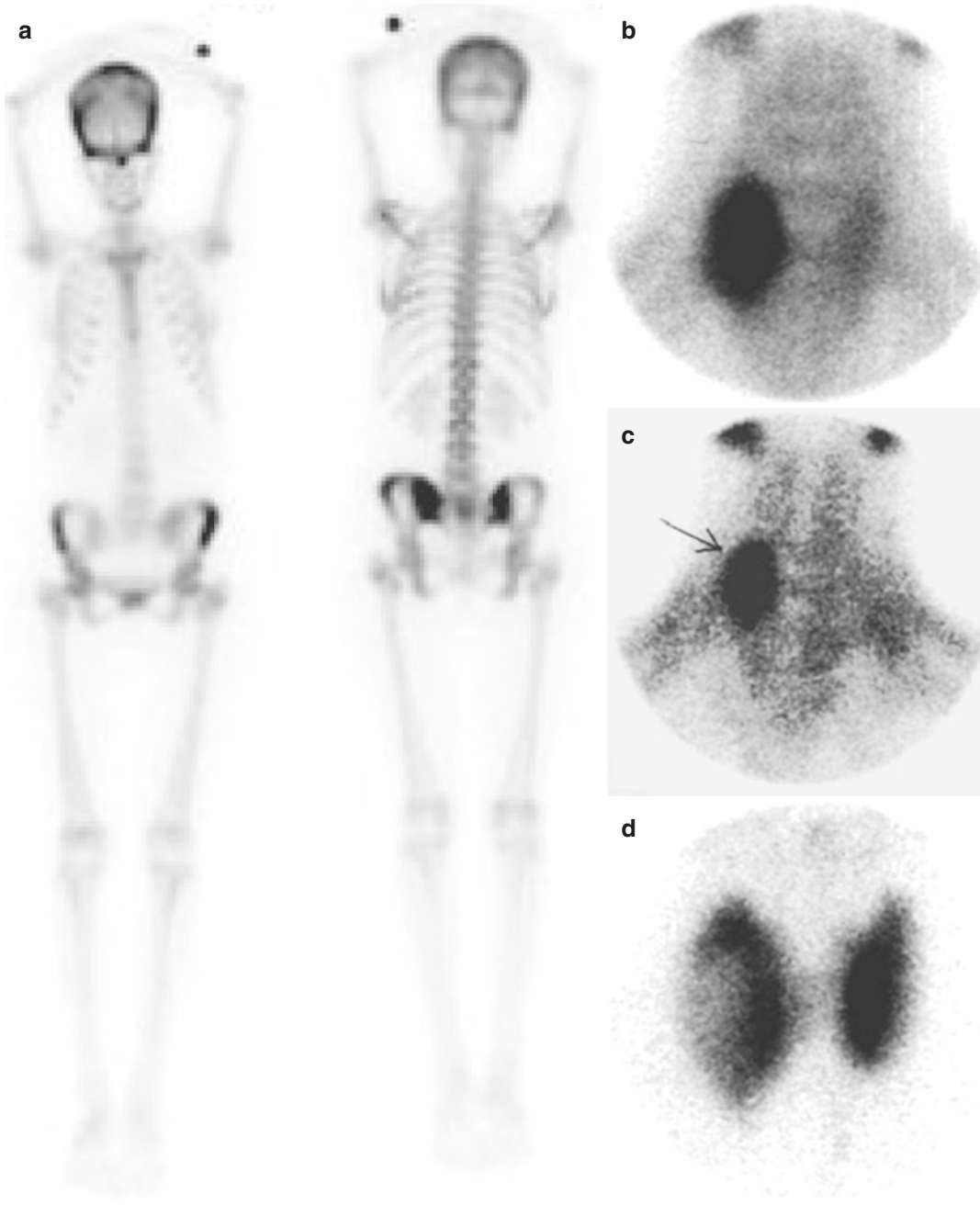

Fig. 5.50 Functioning parathyroid carcinoma. A 45-year-old female was referred for bone scan to evaluate the cause of generalized bony pains. The study (**a**) showed generalized increased bone uptake particularly in the calvarium indicating metabolic bone disease. Parathyroid hormone was found to be high and Tc-99m sestamibi pinhole study was obtained and showed a focus of increased uptake on early image (**b**) with retention of activity (*arrow*) on delayed image (**c**). Tc-99m pertechnetate thyroid scan (**d**) shows a solitary cold nodule corresponding to the finding on sestamibi study and was proved to be parathyroid carcinoma

Conversely, since renal tissue is the site of activation of 25-hydroxycholecalciferol into 1,25-dihydroxy form of vitamin D which is the active form of the vitamin, chronic renal failure causes decrease in the formation of the active form. This leads to reduced gastrointestinal absorption of calcium, producing hypocalcemia.

The major skeletal changes of the disease include osteitis fibrosa, osteitis fibrosa cystica, rickets, osteomalacia, osteosclerosis, and extraosseous calcification including tumoral calcinosis. Slipped capital femoral epiphysis, avascular necrosis including Legg-Calvé-Perthes disease in children, and brown tumors are other associated pathological features [259–263].

Osteitis fibrosa is characterized by extensive medullary fibrosis and increased osteoclastic resorption linked to PTH hypersecretion. When cystic lesions are present, it forms cystitis fibrosa cystica. Osteomalacia is mainly due to vitamin D insufficiency, hypocalcemia, acidosis, aluminum toxicity, and exceptionally to hypophosphatemia. It should be mentioned that aluminum overload directly inhibits the osteoblast.

The clinical presentation of renal osteodystrophy is influenced by the patient's age at onset of renal failure, the etiology of the renal disease, geographic location, dietary contents (protein, phosphate, and calcium), and treatment modalities. The reported prevalence of each bone change mentioned varies and does not correlate well with the clinical findings and laboratory data. Currently, the disease is believed to occur in three major types: high-turnover disease (Table 5.19), low-turnover disease, and a mixed disease [260, 261, 264, 265].

Table 5.19 High-turnover disorders

Generalized disorders
Primary hyperparathyroidism
Renal osteodystrophy (certain forms)
Type 1 (postmenopausal) osteoporosis
Localized disorders
Focal osteoporotic syndromes
Disuse atrophy
CRPS-1 (RSD)
Transient osteoporosis
Paget's disease
Stress fractures

An additional term of adynamic or aplastic bone disease has emerged recently and has been used synonymously as low turn over disease but should be considered actually as an extreme variant of the low-turnover type [266].

The prevalence of different forms of the disease has changed significantly over the last decade. The high-turnover form is the most common and presents typically with osteitis fibrosa and is linked to the development of secondary hyperparathyroidism, and hence, it is sometimes described as "predominant hyperparathyroid bone disease."

High-turnover renal osteodystrophy is usually associated with tubular interstitial nephritis as an underlying disease of renal failure since it is a slowly progressing form of renal pathology compared to glomerular disease which has a rapidly progressive course with a lesser risk of developing high-turnover disease.

The low-turnover type may present with osteomalacia and osteoporosis which can also occur in the high-turnover disease. The mixed form shows both osteomalacia and osteitis fibrosa. Differentiation of different forms is usually based on clinical data, laboratory findings, and standard radiographs although it can be difficult.

Radiologically, skeletal deformities, thickening of cortical bone, thickened irregular trabecular, osteonecrosis, extraosseous, calcification, and brown tumors can all be seen with variable frequency. Brown tumors present as well-defined lytic lesions that may cause expansion on standard radiographs since they may involve the cortical bone.

Scintigraphically, diffusely increased uptake with increased skeletal to renal uptake ratio occurs in high-turnover form. This uptake may be homogenous or heterogenous with focal findings depending on the predominant pathophysiological process (Fig. 5.51). One or more of the typical finding metabolic bone disease on bone scan may be seen (Table 5.20). Low-turnover form shows typically decreased uptake unless complicated by a focal pathology. A mixture of those findings is seen in mixed form. It should be noted that there is no consistency in the patterns seen on standard

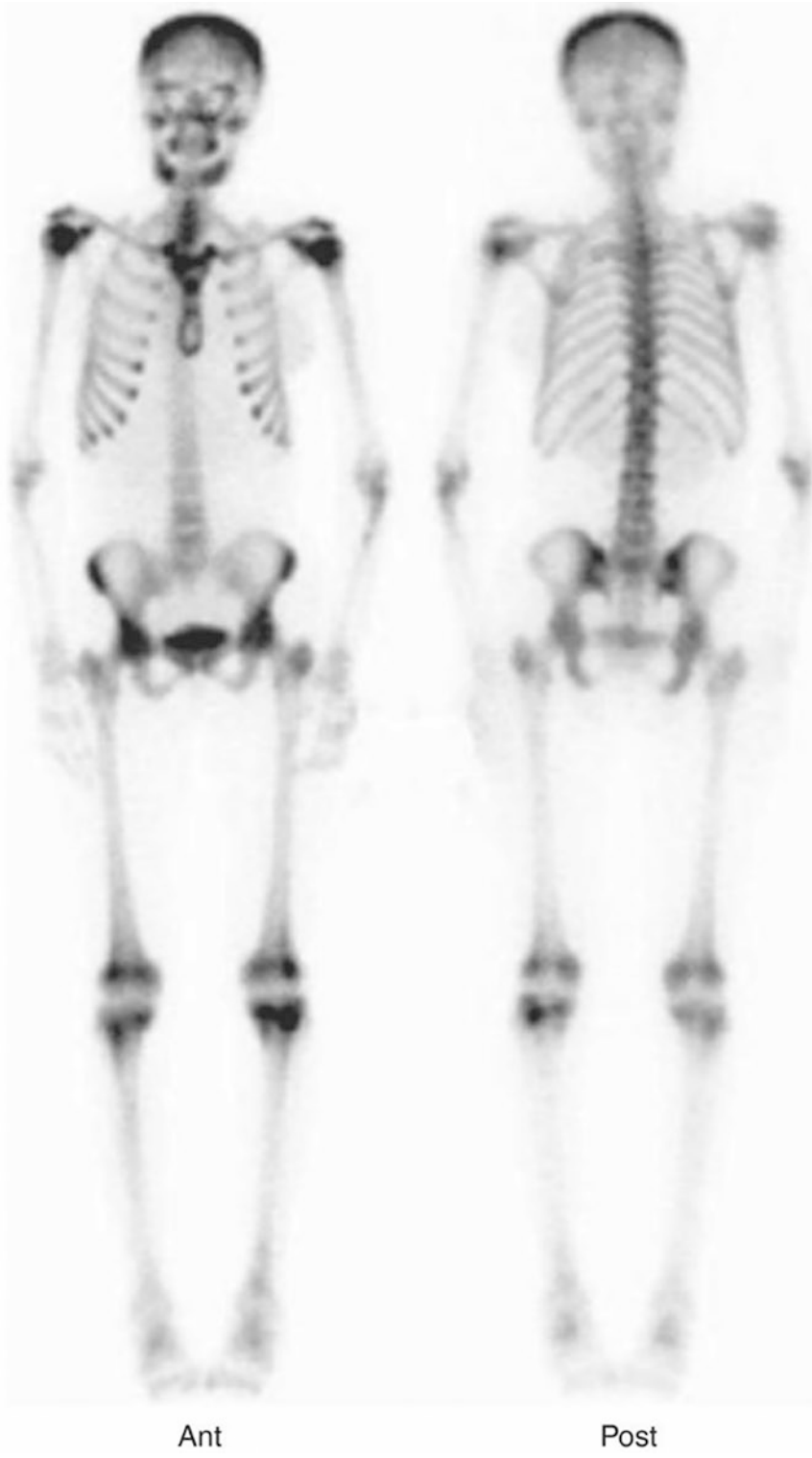

Fig. 5.51 Renal osteodystrophy. A whole-body bone scan of a patient with long-standing renal failure. The scan illustrates diffusely increased skeletal uptake. Note the typical sites of abnormal uptake in the mandible, sternum, and costochondral junctions of this case of renal osteodystrophy

Table 5.20 Bone scan findings in metabolic bone disease

Generalized increased uptake with increased contrast between bone and soft tissue
Generalized decreased uptake
Increased uptake in long bones
Increased uptake in axial skeleton
Increased uptake in periarticular areas
Increased uptake in the calvaria
Increased uptake in the mandible
Increased uptake in the costochondral junctions (beads)
Increased uptake in the sternum (tie sternum)
Foci of increased uptake due to fractures, pseudofractures, and brown tumor
Faint or absent kidney

radiographs and bone scan in patients with renal osteodystrophy. Bone scan can be helpful in differentiating cases with osteitis fibrosa and osteomalacia.

5.3.7.6 Hypertrophic Osteoarthropathy

Hypertrophic osteoarthropathy is a rheumatic disorder characterized by bone pain, joint pain, and nearly always clubbing of fingers and/or toes. Two types of hypertrophic osteoarthropathy are recognized: primary and secondary. The primary type (also called pachydermoperiostosis) is less common and occurs in adolescence, with spontaneous arrest of the process in young adulthood. A variant has been reported in a family [267].

The secondary form follows a variety of pathological conditions, predominantly intrathoracic. Lung cancer and other intrathoracic malignancies, benign lung pathologies, and cyanotic heart disease are common causes. Abdominal malignancies, hepatic and biliary cirrhosis, and inflammatory bowel disease are less common causes [268, 269].

Nasopharyngeal carcinoma has also been reported as a cause [270].

Pathologically, the condition is a form of periostitis and may be painful. Additionally, clubbing of fingers and toes, sweating, and thickening of skin may also be seen. In the tubular bones, there is periosteal new bone formation. This pathological feature explains the typical scintigraphic pattern of diffusely increased uptake along the cortical margins of long bones, giving the appearance of "parallel tracks."

The scintigraphic abnormalities are usually confined to diaphyseal regions, although they may also occur in the epiphyseal bone (Fig. 5.52). The changes are usually bilateral but can be unilateral in approximately 15% of cases [269].

The tibiae and fibulae are affected most commonly, followed by the distal femur, radius, ulna, hands, feet, and distal humerus. Scapula, patella, maxilla, mandible, and clavicle are less frequently affected and rarely the ribs and pelvis. The condition has no prognostic significance as there was no significant difference in survival between lung cancer patients with and others without hypertrophic osteoarthropathy [271].

The changes disappear following successful treatment of the lung cancer or other inciting pathologies, and scintigraphy is useful in evaluating the response to treatment of this paraneoplastic syndrome [272].

5.3.8 Arthropathy

Arthritides may begin primarily with synovial and intra-articular disease or with bone involvement. The characteristics of synovitis include increased blood flow and tissue blood volume, interstitial edema, and cellular infiltration. There is often some overlap with primary periarticular bone disease since synovitis may be associated with bone erosion, and primary bone disease may have an element of synovitis [273].

No unified classification for the many types of joint diseases is available. Arthropathies are grouped into two main categories: inflammatory and noninflammatory [274, 275].

(Table 5.21). The inflammatory joint diseases are further classified into infectious and noninfectious. The infectious type is caused by bacteria, mycoplasmas, fungi, viruses, or protozoa, while the noninfectious type is caused by immune reactions such as rheumatoid arthritis and ankylosing spondylitis or deposition of crystals in and around the joint as in gout, which is caused by

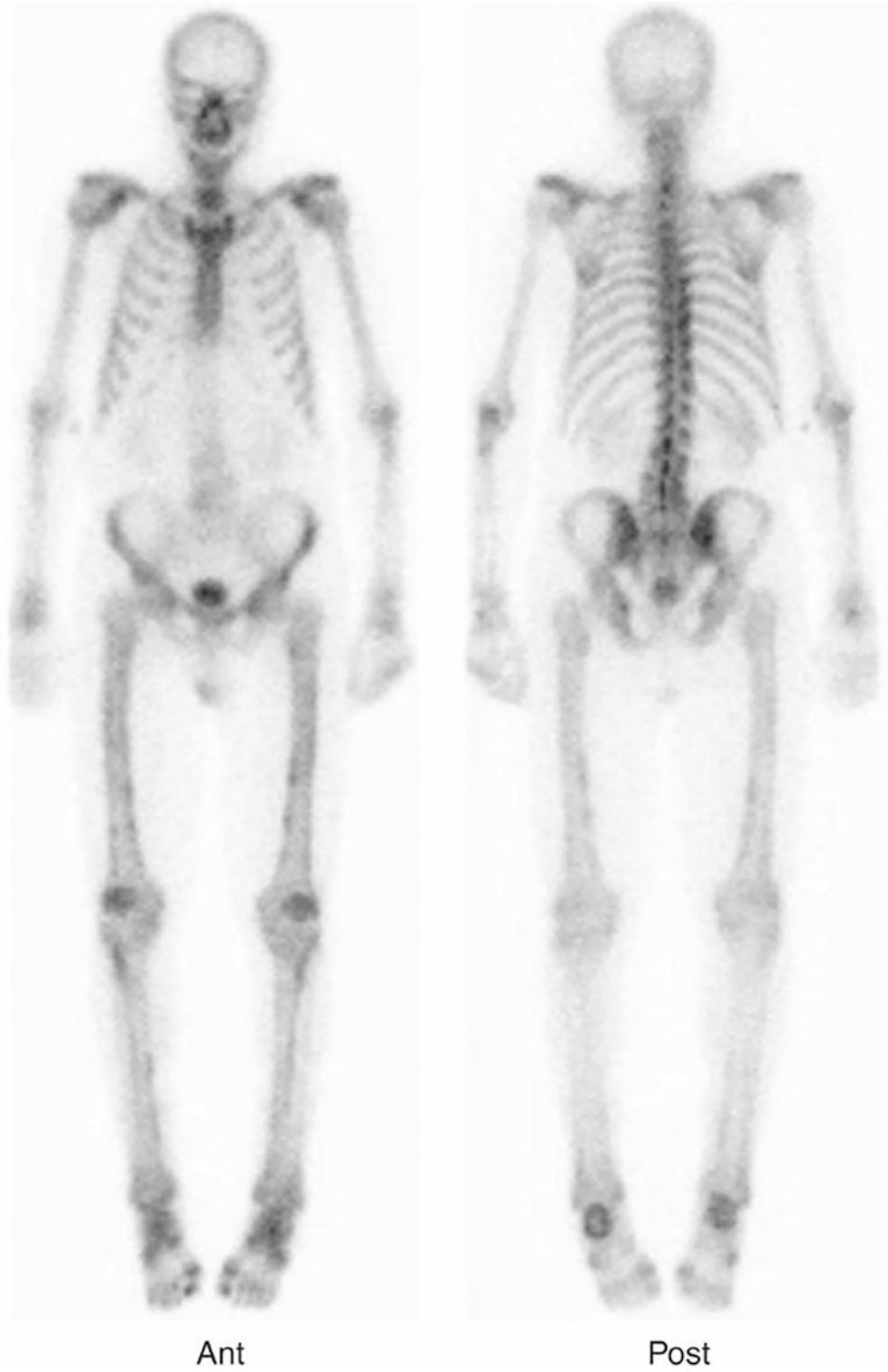

Fig. 5.52 Hypertrophic osteoarthropathy in a patient with lung cancer. Note the diffusely increased uptake in all bones of the lower extremities with a parallel track pattern in the femurs and tibiae

Table 5.21 Main types of joint disease with major examples

A. *Inflammatory joint disease*
1. Infectious
Infectious arthritis
2. Noninfectious
Rheumatoid arthritis
Crystal deposition arthropathies (gouty arthritis, CPPD)
Sacroiliitis
Neuropathic joint disease
Spondyloarthropathies
Ankylosing spondylitis
Psoriatic arthritis
Reactive arthritis (formerly Reiter's disease)
Inflammatory bowel disease-associated arthritis
B. *Noninflammatory joint disease*
1. Primary osteoarthritis
2. Secondary osteoarthritis

deposition of monosodium urate crystals. Alternatively, the group of inflammatory joint disease can also be subclassified into immunoinflammatory such as rheumatoid arthritis; infectious, crystal deposition; and arthritis associated with connective tissue disease such as in systemic lupus erythematosus and those associated with vasculitis such as Behcet's disease. The noninflammatory joint disease is exemplified by the common osteoarthritis or degenerative joint disease, which can be idiopathic (primary) or secondary. It should be noted that certain conditions such as neuroarthropathy and sacroiliitis have multiple overlapping pathogenetic features including immunologic, vascular, and degenerative. MRI, US, bone scintigraphy, and PET have all been used for diagnosis and assessment of disease severity and follow-up of therapy.

5.3.8.1 Rheumatoid Arthritis

Rheumatoid arthritis, an autoimmune disease, causes inflammation of connective tissue, mainly in the joints. It is thought that microvascular injury and mild synovial cell proliferation occur first, along with obliteration of small blood vessels. Synovial inflammatory response is triggered by immune complexes in the blood and synovial tissue through activation of plasma protein complement. This complement activation stimulates release of kinin and prostaglandin, which causes an increase in vascular permeability in the synovial membranes and attracts leukocytes out of the circulation to the synovial membrane. As the condition becomes chronic, synovial proliferation, supported by neovascularization, leads to pannus formation which is highly invasive. Inflammation eventually may spread from the synovial membrane to the articular cartilage, the joint capsule, and the surrounding tendons and ligaments with resultant pain, loss of function, and joint deformity [274, 276]. The small joints of the hands and joints in the feet, wrists, elbows, ankles, and knees are the most commonly affected. On bone scintigraphy, there is increased perfusion and delayed uptake periarticularly in the areas of the joints affecting commonly the small joints of the hand, wrists, and feet and elbows, ankle, and knees. Tc-99m polyclonal human immunoglobulin-G (HIG) has been shown to be a successful agent in the depiction of active inflammation in rheumatoid arthritis [277].

Scintigraphy is more sensitive but less specific than radiography in the depiction of abnormal joints in rheumatoid arthritis, especially in the peripheral joints. Active disease may be detected scintigraphically before becoming clinically evident [278, 279].

The pattern of symmetric peripheral joint involvement can usually be distinguished scintigraphically from that of the rheumatoid variants (ankylosing spondylitis, psoriasis, Reiter's syndrome, etc.), which tend to have more central skeletal involvement and asymmetric peripheral articular uptake. While bone scintigraphy cannot always distinguish progressive disease from joints responding to therapy with osteoblastic repair, radiolabeled IgG and leukocytes have considerable prognostic sensitivity [280, 281].

^{18}F-FDG PET is found to be accurate in assessing the metabolic activity of synovitis and measure the disease activity in rheumatoid arthritis [282, 283]. Since FDG uptake in affected joints have strong correlations with various clinical parameters [282]. It has also been found to be useful in assessing response to therapy [284].

5.3.8.2 Ankylosing Spondylitis

Stiffening and fusion (ankylosis) of the spine and sacroiliac joints causing most frequently low back pain and stiffness characterize the chronic inflammatory joint disease ankylosing spondylitis, which is the most common type of the seronegative spondyloarthropathies. It affects predominantly the axial joints, particularly the sacroiliac joints. Other joints such as the hips, knees, and shoulders are involved in approximately 30% of patients. The condition usually affects boys and begins in adolescence with inflammation of fibrocartilage in cartilaginous joints (primarily in the vertebrae) along with infiltration of inflammatory cells (mainly macrophages and lymphocytes) in the fibrous tissue of the joint capsule, cartilage, and periosteum. This process is followed by repair of cartilaginous structures by proliferation of fibroblasts that secrete collagen, which later becomes organized into fibrous scar. This scar eventually undergoes calcification and ossification, causing loss of flexibility and fusion of joints.

Recent progress in pathophysiology of this disease with immune cells and innate cytokines suggested to be crucial in its pathogenesis, especially human leukocyte antigen (HLA)-B27 and the interleukin-23/17 axis although pathogenesis is still unsettled [285]. Scintigraphically, patterns vary with the disease stage; in early stage scintigraphy reveals typical although not always symmetrical intense tracer uptake in both sacroiliac joints. Later as the spine becomes involved, pinhole scintigraphy reveals patchy uptake in apophyseal joints, horizontal band-like uptake in the discovertebral junctions [286].

5.3.8.3 Gouty Arthritis

Uric acid crystallizes when it reaches certain concentrations in fluids, forming insoluble crystals that can precipitate in the connective tissue of different parts of the body. When this process involves the synovial fluid, it causes acute inflammation of the joints. Although the effect is the same, classic gouty arthritis is caused by deposition of monosodium urate crystals, while deposition of calcium pyrophosphate dihydrate crystals causes pseudogout [287].

The disease is rare in children and premenopausal women and uncommon in men under 30 years of age. Gout is closely linked to purine metabolism and kidney function. An accelerated rate of purine synthesis may occur in some individuals leading to overproduction of uric acid, since the latter is a breakdown product of purine nucleotides. In other individuals, the rate of breakdown (rather than synthesis) of purine nucleotides is accelerated, resulting also in overproduction of uric acid.

Uric acid is eliminated predominantly through the kidney. Urate excretion by the kidney may be sluggish due to a decrease in glomerular filtration of urate or an acceleration of urate reabsorption. Sluggish excretion of urate occurs in primary gout. Urate crystals are deposited in the renal interstitium, causing impaired renal flow, and may also precipitate to cause renal stones.

Monosodium urate crystals trigger an acute inflammatory response in the synovial membrane and other tissues of the joints. Leukocytes, particularly neutrophils, are attracted out of the circulation to phagocytose the crystals. Trauma is the most common aggravating factor. Therefore, because of the chronic strain during walking, the great toe is a common presenting site (50% of initial attacks).

On bone scan, there is increased flow, blood pool activity, and delayed uptake in the areas of the joint involved. The first metatarsophalangeal joint, ankle, and the knee are the joints most often affected on bone scintigraphy with the most typical being that of the metatarsophalangeal joint of the great toe called podagra. A case of gouty tophus of the patella was evaluated by PET using a combination of an amino acid analog emitter L-[3-F-18]-alpha-methyl tyrosine (FMT), which does not accumulate in malignancies showed increased metabolic activity while FDG, did not show appreciable activity suggesting that PET may be useful for the preoperative evaluation of gouty tophus including detection and differentiation from malignant tumors [288].

5.3.8.4 Osteoarthritis

Idiopathic osteoarthritis is the most common type of noninflammatory joint disease. The idiopathic

and the secondary form of osteoarthritis have the same pathological characteristics. Although it affects any joint, those most commonly involved are in the hands, wrists, lower cervical spine, lumbar spine, sacroiliac, hips, knees, ankles, and feet. Aging is an important risk factor, although the cause of osteoarthritis is unknown. Premature cartilage degeneration due to an inherited genetic defect encoding for the structural components of articular cartilage has been suggested as the etiology of this condition.

Primary or osteoarthritis of unknown cause progresses with age. Secondary osteoarthrosis occurs when the predisposing cause is known, e.g., following intra-articular fracture, rheumatoid diseases, neurogenic and metabolic disorders, drugs, and recurrent hemarthrosis as may occur among hemophilic patients. The pain of osteoarthrosis is caused by intracapsular tension, muscle spasm, abnormal stress on the bone, and increased intraosseous venous pressure [289, 290].

Osteoarthritis starts with changes in the articular cartilage. The ability of articular cartilage to repair is very limited. Intrinsic repair occurs in infants, as chondrocytes are still able to proliferate. Extrinsic repair occurs by granulation tissue growing from the adjacent bone. Granulation tissue changes to fibrocartilage, which is inferior to normal cartilage in its mechanical properties.

The changes of articular cartilage in osteoarthritis progress from fibrillation to erosion and then, at the advanced stage, to complete loss of cartilage. With loss of articular cartilage, the exposed bone takes increased stress, becomes more compressed, and shows subarticular sclerosis [290].

Thus, the pathological features of osteoarthritis include gradual loss of articular cartilage, thickening, and hardening (sclerosis) of the bone underneath the cartilage, and formation of osteophytes (spurs). As the articular cartilage erodes, cartilage-coated osteophytes often grow into the joint. Small pieces of osteophyte may break off and become free within the synovial cavity. These pieces, called joint mice, irritate the synovial membrane, resulting in synovitis and joint effusion. In addition, the joint capsule may thicken and in some cases adhere to the underlying bone, causing limitation of movement.

Table 5.22 Typical scintigraphic findings of major joint diseases

Disease	Scintigraphic findings
Rheumatoid arthritis	Symmetric uptake involving small and large joints
Gouty arthritis	Uptake of metatarsophalangeal joint of the great toe and large joints, commonly symmetric
Ankylosing spondylitis	Symmetric intense tracer uptake in both sacroiliac joints and spine
Osteoarthritis	Uptake of large joints, symmetric in primary type
Reactive arthritis	Asymmetric uptake of large and small joints and spine
Psoriatic arthritis	Asymmetric uptake of large and small joints typically of upper extremity including fingers and spine
Infectious arthritis	Uptake involving a large joint
Enteropathic arthritis	Uptake of large joints (asymmetric), sacroiliac joints (symmetric), and spine

Pathological features of arthropathies are translated into various patterns of findings on scintigraphic imaging modalities. Table 5.22 summarizes the typical scintigraphic findings seen on bone scans in major arthropathies.

5.3.9 Soft Tissue Calcification

Pathological calcification is classified mainly into three types, as detailed below.

5.3.9.1 Dystrophic Calcification

Dystrophic calcification is calcification of dying or dead tissue. The mechanism appears to be increased calcium-binding capacity of the exposed denatured proteins of the injured cells which preferentially bind with phosphate ions which in turn react with calcium and form calcium deposits. Examples include calcification in infarcted myocardial muscle, in atheromas, in amyloid tissue, and in the centers of tumors (Fig. 5.53).

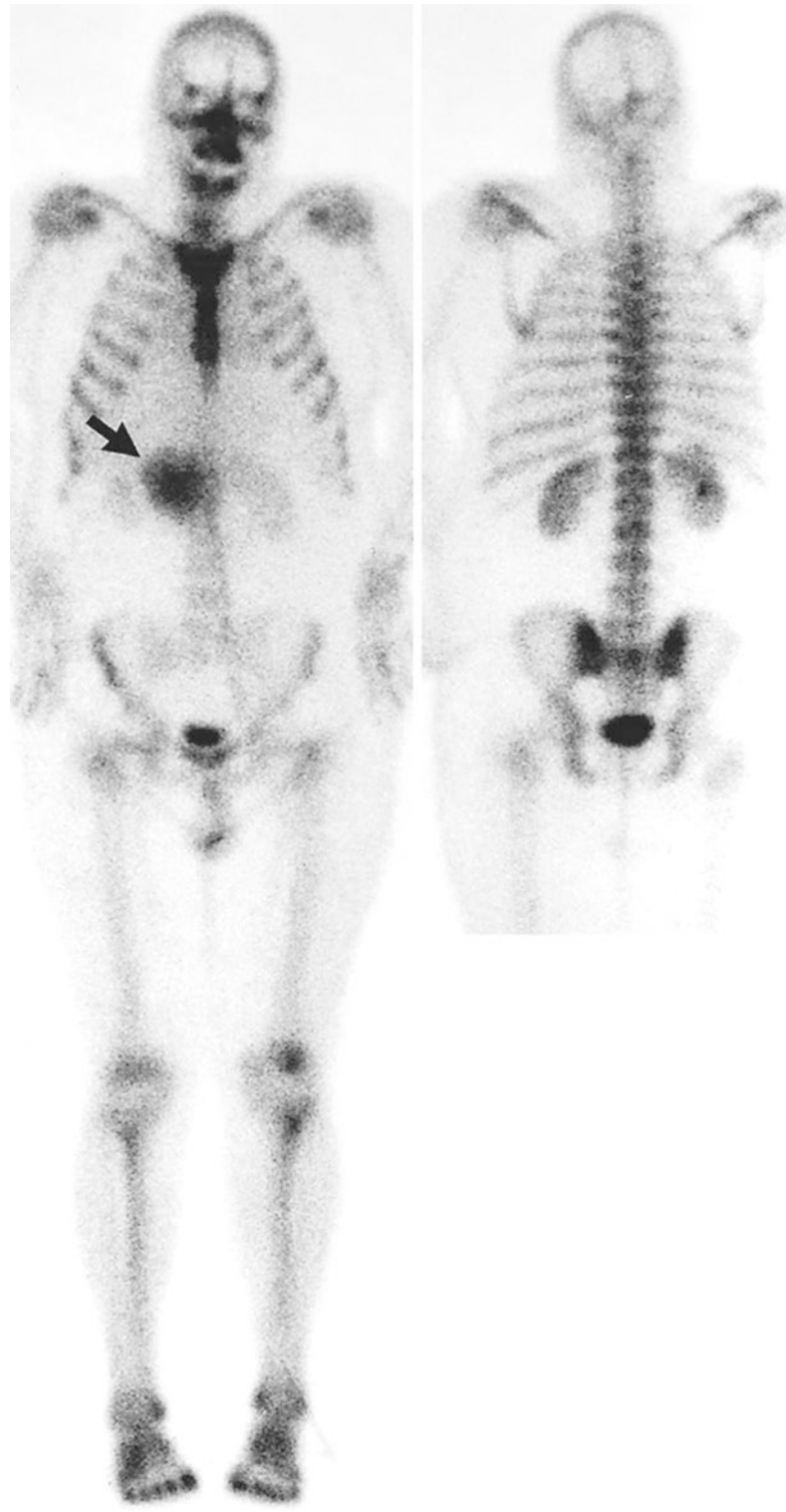

Fig. 5.53 ^{99m}Tc-MDP uptake as an example of dystrophic calcification in a case of hepatoma (*arrow*)

5.3.9.2 Metastatic Calcification

Metastatic calcification describes calcification of viable, undamaged, normal tissue (Fig. 5.54) as a result of hypercalcemia associated with increased calcium phosphate product, locally or systemically. This can be due to metabolic abnormalities as with renal failure, hypervitaminosis D, and hyperparathyroidism or to increased bone demin-

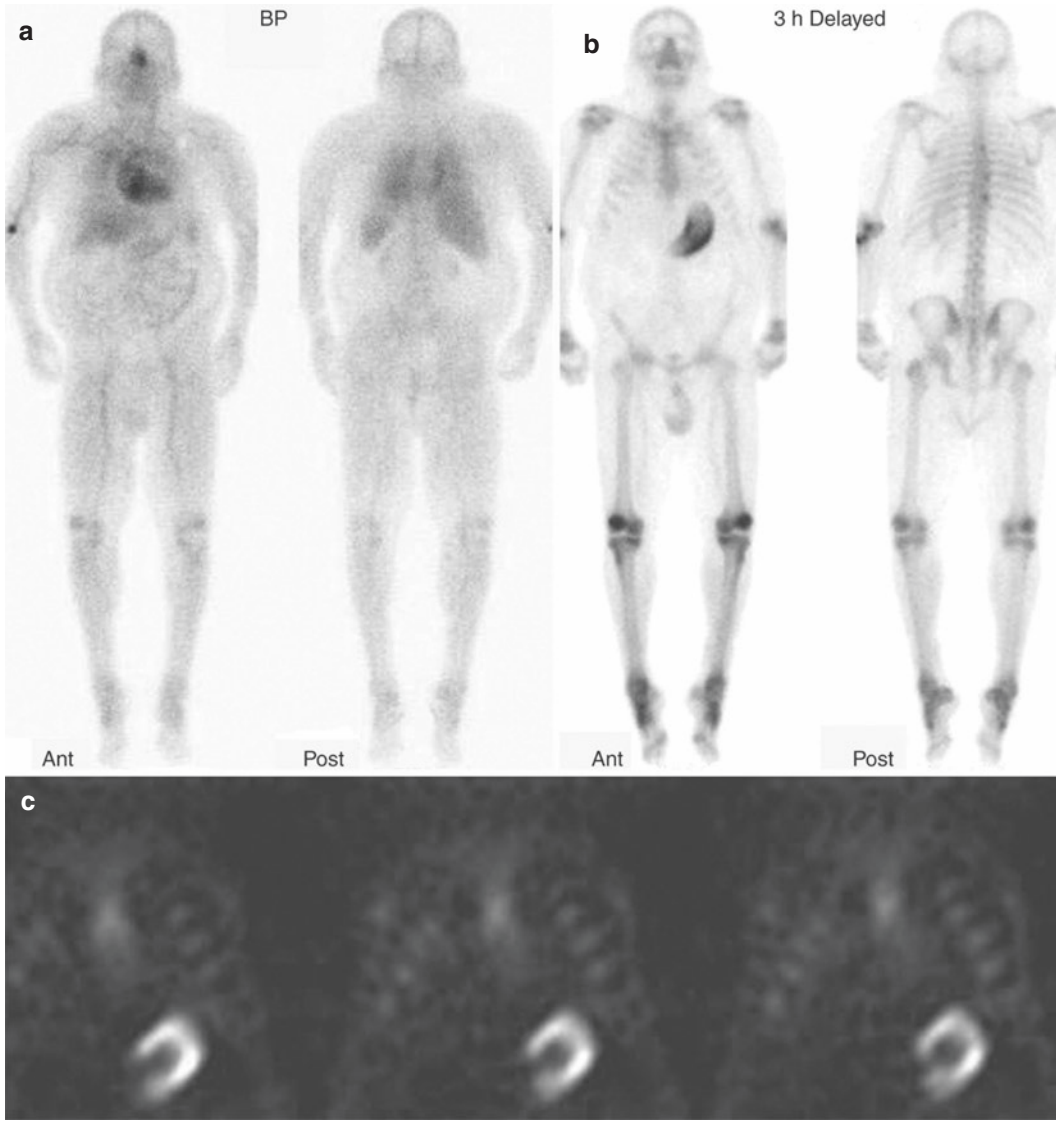

Fig. 5.54 (**a**–**e**) ^{99m}Tc-MDP whole-body blood pool (**a**) and delayed scans and selected SPECT cuts of the chest of a 57-year-old male with a history of chronic renal failure and coronary artery disease presenting with chronic progressive motor demyelinating polyneuropathy. Rule out osteosclerotic melanoma. The patient is thought to have POEMS syndrome. Increased activity in the T spine is likely due to degenerative disease and may represent osteophyte formation. Increased activity in the knees has the appearance of arthropathy. Increased activity in the left elbow is consistent with known olecranon bursitis. Poor visualization of the kidneys is consistent with known chronic renal failure. Intense visualization in the stomach is most likely due to metastatic calcification, which can be seen secondary to numerous metabolic disorders including hyperparathyroidism, which in this patient may be secondary hyperparathyroidism due to chronic renal failure. This is also likely the cause of the increased visualization of the long bones

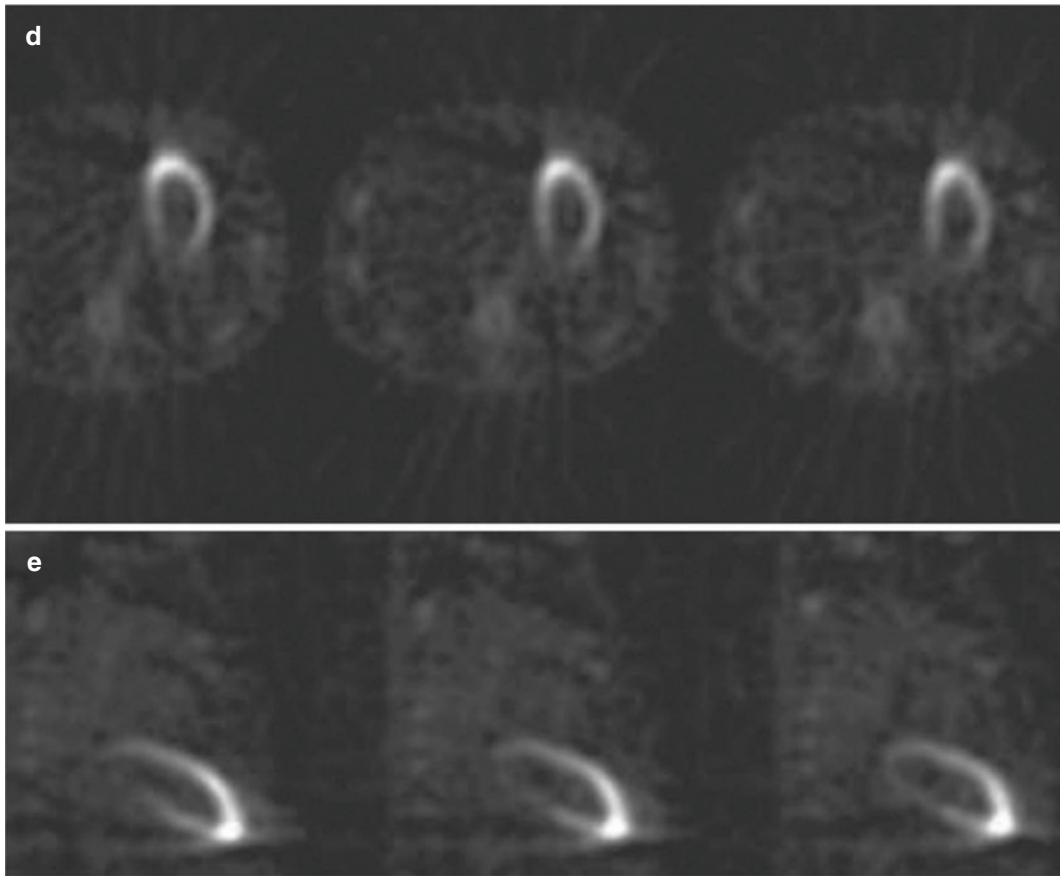

Fig. 5.54 (continued)

eralization from bone tumors or disseminated metastases [59].

5.3.9.3 Heterotopic Bone Formation

Heterotopic bone formation, or increased ectopic osteoblastic activity, is defined as the presence of bone in soft tissue where it does not normally exist. In the vast majority of cases, the condition is acquired. Rarely it can be congenital. The pathogenesis of heterotopic bone formation is still debated. However, it is believed to be secondary to transformation of pluripotent mesenchymal cells, present in the connective tissue septa within muscle, into the osteogenic cell line.

The acquired form of heterotopic bone formation often occurs after trauma. Other associated conditions include burns, sickle cell disease, hemophilia, tetanus, poliomyelitis, multiple sclerosis, toxic epidermal necrolysis, and cancer. It also occurs infrequently in the absence of a precipitating event or condition. Heterotopic bone formation includes the specific entity myositis ossificans, a posttraumatic skeletal muscle ossification usually occurring next to long bones. In many clinical practices, myositis ossificans is usually seen among patients who have sustained trauma such as operative procedures (e.g., total hip arthroplasty), fractures, dislocations, and direct trauma to muscle groups (mainly quadriceps femoris and brachialis muscles). Additional reported sites include abdominal incisions, wounds, and the gastrointestinal tract. The other acquired traumatic form follows trauma to the nervous system, i.e., neurogenic, and is most commonly seen following spinal cord injury. Patients are typically adolescents or adults, with 75% younger than age 30. There is no sex predominance. This subtype often occurs following

closed head injuries, strokes and central nervous system infarctions, and tumors [291, 292].

Anatomically, HBF is always extra-articular, but it may be attached to the joint capsule without disrupting it. Occasionally, HBF may be attached to the cortex of adjacent bone with or without cortical disruption (Fig. 5.55). Tumoral calcinosis describes heterotopic bone formation that has large amounts of bone formation resembling tumor masses (Fig. 5.56).

The incidence of heterotopic bone formation varies greatly in different patient populations. It has been reported to be between 20 and 25% among spinal cord injury patients, while 10–20% of closed head injury patients develop heterotopic bone formation. The onset of heterotopic bone formation has been reported to range from 4 to 12 weeks after injury, most commonly at 2 months, but it has also been reported to occur as early as 20 days' post-injury. The most commonly involved areas, in decreasing order, are the hips, knees, shoulders, and elbows. Rarely, it can occur in the foot.

The course of acquired heterotopic bone formation is relatively benign in 80% or more of cases. The remaining patients often develop significant loss of motion, and ankylosis occurs in up to 10%. Clinical, laboratory, radiographic, and scintigraphic criteria have been used to follow the course of heterotopic bone formation and to assist in treatment.

The most sensitive imaging modality for early detection of heterotopic bone formation is multiphase bone scintigraphy. Blood flow and pool images have detected incipient heterotopic bone formation as early as 2.5 weeks after injury, with delayed scintigraphs becoming positive about 1 week later. These scintigraphic findings precede positive radiographs by 1–4 weeks [292].

The condition is classified as immature when flow and blood pool activity are increased (Fig. 5.57). When flow and blood pool patterns normalize or stabilize after showing decreasing activity, the condition is considered to be mature. As heterotopic bone progresses from immature to mature, the three-phase bone scan typically shows progressive reduction in the activity of all three phases. The majority of bone scans returns to baseline within 12 months, although many patients reach the mature phase much earlier or much later. Since surgical intervention during the immature phase often leads to recurrence, serial bone scans are useful in monitoring the activity of the disease, so as to determine the appropriate

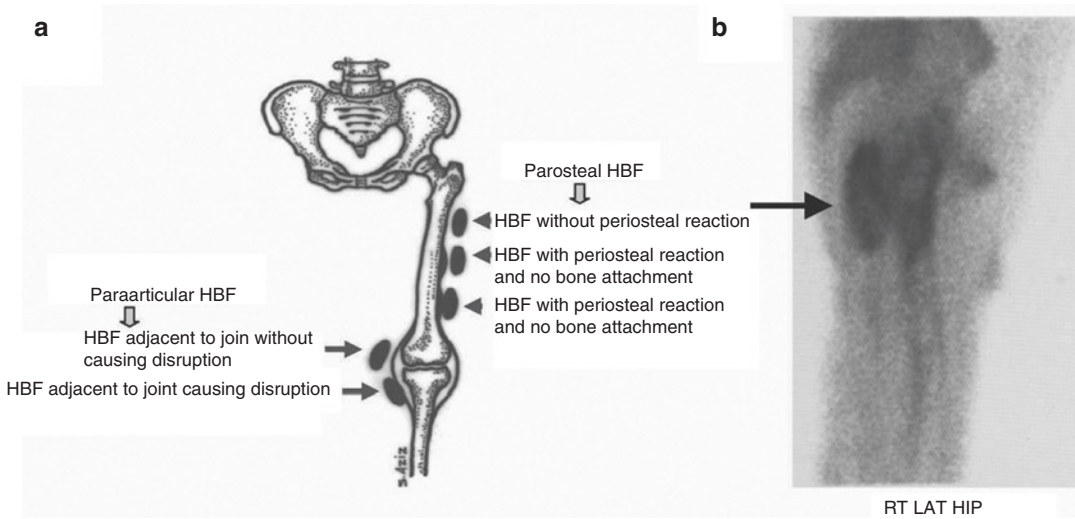

Fig. 5.55 (**a**) Illustration of the relation of heterotopic bone formation to the bone cortex and joints. Heterotopic bone formation is always extra-articular, but may be attached to the cortex of adjacent bone with or without cortical destruction. (**b**) A spot delayed image of a bone scan obtained using ^{99m}Tc-MDP showing a focus of heterotopic bone formation adjacent to the posterior surface of the upper right femur

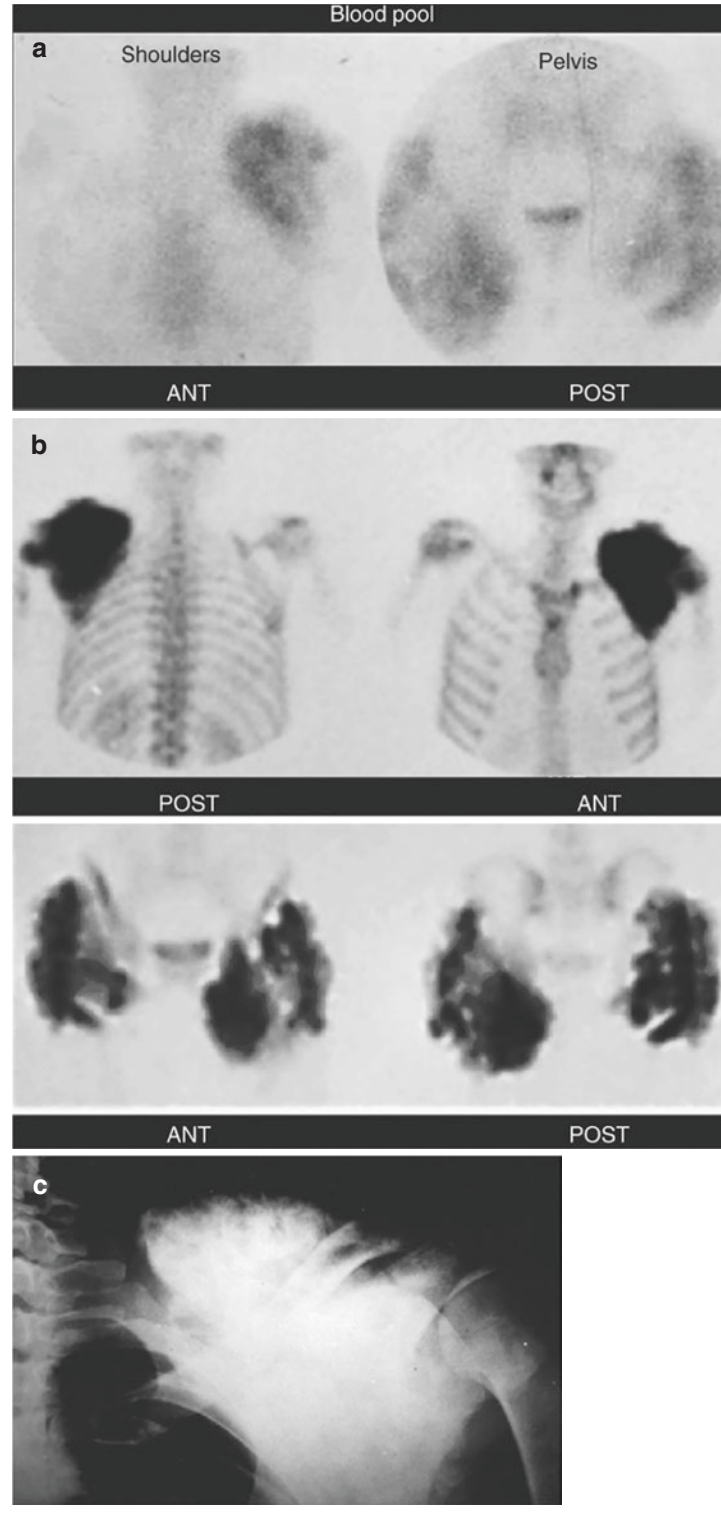

Fig. 5.56 Blood pool (**a**) and spot delayed images (**b**) of Tc99m bone scan of a case of tumoral calcinosis. Note the large amount of soft tissue calcification in the left shoulder and around both hips. X-ray (**c**) of the left shoulder illustrates the tumor-like calcification

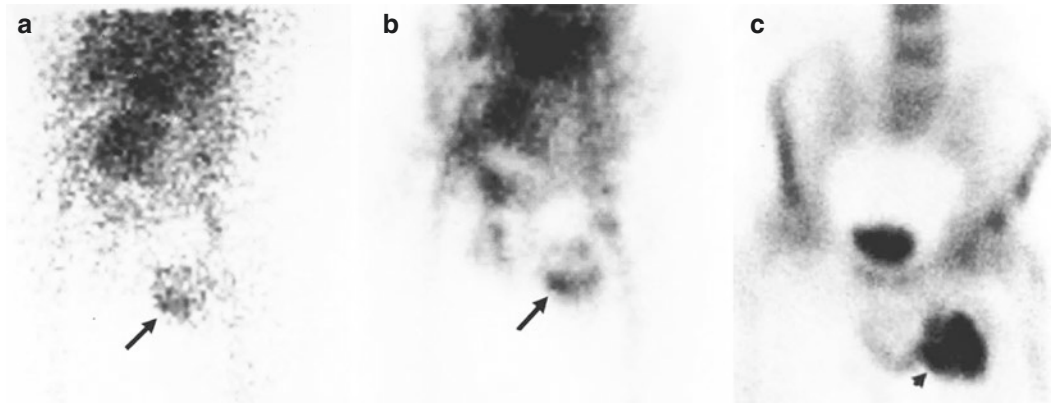

Fig. 5.57 (**a**–**c**) Multiphase bone scan showing increased flow (**a**), blood pool (**b**), and delayed (**c**) soft tissue uptake in the left thigh (*arrows*) and illustrating the finding of immature heterotopic bone formation

time for surgical removal of heterotopic bone with minimal risk of recurrence. In several reported series, preoperative serial bone scans with quantitation of the uptake ratios between heterotopic and normal bone have successfully identified those patients who remained free of heterotopic ossification following surgery (i.e., those patients with decreasing or stable scintigraphic activity as measured by this quantitative technique).

Several pathological conditions can clinically mimic the scintigraphic appearance of early heterotopic ossification [245–248]:

- Infection
- Osteomyelitis
- Cellulitis
- Thrombophlebitis
- Deep vein thrombosis
- Tumor
- Osteosarcoma
- Osteochondroma
- Pyomyositis

Osteomyelitis may represent a difficult diagnostic challenge on scintigraphy, particularly since ^{67}Ga and, rarely, ^{111}In-labeled WBCs accumulate in areas of immature heterotopic bone formation. The uptake of ^{67}Ga by foci of heterotopic bone formation undergoing osteogenesis, with considerable osteoblastic activity, may be explained by the fact that this radionuclide shares some of the properties of bone imaging agents. Fortunately, ^{67}Ga uptake in heterotopic ossification has been found to be proportional to the uptake of Tc diphosphonates, in contrast to its relatively greater uptake in sites of osteomyelitis. Since ^{67}Ga uptake might otherwise be mistaken for infection or tumor, this proportionality can help to differentiate heterotopic ossification from osteomyelitis. Therefore, in the appropriate clinical setting, heterotopic ossification is a diagnostic consideration for patients with a positive ^{67}Ga scan [291].

Two cases of heterotopic bone formation were reported to have been misdiagnosed as pyomyositis at first by clinical signs and MRI findings indicating the deep infection, but extensive intramuscular ossification appeared later on [292]. SPECT/CT is helpful in such situation since it clarifies the location of abnormal uptake [293].

The rare congenital form of heterotopic ossification is called myositis ossificans progressiva, or fibrodysplasia ossificans progressiva [294]. This autosomal dominant congenital disease is often associated with other skeletal abnormalities including malformation of the great toes and shortening of digits, as well as other clinical features such as deafness and baldness. Although symptoms have been reported to develop in patients with this disease prior to 4 years of age, the diagnosis is frequently missed. The soft tissue ossification present may be mistakenly attributed to bruising or even to a sarcoma. Initial failure to

appreciate the significance of the toe and other digit malformations also is common. Progression to severely impaired joint mobility with ankylosis by early adulthood is the hallmark of this disease.

5.3.9.4 Calcinosis Cutis

Calcinosis cutis describes a group of disorders in which calcium deposits form in the skin, subcutaneous tissue, and connective tissue sheaths around the muscles. Etiologically, dystrophic, metastatic, iatrogenic, and idiopathic varieties may be identified. Some rare types may even be variably classified as dystrophic or idiopathic. These include calcinosis cutis circumscripta and calcinosis cutis universalis. Most lesions of calcinosis cutis develop gradually and are asymptomatic. However, the history and evolution of the lesions depend upon the etiology of the calcification.

Calcinosis Cutis Universalis

This entity describes diffuse calcium deposits in the skin, subcutaneous tissue, and connective tissue sheaths around the muscles but not within the muscles as the case with myositis ossificans. It is seen mostly in association with scleroderma and polymyositis. On bone scintigraphy, it shows uptake of variable degrees in a diffuse fashion in large areas of the skin and subcutaneous regions.

Calcinosis Cutis Circumscripta

This condition is a form of localized calcium deposition in the skin. If dystrophic, it is secondary to localized causes of dystrophic calcification such as trauma, insect bites, acne, and certain skin tumors. If metastatic or associated with systemic causes of dystrophic calcifications, it generally occurs earlier and tends to involve the extremities, whereas calcinosis universalis occurs later and usually is more widespread.

Calciphylaxis

This is a condition of soft tissue calcification affecting mainly patients with chronic renal failure. The calcification involves the media of small- and medium-sized cutaneous arterioles with extensive intimal hyperplasia and fibrosis. There is also subcutaneous calcification and necrosis which may lead to sepsis, the main cause of morbidity which may be significant.

Rhabdomyolysis

Rhabdomyolysis, also called myoglobulinuria, is a condition that follows muscle damage secondary to infectious and noninfectious injuries including viral infections, electrical injury, certain drugs, and trauma as in runners and military recruits. The condition can be severe and life threatening. The most severe form is sometimes called crush syndrome. Milder forms are called compartment syndromes. There is excess myoglobulin in the urine since intracellular muscle protein is released with muscle damage and appears in urine. Since variable degrees of muscle death occur, this will increase calcium content which is sensitively identified by ^{99m}Tc-MDP bone scan showing increased uptake in the damaged muscle. Bone scan can be useful to evaluate the degree of muscle necrosis [295].

5.4 Neoplastic Bone Disease

5.4.1 Primary Bone Tumors

Various primary tumors originate from the bone. Based on the cell of origin, primary tumors can be classified as osteogenic, chondrogenic, collagenic, or myelogenic (Fig. 5.58).

5.4.1.1 Osteogenic Tumors

Osteogenic tumors originate from bone cell precursors, the osteoblasts, and are characterized by formation of bone or osteoid tissue. These tumors include osteoid osteomas, osteosarcomas, and osteoblastomas.

Osteoid Osteoma. The benign tumor osteoid osteoma is most common in children, particularly boys. Typically, it presents in the lower extremities, the pelvis, or less commonly the spine. Patients frequently report nocturnal pain which is relieved by aspirin. It is characterized by its small nidus size of less than 2 cm, self-limited growth, and the tendency to cause extensive reactive changes in the surrounding bone tissue. The

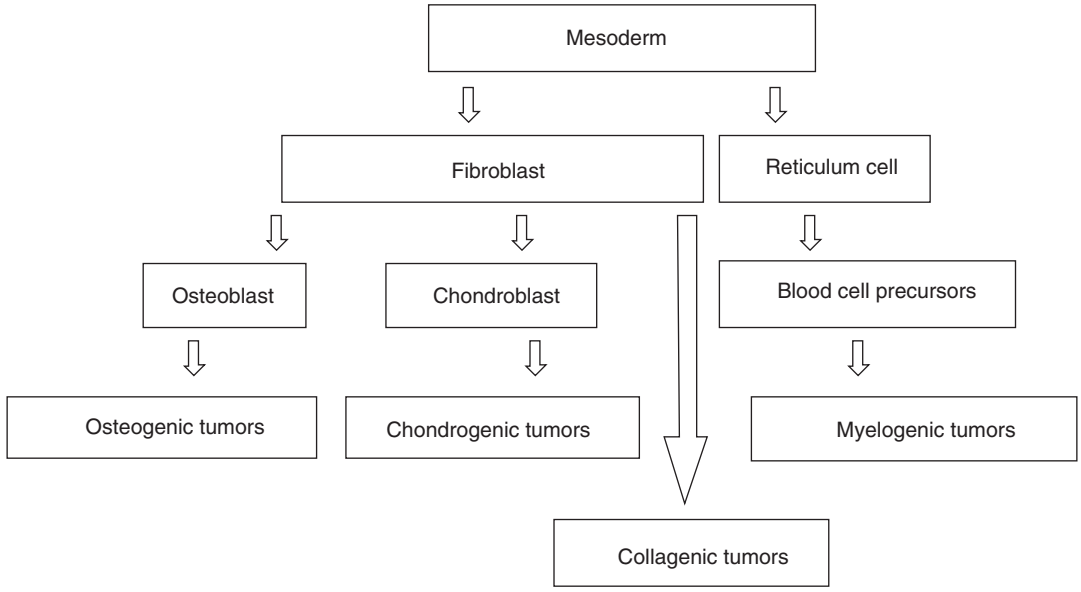

Fig. 5.58 The origin of various primary bone tumors. (Modified from [1], with permission)

lesion classically presents with severe pain at night that is dramatically relieved by nonsteroidal antiinflammatory drugs (NSAIDs). The tumor has been shown to express very high levels of prostaglandins, particularly PGE2 and PGI2. High local levels of these prostaglandins are presumed to be the cause of the intense pain seen in patients with this lesion. Studies have shown strong immunoreactivity to cyclooxygenase-2 (COX-2) in the nidus of the tumor but not in the surrounding reactive bone. COX-2 is one of the mediators of increased production of prostaglandins by osteoid osteomas and may be the cause of the secondary changes depicted by MRI [296]. The usual sites of involvement include bones of the lower extremities, pelvis, and spine.

Osteoblastoma is a tumor related to osteoid osteoma and has almost identical histologic appearance, but the nidus is larger in size measuring more than 2 cm. It is commonly seen in the spine and can occur in any other location. For the appendicular skeleton, the lower extremity is the most common location for osteoblastoma where 35% of the lesions occur.

Osteogenic Sarcoma. Osteogenic sarcoma is an osteogenic tumor with sarcomatous tissue. It is the most common malignant bone-forming tumor

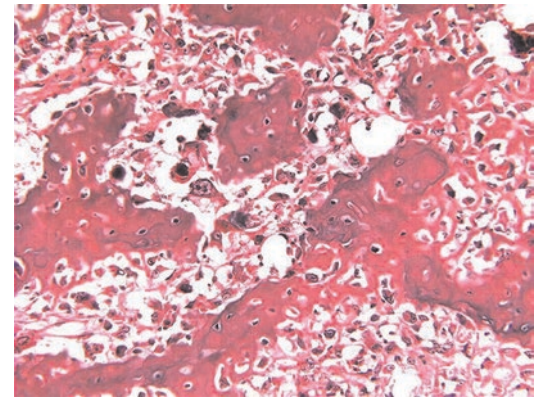

Fig. 5.59 Osteogenic sarcoma pathology

and has the appearance of callus compact contain or cancellous bone produced by anaplastic cells and sometimes chondroid and fibrinoid tissue (Fig. 5.59). The male-to-female ratio is 3:2. Sixty percent of cases occur before the age of 20. A secondary peak incidence is found between 50 and 60 years of age, mainly in patients with a history of prior radiation therapy years earlier [297].

The vast majority of the tumors involve the metaphyses of long bones particularly in the distal femur, with 50% around the knee region (Fig. 5.60).

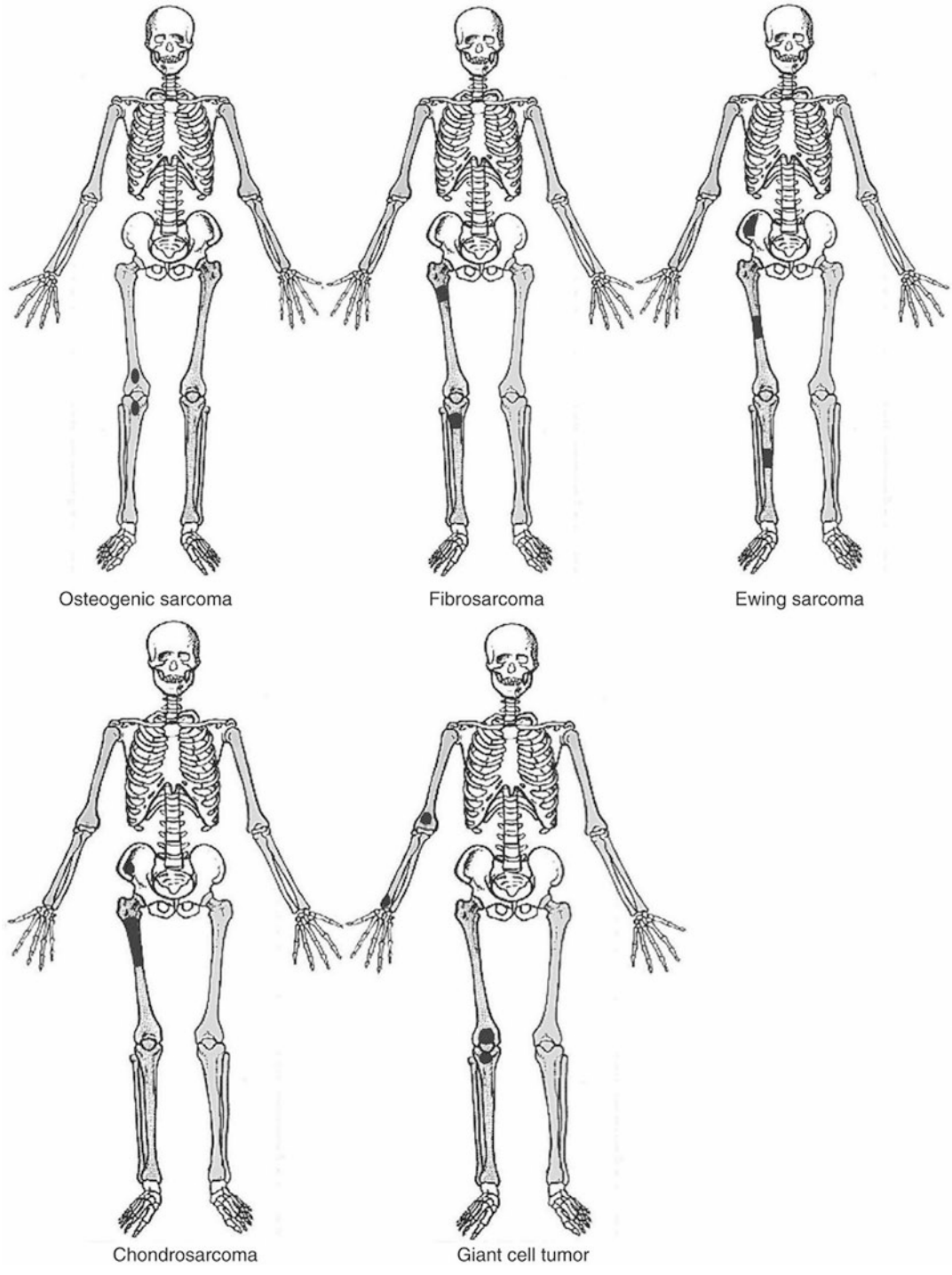

Fig. 5.60 The most common sites of the major primary bone tumors

5.4.1.2 Chondrogenic Tumors

All tumors that produce cartilage, primitive cartilage, or cartilage-like substance are called chondrogenic. The most common malignant chondrogenic tumor is chondrosarcoma. Two types of this malignant tumor are recognized: (a) primary chondrosarcoma, occurring mainly in patients aged 50–70 years, and (b) secondary chondrosarcoma, which is derived from the benign chondrogenic tumor enchondroma and occurs more frequently in patients aged 20–30 years. Chondrosarcoma is more common in men than in women, often arising in the metaphysis or diaphysis of long bones (Fig. 5.60), particularly the femur and in the pelvis. The neoplasm consists of hyaline cartilage with bands of anaplastic cells and fibrous tissue. The tumor may infiltrate the joint spaces located near the end of the long bone. Chondroma is the benign chondrogenic tumor which is an uncommon benign tumor that forms characteristically mature cartilage. The tumor is encapsulated with a lobular growing pattern. It is formed of chondrocytes (cartilaginous cells) that resemble normal cells and produce cartilaginous matrix. It is found mostly in the small bones of the hand and/or feet, although it can also occur in long, tubular bones, primarily the humerus, femur, and ribs. Occasionally, focal areas of myxoid degeneration may result in a mistaken diagnosis of chondrosarcoma. Chondromas are classified according to their location into enchondroma within the medullary cavity of bone, periosteal chondroma found on the surface of the bone, and soft tissue chondroma found in the soft tissue. The primary significance of enchondroma is related to its complications, most notably pathological fracture, and a small incidence of malignant transformation. Enchondromas are usually solitary but may be multiple. Multiple enchondromas occur in three distinct disorders: Ollier disease is a nonhereditary disorder characterized by multiple enchondromas with a predilection for unilateral distribution (Fig. 5.61), and Maffucci syndrome is another nonhereditary disorder which is less common than Ollier disease. This syndrome features multiple hemangiomas in addition to enchondromas. The third form is metachondromatosis which consists of multiple enchondromas and osteochondromas, and it is the only 1 of the 3 disorders that is hereditary as autosomal dominant [298, 299].

5.4.1.3 Collagenic Tumors

Collagenic tumors are primary bone tumors that produce fibrous connective tissue. A fibrosarcoma is a malignant collagen-forming tumor that occurs most frequently in patients between 30 and 50 years of age but also is encountered in younger and older age groups. It is slightly more common among women. A secondary form may occur following Paget's disease, radiation therapy, and long-standing osteomyelitis. The tumor is most frequently located in the metaphysis of the femur or tibia. It begins in the marrow cavity and infiltrates the trabeculae. Histological examination typically reveals collagen, malignant fibroblasts, and occasionally giant cells.

5.4.1.4 Myelogenic Tumors

Myelogenic tumors originate from various cells in the bone marrow.

Myeloma. A myeloma originates from the plasma cells of the reticuloendothelial element of the bone marrow and may be solitary (85%) or multifocal (multiple myeloma). It is a highly malignant tumor that occurs more commonly in patients above 40 years of age and more frequently in men and blacks. It affects mainly the spine, pelvis, ribs, skull, and proximal bones of the extremities. In myeloma there is neoplastic proliferation of plasma cells presenting with skeletal lesions. The neoplastic cells produce immunoglobulins including heavy chains (IgG, IgA, IgM) and light chains, kappa or lambda (Bence Jones proteins). The tumor can present in differenet forms, Multiple myeloma (most common), solitary plasmacytoma, and osteosclerotic myeloma. Osteosclerotic myeloma is rare and is characterised by polyneuropathy, organomegaly, endocrinopathy, M protein, and skin changes. Bone lesions are sclerotic in both axial and appendicular skeleton A rare variant of multiple myeloma,‹3% of all newly diagnosed myeloma is the non-secretory myeloma as no monoclonal gammopathy can be detected in serum or urine

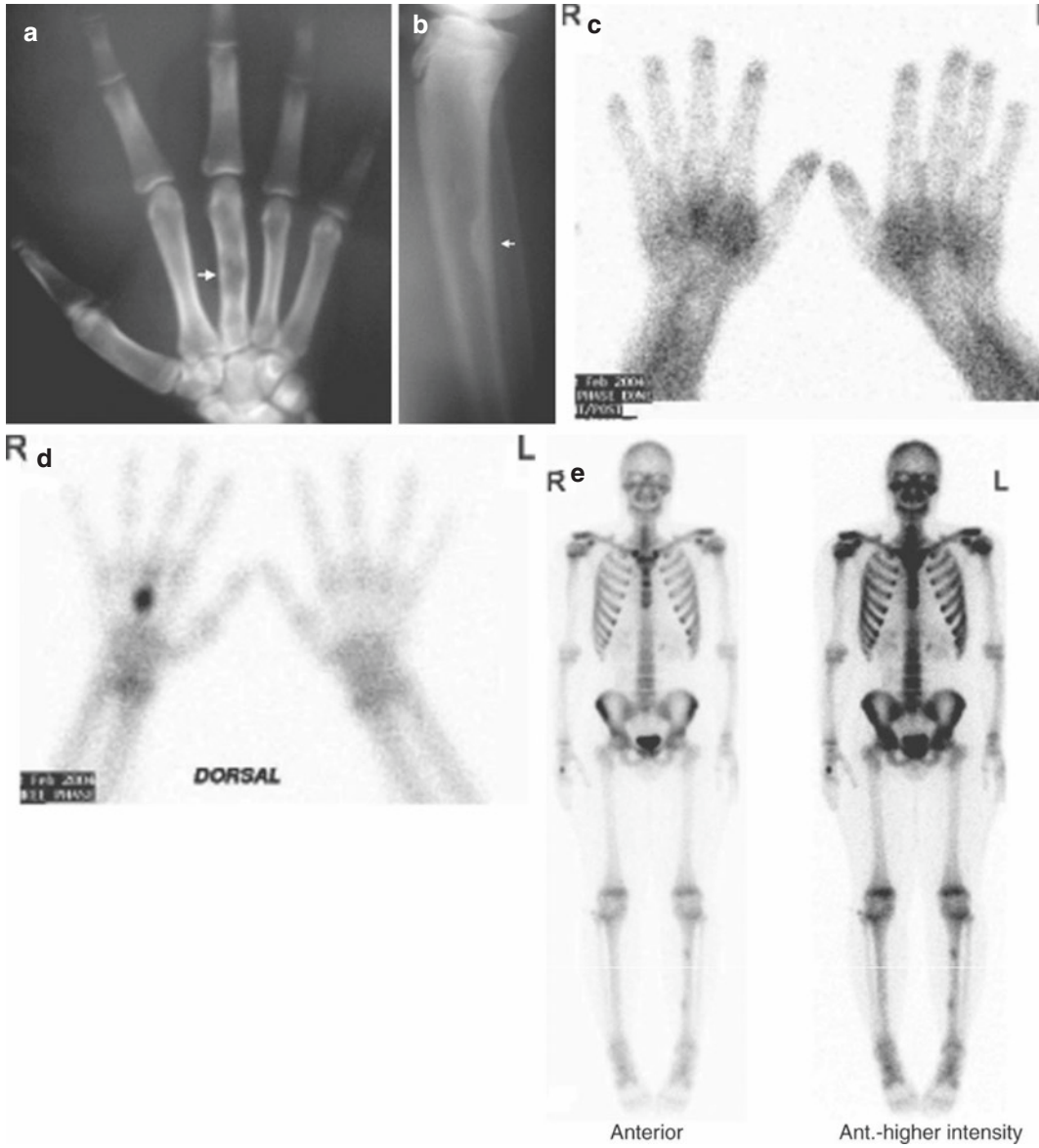

Fig. 5.61 (**a**–**e**) A 17-year-old boy presenting at the age of 12 years with swollen and painful right hand after playing boxing was diagnosed with a benign enchondroma of the third right metacarpal bone. At the age of 14 years, he had a recurrent pain of the upper third of the right leg and was also diagnosed with a benign enchondroma. Follow-up radiography of the right hand (**a**) revealed no changes in the size or characters of the previously diagnosed enchondroma of the middle metacarpal bone (*arrow*). Left leg (**b**) demonstrated a mixed density scalloped eccentric lesion (*arrow*) in the upper half of left tibia believed to be mostly benign. The patient was referred to the Nuclear Medicine Department for an annual follow-up. A three-phase bone scan was obtained 3 h after IV injection of 25.3 MCI of ^{99m}Tc-MDP. The blood pool images (**c**) of both hands show moderate focal increase uptake in the mid-right hand. The delayed images of the hands (**d**) show intense focal uptake in the third right metacarpal bone. The whole-body images (**e**) show two foci of increased uptake in the left tibia, one in the upper third and one in the lower third representing multiple enchondromas

by conventional techniques. In Myeloma, there is increased osteoclastogenesis and suppressed osteoblastogenesis. Osteoblastogenesis is suppressed due to secreted inhibitors and dysregulation of cell-surface "coupling" factors on osteogenic cells resulting in uncoupling of bone remodeling responsible of the related bone disease. Osteoclastogenesis is increased as a consequence of osteoblast deactivation and of production of osteoclast-activating factors [300]. Pain progresses over time during the course of the disease, and pathological fractures may take place. Patients may develop renal failure, anemia, and thrombocytopenia, and their urine shows Bence-Jones protein. The tumor has a poor prognosis, and radiation and chemotherapy have limited success.

Ewing's Sarcoma. Ewing's sarcoma is a malignant tumor originating from the bone marrow and is the second most common bone tumor after osteogenic sarcoma in children and adolescents. The tumor is most frequent in the first three decades of life as 95% of cases are reported between the ages of 4 and 25 years [301]. The peak prevalence is between the ages of 10 and 15 years. The most commonly affected sites are the femur (21% of cases), ilium (12–13%), tibia (8–11%), humerus (10%), fibula (7–9%), ribs (8%), and sacrum (6%). The pelvis, extremities, and ribs account for approximately more than 80% of cases [302].

It is more common in males and in whites. It is characterized by chromosomal translocation between chromosomes 11 and 22. Typically, it occurs in the diaphysis of long bones such as the femur and tibia and in flat bones such as the pelvis; however, any bone may be involved. After arising from marrow, Ewing's sarcoma breaks through the bone cortex to form a soft tissue mass which does not contain osteoid. The tumor metastasizes early to the lung, other bones, lymph nodes, bone marrow, liver, spleen, and central nervous system. Often the prognosis is poor, particularly if the tumor involves the pelvis rather than the long bones.

Giant cell tumor is difficult to classify although many practitioners include it with myelogenic tumors since it is believed to originate from the fibrous tissue of the bone marrow. While giant cell tumor may occur in persons between 10 and 70 years of age, it is more commonly encountered in those between 20 and 40 years old, with women afflicted more often than men from the metaphyseal-epiphyseal region of long bones. The tumor occurs mainly around the knee (50%), in the radius, and in the humerus. It has a high recurrence rate, often extending locally into adjacent soft tissues; distant metastases, however, occur more rarely. It consists particularly of osteoclast-like giant cells and anaplastic stromal cells, with a minor component of osteoid and collagen [303].

Chordoma is a rare slowly growing neoplasm arising from notochordal remnants in the midline of the neural axis and involving the adjacent bone. The main malignant potential of chordomas resides in their critical locations adjacent to important structures, their locally aggressive nature, and their extremely high rate of recurrence. CT and MRI are essential for accurate evaluation. Myelography is used to determine intraspinal extension.

Bone hemangiomas are benign, malformed vascular lesions, overall constituting less than 1% of all primary bone neoplasms. They occur most frequently in the vertebral column (30–50%) and skull (20%), but can occur anywhere in the body, and thus, any bone can be affected including the long bones, short tubular bones, and ribs. It is multiple in approximately one-third of cases particularly within the vertebral column. Osseous hemangioma generally occurs more commonly in females than males, with a ratio of 3:2. The peak incidence is in the fifth decade, although osseous hemangiomas can be encountered at any age. Bone hemangiomas usually occur in the medullary cavity, but uncommonly, surface-based hemangiomas are encountered in the cortex, periosteum, and subperiosteal regions. The rare periosteal and other surface-based hemangiomas tend to occur in younger patients. Bone hemangiomas are usually asymptomatic lesions discovered incidentally on imaging or postmortem examination and mostly encountered in the middle aged. Vertebral hemangiomas are the most common benign tumor of the spinal col-

umn, and they occur most frequently in the lower thoracic and upper lumbar spine. They are usually localized to the vertebral body, less frequently extending into or exclusively affecting the posterior arch. Long bone hemangiomas are uncommon and are found mainly in the tibia, femur, or humerus. They have a predilection for the metaphyseal or diaphyseal regions but can involve the epiphyses and even extend across the joint space. Skull hemangiomas affect most commonly the frontal bone. Gross pathology usually reveals well-demarcated, unencapsulated lesions with cystic red cavities. Microscopic examination shows hamartomatous proliferations of vascular tissue within endothelial-lined spaces.

There are four histologic variants of hemangioma, classified according to the predominant type of vascular channel: cavernous, capillary, arteriovenous, and venous. These types can coexist. Bone hemangiomas are predominantly of the cavernous and capillary varieties. Cavernous hemangiomas most frequently occur in the skull, whereas capillary hemangiomas predominate in the vertebral column; overall, the former type is most common in bone [304, 305].

Multiphase ^{99m}Tc MDP bone scintigraphy may also reveal increased tracer uptake in all phases (perfusion, blood pool, and delayed), with a progressive increase in uptake, most marked in the delayed static images. Single-phase bone scintigraphy, though, has a far lower specificity since hemangiomas vary in their aggressiveness and hence in the degree of bone turnover and may demonstrate either increased or decreased uptake or even normal uptake and therefore generally adds minimal information. SPECT may be helpful in vertebral hemangiomas [306], and Tc99m-labeled red cells will show accumulation by the tumor as the case with hemangiomas at other sites.

5.4.1.5 Imaging of Primary Bone Tumors

Morphological imaging modalities play a major role in evaluating the local extent of the primary tumors of bone. MRI has become the examination of choice for local staging. Bone scintigraphy, however, has a limited role in local staging but is still the very useful for detecting distant metastases. Combining MRI with FDG PET (PET/MR) adds the benefit of providing physiological information that can guide and assess treatment [307]. The effective radiation dose of whole-body FDG PET/MR is more than 50% lower than for FDG PET/CT [308] which makes PET/MR especially attractive for imaging particularly in pediatric and young age group [309].

Functional nuclear medicine imaging plays a minor role in evaluating the local extent of the primary bone tumors. However, utilization of several radiotracers including ^{99m}Tc-MDP, thallium-201, Tc99m MIBI, ^{67}Ga, F-18sodium fluoride, and F18 FDG helps in making diagnosis, grading, and evaluating the response to chemotherapy. Thallium-201, Tc99m MIBI, and F18 FDG can help in differentiating malignant from benign bone lesions [310–314].

PET FDG plays an important role in evaluating prognosis and response to therapy [315, 316]. A study of 17 patients with primary bone tumors (11 osteosarcomas, 5 Ewing's sarcomas) has shown that patients with increasing tumor-to-non-tumor ratios of FDG uptake or decreasing ratios of less than 30% have poor responses [315].

In comparison to bone scan, studies indicate that PET scanning is more sensitive and may detect metastases and other lesions as small as 2 mm [317]. In one study, FDG-PET has been compared to ^{99m}Tc-MDP bone scan in detection of osseous metastases in 70 patients with histologically proved malignant primary bone tumors (32 osteosarcomas, 38 Ewing's sarcomas). FDG-PET showed higher sensitivity of 90%, specificity of 96%, and accuracy of 95% in detection of bone metastases (49 from Ewing's sarcomas and 5 from osteosarcomas) more than bone scan, which showed a limited sensitivity of 71%, specificity of 92%, and accuracy of 88%. Similarly, accuracy of FDG-PET in patients with Ewing's sarcoma was found to be higher than that of bone scan (97 and 82%, respectively). In contrast, in patients with osteogenic sarcoma, FDG-PET detected none of the five cases of osseous metastases detected by bone scan, indicating a lower sensitivity of FDG-PET than bone scan in detection of osteosarcoma-induced osseous metastases [318].

Table 5.23 Scintigraphic patterns of primary benign bone tumors and tumorlike lesions on bone scan

Tumor	Typical pattern on MDP/NaF
Osteoid osteoma	A focal area of increased activity in all three phases and double intensity sign
Osteoblastoma	Increased uptake in all three phases
Osteochondroma	Variable degree of uptake
Giant cell tumor	Increased uptake in all three phases
Chordoma	Increased or normal uptake
Aneurysmal bone cyst	Moderate to intense uptake at the periphery of the lesion with little activity at its center ("doughnut sign")
Bone hemangioma	Variable (increased, decreased or normal uptake)

Table 5.23 summarizes the scintigraphic patterns of the main benign primary bone tumors.

Imaging of Major Specific Tumors

Osteoid Osteoma

Characteristically these lesions are intracortical and diaphyseal in location, although they occasionally involve the metaphysis. On standard radiographs, the characteristic appearance is a small, less than 1.5–2 cm, cortically based radiolucency (nidus) surrounded by marked sclerosis and cortical thickening, combined with the classic clinical history of pain, worse at night, that is relieved by aspirin. On CT, an area of increased bone density surrounding a lucent nidus is typical of this tumor. Scintigraphically there is a focal area of increased flow, increased blood pool activity, and increased delayed uptake [295]. A specific scintigraphic pattern of a double density may be seen more intense uptake corresponding to the nidus and a peripheral less intense activity (Fig. 5.62). Symptoms of osteoid osteoma are cured by removing the nidus. The nidus of the tumor must also be removed during surgery to avoid regrowth. SPECT may help to localize an osteoid osteoma before surgery, and a gamma probe is a useful operating room tool for localizing this tumor [319].

In osteoid osteoma, a typical nidus surrounded by sclerosis or cortical thickening characterizes the tumor on plain radiography and CT. Extensive accompanying bone marrow oedema, soft-tissue alterations, difficulty detecting the nidus, and lesion locations close to a joint (with reactive arthritis) may make a confident diagnosis of osteoid osteoma by MRi imaging difficult. SPECT/CT with Tc99m diphosphonates or PET/CT with F-18 sodium fluoride combines high radionuclide uptake with morphological details and provides accurate diagnosis of osteoid osteoma and provides additional information for treatment planning. FDG is not used as osteoid osteoma is normally FDG-negative, although atypically, some may show increased FDG uptake [320].

"En bloc" resection is often not successful because the nidus is hard to find and remove totally. Since the nidus is best localized with CT [321], surgery under CT control using standard equipment usually available in the operating room has been recently used successfully for CT-guided removal of the nidus [322]. MRI also shows intramedullary high-intensity areas on T2-weighted images in the nidus, and this was suggested to be due to high level of cyclooxygenase-2 (COX-2) expression in neoplastic osteoblasts in the nidus [296].

Intra-articular and intramedullary osteoid osteomas present special problems. Joint effusion and lymphoproliferative synovitis, similar to that seen in rheumatoid arthritis, are often seen with intra-articular lesions and may suggest an arthritic condition, as may the relatively nonspecific symptoms often seen with these lesions and diagnosis may be delayed.

Osteoblastoma

As stated earlier, this tumor is related to osteoid osteoma and affects most commonly the spine and lower extremities. Scintigraphically, osteoblastoma shows intense uptake similar to osteoid osteoma. Radiographically, a pattern of lysis with or without a rim of surrounding sclerosis is characteristic. Extensive surrounding sclerosis is usually absent; however, surrounding inflammatory changes are often identified on MRI.

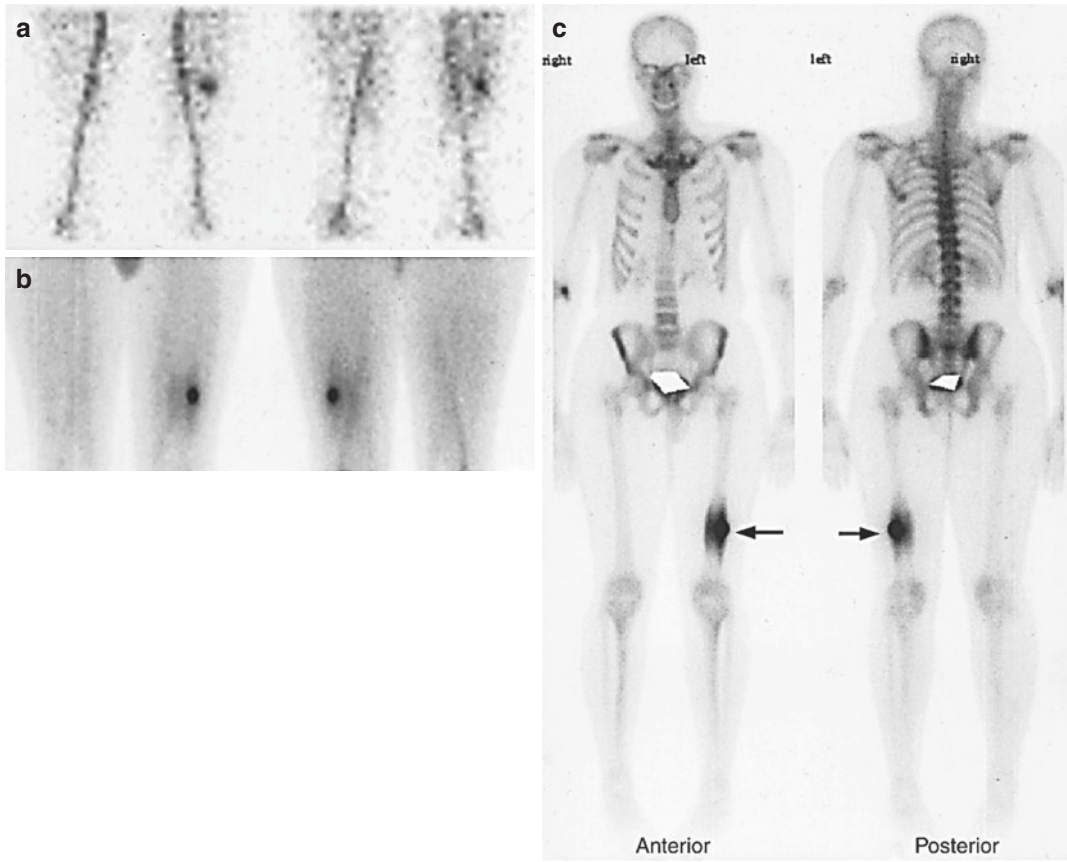

Fig. 5.62 (**a**–**c**) Flow (**a**), blood pool (**b**), and delayed (**c**) images of a patient with osteoid osteoma of the left femur showing intense flow and blood pool activity and on delayed images the specific pattern of double intensity (*arrow*)

Osteochondroma

This tumor could appear as sessile/pedunculated (exostosis) or asessile. The lesions particularly the pedunculated have a central core of cancellous bone surrounded by a shell of cortical bone and covered by a cap of hyaline cartilage. It can be familial and multiple forming the entity of hereditary multiple exostosis that is discovered in childhood [323].

We encountered a case of this condition where the patient has more than 300 lesions, which show variable degree of uptake on bone scintigraphy. Standard radiographs and CT scan usually are enough to detect the lesions; however, bone scan is particularly useful to detect multiplicity and following up patients with hereditary disease since there is a risk of malignant transformation in up to 30% of cases [323].

MRI delineates and assesses the thickness of cartilage cap and is useful in planning biopsy of the lesions. A cartilage cap of 1.5–2 cm thick in a skeletally mature person is highly suggestive of malignant transformation. Scintigraphically a variable degree of uptake (Fig. 5.63) is seen which may reflect the lesion's activity; however, active peripheral lesions particularly if small may not show enough uptake to be detected on bone scans [324–326].

Osteogenic Sarcoma

Scintigraphically, osteogenic sarcoma presents as an area of intense uptake (Fig. 5.64). Rarely, the tumor may present as a cold lesion [327].

CT and particularly MRI are superior to bone scan in evaluating the extent of the tumor. Bloem [328] evaluated the relative value of MRI, CT,

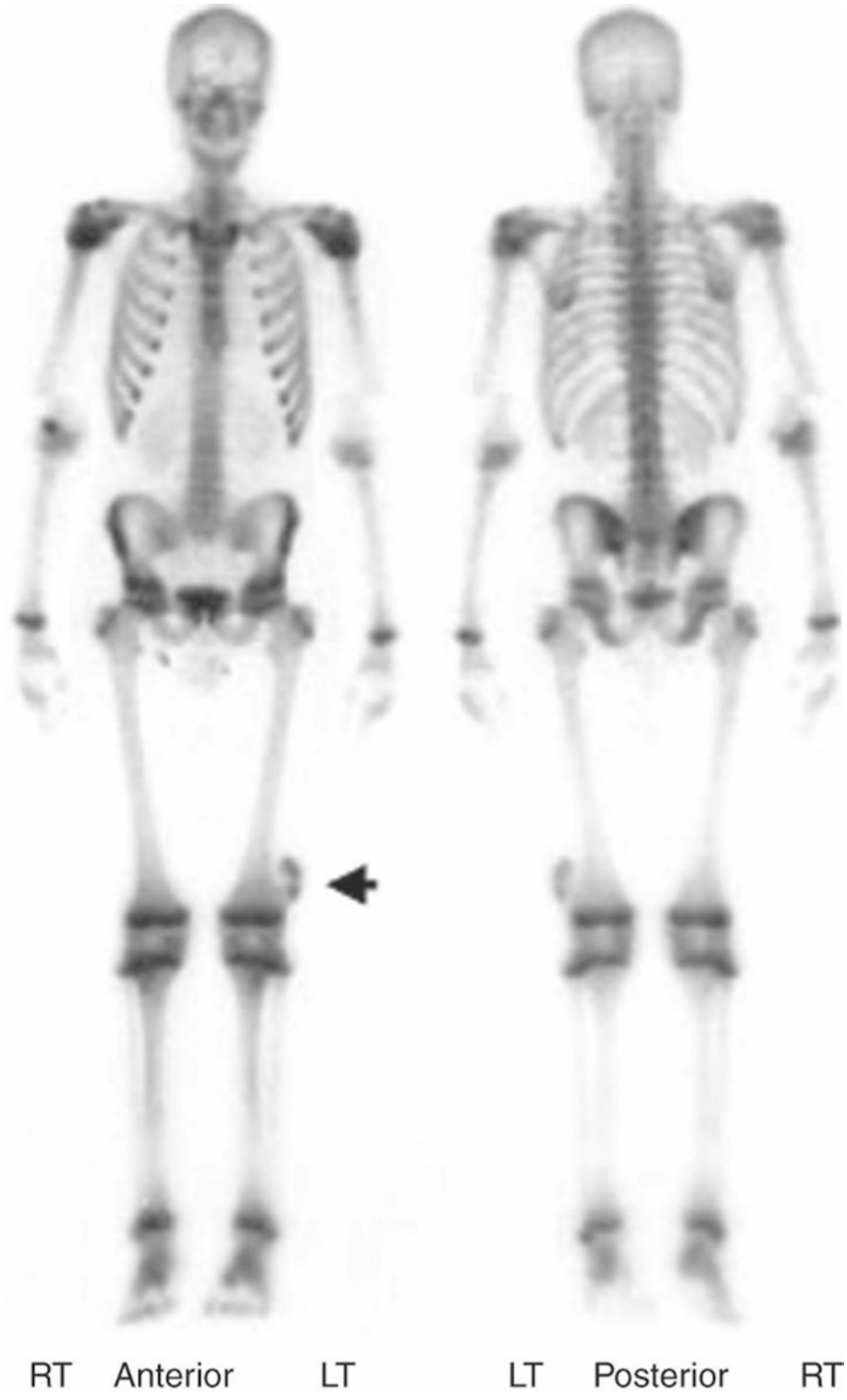

Fig. 5.63 Osteochondroma. A 14-year-old athletic male with pain and swelling of the left distal thigh for 1 week. The patient was referred to rule out trauma or heterotopic bone formation. The scan shows increased blood pool activity in the lateral aspect of the distal left femur representing the typical pattern of pedunculated osteochondroma

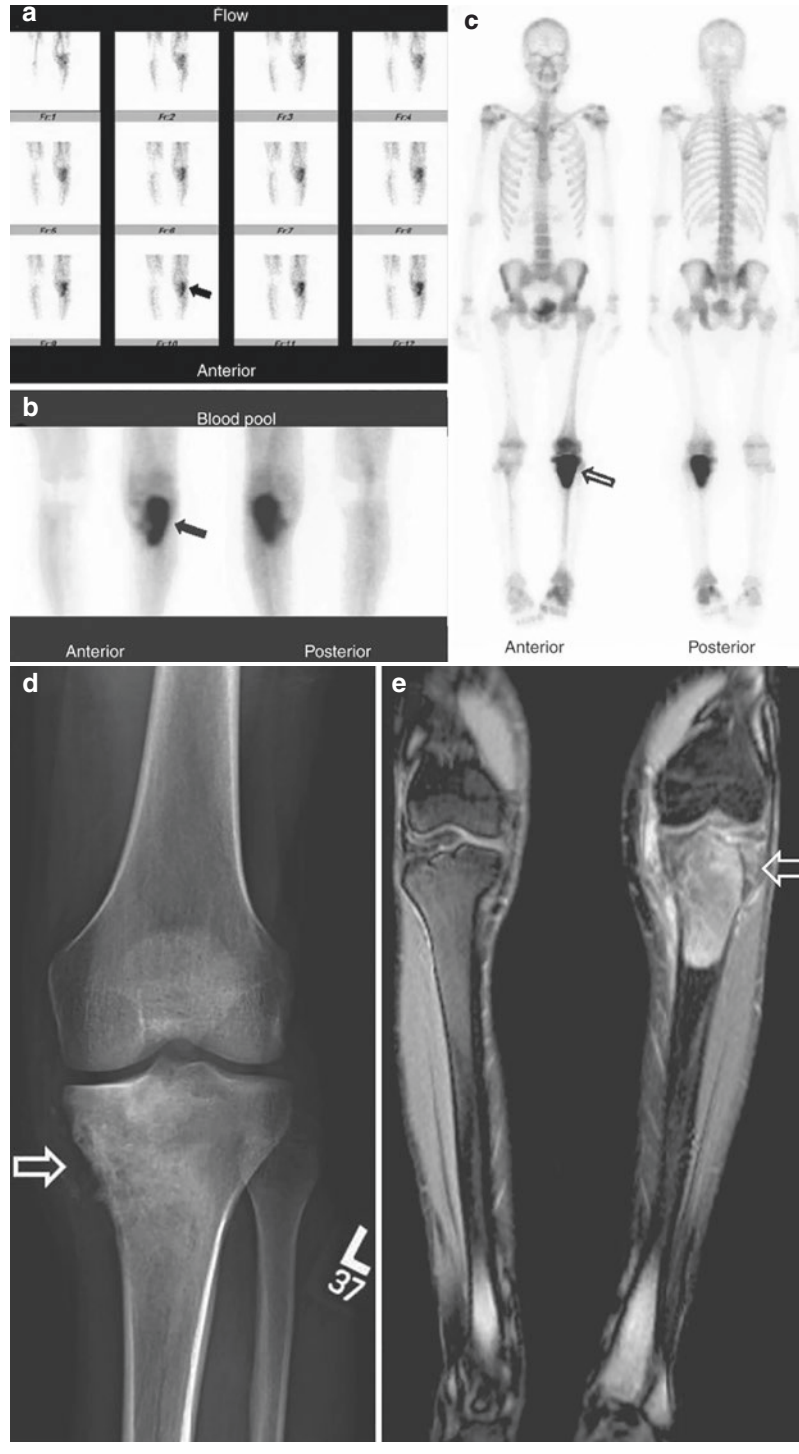

Fig. 5.64 A 14-year-old male with pain and swelling of the left upper leg proven later to be osteogenic sarcoma. Bone scan showing hypervascularity (**a**, **b**) and intense delayed uptake (**c**) corresponding to the X-ray (**d**) and MRI (**e**) findings (*arrows*). Note the mildly diffuse increased uptake in the bones of the left lower extremity due to disuse. No distant metastases. Note the outlines of the tumor on MRI images which are superior to bone scan in regional staging of the tumor

Tc99m bone scintigraphy, and angiography prospectively in local tumor staging in 56 patients with a primary bone sarcoma. MRI was significantly superior to CT and scintigraphy in defining intraosseous tumor lengths and as accurate as CT in demonstrating cortical bone and joint involve-

ment. Additionally, MRI was superior to CT in demonstrating involvement of skeletal muscle. Bone metastases are rare at presentation. McKillop et al. [329] found only one, out of 55 patients, who presented with bone metastases. Conversely, during follow-up, bone metastases developed in 20 patients who developed abnormal bone scan, but approximately half were asymptomatic. The authors concluded that initial bone scan yield is small, but it is a justified procedure on presentation because the results may profoundly alter the treatment of the patient and is indicated in all patients routinely during follow-up even if they are asymptomatic. a more recent study found 4 out of 39 patients with bone metastases at diagnosis. The study also found that 18F-FDG-PET-CT demonstrated superior sensitivity over BS for detecting osseous metastases, supporting the use of 18F-FDG-PET-CT for staging of osteosarcoma [330]. A meta-analysis study on the comparison of PET and PETT/CT to bone scan in the diagnosis. Recurrence and evaluation of response to therapy found that FDG has a pooled sensitivity of 91% and a specificity of 93% for detecting recurrence of osteosarcoma. The study demonstrated that ^{18}F-FDG PET and PET/CT are very accurate for the diagnosis, staging, and recurrence monitoring and the follow-up of the response of the tumor to therapy of osteosarcoma [331] (Fig. 5.60). Tc99m MIBI and thallium-201 have been also useful in the past for this purpose and predict the prognosis. Studies have suggested that P-glycoprotein (Pgp) expression is a prognostic factor for patients with osteosarcoma. Some investigators found relationship between the washout rate of ^{99m}Tc-MIBI and the Pgp score, with a significant difference in washout rate being observed between patients with high and patients with low Pgp expression [332]. Others found that Tc99m-MIBI imaging is not an effective predictor of prognosis since the Tc99m-MIBI half-life and uptake ratio showed no correlation with histological necrosis following induction chemotherapy and did not correlate with P-glycoprotein expression [333].

Using thallium-201, the pattern of doughnut uptake was found to be a predictor of lower event-free survival in patients with extremity osteogenic sarcoma, but does not correlate with histologic response to therapy [334] (Fig. 5.65).

FDG-PET/CT has a high diagnostic accuracy for detecting bone metastases of osteogenic sarcoma (98%) compared to 96% bone scan [335]. In the same study, lesion-based analysis demonstrated that the sensitivity of PET/CT + BS (100%) was significantly higher than that of PET/

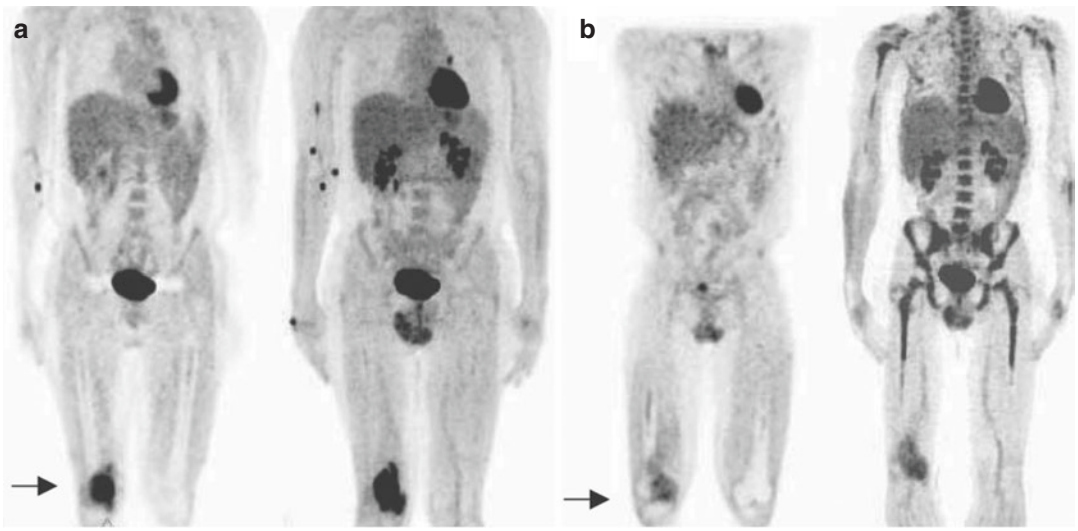

Fig. 5.65 (**a**, **b**) 18F-FDG-PET study of a patient with osteogenic sarcoma of the distal right femur showing increased uptake and SUV value of 9.6. (**b**) Follow-up study obtained after chemotherapy shows a significant decrease in the initial uptake with a drop of SUV to 4.2, indicating a good response

CT (92%) or BS (74%) alone. BS detected significantly less bone metastases in the growth plate region than outside the growth plate region (22 vs. 77%) [335]. FDG-PET imaging provides also prognostic information related to grading and estimating biologic aggressiveness. High F18-FDG uptake correlates with poor outcome, and F18-FDG uptake may be complementary to other well-known factors in judging the prognosis in osteosarcoma [336].

Myeloma

Imaging plays an important role in the management of patients with multiple myeloma. Standard radiograph has traditionally been the standard imaging modality; however, it has low sensitivity in detecting osteolytic lesions and inability to evaluate response to therapy. Accordingly other modalities are being used including whole-body low-dose CT, whole-body MRI, and ^{18}F-FDGPET/CT. In large studies, whole-body low-dose CTWBLDCT was found to be superior to whole-body X-ray in detecting osteolytic lesions due to higher sensitivity and accuracy and in particular in the spine and pelvis.[337, 338].

The European Myeloma Network and the European Society for Medical Oncology guidelines have recommended WBLDCT as the imaging modality of choice for the initial assessment of multiple myeloma related lytic bone lesions. Magnetic resonance imaging is the gold-standard imaging modality for detection of bone marrow involvement, while FDG PET/CT provides valuable prognostic data and is the preferred modality for response to therapy assessment [339].

Bone scan is viewed to be in general unreliable for staging although in a study reviewing the literature comparing the usefulness of conventional skeletal radiography and bone scans in diagnosing the osteolytic lesions of myeloma shows that bone scintigraphy, considered by many to have no role in the detection of osteolytic lesions of myeloma, is in fact more sensitive than radiography in detecting lesions in the ribs, scapula, and spine. Although cold areas are commonly seen on bone scans, increased uptake (Fig. 5.66) is a common scintigraphic pattern. This should not contradict the fact that myeloma is the most common tumor to cause cold lesions on bone scan. Ga-68-PSMA PET/CT was reported recently to show intense uptake in a case of multiple myeloma which may also suggest the possibility of theranostics with 177Lu-PSMA. Tumor neoangiogenesis is the mechanism attributed to increased 68GaPSMA uptake in such nonprostatic malignancies [340].

Ewing's Sarcoma

As with other primary bone tumors, morphologic modalities including CT and MRI are the primary imaging modalities for assessing local extent of this primary tumor. Bone scan however is indicated when metastases need to be excluded particularly if SPECT/CT is used. The detection of osseous metastases of Ewing's sarcoma, therapy monitoring, and the diagnosis of recurrences is potentially useful clinical indications for FDG-PET [341].

FDG-PET was reported to detect more lesions of metastatic Ewing's sarcoma than bone and gallium scans, especially for those with bone marrow involvement [342]. Metastases are best evaluated with bone scintigraphy, FDG PET, or whole-body MR imaging. A study comparing these modalities in detecting metastases in children with Ewing sarcoma found FDG PET (90% sensitivity) superior to bone scintigraphy (82% sensitivity) or whole-body MR imaging (71% sensitivity) [343].

Bone scintigraphy may reveal diminishing uptake of radionuclide in response to therapy [344]. However, FDG PET is more useful in evaluation of tumor response to treatment, with its ability to depict molecular changes before the morphologic abnormalities evaluated with morphologic cross-sectional imaging [345]. As mentioned earlier PET/MR is preferred to PET/CT in pediatric age group [307] due to lower radiation exposure and better bone/soft tissue contrast.

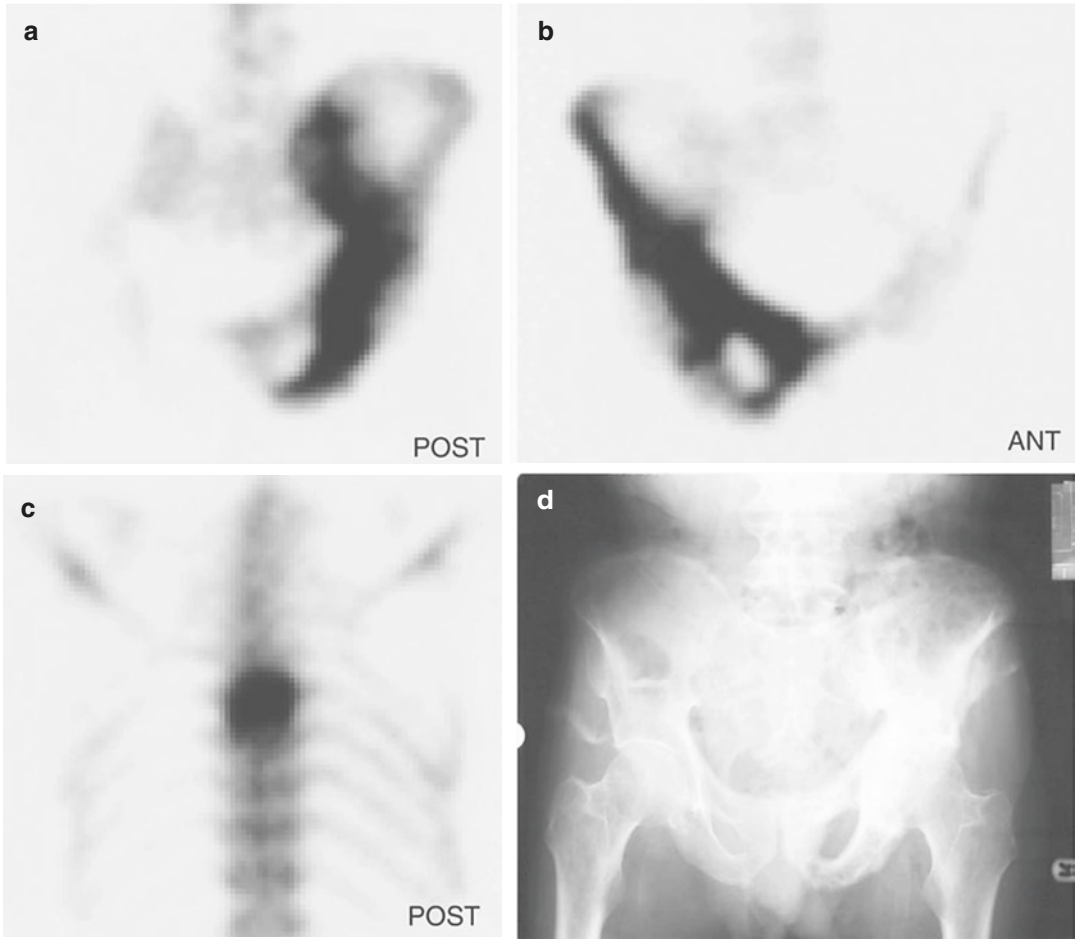

Fig. 5.66 (**a**–**d**) Selected spot images (**a**–**c**) of a bone scan of a patient with known multiple myeloma show areas of increased uptake at the sites of tumor. X-ray of the pelvis (**d**) shows the tumor corresponding to the increased uptake of the left iliac bone. Note that all lesions depicted have increased uptake and the patient had no history of trauma or pathologic fractures

5.4.2 Metastatic Bone Disease

Metastasis means "the transfer of disease from one organ or part to another not directly connected with it" [346].

In general, several events are required for the metastatic spread of tumors (Fig. 5.67). The sequence of these events is as follows:

1. Neoplastic cells separate from primary tumors.
2. They gain access to an efficient lymphatic channel or blood capillary.
3. They survive the transport.
4. They attach to the endothelium of a distant capillary bed.
5. They exit the vessel.
6. They develop a supporting blood supply for the cells at the new site.

The pathophysiology of skeletal metastases includes two major events: transport of viable tumor cells to bone and interaction of these cells with osseous tissue. Once cells are in the site, they proliferate to produce micrometastasis. Further growth to macrometastasis occurs at the expense of the surrounding bone tissue. A variety of agents are implicated in the metastatic process

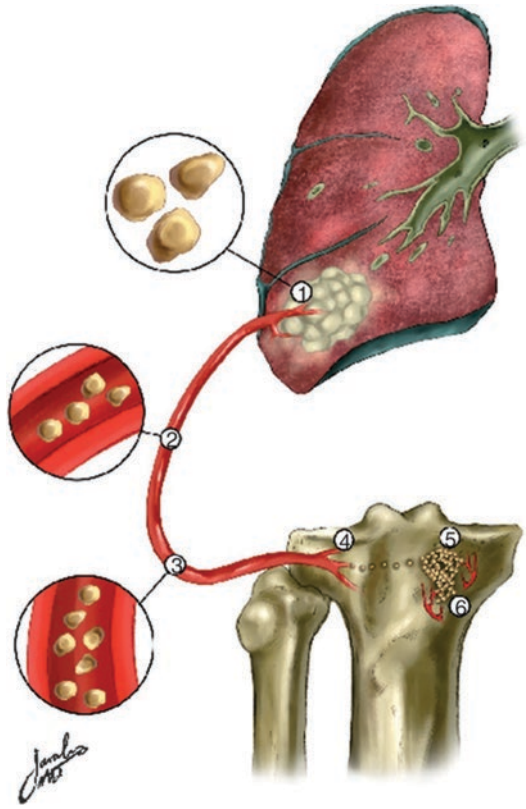

Fig. 5.67 Events required for metastatic spread: (*1*) separation of cells from primary tumor, (*2*) access of separated cells to an efficient lymph channel or blood cap, (*3*) survival of cells during transport, (*4*) successful attachment of cells to the endothelium of a distant cap bed, (*5*) exit of cells from vessel at new site, (*6*) successful development of a supporting blood supply

including proteolytic enzymes, cell adhesion molecules (CAMs), and growth factors [347].

5.4.2.1 Methods of Tumor Cell Transport

In addition to direct extension, tumor cells are transported to produce metastases by:

- *Lymphatic spread*. Lymphatic spread is relatively unimportant for the transport of tumor cells to distant bones. However, metastases in regional draining lymph nodes may secondarily involve the adjacent bones.
- *Hematogenous spread*. Hematogenous spread is a major way of transporting malignant cells to the skeleton; it may happen through the arterial system or through the venous system, particularly the vertebral plexus of the veins of Batson [295]. The relative roles of the arterial and venous systems in the spread of tumor to bone are difficult to define. Metastases occur predominantly in the axial skeleton (especially the spine) and may be present in the absence of pulmonary and other organ involvement, a combination of findings which support the significance of Batson's vertebral plexus in tumor spread. This vertebral plexus consists of an intercommunicating system of thin-walled veins with low intraluminal pressure. These veins frequently are without valves and lie outside the thoracoabdominal cavity. The plexus has extensive communication with veins (Fig. 5.68) in the spinal canal and with the caval, portal, intercostal, pulmonary, and renal systems [348].
- *Intraspinal spread*. Intraspinal dissemination allows secondary deposits in the spinal canal to develop in patients with intracranial tumors. This occurs by subarachnoid spread, secondary to fragmentation of a tumor bathed with cerebrospinal fluid, shedding of portions of the tumor at the time of surgery, ependymal breaching by the primary intracranial tumor, or fissuring secondary to hydrocephalus [348]. Dissemination of intracranial neoplasms via the cerebrospinal fluid represents only one of the mechanisms of spread of metastatic foci to the spinal cord. Arterial, venous, and direct extension pathways are additional routes.

5.4.2.2 Bone Response to Metastases

Hematogenous metastasis in human beings generally begins in the medullary cavity and then involves the cortex. Accordingly, intramedullary injection of tumor cells suspension is used experimentally. There are two types of osseous response to metastasis:

1. Bone resorption

   There is increased bone resorption secondary to malignant disease. Osteoclasts, tumor cells, tumor cell extracts, monocytes, and macrophages may all be involved in the process [349, 350].

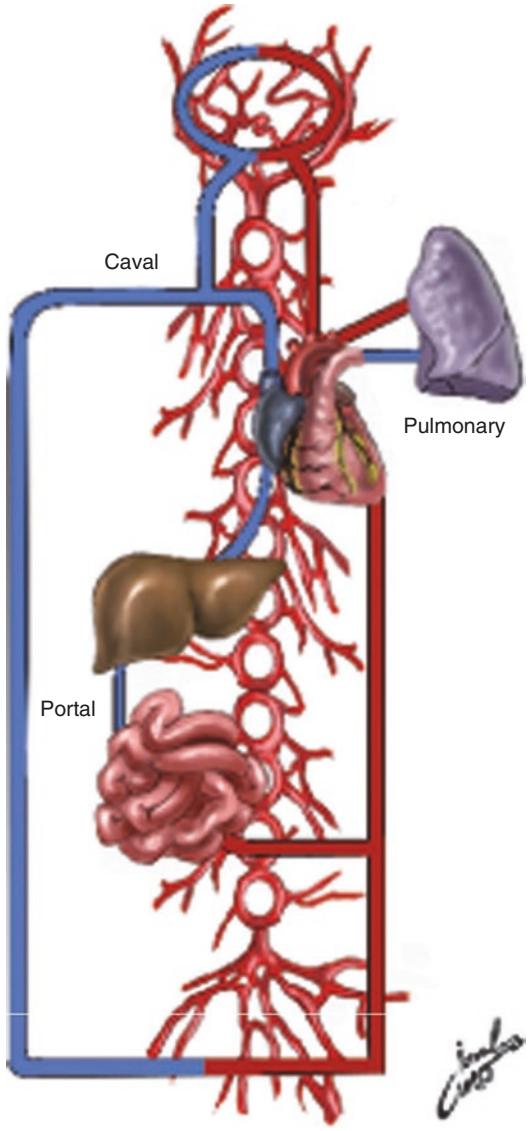

Fig. 5.68 Batson's plexus

2. Bone formation

This response to tumor occurs in two ways:

(a) Stromal bone formation is the earlier and quantitatively less important mechanism of bone formation associated with metastasis. In this type of bone formation, intramembranous ossification takes place in areas of fibrous stroma within the tumor. This occurs only in those skeletal metastases which are associated with the development of fibrous stroma, such as carcinoma of the prostate. Highly cellular tumors have little or no stroma and are not accompanied by this type of bone formation.

(b) Reactive bone formation occurs in response to bone destruction. Immature woven bone is deposited and subsequently converted to lamellar bone. In highly anaplastic, rapidly growing tumors, lymphomas, myelomas, or leukemias, the active bone formation may be only minor or insignificant [351].

5.4.2.3 Distribution of Bone Metastases

The distribution of skeletal metastases varies with the type of primary malignant tumor and age (Fig. 5.69). However, metastases typically involve the axial skeleton, which is the region rich in red bone marrow (Fig. 5.70). Factors favoring the predominant involvement of the red marrow include a large capillary network, a sluggish blood flow, and the suitability of this tissue for the growth of tumor emboli. As mentioned earlier, blood flow is estimated as 5–13 times higher to cancellous bone containing marrow than to cortical bone [7]. In decreasing order, the usual locations of bone metastases are the vertebral column, pelvic bones, ribs, sternum, femoral and humeral shaft, and skull. Less common sites of skeletal metastases include the mandible, patella, and the bones of the extremities distal to the elbows and knees.

The involvement of the spine as the most common site by metastasis can be explained by:

- The fact that Batson's venous plexus provides direct communication between the spine and numerous other locations in the body.
- The large amount of bone mass.

Within the spine, the thoracic and cervical areas involving the lumbar region are the most commonly affected. Within the vertebra, metastases are more common in the vertebral body than in the posterior elements. Possible explanations

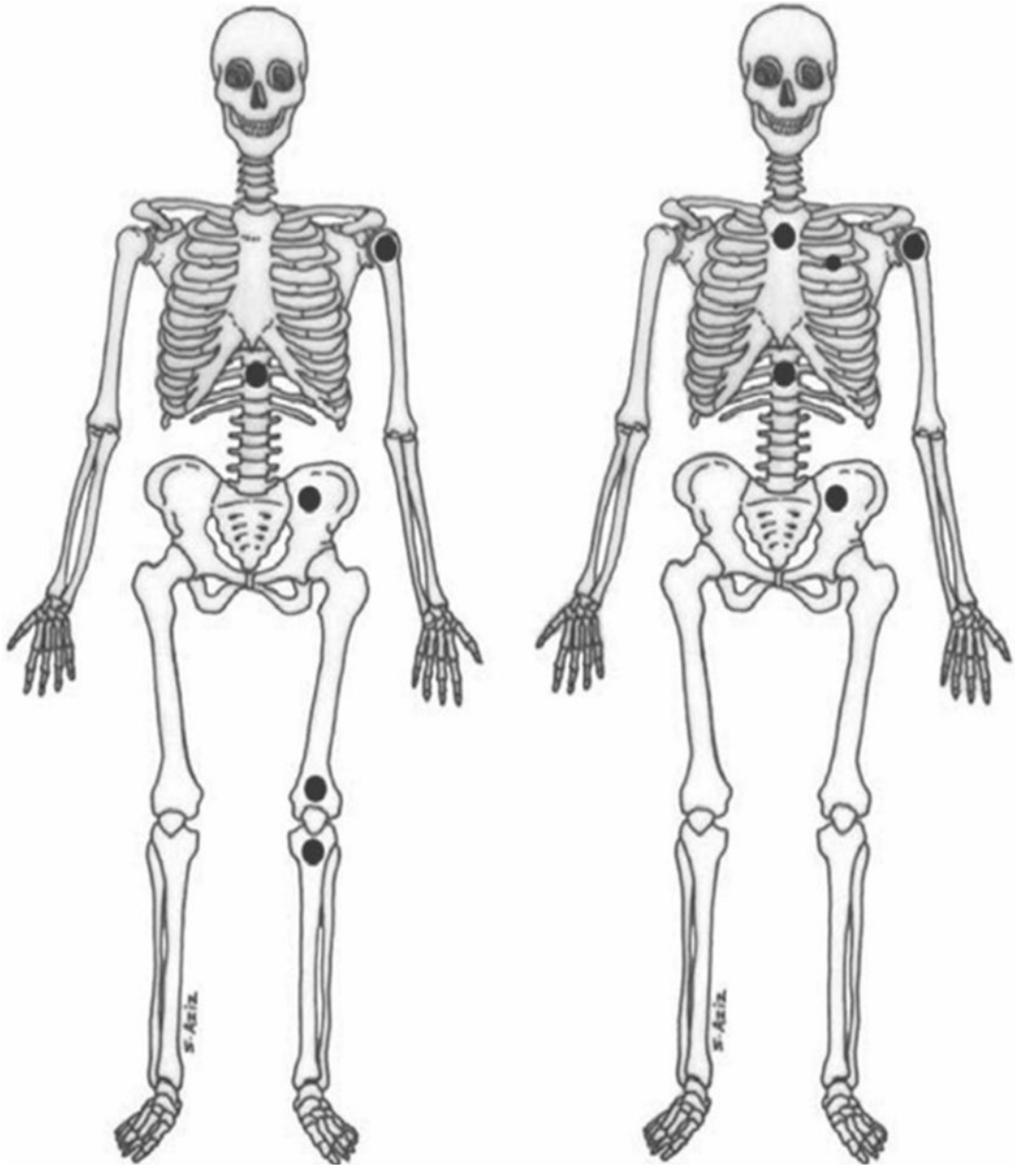

Fig. 5.69 Distribution of bone metastases according to age

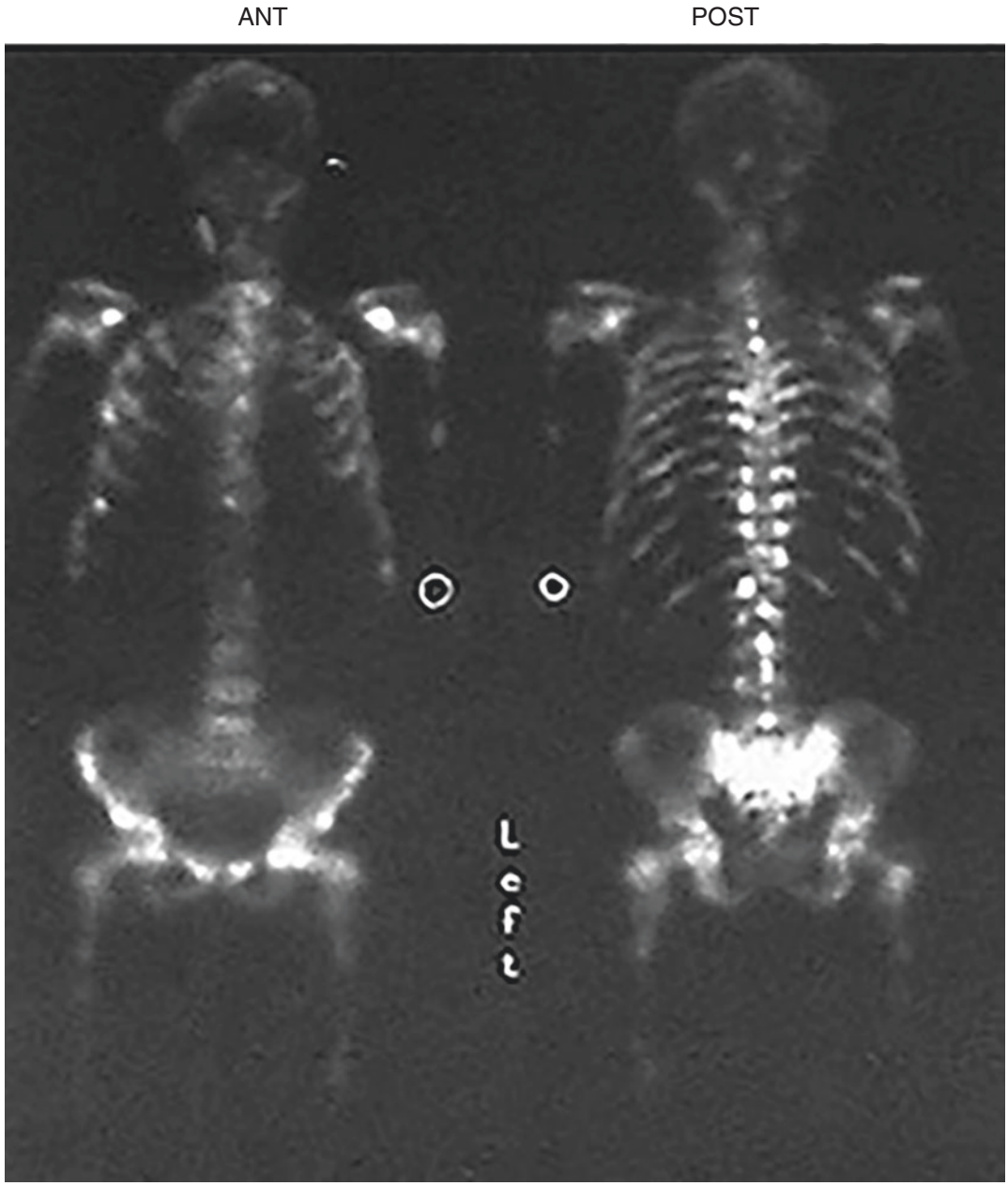

Fig. 5.70 A whole-body bone scan with metastatic bone disease distributed axially illustrating the most common sites and corresponding to the axial skeleton

for the low frequency of metastases in the distal portion of the extremities are:

1. The blood supply, which is essentially limited to the arterial route.
2. The relative absence of red marrow, which is a suitable soil for the growth of metastatic tumor cells.

5.4.2.4 Classification of Bone Metastases

Skeletal metastases begin as medullary lesions. As the lesion enlarges, the surrounding cortical bone undergoes both osteoclastic and osteoblastic changes, and bone may be destroyed directly by the tumor cells or indirectly by specific mediators which stimulate resorption by osteoclasts [351].

Bone metastases can be classified on the basis of several factors, including number of lesions, location, calcium content (as seen on radiographs), and patterns of bone response. Depending on the proportion of these osteoclastic and osteoblastic changes, the radiographic appearance will be lytic, blastic, or mixed [352].

The skeleton might at times respond to the various metastatic foci of a tumor in a uniform manner. However, this is not constant. Sometimes bone metastases show, for example, purely osteoblastic or mixed osteoblastic/osteolytic lesions in certain sites and purely osteolytic lesions in others. Based on the pattern of bone response, metastases can be classified as:

- Purely osteolytic: typically arising from carcinomas of the thyroid, kidney, adrenal, uterus, and gastrointestinal tract. Lytic lesions may be associated with a very rapidly growing metastasis; hence, osteoblastic repair component is unable to keep up with the osteoclastic changes, such as seen with metastases from kidney and lung carcinoma. Metastases with lytic appearance, however, may also be slowly growing so that an osteoblastic response is only minimally stimulated which is seen in metastases derived from myeloma or thyroid carcinoma. Additionally, tumors like myeloma may release a substance that inhibits the osteoblastic response.
- Purely osteoblastic: are seen in bone metastatic tumors with slower growth such as prostatic carcinoma, less often from bronchial carcinoid, carcinoma of the nasopharynx and stomach, neuroblastomas, and medulloblastomas and may actually be a sign of healing of a lytic process [353].
- Mixed osteolytic/osteoblastic: arising from carcinomas of the breast, lung, cervix, ovary, and testis. Tables 5.24, 5.25 and 5.26 lists tumors that produce different types of metastases.

Table 5.24 Tumors producing primarily osteolytic bone metastases

Renal
Thyroid
Ewing's
sarcoma
Uterine carcinoma
Gastrointestinal cancers
Hepatoma
Wilms' tumor
Melanoma
Malignant pheochromocytoma
Squamous cell carcinoma of skin
Myeloma

Table 5.25 Tumors producing primarily osteoblastic bone metastases

Prostate
Medulloblastoma
Medullary carcinoma of thyroid
Carcinoid
Osteogenic sarcoma
Neuroblastoma
Nasopharyngeal carcinoma

Table 5.26 Tumors producing primarily mixed osteoblastic/osteolytic bone metastases

Breast
Lung
Urinary bladder
Pancreatic
Testicular
Cervical
Ovarian

5.4.2.5 Sources of Bone Metastases

Since the vast majority of metastatic bone lesions appear in the middle- and older-aged groups, certain tumors are known to be common sources of bone metastases. The following primary tumors are the most common to metastasize to bone: prostate, breast, kidney, lung, and thyroid. Bladder and uterine carcinomas are less common sources.

In children, skeletal metastases come from neuroblastoma, Ewing's sarcoma, and osteosarcoma. In men, carcinoma of the prostate

accounts for 60% of bone metastases, while in women, breast cancer accounts for 70% of such metastases. Following is a brief presentation of the relevant pathological considerations concerning the major sources of skeletal metastases.

- *Breast Cancer*. Breast cancer is a common source of skeletal metastases. The average incidence of metastases is low at less than 5% in clinical stages 1 and 2, although it ranges from 0 to 40%. In clinical stage 3, the incidence of bone metastases is 20–45%. The tumor usually produces osteolytic or mixed osteolytic/osteoblastic lesions. Rarely, breast cancer gives rise to only osteoblastic lesions. The bone metastases develop most rapidly during the first 2 years. Pain is not a good predictor of bone metastases, since such metastases are found in asymptomatic breast cancer patients and in only 60% of patients with constant pain [354–356].
- *Prostate Cancer*. Prostate cancer is also a common source of bone metastases that are characteristically osteoblastic. Metastases to bone are found in 8–35% of patients at the time of diagnosis. Bone scintigraphy has a crucial role in detecting metastases since it is more sensitive than other imaging and laboratory modalities. Pain has a low predictive value in their detection.
- *Lung Cancer*. Lung cancer produces skeletal metastases in three ways: (a) via lymphatic spread to mediastinal nodes with direct extension to bone; (b) via lymphatic spread to paraaortic nodes, followed by direct extension to bone; and (c) via invasion of pulmonary veins, followed by transport of tumor through the arterial circulation to any part of the skeleton, including the appendicular. The lesions are predominantly osteolytic and mixed, although only osteoblastic lesions can occur in a minority of cases, particularly those with small cell and adenocarcinoma. Among the four major types of lung cancer, small cell is the most aggressive, followed by large cell and adenocarcinoma, squamous cell being the least aggressive [348].
- *Renal Cell Carcinoma*. Renal cell carcinoma produces skeletal metastases rather commonly. Although symptoms related to metastases might be the presenting feature, these symptoms are inconsistent, and pain is not a reliable predictor. The tumor produces skeletal metastases through (a) lymphatic channels to para-aortic, hilar, paratracheal, and/or mediastinal nodes with invasion of bone later and (b) invasion of renal veins which leads to the inferior vena cava, right atrium, and then pulmonary vessels, to be disseminated to bones. The metastatic lesions are predominantly osteolytic and in some cases expansile [355, 357].

5.4.2.6 Sequelae of Skeletal Metastases

Local consequences include:

1. Bone destruction

   Both direct and indirect mechanisms of bone destruction are involved in the bone loss associated with tumor invasion of bone [358].

   Direct stimulation of bone loss: Tumors cause increased osteoclastic activity and consequently bone destruction through secretion of tumor-derived substances that directly stimulate osteoclasts. These substances include parathyroid hormone-related protein, transforming growth factor alpha, transforming growth factor beta, and prostaglandins.

   Indirect stimulation of bone loss by tumors occurs, however, by substances secreted by the tumor that stimulate first the immune cells (Tcells) or activated bone cells which in turn release osteoclast-stimulating cytokines such as tumor necrosis factor (TNF) and interleukin-1 (IL-1) which increase the osteoclastic activity and cause bone destruction (Fig. 5.71).
2. Pathological fractures

   Metastases cause weakening of the involved bones and may lead to fractures in the vertebrae (compression fractures) or long bones, most commonly affecting the proximal portion of the femur [357].

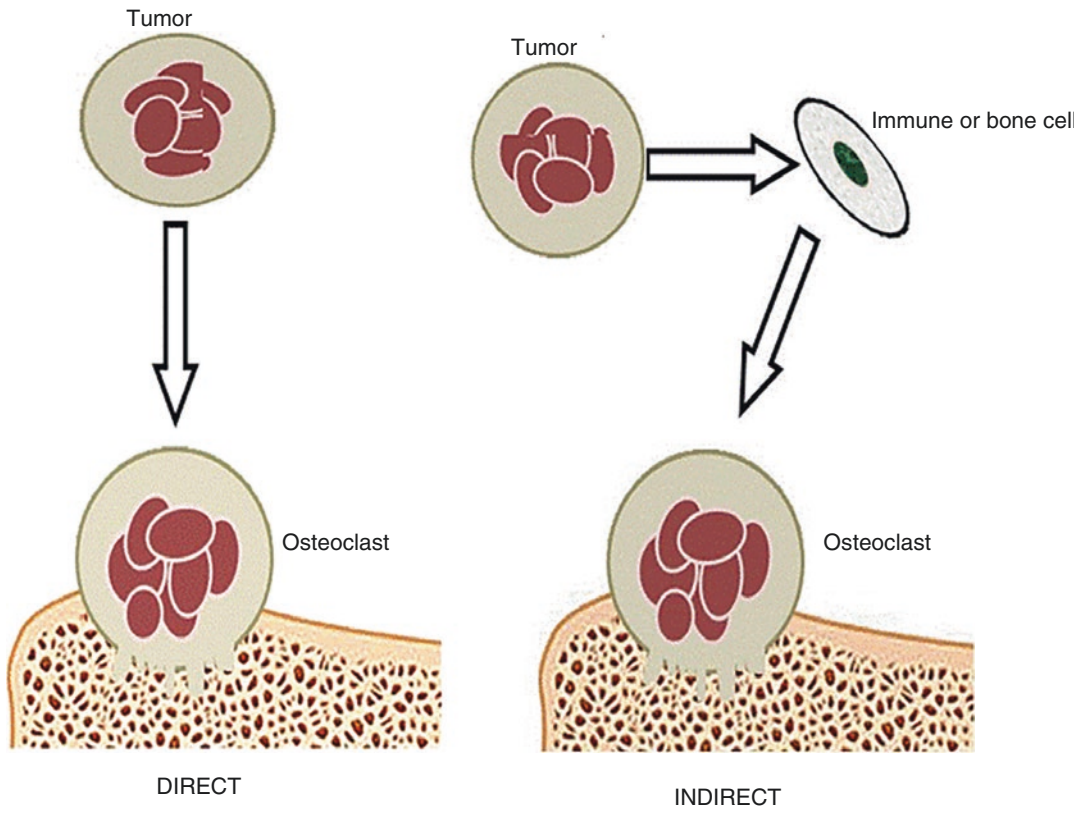

Fig. 5.71 Direct and indirect mechanisms of bone destruction associated with tumor invasion of bone

3. Periosteal new bone formation
   In general, periosteal reaction due to metastases is minimal if present compared with significant new bone formation in association with primary bone tumors.
4. Soft tissue extension
   Soft tissue masses may infrequently present regionally in association with metastases. This occurs particularly with rib lesions in association with myeloma and in the pelvis in association with colon cancer.
5. Bone expansion
   This occurs with both osteolytic and osteoblastic lesions. Carcinomas of the prostate, kidney, and thyroid and hepatocellular carcinoma are particularly known to cause expansile metastatic lesions.

Generalized or metabolic consequences include:

1. Hypercalcemia
   This can be associated with metastases due to destruction of bone, but also with primary tumors not associated with skeletal metastases. Hypercalcemia occurs in up to 20% of cancer patients.
2. Hypocalcemia
   An unidentified humoral substance capable of stimulating osteoclasts in some cancer

patients with skeletal metastases is proposed to be the underlying mechanism behind the presence of hypocalcemia in up to 16% of cancer patients.

3. Osteomalacia

In some patients with skeletal metastases, depressed levels of 1,25-hydroxyvitamin D_3, hypocalcemia, and hypophosphatemia are recognized and associated with generalized weakness and pain of bones and muscles (oncogenic osteomalacia).

5.4.2.7 Imaging of Metastatic Bone Disease

In general, four main modalities are routinely utilized clinically to assess for existence of metastatic lesions. These modalities include standard radiography, CT scan, scintigraphy, and MRI, each alone or in combination (hybrid). Bone metastases are not uncommon at the time of the diagnosis and follow-up of many primary tumors [359–361] (Table 5.27). Incidence varies significantly by tumor type, stage at diagnosis, and by duration after diagnosis.

Three large studies searched the incidence of metastases at the time of the diagnosis of different solid tumors and when later for up to 10 years based on medical records to determine incidence of occurrence [360, 361].

Bone scan is the most widely used modality and is the most practical and cost-effective screening technique for assessing the entire skeleton. In addition, bone scan is very sensitive in detecting the disease. However, there is a variable false-negative rate in assessing lesions in certain locations particularly in the spine and in those confined to bone marrow. MRI has been found to detect more vertebral metastases than bone scan. PET using F-18 sodium fluoride (NaF) is increasingly evaluated for detection of bone metastases and has been shown by several studies to be more sensitive than MDP bone scan and has better sensitivity for smaller and osteolytic lesions than MDP.

Table 5.27 Bone metastasis and type of common tumors at the time of diagnosis and during 10 year follow-up

	Incidence at diagnosis (%)	Incidence range during 10 year follow-up (%)
Lung	16.4	22–27
Prostate	5.1	44–73
Breast	3.6	35–63
Kidney	5.2	5–29
Melanoma	0.8	6–13.5
Colon rectal	1.1	3–12

Data extracted from [359–361]

Tc99m Diphosphonate Bone Scintigraphy

Either direct visualization of tumor cells or identification of secondary bone reaction to the malignant cells establishes a basis for detection of malignant bone lesions. The mechanism of visualizing bone metastases by Tc99m diphosphonates or F-18 sodium fluoride is dependent on detection of the reactive (osteoblastic) response to invading tumor. In most of the cases, osteoblasts are stimulated in response to tumor, and the new bone mineral formed accumulates the radiotracer, consequently producing "hot" spots. In a fewer cases, tumor may produce a predominantly lytic reaction producing a photopenic area.

SPECT is more sensitive than planar scintigraphy; SPECT imaging identifies disease seen on CT but missed on planar scintigraphy in one-third of patients [362].

SPECT is useful in the assessment of metastatic disease because of its precise localization of vertebral involvement as well as greater sensitivity for the detection of vertebral metastases [363].

Appearance of Bone Metastases on Bone Scan

Bone scan is the most widely used modality and is the most practical and cost-effective screening technique for assessing the entire skeleton. In addition, bone scan is very sensitive in detecting the disease. However, there is a variable false-negative rate in assessing lesions in certain locations particularly in the spine and in those confined to bone marrow [364].

On bone scans, metastases have different patterns:

Typical pattern: The most common and typical pattern of bone metastases is that of multiple, randomly distributed foci of increased uptake (Fig. 5.72), usually in the axial skeleton, following the distribution of certain bone marrow

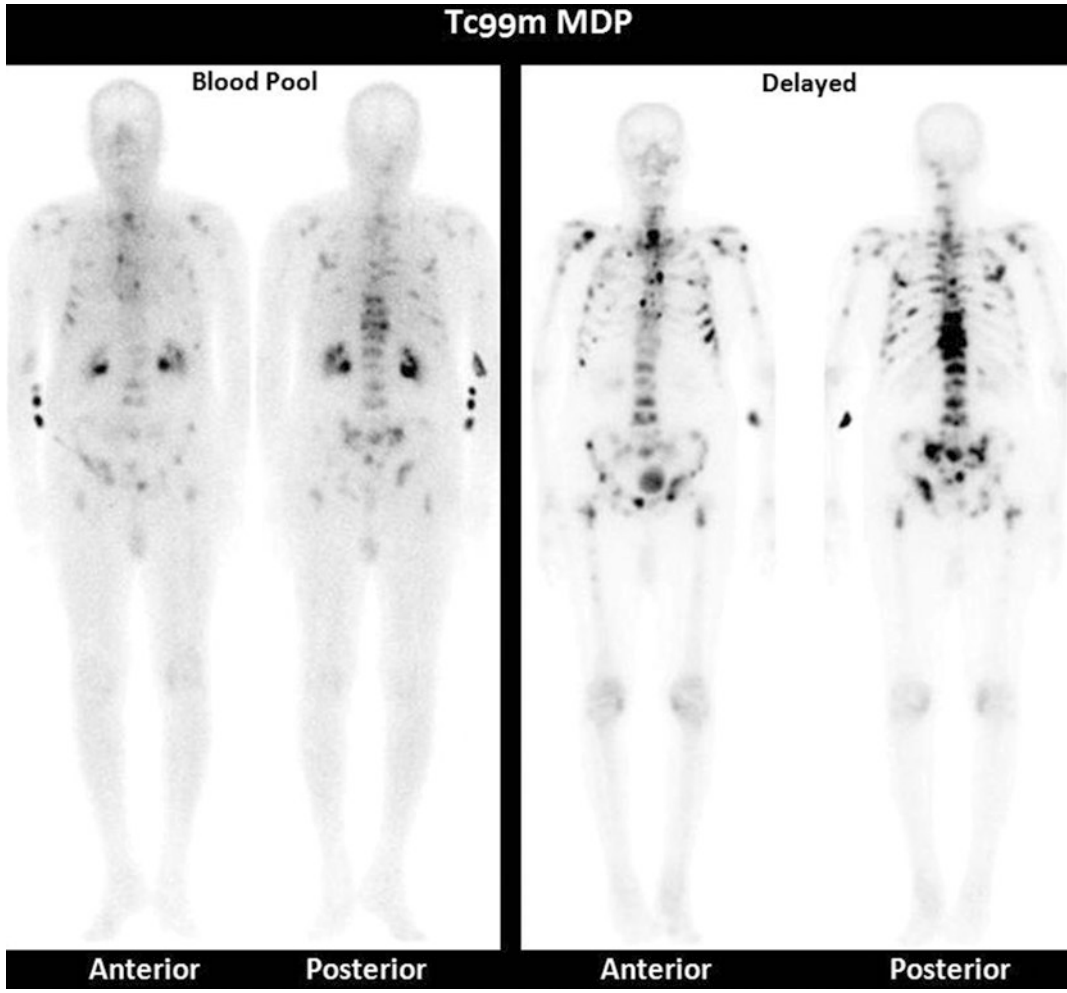

Fig. 5.72 Whole-body blood pool and delayed scans of a 77-year-old male with advanced carcinoma of the prostate. PSA 99 ng/μl. Patient was referred to rule out metastases. The scan shows the typical pattern of metastatic bone diseases of randomly distributed foci of increased uptake

including the shoulder girdle, with relatively less extensive involvement of the ribs. Multiple fractures and multifocal infection may simulate this pattern. The following hematogenously disseminated infections of bone and other pathological conditions [365] can cause a pattern that may mimic metastases:

1. Tuberculosis
2. Atypical mycobacteria
3. Coccidioidomycosis
4. Tertiary syphilis
5. Brucellosis
6. Sarcoidosis
7. Multiple fractures

Atypical patterns include:

1. Solitary lesions
   These occur in the axial and in the appendicular skeleton in a variable percentage of patients (Fig. 5.73). The incidence of malignancy in solitary lesions varies with the location. The incidence is highest in the vertebrae. These lesions are commonly asymptomatic and are not suspected clinically. Less than half

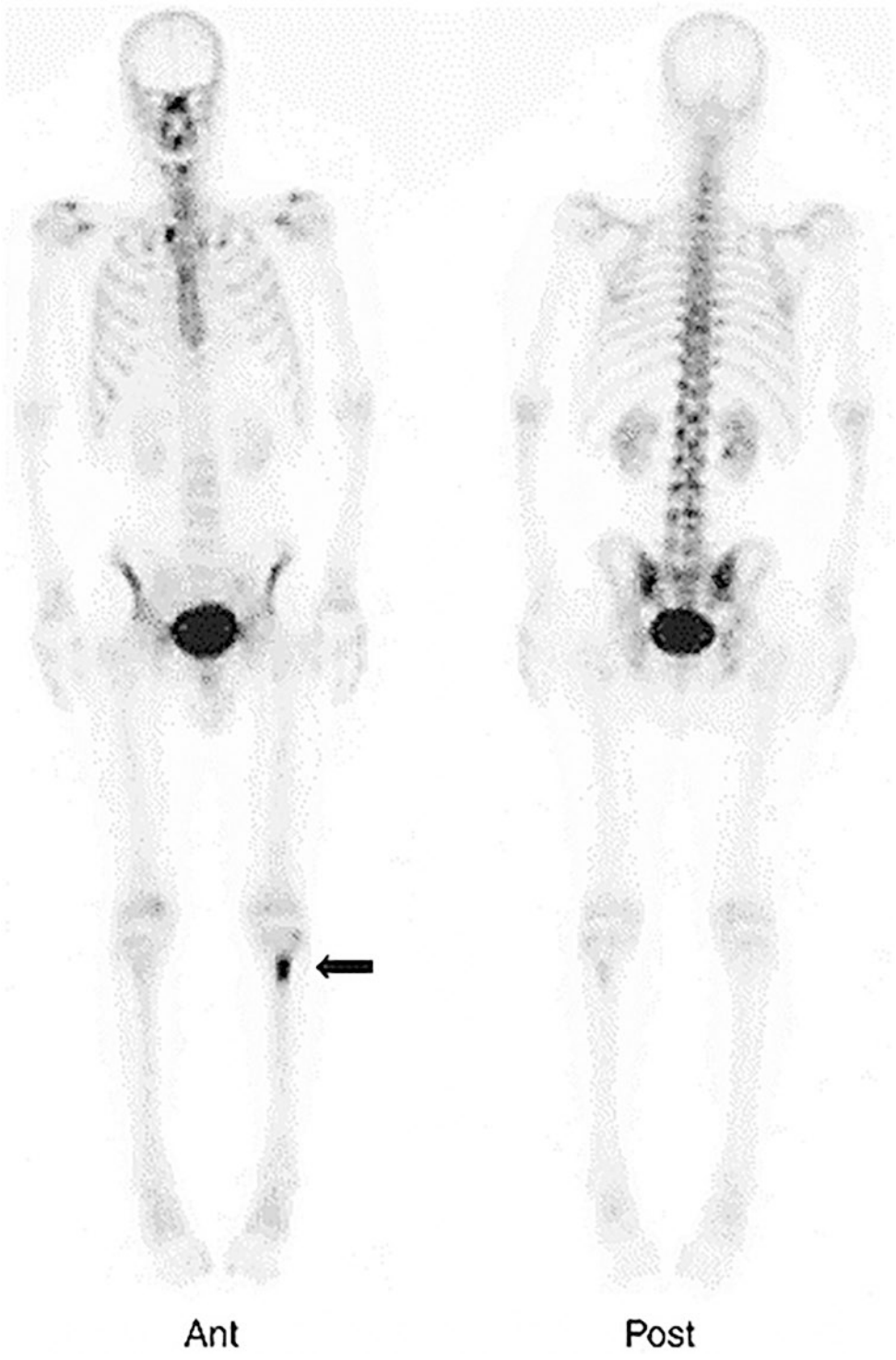

Fig. 5.73 A 63-year-old male with increased alkaline phosphatase and fever. Solitary bone lesion in the left tibia proven to be metastatic

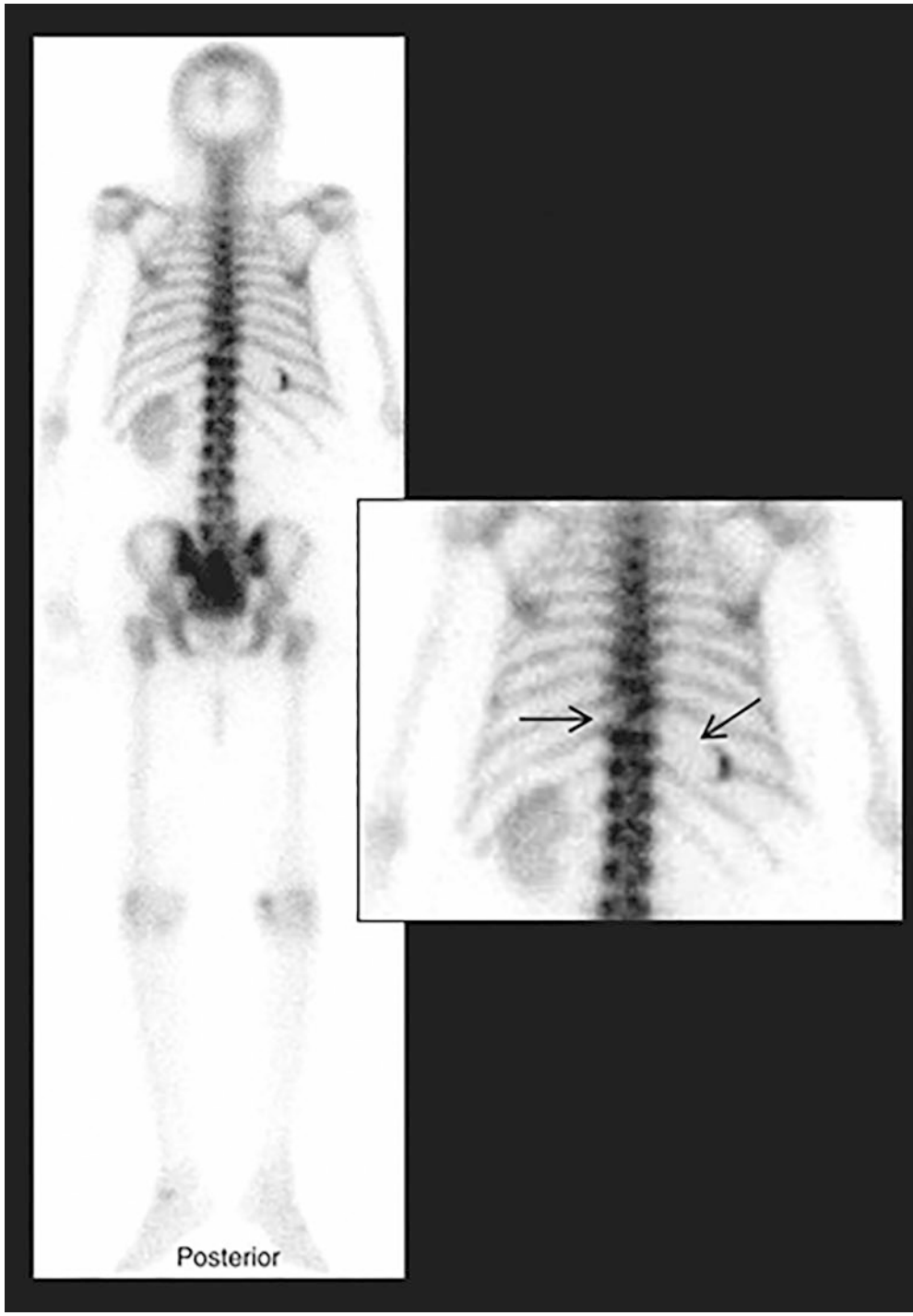

Fig. 5.74 A whole-body bone scan with a magnified image of the thoraco-lumbar region of a patient with renal cell carcinoma and status post right nephrectomy. Two old lesions are seen in the regions of the nineth thoracic vertebra and the medial part of the tenth right rib (*arrows*) representing "old" metastatic pattern that is common with certain aggressive tumors including renal cell carcinoma

of these lesions are evident on X-rays. These facts further emphasize the importance of obtaining a bone scan of the entire skeleton routinely in patients with cancer.

2. Cold lesions
   Aggressive tumors may cause cold lesions at the time of presentation (Fig. 5.74). This is seen frequently in multiple myeloma and renal cell carcinoma, although the most common pattern of multiple myeloma on bone scan is hot spots [366].
3. Equilibrium pattern
   Hot lesions may have a relatively normal appearance with time, reflecting a point of equilibrium between osteoblastic activity and the bone destruction by the tumor. It appears that skeletal lesions may evolve through increased uptake, the equilibrium phase, and then decreased uptake. The second phase can result in minimal abnormalities of focal, nonuniform, minimally increased uptake, or even near-normal patterns that can be missed on scan. This phenomenon has been observed and studied particularly in rib lesions [367].
4. Diffuse pattern
   With advanced metastatic disease, the entire axial skeleton may be involved by a load of tumor cells causing increased extraction of radiopharmaceutical. This pattern may be interpreted as normal depending on the display intensity and should also be differentiated from other causes of diffusely increased uptake in the skeleton (superscan) such as hyperparathyroidism and other metabolic bone diseases (Fig. 5.75) and Paget's disease (Table 5.28).
   A superscan secondary to metastases shows increased uptake that is usually confined to the axial skeleton, while in case of metabolic disorders, it also involves the skull, mandible, sternum, and metaphyses of long bones. Preferential increase of uptake at the osteochondral junctions and joint renal activity are additional features of metabolic disease on assorted superscans.
5. Flare pattern
   Therapy producing healing at the tumor site results in several pathological changes as seen on scintigraphy. As the term healing implies, inflammatory changes with increasing blood flow occur early after therapy. Since the tumors are in bones, reactive bone formation increases with successful therapy [368].
   Following radiation therapy, there is increased activity on blood pool images, and delayed images may be seen early on due to inflammatory reaction. Later, these changes disappear, and decreased uptake is typically seen. It should be noted that the effects of therapeutic radiation depend on the time after treatment and the dose.
   Follow-up scans are more frequently obtained after chemotherapy than after radiation therapy, and the changes that are seen continue for longer periods. Early increased activity on blood pool and delayed images is noted, followed by decreasing activity that can be normalized. Increasing activity may be significant and continue for several months even with successful therapy. This phenomenon may include the appearance of small, new lesions due to healing at the sites of preexisting small or cold lesions that were not resolved on earlier scans.
6. Symmetrical pattern
   Occasionally, symmetrical uptake due to metastases is seen in certain tumors as neuroblastoma and in case of bone marrow involvement in leukemia. This pattern is particularly seen in distal femoral and proximal tibial metaphyses.
   Table 5.29 summarizes correlation between common pathologic changes of bone and the scintigraphic findings on bone scan.

Imaging Metastases with Other Modalities

MRI has been found to detect more vertebral metastases than bone scan. F18 Sodium Fluoride and FDG PET are increasingly evaluated for detection of bone metastases (Fig. 5.76) and was shown to be more sensitive than bone scan [369–372].

Combined Sodium fluoride and FDG PET has also been used and has added benefit. In a comparative study, the diagnostic accuracy of whole-

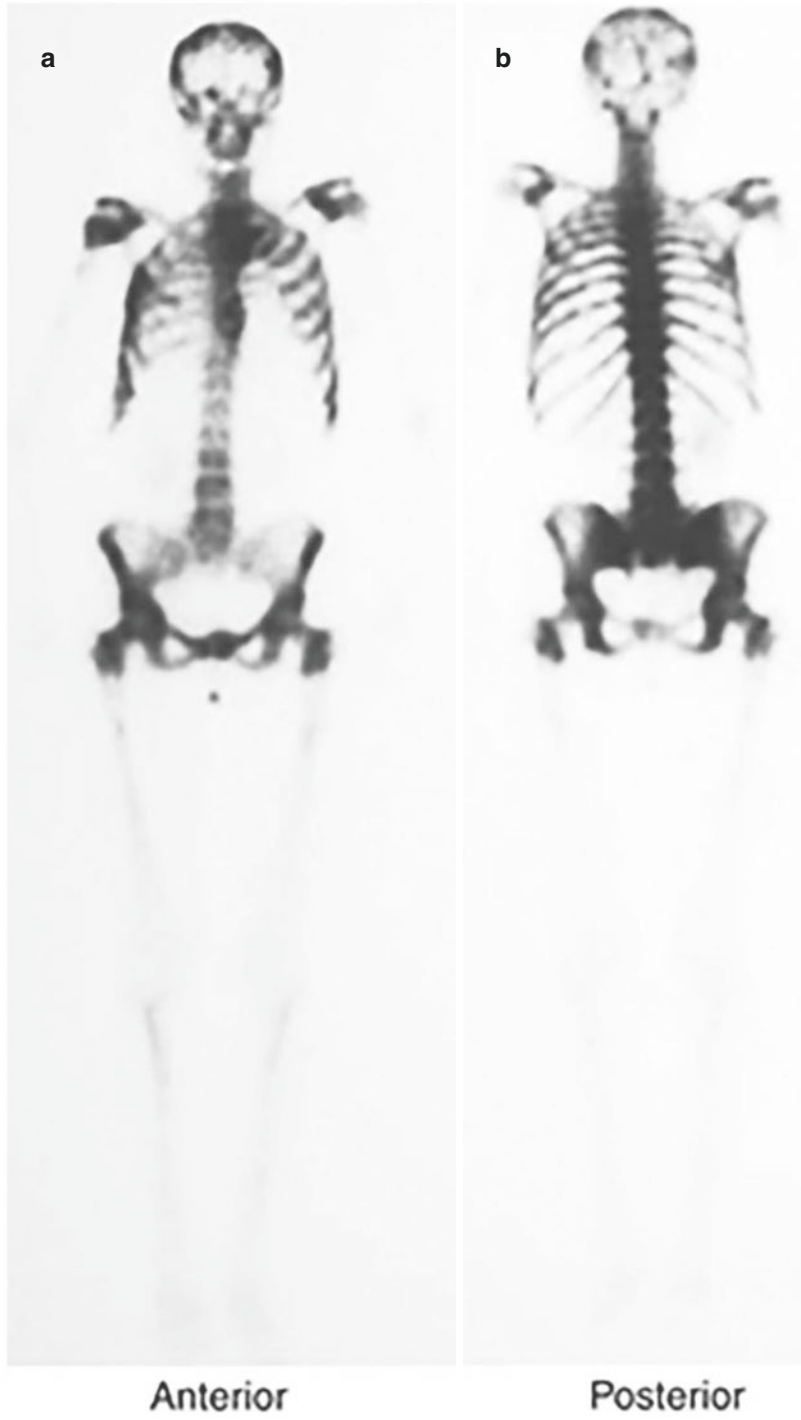

Fig. 5.75 (**a**) A whole-body bone scan illustrating the pattern of diffuse metastases (superscan). Note that the appendicular bones are essentially not involved compared to the pattern of superscan secondary to metabolic bone disease as illustrated in a patient with renal failure (**b**). In this case the increased uptake extends to appendicular bones even distally

Table 5.28 Causes of diffuse increase of radiopharmaceutical uptake by the skeleton

1. Advanced metastatic bone disease
2. Metabolic bone disease
Primary and secondary hyperparathyroidism
Hypertrophic osteoarthropathy
Renal osteodystrophy
Paget's disease
3. Others
Acromegaly
Aplastic anemia
Hyperthyroidism
Leukemia
Waldenström's macroglobulinemia
Myelofibrosis
Hypervitaminosis D

Table 5.29 Scintigraphic pathological correlation

Pathological etiology	Scintigraphic pattern on bone scan
Osteoblastic response	Increased uptake
Increased vascularity	Increased flow and blood pool activity
Angiogenesis	Increased blood pool activity
Bone destruction (infarction, rapidly growing aggressive metastasis)	Cold areas
Large destructive lesion with a rim of new bone formation	Doughnut pattern
Paget's disease, some primary or metastatic tumors	Bone expansion
Arthritis, reflex sympathetic dystrophy	Periarticular increased uptake
Equilibrium of bone destruction and bone formation	Near-normal appearance

body MR imaging, bone scintigraphy, and FDG-PET for the detection of bone metastases in children was determined. Twenty-one patients exhibited 51 bone metastases. Sensitivities for the detection of bone metastases were 90, 82, and 71% for FDG-PET, whole-body MR imaging, and bone scintigraphy, respectively. False-negative lesions were different for the three imaging modalities, mainly depending on lesion location. Most false-positive lesions were seen with FDG-PET [318]. Another study of 56 patients with malignant lymphoma also showed that FDG-PET is more sensitive but, in contrast, more specific than bone scintigraphy []. It is important to remember that PET provides direct visualization of metastases, while bone scan visualizes the reactive bone in response to the presence of metastases. FDG-PET can help differentiate flare from progression and evaluate the tumor status when bone scan is stable [373] (Figs. 5.77 and 5.78).

The use of 18F as the fluoride ion has increased. 18F-sodium fluoride (NaF) PET/CT is used for bone imaging with some established indications. The uptake mechanism of 18F-fluoride resembles that of ^{99m}Tc-methylene diphosphonate (MDP), with better pharmacokinetic characteristics including faster blood (Fig. 5.79) clearance and twofold higher uptake in bone. After diffusing into the extracellular fluid of bone, the fluoride ion is exchanged for a hydroxyl group in the bone crystal and forms fluorapatite [374, 375].

Increased 18F-fluoride uptake may be detected in both sclerotic and lytic lesions. In general, 18F-fluoride is best for blastic lesions. The minimal osteoblastic activity accompanying a lytic lesion, which may not be identified on ^{99m}Tc-MDP bone scan, may be readily identified with 18F-fluoride PET imaging.

^{18}F-fluoride, however, shows also increased uptake in benign bone lesions including degenerative change, fractures, Paget's disease, enchondroma, and osteoma. The use of low-dose CT in conjunction with 18F-fluoride PET improves sensitivity and specificity and improves the ability to distinguish benign from malignant lesions [376–378].

PET/CT studies are valuable in evaluation of metastatic bone disease (Fig. 5.80) and in following patients with bone-dominant metastases. However, there is no definite evidence yet that 18F-fluoride PET is more sensitive in detecting bone metastases to justify replacing conventional bone scan.

PET imaging with 18F-fluoro-2-deoxyglucose (18F-FDG) has also been used to identify bone metastases. 18F-FDG is directly taken by tumor cells and consequently detects cortical and marrow involvement. This indicates that this radiotracer will be best for lytic lesions. Since 18F-FDG-PET has low uptake in normal red marrow, it allows for early detection of malignant

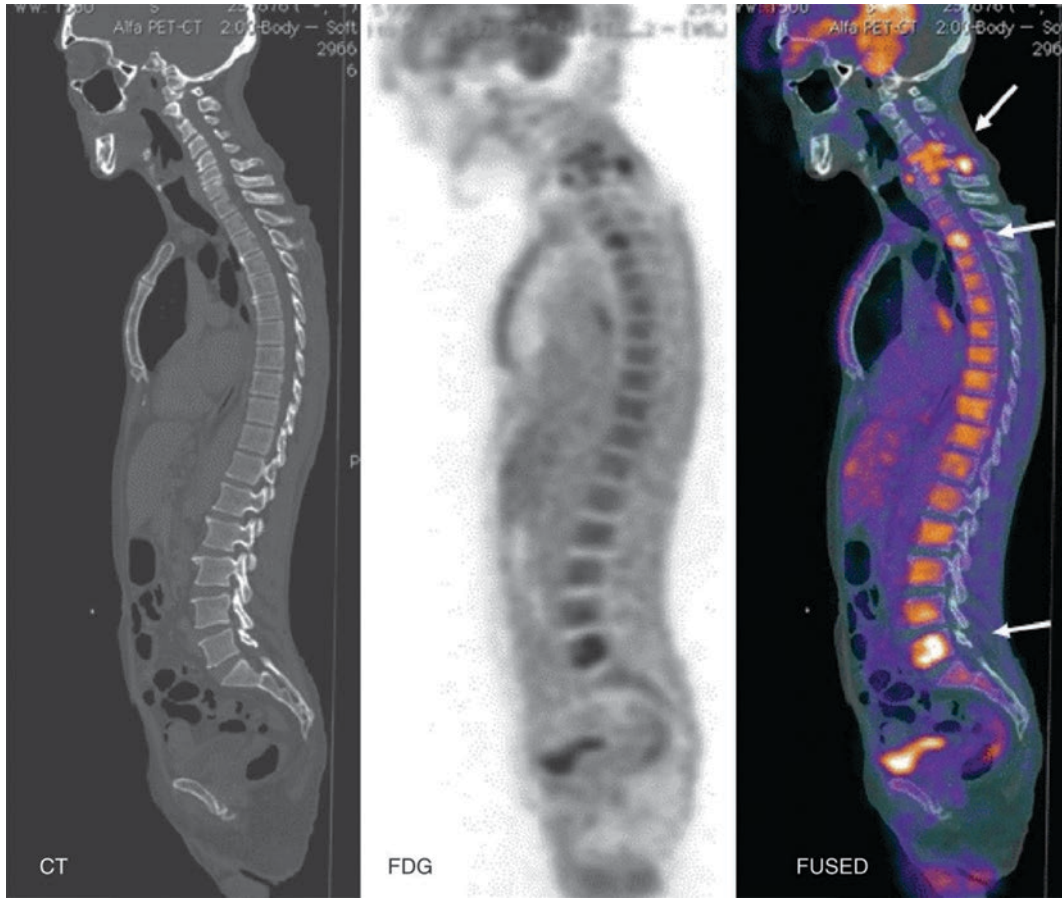

Fig. 5.76 F-18 PET/CT study illustrating multiple hypermetabolic foci in the cervical, thoracic, and lumbar spine representing multiple vertebral metastases. (Courtesy of Prof.SherifElrifae with thanks)

bone marrow involvement preceding detection of bone metastases by bone scan using diphosphonates. 18F-FDG-PET can detect all three types of skeletal metastases including lytic, blastic, and mixed, but preferably 18F-FDG-PET is more sensitive for detection of lytic rather than osteoblastic metastases which are usually less aggressive lesions [327, 379–381].

Cook et al. found 18F-FDG-PET has slightly decreased sensitivity for predominantly osteoblastic lesions but has higher overall sensitivity due to more frequent occurrence of osteolytic bone metastases [382].

Compared to ^{99m}Tc-MDP and 18F-fluoride, 18F-FDG-PET is found to be more sensitive for the detection of bone metastases secondary to lung cancer. For metastases of breast cancer, 18F-FDG appears to be more sensitive for lytic lesions, but less sensitive for sclerotic ones. Conversely, 18F-FDG-PET is also less sensitive in detection of bone metastases from prostate cancer. Accordingly, posttreatment studies which often result in sclerotic lesions are negative with 18F-FDG imaging because they have healed and no longer have viable tumor [383].

FDG-PET/CT was found to have a very high PPV of 98% in the evaluation of bone malignancy when the two portions of the examination are in agreement and when bone window of CT is used. It also can help better differentiate whether FDG-avid lesions are truly located within bone vs. adjacent soft tissue [384, 385].

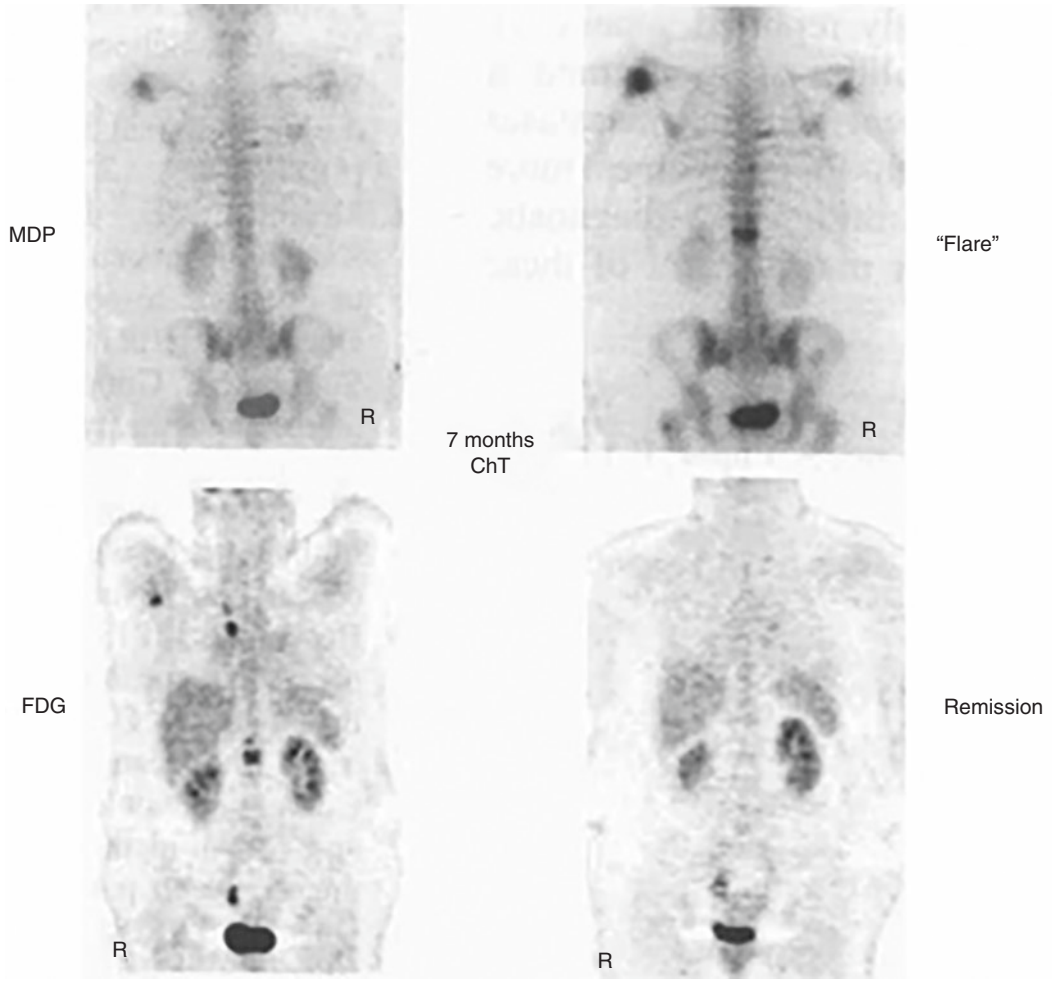

Fig. 5.77 A 49-year-old woman with breast cancer (N1M0) who had undergone mastectomy and axillary lymph node dissection on the right side. The patient had no evidence of disease for 3 years. She presented with an CA 15.3 tumor marker. BS showed uptake in the left humeral head suspicious of necrosis on the basis of long-term corticotherapy and nonspecific uptake in the spine (*top left*). PET showed intense FDG uptake in both the humeral head and the seventh right costovertebral junction and first lumbar vertebra (*bottom left*). The patient was treated with chemotherapy. Seven months after treatment, BS showed persistent uptake in the left humeral head with increased activity in the right humeral head, seventh right costovertebral junction, and first lumbar vertebra (*top right*). PET scan showed resolution of the previous lesions (*bottom right*). On the basis of the PET findings, the results on BS should be interpreted as representing a flare phenomenon. (From [373] with permission)

Most recently fluorocholine (18F) (FCH) PET/CT seems to be promising in detection of bone metastases in patients with prostate cancer. Several clinical studies have found increased sensitivity of combined NaF/FDG-PET/CT for detection of osseous lesions when compared with separate NaF PET/CT and FDG-PET/CT [386–390].

Several tumor-targeted radiotracers have been introduced for molecular imaging of bone metastases particularly 68Ga PSMA, which is very useful in the detection and follow-up of prostatic cancer metastases [391].

Table 5.30 summarizes the role of PET in primary and metastatic bone disease.

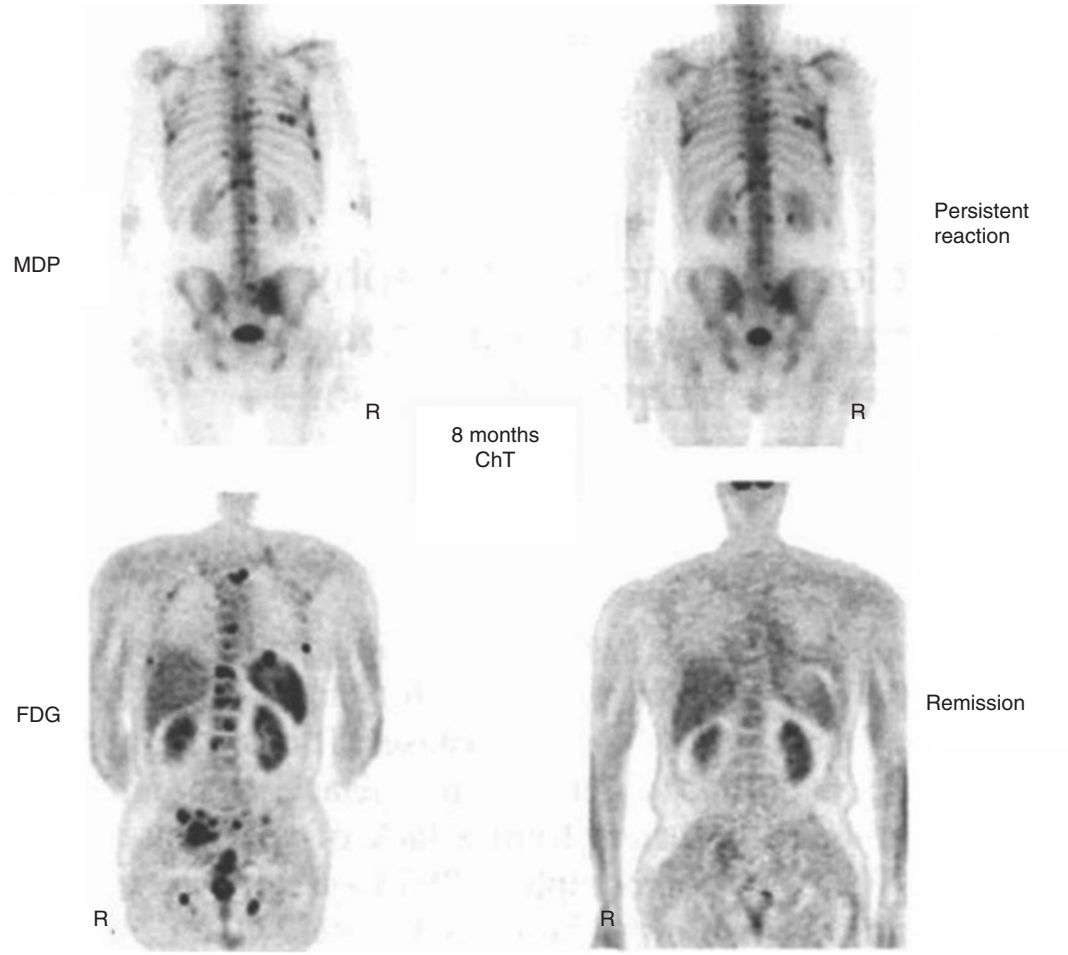

Fig. 5.78 A 55-year-old man recently diagnosed with non-small right lung cell cancer. BS (*top left*) and PET (*bottom left*) in the staging showed multiple bone metastases, with a different distribution, probably due to the lytic/blastic behavior. The patient was treated with chemotherapy. Eight months after treatment, BS remained similar (*top right*). PET scan showed resolution of previous lesions (*bottom right*). On the basis of the PET findings, BS results should be interpreted as representing a persistent bone reaction, not active metastatic disease. (Figure printed with permission from [373])

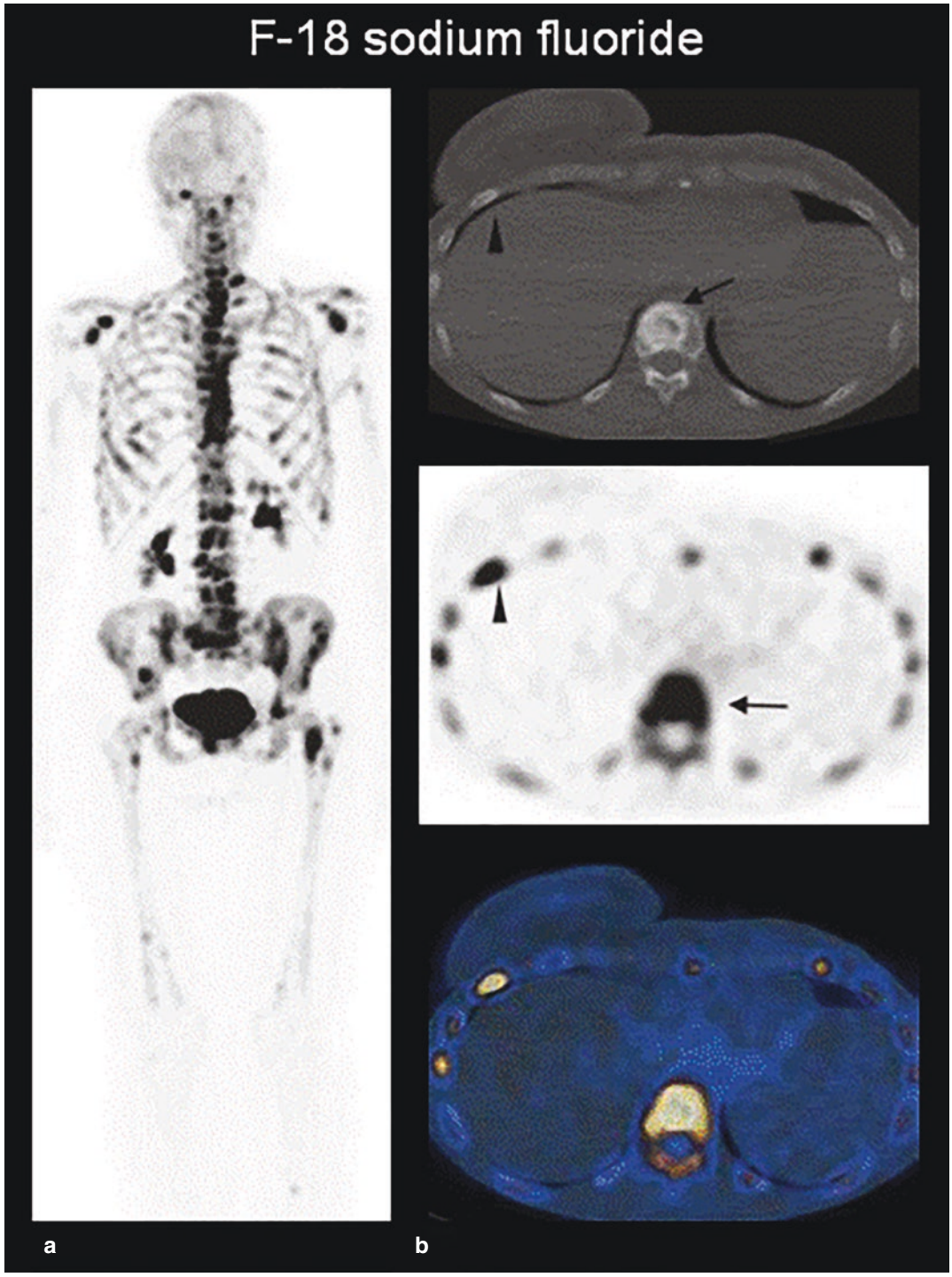

Fig. 5.79 F-18 sodium fluoride PET/CT whole-body MIP (**a**) and selected transaxial CT, PET, and PET/CT fusion images of the chest (**b**) showing increased uptake at the vertebral body (arrow) and rib (arrowhead) corresponding to osteoblastic lesions on the CT images

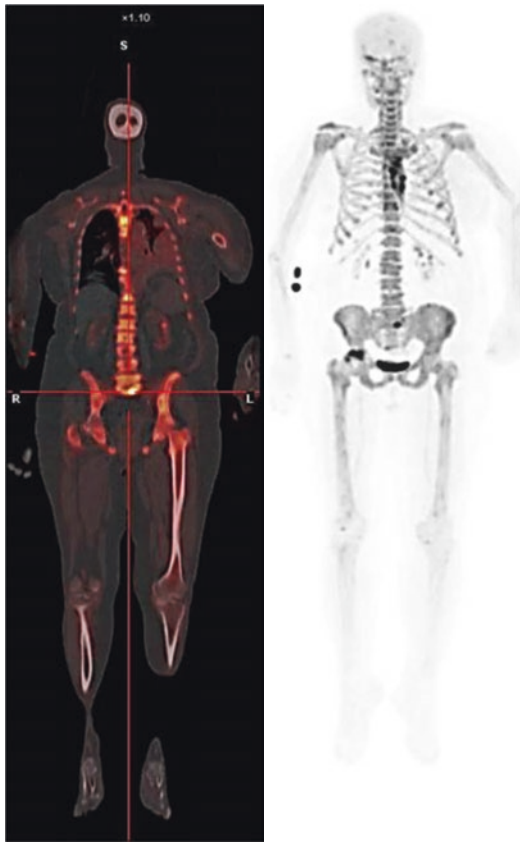

Fig. 5.80 F-18 sodium fluoride bone PET study in a patient with lung cancer illustrating multiple metastases with excellent resolution

Table 5.30 Summary of the role of PET in malignant bone disease

Detection of metastatic bone disease
Evaluation of response to therapy of primary or metastatic bone disease
Detection of recurrence of primary bone malignancies
Early differentiation of progression and flare of metastatic bone disease seen on bone scan
Evaluation of solitary bone lesion

References

1. Mourad LA (1998) structure and function of the musculoskeletal. In: McCane KL, Huether SE (eds) pathophysiology, 3rd edn. Mosby, Philadelphia, pp 1405–1434.
2. Föger-Samwald U, Dovjak P, Azizi-Semrad U, Kerschan-Schindl K, Pietschmann P (2020) Osteoporosis: pathophysiology and therapeutic options. EXCLI J 19:1017–1037. https://doi.org/10.17179/excli2020-2591
3. Clarke BL, Khosla S (2010) Physiology of bone loss. Radiol Clin North Am 48:483–495
4. Pacifici R (2018) Bone remodeling and the microbiome. Cold Spring Harb Perspect Med 2(8):a031203. https://doi.org/10.1101/cshperspect.a031203
5. McCabe L, Britton RA, Parameswaran N (2015) Prebiotic and probiotic regulation of bone health: role of the intestine and its microbiome. Curr Osteoporos Rep 13(6):363–371
6. Watson EC, Adams Ralf H (2018) Biology of bone: the vasculature of the skeletal system. Cold Spring Harb Perspect Med 8:a031559
7. Tondevold E, Eliasen P (1982) Blood flow rates in canine cortical and cancellous bone measured with TC 99 m, labeled human albumin microspheres. Acta Orthop Scand 53:7–11
8. McCarthy EF (1997) Histopathologic correlates of positive bone scan. Semin Nucl Med 27:309–320
9. Ralston SH (2017) Bone structure and metabolism. Medicine 45(9):560–564
10. Benova A, Tencerova M (2020) Obesity-induced changes in bone marrow homeostasis. Front Endocrinol 11:294. https://doi.org/10.3389/fendo.2020.00294
11. Tencerova M, Kassem M (2016) The bone marrow-derived stromal cells: commitment and regulation of adipogenesis. Front Endocrinol 7:127
12. Muruganandan S, Govindarajan R, Sinal CJ (2018) Bone marrow adipose tissue and skeletal health. Curr Osteopor Rep 16:434–442
13. Dalinka MK, Aronchick JM, Haddad JG (1983) Paget's disease. Orthop Clin North Am 4:3–19
14. Vogler JB, Murphy WA (1988) Bone marrow imaging. Radiology 168:679–693
15. Bonakdar-pour A, Gaines VD (1983) The radiology of osteomyelitis. Orthop Clin North Am 14:21–37
16. Francis MD, Martodam RR (2018) Chemical, biochemical, and medicinal properties of the diphosphonates. In: The role of phosphonates in living systems. CRC Press, Boca Raton, pp 55–96
17. Francis MD, Slough CL, Tofe AJ, Silberstein EB (1976) Factors affecting uptake and retention of technetium-99 m-diphosphonate and technetium 99 m pertechnetate in osseous, connective and soft tissues. Cacif Tissue Res 20:303–311
18. Jaramillo D (2011) Infection: musculoskeletal. Pediatr Radiol 41(suppl 1):S127–S134
19. Arnold SR, Elias D, Buckingham SC, Thomas ED, Novais E, Arkader A, Howard C (2006) Changing patterns of acute hematogenous osteomyelitis and septic arthritis: emergence of community-associated methicillin-resistant Staphylococcus aureus. J Pediatr Orthop 26:703–708
20. Gafur OA, Copley LA, Hollmig ST, Browne RH, Thornton LA, Crawford SE (2008) The impact of the current epidemiology of pediatric musculoskeletal infection on evaluation and treatment guidelines. J Pediatr Orthop 28:777–785
21. Haas DW, McAndrew M (1996) Bacterial osteomyelitis in adults: evolving considerations in diagnosis and treatment. Am J Med 101:550–561

22. Cierny G, Mader JT, Pennick H (1985) A clinical staging system of adult osteomyelitis. Contemp Orthop 10:17–37
23. Mandell JC, Khurana B, Smith JT et al (2018) Osteomyelitis of the lower extremity: pathophysiology, imaging, and classification, with an emphasis on diabetic foot infection. Emerg Radiol 25:175–188
24. Hofstee et al (2020) Current concepts of osteomyelitis from pathologic mechanisms to advanced research methods. Am J Pathol 190:1151–1163. https://doi.org/10.1016/j.ajpath.2020.02.007
25. Calhoun JH, Manring MM (2005) Adult osteomyelitis. Infect Dis Clin North Am 19(4):765–786
26. Torda AJ, Gottlieb T, Bradbury R (1995) Pyogenic vertebral osteomyelitis: analysis of 20 cases and review. Clin Infect Dis 20:320–328
27. Song KS, Ogden JA, Ganey T, Guidera KT (1997) Contiguous discitis and osteomyelitis in children. J Pediatr Orthop 17:470–477
28. Babinchak TJ, Riley DK, Rotheram EB (1997) Pyogenic vertebral osteomyelitis of the posterior elements. Clin Infect Dis 25:221–224
29. Lipsky BA, Berendt AR, Cornia PB, Pile JC, Peters EJ, Armstrong DG et al (2012) Infectious Diseases Society of America clinical practice guideline for the diagnosis and treatment of diabetic foot infections. Clin Infect Dis 54(12):e132–e173
30. Jaramillo D, Dormans JP, Delgado J, Laor T, St Geme III, J. W. (2017) Hematogenous osteomyelitis in infants and children: imaging of a changing disease. Radiology 283:629–643
31. Schwartz GS, Berenyi MR, Siegel MW (1969) Atrophic arthropathy and diabetic neuritis. Am J Roentgenol Radium Ther Nucl Med 106:523–529
32. Lee YJ, Sadigh S, Mankad K, Kapse N, Rajeswaran G (2016) The imaging of osteomyelitis. Quant Imaging Med Surg 6(2):184–198
33. Arıcan P, Okudan B, Şefizade R, Naldöken S (2019) Diagnostic value of bone SPECT/CT in patients with suspected osteomyelitis. Mol Imaging Radionucl Ther 28:89–95
34. Elgazzar AH, Abdel-Dayem HM (1999) Imaging skeletal infections: evolving considerations. In: Feeman LM (ed) Nuclear medicine annual. Lippincott/Williams and Wilkins, Philadelphia, pp 157–191
35. Elgazzar AH, Abdel-Dayem HM, Clark J, Maxon HR (1995) Multimodality imaging of osteomyelitis. Eur J Nucl Med 22:1043–1063
36. Issa K, Diebo BG, Faloon M, Naziri Q, Pourtaheri S, Paulino CB, Emami A (2018) The epidemiology of vertebral osteomyelitis in the United States from 1998 to 2013. Clin Spine Surg 31(2):E102–E108
37. Mete B, Kurt C, Yilmaz MH, Ertan G, Ozaras R, Mert A, Tabak F, Ozturk R (2012) Vertebral osteomyelitis: eight years' experience of 100 cases. Rheumatol Int 32:3591–3597
38. Zimmerli W (2010) Clinical practice. Vertebral osteomyelitis. N Engl J Med 362(11):1022–1029
39. Batson OV (1967) The vertebral system of veins as a means for cancer dissemination. Prog Clin Cancer 3:1–18
40. Bamberger DM, Daus GP, Gerding DN (1987) Osteomyelitis in the feet of diabetic patients: long term results, prognostic factors, and the role of antimicrobial and surgical therapy. Am J Med 83:653–660
41. Schwartz GS, Berenyi MR, Siegel MW (1969) Atrophic arthropathy and diabetic neuritis. Am J Roentgenol Radium TherNucl Med 106:523–529
42. Horwitz SH (1993) Diabetic neuropathy. Clin Orthop 296:78–85
43. Gold RH, Tang DTF, Crim JR, Seeger LL (1995) Imaging the diabetic foot. Skeletal Radiol 24:563–571
44. Giurato L, Meloni M, Izzo V, Uccioli L (2017) Osteomyelitis in diabetic foot: a comprehensive overview. World J Diabetes 8:135–142
45. Malhotra R, Chan CS-Y, Nather A (2014) Osteomyelitis in the diabetic foot. Diabetic Foot Ankle 5:24445
46. Mandell GA (1996) Imaging in the diagnosis of musculoskeletal infections in children. Curr Probl Pediatr 26:218–237
47. Rand JA (1995) Preoperative planning for total knee arthroplasty. In: Callaghan JJ, Dennis DA, Paprosky WG, Rosenberg AG (eds) Orthopedic knowledge update. Hip and knee reconstruction. American Academy of Orthopedic Surgeons, Rosemont
48. American Academy of Orthopaedic Surgeons (1995) Proceedings of the American Academy of Orthopaedic Surgeons. AAOS, Rosemont, pp 255–263
49. Griffiths HJ (1995) Orthopedic complications. Radiol Clin North Am 33:401–410
50. Seabald JE, Nepola JV (1999) Imaging techniques for evaluation of postoperative orthopedic infections. Q J Nucl Med 43:21–28
51. Harris WH, Sledge CB (1990) Total hip and total knee replacement (part I). N Engl J Med 323:725–731
52. Johnson JA, Christle MJ, Sandler MP, Parks PF Jr, Horma L, Kayle JJ (1988) Detection of occult infection following total joint arthroplasty using sequential technetium-99 m HDP bone scintigraphy and Indium-111 WBC imaging. J Nucl Med 29:1347–1353
53. Hendrix RW, Anderson TM (1981) Arthrographic and radiologic evaluation of prosthetic joints. Radiol Clin North Am 19:349–364
54. Griffiths HJ, Lovelock JE, Evarts CM (1984) The radiology of total hip replacement. Skeletal Radiol 12:1–11
55. Calvo C, Núñez E, Camacho M, Clemente D, Fernández-Cooke E et al (2001) Epidemiology and management of acute, uncomplicated septic arthritis and osteomyelitis. Pediatr Infect Dis J 35:1288–1293
56. Manz N, Krieg AH, Heininger U, Ritz N et al (2018) Evaluation of the current use of imaging modalities and pathogen detection in children with acute osteomyelitis and septic arthritis. Eur J Pediatr 177:1071–1080
57. Barton LL, Dunkle LM, Habib FH (1987) Septic arthritis in childhood: a 13-year review. Am J Dis Child 141:898–900

58. Mathews CJ, Weston VC, Jones A, Field M, Coakley G (2012) Bacterial septic arthritis in adults. Lancet 375(9717):846–855
59. Silberstein EB, Elgazzar AH, Fernandez-Uloa M, Nishiyama H (1996) Skeletal scintigraphy in non-neoplastic osseous disorders. In: Henkin RE, Bles MA, Dillehay GL, Halama JR, Karesh SM, Wagner PH, Zimmer AM (eds) Textbook of nuclear medicine. Mosby, New York, pp 1141–1197
60. Hofmann SR, Schnabel A, Rösen-Wolff A, Morbach H, Girschick HH, Hedrich CM (2016) Chronic nonbacterial osteomyelitis: pathophysiological concepts and current treatment strategies. J Rheumatol 43:1956–1964. https://doi.org/10.3899/jrheum.160256]
61. Waldvogel FA, Medoff G, Swartz MN (1970) Osteomyelitis: a review of clinical features, therapeutic considerations and unusual aspects, part I. N Engl J Med 282:198–206
62. Paliwal AK, Sahdev R, Deshwal A, Ram B (2021) Role of ultrasound in the diagnosis of paediatric acute osteomyelitis. J Ultrasonogr 21(84):34
63. Llewellyn A, Jones-Diette J, Kraft J, Holton C, Harden M, Simmonds M (2019) Imaging tests for the detection of osteomyelitis: a systematic review. Health Technol Assess 23:1–128
64. Kan JH, Hilmes MA, Martus JE, Yu C, Hernanz-Schulman M (2008) Value of MRI after recent diagnostic or surgical intervention in children with suspected osteomyelitis. AJR Am J Roentgenol 191:1595–1600
65. Liu C, Bayer A, Cosgrove SE, Daum RS, Fridkin SK et al (2011) Clinical practice guidelines by the infectious diseases society of america for the treatment of methicillin-resistant Staphylococcus aureus infections in adults and children: executive summary. Clin Infect Dis. 52:285–292. https://doi.org/10.1093/cid/cir034. PMID: 21217178
66. Hatzenbuehler J, Pulling TJ (2011) Diagnosis and management of osteomyelitis. Am Fam Physician 84:1027–1033
67. Glaudemans AWJM, Jutte PC, Cataldo MA et al (2019) Consensus document for the diagnosis of peripheral bone infection in adults: a joint paper by the EANM, EBJIS, and ESR (with ESCMID endorsement). Eur J Nucl Med Mol Imaging 46:957–970
68. Handmaker H, Leonards R (1976) The bone scan in inflammatory osseous disease. Semin Nucl Med 6:95–105
69. Connolly LP, Connolly SA, Drubach LA, Jaramillo D, Treves ST (2002) Acute hematogenous osteomyelitis of children: assessment of skeletal scintigraphy-based diagnosis in the era of MRI. J Nucl Med 43:1310–1316
70. Tuson GE, Hoffman EB, Mann MD (1994) Isotope bone scanning for acute osteomyelitis and septic arthritis in children. J Bone Joint Surg [Br] 76B:306–310
71. Handmaker H, Giammona ST (1984) Improved early diagnosis of acute inflammatory skeletal – articular diseases in children: a two radiopharmaceutical approach. Pediatrics 73:661–669
72. Sfakianakis GN, Scoles P, Welch M et al (1978) Evolution of the bone imaging findings in osteomyelitis. J Nucl Med 19:706
73. Pennington WT, Mott MP, Thometz JG, Sty JR, Metz D (1999) Photopenic bone scan osteomyelitis: a clinical perspective. J PediatrOrthop 19:695–698
74. Lauri C, Tamminga M, Glaudemans AW, Orozco LEJ, Erba PA, Jutte PC et al (2017) Detection of osteomyelitis in the diabetic foot by imaging techniques: a systematic review and meta-analysis comparing MRI, white blood cell scintigraphy, and FDG-PET. Diabetes Care 40(8):1111–1120
75. Grerand S, Dolan M, Laing P, Bird M, Smith ML, Klenerman L (1996) Diagnosis of osteomyelitis in neuropathic foot ulcers. J Bone Joint Surg [Br] 78B:51–55
76. Ezuddin S, Yuille D, Spiegelhoff D (1992) The role of dual bone and WBC scan imaging in the evaluation of osteomyelitis and cellulitis using both planar and SPECT imaging. J Nucl Med 33:839
77. Johnson JE, Kennedy EJ, Shereff MJ, Patel NC, Collier BD (1996) Prospective study of bone, In-111 labeled white blood cell and gallium scanning for the evaluation of osteomyelitis in the diabetic foot. Foot Ankle Int 17:10–16
78. Hakki S, Harwood SJ, Morrissey MA et al (1997) Comparative study of monoclonal antibody scan in diagnosing orthopedic infection. Clin Orthop 335:275–285
79. Plate A, Weichselbaumer V, Schüpbach R, Fucentese SF, Berli M, Hüllner M, Achermann Y (2020) Diagnostic accuracy of 99mTc-antigranulocyte SPECT/CT in patients with osteomyelitis and orthopaedic device-related infections: a retrospective analysis. Int J Infect Dis 91:79–86
80. Loessel C, Mai A, Starke M, Vogt D, Stichling M, Willy C (2021) Value of antigranulocyte scintigraphy with Tc-99m-sulesomab in diagnosing combat-related infections of the musculoskeletal system. BMJ Mil Health 167:8–17
81. Koort J, Makinen TJ et al (2004) Comparative 18F-FDG PET of experimental S. aureus osteomyelitis and normal bone healing. J Nucl Med 45:1406–1411
82. Kumar V, Boddeti DK (2013) (68) Ga-radiopharmaceuticals for PET imaging of infection and inflammation. Recent Results Cancer Res 194:189–219
83. Lipsky BA, Aragon-Sanchez J, Diggle M et al (2016) IWGDF guidance on the diagnosis and management of foot infections in persons with diabetes. Diabetes Metab Res Rev 32(suppl 1):S45–S74
84. Newman LG, Waller J, Palestro CJ, Schwantz M, Klein MJ, Hermann G, Harrington E, Harrington M, Roman SH, Stagnaro-Green A (1991) Unsuspected osteomyelitis in diabetic foot ulcers: diagnosis and monitoring by leukocyte scanning with In-111 oxyquinoline. JAMA 266:1246–1251
85. Palestro CJ, Mehta HH, Patel M, Freeman SJ, Harrington WN, Tomas MB, Marwin SE (1998)

Marrow versus infection in Charcot joint: indium-111 leukocyte and technetium 99 m sulfur colloid scintigraphy. J Nucl Med 39:349–350
86. Tailji S, Yacoub TY, Abdella N, Albunni A, Mahmoud A, Doza B, Loutfi I, Al-Za'abi K, Heiba S, Elgazzar A (1999) Optimization of simultaneous dual In-111 labeled leukocytes (WK)and Tc-99 m MDP bone scans in diabetic foot. Eur J Nucl Med 26:1201
87. Poirier JY, Garin E, Derrien C, Devillers A, Moisan A, Bourguet P, Maugendre D (2002) Diagnosis of osteomyelitis in the diabetic foot with a 99mTc-HMPAO leucocyte scintigraphy combined with a 99mTc-MDP bone scintigraphy. Diabetes Metab 28:485–490
88. Erdman WA, Buethe J, Bhore R, Ghayee HK, Thompson C, Maewal P, Anderson J, Klemow S, Oz OK (2012) Indexing severity of diabetic foot infection with 99mTc-WBC SPECT/CT hybrid imaging. Diabetes Care 35:1826–1831
89. Heiba S, Kolker D, Ong L, Sharma S, Travis A, Teodorescu V, Ellozy S, Kostakoglu L, Savitch I, Machac J (2013) Dual-isotope SPECT/CT impact on hospitalized patients with suspected diabetic foot infection: saving limbs, lives, and resources. Nucl Med Commun 34:877–884
90. Filippi L, Uccioli L, Giurato L, Schillaci O (2009) Diabetic foot infection: usefulness of SPECT/CT for 99mTc-HMPAO-labeled leukocyte imaging. J Nucl Med 50(7):1042–1046
91. Newman LG, Waller J, Palestro CJ, Hermann G, Klein MJ, Schwatrz M, Harrington E et al (1992) Leukocyte scanning with 111-In is superior to magnetic resonance imaging in diagnosis of clinically unsuspected osteomyelitis in diabetic foot ulcers. Diabetes Care 15:1527–1530
92. Cook TA, Rahim N, Simpson HC, Galland RB (1996) Magnetic resonance imaging in the management of diabetic foot infection. Br J Surg 83:245–248
93. Morrison W, Schweitzer ME, Wapner KL, Hecht PJ, Gannon FH, Behm WR (1995) Osteomyelitis in diabetics: clinical accuracy, surgical utility and cost effectiveness of MR imaging. Radiology 196:557–564
94. Beltran J, Campanini DS, Knight C, McCalla M (1990) The diabetic foot: magnetic resonance imaging. Skeletal Radiol 19:37–41
95. Lauri C, Tamminga M, Glaudemans AWJM et al (2017) Detection of osteomyelitis in the diabetic foot by imaging techniques: a systematic review and meta-analysis comparing MRI, white blood cell Scintigraphy, and FDG-PET. Diabetes Care 40:1111–1120
96. Nickerson EK, Sinha R (2016) Vertebral osteomyelitis in adults: an update. Br Med Bull 117:121–138
97. Modic M, Palestro CJ, Love C, Miller TT (2006) Infection and musculoskeletal conditions: imaging of musculoskeletal infections. Best Pract Res Clin Rheumatol. 20:1197–1218
98. Duarte RM, Vaccaro AR (2013) Spinal infection: state of the art and management algorithm. Eur Spine J 22:2787–2799
99. Cassar-Pullicino VN (2004) MR imaging of spinal infection. Semin Musculoskelet Radiol 8:215–229
100. Quinn SF, Murray W, Clark RA (1988) MR imaging of chronic osteomyelitis. J Comput Assist Tomogr 12:113–117
101. Cahill DW, Love LC, Rechtine GR (1991) Pyogenic osteomyelitis of the spine in the elderly. J Neurosurg 74:878–886
102. Kouijzer IJ, Scheper H, De Rooy JW, Bloem JL, Janssen MJ, van Den Hoven L et al (2018) The diagnostic value of 18 F–FDG-PET/CT and MRI in suspected vertebral osteomyelitis–a prospective study. Eur J Nucl Med Mol Imaging 45(5):798–805
103. Love C, Petel M, Lonner BS, Tomas MB, Palestro CJ (2000) Diagnosing spinal osteomyelitis: a comparison of bone and Ga-67 scintigraphy and magnetic resonance imaging. Clin Nucl Med 25:963–977
104. Love C, Palestro CJ (2016) Nuclear medicine imaging of bone infections. Clin Radiol 71:632–646
105. Tamm AS (2017) Bone and gallium single photon emission computed tomography computed tomography is equivalent to magnetic resonance imaging in the diagnosis of infectious spondylodiscitis: a retrospective study. Can J Radiol 68:41–46
106. Schlaeffer F, Mikolich DJ, Mates SM (1987) Technetium-99m diphosphonate bone scan. False-normal findings in elderly patients with hematogenous vertebral osteomyelitis. Arch Intern Med 147:2024–2026
107. Palestro CJ, Kim CK, Swyer A et al (1991) Radionuclide diagnosis of vertebral osteomyelitis: indium-111-leukocyte and technetium-99m-methylene diphosphonate bone scintigraphy. J Nucl Med 32:1861–1865
108. Whalen IL, Brown ML, McLeod R et al (1991) Limitations of indium leukocyte imaging for the diagnosis of spine infections. Spine 16:193–197
109. Fernandez-Ulloa M, Vasavada PJ, Hanslits MJ et al (1985) Vertebral osteomyelitis imaging with In-111 labeled white blood cells and Tc-99m bone scintigrams. Orthopedics 8:1144–1150
110. Dannoon SF, Al-Fouzan W, Alenezi SA, Alosaimi A, Alhusain M, Elgazzar AH (2019) Effect of causative micro-organisms on patterns of labeled white blood cells in osteomyelitis. Indian J Nucl Med 34:27–31
111. Stumpe KDM, Zanetti M, Weishaupt D, Hodler J, Boos N, Schulthess GK (2002) FDG positron emission tomography for differentiation of degenerative and infectious end plate abnormalities in the lumbar spine detected on MR imaging. AJR Am J Roentgenol 179:1151–1157
112. Gemmel F, Dumarey N, Palestro CJ (2006) Radionuclide imaging of spinal infections. Eur J Nucl Med Mol Imaging 33:1226–1237

113. Palestro CJ (2016) Radionuclide imaging of musculoskeletal infection: a review. J Nucl Med 57:1406–1412
114. Seifen T, Rettenbacher L, Thaler C, Holzmannhofer J, Mc Coy M, Pirich C (2012) Prolonged back pain attributed to suspected spondylodiscitis: the value of 18F-FDG PET/CT imaging in the diagnostic work-up of patients. Nuklearmedizin 51:194–200
115. Fuster D, Tomás X, Mayoral M et al (2015) Prospective comparison of whole-body 18F-FDG PET/CT and MRI of the spine in the diagnosis of haematogenous spondylodiscitis. Eur J Nucl Med Mol Imaging 42:264–271
116. Ioannou S, Chatziioannou S, Pneumaticos SG, Zormpala A, Sipsas NV (2013) Fluorine-18 fluoro2-deoxy-D-glucose positron emission tomography/computed tomography scan contributes to the diagnosis and management of brucellar spondylodiskitis. BMC Infect Dis 13:73
117. Riccio SA, Chu AKM, Rabin HR, Kloiber R (2015) Fluorodeoxyglucose positron emission tomography/computed tomography interpretation criteria for assessment of antibiotic treatment response in pyogenic spine infection. Can Assoc Radiol J 66:145–152
118. Skanjeti A, Penna D, Douroukas A et al (2012) PET in the clinical work-up of patients with spondylodiscitis: a new tool for the clinician? Q J Nucl Med Mol Imaging 6:569–570
119. Tumeh SS, Aliabadi P, Weissman BN, McNeil BJ (1986) Chronic osteomyelitis: bone and gallium scan patterns associated with active disease. Radiology 158:685–688
120. Tumeh SS, Tohmeh AG (1991) Nuclear medicine techniques in septic arthritis and osteomyelitis. Rheum Dis Clin North Am 17:559–583
121. Krznaric E, De Roo M, Verbruggen A, Stuyck J, Mortelinans L (1996) Chronic osteomyelitis: diagnosis with technetium 99 m d,1-hexamethylpropelene amine oxime labeled leukocytes. Eur J Nucl Med 23:792–797
122. Demirev A, Weijers R, Geurts J, Mottaghy F, Walenkamp G, Brans B (2014) Comparison of [18 F] FDG PET/CT and MRI in the diagnosis of active osteomyelitis. Skeletal Radiol 43(5):665–672
123. Sciuk J, Brandau W, Vollet B, Stucker R, Erlemann R, Bartenstein P et al (1991) Comparison of technetium-99 m polyclonal human immunoglobulin and technetium-99 m monoclonal antibodies for imaging chronic osteomyelitis. Eur J Nucl Med 18:401–407
124. Lankinen P, Seppänen M, Mattila K, Kallajoki M, Knuuti J, Aro HT (2017) Intensity of 18F-FDG PET uptake in culture-negative and culture-positive cases of chronic osteomyelitis. Contrast Media Mol Imaging 2017:9754293
125. Basu S, Chryssikos T, Houseni M, Malay DS, Shah JH, Zhuang M et al (2007) Potential role of FDG PET in the setting of diabetic neuro-osteoarthropathy: can it differentiate uncomplicated Charcot's neuroarthropathy from osteomyelitis and soft-tissue infection? Nucl Med Commun 28:465–472
126. Guhlmann A, Brecht-Krauss D, Sugar G, Glatting G, Kotzerke J, Kinzi L, Reske SN (1998) Chronic osteomyelitis: detection with FDG PET and correlation with histopathologic findings. Radiology 206:749–753
127. Zhuang HM, Duarte PS, Poudehnad M et al (2000) The exclusion chronic osteomyelitis with F-18 fluorodeoxyglucose positron tomography imaging. Clin Nucl Med 25:281–284
128. De Winter F, Dierckx R, De Bondt P et al (2000) FDG PET as a single technique is more accurate than the combination bone scan/white blood cell scan in chronic orthopedic infection (COI). J Nucl Med 41:59 (Abstract)
129. Love C, Tomas MB, Marwin SE, Pugliese PV, Palestro CHF (2001) Role of nuclear medicine in diagnosis of the infected joint replacement. Radiographics 21:1229–1238
130. Oswald SG, VanNostrand D, Savory CG, Callaghan JJ (1989) Three phase bone scan and indium white blood cell scintigraphy following porous-coated hip arthroplasty: a prospective study of the prosthetic hip. J Nucl Med 30:1321–1331
131. Oswald SG, VanNostrand D, Savory CG, Anderson JH, Callghan JJ (1990) The acetabulum: a prospective study of three-phase bone and indium white blood cell scintigraphy following porous coated hip arthroplasty. J Nucl Med 31:274–280
132. Rosenthal L, Lepantp L, Raymond F (1987) Radiophosphate uptake in asymptomatic knee arthroplasty. J Nucl Med 28:1546–1549
133. Seabold JE, Nepola JV, Marsh JL et al (1991) Postoperative bone marrow alterations: potential pitfalls in the diagnosis of osteomyelitis with In-111-labeled leukocyte scintigraphy. Radiology 180:741–747
134. Palestro CJ (2015) Radionuclide imaging of osteomyelitis. Semin Nucl Med 45:32–46
135. van der Bruggen W, Bleeker-Rovers CP, Boerman OC, Gotthardt M, Oyen WJ (2010) PET and SPECT in osteomyelitis and prosthetic bone and joint infections: a systematic review. Semin Nucl Med 40:3–15
136. Mariani G, Bruselli L, Kuwert T, Kim EE, Flotats A, Israel O, Dondi M, Watanabe N (2010) A review on the clinical uses of SPECT/CT. Eur J Nucl Med Mol Imaging 37:1959–1985
137. Oyen WJG, VanHorn JR, Claessens RAMJ, Slooff JJH, Van der Meer JWM, Corstens HM (1992) Diagnosis of bone, joint and joint prosthesis infections with In-111-labeled nonspecific human immunoglobulin G scintigraphy. Radiology 182:195–199
138. Lorberboym M, Feldbrin Z, Hendel D, Blankenberg FG, Schachter P (2009) The use of 99mTc-recombinant human annexin V imaging for differential diagnosis of aseptic loosening and low-grade infection in hip and knee prostheses. J Nucl Med 50:534–537

139. Zhuang H, Durate PS, Pourdehnad M et al (2001) The promising role of F-18-FDG PET in detecting infected lower limb prosthesis implants. J Nucl Med 42:44–48
140. Chacko TK, Zhuang H, Stevenson K, Moussavian B, Alavi A (2002) The influence of the location of fluodeoxyglucose uptake in periprosthetic infection in painful; hip prosthesis. Nucl Med Commun 23:851–855
141. Palestro CJ (2013) FDG PET in musculoskeletal infections. Semin Nucl Med 43:367–376
142. Tseng JR, Chang YH, Yang LY et al (2019) Potential usefulness of ^{68}Ga-citrate PET/CT in detecting infected lower limb prostheses. EJNMMI Res 9:2. https://doi.org/10.1186/s13550-018-0468-3
143. Yaddanapudi K, Matthews R, Brunetti V, Martin B, Franceschi D (2017) PET-MRI in diagnosing pedal osteomyelitis in diabetic patients. J Nucl Med 56:307
144. Mitea C, van de Weijer T, van de Meer L, Jacobi L, Loeffen D, Hulsen D, Moonen R (2020) Imaging of osteomyelitis with FDG PET-MR. Infection 5:6
145. Amunden TR, Siegel MJ, Siegel BA (1984) Osteomyelitis and infarction in sickle cell hemoglobinopathies: differentiation by combined technetium and gallium scintigraphy. Radiology 153:807–812
146. Van Kroonenburgh AMJL, Van der Meer WL, Bothof RJP, Van Tilburg M, Van Tongeren J, Postma AA (2018) Advanced imaging techniques in skull base osteomyelitis due to malignant otitis externa. Curr Radiol Rep 6(1):1–14
147. Shavit S, Bernstine H, Sopov V, Nageris B, Hilly O (2019) FDG-PET/CT for diagnosis and follow-up of necrotizing (malignant) external otitis. Laryngoscope 129(4):961–966
148. Porrino J, Richardson ML, Flaherty E, Albahhar M, Ha AS, Mulcahy H, Chew FS (2019) Septic arthritis and joint aspiration: the radiologist's role in image-guided aspiration for suspected septic arthritis. Semin Roentgenol 54:177–189
149. Jaramillo D, Treves ST, Kasser JR, Harper M, Sundel R, Laor T (1995) Osteomyelitis and septic arthritis in children. Appropriate use of imaging to guide treatment. AJR Am J Roentgenol 165:399–403
150. Sundberg SB, Savage JP, Foster BK (1989) Technetium phosphate bone scan in the diagnosis of septic arthritis in childhood. J PediatrOrthop 9:579–585
151. Zhao Y, Ferguson PJ (2018) Chronic nonbacterial osteomyelitis and chronic recurrent multifocal osteomyelitis in children. Pediatr Clin 65:783–800
152. Buch K, Thuesen ACB, Brøns C, Schwarz P (2019) Chronic non-bacterial osteomyelitis: a review. Calcif Tissue Int 104:544–553
153. Hedrich CM, Morbach H, Reiser C, Girschick HJ (2020) New insights into adult and paediatric chronic non-bacterial osteomyelitis CNO. Curr Rheumatol Rep 22:1–11
154. Khanna G, Sato TS, Ferguson P (2009) Imaging of chronic recurrent multifocal osteomyelitis. Radiographics. 29:1159–1177
155. Gicchino MF, Diplomatico M, Granato C, Capalbo D, Marzuillo P, Olivieri AN, Miraglia Del Giudice E (2018) Chronic recurrent multifocal osteomyelitis: a case report. Ital J Pediatr 44:26. https://doi.org/10.1186/s13052-018-0463-3. PMID: 29454377; PMCID: PMC5816363
156. Bahk YW, Chung SK, Kim SH et al (1992) Pinhole scintigraphic manifestations of sternoclavicular hyperostosis: report of a case. Korean J Nucl Med 26:155–159
157. Shandilya R, Gadre KS, Sharma J, Joshi P (2013) Infantile cortical hyperostosis (Caffey disease): a case report and review of the literature--where are we after 70 years? J Oral Maxillofac Surg 71:1195–1201
158. Handmaker H, Kamoun-Goldrat A, le Merrer M (2008) Infantile cortical hyperostosis (Caffey disease): a review. J Oral Maxillofac Surg 66:2145–2150
159. Nouri A, Walmsley D, Pruszczynski B, Synder M (2014) Transient synovitis of the hip: a comprehensive review. J Pediatr Orthop B. 23:32–36
160. Sawyer JR, Kapoor M (2009) The limping child: a systemic approach to diagnosis. Am Fam Physician 79:215–224
161. Kang MS, Jeon JY, Park S-S (2020) Differential MRI findings of transient synovitis of the hip in children when septic arthritis is suspected according to symptom duration. J Pediatr Orthop B 29:297–303
162. Mc Affe JG, Roba RC, Majid M (1995) The musculoskeletal system. In: Wagner HN (ed) Principles of nuclear medicine, 2nd edn. Saunders, Philadelphia, pp 986–1020
163. Graham J, Wood SK (1976) Aseptic necrosis of bone following trauma. In: Davidson JK (ed) Aseptic necrosis of bone. Excerpta Medica, Amsterdam, p 101
164. Achar S, Yamanaka J (2019) Apophysitis and osteochondrosis: common causes of pain in growing bones. Am Fam Physician 99(10):610–618
165. Murphey MD, Foreman KL, Klassen-Fischer MK, Fox MG, Chung EM, Kransdorf MJ (2014) From the radiologic pathology archives imaging of osteonecrosis: radiologic-pathologic correlation. Radiographics 34:1003–1028
166. Agrawal K, Tripathy SK, Sen RK, Santhosh S, Bhattacharya A (2017) Nuclear medicine imaging in osteonecrosis of hip: old and current concepts. World J Orthop 8(10):747–753. https://doi.org/10.5312/wjo.v8.i10.747]
167. Resnick D (1989) Bone and joint imaging. Saunders, Philadelphia, pp 979–999
168. Laine JC, Martin BD, Novotny SA, Kelly DM (2018) Role of advanced imaging in the diagnosis and management of active Legg-Calve-Perthes disease. J Am Acad Orthop Surg 26(15):526–536
169. de Sanctis N, Rondinella F (2000) Prognostic evaluation of Legg-Calvé-Perthes disease by MRI. Part II: pathomorphogenesis and new classification. J PediatrOrthop 20:463–470
170. Fragniere B, Chotel F, Vargas Barreto B, Berard J (2001) The value of early postoperative bone scan in slipped capital femoral epiphysis. J PediatrOrthop B 10:51–55

171. Conway JJ (1993) A scintigraphic classification of Legg-Calve-Perthes disease. Semin Nucl Med 23:274–295
172. Tsao AK, Dias LS, Conway JJ, Straka P (1997) The prognostic value and significance of serial bone scintigraphy in Legg-Calvé-Perthes disease. J Pediatr Orthop 17:230–239
173. Comte F, De Rosa V, Zekri H, Eberle MC, Dimeglio A, Rossi M, Mariano-Goulart D (2003) Confirmation of the early prognostic value of bone scanning and pinhole imaging of the hip in Legg-Calve-Perthes disease. J Nucl Med 44:1761–1766
174. Resnick D, Niwayama G (1998) Osteonecrosis: diagnostic techniques and complications. In: Resnick D, Niwayama G (eds) Diagnosis of bone and joint disorders second editions. Saunders, Philadelphia, p 3268
175. Smith JA (1996) Bone disorders in sickle cell disease. Hematol Oncol Clin North Am 10:1345–1346
176. Keeley K, Buchanan GR (1982) Acute infarction of long bones in children with sickle cell anemia. J Pediatr 101:170–175
177. Skaggs DL, Kim SK, Green NW, Harris D, Miler JH (2001) Differentiation between bone infarct and acute osteomyelitis in children with sickle-cell disease with use of sequential radionuclide bone-marrow and bone scans. J Bone Joint Surg Am 83:1810–1813
178. Jain R, Sawhney S, Rizvi SG (2008) Acute bone crises in sickle cell disease: the T1 fat-saturated sequence in differentiation of acute bone infarcts from acute osteomyelitis. Clin Radiol 63:59–70
179. Bouden AK, Kaïs C, Abdallah NB, Kraiem NH, Jamoussi MM (2005) [MRI contribution in diagnosis of acute bone infarcts in children with sickle cell disease]. Tunis Med 83:344–348
180. Sisayan R, Elgazzar AH, Webner P, Religioso DG (1996) Impact of bone scintigraphy on clinical management of a sickle cell patient with recent chest pain. Clin Nucl Med 21:523–526
181. Kim HK (2012) Pathophysiology and new strategies for the treatment of Legg-Calvé-Perthes disease. J Bone Joint Surg Am 94:659–669
182. Kawai K, Maruno H, Watanabe Y, Hirohata K (1980) Fat necrosis of osteocytes as a causative factor in idiopathic osteonecrosis inheritable hyperlipemic rabbits. Clin Orthop Relat Res 153:273
183. Collier BD, Carrera GF, Johnson RP, Isitman AT, Hellman RS, Knobel J et al (1985) Detection of femoral head avascular necrosis in adults by SPECT. J Nucl Med 26:979–987
184. Greyson ND, Lotem MM, Gross AE (1982) Radionuclide evaluation of spontaneous femoral osteonecrosis. Radiology 142:729–735
185. Janig W, Baron R (2003) Complex regional pain syndrome: mystery explained? Lancet Neurol 2:687–697
186. Shehab D, Al-Jarralah K, Al-Awadhi A et al (1999) Reflex sympathetic dystrophy: an under-recognized entity in Kuwait. APLAR J Rheumatol 3:343–347
187. Cappello ZJ, Kasdan ML, Louis DS (2012) Meta-analysis of imaging techniques for the diagnosis of complex regional pain syndrome type I. J Hand Surg 37:288–296
188. Blockx P, Driessens M (1991) The use of Tc-99-m-HSA dynamic vascular examination in the staging and therapy monitoring of reflex sympathetic dystrophy. Nucl Med Commun 12:725–731
189. Goldstein DS, Tack C, Li TS (2000) Sympathetic innervation and function in reflex sympathetic dystrophy. Ann Neurol 48:49–59
190. Sankaya A, Sankaya I, Pekindil G, Firat MF, Pekindil Y (2001) Technetium-99m sestamibi limb scintigraphy in post-traumatic reflex sympathetic dystrophy: preliminary results. Eur J Nucl Med 28:1517–1522
191. Haensch C, Jorg J, Lerch H (2002) I-123 metaiodobenzyl-guanidine uptake of the forearm shows dysfunction of sympathetic mediated neurovascular transmission in complex regional pain syndrome 1 (CRPS 1). J Neurol 249:1742–1743
192. Yoon D, Xu Y, Cipriano PW, Alam IS, Mari Aparici CA, Tawfik VL et al (2021) Neurovascular, muscle, and skin changes on [18F] FDG PET/MRI in complex regional pain syndrome of the foot: a prospective clinical study. Pain Med 23:339. https://doi.org/10.1093/pm/pnab315
193. Bernateck M, Rolke R, Birklein F et al (2007) Successful intravenous regional block with low-dose tumor necrosis factor α antibbody Infliximab for treatment of complex regional pain syndrome. Anesthesia and analgesia 105:1148–1151
194. Yoon D, Xu Y, Cipriano P, Tawfik V, Curtin C, Carroll I, Biswal S (2019) Musculoskeletal changes on [18F]FDG PET/MRI from complex regional pain syndrome in foot. J Nucl Med 60:94 (abstract)
195. Tsuyuguchi N, Ohata K, Morino M, Takami T, Goto T, Nishio A, Hara M, Sunada I (2002) Magnetic resonance imaging and [11c] methyl-L-methionine positron emission tomography of fibrous dysplasia-two case reports. Neurol Med Chir 42:341–345
196. Papadakis GZ, Manikis GC, Karantanas AH, Florenzano P, Bagci U et al (2019) 18F-NaF PET/CT imaging in fibrous dysplasia of bone. J Bone Miner Res 34:1619–1631
197. Kairemo KJ, Verho S, Dunkel L (1999) Imaging of McCune Albright syndrome using bone single photon emission computed tomography. Eur J Pediatr 158:123–126
198. Mourad A (1998) Alterations of musculoskeletal function. In: McCance KL, Huether SE (eds) Pathophysiology, 3rd edn. Mosby, Philadelphia, pp 1435–1485
199. Schneider R (2005) Radionuclide techniques. In: Resnick D, Kransdorf MJ (eds) Bone and joint imaging, 3rd edn. Elsevier/Saunders, Philadelphia, pp 86–117
200. Zwas TS, Elkanovitch R, Frank G (1987) Interpretation and classification of bone scintigraphic findings in stress fractures. J Nucl Med 28:452–457

201. Brukner P, Bennell K, Matheson G (1999) Diagnosis of stress fractures. In: Stress fractures. Blackwell Science, Victoria, pp 83–96
202. Amin I, Moroz A (2017) Medial tibial stress syndrome (shin splints). In: Musculoskeletal sports and spine disorders. Springer, Cham, pp 281–282
203. Holder LE, Michael RH (1984) The specific scintigraphic pattern of shin splints in the lower leg: concise communication. J Nucl Med 25:865–869
204. Chung CC, Shimer AL (2021) Lumbosacral spondylolysis and spondylolisthesis. Clin Sports Med 40(3):471–490
205. Gaddikeri S, Matesan M, Alvarez J, Hippe DS, Vesselle HJ (2018) MDP-SPECT versus hybrid MDP-SPECT/CT in the evaluation of suspected pars interarticularis fracture in young athletes. J Neuroimaging 28(6):635–639
206. Reed A, Joyner C, Brawnlow H, Simpson H (2001) Radiological classification of human nonunions does not reflect biological activity. In: Proceeding of the 47th annual meeting. Orthopedic Research Society, San Francisco, p 971 (abstract)
207. Sty JR, Starshak RJ (1983) The role of bone scintigraphy in the evaluation of the suspected abused child. Radiology 146:369–375
208. Malki A, Elgazzar A, Ashqar T, Owunwanne A, Abdel-Dayem AH (1992) New technique for assessing muscle damage after trauma. J R Coll Surg Edinb 37:131–133
209. Malki A, Owunwanne A, Elgazzar A, Abdel-Dayem AH (1999) Assessment of skeletal muscle damage in experimental animal using In-111 antimyosin. Int J Surg Investig 1:99–105
210. Sharkey CA, Harcke HT, Mandell GA et al (1986) SPECT techniques in the evaluation of growth plate abnormalities about the knee. J Nucl Med Tech 14:Ab13
211. Harcke HT, Zapf SE, Mandell GA et al (1987) Angular deformity of the lower extremity: evaluation with quantitative bone scintigraphy. Radiology 164:437–440
212. Harcke HT (1978) Bone imaging in infants and children: a review. J Nucl Med 19:324–329
213. Mandell GA (1998) Nuclear medicine in pediatric orthopedics. Semin Nucl Med 28:95–115
214. Etchebehere EC, Caron M, Pereira JA, Lima MC, Santos AO, Ramos CD, Barros FB, Sanches A, Santos-Jesus R, Belangero W, Camargo EE (2001) Activation of the growth plates on three-phase bone scintigraphy: the explanation for the overgrowth of fractured femurs. Eur J Nucl Med 28:72–80
215. Harcke HT, Mandell GA (1993) Scintigraphic evaluation of the growth plate. Semin Nucl Med 23:266–273
216. Etchebehere EC, Etchebehere M, Gamba R, Belangero W, Camargo EE (1998) Orthopedic pathology of the lower extremities: scintigraphic evaluation in the thigh, knee, and leg. Semin Nucl Med 28:41
217. Yamane T, Kuji I, Seto A, Matsunari I (2018) Quantification of osteoblastic activity in epiphyseal growth plates by quantitative bone SPECT/CT. Skeletal Radiol 47:805–810
218. Wioland M, Bonnerot V (1993) Diagnosis of partial and total physeal arrest by single photon emission computed tomography. J Nucl Med 34:1410–1415
219. Peterson HA (1984) Partial growth plate arrest and its treatment. J Pediatr Orthop 4:246–258
220. DeCampo JF, Boldt DW (1986) Computed tomography in partial growth plate arrest: initial experience. Skeletal Radiol 183:119–123
221. Jaramillo D, Hoffer EA, Shapiro F et al (1990) MR imaging of fracture of the growth plate. AJR Am J Roentgenol 155:1261–1265
222. Khan A, Bilezikian J (2000) Primary hyperparathyroidism: pathophysiology and impact on bone. CMAJ 163:184–718
223. Lander PH, Hadjipavlou AG (1986) A dynamic classification of Paget's disease. J Bone Joint Surg [Br] 68B:431–438
224. Boutin RD, Spitz DJ, Newman JS, Lenchik L, Steinbach LS (1998) Complications in Paget disease at MR imaging. Radiology 209:641–651
225. Vandes Berg BC, Malghem J, Lecouvet FE, Maldague B (2001) Magnetic resonance appearance of uncomplicated Paget's disease of bone. Semin Musculoskelet Radiol 5:69–77
226. Cherian RA, Haddaway MJ, Davie MW, McCall IW, Cassar-Pullicino VN (2000) Effect of Paget's disease of bone on areal lumbar spine bone mineral density measured by DXA, and density of cortical and trabecular bone measured by quantitative CT. Br J Radiol 73:720–726
227. Serafini AN (1976) Paget's disease of bone. Semin Nucl Med 6:47–58
228. Fogelman I, Carr D (1980) A comparison of bone scanning and radiology in the evaluation of patients with metabolic bone disease. Clin Radiol 31:321–326
229. King MA, Maxon HR (1984) Paget's disease: the role of nuclear medicine in diagnosis and treatment. In: Silberstein EB (ed) Bone scintigraphy. Futura Publishing, Mount Kisco, pp 333–346
230. Renier JC, Audran M (1997) Polyostotic Paget's disease. A search for lesions of different durations and for new lesions. Rev Rhum Engl Ed 64:233–242
231. Elgazzar AH, Yeung HW, Webner PJ (1996) Indium-111 leukocyte and technetium 99 m sulfur colloid uptake in Paget's disease. J Nucl Med 37:858–861
232. Kaplan FS (1987) Osteoporosis: pathophysiology and prevention. Chin Sympozia 39:2
233. Matkovic V, De Kanic D (1989) Developing strong bones: the teenage female. In: Kleerehoper M, Krane SM (eds) Clinical disorders of bone and mineral metabolism. Mary Ann Liebert Inc., New York, p 165
234. Gillespy T, Gillespy MP (1991) Osteoporosis. Radiol Clin North Am 29:77–84
235. Christiansen C, Riis BJ (1989) Optimizing bone mass in the perimenopause. In: Kleerehoper M, Krane SM (eds) Clinical disorder of bone and mineral metabolism. Mary An Liebert, Inc., New York, p 189

236. Lang P, Steiger P, Faulkner K et al (1991) Current techniques and recent developments in quantitative bone densitometry. Radiol Clin North Am 29:49–76
237. Snyder W (1975) Report of the task group on reference man. Pergamon Press, Oxford
238. Recker RR, Heaney RP (1989) Effects of age, sex and race on bone remodeling. In: Kellerehoper M, Krane SM (eds) Clinical disorders of bone and mineral metabolism. Mary Ann Liebert, Inc., New York, p 59
239. Heaney RP (1989) Optimizing bone mass in the permenopause: calcium. In: Kleerehoper M, Krane SM (eds) Clinical disorders of bone and mineral metabolism. Mary Ann Liebert, Inc, New York, p 181
240. Frost HM (1964) Dynamics of bone remodelling. In: Frost HM (ed) Bone biodynamics. Little, Brown, Boston, pp 315–334
241. Ettinger B, Genant HK (eds) (1987) Osteoporosis update. Radiology Research and Education Foundation, San Francisco
242. Hippisley-Cox J, Coupland C (2009) Predicting risk of osteoporotic fracture in men and women in England and Wales: prospective derivation and validation of Qfracture Scores. BMJ 339:b4229
243. Cooper C, Aihie-Sayer A (1994) Osteoporosis: recent advances in pathogenesis and treatment. Q J Med 87:203–209
244. Simon SR (1994) Osteoporosis: orthopedic basic science. American Academy of Orthopedic Surgeons, Chicago
245. Chen CC, Wang SS, Jeng FS, Lee SD (1996) Metabolic bone disease of liver cirrhosis: is it parallel to the clinical severity of cirrhosis? J Gastroenterol Hepatol 11:417–421
246. Fogelman I (1987) The bone scan in metabolic bone disease. In: Fogelman I (ed) Bone scanning in clinical practice. Springer, Berlin, pp 73–88
247. Lack CA, Rarber JL, Rubin E (1999) The endocrine system. In: Rubin E, Farber JL (eds) Pathology, 3rd edn. Lippincott-Raven, Philadelphia, pp 1179–1183
248. Marshall D, Johnell O, Wedel H (1996) Meta-analysis of how well measures of bone mineral density predict occurrence of osteoporotic fractures. BMJ 312:1254–1259
249. Cummings SR, Black DM, Nevitt MC et al (1993) Bone density at various sites for prediction of hip fractures. Lancet 341:72–75
250. Eastell R (1998) Treatment of postmenopausal osteoporosis. N Engl J Med 338:736–746
251. Njeh CF, Fuerst T, Hans D, Blake GM, Genant HK (1999) Radiation exposure in bone mineral assessment. Appl Radiat Isot 50:215–236
252. WHO Technical Report Series 843 (1994) Assessment of fracture risk and its application to screening for postmenopausal osteoporosis. World Health Organization, Geneva
253. Genant HK, Grampp S, Glüer C-C et al (1994) Universal standardization for dual x-ray absorptiometry: patient and phantom cross-calibration results. J Bone Miner Res 9:1503–1514
254. Basha B, Rao DS, Han ZH, Parfitt AM (2000) Osteomalacia due to vitamin D depletion: a neglected consequence of intestinal malabsorption. Am J Med 108:296–300
255. Reginato AJ, Falasca GF, Pappu R, McKnight B, Agha A (1999) Musculoskeletal manifestations of osteomalacia: report of 26 cases and literature review. Semin Arthritis Rheum 28:287–304
256. Akbunar AT, Orhan B, Alper E (2000) Bone-scan-like pattern with 99Tcm(V)-DMSA scintigraphy in patients with osteomalacia and primary hyperparathyroidism. Nucl Med Commun 21:181–185
257. Leitha T (1998) Rapid changes in the scintigraphic pattern in Tc-99m DPD whole-body scanning in metabolic bone disease. Clin Nucl Med 23:784–785
258. Brasier AR, Nussbaum SR (1988) Hungry bone syndrome: clinical and biochemical predictors of its occurrence after parathyroid surgery. Am J Med 84:654
259. Goen G, Mazzaferro S (1994) Bone metabolism and its assessment in renal failure. Nephron J 67:383–401
260. Rosengerg AE (1991) The pathology of metabolic bone disease. Radiol Clin North Am 29:19–36
261. Dabbagh S (1998) Renal osteodystrophy. Curr Opin Pediatr 10:190–196
262. Cicconetti A, Maffeini C, Piro FR (1999) Differential diagnosis in a case of brown tumor caused by primary hyperparathyroid ism. Minerva Stomatol 48:553–558
263. Loder RT, Hensinger RN (1997) Slipped capital femoral epiphysis associated with renal failure osteodystrophy. J Pediatr Orthop 17:205–211
264. Yalcinkaya F, Ince E, Tumer N, Ensari A, Ozkaya N (2000) Spectrum of renal osteodystrophy in children on continuous ambulatory peritoneal dialysis. Pediatr Int 42:53–57
265. Jorgetti V, Lopez BD, Caorsi H, Ferreira A, Palma A, Menendez P, Douthat W, Olaizola I, Ribeiro S, Jarava C, Moreira E, Cannata J (2000) Different patterns of renal osteodystrophy in IberoAmerica. Am J Med Sci 320:76–80
266. Olaizola I, Aznarez A, Jorgetti V, Petroglia A, Caorsi H, Acuna G, Fajardo L, Ambrosoni P, Mazzuchi N (1998) Are there any differences in the parathyroid response in the different types of renal osteodystrophy? Nephrol Dial Transplant 13(suppl):15–18
267. Seggewiss R, Hess T, Fiehn C (2003) A family with a variant form of primary hypertrophic osteoarthropathy restricted to the lower extremities. Joint Bone Spine 70:230–233
268. Howell DS (1985) Hypertrophic osteoarthropathy. In: Mc Carty DJ (ed) Arthritis and allied conditions, 10th edn. Lea and Febiger, Philadelphia, pp 1195–1201
269. Ali A, Tetalman MR, Fordham EW et al (1980) Distribution of hypertrophic pulmonary osteoarthropathy. AJR Am J Roentgenol 134:771–780
270. Wang CJ, Huang CH, Leung SW, Chen HC, Huang EY (1998) Hypertrophic osteoarthropathy in nasopharyngeal carcinoma patient: two case report. Changgeng Yi Xue Za Zhi 21:222–226

271. Morgan B, Coakley F, Finlay DB, Belton I (1996) Hypertrophic osteoarthropathy in staging skeletal scintigraphy for lung cancer. Clin Radiol 51:694–697
272. Albrecht S, Keller A (2003) Postchemotherapeutic reversibility of hypertrophic osteoarthropathy in a patient with bronchogenic adenocarcinoma. Clin Nucl Med 28:463–466
273. Rosenthall L (1991) Nuclear medicine techniques in arthritis. Rheum Dis Clin North Am 17:585–597
274. McCarthy D (ed) (1984) Arthritis and allied conditions. Lea and Fabiger, Philadelphia
275. Goldenberg DL, Cohen AS (1978) Synovial membrane histopathology in the differential diagnosis of rheumatoid arthritis, gout, pseudogout, systemic lupus erythematosus, infectious arthritis and degenerative joint disease. Medicine 57:239–252
276. Zeman MN, Scott PJ (2012) Current imaging strategies in rheumatoid arthritis. Am J Nucl Med Mol Imaging 2(2):174–220
277. Cindas A, Gokce-Kustal Y, Kirth PO, Caner B (2001) Scintigraphic evaluation of synovial inflammation in rheumatoid arthritis with (99m) technetium-labelled human polyclonal immunoglobulin G. Rheumatol Int 20:71–77
278. Weissberg DI, Resnick D, Taylor A et al (1978) Rheumatoid arthritis and its variants: analysis of scintiphotographic, radiographic and clinical examination. AJR Am J Roentgenol 131:665–673
279. McQueen FM (2013) Imaging in early rheumatoid arthritis. Best Pract Res Clin Rheumatol 27(4):499–522
280. Al-Janabi MA, Solanki K, Critchley M et al (1992) Radioleukoscintigraphy in osteoarthritis. Is there an inflammatory component? Nucl Med Commun 13:706–712
281. Berna L, Torres G, Diez C et al (1992) Technetium-99 m human polyclonal immunoglobulin G studies and conventional bone scans to detect active joint inflammation in chronic rheumatoid arthritis. Eur J Nucl Med 19:173–176
282. Beckers C, Ribbens C, André B, Marcelis S, Kaye O, Mathy L et al (2004) Assessment of disease activity in rheumatoid arthritis with 18F-FDG PET. J Nucl Med 45(6):956–964
283. Kubota K, Ito K, Morooka M, Mitsumoto T, Kurihara K, Yamashita H et al (2009) Whole-body FDG-PET/CT on rheumatoid arthritis of large joints. Ann Nucl Med 23(9):783–791
284. Okamura K, Yonemoto Y, Arisaka Y, Takeuchi K, Kobayashi T, Oriuchi N et al (2012) The assessment of biologic treatment in patients with rheumatoid arthritis using FDG-PET/CT. Rheumatology 51(8):1484–1491
285. Zhu W, He X, Cheng K, Zhang L, Chen D, Wang X et al (2019) Ankylosing spondylitis: etiology, pathogenesis, and treatments. Bone Res 7(1):1–16
286. Bahk Y (2000) Combined scintigraphic and radiographic diagnosis of bone and joint diseases, 2nd edn. Springer, Berlin
287. Mijiyawa M (1995) Gout in patients attending the rheumatology unit of Lome Hospital. Br J Rheumatol 34:843–846
288. Sato J, Watanabe H, Shinozaki T, Fukuda T, Shirakura K, Takagishi K (2001) Gouty tophus of the patella evaluated by PET imaging. J Orthop Sci 6:604–607
289. George E, Creamer P, Dieppe PA (1994) Clinical subsets of osteoarthritis. J Musculoskelet Med 11:14
290. Gelber AC, Hochberg MC, Mead LA, Wang NY, Wigley FM, Klag MJ (2000) Joint injury in young adults and risk of subsequent knee and hip osteoarthritis. Ann Intern Med 133:321–328
291. Orzel JA, Redd TG (1985) Heterotopic bone formation: clinical, laboratory and imaging correlation. J Nucl Med 26:125–132
292. Choi YH, Kim KE, Lim SH, Lim JY (2012) Early presentation of heterotopic ossification mimicking pyomyositis – two case reports. Ann Rehabil Med 36:713–718
293. Hassan F, Enayat M, Mohammed F, Vijayanathan S, Gnanasegaran G (2012) Heterotrophic ossification in a patient suspected of having osteomyelitis: additional value of SPECT/CT. Clin Nucl Med 37:170–171
294. Elgazzar AH, Martich V, Gelfand MJ (1995) Advanced fibrodysplasia ossificans progressiva. Clin Nucl Med 20:519–521
295. Hod N, Fishman S, Horne T (2002) Detection of rhabdomyolysis associated with compartment syndrome by bone scintigraphy. Clin Nucl Med 27:885–886
296. Kawaguchi Y, Hasegawa T, Oka S, Sato C, Arima N, Norimatsu H (2001) Mechanism of intramedullary high intensity area on T2-weighted magnetic resonance imaging in osteoid osteoma: a possible role of COX-2 expression. Pathol Int 51:933–937
297. Dablin DC, Conventry MB (1967) Osteogenic sarcoma: a study of 600 cases. J Bone Joint Surg Am 49:101–110
298. Flemming DJ, Murphey MD (2000) Enchondroma and chondrosarcoma. Semin Musculoskelet Radiol 4(1):59–71
299. Marco RA, Gitelis S, Brebach GT, Healey JH (2000) Cartilage tumors: evaluation and treatment. J Am Acad Orthop Surg 8:292–304
300. Yaccoby S (2010) Advances in the understanding of myeloma bone disease and tumour growth. Br J Haematol 149(3):311–321
301. Maheshwari AV, Cheng EY (2010) Ewing sarcoma family of tumors. J Am Acad Orthop Surg 18:94–107
302. Murphey MD, Kransdorf MJ (2021) Staging and classification of primary musculoskeletal bone and soft tissue tumors based on the 2020 WHO update, from the AJR special series on cancer staging. Am J Roentgenol 217:1038
303. Huvos AG (1991) Bone tumors; diagnosis, treatment and prognosis, 2nd edn. Saunders, Philadelphia
304. Resnik D, Kyriakos M, Greenway GD (2002) Tumors and tumor-like lesions of bone. In: Diagnosis of bone

and joint disorders, 4th edn. Saunders, Philadelphia, pp 3979–3985
305. Choi JJ, Murphey MD (2000) Angiomatous skeletal lesions. Semin Musculoskelet Radiol 4:103–112
306. Han BK, Ryu JS, Moon DH, Shin MJ, Kim YT, Lee HK (1995) Bone SPECT imaging of vertebral hemangioma correlation with MR imaging and symptoms. Clin Nucl Med 20:916–921
307. Gupta A (2018) Ewing sarcoma. In: PET/MR imaging. Springer, Cham, pp 9–11
308. Weber W (2020) Clinical PET/MR. In: Molecular imaging in oncology. Springer, Cham, pp 747–764
309. Gholamrezanezhad A, Guermazi A, Salavati A, Alavi A (2018) Evolving role of PET-computed tomography and PET-MR imaging in assessment of musculoskeletal disorders and its potential revolutionary impact on day-to-day practice of related disciplines. PET Clin 13(4):xiii-xiv
310. Elgazzar AH, Malki AA, Abdel-Dayem HM, Sahweil A, Razzak S, Jahan S, Elsayed M, Omar YT (1989) Role of thallium 201 in the diagnosis of solitary bone lesions. Nucl Med Commun 10:477–485
311. Elgazzar AH, Fernendaz-Ulloa M, Silberstein EB (1993) Thallium 201 as a tumor imaging agent: current status and future consideration. Nucl Med Commun 14:96–103
312. Caner B, Kitapcl M, Unlu M et al (1992) Technetium 99m MIBI uptake in benign and malignant bone lesions: a comparative study with technetium 99m MDP. J Nucl Med 33:319–324
313. Pneumaticos SG, Chatziioannou SN, Moore WH, Johnson M (2001) The role of radionuclides in primary musculoskeletal tumors beyond the bone scan. Crit Rev Oncol Hematol 37(3):217–226
314. Aoki J, Watanabe H, Shinozaki T, Takagishi K, Ishijima H, Oya N, Sato N, Inoue T, Endo K (2001) FDG PET of primary benign and malignant bone tumors: standardized uptake value in 52 lesions. Radiology 219:774–777
315. Franzius C, Sciuk J, Brinkschmidt C, Jurgens H, Schober O (2000) Evaluation of chemotherapy response in primary bone tumors with F-18 FDG positron emission. Clin Nucl Med 25:874–878
316. Dimitrakopoulou-Strauss A, Heichel TO, Lehner B, Bernd L, Ewerbeck V, Burger C, Strauss LG (2001) Quantitative evaluation of skeletal tumors with dynamic FDG PET: SUV in comparison to Patlak analysis. Eur J Nucl Med 28:704–710
317. Johnson JD, Rainer WG, Rose PS, Houdek MT (2020) Utility of bone scintigraphy and PET-CT in the surgical staging of skeletal chondrosarcoma. Anticancer Res 40(10):5735–5738
318. Franzius C, Sciuk J, Daldrup-Link HE, Jurgens H, Schober O (2000) FDG-PET for detection of osseous metastases from malignant primary bone tumors: comparison with bone scintigraphy. Eur J Nucl Med 27:1305–1311
319. Yildiz C, Erler K, Atesalp AS, Basbozkurt M (2003) Benign bone tumors in children. Curr Opin Pediatr 15:58–67
320. Bhure U, Roos JE, Strobel K (2019) Osteoid osteoma: multimodality imaging with focus on hybrid imaging. Eur J Nucl Med Mol Imaging 46:1019
321. Miller SL, Hoffer FA (2001) Malignant and benign bone tumors. Radiol Clin North Am 39:673–699
322. Buhler M, Binkert C, Exner GU (2001) Osteoid osteoma: technique of computed tomography-controlled percutaneous resection using standard equipment available in most orthopaedic operating rooms. Arch Orthop Trauma Surg 121:458–461
323. Clement ND, Porter DE (2014) Hereditary multiple exostoses: anatomical distribution and burden of exostoses is dependent upon genotype and gender. Scott Med J 59(1):35–44. http://www.ncbi.nlm.nih.gov/pubmed/24413927
324. Woerthler K, Linder N, Gosheger G, Brinkschmidt C, Heindel W (2000) MR imaging of tumor-related complications. Eur Radiol 10:832–840
325. Brian WE, Mirra JM, Luck JV Jr (1999) Benign and malignant tumors of bone and joint: their anatomical and theoretical basis with an emphasis on radiology, pathology and clinical biology II, Juxtacortical cartilage tumors. Skeletal Radiol 28:1–20
326. Moody EB, Classman SB, Hansen AV, Lawrence SK, Delbeke D (1992) Nuclear medicine case of the day. AJR Am J Roentgenol 158:1382–1386
327. Siddiqui RA, Ellis JH (1982) "Cold spots" on bone scan at the site of primary osteosarcoma. In: Rosslleigh MA, Smith J, Yeh SDJ et al (1987) Case reports: a photopenic lesion in osteosarcoma. Br J Radiol 60:497–499
328. Bloem JL, Taminiau AHM, Eulderink F, Hermans J, Pauwels EKJ (1988) Radiologic staging of primary bone sarcoma: MR imaging, scintigraphy, angiography, and CT correlated with pathologic examination. Radiology 169:805–810
329. McKillop JH, Etcubanas E, Goris ML (1981) The indications for and limitations of bone scintigraphy in osteogenic sarcoma. Cancer 48:1133–1138
330. Hurley C, McCarville MB, Shulkin BL, Mao S, Wu J, Navid F et al (2016) Comparison of ^{18}F-FDG-PET-CT and bone scintigraphy for evaluation of osseous metastases in newly diagnosed and recurrent osteosarcoma. Pediatr Blood Cancer 63:1381–1386. https://doi.org/10.1002/pbc.26014
331. Liu F, Zhang Q, Zhou D et al (2019) Effectiveness of ^{18}F-FDG PET/CT in the diagnosis and staging of osteosarcoma: a meta-analysis of 26 studies. BMC Cancer 19:323. https://doi.org/10.1186/s12885-019-5488-5
332. Burak Z, Ersoy O, Moretti JL, Erinc R, Ozcan Z, Dirlik A, Sabah D, Basdemir G (2001) The role of 99mTc-MIBI scintigraphy in the assessment of MDR1 overexpression in patients with musculoskeletal sarcomas: comparison with therapy response. Eur J Nucl Med 28:1341–1350
333. Gorlick R, Liao AC, Antonescu C, Huvos AG, Healey JH, Sowers R, Daras M, Calleja E, Wexler LH, Panicek D, Meyers PA, Yeh SD, Larson SM (2001) Lack of correlation of functional scintigraphy

with (99 m)technetium-methoxyisobutylisonitrile with histological necrosis following induction chemotherapy or measures of P-glycoprotein expression in high-grade osteosarcoma. Clin Cancer Res 7:3065–3070
334. Kaste SC, Billips C, Tan M, Meyer WH, Parham DM, Rao BN, Pratt CB, Fletcher BD (2001) Thallium bone imaging as an indicator of response and outcome in nonmetastatic primary extremity osteosarcoma. PediatrRadiol 31:251–256
335. Byun BH, Kong CB, Lim I, Kim BI, Choi CW, Song WS, Cho WH, Jeon DG, Koh JS, Lee SY (2013) Comparison of (18)F-FDG PET/CT and (99 m)Tc-MDP bone scintigraphy for detection of bone metastasis in osteosarcoma. Skeletal Radiol 42:1673–1681
336. Franzius F, Bielack S, Flege S, Sciuk J, Jürgens H, Schober O (2002) Prognostic significance of $^{18F\text{-}FDG}$ and ^{99}Tc-mehylene diphosphonate uptake in primary osteosarcoma. J Nucl Med 43:1012–1017
337. Hillengass J, Moulopoulos LA, Delorme S, Koutoulidis V, Mosebach J, Hielscher T, Terpos E (2017) Whole-body computed tomography versus conventional skeletal survey in patients with multiple myeloma: a study of the International Myeloma Working Group. Blood Cancer J 7(8):e599–e599
338. Gleeson TG, Moriarty J, Shortt CP et al (2009) Accuracy of whole-body low-dose multidetector CT (WBLDCT) versus skeletal survey in the detection of myelomatous lesions, and correlation of disease distribution with whole-body MRI (WBMRI). Skeletal Radiol 38:225–236
339. Zamagn E, Tacchetti P, Cavo M (2019) Imaging in multiple myeloma: how? When? Blood 133:644–651. https://doi.org/10.1182/blood-2018-08-825356
340. Sasikumar A, Joy A, Pilla MRA, Nanabala R, Thomas B (2016) G-68a-PSMA PET/CT imaging in multiple myeloma. Clin Nucl Med 42:e126–e127
341. Connolly LP, Drubach LA, Ted Treves S (2002) Applications of nuclear medicine in pediatric oncology. Clin Nucl Med 27:117–125
342. Hung GU, Tan TS, Kao CH, Wang SJ (2000) Multiple skeletal metastases of Ewing's sarcoma demonstrated on FDG-PET and compared with bone and gallium scans. Kaohsiung J Med Sci 16:315–318
343. Daldrup-Link HE, Franzius C, Link TM et al (2001) Whole-body MR imaging for detection of bone metastases in children and young adults: comparison with skeletal scintigraphy and FDG PET. AJR Am J Roentgenol 177:229–236
344. Mar WA, Taljanovic MS, Bagatell R et al (2008) Update on imaging and treatment of Ewing sarcoma family tumors: what the radiologist needs to know. J Comput Assist Tomogr 32:108–118
345. Gaston LL, Di Bella C, Slavin J, Hicks RJ, Choong PF (2011) 18F-FDG PET response to neoadjuvant chemotherapy for Ewing sarcoma and osteosarcoma are different. Skeletal Radiol 40:1007–1015
346. Dorland WAN (1988) Dorland's Illustrated medical dictionary, 27th edn. Saunders, Philadelphia, p 1016
347. Cuccurullo V, Cascini GL, Rossi A, Tamburrini O, Rotando A, Mansi L (2011) Pathophysiological premises to radiotracers for bone metastases. Q J Nucl Med Mol Imaging 55:353–373
348. Batson OV (1940) The function of the vertebral veins and their role in the spread of metastases. Ann Surg 112:138
349. Resnick D, Niwayama G (1998) Skeletalmetastases. In: Resnick D, Niwayama G (eds) Diagnosis of bone and joint disorders, 2nd edn. Saunders, Philadelphia, pp 3945–4010
350. Resnick D, Niwayama K, Galasko CSD (1981) Bone metastasis studied in experimental animal. Clin Orthop Relat Res 155:269
351. Galasko CSD (1982) Mechanisms of lytic and blastic metastatic disease of bone. Clin Orthop Relat Res 169:20
352. Roodman GD (2004) Mechanism of bone metastasis. N Engl J Med 350:1655–1664
353. Mihailović J, Freeman LM (2012) Bone: from planar imaging to SPECT & PET/CT. Arch Oncol 20(3–4):117–120
354. Padhani A, Husband J (1998) Bone metastases. In: Husband JES, Reznek RH (eds) Imaging in oncology. Isis medical Media Ltd, Oxford, pp 765–787
355. O'Connel MJ, Wahner HW, Alhann DL et al (1978) Value of preoperative radionuclide bone scan in suspected primary breast carcinoma. Mayo Clin Proc 53:221–226
356. Baker RR (1978) Preoperative assessment of patients with breast cancer. Surg Clin North Am 58:681–691
357. Wilner D (1982) Radiology of bone tumors and allied disorders. Saunders, Philadelphia, p 3641
358. Ripamonti C, Fulfaro F, Ticozzi C, Casuccio A, De Conno F (1998) Role of pamidronate disodium in the treatment of metastatic bone disease. Tumori. 84:442–455
359. Huang JF, Shen J, Li X, Rengan R, Silvestris N, Wang M, Derosa L, Zheng X, Belli A, Zhang XL, Li YM, Wu A (2020) Incidence of patients with bone metastases at diagnosis of solid tumors in adults: a large population-based study. Ann Transl Med 8:482
360. Ryan C, Stoltzfus KC, Horn S, Chen H, Louie AV, Lehrer EJ, Trifiletti DM, Fox EJ, Abraham JA, Zaorsky NG (2022) Epidemiology of bone metastases. Bone. 2022;158:115783. https://doi.org/10.1016/j.bone.2020.115783. Epub 2020 Dec 1. PMID: 33276151.
361. Hernandez RK, Wade SW, Reich A, Pirolli M, Liede A, Lyman GH (2018) Incidence of bone metastases in patients with solid tumors: analysis of oncology electronic medical records in the United States. BMC Cancer 18:44
362. Ryan PJ, Evans PA, Gibson T et al (1992) Chronic low back pain: comparison of bone SPECT with radiography and CT. Radiology 13:497–854
363. Bushnell DL, Kahn D, Huston B et al (1995) Utility of SPECT imaging for determination of vertebral metastases in patients with known primary tumors. Skeletal Radiol 24:13–16

364. Ron IG, Striecker A, Lerman H, Bar-Am A, Frisch B (1999) Bone scan and bone biopsy in the detection of skeletal metastases. Oncol Rep 6:185–188
365. Elgazzar AH, Abdel-Dayem HM, Shible O (1991) Brucellosis simulating metastases on Tc99m MDP bone scan. Clin Nucl Med 16:162–164
366. Goris ML, Basso LV, Etcublanaas E (1980) Photopenic lesions in bone scintigraphy. Clin Nucl Med 5:299–301
367. Sy WM, Westring DW, Weinberger G (1975) Cold lesions on bone imaging. J Nucl Med 16:1013–1016
368. Galasko CSB (1980) Mechanism of uptake of bone imaging isotopes by skeletal metastases. Clin Nucl Med 12:565
369. Daldrup-Link HE, Franzius C, Link TM, Laukamp D, Sciuk J, Jurgens H, Schober O, Rummeny EJ (2001) Whole-body MR imaging for detection of bone metastases in children and young adults: comparison with skeletal scintigraphy and FDG PET. AJR Am J Roentgenol 177:229–236
370. Kao CH, Hsieh JF, Tsai SC, Ho YJ, Yen RF (2000) Comparison and discrepancy of 18F-2-deoxyglucose positron emission tomography and Tc-99m MDP bone scan to detect bone metastases. Anticancer Res 20:2189–2192
371. Moog F, Kotzerke J, Reske SN (1999) FDG PET can replace bone scintigraphy in primary staging of malignant lymphoma. J Nucl Med 40:1407–1413
372. Schirrmeister H, Guhlmann A, Elsner K, Kotzerke J, Glatting G, Rentschler M, Neumaier B, Trager H, Nussle K, Reske SN (1999) Sensitivity in detecting osseous lesions depends on anatomic localization: planar bone scintigraphy versus F18 PET. J Nucl Med 40:1623–1629
373. Garcia JR, Simo M, Soler M, Perez G, Lopez S, Lomena F (2005) Relative roles of bone scintigraphy and positron emission tomography in assessing the treatment response of bone metastases. Eur J Nucl Med Mol Imaging 32:1243–1244
374. Toegel S, Hoffmann O, Wadsak W et al (2006) Uptake of bone-seekers is solely associated with mineralization! A study with (99m)Tc-MDP, Sm-EDTMP and fluoride-(18F) on osteoblasts. Eur J Nucl Med Mol Imaging 33:491–494
375. Czernin J, Satyamurthy N, Schiepers C (2010) Molecular mechanisms of bone 18F-NaF deposition. J Nucl Med 51:1826–1829
376. Segall G, Delbeke D, Stabin MG, Even-Sapir E, Fair J, Sajdak R, Smith GT (2010) SNM practice guideline for sodium 18F-fluoride PET/CT bone scans. J Nucl Med 51:1813–1820
377. Yen RF, Chen CY, Cheng MF, Wu YW, Shiau YC, Wu K, Hong RL, Yu CJ, Wang KL, Yang RS (2010) The diagnostic and prognostic effectiveness of F-18 sodium fluoride PET-CT in detecting bone metastases for hepatocellular carcinoma patients. Nucl Med Commun 31:537–545
378. Sheth S, Colletti PM (2012) Atlas of sodium fluoride PET bone scans: atlas of NaF PET bone scans. Clin Nucl Med 37:e110–e115
379. Blake GM, Park-Holohan SJ, Cook GJ et al (2001) Quantitative studies of bone with the use of 18F-fluoride and 99mTc-methylene diphosphonate. Semin Nucl Med 31:28–49
380. Cook GJ, Fogelman I (2001) The role of positron emission tomography in skeletal disease. Semin Nucl Med 31:50–61
381. Even-Sapir E (2005) Imaging of malignant bone involvement by morphologic, scintigraphic, and hybrid modalities. J Nucl Med 46:1356–1367
382. Cook GJ, Houston S, Rubens R et al (1998) Detection of bone metastases in breast cancer by 18-FDG PET: differing metabolic activity in osteoblastic and osteolytic lesions. J Clin Oncol 16:3375–3379
383. Gnanasegaran G, Cook G, Fogelman I (2007) Musculoskeletal system. In: Biersac HJ, Freeman LM (eds) Clinical nuclear medicine. Springer, Berlin, pp 241–262
384. Taira AV, Herfkens RJ, Gambhir SS, Quon A (2007) Detection of bone metastases: assessment of integrated FDG PET/CT imaging. Radiology 243(1):204–211
385. Costelloe CM, Chuang HH, Chasen BA, Pan T, Fox PS, Bassett RL, Madewell JE (2013) Bone windows for distinguishing malignant from benign primary bone tumors on FDG PET/CT. J Cancer 4:524–530
386. Kruger S et al (2009) Detection of bone metastases in patients with lung cancer: 99mTc-MDP planar bone scintigraphy, 18F-fluoride PET or 18F-FDG PET/CT. Eur J Nucl Med Mol Imaging 36:1807
387. Iagaru A et al (2012) Prospective evaluation of (99m) Tc MDP scintigraphy, (18)F NaF PET/CT, and (18) F FDG PET/CT for detection of skeletal metastases. Mol Imaging Biol 14:252
388. Jadvar H et al (2012) Prospective evaluation of 18F-NaF and 18F-FDG PET/CT in detection of occult metastatic disease in biochemical recurrence of prostate cancer. Clin Nucl Med 37:637
389. Lin FI et al (2012) Prospective comparison of combined 18F-FDG and 18F-NaF PET/CT vs. 18F-FDG PET/CT imaging for detection of malignancy. Eur J Nucl Med Mol Imaging 39:262
390. Iagaru A, Mittra E, Mosci C, Dick DW, Sathekge M, Prakash V, Gambhir SS (2013) Combined 18F-fluoride and 18F-FDG PET/CT scanning for evaluation of malignancy: results of an international multicenter trial. J Nucl Med 54(2):176–183
391. Karamzade-Ziarati N, Manafi-Farid R, Ataeinia B, Langsteger W, Pirich C, Mottaghy FM, Beheshti M (2019) Molecular imaging of bone metastases using tumor-targeted tracers. Q J Nucl Med Mol Imaging. 63(2):136–149

Endocrine System

6

Saud A. Alenezi and Abdelhamid H. Elgazzar

6.1 The Thyroid Gland

6.1.1 Anatomical and Physiological Considerations

6.1.1.1 Anatomy

The thyroid gland develops from the foramen cecum of the tongue, to which it is connected by the thyroglossal duct. It descends during fetal life to reach the anterior neck by about the seventh week. Absent or aberrant descent results in ectopic locations, including the sublingual region and superior mediastinum.

The normal adult thyroid gland weighs 14–19 g. It is generally smaller in women than in men, and is barely palpable [1, 2]. The thyroid is located in the mid to lower anterior neck, with the isthmus in front of the trachea, usually just below the cricoid cartilage, and the lobes on the sides of the trachea (Fig. 6.1). In older individuals with shorter necks, the thyroid may lie at or just above the suprasternal notch, and it may often be partly substernal. The thyroid gland moves cephalad during swallowing, a characteristic that aids in palpation and in distinction of thyroid from nonthyroid neck masses.

6.1.1.2 Physiology

The thyroid gland regulates a spectrum of physiological activities such as growth, metabolism, homeostasis, and cell proliferation and differentiation through the secretion of thyroid hormones. The thyroid follicle consists of a colloid center, which acts as a storage site for thyroid hormone, surrounded by epithelial cells (Fig. 6.2). The thyroid epithelial cell has a transport mechanism, also referred to as trapping, that enables thyroid concentration of iodide. The sodium-dependent iodide transport activity of the thyroid gland is mainly attributed to the functional expression of the Na^+/I^- Symporter (NIS) localized at the basolateral membrane of thyroid epithelial cells. Symporter activity is influenced primarily by pituitary thyroid-stimulating hormone (TSH), which increases the transport of iodide. The trapped iodide subsequently undergoes organification and incorporation into thyroid hormones.

Additionally, other anions, such as pertechnetate, thiocyanate, and perchlorate, are also accumulated by the thyroid gland. The uptake of pertechnetate is the basis for ^{99m}Tc-pertechnetate scintigraphy. Thiocyanate, derived from certain foods, decreases thyroid accumulation of iodine and may exacerbate iodine deficiency. Perchlorate has diagnostic and therapeutic applications.

Synthesis of hormone takes place in thyroglobulin, a glycoprotein, which is produced in the thyroid cell and extruded into the colloid. Iodine combines with tyrosine in thyroglobulin to form

S. A. Alenezi (✉) · A. H. Elgazzar
Department of Nuclear Medicine, Faculty of Medicine, Kuwait University, Kuwait City, Kuwait

A. H. Elgazzar (ed.), *The Pathophysiologic Basis of Nuclear Medicine*,
https://doi.org/10.1007/978-3-030-96252-4_6

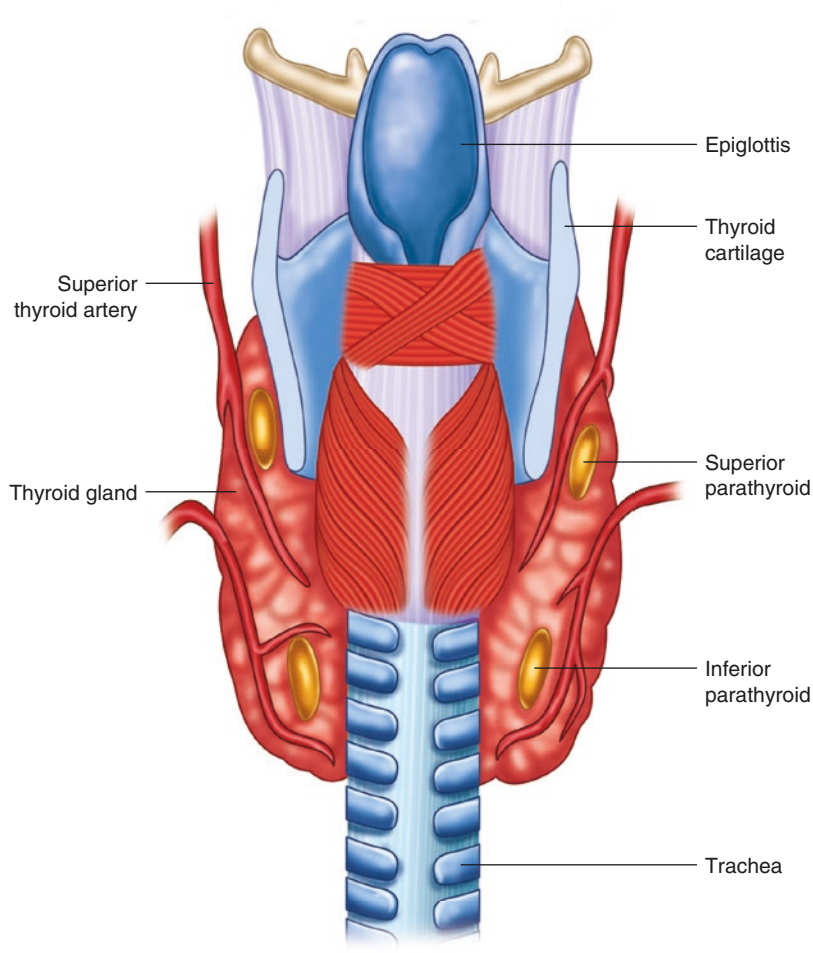

Fig. 6.1 Diagram showingtypical locations of the thyroid and parathyroid glands in the neck

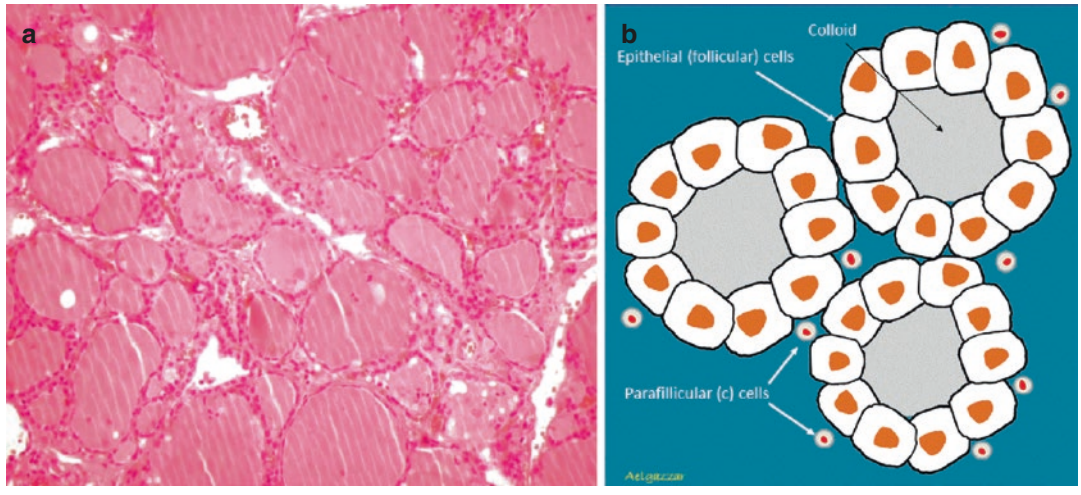

Fig. 6.2 Thyroid follicle. (**a**) Low-power field images of thyroid gland tissue showing the follicles lined by follicular cells and filled with colloid. (**b**) Diagram illustrating thyroid follicles and cells

Table 6.1 Actions and uses of antithyroid drugs

Drug	Mechanism	Uses
Propylthiouracil (PTU)	Blocks iodine organification	Controls hyperthyroidism in Graves' disease and toxic nodular goiter
	Decreases the monodeiodination of T_4 to T_3	
	Decreases in serum levels of thyrotropin receptor autoantibodies	
Methimazole	Blocks iodine organification	Controls hyperthyroidism in Graves' disease and toxic nodular goiter
	Decreases in serum levels of thyrotropin receptor autoantibodies	
Glucocorticoids	Rapid inhibitory effect on peripheral conversion of T_4 to T_3	Thyroid storm, Graves' ophthalmopathy, and protracted subacute thyroiditis
Iodides	Decreases synthesis of thyroid hormones	Thyroid storm
Lithium	Blocks release of thyroid hormone	Adjunct in treatment of severe hyperthyroidism
Potassium perchlorate	Decreases thyroid iodine uptake and discharges unbound iodine	Amiodarone-induced thyroid dysfunction and after accidental exposure to radioactive iodine

monoiodotyrosine (MIT) and diiodotyrosine (DIT). Subsequently, the iodotyrosines are coupled, with the formation of thyroxine (T_4) and triiodothyronine (T_3). The coupling reaction also is mediated by peroxidase.

Release of thyroid hormones occurs in response to TSH, where a small amount of colloid is engulfed by the epithelial cell and proteolyzed, with release of T_3 and T_4, which diffuse into the circulation. Thyroglobulin not undergoing proteolysis also enters the circulation in small quantities. The serum thyroglobulin has been used as a tumor marker in differentiated thyroid cancer. Thyroglobulin decreases and eventually becomes undetectable following thyroidectomy and ^{131}I ablation, and its subsequent rise indicates a recurrence. TSH stimulation, by promoting colloid endocytosis, increases the amount of thyroglobulin released. Consequently, the serum thyroglobulin is a more reliable tumor marker at high TSH levels [3, 4].

Most of the circulating thyroid hormones are bound to plasma proteins, the free fraction comprising about 0.05% of T_4 and 0.2% of T_3. Only the free hormone has metabolic effects, and it is a more accurate measure of thyroid function than the total hormone, which varies with plasma proteins levels. T_3 is considered the active hormone. About 20–30% of the circulating T_3 is secreted by the thyroid gland and the remainder is produced by monodeiodination of T_4 in extrathyroid tissues, notably the liver, kidney, brain, and pituitary [4]. Decrease in the peripheral conversion of T_4 to T_3 is a basis for the use of some antithyroid drugs.

Most antithyroid drugs generally block one or more steps in the synthesis and metabolism of thyroid hormone (Table 6.1). The thiourea derivatives (thionamides), including propylthiouracil (PTU) and methimazole, are the most common antithyroid agents in use [5, 6]. Methimazole is generally the preferred drug since PTU may be associated with serious hepatotoxicity [6]. Other drugs used for their antithyroid actions include glucocorticoids, iodides, lithium, and potassium perchlorate [4].

Thyrotropin-releasing hormone (TRH), a tripeptide originating from the hypothalamic median eminence, stimulates the secretion and synthesis of thyroid-stimulating hormone (TSH, thyrotropin), a glycoprotein, by the anterior pituitary. It increases the transport of iodide, synthesis of hormone, and release of T_3, T_4, and thyroglobulin. The production and release of TSH are influenced by the concentration of T_3 within the pituitary. When the T_3 concentration falls below a set point, TSH secretion increases, and synthesis and release of thyroid hormones are accelerated. Conversely, when the T_3 level rises above the set point, TSH release is inhibited. In addition to its pituitary effect, T_3 inhibits hypothalamic TRH release. Other mechanisms

reported more recently include the inhibitory actions of the released TSH on TRH secretion, and on TSH receptors in the pituitary itself.

In addition to regulation of thyroid function, TSH promotes thyroid growth. If thyroid hormone synthesis is chronically impaired, as in iodine deficiency and autoimmune thyroid disease, chronic TSH stimulation eventually may lead to the development of a goiter.

The serum TSH is a sensitive and specific marker of thyroid function. Normal serum TSH is about 0.45–4.5 μunits/ml, and levels up to 20 μunits/ml are considered normal in newborns because of the contribution of maternal TSH. Serum TSH is increased in primary hypothyroidism and decreased in hyperthyroidism of all etiologies except for the uncommon entity of thyrotropin-induced hyperthyroidism.

The TSH secretion is suppressed by exogenous thyroid hormone to avoid stimulation of tumor growth in patients with differentiated thyroid cancer, and to decrease thyroid size or arrest thyroid growth in the early stages of goiter development.

Stimulation with TSH increases thyroid function and thyroid uptake of radioiodine. This principle is used in differentiated thyroid cancer for the detection and treatment of thyroid remnants and thyroid cancer metastases with radioiodine [6, 7]. Thyroid-stimulating hormone levels are allowed to rise to 30–50 μunits/ml or higher after withholding thyroid hormone supplements, or after administering recombinant human TSH. The latter is becoming popular since it shortens the preparation time and avoids a period of hypothyroidism after stopping thyroid hormone replacement therapy [8, 9]. In thyroid cancer, recombinant TSH is used in diagnosis, monitoring of serum thyroglobulin, and for radioiodine ablation of thyroid remnants after thyroidectomy. FDG PET is optimal at high TSH levels, and it may be combined with radioiodine imaging and thyroglobulin measurement in selected patients [10, 11]. In addition, FDG uptake was found to be of value in identifying metastases in postoperative differentiated thyroid cancer patients and in predicting iodine avidity since SUV higher than four indicate more aggressive disease and higher probability of non-avidity to radioiodine [12].

6.1.1.3 Role of Iodine Metabolism in Thyroid Physiology

Iodine is needed for the production of thyroid hormones. Since the body does not make iodine, it is an essential part of diet. The mean daily turnover of iodine by the thyroid is approximately 60–95 μg in adults in iodine-sufficient areas. The body of a healthy adult contains from 15 to 20 mg of iodine, 70–80% of which is in the thyroid. Iodine is a trace element that is ingested in several chemical forms. Most forms of iodine are reduced to iodide in the gut. Iodide is nearly completely absorbed in the stomach and duodenum [13]. In the basolateral membrane of the thyroid cell, the sodium/iodine symporter transfers iodide into the thyroid across a concentration gradient 20–50 times that of plasma by active transport [13]. Iodine is cleared from the circulation primarily by the thyroid and kidney. Under normal circumstances, plasma iodine has a half-life of approximately 10 h, but this is shortened if the thyroid is overactive, as in iodine deficiency or hyperthyroidism.

Degradation of T_4 and T_3 in the peripheral tissues releases iodine that re-enters the plasma iodine pool. Most ingested iodine is eventually excreted in the urine. Only a small amount appears in the feces.

The mammary glands concentrate iodine and secrete it into breast milk to provide it for the newborn. The salivary glands, gastric mucosa, and choroid plexus also take up small amounts of iodine. The iodine symporter have been reported in trophoblasts, and the placental iodine content is approximately 3% that of the thyroid [14, 15].

Effect of Iodine Insufficiency

Iodine is an essential micronutrient, as it is an integral part of the thyroid hormones thyroxine (T_4) and triiodothyronine (T_3). Severe iodine deficiency results in depleted iodine stores and a failure to sustain normal thyroid hormone levels [16]. The recommended daily intake of iodide is 150 μg for adolescents and adults, and 250 μg in pregnancy and lactation [17].

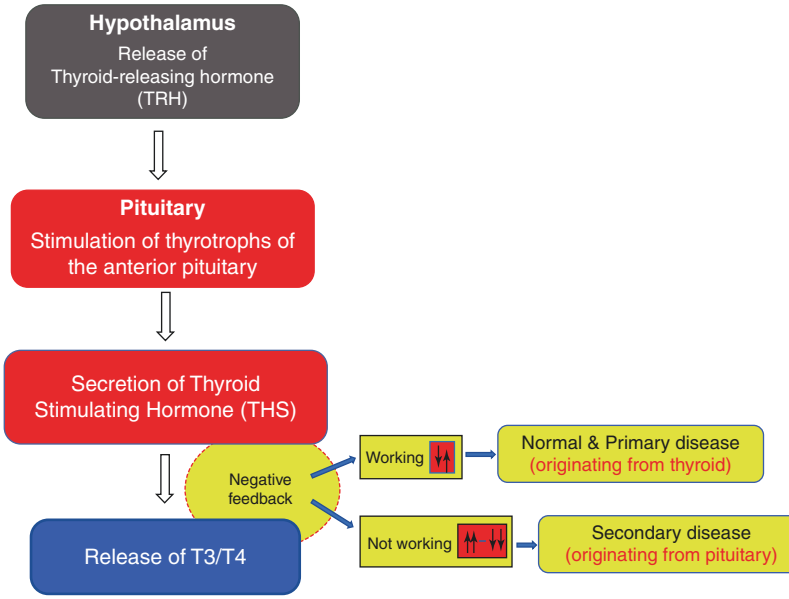

Fig. 6.3 Simple illustration of different hormones related to thyroid function

Reduced synthesis of thyroid hormone is compensated, at least in part, by increased TSH secretion, resulting eventually in goiter formation.

Because an adequate supply of thyroid hormone is needed for fetal neurological development, maternal and fetal hypothyroidism resulting from iodine deficiency is associated with varying degrees of neuropsychological deficits including cretinism.

Effect of Excessive Iodine

When intrathyroid iodine concentrations are significantly increased, the rate of thyroid hormone synthesis is decreased, with a reduction in iodothyronine synthesis and decrease in the DIT/MIT ratio. This response is referred to as the Wolff–Chaikoff effect.

Continued exposure to large amounts of iodine would eventually lead to hypothyroidism, with compensatory increase in TSH and development of goiter. While this does occur occasionally, adaptation or escape from the effects of chronic iodide excess is more likely. The inhibitory effect of iodides on thyroid function is utilized clinically for prompt control of severe hyperthyroidism and thyroid storm. In Graves' disease, large doses of iodide decrease not only hormone synthesis but also hormone release [12]. Since escape from the inhibitory effect is likely, iodide therapy is only a short-term measure for lowering thyroid hormone levels rapidly.

Iodine excess may lead to hyperthyroidism or hypothyroidism [13, 14]. Iodine-induced hyperthyroidism, referred to as Jod-Basedow, characteristically occurs in persons with hyperplastic thyroid glands. Hyperthyroidism occurring after iodine supplementation in endemic goiter areas is a classical example. Iodine-containing medical products, including amiodarone, radiographic dyes, and kelp, also have the potential to cause Jod-Basedow [18, 19]. Amiodarone, a cardiac antiarrhythmic drug, is a benzofuranic product with a very high iodine content and may be associated with either hypo- or hyperthyroidism development.

Figure 6.3 summarizes the mechanism of hormonal interactions related to thyroid gland.

6.1.2 Radiopharmaceuticals for Thyroid Imaging

6.1.2.1 Technetium-99m-Pertechnetate

Technetium-99m-pertechnetate is widely used for imaging the thyroid gland. It is trapped by the thyroid, but unlike iodine, it does not undergo organification and remains in the gland for a rela-

tively short duration. Therefore, imaging is done about 20–30 min after intravenous administration of the radiotracer. Approximately 5–10 mCi (185–370 MBq) are used. The thyroid-to-background activity ratio is not as high as that with radioiodine, so that ^{99m}Tc-pertechnetate is unsuitable for imaging to search for metastatic thyroid carcinoma, which usually functions poorly compared with normal thyroid tissue. Imaging of ectopic mediastinal thyroid tissue also may be suboptimal due to high blood and soft tissue background activity.

6.1.2.2 Iodine-123

Iodine-123 (^{123}I) has ideal characteristics for imaging the thyroid gland, with a short physical half-life of 13 h, absence of beta emissions, and high uptake in thyroid tissue relative to background [17]. However, it is less readily available and more expensive than ^{99m}Tc-pertechnetate. ^{123}I undergoes organic binding in the thyroid gland, and imaging is usually done 4–24 h after oral administration of 200–400 μCi (7.4–14.8 MBq) of radiotracer. Because of its superior biodistribution characteristics, ^{123}I is preferred over ^{99m}Tc-pertechnetate for imaging of poorly functioning and ectopic thyroid glands. ^{123}I also may be used for whole-body imaging in differentiated thyroid cancer. Approximately 2–4 mCi (74–148 MBq) of the radiotracer are used for this purpose.

6.1.2.3 Iodine-131

Iodine-131 (^{131}I) may be used for the measurement of thyroid uptake, which requires only very small amounts of radiotracer. It is no longer used for routine imaging of the thyroid gland but continues to be valuable for the detection of metastases and recurrences in differentiated thyroid cancer [3, 20, 21]. Following appropriate patient preparation to increase TSH levels, 2–4 mCi (74–148 MBq) of ^{131}I are administered orally and imaging is performed 48–96 h later. Radioiodine imaging has diagnostic as well as prognostic value. Iodine-avid tumors tend to be well-differentiated histological features and a favorable prognosis, whereas tumors that do not accumulate iodine are likely to be less differentiated and more aggressive [3, 22, 23].

Iodine-131 delivers a high radiation absorbed dose to the thyroid, with relative sparing of non-thyroid tissues. It is therefore ideal for the treatment of thyroid disease, and used extensively in the management of Graves' disease, toxic nodular goiter, and differentiated thyroid cancer.

6.1.2.4 Fluorine-^{18}F-Fluorodeoxyglucose (^{18}F-FDG)

Positron emission tomography (PET) with ^{18}F-FDG is used in evaluating a variety of neoplasms including differentiated thyroid cancer. In differentiated thyroid cancer, FDG may be used to identify metastases not visualized at radioiodine imaging, and to assess prognosis. Lesions that accumulate FDG tend to follow a more aggressive course than lesions that are not FDG-avid [10]. Whole-body FDG PET, therefore, is useful in evaluating high-risk thyroid cancer. Patient preparation is similar to that for radioiodine scintigraphy, since the uptake and diagnostic sensitivity of FDG are increased by TSH stimulation [11].

Focal uptake of FDG within the thyroid gland, an occasional finding at evaluation of non-thyroid cancers, may be related to a benign or malignant pathology [23]. In patients with thyroid nodules with indeterminate FNA, FDG PET/CT has a moderate ability to correctly discriminate malignant from benign lesions [24]. It may be a reliable option to reduce unnecessary diagnostic surgeries particularly if it is negative at the site of a solitary nodule. On the other hand, diffusely increased FDG uptake in the thyroid gland was found to be associated with chronic thyroiditis and thyroid dysfunction [25].

6.1.3 Major Thyroid Disorders

The most relevant thyroid conditions that commonly need imaging for diagnosis and management include nodular disease, inflammatory conditions, autoimmune disorders, and thyroid cancer:

6.1.3.1 Pathophysiology

Nodular Thyroid Disease

Thyroid nodules are common. The prevalence ranges from 4% to 10% in general adult and 0.2% to 1.5% in children [26] and is greater in countries affected by iodine deficiency. The incidence of thyroid nodules in apparently normal thyroid glands is greater than 50% in autopsy series. Studies using high frequency ultrasound in detecting nodules showed a varying prevalence of up to 68% [27, 28], higher in females compared to males and increasing with age [28].

Most thyroid nodules are benign, particularly in multinodular goiter. Malignancy in clinical thyroid nodules is reported to occur in 5–20% of nodules and is higher in males [29]. Mortality due to thyroid cancer is generally very low.

Types of Thyroid Nodules

Thyroid nodules represent wide spectrum of thyroid diseases. In a normal sized gland or a diffuse goiter, thyroid nodules may be solitary or multiple. In multinodular goiters, a nodule may become clinically dominant in terms of growth, dimensions, and functional characteristics. A clinicopathological classification of thyroid nodules subdivides nodules into: nonneoplastic nodules, true neoplastic nodules (benign or malignant), and micronodules.

Nonneoplastic Nodules (Pseudo-nodules)

These nodules may be seen in patients with thyroid hyperplasia, inflammatory or autoimmune thyroid diseases:

1. Glandular hyperplasia arising spontaneously or following previous partial thyroidectomy.
2. Rare forms of thyroid hemiagenesis which may present as hyperplasia of the existing thyroid tissue, mimicking a thyroid nodule.
3. Hashimoto's thyroiditis associated nodules, indicative of lymphocyte infiltration.
4. Nodules found during the initial phase of subacute thyroiditis, resulting from the inflammatory process.

Neoplastic Nodules

Based on scintigraphy thyroid nodules are classified into functioning (hot) nodules which are able to concentrate radioactive iodine or technetium-99m pertechnetate and non-functioning (cold) which show radiotracer uptake less than that in normal thyroid tissue. Hot nodules represent from 3% to 20% of thyroid nodules, according to the geographical origin of the patients as their incidence is higher in countries where iodine deficiency is still present. They are three to four times more frequent in females and tend to occur in those older than 40 years. In the great majority of cases, hot nodules are benign. Cold nodules account for more than 80% of all thyroid nodules. Three types of nodule are distinguished by ultrasonography: cystic, solid, and mixed (containing solid and cystic components). Cystic nodules (10–20% of all nodules) are almost always benign. Thyroid cancer is found in approximately 10% of cold nodules (solitary and multiple) that are solid or mixed at ultrasonography. More than 75% of malignant nodules are differentiated thyroid cancer of the follicular epithelium (papillary and follicular) with excellent prognosis. The other types of cancer are rare and include anaplastic or undifferentiated carcinoma (2–14% of all thyroid carcinomas), medullary thyroid carcinoma representing 5–10% of thyroid carcinomas and originating from the calcitonin-producing parafollicular C cells of the thyroid [30–32]. Lymphoma and metastases to thyroid are other uncommon malignancies.

Micronodules

Micronodules describe nodules of 1 cm or less in diameter. These nodules are discovered increasingly by the commonly used ultrasonography. In the absence of other suspicious clinical criteria, they only require to be followed by repeated thyroid ultrasonography.

Thyroiditis

Thyroiditis, a group of inflammatory thyroid diseases affecting the gland diffusely or focally, can be infectious, due to microorganisms, or noninfectious. Based on clinical, histopathologic, etio-

logical, and other factors, many classifications and terminologies for the conditions have been proposed. Simply it can be classified into acute, subacute, and chronic [32]. Figure 6.4 shows that classification which we modified to be more inclusive.

Acute Thyroiditis

Acute thyroiditis also called acute suppurative thyroiditis is a rare but serious form secondary to bacteria. Acute thyroiditis requires immediate parenteral antibiotic therapy before abscess formation begins.

Subacute Thyroiditis

Subacute thyroiditis or destructive thyroiditis is characterized by cell membrane breakdown and consequently release of excessive amounts of thyroid hormone into the circulation. The usual causes are autoimmune thyroid disease, viral infection, and amiodarone treatment. Less commonly, thyroiditis may be related to treatment with certain drugs such as interferon alpha, interleukin-2, lymphokine-activated killer (LAK) cells, and lithium. These therapeutic agents probably exacerbate existing autoimmune thyroid disease [3–6, 8–36].

Thyroiditis is typically painful and usually resolves spontaneously. Hyperthyroidism in the active phase is followed by transient hypothyroidism before restoration of the euthyroid state, usually in 6–12 months. Treatment usually consists of β-adrenergic blockers in the hyperthyroid phase and analgesics for pain. Protracted thyroiditis may however require glucocorticoids.

Viral subacute thyroiditis, also known as de Quervain's thyroiditis, usually occurs after an upper respiratory tract infection. The disorder tends to be seasonal and may occur in clusters, occasionally causing mini epidemics. It usually presents as a painful and tender goiter, associated with general malaise and possibly fever. Inflammation frequently begins in one lobe of the

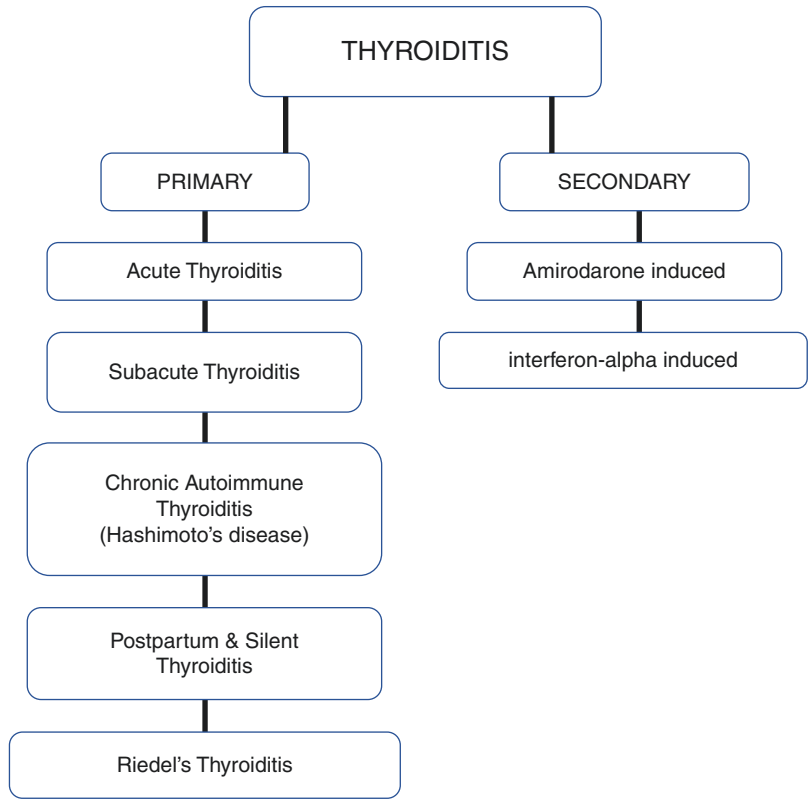

Fig. 6.4 Classification of thyroiditis

thyroid and gradually spreads to involve the entire gland. Permanent hypothyroidism is uncommon.

Postpartum Thyroiditis

Postpartum thyroiditis, also known as painless or subacute lymphocytic thyroiditis, is the principal thyroid disorder in postpartum women. It may be considered an accelerated form of autoimmune thyroid disease, attributed to suppression of immune-related disorders during pregnancy with a rebound after childbirth [37, 38].

For the same reason, Graves' disease also may occur in the postpartum period, though less frequently, and a strong association with insulin-dependent diabetes mellitus, an autoimmune condition, has been noted.

Postpartum thyroiditis, like other forms of destructive thyroiditis, is a self-limited, but tends to reoccur in subsequent pregnancies. Permanent hypothyroidism occurs in 20–25% of patients over a period of 5 years. Elevated thyroid peroxidase (anti-microsomal) antibodies during pregnancy are associated with a sharp increase in postpartum thyroiditis.

Amiodarone-Induced Thyroiditis

Amiodarone is an iodine-rich benzofuran derivative used to treat and prevent cardiac arrhythmias. It may precipitate a number of thyroid conditions including thyroiditis, which appears to be related to a cytotoxic effect [18, 19]. Thyroid hormone synthesis may increase or decrease. Other actions of amiodarone include blocking peripheral conversion of T_4 to T_3, binding of T_3 to its receptors, and thyroid release of T_3 and T_4. These effects may permit the use of amiodarone in very selected cases of hyperthyroidism [39].

Since amiodarone and its metabolite desethylamiodarone have long half-lives of up to 100 days, the thyroid-related effects can be protracted and occasionally may begin after stopping the drug. Amiodarone-induced thyroiditis generally requires treatment with a glucocorticoid. Permanent hypothyroidism is uncommon.

Interferon-Alpha Induced Thyroiditis

Interferon-alpha (IFNα) is an important drug therapy for several malignant and nonmalignant diseases, especially hepatitis C. Interferon induced thyroiditis is a major clinical problem for patients receiving interferon therapy. Studies have shown that up to 15% of patients with hepatitis C receiving IFNα develop clinical thyroid disease, and up to 40% were reported to develop thyroid antibodies. Interferon-alpha induced thyroiditis can be classified as autoimmune type and non-autoimmune type. Autoimmune interferon-alpha induced thyroiditis may be manifested by the development of thyroid antibodies with or without clinical disease. Clinical disease includes both autoimmune hypothyroidism (Hashimoto's thyroiditis) and autoimmune thyrotoxicosis (Graves' disease). Non-autoimmune thyroiditis can manifest as subacute (destructive thyroiditis) or as hypothyroidism with negative thyroid antibodies [40, 41].

Autoimmune Thyroiditis (Hashimoto's Disease)

See following section.

Autoimmune Thyroid Disease

Autoimmune thyroid disease is often observed together with other autoimmune diseases. The coexistence of two or more autoimmune diseases in the same individual is referred to as polyautoimmunity. The occurrence of polyautoimmunity has led to a hypothesis that the affected patients suffer from a generalized dysregulation of their immune system [42].

Autoimmune thyroid disease comprises two major entities, Hashimoto's disease (chronic autoimmune thyroiditis and variants) and Graves' disease. Variants of Hashimoto's disease include subacute thyroiditis, which occurs typically in the postpartum period, and atrophic thyroiditis. The predisposing factors of the disease are listed in Table 6.2 [43–46].

Hashimoto's Disease

Elevation of thyroid peroxidase antibodies is characteristic of Hashimoto's disease. Antithyroglobulin antibodies may also be elevated. Hormone synthe-

Table 6.2 Predisposing factors for autoimmune thyroid disease

Genetic predisposition Immune system dysregulation
Iodine excess
Cigarette smoking
Female gender
Psychological stress
Infection

sis is impaired with immune thyroid disease compensatory increase in TSH secretion, which stimulates thyroid function and growth. Eventually, many patients become hypothyroid. Both overt and subclinical hypothyroidism related to autoimmune disease are widely prevalent in iodine-sufficient regions [47].

Exacerbation of Hashimoto's disease, frequently occurring in the postpartum period, is a cause of subacute thyroiditis.

Graves' Disease

Graves' disease is associated with high levels of thyrotropin receptor autoantibodies(TRAB) that stimulate thyroid growth, and thyroid hormone synthesis and release [46, 48]. Most organ systems are affected by Graves' disease, the cardiovascular manifestations being the most apparent. Increased heart rate and contractility increases the cardiac output. These effects are related to a direct inotropic effect of T3, decreased systemic vascular resistance, increased preload related to a higher blood volume, and heightened sensitivity to sympathetic stimulation. Blood volume is increased by activation of the renin-angiotensin-aldosterone system caused by the reduction in systemic vascular resistance, and by increased erythropoietin activity. Overt cardiac failure may result from severe and prolonged hyperthyroidism, but is rarely seen today. Atrial fibrillation is not an uncommon complication, occurring in up to 15% of patients with hyperthyroidism [49, 50].

Autoimmune Interferon Induced Thyroiditis

The entire spectrum of autoimmune thyroid diseases (AITD) has been described in patients receiving IFNα: Graves' disease (GD), Hashimoto's thyroiditis (HT), and the presence of thyroid antibodies (TAb's) without clinical disease [40, 41].

Thyroid Cancer

In most areas of the world, the incidence of thyroid cancer of follicular origin is increasing. Currently the incidence is approximating 4/100,000 in males and 13.5/100,000 in females. Mortality is stable, at approximately 0.5/100,000 [51]. Based on the histologic classification nuclear medicine has a very important role in the management of thyroid cancer. Table 6.3 summarizes the classification of thyroid cancer. See Chap. 10.

6.1.3.2 Thyroid Scintigraphy

Nodular Disease

When thyroid nodule is discovered, the main problem is distinguishing between a benign and a malignant lesion. This problem has largely been solved by fine-needle biopsy which makes that distinction when performed by experienced cytologists. Nevertheless, nodules labeled as indeterminate by cytology remains a challenge [52]. Neck ultrasound plays a pivotal role in the diagnosis and several ultrasound stratification systems have been proposed in order to predict malignancy and help clinicians in therapeutic and follow-up decision. Despite new technologies in thyroid imaging, diagnostic surgery in 50–70% of patients with indeterminate cytology is still performed. In the last years, various image-guided procedures have been proposed as alternative and less invasive approaches to surgery for symptomatic thyroid nodules. These minimally invasive techniques (laser and radio-frequency ablation, high intensity focused ultrasound and percutaneous microwave ablation) result in nodule shrinkage and improvement of local symptoms, with a lower risk of complications and minor costs compared to surgery. Ultrasound-guided ablation therapy was introduced with promising results as a feasible treatment for low-risk papillary thyroid microcarcinoma or cervical lymph node metastases [52].

Accordingly, the role of thyroid scintigraphy is reserved to the assessment of the functional

Table 6.3 Types of thyroid cancer and main features

Type	Main features
Papillary carcinoma	Most common thyroid malignancy (85%). Derived from the follicular epithelium Has papillary growth pattern with psammoma bodies Has characteristic nuclear changes
Follicular variant papillary carcinoma	Follicular architecture with the characteristic papillary thyroid nuclear pattern
Papillary microcarcinoma	Added relatively recently Of less than 10 mm in size
Follicular carcinoma	Represents 10–20% of thyroid cancers Derived from follicular epithelium with evidence of capsular and/or vascular invasion but without nuclear changes characteristic of papillary thyroid cancer Have a slightly poorer prognosis than papillary cancer. Metastatic spread is hematogenous most commonly to the lung and bone
Oncocytic or Hurthle cell carcinoma	Hurthle cell can occur in any thyroid tumor More commonly associated with follicular carcinomas Prognosis is worse for comparative stage mainly due to poor radioiodine uptake
Poorly differentiated thyroid cancer	Formed of poorly differentiated cells Has a poor prognosis.
Anaplastic carcinoma	Formed of undifferentiated (anaplastic) cells Aggressive and has generally short clinical course and poor prognosis

activity of the nodules and when functional autonomy is suspected (Figs. 6.5, 6.6, and 6.7). Thyroid scintigraphy is performed then when serum TSH is suppressed or low in a patient with a single nodule and in all patients with multinodular goiter, regardless of the TSH result. Iodine-123 and ^{99m}Tc-pertechnetate are routinely used for imaging thyroid nodular disease. The acquisition of multiple projections is important as more than 30% of nodules can be missed with anterior views and only seen on the

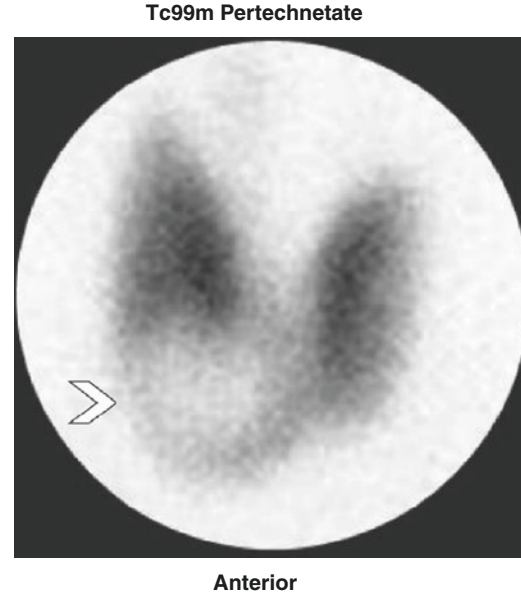

Fig. 6.5 Solitary cold nodule. ^{88m}Tc-pertechnetate thyroid scan anterior pinhole image showing a large solitary cold nodule (*arrow*)

oblique views [53]. ^{18}F-FDG PET has low specificity (63%) in the diagnosis of thyroid nodules but can help to select patients who need surgery when cytology is inconclusive in view of its high (100%) negative predictive value for thyroid cancer [52].

Whole-body ^{131}I and FDG PET have a role in the investigations and follow-up of thyroid cancer (see Chap. 10). On FDG PET scans, a normal thyroid gland demonstrates absent or low-grade FDG uptake. FDG PET may incidentally identify thyroid uptake. In general, a diffuse uptake by the thyroid gland is considered to be benign and very likely secondary to thyroiditis and/or hypothyroidism, while a focal uptake of the thyroid on FDG PET is defined as an incidentaloma, which is more clinically significant due to its high risk of malignancy ranging from 25% to 50% [54, 55].

Thyroiditis

Poor radioiodine/^{99m}Tc-pertechnetate uptake in the thyroid gland is the hallmark of subacute thyroiditis of any etiology (Fig. 6.8). Decreased tracer uptake is related to TSH suppression by excessive thyroid hormone released from

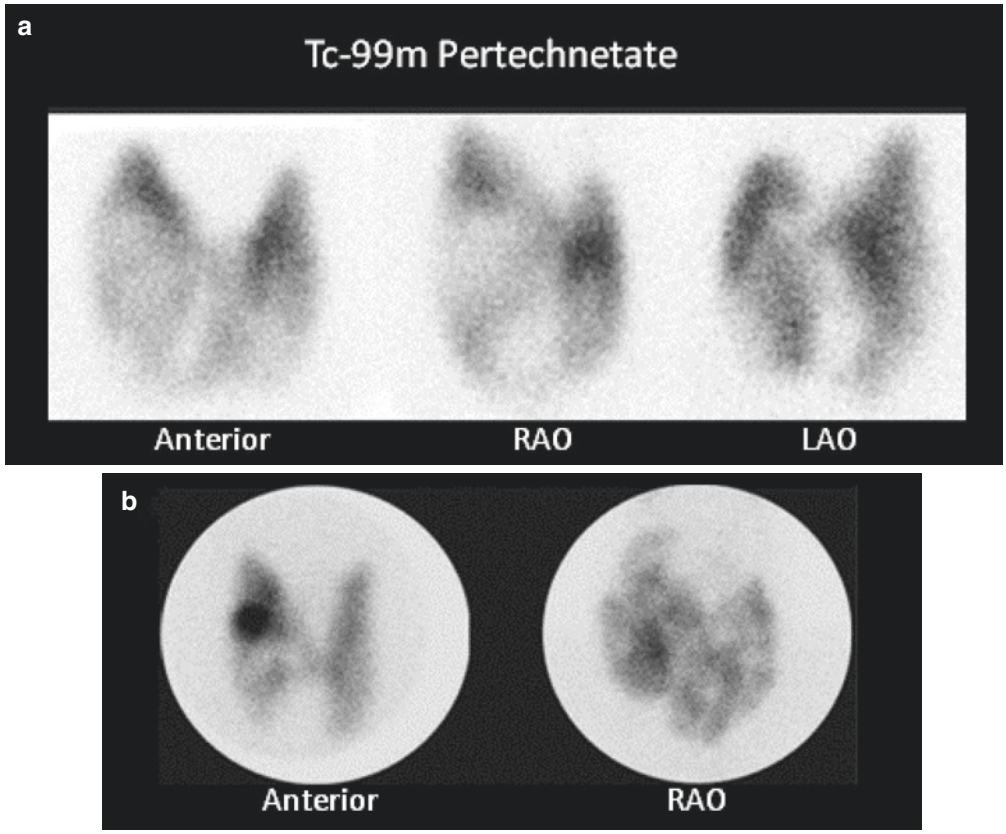

Fig. 6.6 Multinodular goiter as it appears on scintigraphy. (**a**) represents multiple cold nodules a while (**b**) shows mixture of cold and hot nodules

damaged follicles and to decreased hormone synthesis in the damaged gland. The thyroid uptake and scan normalize with resolution of thyroiditis.

Scintigraphy is frequently used in some thyrotoxic patients to differentiate autoimmune thyroiditis, with low uptake, from Graves' disease, with high uptake [48].

A thyroid uptake/scan may be worthwhile in amiodarone-related hyperthyroidism, which may be due to Jod-Basedow or thyroiditis. A low thyroid uptake is frequently found in patients treated with amiodarone and is nondiagnostic, while a normal or high uptake suggests that Jod-Basedow is likely. The thyroid uptake measurement also helps determine the feasibility of ^{131}I treatment in refractory cases.

Scintigraphy is nonspecific in Hashimoto's disease. The thyroid gland is usually symmetrically enlarged with uniform tracer distribution, and the 24-h radioactive iodine uptake is normal. In subacute thyroiditis resulting from exacerbation of Hashimoto's disease, tracer uptake is typically absent or very low.

Graves' Disease

Graves' disease typically shows uniformly increased tracer uptake in a diffusely enlarged thyroid gland (Fig. 6.9a), frequently with visualization of a pyramidal lobe and decreased background activity of various degrees based on the severity of the condition (Fig. 6.9b). However, atypical appearances, particularly in Graves' disease superimposed on nodular goiter, are

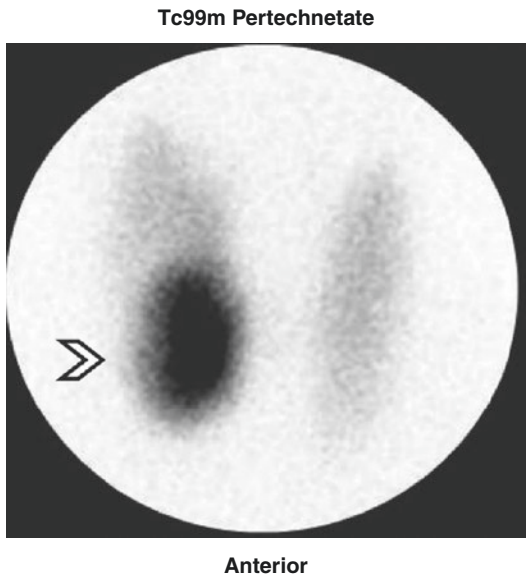

Fig. 6.7 Solitary hot nodule. A study showing a toxic nodule in the right lower lobe (*arrow*) with suppression of the remainder of the gland

occasionally encountered. If needed, TRAB measurement may assist in confirming the diagnosis. The 24-h radioactive iodine uptake is elevated and, typically, much higher than in toxic nodular goiter [49, 56].

6.1.4 Thyroid Dysfunction and Pregnancy

Results from observational studies have indicated that even mild to moderate iodine deficiency in pregnancy might negatively affect child neurodevelopment [57–59]. Low maternal free T_4 (FT4) has been suggested to be associated with poor child neurodevelopment. A recent meta-analysis of individual participants data from 9036 mother–child pairs from three prospective population-based birth cohorts from Spain, Netherlands, and the United Kingdom indicates that low maternal FT4 was consistently associated with a lower child IQ [60].

Hyperthyroidism in pregnancy is generally caused by Gestational Transient Thyrotoxicosis (GTT) or Graves' disease. Management of Graves' disease remains a challenge, with thionamide treatment as the best option. Patients should be monitored closely because undertreatment, with persistently high maternal TRAB, increases the risk of fetal hyperthyroidism, while overtreatment may cause fetal hypothyroidism. Gestational hypothyroidism is usually related to autoimmune thyroid disease, and less frequently to iodine deficiency. The latter may be associated with fetal hypothyroidism as well.

6.1.5 Summary

Synthesis and secretion of thyroid hormone are regulated mainly by thyroid releasing hormone and thyroid-stimulating hormones. Thyroid-stimulating hormone promotes iodide transport and the synthesis and release of thyroid hormones and thyroglobulin. Excessive amounts of iodine may cause hypothyroidism or hyperthyroidism. Endemic goiter is the result of iodine deficiency, with decrease in hormone production and compensatory increase in TSH secretion. Thyroid nodules represent a wide spectrum of thyroid diseases. Thyroid nodules may be solitary or multiple. A clinicopathological classification of thyroid nodules subdivides nodules into nonneoplastic nodules, true neoplastic nodules (benign or malignant), and micronodules. Autoimmune thyroid disorders, including Hashimoto's disease and Graves' disease, are related primarily to genetic susceptibility, with contributions from environmental factors including chronic iodine excess. Subacute thyroiditis is usually caused by exacerbation of autoimmune disease, viral infection, and amiodarone or interferon-alpha therapy. Iodine deficiency in pregnancy might negatively affect child neurodevelopment.

6.2 Parathyroid Gland

6.2.1 Anatomical and Physiological Considerations

Normal parathyroid glands are derived from the pharyngeal pouches, the upper glands from the endoderm of the fourth pouch, and the lower

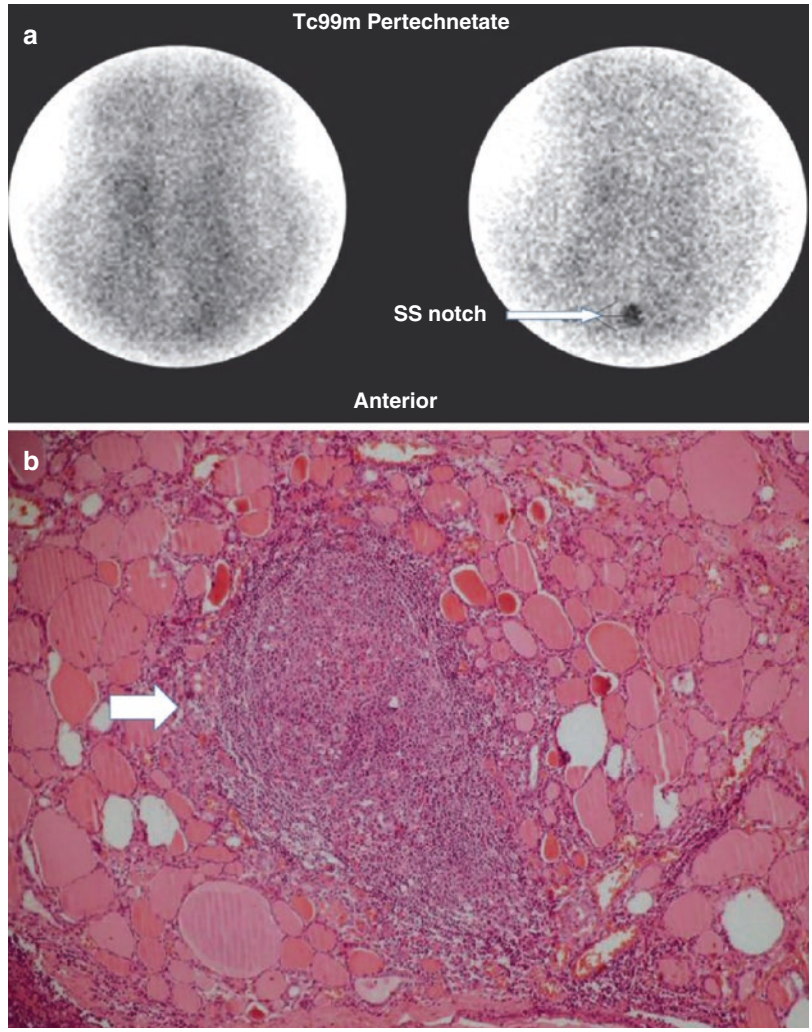

Fig. 6.8 Thyroiditis (**a**, **b**). (**a**) ^{99m}Tc-pertechnetate thyroid scan in an 8-year-old girl with a recent history of upper respiratory infection. The scan shows poor uptake by the thyroid gland with poor delineation of its outlines. The thyroid uptake was 0%. SS notch: suprasternal notch. (**b**) Microscopic illustration of thyroiditis with a focus of inflammatory cells (*arrow*) surrounded by thyroid follicles. (Courtesy of Professor Magda El-Monayeri with thanks)

glands from the third pouch. The parathyroid glands are typically located on the posterior aspect of the thyroid gland (Fig. 6.1). Occasionally one or more glands may be embedded in the thyroid. The normal position of the superior parathyroids is at the cricothyroid junction, above the anatomical demarcation of the inferior thyroid artery and the recurrent laryngeal nerve [61]. The inferior parathyroids are more widely distributed mostly anterolateral or posterolateral to the lower thyroid gland [62]. The accessory glands that can be variously located in humans, from the cricoid cartilage down into the mediastinum [63, 64], are derived from the numerous dorsal and ventral wings of the pouches. Normally, human beings have four glands, but more or fewer than this number are found in some individuals [49]. Among healthy adults, 80–97% have four parathyroids; approximately 5% have fewer than four glands, and 3–13% have supernumerary glands [62]. Location and anatomy of parathyroid glands are essential for surgical planning and for carrying out parathyroidectomies since any unidentified gland, either supernumerary or in ectopic location, can result in unsuccessful treatment and possible reoperation. Recent large meta-analysis study showed that 81.4% of patients have four glands with 15.9% of the glands are ectopic (11.6% in the neck and 4.3% in the mediastinum). Additionally, 51.7% of the neck ectopic

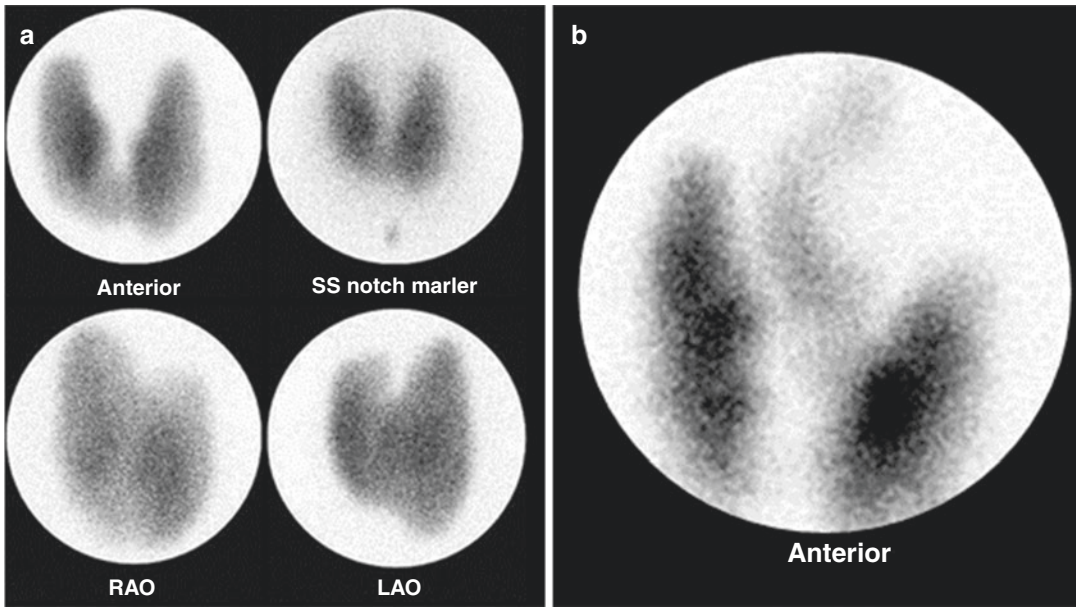

Fig. 6.9 (**a**) Graves' disease. ^{99m}Tc-thyroid scan illustrating the pattern of Graves' disease. There is uniform increased radionuclide distribution with low background activity. (**b**) Anterior view of tc99m pertechnetate illustrating Grave's disease with visualized pyramidal lobe and decreased background uptake

glands are located in retroesophageal/paraesophageal space or in the thyroid gland [63].

The normal glands usually measure 4–6 mm in length, 2–4 mm in width, and 0.5–2 mm in thickness. The glands are usually ovoid or bean shaped but may be elongated, flattened into a leaf-like structure, or multilobulated. The weight of the glands is usually 30 mg each, with the largest normal gland not exceeding 70 mg. The total weight of the glands is less than 210 mg, and the total parenchymal cell weight is less than 145 mg [64]. In normal glands, parenchymal cells are predominantly chief cells which contain cytoplasmic fat droplets. Oxyphilic and transitional oxyphilic cells are sparsely present in children and young adults and increase to 4–5% of the parenchymal cells in old age. These cells tend to form nodules if they increase in number and have a very small amount of fat or no fat at all in their cytoplasm. Ultrastructurally, oxyphil cells are characterized by the presence of closely packed mitochondria, while chief cells contain moderate to high mitochondrial content. Water-clear cells are vacuolated with distended organelles. Each of the three cell types may contain varying amounts of lipid droplets and residual bodies [65]. Table 6.4 summarizes the types of parathyroid cells and their function.

Table 6.4 Cells of the parathyroid glands and their functions

Cell type	Major ultrastructural feature	Function
Chief cell	Slightly eosinophilic cytoplasm, few mitochondria	The active endocrine cell, producing the parathyroid hormone
Oxyphil cell	Rich eosinophilic cytoplasm, tightly packed mitochondria	May be able to produce parathyroid hormone
Transitional oxyphil cell	Less eosinophilic cytoplasm	Variant of oxyphil cell
Clear cell	Foamy and water-clear cytoplasm	Unknown, fundamentally inactive

Parathyroid hormone has four principle actions: (a) to increase calcium absorption from the gastrointestinal tract; (b) to stimulate osteoclastic activity, resulting in resorption of calcium

and phosphate from bone; (c) to inhibit phosphate reabsorption by the proximal renal tubules; and (d) to enhance renal tubular calcium reabsorption. Parathyroid hormone secretion is controlled mainly by the extracellular calcium concentration. The parathyroid cell surface is thought to be equipped with a cation-sensitive receptor mechanism through which ambient calcium regulates the cytosolic calcium ($Ca^{2+}i$) concentration and parathyroid hormone secretion. Activation of this receptor causes also activation of protein kinase C. 1,25-Dihydroxycholecalciferol reduces the secretion of parathyroid hormone independent of any changes in calcium concentration. Parathyroid hormone is metabolized in Kupffer's cells of the liver.

In patients with hyperparathyroidism, pathological parathyroid cells show defective sensing of ambient calcium. The cellular basis of this abnormality is unknown, although increased protein kinase C activity within abnormal parathyroid cells may be the mechanism. Pathological parathyroid glands also have an increased parenchymal cell content, although the extent of hypercalcemia appears more closely related to the defective secretory regulation than to increased parenchymal cell mass [66].

6.2.2 Hyperparathyroidism

Hyperparathyroidism has been diagnosed with increasing frequency in recent years due to awareness of the disease and to the laboratory advancement that allowed for routine chemistry screening. The condition is characterized by excess secretion of parathyroid hormone. The resulting biochemical changes, including increased levels of serum calcium and increased urinary excretion of calcium, may result in calcium wastage, nephrocalcinosis, urolithiasis, bone disease, and neuropsychiatric disturbances. Hyperparathyroidism may occur as a primary, secondary, or tertiary disease. It can also occur as eutopic and ectopic disease. In addition, it may have a familial origin, as in multiple endocrine neoplasia (MEN).

6.2.2.1 Primary Hyperparathyroidism

Primary hyperparathyroidism is a common endocrine disorder of calcium metabolism characterized by hypercalcemia and elevated or inappropriately normal concentrations of parathyroid hormone. Almost always, it is due to a benign overgrowth of parathyroid tissue either as a single gland (80% of cases) or as a multiple gland disorder (15–20% of cases) [67]. It is the most common cause of hypercalcemia in postmenopausal women [68]. Primary hyperparathyroidism occurs due to neoplastic or hyperplastic parathyroid glands or when nonparathyroid tumors such as bronchogenic or renal cell carcinomas secrete ectopically parathyroid hormone or a biologically similar product. The incidence of this disorder in the United States is estimated to be 66 per 100,000 person among women and 25 per 100,000 among men per year [69, 70]. The condition is more prevalent in females than males by a ratio of 3 to 1. More than 80% of patients with primary hyperparathyroidism have a solitary adenoma. Hyperplasia—predominantly of chief cells—occurs in less than 20% of patients. Parathyroid carcinoma is the cause in less than 1% of patients, and very rarely the condition is due to ectopic secretion of parathyroid hormone [64, 65].

Primary hyperparathyroidism occurs as part of MEN. MEN is a hereditary syndrome that involves hyperfunctioning of two or more endocrine organs. Primary hyperparathyroidism, pancreatic endocrine tumors, and anterior pituitary gland neoplasms characterize type 1 MEN. MEN 2A is defined by medullary thyroid carcinoma, pheochromocytoma (about 50%), and hyperparathyroidism caused by parathyroid gland hyperplasia (about 20%). MEN 2B is defined by medullary thyroid tumor and pheochromocytoma. Both MEN 1 and MEN 2 are inherited autosomal dominant cancer syndromes. The gene responsible for MEN 1 is a tumor suppressor gene located on chromosome 11 [71, 72].

Primary hyperparathyroidism is also associated with thyroid pathology in 15–70% of patients [73, 74]. This includes thyroid carcinoma which has been reported in the range of

1.7–6.2% of patients with primary hyperparathyroidism [73–75].

6.2.2.2 Secondary Hyperparathyroidism

Secondary hyperparathyroidism occurs when there is a condition causing chronic hypocalcemia such as chronic renal failure, malabsorption syndromes, dietary rickets, and ingestion of drugs such as phenytoin, phenobarbital, and laxatives, which decrease intestinal absorption of calcium. Secondary hyperparathyroidism is simply a compensatory hyperplasia in response to hypocalcemia. In this condition, reduced renal production of 1,25-dihydroxyvitamin D_3 (active metabolite of vitamin D) leads to decreased intestinal absorption of calcium, resulting in hypocalcemia. Tubular failure to excrete phosphate results in hyperphosphatemia. Hypocalcemia along with hyperphosphatemia is compensated for by hyperplasia of the parathyroids to overproduce PTH. Secondary hyperparathyroidism develops in chronic kidney disease, which is due to a combination of vitamin D deficiency, hypocalcemia, and hyperphosphatemia, and it exists in nearly all patients at the time of dialysis initiation [76].

6.2.2.3 Tertiary Hyperparathyroidism

Tertiary hyperparathyroidism describes the condition of patients who develop hypercalcemia following long-standing secondary hyperparathyroidism due to the development of autonomous parathyroid hyperplasia, which may not regress after correction of the underlying condition, as with renal transplantation.

6.2.2.4 Eutopic Parathyroid Disease

Parathyroid disease with typical location of glands (eutopic) represents 80–90% of all cases. There is a relatively fixed location for the superior parathyroids and are found close to the dorsal aspect of the upper thyroid [61, 62]. On the other hand, inferior parathyroids have a more widespread distribution, which is closely related to the migration of the thymus. Inferior parathyroids are mostly located inferior, posterior, or lateral to the lower thyroid. They may be very close to the thyroid and may be covered by or attached to the thyroid capsule and are sometimes adjacent to or surrounded by remnant thymic tissue. Interestingly, the parathyroid glands demonstrate a remarkably constant symmetry, which is helpful in the surgical exploration of eutopic disease [62].

6.2.2.5 Ectopic Parathyroid Disease

Superior parathyroid adenoma may have an abnormal supero-posterior mediastinal position, such as a retropharyngeal, retroesophageal, or paraesophageal site or the tracheoesophageal groove. The frequency of ectopia (up to 39%) is similar for the right and left superior parathyroids [77]. Intrathyroid superior parathyroid adenomas are rare.

The more common ectopic inferior parathyroids are a well-established entity responsible for 10–13% of all cases of hyperparathyroidism [77]. Ectopic tissue can occur from the angle of the mandible to the mediastinum according to the developmental and migratory aberrations. These sites include the mediastinum, thymus, aortopulmonary window, carotid bifurcation and rarely thyroid, carotid sheath, vagus nerve, retroesophageal region, thyrothymic ligament, and pericardium [77, 78].

6.2.3 Parathyroid Adenoma

Parathyroid adenoma is a benign tumor that is usually solitary, although multiple adenomas are found in a low percentage. The tumor in general is more common in women and varies in weight from less than 100 mg to more than 100 g. The most commonly found adenomas, however, weigh 300 mg to 1 g. The size was found to correlate to the degree of hypercalcemia.

Microscopically, the vast majority of typical adenomas are formed predominantly of chief cells, although a mixture of oxyphil cells and transitional oxyphil cells is also common. Adenomas formed of water-clear cells are very rare. A rim of parathyroid tissue is usually present outside the capsule of the adenoma and can serve to distinguish it from parathyroid

Table 6.5 Variants of parathyroid adenoma [79–88]

Type	Major features	Imaging
Solitary adenoma	Found in 80–85% of patients with primary hyperparathyroidism	^{99m}Tc-MIBI with high sensitivity
	Composed of chief cells or mixture of chief, oxyphil, or transitional oxyphil cells	
Double/ multiple	Occurs in up to 12% of cases of primary hyperparathyroidism	Detection with any imaging modality is not reliable
	Bilateral in 55–88% of cases	^{99m}Tc-MIBI has a sensitivity of less than 37%
	More prominent symptoms and higher parathyroid hormone and alkaline phosphatase levels than with a solitary adenoma or hyperplasia	
Cystic adenoma	Central necrosis or cystic degeneration of adenomas	May not be visualized on ^{99m}Tc-MIBI studies
	Accounts for less than 9% of all parathyroid adenomas	
	Frequently associated with hyperparathyroidism	
Lipoadenoma	Composed of hyperfunctioning parathyroid tissue and fatty stroma	Target-to-background ratio may be low due to the high adipose content
Oncocytic adenoma	Rare subtype formed of 80–100% oxyphil cells	^{99m}Tc-MIBI with high sensitivity

carcinoma. The chief cells in adenomas are usually enlarged, and their nuclei are larger and more variable in size than in normal chief cells. Nuclear pleomorphism may be prominent; this is not considered a sign of malignancy but a criterion for discriminating adenoma from hyperplasia, which lacks this feature. The following variants (Table 6.5) of parathyroid adenoma may be recognized.

6.2.3.1 Solitary Adenoma

Solitary adenoma is found in 80–85% of patients with primary hyperparathyroidism [9]. There is no significant predominance in location among the four parathyroids with each responsible for approximately 25% of all solitary adenomas [77]. The remaining tumor-free parathyroid glands associated with single adenomas usually have lower weight and parenchymal cell mass than the average normal glands and show signs of secretory inactivity on electron microscopy.

6.2.3.2 Double or Multiple Adenomas

Double or multiple adenomas occur in up to 12% of cases of primary hyperparathyroidism [79, 80]. These patients have more prominent symptoms and usually have higher parathyroid hormone and alkaline phosphatase levels than those with a solitary parathyroid adenoma or hyperplasia. Preoperative detection of double or multiple adenomas with any imaging modality is not reliable [81, 82].

6.2.3.3 Cystic Adenoma

Cystic adenomas are thought to represent central necrosis or cystic degeneration of adenomas [85]. Contrary to the asymptomatic true parathyroid cysts which are due to embryologic vestiges of the third and fourth pharyngeal pouches or enlargement of microcysts within the parathyroid as a manifestation of colloid retention [86], cystic adenomas are frequently associated with hyperparathyroidism.

6.2.3.4 Lipoadenoma

Parathyroid lipoadenoma, composed of hyperfunctioning parathyroid tissue and fatty stroma, is a rare entity that occurs in patients beyond the fourth decade of life.

6.2.3.5 Oncocytic Adenoma

Oncocytic adenoma is a rare subtype and has been reported to be associated with hyperparathyroidism. It is found in the sixth or seventh decades and like the typical adenomas is more common in women [88].

6.2.4 Parathyroid Hyperplasia

Parathyroid hyperplasia affects the glands to varying degrees, and commonly one or two glands are of normal size even though microscopic signs of endocrine hyperfunction are present, at least focally, in all glands. Chief cell hyperplasia is the most common and is composed of chief cells or a mixture of chief cells and to a lesser extent oxyphil cells. The cells are arranged diffusely, in nodules, or in a mixture of both patterns. Water-clear cell hyperplasia is rare and is characterized by substantial enlargement of most parathyroid glands. The large water-clear cells are usually arranged in a diffuse pattern [89].

In primary hyperparathyroidism, hyperplasia affects the glands asymmetrically. In secondary hyperparathyroidism, the hyperplastic glands are more uniformly enlarged than with primary chief cell hyperplasia, with two histological types (Table 6.6). In the tertiary form, the glands are more often markedly and asymmetrically enlarged.

Pathologically, it is difficult to differentiate primary chief cell hyperplasia of only one gland from adenoma. Both contain large numbers of active chief cells with cells characterized by aggregated arrays of rough endoplasmic reticulum and a large, complex Golgi apparatus with numerous vacuoles and vesicles. Secretory granules are frequently present in these cells. These changes indicate that most of these cells are in the more active phases of parathyroid hormone synthesis and secretion [90]. Molecular biology techniques used on pathological parathyroid tissue have shown that cell proliferation is monoclonal in many sporadic adenomas and in the largest glands of multiple endocrine neoplasia type I. This monoclonality has not been found in the smaller parathyroid glands of multiple endocrine neoplasia or in sporadic hyperplasia. Additionally, rearrangement of parathyroid hormone gene in chromosome 11 was observed in sporadic adenomas.

Table 6.6 Classification of parathyroid hyperplasia

Type	Major pathological features
Primary hyperplasia	Uniform chief cells with some oxyphil and transitional oxyphil cells
Secondary hyperplasia	
Diffuse(classic) type	Cords, sheets, or follicular arrangement of cells replacing the stromal fat cells. Oxyphil cells are more frequent in this type. This type is indistinguishable from the primary type
Adenomatous-nodular type	Cells are grouped in large islands or nodules. Necrosis is seen more frequently than in diffuse type

6.2.5 Parathyroid Carcinoma

Parathyroid carcinoma is a rare cause of hyperparathyroidism which can arise in any parathyroid gland, including ectopic and mediastinal, although the usual site of involvement is the normally located parathyroids. The tumor is found predominantly in patients between the ages of 30 and 60 years, with no sex preference, and is usually functioning. The tumors tend to be larger than adenomas and appear as lobulated, firm, and uncapsulated masses that often adhere to the surrounding soft tissue structures. The involved glands usually weigh more than 1 g and the diagnosis is restricted histologically to the lesions displaying infiltrative growth into vessel or capsule, since pleomorphism can be seen in many adenomas.

6.2.6 Hyperfunctioning Parathyroid Transplant

Autotransplantation of parathyroid tissue is performed in cases of recurrent, persistent type 1 MEN and symptomatic secondary hyperparathyroidism in association with total parathyroidectomy. After total parathyroidectomy, the most normal glands, usually one or two, are used for the graft. They are diced into small fragments with each fragment placed in an individual bed beneath a muscle sheath and between muscle fibers [91]. A graft site in the forearm is preferred for accessibility. The graft may be functional in 8–9 days after surgery [80]. After autotransplan-

tation, recurrent hyperparathyroidism occurs in approximately 14% of cases [92]. A hyperfunctioning graft in the forearm is easily demonstrated with Doppler US or ^{99m}Tc-sestamibi scintigraphy [92].

6.2.7 Consequences of Hyperparathyroidism

Excess secretion of parathyroid hormone promotes bone resorption and consequently leads to hypercalcemia and hypophosphatemia. The clinical presentation and complications of hyperparathyroidism depend on the rapidity of development and the degree of hypercalcemia. They can be grouped into genitourinary, gastrointestinal and musculoskeletal, neuropsychiatric, and others (Table 6.7).

The five disease-specific symptoms are muscle weakness, polydipsia, dry skin and itching, memory loss, and anxiety. Overall the symptoms, particularly the disease-specific ones, show significant decline after successful parathyroidectomy [93].

Table 6.7 Consequences of hyperparathyroidism

Type of abnormality	Presentation
Genitourinary	Nephrolithiasis
	Nephrocalcinosis
	Renal insufficiency
	Polyuria
	Nocturia
	Decreased urine concentrating ability
Gastrointestinal	Nausea
	Vomiting
	Constipation
	Increased thirst
	Loss of appetite
	Abdominal pain
	Peptic ulcers
	Heartburn (hypercalcemia causes increased gastric acidity)
	Pancreatitis
Musculoskeletal	Myopathy
	Muscle weakness
	Osteoporosis
	Osteomalacia
	Bone and joint pains
	Renal osteodystrophy
	Pseudogout
Neuropsychiatric	Memory loss
	Anxiety
	Sleepiness
	Confusion
	Lassitude, coma
	Depression
	Impaired thinking
	Psychosis
Others	Fatigue
	Hypertension
	Pruritis
	Metastatic calcification including cardiocalcinosis
	Band keratopathy (present in the medial and lateral aspects of the cornea)

6.2.8 Preoperative Parathyroid Localization

Surgery is the major and only current curative modality in treating primary hyperparathyroidism. Identifying the glands can be difficult, however, particularly with removal of multiple glands and with reoperation [94]. Although the success rate is high in experienced hands, up to 25% of the initial explorations fail because the abnormal glands cannot be located. Prolonged exploration was also found to result in a high incidence of recurrent laryngeal nerve damage [94]. Surgical re-exploration with violated anatomy is even more difficult and hazardous and can often be unrewarding.

Preoperative localization of parathyroid lesions is thus desirable to reduce the incidence of missed lesions and to help avoid prolonged neck exploration. Since surgeons' experience with neck exploration is decreasing due to the reduced incidence of thyroid surgery with the expanding use of iodine-131 for therapy of hyperthyroidism, preoperative localization of parathyroid lesions is even more important than before.

In recent years, minimal access parathyroid surgery (small incisions with gamma probe or endoscopic assistance) is increasingly becoming the operation of choice for single parathyroid adenomas [95]. Compared with bilateral neck exploration, it has a shorter hospital stay, less morbidity, and better cosmetic result [95]. The development of this minimally invasive surgical techniques has placed an even greater emphasis on preoperative localization [96].

The forms that preoperative localization can take include computed tomography (CT), ultrasound, magnetic resonance imaging (MRI), arteriography, selective venous sampling, ^{99m}Tc-sestamibi (MIBI) scintigraphy, ^{18}F-fluorodeoxyglucose positron emission tomography (FDG PET), and ^{11}C-methionine PET. The morphological imaging modalities, such as CT, ultrasound, and MRI, have the disadvantage that they cannot distinguish functional parathyroid tissue from other types of tissue. However, they provide excellent image resolution and contrast. Overall their accuracy is inadequate and varies.

6.2.9 Scintigraphic Localization

Scintigraphy using ^{99m}Tc-sestamibi (MIBI) is currently the preferred nuclear medicine method for parathyroid imaging. It is the most sensitive and cost-effective modality for preoperative localization of hyperfunctioning parathyroid tissue. If a single parathyroid adenoma is detected, a unilateral scan-directed neck exploration can be performed. Due to a wide variation in scintigraphic techniques [97], the reported sensitivities of MIBI scan range from 80% to 100%. The mechanism of uptake of this radiopharmaceutical by abnormal parathyroid cells is not fully understood although the mitochondria have been implicated in its uptake [98]. P-glycoprotein, a membrane transport protein encoded for by the multidrug resistance (MDR) gene, may also be additionally responsible for uptake, since it transports other products with structural similarity to MIBI [99]. The uptake and retention of MIBI by the abnormal neoplastic and hyperplastic lesions are probably due to the alterations in the biology of the abnormal parathyroid cells, as noted earlier, and mitochondria are probably the site of retention. The size of the lesions is also an important factor in their visualization but cannot alone explain the uptake and retention. The size and the cellularity of the abnormal gland are also factors in the visualization and correlate with its MIBI uptake (Fig. 6.10) [100, 101]. Additionally, the ectopic disease (Fig. 6.11) may affect the degree of visualization and SPECT with or without CT is better to be used.

Parathyroid lesions detected by ^{201}Tl scintigraphy have been shown to have significantly higher numbers of mitochondria-rich oxyphil cells compared with nonvisualized lesions, indicating further that the uptake depends in part on the metabolic activity of the lesion [102]. Our group found that the amount of mitochondria (Fig. 6.11) in adenoma cells correlates with the degree of uptake [103]. Significant P-glycoprotein or multidrug resistance-related protein expression was reported to limit the sensitivity of MIBI imaging in localizing parathyroid adenomas [98].

The protocol for MIBI parathyroid scintigraphy varies regarding timing of acquisition, SPECT and SPECT/CT. However, the study principle is to acquire early and delayed (Figs. 6.12 and 6.13). The variable behavior of abnormal parathyroid glands is due to the varying ultrastructure of the cells, the various combinations of cell types, and their biological activity. ^{123}I or pertechnetate thyroid imaging for comparison or subtraction is only occasionally needed on an individual basis (e.g., presence of thyroid nodule). If the presence of thyroid pathology is known or suspected clinically, one starts with a thyroid scan to define the morphology and localize the thyroid by injecting 1 mCi ^{99m}Tc-pertechnetate i.v., and the neck is imaged 15 min later.

Tetrofosmin has been also used in a 2-day protocol using ^{99m}Tc-pertechnetate imaging of thyroid and single acquisition of ^{99m}Tc-Myoview next day. Comparing the activity of both scans

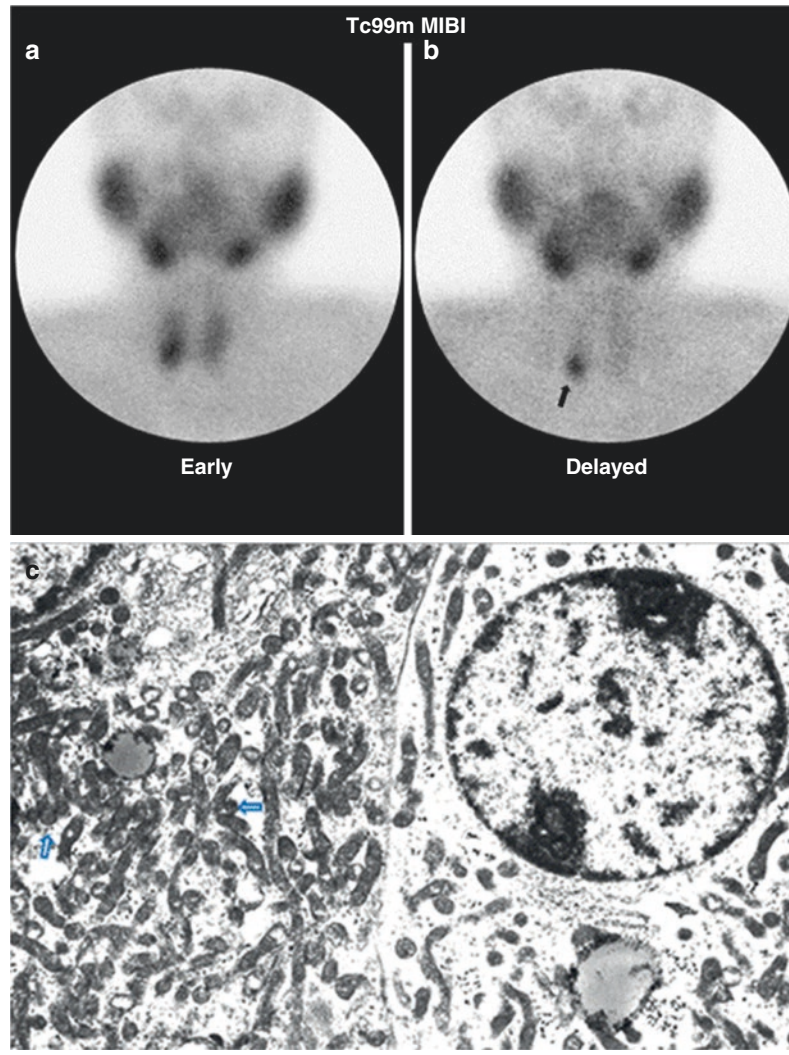

Fig. 6.10 Tc99m sestamibi study for a patient with biochemically proven hyperparathyroidism. Early images (**a**) shows a focus of increased uptake in the region of the right lower pole of the thyroid gland which, in the delayed image (**b**), retains the activity (arrow) with clearance of thyroid uptake consistent with adenoma. Surgery was performed and the lesion was pathologically proven to be adenoma. Sample was sent for electron microscopic study. Electron microscopic photograph (**c**) of this parathyroid adenoma illustrates cells packed with mitochondria (arrows)

obtained 15 min post injection facilitates detecting focal activity of parathyroid adenomas and hyperplastic glands with high accuracy [104].

It was reported that parathyroid scan interpretation by a nuclear medicine physician along with an endocrine surgeon resulted in improved accuracy of gland localization and lateralization compared to a nuclear medicine physician reading alone. This improvement may be due to increased awareness of clinical data and head and neck anatomy [105].

SPECT/CT has proven to be most accurate in localizing parathyroid glands (Fig. 6.14) and is currently the recommended procedure. It has proven to be a useful tool for preoperative assessment, not only for ectopic glands but also for patients with previous neck surgery. It also increases reporting confidence for physicians [106, 107]. It has been reported to be 94% accurate in detecting parathyroid adenoma and 92% in accurate localization [108].

PET has been also investigated for localizing parathyroid glands. Initial studies using FDG showed conflicting results in imaging the parathyroid glands in primary hyperparathyroidism. ^{11}C-methionine PET was suggested to be more promising than FDG in parathyroid localization [109]. In a large recent study of 171 patients,

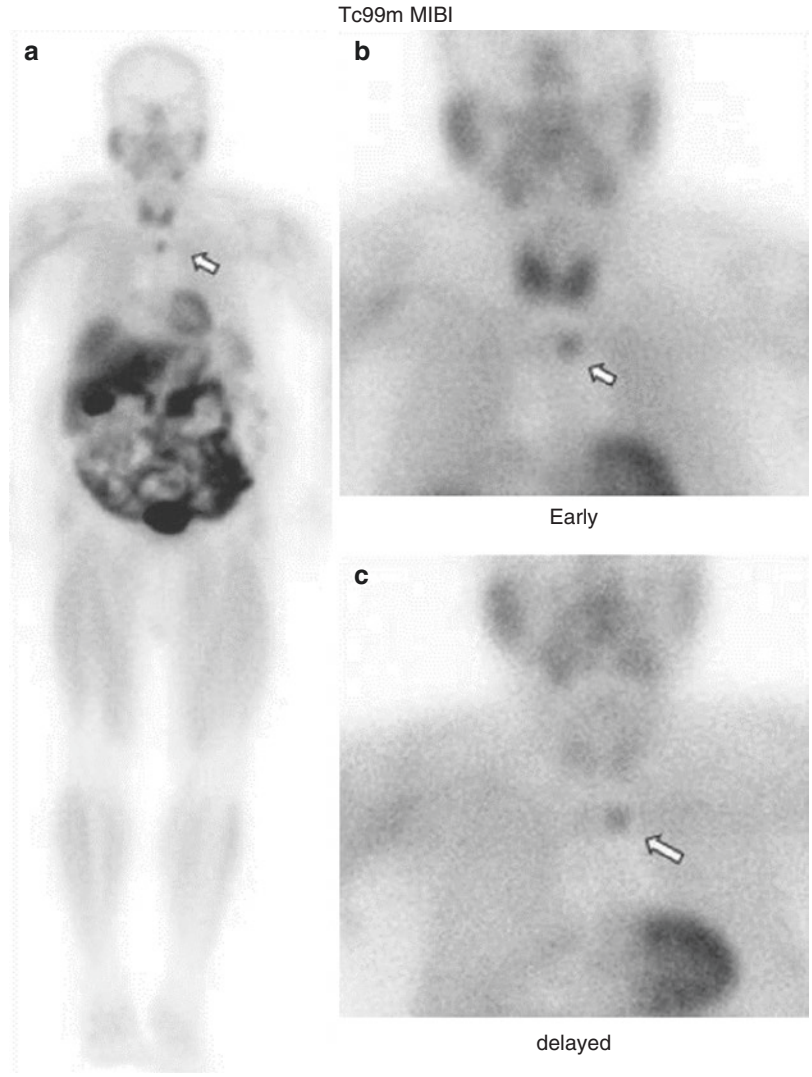

Fig. 6.11 Ectopic parathyroid adenoma (*arrow*) seen on Tc99m MIBI study. Early whole-body (**a**) and spot images (**b**, **c**) with retained activity on delayed spot image

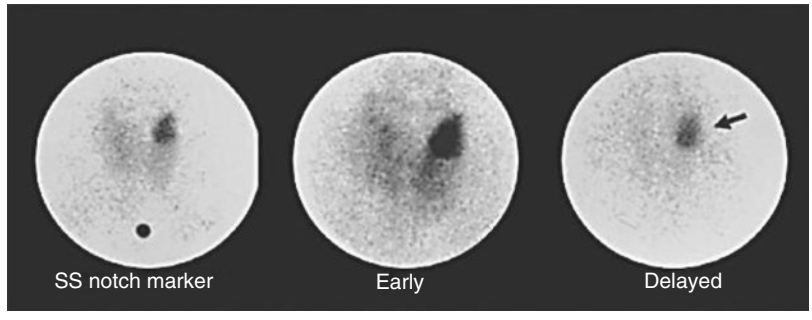

Fig. 6.12 ^{99m}Tc-sestamibi study acquired 15–90 min post injection using pinhole collimator. The delayed image shows differential clearance of activity from the thyroid gland with retained and intense uptake by a large parathyroid adenoma (*arrow*)

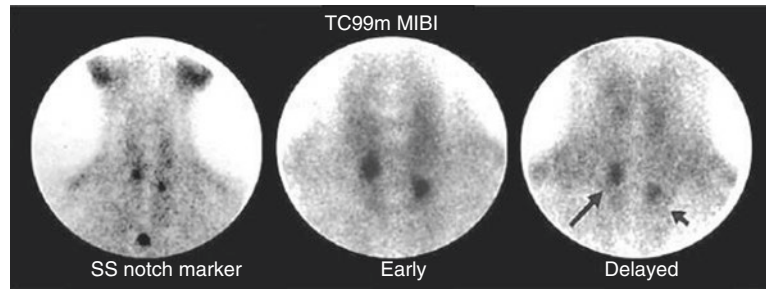

Fig. 6.13 Hyperplastic parathyroid glands (*arrows*) with persistent uptake on delayed ^{99m}Tc-sestamibi image

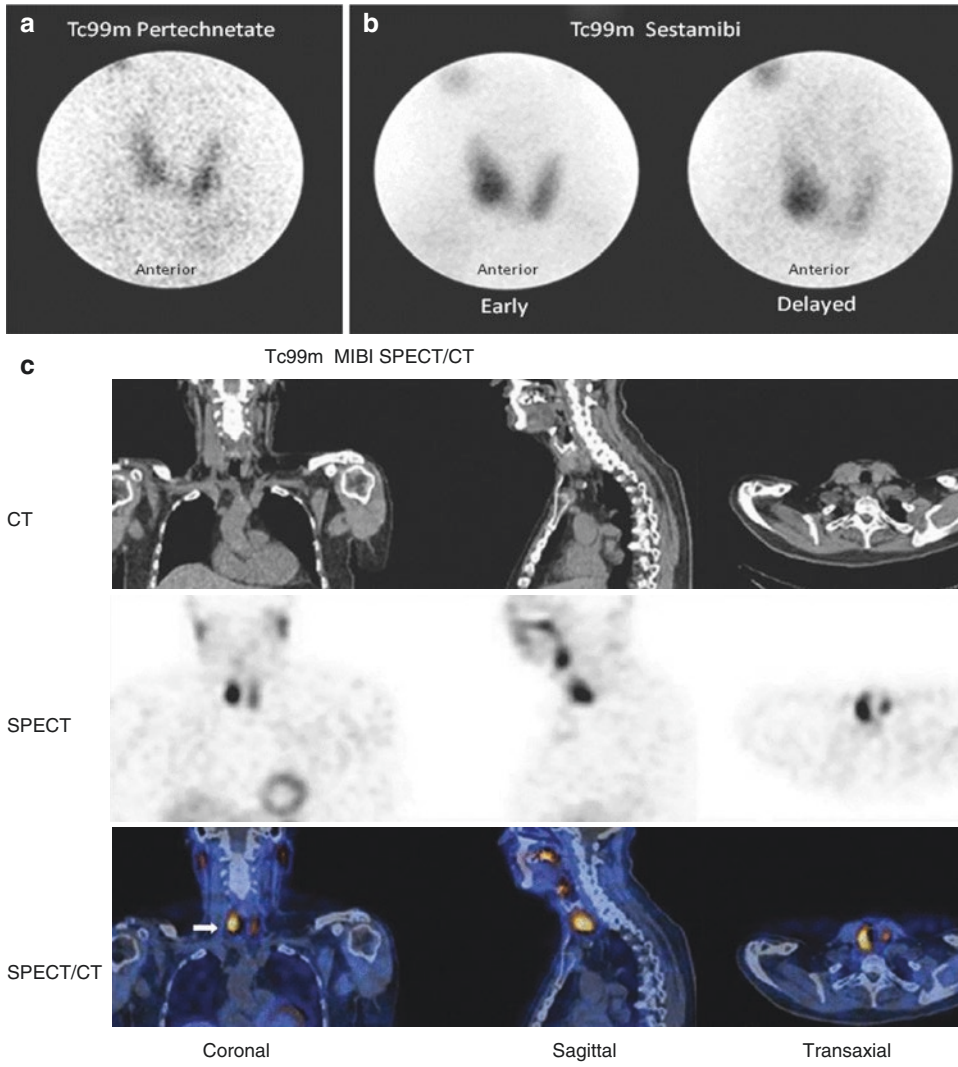

Fig. 6.14 A 70-year-old male with osteoporosis who is on rheumatoid arthritis treatment. He has hypercalcemia and high parathyroid hormone (PTH) levels. Tc-99m pertechnetate thyroid scan (**a**) and Tc-99msestamibi planar (**b**) with SPECT/CT (**c**) were performed. The thyroid scan (**a**) is grossly normal with no focal abnormalities. There is a focus of increases uptake on early sestamibi image (**b**) in the region of the right lower pole of the thyroid which does not show significant washout of activity and becomes more prominent on delayed image. There is normal washout of activity from the thyroid gland. Based on planar images, scintigraphic findings are consistent with parathyroid adenoma at the region of the right lower pole. Selected SPECT/CT images (**c**) demonstrate that this focal activity is located posterior to the lower pole of the right lobe (arrow). Note that SPECT/CT better located the lesion as compared to planar imaging

^{18}F-fluorocholine (FCH) PET/CT, correctly detected 96% and 90%, on a per patient-based and per lesion-based analysis, respectively [110].

6.2.10 Atypical Washout of Radiotracer

As outlined, the diagnosis of parathyroid tumor with MIBI scintigraphy is based on the differential washout rate between the thyroid and diseased parathyroids. Atypical radiotracer clearance whether fast parathyroid or delayed thyroid gland washout will limit the efficacy of detection of parathyroid disease with dual-phase MIBI scintigraphy as well as using the intraoperative probe.

Early parathyroid washout is frequently seen in parathyroid hyperplasia; the detection rate for this entity is approximately half of that for parathyroid adenoma [92]. Scintigraphy performs worse in cases of multisite hyperplasia, in which only the most prominent radiotracer-avid gland is visualized. In addition, rapid washout from a parathyroid adenoma has been attributed, without unanimous confirmation, to the histological composition of the adenoma [92]. Modifying the imaging protocol with additional interval scanning between the standard 15-min and 2–4-h acquisitions may be helpful in demonstrating rapid washout.

Delayed radiotracer washout from the thyroid parenchyma makes dual-phase scintigraphic assessment difficult. It was observed that the delay varies, and significant washout may not occur even several hours after injection of the radiotracer. This retention of MIBI occurs in thyroid diseases such as multinodular goiter, Hashimoto's thyroiditis, thyroid adenoma, and thyroid carcinoma owing to the hypermetabolic characteristics of these diseases [93]. Extended delayed-phase imaging of MIBI along with in-depth clinical examination may be useful in the diagnosis of concomitant thyroid and parathyroid disease.

As rapid washout and small size of parathyroid glands would cause false-negative localization studies, several pathologies can also cause false-positive studies (Table 6.8).

Table 6.8 Causes of false-positive MIBI parathyroid studies

Lymph nodes
Supraclavicular
Axillary
Hyperplastic thymus[a]
Sarcoidosis[b]
Carcinoid tumor
Malignant tumors

[a] Confused with an intrathymic or mediastinal parathyroid adenoma
[b] Thorax

6.2.11 Intraoperative Probe Localization

Localization using intraoperative gamma probe has recently gained popularity. The patient is injected 2 h before surgery, and the probe is used to detect the higher level of activity after exploration by the surgeon. On the day of surgery, the patients receive the same dose of MIBI as for imaging and is taken to the operating room. Prior to skin incision, counts over four quadrants in the neck as well as over the mediastinum are obtained using a gamma probe.

6.3 Adrenal Gland

6.3.1 Anatomical and Physiological Considerations

The adult adrenal glands weigh 8–10 g and lie above and slightly medial to the upper pole of both kidneys. The outer cortex comprises 90% of the adrenal weight, the inner medulla about 10%. The cortex is rich with vessels and receives its main blood supply from branches of the inferior phrenic artery, renal arteries, and the aorta. These small arteries form an arterial plexus beneath the capsule and then enter a sinusoid system that penetrates the cortex and medulla, draining into a single central vein in each gland [111].

Histologically, the adult adrenal cortex is composed of three zones: an outer zona glomerulosa which produces aldosterone, a zona fasciculata, and an inner zona reticularis. The zona fasciculata is the thickest layer and produces cortisol and androgens; its cells are large and contain

more lipid and thus are termed clear cells. The zona reticularis produces weak androgens. The zonae fasciculata and reticularis are regulated by adrenocorticotropic hormone (ACTH).

Cholesterol within the adrenal cortex is the starting point for synthesis of multiple adrenal hormones. Therefore, a radioactive cholesterol is useful in evaluating the functional status of adrenocortical lesions The adrenal medulla is composed histologically of chromaffin cells, which are large ovoid columnar cells arranged in clumps or cords around blood vessels and surrounded by capillaries and sinusoids. They have large nuclei and a well-developed Golgi apparatus; they have a large number of granules containing catecholamines. The adrenal medulla also contains some sympathetic ganglia. The cells of adrenal medulla are innervated by preganglionic sympathetic fibers. Most of the blood supply to the hormonally active cells of the medulla is derived from a portal vascular system arising from the capillaries in the cortex. There is also a network of lymphatics that drain into a plexus around the central vein [112]. The adrenals provide adjustment of heart performance and vascular tone. Epinephrine is found essentially only in the adrenal medulla, and constituting greater than 80% of its output. Norepinephrine is synthesized by adrenergic neurons and cells of the adrenal medulla; therefore, a radioactive norepinephrine analog is used to evaluate adrenomedullary lesions.

6.3.2 Adrenal Cortex

6.3.2.1 Pathophysiology

Primary Aldosteronism (Conn's Syndrome)

In primary aldosteronism (Conn's syndrome), there is increased production of aldosterone by abnormal zona glomerulosa (adenoma or hyperplasia) leading to hypertension through the increased reabsorption of sodium and water from the distal tubules. A benign adenoma accounts for 75% of cases of this syndrome; it is usually small, ranging from 0.5 to 1.5 cm in diameter. It is more common in women than in men (3:1) and usually occurs between the ages of 30 and 50 years. Bilateral, or rarely unilateral, micro- or macronodular adrenal hyperplasia accounts for most of the remaining cases. Two types of familial hyperaldosteronism have recently been identified: Type I is glucocorticoid suppressible and associated with bilateral hyperplasia, and type II is associated with adrenocortical adenoma. Adrenal carcinoma is a very rare cause of this syndrome. The patients typically come to medical attention because of clinical signs of hypokalemia or detection of previously unsuspected hypertension during the course of a routine physical examination. The diagnosis is principally a biochemical one (low plasma renin activity and a high level of aldosterone); imaging is required to localize the lesion and identify its multiplicity. The diagnostic information provided by CT or MRI in localizing adenomas is both accurate and practical, and they are the initial approach of choice. Some smaller adenomas which are not clearly visualized by CT can be depicted by scintigraphy.

Cushing's Syndrome

The most common pathological cause of this syndrome is the stimulation of the zona fasciculata by excess ACTH from the pituitary gland (Cushing's disease) or, less commonly, the ectopic production of ACTH (as in small cell lung cancer and neural crest tumors) or corticotropin-releasing factor (CRF) (as in bronchial carcinoid and prostate cancer). Stimulating this zona may lead to bilateral adrenocortical hyperplasia, which is nodular in 25% and diffuse in 75% of cases. Cushing's syndrome may also be due to autonomous adrenal cortisol production (30–40% of cases) due to adrenal adenoma or hyperfunctioning adrenal carcinoma. ACTH-induced Cushing's disease is more common in adults (25–45 years) and is at least three times more common in women than in men. Cushing's disease resulting from ectopic ACTH secretion is more common in older adults, particularly men. Adrenal tumors rather than pituitary tumors are more common in children, especially girls. Twenty percent of nonfunctional adrenocortical carcinomas tend to be highly malignant, with weights exceeding 1 kg.

Hyperandrogenism

Hyperandrogenism can be the result of hypersecretion of androgens (causing virilization) or estrogens (causing feminization) from the zona reticularis of the adrenal cortex by primary adrenocortical hyperplasia and rarely by adrenal tumors, though the most common cause of this syndrome is polycystic ovary disease (POD). In POD, the chronic anovulation associated with increased circulating LH levels results in increased ovarian stromal stimulation, which leads to increased ovarian androgen production. A testosterone-secreting adrenal adenoma may contain the crystalloids characteristic of Leydig's cells [113].

6.3.2.2 Scintigraphy

Radiolabeled Cholesterol Analogs

NP(^{131}I-7-iodomethyl-19-norcholesterol)-59 (NP-59) is the classic nuclear medicine study used to evaluate some disease processes related to the adrenal cortex. Its main uses are documented cases of adrenal excess secretion and negative or equivocal CT or MRI findings. This radiopharmaceutical is a cholesterol analog that is bound to and transported by low-density lipoproteins (LDL) to specific LDL receptors on adrenocortical cells; therefore, endogenous hypercholesterolemia may limit the number of receptors available for radiocholesterol localization through competitive inhibition. Once liberated from LDL, NP-59 is esterified but is not further converted to steroid hormones [114]. This scan should be done only on patients with clinically hyperfunctioning adrenal cortex verified by lab results, CT, or MRI.

Patient Preparation

1. Suppression of normal adrenal cortex is achieved by oral administration of 1 mg dexamethasone q.i.d. beginning 7 days before and for the duration of the study. This is not required in patients with hypercortisolism.
2. Stop diuretics, spironolactone, and antihypertensive drugs, if feasible for at least 48 h.
3. Saturated solution of kalium iodide (SSKI) is given orally in a dose of one drop t.i.d. starting 2 days before and continuing for 14 days to suppress the thyroid uptake of free radioiodine. Patients allergic to iodine can take potassium perchlorate (200 mg every night after meals), starting 1 day before injection of NP-59, for 10 days.
4. A laxative should be given starting 48 h prior to imaging and continuing till final imaging to diminish bowel activity. Enemas may be required. The dose of ^{131}I-NP-59 is 1 mCi, to be strictly injected i.v. through a secured i.v. line over 2 min. NP-59 background clearance and accumulation in the adrenals occur slowly, but by day 5, accumulation in the normal adrenals is greater than in other organs. Suppressed patients should be imaged on days 3, 4, 5, and 7. If the adrenals are not seen by day 7, dexamethasone should be stopped and the patient imaged on day 10; nonsuppressed patients are imaged on days 5 and 7. Anterior and posterior projections of the adrenals are obtained; in case of hyperandrogenism, the pelvis and genitalia should be included.

The normal distribution is seen in the liver, gallbladder, and colon. In 90% of cases, the right adrenal gland is more cephalad and deeper than the left adrenal gland. In two-thirds of normal subjects, the activity in the right adrenal appears greater than that in the left in the posterior projection; this is because the right adrenal occupies a more posterior location than the left adrenal. In some instances, the gallbladder can be confused with the right adrenal. In the lateral view, the gallbladder is located anteriorly. In difficult cases, cholecystokinin can clear the gallbladder activity. Interfering colonic activity can be reduced by cathartics. Although count rates are low, single photon-emission computed tomography (SPECT) can be performed and may separate adrenals from gut and liver activity.

In primary aldosteronism, early unilateral increased uptake indicates adrenal adenoma, whereas bilateral increased uptake suggests bilateral adrenal hyperplasia. Pituitary ACTH-producing adenoma or ectopic ACTH secretion

can result in bilateral adrenal hyperplasia manifested by bilateral symmetric increased uptake, with ectopic causes producing more uptake of NP-59; this pattern may be asymmetric in the macronodular form of hyperplasia. Adrenal adenoma causes unilateral increased uptake, whereas adrenocortical carcinoma gives rise to bilateral nonvisualization. In hyperandrogenism, early bilateral uptake is compatible with hyperplasia, and early (<5 days) unilateral uptake or markedly a symmetric visualization is indicative of adrenal adenoma.

Positron Emission Tomography Imaging

Since adrenal adenomas are relatively common (2–9%) in the general population, incidental detection of adrenal lesions poses a diagnostic challenge, particularly in patients with a previous clinical history of malignancy [115, 116].

CT is used as the first-line diagnostic modality for screening and determining the nature of the adrenal lesions, and MRI is often performed to further characterize indeterminate masses seen on CT. ^{18}F-FDG PET can help in differentiating malignant from benign adrenal lesions in patients with proven malignancy or in patients with incidentally detected adrenal tumors on CT or MRI studies [116–118]. However, some adenomas show increased FDG tracer uptake similar to cancer and some do not. It has been suggested that the functional state of an adenoma is a factor determining the intensity of uptake, with $^{18F\text{-}FDG}$ uptake being increased in functioning adrenal masses [119]. SUV value can help differentiate adrenal cortical adenomas from adrenal cortical carcinomas [118].

Specific inhibitors of adrenal steroidogenesis, etomidate and metomidate, have recently been used to develop suitable PET tracer. These molecules seem to be suitable as in vivo tracers for specific visualization of the normal adrenal cortex and positive identification of adrenocortical tumors. To date adrenocortical radiocholesterol scintigraphy has been shown to be the most accurate noninvasive imaging technique in differentiating benign cortical adenomas from space-occupying or destructive adrenal lesions.

6.3.3 Adrenal Medulla

6.3.3.1 Pathophysiology

Neuroendocrine tumors are a heterogeneous group of usually slow-growing tumors that arise from neuroendocrine cells from various organs, including adrenal in addition to lung, thymus, thyroid, stomach, duodenum small bowel, large bowel, appendix, pancreas, and skin (see Chap. 12).

Pheochromocytoma

Pheochromocytoma is a rare tumor arising from chromaffin cells of the adrenal medulla. Most pheochromocytomas produce excessive amounts of norepinephrine, attributable to autonomous functioning of the tumor, although large tumors may secrete both norepinephrine and epinephrine [120] and in some cases also dopamine. The release of catecholamine into the circulation causes hypertension, tremor, tachycardia, and other signs. Other catecholamine-producing tumors (e.g., chemodectoma and ganglioneuroma) may also cause a syndrome similar to that seen with pheochromocytoma. Furthermore, they may also produce some active peptides such as somatostatin, ACTH, and calcitonin.

Pheochromocytomas vary in size from less than 1 g to several kilograms; in general, they are small, most weighing under 100 g. They are vascular tumors, tend to be capsulated, and commonly contain cystic or hemorrhagic areas. The cells tend to be large and contain typical catecholamine storage granules. Multinucleated cells, pleomorphic nuclei, mitosis, and extension into capsule and vessels are sometimes seen but do not indicate that the tumor is malignant. The chromogranin existing within secretory granules in the tumor tends to form *Zellballen* (cell balls); these structures are surrounded by sustentacular cells. Five to ten percent of cases are malignant, and malignancy is determined by the only biological behavior of the tumor. It is estimated that 0.1% of hypertensive patients have pheochromocytoma. More than 90% of patients with pheochromocytoma exhibit hypertension, which is sustained in two-thirds of patients. These tumors are observed

more frequently in women than in men and at all ages, including infancy; they are most common in the fifth and sixth decades [120].

Although most patients with functioning tumors have symptoms (sweating, palpitation, headache, dyspnea, and anxiety), most of the time, these vary in intensity, and in about half of the patients, they are paroxysmal. Pheochromocytomas are usually sporadic, but about 10–20% of cases are familial and arise alone or as part of several hereditary syndromes including multiple endocrine neoplasia (MEN) type IIa and type IIb, neuroectodermal disorders (tuberous sclerosis, von Hippel–Lindau disease, and neurofibromatosis type I), Carney's syndrome (pulmonary chondroma, gastric epithelioid leiomyosarcoma, and paraganglioma), and McCune–Albright syndrome. Pheochromocytoma can be found anywhere in the sympathetic nervous system from the neck to the sacrum; it is subdiaphragmatic in about 98% of cases. In 85–90% of these cases, it is found in the adrenal medulla. In sporadic cases of pheochromocytoma, 80% of the tumors are unilateral, 10% bilateral, and 10% extra-adrenal (paraganglioma). In contrast, two-thirds of those occurring in the context of MEN are bilateral. In children, it is extra-adrenal in 30% of cases. These extra-adrenal locations are para-aortic sympathetic chain (8%), organ of Zuckerkandl at origin of the inferior mesenteric artery (2–5%), and gonads, scrotum, and urinary bladder (1%). Fewer than 10% of these tumors are malignant and metastasize by lymphatic or hematogenous routes; metastases are usually found in the skeleton, liver, lymph nodes, and lungs [121]. The differential diagnosis includes thyrotoxicosis, migraine, sympathomimetic drug use, menopausal hot flushes, and anxiety disorders. Patients with persistent symptoms and hypertension may develop complications such as nephropathy, retinopathy, myocardial infarction, cerebrovascular accidents, and congestive heart failure.

The diagnosis is confirmed by assay of catecholamines and their metabolites, followed by MRI or CT to localize the lesion; predominant production of epinephrine, when present, suggests an adrenal location. Dopamine excretion is a sensitive indicator of tumor aggressiveness, and a rising plasma or urinary dopamine level is regarded as a poor prognostic indicator.

MRI is somewhat more successful in locating extra-adrenal tumors and has the advantage of providing bright images of pheochromocytoma with T_2 weighting in contrast to most other adrenal tumors. Only the smallest tumors or those shielded by clips and other metal objects from previous surgery cannot be detected; in these cases, an MIBG study is indicated.

Neuroblastoma

Neuroblastoma is a malignant tumor of the sympathetic nervous system, accounting for up to 10% of childhood cancers and 15% of cancer deaths among children. Seventy-five percent of neuroblastoma patients are younger than 4 years. The tumor is usually more than 5 cm in the largest diameter and tends to extend across the midline; it has the potential to mature into pheochromocytoma or ganglioneuroma. Metastases are the first manifestation in up to 60% of cases. The electron microscopic appearance of NB cells is distinctive. The malignant neuroblasts exhibit peripheral dendritic processes containing longitudinally oriented microtubules, neurosecretory granules, and filaments in the cytoplasm. Neuroblastomas readily infiltrate the surrounding structures and metastasize to the regional lymph nodes, liver, lungs, and bones; metastases to the orbit may result in proptosis [122]. Areas of necrosis, hemorrhage, calcification, and cystic changes are frequently present. Around one-third of cases are found in the adrenal gland, another third in other abdominal sites, and 20% in the posterior mediastinum. More than 90% of these tumors produce catecholamine in excess, but they rarely cause typical clinical syndromes. Severe diarrhea may be caused by secretion of vasoactive intestinal peptides by the neuroblastoma.

Ganglioneuroma

Ganglioneuroma is a benign tumor found in older children and young adults, with no sex predilection. Forty percent of the patients are over 20 years of age. Up to 30% of these tumors occur in the adrenal medulla and 43% in the posterior

mediastinum. Histologically, the tumor consists of mature ganglion cells and is well encapsulated; it is frequently calcified and rarely hormone active.

6.3.3.2 Scintigraphy

Metaiodobenzylguanidine

Metaiodobenzylguanidine (MIBG) is a guanethidine analog chemically similar to noradrenaline. Following i.v. injection, MIBG is rapidly cleared from the vascular compartment; however, a small amount remains in the thrombocytes. It localizes in storage granules of adrenergic tissue (referred to as synaptosomes) by means of energy- and Na-dependent mechanisms (type 1), and it is not metabolized to any appreciable extent. Neural crest tumors have these synaptosomes in abundance.

Preparation. The patient should be given Lugol solution orally (3 drops b.i.d. for 4–5 days, starting 2 days before injection to block the thyroid uptake of free ^{131}I. The patient should stop taking reserpine, imipramine, calcium channel blockers, cocaine, labetalol, amphetamine-like drugs, and others.

The dose of ^{131}I-MIBG is 0.5–1.0 mCi and results in a radiation dose of 50–100 rads/mCi to the adrenal medulla. The dose of ^{123}I-MIBG is 3–10 mCi, with a radiation dose of 0.80 rads/mCi to the adrenal medulla. The normal distribution of ^{123}I-MIBG is to the salivary gland, liver, urinary bladder, gastrointestinal tract, lung, myocardium, normal adrenal gland, thyroid, spleen, and uterus [123–126]; in small children, uptake may also be seen in the nape of the neck, which is currently believed to be related to accumulation in brown adipose tissue [127].

Eighty-five percent of the injected dose is excreted unchanged by the kidneys. Imaging is performed at 24 and 48 h after injection of ^{131}I-MIBG and at 6 and 24 h after injection of ^{123}I-MIBG (Fig. 6.15). When SPECT is used (Figs. 6.16 and 6.17), increased certainty is achieved in interpreting the studies [124]. It is worthy of mention that ^{123}I is better than ^{131}I,

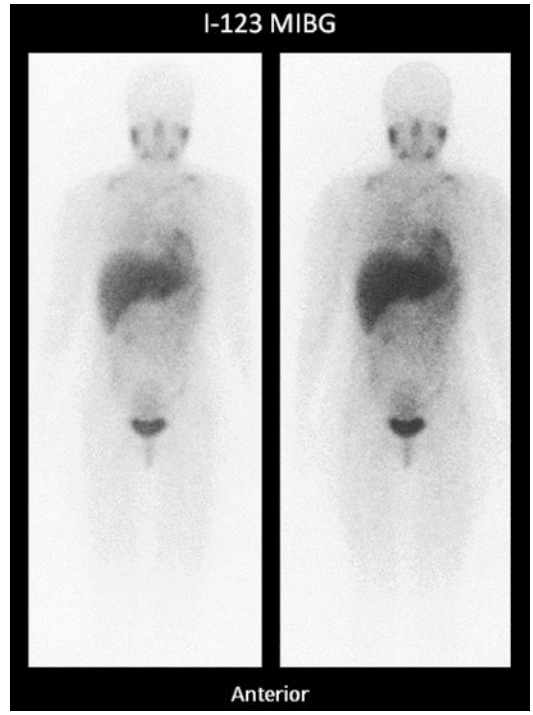

Fig. 6.15 A 32-year-old male with suspected pheochromocytoma. Anterior ^{123}I-MIBG whole-body image with different intensity is shown. There is increased uptake at the supraclavicular region bilaterally. This pattern is due to uptake by brown fat. The remainder of the study shows also physiological distribution of the radiotracer with no abnormalities

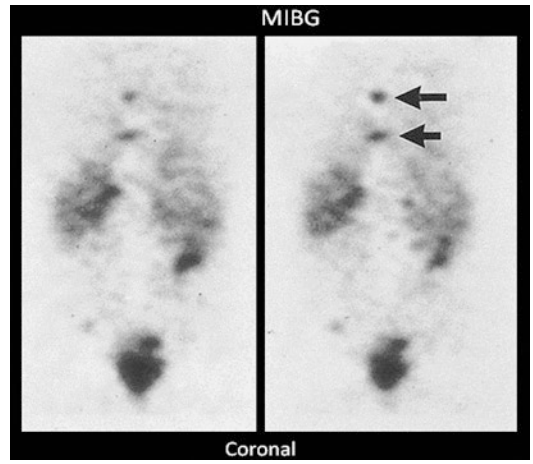

Fig. 6.16 Representative coronal images from a SPECT ^{131}I-MIBG study for a patient with neuroblastoma, showing metastases to the spine (*arrows*)

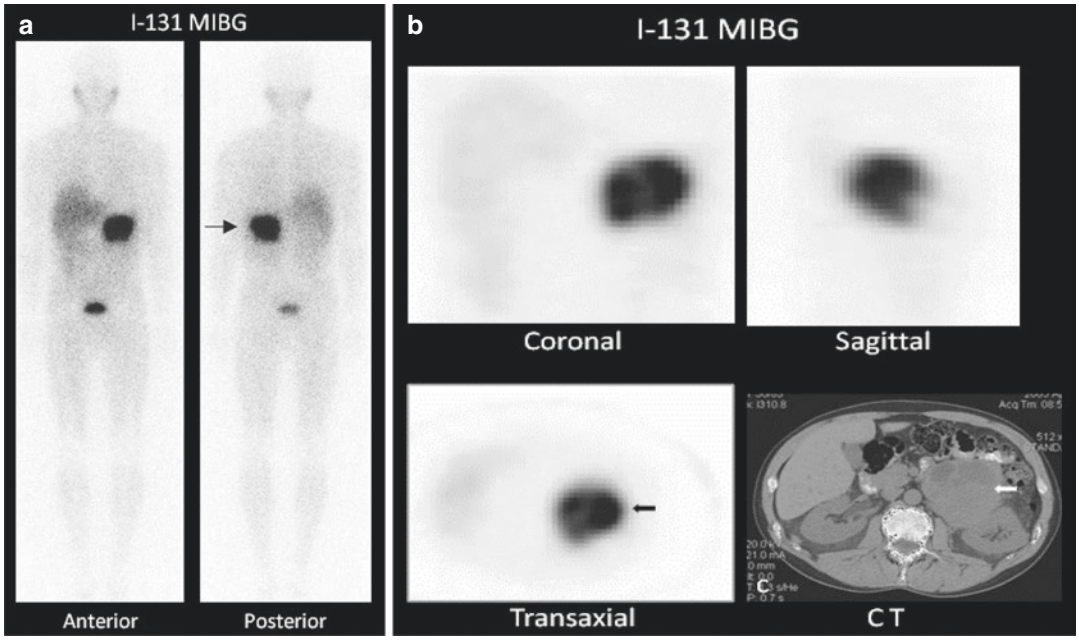

Fig. 6.17 A planar (**a**) and SPECT (**b**) ^{131}I-MIBG study and a CT section of a patient with a large pheochromocytoma (*arrow*s)

especially in the pediatric population, because of the lower radiation exposure to the adrenals in addition to the superior image quality of the former. The sensitivity of ^{131}I-MIBG in pheochromocytoma is 80–90% and specificity is more than 90%; positive MIBG uptake in benign solitary pheochromocytoma occurs in about 90% of patients [128]; tumors as small as 1–2 cm in diameter were detected especially with ^{123}I [129].

Moreover, metastatic and recurrent tumors can also be located (Figs. 6.17 and 6.18). Adrenal medullary hyperplasia found in MEN IIa is difficult to diagnose with CT or MRI. MIBG scintigraphy is uniquely suited to detect this condition. Occasionally, however, some large tumors are not visualized because of extensive tumor necrosis.

MIBG is localized in other neuroendocrine tumors to a lesser degree, including carcinoid, medullary thyroid carcinoma, and paraganglioma. Indium-111 octreotide (a somatostatin analog) is less accurate in the detection of pheochromocytoma, probably due to normal physiological uptake in the liver, spleen, and kidneys and blocking of somatostatin receptors by endogenous somatostatin.

Radiolabeled MIBG imaging is now a well-established examination in the diagnostic evaluation of neuroblastoma. ^{123}I is preferred especially in pediatric patients (dose 3–5 mCi) due to its favorable dosimetry and superior image quality; scintigraphy can be performed as early as 4 h after injection. Elevated catecholamine levels are not necessary for the detection of NB by MIBG. The sensitivity of MIBG in NB is 91%. Somatostatin analog scintigraphy has been reported to visualize MIBG-negative tumor sites in patients with NB. MIBG is essentil [130] as a prelude to ^{131}I-MIBG therapy. In the follow-up of the patients with high-risk neuroblastoma, SPECT/CT MIBG has been found to improve significantly the imaging interpretation and provides positive impact on patient management [131]. Recently, the use of low-dose ^{124}I-MIBG PET/CT for monitoring neuroblastoma in children and evaluating tumor burden showed better tumor detection capability compared to ^{123}I-MIBG planar imaging and SPECT/CT [131].

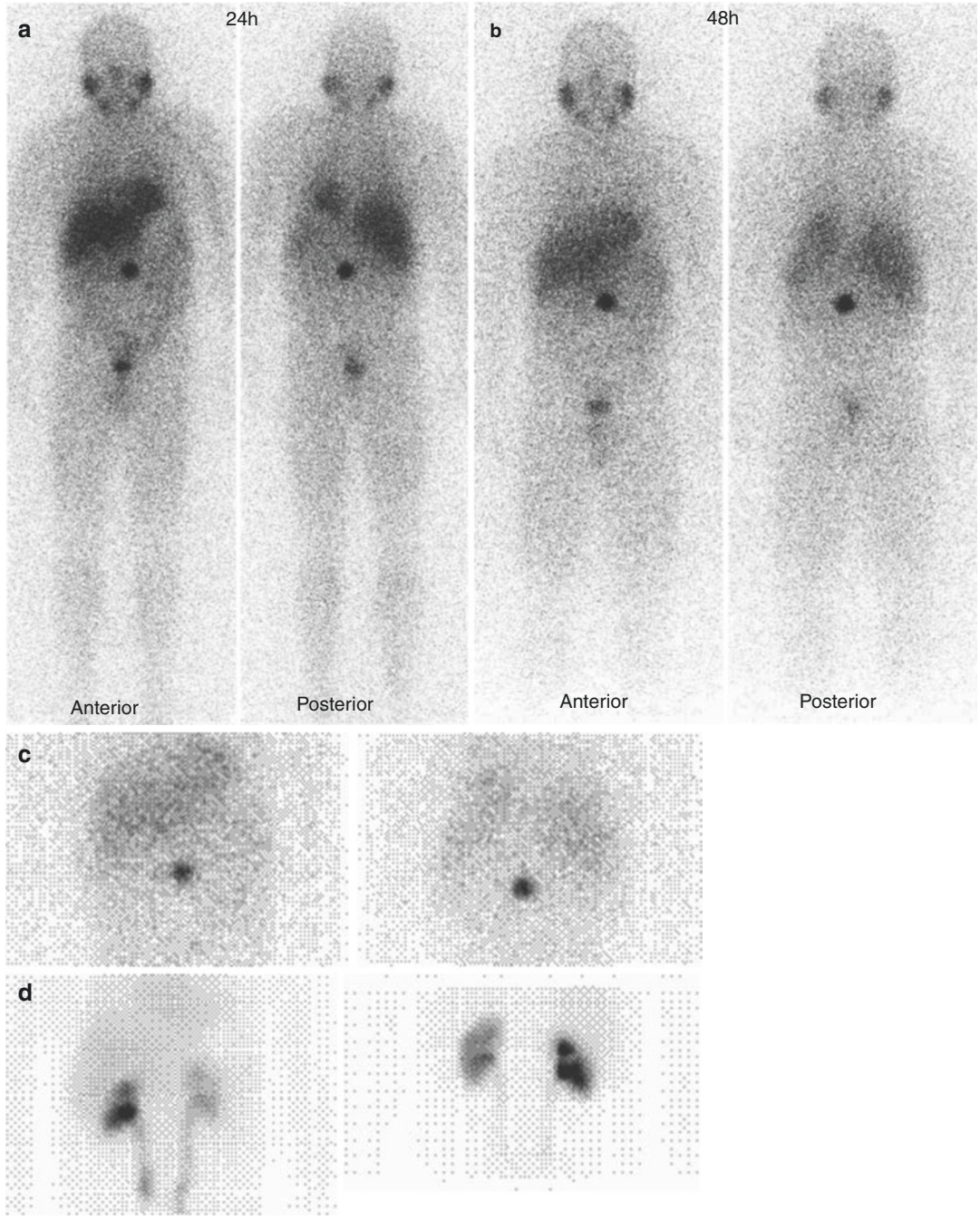

Fig. 6.18 ^{123}I-MIBG whole body (**a**, **b**) of a patient with known pheochromocytoma who was referred for back pain. The study shows a focal area of increased uptake in the midline of the abdomen. Forty-eight hours spot image (**c**) was acquired, and 99mTc-DTPA study (**d**) was also obtained for comparison and lesion appeared away from the kidneys. The study was correlated with 99mTc-MDP spot images of the thoracolumbar spine (**e**) which showed questionable focal abnormality in the midlumbar spine corresponding to the location of I-123 abnormal uptake. MRI (**f**) and CT (**g**) scans were obtained and show a lesion in L-3 representing metastatic pheochromocytoma

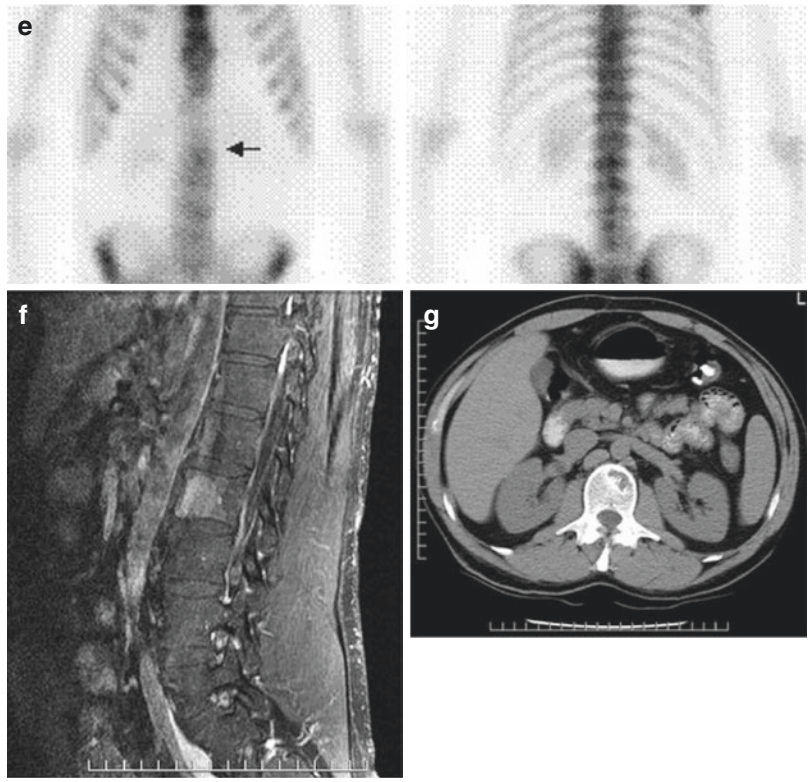

Fig. 6.18 (continued)

Other PET agents are also being used since approximately 10% of the neuroblastomas are non MIBG avid [132].

Indium-111 Octreotide

In healthy human beings, somatostatin, a natural neuropeptide, is produced in various tissues, including the nervous system, endocrine pancreas, and gastrointestinal tract. Somatostatin inhibits the secretion of several hormones, most importantly GH and TSH.

Neuroendocrine (including adrenal medulla) and non-neuroendocrine organs have surface receptors that bind to somatostatin. Octreotide, a somatostatin analog with a half-life of 120 min, is used to evaluate the tumors that contain these receptors, in which case it binds to somatostatin receptor subtypes 2 and 5. Among these tumors are pheochromocytoma, neuroblastoma, paraganglioma, and others including pancreatic tumors and carcinoid.

Octreotide is usually tagged with ^{111}In (Fig. 6.19), although ^{123}I has also been used in the past. It is recommended that octreotide therapy be withheld for at least 72 h prior to the injection of the radiopharmaceutical. Following i.v. injection of a standard dose of 6 mCi, static images are obtained at 4 and 24 h (Fig. 6.19). SPECT images through the region of interest are then obtained at 4 h and at 24 h if needed. This radiopharmaceutical is excreted via glomerular filtration. In a normal patient, octreotide activity is identified in the thyroid, kidneys, liver, spleen, pituitary, gallbladder, and, to a lesser extent, the bowel on delayed images. The kidney and spleen receive the highest absorbed dose. A focal area of intense early radiotracer uptake is considered to be pathological, indicating primary neoplasm or metastasis. A false-negative scan is seen in cases where the tumor is small, has few somatostatin receptors, or both. ^{111}In-octreotide scanning is highly sensitive for

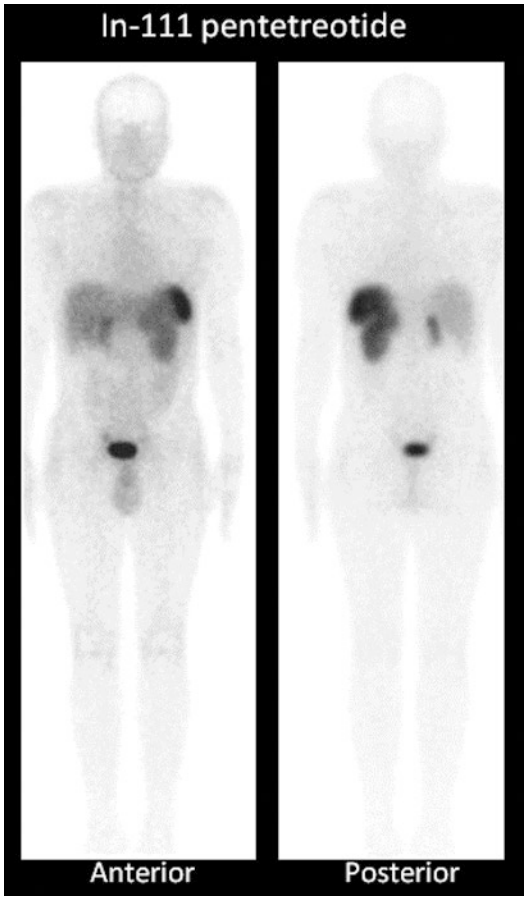

Fig. 6.19 Normal distribution of In-111 pentetreotide includes intense uptake in the spleen as well as uptake in the liver and activity in the kidneys and urinary bladder. Bowel activity is seen usually at 24 h. The pituitary and the thyroid glands may be faintly visualized. Biliary excretion of the tracer occurs with occasional visualization of the gallbladder. Note that the right kidney is smaller than the left in this case

detecting tumors greater than 1.5 cm. Since the expression of somatostatin receptors in neuroblastomas is variable with less receptors in more advanced disease, an accurate sensitivity of ^{111}In-octreotide is not readily definable. In children, several studies have compared ^{111}In-octreotide with MIBG scintigraphy for imaging neuroblastoma; the sensitivity of the former ranged from 55 to 70% and that of the latter 83–94% [133–137]. Several studies reported MIBG-negative tumor sites detected by ^{111}In-pentetreotide in patients with neuroblastomas [133–137]. High affinity of octreotide for the MIBG-negative neuroblastoma cell line has been found. Tenenbaum et al. recommended the use of octreotide to detect somatostatin receptors when results from MIBG scans are negative [134]. Pashankar suggested that neuroblastoma can be imaged by either ^{111}In-octreotide or MIBG depending on local expertise, as they have a complementary role in the initial diagnostic workup particularly since ^{111}In-octreotide additionally correlates with prognosis [136] (Figs. 6.20 and 6.21).

^{111}In-octreotide is currently the agent of choice for nuclear medicine imaging of head and neck paraganglioma, though it is insensitive for lesions less than 1 cm. The recent introduction of SPECT/CT has greatly improved the sensitivity of ^{111}In-octreotide scintigraphy [138].

It was suggested that ^{111}In-DTPA-D-Phe-1--octreotide might be useful for radiation therapy of patients with surgically incurable tumors having high somatostatin receptor densities such as carcinoid [139].

Positron Emission Tomography Imaging

PET has been used to evaluate adrenal masses. The higher spatial resolution of PET scanners (Figs. 6.22, 6.23, and 6.24) enables the detection of small tumors not seen with ^{123}I-MIBG. Malignant adrenal tumors can be detected with FDG PET, but its use in these cases is limited due to the low specificity. FDG PET/CT can help detect certain malignant lesions particularly the minority which are not detected by MIBG. ^{11}C-hydroxyephedrine, the first available positron-emitting tracer of the sympathetic nervous system, was found useful in the detection of pheochromocytomas, with a high level of accuracy [141]. Its uptake reflects catecholamine transport and storage and neuronal reuptake. In detecting metastatic pheochromocytomas, (^{18}F) dopamine was found to be a superior to ^{131}I-MIBG [142–144]. PET imaging is used for the detection, localization, staging, and follow-up of neuroendocrine tumors. It can also be used to determine SSTR status of the tumor and for selecting patients

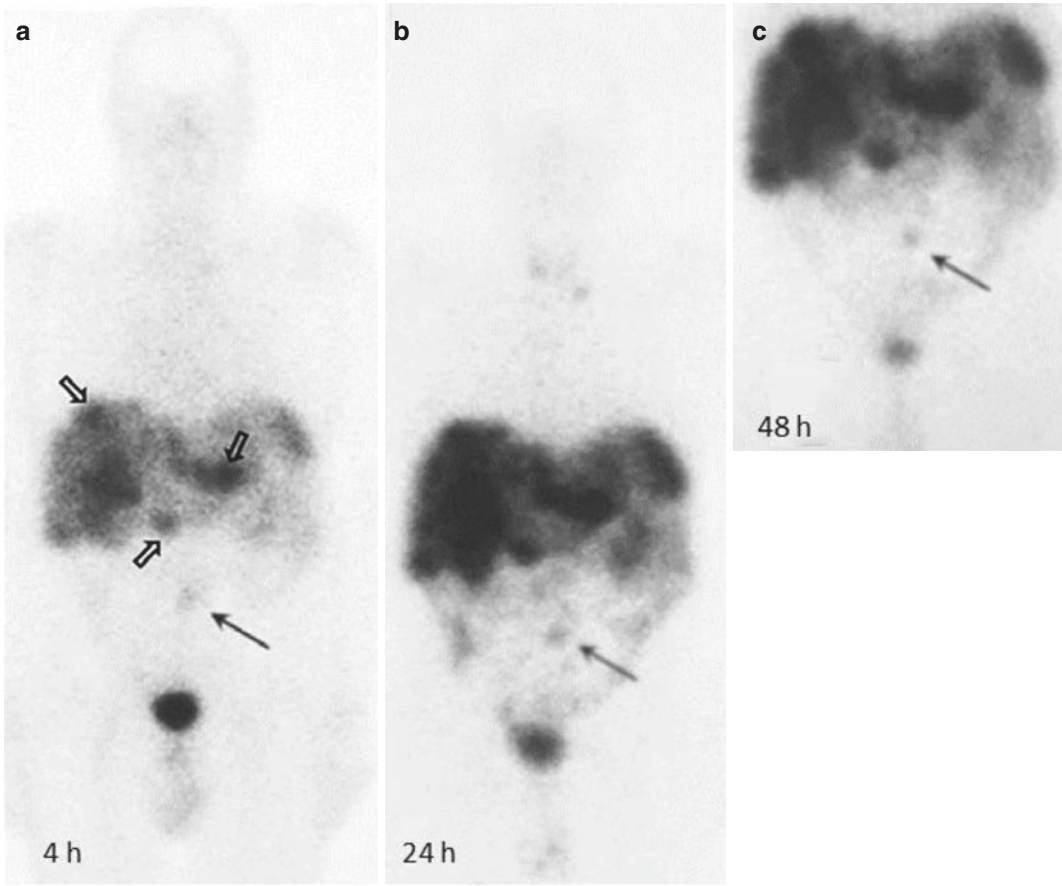

Fig. 6.20 ^{111}In-octreotide imaging study obtained at 4 (**a**), 24 (**b**), and 48 (**c**) h after i.v. injection of 6 mCi of the radiopharmaceutical. The images illustrate—in addition to the foci of metastatic carcinoid to the liver—the physiological uptake in the liver, spleen, kidneys, bowel, and urinary bladder. Note that delayed imaging (**c**) and/or SPECT may be needed to differentiate physiological activity such as in the bowel from true disease (*arrow*) such as in this case

with metastatic disease for SSTR radionuclide therapy with Lutetium-177 (Lu-177)- or Yttrium-90 (Y-90)-labeled somatostatin analogs. 68-Ga-DOTATATE and 64-Cu-DOTATATE are radiolabeled somatostatin analogs for the diagnosis and pretreatment evaluation of neuroendocrine tumors with PET.

PET imaging with Ga-68 DOTA peptides is more accurate and detects more lesions than Octreoscan in carcinoid tumors and other neuroendocrine tumors [142]. Figures 6.22 and 6.23 illustrate normal and abnormal Ga-68 DOTA TATE studies.

6.3.4 Incidental Adrenal Mass

Incidental detection of adrenal lesions is a diagnostic challenge since adrenal adenomas are relatively common (2–9%) in the general population. This is particularly important in patients with a previous clinical history of malignancy. Incidental adrenal lesions are detected in about 2–5% of contrast-enhanced abdominal CT examinations making the diagnosis of adrenal incidentaloma a common clinical problem [145]. In these cases, the patients should be screened for pheochromocytoma clinically and biochemically. Adrenal

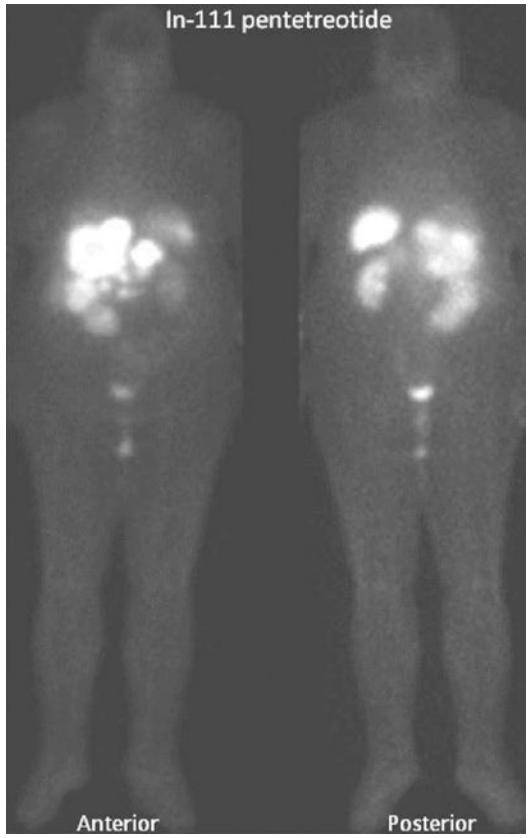

Fig. 6.21 Fifty-three-year-old female presented with carcinoid symptoms for 6 months. She was found to have metastatic disease to the liver and pancreas. In-111 pentetreotide anterior and posterior whole-body planar images at 24 h. Images reveal multiple foci of increased activity in the liver and abdomen consistent with SSTR-positive metastatic disease. SPECT/CT would better locate the abdominal disease

incidentalomas are uncommon in patients younger than 30 years but increase in frequency with age; they occur equally in males and females. Adrenocortical adenoma accounts for 36–94% of incidentalomas detected in patients without a history of malignancy [145]. Only about 10% of incidental adrenal masses are functional [145]. Accordingly, NP-59 would not be an appropriate radiotracer for adrenal incidentaloma because 90% of adrenal masses cannot incorporate NP-59 in their cells. Metomidate is an inhibitor of 11ß-hydroxylase, a key enzyme in the biosynthesis of cortisol and aldosterone by the adrenal cortex. ^{11}C-metomidate is a promising PET tracer to identify incidentalomas of adrenocortical origin [146]. Khan et al. reported on the value of ^{11}C-metomidate in evaluation of adrenocortical cancer [147].

FDG PET/CT can help detect certain malignancy in adrenal incidentalomas particularly when they occur in patients with known extra-adrenal malignancies. The prevalence of adrenal metastases discovered by FDG PET/CT has been reported to be as high as 9.9% in several studies. The upstaging resulting from FDG PET/CT can play an important role in modifying the plans of therapeutic strategies. In some patients, the adrenal metastasis can be the first manifestation of a cancer [148]. It should be noted that functional adrenal adenomas (cortisol secreting was the highest) may show increased FDG uptake in comparison to the nonfunctional adrenal masses [149].

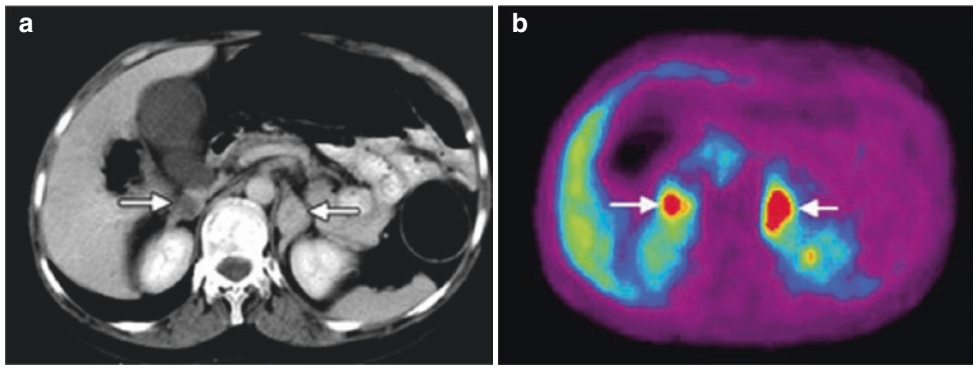

Fig. 6.22 (**a**, **b**) Transverse images obtained in a patient with multiple endocrine neoplasia type 2 and an increase in urinary catecholamine levels. A CT image shows bilateral adrenal tumors (*arrows*) and a 2-cm-diameter tumor on the right side and a 4-cm-diameter tumor on the left side adrenal lesions (*arrows*). HED PET image (**b**) shows intense uptake in both. Surgery revealed bilateral pheochromocytomas. (From Anderson et al. [140] with permission)

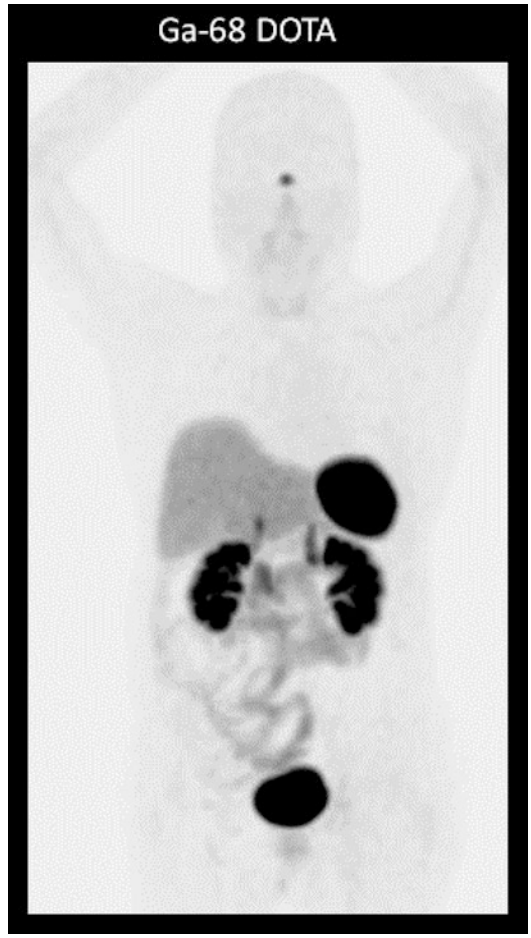

Fig. 6.23 Normal distribution of Ga-68 DOTA peptides includes intense uptake in the spleen with uptake in the pituitary gland, liver, adrenals, and pancreatic head and activity in the kidneys, bowel, and bladder. Salivary and thyroid glands show mild uptake. The prostate gland and breast glandular tissue may show diffuse low uptake. Physiological uptake in the pancreatic head may mimic focal tumor. Uptake in adrenals may be prominent

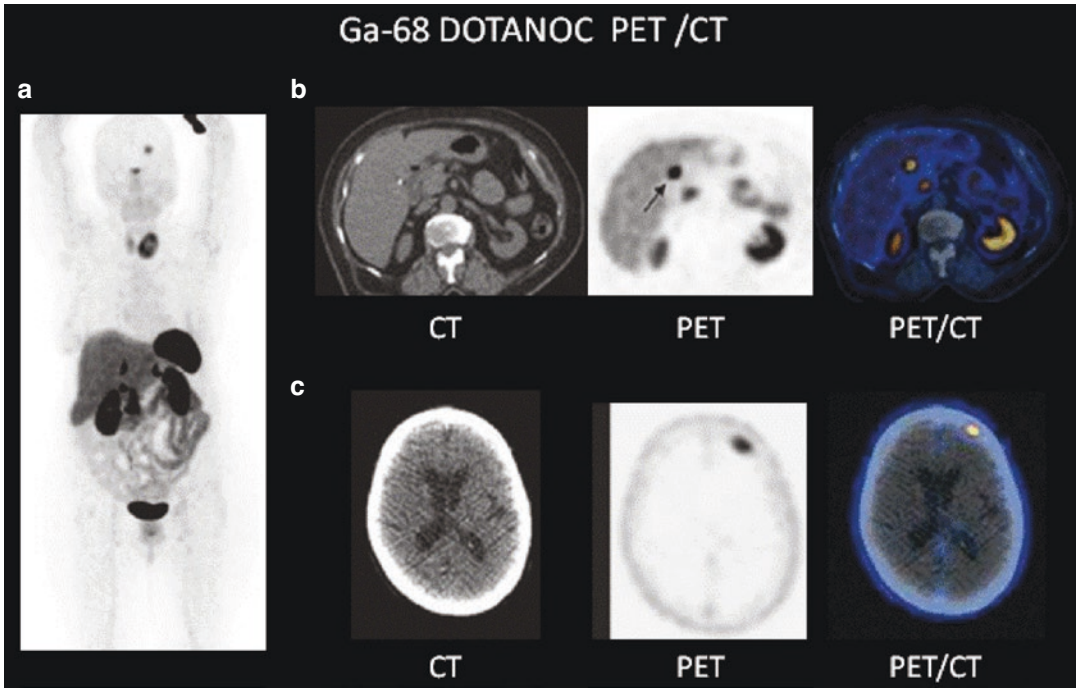

Fig. 6.24 Scintigraphic studies for a 74-year-old woman with duodenal 1 cm polyp, grade 1 carcinoid tumor, for staging. Ga-68 DOTANOC PET/CT whole-body MIP (**a**) and selected transaxial CT, PET, and PET/CT fusion images of the abdomen (**b**) and head (**c**) are shown. There is a focal uptake in the duodenal carcinoid (arrow) which is higher than liver activity. Incidentally, focal uptake is also seen in the left frontal region due to benign meningioma and markedly and heterogeneously increased uptake in the enlarged left thyroid lobe which can be due to medullary thyroid carcinoma, well-differentiated thyroid carcinoma, or carcinoid metastases. Physiological uptake is seen in the pituitary gland, right thyroid lobe, liver, spleen, both adrenal glands, pancreatic head, and bowel with excreted activity in the kidneys and bladder

References

1. Nurunnabi ASM, Alim A, Sabiha M, Manowara B, Monira K, Shamim A (2010) Weight of the human thyroid gland: a postmortem study. Bangladesh J Med Sci 9(1):44–48
2. Ellis H (2007) Anatomy of the thyroid and parathyroid glands. Surgery 25(11): 467–468
3. Sarkar SD (1996) Thyroid pathophysiology. In: Sandler MP, Coleman RE, FJ TW (eds) Diagnostic nuclear medicine. Williams and Wilkins, Baltimore, pp 899–909
4. Cooper DS (2005) Antithyroid drugs. N Engl J Med 352:905–917
5. Malozowski S, Chiesa A (2010) Propylthiouracil-induced hepatotoxicity and death. Hopefully, nevermore. J Clin Endocrinol Metab 95:3161–3163
6. Silberstein EB, Alavi A, Balon HR et al (2012) The SNM practice guideline for therapy of thyroid disease with 131I. J Nucl Med 53
7. Sarkar SD, Savitch I (2004) Management of thyroid cancer. Appl Radiol 33:34–45
8. Tala H, Robbins R, Fagin JA et al (2011) Five-year survival is similar in thyroid cancer patients with distant metastases prepared for radioactive iodine therapy with either thyroid hormone withdrawal or recombinant human TSH. J Clin Endocrinol Metab 96:2105–2111
9. Sarkar SD, Afriyie MO, Palestro CJ (2001) Recombinant human thyroid-stimulating-hormone-aided scintigraphy: comparison of imaging at multiple times after I-131 administration. Clin Nucl Med 26:392–395
10. Moog F, Linke R, Manthey N et al (2000) Influence of thyroid stimulating hormone levels on uptake of FDG in recurrent and metastatic differentiated thyroid carcinoma. J Nucl Med 41:1989–1995
11. Akamizu T, Satoh T, Isozaki O et al (2012) Diagnostic criteria, clinical features, and incidence of thyroid storm based on nationwide surveys. Thyroid 22:661–679

12. Chin BB, Patel P, Cohade C et al (2004) Recombinant human thyrotropin stimulation of fluoro-D-glucose positron emission tomography in well-differentiated thyroid carcinoma. J Clin Endocrinol Metab 89:91–95
13. Bidart JM, Mian C, Lazar V, Russo D, Filetti S, Caillou B et al (2000) Expression of pendrin and the Pendred syndrome (PDS) gene in human thyroid tissues. J Clin Endocrinol Metab 2000(85):2028–2033
14. Mitchell AM, Manley SW, Morris JC, Powell KA, Bergert ER, Mortimer RH (2001) Sodium iodide symporter (NIS) gene expression in human placenta. Placenta 22:256–258
15. Pearce EN, Lazarus JH, Moreno-Reyes R, Zimmermann MB (2016) Consequences of iodine deficiency and excess in pregnant women: an overview of current knowns and unknowns. Am J Clin Nutr 104:918S–923S
16. Koukkou EG, Roupas ND, Markou KB (2017) Effect of excess iodine intake on thyroid on human health. Minerva Med 108:136–146
17. Bogazzi F, Bartalena L, Gasperi M et al (2001) The various effects of amiodarone on thyroid function. Thyroid 11:511–519
18. Daniels GH (2001) Amiodarone-induced thyrotoxicosis. J Clin Endocrinol Metab 86:3–8
19. Laurie AJ, Lyon SG, Lasser EC (1992) Contrast material iodides: potential effects on radioactive iodine thyroid uptake. J Nucl Med 33:237–238
20. Sarkar SD, Kalapparambath T, Palestro CJ (2002) Comparison of I-123 and I-131 for whole body imaging in thyroid cancer. J Nucl Med 43:632–634
21. Ward LS, Santarosa PL, Granja F et al (2003) Low expression of sodium iodide symporter identifies aggressive thyroid tumors. Cancer Lett 200:85–91
22. Bertagna F, Treglia G, Piccardo G et al (2012) Diagnostic and clinical significance of F-18-FDG-PET/CT thyroid incidentalomas. J Clin Endocrinol Metab 97:3866–3875
23. Castellana M, Trimboli P, Piccardo A, Giovanella L, Treglia G (2019) Performance of 18F-FDG PET/CT in selecting thyroid nodules with indeterminate fine-needle aspiration cytology for surgery. A systematic review and a meta-analysis. J Clin Med 8:1333
24. Kim YH, Chang Y, Kim Y, Kim SJ, Rhee EJ et al (2019) Diffusely increased 18F-FDG uptake in the thyroid gland and risk of thyroid dysfunction: a cohort study. J Clin Med 8:443
25. Padma V, Ramakrishnan C (2019) Malignancy in solitary thyroid nodules: a study on incidence & evaluation of risk. Indian J Public Health Res Dev 10:4253–4255
26. Kishan AM, Prasad K (2018) Prevalence of solitary thyroid nodule and evaluation of the risk factors associated with occurrence of malignancy in a solitary nodule of thyroid. Int Surg J 5(6):2279–2285
27. Guth S, Theune U, Aberle J, Galach A, Bamberger CM (2009) Very high prevalence of thyroid nodules detected by high frequency (13 MHz) ultrasound examination. Eur J Clin Investig 39:699–706
28. Jiang H, Tian Y, Yan W, Kong Y, Wang H, Wang A et al (2016) The prevalence of thyroid nodules and an analysis of related lifestyle factors in Beijing communities. Int J Environ Res Public Health 13:1–11
29. Holm LE, Blomgren H, Lowhagen T (1985) Cancer risks in patients with chronic autoimmune thyroiditis. N Engl J Med 312:601–604
30. Belfiore A, La Rosa GL, La Porta GA, Giuffrida D, Milazzo G, Lupo L et al (1992) Cancer risk in patients with cold thyroid nodules: relevance of iodine intake, sex, age, and multinodularity. Am J Med 93:363–369
31. Fabrizio Monaco F (2003) Classification of thyroid diseases: suggestions for a revision. J Clin Endocrinol Metabol 88:1428–1432
32. Fernandez-Soto L, Gonzalez A, Escobar-Jimenez F et al (1998) Increased risk of autoimmune thyroid disease in hepatitis C vs hepatitis B before, during, and after discontinuing interferon therapy. Arch Intern Med 158:1445–1448
33. Hooft L, Hoekstra OS, Deville W et al (2001) Diagnostic accuracy of ^{18}F-fluorodeoxyglucose positron emission tomography in the follow-up of papillary or follicular thyroid cancer. J Clin Endocrinol Metab 86:3779–3786
34. Sarkar SD, Becker DV (1995) Thyroid uptake and imaging. In: Becker KL (ed) Principles and practice of endocrinology and metabolism. Lippincott, Philadelphia, pp 307–313
35. Dang AH, Hershman JM (2002) Lithium-associated thyroiditis. Endocr Pract 8:232–236
36. Amino N, Tada H, Hidaka Y et al (1999) Screening for postpartum thyroiditis. J Clin Endocrinol Metab 84:1813
37. Stagnaro-Green A (2002) Postpartum thyroiditis. J Clin Endocrinol Metab 87:4042–4047
38. Premawardhana LDKE, Parkes AB, John R et al (2004) Thyroid peroxidase antibodies in early pregnancy: utility for prediction of postpartum thyroid dysfunction and implications for screening. Thyroid 14:610–615
39. Mandac JC, Chaudhry S, Sherman KE, Tomer Y (2006) The clinical and physiological spectrum of interferon-alpha induced thyroiditis: toward a new classification. Hepatology 43(4):661–672
40. Oppenheim Y, Ban Y, Tomer Y (2004) Interferon induced autoimmune thyroid disease (AITD): a model for human autoimmunity. Autoimmun Rev 3:388–393
41. Bliddal S, Nielsen CH, Feldt-Rasmussen U (2017) Recent advances in understanding autoimmune thyroid disease: the tallest tree in the forest of polyautoimmunity. F1000 Res 6:1776. https://doi.org/10.12688/f1000research.11535.1
42. Vestergaard P, Rejnmark L, Weeke J et al (2002) Smoking as a risk factor for Graves' disease, toxic nodular goiter, and autoimmune hypothyroidism. Thyroid 12:69–75

43. Fountoulakis S, Tsatsoulis A (2004) On the pathogenesis of autoimmune thyroid disease: a unifying hypothesis. Clin Endocrinol 60:397–409
44. Li Y, Teng D, Shan Z et al (2008) Antithyroperoxidase and antithyroglobulin antibodies in a five-year follow up survey of populations with different iodine intakes. J Clin Endocrinol Metab 93:1751–1757
45. Nygaard B, Knudsen JH, Hegedus L et al (1997) Thyrotropinreceptor antibodies and Graves' disease, a side-effect of I-131 treatment in patients with nontoxic goiter. J Clin Endocrinol Metab 82:2926–2930
46. Surks MI, Ortiz E, Daniels GH et al (2004) Subclinical thyroid disease: scientific review and guidelines for diagnosis and management. JAMA 291:228–238
47. Weetman AP (2000) Graves disease. N Engl J Med 343:1236–1248
48. Ahmed A, Craig W, Krukowski ZH (2012) Quality of life after surgery for Graves' disease: comparison of those having surgery intended to preserve thyroid function with those having ablative surgery. Thyroid 22:494–500
49. Burch HB, Burman KD, Cooper DS (2012) A 2011 survey of clinical practice patterns in the management of Graves' disease. J Clin Endocrinol Metab 97:4549–4558
50. La Vecchia C, Malvezzi M, Bosetti C, Garavello W, Bertuccio P, Levi F, Negri E (2015) Thyroid cancer mortality and incidence: a global overview. Int J Cancer 136:2187–2195
51. Tumino D, Grani G, Di Stefano M, Di Mauro M, Scutari M et al (2020) Nodular thyroid disease in the era of precision medicine. Front Endocrinol 10:907
52. Elgazzar AH, Alenezi S, Alshammari JM, Ghanem M, Asa'Ad S (2015) Value of oblique view in nodular thyroid disease; revisiting fundamentals. World J Nucl Med 14:125
53. Liu Y (2009) Clinical significance of thyroid uptake on F18-fluorodeoxyglucose positron emission tomography. Ann Nucl Med 23:17–23
54. Soto GD, Halperin I, Squarcia M, Lomeña F, Domingo MP (2010) Update in thyroid imaging. The expanding world of thyroid imaging and its translation to clinical practice. Hormones 9:287–298
55. Sarkar SD (2006) Benign thyroid disease: what is the role of nuclear medicine? Semin Nucl Med 36:185–193
56. Bath SC, Steer CD, Golding J, Emmett P, Rayman MP (2013) Effect of inadequate iodine status in UK pregnant women on cognitive outcomes in their children: results from the Avon Longitudinal Study of Parents and Children (ALSPAC). Lancet 382:331–337
57. Hynes KL, Otahal P, Burgess JR, Oddy WH, Hay I (2017) Reduced educational outcomes persist into adolescence following mild iodine deficiency in utero, despite adequacy in childhood: 15-year follow-up of the Gestational Iodine Cohort investigating auditory processing speed and working memory. Nutrients 9:pii:E135477
58. Abel MH, Caspersen IH, Meltzer HM, Haugen M, Brandlistuen RE, Aase H, Alexander J, Torheim LE, Brantsaeter AL (2017) Suboptimal maternal iodine intake is associated with impaired child neurodevelopment at 3 years of age in the Norwegian mother and child cohort study. J Nutr 147:1314–1324
59. Levie D, Tim I, Korevaar M, Bath SC, Dalmau-Bueno A et al (2018) Thyroid function in early pregnancy, child IQ, and autistic traits: a meta-analysis of individual participant data. J Clin Endocrinol Metabol 103:2967–2297
60. Taterra D, Wong LM, Vikse J, Sanna B, Pękala P, Walocha J, Cirocchi R, Tomaszewski K, Henry BM (2019) The prevalence and anatomy of parathyroid glands: a meta-analysis with implications for parathyroid surgery. Langenbeck's Arch Surg 404(1):63–70. 55
61. Alenezi SA, Asa'ad SM, Elgazzar AH (2015) Scintigraphic parathyroid imaging: concepts and new developments. Res Rep Nucl Med 5:9–18
62. Quiros RM, Warren W, Prinz RA (2004) Excision of a mediastinal parathyroid gland with use of video-assisted thoracoscopy, intraoperative 99mTc-sestamibiscanning, and intraoperative monitoring of intact parathyroid hormone. Endocr Pract 10:45–48
63. Taterra D, Wong LM, Vikse J, Sanna B, Pękala P, Walocha J et al (2019) The prevalence and anatomy of parathyroid glands: a meta-analysis with implications for parathyroid surgery. Langenbeck's Arch Surg 404:63–70
64. Akerstrom G, Grimelius L, Johansson H, Lundquist H, Pertoft H, Bergstrom R (1981) The parenchymal cell mass in normal human parathyroid glands. Acta Pathol Microbiol Immunol Scand 89(A):367
65. Akerstrom G, Rudberg C, Grimelius L et al (1986) Histologic parathyroid abnormalities in an autopsy series. Hum Pathol 17:520–527
66. Heath H III (1991) Clinical spectrum of primary hyperparathyroidism: evolution with changes in medical practice and technology. J Bone Mineral Res 6:S63–S70
67. Bilezikian JP, Bandeira L, Khan A, Cusano NE (2018) Hyperparathyroidism. Lancet 391(10116):168–178
68. Silva BC, Cusano NE, Bilezikian JP (2018) Primary hyperparathyroidism. Best Pract Res Clin Endocrinol Metab 32(5):593–607
69. Yeh MW, Ituarte PHG, Zhou HC et al (2013) Incidence and prevalence of primary hyperparathyroidism in a racially mixed population. J Clin Endocrinol Metab 98(3):1122–1129
70. Ljunghall S, Hellman P, Rastad J, Akerström G (1991) Primary hyperparathyroidism: epidemiology, diagnosis and clinical picture. World J Surg 15(6):681–687
71. Herfarth KK, Wells SA (1997) Parathyroid glands and the multiple endocrine neoplasia syndromes and familial hypocalciuric hypercalcemia. Semin Surg Oncol 13:114–124
72. Duh QY, Hybarger CP, Geist R, Gamsu G, Goodman PC, Gooding GA, Clark OH (1987) Carcinoids asso-

ciated with multiple endocrine neoplasia syndromes. Am J Surg 154:142–148
73. Beus KS, Stack BC (2004) Synchronous thyroid pathology in patients presenting with primary hyperparathyroidism. Am J Otolaryngol 25:308–312
74. Sidhu S, Campbell P (2000) Thyroid pathology associated with primary hyperparathyroidism. Aust NZJ Surg 70:285–287
75. Hedman IL, Tisell LE (1984) Associated hyperparathyroidism and non-medullary thyroid carcinoma: the etiological role of radiation. Surgery 95:392–397
76. Lau WL, Obi Y, Kalantar-Zadeh K (2018) Parathyroidectomy in the management of secondary hyperparathyroidism. Clin J Am Soc Nephrol 13(6):952–961
77. Thompson NW, Eckhauser FE, Harness JK (1982) The anatomy of primary hyperparathyroidism. Surgery 92:814–821
78. Simeone DM, Sandelin K, Thompson NW (1995) Undescended superior parathyroid gland: a potential cause of failed cervical exploration for hyperparathyroidism. Surgery 118:949–956
79. Tezelman S, Shen W, Shaver JK et al (1993) Double parathyroid adenomas: clinical and biochemical characteristics before and after parathyroidectomy. Ann Surg 218:300–309
80. Bartsch D, Nies C, Hasse C et al (1995) Clinical and surgical aspects of double adenoma in patients with primary hyperparathyroidism. Br J Surg 82:926–929
81. Nguyen BD (1999) Parathyroid imaging with Tc-99msestamibiplanar and SPECT scintigraphy. Radiographics 19:601–614
82. Clark OH, Duh QY (1989) Primary hyperparathyroidism: a surgical perspective. Endocrinol Metab Clin N Am 18:701–714
83. McHenry CR, Lee K, Saadey J et al (1996) Parathyroid localization with technetium-99m-sestamibi: a prospective evaluation. J Am Coll Surg 183:25–30
84. Bergenfelz A, Tennvall J, Valdermarsson S et al (1997) Sestamibiversusthallium subtraction scintigraphy in parathyroid localization: a prospective comparative study in patients with predominantly mild primary hyperparathyroidism. Surgery 121:601–605
85. Rogers LA, Fetter BF, Peete WPJ (1969) Parathyroid cyst and cystic degeneration of parathyroid adenoma. Arch Pathol 88:476–479
86. Fallon MD, Haines JW, Teitelbaum SL (1982) Cystic parathyroid gland hyperplasia-hyperparathyroidism presenting as a neck mass. Am J Clin Pathol 77:104–107
87. Turner WJD, Baergen RN, Pellitteri PK, Orloff LA (1996) Parathyroid lipoadenoma: case report and review of the literature. Otolaryngol Head Neck Surg 114:313–316
88. Cummings CW (2005) Otolaryngology: head and neck surgery, 4th edn. Mosby, Philadelphia
89. Cheng L, Bostwick DG (2011) Endocrine pathology. In: Essentials of anatomic pathology, 3rd edn. Springer, Berlin, pp 927–928
90. Rinsho N (1995) Primary hyperparathyroidism, pathologic findings and ultrastructure. Jpn J Clin Med 53:861–863
91. Chen CC, Premkumar A, Hill SC, Skarulis MC, Spiegel AM (1995) Tc-99msestamibi imaging of a hyperfunctioning parathyroid autograft with Doppler ultrasound and MRI correlation. Clin Nucl Med 20:222–225
92. Lee VS, Spritzer CE, Coleman RE, Wilkinson RH Jr, Coogan AC, Leight GS Jr (1995) Hyperparathyroidism in high-risk surgical patients: evaluation with double-phase technetium-99msestamibiimaging. Radiology 197:627–633
93. Walker RP, Paloyan E, Gopalsami C (2004) Symptoms in patients with primary hyperparathyroidism: muscle weakness or sleepiness. Endocr Pract 10:404–408
94. Wang CA (1977) Parathyroidre-exploration: a clinical and pathological study of 112 cases. Ann Surg 186:140
95. Assalia A, Inabnet WB (2004) Endoscopicparathyroidectomy. Otolaryngol Clin N Am 37:871–886
96. O'Doherty MJ, Kettle AG (2003) Parathyroid imaging: preoperative localisation. Nucl Med Commun 24:125–131
97. Mitchell BK, Merrell RC, Kinder BK (1995) Localization studies in patients with hyperparathyroidism. Endocr Surg 75:483–498
98. Kao A, Shiau YC, Tsai SC, Wang JJ, Ho ST (2002) Technetium-99mmethoxyisobutylisonitrile imaging for parathyroid adenoma: relationship to P-glycoprotein or multidrug resistance-related protein expression. Eur J Nucl Med Mol Imaging 29:1012–1015
99. Goris ML, Basso LV, Keeling C (1991) Parathyroid imaging. J Nucl Med 32:887–889
100. O'Doherty MJ, Kettle AG, Wells P, Collins RE, Coakley AJ (1992) Parathyroid imaging with technetium99m-sestamibi: preoperative localization and tissue up take studies. J Nucl Med 33: 313–318
101. Takebayashi S, Hidai H, Chiba T, Takaga Y, Nagatani Y, Matsubara S (1999) Hyper functional parathyroid glands with Tc-99mMIBI scan: semiquantitative analysis correlated with histologic findings. J Nucl Med 40:1792–1797
102. Sandrock D, Merino MJ, Norton JA, Neumann RD (1993) Ultrastructural histology correlates with results of thallium-201/technetium-99m parathyroid subtraction scintigraphy. J Nucl Med 34:24–29
103. Naddaf S, Anim JJ, Farghaly MM, Behbehani AE, Alshomar KA, Elgazzar AH (2004) Ultrastructure of hyperfunctioning parathyroid glands: does it explain various patterns of sestamibi uptake. Proceedings of the 9th annual Health science poster day and conference, Kuwait, April 19–21, p 61
104. Dontu VS, Kettle AG, O'Doherty MJ, Coakley AJ (2004) Optimization of parathyroid imaging by simultaneous dual energy planar and single pho-

ton emission tomography. Nucl Med Commun 25:1089–1093
105. Melton GB, Somervell H, Friedman KP, Zeiger MA, Cahid CA (2005) Interpretation of ^{99m}Tcsestamibiparathyroid SPECT scan is improved when read by the surgeon and nuclear medicine physician together. Nucl Med Commun 26:633–638
106. Parikh AM, Suliburk JW, Morón FE (2018) Imaging localization and surgical approach in the management of ectopic parathyroid adenomas. Endocr Pract 24(6):589–598
107. Takahashi H et al (2013) Fusion images of MIBISPECT and MDCT improved iagnostic performance of localization study in hyperparathyroidism with multigland disease. J Nucl Med 54:44
108. Zeng M, Liu W, Zha X, Tang S, Liu J, Yang G et al (2019) 99mTc-MIBI SPECT/CT imaging had high sensitivity in accurate localization of parathyroids before parathyroidectomy for patients with secondary hyperparathyroidism. Ren Fail 41(1):885–892
109. Beggs AD, Hain SF (2005) Localization of parathyroid adenomas using ^{11}C-methionine positron emission tomography. Nucl Med Commun 26:133–136
110. Broos WA, Wondergem M, Knol RJ, van der Zant FM (2019) Parathyroid imaging with 18 F-fluorocholine PET/CT as a first-line imaging modality in primary hyperparathyroidism: a retrospective cohort study. EJNMMI Res 9:1–7
111. Erickson LA (2014) Adrenal gland histology. In: Atlas of endocrine pathology. Springer, New York, NY, pp 147–153
112. Aron DC, Tyrrell JB (1997) Glucocorticoids and adrenal androgens. In: Greenspan FS, Strewler GJ (eds) Basic and clinical endocrinology, 5th edn. Appleton and Lange, Norwalk, p 318
113. Goldfien A (1997) Adrenal medulla. In: Greenspan FS, Strewler GJ (eds) Basic and clinical endocrinology, 5th edn. Appleton and Lange, Norwalk, p 382
114. Ryan JJ, Rezkalla MA, Rizk SN, Peterson KG, Wiebe RH (1995) Testosterone-secreting adrenal adenoma that contained crystalloids of Reinke in an adult female patient. Mayo Clin Proc 70:380–383
115. Lynn MD, Gross MD, Shapiro B, Bassett D (1986) The influence of hypercholesterolemia on the adrenal uptake and metabolic handling of I-1316β-iodomethyl-19-norcholesterol(NP-59). Nucl Med Commun 1:631–635
116. Hedeland H, Ostberg G, Hokfelt B (1968) On the prevalence of adrenocortical adenomas in an autopsy material in relation to hypertension and diabetes. Acta Med Scand 184:211–214
117. Copeland PM (1983) The incidentally discovered adrenal mass. Ann Intern Med 98:940–945
118. Vos EL, Grewal RK, Russo AE, Reidy-Lagunes D, Untch BR, Gavane SC et al (2020) Predicting malignancy in patients with adrenal tumors using 18F-FDG-PET/CT SUVmax. J Surg Oncol 122(8):1821–1826
119. Volpe C, Enberg U, Sjögren A et al (2008) The role of adrenal scintigraphy in the preoperative management of primary aldosteronism. Scand J Surg 97:248–253
120. Evangelista L, DeFalco T, di Nuzzo C et al (2008) Utility of adrenal cortical scintigraphy with I-6-$-methyl-131 norcholesterol in a case of mismatch between morphological and functional PET imaging. Thyroid Sci 3:CR1–CR3
121. Omura M, Saito J, Yamaguchi K, Kakuta Y, Nishikawa T (2004) Prospective study on the prevalence of secondary hypertension among hypertensive patients visiting a general outpatient clinic in Japan. Hypertens Res 27:193–202
122. Huether SE, Tomky D (1998) Alterations of hormonal regulation. In: McCance KL, Huether SE (eds) Pathophysiology, the biologic basis for disease in adults and children, 3rd edn. Mosby, St Louis, p 700
123. Spencer RP (1998) Tumor-seeking radiopharmaceuticals: nature and mechanisms. In: Murray IP, Ell PJ (eds) Nuclear medicine in clinical diagnosis and treatment, 2nd edn. Churchill Livingstone, Hong Kong, p 764
124. Elgazzar AH, Gelfand MJ, Washburn LC, Clark J, Nagaraj N, Cummings D, Hughes J et al (1995) I-123MIBGscintigraphy in adults, are port of clinical experience. Clin Nucl Med 20:147
125. Gelfand MJ, Elgazzar AH, Kriss VM, Masters PR, Golsch GJ (1994) Iodine-123MIBGSPECT versus planar imaging in children with neural crest tumors. J Nucl Med 35:1753–1756
126. Parisi MT, Sandler ED, Hattner RS (1992) The biodistribution of metaiodobenzylguanidine. Semin Nucl Med 22:46–48
127. Okuyama C, Ushijima Y, Kubota T, Yoshida T, Nakai T, Kobayashi K, Nishimura T (2003) 123I-Metaiodobenzyl guanidine up take in the nape of the neck of children: likely visualization of brown adipose tissue. J Nucl Med 44:1421–1425
128. Shapiro B, Copp JE, Sisson JC, Eyre PL, Wallis J, Beierwaltes WH (1985) Iodine-131metaiodobenzyl-guanidine in the locating of suspected pheochromocytoma: experience in 400 cases. J Nucl Med 26:576
129. Paltiel HJ, Gelfand MJ, Elgazzar AH, Washburn LC, Harris RE, Masters PR, Golsch GJ (1994) Neural crest tumors: I-123MIBG imaging in children. Radiology 190:118
130. Liu B, Servaes S, Zhuang H (2018) SPECT/CT MIBG imaging is crucial in the follow-up of the patients with high-risk neuroblastoma. Clin Nucl Med 43(4):232–238
131. Aboian MS, Huang SY, Hernandez-Pampaloni M, Hawkins RA, VanBrocklin HF, Huh Y et al (2021) 124I-MIBG PET/CT to monitor metastatic disease in children with relapsed neuroblastoma. J Nucl Med 62(1):43–47
132. Samim A, Tytgat GA, Bleeker G, Wenker S, Chatalic KL, Poot AJ et al (2021) Nuclear medicine imaging in neuroblastoma: current status and new developments. J Personal Med 11(4):270

133. Shalaby-Rana E, Majd M, Andrich MP, Movassaghi N (1997) In-111pentetreotidescintigraphy in patients with neuroblastoma. Comparison with I-131MIBG, N-Myconcogene amplification, and patient outcome. Clin Nucl Med 22:315–319
134. Kropp J, Hofmann M, Bihl H (1997) Comparison of MIBG and pentetreotidescintigraphy in children with neuroblastoma. Is the expression of somatostatin receptors aprognostic factor? Anticancer Res 17:1583–1588
135. Tenenbaum F, Lumbroso J, Schlumberger M, Mure A, Plouin PF, Caillou B, Parmentier C (1995) Comparison of radiolabeled octreotide and metaiodobenzylguanidine (MIBG) scintigraphy in malignant pheochromocytoma. J Nucl Med 36:1–6
136. Pashankar FD, O'Dorisio MS, Menda Y (2005) MIBG and somatostatin receptor analogs in children: current concepts on diagnostic and therapeuticuse. J Nucl Med 46(Suppl 1):55S–61S
137. Manil L, Edeline V, Jlumbroso J, Lequen H, Zucker JM (1996) Indium-111-pentetreotidescintigraphy in children with neuroblast-derived tumors. J Nucl Med 37:893–896
138. Krausz Y, Keidar Z, Kogan I, Even-Sapir E, Bar-Shalom R, Engel A, Rubinstein R et al (2003) SPECT/CT hybrid imaging with ^{111}In-pentetreotide in assessment of neuroendocrine tumours. Clin Endocrinol 59:565–573
139. Andersson P, Forssel-Aronsson E, Johanson V, Wangberg B, Nilsson O, Fjalling M, Ahlman H (1996) Internalization of indium-111intohuman neuroendocrine tumor cells after incubation with indium-111-DTPA-D-Phe1-Octreotide. J Nucl Med 37:2002–2006
140. Andersson P, Forssel-Aronsson E, Johanson V, Wangberg B, Nilsson O, Fjalling M, Ahlman H (1996) Internalization of indium-111 into human neuroendocrine tumor cells after incubation with indium-111-DTPA-D-Phe 1-octreotide. J Nucl Med 37:2002–2200
141. Trampal C, Engler H, Juhlin C, Bergstrom M, Langstrom B (2004) Pheochromocytomas: detection with C-11hydroxyephedrine PET. Radiology 230:423–428
142. Ruf J, Hueck F, Schiefer J, Denecke T, Elgeti F et al (2010) Impact of multiphase 68Ga-DOTATOC-PET/CT on therapy management in patients with neuroendocrine tumors. Neuroendocrinology 91:101–109
143. Ilias I, Yu J, Carrasquillo JA, Chen CC, Eisenhofer G, Whatley M, McElroy B et al (2003) Superiority of 6-[18F]-fluorodopamine positron emission tomography versus [131I]-metaiodobenzylguanidinescintigraphy in the localization of metastatic pheochromocytoma. J Clin Endocrinol Metab 88:4083–4087
144. Brunt LM, Moley JF (2001) Adrenal incidentaloma. World J Surg 25:905–913
145. Mantero F, Masini AM, Opocher G, Giovagnetti M, Arnaldi G (1997) Adrenal incidentaloma: an overview of hormonal data from the National Italian Study Group. Horm Res 47:284–289
146. Minn H, Salonen A, Friberg J, Roivainen A, Viljanen T, Langsjo J, Salmi J et al (2004) Imaging of adrenal incidentalomas with PET using C-11metomidate and 18F-FDG. J Nucl Med 45:972–979
147. Khan TS, Sundin A, Juhlin C, Langstrom B, Bergström M, Eriksson B (2003) 11C-metomidatePET imaging of adrenocortical cancer. Eur J Nucl Med Mol Imaging 30:403–410
148. Rubello D, Bui C, Casara D et al (2002) Functional scintigraphy of the adrenal gland. Eur J Endocrinol 147:13–28
149. Akkuş G, Güney IB, Ok F, Evran M, Izol V et al (2019) Diagnostic efficacy of 18F-FDG PET/CT in patients with adrenal incidentaloma. Endocr Connect 8:838–845

Genitourinary System

7

Mohammad Ghanem
and Abdelhamid H. Elgazzar

7.1 Anatomic and Physiologic Considerations

7.1.1 Major Structures

The urinary system consists of a pair of kidneys, which filters the blood, form urine, and help regulate various metabolic processes; a pair of tubular ureters, which transport urine away from the kidneys; a saclike urinary bladder, which serves as urine reservoir; and a tubular urethra, which conveys urine to the outside of the body.

Kidneys are paired bean-shaped retroperitoneal organs situated in the posterior part of the abdomen on each side of the vertebral column against the psoas major muscle. The upper pole of each kidney lies at the level of the twelfth thoracic vertebra, and the lower pole lies opposite the third lumbar vertebra. The right kidney is usually slightly more caudal in position. Each kidney's weight ranges from 120 g to 170 g in the adult male and from 115 g to 155 g in the adult female. It is approximately 11 × 6 × 2.5 cm in dimension. Each kidney's concave medial surface has a slit-like aperture called the hilum, through which the renal pelvis, the renal artery, and vein, the lymphatics, and a nerve plexus pass into the kidney. A tough fibrous capsule surrounds the organ.

On cut sections, two distinct regions can be identified: a pale outer region, the cortex, and a darker inner region, the medulla. In humans, the medulla is divided into 4–18 striated conical masses, the renal pyramids (average 8). Each pyramid's base is positioned at the corticomedullary boundary, and the apex extends toward the renal pelvis to form a papilla. On the tip of each papilla are 10–25 small openings representing the distal ends of the collecting ducts. A funnel-shaped minor calyx caps the apex of each medullary pyramid. The minor calyx receives the urine from the kidney and passes it to the extrarenal collecting system (Fig. 7.1).

Since renal blood flow of approximately 400 mL/100 g to 1.0 and 1.2 L/min per 1.73 m^2 of body surface area—is much higher than that of any other well-perfused organs such as the heart and brain, kidney tissue is prone to be exposed to a significant amount of any potentially harmful circulating substances [1].

Additionally, glomerular capillaries vulnerable to hemodynamic injury, in contrast to other capillary beds because glomerular filtration is dependent on high intra- and trans-glomerular pressure. The nephron's microvasculature organization facilitates the spreading of glomerular injury to the tubulointerstitial compartment in disease, exposing tubular epithelial cells to abnormal ultrafiltrate. Accordingly, the concept

M. Ghanem (✉) · A. H. Elgazzar
Department of Nuclear Medicine, Faculty of Medicine, Kuwait University, Kuwait City, Kuwait
e-mail: mohammad.sghanem@ku.edu.kw

A. H. Elgazzar (ed.), *The Pathophysiologic Basis of Nuclear Medicine*,
https://doi.org/10.1007/978-3-030-96252-4_7

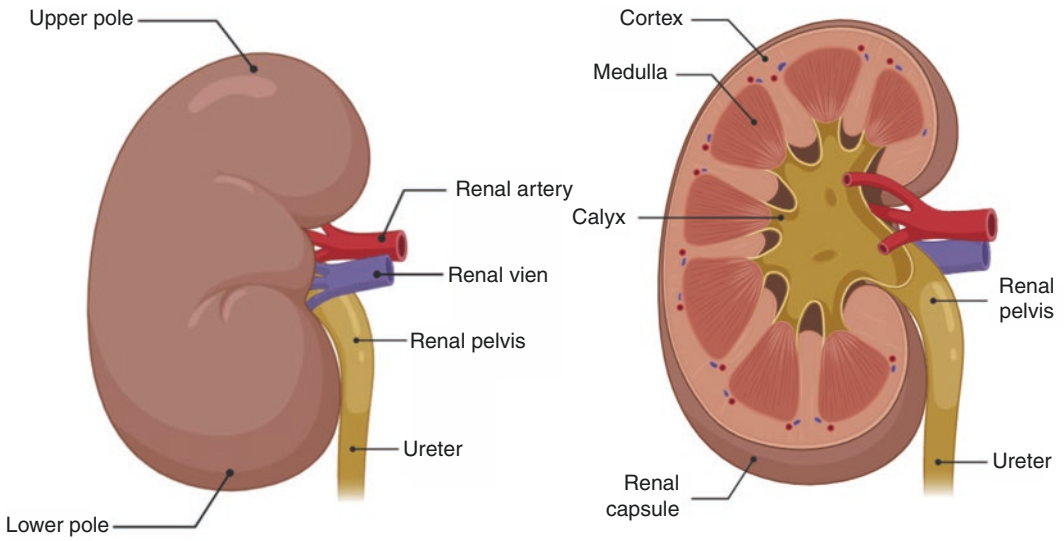

Fig. 7.1 A diagram illustrating main surface renal anatomy. (Created with BioRender.com)

of the nephron as a functional unit applies not only to renal physiology but also to the pathophysiology of renal diseases.

7.1.2 The Nephron

The main functions of the kidneys are the maintenance of water, electrolyte, acid-base balance, elimination of waste products, and blood pressure regulation. The functional unit of the kidney is the nephron, which consists of a glomerulus and a tubule. The *glomerulus* consists of a network of capillaries derived from the afferent glomerular arteriole. They can be broadly divided into several portions: the proximal tubule, loop of Henle, distal tubule, and collecting tubule (Fig. 7.2).

Urine is formed as a result of glomerular filtration, tubular reabsorption, and tubular secretion [2]. The glomerular capillary tuft acts as a filter for plasma. Two epithelial layers encase it, the inner layer becoming part of the outer capillary wall and the outer layer lining Bowman's space (capsule), which receives the filtered fluid. The glomerular filtration rate (GFR) mainly depends on the hydrostatic and colloid osmotic pressure in the glomerular capillaries and the hydrostatic pressure in Bowman's space. Filtered fluid from Bowman's space enters the *tubule*. The *proximal tubule* plays a crucial role in reabsorbing filtered solutes. About half to two-thirds of the sodium, chloride, and potassium are reabsorbed in this segment. Reabsorption of solutes is accompanied by passive osmotic diffusion of water. The *loop of Henle*, consisting of a descending limb and an ascending limb, is the reabsorption site of about 25% of the filtered solutes. Reabsorption occurs primarily in the "thick" ascending limb, where the epithelial cells are thick and metabolically very active. In this section, "loop" diuretics such as furosemide exert their effects (see later). The reabsorbed solutes enter the medullary interstitium and contribute to its hypertonicity.

The *distal tubule* transports sodium, chloride, and potassium, but not water, from its proximal part, similar to the loop of Henle. The terminal distal tubule shares similar functions with the collecting tubules (see later). At the very beginning of the distal tubule is the *macula densa*, a region of specialized cells in the vicinity of the juxtaglomerular (JG) cells in the afferent arteriole that store renin. In response to sodium and chloride concentration changes in this portion of the tubule, the macula densa sends signals to the JG cells to release renin that mainly increases arterial blood pressure.

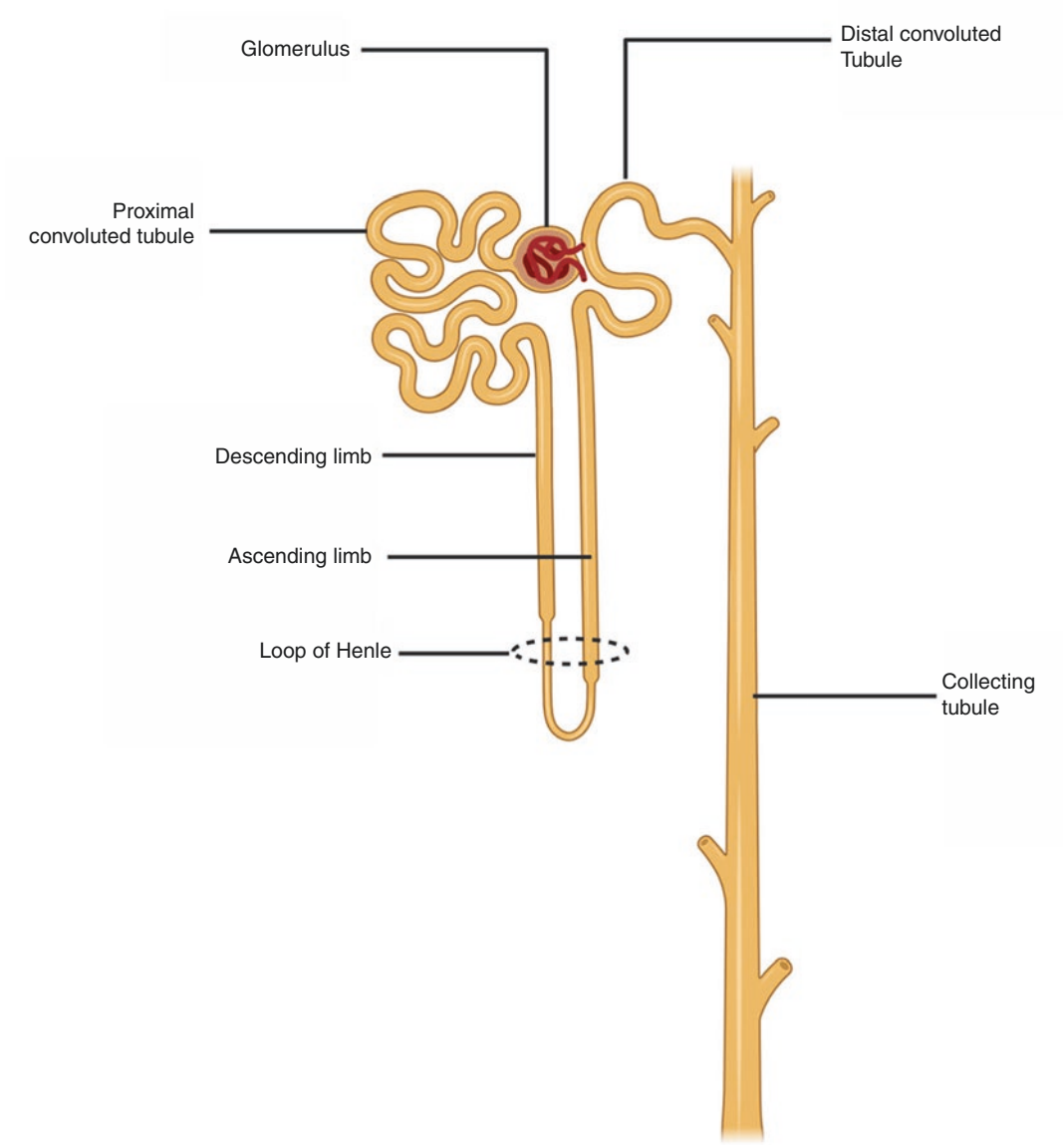

Fig. 7.2 The components of the nephron. (Created with BioRender.com)

7.1.3 Renal Vasculature

Each kidney is supplied normally by a single renal artery in the human body. However, one or more accessory renal arteries is not uncommon, which may occur in 30% of the population [3]. The renal artery enters through the hilum of the kidney and branches successively into the interlobar arteries, arcuate arteries, interlobular arteries, and afferent arterioles. Each afferent arteriole eventually branches into the glomerular capillaries. The distal glomerular capillaries merge to form the efferent arteriole. Efferent arterioles subdivide to form peritubular capillaries in the cortex or the vasa recta in the medulla. Changes in the afferent or efferent arteriolar tone play an important role in regulating the GFR.

7.1.4 Juxtaglomerular Apparatus

The afferent arteriole has specialized smooth muscle cells called juxtaglomerular (JG) cells that store renin and stretch receptors that respond to arteriolar pressure changes. Renin is released as a result of decreased stretch of the arteriolar wall when arteriolar pressure is decreased. Another stimulus for renin comes from the macula densa, which consists of specialized cells in the first part of the distal tubule, located close to the JG cells. The macula densa signals the JG cells to release renin when the sodium and chloride content of this part of the tubule is low. Finally, the sympathetic nervous system can stimulate renin release in response to systemic baroreceptor stimuli.

7.2 Renal Radiopharmaceuticals

Renal radiopharmaceuticals can be described in two broad classes—those excreted rapidly into the urine and those retained for prolonged periods in the renal parenchyma.

7.2.1 Rapidly Excreted Radiopharmaceuticals

The rapidly excreted radiopharmaceuticals are used in dynamic imaging studies to assess individual renal function and include [3–6]:

- ^{99m}Tc-mercaptoacetyltriglycine (MAG_3), the agent of choice, is 90% protein-bound and excreted almost exclusively by the renal tubules. High renal-to-background count ratios provide excellent images and permit visualization of poorly functioning kidneys.
- ^{99m}Tc-diethylenetriamine penta-acetic acid (DTPA) was the most popular radiopharmaceutical in its category prior to the introduction of ^{99m}Tc-MAG_3. It shows little protein binding (about 5%) and is excreted exclusively by glomerular filtration. Renal uptake of ^{99m}Tc-DTPA is limited because the glomeruli filter only 20% of the renal blood flow. The 20% extraction fraction is considerably lower than that of ^{99m}Tc-MAG_3 and yields lower renal-to-background uptake ratios. However, it is less costly and may be used as an alternative to ^{99m}Tc-MAG_3, particularly if a quantitative estimate of GFR is in question. Functional assessment with 99m Tc-MAG3 and 99m Tc-DTPA generally is concordant. However, differences may be noted with glomerular-tubular dissociation in some cases of tubulointerstitial disease. Orthoiodohippurate is about 70% protein bound. Approximately 15–20% of the radiotracer is excreted by glomerular filtration and the remainder by tubular secretion. The use of 131 I-OIH for scintigraphy has been largely abandoned because of the limitations of higher radiation exposure [7] and poor image quality related to a lower administered dose (1/15 that of 99m Tc-MAG3). Radiation exposure with 123 I-labeled OIH is lower, and better images can be obtained using larger amounts of the radiotracer. However, this radiopharmaceutical is expensive and not readily available. The extraction fraction of OIH, while not optimum (since it is not completely extracted by the kidneys), is the highest among the radiopharmaceuticals in use today. Therefore, it can be used for the quantification of renal blood flow.

7.2.2 Slowly Excreted Radiopharmaceuticals

The slowly excreted radiopharmaceuticals include ^{99m}Tc-dimercaptosuccinic acid (DMSA) and ^{99m}Tc-glucoheptonate. Prolonged cortical retention of these radiopharmaceuticals allows the assessment of parenchymal morphology. Since accumulation occurs only in functioning tubules, uptake can be quantified to accurately assess the differential renal function [3, 4]. The preferred agent, Technetium-99m-DMSA, is 90% protein-bound and accumulates in functioning tubules. Since very little of the radiotracer is excreted, interference from collecting system activity, particularly on delayed images, is minimal. A total of about 40% of the administered amount is accumulated in the renal cortex.

7.3 Renal Scintigraphy

According to the types of renal radiopharmaceuticals, renal scintigraphy can be of dynamic or static nature.

- *Dynamic studies* are obtained using rapidly excreted radiopharmaceuticals, while static studies are obtained utilizing slowly excreted tracers. Dynamic studies start by rapidly acquiring image frames upon injection of the tracer to follow activity passing through the blood vessels until reaching the kidneys to evaluate the blood flow. This phase is followed by another series of imaging frames every 10–20 s of the kidneys for approximately 30 min to evaluate the renal functional handling of the radiotracer. This phase will then be computer-processed to generate a time-activity curve (renogram) for both kidneys to illustrate the uptake, build up, and excretion of the radiopharmaceutical by each kidney and generate the percent contribution of each kidney to the total renal function (split or differential renal function).
- *Static studies* using slowly secreted radiopharmaceuticals, particularly ^{99m}Tc-DMSA, are acquired 3 h after intravenous injection of the radiotracer and optionally up to 24 h based on the individual case and the kidney function. These studies are predominantly used to determine the split renal function accurately and in cases of urinary tract infections to evaluate the pathologic changes, including cortical scars. Anterior, posterior, left and right posterior oblique planar views are obtained routinely with optional SPECT or SPECT/CT. Using the anterior and posterior views, the split renal function is calculated by the geometric mean of the background-subtracted kidney counts.

7.3.1 Principles of Interpretation

7.3.1.1 Dynamic Studies

Assessment of function on dynamic studies is based on several criteria, including initial cortical uptake of the radiotracer, cortical retention, first visualization of the collecting system, and time to peak cortical activity. These parameters, however, may be affected by the state of hydration. Prolonged radiotracer uptake, reduced excretion, and cortical retention can be noted in cases of dehydration [8, 9]. An adequate assessment of renal function should include analysis of both the scintigraphic images and the time-activity curves.

Cortical uptake: The first minute after radiotracer administration represents the vascular delivery phase. The next 2 min constitute the parenchymal phase. Uptake in the kidney during this interval (between 1 and 3 min after radiotracer injection) is proportional to its function, using either tubular or glomerular agents.

Cortical retention: The cortical retention of the radiotracer, quantified by expressing renal counts at 20–30 min on the time-activity curve as a percentage of the peak uptake, is a measure of the rapidity with which the kidney excretes the radiotracer. As renal function deteriorates, the percentage of retained radiotracer increases. This index can help monitor patients with renal transplants or assess renovascular hypertension [10]. An apparent increase in retention may occur with urine stasis in the collecting system.

First visualization of collecting system: The interval between radiotracer administration and excretion of activity into the collecting system (pelvis and/or calyces) is a measure of *cortical* function. This interval is obtained from the sequential images. The delayed appearance of the collecting system is associated with impaired function.

Time to peak: This parameter is easily measured from the time-activity curve. However, an accurate estimate may not be possible in the absence of a peak, which is often the case in significant renal dysfunction. Prolonged values for the time to peak can be seen in physiologic retention of the tracer in the renal calyces or pelvis [11].

7.3.1.2 Static Studies

Scintigraphy with ^{99m}Tc-DMSA and ^{99m}Tc-glucoheptonate is done between 3 and 24 h after

radiotracer administration. It is usually used to detect renal parenchymal defects associated with pyelonephritis, scars, and infarcts. Since only functioning tubular cells accumulate these radiopharmaceuticals, the total renal uptake is a measure of individual renal function. Relative renal function can also be measured as with the rapidly excreted radiopharmaceuticals.

7.4 Major Diseases

7.4.1 Renovascular Hypertension (RVH)

Approximately 5% of hypertension is renovascular in origin. It accounts for about 5.4% as a cause of secondary hypertension in adults [12–14]. Renal artery stenosis is generally due to atherosclerotic plaques or fibromuscular dysplasia, the latter occurring in younger individuals. Significant' stenosis that would trigger the activation of the renin-angiotensin system and lead to the development of renovascular hypertension has been defined as a reduction in intraluminal diameter by 50% or greater. However, the degree of anatomically defined renal artery stenosis does not always correlate with the presence of renovascular hypertension.

7.4.1.1 Pathophysiology

The renin-angiotensin system serves as maintenance of systemic blood pressure in such conditions as hypotension and shock. However, with significant renal artery stenosis, the renin-angiotensin system limits a fall in GFR but causing systemic (renovascular) hypertension. Systemic blood pressure is maintained primarily by the increase in vascular tone and sodium and water retention. At the same time, a sharp reduction in GFR is prevented by the increase in the glomerular capillary hydrostatic pressure.

Glomerular capillary hydrostatic pressure is modulated by the tone of the afferent and efferent glomerular arterioles. Increased tone in the efferent arteriole or decreased tone (increased flow) in the afferent arteriole raises capillary hydrostatic pressure and GFR. In contrast, the decreased tone in the efferent arteriole or increased tone (decreased flow) in the afferent arteriole lowers GFR.

The first step in the activation of the renin-angiotensin system is the release of *renin* by the renal JG cells by several mechanisms through [15, 16].

(1) signals from *baroreceptors* ("stretch" receptors) in the afferent arteriole modulated by prostaglandins, (2) chemoreceptor signals from the *macula densa* (located in the initial portion of the distal tubule) related to decreased sodium and chloride in the distal tubule and modulated by prostaglandins and adenosine, and (3) increased *sympathetic activity* due to activation of systemic cardiopulmonary and carotid sinus baroreceptors by hypotension.

Renin released due to these stimuli converts circulating *angiotensinogen*, an $alpha_2$ globulin produced by the liver, to *angiotensin I*, a decapeptide. Angiotensin I is then converted to the active octapeptide form, *angiotensin II*, by *angiotensin-converting enzyme* (ACE), found in vascular endothelium. The bulk of this conversion occurs in the pulmonary vascular bed. Angiotensin II is also produced in the kidney. Angiotensin II is a powerful vasoconstrictor that raises systemic blood pressure primarily by increasing vascular tone and stimulating the synthesis and secretion of aldosterone from the zona glomerulosa of the adrenal cortex, which promotes sodium and water reabsorption from the renal tubules.

The intrarenal effects of angiotensin II help counter a fall in GFR due to decreased afferent arteriolar and glomerular capillary hydrostatic pressure [15–18]. First, angiotensin II raises GFR by preferential constriction of the efferent glomerular arteriole. Second, angiotensin II increases tubular reabsorption of sodium and water directly and indirectly (increased tone in efferent arteriole decreases hydrostatic pressure in peritubular capillaries with a resultant increase in sodium and water reabsorption). GFR remains unchanged in the contralateral normal kidney in unilateral renal artery stenosis

because the increased efferent arteriolar tone is offset by an increase in afferent arteriolar tone in response to a higher systemic blood pressure. The effects of angiotensin II eventually lead to inhibition of renin release. In unilateral renovascular disease, sodium retention is offset by pressure natriuresis (decreased sodium chloride reabsorption in the proximal tubule) by the normal kidney. The process limits the expansion in blood volume, so the pressure in the afferent arteriole of the stenotic kidney remains low. In bilateral renovascular disease, however, blood volume expansion may be sufficient to increase afferent arteriolar pressure and decrease (but not necessarily normalize) renin secretion. Angiotensin II also has a direct inhibitory effect on the JG cells.

7.4.1.2 Scintigraphy for RVH

Basis

The scintirenographic diagnosis of renovascular hypertension is based on the demonstration of renal physiology changes following the administration of an ACE inhibitor [19–21]. As noted above, angiotensin II, formed by the activation of the renin-angiotensin system, helps maintain GFR by increasing the tone of the efferent glomerular arteriole, raising the glomerular capillary hydrostatic pressure. These changes are reversed by ACE inhibitors, which block the conversion of angiotensin I to angiotensin II. Consequently, there is a sharp drop in GFR and proximal tubular urine flow.

Decreased GFR and tubular flow after administering an ACE inhibitor will decrease uptake and prolonged cortical retention of ^{99m}Tc-DTPA. Since renal blood flow generally is not significantly changed, ^{99m}Tc-MAG_3 shows only prolonged cortical retention without decreased uptake. Rarely, uptake of ^{99m}Tc-MAG_3 may decrease, presumably due to a fall in blood pressure below a critical level required to maintain perfusion in the stenotic kidney. The general principles of ACE-inhibitor renography also apply to patients receiving chronic treatment with angiotensin II (AT1) receptor antagonists [22].

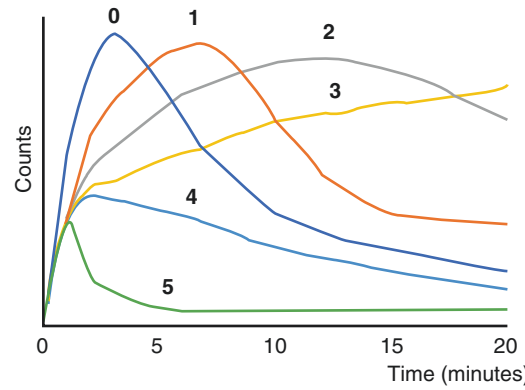

Fig. 7.3 Renographic curve patterns with the grading of suspicion for renovascular hypertension: 0, normal; 1, minor abnormalities; 2, delayed excretion rate with preserved washout phase; 3, delayed excretion rate without washout phase; 4, renal failure pattern with measurable kidney uptake; 5, renal failure pattern without measurable kidney uptake (blood-background type curve). (Adapted from [24])

Interpretation

Scintigraphic studies are generally interpreted by comparing a baseline examination with the one performed after the ACE inhibitor administration. Visual analysis of the time-activity curves of both kidneys using a grading system as shown in Fig. 7.3 can be a valuable method to define the degree of suspicion of renal artery stenosis [23]. Both the images and the time-activity curves are evaluated using the traditional parameters of function discussed earlier, and the following changes after ACE inhibition are considered significant for renovascular hypertension [21–24]:

1. Increase in cortical retention by at least 15% or a change ≥2 in the renogram grade, i.e., 0 to 2 or 1 to 3.
2. Delay in collecting system visualization by at least 2 min.
3. Decrease in initial cortical uptake by at least 10%.
4. Increase in time to peak by at least 2 min.

Factors Influencing ACE Inhibitor Scintigraphy

ACE inhibitor renography is subject to several variables that may result in false-positive or false-negative studies.

1. Hypotension or a marked change in blood pressure after ACE inhibitor administration is often associated with *bilateral symmetrical* renal retention of the radiotracer.
2. Dehydration with or without diuretics. An additional oral fluid load of 5–10 mL/kg of body weight 30–60 min before the procedure is advised to ensure proper hydration [25, 26].
3. Chronic ACE inhibitor therapy may potentially lower scintigraphic sensitivity and should be discontinued before the test. Alternatively, if the ACE inhibitor cannot be discontinued, scintigraphy may be performed while the patient is on therapy. If renal function appears symmetrical, renovascular hypertension is unlikely, and a baseline study need not be done. However, if the function is asymmetrical, the ACE inhibitor should be discontinued before the baseline study.
4. Aspirin and other nonsteroid anti-inflammatory agents such as indomethacin may decrease the sensitivity of the test. These drugs decrease prostaglandin activity and, therefore, indirectly decrease renin-angiotensin activity. This is particularly true with the use of DTPA, and hence MAG_3 is preferred in patients who take nonsteroidal anti-inflammatory drugs [24].
5. Calcium channel blocking drugs are commonly used in renovascular hypertension. Although their effect on GFR is not as pronounced as that of ACE inhibitors, these drugs have been implicated as a cause of false-positive studies [27]. The mechanisms responsible for this finding are not entirely clear. It appears that the effect of angiotensin II on efferent arteriolar constriction requires the presence of extracellular calcium and, therefore, can be attenuated by calcium channel blockers. Perhaps a marked decrease in GFR resulting from the combined effect of calcium channel blockers and captopril may explain the above findings.

7.4.2 Urine Outflow Obstruction

Urinary tract obstruction may be complete or partial, and it may occur at various locations, including the ureteropelvic junction (UPJ), ureterovesical junction (UVJ), and bladder outlet. The clinical consequences are quite dramatic and predictable in an acute and complete obstruction, but not in a partial and chronic one, exemplified by UPJ obstruction in children. Chronic UPJ obstruction, however, may eventually lead to renal cortical atrophy.

Hydronephrosis may be due to obstruction or non-obstructive conditions such as vesicoureteral reflux, urinary tract infection, and congenital dysmorphism. It may be temporary with spontaneous resolution in infants and young children, intermittent, or progressive with eventual stabilization.

7.4.2.1 Diuretic Renography

Furosemide, used for the scintigraphic evaluation of urine outflow for diagnosis of urinary tract obstruction, and other loop diuretics block the reabsorption of sodium, chloride, and potassium in the thick ascending limb of the loop of Henle. Increased tubular sodium decreases water reabsorption by an osmotic effect. Additionally, decreased sodium reabsorption into the medullary interstitium reduces its osmolarity, which in turn reduces water reabsorption from the collecting tubules.

Diuretic renography [28–31] is based on the principle that increased urine flow resulting after furosemide administration causes rapid "washout" of radiotracer from the unobstructed collecting system (Fig. 7.4), but delayed washout is noted if obstruction is present (Fig. 7.5). While furosemide generally is administered intravenously after filling the pelvicalyceal system, administration at the time of or before radiotracer administration has also been used. The standard adult dose of furosemide is 0.5 mg/kg or 40 mg, producing maximal diuresis within 3–6 min in patients with normal renal function. A higher dose of furosemide may be required in patients with impaired renal function to achieve an adequate diuretic response [32]. The washout half-time following diuretic injection is determined from the time-activity curve. A half time of 10 min or less is considered normal, 10–20 min equivocal, and more than 20 min abnormal. However, over-reliance on the washout half-time may not be justified because many factors may

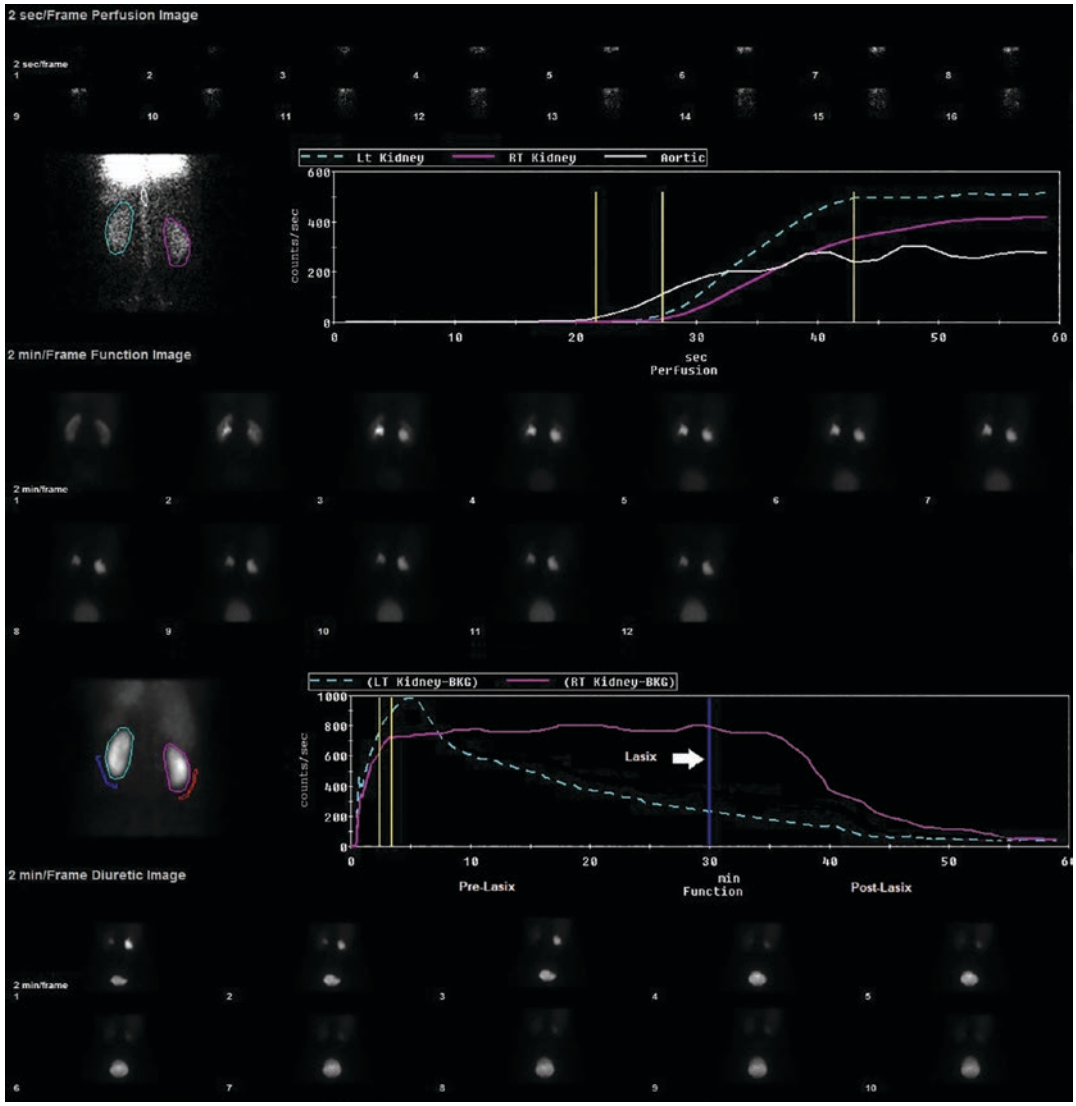

Fig. 7.4 A radionuclide diuretic renography study is illustrating hold-up activity in the right functioning kidney by the end of the pre-Lasix study with rapid washout on post Lasix study, which is clearly illustrated on the time-activity curve. These exemplify the non-obstructed pattern

influence the diuretic renogram, including renal dysfunction, dehydration, inadequate furosemide dosage, atonic pelvis (redundant tissue).

Some steps may be taken to optimize the radionuclide evaluation of urinary tract obstruction. Since renal function preservation is the overriding concern, it has been suggested that renal cortical function evaluation should be the primary focus of scintigraphic assessment. Additionally, since renal impairment or its progression is unpredictable, a single study in the infant with UPJ obstruction is of limited value. Instead, *periodic scintigraphic assessments* at intervals of 3 months are more desirable. Undue reliance on a single post-diuresis washout half-time also appears unwarranted for the reasons noted earlier. If the methodology is standardized, periodic evaluation as for functional assessment may improve the predictive ability of the washout parameter as well. An increasing washout time probably is more meaningful than a single "positive" study [28].

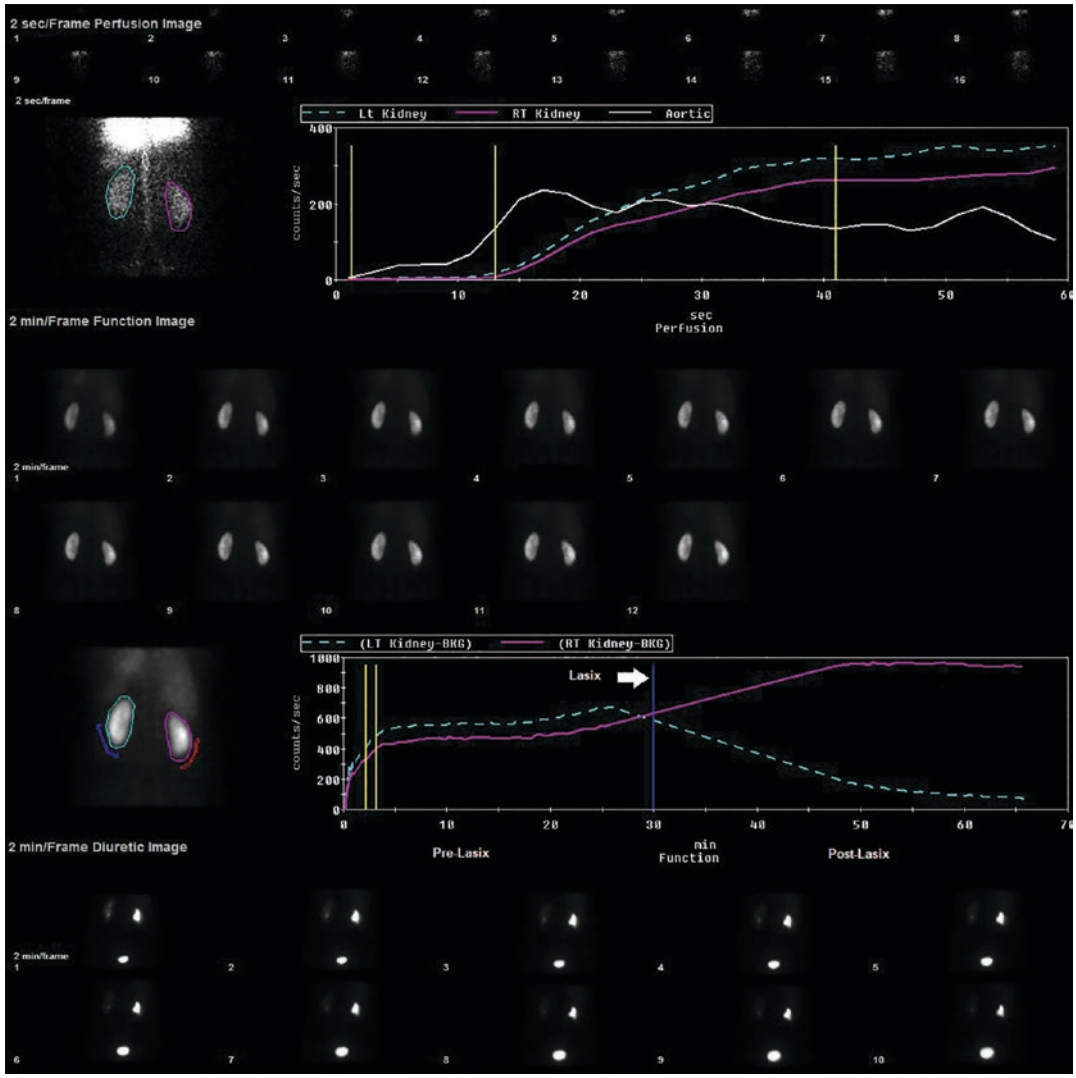

Fig. 7.5 A diuretic renography study in an adult patient illustrating obstructive pattern on the left side. Note the left kidney time activity curve, which shows no clearance before Lasix and no response to Lasix

7.4.3 Urinary Tract Infection

7.4.3.1 Pathophysiology

Urinary tract infections (UTIs) are particularly important in the pediatric age group as it is one of the most common diseases in children. UTIs' overall incidence in children ranges between 1.5% and 2% [29–31]. In the neonatal period, UTIs are relatively rare and are usually caused by bacteria from the bloodstream. The incidence in newborns is higher for boys, while girls are affected (1%) more than boys (0.3%) between the ages of 1 and 5 years [29–31]. The incidence increases up to 5% among girls of school age. The most common age for UTIs in girls is 7–11 years, resulting from bacterial infection – usually a pathogenic strain of *Escherichia coli*—ascending the urethra.

Many predisposing factors affect the incidence and the severity of the disease in different age groups. These factors include individual susceptibility, bacterial virulence, and the host's anatomical abnormalities such as the presence of vesicoureteral reflux (VUR), obstruction, stasis,

Table 7.1 Factors predisposing to and affecting the severity of UTI in children

Individual susceptibility
Bacterial virulence
High-grade vesicoureteral reflux
Obstruction and stasis
Hydronephrosis with or without pelviureteric junction obstruction
Horseshoe kidney
Crossed renal ectopia
Renal duplication with ectopic ureters
Urethral polyps or diverticula
Posterior urethral valves or ureterocele
Lack of circumcision (boys)
Sexual activity (girls)
Indwelling urinary catheter
Trauma to the urinary tract
Diabetes

or stones (Table 7.1). However, UTIs may also occur in healthy children with an anatomically normal urinary tract. Individual susceptibility may be variable and can be related to familial or hereditary factors.

Chronic pyelonephritis is a result of recurrent or untreated acute pyelonephritis. It occurs almost exclusively in patients with major anatomic anomalies, including urinary tract obstruction, renal dysplasia, or, most commonly, vesicoureteral reflux (VUR) in young children.

Although pseudomonas infection is common in UTIs following reflux, particularly the severe cases [33], the usual pathogenesis of UTIs is the proliferation of *E. coli* in the colon. This bacterial proliferation allows the movement of the bacteria into the periurethral mucosa. To be able to multiply, bacteria that reach the urinary tract must overcome the tendency to be washed away by urine flow and bladder voiding. Accordingly, prolonged intervals between voiding, increased storage pressure, or significant residual urine volume favor bacteria's growth and allowed even relatively nonpathogenic bacteria to cause significant infections. Vaginal filling secondary to high voiding velocity and turbulent urine flow related to a dysfunctional voiding pattern is an important factor in bacterial contamination and urinary infections in girls [34].

Urinary tract infections are divided into lower and upper infections. Lower UTI or infection of the bladder (cystitis) results in mucosal inflammation and congestion, which causes hyperactivity of the detrusor muscle and decreasing the bladder capacity [35]. This also can lead to urine reflux up the ureter. This reflux can send bacteria to the kidney, leading to acute or chronic pyelonephritis, which may cause renal abscesses or scarring. Acute pyelonephritis requires more vigorous treatment than lower urinary tract infection and, if left untreated, can lead to scarring and renal insufficiency. Consequently, identifying renal involvement is critical in children with suspected urinary tract infection and parenchymal scintigraphy with the tubular agent, Tc-99m-dimercaptosuccinic acid (DMSA), can play an important role in their diagnostic evaluation.

Ascending infection from the lower urinary tract is the usual cause of pyelonephritis. The infection appears to originate in the urethra or the vaginal introitus, colonized by enteric flora, predominantly *Escherichia coli*. It is more common in females, presumably due to their shorter urethra. The ascending infection eventually reaches the renal calyces, from which micro-organisms enter the parenchyma through the papillae by intrarenal reflux.

Severe long-term sequelae, such as hypertension and renal failure, may develop if urinary infection leads to acute pyelonephritis and subsequently to renal scarring. The pathophysiology of renal scarring is still obscure. Numerous factors may contribute to tissue damage following acute infection. It was found that patients with increased Transforming growth factor-beta1 (TGF-beta1), a potent proinflammatory and fibrogenic cytokine known to have a key role in regulating the renal tissue fibrosis, may be at higher risk for renal damage following reflux [36].

Nonsecretor status of blood type antigen has also been associated with a higher risk of urinary tract infection (UTI) in women. A study has shown that the nonsecretor status significantly correlated with the presence of focal renal scarring (41% vs. 22% for children with and without scarring, respectively) as determined by ^{99m}Tc-DMSA renal scan [37].

Scarring of the renal parenchyma is a common cause of hypertension and, if sufficiently extensive, can lead to progressive renal insufficiency and end-stage renal disease. Vesicoureteral reflux, particularly of a higher grade, is frequently associated with scarring.

The upper UTIs cannot be easily differentiated clinically from cystitis based only on symptoms. However, differentiation between upper and lower UTI is important since the former is often associated with renal parenchymal damage. It is particularly difficult in infants, who usually develop nausea, vomiting, diarrhea, or jaundice. In children, fever, frequency, urgency, enuresis or incontinence in a previously dry child, abdominal pain, foul-smelling urine, and sometimes hematuria are the most common clinical presentations. It is estimated that up to 40% of children with UTI are asymptomatic [38].

7.4.3.2 UTI Scintigraphy

Imaging strategies in pediatric urinary tract infections are controversial. The recent literature illustrates the complementary roles of ultrasound, computed tomography (CT), and nuclear medicine [39–41].

Imaging renal parenchyma with ^{99m}Tc-DMSA offers a simple and accurate method for detecting acute pyelonephritis in a child with urinary tract infection. ^{99m}Tc-DMSA localizes in functioning proximal tubular cells and is not excreted in significant amounts. Imaging at 3–24 h after radiopharmaceutical administration reveals primarily cortical uptake without interfering activity in the collecting system. A cortical defect due to pyelonephritis is characterized by the preservation of renal contour, whereas scarring (from a previous infection) typically results in organ volume contraction (Fig. 7.6).

In addition to imaging during the acute phase of the disease, follow-up studies are done to confirm the resolution of the pyelonephritic defect(s) and the absence of cortical scarring. Patients with scars are followed periodically with imaging and relative function measurements to assess for progressive renal insufficiency (Fig. 7.7).

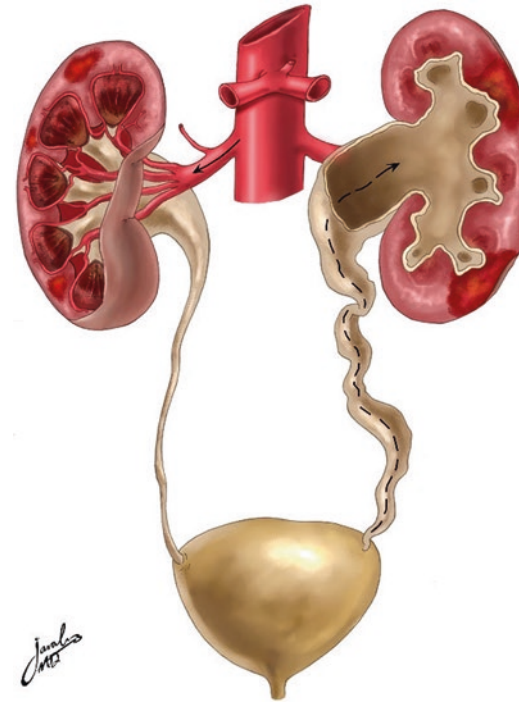

Fig. 7.6 Diagram illustrating the routes of inducing urinary tract infection. The *left-hand side* represents the hematogenous route, while the *right-hand side* represents the retrograde route such as with vesicoureteral reflux

The importance of ^{99m}Tc-DMSA for patients with urinary tract infections for initial evaluation and follow-up of children with UTI was re-emphasized by many studies [42–45].

Ultrasonography is recommended by newer guidelines to be used more than before; Spiral CT and Magnetic resonance imaging (MRI) are other modalities that may help evaluate pyelonephritis [40, 41].

7.4.4 Renal Transplantation Complications

Renal transplantation surgery has shown significant improvement in graft survival and an increase in the number of transplantations. Graft survival is best when the donor is an HLA-identical sibling and better for living-related than cadaver donors with similar HLA matches. Other factors, including harvesting and transplantation technique, cold

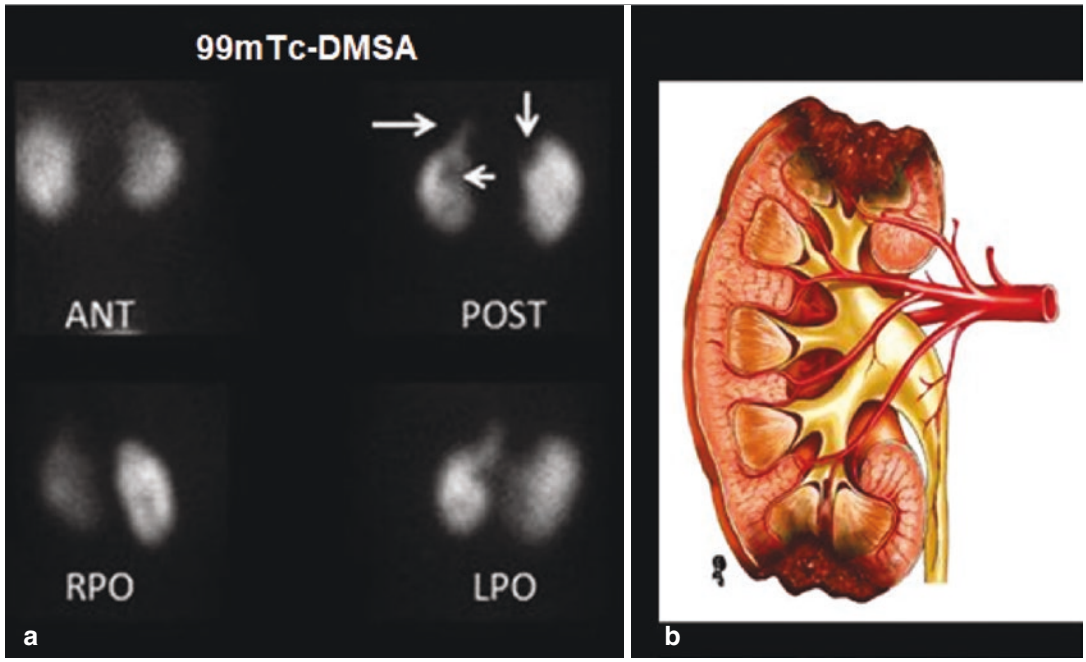

Fig. 7.7 ^{99m}Tc-DMSA study (**a**) demonstrating bilateral upper pole defects and a mid-left kidney defect (arrows). A diagram (**b**) illustrates how scars affect the kidney contour

ischemia time (between harvest and transplantation), donor/recipient age, recurrence of primary renal disease, and race, also play an important role in graft survival. Several complications, surgical and/or medical (Table 7.2), occur following transplantation and need to be detected and evaluated to avoid graft failure and outcome.

Table 7.2 Renal transplantation complications

Surgical complications
Urine extravasation, ureteral obstruction
Hematoma, lymphocele
Renal artery stenosis
Medical complications
Acute tubular necrosis
Rejection
Antibody-mediated rejection
Hyperacute rejection
Accelerated acute rejection
Acute/active rejection
Chronic/sclerosing allograft nephropathy
Nephrotoxicity of drugs

7.4.4.1 Surgical Complications

Urine Extravasation, Ureteral Obstruction

Extravasation of urine ("urinoma") may result from ischemic injury related to devascularization during harvesting or leakage at the ureterovesical anastomosis. It may predispose to infection and therefore requires a timely diagnosis. While routine renal scintigraphy performed after transplantation may detect urine extravasation, it is often used to confirm a leak suspected clinically or sonographically. The scintigraphic appearance is an area of increased radiotracer activity, although such increase may not be apparent for up to 2–3 h after radiotracer administration in some instances.

Ureteral obstruction is thought to be usually due to ischemia or postischemic scarring. Extrinsic compression by a lymphocele or hematoma is another cause. If needed, dilatation of the ureter or stent placement/reoperation may be done. Scintigraphy, with the aid of furosemide-induced diuresis in some cases, maybe helpful in the diagnosis and post-treatment evaluation of this condition.

Hematoma, Lymphocele

Hematomas are generally perinephric or intravesical in location. Scintigraphy can be positive, demonstrating a photopenic region, i.e., with activity less than the background. Hematomas are usually self-limited.

Lymphoceles are extrarenal collections of lymphatic fluid from the kidney, occurring most frequently about 2–3 months after transplantation. They may be exacerbated by rejection, which increases renal lymph flow. Most lymphoceles are inconsequential, though some may be associated with ureteral compression, as noted earlier, or iliac vein compression resulting in lower extremity edema. Treatment consists of sclerotherapy, drainage, or the creation of a peritoneal window. The characteristic scintigraphic finding with lymphoceles is a perinephric photopenic region, which is easier to visualize if a high-intensity image is obtained at the end of the study to accentuate the body background. However, it should be noted that lymphoceles occasionally may become isointense with the background or exceed background activity on later images.

Renal Artery Stenosis

Hypertension is usually due to pathology in the native kidneys, transplant rejection, or cyclosporine/tacrolimus treatment, and, less frequently, renal artery stenosis. The stricture is generally at the anastomotic site or distal to it. The pathophysiological consequences of renal artery stenosis in the transplanted kidney are somewhat different from unilateral stenosis in patients with two kidneys. In the latter, the elimination of sodium is decreased on the stenosed side, but increased sodium excretion by the normal kidney helps keep the blood volume from increasing. In a transplanted kidney with renal artery stenosis, a normal kidney is not available to eliminate excess sodium. Therefore, depending on the level of salt intake, the initial renin-dependent hypertension develops into volume-dependent hypertension. Consequently, the fall in GFR in response to an ACE inhibitor may be less than expected and inapparent on the scintigraphic study. However, most of these patients are on diuretics and/or a salt-restricted diet, which will help to limit the rise in blood volume.

7.4.4.2 Medical Complications

Acute Tubular Necrosis

Acute tubular necrosis (ATN), characterized by ischemic necrosis of the tubular epithelial cells and decreased GFR, is frequently associated with cadaver renal transplants. Possible causes are hypotension/hypovolemia in the donor and the prolonged interval between harvest and transplantation. Urine output usually starts to decrease within the first 24 h or so and improves spontaneously after a few days, although ATN may occasionally last a few weeks. It is often difficult to make a clinical distinction between ATN and rejection in the post-transplantation period. A clear scintigraphic distinction between these two conditions also has remained elusive for two reasons. First, the scintigraphic diagnosis of ATN rests on the premise that graft perfusion is preserved despite decreasing function (Fig. 7.8), in contrast to rejection, where both perfusion and function decrease in parallel (Fig. 7.9). However, depending on the severity/stage of ATN, graft perfusion may vary. Second, ATN and acute rejection may coexist. From a clinical standpoint, a cadaver transplant with impaired function is assumed to have ATN. An aggressive search/treatment for rejection is initiated if the expected recovery in graft function fails to occur. Such recovery can best be ascertained by serial scintigraphy, a sensitive measure of graft function, although the two may be indistinguishable.

Rejection

The histopathological criteria for the diagnosis and classification of rejection have improved significantly in recent years and continue to evolve [46–48]. From a large body of literature, a consensus referred to as the *Banff Classification* has emerged. The new classification shifts the focus from diagnosis of rejection to prognosis to facilitate patient management. The distinction is made between rejection with *tubulointerstitial* changes, milder disease, and rejection with *vasculitis*, where the outcome is poorer. The types of rejection are discussed below.

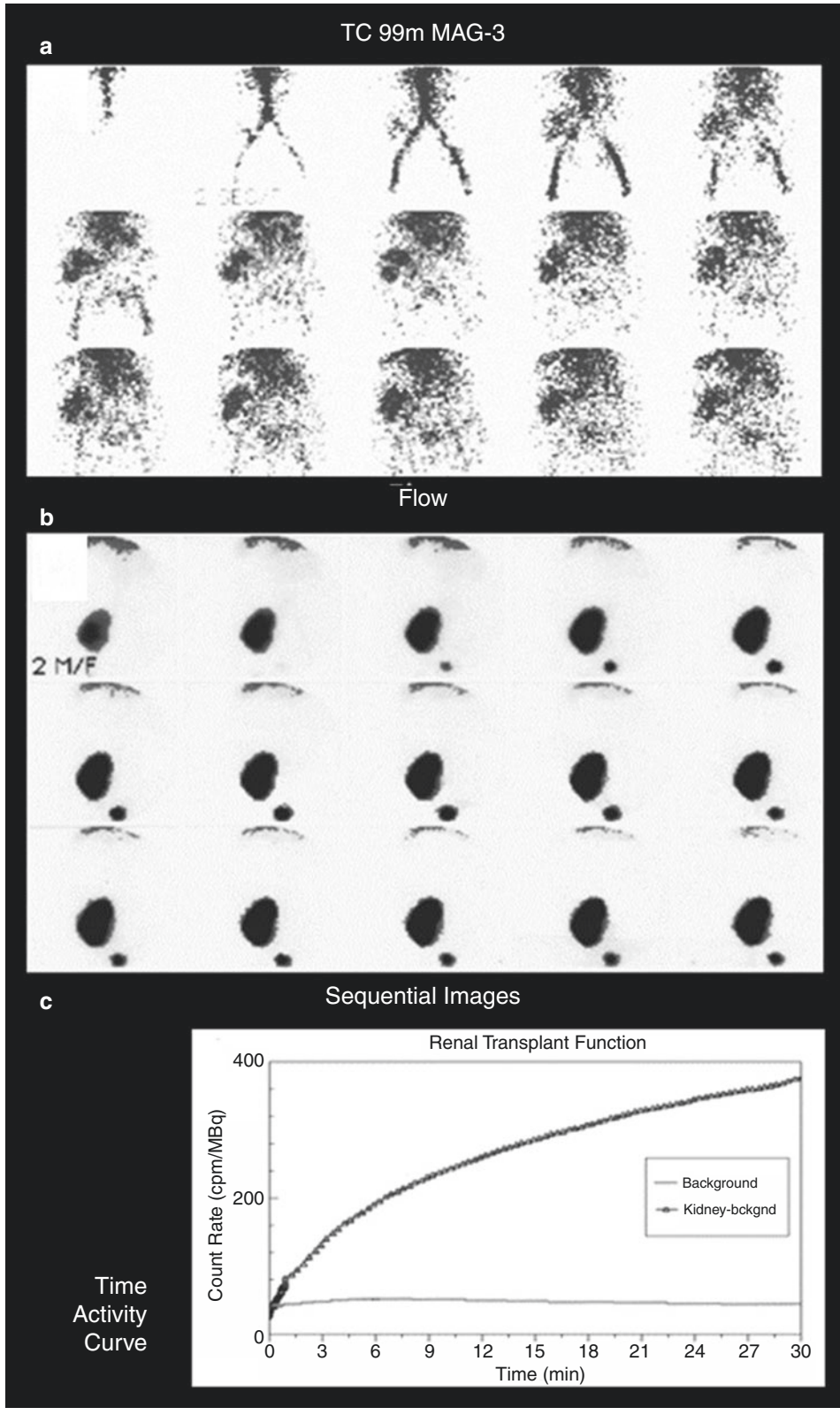

Fig. 7.8 Acute tubular necrosis following renal transplantation. The perfusion is preserved (**a**), while the renal dysfunction is noted through the parenchymal retention (**b**) and rising time-activity curve (**c**). (Courtesy of Dr. A. Omar)

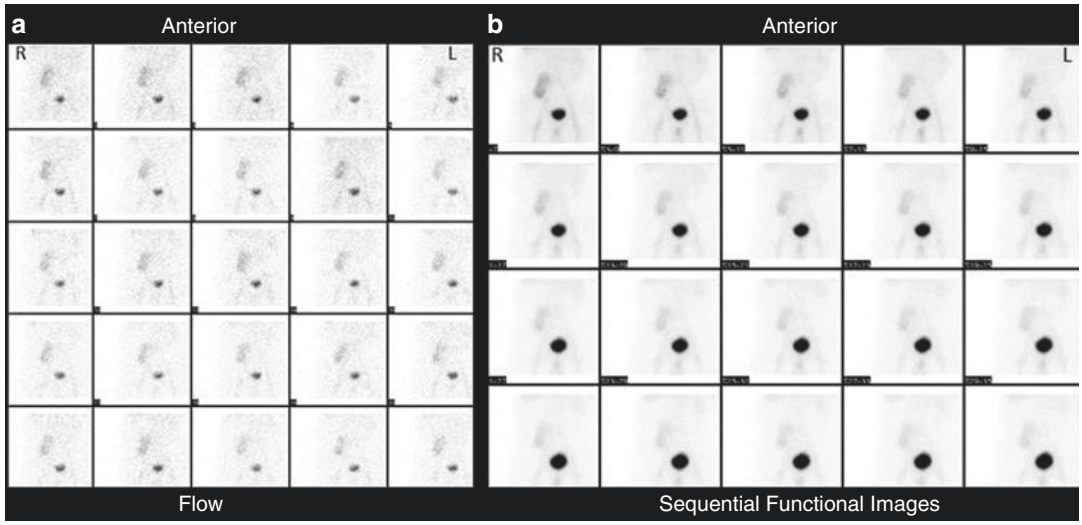

Fig. 7.9 Tc 99m MAG-3 study for a patient with renal transplantation showing decreased perfusion (**a**) and function (**b**) of the graft illustrating the scintigraphic findings of rejection

1. Antibody-mediated rejection:

   Two types of antibody-mediated rejection are described, immediate or hyperacute and delayed or accelerated acute. *Hyperacute rejection* is caused by preformed anti-donor antibodies and is characterized by intense vasculitis, fibrin-platelet thrombi, and infarction of the renal cortex, with graft loss. Rejection may begin within minutes or hours and is usually apparent during surgery. Scintigraphy shows a *photopenic* region corresponding to the avascular graft. Fortunately, hyperacute rejection is rare nowadays and largely preventable by appropriate screening tests.

   Accelerated acute rejection may be considered a "slow" variant of hyperacute rejection, mediated primarily by anti-donor antibodies. It usually occurs on the second or third day following transplantation, after allograft function has been established. Clinical manifestations include fever, pain, swelling, tenderness in the transplant region, hypertension, oliguria, or anuria. Scintigraphy generally shows poor radiotracer uptake in the graft.
2. Acute/active rejection:

   Acute rejection is the most frequent type of rejection confronting the nuclear medicine physician. It is most common in the first 4 weeks following transplantation but may occur at any time between 3 days and 10 or more years. Clinical findings generally are not as dramatic as in accelerated rejection. Acute rejection is predominantly a cell-mediated process with mononuclear cell infiltration and tubulitis, although the more severe forms are associated with a humoral component with various degrees of vasculitis. Accordingly, the Banff system grades acute rejection from I to III, with subdivisions for the severity of changes. The lowest grade represents interstitial infiltration and moderate tubulitis, while the highest grade is associated with transmural arteritis and/or arterial fibrinoid change and necrosis of medial smooth muscle cells.
3. Chronic/sclerosing allograft nephropathy:

   Generally occurs 6 months to years after transplantation. It may be related to many causes, including chronic rejection, hypertension, infectious/noninfectious inflammatory process, and medications' effects (see below). If present, rejection may respond to treatment, though the diagnosis may not be apparent on biopsy. Histopathological changes in the condition also can be graded, depending on the severity of interstitial fibrosis and tubular atrophy.

Nephrotoxicity of Drugs

Cyclosporine and, more recently, tacrolimus (FK506) have been used routinely as immunosuppressive agents. Clinically, nephrotoxicity resulting from these drugs may be difficult to distinguish from rejection, and the conditions may be superimposed. Toxicity is generally associated with elevated blood levels of the drug, improving after dose reduction. Histopathological findings of microvascular injury, with fibrin thrombi in the glomerular arterioles and capillaries, have been noted but, unfortunately, are not diagnostic for cyclosporine or tacrolimus toxicity [49–51].

7.4.5 Vesicoureteral Reflux

7.4.5.1 Pathophysiology

VUR is the retrograde flow of the urine from the bladder into the ureter. Normally, urine is propelled from the kidney to the urinary bladder through the ureter in only one direction. The valvular role of the ureterovesical junction depends on the anatomical relationship between the ureter and the bladder. The ureter follows a retroperitoneal course from the kidney to the bladder. After penetrating the bladder wall, the ureter is securely anchored to it throughout its entire transmural course. A specific arrangement serves to maintain a competent one-way valve at the ureterovesical junction with a mechanism that is best described as a flap valve.

VUR allows the infected urine to be repeatedly returned to the kidneys from the bladder, and the reflux drains back into the bladder at the end of each voiding. Pyelonephritis, especially in children younger than 3 years, is often a result of combined reflux and infection. VUR occurs more frequently in girls by a ratio of 10:1, and the incidence is approximately 1 in 1000 children. Reflux may be unilateral or bilateral and is commonly classified by the international radiologic grading system (Table 7.3). The international radiologic grading includes five grades using detailed anatomy, such as the characterization of the fornices that are impossible to achieve by scintigraphic studies. Accordingly, a more simplified scintigraphic grading attempt classifies reflux into three grades (Table 7.4 and Fig. 7.10) grades; mild (I), moderate (II), and severe (III) [52].

Table 7.3 Radiologic grading of vesicoureteral reflux

I	Reflux into a non-dilated ureter.
II	Reflux into the upper collecting system without dilatation.
III	Reflux into mildly dilated ureter and pelvicalyceal system.
IV	Reflux into a grossly dilated ureter and pelvicalyceal system.
V	Massive reflux with marked ureteral dilatation and tortuosity and marked dilatation of the pelvicalyceal system.

Table 7.4 Scintigraphic grading of vesicoureteral reflux

Grade I	Reflux into the ureter.
Grade II	Reflux into the pelvicalyceal system.
Grade III	Reflux into the pelvicalyceal system with apparently dilated pelvis or both pelvises and ureters.

The flap mechanism of the ureterovesical junction depends on several anatomical relationships and physiological parameters. Any condition that alters these relationships can lead to reflux. Examples include abnormal obliquity of the ureter during its intramural course, conditions that weaken the bladder's muscular support to the ureter, and sphincter dyssynergia. VUR may be primary or secondary [53, 54].

Primary reflux results from a congenitally abnormal or ectopic insertion of the ureter into the bladder. Occasionally, the condition is hereditary [55]. Siblings of patients with vesicoureteral reflux (VUR) are at greater risk of reflux than the general population, and screening in this group is widely accepted. In a recent study, at 48 months after diagnosis, 75% of mild reflux cases (I–III) and 37% of severe reflux (IV and V) of prenatally detected primary VUR had resolved, indicating a relatively benign clinical course.

Secondary reflux is more serious and may be transient or persistent [35]. It develops in association with infection, malformations of the ureterovesical junction, increased intravesical pressure, and surgery to the ureterovesical junction.

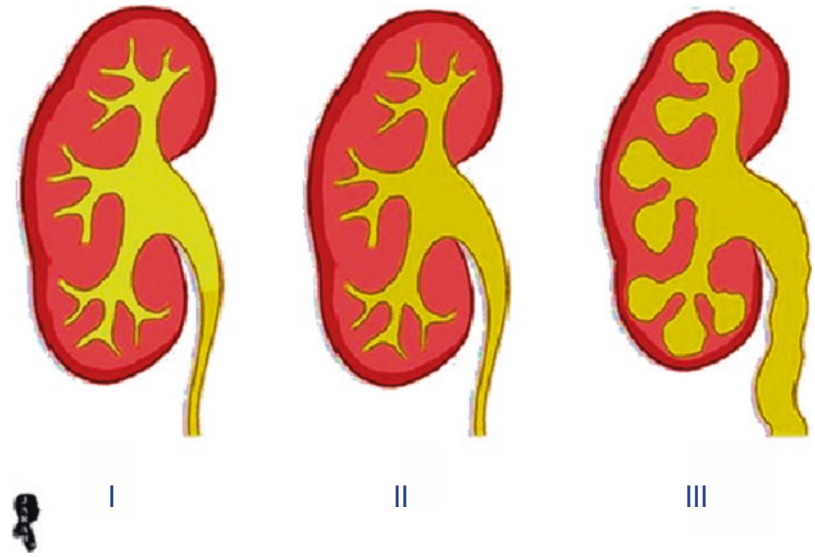

Fig. 7.10 Grades of vesicoureteral reflux used for radionuclide studies

The interstitial cells of Cajal (ICCs) are pacemaker cells that create and coordinate peristaltic motility. It was recently found that refluxing ureteral endings significantly lack these pacemaker cells, implying a malfunctioning valve mechanism permitting VUR. Connexin 43 (gap junction protein) immunoreactivity was significantly decreased in all refluxing ureteral specimens, whereas; it was homogeneously distributed in normal controls. A substantial decrease in gap junctions in this region adversely affects intercellular signaling, aggravating coordinated peristalsis, which is essential for a competent anti-reflux mechanism [53].

7.4.5.2 Reflux Scintigraphy

Voiding radionuclide cystography is a sensitive procedure for the early detection and monitoring of VUR. Early diagnosis of VUR with subsequent follow-up helps to prevent cortical scarring. It is especially attractive because of its excellent sensitivity and low absorbed radiation dose compared with the radiographic MCUG. It was estimated that its radiation exposure is less than 1/20 of the conventional contrast-enhanced micturating cystourethrogram (MCU) [53]. The sensitivity of indirect voiding urosonography without contrast media and without filling the bladder through a catheter to detect vesicoureteral reflux (VUR) in children is inadequate; its overall sensitivity is only 49% [56].

Approximately 20% of patients with vesicoureteral reflux diagnosed before 6 months of age demonstrated dysfunctional voiding after the age of toilet training [57]. Accordingly, follow-up of patients is important. The duration and methods of follow-up of VYR patients are controversial. Voiding cystography, however, may not be used in certain groups of patients for routine follow-up. For instance, the follow-up of uncomplicated ureteral reimplantation in children is usually done by ultrasonography. Additionally, in this group of patients, follow-up for more than 1 year postoperatively is not warranted, and ultrasonography can be eliminated beyond the year [57].

Similarly, ultrasonography is used for screening for siblings of patients with vesicoureteral reflux who are at higher risk than the general population. If ultrasonography is abnormal, the gold-standard test, the radionuclide voiding cystography, is performed [58].

On the other hand, follow-up of newborns with prenatally detected VUR might require voiding cystourethrogram (VCUG) and DMSA scan. In a study [59], 58% of such infants had bilateral VUR. Severe reflux (grades IV and V) was more common and present in 54% of infants. Renal damage was detected in 34% of the kidneys on the first renal scan, with a significant correlation between severe reflux and renal damage scars [59].

Generally, voiding cystourethrograms are associated with significant trauma to patients and should not be used routinely according to the recent guidelines. VCUG is indicated if renal and bladder ultrasonography reveals hydronephrosis, scarring, or other findings that would suggest either high-grade vesicoureteral reflux (VUR) or obstructive uropathy, as well as in other atypical or complex clinical circumstances [40, 41].

7.4.6 Testicular Torsion

7.4.6.1 Pathophysiology

Testicular torsion occurs when the spermatic cord is twisted, and it has been argued that the correct term should be spermatic cord torsion [60, 61]. Although various factors may predispose to torsion [62], a narrow mesenteric attachment from the spermatic cord to the testis and epididymis is regarded as the dominant cause, i.e., a slender attachment occurring as a result of a narrowed testicular bare area. This bare area may reach nearly one-third of the testicular circumference, allowing the testis to fall forward within the cavity of the tunica vaginalis and to rotate like a bell-clapper; the intravaginal type of torsion [63].

Other forms of testicular torsion are recognized. In neonates, the gubernaculum is not attached to the scrotal wall, and the testis is susceptible to torsion. This is termed extravaginal torsion, as the entire testis, epididymis, and tunica vaginalis twist in a vertical axis on the spermatic cord. Some vestigial testicular appendages are susceptible to torsion. There are four testicular appendages: the paradidymis (organ of Giraldés), the appendix testis (hydatid of Morgagni), the appendix epididymis, and the vas aberrans of Haller (divided into superior and inferior components). The appendix testis was most consistently present in 92% of autopsies and found to be multiple in 8% [63, 64].

Two factors are critical in testicular torsion: the extent of spermatic cord twist and the torsion duration. The degree of torsion can vary from 90° to three complete turns of the vascular pedicle. Not surprisingly, blood flow may be variably compromised. The initial disruption will be to the venous and lymphatic drainage, rather than to the arterial input of the testis, and venous infarction occurs earlier and at lesser levels of torsion [65].

Experimentally, complete cessation of blood flow to the testis occurs with the spermatic cord twisting 720° [66]. A 450° twist consistently produced no flow and testicular infarction in the normal rabbit testis, whereas a 360° twist resulted in decreased flow [67].

In patients with torsion, a twist between 360° and 720° is found. Experimental studies have shown that testicular infarction begins to appear within 2 h of complete occlusion of the testicular artery [67]; irreversible ischemia occurs after 6 h [68–70], and complete infarction is established by 24 h.

With complete vascular occlusion, the testis appears grossly swollen and hemorrhagic. Microscopically, the picture is that of hemorrhagic infarction. The degree of necrosis depends upon the duration of occlusion. If this has been longer than 10 h, the necrosis of the seminiferous epithelium is usually complete and irreversible. With incomplete occlusion, necrosis may be delayed. Torsion that lasts less than 6 h probably will not cause a testicular infarct. If torsion lasts longer than 24 h, the test is almost certainly will infarct [60, 61]. Although exceedingly rare, testicular torsion can be asynchronously bilateral [71].

The condition may be acute (symptoms last less than 6 weeks) or chronic (more than 3 months). Acute epididymitis is almost always unilateral. Gram-negative bacilli commonly cause acute epididymitis in children or following urinary tract instrumentation. The epididymis is sometimes the site of metastatic infection, such as tuberculosis.

7.4.6.2 Diagnosis

Testicular torsion results in acute pain and ischemia. The most common signs and symptoms include red, swollen scrotum, and acutely painful testicle, often in the absence of trauma. Nausea and vomiting are common. The most common conditions in the differential diagnosis include epididymitis, strangulated inguinal hernia, traumatic hematoma, testicular tumor, or testicular fracture. Physical examination techniques such

as scrotal elevation can help differentiate between epididymitis and testicular torsion. However, clinical examination of the scrotum is difficult due to the small size of the testes and the epididymis in infants and young children, and eliciting patients' history is challenging. Epididymitis has been considered uncommon in childhood, but its frequency has increased among children admitted with acute scrotum diagnosis [72].

The long-term prognosis for a functional, nonatrophied testicle is improved the sooner the torsion is diagnosed and treated. Therefore, confirming the diagnosis and quick management is crucial. Accordingly, imaging of the scrotum in children suspected of having the condition bears great importance [73, 74].

7.4.6.3 Scrotal Imaging

The classification of scrotal disorders in children into three typical clinical manifestations, namely acute scrotal disorders, scrotal masses, and cryptorchidism, is a helpful and practical basis for choosing the most suitable imaging modality available and commonly used modalities. These include sonography, scintigraphy, and magnetic resonance (MR) imaging. Either scintigraphy or sonography may be used as the first imaging study, and both can help distinguish among the disorders to different degrees. Although sonography provides superior anatomic details to scintigraphy, it may not be as accurate as it is thought to diagnose the most serious emergency reason for scrotal pain [74]. Scrotal masses are also best depicted with sonography with MRI as an adjunctive modality. In suspected cryptorchidism with equivocal clinical findings, both sonography and MR imaging are useful, but sonography is usually the initial study [75].

This strategy for imaging for acute scrotal disorders most relevant to nuclear medicine is not uniform and varies between the institutions based on the experience. In most institutions, Doppler ultrasound is used most commonly as the standard imaging technique of choice to confirm the diagnosis in most cases.

7.4.6.4 Scrotal Scintigraphy

Scintigraphy is used when color Doppler is inadequate, the diagnosis remains unclear, or if complications occur during the course of the disease. Radionuclide testicular scintigraphy is also used more commonly after the acute phase of the first 12 h, and vascular compromise has prolonged [76–78]. Recent studies comparing both modalities indicate similar sensitivity; the two studies may provide complementary information in indeterminate cases [79–81].

A study on 41 boys with suspected testicular torsion scintigraphy and Doppler ultrasound were performed and compared. There was no statistically significant difference in the sensitivity of both modalities. Specificity was 77% for color Doppler US and 97% for scintigraphy ($P = 0.05$). Due to the higher specificity, scintigraphy can help avoid unnecessary surgery when color Doppler US shows equivocal flow [81]. In another two studies of 21 and 37 patients, respectively, scintigraphy was more accurate than Doppler ultrasonography. It also has the advantage of being simple, fast, and accurate but without any detrimental effect on the human body [80, 82].

Findings on a normal scan are symmetrical perfusion with little uptake in the blood pool images. In acute torsion (early), there will be decreased perfusion on flow images, and the blood pool images will show no activity in the affected side (Fig. 7.11).

In missed torsion (late), there will be a halo of activity surrounding the torsion (a doughnut shape) due to increased perfusion to the surrounding tissue through the pudendal vessels (Fig. 7.12). There will be increased perfusion and hyperemia in acute epididymitis in the affected side due to vascular changes associated with the inflammation (Fig. 7.13) [83].

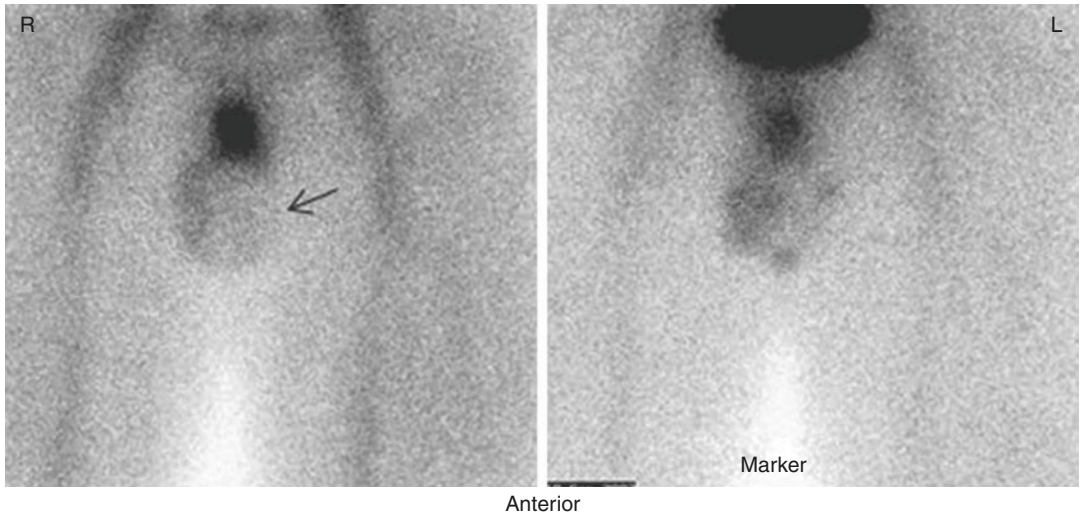

Fig. 7.11 99mTc-pertechnetate scrotal scan of a patient with acute scrotal pain in the left side. The study shows (**a**) essentially absent activity in the region of the left hemi-scrotum (arrow) corresponding to the left testicle by palpation markers (**b**). This case illustrates a pattern of acute testicular torsion

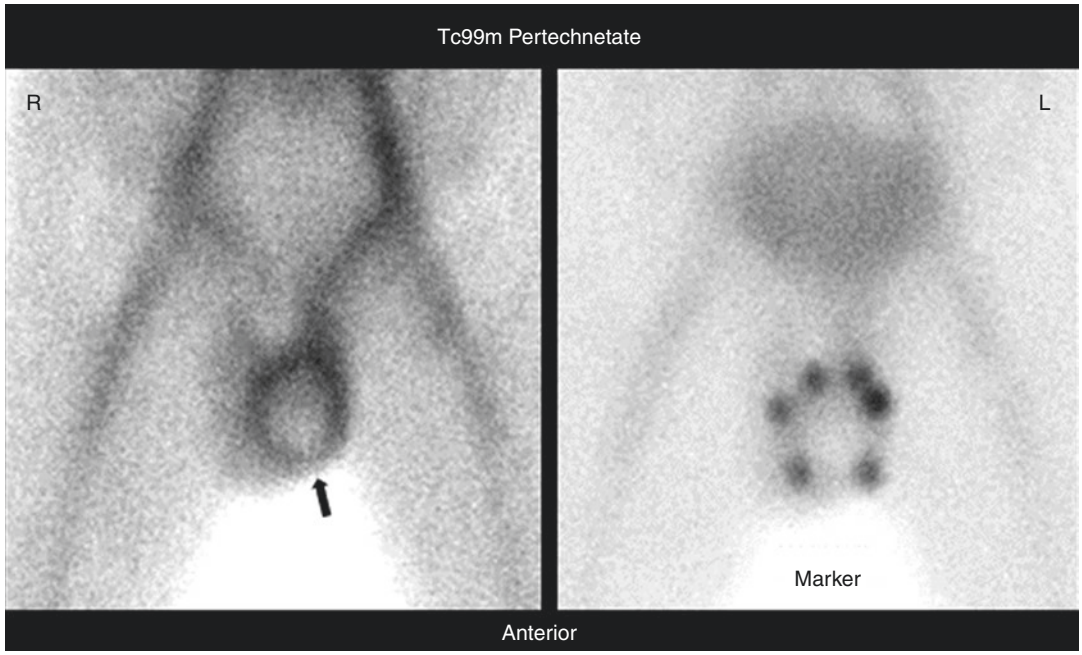

Fig. 7.12 99mTc-pertechnetate testicular imaging study showing the rim of increased uptake around the area of decreased uptake, illustrating the classic pattern of missed torsion of the left testis (arrow)

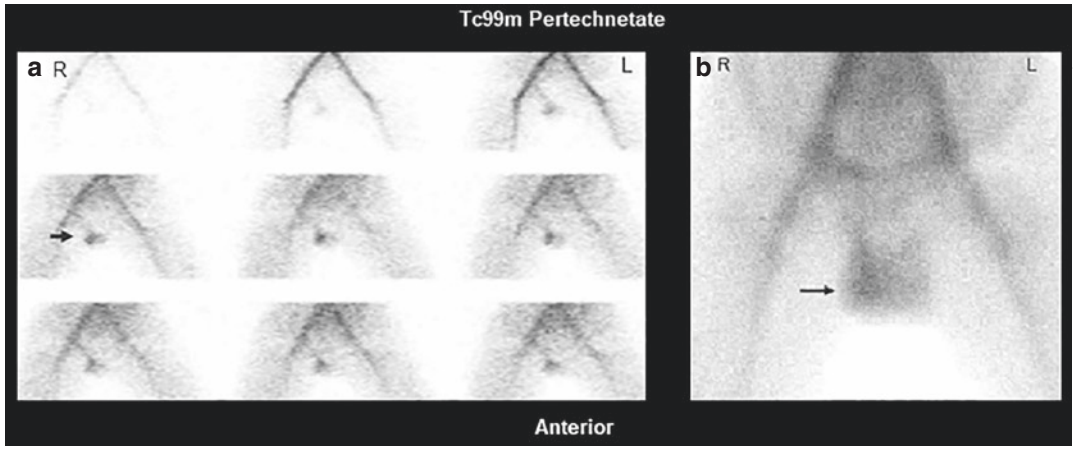

Fig. 7.13 A 14-year-old male was referred for a testicular scan to rule-out testicular torsion. The patient presented with 4 h-history of right-sided acute testicular pain and swelling. The pain was dull in nature, with no radiation, and was associated with nausea and vomiting. There was no history of fever or any urinary symptoms. The patient denied any history of trauma. On examination: Temperature was 37.4 °C. Left testis was grossly normal, and the right testis was tender and swollen. Lab investigations showed leukocytosis at 14,400. Testicular scan was performed, using l7-mCi Tc-99m Pertechnetate given äs a bolus intravenous injection. The scan shows increased flow (**a**) and blood pool (**b**) activity in the right hemiscrotum (arrows) in comparison to the left testis, indicating an inflammatory process in the right hemi-scrotum consistent with right epididymitis

References

1. Field M, Harris D, Pollock C (2010) 5-Glomerular filtration and acute kidney injury. In: Field M, Pollock C, Harris D (eds) The renal system, 2nd edn. Elsevier, pp 57–67
2. Chang A, Laszik ZG (2020) The kidney. In: Robbins pathologic basis of disease, 10th edn. WB Saunders Company
3. Chung AA, Millner PR (2020) Accessory renal artery stenosis and secondary hypertension. Case Rep Nephrol 2020:8879165. https://doi.org/10.1155/2020/8879165
4. Eshima D, Fritzberg AR, Taylor A Jr (1990) 99mTc renal tubular function agents: current status. Semin Nucl Med 20(1):28–40. https://doi.org/10.1016/s0001-2998(05)80174-6
5. Blaufox MD (1991) Procedures of choice in renal nuclear medicine. J Nucl Med 32(6):1301–1309
6. Rutland MD (1985) A comprehensive analysis of renal DTPA studies. I. Theory and normal values. Nucl Med Commun 6(1):11–20. https://doi.org/10.1097/00006231-198501000-00003
7. Jafri RA, Britton KE, Nimmon CC, Solanki K, Al-Nahhas A, Bomanji J, Fettich J, Hawkins LA (1988) Technetium-99m MAG3, a comparison with iodine-123 and iodine-131 orthoiodohippurate, in patients with renal disorders. J Nucl Med 29(2):147–158
8. Stabin M, Taylor A Jr, Eshima D, Wooter W (1992) Radiation dosimetry for technetium-99m-MAG3, technetium-99m-DTPA, and iodine-131-OIH based on human biodistribution studies. J Nucl Med 33(1):33–40
9. Raber SA, Schraml FV, Silverman ED (1997) Renal cortical retention of Tc-99m MAG3 in hypertension. Clin Nucl Med 22(3):190–192. https://doi.org/10.1097/00003072-199703000-00016
10. Levey CS, Schraml FV, Abreu SH, Silverman ED (1999) False-positive result of a captopril-enhanced radionuclide renogram in a child secondary to dehydration. Clin Nucl Med 24(1):6–8. https://doi.org/10.1097/00003072-199901000-00002
11. Taylor A Jr, Nally JV (1995) Clinical applications of renal scintigraphy. Am J Roentgenol 164(1):31–41. https://doi.org/10.2214/ajr.164.1.7998566
12. El-Maghraby TA, de Fijter JW, van Eck-Smit BL, Zwinderman AH, El-Haddad SI, Pauwels EK (1998) Renographic indices for evaluation of changes in graft function. Eur J Nucl Med 25(11):1575–1586. https://doi.org/10.1007/s002590050338
13. Olin JW, Piedmonte MR, Young JR, DeAnna S, Grubb M, Childs MB (1995) The utility of duplex ultrasound scanning of the renal arteries for diagnosing significant renal artery stenosis. Ann Intern Med 122(11):833–838. https://doi.org/10.7326/0003-4819-122-11-199506010-00004
14. Chrysochou C, Kalra PA (2009) Epidemiology and natural history of atherosclerotic renovascular disease. Prog Cardiovasc Dis 52(3):184–195. https://doi.org/10.1016/j.pcad.2009.09.001

15. Noilhan C, Barigou M, Bieler L, Amar J, Chamontin B, Bouhanick B (2016) Causes of secondary hypertension in the young population: a monocentric study. Ann Cardiol d'angeiol 65(3):159–164. https://doi.org/10.1016/j.ancard.2016.04.016
16. Safian RD, Textor SC (2001) Renal-artery stenosis. N Engl J Med 344(6):431–442. https://doi.org/10.1056/NEJM200102083440607
17. Martinez-Maldonado M (1991) Pathophysiology of renovascular hypertension. Hypertension 17(5):707–719. https://doi.org/10.1161/01.hyp.17.5.707
18. Sparks MA, Crowley SD, Gurley SB, Mirotsou M, Coffman TM (2014) Classical renin-angiotensin system in kidney physiology. Compr Physiol 4(3):1201–1228. https://doi.org/10.1002/cphy.c130040
19. Herrmann SM, Textor SC (2019) Renovascular hypertension. Endocrinol Metab Clin N Am 48(4):765–778. https://doi.org/10.1016/j.ecl.2019.08.007
20. Fine EJ, Sarkar S (1989) Differential diagnosis and management of renovascular hypertension through nuclear medicine techniques. Semin Nucl Med 19(2):101–115. https://doi.org/10.1016/s0001-2998(89)80005-4
21. Hricik DE, Browning PJ, Kopelman R, Goorno WE, Madias NE, Dzau VJ (1983) Captopril-induced functional renal insufficiency in patients with bilateral renal-artery stenoses or renal-artery stenosis in a solitary kidney. N Engl J Med 308(7):373–376. https://doi.org/10.1056/NEJM198302173080706
22. Blaufox MD, De Palma D, Taylor A, Szabo Z, Prigent A, Samal M, Li Y, Santos A, Testanera G, Tulchinsky M (2018) The SNMMI and EANM practice guideline for renal scintigraphy in adults. Eur J Nucl Med Mol Imaging 45(12):2218–2228. https://doi.org/10.1007/s00259-018-4129-6
23. Picciotto G, Sargiotto A, Petrarulo M, Rabbia C, De Filippi PG, Roccatello D (2003) Reliability of captopril renography in patients under chronic therapy with angiotensin II (AT1) receptor antagonists. J Nucl Med 44(10):1574–1581
24. Fommei E, Ghione S, Hilson AJ, Mezzasalma L, Oei HY, Piepsz A, Volterrani D (1993) Captopril radionuclide test in renovascular hypertension: a European multicentre study. European multicentre study group. Eur J Nucl Med 20(7):617–623. https://doi.org/10.1007/BF00176558
25. Taylor A, Nally J, Aurell M, Blaufox D, Dondi M, Dubovsky E, Fine E, Fommei E, Geyskes G, Granerus G, Kahn D, Morton K, Oei HY, Russell C, Sfakianakis G, Fletcher J (1996) Consensus report on ACE inhibitor renography for detecting renovascular hypertension. Radionuclides in Nephrourology Group. Consensus group on ACEI renography. J Nucl Med 37(11):1876–1882
26. Prigent A, Cosgriff P, Gates GF, Granerus G, Fine EJ, Itoh K, Peters M, Piepsz A, Rehling M, Rutland M, Taylor A Jr (1999) Consensus report on quality control of quantitative measurements of renal function obtained from the renogram: international consensus committee from the scientific committee of radionuclides in nephrourology. Semin Nucl Med 29(2):146–159. https://doi.org/10.1016/s0001-2998(99)80005-1
27. Mustafa S, Elgazzar AH (2013) Effect of the NSAID diclofenac on 99mTc-MAG3 and 99mTc-DTPA renography. J Nucl Med 54(5):801–806. https://doi.org/10.2967/jnumed.112.109595
28. Ludwig V, Martin WH, Delbeke D (2003) Calcium channel blockers: a potential cause of false-positive captopril renography. Clin Nucl Med 28(2):108–112. https://doi.org/10.1097/01.RLU.0000048679.45832.F3
29. Sarkar SD (1992) Diuretic renography: concepts and controversies. Urol Radiol 14(2):79–84. https://doi.org/10.1007/BF02926908
30. Fine EJ (1999) Interventions in renal scintirenography. Semin Nucl Med 29(2):128–145. https://doi.org/10.1016/s0001-2998(99)80004-x
31. Pohl HG, Rushton HG, Park JS, Belman AB, Majd M (2001) Early diuresis renogram findings predict success following pyeloplasty. J Urol 165(6 Pt 2):2311–2315. https://doi.org/10.1097/00005392-200106001-00024
32. Heyman S (1994) Radionuclide studies of the genitourinary tract. In: Miller J, Gelfand M (eds) Pediatric nuclear imaging. Saunders, Philadelphia, pp 195–211
33. Taylor AT, Brandon DC, de Palma D, Blaufox MD, Durand E, Erbas B, Grant SF, Hilson A, Morsing A (2018) SNMMI procedure standard/EANM practice guideline for diuretic renal scintigraphy in adults with suspected upper urinary tract obstruction 1.0. Semin Nucl Med 48(4):377–390. https://doi.org/10.1053/j.semnuclmed.2018.02.010
34. Ring P, Huether SE (2017) Alteration of renal and urinary tract function in children. In: McCance KL, Huether SE (eds) Pathophysiology, 8th edn. Mosby, Philadelphia, pp 1278–1295
35. Strand WR (1999) Urinary infection in children: pathogenesis, bacterial virulence, and host resistance. In: Bauer SB, Gonzales E (eds) Pediatric urology practice. Lippincott Williams & Wilkins, Philadelphia, pp 433–461
36. Kaefer M, Diamond D (1987) Vesicoureteral reflux. In: Retik A, Cukier J (eds) Pediatric urology. Williams and Wilkins, Baltimore, pp 463–486
37. Solari V, Owen D, Puri P (2005) Association of transforming growth factor-beta1 gene polymorphism with reflux nephropathy. J Urol 174(4 Pt 2):1609–1611. https://doi.org/10.1097/01.ju.0000179385.64585.dc
38. Kanematsu A, Yamamoto S, Yoshino K, Ishitoya S, Terai A, Sugita Y, Ogawa O, Tanikaze S (2005) Renal scarring is associated with nonsecretion of blood type antigen in children with primary vesicoureteral reflux. J Urol 174(4 Pt 2):1594–1597. https://doi.org/10.1097/01.ju.0000176598.60310.90
39. Shaikh N, Osio VA, Wessel CB, Jeong JH (2020) Prevalence of asymptomatic bacteriuria in children: a meta-analysis. J Pediatr 217:110–117.e4. https://doi.org/10.1016/j.jpeds.2019.10.019
40. Mahyar A, Ayazi P, Mavadati S, Oveisi S, Habibi M, Esmaeily S (2014) Are clinical, laboratory, and

imaging markers suitable predictors of vesicoureteral reflux in children with their first febrile urinary tract infection? Korean J Urol 55(8):536–541. https://doi.org/10.4111/kju.2014.55.8.536
41. Subcommittee on urinary tract infection (2016) Reaffirmation of AAP clinical practice guideline: the diagnosis and management of the initial urinary tract infection in febrile infants and young children 2-24 months of age. Pediatrics 138(6):e20163026. https://doi.org/10.1542/peds.2016-3026
42. National Institute for Health and Clinical Excellence (NICE) (2018) Clinical guideline 54—Urinary tract infection in under 16s: diagnosis and management. Clinical guideline Published: 22 August 2007. www.nice.org.uk/guidance/cg54
43. Pokrajac D, Sefic-Pasic I, Begic A (2018) Vesicoureteral reflux and renal scarring in infants after the first febrile urinary tract infection. Med Archiv 72(4):272–275. https://doi.org/10.5455/medarh.2018.72.272-275
44. Roupakias S, Sinopidis X, Tsikopoulos G, Spyridakis I, Karatza A, Varvarigou A (2017) Dimercaptosuccinic acid scan challenges in childhood urinary tract infection, vesicoureteral reflux and renal scarring investigation and management. Minerva Urol Nefrol 69(2):144–152. https://doi.org/10.23736/S0393-2249.16.02509-1. Epub 2016 Jun 29. PMID: 27355216
45. Breinbjerg A, Jørgensen CS, Frøkiær J et al (2021) Risk factors for kidney scarring and vesicoureteral reflux in 421 children after their first acute pyelonephritis, and appraisal of international guidelines. Pediatr Nephrol 36(9):2777–2787
46. Ramos CD, Onusic DM, Brunetto SQ, Amorim BJ, Souza TF, Saad S, Lima M (2019) Technetium-99m-dimercaptosuccinic acid renal scintigraphy and single photon emission computed tomography/computed tomography in patients with sickle cell disease. Nucl Med Commun 40(11):1158–1165. https://doi.org/10.1097/MNM.0000000000001086
47. Vasco M, Benincasa G, Fiorito C, Faenza M, De Rosa P, Maiello C, Santangelo M, Vennarecci G, Napoli C (2021) Clinical epigenetics and acute/chronic rejection in solid organ transplantation: an update. Transplant Rev 35(2):100609. https://doi.org/10.1016/j.trre.2021.100609
48. Hruba P, Madill-Thomsen K, Mackova M, Klema J, Maluskova J, Voska L, Parikova A, Slatinska J, Halloran PF, Viklicky O (2020) Molecular patterns of isolated tubulitis differ from tubulitis with interstitial inflammation in early indication biopsies of kidney allografts. Sci Rep 10(1):22220
49. Callemeyn J, Ameye H, Lerut E, Senev A, Coemans M, Van Loon E, Sprangers B, Van Sandt V, Rabeyrin M, Dubois V, Thaunat O, Kuypers D, Emonds MP, Naesens M (2020) Revisiting the changes in the Banff classification for antibody-mediated rejection after kidney transplantation. Am J Transplant 21(7):2413–2423. https://doi.org/10.1111/ajt.16474
50. Randhawa PS, Tsamandas AC, Magnone M, Jordan M, Shapiro R, Starzl TE, Demetris AJ (1996) Microvascular changes in renal allografts associated with FK506 (Tacrolimus) therapy. Am J Surg Pathol 20(3):306–312. https://doi.org/10.1097/00000478-199603000-00007
51. Asher J, Vasdev N, Wyrley-Birch H, Wilson C, Soomro N, Rix D, Jaques B, Manas D, Torpey N, Talbot D (2014) A prospective randomised paired trial of sirolimus versus tacrolimus as primary immunosuppression following non-heart beating donor kidney transplantation. Curr Urol 7(4):174–180. https://doi.org/10.1159/000365671
52. Munib S, Ahmed T, Ahmed R, Najam-Ud-Din (2021) Renal allograft biopsy findings in live-related renal transplant recipients. J College Physic Surg 31(2):197–201. https://doi.org/10.29271/jcpsp.2021.02.197
53. Lebowitz RL, Olbing H, Parkkulainen KV, Smellie JM, Tamminen-Möbius TE (1985) International system of radiographic grading of vesicoureteric reflux. International reflux study in children. Pediatr Radiol 15(2):105–109. https://doi.org/10.1007/BF02388714
54. Williams G, Fletcher JT, Alexander SI, Craig JC (2008) Vesicoureteral reflux. J Am Soc Nephrol 19(5):847–862. https://doi.org/10.1681/ASN.2007020245
55. Rodriguez MM (2004) Developmental renal pathology: its past, present, and future. Fetal Pediatr Pathol 23(4):211–229. https://doi.org/10.1080/15227950490923453
56. Jana S, Blaufox MD (2006) Nuclear medicine studies of the prostate, testes, and bladder. Semin Nucl Med 36(1):51–72. https://doi.org/10.1053/j.semnuclmed.2005.09.001
57. Kopac M, Kenig A, Kljucevsek D, Kenda RB (2005) Indirect voiding urosonography for detecting vesicoureteral reflux in children. Pediatr Nephrol 20(9):1285–1287. https://doi.org/10.1007/s00467-005-1961-2
58. Charbonneau SG, Tackett LD, Gray EH, Caesar RE, Caldamone AA (2005) Is long-term sonographic followup necessary after uncomplicated ureteral reimplantation in children? J Urol 174(4 Pt 1):1429–1432. https://doi.org/10.1097/01.ju.0000173128.73742.bc
59. Giel DW, Noe HN, Williams MA (2005) Ultrasound screening of asymptomatic siblings of children with vesicoureteral reflux: a long-term followup study. J Urol 174(4 Pt 2):1602–1605. https://doi.org/10.1097/01.ju.0000176596.87624.a3
60. Penido Silva JM, Oliveira EA, Diniz JS, Bouzada MC, Vergara RM, Souza BC (2006) Clinical course of prenatally detected primary vesicoureteral reflux. Pediatr Nephrol 21(1):86–91. https://doi.org/10.1007/s00467-005-2058-7
61. Muschat M (1932) The pathological anatomy of testicular torsion: explanation of its mechanism. Surg Gynaecol Obstet 54:758–763
62. Allan WR, Brown RB (1966) Torsion of the testis: a review of 58 cases. Br Med J 1(5500):1396–1397. https://doi.org/10.1136/bmj.1.5500.1396

63. Scorer CG, Farrington GH (1971) Congenital deformities of testis and epididymis, 1st edn. Butterworth, London
64. Corriere JN Jr (1972) Horizontal lie of the testicle: a diagnostic sign in torsion of the testis. J Urol 107(4):616–617. https://doi.org/10.1016/s0022-5347(17)61093-0
65. Skoglund RW, McRoberts JW, Ragde H (1970) Torsion of testicular appendages: presentation of 43 new cases and a collective review. J Urol 104(4):598–600. https://doi.org/10.1016/s0022-5347(17)61790-7
66. Rencken RK, du Plessis DJ, de Haas LS (1990) Venous infarction of the testis—a cause of non-response to conservative therapy in epididymo-orchitis. A case report. S Afr Med J 78(6):337–338
67. Kogan SJ (2002) Swellings of the intrascrotal contents. In: Gillenwalter JY (ed) Adult and pediatric urology, 4th edn. Lippincott Williams & Wilkins, Philadilphia
68. Frush DP, Babcock DS, Lewis AG, Paltiel HJ, Rupich R, Bove KE, Sheldon CA (1995) Comparison of color Doppler sonography and radionuclide imaging in different degrees of torsion in rabbit testes. Acad Radiol 2(11):945–951. https://doi.org/10.1016/s1076-6332(05)80693-2
69. Luker GD, Siegel MJ (1994) Color Doppler sonography of the scrotum in children. Am J Roentgenol 163(3):649–655. https://doi.org/10.2214/ajr.163.3.8079863
70. Herbener TE (1996) Ultrasound in the assessment of the acute scrotum. J Clin Ultrasound 24(8):405–421. https://doi.org/10.1002/(SICI)1097-0096(199610)24:8<405::AID-JCU2>3.0.CO;2-O
71. Patriquin HB, Yazbeck S, Trinh B, Jéquier S, Burns PN, Grignon A, Filiatrault D, Garel L, Dubois J (1993) Testicular torsion in infants and children: diagnosis with Doppler sonography. Radiology 188(3):781–785. https://doi.org/10.1148/radiology.188.3.8351347
72. Olguner M, Akgür FM, Aktuğ T, Derebek E (2000) Bilateral asynchronous perinatal testicular torsion: a case report. J Pediatr Surg 35(9):1348–1349. https://doi.org/10.1053/jpsu.2000.9330
73. Pogorelić Z, Mustapić K, Jukić M, Todorić J, Mrklić I, Mešštrović J, Jurić I, Furlan D (2016) Management of acute scrotum in children: a 25-year single center experience on 558 pediatric patients. Can J Urol 23(6):8594–8601
74. Laher A, Ragavan S, Mehta P, Adam A (2020) Testicular torsion in the emergency room: a review of detection and management strategies. Open Access Emerg Med 12:237–246. https://doi.org/10.2147/OAEM.S236767
75. Hörmann M, Balassy C, Philipp MO, Pumberger W (2004) Imaging of the scrotum in children. Eur Radiol 14(6):974–983. https://doi.org/10.1007/s00330-004-2248-x
76. Shin J, Jeon GW (2020) Comparison of diagnostic and treatment guidelines for undescended testis. Clin Exp Pediatr 63(11):415–421. https://doi.org/10.3345/cep.2019.01438
77. Lavallee ME, Cash J (2005) Testicular torsion: evaluation and management. Curr Sports Med Rep 4(2):102–104. https://doi.org/10.1097/01.csmr.0000306081.13064.a2
78. Ring N, Staatz G (2017) Bildgebende Diagnostik beim akuten Skrotum [Diagnostic imaging in cases of acute scrotum]. Aktuelle Urol 48(5):443–451. https://doi.org/10.1055/s-0043-100497
79. Saleh O, El-Sharkawi MS, Imran MB (2012) Scrotal scintigraphy in testicular torsion: an experience at a tertiary care centre. IIUM Med J Malaysia 11(1). https://doi.org/10.31436/imjm.v11i1.540
80. Yuan Z, Luo Q, Chen L, Zhu J, Zhu R (2001) Clinical study of scrotum scintigraphy in 49 patients with acute scrotal pain: a comparison with ultrasonography. Ann Nucl Med 15(3):225–229. https://doi.org/10.1007/BF02987836
81. Nussbaum Blask AR, Bulas D, Shalaby-Rana E, Rushton G, Shao C, Majd M (2002) Color Doppler sonography and scintigraphy of the testis: a prospective, comparative analysis in children with acute scrotal pain. Pediatr Emerg Care 18(2):67–71. https://doi.org/10.1097/00006565-200204000-00001
82. Wu HC, Sun SS, Kao A, Chuang FJ, Lin CC, Lee CC (2002) Comparison of radionuclide imaging and ultrasonography in the differentiation of acute testicular torsion and inflammatory testicular disease. Clin Nucl Med 27(7):490–493. https://doi.org/10.1097/00003072-200207000-00005
83. Saha GB (2010) Fundamentals of nuclear pharmacy, 6th edn. Springer, Berlin

Respiratory System

8

Abdelhamid H. Elgazzar and Naheel Alnafisi

8.1 Anatomic and Physiologic Considerations

The pulmonary system consists of the lungs, airways, pulmonary and bronchial circulation, and chest wall. The lungs consist of lobes, three in the right (upper, middle, and lower) and two in the left lung (upper and lower). Each lobe is again divided into segments and lobules (Fig. 8.1). The airway system consists of upper airways (nasopharynx and oropharynx) and lower airways (trachea, bronchi, bronchioles, and alveolar ducts) connected by the larynx (Fig. 8.2).

8.1.1 Respiratory Airways

The *upper airways* are lined by a ciliated mucosa, richly supplied with blood, which warm and humidify the inspired air and get rid of foreign particles. The air normally flows by way of the nose, nasopharynx, and oropharynx to the lower airways. When the nose is obstructed or additional flow of air is needed, as during exercise, air flows via the mouth and oropharynx to the lower airways. Foreign particle removal and humidification are not efficient with mouth breathing as compared with the usual breathing through the nose.

The *lower airways* are formed of a conducting system and a gas exchange system (Fig. 8.3). The trachea divides into two main bronchi at the carina, and each bronchus enters the corresponding lung at the hilum along with the pulmonary blood vessels and lymphatic channels. The trachea measures up to 25 cm in length and 2.5 cm in diameter. The right main bronchus extends to the right lung more vertically than the left bronchus to the left lung. This explains the more frequent aspiration of foreign material in the right side. At the hila, the bronchi divide to lobar bronchi, then segmental and subsegmental bronchi, and then into smaller bronchioles, and at the 16th division, the tracheobronchial tree ends in the tiny terminal bronchioles which form the ends of the conducting airways and are followed by the gas exchange airways. The lung segments are individual units with their bronchovascular supply; hence, they can be individually resected. The airways responsible for conducting air from outside the body into the lungs are lined by ciliated mucous membranes. The cilia, which are hairlike projections, act as sweepers to prevent dust and foreign particles from passing distally into the lungs. Damage to the respiratory epithelium and its cilia allows bacteria and viruses to proliferate and induce infection.

The gas exchange airways start where the terminal bronchioles divide further into smaller,

A. H. Elgazzar (✉) · N. Alnafisi
Department of Nuclear Medicine, Faculty of Medicine, Kuwait University, Kuwait City, Kuwait

A. H. Elgazzar (ed.), *The Pathophysiologic Basis of Nuclear Medicine*,
https://doi.org/10.1007/978-3-030-96252-4_8

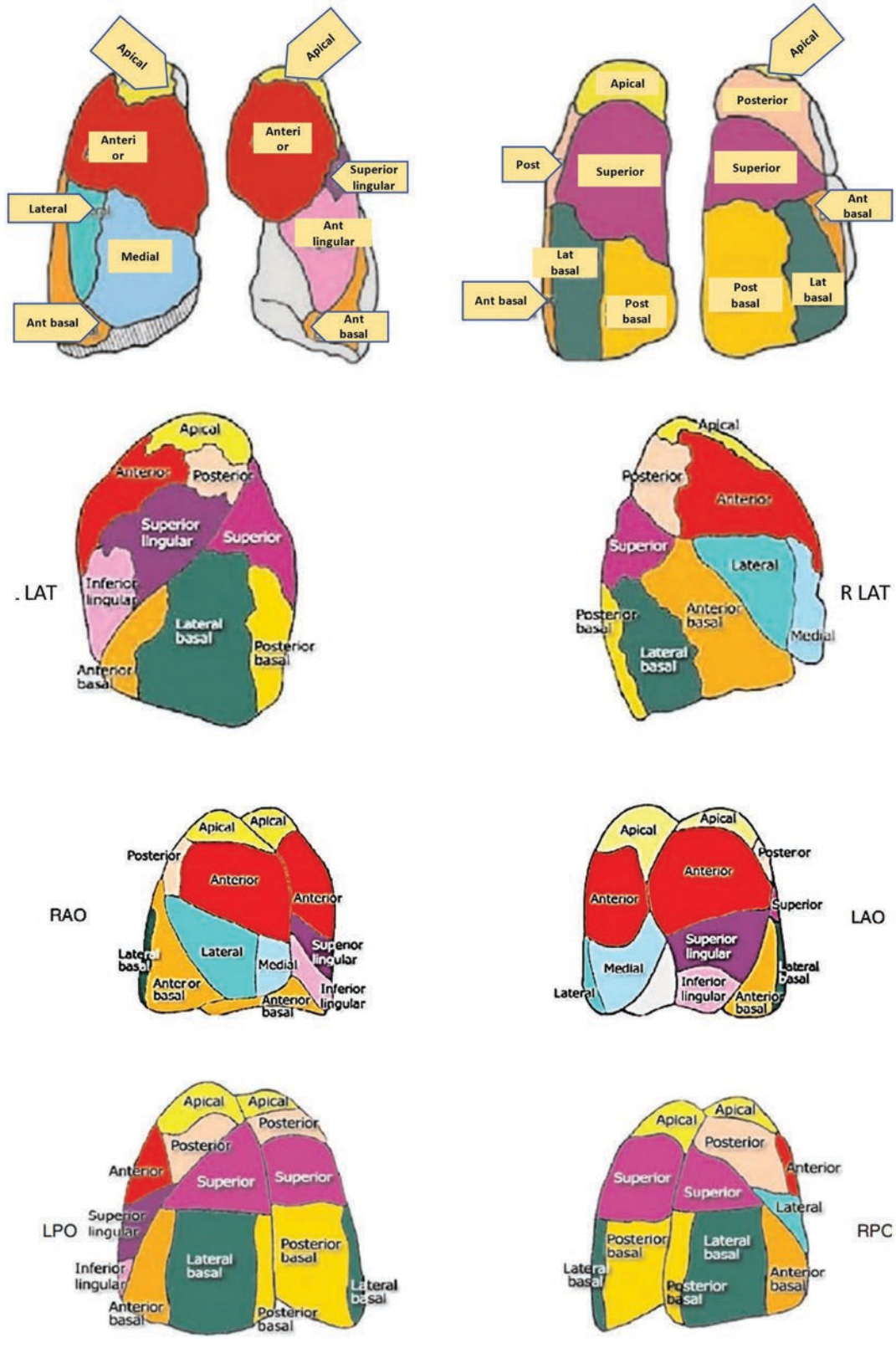

Fig. 8.1 Diagram of the lobes and segments of the lungs

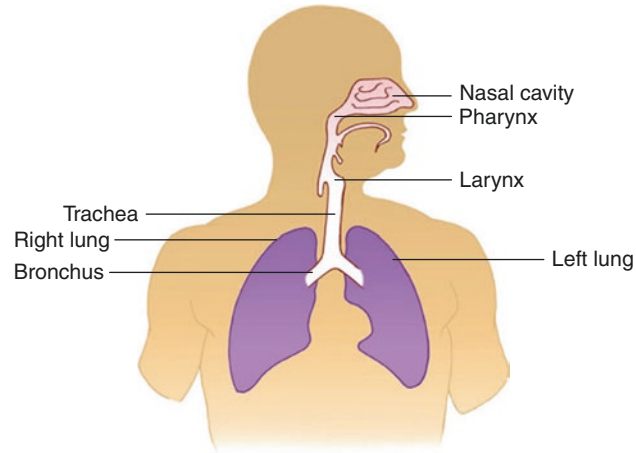

Fig. 8.2 Simple diagram of the upper and lower airways

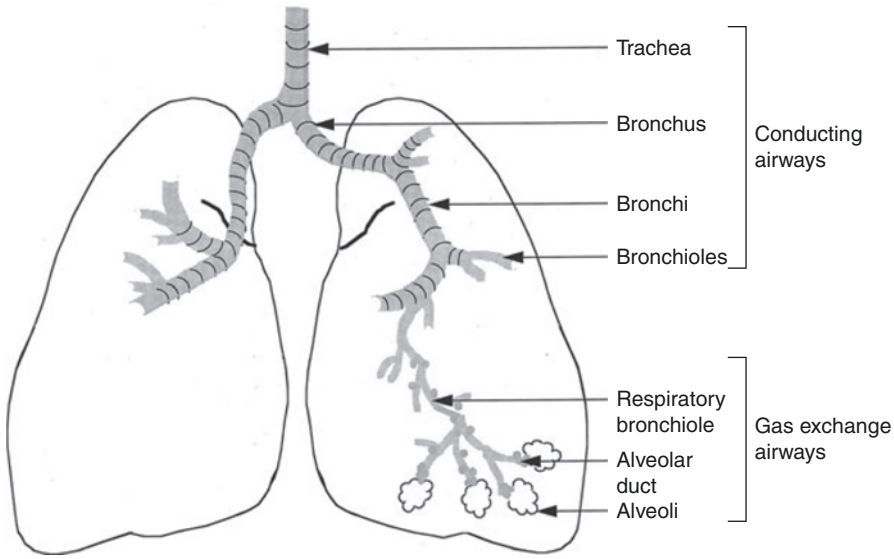

Fig. 8.3 The trachea, bronchi, and bronchioles form the tracheobronchial tree, so-called since it resembles an inverted tree. The conducting system is composed of the trachea, bronchi, and bronchioles up to the 16th division and is lined by ciliated mucosa. The gas exchange system consists of the more distal bronchioles (respiratory) and the alveoli that are lined by nonciliated mucus membrane

respiratory bronchioles which include increasing numbers of alveoli as the division progresses. By the 23rd division, the respiratory bronchioles end in alveolar ducts that lead to alveolar sacs which are made up of numerous alveoli. The alveoli are extremely thin-walled sacs surrounded by capillaries and are the primary site of gas exchange. At birth there are approximately 25 million alveoli; this increases to 300 million in adults. The alveoli are lined by type I alveolar cells that provide structure to the alveolar wall and type II cells that secrete a lipoprotein, the surfactant which coats the alveolar inner surface and aids its expansion during inspiration [1].

Ventilation describes the process by which air flows in and out of the gas exchange airways. Ventilation is involuntary most of the time and is controlled by the sympathetic and parasympathetic autonomic nervous systems, which adjust the caliber of the airway via contraction and relaxation of the bronchial smooth muscle and control the depth and rate of ventilation.

The nose and trachea trap most particles of more than 10 μm in diameter, while the cilia of the bronchi and bronchioles pick up particles 2–10 μm in diameter that are deposited in these airways. Smaller particles remain airborne till they are deposited in the alveoli and removed by macrophages. Extremely small particles behave as a gas and are breathed out. This is the basis of scintigraphic ventilation studies using radioactive aerosols and gases. The flow of oxygen through the ^{99m}Tc DTPA reservoir should create small aerosol particles to be airborne and deposited distally in the alveoli. Larger particles are deposited in the more proximal airways and influence the quality of ventilation studies. This also explains the longer biologic clearance of aerosols compared with radioactive gases, which are breathed out without deposition.

8.1.2 Pulmonary Vasculature

The lung is supplied by two different blood circulations. The pulmonary circulation is a low-pressure, low-resistance system through which oxygen enters and carbon dioxide is removed. The bronchial circulation is a part of the high-pressure systemic circulation that supplies oxygenated blood to the lung tissue itself.

The pulmonary circulation contains the vast majority of blood present in the lung, and since it has lower pressure than systemic circulation, its vessels have a thinner muscle layer. The mean pulmonary artery pressure is 18 mmHg, compared with 90 mmHg for the aorta. The gas exchange airways are served by this pulmonary circulation, which is considered a separate division of the circulatory system. The pulmonary circulation is carried through the pulmonary artery, which branches out to two main pulmonary arteries, one to each lung, entering at the hilum. It then divides progressively into smaller branches, following the branches of the bronchial tree to the smallest, precapillary arterioles, which divide to form a capillary network surrounding the alveoli. The membrane that surrounds the alveoli and contains the capillaries is called the alveolocapillary membrane [2].

The precapillary arterioles are approximately 35 μm in diameter and number approximately 300 million in adults. The capillaries, 7–10 μm in diameter, number 300 billion in adults. The more proximal terminal arterioles have a diameter of approximately 100 μm. This basic anatomical fact is important in determining the size of particles injected for perfusion studies; they should be less than 100 μm to prevent blocking of the terminal arterioles [3].

Although the pulmonary circulation is innervated by the autonomic nervous system, vasodilation and vasoconstriction are controlled mainly by local and humoral factors, particularly arterial oxygenation, and acid–base balance. Vasoconstriction of the pulmonary arterial system occurs secondary to alveolar hypoxia and acidemia and by the presence of inflammatory mediators such as histamine, bradykinin, serotonin, and prostaglandin.

The bronchial circulation, on the other hand, carries approximately 5% of the blood coming to the lungs and is part of the systemic circulation. In contrast to the pulmonary circulation, it does not participate in gas exchange. It supplies the tracheobronchial tree, large pulmonary vessels, and other structures of the lungs, including the pleurae, with blood.

8.1.3 Respiratory Function

The major function of the respiratory system is to oxygenate the blood and remove waste products of the body in the form of carbon dioxide. Oxygen in the inhaled air diffuses from the alveoli into the surrounding blood in the capillaries, where it attaches to hemoglobin molecules and red blood cells and is carried to the various tissues of the body. Carbon dioxide, on the other hand, as a waste product of cellular metabolism, diffuses in the opposite direction, from the blood in capillaries into the alveoli, and is removed from the body during expiration.

The respiration is controlled by the respiratory center in the medulla at the base of the brain. The respiratory center in the brain stem sends impulses to respiratory muscles to contract and relax. The respiratory center also receives impulses from two main types of peripheral receptors, neuro- and chemoreceptors.

Neuroreceptors (lung receptors) monitor the mechanical aspects of ventilation such as the need to expel unwanted substances and expansion of the lungs. The chemoreceptors in the brain circulatory system monitor the pH status of the cerebrospinal fluid and arterial oxygen content (PO_2) to regulate ventilation accordingly.

Any change in the carbon dioxide in the blood will affect the rate and depth of respiration. A slight increase in carbon dioxide concentration in the blood increases the rate and depth of respiration, such as when the individual exercises, since the accumulated waste gas must be removed from the body.

This increase in respiratory rate and depth is secondary to the stimulation of the muscles of respiration, which include the diaphragm and the intercostal muscles, by the respiratory center. Contraction of these muscles causes the volume of the chest cavity to increase, with a consequent drop in the pressure within the lungs, and forces air to move into the tracheobronchial tree. When these respiratory muscles relax, the volume of the chest cavity decreases, the pressure increases, and the air is pushed out of the lungs. When breathing is difficult, or in patients with obstructive airway disease, special muscles of expiration, abdominal and internal intercostal muscles, may be additionally needed.

8.1.4 Distribution of Ventilation and Perfusion

Normally, the lower zones of the lungs are better perfused and ventilated because of the effect of gravity. This gradient is more pronounced in perfusion than in ventilation (Fig. 8.4). This physiological fact will usually cause the perfusion to appear less than the ventilation in the lung apices on scintigraphy. This should not be confused with a mismatching pattern. ^{99m}Tc-macroaggregated albumin (MAA) is injected for perfusion imaging while the patient is in the supine position to minimize the gradient. Injection while the patient is taking a deep breath also helps.

8.2 Pulmonary Embolic Disease

Venous thromboembolism, clinically presenting as DVT or PE, is the third most frequent acute cardiovascular syndrome globally with around ten million cases per year worldwide [5, 6]. The true incidence of PE is unknown, but in the USA, it is estimated that nearly one-third of hospitalized patients are at risk of developing venous thromboemboli and up to 600,000 cases of VTE are diagnosed per year [7].

Pulmonary embolism is potentially fatal and the most common pathological condition involving the lungs of hospitalized patients. The majority of fatal emboli are not recognized or suspected prior to death.

8.2.1 Pathogenesis and Risk Factors

The vast majority of pulmonary emboli are thromboemboli originating from deep veins mostly from lower extremity [8, 9].

Fat, air, or tumor emboli are rare [10]. Fat emboli are reported with long bone fractures and liposuction, while air emboli occur in cardiac and

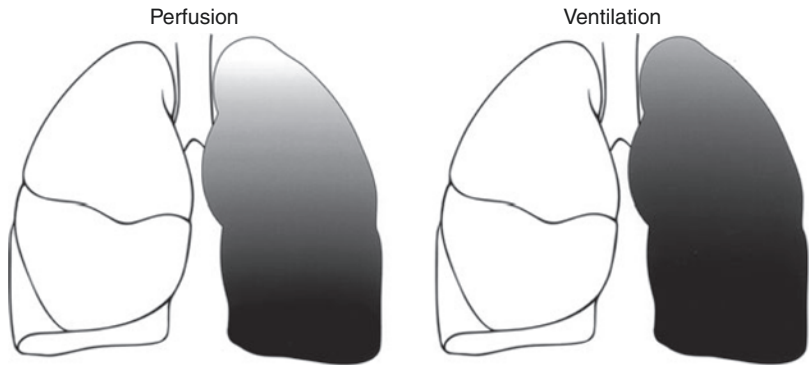

Fig. 8.4 The gradient pattern in perfusion and ventilation of the lungs. (From Elgazzar et al. [4] with permission)

neurosurgeries. Renal cell carcinoma with invasion reaching inferior vena cava is a clinical setting that may lead to tumor emboli. Data indicate that 90% of pulmonary thromboemboli originate from the lower extremities and pelvis. The remainder comes from thrombi that occur in the right side of the heart or in bronchial or cervical veins. Embolization and symptomatology are proportional to how proximal is the vein that contains the thrombus. The vast majority of pulmonary thromboemboli originating from thrombi of the lower extremities come more frequently from the thigh and pelvis (75%) than from smaller veins of the calf and feet [9, 11, 12]. Only 6% of the time upper extremity DVTs cause PE [13]. Septic embolus refers to an infected thromboembolus which occurs either on site or secondary to detachment of an infected vein thrombus of the lower extremities. The risk of pulmonary embolus is also directly related to the presence of a residual clot at the site of a venous thrombus [14].

Recently a common, yet not novel, risk factor for thromboembolism and PE is established with the Corona Virus Disease (COVID 2019) infection. Early in COVID-19 pandemic, multiple clinical, pathological, laboratory, and imaging reports demonstrated an association between COVID-19 infection and coagulopathies. These coagulopathies manifested as PE or venous, arterial, and/or microvascular thrombosis which are associated with severe viral injury of lung endothelium. In the available early and limited data, coagulopathy was reported in up to 50% of patients with severe COVID-19 manifestations. Deep vein thrombosis and PE was reported in up to 40% of patients. Current evidence is limited by small retrospective studies, and the true prevalence of thrombosis in COVID-19 is yet to be evaluated.

Pathogenesis of viral coagulopathy in the previously known various coronavirus infections has been extensively investigated. Some of the mechanisms proven include platelets consumption, thrombin generation, and increased fibrin degradation product (FDP) leading to disseminated intravascular coagulation (DIC)-like syndrome.

The specific mechanisms increasing the risk of thrombotic complications in patient with COVID-19 is currently under extensive investigation. Many factors are considered including the high levels of D-dimer and FDPs, the high levels of proinflammatory cytokines, and the endothelial dysfunction associated with the infection. It is hypothesized that an imbalance between coagulation and inflammation may result in COVID-19 hypercoagulable state. It is also suggested that COVID-19 coagulopathy is distinct from sepsis induced DIC and it reflect dysregulated hemostasis [15–20].

8.2.2 Deep Venous Thrombosis

The best solution to the problem of embolism is to prevent it. However, prevention requires identification of those at risk. Perhaps the most important step in defining who is at risk for this disorder has been the recognition that pulmonary emboli arise from the sites of deep venous thrombosis, almost exclusively in the lower extremity veins. Therefore, those at risk for deep venous thrombosis are those at risk for pulmonary embolism. The classical risk triad elucidated by Virchow in the nineteenth century includes venous stasis, intimal injury, and alteration in coagulation. These are the primary factors in the pathogenesis of venous thrombosis. Deficiencies of antithrombin III, protein C, protein S, and protein Z are clearly important, as is the presence of lupus anticoagulant. There are other rarer conditions such as homocystinuria and deficiencies of the fibrinolytic system. More factors are being identified, but at the present time, up to 90% of all patients with thromboembolism have no identifiable coagulopathy. Thus, in most patients, some clinical states associated with venous stasis, intimal injury, or both are the basis for an increased risk of deep venous thrombosis. These clinical states include injury to the pelvis or lower extremities, surgery involving the lower extremities, all surgical procedures requiring prolonged (at least 30 min) general anesthesia, burns, pregnancy and the postpartum state, previous venous thrombosis with residual obstruction, right ventricular failure

Table 8.1 Risk factors for deep vein thrombosis and pulmonary thromboembolism[a]

Inherited factors
1. Antithrombin deficiency
2. Protein C deficiency
3. Protein S deficiency
4. Factor V Leiden
5. Prothrombin gene mutation
Acquired factors
1. Postoperative state especially following operations on the abdomen and pelvis
2. Trauma, including fractures, particularly of the lower extremities
3. Neoplasms
4. Prior history of thromboembolic disease
5. Venous stasis
6. Vascular spasm
7. Intimal injury
8. Hypercoagulability states
9. Immobilization
10. Infection of the area in the immediate of veins
11. Heart disease, especially:
Myocardial infarction
Atrial fibrillation
Cardiomyopathy
Congestive heart failure
12. Pregnancy
13. Polycythemia
14. Hemorrhage
15. Obesity
16. Old age
17. Extensive varicose veins
18. Certain drugs such as oral contraceptives, estrogens
19. Following cerebrovascular accidents
20. Smoking
21. Central venous instrumentation within the past 3 months
22. Homocystinemia
23. Homocystinuria
24. Hyperlipidemia
25. Hypertension
26. COVID-19 disease

[a] [7, 15–21]

of any cause, occupations in which prolonged venous stasis is involved, and any cause of immobility. Other risk factors are age (particularly above 70 years), obesity, cancer, and the use of estrogen-containing medications, neoplasm, infection in the immediate area of veins, and hypercoagulability (Table 8.1).

An important point to note is that risk factors should be regarded as cumulative, not independent. These factors allow the establishment of a "risk profile" for a given patient, a profile that conditions the intensity of prophylactic initiatives. The anatomical location of the deep venous thrombosis affects as well the likelihood of extending into a pulmonary embolism as noted earlier.

Venous thrombi appear to begin either in the vicinity of a venous valve, where eddy current arises, or at the site of intimal injury. Platelet aggregation and release of mediators initiate the sequence. With stasis, there is local accumulation of coagulation factors; the coagulation cascade is activated, and the characteristic red fibrin thrombus develops. Pathologically there will be a platelet nidus from which a large fibrin thrombus extends.

Regarding the natural history, one of three events can happen after the formation of the thrombus. First, the red thrombus grows explosively and obstructs the vein completely. This can happen even within a few minutes. Second, partial venous obstruction may occur. Blood flow therefore continues over the thrombus surface. Under this circumstance, thrombus growth tends to occur by the progressive layering of platelets and fibrin on the clot surface, pathologically seen as the lines of Zahn. Third, probably the most common scenario, a small thrombus is swept away before it reaches an appreciable size. It lodges in the pulmonary vasculature without symptoms.

Unless fibrinolytic resolution is prompt, organization of the thrombus begins within hours of formation. The thrombus is slowly replaced by granulation tissue. This process anchors the thrombus to the venous wall.

The dynamic battle between fibrinolysis and thrombus formation is fought out over a period of 7–10 days, at the end of which time either complete resolution has occurred or an endothelialized residual is present. At any time during this period, a portion or all of the thrombus can detach as an embolus. This risk is highest early, before significant dissolution or organization occur [12].

8.2.3 Pulmonary Thromboembolism

8.2.3.1 Consequences

Pulmonary thromboemboli occur more commonly in the lower lobes because of the preferential blood flow to these regions. This also applies to the right lung because of the straighter course of the pulmonary artery. Immediately after acute embolism, there is a decrease of perfusion distal to the occluded vessel along with a transient decrease of ventilation to the affected segment. The blood flow is diverted to the other portions of the lung, and pulmonary artery pressure may increase, although cardiac output usually remains stable. The resultant tissue ischemia disturbs certain metabolic functions of the lung such as the production of surfactant. Reduction of the surfactant concentration reduces the alveolar surface tension and may cause the atelectasis that often accompanies embolism. If the embolus completely occludes an artery or an arteriole and the collateral bronchial circulation is insufficient to sustain tissue viability, infarction occurs over 24–48 h. Pulmonary infarction with coagulative necrosis results in an area of radiographic opacity that requires an average of 20 days to resolve but occurs in less than 10–15% of patients with pulmonary embolism. There is significant inflammatory component in pulmonary infarcts which is the basis behind the reported significant FDG uptake in recent lung infarcts and can cause false-positive interpretation for lung malignancy [22]. More frequently, incomplete infarction with hemorrhage but without necrosis occurs. This type of injury resolves quickly and produces only transient radiographic opacities. Infarction always involves the pleural surface of the lung (peripheral) and more frequently involves the lower lobes than other sites.

The regional decrease in ventilation is due to local bronchoconstriction with a tendency for redistribution of ventilation away from the hypoperfused segment. This probably occurs due to decreased regional alveolar and airway carbon dioxide tension, which is the usual stimulus for bronchodilation. This hypocapnia is corrected quickly, since patients inhale carbon dioxide-rich tracheal "dead space air" into the alveolar zones after the embolic event, raising the alveolar pCO_2 [12]. The release of neurohumoral factors, most importantly serotonin and thromboxane A_2, also causes bronchoconstriction. These factors are released after embolization by activated platelets and mediate bronchospasm of small airways through their effects on the smooth muscles [23]. The ventilation of the hypoperfused areas returns to normal within several hours after acute embolism [24, 25]. This concept is the pathophysiological basis for the scintigraphic interpretation of ventilation and perfusion scans, which show segmental perfusion defects with preserved ventilation as a typical scintigraphic pattern for pulmonary embolism. Those showing only regions of matched perfusion and ventilation defects carry a low probability of pulmonary embolism if no chest X-ray abnormalities are noted at the same sites, since this pattern is more likely associated with nonembolic conditions and is more typical of parenchymal lung disease. Because patients with pulmonary emboli usually arrive at the hospital after normalization of the ventilation at the site of pulmonary emboli, the mismatching pattern is typical of pulmonary emboli. However, inpatients may have their V/Q scans within a short time after presentation and matching abnormalities may be associated with pulmonary emboli. This has to be borne in mind, and the duration of symptoms should be a factor in decision-making regarding the management of pulmonary embolism.

Some degree of arterial hypoxemia may also occur, one reason being the widening of the arteriovenous oxygen difference caused by acute right ventricular failure. Another reason is the enhanced perfusion of poorly ventilated or nonventilated lung zones. Loss of pulmonary surfactant may add to the hypoxemia. Hyperventilation almost always occurs and may partly explain the normal levels of oxygen arterial pressure seen in 10–25% of patients with pulmonary emboli.

An increase in the resistance of the pulmonary arterial circulation, due primarily to mechanical blockage by numerous small emboli in the pulmonary vasculature and also to humorally mediated vasoconstriction, may follow pulmonary

emboli. These hemodynamic consequences may include increased pulmonary arterial resistance with elevated pulmonary arterial and right ventricular systolic pressures and hypoxemia. When pulmonary hypertension occurs, it indicates at least 25% obstruction of pulmonary vascular tree as assessed by angiography [26]. The higher the degree of obstruction, the more severe the abnormalities of the cardiopulmonary hemodynamics become. When over 50% of the pulmonary vasculature is included (massive pulmonary embolism), acute pulmonary hypertension and/or right ventricular failure (cor pulmonale) occurs [26]. Systemic hypoxemia results from pulmonary arteriovenous shunting and from perfusion of hypoventilated lung segments (V-P imbalances). The AV shunting accounts for the clinical observation that administration of 100% oxygen will only partially correct hypoxemia induced by pulmonary emboli [27].

The physiological consequences of pulmonary embolism depend on the size of the embolic mass and the general status of the pulmonary circulation. In young individuals with good cardiovascular function and good collateral circulation, thrombi of a large central vessel may be associated with only minimal functional impairment if any. On the other hand, in patients with cardiovascular or severely debilitating diseases, pulmonary embolism may lead to infarction.

8.2.3.2 Resolution

Pulmonary emboli may, spontaneously or with treatment, fragment into smaller portions that travel distally and block smaller arterioles (Fig. 8.5). This may create new, smaller perfusion defects that are more peripherally located in comparison to the original defect caused by the original embolus. This pattern should not be mistaken for recurrent pulmonary emboli on a follow-up scan. If this pattern is the only interval change with no other defects seen in areas other than those in the vicinity of the distribution of the original embolus, it does not suggest recurrent emboli [26].

Resolution of pulmonary thromboembolus may start within hours. It can be seen on perfusion scans as early as 24 h and is progressively noted up to 3 months, with insignificant change after 6 months (Fig. 8.6). This is the basis of the recommendation that follow-up ventilation and perfusion scans are performed 3 months after the initial incident for evaluation of resolution and function as a baseline for future incidents to dif-

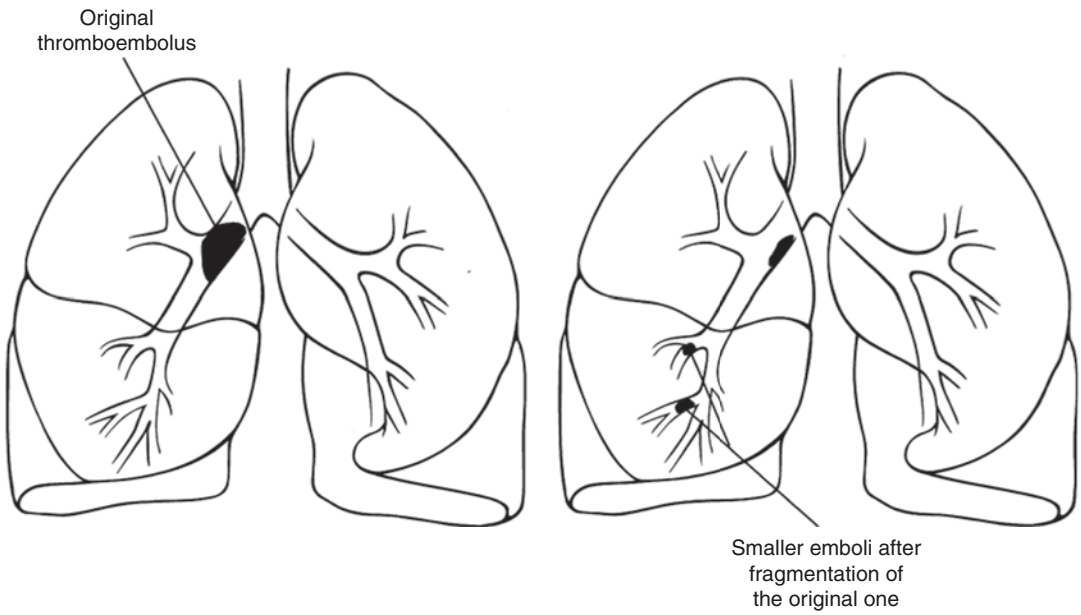

Fig. 8.5 The phenomenon of fragmentation of the thromboemboli. (From Elgazzar [4] with permission)

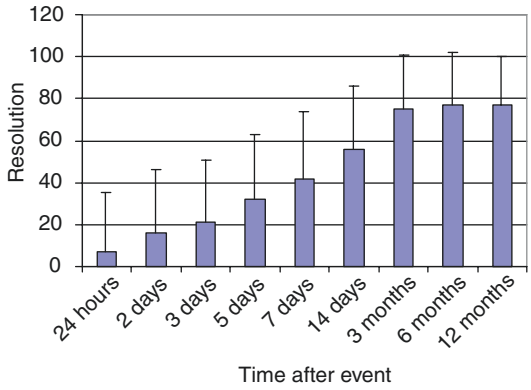

Fig. 8.6 Histogram illustrating the percent resolution of pulmonary emboli. Note that there is progressive increase of the percentage over time until 3 months after the event with no significant increase afterwards. (Data are based on the Urokinase Study [27, 28])

ferentiate between acute and unresolved old emboli. This resolution is dependent on the age of the patient, with complete resolution in young age groups and less complete and less significant resolution in older age groups [26, 27]. Other factors include age of the thromboembolus or length of time between formation of the embolus and the institution of proper anticoagulation. This is the basis behind the relatively recent trend of starting anticoagulant therapy in most patients with pulmonary emboli who have no contraindication for anticoagulation immediately when a pulmonary thromboembolus is suspected before finishing the workup for the condition. Anticoagulant therapy may then be stopped if the condition is excluded.

8.2.3.3 Chronic Pulmonary Thromboembolism

Incomplete resolution of acute pulmonary embolism is frequently observed and may rarely result in chronic thromboembolic pulmonary hypertension [29]. Chronic thromboembolic disease is characterized by intraluminal thrombus organization and fibrous stenosis or complete obliteration of pulmonary arteries. The consequence is an increased pulmonary vascular resistance resulting in pulmonary hypertension and progressive right heart failure. Pulmonary endarterectomy is the preferred treatment [30].

8.2.3.4 Recurrence

Pulmonary thromboemboli recur in up to 50% of patients [31], although the incidence in treated PIOPED patients was only 8.3% [32]. The vast majority of deaths among pulmonary embolism patients are due to recurrent emboli. In the PIOPED study population, it was found that nine of ten people who died had a recurrent pulmonary embolus [33]. Recurrence has been reported to occur at the same site as the original thromboembolus [34].

8.2.3.5 Diagnosis

The clinical diagnosis of pulmonary thromboembolism is difficult and unreliable, due to the nonspecificity of its symptoms and signs as well as the laboratory and chest X-ray findings [35, 36]. Chest X-ray however must be obtained since it may show many parenchymal diseases and must be available for lung scan interpretation (Fig. 8.7). Pulmonary embolism may also be asymptomatic. In the literature, only 24% of fatal emboli were diagnosed antemortem (Table 8.2) [37–46]. Furthermore the presentation is commonly more difficult and atypical in older age group compared to younger patients [47, 48]. Accordingly only 24% of fatal emboli were diagnosed antemortem (Table 8.2). Data indicate that the mortality of pulmonary embolism is more than 30% if untreated. Promptly diagnosed and treated, emboli have a mortality of 2.5–8% [27, 28, 33]. The mortality of PE was found to vary among patients with or without cardiac disease. Paraskos et al. [49] reported survival rates at a mean follow-up period of 29 months of 19% among patients with prior congestive heart failure and 86% for those with no prior congestive heart failure. Pulmonary angiography is the most accurate modality for the diagnosis of pulmonary emboli with an accuracy of 96% [50]. However, angiography is invasive and is not suitable as a screening imaging modality for the disease.

D-dimer is a fibrin degradation product present in the blood after a thrombus is degraded through fibrinolysis. The blood test to determine D-dimer concentration helps diagnose thrombosis. Although a negative result practically rules out thrombosis, a positive result can indicate

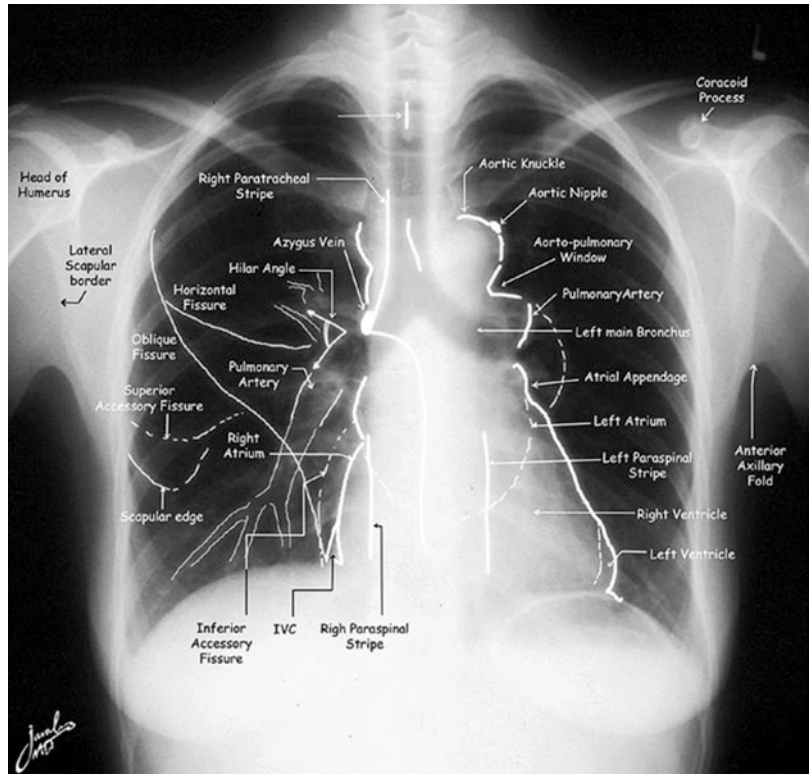

Fig. 8.7 Normal chest X-ray illustrating the important structures that may show variants on perfusion scans

Table 8.2 Antemortem diagnosis of PE

Author	Year	No. (%) of cases with antemortem PE diagnosis
Stein and Henry [37]	1995	6/20 (30)
Morgenthaler and Ryu [38]	1995	29/92 (32)
Morpurgo and Schmid [39]	1991	26/92 (28)
Sperry et al. [40]	1990	275/812 (34)
Karwinski and Svendsen [41]	1989	267/1450 (18.4)
Gross et al. [42]	1988	7/18 (39)
Dismuke and Wagner [43]	1986	41/203 (20)
Goldhaber et al. [44]	1982	16/54 (30)
Rubio-Jurado et al. [45]	2003	9/66 (14)
Total		675/2807 (24)

thrombosis but does not rule out other potential causes. Its main use, therefore, is to exclude thromboembolic disease where the clinical probability is low. On the other hand, the positive predictive value of elevated D-dimer levels is low and D-dimer testing is not useful for confirmation of PE. D-dimer is also more frequently elevated in patients with cancer [51], in hospitalized patients [51–53], in severe infection or inflammatory disease, and during pregnancy [54].

Imaging

Scintigraphy remains the most cost-effective noninvasive screening modality. The major advantages include its ability to provide regional and quantitative information useful for the diagnosis, as well as for mapping to guide selective angiography if needed for the diagnosis. SPECT V/P scan has been strongly recommended as it is more accurate than planar imaging in establishing the diagnosis of PE even in the presence of

diseases such as COPD, heart failure, and pneumonia. Furthermore, adding low dose CT(SPECT/CT) improves the scan specificity especially in patients with other lung diseases [55].

CTPA is useful in detecting central emboli which has become the most commonly used modality in many centers at the expense of scintigraphy although data are still controversial for peripheral emboli [56–59]. Multislice CT was found to have no added value in patients with high-probability V/Q scans and has a comparable diagnostic value with SPECT V/Q scans [60]. CT also as a single study is not cost-effective [61]. It also requires the use of iodinated contrast media with its risk of renal failure and ionizing radiation with its risk of cancer induction [62, 63]. And it was also found to result in overdiagnosis of pulmonary emboli [58]. MRI pulmonary angiography will play a greater role [64]; however, the use of contrast media is still a shortcoming. In an experimental study, reversible PE was induced by inflating a nondetachable silicon balloon in the left pulmonary artery of five New Zealand white rabbits. MR V/Q scans were obtained prior to, during, and after balloon deflation. High-resolution contrast-enhanced MR pulmonary angiography was also used to confirm the occlusion of the pulmonary artery. Similar to radionuclide ventilation/perfusion technique, acute PE produced a mismatched defect in the MR V/Q scan. MRA verified the occlusive filling defect in the left pulmonary artery. The study suggests that high-resolution MRA and MR V/Q imaging of the lung is feasible and allows comprehensive assessment of pulmonary embolism in one imaging session [64]. Recently, non-contrast MRI has been studied in the diagnosis of PE [65].There are growing evidence-based outcome data that Contrast-enhanced pulmonary MRA is a safe and accurate and radiation-free examination for the exclusion of clinically significant PE [66].

Scintigraphy is also valuable in pregnancy. When indicated low activity of 1 mCi (37 MBq) is used for perfusion, if the perfusion study is abnormal, then ventilation and chest X-ray (if not obtained earlier) are obtained as needed. Based upon the available data, there are no apparent short- or long-term consequences to the fetus from the radiation received as a result of diagnostic ventilation/perfusion scintigraphy. For a V/Q scan, fetal dose would mostly come from tracer accumulating in the bladder, with some internal scatter from the lungs. Either Xenon133 or ^{99m}Tc agents can be used safely for the ventilation portion of the exam. Xenon103 has the advantage of not being excreted via the urine.

Scintigraphic Agents

Several agents have been used for ventilation (Table 8.3). Every agent has certain advantages and limitations. Xenon 133 (Fig. 8.8) is useful in evaluating obstructive airway disease. Krypton-81 (Fig. 8.9), ^{99m}Tc-DTPA (Fig. 8.10), and Technegas (Fig. 8.11) provide the ability to perform ventilation studies after the perfusion, particularly krypton-81. ^{99m}Tc-macroaggregated albumin is used for perfusion. For proper interpretation of lung perfusion/ventilation study, chest X-ray must be available and should be obtained within 12 h of the time of the scans.

Table 8.3 Ventilation agents

Agent	Advantages and limitations
Aerosols	
^{99m}Tc-DTPA aerosol	Lung half-clearance time = 58 min
	Pre- or post-perfusion
	Multiple projections
^{99m}Tc-pyrophosphate aerosol	Post perfusion
	Suitable for SPECT
Technegas	Multiple projections
	Good peripheral deposition
Gases	
Xenon-133	Ability to obtain single breath, equilibrium, and washout images
	Very sensitive for obstructive airway disease
	Only posterior view is possible in most patients
	Low energy of 81 keV
	Pre-perfusion acquisition
Krypton-81m	Expensive—available only in some areas
	Energy: 190 keV
	Half-life: 13 s
	Multiple views
	Pre- or post-perfusion

The particle size of ^{99m}Tc-macroaggregated albumin (^{99m}Tc-MAA) is generally between 10 and 90 μm (90% of particles), and no particles should be larger than 150 μm. ^{99m}Tc-MAA is injected slowly IV and lodges in precapillary arterioles, obstructing approximately 0.1% of their total number. The particles clear by enzymatic hydrolysis and are phagocytized by RE cells (the agent has a biologic half-life in the lungs of between 6 and 8 h). Normally, only 3–6% of the injected ^{99m}Tc-MAA will bypass the pulmonary vasculature. The critical organ is the lungs which receive a dose of about 1 rad (1 cGy) from a typical 5 mCi dose. The kidneys and bladder receive moderate exposure largely from the excretion of degraded albumin.

^{99m}Tc-DTPA aerosol is commonly used for ventilation studies worldwide. Using an aerosol delivery system that generates submicronic particles, 30 mCi of Tc-DTPA in 3 mL of saline (3–5 min of rebreathing on the system with the oxygen at 8–10 L/min) delivers about 500–750 mCi of tracer to the lungs. This dose yields 100 K count images in about 2 min on a standard gamma

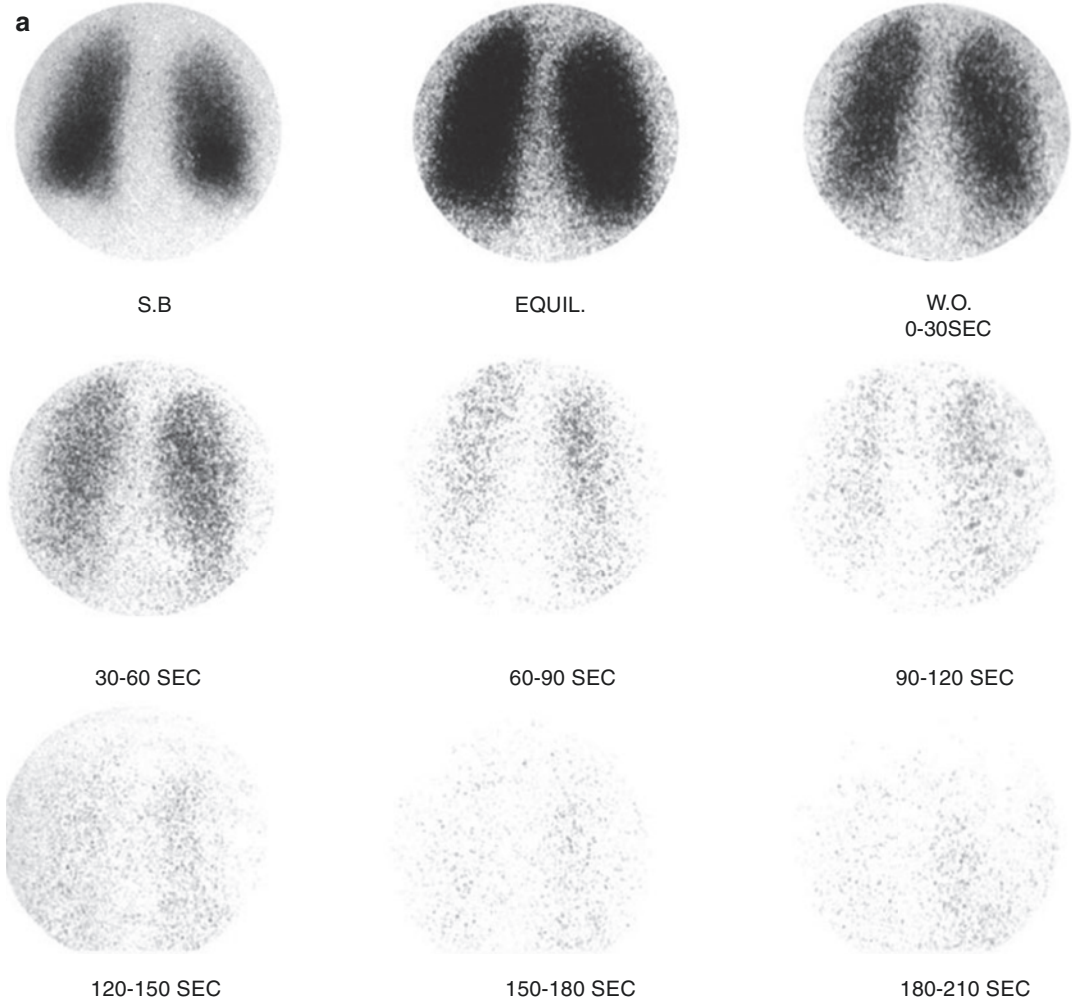

Fig. 8.8 (**a**, **b**) Xenon-133 ventilation studies. (**a**) Normal study with uniform distribution of the radiotracer in both lungs on single breath and equilibrium images. The washout images reveal prompt clearance with no significant retained activity. (**b**) Washout images of a patient with obstructive airway disease showing retained activity in lower zones of both lungs by the end of the study

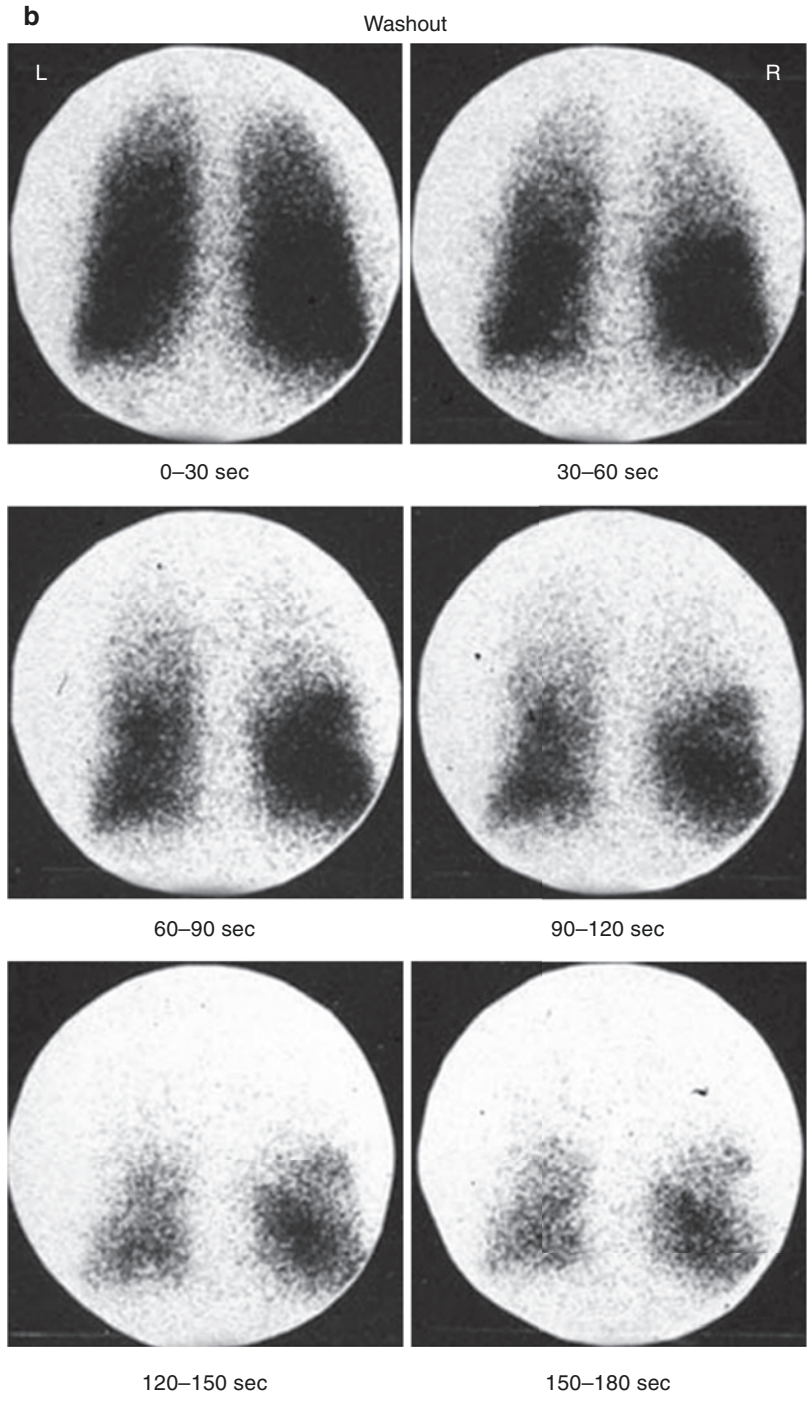

Fig. 8.8 (continued)

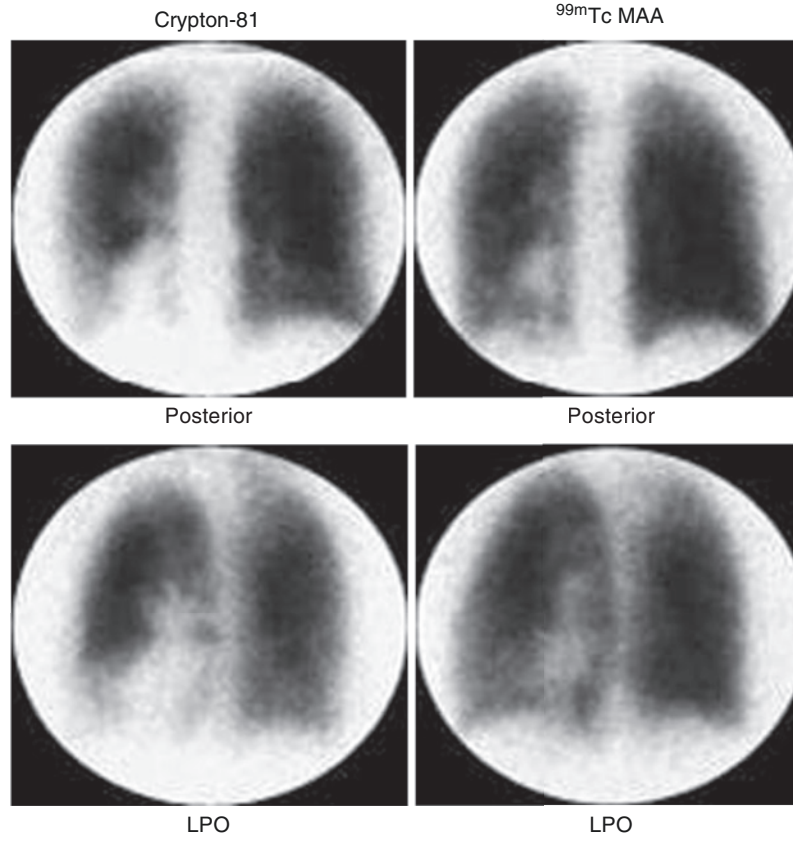

Fig. 8.9 Representative images of krypton-81 ventilation study obtained post perfusion. Note the good quality of images. The shown anterior and left posterior oblique (LPO) images illustrate the ability to evaluate the ventilation status at the regions of the perfusion abnormalities seen on the same projections

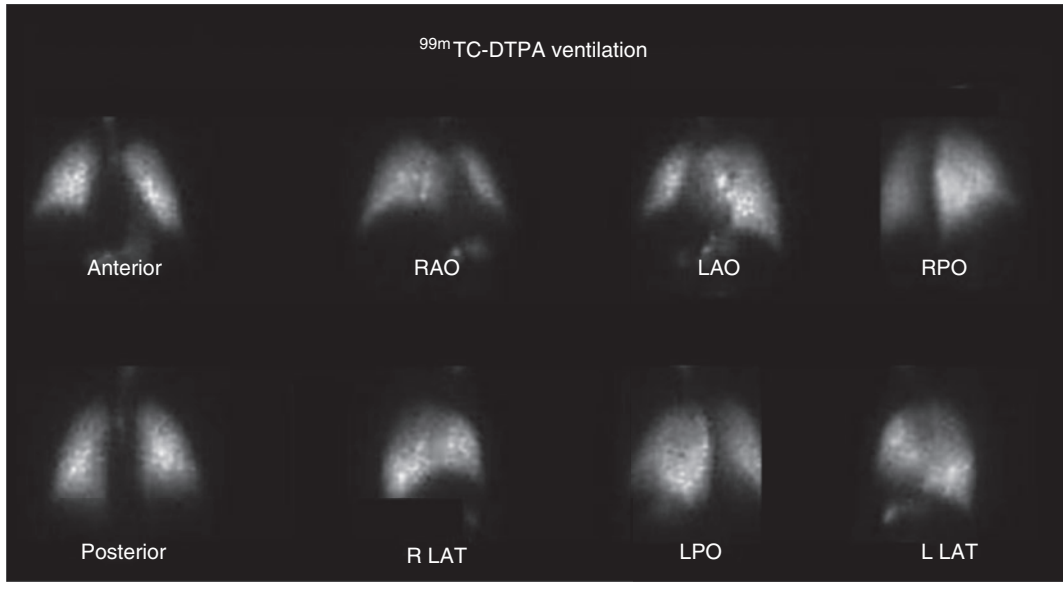

Fig. 8.10 ^{99m}Tc-DTPA aerosol ventilation study. Images show no abnormalities. Observe the activity in the esophagus and stomach due to swallowed activity

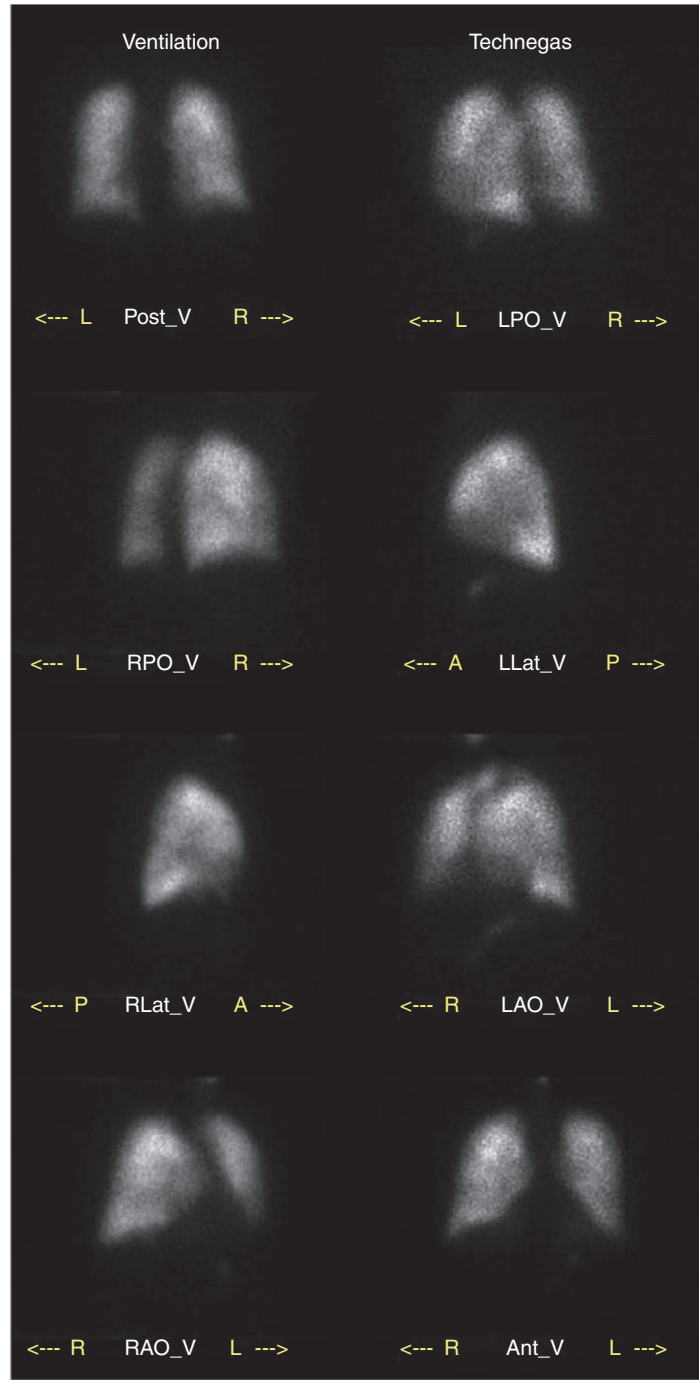

Fig. 8.11 ^{99m}Tc-Technegas ventilation study for a patient suspected of having pulmonary embolism. The study shows no abnormalities and illustrates the good quality of ventilation studies obtained using this agent. The perfusion, on the other hand, reveals perfusion defects in both lungs and no matching ventilation or X-ray abnormalities, indicating a high probability of pulmonary embolism

camera with a low-energy general-purpose collimator. The typical radiation exposure to the lungs is about 100 mrad. This is less than the several hundred milliard exposure from a typical Xe133 rebreathing ventilation exam. The dose to the lungs is also less than that from a Kr-81. Images should be acquired for 100 K counts or 5 min. Exposure to personnel is usually less than that delivered a Xenon study.

Technegas is a ventilation aerosol agent that gained popularity recently. It is ultrafine labeled carbon particles produced by heating ^{99m}Tc-

pertechnetate to very high temperatures of approximately 2500 °C in the presence of 100% argon gas. An ash material is produced that acts like a gas with good peripheral deposition because the particles are so small, with a median size of 0.05–0.15 μm. Technegas has a half-clearance time of 4–6 h. Since the material produced is not filtered and contains up to 50% of the initial radioactivity, a large number of appropriately sized particles are inhaled with each breath. Thus, only a few inspirations (typically 2–10) are needed to reach an adequate dose. Usually about 1 mCi is deposited in the lung. Extrapulmonary activity in the oropharynx, trachea, and stomach can be seen in about 30% of patients. The exam may be technically inadequate in up to 15% of patients particularly in severely ill patients that cannot be instructed for inhalation or in patients with very shallow or rapid breathing. If the Technegas portion of the exam is performed following the perfusion study, a counting rate of at least two times the count rate of the perfusion exam is considered adequate.

Another agent, pertechnegas, which is a vapor of pertechnetate, is prepared similarly but, in the presence of 2–5% oxygen, has a shorter clearance time and shows excellent deposition in the lungs. Table 8.4 summarizes the essential information relevant to its use in obtaining adequate perfusion scan.

Table 8.4 Characteristics of ^{99m}Tc-macroaggregated albumin (^{99m}Tc-MAA)

Size	10–90 μm (mostly 20–50)
Minimum number of particles to be used in adults	100,000 unless pulmonary hypertension or right to left shunt is present
Ideal number of particles	200,000–500,000
Biologic half-life	4–8 h
Injection	Slow intravenous. Care should be taken not to cause particle aggregates that can produce hot spots
Safety	Particles block <1/1000 of the capillaries and precapillary arterioles

Interpretation of V/Q Scan

For proper interpretation of lung perfusion/ventilation study, chest X-ray must be available and should be obtained within 12 h of the time of the scans.

Normal perfusion study (Fig. 8.12) rules out any clinically significant pulmonary emboli. Since the ventilation and perfusion lung scans lack specificity (Table 8.5), probabilities have been used for the interpretation of abnormal studies. Based on the pathophysiological changes and scintigraphic observations, several scintigraphic features of perfusion abnormalities are known to affect the probability of a scan for pulmonary emboli (Table 8.6). One of the important features is the size of segmental perfusion defects. A small defect occupies up to 25% of the segment, a moderate defect between 25 and 75%, while a large defect takes up 75% or more. Using these features, several retrospective and prospective studies were conducted to refine the interpretation of ventilation and perfusion scans and assess their value in managing patients suspected of having embolic disease [67–71]. PIOPED study [32] established the value of normal and high-probability scans in excluding and diagnosing pulmonary embolism. It validated the segment equivalent concept (Fig. 8.13) and clarified the use of Bayesian analysis utilizing the clinical pre-scan and scan probabilities to figure the post-scan or diagnostic probability. The study showed clearly that when the clinical odds agree with the scan probability in the low- and high-probability categories, pulmonary embolism can be ruled out or confirmed with a high degree of certainty.

Based on the modifications of PIOPED criteria and other validated criteria, a simplified set is shown in Table 8.7. Small perfusion defects indicate low probability of pulmonary emboli as well as matching perfusion and ventilation defects regardless of size with no matching X-ray abnormalities (Fig. 8.14). Nonsegmental defects also indicate low probability. When perfusion defects match the X-ray abnormalities, it may indicate low, intermediate, or high probability based on the relative size of perfusion compared to the X-ray densities. When the perfusion defect is of

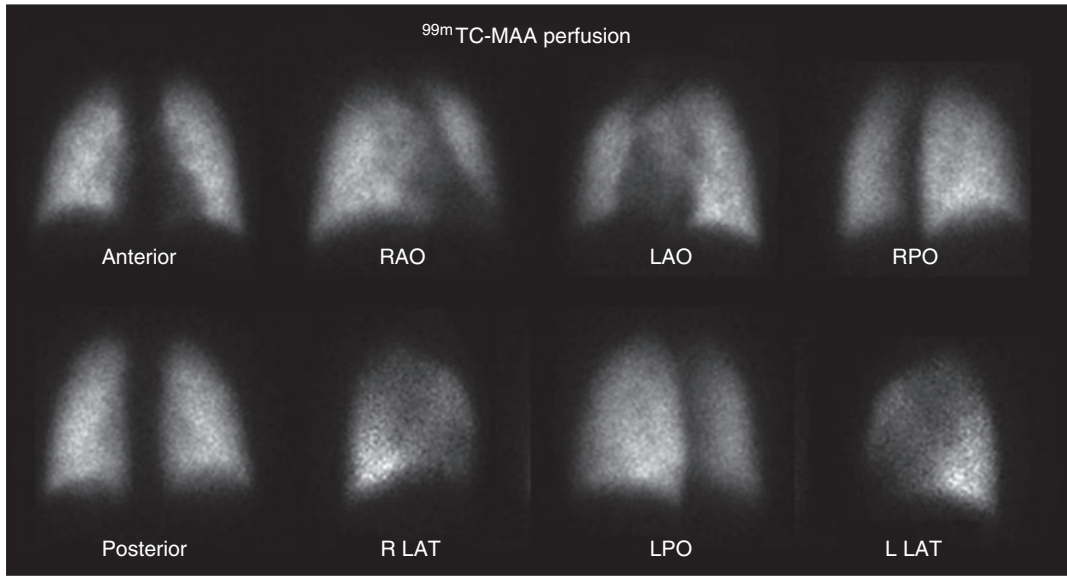

Fig. 8.12 Normal perfusion study. A ^{99m}Tc-MAA perfusion scan of a patient suspected of having pulmonary embolism. The perfusion study reveals uniform perfusion throughout both lungs with no defects. Note the parallel medial borders of both lungs on the posterior view and the sharp delineation of the costophrenic angles

Table 8.5 Causes of abnormal perfusion lung scintigraphy

Emphysema
Inflammatory diseases
Pneumonia
Abscess
Granulomatous disease (sarcoidosis, tuberculosis)
Pulmonary fibrosis
Bronchial obstruction
Infection
Neoplasm
Acute and chronic asthma
Mucus plug
Foreign body
Rib fractures (reduced lung excursion)
Congenital hypoplasia or absence of the pulmonary arteries
Peripheral pulmonary artery stenosis
Thromboembolic disease
Thrombus
Tumor embolism
Fat embolism
Air embolism
Extrinsic vessel compression (tumor, inflammation)
Left ventricular failure
Mitral valve disease
Veno-occlusive disease
Prior lung resection
Radiation

Table 8.6 Features of perfusion defects associated with higher probability of pulmonary emboli

Size	Moderate and large
Larger relative size compared with that of chest X-ray densities	
Location	Pleural-based defects
Lower lobes	
Shape	Wedge shaped
Type	Segmental
Relation to ventilation pattern	Mismatching
Number	Multiple

the same approximate size of the matching X-ray density (Fig. 8.15), it indicates intermediate probability (approximately 25%).

The minimum number of mismatching perfusion defects is two segment equivalent defects with no matching chest X-ray abnormalities to make a high-probability interpretation (Fig. 8.16). However, a study analyzing PIOPED data indicated that defects equivalent of 1.5 segments are indicating high probability among patients with no prior cardiopulmonary diseases [72].

To improve interpretation, SPECT is being used more frequently in V/Q scans. SPECT scintigraphy has been reported to be strongly preferred to V/Q planar as it provides more accurate

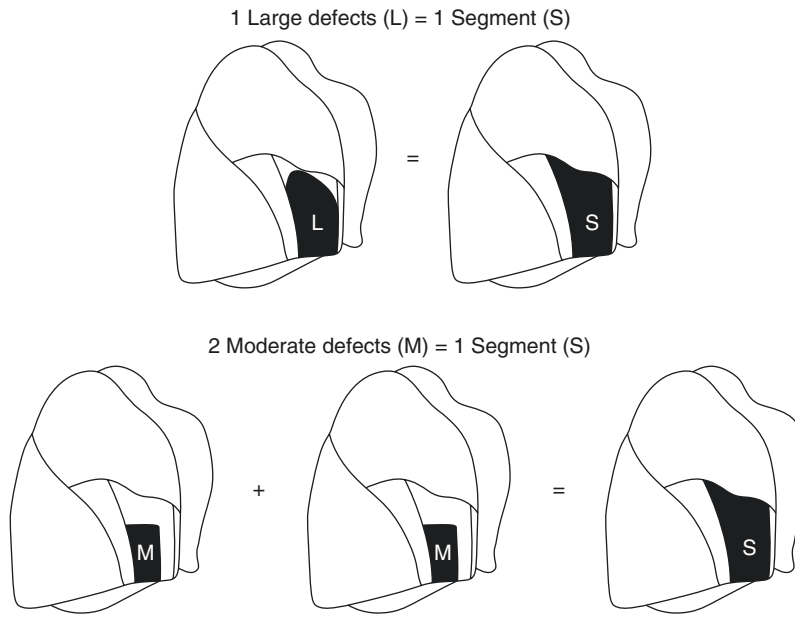

Fig. 8.13 The segment equivalent concept. (From Morpurgo and Schmid [39] with permission)

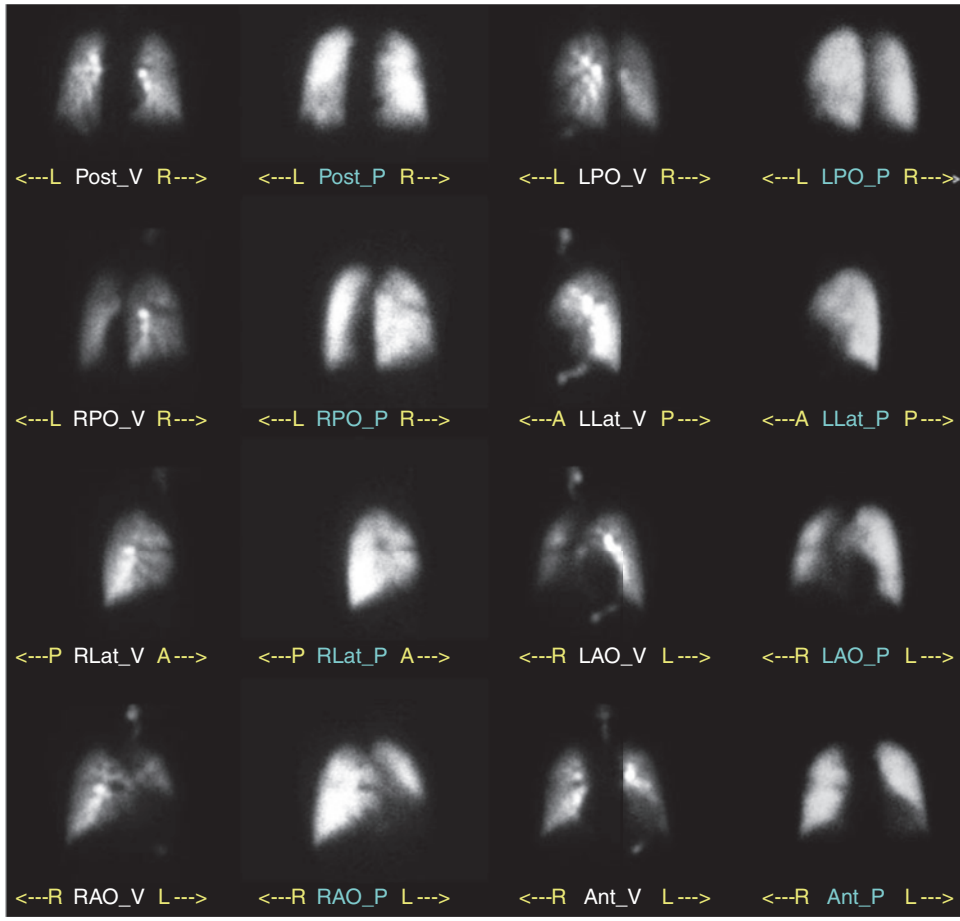

Fig. 8.14 ^{99m}Tc-DTPA aerosol ventilation and ^{99m}Tc-MAA perfusion studies of a patient suspected of having pulmonary embolism. The X-ray was normal. The perfusion study shows multiple small perfusion defects matching the ventilation pattern indicating low probability of pulmonary emboli

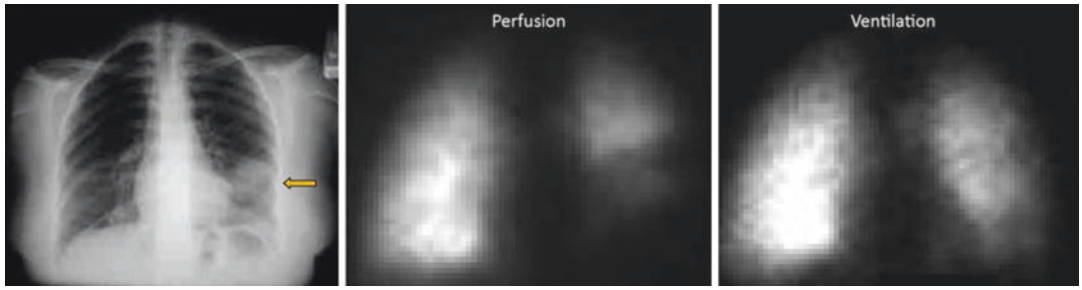

Fig. 8.15 Chest X-ray of a patient referred to rule out pulmonary embolism with a density in the left lower lobe (arrow) matching the perfusion defect on ^{99m}Tc-MAA scan and is of the same approximate size indicating intermediate probability of pulmonary emboli

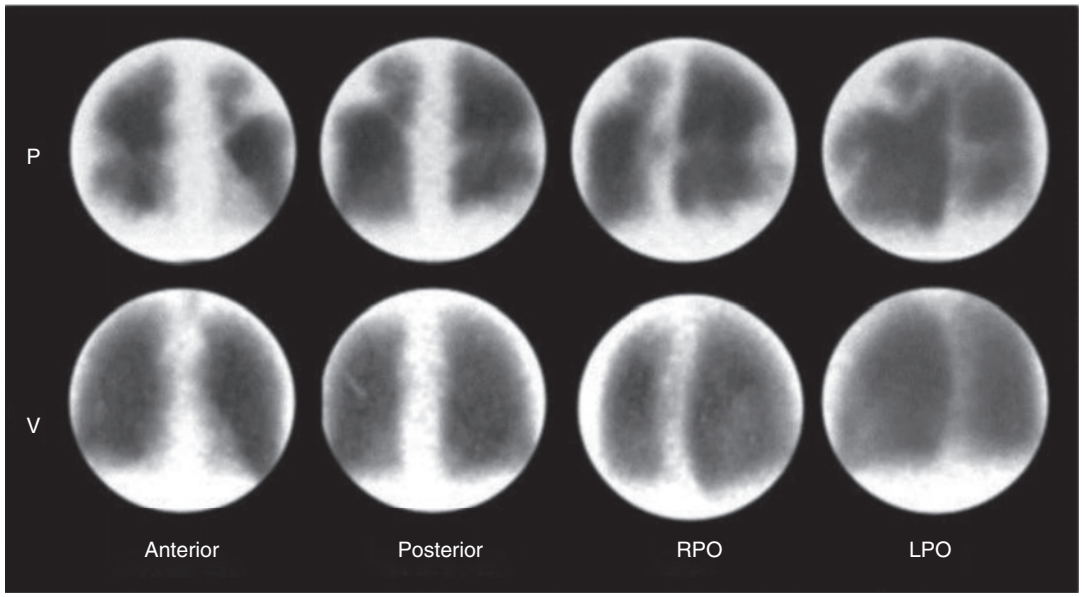

Fig. 8.16 Ventilation and perfusion scans of a 74-year-old man with history of fracture of left femur 3 days earlier treated with internal fixation. Patient was referred to rule out pulmonary emboli because of acute onset of shortening of breath. Perfusion study shows multiple perfusion defects equivalent to more than two segments with no matching abnormalities on ventilation study and no corresponding changes in the chest X-ray which was normal. This illustrates a typical pattern of high probability of pulmonary emboli on ventilation/perfusions scans

diagnosis of PE even in the presence of comorbid diseases such as COPD and pneumonia [64, 65, 73, 74].

Recently, trinary interpretative system for V/Q scans has been proposed and validated in some studies. This system is similar to the interpretative strategy for CT. V/Q scans were interpreted as "PE present," "PE absent," or "nondiagnostic." According to this system, the normal, very low (near normal), and low probabilities are grouped together and reported as PE absent. The high-probability pattern is reported as PE present, while the intermediate patterns are reported as nondiagnostic [75].

This approach can simplify the scan report for the referring physicians since the probability system still causes confusion. This leads to decrease in the utilization of V/Q scans although recent data show increasing evidence that lung scintigraphy is not only safe but also accurate enough to

Table 8.7 Criteria for the interpretation of ventilation/perfusion lung scans

Category	Pattern on V/Q images
Normal	No perfusion defects. Allow for impressions explained by enlarged heart or other hilar structures as seen on chest X-ray
Near normal	Nonuniform uptake with no definite segmental or subsegmental perfusion defects
Low	Nonsegmental perfusion defects other than those explained by cardiomegaly or other prominent hilar structures
	Matching V/Q defects with no corresponding CXR abnormalities
	Any number of only small defects regardless of ventilation and CXR patterns
	Stripe sign
	Perfusion defect substantially smaller than CXR abnormality
High	Two or more large mismatching defects or their equivalent (4 moderate or 1 large plus 2 moderate defects) with no corresponding CXR abnormalities
	Perfusion defect substantially larger than CXR abnormality[a]
Intermediate	Perfusion defect matching chest X-ray abnormality and of the same approximate size.
	Single moderate up to less than two segmental mismatching defects with no corresponding chest X-ray abnormalities
	Difficult to categorize as low or high

[a] 1.5 in patients with no prior cardiopulmonary disease can be considered high probability

be quite useful clinically in patients with suspected PE. It is available conveniently in the clinical setting. Additionally, using the scintigraphic diagnostic strategy results in an important reduction of radiation dose, particularly for the female breast [76].

Many algorithms have been developed to diagnose PE utilizing D-dimer test, echo cardiography, Doppler ultrasound, scintigraphy, and multislice CT. None of these algorithms have gained uniform acceptance, and many variations were found in practice patterns among physicians, geographic locations, available resources, and experience [77].

Till further development, proper utilization of V/Q scans along with the DVT imaging and laboratory tests and CT solves most diagnostic problems and minimizes the need for angiograms (Table 8.7) [78].

8.3 Pulmonary Hypertension

Normal pulmonary artery systolic pressure at rest is 18–25 mmHg, with a mean pulmonary pressure ranging from 12 to 16 mmHg. This low pressure is due to the large cross-sectional area of the pulmonary circulation, which results in low resistance. An increase in pulmonary vascular resistance or pulmonary blood flow results in pulmonary hypertension. It is defined as a pulmonary artery systolic pressure higher than 30 mmHg or a pulmonary artery mean pressure higher than 20 mmHg.

Pulmonary hypertension may have no cause (primary) which is rare or may follow cardiac or pulmonary disorders (secondary). Pathophysiologically, three predominant mechanisms may be involved in the pathogenesis of secondary pulmonary hypertension, (1) hypoxic vasoconstriction, (2) decreased area of the pulmonary vascular bed, and (3) volume/pressure overload.

Chronic hypoxemia such as due to COPD causes pulmonary vasoconstriction by a variety of actions on pulmonary artery endothelium and smooth muscle cells.

A variety of causes may decrease the cross-sectional area of the pulmonary vascular bed, primarily due to disease of the lung parenchyma. Examples of these conditions include collagen vascular diseases particularly systemic scleroderma or CREST (calcinosis cutis, Raynaud phenomenon, esophageal motility disorder, sclerodactyly, and telangiectasia) syndrome and acute and chronic pulmonary emboli [29, 30].

Disorders of the left heart may cause secondary pulmonary hypertension, resulting from volume and pressure overload. Pulmonary blood

volume overload is caused by left-to-right intracardiac shunts, such as in patients with atrial or ventricular septal defects. Left atrial hypertension causes a passive rise in pulmonary arterial systolic pressure in order to maintain a driving force across the vasculature.

8.4 *Pneumocystis carinii* (*jiroveci*) Pneumonia

Pneumocystis carinii (*jiroveci*) is an opportunistic pathogen currently classified as a fungus [79]. It is a significant cause of morbidity and mortality in human immunodeficiency virus and nonhuman immunodeficiency virus-associated immunosuppressed patients [80, 81] although it also occurs in non-immunocompromised patients [82–85]. Highly effective active antiretroviral therapy in industrialized nations however has led to dramatic declines in the incidence of AIDS-associated complications, including PCP, but no decline has occurred in the developing countries [80, 81]. The organism attaches to the alveolar macrophages through a mechanism that involves fibronectin. The trophozoite develops into cysts that produce daughter trophozoites. As the number of organisms increase, the permeability of the alveolar capillary endothelium increases, producing respiratory distress. Typically, infection with *P. carinii* (now called *P. jiroveci*) produces a patchy or lobar interstitial pneumonia or, rarely, a bronchopneumonia pattern. Severe infections produce diffuse alveolar damage. The classical histological findings consist of alveolar exudates having a granular or foamy appearance that represent nonstaining clusters of the cysts and trophozoites of *P. carinii* within an eosinophilic staining background of the organism's filopodia and host cellular debris. Atypical pulmonary reactions include the formation of granulomas, focal pulmonary infection, and cavitary lesions. In extremely immunosuppressed persons, the inflammatory reaction may be minimal and consist only of sparse collections of alveolar macrophages. Since clinical manifestations of *P. carinii* pneumonia (PCP) in AIDS patients may precede X-ray changes by at least 2 weeks and as long as 18 months, ^{67}Ga has an important role in the diagnosis of early PCP. ^{67}Ga is more sensitive than chest X-ray for early PCP and is more accurate in measuring the extent of inflammation. The pattern of uptake is typically diffuse and bilateral (Fig. 8.17), although other patterns may be noted [84, 85]. Localized lung uptake and perihilar uptake patterns can be seen in addition to the diffuse pattern, which may be further classified into homogeneous and heterogeneous diffuse patterns. The heterogeneous pattern has the highest positive predictive value, which is even more specific when it is of high-grade uptake and when accompanied by normal chest radiograph.

8.5 Idiopathic Pulmonary Fibrosis

Idiopathic pulmonary fibrosis is a rare disease characterized by chronic, progressive irreversible interstitial lung fibrosis along with inflammatory changes of unknown cause. Clinically, the condition is often diagnosed at an advanced stage, carry a poor prognosis. The median estimated survival time from the time of diagnosis is 2–5 years. Recently several subtypes have been clearly identified with different outcomes [86, 87]. Idiopathic pulmonary fibrosis is characterized by parenchymal inflammation and interstitial fibrosis that may eventually be fatal. The inciting factors in the development of IPF remain unknown. A widely held hypothesis is that this disorder occurs in susceptible individuals following some unknown stimuli. The inciting agent initiates a cascade of events that involve factors controlling inflammatory, immune, and fibrotic processes in the lung. Viral, immunological, and genetic (supported by finding familial cases) factors appear to play an important role [87]. The main feature in IPF is alveolitis, which is chronic inflammation of the alveolar unit followed by fibrosis. The destruction is mediated by inflammatory (neutrophils and macrophages) and immune (immune complex disease) processes, where immune effector cells injure lung cells and induce connective tissue proliferation. The chronic active inflammation is important and

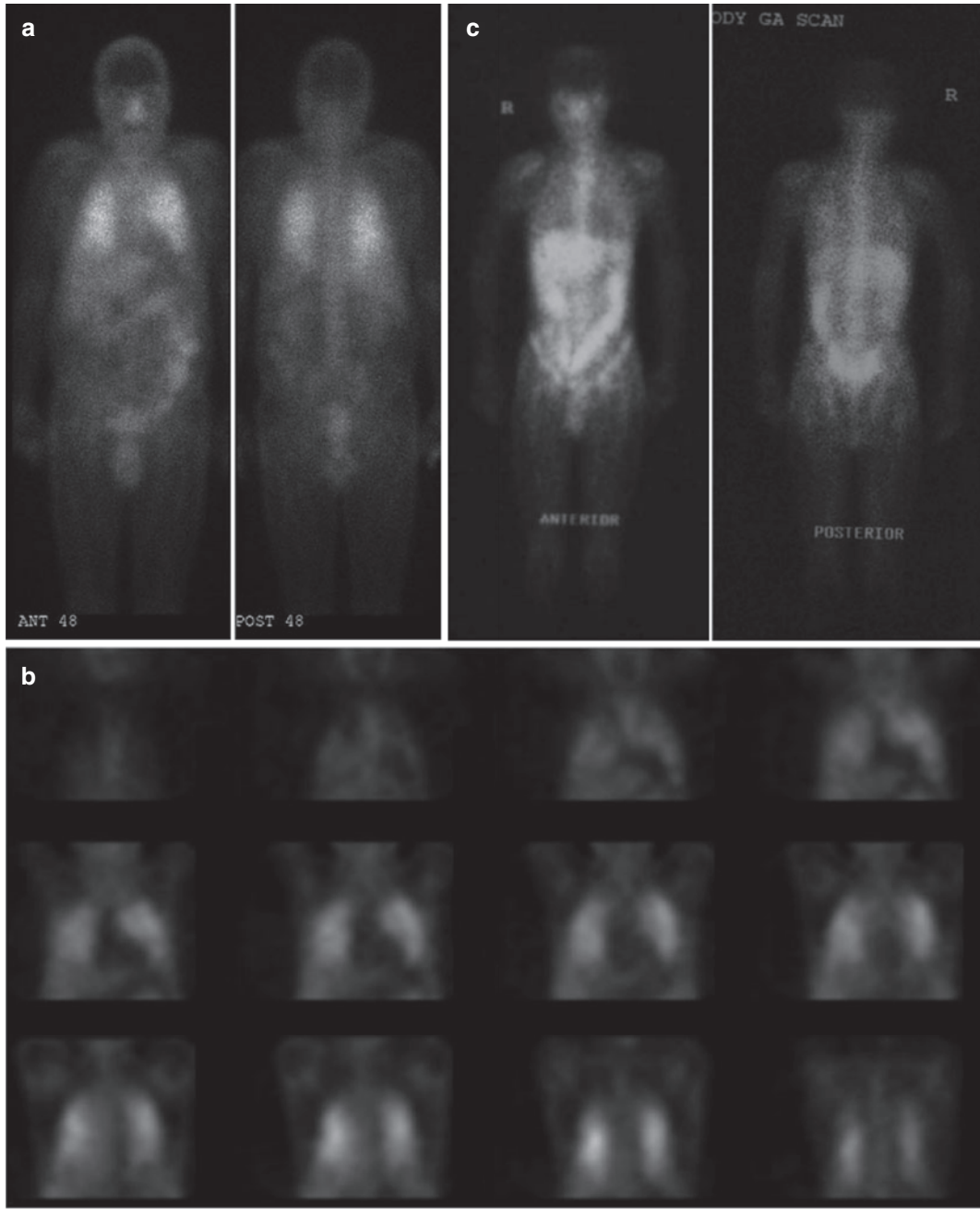

Fig. 8.17 (**a**–**c**) Gallium-67 images of two AIDS patients with PCP obtained 48 h post-injection. Planar (**a**) and SPECT (**b**) of one patient show significantly increased accumulation of the radiotracer illustrating severe infection. Planar image of the other patient (**c**) shows slightly increased accumulation of the radiotracer in both lungs diffusely illustrating mild form of PCP infection

directs the investigations for diagnosis. The fibrotic and destructive changes distort the normal lung architecture and result in morbidity.

The major histopathological findings vary from active alveolitis and minimal fibrosis in early cases to severe fibrosis and honeycombing with minimal alveolitis in late stages. The alveolitis is characterized by an outpouring of mononuclear cells, macrophages, and lymphocytes into the alveolar space, with relatively intact alveolar walls which will be deranged by edema, fibrinous exudate, mononuclear cell infiltration, and fibroblast proliferation [86]. Connective tissue alteration occurs later in the process. Recent classification of the type of fibrosis depends on the predominant cell type. Patients with more cellular findings respond to treatment favorably and have a better long-term prognosis compared with those with more fibrotic changes. ^{67}Ga has an important role in evaluating the activity of the disease and in following up the response to treatment. The degree of ^{67}Ga uptake correlates with the degree of interstitial and alveolar cellularity as seen on lung biopsies. Accordingly, it helps evaluate the extent and activity of the disease by visual assessment and/or quantitation of the uptake [88].

8.6 Pulmonary Sarcoidosis

Sarcoidosis, a multisystem granulomatous disorder, occurs most commonly in young adults, more commonly in blacks and in temperate areas. A second peak is known to occur in older age group (over age 60) [89]. The exact etiology of the disease is unknown, but it is believed to be due to exaggerated cellular immune response on the part of helper/inducer T lymphocytes to exogenous or autoantigens. It presents most frequently as bilateral hilar adenopathy, pulmonary infiltrates, and skin and eye lesions. It may be acute or chronic. Current evidence points to genetic predisposition and exposure to yet unknown transmissible agent(s) and/or environmental factors as etiological agents. Recently it has been recognized to be a Th1 mediated disease as it is dominated by gene signatures associated with IFNȳ signaling [90, 91].

The acute variant has an abrupt onset and may commonly show spontaneous remission within 2 years; the response to steroids is excellent. The chronic variant has an insidious onset and is more likely to cause progressive disease with fibrosis. The disorder is characterized by the presence of epithelioid (correct spelling) granuloma in affected organs that may lead to fibrosis and organ dysfunction. Granulomas of sarcoidosis often exist diffusely throughout the body despite the lack of clinical evidence of disease. Histological features are usually quite typical, but not specific. The architecture of the lesion is that of multiple similar granulomas, consisting of whorls of elongated cells (fibroblasts and epithelioid cells) with mononuclear inflammatory cells at their periphery. Giant cells are located within the granulomas (Fig. 8.18), and multinucleated cellular inclusion bodies are frequently found. Scarring with fibrosis suggests chronicity. Epithelioid cells secrete a number of cytokines and other mediators including angiotensin-converting enzyme (ACE) which is suggested to reflect the granuloma burden in sarcoidosis and may play a role in its pathophysiology. Lung is involved in more than 90% of cases. Pulmonary sarcoidosis starts as diffuse interstitial alveolitis, followed by the characteristic granulomas. Granulomas are present in the alve-

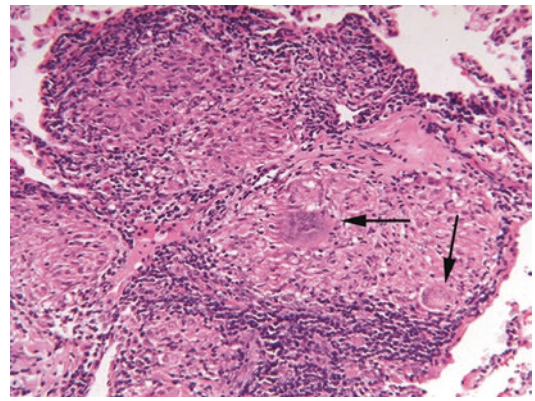

Fig. 8.18 Microphotograph of a noncaseating granuloma of a case of sarcoidosis. Note multinucleated giant cells (*arrows*)

olar septa as well as in the walls of the bronchi and pulmonary arteries and veins. The center of the granuloma contains epithelioid cells derived from mononuclear phagocytes, multinucleated giant cells, and macrophages. Lymphocytes, macrophages, monocytes, and fibroblasts are present at the periphery of the granuloma [92]. Sarcoidosis represents a challenge to clinical investigation because of its unpredictable course, uncertain response to therapy, and diversity of potential organ involvement and clinical presentations [93].

The diagnosis is based on a compatible clinical and/or radiologic picture, histopathological evidence of noncaseating granulomas in tissue biopsy specimens, and exclusion of other diseases capable of producing similar clinical or histopathological appearances [59]. Patients with pulmonary sarcoidosis may have no symptoms and are discovered by chest X-ray obtained for nonpulmonary reasons. When symptomatic, dyspnea, chest pain, and cough are the most common chest symptoms [93]. For many years, pulmonary sarcoidosis has been staged into four stages (Table 8.8) based on chest X-ray findings [94]. The distinction between sarcoidosis and tuberculosis can be difficult at times, and the two diseases may coexist in the same patient. Similar granulomas may occur in a wide variety of other diseases, such as with malignancy or immune deficiencies, berylliosis, and foreign body reactions. ^{67}Ga is useful in evaluating the activity of the disease and the response to therapy. Semiquantitative and quantitative methods of grading ^{67}Ga uptake can be helpful. Diffuse lung uptake and bilateral hilar uptake (Fig. 8.19) are the most common patterns seen, but they lack specificity [94]. The major value of ^{67}Ga is in evaluating the activity of the disease, in detecting extrathoracic sites of involvement, and in evaluating the response to therapy. Ventilation and perfusion scans do not have a specific role in sarcoidosis. However, it should be known that a mismatching pattern is among those seen in the disease and can be falsely interpreted as indicating a high probability of pulmonary emboli.

Table 8.8 Radiologic staging of pulmonary sarcoidosis

Stage 1	Hilar adenopathy alone
Stage 2	Adenopathy plus infiltrates
Stage 3	Infiltrates only
Stage 4	Fibrosis

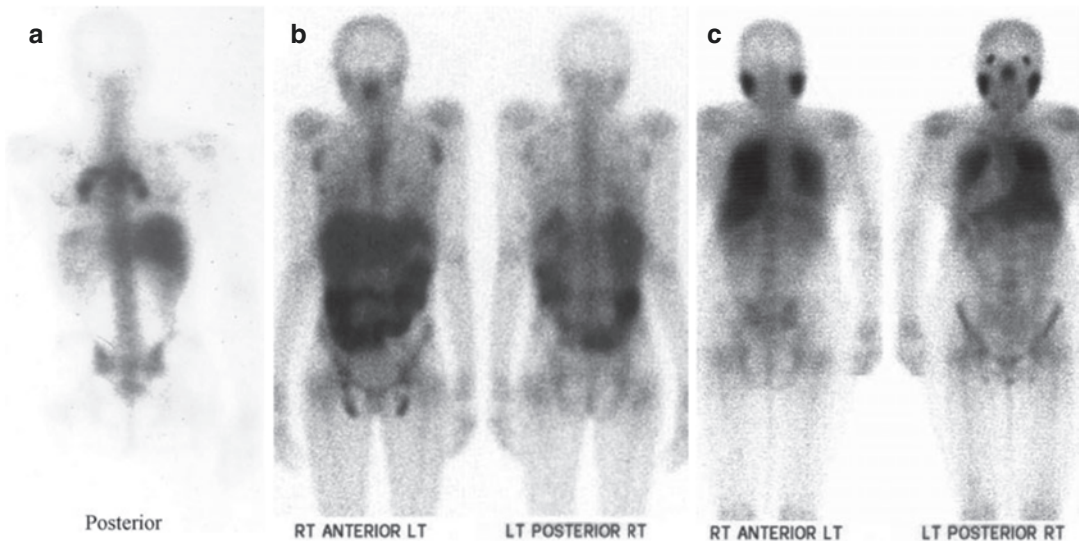

Fig. 8.19 Forty-eight-hour Ga-67 posterior image of a patient with sarcoidosis showing uptake in the hilar nodes bilaterally (**a**). Another patient's study is shown (**b**) Ga-67 images for a patient with sarcoidosis illustrating uptake in the axillary and inguinal lymph nodes as we as mild diffuse accumulation in the lungs and (**c**) a patient with diffuse lung uptake and intense uptake in the parotids and lacrimal gland

FDG uptake in sarcoidosis (Fig. 8.20) is nonspecific in both intensity and pattern and is not generally useful in making an initial diagnosis. FDG uptake can decrease when sarcoidosis is treated, and PET can be useful in monitoring the effectiveness of therapy. Accordingly, PET/CT can be useful in monitoring disease progression or remission [95].

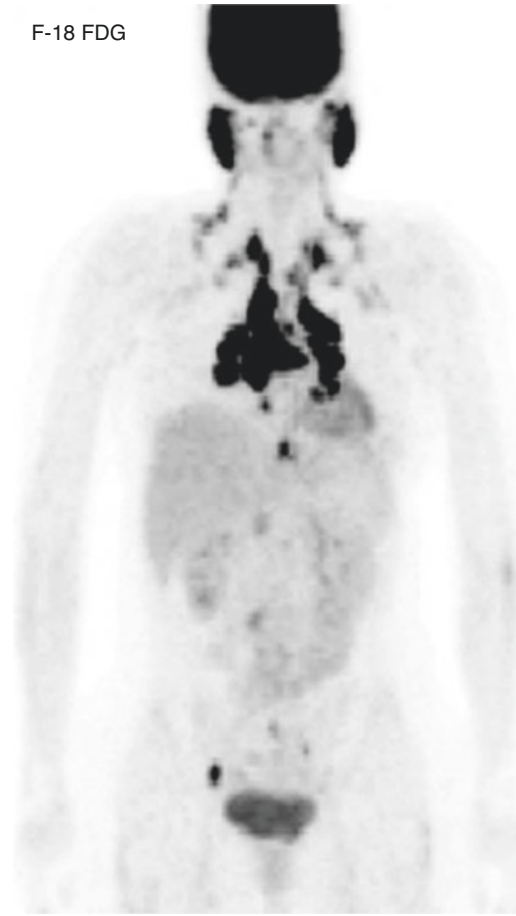

Fig. 8.20 F-18 FDG image of a 35-year-old female with proven sarcoidosis. The study shows uptake in the areas of active inflammation in mediastinum, pulmonary hilus, salivary glands, and cervical, supraclavicular, axillary, para-aortic, iliac, and inguinal lymph nodes. (Courtesy of Professor Osama Sabry)

8.7 Obstructive Airway Disease

Chronic bronchitis, emphysema, and bronchial asthma are collectively known as obstructive airway disease. Chronic bronchitis and emphysema are common among smokers but are also caused by air pollutants. In chronic bronchitis, the walls of the bronchi and bronchioles are inflamed with edema, cellular infiltrates, fibrosis, and an increase in the mucus glands and bronchial secretions and thickening of the bronchial walls. All these changes result in progressive narrowing of the lumina of the bronchi and bronchioles.

Emphysema indicates irreversible dilation of the alveoli, and destruction of their septa can occur alone or, commonly, in association with chronic bronchitis as part of chronic obstructive airway disease. Hyperinflation of the alveoli and septal destruction may lead to formation of large air spaces (bullae). Air spaces formed adjacent to the pleura are called blebs. There are three types of emphysema:

1. In centrilobular emphysema, the central areas of the lungs are affected by alveolar dilation. This type is most commonly associated with chronic bronchitis in smokers. It affects more the upper lobes and usually spares the alveoli.
2. Panlobular emphysema involves an entire lobule with randomly distributed damage. It involves more the lower lobes of the lungs, older individuals, and patients with alpha 1 antitrypsin deficiency.
3. Localized (previously paraseptal) emphysema is characterized by emphysematous changes in only one or at most a few locations, with the remainder of the lung normal. It is usually of no clinical significance; however, the rather common subpleural bullae may rupture and cause spontaneous pneumothorax.

Bronchial asthma is characterized by episodes of airflow obstruction, which affect both large and small airways. Decreased ventilation and perfusion can be seen on ventilation and perfusion scans within moments of the asthma attack.

Obstructive airway disease can cause an abnormal ventilation scan with or without abnormal perfusion. Xenon-133 is the most sensitive agent for detecting the ventilation abnormalities, particularly in the washout phase. ^{99m}Tc-DTPA aerosol

studies show nonuniformity with varying degrees of central deposition of the particles, depending on the severity of bronchial narrowing (Fig. 8.21). The associated perfusion abnormalities range from minimal nonuniformity to complete absence of perfusion, matching the ventilation defects. Obstructive airway disease is commonly seen among patients suspected of having pulmonary emboli. This may pose difficulty in interpreting the ventilation and perfusion images to establish whether a matching pattern is present [96], but the same criteria of interpretation are applied to determine the probability of pulmonary emboli as in patients with no obstructive airway disease.

8.8 Pleural Effusions

Many etiologies can cause pleural effusion, including inflammatory, traumatic, and neoplastic diseases, and disturbance in organ functions. Pulmonary embolism is not uncommonly associated with pleural effusion. Based on the underlying cause, pleural effusion may consist of transudate, exudate, pus, or blood. With pleural effusions, there is diminished ventilation and perfusion, which is proportional to the amount of effusion [97]. Elevated hemidiaphragm causes a similar pattern. The appearance of pleural effusion may change with the position of the patient

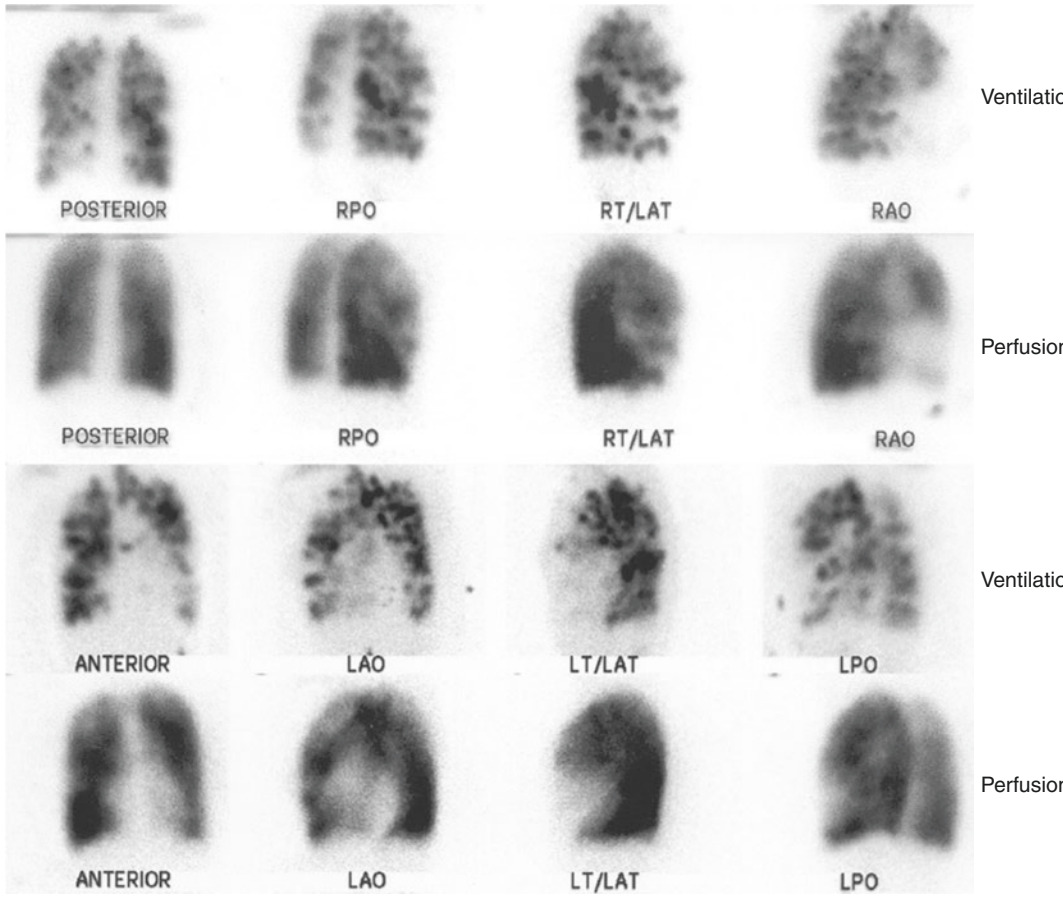

Fig. 8.21 ^{99m}Tc-DTPA aerosol image of a patient with severe obstructive airway disease. Note the central deposition of the radiotracer at the sites of the narrowed openings of the bronchi and bronchioles

when effusion is freely mobile or may not change when the effusion is loculated or encapsulated.

8.9 Pneumonia

Pneumonia is an acute inflammation of the lung parenchyma, which often impairs gas exchange. The condition is prevalent in infants, old individuals, and immunocompromised patients. It is the leading secondary cause of death in the USA. Three major types can be recognized: lobar, lobular (bronchopneumonia), and interstitial. Lobar pneumonia is usually bacterial and involves the alveoli of one lobe or more, but not the bronchi. Chest X-ray and other imaging modalities show varying degrees of abnormalities based on the amount of inflammatory exudate. X-ray will show opacities of different degrees, while nuclear medicine procedures such as labeled WBC or ^{67}Ga (Fig. 8.22) show abnormalities correlating in size and intensity with the severity of inflammation and its duration (see Chap. 4). Lobular pneumonia (bronchopneumonia) shows inflammation of bronchi, bronchioles, and alveoli in a patchy manner. Interstitial pneumonia, also called pneumonitis or viral pneumonia, is a milder form that usually accompanies other viral conditions such as measles. Typically, no exudates are present in the alveoli.

8.10 Bronchial Obstruction

Bronchial obstruction may be caused by obstruction from within or from outside the bronchi. It may be acute, such as obstruction due to a foreign body or mucus plug, or gradual, as in some patients with bronchial compression by an adjacent mass. Depending on the level and severity of obstruction, the ventilation and perfusion are affected. Usually the ventilation is affected more severely than the perfusion and may be totally absent with complete obstruction (Fig. 8.23).

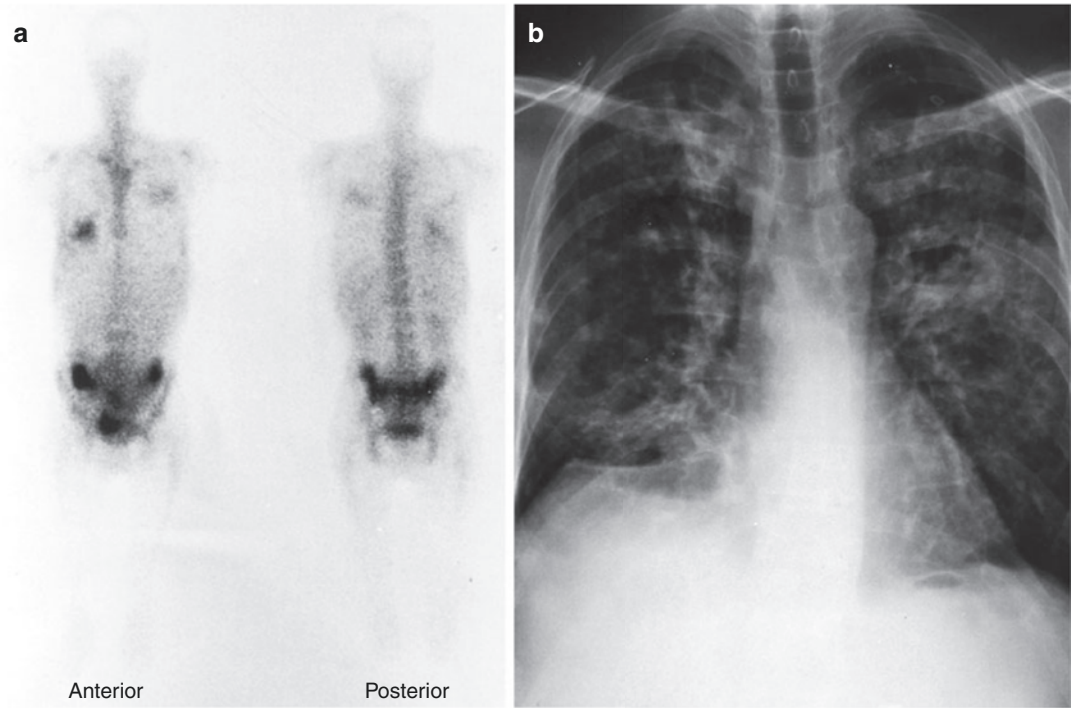

Fig. 8.22 Gallium-67 48-h study (**a**) shows two areas of increased accumulation of the radiotracer in the right lower and left mid lung zones in a patient with pneumonia. Chest X-ray (**b**) of the same patient shows infiltrates

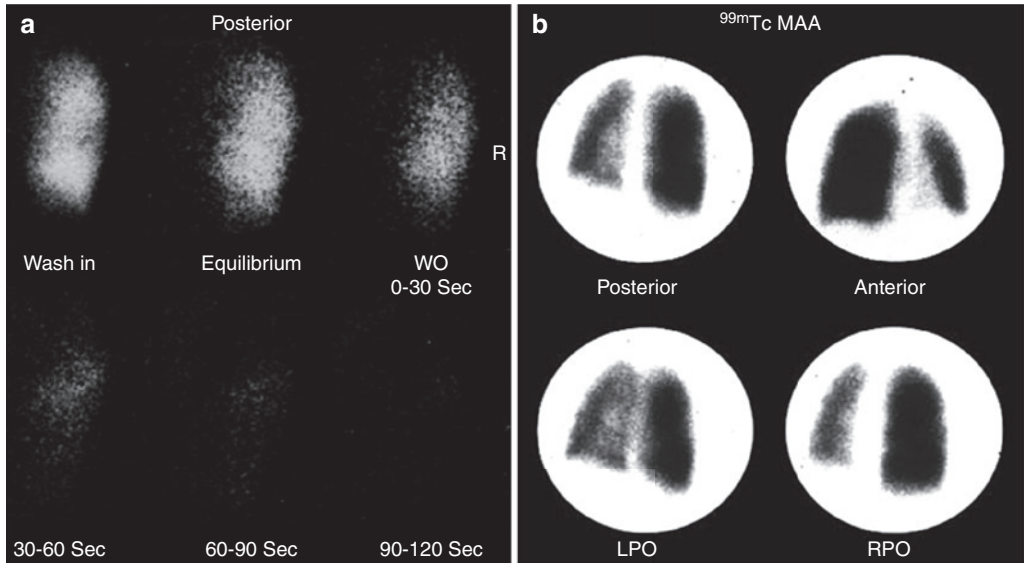

Fig. 8.23 (**a**, **b**) Xenon-133 washout images of a patient complaining of severe shortness of breath. The images reveal nonvisualized left lung. ^{99m}Tc-MAA perfusion study of the same patient shows decreased perfusion to same lung diffusely. This pattern suggests bronchial obstruction with reflex vasoconstriction. The patient has a mucus plug obstructing the left main bronchus

8.11 Lung Cancer (See Chap. 12)

Lung cancer is the second most common cancer in both men and women (second to prostate and breast cancers). It is, however, the leading cause of cancer death in both men and women [98].

FDG-PET/CT is useful for imaging lung cancer since the tumor cells have both an increased uptake of glucose due to a higher number of Glut-1 surface proteins as well as a higher rate of glycolysis compared to nonneoplastic cells [99].

Histologically, lung cancer may be squamous (epidermoid), adenocarcinoma (bronchogenic carcinoma), small cell carcinoma, adenosquamous carcinoma, and anaplastic carcinoma. The role of nuclear medicine particularly PET/CT (Fig. 8.24) lies in the detection of the primary tumor in some patients, and more importantly staging of the tumor determines the best treatment choice, evaluating the response to therapy and sometimes predicting its success [100] (see Chap. 10). When pneumonectomy is planned for lung cancer, postoperative lung function can be predicted with optimal accuracy by a preoperative perfusion scan in the upright or supine positions. The ventilation scan is less accurate [101].

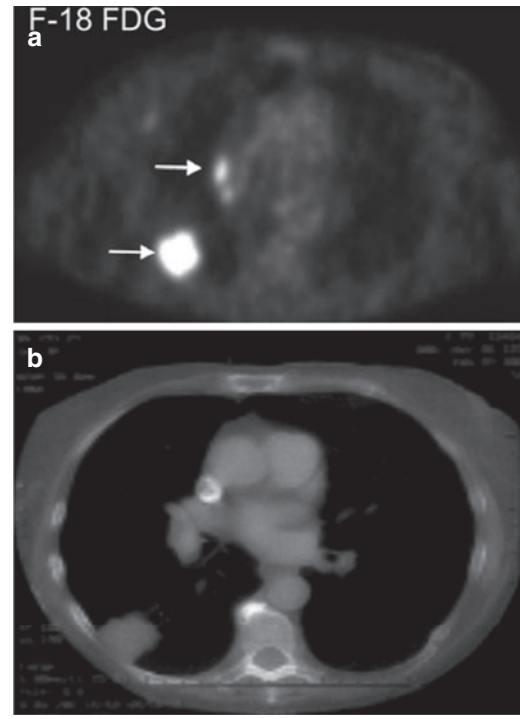

Fig. 8.24 (**a**, **b**) FDG-PET study illustrating right lung nodule with intense uptake and a mediastinal involvement (*arrows*) corresponding to lesions seen on CT scan. These represent non-small cell lung cancer. The example demonstrates the value of FDG in determining the nature of morphologic findings of nodules and in staging the disease

When pneumonectomy is planned for lung cancer, postoperative lung function can be predicted with optimal accuracy by a preoperative perfusion scan in the upright or supine positions. The ventilation scan is less accurate.

References

1. Brashers BL, Davey SS (1998) Structure and function of the pulmonary system. In: McCance KL, Huether SE (eds) Pathophysiology, the biologic basis for disease in adults and children, 3rd edn. Mosby, St Louis, pp 1131–1157
2. Thibodeau GA, Patton KI (1996) Anatomy and physiology, 3rd edn. Mosby, St Louis
3. De Nardo GL, De Nardo SJ (1984) Thelungs. In: Freeman LM, Johnson PM (eds) Clinical radionuclide imaging, 3rd edn. Grune and Stratton, Orlando, pp 1051–1139
4. Elgazzar AH (1997) Scintigraphic diagnosis of pulmonary embolism: unraveling the confusion seven years after PIOPED. In: Nuclear medicine annual. Lippincott, Raven, pp 69–101
5. Raskob GE, Angchaisuksiri P, Blanco AN, Buller H, Gallus A, Hunt BJ, Hylek EM, Kakkar A, Konstantinides SV, McCumber M, Ozaki Y, Wendelboe A, Weitz JI (2014) Thrombosis: a major contributor to global disease burden. Arterioscler Thromb Vasc Biol 34:23632371
6. Anderson FA Jr, Zayaruzny M, Heit JA, Fidan D, Cohen AT (2007) Estimated annual numbers of US acute-care hospital patients at risk for venous thromboembolism. Am J Hematol 82:777–782
7. Turetz M, Sideris AT, Friedman OA, Triphathi N, Horowitz JM (2018) Pulmonary embolism: epidemiology, pathophysiology, and natural history of pulmonary embolism. In: Seminars in interventional radiology, vol 35, No. 2. Thieme Medical Publishers, New York, p 92
8. Kucher N, Tapson VF, Goldhaber SZ, DVT FREE Steering Committee (2005) Risk factors associated with symptomatic pulmonary embolism in a large cohort of deep vein thrombosis patients. Thromb Haemost 93:494–498. https://doi.org/10.1160/TH04-09-0587. PMID: 15735800
9. Stein PD, Matta F, Musani MH, Diaczok B (2010) Silent pulmonary embolism in patients with deep venous thrombosis: a systematic review. Am J Med 123(5):426–431
10. Frieman DG, Suyemoto J, Wessler S (1965) Frequency of pulmonary thromboembolism in man. N Engl J Med 272:1278–1280
11. McLachlin J, Patterson JC (1961) Some basic observations on venous thrombosis and pulmonary embolism. Surg Gynecol Obstet 93:1–8
12. Moser KM (1990) Venous thromboembolism: state-of-the-art. Am Rev Respir Dis 141:235–249
13. Muñoz FJ, Mismetti P, Poggio R et al (2008) Clinical outcome of patients with upper-extremity deep vein thrombosis: results from the RIETE Registry. Chest 133(1):143–148
14. Palevsky HI, Alavi A (1991) Noninvasive strategy for management of patients suspected of pulmonary embolism. Semin Nucl Med 21:325–331
15. Miesbach W, Makris M (2020) COVID-19: coagulopathy, risk of thrombosis, and the rationale for anticoagulation. Clin Appl Thromb Hemost 26:1076029620938149. https://doi.org/10.1177/1076029620938149. PMID: 32677459; PMCID: PMC7370334
16. Kipshidze N, Dangas G, White CJ, Kipshidze N, Siddiqui F, Lattimer CR, Carter CA, Fareed J (2020) Viral coagulopathy in patients with COVID-19: treatment and care. Clin Appl Thromb Hemost 26:1076029620936776. https://doi.org/10.1177/1076029620936776
17. Salabei JS, , Fishman TJ, Asnake ZT, Ali A, Iyer UG, et al (2021). COVID-19 coagulopathy: current knowledge and guidelines on anticoagulation. Heart Lung; 50: 357–360
18. Colling ME, Kanthi Y (2020) COVID-19-associated coagulopathy: an exploration of mechanisms. Vasc Med 25:471–478
19. Malas MB, Naazie IN, Elsayed N, Mathlouthi A, Marmor R, Clary B (2020) Thromboembolism risk of COVID-19 is high and associated with a higher risk of mortality: a systematic review and meta-analysis. EClinicalMedicine 29–30:100639
20. Akel T, Qaqa F, Abuarqoub A, Shamoon F (2020) Pulmonary embolism: a complication of COVID 19 infection. Thromb Res 193:79–82
21. Bělohlávek J, Dytrych V, Linhart A (2013) Pulmonary embolism, part I: epidemiology, risk factors and risk stratification, pathophysiology, clinical presentation, diagnosis and nonthrombotic pulmonary embolism. Exp Clin Cardiol 18(2):129–138
22. Kamel E, Mckee T, Calcagni M, Schmidt S, Markl S, Bischof Delaloye A (2005) Occult lung infarction may induce false interpretation of F19 FDG PET in primary staging of pulmonary malignancies. Eur J Nucl Med Mol Imaging 32:641–646
23. Manny J, Hechtman HB (1985) Vasoactive humoral factors. In: Goldhaber SZ (ed) Pulmonary embolism and deep venous thrombosis. Saunders, Philadelphia, p 283
24. Dass H, Hcekscher T, Anthonisen NR (1967) Regional pulmonary gas exchange in patients with pulmonary embolism. Clin Sci 33:355–364
25. Smith R, Alderson PO (1987) Ventilation perfusion scintigraphy in pulmonary embolism in pulmonary nuclear medicine. In: Loken MK (ed) Pulmonary nuclear medicine. Appleton and Lange, Norwalk, pp 51–79
26. Wolfe MW, Skibo LK, Goldhaber SZ (1993) Pulmonary embolic disease: diagnosis, pathophysiologic aspects and treatment with thrombolytic therapy. Curr Probl Cardiol XVIII:587–633

27. National Heart, Lung and Blood Institute (1970) Urokinase pulmonary embolism trial – phase I results. JAMA 214:2163–2172
28. National Heart, Lung and Blood Institute (1974) Urokinase pulmonary embolism trial – phase II results. JAMA 229:1606–1613
29. Elgazzar AH, Jobalia R, Subramanian P, Ryan J, Hughes JA (1994) Multiple ventilation and perfusion (V/Q) scans in patients with and without pulmonary emboli (PE). J Nucl Med 35:239
30. Klok FA, Mos IC, van Kralingen KW, Vahl JE, Huisman MV (2012) Chronic pulmonary embolism and pulmonary hypertension. Semin Respir Crit Care Med 33:199–204
31. Hoeper MM, Mayer E, Simonneau G, Rubin LJ (2006) Chronic thromboembolic pulmonary hypertension. Circulation 110:2011–2020
32. PIOPED Investigators (1990) Value of the ventilation/perfusion scan in acute pulmonary embolism: results of the prospective investigation of pulmonary embolism diagnosis (PIOPED). JAMA 263:2753–2759
33. Carson JL, Kelley MA, Duff A, Weg JG, Fulkerson WJ, Palevsky HI, Schwartz JS, Thompson BT, Popovich J Jr, Hobbins TE et al (1992) The clinical course of pulmonary embolism. N Engl J Med 326:1240–1245
34. Schober B (1980) Do pulmonary emboli lodge preferentially in prior foci? J Nucl Med 21:659–661
35. Hoffman JM, Lee A, Grafton S, Bellamy P, Hawkins RA, Webner M (1994) Clinical signs and symptoms in pulmonary embolism. A reassessment. Clin Nucl Med 19:803–808
36. Stein PD, Terrin ML, Hales CA, Palevsky HI, Saltzman HA, Thompson BT, Weg JG (1991) Clinical, laboratory, roentgenographic, and electrocardiographic findings in patients with acute pulmonary embolism and no pre-existing cardiac or pulmonary disease. Chest 100:598–603
37. Stein PD, Henry JW (1997) Prevalence of acute pulmonary embolism in central and subsegmental pulmonary arteries and relation to probability interpretation of ventilation/perfusion lung scans. Chest 111:1246–1248
38. Morgenthaler TI, Ryu JH (1995) Clinical characteristics of fatal pulmonary embolism in a referral hospital. Mayo Clin Proc 70:417–424
39. Morpurgo M, Schmid C (1995) The spectrum of pulmonary embolism. Clinicopathologic correlations. Chest 107:18S–20S
40. Sperry KL, Key CR, Anderson RE (1990) Towards a population-based assessment of death due to pulmonary embolism in New Mexico. Hum Pathol 21:159–165
41. Karwinski B, Svendsen E (1989) Comparison of clinical and postmortem diagnosis of pulmonary embolism. J Clin Pathol 42:135–139
42. Gross JS, Neufeld RR, Libow LS, Gerber I, Rodstein M (1988) Autopsy study of the elderly institutionalized patient: review of 234 autopsies. Arch Intern Med 1:173–176
43. Dismuke SE, Wagner EH (1986) Pulmonary embolism as a cause of death. JAMA 225:2039–2042
44. Goldhaber SZ, Hennekens CH, Evans DA, Newton EC, Goldleski JJ (1982) Factors associated with correct antemortem diagnosis of major pulmonary embolism. Am J Med 73:822–826
45. Rubio-Jurado B, Albores-Arguijo RC, Guerra-Soto A, Plasencia-Ortiz T, Tavarez-Macías G, Huerta-Hernández J et al (2020) Concordance between clinical diagnosis of pulmonary thromboembolism at hospital discharge and anatomopathological diagnosis. Int J Immunopathol Pharmacol 34:2058738420942390
46. Timmons S, Kingston M, Hussain M, Kelly H, Liston R (2003) Pulmonary embolism: differences in presentation between older and younger patients. Age Ageing 32:601–605
47. Berman AR, Arnsten JH (2003) Diagnosis and treatment of pulmonary embolism in the elderly. Clin Geriatr Med 19:157–175
48. Paraskos JA, Adelstein SJ, Smith RE, Rickman FD, Grossman W, Dexter L, Dalen JE (1973) Late prognosis of acute pulmonary embolism. N Engl J Med 239:55–58
49. Stein PD, Athanasoulis C, Alavi A, Greenspan RH, Hales CA, Saltzman HA, Vreim CE, Terrin ML, Weg JG (1992) Complications and validity of pulmonary angiography in acute pulmonary embolism. Circulation 85:462–468
50. Righini M, Le Gal G, De Lucia S, Roy PM, Meyer G, Aujesky D, Bounameaux H, Perrier A (2006) Clinical usefulness of D-dimer testing in cancer patients with suspected pulmonary embolism. Thromb Haemost 95:715719
51. Douma RA, Mos IC, Erkens PM, Nizet TA, Durian MF et al (2011) Performance of 4 clinical decision rules in the diagnostic management of acute pulmonary embolism: a prospective cohort study. Ann Intern Med 154:709718
52. Miron MJ, Perrier A, Bounameaux H, de Moerloose P, Slosman DO, Didier D, Junod A (1999) Contribution of noninvasive evaluation to the diagnosis of pulmonary embolism in hospitalized patients. Eur Respir J 13:13651370
53. Chabloz P, Reber G, Boehlen F, Hohlfeld P, De Moerloose P (2001) TAFI antigen and D-dimer levels during normal pregnancy and at delivery. Br J Haematol 115(1):150–152
54. Bajc M, Schümichen C, Grüning T, Lindqvist A, Le Roux PY, Alatri A et al (2019) EANM guideline for ventilation/perfusion single-photon emission computed tomography (SPECT) for diagnosis of pulmonary embolism and beyond. Eur J Nucl Med Mol Imaging 46(12):2429–2451
55. Schoepf UJ, Goldhaber SZ, Costello P (2004) Spiral computed tomography for acute pulmonary embolism. Circulation 109:2160–2167

56. Radan L, Mor M, Gips S, Schlang-Eisenberg D, Lurie Y, Dickstein K, Bitterman H, Ben-Haim S (2004) The added value of spiral computed tomographic angiography after lung scintigraphy for the diagnosis of pulmonary embolism. Clin Nucl Med 29:255–261
57. Wiener RS, Schwartz LM, Woloshin S (2013) When a test is too good: how CT pulmonary angiograms find pulmonary emboli that do not need to be found. BMJ 347:3368
58. Aviram G, Levy G, Fishman JE, Blank A, Graif M (2004) Pitfalls in the diagnosis of acute pulmonary embolism on spiral computed tomography. Curr Probl Diagn Radiol 33:74–84
59. Perrier A (2001) Pulmonary embolism: from clinical presentation to clinical probability assessment. Semin Vasc Med 1:147–154
60. Kanne JP, Lalani TA (2004) Role of computed tomography and magnetic resonance imaging for deep venous thrombosis and pulmonary embolism. Circulation 109(12 Suppl 1):115–121
61. Mitchell AM, Kline JA (2007) Contrast nephropathy following computed tomography angiography of the chest for pulmonary embolism in the emergency department. J Thromb Haemost 5:50–54
62. Smith-Bindman R, Lipson J, Marcus R et al (2009) Radiation dose associated with common computed tomography examinations and the associated lifetime attributable risk of cancer. Arch Intern Med 169:2078–2086
63. Altes TA, Mai VM, Munger TM, Brookeman JR, Hagspiel KD (2005) Pulmonary embolism: comprehensive evaluation with MR ventilation and perfusion scanning with hyperpolarized helium-3, arterial spin tagging, and contrast-enhanced MRA. J Vasc Interv Radiol 16:999–1005
64. Mudge CS, Healey TT, Atalay MK, Pezzullo JA (2013) Feasibility of detecting pulmonary embolism using noncontrast MRI. Radiology 2013:1–5
65. Benson DG, Schiebler ML, Repplinger MD, François CJ, Grist TM, Reeder SB, Nagle SK (2017) Contrast-enhanced pulmonary MRA for the primary diagnosis of pulmonary embolism: current state of the art and future directions. Br J Radiol 90(1074):20160901. https://doi.org/10.1259/bjr.20160901. Epub 2017 Apr 12. PMID: 28306332; PMCID: PMC5602179
66. Biello DR, Mattar AG, McKnight RC, Siegel BA (1979) Ventilation-perfusion studies in suspected pulmonary embolism. AJR Am J Roentgenol 103:1033–1037
67. Hull RD, Hirsh J, Carter CJ, Jay RM, Dodd PE, Ockelford PA, Coates G, Gill GJ, Turpie AG, Doyle DJ, Buller HR, Raskob GE (1983) Pulmonary angiography, ventilation lung scanning, and venography for clinically suspected pulmonary embolism with abnormal perfusion lung scan. Ann Intern Med 98:891–899
68. Onyedika C, Glaser JE, Freeman LM (2010) Pulmonary embolism: role of ventilation-perfusion scintigraphy. Semin Nucl Med 43(2):82–87
69. Freeman LM, Glaser JE, Haramati LB (2012) Planar V/Q imaging for pulmonary embolism: the case for "outcomes" medicine. Semin Nucl Med 42(1):3–10
70. Burns SK, Haramati LB (2012) Diagnostic imaging and risk stratification of patients with acute pulmonary embolism. Cardiol Rev 20:15–24
71. Stein PD, Coleman ER, Gottscalk A, Saltzman H, Terrin ML, Weg JG (1991) Diagnostic utility of ventilation/perfusion lung scans in acute pulmonary embolism is not diminished by pre-existing cardiac or pulmonary disease. Chest 100:604–606
72. Harris B, Bailey D, Miles S, Bailey E, Rogers K, Roach P, Thomas P, Hensley M, King GG (2007) Objective analysis of tomographic ventilation–perfusion scintigraphy in pulmonary embolism. Am J Respir Crit Care Med 175:1173–1180
73. Bajc M, Neilly JB, Miniati M, Schuemichen C, Meignan M, Jonson B (2009) EANM guidelines for ventilation/perfusion scintigraphy. Part 1. Pulmonary imaging with ventilation/perfusion single photon emission tomography. Eur J Nucl Med Mol Imaging 36:1056–1070
74. Glaser JE, Chamarthy M, Haramati LB, Esses D, Freeman LM (2011) Successful and safe implementation of a trinary interpretation and reporting strategy for V/Q lung scintigraphy. J Nucl Med 52:1508–1512
75. Sostman HD, Pistolesi M (2011) Scintigraphy for pulmonary embolism: too old to rock 'n' roll, too young to die? J Nucl Med 52:11A–12A
76. Bhargavan M, Sunshine JH, Lewis RS, Jha S, Owen JB, Vializ J (2010) Frequency of use of imaging tests in the diagnosis of pulmonary embolism: effects of physician specialty, patient characteristics, and region. AJR Am J Roentgenol 194:1018–1026
77. The Task Force for the Diagnosis and Management (2008) Guidelines on the diagnosis and management of acute pulmonary embolism. Eur Heart J 29:2276–2315
78. Wazir JF, Ansari NA (2004) Pneumocystis carinii infection: update and review. Arch Pathol Lab Med 128:1023–1027
79. Feldman C (2005) Pneumonia associated with HIV infection. Curr Opin Infect Dis 18:165–170
80. Morris A, Lundgren JD, Masur H, Walzer PD, Hanson DL, Frederick T, Huang L, Beard CB, Kaplan JE (2004) Current epidemiology of Pneumocystis pneumonia. Emerg Infect Dis 10:1713–1720
81. Medrano FJ, Montes-Cano M, Conde M, de la Horra C, Respaldiza N, Gasch A, Perez-Lozano MJ, Varela JM, Calderon EJ (2005) Pneumocystis jirovecii in general population. Emerg Infect Dis 11:245–250
82. Al Soub H, Taha RY, El Deeb Y, Almaslamani M, Al Khuwaiter JY (2004) Pneumocystis carinii pneumonia in a patient without a predisposing illness: case report and review. Scand J Infect Dis 36:618–621
83. Kramer EL, Sanger JJ (1989) Detection of thoracic infections by nuclear medicine techniques in the acquired immunodeficiency syndrome. Radiol Clin N Am 27:1067–1075

84. Woolfenden JM, Carrasquillo JA, Larson SM, Simmons JT, Masur H, Smith PD, Shelhamer JH, Ognibene FP (1987) Acquired immunodeficiency syndrome: Ga-67 citrate imaging. Radiology 162:383–387
85. Raghu G, Collard HR, Egan JJ, Martinez FJ, Behr J et al (2011) An official ATS/ERS/JRS/ALAT statement: idiopathic pulmonary fibrosis: evidence-based guidelines for diagnosis and management. Am J Respir Crit Care Med 183:788–824
86. Travis WD, Costabel U, Hansell DM, King TE Jr, Lynch DA et al (2013) An official American Thoracic Society/European Respiratory Society statement: update of the international multidisciplinary classification of the idiopathic interstitial pneumonias. Am J Respir Crit Care Med 188:733–748
87. Noble PW, Homer RJ (2004) Idiopathic pulmonary fibrosis: new insights into pathogenesis. Clin Chest Med 25:749–758
88. Line BR, Fulmer JD, Reynolds HY, Roberts WC, Jones AE, Harris EK, Crystal RG (1978) Gallium-67 citrate scanning in the staging of idiopathic pulmonary fibrosis: correlation with physiologic and morphologic features and bronchoalveolar lavage. Am Rev Respir Dis 118:355–365
89. Baughman RP (2004) Pulmonary sarcoidosis. Clin Chest Med 25:521–530
90. Culver DA, Valeyre D (2016) Emerging ideas about sarcoidosis pathophysiology. Curr Opin Pulm Med 22:466–468. https://doi.org/10.1097/MCP.0000000000000310]
91. Mandel J, Weinberger SE (2001) Clinical insights and basic science correlates in sarcoidosis. Am J Med Sci 321:99–107
92. ACCESS Research Group (1999) Design of a case control etiologic study of sarcoidosis (ACCESS). J Clin Epidemiol 52:1173–1186
93. Scadding JG (1961) Prognosis of intrathoracic sarcoidosis in England. Br Med J 4:1165–1172
94. Gupta RG, Beckerman C, Silcian L et al (1982) Gallium citrate scanning and serum angiotensin converting enzyme levels in sarcoidosis. Radiology 144:895–899
95. Prabhakar HB, Rabinowitz CB, Gibbons FK, O'Donnell WJ, Shepard JA, Aquino SL (2008) Imaging features of sarcoidosis on MDCT, FDG PET, and PET/CT. AJR Am J Roentgenol 190:s1–s6
96. Elgazzar AH, Silberstien EB, Hughes J (1995) Perfusion and ventilation scans in patients with diffuse obstructive airway disease: utility of single breath (wash in) xenon-103. J Nucl Med 36:64–67
97. Anthonisen NR, Martin RR (1977) Regional lung function in pleural effusion. Am Rev Respir Dis 116:201–207
98. American Cancer Society (2013) Cancer fact & figures. American Cancer Society, Atlanta, p 2013
99. Higashi K, Ueda Y, Sakuma T et al (2001) Comparison of [(18)F]FDG PET and (201)Tl SPECT in evaluation of pulmonary nodules. J Nucl Med 42:1489–1496
100. Tümkaya E, Büyükdereli G (2013) The role of F-18-FDG PET and PET/CT in lung cancer. Arch Med Rev J 22:470–485
101. Kristersson S (1974) Prediction of lung function after lung surgery. A Xe-133 radiospirometric study of regional lung function in bronchial cancer. Scand J Thorac Cardiovasc Surg 18(Suppl):5–44

9 Circulatory System (Cardiovascular and Lymphatic Systems)

Abdelhamid H. Elgazzar, Saud A. Alenezi, and Mohamed A. Elfawal

9.1 Introduction

This chapter will review anatomic, physiologic, and pathophysiologic principles of major nuclear medicine relevant heart diseases. It will also discuss the role of radionuclide imaging in the diagnosis and management of these conditions including coronary artery disease, acute ischemic syndromes, and heart failure. The chapter includes the pertinent radiotracers and imaging techniques and the clinical circumstances under which these tools are applied to clinical decision making. The chapter will also review the lymphoscintigraphy and its basis and applications.

9.2 Anatomical Considerations

The heart consists of muscle, valves, specialized tissue, coronary arteries, and pericardium. In the embryo, during the first month of gestation, a primitive straight cardiac tube is formed. The tube comprises the sinoatrium, the bulbus cordis, and the truncus arteriosus. In the second month of gestation, this tube doubles over on itself to form two parallel pumping systems, each with two chambers and a great artery. The two atria develop from the sinoatrium; the right and left ventricles develop from the bulbus cordis. Differential growth of myocardial cells causes the straight cardiac tube to bear to the right, and the ventricular portion of the tube doubles over on itself, bringing the ventricles side by side (Fig. 9.1) [1].

The coronary arteries originate from the left and right coronary sinuses of the aorta (Fig. 9.2). The left main coronary artery, which comes off the left coronary sinus, continues for a variable distance before it divides into two major arteries, the left anterior descending and circumflex arteries [2]. The left anterior descending artery (LAD) descends in the anterior interventricular groove and, most of the time, continues to the apex, supplying the apical and inferior apical portion. The LAD gives off septal branches that course deep into the interventricular septum. The septal branches vary in size and number. The anterior two thirds of the septum derive their supply from the septal LAD branches, while the rest of the septum is supplied by the perforator branches from the posterior descending branch of the right coronary artery. The LAD provides also diagonal branches, which run on the epicardial surface diagonally to supply the lateral wall of the left ventricle. Usually, the first one or two diagonal branches are large enough for angioplasty or bypass consideration.

A. H. Elgazzar (✉) · S. A. Alenezi
Department of Nuclear Medicine, Faculty of Medicine, Kuwait University, Kuwait City, Kuwait

M. A. Elfawal
Department of Pathology, Faculty of Medicine, Kuwait University, Kuwait City, Kuwait

A. H. Elgazzar (ed.), *The Pathophysiologic Basis of Nuclear Medicine*,
https://doi.org/10.1007/978-3-030-96252-4_9

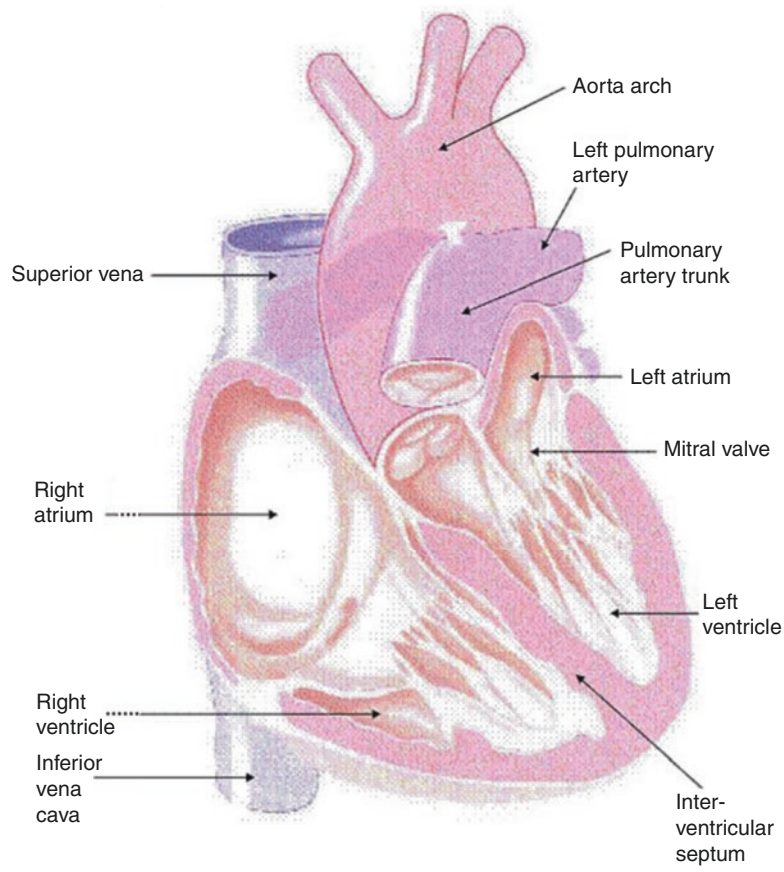

Fig. 9.1 Cutaway view of the heart

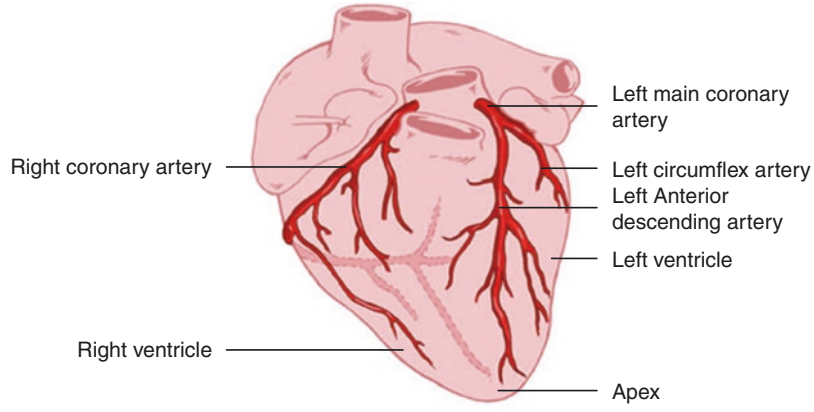

Fig. 9.2 Heart showing the origination of the coronary arteries from the left and right coronary sinuses of the aorta

The left circumflex artery (LCx) branches off from the left main artery and runs in the left atrioventricular groove. It then continues to the left and posteriorly. It supplies several posterolateral ventricular branches, which in turn supply the posterior lateral surface of the left ventricle and parallel the diagonal branches of the LAD. In most cases, the LCx continues as a small terminal posterior left ventricular branch.

The right coronary artery (RCA) arises from the right coronary sinus and descends in the right atrioventricular (AV) groove. Its first supply is to the proximal pulmonary conus and right ventricular outflow region. Normally, there are also two

or three large right ventricular branches that course diagonally over the right ventricle and supply the right ventricular myocardium. Most of the time the RCA continues along the diaphragmatic surface of the heart in the AV groove to reach the crux. At the crux, the RCA divides into a posterior descending artery (PDA) and posterior left ventricular branch. The PDA branch is usually a large artery that runs in an anterior direction in the inferior interventricular groove. The PDA supplies the inferior third of the septum. The PDA septal branches can provide a rich collateral pathway via septal perforating arteries of the LAD. The other terminal branch of the RCA, the posterior left ventricular branch, continues in the AV groove and communicates with the terminal branch of the Cx.

9.3 Physiological Considerations

9.3.1 Physiology of Coronary Blood Flow

The heart is continuously filled with blood throughout the whole life although blood within the cardiac chambers does not significantly contribute to the function, viability and maintenance of cardiac tissue. A specialized separate coronary circulation provides the myocardial tissue with oxygen and substrates to ensure normal function and viability.

Based on the demands for operating a constantly functioning contractile organ, the heart has the highest per gram oxygen consumption of any organ (50–100 μL O_2/min/g) and hence it extracts 70–80% of delivered oxygen even under resting conditions compared to skeletal muscle which utilizes only about 30–40% of delivered oxygen at rest [3, 4].

Coronary blood supply depends on coronary vascular resistance. Coronary vascular resistance depends on several factors (Fig. 9.3) and is continuously regulated to deliver sufficient quantities of oxygen supply to meet any change in the metabolic demand of the myocardial tissue (metabolism-perfusion matching) [3, 5, 6].

Regional myocardial blood flow can be currently measured noninvasively in the units of milliliters blood per minute per gram myocardium. These noninvasive measurements are achieved by positron emission tomography (PET) and can also be done using MRI and CT. Flow estimates with these different imaging modalities were found in animal experimental studies to correlate well with invasive flow estimates by the arterial blood sampling-microsphere technique which is considered the "gold standard" of blood flow measurements [7].

Measuring myocardial blood flow at rest provides limited diagnostic information as even in patients with advanced cardiovascular disease such as dilated cardiomyopathy, hypertrophic cardiomyopathy, or coronary artery disease, resting myocardial blood flows frequently are similar to those in normal individuals [7]. With pharmacologic or physiologic interventions, the response of coronary blood flow can uncover the presence of functional or structural disease-related alterations of the coronary circulation.

Changes in myocardial work and, consequently, in energy demand, are accompanied by proportional changes in coronary blood flow. This flow increase is initiated by a metabolically-

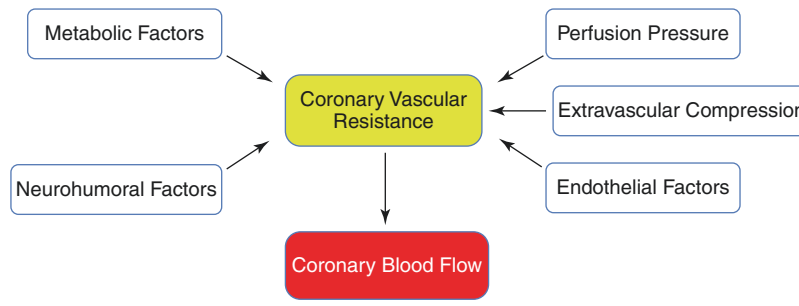

Fig. 9.3 Diagram illustrating factors affecting coronary vascular resistance, the main determinant of coronary blood flow

mediated decrease in microvascular resistance with vascular smooth muscle relaxation and hence to adjust the vessel diameter [7].

Seven to 15% of patients with acute coronary syndrome have nonobstructed coronary arteries and myocardial infarction is not accompanied with obstructed coronary arteries [8]. Quantitative measurements of myocardial blood flow identify functional rather than structural disturbances that may reflect adverse effects of coronary risk factors on endothelial function or early stages of developing coronary artery disease.

Measurements of myocardial blood flow in absolute units allows improved characterization of the extent and severity of coronary artery disease, its impact is likely to be the greatest in patients with microvascular disorders. It is in this particular disease entity where flow measurements offer a means for estimating the true ischemic burden of the myocardium and its associated cardiac risk. Furthermore, it aids to distinguish between functional and structural alterations and, at the same time, identifies potential reversibility and thus therapeutic strategies [9, 10].

The most useful application of measuring myocardial blood flow is in cases with coronary disease confined to microvasculature with angiographically nonidentifiable coronary disease. In other words, there is coronary disease affecting microvessels with no apparent macrovascular alterations. This condition may also show diffuse luminal narrowing without discreet coronary stenosis [7]. This condition is now known to be associated with several conditions such as diabetes and cardiomyopathy (Table 9.1) [11–13]. In addition to normal agiography or a finding of diffuse narrowing, myocardial perfusion studies can also be normal even in the presence of symptoms [7]. However, myocardial blood flow is typically diminished in response to vasodilator stress, although it is most likely be in the range of normal in resting status.

Table 9.1 Major causes of microvascular coronary disease

Diabetic microangiopathies
Hypertrophic cardiomyopathy
Systemic vasculopathies associated with inflammatory disorders
Transplant vasculopathies

9.3.2 Myocardial Contractility

Cardiac muscle has two essential properties: electrical excitability and contractility.

9.3.2.1 Electrical Excitation

The conduction system is composed of modified cardiac cells. The sinoatrial and atrioventricular nodes have cells with high electrical impulse automaticity, while the His bundle and the Purkinje system cells have higher rapid impulse conductivity. The contraction of the heart is normally initiated by an impulse in the sinoatrial node and then spreads over the atrial muscles to the atrioventricular node. The impulse then runs through the His bundle and the Purkinje system to reach all areas of both ventricles at approximately the same time [1, 14].

9.3.2.2 Contraction

The ability of myocardial muscles to shorten and generate the force necessary to maintain blood circulation is a fascinating property of the heart. This is achieved primarily through the unique contractile function of two proteins of the sarcomere (actin and myosin) of the syncytially arranged myocardial fibers. The two main mechanisms that can alter cardiac muscle performance are a change in initial muscle length (Frank-Starling mechanism) and a change in contractile state. In the intact heart, these are determined by preload status, afterload status, the contractile state under a given set of loading conditions, and the heart rate. There is a passive exponential relationship between the length and the tension of muscle fibers. Cardiac muscle tissue, like other body tissue, is not entirely elastic. Thus, this relationship does not exist beyond certain muscle stretch limits. Additionally, there is an active proportional relationship between the initial length of myocardial muscle and the force generated by this muscle, again up to certain length limits [1, 2, 14].

Unlike skeletal muscles, cardiac muscle cells are connected to each other by intercalated disks

and do not run the length of the whole muscle. Also, heart muscle has a rich supply of the high-energy phosphate needed for the contraction. Therefore, it may not easily develop an oxygen deficit as skeletal muscle does when its work exceeds its oxygen supply. Cardiac sarcomeres are limited by the fact that they can be extended only to a certain limit (the optimum length of 2.2 μm), whereas sarcomeres of skeletal muscles can be stretched out beyond that. Finally, cardiac muscle has all-or-none twitch contraction and cannot be physiologically tetanized as skeletal muscle can.

9.3.2.3 Left Ventricular Performance

Left Ventricular Function Curve

The left ventricular function curve usually refers to plotting of some of the LV performance measurements such as stroke volume or work against some of the preload indices such as pulmonary capillary wedge pressure [2, 15]. This analysis requires invasive measurements and is useful not only for providing prognostic information in acute cardiac conditions but also for monitoring response to therapeutic interventions.

Ejection Fraction

The ejection fraction is the most useful single number of the LV performance, defined as the stroke volume divided by the end-diastolic volume. This functional index can be measured by both invasive and noninvasive techniques. Ejection fraction is closely related to the LV function curve; however, it is very sensitive to loading conditions [2, 15].

Pressure–Volume Relationship Measurement

By studying the pressure–volume relationship, a stroke work index can be obtained [2, 15]. This is defined as stroke volume × (mean LV systolic ejection pressure − mean LV diastolic pressure). It is a very sensitive index since it is affected by all factors that may alter LV performance.

Regional Wall Motion Assessment

The assessment of regional wall motion is extremely useful in confirming and locating the site of coronary artery disease (CAD). As with LV ejection fraction measurement, it can be studied using both invasive and noninvasive methods.

Diastolic Function

Diastolic function is usually assessed by studying the relationship between LV passive pressure and volume and by examining the rate of relaxation after contraction. Several important measurements have been derived from various invasive and noninvasive techniques that can be used for both evaluating and monitoring the changes in diastolic function [15].

9.4 Pathophysiological Considerations

9.4.1 Heart Failure

Heart failure is considered a pathophysiological condition rather than a specific disease. In such a condition, the heart fails to supply enough blood to meet the metabolic demand of the tissues. Most cases of heart failure are due to primary myocardial dysfunction or intrinsic abnormalities, which include hypertensive myocardial hypertrophy, ischemic heart disease, valvular heart disease, pulmonary hypertension, pericardial disease, and other cardiomyopathies (Table 9.2). Various extrin-

Table 9.2 Major causes of heart failure

A. Systolic dysfunction:
1. Ischemic heart disease (e.g., chronic ischemia, myocardial infarction)
2. Valvular heart disease (e.g., mitral regurgitation, aortic regurgitation)
3. Dilated cardiomyopathy (idiopathic and nonidiopathic)
4. Chronic uncontrolled arrhythmia
B. Diastolic dysfunction:
1. Hypertension
2. Ischemic heart disease (e.g., acute ischemia)
3. Infiltrative myocardial disease (e.g., amyloid)
4. Left ventricular outflow tract obstruction (e.g., hypertrophic obstructive cardiomyopathy, aortic stenosis)
5. Uncontrolled arrhythmia

sic abnormalities can cause heart failure as well, despite normal ventricular function; this is referred to as secondary heart failure. Heart failure in this situation could have many reasons: inadequate blood volume as in hemorrhage, inadequate oxygen delivery as in anemia, inadequate venous return as in tricuspid stenosis, profound capillary vasodilatation as in toxic shock, and peripheral vascular abnormalities as in arteriovenous shunts.

Under normal conditions, the heart receives blood at low pressure in diastole, then ejects it at higher pressure during systole. Heart failure occurs when the heart fails to maintain adequate cardiac output (CO) to meet the body's metabolic demands. CO is the ejected amount of blood by the ventricle per minute. It is equal to the stroke volume (SV) multiplied by the heart rate (HR), i.e., CO = SV × HR. Stroke volume is the amount of blood ejected from the ventricle during systole, which is equal to the end-diastolic volume (EDV) minus end-systolic volume (ESV). SV depends on three determinants; preload, afterload, and contractility. Preload is the ventricular pressure at the end of diastole, while afterload is the pressure during ventricular systolic contraction. Myocardial contractility accounts for the change in contraction intensity. Ventricular SV increases when there is an increase in preload, a decrease in afterload, or enhanced contractility. When a cardiac muscle is passively stretched before contraction, and then stimulated to contract, the generated force depends on the length of the muscle fiber. The Frank-starling law explains how the SV increases if the preload is increased in relation to the myocytes stretching which results in increased systolic contraction. In other words, the more the ventricle is distended with blood during diastole, the more is the volume of blood ejected during systole. Ejection fraction (EF) is the portion of EDV ejected from the ventricle during each systole (EF = SV ÷ EDV). The normal EF range is between 55% and 75% [16].

Chronic heart failure occurs when the afterload increases, or ventricular contractility is reduced, a condition termed "systolic dysfunction." Essential causes of increased afterload are systemic hypertension and severe aortic stenosis. Significant causes of impaired contractility are coronary atherosclerosis, mitral regurgitation, aortic regurgitation, and dilated cardiomyopathies. Chronic heart failure may also result from impaired ventricular filling and diastolic relaxation which is known as "diastolic dysfunction." Causes include left ventricular hypertrophy, myocardial fibrosis, restrictive cardiomyopathies, and constrictive pericarditis or cardiac tamponade. Accordingly, heart failure has been categorized into two groups; heart failure with reduced EF, i.e., systolic dysfunction and heart failure with normal EF, i.e., diastolic dysfunction [17]. In heart failure with reduced EF, the incomplete ventricular emptying and increased EDV cause elevation of the LV pressure during diastole. This, in turn, is transmitted to the left atrium and the pulmonary vasculature. When pulmonary pressure is significantly elevated, i.e., more than 20 mmHg, pulmonary congestion and pulmonary edema will occur and generalized venous congestion and generalized edema will then follow. On the other hand, in heart failure with normal EF, diastolic filling occurs at a higher pressure due to reduced ventricular compliance. This elevated ventricular pressure is retrogradely transmitted to the left atrium, pulmonary and systemic venous circulation with similar consequences as described in heart failure with reduced E.F.

Compensatory mechanisms in heart failure include the Frank-Starling mechanism. When LV contractile function is impaired, this results in incomplete emptying and increased LV pressure. Myocardial fibers act through the Frank-Starling mechanism, increase stretch to induce a greater stroke volume which helps to empty the enlarged LV and maintain a normal cardiac output. The second compensatory mechanism is neurohormonal activation which comprises increased adrenergic activation, renin-angiotensin-aldosterone system, and increased antidiuretic hormone. The third (space)mechanism includes ventricular hypertrophy and remodeling. All such compensatory mechanisms can be beneficial within limits, but eventually fail to maintain adequate cardiac output [18].

All the physiological principles described in heart failure are essentially applied to both left-

sided and right-sided failure. However, the right ventricle is highly compliant compared to the left ventricle and therefore can accept larger volumes of blood with little changes in its filling pressure. Apart from the fact that left-sided heart failure is the commonest cause of right-sided heart failure, as a result of increased pulmonary vascular pressure, isolated right ventricular failure may occur following chronic obstructive pulmonary disease, reflecting the increased right ventricular afterload. The most common cause of acute right-sided heart failure is massive pulmonary embolism due to sudden increase of right ventricle afterload [16].

Heart failure may occur due to ventricular dysfunction as a result of various causes which include systemic hypertension, ischemic heart disease, cardiac valve disease, cardiomyopathies, chronic pulmonary disease, pericardiac disease, among other conditions. Other conditions may also lead to heart failure despite of normal ventricular function, such as hypovolemia, anemia, distribution shock, among other causes [19].

9.4.2 Systemic Hypertension

Blood pressure (BP) is the result of cardiac output (CO) and peripheral resistance (PR), i.e., $BP = CO \times PR$. There are four structures that are responsible for regulation of BP. These include the heart or the pump that creates the ejecting pressure; blood vascular tone which is responsible for peripheral resistance; the kidneys which control the intravascular volume; and neurohormones that moderate the previous three structures. However, a fourth short-term regulatory mechanism of BP is through the baroreceptor reflex, which plays a significant role in momentary changes in BP. Such receptors are present in the walls of the aortic arch and carotid sinuses. Whenever BP rises, baroreceptors are stimulated and transmit impulses to the brain stem medulla, which sends negative feedback signals through the autonomic nervous system, causing inhibition of the sympathetic nervous system and stimulation of the parasympathetic system with a consequent fall in BP. Contrarily, baroreceptors transmit fewer impulses to the medulla following a transient fall in BP, resulting in restoration of BP [20].

Hypertension increases the workload of the heart and damages the systemic arterial vasculature. It increases the afterload and can cause systolic dysfunction, left ventricular hypertrophy, which if uncontrolled, can eventually end in diastolic dysfunction. All of such effects can lead to left ventricular failure. Increased afterload will, in turn, increase the myocardial oxygen demands, which can lead to chronic myocardial ischemia. In addition, hypertension causes vascular endothelial damage, the most significant triggering mechanism for the initiation of atherosclerosis [21]. Hence, the role of hypertension as a risk factor for atherosclerosis cannot be overstated. In addition to its atherogenic role, hypertension contributes to many arterial pathological complications, which include tissue ischemia, thrombosis, embolism, aneurysm, and hemorrhage. Such effects may influence important and vital target organs, such as the heart, brain, kidneys, and the eyes.

The increased arterial peripheral resistance raises pressure inside the LV with increased afterload. As a compensatory mechanism, LV hypertrophy ensues in the form of concentric hypertrophy, mostly without dilatation. Increased LV muscular rigidity results in diastolic dysfunction [2, 22]. In such conditions, HF is manifested with a normal ejection fraction (EF). It follows that LV hypertrophy in such cases will result in pulmonary congestion and will eventually cause RV hypertrophy and congestive heart failure. Clinically, increased LV mass as a result of hypertrophy can be manifested by heaving LV impulse on chest palpation, and a fourth heart sound (S4) is present, since the left atrium is contracting into a rigid LV. In hypertensive patients, cardiac morbidity is proportionate to the extent of LV hypertrophy. This is valid in many cardiac illnesses, such as acute coronary syndrome, congestive heart failure, arrhythmias and, unsurprisingly, sudden death.

In patients with advanced hypertension, however, the increased LV pressure outweighs the LV mass built up throughout LV hypertrophy. This

will result in LV systolic dysfunction, with low CO and reduced EF, pulmonary congestion, and congestive HF. Myocardial ischemia, due to the likely associated coronary atherosclerosis, and the increased LV mass due to LV hypertrophy, plays a significant contributory role to LV systolic dysfunction.

9.4.3 Pulmonary Hypertension

The degree of pulmonary blood flow is affected mainly by the lumen size of the pulmonary vessels [23].

Furthermore, the pulmonary vascular resistance is defined as the difference of mean alveolar pressure and left atrial (LA) pressure divided by pulmonary blood flow. A change in any of these factors may therefore give rise to pulmonary hypertension. Pulmonary hypertension can be either primary or secondary to many other causes. In congenital heart diseases, increased medial thickening and atherosclerotic changes of the pulmonary vasculature are observed [24]. Such changes are also seen in patients with systemic to pulmonary collateral circulation. The sudden rise of PA pressure with irreversible RV failure and the usual significant decrease in LV systolic function association in acute pulmonary embolization are the cause of high mortality within the first hour in these patients [25]. Conversely, intimal fibrosis due to thrombus organization is the reason behind the cor pulmonale in chronic pulmonary embolization [26].

Pulmonary hypertension can also develop due to a rise of pulmonary venous pressure caused by LV diastolic dysfunction or high LA pressure. If such a condition persists long enough, medial thickening and arterialization of pulmonary veins will develop, which results in pulmonary fibrosis and destruction of alveolar capillaries [23]. The most common chronic lung disease associated with cor pulmonale is chronic bronchitis. The increased pulmonary vascular resistance in this case is caused by a reduction in the total area of the pulmonary vascular tree as well as mild thickening of the pulmonary arterioles [27, 28].

Unlike the LV, the RV is a high-volume, low-pressure pump. Consequently, as pulmonary vascular resistance increases, a decrease in RV stroke volume and EF is observed [29].

An increase in heart rate does not usually provide enough compensation, and a decrease in cardiac output is inevitable. Additionally, signs and symptoms of systemic venous congestion are seen due to high-pressure transmission from the RV. Diastolic LV dysfunction due to RV failure could be caused by the decrease in both the LV distensibility and the myocardial blood flow from the accompanied elevation in coronary venous pressure [30].

9.4.4 Atherosclerosis

Currently, atherogenesis is largely viewed as a chronic inflammatory process. Several decades back, it was regarded as a simple imbibition of elevated plasma lipoproteins through permeable vascular endothelium. The evolution of early atheromatous lesions, i.e., fatty streaks, may commence as early as during infancy [31]. Atherogenesis is a complex and incompletely understood multifactorial procedure. There are two adopted theories of atherogenesis; the first is the response to Injury, which probably contributes to the build-up of atherosclerotic lesions during the early stages of the disease. The second, thrombogenic theory, possibly participates in the progression of a pre-existing plaque that undergoes thrombotic formation (Fig. 9.4), with healing by organization and reendothelialization, and further progressive narrowing of the arterial lumen. The current view of atherogenesis incorporates elements of both theories and includes the recognized modifiable and unmodifiable risk factors [32].

The response to injury theory entails dynamic interaction between (1) endothelial dysfunction, (2) subendothelial inflammation, and (3) vascular smooth muscle cells response [33].

Endothelial dysfunction can be initiated by a number of risk factors, which include sheer mechanical stress related to hypertension, oxi-

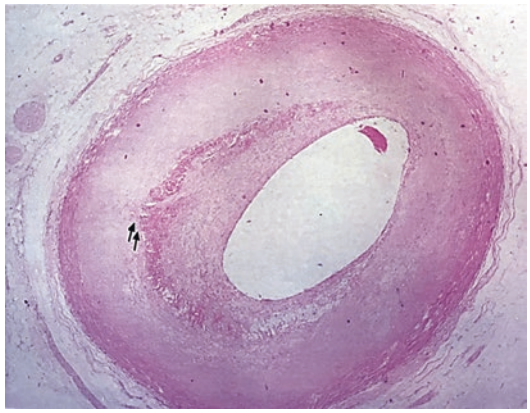

Fig. 9.4 Coronarynatherosclertic plaque showing an organized thrombus (arrows) building up the atheromatous growth

dized low-density lipoprotein (OxLDL), diabetes mellitus, smoking, elevated homocysteine levels, infectious agents, among others. Such physical and chemical stressors impair endothelial permeability, promote the release of inflammatory cytokines, increase monocytes adhesion, alter the release of vasoactive substances (e.g., prostacyclin and nitric oxide), and interfere with normal antithrombotic properties. Dysfunctional endothelium leads to (a) increased permeability to lipoproteins and (b) promoting passage of monocytes across the endothelium. The low-density lipoprotein (LDL) trapped in the subendothelium undergoes oxidation (OxLDL). The resultant inflammatory reaction involves incorporation of OxLDL in the subendothelium into the modified macrophages, forming foam cells that represent the earliest lesions known as fatty streaks or the precursor lesions. Fatty streaks are observed in the aorta and coronary arteries of most individuals by 20 years of age. The intimal thickening in fatty streaks is due to the accumulation of monocyte-derived macrophages filled with lipid (cholesterol esters) forming foamy cells [34].

Some fatty streaks, especially those involving the coronary arteries, have been shown to progress to the classic atherosclerotic plaques, as because of progressive lipid accumulation and migration and proliferation of smooth muscle cells. Some fatty streaks may regress, while others remain unchanged.

The pathogenesis of the atherosclerotic plaque involves the entry of LDL into the intima, where it binds to receptors of macrophages to form foam cells as described before. Once within the intima, LDL becomes chemoattractant to more blood monocytes and also causes macrophage aggregation, as well as further injury to the endothelium [34, 35].

Monokines from the activated macrophages also attract migration of smooth muscle cells from the media into the intima where they proliferate under the influence of platelet-derived growth factor (PDGF) and other cytokines released by endothelial cells, activated macrophages, and the smooth muscle cells themselves [36, 37].

Smooth muscles then modify into collagen fibers to form the fibrous component of the atheromatous plaque. By this fashion, fatty streaks progress into fibrofatty lesions or plaques. Instead of following a sequential pathway, the cells constantly interact and modify each other's behavior, forming plaques in one of many possible configurations.

The proportion of fibrous and fatty elements within the plaque varies from one lesion to another, i.e., some lesions are predominantly soft and fatty (with a thin fibrous cap and necrotic core), while others are largely hard and fibrous (with a thick fibrous cap). Beneath the cap is an accumulation of smooth muscle cells and macrophages containing lipid (foamy cells), as well as areas of necrosis (due to the toxic effects of oxidized extracellular lipid) and pools of lipid consisting of soluble cholesterol (cholesterol crystals). There is usually an associated chronic inflammatory infiltrate of lymphocytes and plasma cells. In large arteries (e.g., aorta), the lesions may appear as isolated or confluent plaques which eventually cover the entire intimal surface. In smaller arteries, however, e.g., coronary and cerebral, the involvement of the intima may be eccentric, reducing and pushing the lumen to one side, or it may be circumferential and concentric with a narrowed central lumen depending on the extent of intimal thickening. It is noteworthy that eccentric plaques may undergo outward plaque remodeling, which

can partly compensate for progressive growth of atherosclerotic lesions. However, such outward remodeling can possibly conceal angiographic diagnosis of large-sized plaques, and may be associated with an increased risk of plaque rupture [38].

Advanced or complicated plaques(space) may show ulceration, superimposed thrombosis (Fig. 9.5), or dystrophic calcification within the necrotic material in the intima. The size of the plaque determines the extent to which blood flow in the vessel is reduced. In the coronary artery, a plaque occupying >75% of cross-sectional area of the vessel (or >50% reduction of the lumen diameter) would cause significant interference with blood flow manifested as chronic ischemia in stable angina. Dynamic changes within the plaque may trigger fissuring or "rupture" of a thin fibrous cap (as in the vulnerable soft lipid plaque), thus exposing the circulating blood to potentially thrombogenic contents of the plaque. The clinical consequence of coronary plaque rupture depends upon a variety of elements. The site, i.e., proximal or distal, and caliber of the ruptured artery are crucial factors. Type of coronary circulation, i.e., right or left dominant circulation, will also influence the outcome. The nature of the composition of the ruptured plaque, i.e., soft fatty or hard fibrous, is another significant determinant factor. Finally, the presence of adequate collateral circulation at the area supplied by the ruptured vessel plays a very important role in such context.

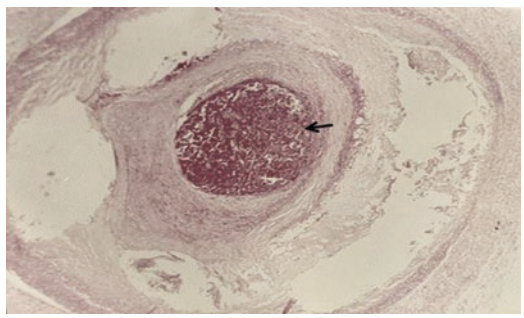

Fig. 9.5 Occluding recent thrombus (arrow) in a severely narrowed coronary artery by a predominantly fatty concentric atherosclerotic plaque

Ruptured plaque may result in luminal thrombus formation, with partial occlusion manifested by unstable angina or total (or near-total) occlusion leading to myocardial infarction or sudden death. Alternatively, a ruptured cap may admit blood inside the plaque causing intimal hemorrhage and/or intimal (intramural) thrombosis. Either of these may lead to rapid plaque enlargement, with the potential to occluding the lumen, partially or completely, as a result of pressure from inside the plaque. Ruptured plaque and subsequent intraluminal thrombosis may be also followed by organization of the thrombus and its incorporation within the plaque with further progressive arterial stenosis (thrombogenic theory). Furthermore, plaque erosion, or a small plaque fissuring may predispose to sudden coronary spasm without thrombosis, and the recognized manifestations of variant or Prinzmetal angina.

Extracellular matrix fortifies the fibrous cap(space) and (space) separates the thrombogenic plaque (space)core(space) from coagulating substrates within the circulation [39]. Macrophages, T-cells and their mediators play an important role in the pathogenesis of plaque rupture. Inflammatory signals alter collagen metabolism by reducing the synthesis and promoting the breakdown of collagen throughout the overproduction of matrix metalloproteinases (MMPs). In such conditions, the consequent thin and friable fibrous cap renders the plaque vulnerable to rupture and thrombotic complications. These inflammatory signals not only alter collagen synthesis and breakdown, but also increase the potential for thrombosis through excessive production of tissue-factor procoagulant. Such dual actions elucidate the strong association between inflammation and thrombosis in atherosclerosis [40].

Meanwhile, favorable effects of lipid lowering include reduction of the inflammatory signaling in plaques, with consequent reduction of the expression of MMPs, and increasing endothelial nitric oxide synthase. Coupled with the well-known anti-inflammatory effects of statins, low lipid levels seem to have a beneficial impact in stabilizing atherosclerotic plaques and reducing thrombotic potential [41].

Although it is essentially an intimal disease, atherosclerosis is frequently associated with thinning, atrophy and weakening of the media. This is due to indirect consequences of the intimal changes and can predispose to aneurysm formation. This is best seen in large arteries, e.g., abdominal aorta and iliac arteries. The adventitia also demonstrates neovascularization, arising from vasa vasorum, in addition to chronic inflammatory changes as a response to oxidized lipids within the plaque.

In summary, one or more of the risk factors, such as hypertension, diabetes mellitus, smoking, dyslipidemia, and others, can induce injury to the arterial endothelium, which promotes entry of LDL and monocyte-derived macrophages into the intima. This initial step is followed by a cascade of events that lead to the formation of the atherosclerotic plaque. Further evolution of changes within the plaque leads to increased intimal thickening with further arterial stenosis and chronic ischemic effects or acute plaque events resulting in acute ischemic episodes. Stages of atheroma include fatty streaks, atheromatous plaque, and complicated lesions, namely ulceration, thrombosis, and calcification. Diseases commonly associated with atherosclerosis result either from acute ischemia, e.g., myocardial infarction, stroke, and sudden death, or prolonged ischemic effects such as angina, chronic ischemic heart failure, vascular dementia, chronic renal ischemia, intermittent claudication, gangrene, among other chronic health impediments. Consequences of large-size arterial lesions, e.g., aorta, include aneurysm formation, which may lead to rupture or thrombo-embolic complications.

9.4.5 Ischemic Heart Disease

Ischemic heart disease (IHD) is a group of closely related syndromes due to myocardial ischemia, which means an imbalance between coronary blood supply and metabolic demands of the heart for oxygenated blood. In normal individuals, if the myocardial metabolic requirements are increased, even following forceful physical exertion, the oxygen supply to the heart matches such an upsurge, in order to maintain this balance [42].

Myocardial oxygen demand is proportionate to both the heart rate and myocardial contractility; when demand is increased both the rate and contractility are increased as well. Commonly referred to as coronary artery disease (CAD), IHD in the vast majority of cases, probably more than 98%, is due to advanced coronary atherosclerosis. Other minor causes include congenital ostium stenosis, arteritis, aneurysm, and thromboembolism. Two factors influence coronary artery flow: (a) coronary perfusion pressure and (b) coronary vascular resistance. The greatest coronary perfusion occurs during diastole, i.e., during myocardial relaxation to allow adequate coronary filling, which is unlike other arterial systems in the body. Hence, conditions that impair the aortic pressure, such as hypotension and aortic regurgitation, can have a negative impact on coronary perfusion.

Normally, physical or mental stress are associated with coronary vasodilatation. This is regulated by activation of the sympathetic nervous system, with enhanced blood flow and release of endothelial-derived vasodilators, such as nitric oxide (NO). The relaxation effect of NO seems to outweigh the direct constricting effect of catecholamines on arterial smooth muscle. Risk factors for atherosclerosis, such as hypertension, diabetes mellitus, smoking, and hypercholesterolemia, are associated with the diminished release of NO into the arterial wall, either because of impaired synthesis or due to excessive oxidative degradation. Diminished NO bioactivity may cause constriction of coronary arteries during physical or mental stress, thus contributing to myocardial ischemic injury. Additionally, diminished NO may facilitate vascular inflammation, thus promote oxidation of lipoproteins and foam cell formation in the pathogenesis of atherosclerosis [43].

In patients suffering from atherosclerosis, coronary perfusion is influenced by fluid mechanics, as well as the anatomy of the affected arteries. Fluid mechanics are essentially determined by the degree of coronary stenosis. From the anatomical point of view, distal intramural small-

caliber arteries are less affected by atherosclerosis, compared to proximal epicardial large coronaries, which display more frequent extents of atherosclerotic narrowing. Nevertheless, such small coronary vessels can play a significant compensatory role, by vasodilatation, in cases of proximal atherosclerotic narrowing. Thus, the hemodynamic impact of coronary stenosis is dependent upon the degree of epicardial proximal coronary stenosis, as well as the vasodilatation capability of the distal arteries. However, remodeling of plaques with outward expansion of the arterial wall allows sizable atheromatous lesions to reside in the walls of affected arteries without causing significant narrowing of the lumen. Thus, such plaques are undetectable on arteriograms and conceal warning symptoms or signs to both the patients and clinicians [41].

Although atherosclerotic plaques are usually developed over many years or even decades, they frequently produce clinical manifestations suddenly and without warnings. IHD may be manifested by a variety of presentations. The most popular form is through chest pain or "angina"; (Angina Pectoris = chest pain). Angina pectoris in its broad term is an uncomfortable feeling in the chest and neighboring anatomic structures produced by myocardial ischemia. Clinical presentation of coronary atherosclerosis can be gradual, as a result of progressive flow-limiting stenosis and exertional angina, or dramatic, with plaque rupture and thrombosis triggering unstable angina, myocardial infarction, (Figs. 9.6 and 9.7) or even sudden death. "Stable angina" is associated with stable coronary plaques of more than 75% cross-sectional stenosis and without acute coronary pathology, e.g., plaque rupture or thrombus formation. In such patients, pain occurs following physical exertion, i.e., increased demands. "Unstable angina," on the other hand, is a consequence of acute coronary lesions, mainly plaque rupture and subsequent thrombosis. However, the myocardial ischemia in such patients is not severe enough to cause permanent death of the myocardial cells. The third, less common form of anginal chest pain, is due to transient ischemia as a result of short-term coronary spasm and is known as "variant" or "Prinzmetal angina." A more severe clinical form of IHD is the "acute myocardial infarction" (MI). This follows severe, commonly occlusive, coronary thrombosis that results in an everlasting

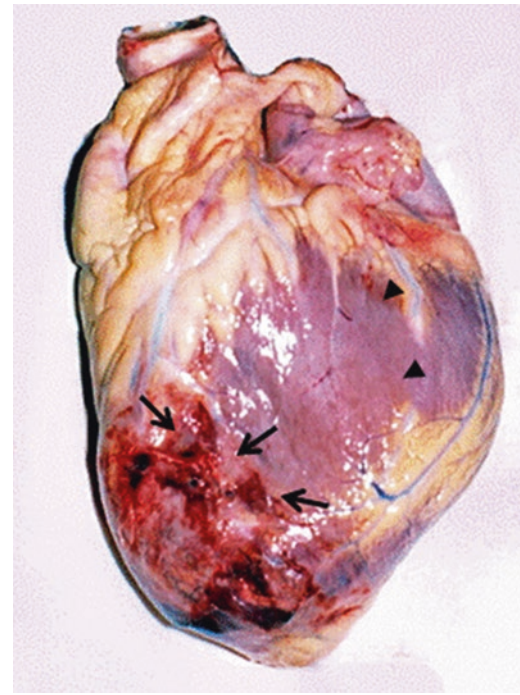

Fig. 9.6 Acute MI (Arrows) note the discoloration of the cardiac muscle with bloody spots compared to the adjacent viable muscle (arrow heads)

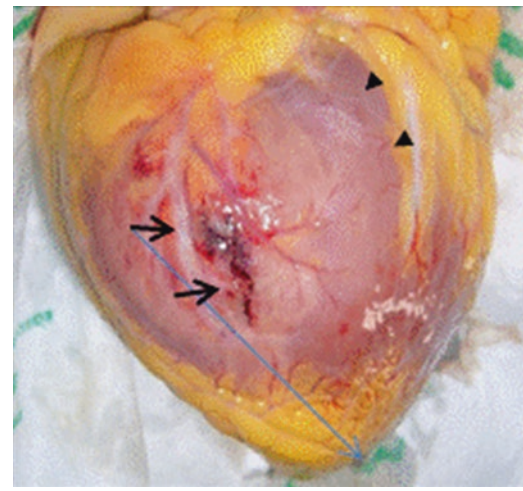

Fig. 9.7 Ruptured MI (arrows) of the anterior wall of the left ventricle. Note the adjacent viable cardiac muscle (arrowheads)

myocardial cell necrosis. Therefore, plaque rupture underlies most unstable angina, myocardial infarction, and sudden death due to IHD. Chronic IHD with CHF is the consequence of either chronic myocardial ischemia, in which there is scattered focal myocardial fibrosis following focal necrosis, or as secondary to the healing of an acute MI with replacement fibrosis [39].

9.4.6 Cardiomyopathies

Cardiomyopathy entails a diverse group of disorders with a primary myocardial dysfunction. Secondary myocardial changes, e.g., ischemic, hypertensive, valvular, etc., can lead to extrinsic cardiomyopathy, i.e., myocardial dysfunction with the primary pathology is not within the myocardium.

9.4.6.1 Dilated Cardiomyopathy

Dilated cardiomyopathy (DCM) is the most common form and accounts for almost 90% of cases. The etiology can be idiopathic and is possibly related to genetic, viral, or immunologic factors. DCM may also follow viral myocarditis with Coxsackie B virus, child birth, exposure to toxins or drugs e.g., cocaine, cobalt, or alcohol. The four cardiac chambers are markedly dilated, although areas of ventricular hypertrophy may be shown. Ventricular dysfunction is systolic as a result of impaired contractility. Thrombo-embolic complications are not uncommon. Functional mitral and tricuspid regurgitation are frequent consequences due to valve annular dilatation [44].

9.4.6.2 Hypertrophic Cardiomyopathy

Hypertrophic cardiomyopathy (HCM) is almost exclusively genetic [45].

It is characterized by asymmetric myocardial hypertrophy, particularly of the left ventricle. Thickness of the interventricular septum exceeds that of left ventricle free wall, and may cause obstruction of the blood flow in one third of the cases; a condition termed hypertrophic obstructive cardiomyopathy (HOCM). Diastolic dysfunction is due to ventricular stiffness and impaired compliance [46].

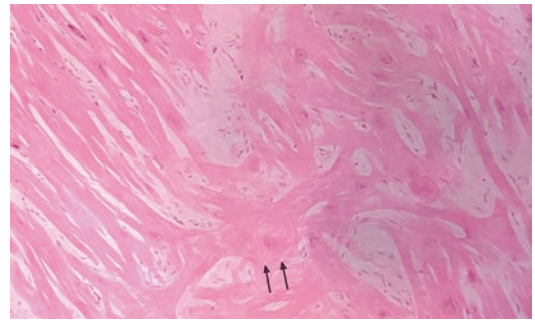

Fig. 9.8 Microphotograph of the myocardium illustrating the disarray of hypertrophied myocytes (arrows) in a case of HCM

Microscopically, the hallmark is the disorganized alignment or disarray of hypertrophied myocardial fibers (Fig. 9.8). Massive ventricular hypertrophy, high left ventricular pressure, and intramural coronary dysplasia (medial thickening and luminal narrowing) can lead to ischemic effects with anginal pain in the absence of coronary atherosclerosis.

9.4.6.3 Restrictive Cardiomyopathy

The restrictive cardiomyopathies are less common than DCM and HCM. The ventricles are abnormally rigid, but not necessarily thickened. This results in impaired cardiac filling with diastolic dysfunction, although the systolic function is usually normal [47].

There are two forms of restrictive cardiomyopathy; the first comprises a group of rare endomyocardial diseases which are of poorly understood etiology, including endomyocardial fibrosis (EMF), hypereosinophilic syndrome, and endocardial fibroelastosis (EFE). In EMF, the endocardium and the subendocardial layer of the myocardium display thickening with fibrotic plaques of variable extents. The second form is the infiltrative cardiomyopathy, with infiltration of the myocardium by an abnormal substance. The commonest cause of this form is amyloidosis. Other causes include sarcoidosis, radiation fibrosis, and hemochromatosis.

9.4.7 Pericardial Effusion

The pericardium is a sac surrounding the heart, composed of two layers, a layer on the heart (visceral pericardium) which is mesothelium, while the external portion (parietal pericardium) is mesothelium internally and fibrous externally. Normally, 15–35 mL of serous fluid surrounds the heart. The pericardium prevents the displacement of the heart and large vessels, prevents sudden dilatation of the heart, and the spread of infection or cancer from the pleura or lung as well as minimizes friction between the heart and surrounding structures [48]. Pericardial effusion is considered to be present when the amount of fluid in the pericardial space exceeds 50 mL. It may be presented as an incidental finding to a life-threatening emergency. Pericardial effusion can be associated with generalized processes not related to the pericardium, as the pericardium may be involved in a large number of systemic diseases (space) such as congestive heart failure, hypoalbuminemia, volume overload, and pulmonary hypertension or may be diseased, as an isolated process. The numerous causes of pericardial effusion can generally be divided into inflammatory and non-inflammatory etiologies (Table 9.3) [48, 49].

The most common causes are neoplastic, uremic, infectious, and idiopathic pericarditis. The hemodynamic consequences of pericardial effusion depend on the rate at which the effusion is developing and the compliance of both the pericardium and the ventricles. With significant increase in the pericardial fluid pressure, the filling pressure of both ventricles may decrease, which subsequently leads to a decrease in cardiac output. This condition is called pericardial tamponade and in severe cases is associated with a high mortality. Echocardiography is an excellent tool for the diagnosis and follow-up of pericardial effusion. The condition is also invariably seen with equilibrium radionuclide angiography (ERNA); however, an effusion of more than 400 mL is usually needed to be well recognized. The identification of pericardial effusion is important to be able to start an appropriate workup for this potentially lethal condition.

Table 9.3 Causes of pericarditis

A. Infectious
Viral (common), bacterial, parasitic, or fungal
B. Non-infectious
Auto immune diseases
Cancer
Metabolic conditions (e.g. end stage renal disease)
Trauma, direct and indirect (e.g. post-myocardial infarction, post-pericardiotomy, penetrating injury)
Drugs (e.g. chemotherapy)
Miscellaneous: amyloidosis, chronic heart failure. Idiopathic

[49–51]

9.5 Correlative Scintigraphic Evaluation of Cardiac Diseases

9.5.1 Evaluation of Ventricular Function

Radionuclide techniques including first pass, equilibrium blood pool, gated myocardial SPECT provide both accurate and noninvasive means of evaluating cardiac function with simple indices, such as left ventricular volumes and ejection fraction (LVEF). It provides diagnostic and prognostic implications in the spectrum of cardiac diseases [52].

Although most ventricular function studies are performed with the patient at rest, exercise functional studies can also be done to assess regional and global myocardial contraction changes with stress. The cardiac information obtained by these methods is summarized in Table 9.4 [53].

Nuclear medicine techniques are accurate and reproducible for cardiac function evaluation.

Table 9.4 Information obtained by radionuclide evaluation of ventricular function

1. Global left and right ventricular ejection fraction
2. Regional right and left ventricular function
3. Absolute ventricular volumes
4. Systolic emptying and diastolic filling rates
5. Detection and quantitation of cardiac shunts

They provide important information that is useful in the diagnosis and management of the following clinical situations: assessment and prognosis of congestive heart failure, monitoring drug therapy and exposure to cardiotoxins and also for diagnosis of coronary artery disease. Echocardiography made the utilization of gated blood pool studies more limited [54].

The left ventricular (LV) ejection fraction is the preferred parameter applied for the noninvasive evaluation of LV systolic function in clinical practice. It has an established and important extensive role in the clinical management of numerous cardiac conditions.

9.5.1.1 Equilibrium Radionuclide Angiography

Radiopharmaceuticals. Studies with radiopharmaceuticals require the use of an intravascular tracer that equilibrates within the blood pool. The ease with which ^{99m}Tc-pertechnetate can be attached to the patient's own red blood cells (RBCs) makes labeled RBCs the preferred technique over labeled pooled human serum albumin. The usual adult dose is about 30 mCi. Three methods of labeling the RBCs are commonly used: in vivo, modified in vitro, and in vitro. The characteristics of each method are described below. All three methods allow the ^{99m}Tc to bind irreversibly to the hemoglobin and remain in the intravascular space, allowing serial studies to be performed for up to 6–8 h following labeling of the RBCs [55].

In Vivo Technique. The patient first receives stannous pyrophosphate intravenously. The stannous ion (tin) enters the RBCs and creates the optimal oxidation-reduction environment for reduction and binding of the ^{99m}Tc-pertechnetate, which is injected intravenously 15–20 min later. Once the ^{99m}Tc-pertechnetate is in the RBCs, it is trapped inside by strong binding to the beta chain of the hemoglobin. Approximately 70–80% of the ^{99m}Tc is attached to RBCs, but in some patients as little as 50% or less may be attached. This makes identifying the edges of the blood pool during processing and analysis more difficult. In some laboratories, this method is used only when a first-pass study precedes ERNA or the patient has limited venous access. The major advantages of this method are the simplicity of use, shorter labeling time, and lower cost.

Modified In Vitro Technique. This technique is used by many laboratories because it is easier to perform than the in vitro technique and results in a higher labeling efficiency than the in vivo method. As in the previous method, stannous pyrophosphate is first injected intravenously. The blood is then drawn from the patient into an anticoagulant acetate dextrose solution (ACD) or a heparin-treated, lead-shielded syringe containing ^{99m}Tc-pertechnetate. Subsequently, the syringe is placed in a mechanical rocker or rotated slowly by the technician for 10–15 min, and the RBCs are then reinjected into the patient. Labeling efficiency is usually greater than 90%. This method offers the best compromise between ease of use and high labeling efficiency. Total labeling time averages 30 min.

In Vitro Technique. The labeling efficiency of this method approaches 100%. Patient blood is drawn and the RBCs are separated, washed with saline, and incubated first with stannous pyrophosphate and then with ^{99m}Tc-pertechnetate. The cells are washed with normal saline before and after each step to eliminate unbound material. Finally, the labeled cells are reinjected into the patient with very little or no free ^{99m}Tc-pertechnetate. The average labeling time is slightly more than 30 min. This technique also requires handling blood during multiple steps and using needles to inject blood into sealed vials.

RBCs from patients receiving heparin therapy are sometimes difficult to label, and in such cases the use of ACD as an anticoagulant is preferred to increase the labeling efficiency. Inadequate anticoagulation or too aggressive shaking of cells may cause thrombus formation and result in hot spots in the lungs. Likewise, stannous pyrophosphate can be oxidized by water in glucose solutions, and this may lead to poor RBC labeling.

Image Acquisition

Assessing ejection fraction and regional wall motion requires measurement of volume changes and wall motion at different intervals throughout

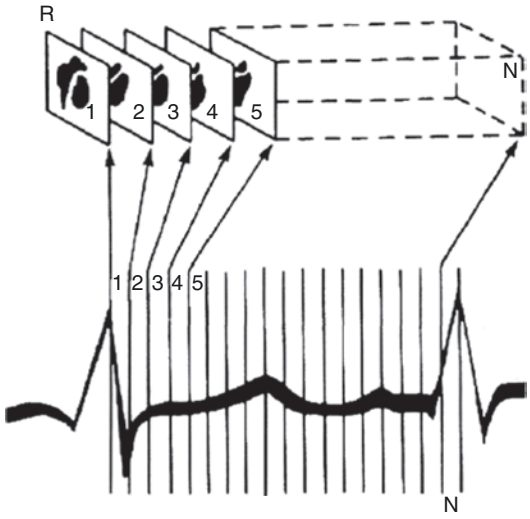

Fig. 9.9 Method by which the computer generates multiple gated images. The cardiac cycle is divided into a preselected number of frames of equal duration. Scintigraphic data from successive beats are placed into separate parts of the computer memory, depending on the temporal relation of the scintigraphic data to the R-wave marker (R). For each frame (*1*…*N*), scintigraphic data from successive beats are accumulated either until a preset time is reached (e.g., 2 min for exercise scintigraphy) or until the average cardiac image contains a predetermined number of counts (e.g., 200,000 counts for typical resting studies). (Reproduced with permission from Berman et al. [56])

the cardiac cycle. Acquisition of multiple timed images of the blood pool activity in the heart will then be triggered by each R wave (Fig. 9.9). The duration of every frame may be 1–60 ms. Multiple beats are acquired to obtain adequate counts in each frame, and typically a complete radionuclide ventriculographic study will consist of 200–800 summed beats for each of the three planar views [53] (Fig. 9.10).

A minimum of three different views of the heart are needed to assess all walls of the LV as well as all four cardiac chambers. The best septal views are left anterior oblique (LAO), anterior (ANT), which is 45° to the right from LAO, and left lateral (LLT), which is 45° to the left of LAO. Following labeling of the RBC pool, the LAO view is obtained first, as this view allows the best quantitation of the ejection fraction. In the LAO view, the camera is positioned so that the RV and LV are well separated. The other views are obtained for a similar number of counts as the LAO view. The closer the head of the camera is to the patient, the better the spatial resolution of the images. A 10° caudal tilt is used in the LAO view to minimize overlap of the left atrium (LA) and LV counts. Alternatively, a slanted hole collimator may be used to give optimal separation while allowing the camera head to be closer to the patient on the LAO view. The general all-purpose (GAP) collimator offers a compromise between the high-resolution and high-sensitivity collimators and is the one most frequently used in clinical imaging. A dedicated computer system is required to acquire, store, and process the information.

Studies may be acquired for a fixed number of heartbeats or for the total counts in the complete study. Fixed-beat studies usually acquire 200–800 individual beats, and the time of acquisition is dependent on the heart rate. Fixed-count studies usually require six million counts for the entire study or they may be acquired until a fixed number of counts are reached within each image or in the LV region.

Modes of Acquisition

There are three possible modes of acquiring ERNA: list, frame, and dynamic arrhythmia filtration. Each method has its advantages and disadvantages, as described below and summarized in Table 9.5.

List Mode. During acquisition the computer records the spatial location of each photon, the ECG gating signal, and rimming markers, usually every millisecond. Following acquisition, each individual beat can be reviewed to eliminate atrial or ventricular premature beats that exceed a determined R-R interval duration (arrhythmia rejection). The acceptable beats can then be framed in the most appropriate timing interval for the type of analysis that is needed.

Frame Mode. Prior to starting frame mode acquisition, the patient's heart rate is sampled for 10–20 s, and the mean R-R interval is used to set the time limits or window for acceptable sinus beats. For clinical studies, beats 10% shorter or longer than the mean R–R interval are rejected as possible premature beats. The beat following the early rejected beat is also rejected, as it has a pro-

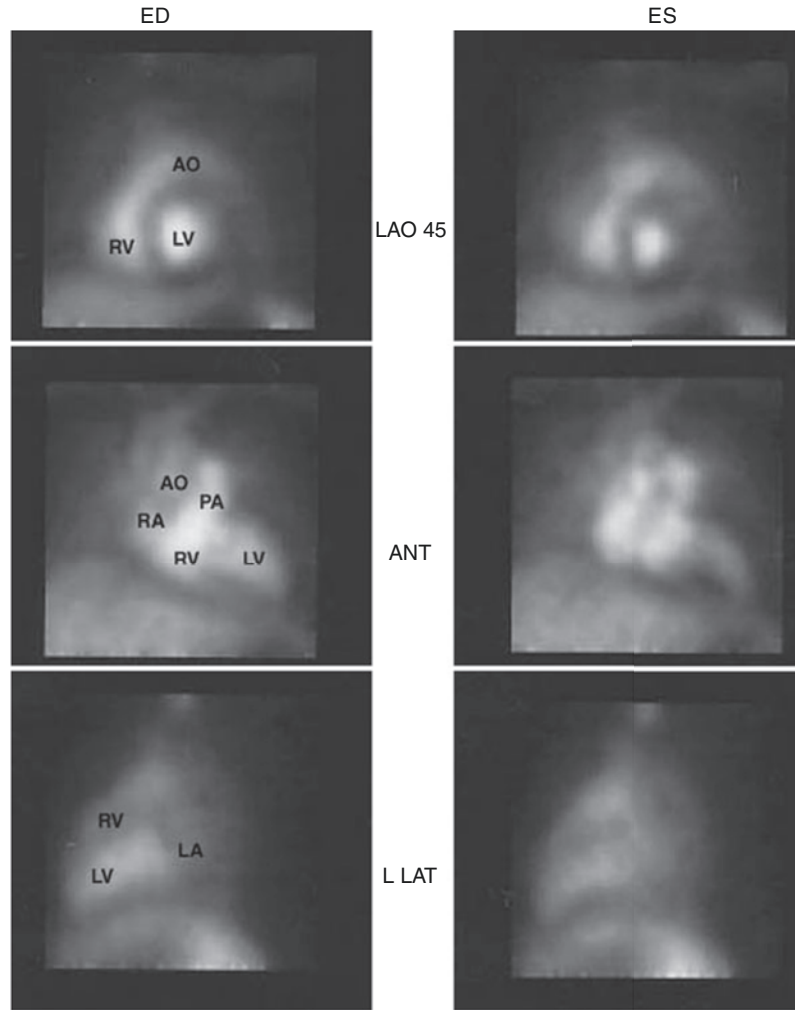

Fig. 9.10 Example of a normal gated blood pool study. The pictures on the *left* represent end-diastolic (*ED*) frames, while the images on the *right* represent end-systolic (*ES*) frames. The main structures are identified in each projection: *AO* aorta, *RV* right ventricle, *LV* left ventricle, *RA* right atrium, *PA* pulmonary artery, *LA* left atrium

longed filling interval and will result in a higher ejection fraction. Frame mode studies are generally acquired for 16–32 frames. It is extremely important that patients be in a resting state during the heart rate sampling prior to starting acquisition and throughout acquisition. Major shifts in heart rate will cause many beats to be rejected and prolong the acquisition.

Dynamic Arrhythmia Filtration. This technique allows the acquisition parameters (duration of each frame, percent R-R variability allowed for beat rejection, and total number of frames) to be set at the beginning of acquisition. Once acquisition starts, each beat is placed in a temporary memory buffer where it is examined with regard to the preset parameters. If it meets all criteria, it is accepted and included in the final data set. If it does not meet all the criteria, it is rejected. Thus, greater flexibility in beat selection is possible than with frame mode, but without the memory requirements and longer processing time required by list mode acquisition.

Regardless of the method of acquisition used, it is important to confirm that only the R wave from the ECG signal is detected as the trigger signal and as appropriately gating the acquisition. This can be done by examining an ECG rhythm strip and identifying the triggering signal. Gating may sometimes occur incorrectly on the P-, T-, or R-wave signal as well as muscle artifact and pacing spikes from artificial pacemakers. If this occurs, the lead placement needs to be changed

Table 9.5 Comparison between the different modes of computer acquisition

Mode of acquisition	Advantages	Disadvantages
List mode	Optimal temporal resolution	Intensive memory requirement
	Excellent arrhythmia rejection	Longer processing time
Frame mode	Easy setup	Count drop-off
	Minimum memory	Fixed temporal resolution
		Poor arrhythmia rejection
Dynamic arrhythmia (buffered beat) mode	Flexible temporal resolution and arrhythmia rejection	Longer setup for greater options
	Less memory than list	
	Accurate systole/diastole	

or the voltage amplitude adjusted to avoid inappropriate gating [56].

Simple LV ejection fraction calculations (Fig. 9.11) usually require time intervals of 40–50 ms to adequately define the end-systolic point in the heart cycle, where the heart has the smallest volume. For analysis of diastolic function, timing intervals of 10–20 ms give the most reliable information for the ventricular filling portion of the heart cycle. Even with list mode and dynamic arrhythmia filtration, there is still slight R-R interval variability that can lower the counts and distort the last few frames of the time-activity curve. This count drop-off does not affect ejection fraction calculation but is deleterious for diastolic function analysis. This limitation can be overcome by generating separate forward and backward time-activity curves and combining them in a final curve for analysis.

Patients in atrial fibrillation have variable diastolic filling intervals, and this results in a different ejection fraction for each beat. LV ejection fraction measurement by ERNA during atrial fibrillation has been shown to be an accurate reflection of the summed ejection fraction of each of the individual bats. Thus, it is an accurate reflection of overall ventricular systolic function [55].

Contrast ventriculography and echocardiography will sample only a few beats for ejection fraction calculation and may be less representative of true function.

9.5.1.2 ECG-Gated Myocardial Perfusion SPECT

Gated myocardial perfusion SPECT studies provide information on both myocardial perfusion and ventricular function. Quantification of gated SPECT images provides a global LVEF, plus indices of regional wall motion and wall thickening, useful in the evaluation of ventricular function and LV dyssynchrony that occurs with primary contractile dysfunction [57] (see later). Recently, a low-dose SPECT (as low as 8 mci) gated bloodpool SPECT for quantification of LV function was used [58, 59]. The low-dose ^{99m}Tc-RBC imaging method was proved to provide precise quantification of LV function and resulted in the most consistent assessment of LV function compared with the gold standard high-dose ERNA method, along with excellent inter-observer reproducibility with a greater than 67% reduction in radiation dose [58].

9.5.2 Evaluation of Myocardial Perfusion

9.5.2.1 Myocardial Perfusion SPECT Imaging

Clinical manifestations of coronary artery disease include angina pectoris, myocardial infarction, congestive heart failure, and sudden death. It may be asymptomatic until advanced in severity or complications. Most diagnostic methods, both invasive and noninvasive, depend on the detection of luminal narrowing of the epicardial coronary vessels. Vessel narrowing of up to 75% of the cross-sectional area (or <50% of luminal narrowing) does not affect the resting coronary flow. Increase of coronary flow caused by exercise or pharmacological stress exaggerates flow nonuniformity, through either increased metabolic demand or vasodilation [60].

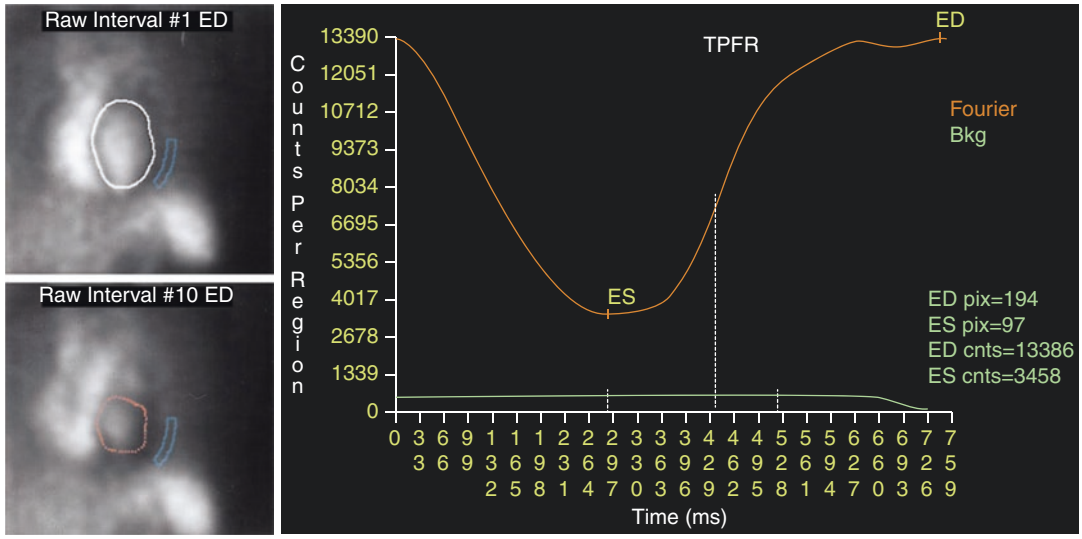

Fig. 9.11 Ejection fraction calculation of an LAO radionuclide ventriculogram. Shown are left ventricular edges as determined by an automated computer algorithm for end diastole (*top left*) and end systole (*bottom left*), chosen area for background subtraction, volume curve (*right*), and ejection fraction (60%) of the left ventricle. Specific information on heart rate and time/frame is also provided

The easiest method of increasing coronary flow is physical exercise, using a motorized treadmill or a stationary bicycle. In patients who are unable to exercise adequately, pharmacological agents are used for transient elevation of coronary flow.

SPECT Radiotracers

The ideal tracer of coronary flow would be extracted by the myocardium with 100% efficiency, like microspheres. Its myocardial uptake would be linearly related to coronary flow, and the tracer isotope would have optimal emission photon energy for imaging with a gamma camera. Currently, this ideal tracer is not present and two classes of tracers are widely used for conventional MPI: thallium-201 and the Tc-99m-labeled tracers.

Thallium-201

Thallium-201 (Tl-201) has been in clinical use for decades. Tl-201 is a metal in group III-A of the periodic table and, as an isotopic cationic tracer, has properties similar to those of potassium. Tl-201 is extracted with a high extraction fraction by the ATPase-dependent Na^+/K^+ channels (Table 9.6). Diagnostic and prognostic data on Tl-201 are extensive. An advantage of Tl-201 is the ease of use since one injection only is needed (Fig. 9.12). Tl-201 is the preferred radiotracer for evaluation of myocardial viability among the conventional SPECT agents. Major drawbacks of Tl-201 include low energy of its principle X-ray photons (69–80 keV) and its long half-life (72 h), which limits the injected dose, due to its relatively higher radiation dose to the patient. The limited dose leads to suboptimal image quality due to noise [61].

Tc-99m Sestamibi and Tc-99m Tetrofosmin

Tc-99m sestamibi (MIBI) and Tc-99m tetrofosmin have shorter physical half-life of Tc-99m (6 h) allowing the use of higher tracer doses (up to 50 mCi/day) (Table 9.6). Combined with the more optimal photon energy for gamma camera imaging (140 keV) compared with Tl-201, image quality is less noisy, and frequency and severity of attenuation artifacts are decreased. Negligible washout of Tc-99m-based tracers [62] requiring the use of two separate tracer injections: one for rest imaging and one for stress imaging. SPECT imaging is usually started 20–60 min after tracer injection. The delay is needed for blood pool

Table 9.6 Radiotracers for SPECT myocardial perfusion imaging

	Thallium-201	Tc-99m sestamibi	Tc-99m tetrofosmin
Brand name	N/A	Cardiolite	Myoview
Class	K^+ analog	Isonitrile	Diphosphine
Preparation	Cyclotron	Kit (heated)	Kit (cold)
Charge	Cation	Cation	Cation
Lipophilicity	Low	High	High
Redistribution	Yes	Minimal	Minimal
Tissue clearance	50%/4 h	>6 h	>6 h
Excretion	Renal	GI (renal)	GI (renal)
Time of imaging (min)	5–10	20–60	10–45
Completion time (h)	4–6	3–4	3–4
Counts	Adequate	High	High
SPECT	Yes	Yes	Yes
Extraction	0.85	0.39	0.24
Gating	±	Yes	Yes
Heart-liver (1 h)	2.6	1.2	1.4
TEDE (rem/3.5 mCi)	2.1	1.1	0.8
Clinical use			
Diagnosis	Yes	Yes	Yes
Prognosis	Yes	Yes	Yes
Viability	Yes	Yes	Yes

[a] *N/A* not applicable

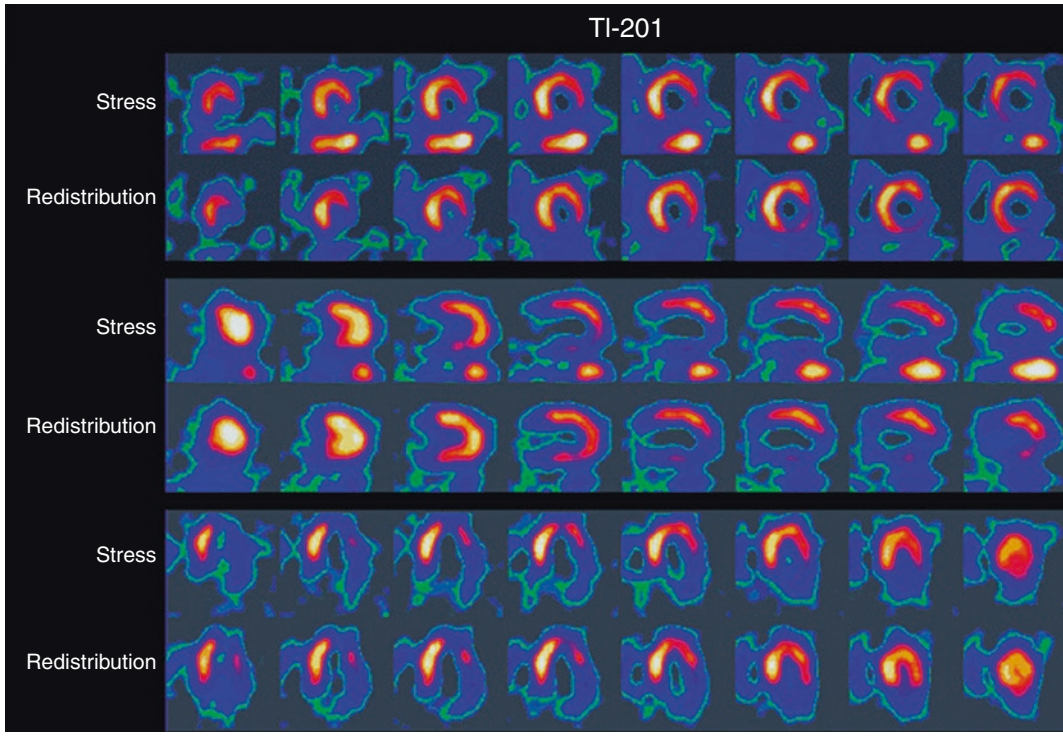

Fig. 9.12 Thallium-201 stress and redistribution images of a patient showing a severe fixed inferolateral defect; a severe, partially reversible basal inferolateral defect; a reversible basal inferoseptal defect; and a mild to moderate reversible anterolateral defect

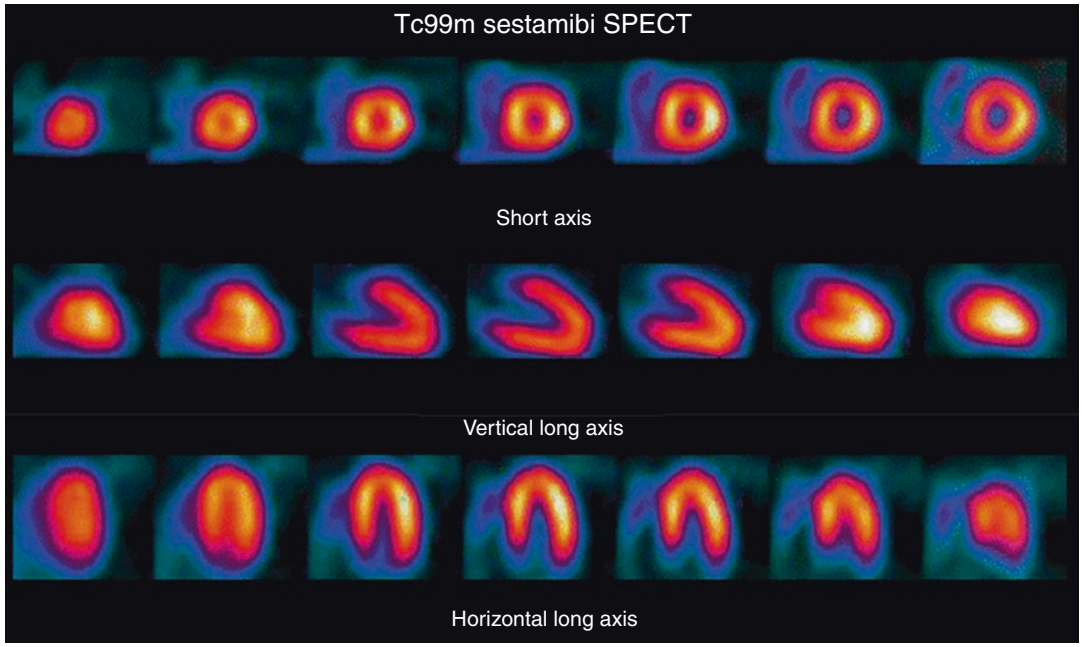

Fig. 9.13 Normal stress Tc-99m sestamibi myocardial perfusion SPECT images in short axis, vertical axis, and horizontal long. There is homogeneous distribution of the radiotracer in the left ventricular wall. The short axis views have a doughnut shape distribution of radioactivity, while the horizontal and vertical long axis views are like a horse shoe. These views depict different parts of the left ventricle: apex, anterior wall, septum, lateral wall, and inferior wall, as well as the right ventricle. Gated images show uniform motion and thickening of ventricular walls with left ventricular ejection fraction (LVEF) greater than 50%. Left ventricular end-diastolic and end-systolic volumes were within normal limits. There is mild uptake in the normal right ventricle

clearance and partial liver clearance (Fig. 9.13). Gating of Tc-99m sestamibi or Tc-99m tetrofosmin images made possible because of the high photon flux, allows simultaneous evaluation of perfusion and function.

Excretion of the Tc-99m tracers is through the hepatobiliary and, to a lesser extent, renal systems. High subdiaphragmatic uptake in the liver or intestines occasionally interferes with the evaluation of cardiac perfusion.

In an attempt to utilize advantages of both types of tracers, dual-tracer protocols were developed: Tl-201 is injected at rest, and rest imaging is started within 15 min. Exercise or pharmacological stress is followed by Tc-99m MIBI or Tc-99m tetrofosmin injection at peak stress. The test is completed in less than 3 h [63].

A drawback from the different pharmacokinetic properties of the tracers results in nonparallel flow-uptake relationships and different spatial contrast due to different isotope energies.

Tc-99m teboroxime was another perfusion agent that was marketed. This highly lipophilic agent readily crosses myocardial cellular membranes but, unlike MIBI, rapidly diffuses out of the cells in 6–10 min, allowing only a few minutes for imaging [64].

It requires separate rest and stress injections. There is some evidence that the differential washout rate of Tc-99m teboroxime obtained from stress-redistribution images can differentiate between ischemic and infarcted myocardium [65].

One advantage of teboroxime is its very high extraction fraction, which is higher than any of the other conventional SPECT agents at high flow rates during pharmacological vasodilation. Due to the demanding rapid imaging protocol required, its use never became extensively applied, in spite of examples of good quality images obtained with either multiheaded or single-headed gamma cameras in some laborato-

ries. Its commercial availability has been stopped for years.

99mTc-3SPboroximine is a newer perfusion radiotracer since its cardiac uptake is largely relies on the regional blood flow. It can be used for the detection of perfusion abnormalities, accurate quantification, and determination of regional blood flow rate [66–68].

Methods of Stress

Exercise Stress

Exercise stress is the most frequently used test for noninvasive diagnosis of coronary artery disease (CAD). This form of stress is usually performed with exercise protocols using either a treadmill or bicycle. Exercise is associated with sympathetic stimulation and changes in coronary vasomotor tone which affects coronary blood flow through dilatation of coronary arteries. Exercise results in increase in myocardial oxygen demand and coronary vasodilation allowing increased oxygen delivery which is crucial to myocardial perfusion to prevent ischemia. This hyperemic effect is behind the identification of ischemia, as stenotic vessels do not vasodilate efficiently [69].

Sensitivity of a symptom-limited exercise treadmill test (ETT) for the diagnosis of CAD is 65–70% [70].

When combined with myocardial perfusion imaging, the sensitivity increases to 85–90%, while specificity is increased as well [61]. This combination of results also provides the best prognostic value and risk stratification for patients with coronary artery disease [71].

ETT evaluates the hemodynamic changes and provides independent prognostic information including total exercise time and capacity, heart rate response, blood pressure response, and symptoms during stress [71]. Systolic blood pressure is expected to increase during stress to maintain adequate cardiac output. Any drop in blood pressure during exercise may indicate the presence of coronary artery disease and, therefore, poor prognosis and outcome [72, 73]. Heart rate is also expected to increase during the exercise preferably up to 85% of the maximum age predicted heart rate (MPHR) which can be calculated by subtracting the patient age from 220 [74]. However, achievement of 85% of MPHR is not an indication for termination of the test and ETT should rather be symptom-limited. Slow heart rate during exercise can be normally seen in athletes. On the other hand, heart rate that is slow to return to baseline during recovery may indicate inability of the heart to recover from this increased demand resulting in exercise intolerance. This can be seen in patients with coronary artery disease and congestive heart failure and is considered as an independent predictor of risk for major cardiac events [71]. Metabolic equivalent (MET) is another parameter that is routinely recorded during exercise. One MET equals about 3.5 mL of oxygen/kg of body weight [72]. This parameter can be used to assess the functional status of patients and help in treatment options by categorizing patients into three classes. Class I patients can exercise beyond 7 or 8 METs, class II patients get symptom-limited exercise at 5 or 6 METs, while class III patients get symptom-limited exercise at 3–4 METs. Healthy people can usually exercise beyond 10–11 METs [71].

The single most powerful prognostic predictor in both men and women is the exercise capacity (length of the exercise) [75].

Pharmacological Stress

Patients who cannot exercise for noncardiac reasons (e.g., orthopedic, neurological, peripheral vascular) or are unable to exercise adequately (for a meaningful period of time and/or to an adequate heart rate) are candidates for pharmacological stress testing. Five agents are currently approved for use in conjunction with MPI: adenosine, dipyridamole, regadenoson, dobutamine, and arbutamine. Adenosine, dipyridamole, and regadenoson are coronary vasodilators. Dobutamine and arbutamine are beta-adrenergic agonists and increase myocardial oxygen demand; they also have some direct vasodilatory effect [76].

Pharmacological stress makes possible evaluation of patients unable to exercise for noncardiac reasons, including sick and debilitated patients. However, physiologically useful param-

eters derived from an exercise test, valuable for a comprehensive evaluation, are lost.

Adenosine

Adenosine is an endogenous coronary vasodilator produced from ADP and AMP in myocardial and vascular smooth muscle cells. Adenosine affects two kinds of receptors: A1 and A2. Activation of the A1 receptor slows AV conduction. Activation of the A2 receptor leads to coronary vasodilation (Fig. 9.14, Table 9.7). The half-life of adenosine is extremely short (seconds only). Perfusion tracers are therefore injected during continuous adenosine infusion (140 μg/kg/min for 6 min). Side effects of adenosine include flushing in 37% of patients, chest pain in 35%, shortness of breath in 35%, and gastrointestinal symptoms in 15%. Chest pain is not indicative of myocardial ischemia. Vasodilation causes a modest blood pressure drop, usually accompanied by compensatory tachycardia, although transient second-degree AV block is seen in 3–4% of patients and third-degree AV block in <1% of tested patients. All side effects and hemodynamic changes are transient and reversible. Use of an antidote (IV aminophylline) is very rarely needed. Most situations can be controlled by decreasing the infusion rate and/or by shortening the duration of the infusion. Adenosine may trigger bronchospasm and should not be used in patients with bronchospastic disease, particularly those who have clinical asthma and/or are being treated with bronchodilators. Caffeine, theophylline, and their metabolites competitively block adenosine receptors. Therefore, patients should abstain from caffeine-containing beverages and medication for 12–24 h prior to the test [74].

Dipyridamole

Dipyridamole is an indirect vasodilator: It increases intravascular concentration of endogenously produced adenosine by blocking its cel-

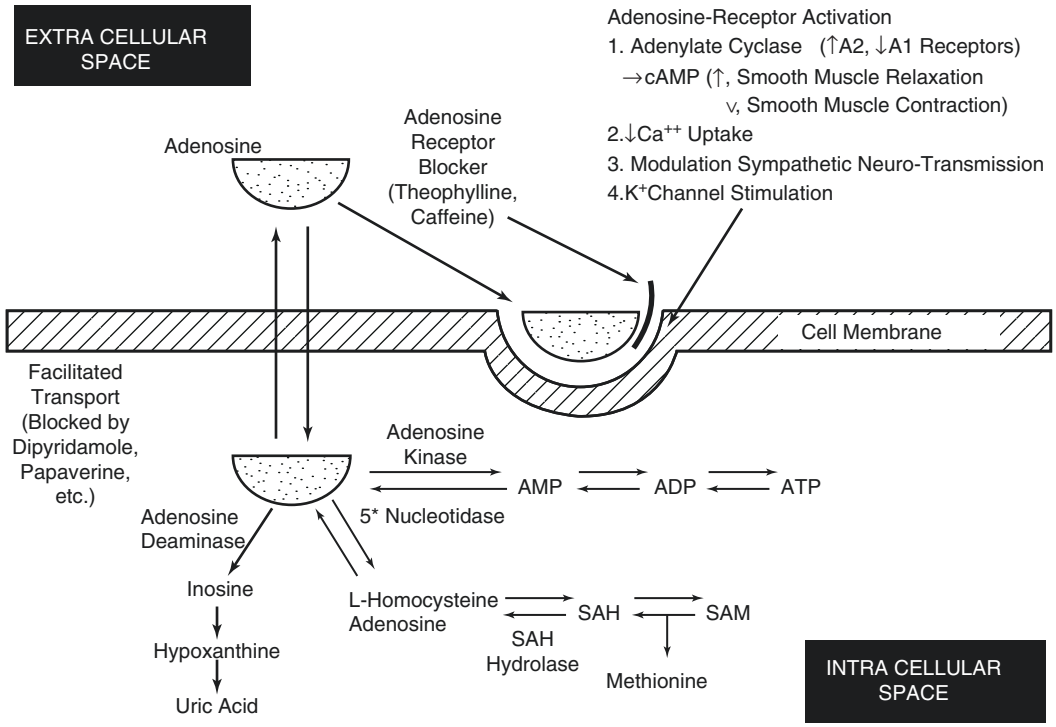

Fig. 9.14 Mechanisms of the vasodilating stress agents. Adenosine is synthesized intracellularly and leaves the cells to act on surface membrane receptors. Dipyridamole blocks adenosine reentry into the cell, increasing extracellular adenosine that can bind to the receptor. Methylxanthines, such as theophylline and caffeine, competitively block the receptor sites. (Reproduced from Iskandrian et al. [77] with permission)

Table 9.7 Main coronary vasodilators

	Adenosine	Regadenoson	Dipyridamole
Effect	Direct	Direct	Indirect
Half-life	<10 s	8.5 min	Minutes
Onset of action	Seconds	Seconds	Minutes
Time to peak effect	ca. 1 min	20–40 s	ca. 7 min
AV block	7%	3%	0%
Diagnostic utility	Inability to exercise	Inability to exercise	Inability to exercise
Contraindications	Bronchospasm		Bronchospasm
	Unstable/severe ischemia	Unstable/severe ischemia	Unstable/severe ischemia

lular reuptake (Fig. 9.14). Dipyridamole has a longer half-life than adenosine and does not affect AV conduction. Dipyridamole is usually infused for 4 min. The perfusion tracer is injected at 7 min. In some laboratories, the patient is asked to perform low-level exercise or handgrip exercise to enhance its effects. Contraindications for dipyridamole use are similar to those for adenosine, although chest pain is less frequent. An effective antidote is IV aminophylline (50–100 mg IV), which can be used to normalize hemodynamic changes, relieve ischemia, and/or treat side effects [74].

Dipyridamole potentiates the effects of exogenously infused adenosine. Therefore, oral dipyridamole, when being taken for its antiplatelet effects, should be discontinued on the day of the stress test.

Regadenoson

The first historically available vasodilator stress agents, dipyridamole and adenosine, are effective and useful, but they do have significant side effects, making stress testing an unpleasant experience in many patients, and are contraindicated in patients with bronchospastic disease. It has been established that there are four adenosine receptor subtypes distributed in various locations: A_1, A_{2A}, A_{2B}, and A_3. The selective activation of A_{2A} receptors leads to coronary vasodilation, while A_1 are responsible for decreased AV conduction and chest pain, while the stimulation of A_{2B} receptors leads to peripheral vasodilation, mast cell degranulation, and bronchiolar constriction, and the stimulation of A_3 leads to ischemic preconditioning and mast cell degranulation [78].

Regadenoson is an A_{2A} receptor agonist that is a coronary vasodilator with very weak affinity for A_1, A_{2B}, and A_3 receptors that are associated with adenosine's unpleasant side effects. It is supplied in prefilled syringe doses of 0.4 mg in 5 mL of solution. It is administered as a single-dose bolus (less than 10 s), which leads to increased coronary blood flow to more than twice baseline levels within 30 s, with maximal vasodilation 1–4 min after injection, and decreases to less than twice baseline within 10 min. This is accompanied by decrease in systolic and diastolic blood pressure and increase in heart rate [79].

In the ADVANCE MPI multicenter trial comparing myocardial perfusion imaging with regadenoson compared to adenosine pharmacological stress, it was demonstrated that regadenoson was similar to adenosine for the detection of ischemia [79].

Methylxanthines block the effects of regadenoson, as for adenosine. Patients should be instructed to avoid consumption of any products containing methylxanthines, including caffeinated coffee, tea, and other caffeine-containing beverages of drug products for at least 12 h prior use. In clinical trials conducted during regadenoson's development, where side effects were compared to adenosine, 80% of subjects had some kind of adverse reaction, including dyspnea (28%), headache (26%), flushing (16%), chest discomfort (13%), angina or ST segment depression as evidence of myocardial ischemia (12%), dizziness (8%), chest pain (7%), and nausea (6%). In most categories, this profile was similar to side effects from adenosine, except for a lower rate of chest discomfort (13% vs. 18%) or evidence of ischemia (12% vs. 18%). There was a

similar rate (26% vs. 30%) of rhythm or conduction abnormalities, but a lower rate of first-degree block (3% vs. 7%) or second-degree AV block (0.1% vs. 1%). There was a higher rate of respiratory adverse reactions, such as dyspnea or wheezing compared to placebo (12.9% in the asthma group and 19% in the COPD patient group), but most respiratory adverse reactions resolved without therapy. Aminophylline was used 3% of the time to treat side effects from regadenoson, versus 2% for adenosine. As for dipyridamole and adenosine, serious ischemia, leading to myocardial infarction, ventricular arrhythmias, and cardiac arrest, has occurred following regadenoson injection [80].

Dobutamine and Arbutamine

Dobutamine is a synthetic catecholamine with predominantly β1 affinity and short plasma half-life (approximately 2 min). In the presence of significant epicardial coronary artery stenosis, the increase in oxygen demand caused by positive inotropic and chronotropic effects of dobutamine can induce myocardial ischemia. Additionally, dobutamine at higher doses induces coronary vasodilation. The infusion rate used for diagnostic imaging (40–50 μg/kg/min) is higher than the customary therapeutic infusion rate of dobutamine (10–20 μg/kg/min) used for inotropic support in the intensive care units. The side effects of dobutamine in our patient series included supraventricular and ventricular arrhythmia (6% of patients), palpitations (40%), chest pain (20%), shortness of breath (17%), headache (15%), and GI symptoms (5%). Dobutamine was used mostly in patients who are unable to exercise and have bronchospastic disease [81], but its use has decreased since the introduction of the selective A_{2A} vasodilator agonist regadenoson.

Arbutamine is also a synthetic catecholamine. It has been marketed with a computerized feedback system between arbutamine infusion rate and the heart rate. This approach attempts to minimize the time required to reach a selected peak heart rate. However, added complexity and expense of this approach limited its widespread use [81].

Combined Exercise and Pharmacological Stress

Many laboratories have found it useful to combine low-level treadmill exercise with either adenosine, regadenoson, or dipyridamole. This has been found to reduce the unpleasant side effects of flushing, headache, dizziness, or nausea due to either stressor. Image quality is also improved through a decrease in hepatic and gut uptake of the technetium-99m perfusion tracers, which is more common with adenosine or dipyridamole, compared to exercise [82].

On the other hand, the incidence of stress-inducible ischemia is more common due to increased myocardial demand, leading to a higher prevalence of ischemic chest pain and ischemic ECG changes. The combination of adenosine or regadenoson and symptom-limited exercise in patients who can exercise but where it is not certain that they can attain maximal heart rate has been found safe and useful to achieve maximal level of stress [83].

Combined exercise with pharmacological stress should be avoided in patients with left bundle branch block or RV pacemaker, since the likelihood of false-positive myocardial perfusion stress images is increased with exercise.

Methods of SPECT Imaging

SPECT

Single-photon emission computed tomography (SPECT) has by now been well standardized and optimized for either thallium-201 or Tc-99m sestamibi or Tc-99m tetrofosmin imaging as well as optimized for each imaging system manufacturer. This includes timing of acquisition, choice of collimators, choice of step-and-shoot versus contiguous acquisition, circular versus elliptical orbits, filtered versus iterative reconstruction, filtering, display, quantification, and correction for movement artifact. The greatest area of concern and therefore undergoing the greatest evolution is the challenge of addressing inaccuracies in diagnoses and inefficiencies in patient management arising from mistaking soft tissue attenuation artifacts from true perfusion defects.

Solutions to the problem of soft tissue attenuation include training in recognition by the technologist and the interpreting physician and the utilization of various compensation strategies, such as prone imaging, ECG gating, image quantification, and the use of attenuation correction hardware and corrective reconstruction.

The inspection of the original multiplanar images allows one to detect movement artifact, as well as ascertain the presence of overlapping soft tissue likely to cause attenuation artifact, either due to an overlapping diaphragm, causing inferior wall defects, or in women and obese men, overlapping breast tissue, causing anterior, anteroseptal, or anterolateral defects. This allows the interpreting physician to properly evaluate the obtained images and avoid an unnecessarily false-positive reading.

If an inferior wall defect is recognized early, while the patient is still in the laboratory, it has been demonstrated that inferior wall defects due to attenuation artifact seen in the standard supine position resolve after repeat imaging in the prone position, which improves diagnostic accuracy. Limitations of this approach include the creation of a new anterior wall attenuation defect and the apparent lack of efficacy in anterior wall attenuation artifacts [84, 85]. This strategy is useful when other means are not available or in combination with gated SPECT imaging.

Gated SPECT

ECG gating of the SPECT myocardial perfusion images provides, independently from the perfusion information, important information on global LV and RV function, LV ejection fraction, and regional wall motion and thickening. This information provides information that incrementally add to the value of myocardial perfusion imaging alone. It can also help enhance the accuracy of perfusion imaging. When there is a wall motion abnormality corresponding to a perfusion abnormality, the presence of disease can be made with greater confidence, resulting in enhanced accuracy [86].

However, normal wall motion associated with a reversible perfusion defect does not exclude reversible ischemia. Normal wall motion in the presence of mild to moderate fixed perfusion abnormality could be due to non-transmural wall injury, insufficient to cause a discernible wall motion abnormality.

Quantification of gated SPECT images provides a global LVEF, plus indices of regional wall motion and wall thickening, useful in the evaluation of function. Whereas its original use was applied in planar gated blood pool imaging, it has been applied to three-dimensional SPECT gated blood pool images to overcome problems of overlap of adjacent cardiac structures and inaccurate localization of left ventricular and right ventricular abnormalities [87], which was subsequently applied to myocardial perfusion imaging [88].

This technique has been found useful in patients with advanced systolic heart failure and evidence of dyssynchrony on ECG due to conduction abnormalities, single ventricle pacing, in predicting which patients would benefit from cardiac resynchronization therapy [89].

Clinical Uses of Myocardial Perfusion Imaging

Initially, myocardial perfusion imaging was a primarily diagnostic method for noninvasive detection of coronary artery disease (Figs. 9.15 and 9.16). Later applications have extended to evaluation of prognosis to assess the patient risk and outcome (Table 9.8) [90, 91].

Advances in surgical, percutaneous, and medical therapy of CAD have fundamentally changed the natural history of the disease. Thus, appropriate identification of high-risk patients, followed by appropriate therapy, favorably modifies prognosis. Conversely, the identification of low-risk patients with a benign prognosis reduces the need for costly and potentially detrimental invasive testing and therapy. A normal SPECT myocardial perfusion imaging study has been shown to be extremely effective in predicting a good prognosis in a variety of settings.

Diagnosis

Appropriate candidates for stress testing with MPI are patients with intermediate pretest

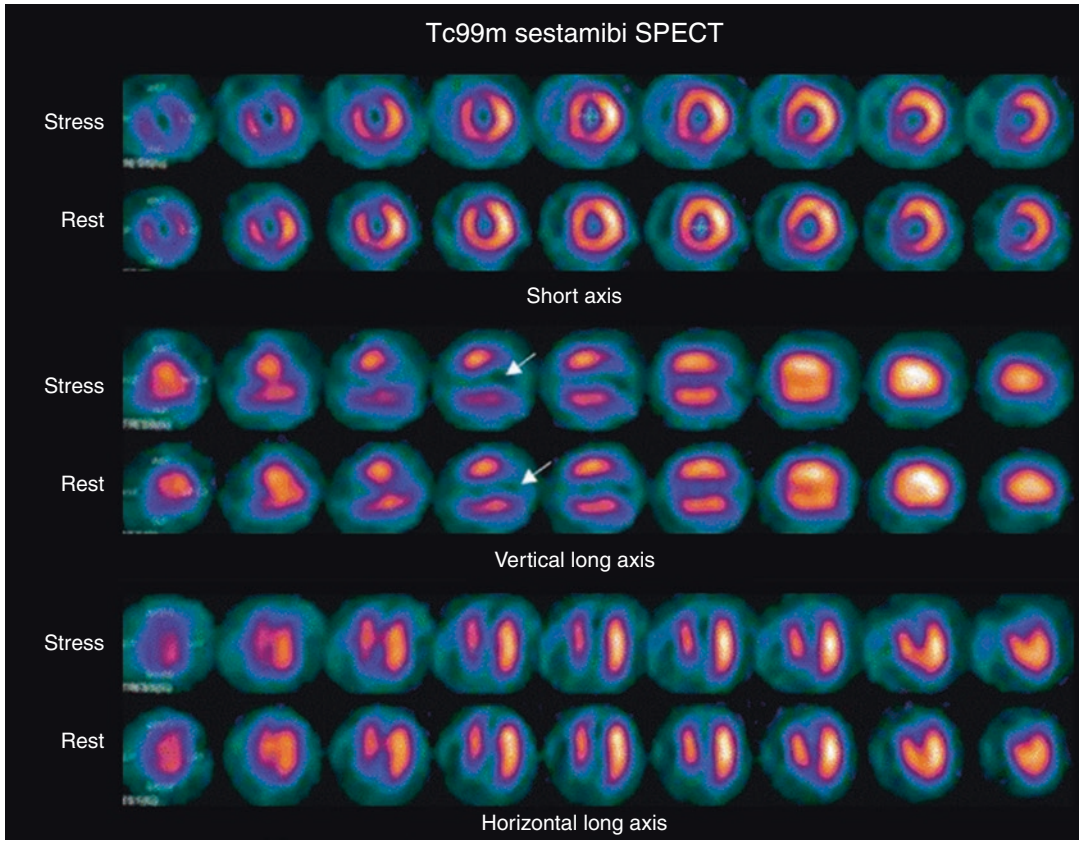

Fig. 9.15 Stress and rest Tc99m sestamibi myocardial perfusion SPECT images in short axis, vertical long axis, and horizontal long axis. SPECT images demonstrate fixed perfusion defect in the apex (arrows). There was also akinetic wall motion in this region. Findings are consistent with apical scar/infarct with possible aneurysm suggested by slight divergence of left ventricular walls as they approach the apex, instead of normal convergence on horizontal long axis images

probability for the presence of coronary artery disease. The pretest probability is determined from easily obtained parameters: age, gender, symptoms, and rest ECG [92]. Such patients might be chronically symptomatic with some atypical features at presentation. MPI is inappropriate for patients with a low pretest probability due to the high rate of false-positive results in such patients. Patients with several risk factors for CAD and typical symptoms with a high probability of CAD do not gain so much from MPI for diagnosis, as the diagnosis is nearly certain on clinical grounds. However, such patients would benefit from MPI for risk stratification. Exercise stress testing without MPI is inadequate for diagnostic purposes in patients who are unable to exercise adequately and in those with nondiagnostic baseline ECG, such as LBBB, paced rhythm, left ventricular hypertrophy, or users of digoxin [93].

In other patients, MPI adds to the diagnostic accuracy of ECG stress testing alone.

Average sensitivity and specificity of MPI for diagnosis of CAD have been reported close to 90 and 70%, respectively. The gold standard for diagnosis of CAD remains coronary angiography, despite its known limitations and likely systematic underestimation of the extent of disease. True sensitivity and specificity with each new tracer and each new imaging protocol have been difficult to ascertain because of posttest angiographic referral bias. Patients with negative results on MPI are rarely referred for coronary angiography, except where clini-

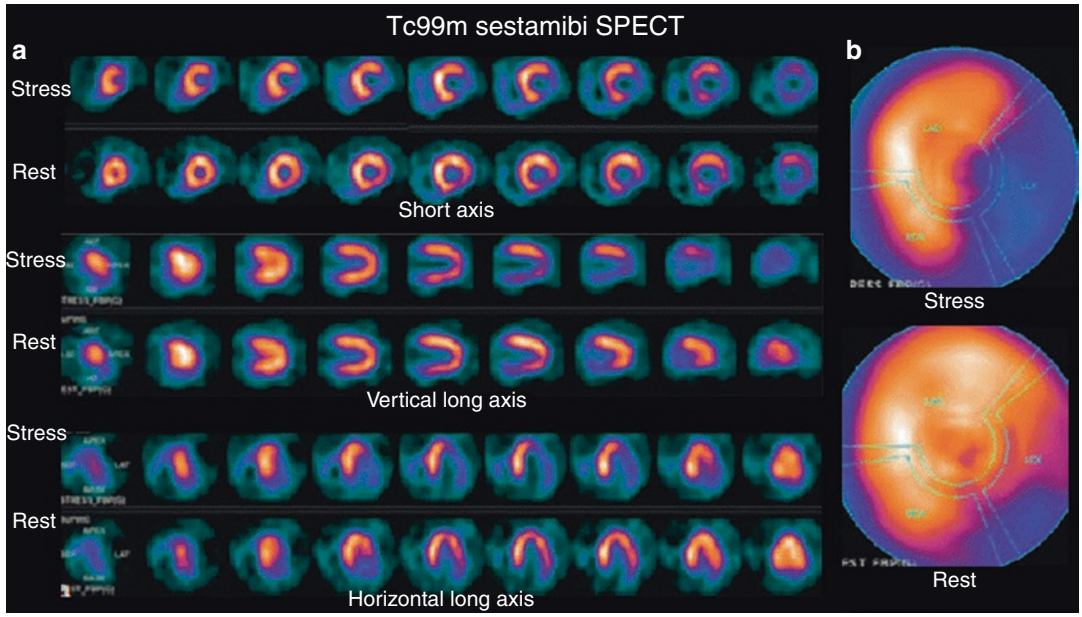

Fig. 9.16 Sixty-year-old male with history of hypertension and CAD and currently complains of shortness of breath**.** Stress and rest myocardial perfusion SPECT images in short axis, vertical long axis, and horizontal long axis (**a**) and stress and rest bullseye polar maps (**b**). There is a large area of significant reversible perfusion defect involving the lateral wall, and inferolateral regions, which is consistent with stress-induced ischemia. A small fixed defect in the inferolateral base

Table 9.8 Candidate patients for MPI for prognostic and risk stratifications

1. Stable CAD evaluated for prognosis
2. Acute chest pain syndromes
3. Post-acute myocardial infarction
4. Post-revascularization procedures (CABG, PTCA, coronary stenting)
5. Before noncardiac surgery
6. Post-cardiac transplantation

cal ECG responses or clues in the MPI images suggest possible global "balanced ischemia." This practice is justified because of the known excellent prognosis of patients with a normal MPI study [94].

Nevertheless, this referral bias limits the usefulness of retrospective validation studies using a clinical test population.

Prognosis

Several distinct patient groups are commonly referred for MPI for prognostic assessment.

1. **Prognosis Assessment in Stable CAD**

Current guidelines recommend that the care for ishemic heart disease patients is driven by risk assessment. Structural and functional information provided by different imaging techniques aids the physician in assessing different aspects of the disease. The recent shift in the management of these patients from an anatomical to a functional gold standard which further emphasized the importance of functional imaging techniques. Recent technological advances in image acquisition and processing such as tomographic imaging (SPECT), gating, attenuation correction, and Tc-99m-based tracers allow for more accurate simultaneous evaluation of myocardial perfusion and function. Perfusion abnormalities can be classified according to size, localization, severity, and reversibility. Left ventricular volumes, systolic wall thickening, segmental wall motion, and ejection fraction can be quantified. Right ventricular size and function can be assessed.

Retrospective and prospective observations have defined patterns which are compatible with high-risk prognosis as well as benign prognosis. A normal perfusion pattern in patients with an adequate level of stress and with high-quality study is consistent with an excellent short-term prognosis, regardless of coronary anatomy [94]. The extent of perfusion abnormalities characterized by number of abnormal segments, severity of defects, and extent of reversibility (ischemia) defines prognosis. When integrated with results of the exercise stress test and parameters of left and right ventricular function, combined information has a prognostic value which exceeds prognostication based on performance of coronary angiography [91]. The average annual cardiac event rate in patients with abnormal images is 12-fold than in patients with normal images. Both fixed and reversible defects are prognostically significant. Fixed defects are a predictor of death, whereas reversible defects are an important predictor of nonfatal myocardial infarction [95].

The event rate is significantly greater in patients with severe than in those with mild abnormalities (10.6% annual hard event rate vs. 3.5%) [93]. Incorporation of other SPECT variables, such as stress-induced LV dilation, LVEF, and LV volumes, further enhances the prognostic power of SPECT imaging [93, 96].

A high likelihood of multivessel (hence surgical) CAD is indicated by the presence of perfusion defects in each of the three coronary artery territories, diffuse slow washout of Tl-201, prominent pulmonary Tl-201 activity, transient stress-induced LV dilation, fall in LVEF on the gated stress SPECT MPI images, and the "left main pattern" of anterior, septal, and posterolateral defects [97].

2. **Prognosis Assessment in Acute Chest Pain Syndromes**

Acute chest pain may be due to myocardial ischemia as a result of a coronary artery plaque rupture and may be potentially life threatening. However, in only 40% of emergency department (ED) visits for chest pain the pain of cardiac origin. Rapid and reliable triage is needed for speedy diagnosis of acute myocardial infarction and to prevent unnecessary hospitalizations and inappropriate discharges from the ED [98].

Current diagnostic tools include clinical observation, serial ECGs, ST segment monitoring, serial measurements of serum markers of myocardial necrosis (such as CK-MB, troponins), and noninvasive cardiac imaging. Some centers perform MPI at rest. Abnormal results lead to hospital admission. Others perform stress testing, with or without MPI, 6–12 h after a negative workup for an acute MI [99, 100]. Based on the results of MPI, a patient's short-term prognosis can be determined.

3. **Prognosis Assessment After an Acute Myocardial Infarction**

The purposes of early or predischarge MPI evaluation after an acute myocardial infarction are (a) to assess the extent of sustained damage, including determination of the ejection fraction, and (b) to detect residual ischemia, both in the infarct-related territory and in the other vascular territories using either exercise MPI or pharmacological stress. In the era of acute interventions (i.e., thrombolysis, PTCA, stenting), the urge to perform invasive assessment (by angiography) is often irresistible. However, recent reports support a less aggressive approach: Patients with a limited amount of ischemia after an acute myocardial infarction can be risk stratified noninvasively and, if found to have a low-risk profile, treated medically with the same results as those treated with interventions [101, 102].

4. **Prognosis Assessment After Revascularization Procedures**

In view of the possibility of restenosis after percutaneous revascularization and of aorto-coronary bypass graft closure after coronary artery bypass surgery, and the frequent absence of reliable symptoms, MPI is an efficient means to determine the need for additional and/or repeat interventions, especially when the clinical symptoms are vague or nonspecific [103].

5. **Risk Assessment Prior to Noncardiac Surgery**

   Preoperative evaluation for noncardiac surgery depends partly on a patient's risk factors. These include severity and/or stability of known heart disease; the presence of concomitant conditions such as diabetes mellitus, peripheral vascular disease, renal insufficiency, and pulmonary disease; urgency of the surgery (emergency vs. elective); and type of surgery planned. Several principles for preoperative evaluation are summarized in the 2002 AHA/ACC Task Force guideline update recommendations [104].

   There is currently no evidence that preoperative revascularization alters the outcome of noncardiac surgery. However, risk stratification based on preoperative testing can help the patient and physician choose the best type and timing of surgery, perioperative care, and long-term postoperative management.

6. **Prognosis Assessment After Cardiac Transplantation**

   Long-term survival after heart transplantation, in excess of 80% after 1 year, is now common [105, 106].

   Immunologically mediated obstructive coronary vasculopathy has emerged as the most devastating late complication. Pain symptoms of myocardial ischemia are absent because of denervation of the transplanted heart. Frequent invasive (angiographic) evaluation is not practical. MPI and perhaps stress echocardiography are emerging as surveillance methods for detection of asymptomatic myocardial ischemia [107, 108].

9.5.2.2 PET Myocardial Perfusion Imaging

Currently, PET is considered the gold standard for noninvasive quantitative assessment of myocardial perfusion and metabolism although the availability is still limited. Although the role of SPECT MPI in the diagnosis and management of ischemic heart disease is well established and its qualitative or semi-quantitative assessment of regional perfusion is most used in clinical practice, it has limitations in determining the extent of the disease particularly in patients with multivessel disease and its inability to delineate the extent and severity of diffuse atherosclerosis and microvascular dysfunction. On the other hand, PET enables better assessment of disease by analyzing myocardial perfusion, function, and metabolism (Table 9.9).

Table 9.9 Advantages of PET imaging in heart disease

Offers reliable attenuation correction
Higher resolution
Ability to reliably detect coronary disease down to about 50% occlusion
Ability to delineate the extent and severity of diffuse atherosclerosis and microvascular dysfunction
More reliable in obese patients
Absolute perfusion quantitation
Lower radiation than SPECT MPI

Myocardial Perfusion PET imaging

The tracers used most commonly are 82Rb-chloride and 13N-ammonia [109]. Less commonly used are and O-15 water and F-18flurpiridaz (Table 9.10). Each has specific features that make one preferable over another in individual situations.

The perfusion tracer is injected intravenously at rest, followed by a PET acquisition, and again during pharmacological stress with either intravenous regadenoson, dipyridamole, adenosine, or dobutamine/arbutamine.

The rest and stress perfusion studies can and should be gated, if possible, providing valuable information about LV function at rest and during stress. With a PET-CT scanner, a CT transmission scan with each of the rest and stress perfusion scans is performed. For N-13 ammonia or F-18 flurpiridaz, it is possible to perform either exercise or pharmacological stress, although pharmacological stress is been used in most patients. In the USA, regadenoson is the agent utilized most commonly for inducing coronary vasodilation [110]. Exercise stress is challenging technically because of the short half-lives of PET radiotracers, size of PET gantry for supine bicycles, and motion artifacts with exercise [109].

Table 9.10 Positron-emitting tracers for myo cardial perfusion

Tracer	Physical half-life	Mean range (mm)	Production	Scan duration	Mechanism	Require on-site cyclotron
N-13 ammonia	9.8 min	0.7	Cyclotron	20 min	Metabolic trapping in myocardium	Yes
Rubidium-82	75 s	2.4	Generator	6 min	Free diffusion, metabolically inert	No
F-18 flurpiridaz	110 min	0.2	Cyclotron	20 min	Metabolic trapping in myocardium	Yes
O-15 water	2.0 min	1.1	Cyclotron	6 min	Metabolic trapping in myocardium	No

1. **N-13 Ammonia**

In the bloodstream, N-13 ammonia consists of the neutral NH_3 molecule in equilibrium with NH_4^+. At normal pH, NH_4^+ is the predominant form. The neutral, lipid-soluble NH_3 readily crosses cell membranes by diffusion. Inside the cell, the NH_3 converts into $NH_4^+$and is trapped in the cell as glutamine in a reaction catalyzed by glutamine synthase [111].

Egress from the cell is slow, mostly through catabolism of proteins and amino acids. N-13 ammonia has been used as a PET myocardial perfusion agent since 1972 [112] with either pharmacological or exercise stress. Its extraction fraction remains high even with high flows during pharmacological vasodilation, although under severe metabolic derangement, the glutamine synthase pathway can be blocked and the uptake of N-13 ammonia can become low [113].

Its half-life allows high-quality image acquisition and gating. In dogs, Gould et al. demonstrated that coronary stenoses of 47% or greater can be detected by perfusion imaging with N-13 ammonia in conjunction with IV dipyridamole [114].

In human beings, Schelbert et al. correctly identified 52 of 58 stenosed vessels (90% sensitivity per vessel) and correctly diagnosed the presence of CAD in 31 of 32 patients (97% sensitivity) [111]. Tamaki et al. [115] demonstrated a sensitivity of 95% for N-13 ammonia rest and exercise stress imaging (Fig. 9.17).

2. **Rubidium-82**

Rubidium-82 is a potassium analog. Like Tl-201, Rb-82 is transported into cells by the Na^+/K^+ ATPase pump. Like Tl-201, Rb-82 extraction decreases at high blood flow and can be altered by drugs, severe acidosis, hypoxia, and ischemia [116, 117].

With ischemia, segmental reduction of Rb-82 uptake can persist following exercise, even after symptoms and ECG abnormalities have resolved, for up to 30 min. Owing to its short half-life (75 s), Rb-82 is injected at a high dose (30–60 mCi); this is followed by a short acquisition lasting 4–6 min. The imaging sequence can be fast and efficient. An example of rest and stress Rb-82 PET myocardial perfusion images and gated resting images is shown in Fig. 9.18. In chronically instrumented dogs, Gould et al. detected coronary stenoses of 50% or greater with Rb-82 imaging and dipyridamole stress [118].

Gould et al. [119] compared Rb-82 rest and dipyridamole-handgrip stress imaging with a validated quantitative flow reserve index obtained from contrast angiograms. The results showed a sensitivity of 95% and a specificity of 100% for impaired flow reserve. Studies performed to study the accuracy of Rb-82 PET perfusion MPI for the detection of CAD showed a sensitivity from 85 to 93% and a specificity of 50–90% (Fig. 9.19).

The normal myocardial distribution of Rb-82 is similar to Tc-99m-labeled SPECT tracers, but the image resolution is better (Fig. 9.18).

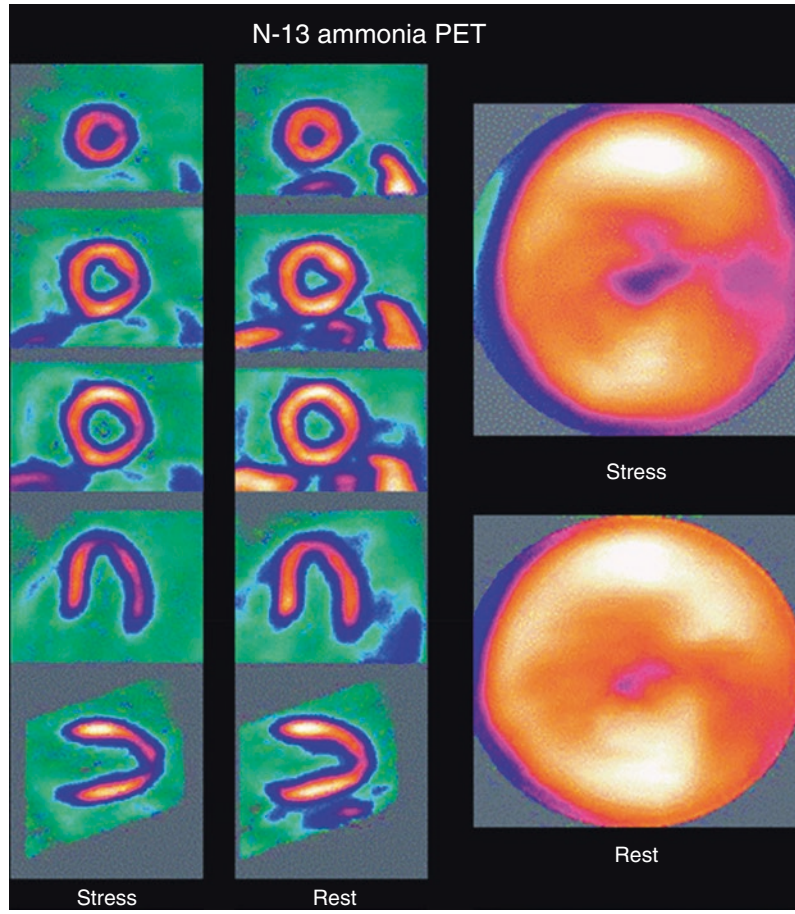

Fig. 9.17 Stress and rest N-13 ammonia PET images demonstrating a mild lateral wall defect during stress, with normal distribution at rest

3. **Oxygen-15 Water**

   The use of O-15 water is limited to quantification of coronary blood flow. Water enters all cells by diffusion, with a high extraction fraction even at high myocardial flow. Owing to the very short half-life of O-15, the tracer must be produced by an on-site cyclotron.

4. **Fluorine-18 Flurpiridaz**

   F-18 flurpiridaz is lipophilic and, like Tc-99m sestamibi, binds to mitochondria with high affinity. Preclinical studies showed that the extraction fraction of F-18 flurpiridaz was greater than that of N-13 ammonia, R-82, thallium-201 (201Tl), or technetium-99m (Tc-99m) sestamibi and was in fact found to be greater than 90%. Both sensitivity and absolute quantification of MBF would be expected to be more suitable with this high-extraction-fraction tracer because there is significantly less roll-off in extraction at high flows than there is with other tracers [119]. In Phase I trials, the heart exhibited high and sustained retention of F-18 flurpiridaz from the earliest images through approximately 5 h after injection [120].

   Similar to the Tc-99m perfusion agents, one administers a slightly lower for resting study dose (approximately 74–111 MBq (2–3 mCi)). After waiting for approximately 50–70 min, perform exercise or pharmacological stress, and administer a higher (approximately 240 MBq (6.5 mCi)) during stress for stress study (Fig. 9.20). In a Phase II study comparing F-18 flurpiridaz MPI to Tc-99m sestamibi SPECT MPI in the same 143 subjects in 21 centers, a higher percentage of images was rated as excellent or good on PET versus SPECT imaging, with a higher diagnostic certainty. In 86 patients who underwent coronary angiography, sensitivity of

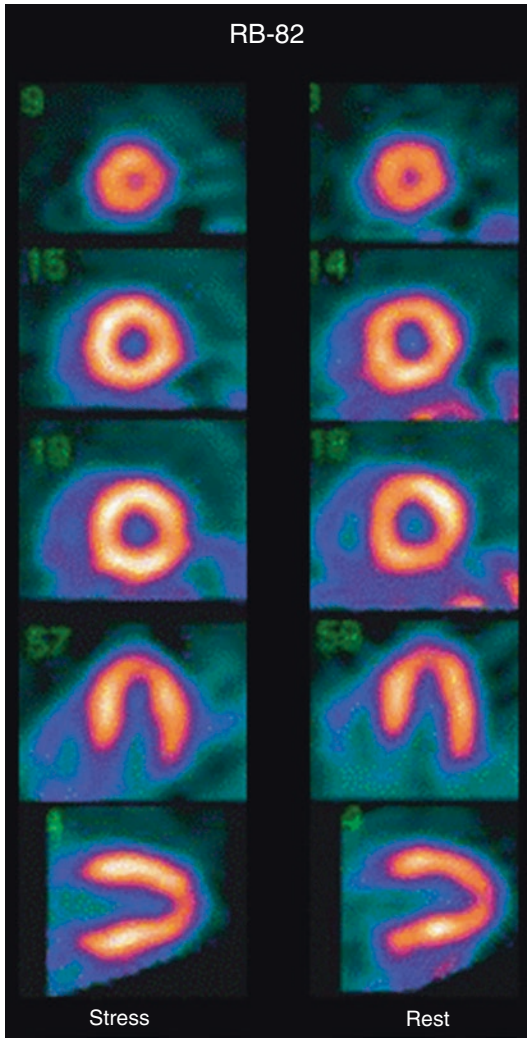

Fig. 9.18 Stress and rest selected Rb-82 short axis and horizontal and vertical long axis images demonstrating normal perfusion

F-18 flurpiridaz PET for individual coronary vessel disease was higher than SPECT MPI, 79% versus 62%, with similar specificity, and a normalcy of 90% with F-18 flurpiridaz PET versus 97% with SPECT. In patients with CAD on angiography, the magnitude of reversible defects was greater with PET compared to SPECT [121].

Myocardial Metabolism FDG PET Imaging

The major source of ATP in a normal heart is oxidation of free fatty acids, rather than of carbohydrate. With ischemia, reversible metabolic adaptation will occur to enable myocytes to survive in a low oxygen environment. Mitochondrial oxidation is supressed and anaerobic metabolism may occur. Exogenous glucose uptake and glycogen breakdown are increased with stimulation of glycolysis and ATP production from the anaerobic catabolism of glucose. Accordingly F-18 FDG is the radiotracer used for PET metabolic imaging [122].

FDG is a glucose analogue that is transported into the myocyte by the same carriers (GLUT-1 and GLUT-4) as glucose and phosphorylated to FDG-6-phosphate by hexokinase. PET imaging of regional glucose uptake reflects overall cell glucose uptake. FDG uptake may be increased in hibernating but viable myocardium; uptake in regions with reduced blood flow at rest has become a marker of hibernation.

Clinical Uses of PET in Heart Diseases

Positron emission tomography is increasingly used in the diagnosis and risk stratification of patients with ischemic heart disease (Table 9.11). PET myocardial perfusion imaging has a mean sensitivity and specificity of around 90% for the detection of angiographically significant coronary artery disease, and is also highly accurate for assessing the prognosis of patients with ischemic heart disease. Based on the tracer used, it can provide information not only on myocardial perfusion but also on myocardial metabolism, which is important for myocardial viability evaluation. The value of this imaging technique has been further enhanced with the introduction of hybrid scanners (PET/CT and PET/MR), offering integrated morphological and functional information and consequently comprehensive assessment of atherosclerosis effect on the myocardium [123].

PET in the Diagnosis of Ischemic Heart Disease

FDG-PET has several advantages including higher sensitivity and specificity over perfusion tracer, reliable attenuation correction, thus avoiding the attenuation artifacts seen frequently in SPECT imaging, although caution needs to be exercised to recognize and correct for PET emis-

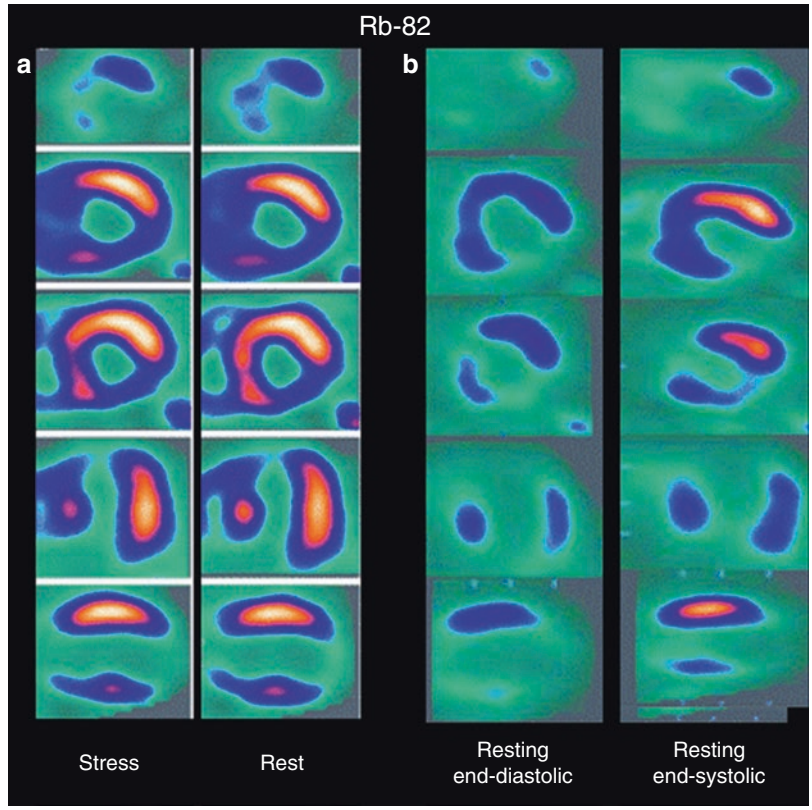

Fig. 9.19 (**a**) Stress and rest of Rb-82 PET images demonstrating severe extensive apical, septal, and inferior scarring and only minimal basal septal ischemia. (**b**) Resting end-diastolic and end-systolic gated images, showing poor or absent contractility in the scarred regions and poor overall LV function

sion-transmission misregistration artifacts. PET imaging also offers higher resolution. A number of studies have shown a higher accuracy of coronary disease detection by stress PET imaging compared with SPECT imaging [111, 120, 124, 125]. The high extraction fraction of the PET tracers, especially N-13 ammonia and O-15 water, assures higher sensitivity for disease at high flows during pharmacological stress, resulting in the ability to reliably detect coronary disease down to about 50% occlusion [124, 126]. Comparisons of sestamibi and PET perfusion imaging showed that adenosine stress MIBI SPECT imaging significantly underestimates ischemia and defect severity compared with N-13 ammonia PET [127, 128].

Many studies indicate that PET imaging consistently yield higher diagnostic accuracy for detection of coronary artery disease compared to gated Tc-99m sestamibi SPECT imaging, both with and without SPECT attenuation correction [129–135]. One study performed head-to-head comparison of 208 adults of coronary computed tomography angiography, single-photon emission tomography, $[^{15}O]H_2O$ positron emission tomography, and hybrid imaging for the diagnosis of myocardial ischemia [133]. demonstrated highest diagnostic accuracy for Positron emission tomography compared with single-photon emission tomography and coronary computed tomography angiography.

The gating of MPI at rest and during stress with PET imaging allows the additional diagnostic and prognostic relevant information about the severity of disease. During gated vasodilator stress Rb-82 PET imaging, LVEF increases with vasodilator stress in patients without significant stress-induced perfusion defects or severe left main/3-vessel CAD. A high LVEF reserve appears to be an excellent tool to exclude left main/3-vessel CAD noninvasively [136].

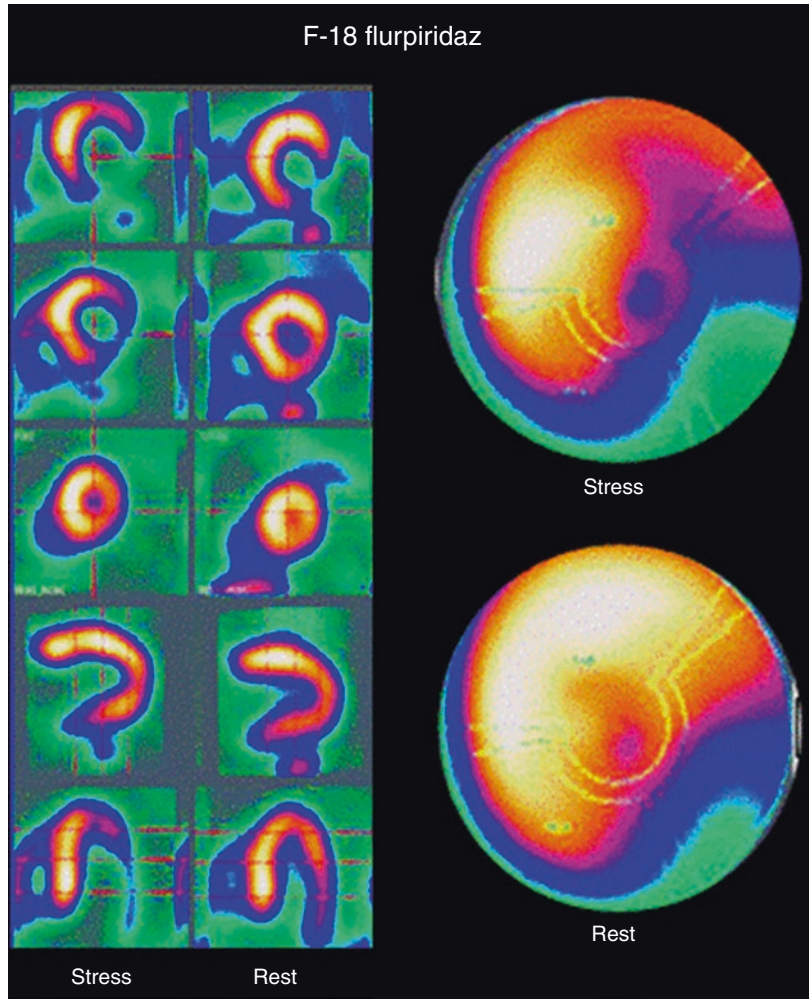

Fig. 9.20 Stress and rest PET images with F-18 flurpiridaz, demonstrating severe inferolateral and mild anterolateral and apicolateral defects with stress, with complete improvement in the anterolateral and apicolateral wall and partial improvement in the inferolateral wall

Table 9.11 Clinical applications of PET in heart diseases

1. Perfusion assessment
2. Absolute quantification of myocardial blood flow
3. Assessment of myocardial viability
4. Prognostic assessment
5. Assessing ventricular function
6. Cardiovascular prosthetic infection
7. Cardiac sarcoidosis, amyloidosis

Quantation of myocardial perfusion in absolute units by PET further improves its diagnostic accuracy. Patients with multivessel disease, microvascular disease, and obese patients may benefit most from this quantitative assessment [137, 138].

Quantification of Myocardial Blood Flow

In addition to qualitative and semi-quantitative grading, PET enables absolute quantification of perfusion. Absolute quantification of myocardial blood flow expands the scope of conventional relative MPI from identifying only end-stage epicardial IHD to the earlier identification and characterization of abnormalities in coronary endothelial function and subclinical stages of IHD (microvascular dysfunction) [139]. Quantitation of myocardial perfusion offers an objective parameter which is more reproducible than visual interpretation. PET has become the noninvasive imaging modality of choice for the quantification of MBF. In conclusion, it adds not

only to diagnostic certainty but also provides prognostic value (see later).

PET in Prognosis Assessment

PET MPI, similarly to SPECT MPI, has great prognostic value in patients with known or suspected IHD. Marvick et al. noted that defect severity with PET was related to outcome [140, 141]. Normal ribidium-82 PET MPI have good prognosis, regardless of ECG changes during stress including patients whose diagnosis was uncertain after SPECT MPI and in obese patients [142–144]. A multicenter observational registry in 7061 patients from 4 centers underwent a clinical indicated rest-stress Rb-82 PET MPI, with a mean follow-up of 2.2 years. The investigators found that the risk-adjusted hazard of cardiac death increased with 10% with abnormal stress PET, compared to normal PET results. The model worked even better when clinical risk factors were combined with PET MPI findings [145]. In a related work, Rb-82 PET findings were particularly helpful in identifying high-risk, older women [146]. Similarly, perfusion findings on 256 N-13 ammonia PET MPI studies were shown to be strong predictors of clinical outcome [147]. Dorbala et al. [148] demonstrated that not only vasodilator stress Rb-82 PET MPI provides incremental prognostic value to historical/clinical variables to predict risk of cardiac events and all-cause death, but also the left ventricular ejection fraction reserve provides significant independent and incremental value to Rb-82 MPI for predicting the risk of future adverse events. The extent and severity of PET perfusion defect, rest left ventricular (LV) ejection fraction (LVEF), stress LVEF and LVEF reserve (stress LVEF - rest LVEF), LV volumes and myocardial flow reserve provide valuable prognostic information [144–146, 149]. Even in the presence of angiographically significant IHD, normal findings on stress MPI are generally associated with a low risk of CV events (around 1% per year) [150].

The risk of cardiac events, however, must consider all factors besides imaging information. Ceratin groups of patients such as diabetics, those with known IHD, old age group were found to have higher annual event rate (1.4–1.8%) despite normal MPI. The warranty period of a normal PET MPI in is around 2 years [151] depending on risk factor control.

Myocardial flow reserve was found to independently augment clinical outcome prediction. The quantification of blood flow at rest and during maximal pharmacological stress allows measurement of flow reserve in various hypertrophies and cardiomyopathies, post-transplant CAD [152], syndrome X, and other vascular endothelial disorders and to study the effects of smoking, diabetes, various medications [153–156], and lipid control [157–159].

Multiple studies documented the greater prognostic value of PET-derived myocardial flow reserve (MFR) compared to clinical factors and perfusion defect size and severity in patients with known or suspected IHD [160, 161]. Addition of PET derived MFR, led to correct reclassification of estimated risk categories in 35% of patients with previously intermediate risk of death [162]. Since MFR indirectly reflects microvascular disease, it also has prognostic value in diabetic patients with diabetes and in patients with chronic kidney disease [163].

In viability imaging, FDG PET has the greatest sensitivity for predicting global LV functional recovery following revascularization, compared with SPECT, dobutamine stress echocardiography, and cardiac MRI [164–166].

The amount of tissue of scarring as well as hibernating myocardium on FDG PET has also been shown to be an important predictor of improvement in LVEF following revascularization [167–169]. Additionally, compared to scar, dysfunctional myocardium diagnosed as hibernating or stunned by PET has a high chance of functional improvement following revascularization [169].

PET in Assessment of Myocardial Viability

PET is very valuable in assessing viability in stunned myocardium (Delayed functional recovery myocardium) and hibernating myocardium (chronically depressed function of hypoperfused myocardium). Demonstration of preserved glucose metabolism by FDG is a marker of myocardial viability (Fig. 9.21) While matching defect on perfusion and FDG indicates non-viable myocardium (Fig. 9.22). The detection of viable myo-

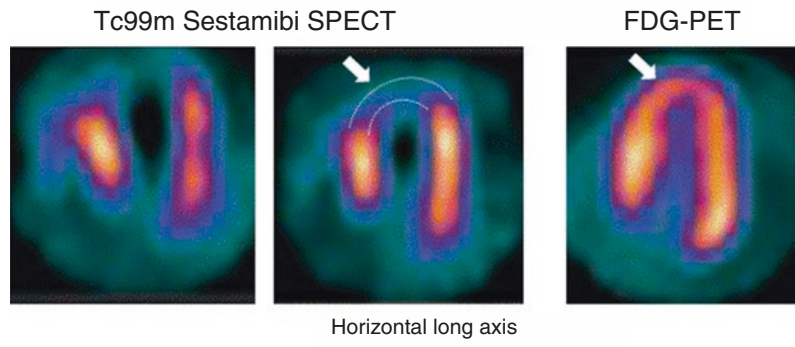

Fig. 9.21 Viable myocardium pattern

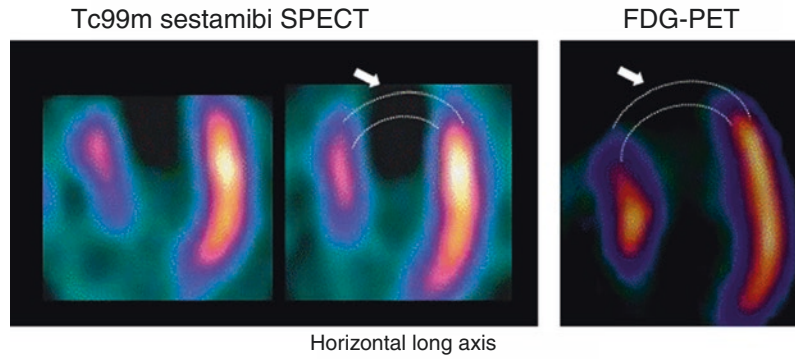

Fig. 9.22 Pattern of non-viable myocardium

cardium is accurately estimated by referencing the level of myocardial glucose metabolism to the level of MBF [123, 169]. Sequential perfusion-metabolism imaging gives the most complete information, yielding different interpretation scenarios. See later more details.

PET in Assessing Ventricular Function

Gated first-pass ^{18}F-FDG PET has also been introduced for assessing ventricular function [170].

PET in Endocarditis and Cardiovascular Prosthetic Infection

Cardiovascular prosthetic infection is a difficult condition to diagnose. PET has a major role in the diagnosis of endocarditis and prosthetic infections (Pathophysiology and diagnosis is presented in Chap. 4).

PET in Assessing Ventricular Function

Gated first-pass ^{18}F-FDG PET has also been introduced for assessing ventricular function [170].

PET in Endocarditis and Cardiovascular Prosthetic Infection

Infective endocarditis is among the most severe infectious diseases. Patients with damaged or artificial heart valves and heart defects are at greatest risk for endocarditis. Cardiovascular prosthetic infection is a difficult condition to diagnose. PET has a major role in the diagnosis of endocarditis and prosthetic infections Fig. 9.23 (see details in Chap. 4).

PET in Cardiac Sarcoidosis and Amyloidosis

Sarcoidosis and Amyloidosis are both multiorgan systemic diseases. Diagnosis of cardiac involvement is particularly important because it can be fatal. Sarcoidosis is a multisystem granulomatous disorder affecting the heart in up to 25% of patients. Cardiac involvement is often associated with a poor prognosis [171] as it may lead to advanced heart block, cardiomyopathy, arrhythmias, or death. PET may be essential in the diagnosis, risk stratification, and patient management [172, 173]. When sarcoidosis involves the heart it affectst left ventricular subepicardial regions,

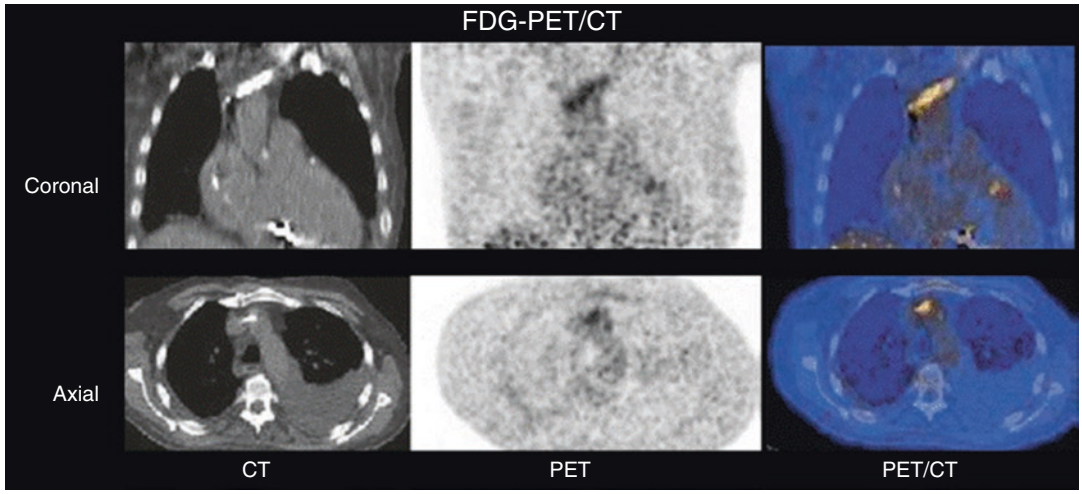

Fig. 9.23 FDG PET/CT study for a 68-year-old male with bacteremia and questionable infectious endocarditis. There is increased FDG accumulation around electrode in the left subclavian vein near superior vena cava. Findings are consistent with infection. Note successful suppression of normal cardiac uptake of FDG after 6–12 h fasting and unfractionated iv heparin administration

septal, and right ventricular free wall in >90% of cases [174]. F-18 FDG PET and 18-FDG PET/MRI are useful in the diagnosis of cardiac involvement of sarcoidosis [175, 176]. Cardiac sarcoidosis may be an incidental finding cardiac MR or PET show similar accuracy in the diagnostic workup of CS compared with autopsy studies. Combining 18F-FDG-PET/CT study with SPECT/CT perfusion is particularly useful, as the finding of multiple uptake areas associated with the matching perfusion abnormalities seen in SPECT/ CT indicate high probability of an accurate diagnosis 18F-FDG-PET/CT may also be useful to assess the therapeutic and prognostic factors [177].

Amyloidosis is the clinical condition caused by the deposition of unstable misfold proteins as amyloid fibrils. Cardiac amyloidosis is the condition in which the primary interstitial protein deposition occurs in the extracellular space of the heart. Systemic amyloidosis represents a debilitating, under-diagnosed but increasingly recognized group of disorders characterized by the extracellular deposition of these misfolded proteins in one or more organs. Cardiac amyloid deposition leads to an infiltrative or restrictive cardiomyopathy and is the major contributor to poor prognosis in patients with systemic amyloidosis. Many proteins can form amyloid fibrils, but the two main types that can infiltrate the heart are monoclonal immunoglobulin light-chain amyloid and transthyretin amyloid. Cardiac amyloidosis is classified into amyloid immunoglobulin light chain (AL) and amyloid transthyretin (ATTR) types [178]. These two most common types of cardiac amyloidosis have distinct therapeutic management and prognosis. Cardiac amyloidosis can be acquired in older individuals or inherited from birth. Early and accurate diagnosis of cardiac amyloidosis is crucial for the implementation of appropriate patient care and is now more important than ever given the availability of new therapies [179].

Cardiac amyloidosis is currently diagnosed more frequently than in the past owing to the advanced diagnostic modalities. Echocardiography and Cardiac MRI play a crucial role in the diagnostic workup of cardiac amyloidosis; however, the differentiation between the subtypes of cardiac amyloidosis is still difficult [177]. Scintigraphy is valuable in the diagnosis and follow-up of the disease. Radiotracers for amyloidosis include (1) bone tracers including PYP, (2) amyloid-directed molecules, (3) PET amyloid agents, and (4) I-123-

MIBG. Bone tracers are particularly sensitive in the detection of ATTR type amyloidosis, whereas PET amyloid agents show a higher affinity for the AL type. An important limitation of ^{18}F-FDG is the physiologic uptake in the myocardium, which may remain in approximately 20% of patients even after proper preparation [178]. This fact limited the FDG PET scan's sensitivity for detection of cardiac involvement to 62.5% [180]. ^{11}C-Labeled Pittsburgh compound B (^{11}C-PiB), a radio-labeled derivative of thioflavin-T that is used to detect Aβ amyloid deposition in Alzheimer's disease [181]. The findings of ^{11}C-PiB PET were found to correlate well with post-mortem histopathological samples [180]. Finally, 123I-MIBG scintigraphy is capable of detecting cardiac sympathetic denervation in cardiac amyloidosis [181].

9.5.2.3 Hybrid Myocardial Perfusion and CT Imaging

CT Attenuation Correction

Combining PET and CT imaging as a single combined PET-CT unit has become the preferred approach for PET imaging in oncology. For cardiac PET imaging, the scout CT checks the position of the patient in a few seconds. The CT transmission scan, lasting 10–30 s, saves a significant amount of time compared to transmission imaging using radiation pin-sources. The CT transmission scan is relatively noise free, compared to the dedicated PET transmission scan. It enables one to perform an entire rest and pharmacological stress PET perfusion imaging study with rubidium-82 in 30–40 min, compared to 45–60 min for a dedicated PET scanner.

Calcium Scoring

Another application of PET-CT and SPECT-CT is the possibility of obtaining coronary calcium scores in the same imaging session as the PET or SPECT MPI, which is feasible with an 8-, 16-, or 64-slice multidetector CT scanner. Calcium scoring requires gating and a higher current from the CT scanner than a transmission scan, resulting in higher patient radiation exposure, but still lower than diagnostic CT imaging [182–185].

CT Coronary Angiography

The possibility of performing CT coronary angiography performed together with PET or SPECT MPI in selected patients can be very valuable.

9.5.2.4 Assessment of Myocardial Viability

Nonfunctioning but viable myocardium includes stunned and hibernating myocardium and also remodeling.

1. Stunned myocardium reoresents reversible regional decreased contractility after an episode of prolonged ischemia, but intact blood flow at the time of observation [169]. Oxygen-derived free radicals contribute to postischemic dysfunction [186]. Stunned myocardium generally improves without further intervention. In most cases of exercise-induced ischemia, this may take a few minutes or, uncommonly, several hours. Following an acute coronary occlusion and thrombolysis, most of the improvement takes place over 7–10 days, but it may take longer in the presence of residual stenosis and/or repeated stunning [187]. Patients may experience repeated episodes of ischemia, often silent, in the same territory, and the stunned myocardium may not be able to recover, leading to a quasi-permanent state of stunning [188, 189] and progressing to hibernation [190]. When superimposed on an already severely dysfunctional heart, it may become dangerous, and the patient may require hemodynamic support. Recovery of myocardial function is spontaneous provided that myocardial perfusion remains normal. The duration of stunning is directly proportional to the duration of the preceding ischemia.
2. Hibernation occurs in myocardium that has undergone a downregulation of contractile function, thus reducing cellular demand for energy, in response to chronic or repetitive ischemia [123]. Hibernation may represent a spectrum, with chronic repetitive stunning showing normal or near normal resting perfusion and impaired MFR at one end and reduced rest MBF at the other. In most cases, the impair-

ment is only detected through reduced MFR, with reduced rest MBF only being seen in the most advanced cases [123]. Hibernation, by definition, requires the restoration of blood flow in order to improve function. Benefit also may be expected from reduced metabolic demand via hemodynamic support.

3. Remodeling may result in dysfunctional myocardium in the area adjacent to an infarct or hibernation also that may or may not improve with revascularization [169].

Normal myocardium uses several different metabolic substrates (predominantly glucose or fatty acids) for its energy needs. In the fasting state, the myocytes predominantly use fatty acids, whereas in the post-prandial state, they switch to use glucose [191]. The majority of dysfunctional but viable segments are in fact due to stunning (72%), with only a minority (28%) due to hibernation [192]. The definition of either stunning or hibernation includes the recovery of function, either spontaneously or after intervention. Other potential benefits from the reversal of stunning or hibernation, including prevention of remodeling or arrhythmias.

Dysfunctional but viable myocardium is not uncommon. Up to 50% of patients with previous infarction may have areas of dysfunctional viable myocardium mixed with scar tissue, even in areas with Q waves on the ECG [191].

Resting wall motion imaging identifies myocardium which is thickening and moving well and that which is not. It cannot differentiate dysfunctional viable myocardium from permanently scarred myocardium, except by documenting serial changes in function over time. Stimulation by exercise, catecholamines, or nitrates and post-exercise and post-PVC potentiation are all evidence of viability, but with limited sensitivity. Low-dose dobutamine (LDDE) and high-dose dobutamine echocardiography (LDDE) showed that both biphasic response (improvement at low dose and deterioration at high dose) and sustained improvement of wall motion (improvement at both low dose and high dose) in dysfunctional segments were highly predictive of reversible dysfunction [193], with a combined sensitivity of 84% and specificity of 81% [193–196].

The uptake and retention of myocardial perfusion agents is good evidence of myocardial viability. However, impaired retention of perfusion tracers can be seen in dysfunctional, stunned myocardium, while decreased uptake due to decreased perfusion is often seen in hibernation [195]. Simple stress-redistribution imaging with Tl-201 has been shown to underestimate the presence of viability. Augmentation with late (12–24 h) imaging and/or resting reinjection was found to increase sensitivity for viability [196–199]. The latter approach yielded a combined mean sensitivity of 86% but at the cost of a lower specificity [194] (Table 9.12). In patients who cannot exercise owing to poor LV function and clinical CHF, rest-redistribution Tl-201 imaging has shown a combined sensitivity of 90% and specificity of 54% [194]. Comparisons showed LDDE to be slightly less sensitive but more specific.

Myocardial perfusion imaging with Tc-99m sestamibi has yielded a slightly lower sensitivity of 83% but higher specificity of 69% [202]. Tc-99m sestamibi imaging combined with nitrate administration has yielded an improved sensitivity of 91% and specificity of 88% [194]. Gated Tc-99m sestamibi imaging with nitroglycerin (NTG) administration can be used successfully as an alternative to rest-redistribution Tl-201 SPECT imaging [203]. Tc-99m tetrofosmin showed performance similar to that of Tl-201 stress-redistribution imaging and slightly lower sensitivity than rest-late redistribution Tl-201 imaging [204].

Table 9.12 Sensitivity and specificity of various methods of imaging for myocardial viability

Method	Patients	Sensitivity	Specificity
Dobutamine stress echocardiography	1869	76	81
Tc99m	695	83	69
Tl-201	1067	87	51
F-18 FDG PET	930	90	68
Dobutamine cardiovascular magnetic resonance (Db CMR)	247	81	91
Late gadolinium-enhanced cardiovascular magnetic resonance (LGE-CMR)	331	95	51

Data extracted from [193, 200, 201]

Myocardial perfusion can be imaged with N-13 ammonia or Rb-82 with PET imaging or Tl-201, Tc-99m sestamibi, or Tc-99m tetrofosmin imaging using SPECT (Figs. 9.24, 9.25, and 9.26).

Stunned myocardium shows relatively preserved flow and either matched or excessive FDG accumulation. At times, stunning results in impaired FDG accumulation, producing an underestimation of viability [205]. Hibernation

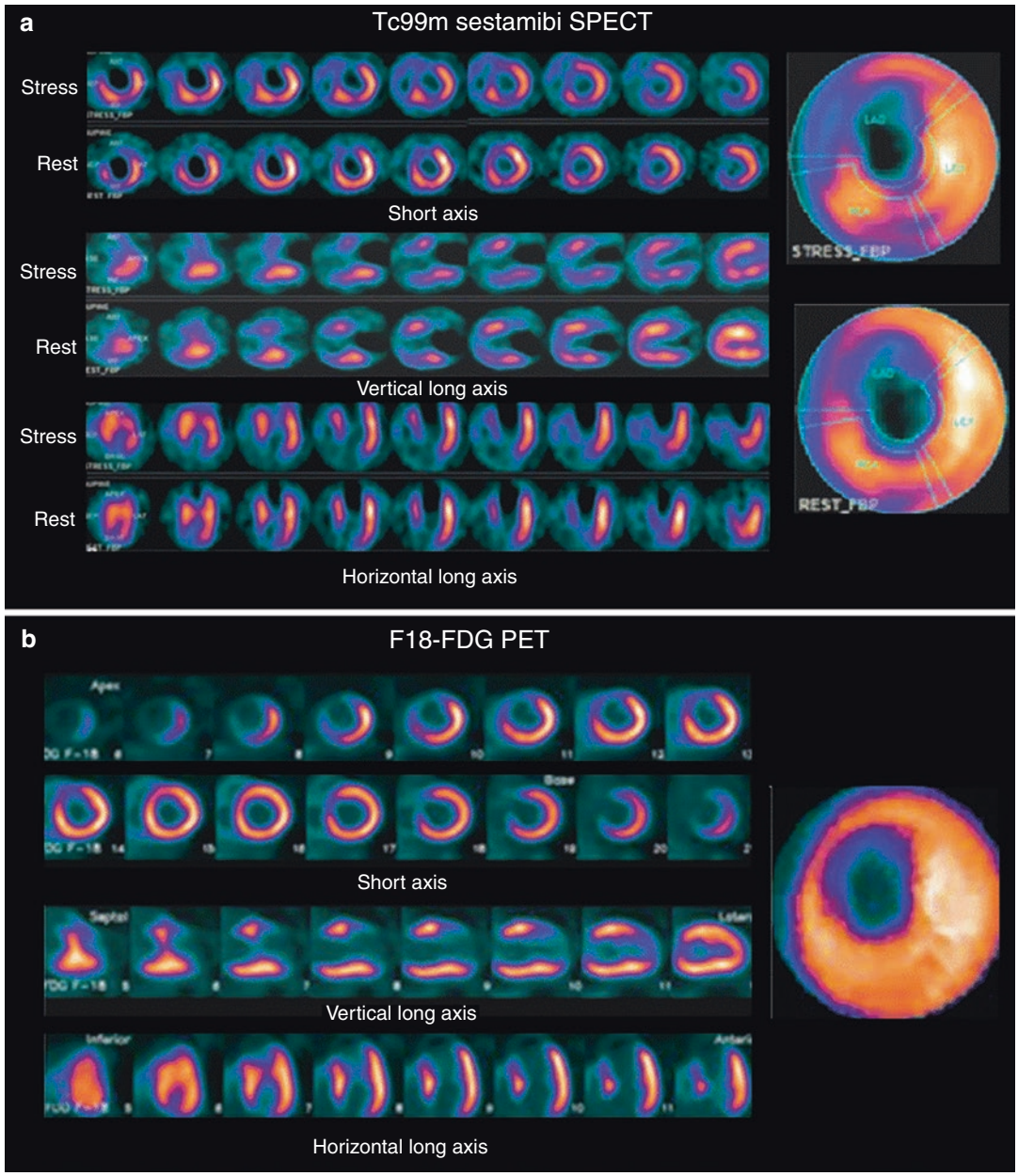

Fig. 9.24 Tc-99m sestamibi stress and rest myocardial perfusion SPECT images and polar maps (**a**) and F-18 FDG studies (**b**) for a 62-year-old male with dyslipidemia, smoking, and fixed perfusion defect on myocardial perfusion SPECT. The patient was referred for viability study. Tc-99m sestamibi SPECT images (**a**) demonstrate a large area of fixed perfusion defect involving apex and mid-anteroseptal region with stress-induced ischemia in the anteroseptal base. FDG PET images (**b**) demonstrate absent glucose metabolism in the same region. Findings are consistent with nonviable/scar tissue in the apex/mid anteroseptal region

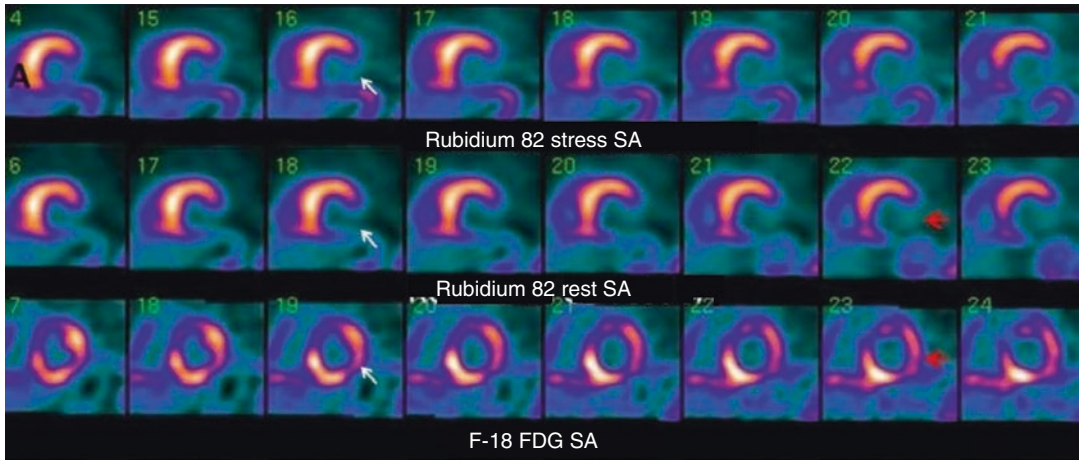

Fig. 9.25 Selected short axis frames of Rubidium-82 and F-18 FDG are shown. Viable myocardium is indicated by filling of the inferior-lateral defect by activity on FDG images (arrows) while is fixed on the perfusion study obtained utilizing Rubidium-82

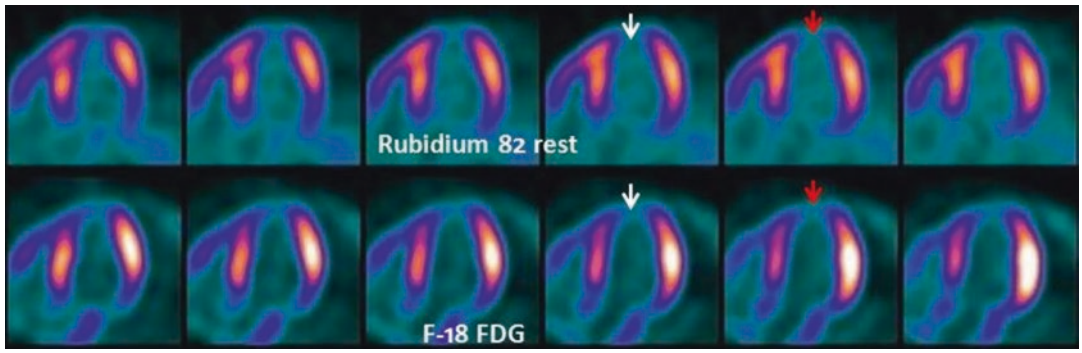

Fig. 9.26 Rubidium-82Perfusion (upper) and FDG metabolic (lower) images show no difference in an apical defect indicating a scar with no viability

has been shown to demonstrate decreased perfusion and relatively preserved or disproportionately increased FDG accumulation [202, 206]. Infarcted myocardium shows a matched decrease in both perfusion and FDG uptake (Figs. 9.25 and 9.26) while ischemia shows a mismatched pattern.

Addition of metabolic imaging to perfusion imaging using analogs of either free fatty acids or glucose imaging is valuable. Injured myocardium frequently demonstrates impaired oxidative metabolism, impaired free fatty acid utilization, and an excess of glucose utilization relative to flow. Myocardial FFA uptake is proportional to blood flow. FFA beta-oxidation is reduced in the presence of ischemia, stunning, and hibernation, which increases the proportion of FFAs accumulating in the triglyceride pool. Myocardial imaging with iodine-123-labeled FFAs shows uptake and rapid clearance in the normal myocardium and delayed clearance or accumulation in the presence of impaired oxidation. Thus, impaired FFA clearance represents recoverable myocardium [207, 208]. Labeled FFAs are only investigational in the USA. BMIPP is approved for clinical use in Japan. Where FDG production and PET imaging equipment are unavailable, I-123-labeled FFA imaging is a feasible alternative to FDG imaging.

More recently, several studies tried to address the role of viability imaging in routine decision

making, with complex results. In the PARR-1 study, in 82 patients with severe LV dysfunction who had FDG PET perfusion imaging before revascularization, the amount of scar was a significant independent predictor of LV function recovery after revascularization. A combination of PET and clinical parameters predicted the degree of recovery [209]. In PARR-2 the investigators conducted a randomized trial to assess the effectiveness of FDG PET-assisted management in a patient with severe LV dysfunction followed for 1 year for cardiac death, myocardial infarction, or recurrent hospital stay. Two hundred and eighteen patients were randomized to management assisted by FDG PET or 212 randomized to standard care. The study did not demonstrate a significant reduction in cardiac events for FDG PET-assisted management versus standard care. Given that there was a substantial proportion where the recommendations based on FDG PET were not followed, a separate analysis of patients where management adhered to PET recommendations and in patients without recent angiography, significant benefits in event-free survival were observed, thus supporting the utility of viability FDG PET imaging [210]. The complexity of the relationship between clinical factors and viability imaging and management decisions was also illustrated in the STICH trial. Among 1212 patients with CAD and LV dysfunction enrolled, 601 were randomized to assessment of myocardial viability. Of these, 298 were randomized to medical therapy plus CABG, and 303 were randomized to medical therapy alone. While 37% of 487 patients have viable myocardium and 51% without viable myocardium, seemingly confirming utility of viability imaging, after adjustment for baseline variable, the association between mortality and viability was no longer significant. One potential weakness of the study was that the viability studies were a mixture of SPECT MPI and dobutamine stress echocardiography [211].

9.5.2.5 Imaging of Myocardial Metabolism

While gated myocardial perfusion SPECT imaging offers invaluable diagnostic and prognostic information for the evaluation of patients with suspected or known coronary artery disease, advances in the cellular and molecular biology of the cardiovascular system lead to molecular imaging, which can play a role in in the early detection of CAD at the level of the vulnerable plaque, the evaluation of cardiac remodeling, and monitoring of important new therapies including gene therapy and stem cell therapy [212].

Unlike skeletal muscle, cardiomyocytes sustain an everlasting cycles of contraction and relaxation in order to supply the body with blood and maintain the homeostasis of nutrients and metabolic gases [213]. Cardiomyocytes are specialized for aerobic metabolism of fatty acids and are packed with mitochondria performing oxidative phosphorylation and β-oxidation. Cardiac health is dependent on the heart's ability to utilize different substrates to support overall oxidative metabolism to generate ATP. In other words, it is a process that converts energy-providing fuels to ATP, the energy currency in the cell. ATP is largely used to maintain myocardial contraction and to regulate the membrane pumps and movements of ions in and out of the cell. Cardiac health is dependent on the heart's ability to utilize different substrates to support overall oxidative metabolism to generate ATP.

For a given physiologic environment, the heart consumes the most efficient metabolic fuel. In the normally oxygenated heart, fatty acids account for the majority of ATP production with glucose making only a small contribution to the ATP production, unless there is an insulin surge. During an acute increase in work load (for example, inotropic stimulation), the heart immediately mobilizes its metabolic reserve contained in glycogen (transient increase in glycogen oxidation) and meets the needs for additional energy from the oxidation of carbohydrate substrates (glucose and lactate). When the oxygen supply is decreased, the heart protects itself from an oxygen-deficient state by switching its energy source to glycolysis, downregulating mitochondrial oxidative metabolism, and reducing contractile function. A substrate preference is characteristic of a variety cardiac diseases such as diabetic heart disease, in which fatty acid metabolism predominates, and dilated cardiomyopathy, in which glucose metabolism predomi-

Table 9.13 Main conditions evaluated by molecular imaging for evaluating metabolic alterations

Radiotracer	Condition evaluated	Basis of uptake
F-18 FDG	Myocardial viability	Glucose metabolism
C-11 palmitate	Idiopathic dilated cardiomyopathy	Fatty acid metabolism
C-11 acetate	Hypertrophic cardiomyopathy	Tricarboxylic acid flux
F-18 FTHA	CAD	Fatty acid metabolism
F-18 FTP	Diabetes type-2	Fatty acid metabolism
F-18 FCPHA	CAD	Fatty acid metabolism

nates [214]. Thus, the tight coupling between metabolism and contractile function in the heart offers a unique opportunity to assess cardiac performance at different levels in vivo: coronary flow, myocardial perfusion, oxygen delivery, metabolism, and contraction [215].

Based of understanding the metabolic changes of several cardiac diseases, several tracers are used for evaluation such diseases. Table 9.13 summarizes the main tracers and conditions evaluated.

9.5.2.6 Cardiac Shunt Evaluation

Two distinctive types of studies can be obtained to both qualitatively and quantitatively evaluate cardiac shunts, depending on the type of shunt suspected.

Left-to-Right Shunt

A first-pass study should be performed to assess patients with this type of shunt. Subsequently, a time-activity curve is generated from a region of interest drawn in the lung field. The pulmonary transit time is normally shown as a narrow spike, with symmetric limbs that represent the pulmonary blood flow of the radioactivity. However, this curve, particularly the descending limb, is distorted in left-to-right shunts due to early recirculation of pulmonary blood from the shunt. Calculation of the pulmonary-to-systemic flow ratio can be obtained by subtracting the fitted shunt curve from the pulmonary one. This is a sensitive method for detecting pulmonary-to-systemic blood flow shunts between 1.2 and 3.0, provided that the patient has no pulmonary hypertension, congestive heart failure, or tricuspid regurgitation [53].

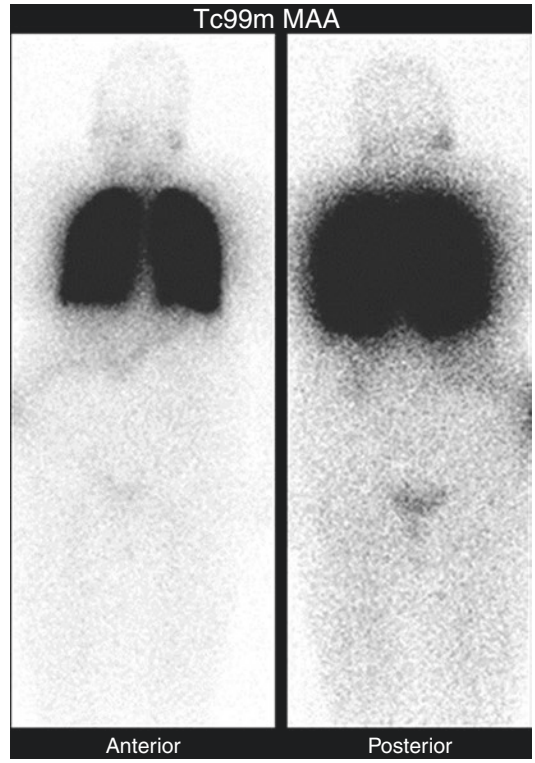

Fig. 9.27 Tc99m MAA shunt study illustrating normal findings. There is intense activity is een in the lungs, and no abnormal activity in the brain or kidney parenchyma. Mild activity in the kidneys is due to excreted activity in pelvicalyceal structures

Right-to-Left Shunt

This can be suggested from visual examination of a first-pass study, where there will be early visualization of the LV. A more accurate and quantitative method of assessing these types of shunt is to inject ^{99m}Tc-macroaggregated albumin (Fig. 9.27). The small particles of this radiopharmaceutical, used mainly in perfusion lung scan, are trapped in the capillary beds as they pass through the pulmonary arteries. However, in the presence of a right-to-left shunt, the pulmonary capillary system is bypassed and the particles enter the systemic circulation, where they are trapped in end organs such as the brain and the kidneys. Qualitative as well as

quantitative analysis of activity within the body can be accurately obtained. A significant right-to-left shunt is present if the organ counts are greater than 7% of the total lung uptake [55]. Complication because of capillary blockage is not a clinical concern with this procedure, as the number of particles used is very small compared with the number of capillaries in any organ.

9.6 Lymphatic System

9.6.1 Anatomic and Physiologic Considerations

The lymphatic system is the second vascular system, after blood circulation, in mammalian species. The function of the lymphatic system includes drainage of excess interstitial fluid, absorption of fat, and immune surveillance. Knowledge of the normal anatomy of the lymphatic system is crucial for predicting which lymph nodes may be the site of metastatic disease for primary tumors and for understanding the pathophysiological changes of lymphatic disorders such as lymphedema. The lymphatic system is composed of many structures including lymph nodes, tonsils and adenoids, bone marrow, thymus, and spleen, all of which are connected via a network of lymphatic vessels (Table 9.14) that run parallel to the venous circulation. Lymphatic vessels form a complex network that transport the ultrafiltrate of extracellular fluid back to the intravascular space. The lymphatic capillary network wraps around the surface of the body and also lines the internal surface of the gastrointestinal and respiratory tract. Normally, some fluid is forced out of the vascular space at the arterial end of the capillary bed but is reabsorbed at the venous end. Capillary egress, however, exceeds venous reabsorption by approximately 3 L/day (approximately 10% of capillary contents), leaving behind fluid in the interstitial tissue [99]. This fluid can contain protein and often fat, especially after meals. The peripheral lymphatic capillary collection site has a single layer of overlapping endothelial cells with a poorly developed basement membrane [216]. When the volume of fluid in the interstitial space increases, the intercellular gaps between the endothelial cells widen to allow the surplus of fluid to enter [216]. Lymphatic vessels coalesce into increasingly larger vessels that eventually contain smooth muscle and one-way valves to promote forward flow back toward the vascular space via the thoracic duct or the right lymphatic duct. Fluid travels through the lymphatic system at an average rate of 120 mL/h or 2–3 L/day, encountering numerous lymph nodes which serve as filters to remove foreign elements such as tumor cells and bacteria. Lymph enters the nodes through the afferent lymphatic vessel, filtering through the sinusoids of the node and subsequently leaving through the efferent lymphatic vessel. The lymphatic system plays an important role in the dynamic control of fluid volume, protein concentration, and, consequently, the pressure in the interstitial space.

Table 9.14 Components of lymphatic system

a. Organs
I. Primary lymphoid organs
1. Bone marrow
2. Thymus
II. Secondary lymphoid organs
1. Spleen
2. Lymph nodes
3. Tonsils and adenoids
b. Tissue
1. Peyer's patches
2. Vermiform appendix
c. Lymphatic vessels
d. Collecting ducts

The lymphatic system is distributed throughout the entire human body, except CNS (not including the dura mater), the bone marrow and cartilage [217], endomysium of muscle [216]. All human beings have similar lymphatic system anatomy; however, there can be considerable variation in the exact route of drainage from different locations of the body. The lymphatic vessels are usually located in close proximity to the venous system. Approximately 800 lymph nodes are present in the human body, with a short axis diameter that ranges from a few millimeters to 1 cm [218, 219]. Lymph nodes contain reticuloendothelial cells, primarily tissue phagocytes, that remove abnormal substances.

Lymphatic vessels have the capability of regeneration and can establish their own anastomoses within a short period (weeks) after organ transplantation [220, 221]. Additionally, new lymph tracts can develop and may subsequently reconnect to the main system. This occurs when small lymphatics are surgically transected or there is an attempt to circumvent flow obstruction.

Lymphatic vessels are divided into three categories according to their structural characteristics: lymph capillaries, pre-collectors, and lymph collecting vessels [222]. The lymph capillaries (between 20 and 70 μm in diameter) do not have a valvular structure. The lymph capillary begins with a blind ending. The endothelial cells that form the lymph capillary connect with each other loosely. A fibrous structure called an anchoring filament connects the endothelial cell with the surrounding tissue [223]. When the tissue increases in volume owing to extra interstitial fluid (edema), the anchoring filaments pull the endothelial cells outward so that the junctions between the cells open up to capture the extra interstitial fluid into the lumen [217].

The lymph capillaries connect to pre-collectors (70–150 μm in diameter) which have a valvular structure that regulates the direction of lymph flow unidirectionally. The pre-collectors connect to the lymph-collecting vessels, or collectors. These collectors (between 150 and 500 μm in diameter). The lymph-collecting vessels have a three-layered wall made of endothelial cells, smooth muscle cells, and collagen fibers with fibroblasts that contracts rhythmically to propel lymph flow [217].

The lymph node barrier theory postulates that each lymphatic vessel connects to at least one lymph node before connecting to the vein. Lymph nodes are classified as regional or interval, according to their location. Regional lymph nodes are groups of lymph nodes that form lymphatic basins into which lymph drains from different skin regions or organs. The regional lymph nodes are the target of lymph node dissection in cancer treatment to halt the spread of cancer cells, with neck dissection for tongue cancer, axillary dissection for breast cancer, and inguinal dissection for lower extremity melanoma. Interval lymph nodes are located in the limbs, and the lymph vessels pass through them on the way to the regional lymph nodes. The superficial lymphatic system in the upper extremities originates in the lymph capillaries in the fingertips and palm while the superficial lymphatic system in the lower extremities originates in the lymph capillaries in the toes and soles of the feet [217].

9.6.2 Pathophysiology of Relevent Lymphatic Disorders

9.6.2.1 Lymphedema

Lymph is a body fluid with low protein content, high fat level, and circulating lymphocytes. Lymph drains from peripheral tissues in blind-ended lymph vessels passing through lymph nodes and ending into the central venous circulation. Failure of lymph drainage from an area of the body results in lymphedema. Lymph drainage can be studied by following the movement of radiolabeled microparticles injected intradermally by scintillation camera imaging.

Lymphedema is the excess accumulation of protein-rich fluid in the interstitial space. It may develop due to excess production of lymph, obstruction of lymphatic drainage, or disruption of the integrity of the lymphatic system. Excess production occurs when there is (a) obstruction of the capillary or venous system with resultant increased pressure, (b) excessive fluid migration from the vascular space due to low oncotic pressure, or (c) a leak in the system. Obstruction of lymphatic drainage occurs secondary to scarring following trauma, radiation, surgery, and infection or when there is abnormal development of the lymphatic system or compression of a main lymphatic by a mass [224]. These conditions force fluid to travel back to the vascular space via the nearest accessible lymphatic route.

Lymphedema may be primary or secondary (Table 9.15). The primary type is uncommon, may be congenital or developmental, and usually causes only minimal disturbances in lymphatic flow. Primary lymphedemas have been subclassified on the basis of their onset into congenital, peripubertal (lymphedema Praecox) and late-

Table 9.15 Causes of lymphedema

Class	Pathogenesis
Primary	Defects in genes involved in lymphatic vessel development
Secondary	Damage or physical obstruction of lymphatic vessels or LNs due to Inflammation Malignancy Radiation therapy Filariasis Surgical dissection Trauma Recurrent dermatitis

onset lymphedema (Tarda). Many genes have been associated with different forms of primary lymphedemas including VEGFC-VEGFR3, CCBE1, PTPN14, FOXC2, and SOX18 [225]. The more common secondary type can be due to several factors including infection, trauma, and other venous disorders. Since lymph is rich in protein, it promotes a cycle of inflammation that may be followed by fibrosis, leading to progressive scar formation which can worsen lymphatic obstruction [224]. Lymphedema should not be confused with lipedema which is a chronically progressive accumulation of adipose tissue primarily in the lower extremities but can also affect arms. It affects almost exclusively woman and can be inherited. It is symmetrical (Lymphedema is assymetrical) and does not involve feet (affected by Lymphedema) [226].

Severe edema of the upper limb may complicate the effective treatment of breast cancer. The surgical removal and irradiation of the breast and associated axillary lymph nodes result in lymphedema in 4–49% of patients [224, 226].

The most dramatic example of secondary lymphedema is seen in lymphatic filariasis, a neglected tropical disease that affects about 40 million people in the endemic areas of Africa, South America, and South-East Asia. This disease is caused by mosquito-transmitted parasitic nematodes, such as *Wuchereriabancrofti* (in 90% of the cases), which targets and dwell in lymphatic vessels and LNs for years, resulting in extensive fibrosis. This may cause significant edema of the lower limbs and external genitalia that is so massive to be named elephantiasis [225].

Podoconiosis (endemic nonfilarial elephantiasis), another tropical secondary lymphedema visa noninfectious geochemical disease of the lower limb lymphatic vessels resulting from chronic barefoot exposure to red-clay soil derived from volcanic rock. Pathogenesis was suggested to be due to mineral particles in red-clay soils are absorbed through the skin of the foot and engulfed by macrophages in the lymphatic system of the lower limbs, inducing an inflammatory response in the lymphatic vessels resulting in fibrosis and vessel obstruction [227].

9.6.2.2 Lymph Nodes with Metastases

In general, tumors can metastasize by several routes including venous, arterial, lymphatic, and local invasion. It is believed that while most tumors initially spread through the lymphatic system, temporarily being retained at successive levels of lymph nodes by the body's defense system, some tumors may spread through both the vascular and lymphatic systems nearly simultaneously. Since lymph nodes are common sites of metastasis, knowledge of their involvement is crucial for patient management and prognosis. When small numbers of tumor cells (micrometastases) are found in lymph nodes, the architecture and physiological characteristics of the lymph node are not altered. Even with larger tumor loads, lymph nodes may remain normal in size, making them difficult to detect with anatomical imaging studies. Determination of focal defects within lymph nodes secondary to tumor infiltration is usually unreliable with all current imaging modalities.

9.6.2.3 Sentinel Node

The lymph node(s) that receives initial lymphatic drainage from a location harboring tumor has been termed the "sentinel node." There can be single or multiple nodes which may be located in one or different lymphatic beds [228]. Since determination of lymph node involvement is an integral part of tumor staging and management, lymph node excision with pathological evaluation is commonly performed. A complete nodal dissection (often involving large areas of tissue), however, can cause considerable morbidity, including lymphedema, and still fail to remove small diseased nodes [228, 229]. If the sentinel node(s) can be identified, extensive pathological examination of the node(s) can forecast whether

tumor dissemination has occurred, since it is the first filter that metastatic cells encounter. Identification of the sentinel node can be done by injections of blue dye around the tumor just before surgery or by using a radiopharmaceutical injected in a similar fashion.

9.6.3 Scintigraphy of Lymphatic System

Tracer is injected into a specific location, and imaging is then performed while the material crosses into the lymphatic system and migrates toward the vascular space. Agent movement will depend on the specific radiopharmaceutical used and the location of the injection. Particulate agents such as colloids are not transported into the peripheral collection sites as well because of their larger size. However, they are better retained in the lymph nodes because of their localization within RES cells. Nonparticulate agents travel much faster and efficiently but are not retained within a lymph node because they do not localize to any of the tissue components but are simply passing through. Because of the very rich supply of lymphatics in the skin, injections into this location will show very efficient uptake and movement of tracer, while breast injections move much slower due to a much sparser lymphatic system.

9.6.3.1 Detection and Follow-Up of Lymphedema

Lymphoscintigraphy can demonstrate (a) clearance of radiolabeled colloid from an interstitial injection and (b) flow to regional lymph node(s), along with some lymph node anatomical features. Several acquisition protocols can be used. The procedure usually consists of a 45-min dynamic acquisition followed by delayed imaging, usually at 90 min post injection. For lower extremity disease, if movement of the tracer through the lymphatic system is not seen on early images, patients may be instructed to exercise their calf muscles by walking. Interpretation of images includes visual assessment of the injection sites, lymphatic tracts, lymph nodes, and time-activity curves, along with review of the early dynamic acquisition via a computer-generated cine display. Several quantitative procedures have been advocated for use in detecting lymphatic flow disturbances, with some attempting to define the cause of the disease. These include determination of the timing as well as the amount of tracer uptake in the draining lymph nodes. However, care is advised when using such measures because there is a normal decrease in lymphatic flow parameters with age, and the use of different radiopharmaceuticals, different injection techniques, and additional procedures such as exercise can alter expected values.

Normally, there is rapid and fairly symmetrical transport of the radiotracer from foot injections through one or two lymphatic vessels in the calf and one lymphatic vessel in the thigh. Multiple pelvic lymph nodes should be clearly visualized within 1 h (Fig. 9.28) but may be seen within 6 min when a nonparticulate agent such as ^{99m}Tc-HSA is used [230]. Upper extremity findings in normal flow are similer (Fig. 9.29).

Scan findings in patients with lymphedema will depend on the cause of the swelling, the length of time that the process has been present, and compensatory mechanisms that have developed to circumvent the flow disturbance [231]. Figure 9.20 shows the pathological mechanisms that lead to lymphedema and the corresponding scan patterns. Figures 9.30, 9.31, and 9.32 illustrate a lymphedema studies.

9.6.3.2 Detection of Lymph Node Metastases

Since lymph nodes have reticuloendothelial cells that phagocytose foreign material, radiocolloids are used to visualize them. Direct determination of the presence of tumor is extremely difficult, since the desired space-occupying defects caused by tumor infiltration require a significant portion of the node to be involved. When lymphatic tissue is largely replaced by tumor, lymph nodes

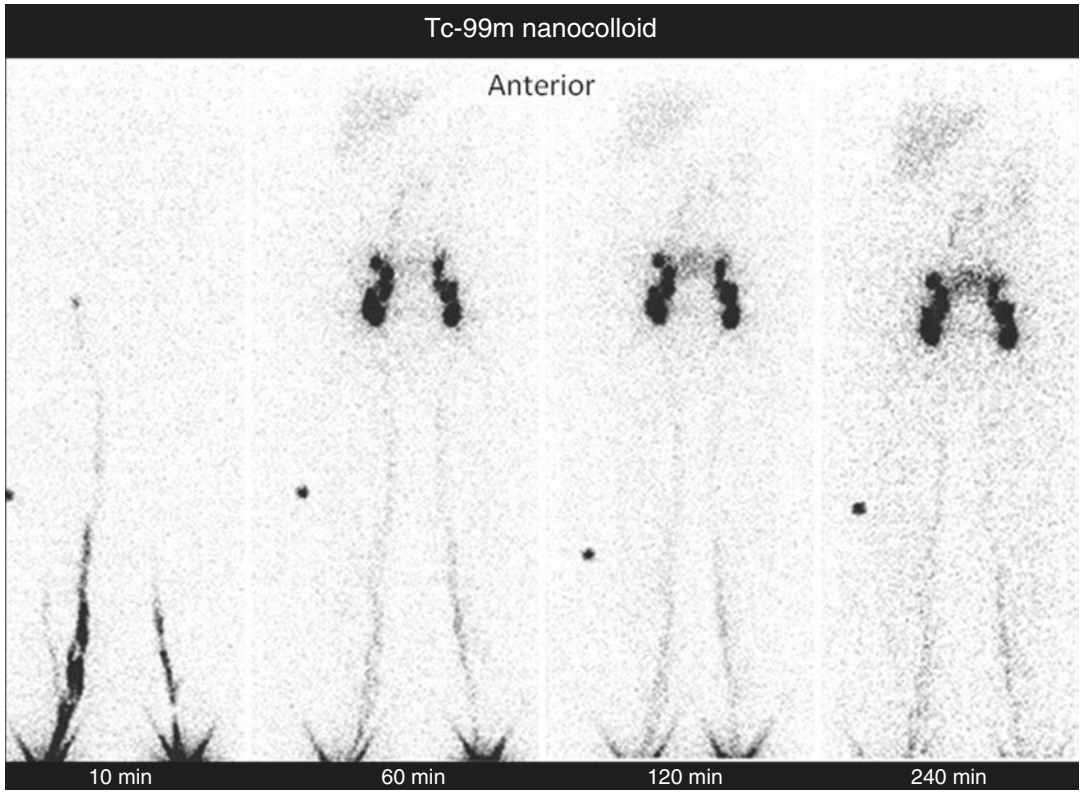

Fig. 9.28 Tc-99m nanocolloid images of the lower extremities. Anterior view images at 10, 60, 120, and 240 min. Images demonstrate normal ascend of activity throughout the lymphatic channels, particularly the medial band, and localization in the inguinal nodes bilaterally within 1 h. The lymph nodes are in symmetric appearance and similar number

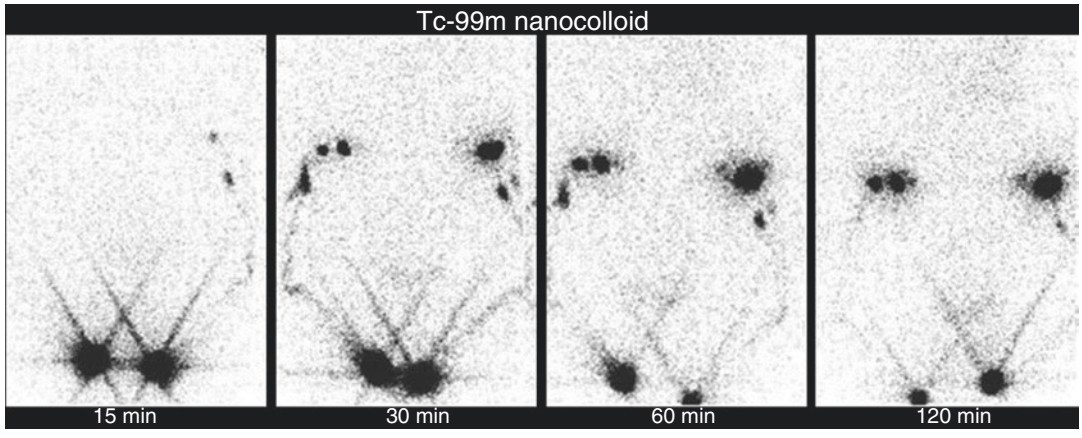

Fig. 9.29 Tc-99m nanocolloid lymphoscintigraphy images of the upper extremities. Anterior view images at 15, 30, 60, and 120 min. Normal upper extremity lymphoscintigraphy images demonstrate normal ascend of activity through lymphatic channels and localization in axillary lymph nodes bilaterally within 30 min. The lymph nodes are in symmetric appearance and similar number

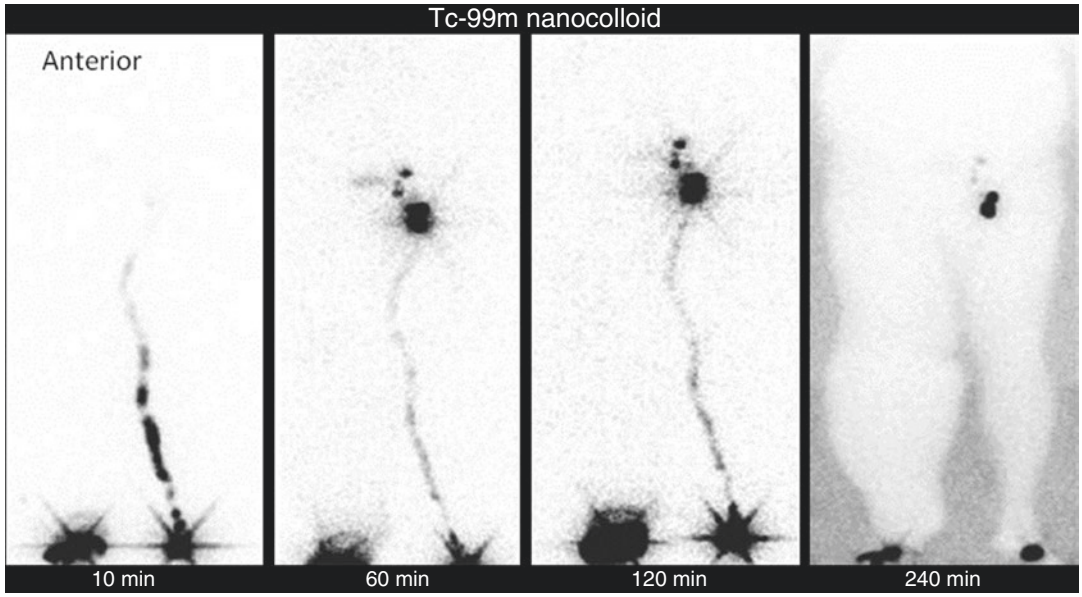

Fig. 9.30 Forty-seven-year-old male with severe right leg swelling. No lymphatic channels or lymph nodes are identified in the significantly swollen right leg and inguinal region (primary lymphedema). Findings are normal on the left side with normal visualization of lymphatic channels and inguinal lymph nodes which are in normal appearance

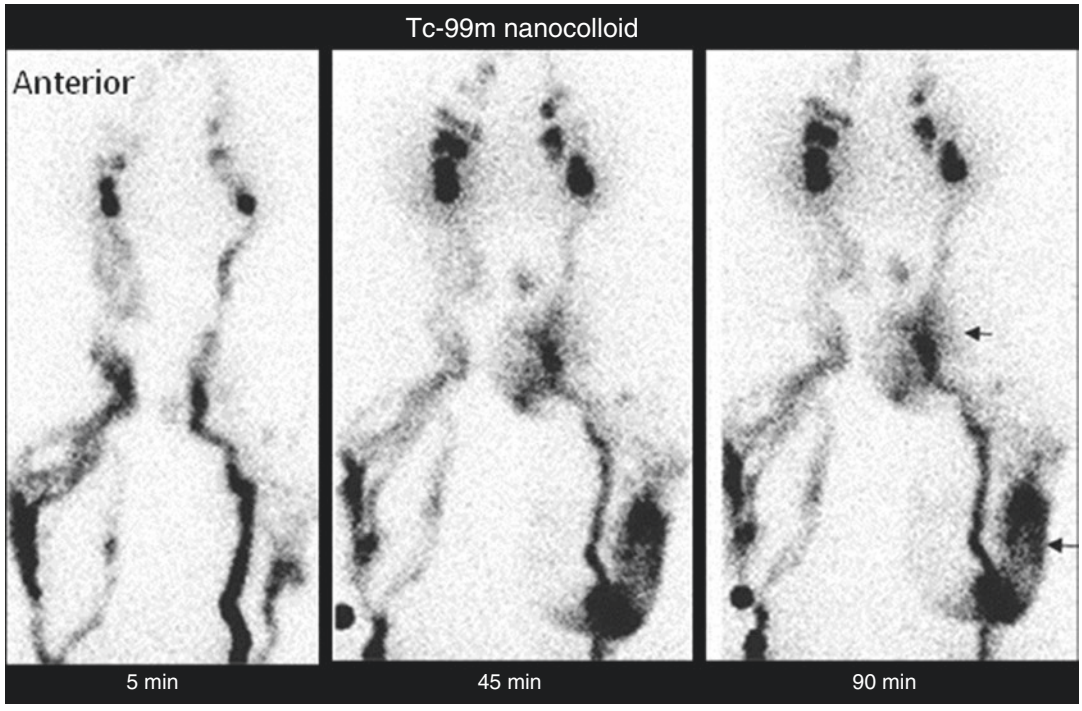

Fig. 9.31 Bilateral Lower Limb Lymphedema in a 65-year-old female with bilateral leg swelling for 2 years. Images were obtained at 5, 45, and 90 min and demonstrate prominent lymphatic channels and dermal backflow in the left lower and upper leg (arrows) indicating secondary lymphedema in bilateral legs

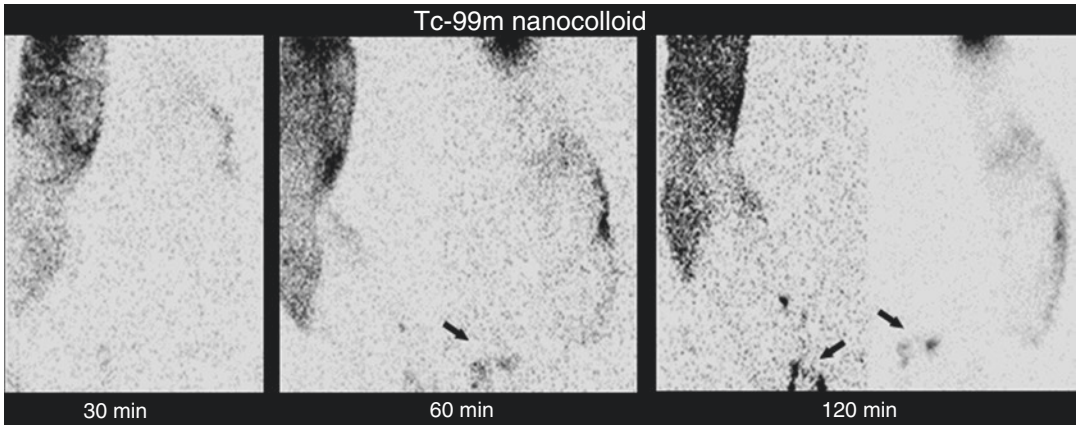

Fig. 9.32 Lymphoscintigraphy of the upper extremities for a 75-year-old woman with history of long-standing lymphedema in upper limbs. There is dermal backflow which is significant in the right arm and mild in the left arm. No lymphatic channels are identified in both arms. There is activity in few lymph nodes in both axilla (arrows)

may not be visualized because the tracer is blocked from entering. Tumor-involved nodes can even show more tracer uptake than normal nodes. This may be explained by reactive changes in the lymph node, with increased numbers of RES cells being present, possibly in reaction to the presence of tumor antigens.

Lymphoscintigraphy with radiolabeled anti-tumor antibodies such as anti-CEA has been used to detect occult tumor in lymph nodes. Contrary to radiocolloid lymphoscintigraphy, which depends on phagocytosis, radiolabeled antibody localization requires attachment of the antibody directly to tumor cells. Interstitial injection of these agents has the advantage of producing a higher concentration of tracer at the tumor site in the lymph node than when the antibody is injected intravenously. However, the presence of a definitive number of metastatic cells is required for detection, depending on the agent and the imaging technique used. More recently FDG PET is being used to detect more effectively lymph node metastasis of many tumors. It has proven useful in detecting lymph node metastasis of lung cancer changing the mode of therapy in a significant number of cases [232, 233].

9.6.3.3 Sentinel Node Detection

Radioactive sentinel nodes can be detected using imaging with a gamma camera and/or a gamma probe at surgery. Lymphoscintigraphy using dynamic and static imaging better defines the sequence of lymphatic flow from the tumor site to draining lymph nodes, especially the sentinel node (Fig. 9.33) SPECT/CT is much better in achieving accurate localization, (Fig. 9.34) (see Chap. 12 for more details).

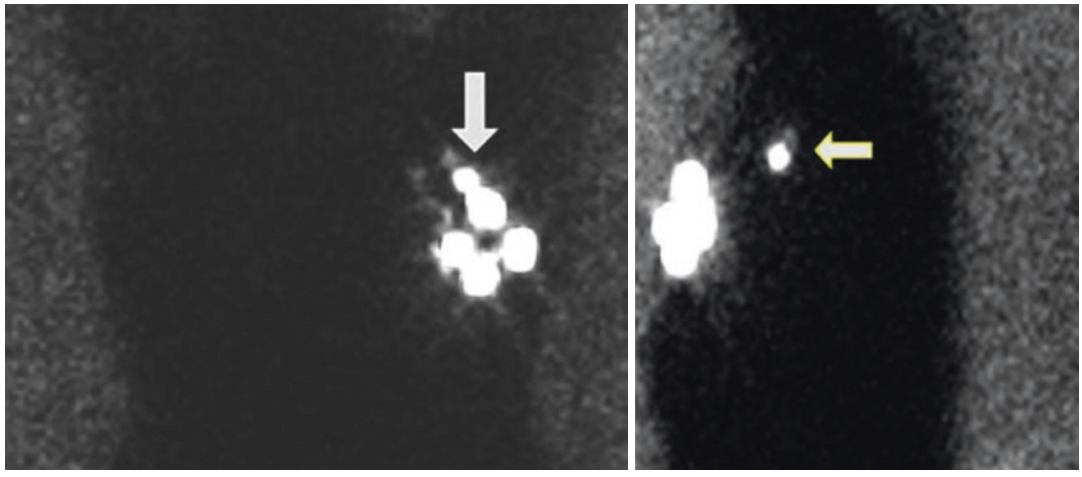

Fig. 9.33 A sentinel lymph node localization study in a patient with left breast cancer showing visualization of a sentinel lymph node in the anterior projection and more clearly in the left lateral projection (*arrows*)

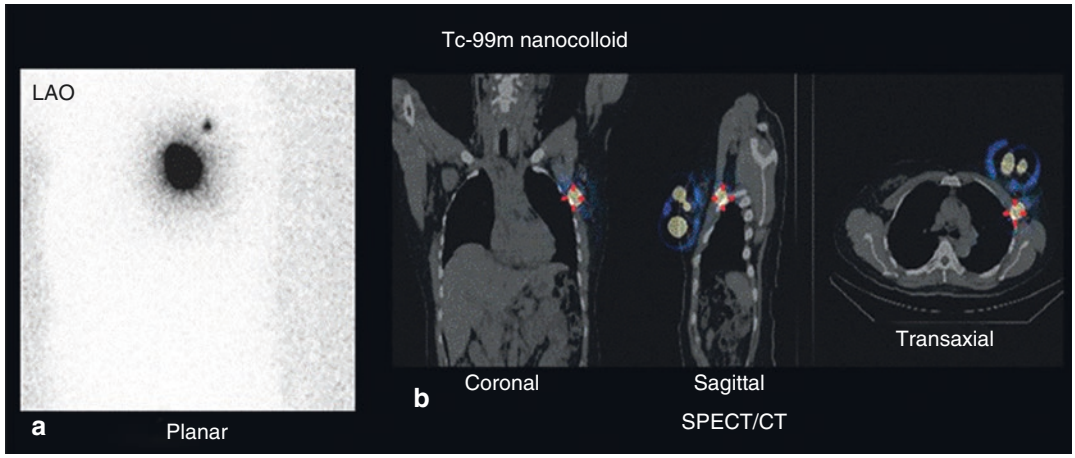

Fig. 9.34 Tc-99m nanocolloid sentinel node scintigraphy in a patient with breast cancer. Anterior oblique view of the left breast and axilla (**a**) and selected coronal, sagittal, and transaxial SPECT/CT fusion images of the chest (**b**). Breast lymphatic tracts, nodes, and their surgical classification. Images show intense activity at the injection site in the left breast as well as radiotracer accumulation in the left axillary sentinel lymph node. SPECT/CT better locates the lymph node in the axilla (level 1)

References

1. Parmley WW, Wikman-Coffelt J (1991) Physiology of cardiac muscle contraction. In: Parmley WW, Chatterjee K (eds) Cardiology. Lippincott, Philadelphia, pp 1–26
2. Parmley WW (1991) Ventricular function. In: Parmley WW, Chatterjee K (eds) Cardiology. Lippincott, Philadelphia, pp 1–20
3. Duncker DJ, Bache RJ (2008) Regulation of coronary blood flow during exercise. Physiol Rev 88:1009–1086
4. Tune JD (2014) Coronary circulation. Morgan & Claypool Life Sciences, San Francisco
5. Ardehali A, Ports TA (1990) Myocardial oxygen supply and demand. Chest 98:699–705
6. Goodwill AG, Dick GM, Kiel AM, Tune JD (2017) Regulation of coronary blood flow. Compr Physiol 7(2):321–382

7. Schelbert HR (2010) Anatomy and physiology of coronary blood flow. J Nucl Cardiol 17:545–554
8. Niccoli G, Scalone G, Crea F (2015) Acute myocardial infarction with no obstructive coronary atherosclerosis: mechanisms and management. Eur Heart J 36:475
9. Campisi R, Czernin J, Schoder H, Sayre JW, Schelbert HR (1999) L-arginine normalizes coronary vasomotion in long-term smokers. Circulation 99:491–497
10. Schindler TH, Nitzsche EU, Munzel T, Olschewski M, Brink I, Jeserich M et al (2003) Coronary vasoregulation in patients with various risk factors in response to cold pressor testing: contrasting myocardial blood flow responses to short- and long-term vitamin C administration. J Am Coll Cardiol 42:814–822
11. Gould KL, Nakagawa Y, Nakagawa K, Sdringola S, Hess MJ, Haynie M et al (2000) Frequency and clinical implications of fluid dynamically significant diffuse coronary artery disease manifest as graded, longitudinal, base-to-apex myocardial perfusion abnormalities by noninvasive positron emission tomography. Circulation 101:1931–1939
12. Cecchi F, Olivotto I, Gistri R, Lorenzoni R, Chiriatti G, Camici PG (2003) Coronary microvascular dysfunction and prognosis in hypertrophic cardiomyopathy. N Engl J Med 349:1027–1035
13. Neglia D, Michelassi C, Trivieri MG, Sambuceti G, Giorgetti A, Pratali L et al (2002) Prognostic role of myocardial blood flow impairment in idiopathic left ventricular dysfunction. Circulation 105:186–193
14. Bombardini T (2005) Myocardial contractility in the echo lab: molecular, cellular and pathophysiological basis. Cardiovasc Ultrasound 3:27. https://doi.org/10.1186/1476-7120-3-27
15. Dandel M, Hetzer R (2021) Ventricular systolic dysfunction with and without altered myocardial contractility: clinical value of echocardiography for diagnosis and therapeutic decision-making. Int J Cardiol 327:236–250
16. Miranda D, Lewis GD, Fifer MA (2016) Heart failure, Chapter 9. In: Lilly LS (ed) Pathophysiology of heart disease: a collaborative project of medical students and faculty, 6th edn. Wolters Kluwer, Alphen aan den Rijn, pp 220–248
17. Gazewood JD, Turner PL (2017) Heart failure with preserved ejection fraction: diagnosis and management. Am Fam Physician 96(9):582–588
18. Hartupee J, Mann DL (2017) Neurohormonal activation in heart failure with reduced ejection fraction. Nat Rev Cardiol 14(1):30–38
19. Hayley BD, Burwash IG (2012) Heart failure with normal left ventricular ejection fraction: role of echocardiography. Curr Opin Cardiol 27(2):169–180
20. Patel PA, Ali N (2017) Mechanisms involved in regulation of systemic blood pressure. Arch Clin Hypertension 3(1):016–020
21. Harrison DG, Florentine MS, Brooks LA et al (1988) The effect of hypertension and left ventricular hyper trophy on the lower range of coronary autoregulation. Circulation 77:1108
22. Oktay AA, Shah SJ (2014) Current perspectives on systemic hypertension in heart failure with preserved ejection fraction. Curr Cardiol Rep 16:545. https://doi.org/10.1007/s11886-014-0545-9
23. Franch RH, Gravanis MB (1993) Pulmonary hypertension and core pulmonale. In: Gravanis M (ed) Cardiovascular disorders: pathogenesis and pathophysiology. Mosby, St Louis, pp 139–177
24. Haworth SG (1987) Pulmonary vascular disease in ventricular septal defect: structural and functional correlations in lung biopsies from 85 patients with outcome of intracardiac repair. J Pathol 152:157–168
25. Sharma GV, McIntyre KM, Sharma S et al (1984) Clinical and hemodynamic correlates in pulmonary embolism. Clin Chest Med 5(421):37
26. Palevsky HI, Weiss DW (1990) Pulmonary hypertension secondary to chronic thromboembolism. J Nucl Med 31:1–9
27. Fishman AP (1988) Pulmonary hypertension and cor pulmonale. In: Fishman AP (ed) Pulmonary diseases and disorders, 2nd edn. McGraw-Hill, New York
28. Dunnill MS (1961) An assessment of the anatomical factor in cor pulmonale in emphysema. J Clin Pathol 14:246
29. Berger HJ, Matthay RA, Lake J et al (1978) Assessment of cardiac performance with quantitative radionuclide angiocardiography: right ventricular ejection fraction with reference to findings in chronic obstructive pulmonary disease. Am J Cardiol 41:897–905
30. Grossman W (1991) Diastolic dysfunction in congestive heart failure. N Engl J Med 325:1557
31. McGill HC Jr, McMahan CA, Herderick EE, Malcom GT, Tracy RE, Strong JP (2000) Origin of atherosclerosis in childhood and adolescence. Am J Clin Nutr 72(5 Suppl):1307S–1315S
32. Tegos TJ, Kalodiki E, Sabetai MM, Nicolaides AN (2001) The genesis of atherosclerosis and risk factors: a review. Angiology 52(2):89–98
33. Shahawy S, Libby P (2016) Atherosclerosis, Chapter 5. In: Lilly LS (ed) Pathophysiology of heart disease: a collaborative project of medical students and faculty, 6th edn. Wolters Kluwer, Alphen aan den Rijn, pp 112–133
34. Moore KJ, Sheedy FJ, Fisher EA (2013) Macrophages in atherosclerosis: a dynamic balance. Nat Rev Immunol 13(10):709–721
35. Borén J, Chapman MJ, Krauss RM, Packard CJ, Bentzon JF et al (2020) Low-density lipoproteins cause atherosclerotic cardiovascular disease: pathophysiological, genetic, and therapeutic insights: a consensus statement from the European Atherosclerosis Society Consensus Panel. Eur Heart J 41:2313–2330
36. He C, Medley S, Hu T, Hindstale ME, Lupu F, Virmani R, Olsen LE (2015) PDGFRβ signalling regulates local inflammation and synergizes with hypercholesterolaemia to promote atherosclerosis. Nat Commun 6:7770
37. Ramji DP, Davies TS (2015) Cytokines in atherosclerosis: key players in all stages of disease and

promising therapeutic targets. Cytokine Growth Factor Rev 26(6):673–685
38. Ward MR, Pasterkamp G, Yeung AC, Borst C (2000) Arterial remodeling mechanisms and clinical implications. Circulation 102:1186–1191
39. Wilder J, Sabatine MS, Lilly LS (2016) Ischemic heart disease, Chapter 6. In: Lilly LS (ed) Pathophysiology of heart disease: a collaborative project of medical students and faculty, 6th edn. Wolters Kluwer, Alphen aan den Rijn, pp 134–161
40. Croce K, Libby P (2007) Intertwining of thrombosis and inflammation in atherosclerosis. Curr Opin Hematol 14:55–61
41. Libby P (2013) Mechanisms of acute coronary syndromes. N Engl J Med 369:883–884
42. Antonopoulos AS, Goliopoulou A, Vogiatzi G, Tousoulis D (2018) Myocardial oxygen consumption, Chapter 2.2. In: Tousoulis D (ed) Coronary artery disease from biology to clinical practice. Academic, New York, pp 127–136
43. Cannon RO 3rd. (1998) Role of nitric oxide in cardiovascular disease: focus on the endothelium. Clin Chem 44(8 Pt 2):1809–1819
44. Arbustini E, Narula J, Tavazzi J et al (2014) The MOGE(S) classification of cardiomyopathy or clinicians. J Am Coll Cardiol 64:304–318
45. Garfinkel AC, Seidman JG, Seidman CE (2018) Genetic pathogenesis of hypertrophic and dilated cardiomyopathy. Heart Failure Clin 14:139–146
46. Maron BJ, Ommen SR, Semsarian C et al (2014) Hypertrophic cardiomyopathy: present and future, with translation into contemporary cardiovascular medicine. J Am Coll Cardiol 64:83–99
47. Rammos A, Meladinis V, Vovas G, Patsouras D (2017) Restrictive cardiomyopathies: the importance of noninvasive cardiac imaging modalities in diagnosis and treatment—a systematic review. Radiol Res Pract 2017:2874902
48. Jung HO (2012) Pericardial effusion and pericardiocentesis: role of echocardiography. Korean Circ J 42(11):725–734
49. Vakamudi S, Ho N, Cremer PC (2017) Pericardial effusions: causes, diagnosis, and management. Prog Cardiovasc Dis 59(4):380–388
50. Cheong XP, Law L, Seow SC, Tay L, Tan HC, Yeo WT, Low AF, Kojodjojo P (2020) Causes and prognosis of symptomatic pericardial effusions treated by pericardiocentesis in an Asian academic medical centre. Singap Med J 61(3):137–141
51. Albugami S, Al-Husayni F, AlMalki A, Dumyati M, Zakri Y, AlRahimi J (2020) Etiology of pericardial effusion and outcomes post pericardiocentesis in the western region of Saudi Arabia: a single-center experience. Cureus 12:e6627
52. Sachpekidis V, Moralidis E, Arsos G (2018) Equilibrium radionuclide ventriculography: still a clinically useful method for the assessment of cardiac function? Hell J Nucl Med 21(3):213–220
53. Heiba SI, Cerqueira MD (1994) Evaluation of cardiac function. In: Cerqueira MD (ed) Nuclear cardiology. Blackwell Scientific, Cambridge, pp 53–117
54. Soufer A, Liu C, Henry ML, Baldassarre LA (2020) Nuclear cardiology in the context of multimodality imaging to detect cardiac toxicity from cancer therapeutics: established and emerging methods. J Nucl Cardiol 27:1210–1224
55. Berger HJ, Zaret BL (1984) Radionuclide assessment of cardiovascular performance. In: Freeman L (ed) Freeman and Johnson's clinical radionuclide imaging. Saunders, Philadelphia
56. Berman DS, Maddahi J, Garcia EV et al (1981) Assessment of left and right ventricular function with multiple gated equilibrium cardiac blood pool scintig raphy. In: Berman DS, Mason DT (eds) Clinical nuclear cardiology. Grune and Stratton, New York
57. Scatteia A, Silverio A, Padalino R, De Stefano F, America R, Cappelletti AM et al (2021) Non-invasive assessment of left ventricle ejection fraction: where do we stand? J Pers Med 11(11):1153
58. Liu YH, Fazzone-Chettiar R, Sandoval V et al (2021) New approach for quantification of left ventricular function from low-dose gated blood-pool SPECT: validation and comparison with conventional methods in patients. J Nucl Cardiol 28:939–950
59. Ramon AJ, Yang Y, Wernick MN, Pretorius PH, Johnson KL, Slomka PJ, King MA (2020) Evaluation of the effect of reducing administered activity on assessment of function in cardiac gated SPECT. J Nucl Cardiol 27(2):562–572
60. Gould KL, Lipscomb K, Hamilton GW (1974) A physiological basis for assessing critical coronary stenosis: instantaneous flow response and regional distribution during coronary hyperemia as measures of coronary flow reserve. Am J Cardiol 33:84
61. Maddahi J, Rodrigues E, Kiat J, Van Train KF, Berman DS (1995) Detection and evaluation of coronary artery disease by thallium-201 myocardial perfusion scintigraphy. In: DePuey EG, Berman DS, Garcia E (eds) Cardiac SPECT imaging. Raven, New York
62. Okada RD (1988) Myocardial kinetics of technetium-99m hexakis 2-methoxyl 2 methylopropylisonitrile. Circulation 77:491
63. Berman DS, Kiat H, Friedman JD, Wang FP, Van Train K, Metzer L, Maddahi J, Germano G (1993) Separate acquisition rest thallium-201/stress technetium 99m sestamibi dual-isotope myocardial perfusion single-photon emission computed tomography: a clinical validation study. J Am Coll Cardiol 22:1455–1464
64. Seldin DW, Johnson LL, Blood DK (1989) Myocardial perfusion imaging with technetium-99m SQ30217: comparison with thallium-201 and coronary anatomy. J Nucl Med 30:312–319
65. Henzlova MJ, Machac J (1994) Clinical utility of technetium-99m-teboroxime myocardial washout imaging. J Nucl Med 35:575–579
66. Fang W, Liu S (2019) New 99mTc radiotracers for myocardial perfusion imaging by SPECT. Curr Radiopharm 12:171–186

67. Saha GB (2018) Radiopharmaceuticals and general methods of radiolabeling. In: Fundamentals of nuclear pharmacy. Springer, Cham, pp 93–121
68. Norenberg JP (2021) Fundamentals of medical radionuclides. In: Remington. Academic, New York, pp 187–204
69. Vilcant V, Zeltser R (2022) Treadmill stress testing. In: StatPearls [Internet]. StatPearls Publishing, Treasure Island
70. Heiba SI, Jacobson AF, Cerqueira MD, Shattuc S, Sharma S (1999) The additive values of radionuclide ventriculography and extent of myocardium at risk to dipyridamole thallium-201 imaging for optimal risk stratification prior to vascular surgery. Nucl Med Commun 20:887–894
71. Mann A, Williams J (2020) Considerations for stress testing performed in conjunction with myocardial perfusion imaging. J Nucl Med Technol 48:114–121
72. Wasserman K, Hansen JE, Sue DY et al (2012) Principles of exercise testing and interpretation, 5th edn. Wolters Kluwer/Lippincott Williams & Wilkins, Philadelphia
73. Farell MB (2016) Myocardial perfusion imaging 2015: quality, safety, and dose optimization. Society of Nuclear Medicine and Molecular Imaging Technologist Section, Reston
74. Heller GV, Hendel R, Mann A (2009) Nuclear cardiology: technical applications. McGraw Hill, New York
75. Roger VL, Jacobsen SI, Pelikka PA et al (1998) Prognostic value of treadmill exercise testing. a population based study in Olmsted County, Minnesota. Circulation 98:2836–2841
76. Young M, Pan W, Wiesner J et al (1994) Characterization of arbutamine: a novel catecholamine stress agent for diagnosis of coronary artery disease. Drug Dev Res 32:19–28
77. Iskandrian AS, Verani MS, Heo J (1994) Pharmacologic stress testing: mechanism of action, hemodynamic responses, and results in detection of coronary artery disease. J Nucl Cardiol 1:94–111
78. Lieu HD, Shryock JC, von Mering GO et al (2007) Regadenoson, a selective A2A adenosine receptor agonist, causes dose-dependent increases in coronary blood flow velocity in humans. J Nucl Cardiol 14:514–520
79. Iskandrian AE, Bateman TM, Belardinelli L et al (2007) Adenosine versus regadenoson comparative evaluation in myocardial perfusion imaging: results of the ADVANCE phase 3 multicenter international trial. J Nucl Cardiol 14:645–658
80. Cerqueira MD, Nguyen P, Staehr P et al (2008) Effects of age, gender, obesity and diabetes on the efficacy and safety of the selective A2A agonist, regadenoson versus adenosine in myocardial perfusion imaging: integrated ADVANCE-MPI trial results. JACC Cardiovasc Imaging 1:207–216
81. Travin MI, Wexler JP (1999) Pharmacological stress testing. Semin Nucl Med 29:298–318
82. Vitola JV, Brambatti JC, Caligaris F et al (2001) Exercise supplementation to dipyridamole prevents hypotension, improves electrocardiogram sensitivity, and increases heart-to-liver activity ratio on Tc-99m sestamibi imaging. J Nucl Cardiol 8:652–659
83. Pennell DJ, Mavrogeni SI, Forbat SM et al (1995) Adenosine combined with dynamic exercise for myocardial perfusion imaging. J Am Coll Cardiol 25:1300–1309
84. Kiat H, VanTrain KF, Friedman JD et al (1992) Quantitative stress-redistribution thallium-201 SPECT using prone imaging: methodologic development and validation. J Nucl Med 33:1509–1512
85. Hayes SW, DeLorenzo A, Hachamovich R et al (2003) Prognostic implications of combined prone and supine myocardial perfusion SPECT. J Nucl Med 44:1633–1640
86. DePuey EG (1994) How to detect and avoid myocardial perfusion SPECT artifacts. J Nucl Med 35:699–702
87. Neumann DR, Go RT, Myers BA et al (1993) Parametric phase display for biventricular function from gated cardiac blood pool single-photon emission tomography. Eur J Nucl Med 20:1108–1111
88. Chen J, Garcia EV, Folks RD et al (2005) Onset of left ventricular contraction determined by phase analysis of ECG-gated myocardial perfusion SPECT imaging: development of a diagnostic tool for assessment of cardiac mechanical dyssynchrony. J Nucl Cardiol 6:687–695
89. Samad Z, Atchley AE, Trimble MA et al (2011) Prevalence and predictors of mechanical dyssynchrony as defined by phase analysis in patients with left ventricular dysfunction undergoing gated SPECT myocardial perfusion imaging. J Nucl Cardiol 18:24–30
90. Bateman TM, O'Keefe JH Jr, Dong VM et al (1995) Coronary angiographic rates after stress single photon emission computed tomographic scintigraphy. J Nucl Cardiol 2:217–223
91. Hachamovich R, Berman DS, Shaw IJ et al (1998) Incremental prognostic value of myocardial perfusion single photon emission computed tomography for the prediction of cardiac death: differential stratification for risk of cardiac death and myocardial infarction. Circulation 97:535–543
92. Diamond GA, Forrester JS (1979) Analysis of probability as an aid in the clinical diagnosis of coronary artery disease. N Engl J Med 300:1350
93. Hachamovitch R, Berman DS, Kiat H et al (1996) Exercise myocardial perfusion SPECT in patients without known CAD. Incremental prognostic value and use in risk stratification. Circulation 93:905–914
94. Bateman TM (1997) Clinical relevance of a normal myocardial perfusion scintigraphic study. J Nucl Cardiol 4:172–173
95. Iskander S, Iskandrian AE (1998) Risk assessment using single-photon emission computed tomographic technetium-99m sestamibi imaging. J Am Coll Cardiol 32:57–62
96. Mazzanti M, Germano G, Kiat H (1997) Identification of severe and extensive coronary artery disease by automatic measurement of transient ischemic dilatation of the left ventricle in dual isotope myocardial perfusion SPECT. J Am Coll Cardiol 27:1612–1620

97. Gerson MC, Gerson MC (1997) Test accuracy, test selection, and test result interpretation in chronic coronary artery disease, Chap 20. In: Gerson MC (ed) Cardiac nuclear medicine, 3rd edn. McGraw-Hill, New York
98. Farkouh ME, Smars RA, Reeder GS, Zinsmeiter AR, Evans RW, Meloy TD, Kopecky SL, Allen M, Allison TG, Gibons RJ, Gabriel SE (1998) A clinical trial of a chest-pain observation unit for patients with unstable angina. N Engl J Med 339:1882–1888
99. Tatum JL, Jesse RI, Kontros MC et al (1997) Comprehensive strategy for the evaluation and triage of the chest pain patient. Ann Emerg Med 29:116–125
100. Heller GV, Stowers SA, Hendel RC et al (1998) Clinical value of acute rest technetium-99m tetrofosmin tomographic myocardial perfusion imaging in patients with acute chest pain and nondiagnostic electrocardiograms. J Am Coll Cardiol 31:1011–1017
101. Boden WE, O'Rourke RA, Crawford MH et al (1998) Outcomes in patients with acute non-Q-wave myocardial infarction randomly assigned to an invasive as compared with a conservative management strategy. Veterans Affairs Non-Q-Wave Infarction Strategies in Hospital (VANQUISH) Trial Investigation. N Engl J Med 338:1785–1792
102. Mahmarian JJ, Mahmarian AC, Marks GF et al (1995) Role of adenosine thallium-201 tomography for defining long-term risk in patients after acute myocardial infarction. J Am Coll Cardiol 25:1333–1340
103. Iskandrian AE, Hage FG, Shaw LJ, Mahmarian JJ, Berman DS (2014) Serial myocardial perfusion imaging: defining a significant change and targeting management decisions. JACC Cardiovasc Imaging 7:79–96
104. Gibbons RJ, Balady GJ, Bricker TJ et al (2002) ACC/AHA guideline update for exercise testing: summary article—a report of the American College of Cardiology/American Heart Association Task Force on Practice Guidelines (Committee to Update the 1997 Exercise Testing Guidelines). J Am Coll Cardiol 40:1531–1540
105. Young JD (1998) Cardiac transplantation: three decades of experience defines our challenge. Transplant Proc 30:1885–1888
106. Oyer PE, Stinson EB, Jamieson SW et al (1983) Cyclosporine in cardiac transplantation: 2 and 1/2 year follow-up. Transplant Proc 15:2546–2552
107. Mairesse GH, Marwick TH, Hanet C et al (1995) Use of exercise electrocardiography, technetium-99m MIBI perfusion tomography for coronary disease surveillance in a low-prevalence population of heart transplant recipients. J Heart Lung Transplant 14:222–229
108. Fang JC, Roco T, Jarcho J et al (1998) Noninvasive assessment of transplant-associated arteriosclerosis. Am Heart J 125:980–987
109. Manapragada PP, Andrikopoulou E, Bajaj N, Bhambhvani P (2021) PET cardiac imaging (perfusion, viability, sarcoidosis, and infection). Radiol Clin N Am 59:835–852
110. Bateman TM, Dilsizian V, Beanlands RS et al (2016) American Society of Nuclear Cardiology and Society of Nuclear Medicine and molecular imaging joint position statement on the clinical indications for myocardial perfusion PET. J Nucl Cardiol 23(5):1227–1231
111. Schelbert HR, Wisenberg G, Phelps ME et al (1982) Noninvasive assessment of coronary stenoses by myocardial imaging during pharmacologic coronary vasodilation, VI: detection of coronary artery disease in human beings with intravenous N-13 ammonia and positron computed tomography. Am J Cardiol 49:1197–1207
112. Monahan WG, Tilbury RS, Laughlin JS (1972) Uptake of H-13 labeled ammonia. J Nucl Med 13:274
113. Bergmann SR, Hack S, Tewson T et al (1980) The dependence of accumulation of N-13-NH3 by myocardium on metabolic factors and its implications for quantitative assessment of perfusion. Circulation 61:34
114. Gould KL, Schelberth H, Phelps H et al (1979) Noninvasive assessment of coronary stenosis with myocardial perfusion imaging during pharmacologic coronary vasodilation. V. Detection of 47 percent diameter coronary stenosis with intravenous N-14 ammonia and emission-computed tomography in intact dogs. Am J Cardiol 43:200
115. Tamaki N, Yonekura Y, Senda M et al (1985) Myocardial positron computed tomography with N-13 ammonia. Eur J Nucl Med 11:246–251
116. Selwyn AP, Allan RM, L'Abbate A et al (1982) Relation between regional myocardial uptake of rubidium-82 and perfusion: absolute reduction of cation uptake in ischemia. Am J Cardiol 50:112–121
117. Goldstein RA, Mullani NA, Marani SK et al (1983) Myocardial perfusion with rubidium-82. II. Effects of metabolic and pharmacological interventions. J Nucl Med 24:907–915
118. Schelbert HR, Ashburn WL, Chauncey DM et al (1977) Comparative myocardial uptake of intravenously administered radionuclides. J Nucl Med 15:1092
119. Gould KL (1978) Assessment of coronary stenoses by myocardial perfusion imaging during pharmacologic coronary vasodilatation. IV. Limits of stenosis detection by idealized experimental, cross-sectional myocardial imaging. Am J Cardiol 42:761–768
120. Maddahi J, Czernin J, Lazewatsky J et al (2011) Phase I, first-in-human study of BMS747158, a novel F18-labeled tracer for myocardial perfusion PET: dosimetry, biodistribution, safety, and imaging characteristics after a single injection at rest. J Nucl Med 52:1490–1498
121. Berman DS, Maddahi J, Tamarappoo BK et al (2013) Phase II safety and clinical comparison with single-

photon emission computed tomography myocardial perfusion imaging for detection of coronary artery disease. J Am Coll Cardiol 61:469–477
122. Wackers FJ, Soufer R, Zaret BL et al (2012) Nuclear cardiology. In: Mann Z, Bonow L (eds) Braunwald's heart disease: a textbook of cardiovascular medicine. Elsevier/Saunders, Philadelphia, pp 293–339
123. Santos BS, Ferreira MJ (2019) Positron emission tomography in ischemic heart disease. Rev Port Cardiol 38(8):599–608
124. Momose M, Kondo C (2007) Assessment of myocardial viability by FDG-PET. Rinsho Byori 55:639–647
125. Blume ED, Altmann K, Mayer JE et al (1999) Evolution of risk factors influencing early mortality of the arterial switch operation. J Am Coll Cardiol 33:1702–1709
126. Gould KL (1991) PET perfusion imaging and nuclear cardiology. J Nucl Med 32:579–606
127. Arrighi JA, Dione DP, Condos S et al (1999) Adenosine Tc-99m sestamibi SPECT underestimates ischemia compared with N-13 ammonia PET in a chronic canine model of ischemia. J Nucl Med 40:6P (abstract)
128. Di Carli M, Czernin J, Hoh CK et al (1995) Relation among stenosis severity, myocardial blood flow, and flow reserve in patients with coronary artery disease. Circulation 91:1944–1951
129. Bateman TM, Heller GV, McGhie AI et al (2006) Diagnostic accuracy of res/stress ECG-gated Rb-82 myocardial perfusion PET: comparison with ECG-gated Tc-99m sestamibi SPECT. J Nucl Cardiol 13:24–33
130. Jaarsma C, Leiner T, Bekkers SC et al (2012) Diagnostic performance of noninvasive myocardial perfusion imaging using single-photon emission computed tomography, cardiac magnetic resonance, and positron emission tomography imaging for the detection of obstructive coronary artery disease: a meta-analysis. J Am Coll Cardiol 59:1719–1728
131. Mc Ardle BA, Dowsley TF, deKemp RA et al (2012) Does rubidium-82PET have superior accuracy to SPECT perfusion imaging for the diagnosis of obstructive coronary disease? A systematic review and meta-analysis. J Am Coll Cardiol 60:1828–1737
132. Bateman TM, Heller GV, McGhie AI et al (2005) Attenuation-corrected Tc-99m sestamibi SPECT compared with Rb-82 myocardial perfusion PET. J NuclCardiol 12:S118 (abstract)
133. Bateman TM, Heller GV, McGhie AI et al (2006) Diagnostic accuracy of rest/stress ECG-gated Rb-82 myocardial perfusion PET: comparison with ECG-gated Tc-99m sestamibi SPECT. J Nucl Cardiol 13(1):24–33
134. Danad I, Raijmakers PG, Driessen RS, Leipsic J, Raju R, Naoum C et al (2017) Comparison of coronary CT angiography, SPECT, PET, and hybrid imaging for diagnosis of ischemic heart disease determined by fractional flow reserve. JAMA Cardiol 2:1100–1107
135. Angelidis G, Giamouzis G, Karagiannis G, Butler J, Tsougos I et al (2017) SPECT and PET in ischemic heart failure. Heart Fail Rev 22(2):243–261
136. Dorbala S, Vangala D, Sampson U et al (2007) Value of vasodilator ventricular ejection fraction reserve in evaluating the magnitude of myocardium at risk and the extent of angiographic coronary artery disease: a 82Rb PET/CT study. J Nucl Med 48:349–358
137. Danad I, Uusitalo V, Kero T et al (2014) Quantitative assessment of myocardial perfusion in the detection of significant coronary artery disease: cutoff values and diagnostic accuracyof quantitative [(15)O]H2O PET imaging. J Am Coll Cardiol 64:1464–1475
138. Hajjiri MM, Leavitt MB, Zheng H et al (2009) Comparison of positron emission tomography measurement of adenosine-stimulated absolute myocardial blood flow versus relative myocardialtracer content for physiological assessment of coronary arterystenosis severity and location. JACC Cardiovasc Imaging 2:751–758
139. Ohira H, Dowsley T, Dwivedi G et al (2014) Quantification of myocardial blood flow using PET to improve the management of patients with stable ischemic coronary artery disease. Future Cardiol 10:611–631
140. Marwick TH, Shan K, Patel S et al (1997) Incremental value of rubidium-82 positron emission tomography for prognostic assessment of known or suspected coronary artery disease. Am J Cardiol 80:865–870
141. Yoshinaga K, Chow BJW, de Kemp R et al (2004) Prognostic value of rubidium-82 perfusion positron emission tomography: preliminary results from the consecutive 153 patients. J Am Coll Cardiol 43:338A (abstract)
142. Chow BJW, Wong JW, Yoshinaga K et al (2005) Prognostic significance of dipyridamole-induced ST depression in patients with normal Rb-82 PET myocardial perfusion imaging. J Nucl Med 46:1095–1101
143. Nemirovsky D, Henzlova MJ, Machac J et al (2005) Prognosis of normal rubidium-82 myocardial perfusion study. J Nucl Cardiol 12:S118 (abstract)
144. Yoshinaga K, Chow BJW, Williams K et al (2006) What is the prognostic value of myocardial perfusion imaging using rubidium-82 positron emission tomography? J Am Coll Cardiol 48:1029–1039
145. Dorbala S, DiCarli MF, Beanlands RS et al (2013) Prognostic value of stress myocardial perfusion positron emission tomography: results from a multicenter observational registry. J Am Coll Cardiol 61:176–184
146. Kay J, Dorbala S, Goyal A et al (2013) Influence of sex on risk stratification with stress myocardial perfusion Rb-82 positron emission tomography: results from the PET prognosis multicenter registry. J Am Coll Cardiol 62:1866–1876
147. Herzog BA, Husmann L, Valenta I et al (2009) Long-term prognostic value of N13-ammonia myocardial perfusion positron emission tomography: added

value of coronary flow reserve. J Am Coll Cardiol 54:150–156
148. Dorbala S, Hachamovich R, Curillova Z et al (2009) Incremental value of gated Rb-82 positron emission tomography myocardial imaging over clinical variables and rest LVEF. J Am Coll Cardiol Imaging 2:846–854
149. Dorbala S, Di Carli MF (2014) Cardiac PET perfusion: prognosis,risk stratification, and clinical management. Semin Nucl Med 44:344–357
150. Shaw LJ, Iskandrian AE (2004) Prognostic value of gated myocardialperfusion SPECT. J Nucl Cardiol 11:171–185
151. Hachamovitch R, Hayes S, Friedman JD et al (2003) Determinants of risk and its temporal variation in patients with normal stress myocardial perfusion scans: what is the warranty period of anormal scan? J Am Coll Cardiol 41:1329–1340
152. Pethig K, Heublein B, Meliss RR et al (1999) Volumetric remodeling of the proximal left coronary artery: early versus late after heart transplantation. J Am Coll Cardiol 34:197–203
153. Julius BK, Vassalli G, Mandonow L et al (1999) Alpha-adrenergic blockade prevents exercise-induced vasoconstriction of stenotic coronary arteries. J Am Coll Cardiol 33:1499–1505
154. O'Driscoll G, Green D, Maiorana A et al (1999) Improvement in endothelial function by angiotensin-converting enzyme inhibition in non-insulin-dependent diabetes mellitus. J Am Coll Cardiol 33:15–16
155. Kugiyama K, Motoyama T, Doi H, Kawano H et al (1999) Improvement of endothelial vasomotor dysfunction by treatment with alpha-tocopherol in patients with high remnant lipoproteins levels. J Am Coll Cardiol 33:1512–1518
156. Gould KL, Martucci JP, Goldberg DI, Hess MJ, Edens RP, Latifi R, Dudrick SJ (1994) Short-term cholesterol lowering decreases size and severity of perfusion abnormalities by positron emission tomography after dipyridamole in patients with coronary artery disease. A potential noninvasive marker of healing coronary endothelium. Circulation 89:1530–1538
157. Huggins GS, Pasternak RC, Alpert NM et al (1998) Effects of short-term treatment of hyperlipidemia on coronary vasodilator function and myocardial perfusion in regions having substantial impairment of baseline dilator reverse. Circulation 98:1291–1296
158. Yokoyama J, Memomura S, Oktake T, Yonekura K et al (1999) Improvement of impaired myocardial vasodilation due to diffuse coronary atherosclerosis in hypercholesterolemics after lipid-lowering therapy. Circulation 100:117–122
159. Gould KL, Martucci JP, Goldberg DL et al (1994) Short-term cholesterol lowering decreases disease in patients on a regimen of intensive physical exercise and low fat diet. J Am Coll Cardiol 19:34–42
160. Murthy VL, Naya M, Foster CR et al (2011) Improved cardiac riskassessment with noninvasive measures of coronary flow reserve. Circulation 124:2215–1224
161. Ziadi MC, Dekemp RA, Williams KA et al (2011) Impaired myocar-dial flow reserve on rubidium-82 positron emission tomographyimaging predicts adverse outcomes in patients assessed formyocardial ischemia. J Am Coll Cardiol 58:740–748
162. Murthy VL, Lee BC, Sitek A et al (2014) Comparison and prognosticvalidation of multiple methods of quantification of myocardialblood flow with 82Rb PET. J Nucl Med 55:1952–1958
163. Taqueti VR, Di Carli MF (2015) Radionuclide myocardial perfusion imaging for the evaluation of patients with known or suspectedcoronary artery disease in the era of multimodality cardiovascular imaging. Prog Cardiovasc Dis 57:644–653
164. Schinkel AF, Bax JJ, Poldermans D et al (2007) Hibernating myocardium: diagnosis and patient outcomes. Curr Probl Cardiol 32:375–410
165. Underwood SR, Bax JJ, vom Dahl J et al (2004) Imaging techniques for the assessment of myocardial hibernation report of a study group of the European Society of Cardiology. Eur Heart J 25:815–836
166. Schinkel AF, Bax JJ, Delgado V et al (2010) Clinical relevance of hiber-nating myocardium in ischemic left ventricular dysfunction. Am J Med 123:978–986
167. Beanlands RS, Ruddy TD, deKemp RA et al (2002) Positron emission tomography and recovery following revascularization (PARR-1):the importance of scar and the development of a prediction rule for the degree of recovery of left ventricular function. J Am Coll Cardiol 40:1735–1743
168. D'Egidio G, Nichol G, Williams KA et al (2009) Increasing benefit from revascularization is associated with increasing amounts of myocardial hibernation: a substudy of the PARR-2 trial. JACC Cardiovasc Imaging 2:1060–1068
169. Ohira H, Mc Ardle B, Cocker MS et al (2013) Current and future clinical applications of cardiac positron emission tomography. Circ J 77:836–848
170. Ben Bouallègue F, Maïmoun L, Kucharczak F et al (2021) Left ventricle function assessment using gated first-pass ^{18}F-FDG PET: validation against equilibrium radionuclide angiography. J Nucl Cardiol 28:594–603
171. Sauer WH, Stern BJ, Baughman RP, Culver DA, Royal W (2017) High-risk sarcoidosis: current concepts and research imperatives. Ann Am Thorac Soc 14:S437–S444
172. Ramirez R, Trivieri M, Fayad ZA, Ahmadi A, Narula J, Argulian E (2019) Advanced imaging in cardiac sarcoidosis. J Nucl Med 60(7):892–898
173. Ramsay SC, Cuscaden C (2020) The current status of quantitative SPECT/CT in the assessment of transthyretin cardiac amyloidosis. J Nucl Cardiol 27(5):1464–1468
174. Okasha O, Kazmirczak F, Chen KHA, Farzaneh-Far A, Shenoy C (2019) Myocardial involvement in patients with histologically diagnosed cardiac sarcoidosis: a systematic review and meta-analysis of gross pathological images from autopsy or cardiac transplantation cases. J Am Heart Assoc 8(10):e011253

175. Youssef G, Leung E, Mylonas I et al (2012) The use of 18F-FDG PET in the diagnosis of cardiac sarcoidosis: a systematic review and metaanalysis including the Ontario experience. J Nucl Med 53:241–248
176. White JA, Rajchl M, Butler J, Thompson RT, Prato FS, Wisenberg G (2013) Active cardiac sarcoidosis: first clinical experience of simultaneous positron emission tomographyDOUBLEHYPHENmagnetic resonance imaging for the diagnosis of cardiac disease. Circulation 127:e639–e641
177. Cegła P, Ciepłucha A, Pachowicz M, Chrapko B, Piotrowski T, Lesiak M (2020) Nuclear cardiology: an overview of radioisotope techniques used in the diagnostic workup of cardiovascular disorders. Kardiol Pol 78:520–528
178. Hotta M, Minamimoto R, Awaya T, Hiroe M, Okazaki O, Hiroi Y (2020) Radionuclide imaging of cardiac amyloidosis and sarcoidosis: roles and characteristics of various tracers. Radiographics 40(7):2029–2041
179. Martinez-Naharro A, Baksi AJ, Hawkins PN, Fontana M (2020) Diagnostic imaging of cardiac amyloidosis. Nat Rev Cardiol 17:413–426
180. Fontana M, Ćorović A, Scully P, Moon JC (2019) Myocardial amyloidosis: the exemplar interstitial disease. JACC Cardiovasc Imaging 12(11 Part 2):2345–2356
181. Kyriakou P, Mouselimis D, Tsarouchas A, Rigopoulos A, Bakogiannis C, Noutsias M, Vassilikos V (2018) Diagnosis of cardiac amyloidosis: a systematic review on the role of imaging and biomarkers. BMC Cardiovasc Disord 18(1):1–11
182. Shaw LJ, Raggi P, Schisterman E et al (2003) Prognostic value of cardiac risk factors and coronary calcium screening for all-cause mortality. Radiology 228:826–833
183. Berman DS, Wong ND, Gransar H et al (2004) Relationship between stress-induced myocardial ischemia and atherosclerosis measured by coronary calcium tomography. J Am Coll Cardiol 44:923–930
184. Kim JH, Machac J, Travis A et al (2013) Coronary artery and thoracic aorta calcification is inversely related to coronary flow reserve as measured by Rb-82 PET/CT in intermediate risk patients. J Nucl Cardiol 20(3):375–384. https://doi.org/10.1007/s12350-013-9702-6
185. Schenker MP, Dorbala S, Hong EC et al (2008) Interrelation of coronary calcification, myocardial ischemia, and outcomes in patients with intermediate likelihood of coronary artery disease. Circulation 117:1693–1700
186. Bolli R (1990) Mechanism of myocardial stunning. Circulation 82:723–772
187. Ferrari R, LaCanna G, Giubbini R et al (1994) Left ventricular dysfunction due to stunning and hibernation in patients. Cardiovasc Drugs Ther 8(Suppl 2):371–380
188. Fuster V, Badimon L, Badimon JJ et al (1992) The pathogenesis of coronary artery disease and the acute coronary syndromes. N Engl J Med 326(242–250):310–318
189. Homans DC, Laxson DD, Sublett E et al (1989) Cumulative deterioration of myocardial function after repeated episodes of exercise-induced ischemia. Am J Phys 256:H1462–H1471
190. Shivalkar B, Flameng W, Szilard M et al (1999) Repeated stunning precedes myocardial hibernation in progressive multiple coronary artery stenosis. J Am Coll Cardiol 34:2126–2136
191. Brunken R, Tillisch J, Schwaiger M et al (1986) Regional perfusion, glucose metabolism, and wall motion in patients with chronic electrocardiographic Q-wave infarctions: evidence for persistence of viable tissue in some infarct regions by positron emission tomography. Circulation 73:951–963
192. Partington SL, Kwong RY, Dorbala S (2011) Multimodality imaging in the assessment of myocardial viability. Heart Fail Rev 16:381–395
193. Smart S, Wynsen J, Sagar K (1997) Dobutamine-atropine stress echocardiography for reversible dysfunction during the first week after myocardial infarction: limitations and determinations of accuracy. J Am Coll Cardiol 30:1669–1678
194. Bax JJ, Wijns W, Cornel JH et al (1997) Accuracy of currently available techniques for prediction of functional recovery after revascularization in patients with left ventricular dysfunction due to chronic coronary artery disease: comparison of pooled data. J Am Coll Cardiol 30:1451–1460
195. Dilsizian V, Bonow RO (1992) Differential uptake and apparent Tl-201 washout after thallium reinjection: options regarding early redistribution imaging before reinjection or late redistribution imaging after reinjection. Circulation 85:1032–1038
196. Dilsizian V, Bonow RO (1993) Current diagnostic techniques of assessing myocardial viability in patients with hibernating and stunned myocardium. Circulation 87:1–20
197. Dilsizian V, Rocco TP, Freedman NMT et al (1990) Enhanced detection of ischemic but viable myocardium by the reinjection of thallium after stress-redistribution imaging. N Engl J Med 323:141–146
198. Dilsizian V, Freedman NMT, Bacharach SL et al (1992) Regional thallium uptake in irreversible defects: magnitude of change in thallium activity after reinjection distinguishes viable from nonviable myocardium. Circulation 85:627–634
199. Perrone-Filardi P, Bacharach SL, Dilsizian V et al (1992) Regional left ventricular wall thickening: relation to regional uptake of F-18-fluorodeoxyglucose and Tl-201 in patients with chronic coronary artery disease and left ventricular dysfunction. Circulation 86:1125–1137
200. Romero J, Xue X, Gonzalez W, Garcia MJ (2012) CMR imaging assessing viability in patients with chronic ventricular dysfunction due to coronary artery disease: a meta-analysis of prospective trials. JACC Cardiovasc Imaging 5:494–508

201. Schinkel AF, Bax JJ, Poldermans D, Elhendy A, Ferrari R, Rahimtoola SH (2007) Hibernating myocardium: diagnosis and patient outcomes. Curr Probl Cardiol 32:375–410
202. Maes A, Flameng W, Nuyts J et al (1994) Histological alterations in chronically hypoperfused myocardium: correlation with PET findings. Circulation 90(735–745):208
203. Kim YK, Lee DS, Cheon J et al (1999) Myocardial viability assessment by nitroglycerine gated Tc-99m MIBI SPECT: comparison with rest-24-hour redistribution Tl-201 SPECT. J Nucl Med 40:1P (abstract)
204. Gunning MG, Anagnostopoulos C, Knight CJ et al (1998) Comparison of Tl-201, Tc-99m-tetrofosmin, and dobutamine magnetic resonance imaging for identifying hibernating myocardium. Circulation 98:1869–1874
205. Perrone-Filardy P, Bacharach S, Dilsizian V et al (1994) Clinical significance of regional myocardial glucose uptake in regions with normal blood flow in patients with chronic coronary artery disease. J Am Coll Cardiol 23:608–616
206. Fallavolita JA, Canty JM (1997) F-18 FDG utilization is regionally increased in fasting pigs with hibernating myocardium. J Am Coll Cardiol 29:130A (abstract)
207. Hansen CL, Corbett JR, Pippin JJ et al (1988) 123-I-phenylpentadecanoic acid and single photon emission computed tomography in identifying LV regional metabolic abnormalities in patients with coronary heart disease: comparison with thallium-201 myocardial tomography. J Am Coll Cardiol 12:78–87
208. Hansen CL, Rastogi A, Sangrigoli R et al (1998) On myocardial perfusion, metabolism, and viability. J Nucl Cardiol 5:202–204
209. Beanlands RSB, Ruddy TD, deKemp RA et al (2002) Positron emission tomography and recovery following revascularization (PARR-1): the importance of scar and the development of a prediction rule for the degree of recovery of left ventricular function. J Am Coll Cardiol 40:1735–1743
210. Beanlands RSB, Nichol G, Huszti E et al (2007) F-18-fluorodeoxyglucose positron emission tomography imaging-assisted management of patients with severe left ventricular dysfunction and suspected coronary disease: a randomized, controlled trial (PARR-2). J Am Coll Cardiol 50:2002–2012
211. Bonow RO, Maurer G, Lee KL et al (2011) Myocardial viability and survival in ischemic left ventricular dysfunction. N Engl J Med 364:1617–1625
212. Russell RR III, Zaret BL (2006) Nuclear cardiology: present and future. Curr Probl Cardiol 31(9):557–629
213. Lopaschuk GD et al (2010) Myocardial fatty acid metabolism in health and disease. Physiol Rev 90:207–258
214. Luyten K, Schoenberger M (2017) Molecular imaging of cardiac metabolism, innervation, and conduction. EMJ Cardiol 5(1):70–78
215. Taegtmeyer H, Dilsizian V (2013) Imaging cardiac metabolism. In: Atlas of nuclear cardiology. Springer, New York, pp 289–321
216. Guyton AC, Hall JE (1966) Textbook of medical physiology, 9th edn. Saunders, Philadelphia, pp 193–197
217. Suami H, Scaglioni MF (2018) Anatomy of the lymphatic system and the lymphosome concept with reference to lymphedema. In: Seminars in plastic surgery, vol 32, No. 1. Thieme Medical Publishers, New York, pp 05–11
218. Weissleder R, Thrall JH (1989) The lymphatic system: diagnostic imaging studies. Radiology 172:315–317
219. Weiss L (1988) Cell and tissue biology, 6th edn. Urban and Schwarzenberg, Baltimore, pp 499–514
220. Ruggiero R, Muz J, Fietsam R Jr (1993) Reestablishment of lymphatic drainage after canine lung transplantation. J Thorac Cardiovasc Surg 106:167–171
221. Ruggiero R, Fietsam R Jr, Thomas GA (1994) Detection of canine allograft lung rejection by pulmonary lymphoscintigraphy. J Thorac Cardiovasc Surg 108:253
222. Suami H, Pan WR, Mann GB, Taylor GI (2008) The lymphatic anatomy of the breast and its implications foe sentinel lymph node biopsy: a human cadaver study. Ann Surg Oncol 15:863–871
223. Leak LV (1970) Electron microscopic observations on lymphatic capillaries and the structural components of the connective tissue lymph interface. Microvasc Res 2:361–391
224. Clodius L (1990) Lymphedema. In: McCarthy JG (ed) Plastic surgery. Saunders, Philadelphia, pp 4093–4120
225. Aspelund A, Robciuc MR, Karaman S, Makinen T, Alitalo K (2016) Lymphatic system in cardiovascular medicine. Circ Res 118(3):515–530
226. Zuther JE, Norton S (2013) Lymphedema management. The comprehensive guide for practitioners, 3rd edn. Thieme Medical Publishers, New York
227. Warren AG, Brorson H, Borud LJ, Slavin SA (2007) Lymphedema. Ann Plast Surg 59:464–472
228. Chen SL, Iddings DM, Scheri RP, Bilchik AJ (2006) Lymphatic mapping and sentinel node analysis: current concepts and applications. CA Cancer J Clin 56:292–309
229. Krag DN, Anderson SJ, Julian TB et al (2010) Sentinel-lymph-node resection compared with conventional axillary-lymphnode dissection in clinically node-negative patients with breast cancer: overall survival findings from the NSABP B-32 randomised phase 3 trial. Lancet Oncol 11:927–933

230. Nawaz MK, Hamad MM, Abdel-Dayem HM (1990) Tc-99m human serum albumin lymphoscintigraphy in lymphedema of the lower extremities. Clin Nucl Med 15:794–799
231. Szuba A, Shin WS, Strauss HW, Rockson S (2003) The third circulation: radionuclide lymphoscintigraphy in the evaluation of lymphedema. J Nucl Med 44(1):43–57
232. Mavi A, Lakhani P, Zhuang H, Gupta NC, Alavi A (2005) Fluorodeoxyglucose-PET in characterizing solitary pulmonary nodules, assessing pleural diseases and the initial staging, restaging, therapy planning, and monitoring response of lung cancer. Radiol Clin N Am 43(1):1–24
233. Koolen BB, Valdés ORA, Vogel WV et al (2012) 18F-FDG PET/CT for the assessment of locoregional lymph node involvement and radiotherapy indication in stage II-III breast cancer treated with neoadjuvant chemotherapy. Cancer Res 72:nr:P4–02–01 (abstract)
234. Rijke AM, Croft BY, Johnson RA (1990) Lymphoscintigraphy and lymphedema of the lower extremities. J Nucl Med 31:990–998

Digestive System

10

Abdelhamid H. Elgazzar and Saud A. Alenezi

10.1 Gastrointestinal Tract

The digestive system consists of the gastrointestinal tract, hepatobiliary system (Fig. 10.1), pancreas, and salivary glands. Nuclear medicine is concerned with the evaluation of normal and abnormal functions of the gastrointestinal tract and hepatobiliary system. To date, the role of nuclear medicine in pancreatic disorders is limited to evaluation of its tumors which is dealt with elsewhere in the book.

10.1.1 The Esophagus

10.1.1.1 Anatomic and Physiological Considerations

The esophagus is a 18–25 cm long muscular tube that passes through the mediastinum, connecting the pharynx and the stomach. The cervical esophagus is composed of striated muscles whereas the thoracic esophagus consists of smooth muscles. Physiologically, the main function of the esophagus is to transport swallowed food from the hypopharynx to the stomach. Moreover, the normal function of the esophagus prevents the regurgitation of food from the upper esophagus into the hypopharynx and gastric contents from the stomach to the esophagus. The disruption of the normal function of the esophagus results in dysphagia and/or regurgitation. Functionally, the esophagus has three components: the upper esophageal sphincter (UES), the body, and the lower esophageal sphincter (LES) [1]. The components work together to keep the esophagus empty. Esophageal motility disorders result from sphincter dysfunction or abnormal peristalsis in the body of the esophagus or both. The diagnosis and treatment of esophageal dysmotility rest on the understanding of the functional anatomy of the UES, esophageal body, and the LES.

Upper Esophageal Sphincter

The UES is a 3–4-cm-long high-pressure zone that forms a barrier between the esophagus and the pharynx. It opens and closes intermittently to allow the passage of food or liquid. The UES closure muscles comprise the cervical esophagus, cricopharyngeus, and interior pharyngeal constrictor. The UES opening muscles consist of the superior and inferior hypoid muscles and superior pharyngeal muscles [1–3]. All UES muscles are striated and are innervated by the glossopharyngeal, branches of the vagus, ansa cervicalis, and sympathetic nerves from the cervical ganglion. The vagus nerve is the major motor nerve of the UES. Nerve cell bodies of the vagus efferent fibers are located in the nucleus ambiguus (medulla oblongata). Between swallows, the UES is tonically contracted to prevent reflux of

A. H. Elgazzar (✉) · S. A. Alenezi
Department of Nuclear Medicine, Faculty of Medicine, Kuwait University, Kuwait City, Kuwait

A. H. Elgazzar (ed.), *The Pathophysiologic Basis of Nuclear Medicine*,
https://doi.org/10.1007/978-3-030-96252-4_10

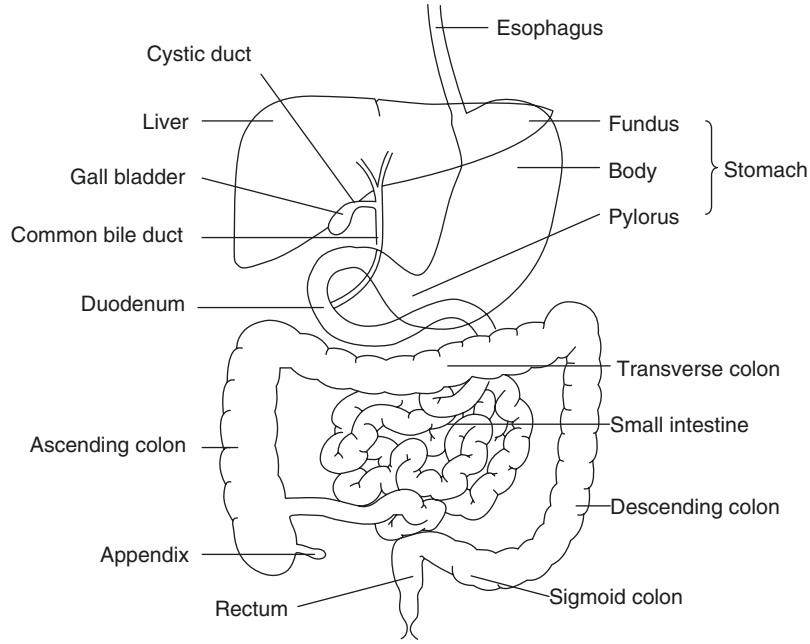

Fig. 10.1 Diagram of the relevant parts of the digestive system

esophageal contents and entry of air from the pharynx during inspiration. During swallowing, the cricopharyngeal and inferior pharyngeal constrictor muscles relax and the suprahyoid muscles contract.

Esophageal Body

The esophageal body extends from the UES to the LES and measures 18–25 cm. The esophageal wall consists of mucosa, submucosa, and the tunica muscularis and adventitia. The esophageal body is not surrounded by a tunica serosa. The esophageal mucosa is of the stratified squamous epithelium type, except for the distal 2 cm, where columnar epithelium of the gastric cardia type may be encountered. More proximal extension of gastric-type epithelium or the presence of intestinal-type columnar epithelium defines the pathological entity known as Barrett's esophagus (Fig. 10.2). Outside the epithelial lining is a thin layer of longitudinally oriented smooth muscle fibers, the muscularis mucosa. Below the muscularis mucosa is the submucosa, which consists of connective tissue. The muscularis propria is made up of an inner, circular, muscle layer and an outer, longitudinal, muscle layer. In the proximal 5% of the esophageal body, the muscularis propria is made up of striated muscle fibers. The distal 50–60% consists entirely of smooth muscle. The middle 35–40% is composed of a mixture of smooth and striated muscle fibers.

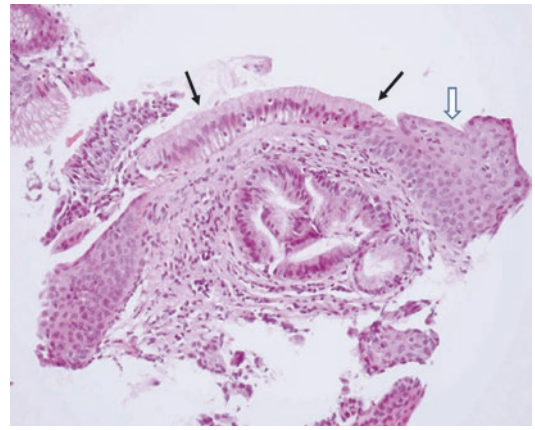

Fig. 10.2 Barrett's esophagus. *Solid arrows* point to columnar metaplasia. *Open arrow* points to the normal stratified squamous epithelium. (Courtesy of Prof. M. Elmonayeri)

Neuronal control of esophageal body motility is complex [4]. The esophageal wall receives extrinsic innervation via the vagus nerve. Striated muscle fibers are directly innervated

by postganglionic neurons originating in the nucleus ambiguus and terminating on the motor end plate. Smooth muscle fibers are controlled by preganglionic nerve fibers originating in the dorsal motor nucleus. These cholinergic nerve fibers terminate on the intrinsic neurons of the myenteric plexus located between the circular and longitudinal muscle layers. Within the myenteric plexus, two types of neurons have been identified. Excitatory neurons mediate contraction of both longitudinal and circular muscle layers via nicotinic cholinergic nerve receptors. Inhibitory neurons mediate the relaxation of mainly circular muscle fibers via noncholinergic, nonadrenergic neurotransmitters, most probably nitrous oxide and vasoactive intestinal peptide (VIP) [5]. Intrinsic sensory (afferent) neurons are within Meissner's plexus located in the submucosa. Sensory impulses are conveyed to the central nervous system via both vagal and thoracic sympathetic nerve fibers.

Swallowing initiates a progressive series of coordinated propulsive contractions throughout both the striated and the smooth muscle portions of the esophageal body. This form of esophageal motor activity is referred to as primary peristalsis. Intraluminal distention of the esophageal body results in a peristaltic wave at or proximal to the site of distention. This wave is termed secondary peristalsis and serves to clear the esophagus from contents that have not been cleared by primary peristalsis, or refluxed gastric contents. Primary and secondary peristaltic waves have similar amplitudes and travel at a velocity of 3–5 cm/s.

Deglutitory inhibition is a unique physiological phenomenon whereby repetitive swallowing inhibits all esophageal body activity while the LES is relaxed. A normal peristaltic contraction will follow the last swallow of such a series and clear the esophagus completely [6].

Lower Esophageal Sphincter

The LES is a high-pressure zone measuring 2–5 cm in length located between the esophageal body and the stomach. Ultrastructural studies show that this high-pressure zone consists of a specialized thickened region of the circular muscles layer of the distal esophagus, albeit the muscle fibers are not circular, rather they are organized as clasp and sling fibers [7]. At rest the sphincter is tonically contracted with a normal pressure ranging from 10 to 45 mmHg. The basal LES tones are determined by three factors: myogenic tone that is independent of neural influences, cholinergic excitatory tone, and nitrergic inhibitory tone. The LES relaxes after swallowing. Relaxation is mediated by the nitrergic inhibitory neurons. The LES may also relax without swallowing, a phenomenon referred to as transient lower esophageal sphincter relaxation (TLESR). These relaxations are believed to play a major role in the pathogenesis of gastroesophageal reflux disease.

A number of endogenous compounds affect the LES tone when administered in pharmacological doses. For instance, large doses of gastrin increase the tone of LES. Exogenous substances such as beta-adrenergic receptor agonists and calcium channel blockers may induce relaxation of the LES.

10.1.1.2 Esophageal Motor Disorders

Disorders of the UES and Cervical Esophagus

Motor disorders affecting the skeletal (proximal) part of the esophagus result from either neurological abnormalities affecting the extrinsic innervation of the proximal esophagus, or skeletal muscle or neuromuscular disorders. More specifically these include:

- Neurological diseases
  - Cerebrovascular accident
  - Parkinsonism
  - Amyotrophic lateral sclerosis
  - Cranial nerve palsy
- Skeletal muscular disorders
  - Dermatomyositis
  - Polymyositis
  - Muscular dystrophy
- Cricopharyngeus dysfunction
- Others
  - Myasthenia gravis
  - Amyloidosis

Table 10.1 Classification of primary esophageal body and LES disorders

Achalasia
Nonspecific esophageal dysmotility
Hypercontractile esophagus
Nutcracker esophagus
Hypertensive lower esophageal sphincter
Hypocontractile esophagus
Ineffective esophageal motility
Hypotensive lower esophageal sphincter
Discoordinated motility
Diffuse esophageal spasm

Because of the difficulty of transferring food bolus from the hypopharynx into the esophageal body across the UES, most patients experience choking or regurgitation of liquids and/or solids. Videofluoroscopy is the best diagnostic modality for diagnosing oropharyngeal dysphagia. Scintigraphy is of limited value.

Disorders of Esophageal Body and LES

Disorders of the distal esophageal body (smooth muscle) and LES can be broadly classified into achalasia and nonspecific esophageal dysmotility according to conventional stationary esophageal manometry (Table 10.1).

Achalasia

Achalasia is a primary motor disorder of the esophagus with absence of peristalsis and insufficient lower esophageal sphincter relaxation [8].

It is the best-studied motor disorder of the esophagus. It occurs at a rate of 1:100,000 and affects both sexes equally. Age of onset is usually 25–65 years. It results from the degeneration of the inhibitory myenteric neurons in the body and the LES region. This leads to a hypertensive LES which relaxes poorly and also causes aperistalsis in the body of the esophagus. Patients usually present with dysphagia to liquids and solids. Barium esophagogram may show dilatation of the esophagus and "bird beaking" of the distal esophagus. Esophageal manometry confirms the diagnosis of achalasia. Typically, there is incomplete relaxation of the LES and aperistalsis. LES hypertension is detected in 20–40% of patients [7]. Although these changes are highly suggestive of achalasia, they are by no means pathognomonic. Other conditions that might mimic achalasia include adenocarcinoma of the cardia, esophageal squamous cell carcinoma, Chagas' disease, and lung cancer.

Several other spastic disorders have been characterized in patients with noncardiac chest pain (Table 10.1). They all share a similar clinical presentation. Diffuse esophageal spasm (DES) is the most severe form. It is less common than achalasia. The mean age at presentation is 40 years. Patients frequently complain of intermittent nonprogressive dysphagia for solids and liquids. Hot or cold liquids and stress may precipitate chest pain. Some patients with DES progress to achalasia.

Nonspecific Esophageal Dysmotility

Nonspecific esophageal motility disorders are further classified into hypercontractile, hypocontractile, and discoordinated motility. Patients with hypercontractile esophagus usually present with chest pain and dysphagia. Nutcracker esophagus is a hypercontractile disorder characterized by increased lower esophageal peristalsis amplitude and duration. Hypertensive LES is associated with an LES resting pressure of >45 mmHg [9].

Patients with hypocontractile esophageal disorders complain of heartburn, regurgitation, and occasional dysphagia. Ineffective esophageal motility is characterized by low-amplitude peristalsis. Hypotensive LES is defined as an LES pressure below 10 mmHg. A number of systemic conditions are associated with esophageal hypocontractility including scleroderma, diabetes mellitus, and amyloidosis.

Diffuse esophageal spasm is a rare condition that presents with atypical chest pain that can radiate to the throat and back. Dysfunction in nitrous oxide synthesis or degradation is believed to be the cause of the spastic component. The manometric hallmark of diffuse esophageal spasm is simultaneous discoordinated contractions in more than 20% of swallow. The resultant tertiary contractions give the corkscrew appearance on barium swallow.

Gastroesophageal Reflux Disease

Gastroesophageal reflux disease (GERD) involves the reflux of chyme from the stomach to the esophagus. The LES may relax spontaneously and transiently 1–2 h after the patient has eaten, allowing gastric contents to regurgitate into the esophagus. The acid is normally neutralized and cleared by peristalsis from the esophagus within 3 min and the tone of the sphincter is stored. When the reflux does not cause symptoms, it is known as physiological but in some individuals it may cause a spectrum of inflammatory responses in the esophagus. GERD is the most prevalent condition originating from the gastrointestinal tract. It is estimated than 20% of the Western adult population suffers from heartburn more than three times a month [9]. It is particularly important in the pediatric age group. Also, GERD is common among pregnant women, especially during the third trimester.

The typical symptom of GERD is heartburn. However, a number of atypical symptoms are also linked to GERD, such as noncardiac chest pain, hoarseness, asthma, water brash, teeth erosion, and halitosis.

Most children affected with gastroesophageal reflux (GER) are between 6 months and 2 years old; they suffer from poor weight gain, vomiting, aspiration, choking, asthmatic episodes, stridor, apnea, and failure to thrive. A small amount of physiological reflux occurs in infants and resolves spontaneously by 8 months of age. The Tuttle acid reflux test is generally considered the reference standard but is technically demanding. The radionuclide method has a number of potential advantages. It is physiological, easily performed, well tolerated by the patient, and quantitative and involves a low radiation dose to the child.

Pathophysiology

GERD is a multifactorial process. Causes of GERD can be categorized as follows: (a) decreased pressure of LES, (b) transient increase in intra-abdominal pressure, and (c) short intra-abdominal esophageal segment. Mechanisms involved are summarized in Table 10.2. As mentioned earlier, transient LES relaxation appears to be the most common mechanism of GERD, especially in patients without endoscopic evidence of esophagitis [10]. In patients with moderate to severe esophagitis, LES incompetence plays a more important role in promoting reflux. The relation between a sliding hiatus hernia and GERD is controversial. Although most patients with severe GERD have hiatus hernia, most patients with hiatus hernia are asymptomatic. Recent data suggest that a large hiatus hernia may impair acid clearance [11, 12].

Table 10.2 Mechanisms of gastroesophageal reflux disease

Mechanism	Causes
Anti-reflux barrier	Transient LES relaxation
	Incompetent LES
	Sliding hiatus hernia
Esophageal clearance	Impaired peristalsis
	Decreased salivary output
Refluxate composition nature	Acid
	Pepsin
	Bile salts
	Pancreatic enzymes
Gastric factors	Delayed gastric emptying
	Acid hypersecretion
	Helicobacter pylori
Defective esophageal mucosal protection	Lack of HCO_3 secretion
	Lack of mucus secretion

Esophageal body peristalsis plays an important role in clearing refluxed acid in both the upright and the supine position. Defective primary or secondary peristalsis leads to incomplete clearance of acid. Furthermore, salivary HCO_3 usually neutralizes acid that remains in contact with the esophageal mucosa. Thus, impaired salivation may contribute to mucosal injury [13].

There is consensus about the fact that the potency of the contents of the refluxate, particularly acid/pepsin, is important in the pathogenesis of reflux esophagitis. Bile and pancreatic enzymes may be additional contributing factors.

Delayed gastric emptying is documented in 6–30% of patients with GERD. Theoretically,

gastric stasis can contribute to GERD. However, the relative importance of delayed gastric emptying is not well established [13]. *Helicobacter pylori* has recently been implicated as having a potential role in the pathogenesis of GERD [5]. *H. pylori* may secrete proinflammatory substances that can damage esophageal mucosa and sensitize vagal afferent nerves or lead to the reduction of LES tone. In contrast, there are data suggesting a protective role for *H. pylori* against GERD [6].

Finally, a significant proportion of patients with proven esophagitis do not have increased exposure to acid/pepsin. These patients probably have disruption of mucosal defense mechanisms such as the mucus layer, intercellular junctional complexes, intracellular mechanisms of handling acid, and blood flow to the esophagus [14].

10.1.2 The Stomach

10.1.2.1 Anatomic and Physiological Considerations

Anatomic Features

The stomach is a storage sac located between the esophagus and duodenum (Fig. 10.1). The proximal stomach consists of the cardia, fundus, and body. The antrum forms the distal stomach and is separated from the duodenum by the pyloric ring. The wall structure of the stomach is similar to that of the rest of the gastrointestinal tract, i.e., it consists of the mucosa, submucosa, muscularis propria, and serosa. However, unlike other parts of the gastrointestinal tract, the muscularis consists of three layers—circular, longitudinal, and oblique. This facilitates distension of the stomach and storage of food. The muscle layer in the antrum is modified to aid the mixing of food. The pyloric ring regulates the emptying of the stomach.

Overall Functions

Besides storage, the stomach has a number of exocrine, paracrine, and endocrine functions. The exocrine secretions consist of HCI and pepsin produced by the mucosal parietal cells and chief cells, respectively. These cells are located in the fundus and body of the stomach. Most cells within the lamina propria and submucosa are responsible for the main paracrine function, namely, the release of histamine, which in turn stimulates the parietal cells to secrete acid. The antrum secretes the hormone gastrin which enhances gastric emptying and acid secretion.

The intrinsic factor (IF) is a glycoprotein secreted by parietal cells. It binds to Vitamin B-12. The IF-B12 complex in turn binds to specific receptors on the terminal ileal epithelium. Without IF, B12 cannot be absorbed and pernicious anemia develops. Usually failure to secrete IF results from gastric atrophy which causes the destruction of parietal cells.

Gastric Motor Physiology

The motor activity of the stomach serves two main functions: (a) to act as a reservoir for ingested meal and ensure timed delivery of food particles to the duodenum at a rate compatible with optimal digestion and (b) to disperse solids into small particles and to mix them with gastric juice. The functions are accomplished by the coordinated activity of three functionally distinct parts of the stomach: (a) the proximal stomach, including the fundus and proximal body; (b) the distal stomach, including distal body and antrum; and (c) the pylorus, as part of the pyloroduodenal unit.

The proximal stomach has three muscle layers, longitudinal, circular, and oblique. No myoelectrical activity is recorded from the fundus during fasting except for the interdigestive migratory motor complexes (see below). In the fed state, the fundus exhibits two forms of motor activity: receptive relaxation and accommodation. Receptive relaxation refers to the reduction in proximal stomach tone initiated by swallowing or pharyngeal stimulation. Accommodation is reflex relaxation of the proximal stomach in response to gastric distention. It is not induced by swallowing or pharyngeal stimulation. Truncal vagotomy abolishes both receptive relaxation and accommodation, suggesting that they are mediated by the vagus nerve. Some gastrointestinal peptides such as cholecystokinin, secretin, VIP, and gas-

trin induce proximal stomach relaxation, whereas motilin increases fundic pressure [15, 16].

The distal stomach is comprised of two muscle layers: the longitudinal and circular. Slow waves or slow pacer potentials originate in the pacemaker region, located on the greater curvature of the stomach near the junction of the proximal and distal stomach. Slow waves pace the normal 3 min^{-1} corpus-antral peristalsis, which mixes solid and liquid food with gastric juice and triturates larger particles. The distal gastric motor activity is regulated by cholinergic and noncholinergic, vagal efferent nerve fibers. Cholinergic pathways stimulate antral contraction whereas noncholinergic vagal nerve stimulation inhibits antral activity through VIP and possibly nitrous oxide release from inhibitory neurons within the myenteric plexus.

The pyloric sphincter functions, in coordination with the duodenum, as a sieve allowing particles l mm or smaller to pass into the duodenum in 2–4-mL aliquots with each gastric peristalsis [17]. Emptying of inert liquids such as 0.9% saline follows first-order kinetics; i.e., the volume of liquid emptied into the duodenum in a given time is a constant fraction of the volume that remains in the stomach (Fig. 10.3) [18]. Emptying of digestible solid particles is characterized by a lag phase and a linear phase (Fig. 10.4) [19]. However, the caloric density, viscosity, osmolarity, and volume of any specific meal will influence gastric emptying rates. Fibrous material in the stomach is emptied in the interdigestive state by migrating myoelectrical-contractile complexes comprising 3–10 min of strong lumen-obliterating antral contractions [8].

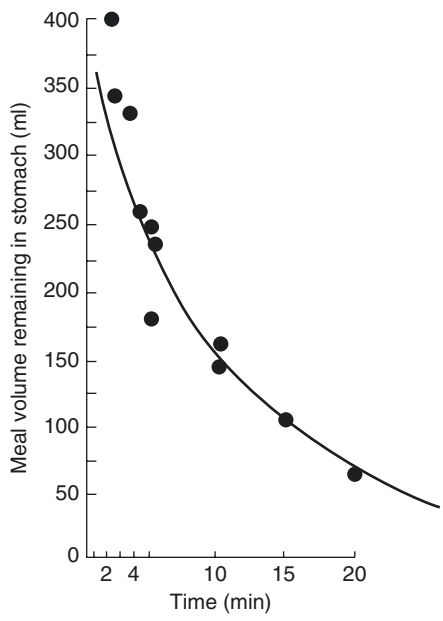

Fig. 10.3 Gastric emptying of 0.9% normal saline follows first-order kinetics. (From [18])

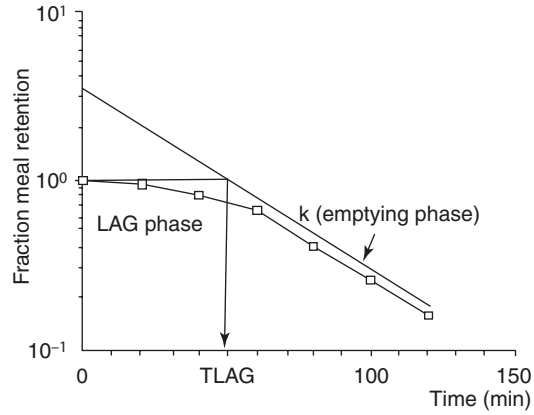

Fig. 10.4 Emptying of digestible solid particles lag phase and a linear phase. The *curve* represents modified power exponential function. (From Siegel et al. [19])

10.1.2.2 Disorders of Gastric Emptying

Conditions that cause abnormal gastric emptying can be divided into two groups: disorders associated with delayed emptying and disorders associated with dumping (Table 10.3). Diabetes is one of the most common causes of delayed gastric emptying in clinical practice. Most afflicted patients have had type I diabetes for more than 10 years, complicated by autonomic and peripheral neuropathy. Delayed emptying of both solids and liquids is attributed to the dysfunction of the proximal and distal stomach, as well as to increase pyloric resistance [20, 21].

Idiopathic gastroparesis is also encountered frequently in patients with bloating, early satiety, and nausea. The exact cause is unclear but it may be related to post-viral gastroenteritis [5]. Delayed gastric emptying is a known and frequent complication of gastric surgery. For instance, vagotomy delays emptying of solids but

Table 10.3 Causes of gastric dysmotility

Condition	Causes
	Mechanical obstruction
	Gastric outlet obstruction (e.g., tumor, peptic ulcer)
	Small intestinal obstruction
	Decreased gastric motility
	Postsurgical gastroparesis (vagotomy Roux-en-Y, fundoplication, etc.)
	Endocrine disorders (DM, hypothyroidism, Addison's disease, hyper- or hypoparathyroidism)
	Drugs (narcotics, anticholinergics, calcium channel blockers)
	Connective tissue diseases (e.g., scleroderma, SLE)
	Muscular disorders (myotonic dystrophy, dermatomyositis)
	Paraneoplastic
	Post-viral
	Neurological disorders (migraine, CVA, Parkinson, dysautonomia)
	Intestinal pseudo-obstruction
	Idiopathic gastroparesis
	Others (anorexia nervosa, uremia, ischemic gastroparesis, pregnancy)
Rapid gastric emptying (dumping)	Duodenal ulcer disease (including ZE syndrome)
	Vagotomy
	Antrectomy
	Idiopathic

promotes liquid emptying. Similarly, antrectomy can cause rapid emptying of undigested solids and liquids due to the loss of mixing function and loss of pyloric resistance. Symptoms of delayed gastric emptying include early satiety, nausea, vomiting, postprandial abdominal bloating, distention, and pain. The symptoms of gastroparesis are nonspecific and cannot be easily differentiated from those of mechanical obstruction. Other diseases such as gastritis, irritable bowel syndrome, and nonnuclear dyspepsia may cause similar complaints.

10.1.2.3 Duodenogastric Reflux

Duodenogastric reflux (DGR) has been suggested to occur in normal individuals in both fasting and postprandial periods [22, 23], although others have suggested that it does not occur physiologically [24]. The amount of refluxed bile in normal subjects is reported to be small and clears rapidly from the stomach [25]. This feature helps separate normal from abnormal subjects in the fasting state.

Table 10.4 Causes of duodenogastric reflux

Causes	
Duodenal ulcer	Gastritis
Acute cholecystitis	Chronic cholecystitis
Enteritis	Pancreatitis
Gastric carcinoma	Surgery
Post-traumatic stress ulceration	Gastric surgery/ vagotomy
Duodenal hematoma	Cholecystectomy
Erosive esophagitis	Gallstone dyspepsia
Physiological/unknown cause	

Pathologically, DGR has been associated with many conditions (Table 10.4), including postgastrectomy/vagotomy, gastric and duodenal ulcers, cholecystitis, and gastritis [26]. In some of these conditions, such as duodenal ulcer, duodenal hematoma, and cholecystitis, duodenal irritation is probably the underlying mechanism. Other causes may irritate the duodenal mucosa by the adjacent pancreatic inflammation. Slavin also proposed that the deficiency of pancreatic secretions can explain DGR since volume, the alkaline pH, and the physiological components of the pancreatic secretions may be important for maintaining the outward flow of gastric contents [27].

10.1.3 The Intestines

10.1.3.1 The Small Intestine

Anatomic and Histologic Considerations

The small intestine is a hollow muscular cylinder that measures 5–6 m in length. It consists of three regions: duodenum, jejunum, and ileum. The intestinal wall is made up of four layers: the mucosa, the submucosa, the muscularis, and the serosa. The small intestinal mucosa is fashioned into villi and crypts to increase the surface area and enhance the absorptive function of the small bowel. The mucosa of the villi consists of absorp-

tive columnar epithelial cells (enterocytes) and mucus-secreting goblet cells. Within the crypts the most common cell type is the undifferentiated crypt cell which secretes chloride and water into the lumen. The crypt also contains pluripotent stem cells. Furthermore, the small bowel harbors the enteroendocrine cells which secrete a number of hormones including secretin, cholecystokinin, gastrin, gastric inhibitory peptide, motilin, glucagon, vasoactive intestinal peptide, somatostatin, and others. These hormones play an important role in gastrointestinal motility. Finally, the intestinal mucosa and lamina propria contain the largest lymphoid organ in man: the gut-associated lymphoid tissue (GALT) [28]. The latter consists of:

- M-cells
- Intraepithelial lymphocytes (IELs)
- Peyer's patches (lymphoid follicles)
- Lamina propria T and B lymphocytes
- Dendritic cells
- Macrophages

The M-cells are specialized epithelial cells overlying lymphoid follicles. Because they are not covered by mucus, antigens can bind to M-cells which take in the antigens, process them, and present them to lymphocytes and macrophages. However, the binding to antigens is highly selective. For instance, only pathogenic bacteria can attach to M-cells, whereas commensals cannot. IELs are specialized T lymphocytes situated between the basolateral membranes of mucosal epithelial cells and the lamina propria. They appear to have an important immunologic function as they express CD45RO a marker of memory cells. Dendritic cells are derived from the bone marrow and reside beneath M-cells. They capture antigens, carry them across the mucosal barrier, and present them to T lymphocytes.

The submucosa consists of connective tissue, lymphocytes, plasma cells, macrophages, mast cells, fibroblasts, eosinophils, nerve fibers, ganglion cells (Meissner's plexus), blood vessels, and lymphatics.

The muscularis is made of inner circular and an outer longitudinal muscle fibers. Between these two layers of smooth muscle lies the myenteric plexus, the network of intramural neurons that is essential for all coordinated and organized motor activity. The extrinsic (autonomic) nerves affect the gastrointestinal motility by means of these enteric nerves.

Functional Considerations

Most of the digestion and absorption of nutrients takes place in the small bowel. Moreover, the motor function of the small bowel ensures the mixing of chyme with digestive enzymes and the propulsion of chyme toward the colon. Also, the small bowel plays an important role as a first line of defense against pathogenic microorganisms and harmful food antigens.

In most instances, nutrients cannot be absorbed by the cells that line the gastrointestinal tract in the forms in which they are ingested. *Digestion* is the breakdown of ingested molecules into small ones via reactions catalyzed by enzymes produced by the gastrointestinal organs.

The small intestinal epithelium participates in digestion by secreting oligosaccharidases such as lactase, enterokinase, and peptidases.

Absorption refers to the process of transporting molecules through the epithelial lining of the gastrointestinal tract into the blood or lymph.

Water, electrolytes, monosaccharides, amino acids, small peptides, glycerol, fatty acid, vitamins, and minerals are all absorbed via a number of mechanisms including passive diffusion, facilitated diffusion, active transport, and endocytosis. Although absorption takes place along the entire length of the small intestine, the mucosa in certain regions selectively absorbs specific molecules. For instance, iron is primarily absorbed in the duodenum and proximal jejunum, whereas the terminal ileal mucosa has specific receptors for binding and absorbing vitamin B-12 and bile salts [29].

Under physiological conditions the small bowel exhibits two main motor patterns. During the fed state, and as a result of contact with nutrients, a number of neuronal and hormonal signals are elicited including afferent vagal stimulation and the release of cholecystokinin which mediate *segmentation* and *peristalsis. Segmentation* is the

most frequent movement in the small bowel and is characterized by closely spaced contractions of the circular muscle layer. These contractions divide the small intestine into short neighboring segments. Segmentation helps mix chyme with digestive enzymes. *Peristalsis*, on the other hand, is the progressive contraction of successive sections of circular smooth muscle resulting in the propulsion of chyme toward the colon. Furthermore, during the fed state, the small intestine especially the duodenum exerts negative feedback control on gastric emptying via neural and hormonal mechanisms (secretin, cholecystokinin, and gastric inhibitory peptide).

During the fasting phase, the small intestine exhibits a different pattern of motility characterized by bursts of intense electrical and contractile activity separated by periods of lack of activity. This pattern is called *migrating myoelectric complex* (MMC). In humans MMC occurs every 90–120 min, originates from the stomach, and sweeps through the small bowel till the terminal ileum. The function of MMC is to clear undigested particles and propagate them to the colon [30].

Small Intestinal Dysmotility

Motor disorders of the small bowel can lead to symptoms and signs of "functional" as opposed to mechanical small bowel obstruction. Patients frequently complain of abdominal distension, bloating, and abdominal pain, and when small intestinal dysmotility is associated with gastroparesis, nausea, and vomiting may be prominent. On physical examination, the abdomen is usually distended and bowel sounds are diminished. Features of bacterial overgrowth may be observed.

Small intestinal dysmotility may be acute or chronic. Acute dysmotility is termed adynamic ileus and is commonly seen following abdominal surgery, severe septicemia, or electrolyte disturbances such as hypokalemia. Chronic dysmotility is termed pseudo-obstruction (Table 10.5).

Most cases of pseudo-obstruction are secondary to endocrine and metabolic causes, such as diabetes mellitus and hypothyroidism; neurological disorders, such as Chagas' disease and Parkinsonism; or drug induced (e.g., phenothiazines, narcotics). Primary pseudo-obstruction is rare. Few cases are due to familial visceral neuropathies and myopathies. However, the majority of cases of primary pseudo-obstruction are sporadic.

Table 10.5 Motor disorders of the small intestine

Cause	Mechanism	Outcome
Acute illness	Impaired smooth muscle contraction	Adynamic ileus
	Altered neurotransmission	
Pregnancy	Decreased smooth muscle contraction (progesterone)	Slow transit
Diabetes mellitus	Autonomic dysfunction	Slow or rapid transit
Scleroderma	Smooth muscle fibrosis	Weak contractions
	Neuronal loss in gut wall	Slow transit
Primary pseudo-obstruction	Neuronal loss, plexus degeneration	Weak contractions
		Abnormal MMC
		Slow transit
Myopathies	Myocyte and mitochondrial abnormalities	Weak segmentation and peristalsis

Malabsorption

Malabsorption syndrome is an alteration in the ability of the GI tract, usually the small intestine to absorb one or more nutrients adequately from diet into the bloodstream. These may include fats, proteins, carbohydrates, vitamins, or others. This may result from acquired or congenital defects. The syndrome may present with anemia (most commonly vitamin B-12, folate, and iron deficiency); diarrhea; steatorrhea (excessive amount of fat in the stool); abdominal distention edema; malnutrition and weight loss; muscle cramping due to decreased vitamin D, calcium, and potassium levels; muscle wasting and atrophy due to decreased protein absorption and metabolism; and perianal skin burning, itching, or soreness due to frequent loose stools. Protein depletion can lead to impaired bone formation and osteoporosis, and calcium deficiency leads to weak-

ening and demineralization of the bone, causing osteomalacia.

Common causes of malabsorption syndrome include inflammatory bowel disease, tropical sprue, Whipple's disease, lactase deficiency, and parasitic diseases; other causes are past intestinal surgeries, bacterial overgrowth, gluten enteropathy (nontropical sprue), AIDS, radiation to the abdomen, diabetes, lymphoma, or motility disorders. In addition to small bowel disease, malabsorption can occur in those who have had portions of their stomachs removed surgically. The pancreas produces enzymes that help digest food, so if a condition exists where enzymes are not being produced, it can result in maldigestion or malabsorption. This could include chronic alcoholic pancreatitis, trauma, cystic fibrosis, tumors, or postsurgical states. The diagnosis of malabsorption syndrome and identification of the underlying cause can require extensive diagnostic testing. Generally, an endoscopy is performed under mild sedation, at which time a biopsy can be obtained to be analyzed under the microscope. In addition, various blood tests are helpful to determine if a malnourished condition exists. These tests may include serum cholesterol; serum sodium, potassium, and chloride; serum calcium; serum protein and albumin; serum vitamin A and carotene; D-xylose test; Schilling test; and others. Stool collections and cultures are useful as well as certain breath and hormone tests. Scintigraphic imaging and quantitation is also used in some forms.

Protein-Losing Enteropathy (PLE)

PLE is a condition in which excess protein loss into the gastrointestinal lumen is severe enough to produce hypoproteinemia. It occurs with many of the previously listed conditions causing malabsorption. Furthermore, diseases such as constrictive pericarditis, congestive heart failure, intestinal lymphangiectasia, nephrotic syndrome, and systemic lupus erythematosus may also cause protein loss from the gastrointestinal tract without any observable mucosal lesions in the bowel. The mechanism of the loss of plasma protein into the gastrointestinal tract in these diseases is not yet fully understood [5].

The previously reported materials used for the detection of protein loss have many limitations, such as rapid reabsorption of the radiolabel, unstable protein binding both in vivo and in vitro, and limited availability. The need for measurement of fecal radioactivity over 3–4 days has also been a drawback with some of the methods in which these materials are used. Imaging with other radioisotope-labeled materials such as ^{111}In chloride and ^{111}In transferrin has been reported [6].

^{99m}Tc–labeled HSA has been used to image protein-losing enteropathy since its introduction in 1986 [31]. Serial imaging for up to 24 h is useful in detecting protein loss from the gut, possibly because of the intermittent nature of this protein loss. Tc-99m HSA is also useful in viewing the entire gastrointestinal tract at one time to permit detection of multiple potential sites of protein loss. A new scintigraphic method using ^{99m}Tc-labeled dextran was first described in 1995 by Bhatnagar et al. [32]. This method demonstrates significant intestinal radiotracer accumulation at 3–4 h postinjection in 22 patients, giving information about localization and extension of the disease. In 4 of 12 healthy subjects, there was minimal abdominal accumulation occurring late in the study [33]. These polysaccharides of molecular weight between 60,000 and 90,000 are being used as a plasma expander and, in radioactive tagged form, for lymphoscintigraphy and blood pool agents. Add brief details on the procedure.

Vitamin B-12 Malabsorption

Vitamin B-12 deficiency due to pure dietary inadequacy of this vitamin is very rare and occurs mainly in strict vegetarians. More often gastrointestinal disorders, atrophic gastritis, pernicious anemia, congenital lack or abnormality of gastric IF, or total or partial gastrectomy cause malabsorption and consequent deficiency of this vitamin. Diseases involving the distal ileum such as Crohn's disease, intestinal stagnant loop syndrome, and rarely congenital selective ileal malabsorption with proteinuria (Imerslund-Grasbeck syndrome) may also result in malabsorption of vitamin B-12.

10.1.3.2 The Colon

Anatomic and Functional Considerations

The colon is a tubular structure that extends from the ileocecal valve to the anal verge (Fig. 10.1). It measures approximately 1–5 m and consists of the cecum; ascending, transverse, descending, and sigmoid colon; and rectum. Like the small intestine, the colonic wall consists of the mucosal submucosa, muscularis, and serosa. However, the colonic mucosa lacks villi. Also, unlike the small intestine, the external longitudinal muscular layer is gathered into three flat longitudinal ribbons of smooth muscle called teniae coli. The continuous contractions of the teniae coli cause sacculations of the wall termed haustrations.

The primary function of the colon is to absorb water and electrolytes from its contents and to pack feces until defecation. The motility of the colon is geared toward this function. As stated above, throughout the colon, localized segmental contractions take place and result in mixing chyme. In the cecum and ascending colon, retrograde (antipropulsive) contractions also occur. The net effect of these motility patterns is to slow transit and facilitate the absorption of water and electrolytes. Periodically, massive contractions start in the proximal colon to propel fecal material toward the sigmoid colon where it is stored. One to three times a day, mass contractions sweep the stool toward the rectum. Distension of the rectum by feces initiates the defecation reflex which is mediated by the pelvic nerves and integrated at the level of the sacral spinal cord.

Pathophysiology of Relevant Colon Diseases

Inflammatory Bowel Disease

Inflammatory bowel disease (IBD) refers to two disorders: Crohn's disease (CD) and ulcerative colitis (UC). Both conditions are characterized by chronic relapsing intestinal inflammation. UC affects the colon only, and the inflammation is limited to the mucosa + submucosa in most cases. CD can affect the entire gastrointestinal tract from mouth to anus. The inflammation in CD is granulomatous and transmural. Besides inflammation of the gut, IBD is associated with a number of systemic manifestations including anterior uveitis, axial and peripheral arthropathy, primary sclerosing cholangitis, erythema nodosum, and pyoderma gangrenosum.

The etiology of IBD is not totally settled. Proposed factors include environmental, infectious, genetic, autoimmune, and host factors. After first described by Burrill B. Crohn, Crohn's disease was considered an infectious disease. Crohn's disease and ulcerative colitis were thought to be autoimmune diseases, and currently, microbial factors, as well as other direct environmental influences, have been proposed [34].

A lot of research has been performed to discover potential genes linked to IBD. One of the early linkages discovered was on chromosome 16 (IBD1 gene), which led to the identification of the NOD2 gene (now called CARD15) as the first gene clearly associated with IBD (as a susceptibility gene for Crohn's disease). Studies have also provided strong support for IBD susceptibility genes on chromosomes 5 (5q31) and 6 (6p21 and 19p). None of these mechanisms has been implicated as the primary cause, but they are postulated as potential causes.

The pathophysiology of IBD is still incompletely understood and is under active investigation, but the common end pathway is inflammation of the mucosal lining of the intestinal tract, causing ulceration, edema, bleeding, and fluid and electrolyte loss. The inflammation of the intestinal mucosa includes both acute inflammation with neutrophilic infiltration and chronic with mononuclear cell infiltration, predominantly lymphocytes [35].

Many of the immunologic and molecular mechanisms that mediate inflammation have been elucidated in recent years. Three groups of factors seem to play a role: genetic predisposition, mucosal immune dysregulation, and environmental agents (Table 10.6). The importance of genetic factors in the pathogenesis of IBD is evidenced by familial aggregation of CD and UC cases. Approximately 10–20% of patients with IBD have an affected relative. Concordance among monozygotic twins especially in CD also

Table 10.6 Pathogenesis of inflammatory bowel disease

Genetic predisposition	Environmental factors	Immunologic dysregulation
Family clustering	Infectious agents	Proinflammatory mediators
NOD_2 gene variants	Dietary antigens	Anti-inflammatory mediators
Gene loci on Chr. 2,3,12	Intestinal commensals	

supports the notion of genetic predisposition. . One of the early linkages discovered was on chromosome 16 (IBD1 gene), which led to the identification of the NOD2 gene (now called CARD15) as the first gene clearly associated with IBD (as a susceptibility gene for Crohn's disease). Studies have also provided strong support for IBD susceptibility genes on chromosomes 5 (5q31) and 6 (6p21 and 19p). None of these mechanisms has been implicated as the primary cause, but they are postulated as potential causes [35].

This gene mediates the innate immune response to microbial pathogens. Similarly a number of other susceptibility genes have been identified in relation to CD and UC.

In genetically predisposed individuals, environmental factors can precipitate the disease by inducing an abroad immunologic response characterized by an imbalance between anti-inflammatory mediators.

The mucosal immune system plays a central role in the pathogenesis of IBD. A defective mucosal barrier may allow the uptake of microbial and ingested antigens. Under physiological conditions, GALT selectively removes harmful antigens. This process is mediated by the dendritic cells which are the main antigen presenting cells in GALT. The interaction of dendritic cells with T lymphocytes results in immunosuppression (tolerance) toward commensals and beneficial antigens. In IBD patients, tolerance is lost due to a number of immunoregulatory abnormalities including an imbalance between proinflammatory and anti-inflammatory mediators in favor of the former. For instance, the levels of IL-1, IL-6, IL-18, tumor necrosis factor alpha (TNF alpha), and interferon gamma are raised in patients with CD (TH1 response), whereas the levels of IL-1ra, TGF beta, 4-Y, IL-10 (TH2 response), and prostaglandin E_2 are reduced. The role of TNF alpha is of particular therapeutic significance. Monoclonal antibodies to TNE alpha have been shown to be effective in treating CD.

The rising incidence of IBD especially CD in recent years is highly suggestive of the role of environmental factors in modulating the immune response. Furthermore, a number of studies have shown a positive correlation between smoking and CD and a negative association with UC. Other factors that have been implicated as environmental precipitants of IBD include the use of NSAIDS, antibiotics, infective diarrheal illnesses, and increased intake of refined sugar. In the genetically susceptible rodent model of IBD, colitis does not develop when the gut is sterile, and IBD is precipitated by the introduction of bacteria into the diet [36, 37].

The primary pathophysiologic change of UC is inflammation of the mucosa and the submucosa and formation of crypt abscesses and mucosal ulceration with skip areas. The small intestine is essentially not involved. UC primarily involves the mucosa and the submucosa, with formation of crypt abscesses and mucosal ulceration.

CD consists of segmental involvement by a nonspecific granulomatous inflammatory process involving all layers of bowel with skip areas. The disease involves the small bowel in addition to the colon, and rectal sparing is typical. Less commonly it involves the mouth, tongue, esophagus, stomach, and duodenum.

Acute Appendicitis

The appendix is a diverticulum of an average of 10 cm in adults arising from the posteromedial wall of the cecum with its fixed to the cecum, while the remainder of the appendix is free. This fact accounts for its variable positions (retrocecal, subcecal, retroileal, pre-ileal, or pelvic) and behind much of the diversity in clinical presentations among patients with acute appendicitis [38].

The pathophysiology of appendicitis begins with obstruction of the narrow appendiceal lumen by causes, including fecaliths, lymphoid hyperplasia (related to viral illnesses such as upper respiratory infections, mononucleosis, or gastroenteritis), gastrointestinal parasites, foreign bodies, and Crohn's disease. Continued secretion of mucus results in elevated intraluminal pressure, leading to tissue ischemia, overgrowth of bacteria, transmural inflammation, appendiceal infarction, and possible perforation. Inflammation may subsequently extend into the parietal peritoneum and adjacent structures causing abdominal abscesses.

Acute appendicitis is the most common reason for emergency abdominal surgery and must be differentiated from other causes of abdominal pain. The overall diagnostic accuracy achieved by medical history, physical examination, and laboratory tests has been approximately 80% as the presentation may be atypical. In atypical cases, ultrasonography and computed tomography (CT) may help lower the rate of unnecessary surgeries. The accuracy rates for ultrasonography range from 71 to 97% and the modality is highly operator dependent and difficult in patients with a large body habitus. The accuracy rate of CT scanning is between 93 and 98%. However, there is controversy regarding the use of contrast media and which CT technique is best. Additionally, radiation exposure, cost, and possible complications from contrast media are disadvantages [4].

Colorectal Cancer

The incidence of colorectal cancer is highest in developed countries, such as the USA and Japan, and lowest in developing countries in Africa and Asia. It is the third most common type of cancer in both men and women in the USA. Pathologically most (over 95%) of colorectal cancers are adenocarcinomas. Surgery, chemotherapy, radiation therapy, and immunotherapy are the lines of treatment. Nuclear medicine has an important role in the follow-up to detect recurrence (see Chap. 12). FDG-PET has an important role as it is more sensitive than computed tomography for the detection of metastatic or recurrent colorectal cancer (Fig. 10.5) and may improve clinical management in more than 25% of cases [39]. It is of particular importance to differentiate post-therapy fibrosis and inflammation from viable tumor in the presacral region.

Gastrointestinal Bleeding

The localization of the specific bleeding site in patients presenting with acute GI bleeding remains a serious clinical problem. Scintigraphy has emerged as the imaging modality of first choice for localizing bleeding sites in the lower gastrointestinal tract.

Acute gastrointestinal bleeding (GIB) can be divided into bleeding in the upper (proximal to the ligament of Treitz) or lower tract. If acute upper GIB is a possibility, lavage with a nasogastric tube should identify acute or subacute bleeding. Endoscopy will localize 80–97% cases of acute upper bleeding; of these, 75% will resolve spontaneously or with conservative medical therapy and 10% will require surgery. Because of the length and tortuosity of the colon and contamination of fecal matter and blood, endoscopy is not that successful in lower GIB cases. Peptic ulcers are the most common cause of upper GIB; other causes include gastritis, esophageal varices, Mallory Weiss tear, esophagitis with or without hiatal hernia, and carcinoma [40]. The three leading causes of lower GIB are diverticular disease, angiodysplasia, and colorectal cancer. Other causes include inflammatory bowel disease, ischemic colitis, infectious colitis (inflammation of the colon due to an **infective** cause, including bacterial, viral, fungal, or parasitic), and anorectal disease (Table 10.7). This bleeding usually resolves spontaneously in 80% of cases and rebleeds in 25%. Angiodysplasias account for 20% of significant lower GIB and tend to rebleed.

Meckel's diverticulum is a vestige of the omphalomesenteric duct that is present in about 2% of the population with two thirds younger than 2 years. It is an outpouch usually found on the antimesenteric border of the ileum, 50–80 cm proximal to the ileocecal valve. Ectopic gastric mucosa is present in about 30% of cases. Nearly all diverticula responsible for

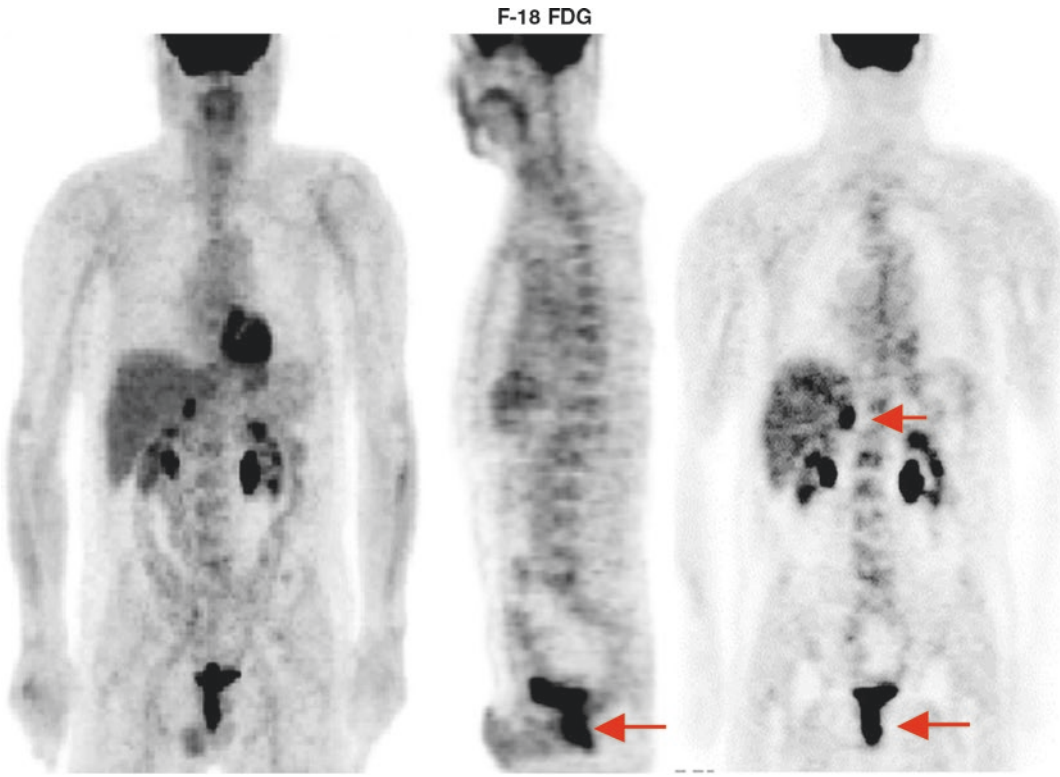

Fig. 10.5 F-18 FDG study of a patient who had rising CEA 5 years after resection of rectal adenocarcinoma. MRI and CT were inconclusive. Five biopsies were obtained from the rectum and were negative. The FDG study shows clearly viable local tumor recurrence and metastases in the right adrenal gland (*arrows*)

Table 10.7 Causes of GI bleeding[a]

Upper gastrointestinal bleeding
Esophageal, gastric, and duodenal ulcers
Mallory Weiss tears
Esophagitis, gastritis, duodenitis, pancreatitis
Neoplasms
Vascular malformations
Varices
Lower gastrointestinal bleeding
Post-polypectomy bleeding
Ischemic colitis
Colorectal polyps/neoplasms
Inflammatory bowel disease
Infectious colitis
Meckel's diverticulum
Neoplasia
NSAID ulcers
Dieulafoy's lesion
Anorectal conditions **as** rectal varices **and radiation** proctitis

[a] [41–44]

rectal bleeding contain ectopic gastric mucosa. Bleeding, which is usually massive and painless, may result from ileal mucosal ulceration due to acid secretion.

Scintigraphy and computed tomography angiography (CTA) are the most important noninvasive imaging tests that can identify presence of and help locate the site of bleeding [41]. Patients with lower GIB should be stabilized and supported while diagnostic studies are performed. More commonly, a nuclear medicine study is performed first to localize the bleeding because it is more sensitive for slow or intermittent bleeding, which is a common occurrence. If the scan is positive, arteriography can be employed to deliver vasopressin or embolic agents selectively into the bleeding artery. The most recent ACR appropriateness criteria guidelines for stable patients with lower GI bleeds give equal weight to Tc-99m RBC scan and CTA [45].

10.1.4 Salivary Gland

10.1.4.1 Anatomic and Physiologic Considerations

The major salivary glands include the parotid and the submandibular gland. The parotid gland is located behind the mandible and consists of a superficial and a deep part. The main parotid duct (Stensen's duct) runs anteriorly to pierce the buccinator muscle, opening on a papilla on the buccal mucosa opposite the second upper molar tooth. The submandibular gland is smaller than the parotid and lies in the submaxillary triangle just below the mandible. The main duct (Wharton's duct) passes forward and medially to open on a papilla lateral to the frenulum at the base of the tongue. The sublingual glands are situated anteriorly in the floor of the mouth above the mylohyoid muscle, and each gland opens into the oral cavity through several small ducts.

Salivary glands secrete saliva which is a clear, viscous, and watery fluid that contains two major types of protein secretions, a serous secretion containing the digestive enzyme ptyalin and a mucus secretion containing the lubricating aid mucin. Saliva also contains large amounts of potassium and bicarbonate ions and to a lesser extent sodium and chloride ions as well as several antimicrobial constituents, including thiocyanate, lysozyme, immunoglobulins, lactoferrin, and transferrin. Accordingly saliva provides many several functions including antimicrobial activity, mechanical cleansing action, control of pH, removal of food debris from the oral cavity, lubrication of the oral cavity, remineralization, and maintaining the integrity of the oral mucosa.

10.1.4.2 Pathophysiology of Relevant Disorders

Nuclear medicine-relevant conditions affecting salivary glands are numerous. These include inflammatory, neoplastic, and mechanical disorders affecting the parenchyma and duct system. Xerostomia is defined as dry mouth resulting from reduced or absent saliva flow. It is not a disease but is a symptom of various medical conditions. Xerostomia may result from such conditions as mumps, Sjögren's syndrome, sarcoidosis, radiation-induced atrophy, and drug sensitivity.

Inflammation of salivary glands usually presents as diffuse enlargement of the glands, unilateral or bilateral. Bilateral enlargement is caused by inflammation (mumps, Sjögren's syndrome), granulomatous disease (sarcoidosis), or diffuse neoplastic involvement (leukemia and lymphoma). The vast majority of salivary neoplasms occur in the parotid gland. Over two thirds represent benign mixed or pleomorphic adenomas. Warthin's tumor is another benign tumor that can be bilateral. The more common malignant tumors include mucoepidermoid carcinoma, adenocarcinoma, and squamous cell carcinoma. Plain films are of limited use for evaluating these tumors. Sialography in conjunction with CT is the preferred technique [46, 47]. The CT sialogram demonstrates the location of the tumor within the gland and also defines any involvement of the deep structures of the neck.

The duct system of the parotid and the submandibular glands can be demonstrated by sialography, and the technique is particularly valuable in the diagnosis of diseases which affect the duct system such as calculus, stricture, and sialectasia.

10.1.5 Ascites

Ascites is the accumulation of excess fluid within the peritoneal cavity. It is most frequently encountered in patients with cirrhosis and other forms of severe liver disease, but a number of other disorders may lead to either transudative or exudative ascites. Serous effusion into the peritoneum occurs in cases of general edema of both the cardiac and renal type and is sometimes abundant; some fluid may accumulate also in severe anemias and wasting disease. The most severe ascites, however, results from portal obstruction, the most common cause being cirrhosis of the liver. Hepatic vein occlusion (Budd–Chiari syndrome) is also accompanied by gross ascites.

The pathogenesis of ascites is complex, and multiple factors have been postulated to

be involved. In cirrhosis the major vascular obstruction is post-sinusoidal, and the flow of lymph is considerably augmented. The lymphatic vessels, including the thoracic duct, are dilated but nevertheless appear inadequate to deal with the increased volume of lymph. Fluid oozes from the liver surface; this is called the weeping liver.

Another factor in the pathogenesis of ascites is hypoalbuminemia, since if this is combined experimentally with portal vein obstruction, ascites develops. It has been postulated that the major factor in the formation of ascites is retention of salt and water by the kidney, followed by an outflow of fluid into the peritoneal cavity. Another factor to consider in the pathogenesis of ascites is the increased capillary pressure in the splanchnic area secondary to portal hypertension. This leads to the formation of transudate.

Surgical management of ascites includes various shunt operations. Most are performed as therapy for esophageal bleeding. Which shunt operation is most effective in relieving ascites has not been established; in fact, ascites is reduced after any type of portosystemic shunt as a consequence of decreased portal flow and decreased intrahepatic congestion. Among the most commonly performed shunts, splenorenal and splenocaval shunts and their variants have proven effective in relieving ascites. Transjugular intrahepatic portosystemic shunt (TIPS) has been used to reduce portal hypertension in patients with bleeding esophageal varices. TIPS has been shown to relieve intractable ascites as well.

The peritoneovenous shunt is a pressure-activated shunt devised by LeVeen. One line of this shunt lies free in the peritoneal cavity, and the venous opening of the efferent inserts into the SVC near its entrance into the right atrium. Flow into the shunt is maintained if there is 3–5 cmH_2O pressure gradient between the valve and its venous end. Radionuclide studies using Tc99m-macroaggregated albumin (MAA) injected intraperitoneally are used to evaluate the patency of the shunts [48–50].

10.1.6 Gastrointestinal Scintigraphy

10.1.6.1 Radionuclide Esophageal Transit Time Study

This study has proven useful and sensitive in detecting esophageal disorders and its involvement in certain systemic disorders.

The patient should fast for 4–6 h. A dose of 250–500 μCi Tc-99m-SC in 10 mL of water is taken through a straw. The multiple-swallow technique is preferred over the single-swallow test because of the considerable intraindividual variations in esophageal emptying among normal subjects and patients. It is preferable to do the imaging with the subject in the supine position to eliminate the effect of gravity; images of 1 s each are acquired to characterize the esophageal transit. Delayed images at 10 min may be helpful in patients with significant stasis of radioactivity in the esophagus. A time-activity curve can be generated; the esophageal transit time is the time interval between the peak activity of the proximal esophageal curve and the peak activity of the distal esophageal curve.

The normal transit time is 15 s, with a distinct peak in each third of the esophagus. A slowing of bolus progression can be noted at the mid-esophagus because of compression by the tracheal bifurcation and aortic arch. Prolonged transit time might be found in several esophageal and systemic disorders such as achalasia, progressive systemic sclerosis, diffuse esophageal spasm, nonspecific motor disorders, nutcracker esophagus, Zenker's diverticulum (an outpouch above the UES that is acquired), esophageal tumors, and esophageal stricture.

10.1.6.2 Gastroesophageal Reflux Study

The patient should fast for 4 h. The dose is 0.5–1 mCi Tc-99m-SC in 300 mL of acidic orange juice. Imaging is performed with the subject in a supine position at a rate of 1 frame/10 s for 60 min. All frames should be reviewed with contrast enhancement. GER is seen as distinct spikes of activity into the esophagus (Fig. 10.6).

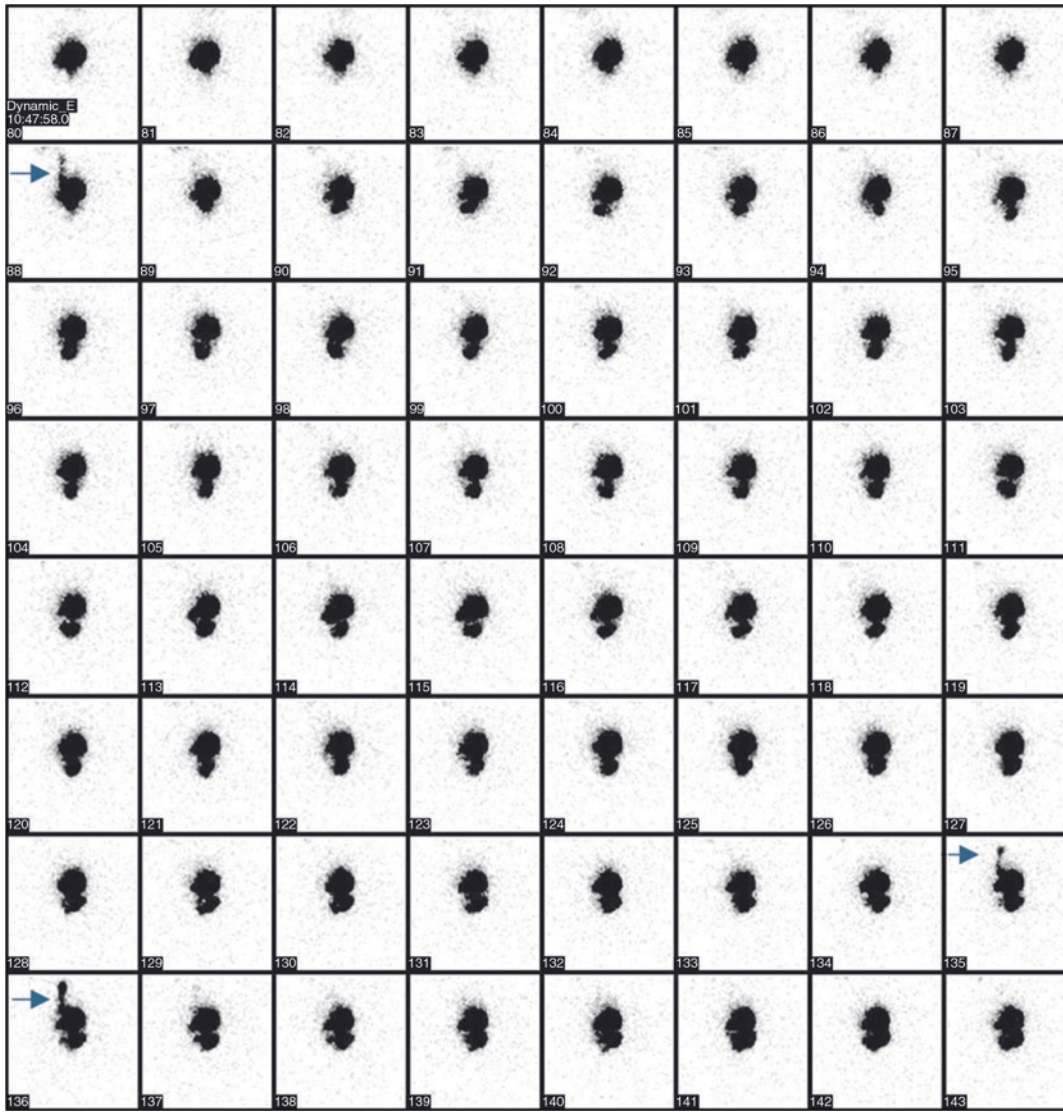

Fig. 10.6 A gastroesophageal reflux study obtained using ^{99m}Tc-sulfur colloid for a 2-year-old boy demonstrates reflux in three frames (*arrows*)

The episodes of reflux are graded as high or low level, by duration (less or more than 10 s), and by their temporal relationship to meal ingestion. The salivagram can often reveal aspiration when a GER study is negative.

This scintigraphic study has 89% correlation with the acid reflux test. The evidence of pulmonary aspiration is valuable in the pediatric age group, though it is seen in up to 25% of cases of aspiration with reflux.

10.1.6.3 Gastric Emptying Study

The patient should avoid smoking, since it affects emptying, and should fast overnight. The dose is 0.5–1.0 mCi Tc-99m-SC mixed with egg white or liver pâté as a solid meal. Dynamic images can be taken for 60 min or longer (Figs. 10.7 and 10.8), and if necessary, static delayed images are taken every 15 min until at least 50% of the stomach activity (content) has gone into the bowel. Normally, the stomach should empty 50% of the

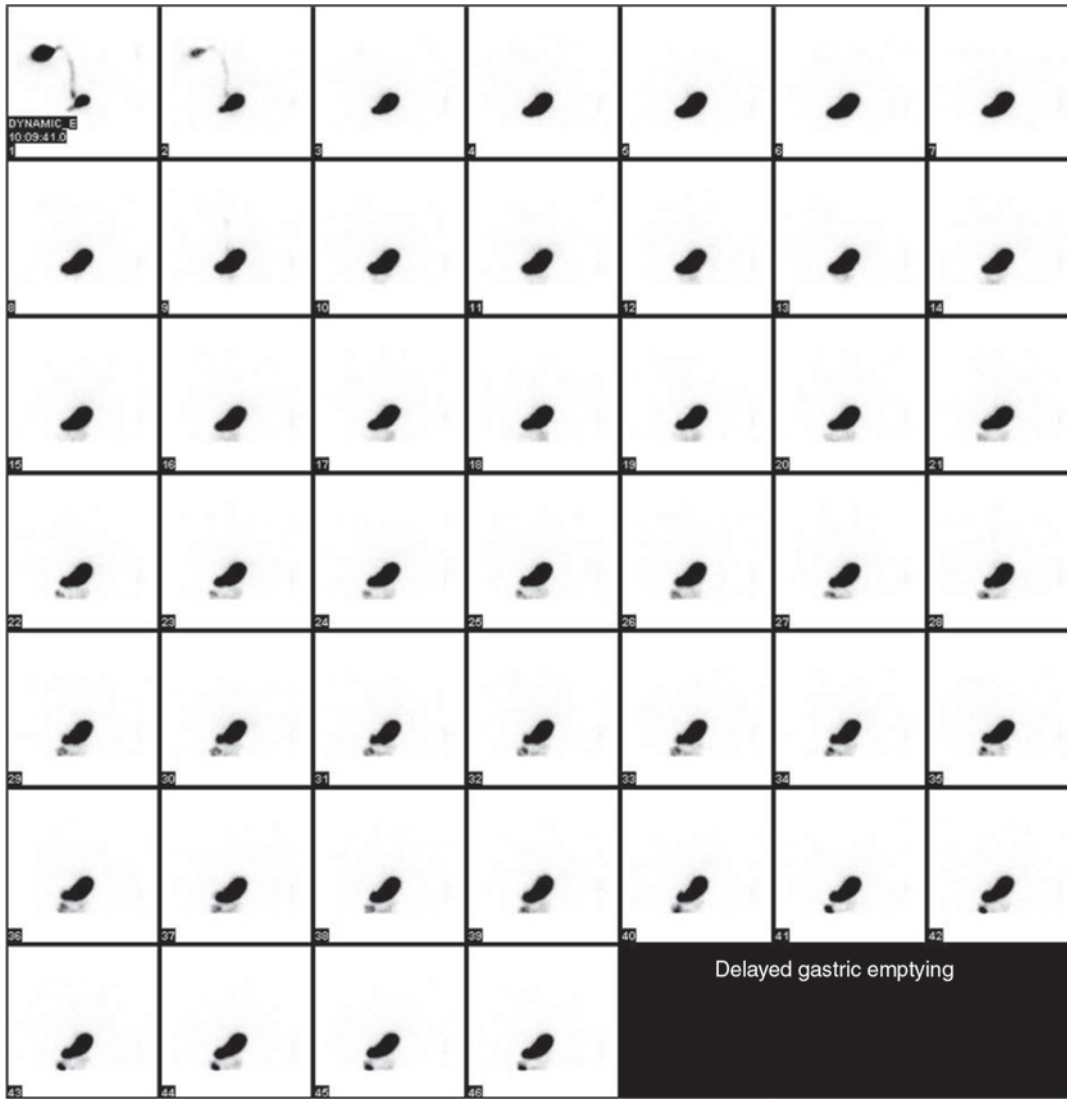

Fig. 10.7 Abnormal gastric emptying study. ^{99m}Tc-sulfur colloid gastric emptying study is shown. Gastric emptying half-clearance time was more than 160 min. Note activity in the stomach is not decreasing with time indicating delayed clearance. Compare with the normal pattern in Fig. 10.8

activity measured at time zero, by 90 min. The lag phase corresponds to maximal filling of the distal stomach when trituration has been completed and the suspended solid particles begin to empty. Lag phase abnormality may be the earliest finding in diabetic gastroparesis and can be corrected by the drugs used to treat this condition [15, 21]. Solids leave the stomach in a linear fashion. Acutely delayed emptying is seen in stress (as in cold or pain), due to drugs (morphine, anticholinergics, levodopa, nicotine, beta blockers) and due to hyperglycemia and hypokalemia.

Chronically delayed gastric emptying is encountered most frequently in gastric outlet obstruction, postvagotomy, gastric ulcer, scleroderma, dermatomyositis, hypothyroidism, diabetes mellitus,

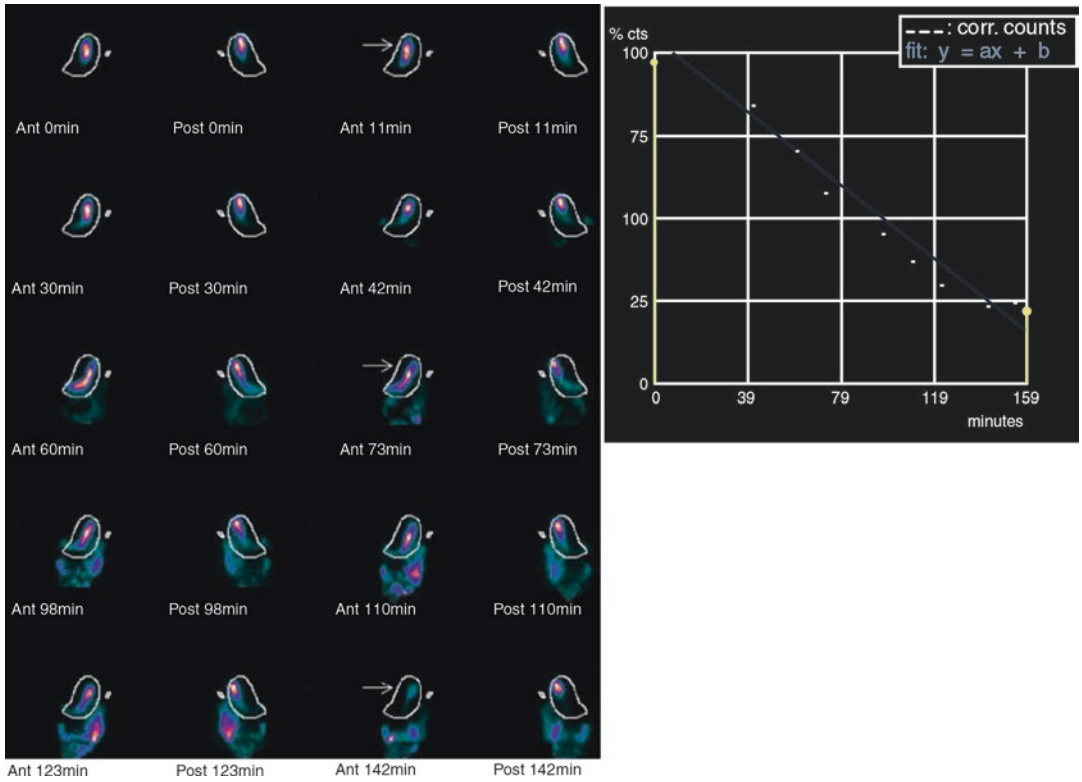

Fig. 10.8 Normal gastric emptying study. The study revealed normal gastric emptying quantitatively. Note the decreasing activity of gastric activity with time during the study, indicating prompt clearance

amyloidosis, and uremia. Abnormally rapid gastric emptying is found in gastric surgery, Zollinger-Ellison syndrome, duodenal ulcer, hyperthyroidism, and diabetes.

It should be noted that the reproducibility of gastric emptying studies is only moderately as in 30% of studies repeat studies can be different [51]. Accordingly, the diagnosis of gastroparesis based on a single study may occasionally be inaccurate.

An ingestible, telemetric device (the wireless motility capsule: WMC) is now commercially available, enabling the measurement of both regional and total GI transit times in a minimally invasive manner without radiations is an alternative to scintigraphy. The wireless motility capsule measures pH, pressure, and temperature throughout the GI tract, and is used also to calculate gastric emptying [52].

10.1.6.4 Duodenogastric Reflux Study

The way of detecting duodenogastric reflux is to administer a radiopharmaceutical that can go to the duodenum without passing through the stomach. This can be achieved by using hepatobiliary radiopharmaceuticals in conjunction with stimulation of the gall bladder to empty by a fatty meal. This helps to increase the activity in the duodenum and thus to detect the reflux. The usual protocol is to acquire dynamically for 60 min following i.v. administration of Tc99m-IDA derivative (Fig. 10.9). The fatty meal is then ingested by the patient and another dynamic study is obtained for 30 min.

10.1.6.5 Gastrointestinal Bleeding Localization Study

This radionuclide study can detect a bleeding rate as low as 0.1 mL/min. The two common

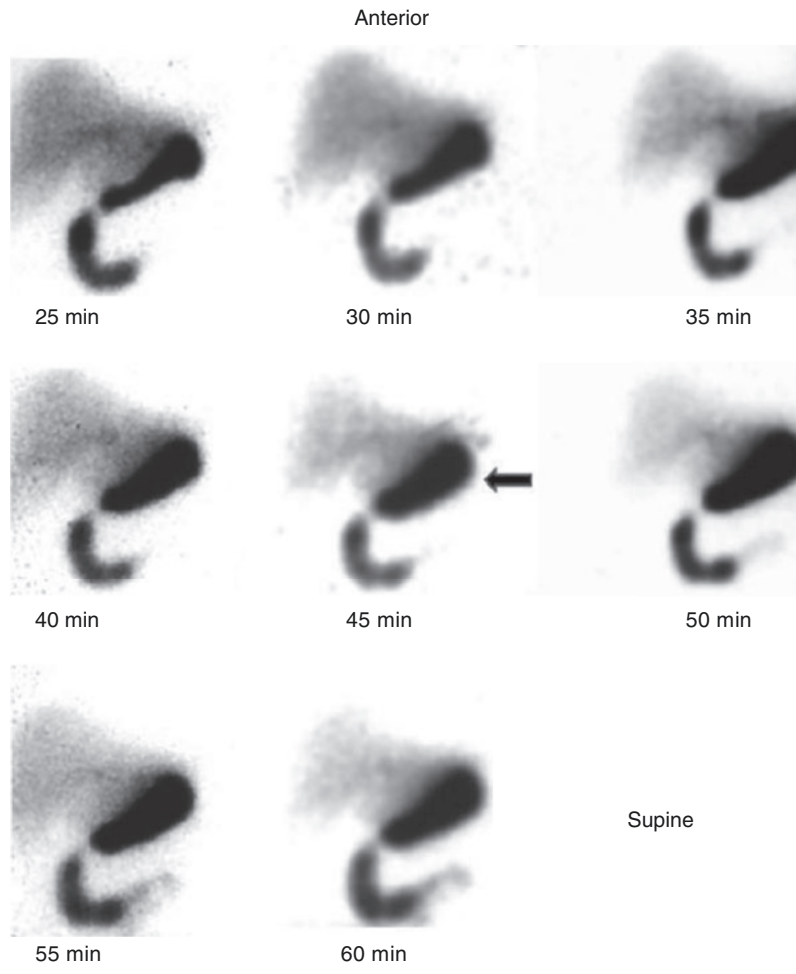

Fig. 10.9 Representative images of a hepatobiliary study of a 32-year-old male patient suspected of having acute cholecystitis. In addition to the nonvisualized gallbladder by 60 min shown in the images presented, significant duodenogastric reflux is seen (*arrow*)

indications for a radionuclide bleeding scan are as follows:

1. Suspected acute ongoing or intermittent lower GIB of unknown localization with nondiagnostic endoscopy.
2. Follow-up of known bleeding to assess treatment effectiveness.

A radionuclide bleeding scan plays only a very small role in the evaluation of upper GIB because of the high accuracy of endoscopy and because of potential interference from radiotracer activity normally excreted by the gastric mucosa. All patients with prior aortic graft surgery and GIB should be considered to have an aortoenteric fistula until proven otherwise.

Two radiopharmaceuticals are available for the study of lower GIB: Tc-99m-labeled RBCs and Tc-99m-sulfur colloid.

1. Using Tc-99m-labeled RBCs is the most commonly used method. The patient's RBCs should be labeled in vitro to get the highest labeling efficiency. Imaging is begun with injection of the radiolabeled RBCs, where dynamic images are taken at a rate of 1 frame/10–60 s. Rapid bleeding can be detected with first-minute flow images taken at a rate of 1 s/frame. The extravasation manifests as focal activity that appears during the blood pool phase, initially intensifies, and moves anterograde and retrograde in a bowel-like trajectory on subsequent images

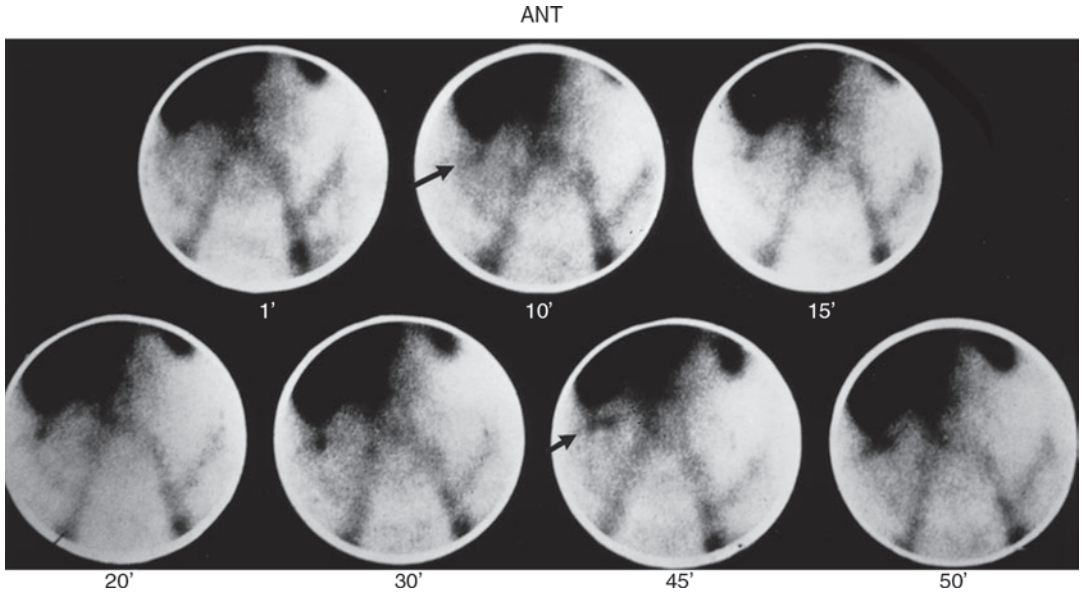

Fig. 10.10 ^{99m}Tc-labeled RBC study for localization of gastrointestinal bleeding showing a focus of extravasated activity in the right hepatic flexure, which progressed later during the study (*arrows*)

(Fig. 10.10). It is extremely important to view the study in a cine mode, which can clarify difficult cases. If transit time is rapid, 1 mg glucagon can be given i.v. to reduce bowel motility. The sensitivity of this cinematic method is more than 90% [53].

To localize the bleeding site, 5 cc or more of extravasation may be needed. The patients can be monitored for up to 24 h; however, the site of extravasation may be easily misinterpreted [54]. A negative radionuclide study is good evidence that angiography will not detect the site of hemorrhage.

2. In the Tc-99m-sulfur colloid method, the study can be performed in approximately 30 min, in cases of active lower GIB (if no time is available for labeling the RBCs) where time is vital for the management of the patient. This tracer is cleared from the circulation with a half-time of 2.5–3.5 min. By 12–15 min, most of the activity is cleared from the vascular system (background), resulting in a high target-to-background ratio. The clearance is delayed in patients with diffuse liver disease. The study is fast and sensitive with quick results, but intermittent bleeding sites may be missed. Small bowel bleeding can be differentiated from colonic bleeding by the appearance of blood filling multiple loops of small bowel.

The technique of Tc-99m-labeled RBCs is preferred. However, for acute or continuous bleeding, a Tc-99m-SC study may be used, and in this case, images are taken for 30 min, which can detect a blood loss of 0.1 mL/min. If this is negative or blood loss is known to be intermittent, a labeled RBC study is used.

10.1.6.6 Meckel's Diverticulum Study

Scintigraphy is performed using Tc-99m-pertechnetate, since it is taken up by the gastric mucosa contained in Meckel's diverticulum (Figs. 10.11 and 10.12). The radiotracer accumulates in and is excreted from the mucus-secreting cells in the ectopic gastric mucosa regardless of the presence of parietal cells.

The patient should be fasting for 4–6 h to reduce gastric secretion passing through the bowel. With Tc-99m-pertechnetate, Meckel's diverticulum appears at the same time as the stomach and the activity increases in intensity with the stomach; it may change in position during the study and may empty its contents

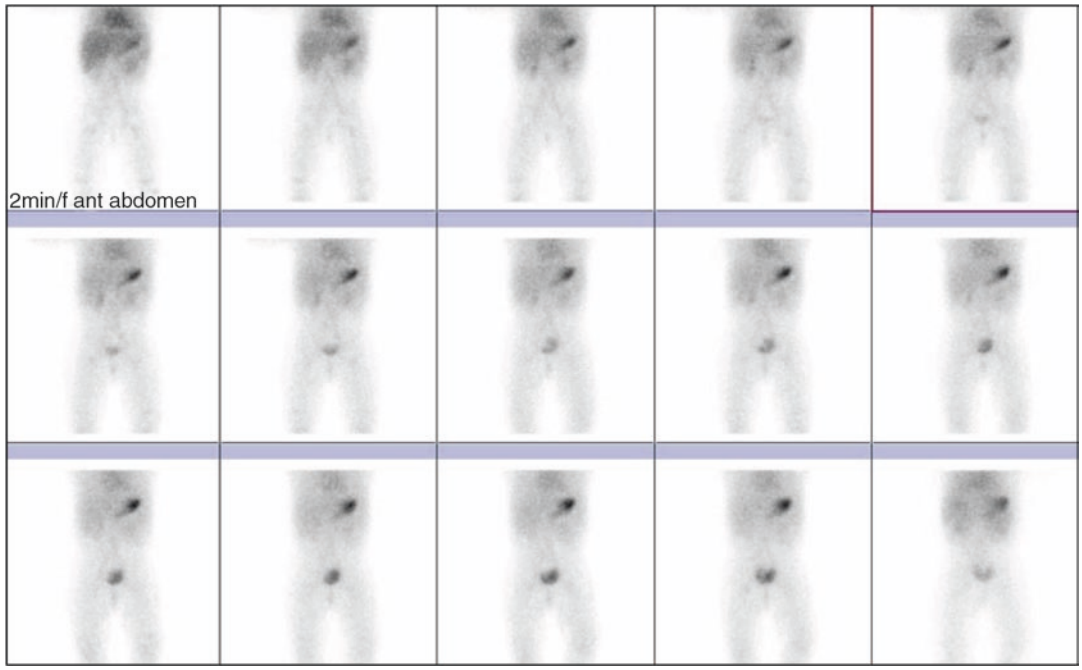

Fig. 10.11 Negative Meckel's diverticulum study

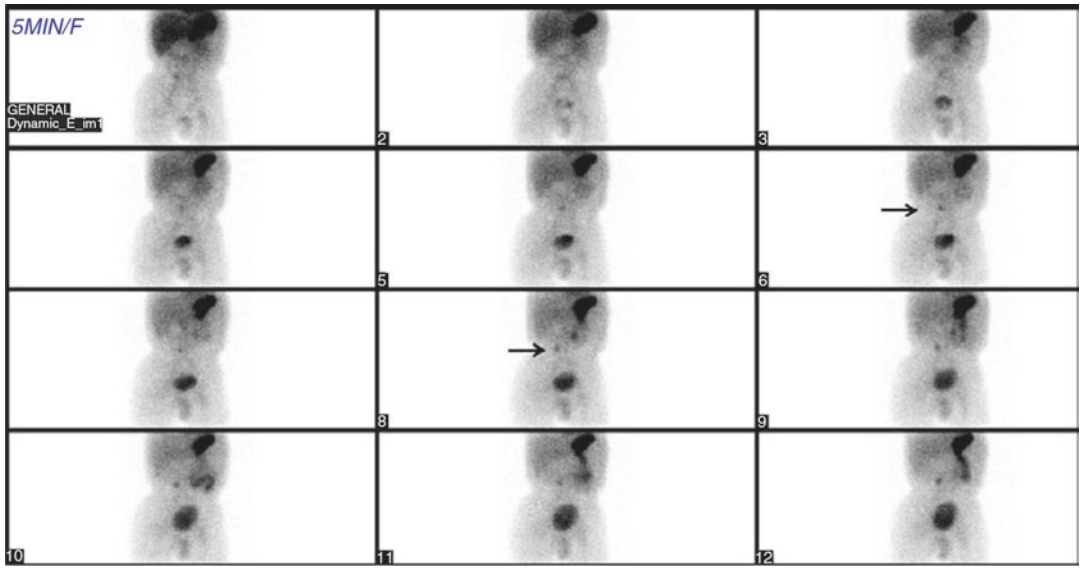

Fig. 10.12 Positive study for Meckel's diverticulum (*arrows*)

into the bowel. Pharmacological intervention improves the sensitivity of the study. Cimetidine enhances gastric uptake and blocks pertechnetate release from the mucosa. Glucagon is given i.v. 10 min after pertechnetate to inhibit peristalsis and delay emptying of gastric contents into the small bowel.

Any blood leaking into the bowel would be apparent, although it would not show the rounded appearance of Meckel's diverticulum. Among the

false-positive cases are renal transplant, renal pelvis, ureter, bladder diverticulum, iliac vessels and uterus, ectopic gastric mucosa in small bowel other than Meckel's diverticulum, infection (as in acute appendicitis), and intussusception. Among the false-negative cases are absence of ectopic gastric mucosa in the diverticulum and diverticulum hidden by bladder or stomach. The sensitivity of Tc-99m-pertechnetate is overall more than 85%, but it drops after adolescence because patients asymptomatic throughout childhood are less likely to have ectopic gastric mucosa. In a recent study on children under 18 years of age, the sensitivity, specificity, PPV, NPV, and accuracy values were 84%, 97%, 90%, 95%, and 94%, respectively [55].

10.1.6.7 Imaging of Inflammatory Bowel Disease

The diagnosis of inflammatory bowel disease (IBD) needs a complex workup. Besides verifying the disease itself, it is fundamental to assess disease extent and activity and to detect associated complications, to help select the most effective treatment and for follow-up. Scintigraphy with radiolabeled leukocytes (Fig. 10.13) is able to provide a complete survey of the whole intestinal tract, both the small and large bowel, and detects septic complications successfully with negligible risk. Radionuclide procedures are useful in establishing or ruling out IBD in patients with intestinal complaints, in assessing disease severity, and in the evaluation of extraintestinal septic complications [56]. Radiolabeled leukocytes studies offer an accepted radionuclide method for imaging inflammation. Because of many advantages of tecnetium-99m (^{99m}Tc) over indium-111 (111In), ^{99m}Tc-HMPAO-leukocyte scintigraphy is preferred for the investigation of IBD. The ^{99m}Tc-HMPAO-leukocyte scintigraphy technique is highly accurate within the first few hours postinjection. It can reliably assess disease activity, but a normal scintigraphy does not exclude mild inflammation [57]. Recently the immunoscintigraphy with ^{99m}Tc-antigranulocyte antibodies has been carried out; however, ^{99m}Tc-HMPAO is the first-choice agent with SPECT/CT preferred (Figs. 10.13 and 10.14). FDG-PET/CT is very helpful in localization of activity . It is an excellent method for the noninvasive quantification of bowel inflammation and in assessing advancement of the disease [58]. For more details, please refer to Chap. 4.

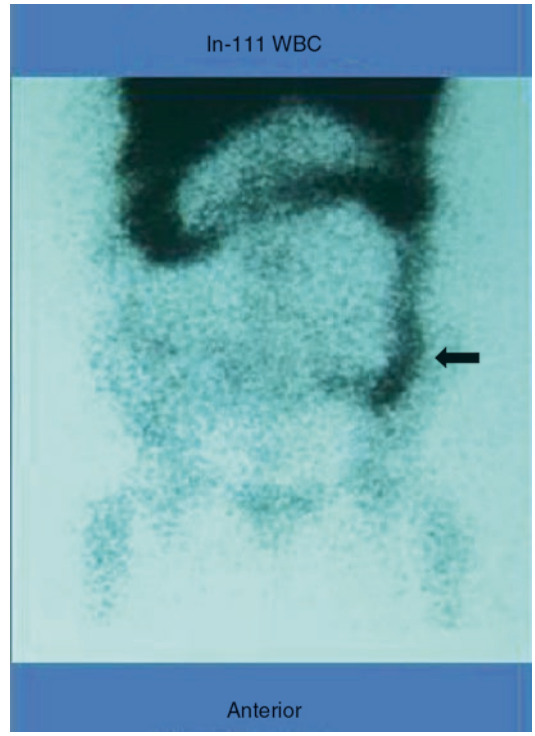

Fig. 10.13 In 111 WBC study in a patient with known inflammatory bowel disease showing significant uptake by the colon (*arrow*) indicating active disease

10.1.6.8 Salivary Gland Imaging

Several modalities can be used for the diagnosis of salivary gland disorders. Standard radiographs are of limited value. Sialography is particularly useful for duct system conditions. Parenchymal diseases like tumors are better shown by CT and US. CT can be combined with sialography, and this combination is currently the most sensitive technique for localizing small tumors [46]. Scintigraphy is needed in some conditions that cannot be evaluated by morphologic modalities particularly functional conditions such as xerostomia.

Salivary gland scintigraphy is carried out after 5–15 mCi (185–550 MBq) of Tc99m-pertechnetate injected in the patient intravenously.

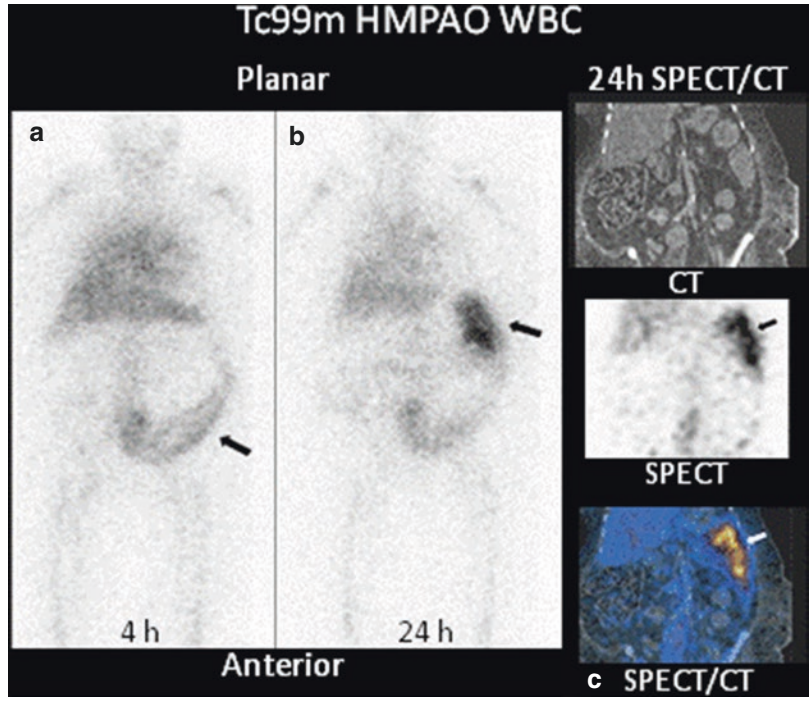

Fig. 10.14 In 111 WBC study of a patient with inflammatory bowel disease. On 4-h In-111 WBC images (**a**), there is mild diffuse labeled WBC accumulation in the descending and sigmoid colon (arrow). On 24-h images (**b**), the accumulation in the upper part of the descending colon and splenic flexure are more intense (arrow). SPECT/CT (**c**) more clearly shows the uptake in the colon's splenic flexure (arrow) since there is a superimposition of the spleen and splenic flexure on planar images

Dynamic images are obtained as 1-min frames for 15–20 min. The patient is asked to drink two glasses of water before the study, and a sialagogue (20-mL lemon juice) is given at 10 min to stimulate salivation. The images are obtained for the anterior face and neck in the sitting position, using a low-energy, high-resolution collimator. Extra images for right and left laterals are obtained for 2 min each to localize the activity. Regions of interest (ROI) are drawn and a graph is plotted to assess the function of the salivary glands.

Findings on a normal scan are a stepwise rising curve of activity with an abrupt drop after the sialagogue and a subsequent rise again (Fig. 10.15). In Sjögren's syndrome there will be decreased accumulation of radiotracer compared with the thyroid gland and delayed clearance (Fig. 10.16). In Warthin's tumor (adenolymphoma), there is an intense increase in the focal area of activity because it mimics thyroid tissue in pertechnetate uptake [59–61].

10.1.6.9 Imaging of Appendicitis

Radioisotope imaging using labeled white blood cells and more recently antigranulocyte antibody technetium (99mTc) fanolesomab (NeutroSpec) has been used for appendicitis imaging patients with equivocal signs and symptoms of appendicitis. Localized uptake of tracer in the RLQ suggests appendiceal inflammation. Tc99m HMPAO labeled leukocyte showed a sensitivity of 90–98% and specificity of 92–96% [62, 63]. Recent reports suggest a possible role of FDG-PET/CT to diagnose appendicitis [64].

10.1.6.10 Scintigraphic Non-imaging Procedures

Carbon-14 Breath Tests

This simple carbon-14 breath test has been utilized increasingly in recent years in gastrointestinal practice. The test is based on detection and quantitation of radioactive carbon dioxide originating in the stomach or small intestines and exhaled through the respiratory system after being absorbed into the blood stream. This is based on the ability of the *H. pylori* urease enzyme to break down an isotope-labeled urea solution ingested by the patient into carbon dioxide and ammonia [65]. The test is useful in

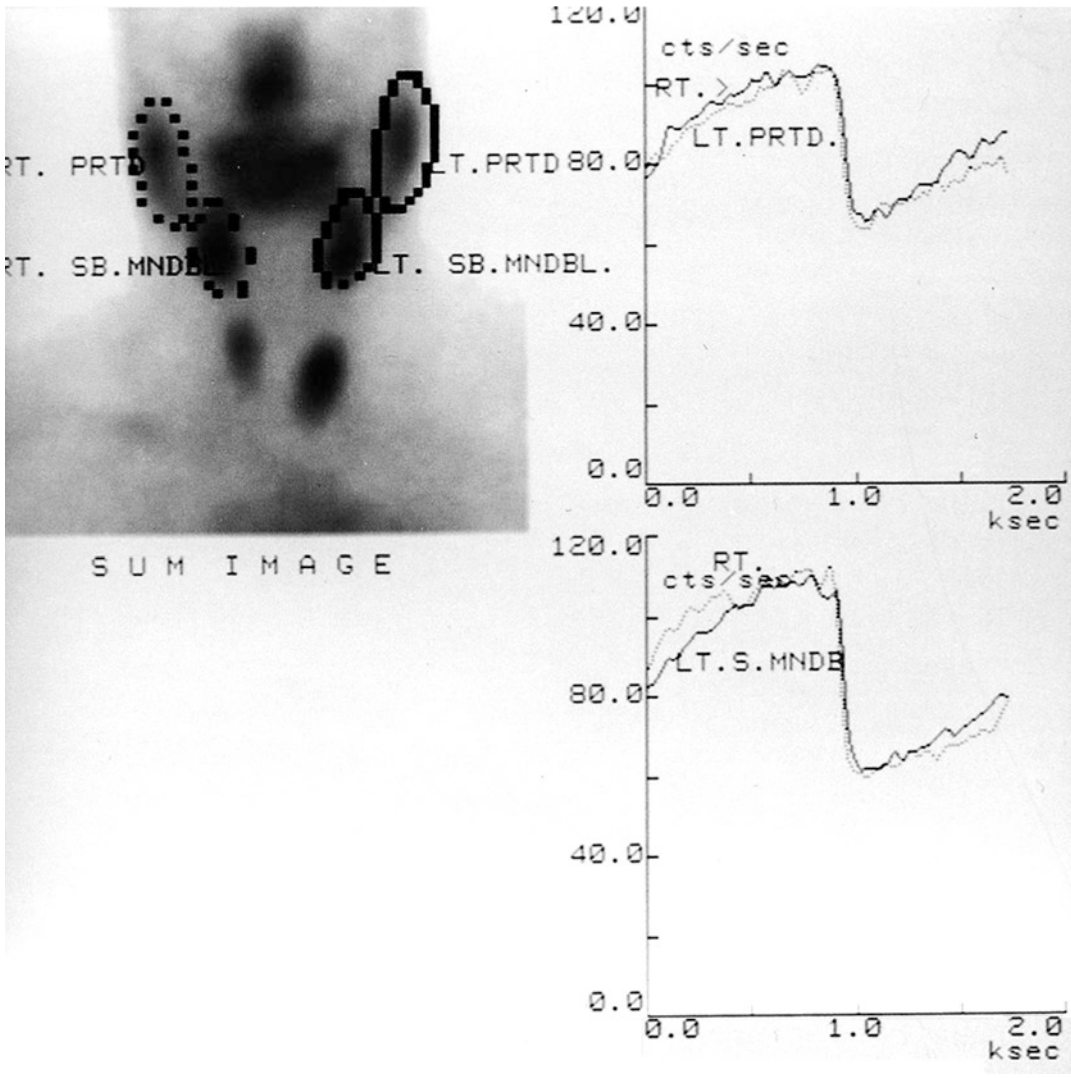

Fig. 10.15 Normal pattern on a salivary radionuclide study. Note the adequate accumulation of the radiotracer with good clearance

the diagnosis of several disease processes, particularly *Helicobacter pylori* infections, lactose intolerance, and malabsorption due to bacterial deconjugation of bile acids.

Helicobacter pylori Infections

Helicobacter pylori has been known for many years and was previously called *Campylobacter pylori* or *Campylobacter pyloridis*. It is a small, curved, gram-negative rod found in the stomach (Fig. 10.17) and duodenum of many individuals. The prevalence correlates best with socioeconomic status. In the USA, the overall probability of infection is 20–30%. Among African-Americans the probability is about 50%, and approximately 60% of immigrants such as Latinos are affected. The infection approaches 90% in third-world countries, where it occurs in 10% of children between the age of 2 and 8 years per year and most teens become infected [65–72].

H. pylori infection is known to be associated with several pathological disorders. The organism causes the most common type of nonerosive gastritis, which characteristically involves the antrum

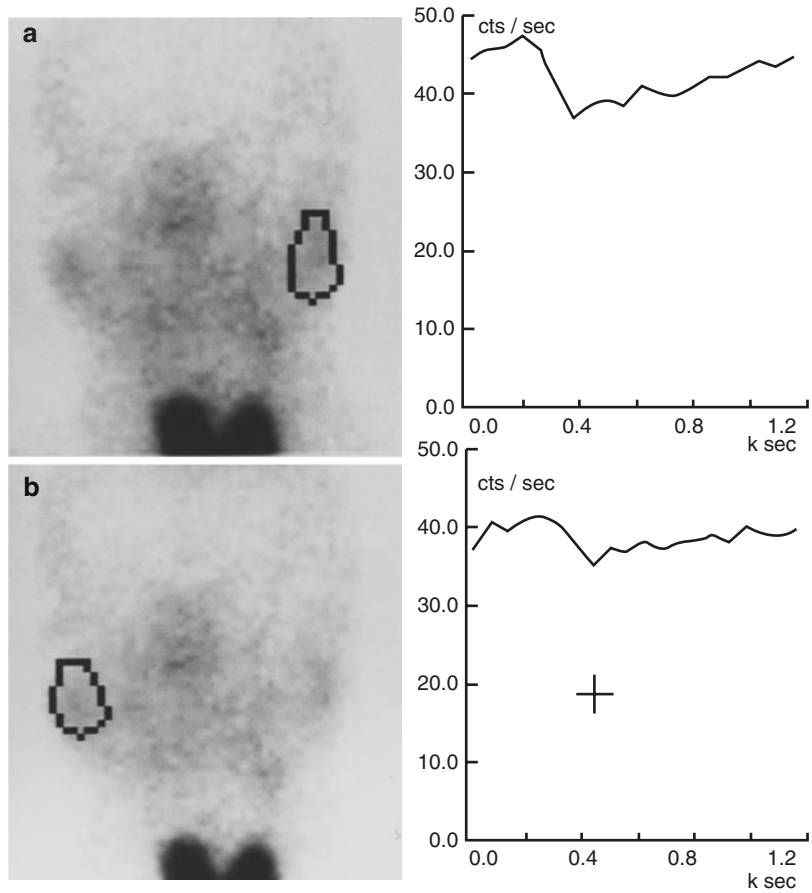

Fig. 10.16 ^{99m}Tc-pertechnetate salivary gland study showing poor uptake and clearance of the radiotracer in a patient with Sjögren's syndrome. Visually (**a**) and on time-activity curves (**b**)

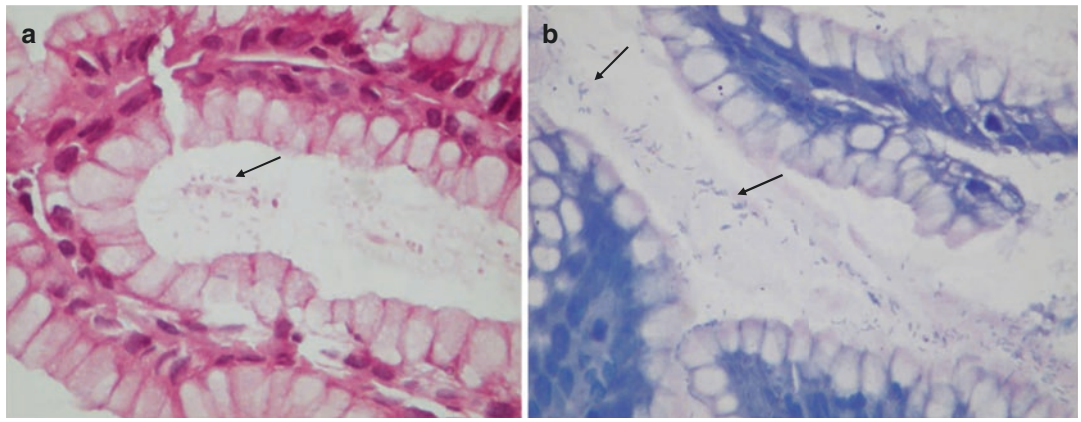

Fig. 10.17 *Helicobacter pylori* as seen on H & E stain (**a**) and Giemsa stain (**b**). (Courtesy of Prof. M. Elmonayeri with thanks)

and body of the stomach. It is found in almost all patients with duodenal ulcers and approximately 80% of those with gastric ulcer. Other conditions such as gastric adenocarcinoma and lymphoma, chronic fatigue syndrome, and acne rosacea are also linked to the organism [63, 64]. Recently it has also been suggested to be involved in the pathogenesis of coronary artery disease.

The diagnosis of *H. pylori* may be obtained by endoscopy specimen, by a blood test identifying anti-*Helicobacter* infection antibody or by a carbon-13 or carbon-14 urea breath test. Endoscopy is needed in many cases to detect ulcers and other gross pathological changes. During endoscopy, biopsy material is obtained and examined microscopically, in addition to culturing for *H. pylori*. However, endoscopy cannot be used just to find whether *Helicobacter* infection is present and is not justified as a follow-up technique to evaluate the response to therapy. Antibody testing, on the other hand, has the shortcoming of not being suitable for patient follow-up since antibodies decline slowly after treatment and may remain elevated long after *Helicobacter* has been killed.

H. pylori is able to fight stomach acid containing a large amount of the enzyme urease. Urease converts urea, present in the saliva and gastric juices, into bicarbonate and ammonia, which are strong bases and act as acid-neutralizing agents around the *H. pylori*, protecting it from the stomach acidity. This action of urea hydrolysis is the basis of carbon-14 and carbon-13 urea breath tests (Fig. 10.18).

The test can be performed using a capsule or a liquid containing a minimal amount (2 μCi) of carbon-14 urea. The patient swallows a drink or capsule and 10–20 min later, samples of breath are taken with the patient blowing into a small bottle of liquid. The amount of radioactive carbon dioxide in blood and expired in breath is detected and quantitated by scintillation counter. In the presence of *H. pylori* infections, the count will be higher than normal. Carbon-14 urea contains a tiny amount of radioactive material, which passes out of the body in a day or so in the urine or breath [73]. The amount of radioactive exposure to the patient from the test is less than the individual normally receives in a half day from nature [67]. It is also equivalent to the radiation dose that an individual absorbs when flying in an airplane for 1 h. Since urea is present in saliva, patients must brush and rinse their teeth before taking the test.

Lactase Deficiency

Acquired lactase deficiency is a common disorder of carbohydrate absorption. The deficiency of intestinal lactase leads to decreased hydrolysis of ingested lactase in the small intestinal cells as occurs normally. Lactase is one of the most common disaccharides in diet and is a main constituent of milk and other dairy products. The intact lactose is not absorbed and increases the osmotic effect of the small intestinal contents, with subsequent outpouring of liquid into the intestinal lumen. This will result in increased intestinal motility with abdominal cramps, distention, and diarrhea when a patient ingests milk [74, 75].

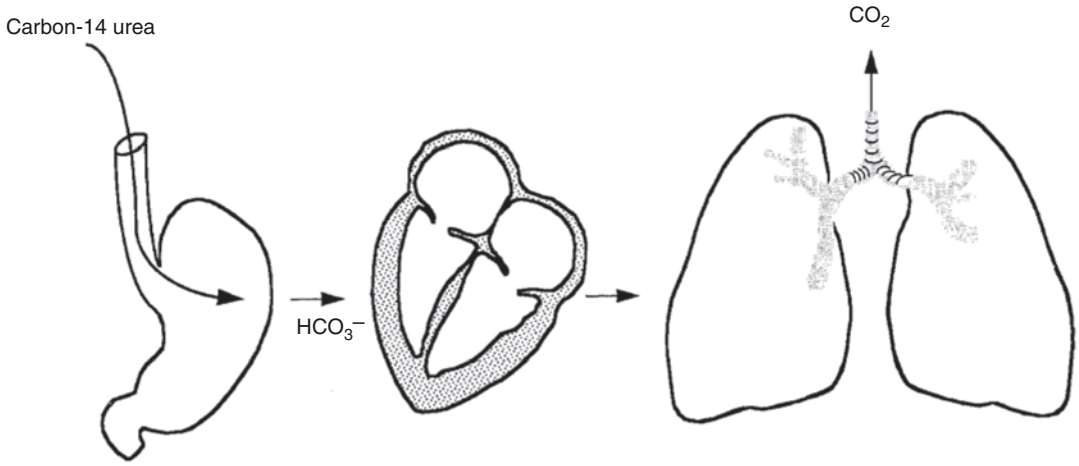

Fig. 10.18 The principle of carbon-14 breath tests

For lactose intolerance, lactose-1-C-14 together with carrier lactose (50 g) dissolved in 400 mL of water is used. In patients with lactose intolerance, lactase deficiency leads to the inability to split lactose into glucose and galactose and subsequently to CO_2. When carbon-14-labeled lactose-1 is administered to patients with lactase deficiency, there will be decreased exhalation of labeled carbon dioxide.

Malabsorption Secondary to Bacterial Overgrowth

Bacterial overgrowth is one of the major reasons for luminal phase malabsorption. Bacterial overgrowth causes deconjugation of bile salts which are absorbed and cycled normally through the enterohepatic circulation but are ineffective in micelle formation. Since micelle formation is essential for the normal absorption of free fatty acids and monoglycerides, malabsorption results. Carbon-14-glycine cholate and more recently the carbon-14-xylose breath test are useful in the diagnosis of malabsorption secondary to bacterial overgrowth [75, 76]. Since carbon-14-glycine cholate is a conjugated bile salt, it is absorbed by the ileum and metabolized in the liver. Only a small portion is attached normally by bacteria and causes deconjugation leading to the formation of carbon dioxide that is exhaled. The deconjugation increases with increased bacterial colonization in the intestines, and consequently the amount of labeled carbon dioxide present in the exhaled breath increases [77]. This test is useful in the diagnosis of blind or stagnant loop syndrome and of ileal absorptive function.

Schilling Test

This procedure uses an oral test dose of radiolabeled cyanocobalamin (usually ^{57}Co-B-12) with or without added Intrinsic factor (IF). The absorption is most frequently measured indirectly by measuring the urinary excretion of the radiolabeled vitamin B-12. The vitamin is flushed out into a 24-h collection of urine sample by a large parenteral dose (1 mg) of nonradioactive vitamin B-12 injected intramuscularly usually 1 h after administration of the oral test dose. The test is done once without IF and then repeated with IF. A convenient method is to use two radioisotopes of cobalt, ^{58}Co-labeled cyanocobalamin with IF and ^{57}Co-cyanocobalamin without IF (often referred to as the Dual-Isotope method). Normal subjects with no abnormality of Vitamin B-12 absorption show urinary excretion of free radioactive vitamin B-12 of 9% or more, with IF-bound to free cobalamin ratio of between 0.8 and 1.2.

10.2 Hepatobilitary system

10.2.1 Anatomical and Physiological Considerations

The liver is the largest organ in the body, weighing between 1200 and 1800 g. The liver lies in the abdominal cavity, where it is split into a large right and a small left lobe by the falciform ligament extending from the anterior abdominal wall. The Couinaud classification divides the liver into eight independent segments numbered 1–8, each of which has its own vascular inflow, outflow, and biliary drainage. The Couinaud segments and their corresponding traditional nomenclature are shown in Fig. 10.19.

Within the lobes and segments are multiple, smaller anatomical units called liver lobules. These lobules are formed of plates of hepatocytes, which are the functional cells of the liver. In addition, the parenchyma of the liver is composed of another type of cells: the reticuloendothelial cells or Kupffer's cells. Almost 90% of the reticuloendothelial cells in the body are found in the liver. The sinusoids are capillaries located between the plates of hepatocytes; they receive a mixture of venous and arterial blood from branches of the portal vein and the hepatic artery, respectively. Blood from the sinusoids drains to central veins that continue to empty into the hepatic vein, which enters the inferior vena cava. Kupffer's cells line the sinusoids and destroy microorganisms.

The liver has digestive, metabolic, hematological, and immunological functions. The hepatocytes synthesize approximately 1 L of bile per day and secrete it into the bile canaliculi, which are small channels between the hepatocytes. The bile canaliculi empty into bile ducts that unite and finally

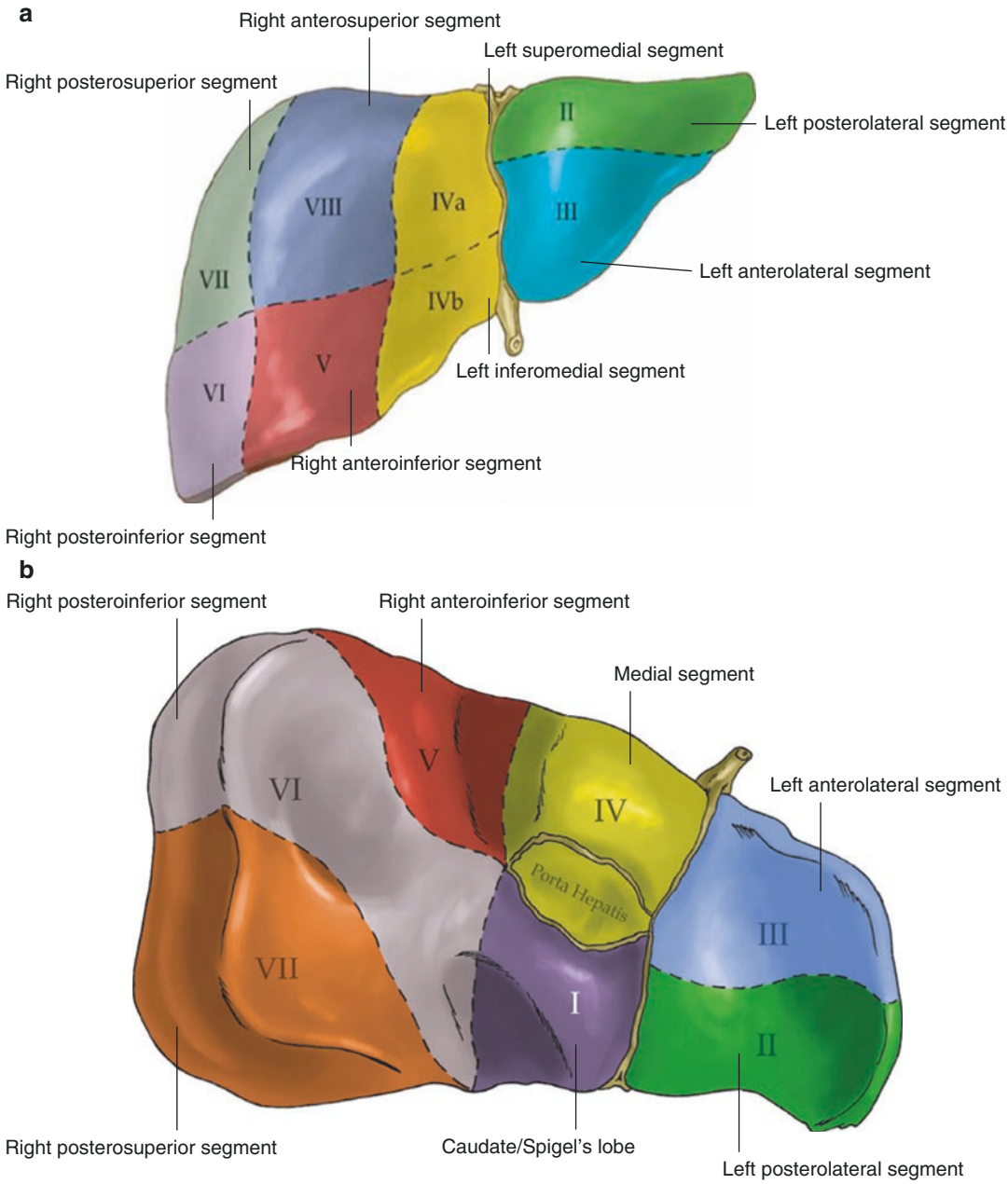

Fig. 10.19 (**a**, **b**) The Couinaud segments of the liver. (**a**) Anterior surface view; (**b**) visceral surface view. *I*, caudate/Spigel's lobe; *II*, left, posterolateral segment; *III*, left anterolateral segment; *IVa*, left superomedial segment; *IVb*, left inferomedial segment; *V*, right anteroinferior segment; *VI*, right posteroinferior segment; *VII*, right posterosuperior segment; *VIII*, right anterosuperior segment

form the right and left hepatic ducts, which join to form the common hepatic duct. Past the point where the cystic duct begins, the hepatic duct is called the common bile duct, which drains into the duodenum through the major duodenal papilla. Bile is necessary for fat digestion and absorption. Unconjugated bilirubin is converted to water-soluble, conjugated bilirubin by hepatocytes and is secreted with bile. The gallbladder stores bile and ejects it when chyme enters the duodenum and stimulates the

secretion of cholecystokinin. The hepatocytes are capable of regeneration. Most regeneration takes place in the left lobe in disease states such as alcoholic damage or chronic hepatitis.

10.2.2 Hepatobiliary Radiopharmaceuticals

Several radiopharmaceuticals are used for scintigraphic assessment of liver and hepatobiliary disorders (Table 10.8). Technetium-99m (Tc-99m)-sulfur colloid (SC) is a radiopharmaceutical for liver/spleen imaging. This compound is cleared by cells of the reticuloendothelial system: approximately 85% by Kupffer's cells in the liver, 10% by the spleen, and 5% by the bone marrow. Tc-99m-phytate is also used for liver/spleen imaging in some countries. However, due to smaller particle size, its splenic uptake is significantly less than that of SC.

Iminodiacetic acid derivatives are used for cholescintigraphy. Tc-99m-disofenin (2,6-diisopropyl iminodiacetic acid (DISIDA)) and Tc-99m-mebrofenin (2,4,6-trim-ethyl, 5-bromoiminodiacetic acid (BrIDA)) are exclusively used for cholescintigraphy by most laboratories in the USA. Various other iminodiacetic acid (IDA) compounds are available in other countries. These compounds, after being injected intravenously, are bound to plasma albumin, transported to the liver, and actively taken up by the hepatocytes via carrier-mediated, non-sodium-dependent, organic anionic pathways similar to those responsible for bilirubin uptake [84]. The IDA compounds are not conjugated. They are excreted into the bile canaliculi by both active and passive transport mechanisms [85]. Compared with Tc99m-disofenin, mebrofenin demonstrates higher hepatic excretion and lower urinary excretion, especially in patients with a high bilirubin level [85]. Depending on the agents used, 2–15% of the injected dose is excreted in urine. The more severe the hepatic dysfunction, the greater the renal excretion [86, 87].

Tc-99m-aglactosyl-neoglycoalbumin (Tc-99m-NGA) and Tc-99m-galactosyl human serum albumin (Tc-99m-GSA) are liver imaging agents that bind to the hepatocyte-specific asialoglycoprotein membrane receptors (ASGCP receptor) [78, 79]. These agents have been used primarily to evaluate the functional liver mass/reserve in various clinical settings.

10.2.3 Evaluation of Liver Diseases

10.2.3.1 Functional Hepatic Mass/Reserve

Assessment of hepatic functional reserve is important prior to major hepatic resection for predict-

Table 10.8 Radiopharmaceuticals for hepatobiliary scintigraphy (cholescintigraphy)[a]

Radiopharmaceutical	Uptake mechanism	Use
Tc-99m sulfur colloid	Kupffer cell	Focal nodular hyperplasia, splenosis, liver function
Tc-99m red blood cells	Blood pool distribution	Hemangioma, splenosis
Tc-99m disofenin	Extracted and excreted by the liver similar to bilirubin	Gall bladder and hepatobiliary disorders
Tc-99m MAA	Blood flow, capillary occlusion	Hepatic arterial perfusion
Tc-99m mebrofenin	Extracted and excreted by the liver similar to bilirubin	Gall bladder and hepatobiliary disorders
F-18 FDG	Glucose metabolism	Tumor/infection imaging
Gallium-67 citrate	Iron binding	Tumor/infection imaging
Tc-99m-aglactosyl-neoglycoalbumin (Tc-99m-NGA) and Tc-99m-galactosyl human serum albumin (Tc-99m-GSA)	Binding to the hepatocyte-specific asialoglycoprotein membrane receptors	Assessment of functional liver mass/reserve

[a] [78–83]

ing the outcome of surgery because postoperative liver failure can significantly affect the clinical course. This may require imaging of both the anatomical structure of the liver and the regional functional reserve. Hepatobiliary scintigraphy with technetium-99m (^{99m}Tc) iminodiacetic acid or ^{99m}Tc galactosyl human serum albumin (GSA) has been used to assess regional hepatic function. Galactosyl human serum albumin (GSA) is a ligand specific to the asialoglycoprotein receptor present exclusively on the plasma membrane of hepatocytes. GSA is bound only by this receptor and then providing valuable information about receptor population density as well as functioning hepatocyte mas [79, 83]. Tc-99m GSA does not compete with bilirubin, which is an additional advantage in the evaluation of hepatic reserve in patients with hyperbilirubinemia [88].

10.2.3.2 Primary Hepatic Neoplasms and Tumor-Like Conditions

Hepatocellular Carcinoma

While hepatocellular carcinoma (HCC) usually displays marked arterial vascularity on dynamic perfusion imaging, its appearance on static colloid imaging (focally decreased activity) is nonspecific. Sulfur colloid imaging can be used to differentiate regenerating nodules from HCC in a cirrhotic liver. The presence of colloid uptake typically represents regenerating nodules, while decreased uptake is nonspecific but may include HCC [89].

Depending on the degree of differentiation, approximately 40–50% of HCCs concentrate hepatobiliary tracers (Fig. 10.20), i.e., Tc-99m-IDA or Tc-99m-PMT. The degree of uptake seems to correlate with tumor differentiation, as well as with survival [90, 91]. Tc-99m-IDA uptake was seen in 70% of well-differentiated tumors, in 30% of moderately differentiated tumors, and in no poorly differentiated tumors [90]. In another series of 162 patients, the median survival of 82 patients with increased tumor uptake on delayed Tc-99m-PMT imaging was 1013 days, compared with 398.5 days in 80 patients with no tumor uptake [91].

Uptake of hepatobiliary tracers on delayed imaging can be present in other liver lesions that contain hepatocytes, such as focal nodular hyperplasia (FNH) [92]. Kotzerke et al. claimed that the distinction between FNH and HCC is possible with 3-phase imaging (perfusion, 5–10 min, and 2–3 h) [93]. In their series, most FNH exhibited normal or increased uptake at 5–10 min, whereas most HCC displayed decreased or no uptake during this phase.

Gallium-67 and thallium-201 were used in the past for evaluation of HCC in various clinical settings. However, the utility of these tracers in HCC appears to have been replaced largely by positron-emitting tracers recently.

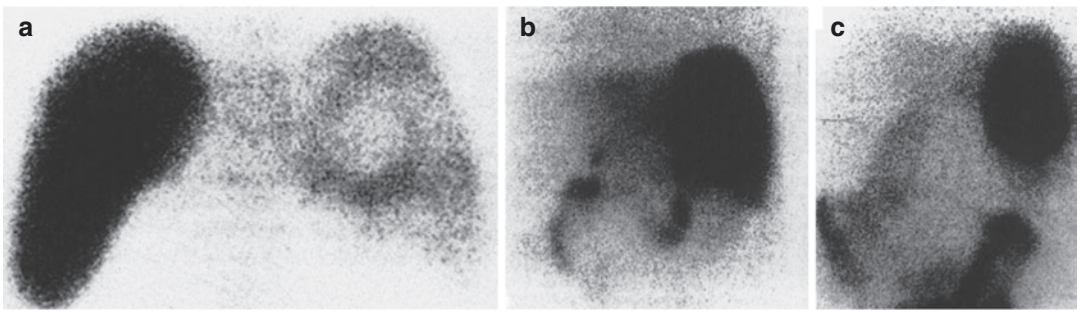

Fig. 10.20 (**a**) Hepatic scintigraphy with Tc-99m-SC in a patient with hepatoma complicating liver cirrhosis. A defect is observed in the posterior view. (**b**) Hepatic scintigraphy with Tc-99m-DISIDA 15 min after tracer administration (posterior view). Marked tracer uptake fills the cold area previously observed, as well as the rest of the liver parenchyma. (**c**) Hepatic scintigraphy with Tc-99m-DISIDA 3 h after tracer administration (posterior view). Tracer is clearly retained in the HCC area while it has been excreted from the nontumoral liver. (Reprinted from Calvet et al. [90] with permission)

10.2.3.3 Hepatic Hemangioma

Hemangioma is the most common benign tumor of the liver. Cavernous hemangioma occurs at all ages but most commonly in adults. Most hemangiomas are of the cavernous type, constituted by dilated nonanastomotic vascular spaces lined by flat endothelial cells and supported by fibrous tissue. Thrombi in different stages of organization are often encountered. Long-standing lesions can show extensive hyalinization or calcification [94–96].

The classic finding of hepatic cavernous hemangiomas (HH) on Tc-99m-RBC imaging was described as lack of increased activity on early flow images and a gradual increase in activity on blood pool images over time [97] while HCCs show increased flow as well as increased activity on delayed images; however, other studies found no cases in which HCC demonstrated increased activity on either planar or SPECT-delayed images [98]. In addition, perfusion in small and/or deeply situated lesions is difficult due to the limited resolution of dynamic imaging. Moreover, it quickly became obvious that the sensitivity of planar Tc-99m-RBC imaging is unacceptably low, ranging from 30 to 53% [98–104]. The sensitivity of SPECT RBC imaging is but still heavily dependent on the lesion size. Reports published in the 1990s showed overall sensitivity of 70–80% using single-head SPECT [101–103, 105]. Using triple-head cameras [99, 104], the sensitivity was 17–20% for the detection of lesions smaller than 1 cm, 65–80% for lesions between 1 and 2 cm, and virtually 100% for lesions equal to or larger than 1.4 cm (Fig. 10.21). It is remarkable that the specificity and positive-predictive value of both planar and SPECT RBC (Fig. 10.22) imaging is essentially 100% [98–104]. For all of these reasons, neither flow nor delayed planar imaging needs to be a

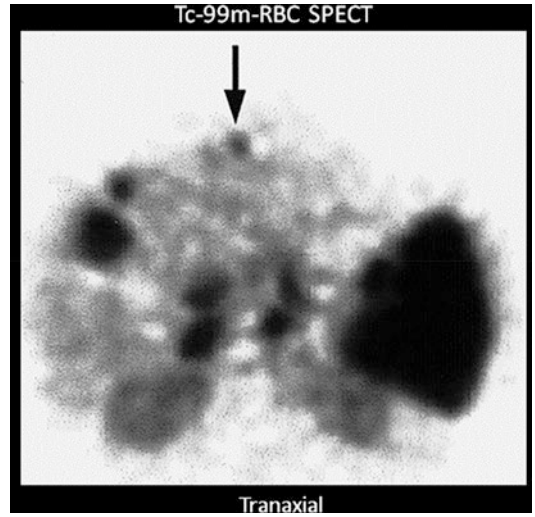

Fig. 10.21 Selected image of Tc-99m-RBC SPECT images of the liver reveal multiple hemangiomas. The smallest one (*arrow*) was 0.7 cm

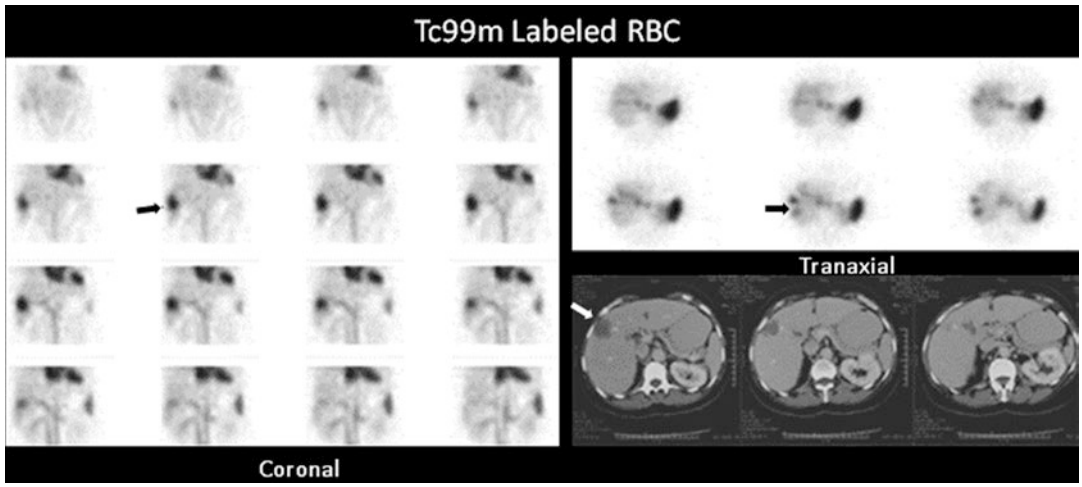

Fig. 10.22 Representative images of a tomographic radionuclide hemangioma study showing a solitary hemangioma (*arrow*) corresponding to the finding on CT but clarifying its nature with high specificity

routine part of the Tc-99m RBC study for evaluation of HH.

False-negative results were reported in cases of HH with extensive thrombosis and/or fibrosis [97]. Several false-positive cases related to various malignancies, including HCC as mentioned above, angiosarcomas, metastases, and hepatic lymphoma, have been reported in the literature [105–107]. However, the occurrence of such false-positive results seems extremely rare in view of the 100% specificity in virtually all studies other than case reports.

When dedicated SPECT imaging is performed, a lesion situated adjacent to large intrahepatic vessels, inferior vena cava, or right kidney needs to be cautiously evaluated to avoid either false-negative or false-positive results [108]. A SPECT/CT hybrid system is becoming more widely available, and fusion imaging lowers the false results [109, 110].

Tc-99m RBC SPECT imaging was reported to be more useful than MRI for evaluation of HH in 1990 because of the lower cost and higher specificity [111]. Despite its near-perfect specificity and positive-predictive value, Tc-99m RBC imaging does not appear to be fully utilized, which may be in part due to improved specificity of other anatomical imaging modalities [112, 113]. Given that, a new prospective head-to-head comparison of SPECT/CT with MRI or ultrasound for evaluation of HH may be needed.

10.2.3.4 Focal Nodular Hyperplasia

Focal nodular hyperplasia contains variable quantities of normal hepatic cellular elements, including Kupffer's cells, hepatocytes, and bile ducts arranged in a characteristic pattern. The characteristic triad suggesting FNH has been described as arterial blood flow (Fig. 10.23), normal colloid uptake, and accumulation of Tc-99m-IDA tracer [115].

Thirty to seventy percent of FNHs have either normal or increased Tc-99m-colloid uptake (Fig. 10.23a) [97, 116], reflecting the variable quantity of Kupffer's cells. Decreased Tc-99m-colloid uptake may be seen in approximately one-third of cases (Fig. 10.23b) [116]. Because of the presence of hepatocytes in FNH, Tc-99m-IDA scintigraphy has also been evaluated for the diagnosis of FNH. Of 25 FNHs in a study, 19 (76%) showed hyperperfusion during the flow phase and 23 (92%) appeared as focal regions of increased uptake during the clearance phase of hepatobiliary imaging. Normal sulfur colloid uptake was seen in 16 (64%) [92]. The detectability of FNH by Tc-99m-IDA scintigraphy was 92%, greater than that of CT (84%) or MRI (84%).

10.2.3.5 Hepatocellular Adenoma

Hepatocellular adenomas typically appear as photopenic defects on Tc-99m-colloid scintigraphy. In the past, this was attributed to the absence of Kupffer's cells [117]. However, a pathological study demonstrated that all hepatic adenomas studied contained Kupffer's cells [118]. Yet most of these lesions (77%) did not demonstrate Tc-99m-colloid uptake for unknown reasons. The authors found no significant histological difference between those lesions that accumulate colloids and those that do not. They also suggested that adenoma should be added to the differential diagnosis of a hepatic lesion with Tc-99m-colloid uptake because of the presence of uptake in 23% of their cases.

10.2.4 Biliary Tract Diseases

Bile flowing through the common hepatic duct may flow either into the gallbladder or through the common bile duct (CBD) into the duodenum. The quantity of bile flowing in either direction is determined to a major degree by the pressure developed by the sphincter of Oddi. In normal individuals, bile flows into the gallbladder when the sphincter of Oddi is contracted. Foods containing lipids and amino acids enter the duodenum and cause release of endogenous cholecystokinin (CCK) from the duodenum to the upper jejunum, which in turn contracts the gallbladder, dilates the sphincter of Oddi, and increases bile secretion from the hepatocytes. All of these enhance the flow of bile into the duodenum.

On a typical normal cholescintigram performed with Tc-99m-IDA agents, the CBD and gallbladder are visualized 10–20 min following

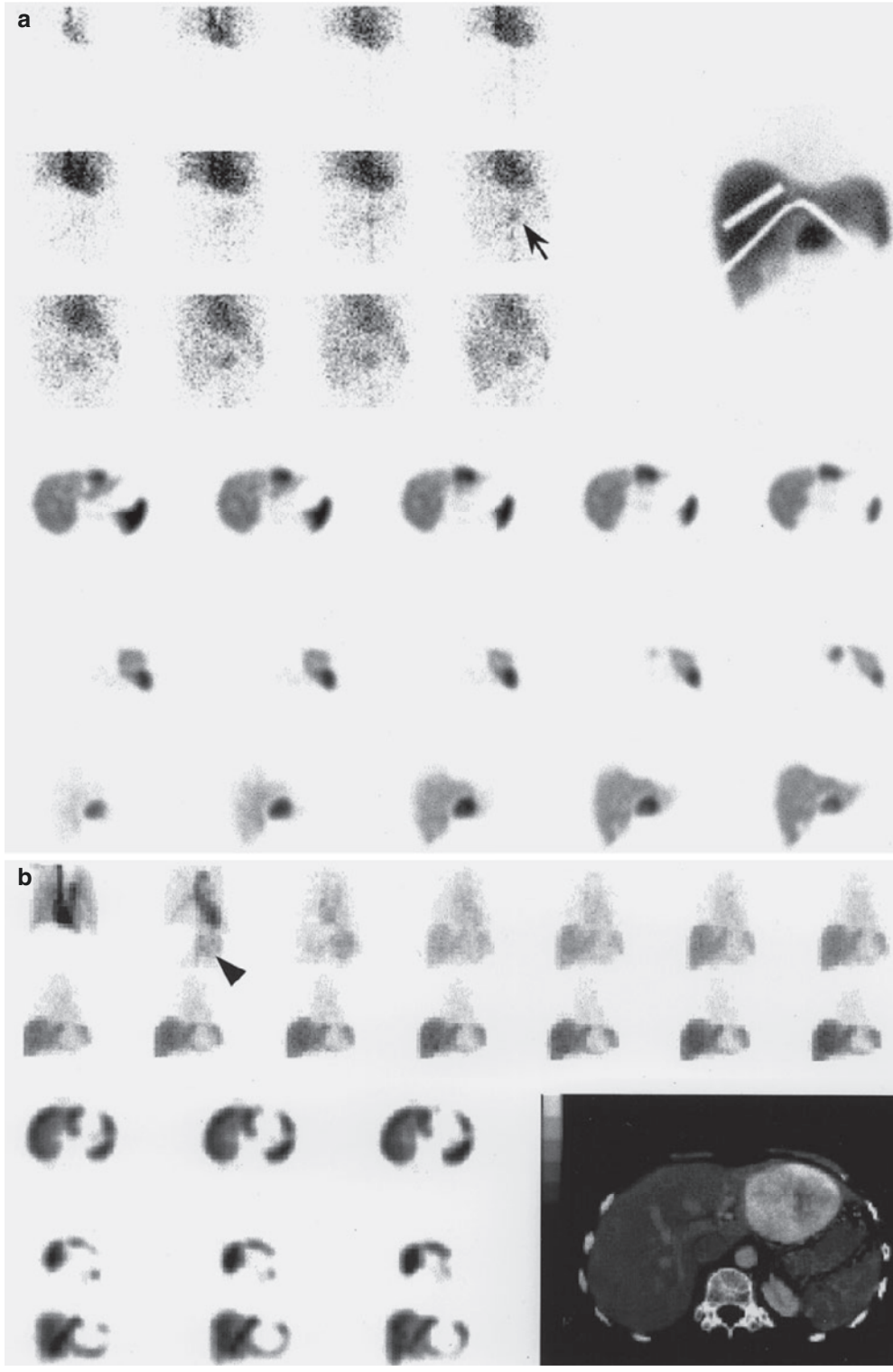

Fig. 10.23 (**a**, **b**) Tc-99m sulfur colloid studies in two cases of focal nodular hyperplasia. While both case **a** and case **b** show increased early arterial flow (*arrow, arrowhead*), colloid uptake is increased in case **a** and decreased in case **b** on delayed views. (Reprinted from Kim et al. [114] with permission)

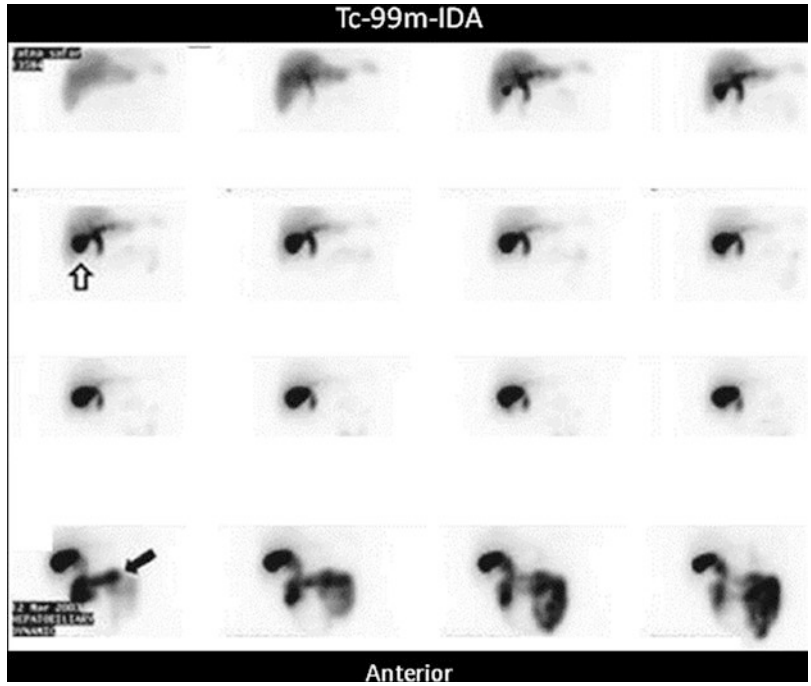

Fig. 10.24 Normal radionuclide hepatobiliary study with prompt visualization of gall bladder (*open arrow*) and intestinal activity (*solid arrow*)

the intravenous administration of Tc-99m-IDA (Fig. 10.24). Visualization of the small bowel varies depending on the sphincter tone and the degree of gallbladder filling.

10.2.4.1 Acute Cholecystitis

Although it is generally known that acute cholecystitis in 90–95% of cases begins with obstruction of the neck of the gallbladder or the cystic duct by a gallstone, some authors feel that obstruction does not necessarily lead to acute cholecystitis [119]. Nevertheless, obstruction is present in almost all cases of acute cholecystitis. There are other important factors in the pathogenesis of acute cholecystitis, including chemical factors such as prostaglandins and bacterial growth . Injury to the gallbladder mucosa by a mechanical or chemical factor stimulates the epithelial cells to secrete fluid. Active fluid secretion in the obstructed gallbladder lumen increases the intraluminal pressure, which may cause impairment of circulation and ischemia of the gallbladder mucosa (Fig. 10.25) and wall. Distention of the gallbladder further enhances formation of

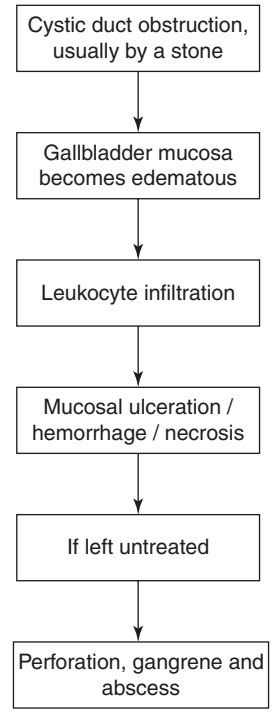

Fig. 10.25 Pathophysiologic features of acute cholecystitis

prostaglandin, establishing a vicious cycle [120]. Active fluid secretion in the gallbladder wall is markedly reduced by morphine. The acceleration of the process can be reduced by morphine [121].

Approximately 60–70% of patients report prior attacks that resolved spontaneously. The factors regulating the intraluminal pressure may determine the course of an attack of acute cholecystitis. Of the 75% of patients with acute cholecystitis who experience remission of symptoms, approximately one quarter will experience a recurrence of cholecystitis within 1 year, and 60% will have at least one recurrent attack within 6 years [122]. Therefore, the histological pattern of acute cholecystitis is superimposed upon chronic inflammatory changes in at least 90% of cholecystectomy specimens [123].

Acalculous form of acute cholecystitis is less common (less than 10%) of patients with acute cholecystitis [124]. Despite the absence of gallstones, the cystic duct is frequently obstructed by viscous bile, sludge, cellular debris or edema associated with dehydration [125]. Precipitating factors include severe trauma or burns, the postpartum period following prolonged labor, a major operation, prolonged parenteral hyperalimentation, vasculitis, obstructing tumor of the gallbladder, and parasitic infestation of the gallbladder. It also may be seen with a variety of other systemic diseases (sarcoidosis, cardiovascular disease, tuberculosis, syphilis, actinomycosis, etc.) [122]. Apart from the absence of stones, the pathology of acalculous and calculous cholecystitis is essentially identical [126].

10.2.4.2 Imaging for Acute Chelecyctitis

Acute cholecystitis is the most common indication for cholescintigraphy, which is considered the procedure of choice for its diagnosis [127]. Generally, nonvisualization of the gallbladder up to 4 h after radiotracer administration or within 30 min after the administration of morphine sulfate is interpreted as consistent with cystic duct obstruction, provided that there is normal hepatic uptake and excretion. Gallbladder visualization anytime during imaging virtually excludes the presence of acute cholecystitis. The study can be obtained as planar, SPECT, or SPECT/CT.

Meta-analysis of 2466 patients showed a sensitivity of 97% and specificity of 90% [127]. Conventional imaging protocols frequently require delayed imaging for up to 4-h postinjection or even up to 24 h in patients with severe intercurrent disease to achieve a sufficiently high level of accuracy. Delayed imaging is logistically inconvenient. It can be potentially disadvantageous to the patient, and it may not be feasible in some clinical settings. Efforts to increase the specificity of the test and/or to shorten the total imaging time were made using pharmacological interventions, which include morphine augmentation and CCK pretreatment [128].

Despite the superiority of cholescintigraphy over ultrasonography (US) for evaluation of acute cholecystitis that has been known for decades and confirmed repeatedly as the best single noninvasive test for the diagnosis of acute checystitis [128]. US is still often the first diagnostic test being ordered in many institutions. A most recent (and seemingly largest) meta-analysis report, including 57 studies and 5859 patients, published in 2012 confirmed that cholescintigraphy has the highest diagnostic accuracy of all imaging modalities in the detection of acute cholecystitis [129].

10.2.4.3 Causes of False-Positive Results of Cholescitigraphy for Acute Cholesystitis

Several conditions are known to be potential causes for false-positive results on cholescitigraphy resulting in false non visualization of gall bladder (Table 10.9). Insufficient fasting will result in gallbladder contraction induced by circulating endogenous CCK, thereby inhibiting

Table 10.9 False-positive cholescintigraphy for acute cholecytitis

1. Non-fasting (less than 3–4 h)
2. Prolonged fasting (more than 24 h)
3. Total parentenral nutrition
4. Severe concurrent disease
(a) Severe postoperative complications
(b) Massive trauma
(c) Sepsis
(d) Acute respiratory syndrome
5. Hepatocellular disease
6. Chronic cholecystitis

bile flow into the gallbladder. Delayed imaging and certain interventions are used to minimize false-positive results.

Secondary Scintigraphic Signs of Acute Cholecystitis

Rim Sign

This pattern represents increased IDA activity in the liver parenchyma around the gallbladder fossa "rim sign" (Fig. 10.26). The presence of this sign is frequently associated with acute cholecystitis, which is often complicated, i.e., gangrenous gallbladder [128]. This pericholecystic activity appears to be caused by increased blood flow to [130] and/or delayed bile excretion from inflamed liver parenchyma adjacent to an inflamed gallbladder [131].

At times, a rim sign with marked tracer retention may mimic the gallbladder appearance

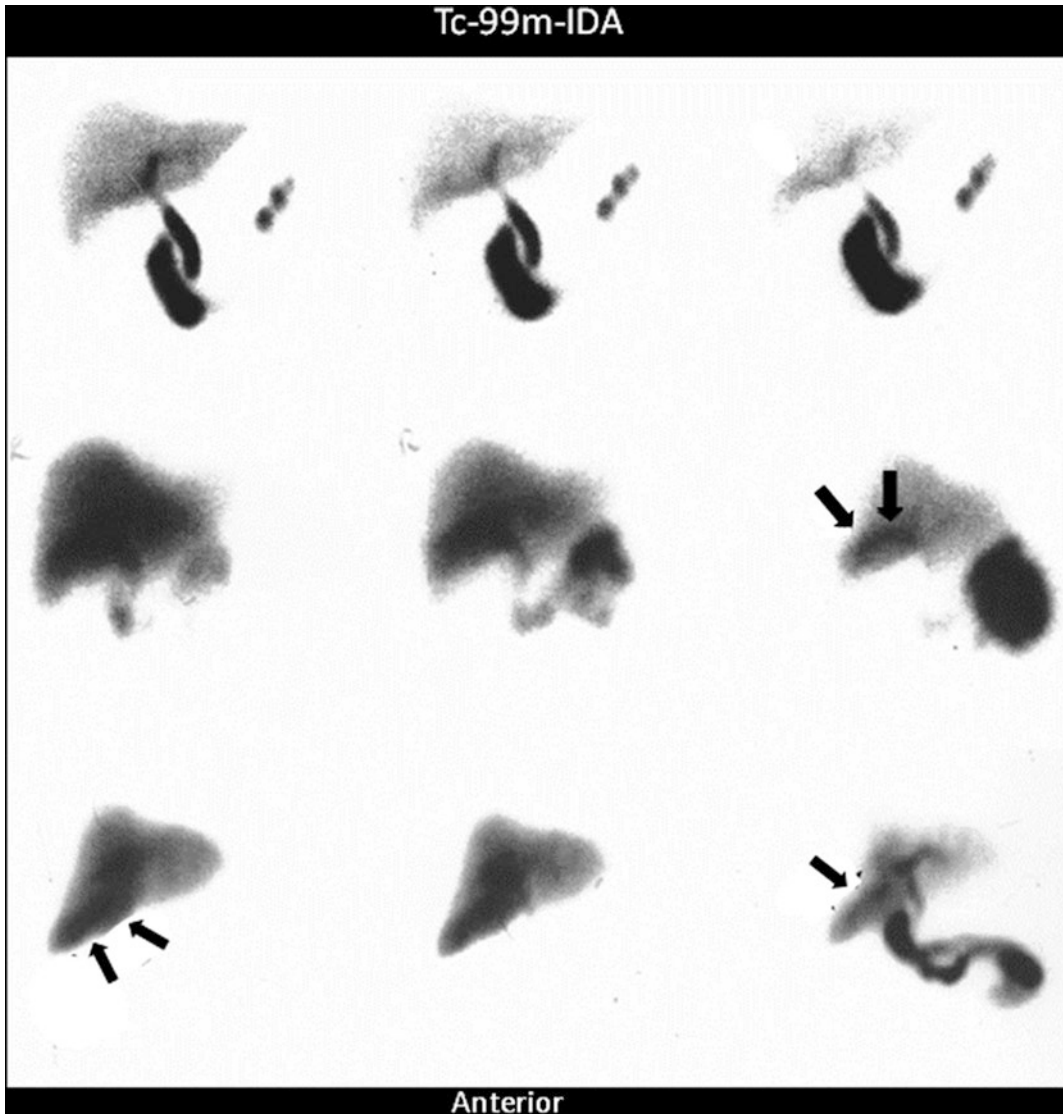

Fig. 10.26 A spectrum of rim signs. A mild rim sign is seen in the Tc-99m-IDA study of patient 1 (*arrow*). The rim sign in patient 2 is quite prominent and clearly seen as a rim. The rim sign in patient 3 is more diffuse and may be confused with the gallbladder. However, this activity is present on the early image (*large arrows*) even before the tracer activity appears in the bile ducts. (From Kim [108] with permission)

(patient 3 in Fig. 10.26), in which case the presence of such activity on the early images before the appearance of bile duct activity can help to exclude the possibility of gallbladder filling. The rim sign, though suggestive of acute cholecystitis, is not sufficiently specific to obviate interventions such as delayed imaging or morphine augmentation.

10.2.4.4 Chronic Acalculous Biliary Syndromes

This group includes chronic acalculous cholecystitis, cystic duct syndrome, and gall bladder dyskinesis. Approximately 98% of patients with symptomatic gallbladder disease have gallstones. Occasionally, patients have signs and symptoms of gallbladder disease, but no stone can be demonstrated by repeated ultrasound or oral cholecystography [132]. Chronic biliary-type pain in patients with no stones may be due to chronic acalculous biliary disorders, including chronic acalculous cholecystitis, cystic duct syndrome, a functional disorder such as gallbladder dyskinesia, and sphincter of Oddi dysfunction. Nonbiliary disease such as the irritable bowel syndrome may cause the same symptoms. Sincalide has been used for the evaluation of gallbladder ejection fraction (GBEF) or sphincter of Oddi response in this patient group to determine who might benefit from cholecystectomy, sphincterotomy, or smooth muscle relaxants.

The pathological findings of chronic acalculous cholecystitis are nearly identical to those of chronic calculous cholecystitis, except for the absence of stones [133]. Intermittent acalculous cystic duct obstruction and chronic ischemia with active inflammatory changes have both been postulated as possible pathogenic mechanisms.

The cystic duct syndrome results from a partial acalculous obstruction or narrowing of the cystic duct [124], which may be due to fibrosis, kinking, or adhesion.

Gallbladder dyskinesia histologically show no abnormal findings. Abnormal and/or inhomogeneous CCK receptors within the gallbladder, which cause a paradoxical or inhomogeneous response to cholecystokinetic agents, were suggested as a possible mechanism [134]. In this condition, right upper quadrant pain occurs following meals as a result of increased intraluminal gallbladder pressure. Other possible mechanisms of impaired gallbladder motility include a primary smooth muscle disorder and altered release of endogenous CCK [135].

In cholesterosis, the mucosa of the gallbladder is studded with minute yellow lipid flecks, producing the strawberry appearance [125]. In some patients suspected of having chronic acalculous biliary disease, cholesterosis has occasionally been the only histological finding, without evidence of other diseases [136]. Although cholesterosis is not often of clinical significance [125], cholecystectomy is indicated when the condition is symptomatic.

Biliary Sphincter (Sphincter of Oddi) Stenosis/Obstruction

Biliary Sphincter disorder occurs mostly in patients after cholecystectomy. It is much more common in female patients can be classified into two broad categories: stenosis (by stone or a fixed structural narrowing) and dyskinesia (functional disorder: a primary disorder of tonic/phasic motor activity) [137].

Measurement of the sphincter of Oddi pressure using sphincter manometry is considered the gold standard for the diagnosis. An elevated basal pressure (>40 mmHg) is considered the only consistent manometric criterion which is correlated with patients' symptoms and also with relief of symptoms with therapy [138].

The treatment of choice for patients with sphincter of Oddi stenosis is endoscopic sphincterotomy.

Hepatobiliary imaging with or without pharmacological intervention has also been shown to be useful in patients with SOD, and investigations have focused primarily on patients after cholecystectomy. A number of parameters have been derived from the time-activity curves of the liver parenchyma, hilum, CBD, entire hepatobiliary tract (liver and bile ducts), and bowel. These include the time of peak activity (T_{max}), excretion half-time ($T1/2$), percentage of excretion at a certain time (i.e., 45, 60 min), excretion rate, and mean transit time. Visual parameters such as

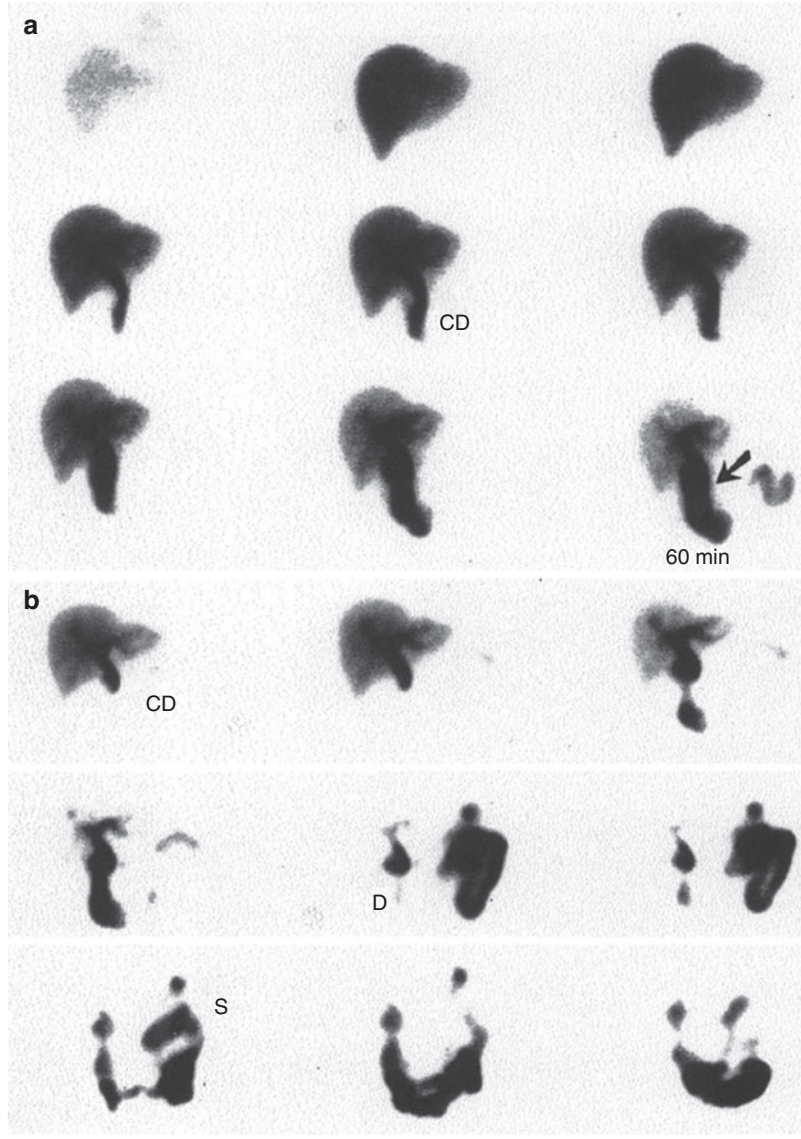

Fig. 10.27 (**a**, **b**) SOD: stenosis. This 50-year-old woman was seen at 3 years' postcholecystectomy with chronic recurrent pain. ERCP showed no mechanical obstruction, but the basal sphincter of Oddi pressure was elevated (45 mmHg). (**a**) Preoperative cholescintigraphy shows delayed hepatobiliary clearance with retention of activity in the common bile duct (*CD*) at 60 min (*arrow*). Increasing activity within the duodenum (*D*) is noted. A second preoperative study (not shown here) with constant CCK infusion (40 ng/kg/60 min) was not significantly different (i.e., there was a fixed papillary stenosis). (**b**) Postsphincterotomy study in the same patient shows significant improvement with rapid hepatobiliary and common duct clearance compared with the preoperative study. *S*, stomach. (Reprinted from Ziessman [139] with permission)

the time of first appearance of the intrahepatic biliary tree, and the bowel, CBD emptying, and CBD-to-liver ratio (comparison of CBD activity at 60 min with liver activity at 15 and 60 min) have been added to the above semiquantitative parameters [139].

These parameters have also been found useful in assessing the benefit of endoscopic sphincterotomy (Figs. 10.27 and 10.28) [140].

Although scintigraphic studies on this subject have focused primarily on the differentiation between the presence and absence of SOD, it can be also useful in discriminating between stenosis and functional dyskinesia [140] (Fig. 10.29).

10.2.5 Interventions in Cholescintigraphy

Several drugs, including cholecystokinin (CCK), morphine, and phenobarbital, have been used to alter biliary kinetics at different levels (i.e., hepatocytes, gallbladder, and/or sphincter of Oddi) in an effort to increase the efficacy of hepatobiliary

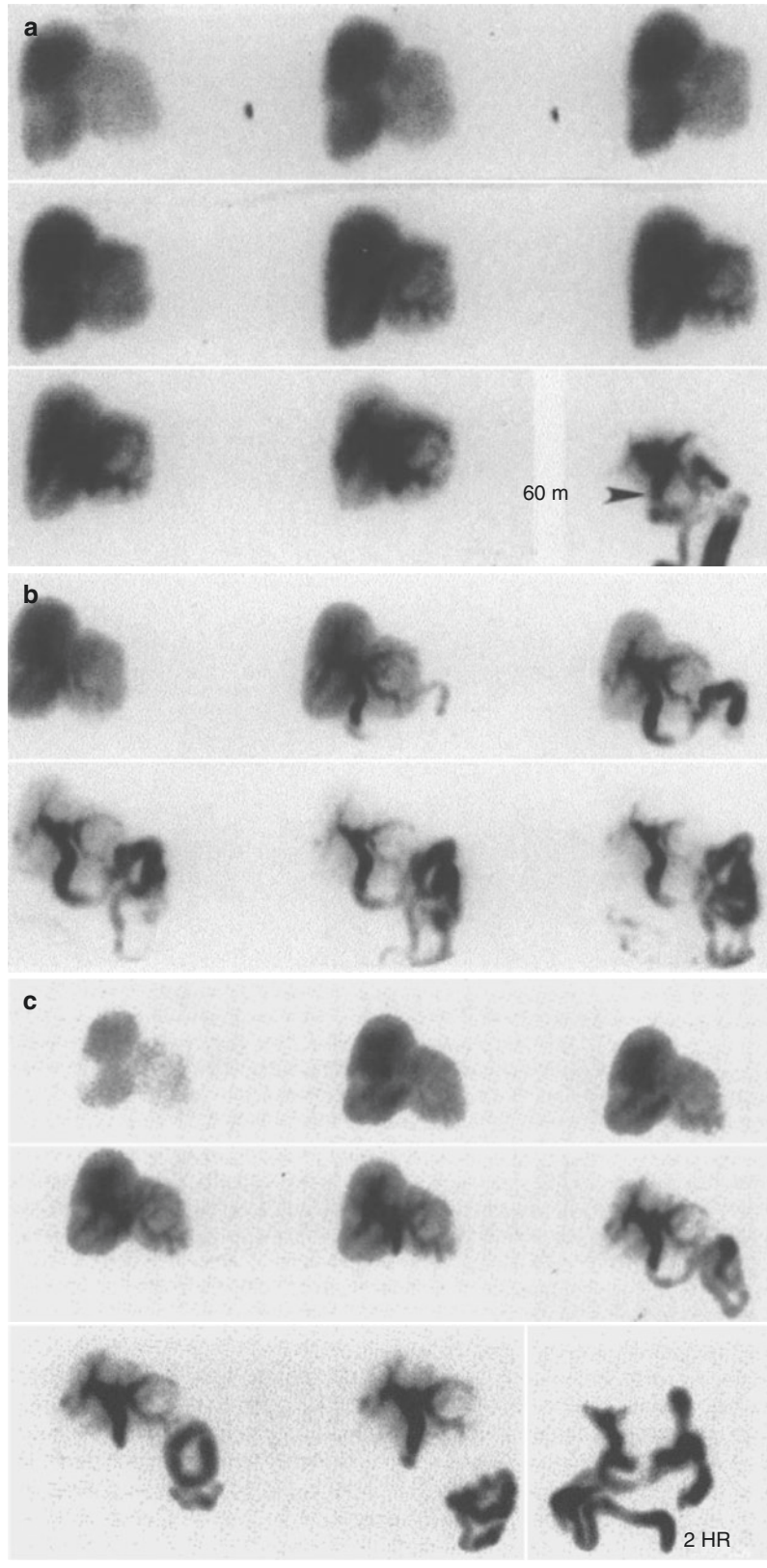

Fig. 10.28 (**a**–**c**) SOD: dyskinesia. Postcholecystectomy pain syndrome. An ERCP showed no mechanical obstruction. The sphincter of Oddi pressure was 48 mmHg. A sphincterotomy was performed. (**a**) Preoperative study. Sequential analog images over 60 min show a prominent intrahepatic collection system with dilatation in the region of the common hepatic duct at 60 min. A delayed image at 2 h shows that the obstruction is really at the level of the sphincter of Oddi (*arrowhead*). (**b**) Preoperative study with a continuous infusion of sincalide, 40 ng/kg/60 min. Hepatobiliary clearance is more rapid than the study without CCK. However, at the end of 60 min, there is retained activity in a prominent common duct. This is an obstructed dyskinetic sphincter of Oddi. (**c**) Postsphincterotomy study. There is still prominent retention in the common duct, but hepatobiliary clearance has significantly improved since the baseline study (**a**) and, interestingly, looks similar to the preoperative CCK study (**b**). (From Ziessman [139] with permission)

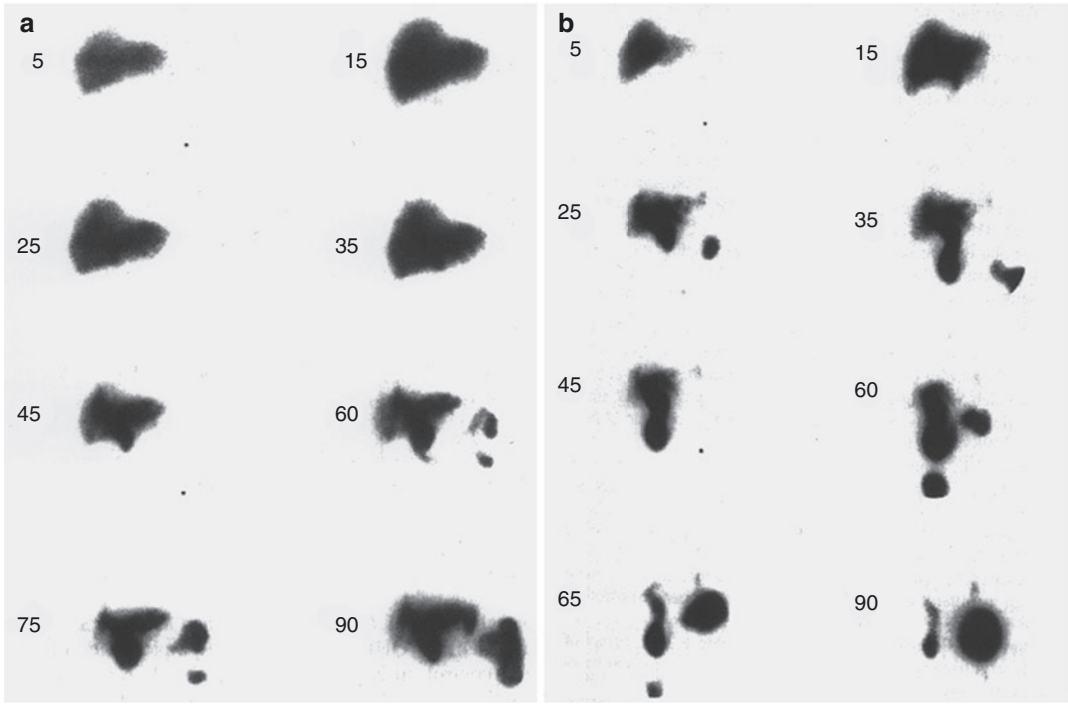

Fig. 10.29 (**a**) Stenosis of the sphincter of Oddi (structural SOD). Biliary tree activity is initially visualized at 25 min after injection of Tc-99m-IDA. The CBD and intrahepatic biliary tree appear prominently at 45 min and do not change significantly during amyl nitrate inhalation from 60 to 90 min. (**b**) Sphincter of Oddi dyskinesia (functional SOD). Biliary tree activity is first visualized at 15 min. The CBD and intrahepatic biliary tree appear prominently from 25 up to 60 min. The small bowel is first visualized at 25 min. Note a marked decline in CBD activity during amyl nitrate inhalation from 60 to 90 min. (From Madacsy et al. [141] with permission)

imaging. Sincalide, a synthetic C-terminal octapeptide of CCK, has been used in the diagnosis of acute cholecystitis in order to empty the gallbladder before cholescintigraphy, so that gallbladder filling can be enhanced during the study if the cystic duct is patent. These agents are also used to evaluate gallbladder ejection fraction (GBEF) and/or sphincter of Oddi response in patients with suspected chronic, acalculous biliary tract diseases to determine who might benefit from cholecystectomy or sphincterotomy.

10.2.5.1 Cholecysystokinin (CCK) Administration

CCK is a polypeptide hormone normally released from mucosal cells of the proximal small bowel in response to fat and protein ingested. CCK is bound to receptors in the gall bladder and sphincter of Oddi resulting in gall bladder wall contraction and sphincter of Oddi relaxation. CCK can be used in several situation as one of the interventions with cholescintigraphy. It may be administered before cholescintigraphy or after the 60 min study ends (Table 10.10).

Table 10.10 Uses of CCK associated with cholescitigraphy

1. Administration prior to cholescitigraphy
(a) Prolonged fasting and total parenetral nutrition
(b) Suspected biliary sphincter (Sphincter of Oddi) dysfunction
2. Administration after 60 min study
(a) Chronic acalculous cholecystitis
(b) Differentiate common bile duct obstruction from functional etiology
(c) Exclude acalculous form of acute cholecystitis when gall bladder is visualized

CCK Pre-cholescingraphy Administration for the Diagnosis of Acute Cholecystitis

Administration of CCK prior to injection of Tc-99mIDA will induce gallbladder empty-

ing with a reduction of intraluminal pressure. It was introduced as a means of reducing potential false-positive results for acute cholecystitis and of shortening the total imaging time [140]. The rationale of this approach is that gallbladder emptying before initiating the study is generally followed by more reliable gallbladder filling during the cholescintigraphy. Although sincalide pretreatment of all patients may not be necessary, it is often used in conditions such as alcoholism and total parenteral nutrition and during a prolonged fasting state, because functional resistance to tracer inflow may result from distention of the gallbladder with viscous contents. Fasting for 24 h or longer is a routine indication for the preadministration of sincalide in many laboratories.

It should be noted that a meticulous sincalide infusion technique is important to ensure good gallbladder emptying. At a dose of 0.02 μg/kg the drug is infused slowly over 30 and up to 60 min [85]. If this long infusion is logistically inconvenient, a 3-min infusion at the physiological rate of 3.3 ng/kg/min [86], or an infusion for up to 10 min at the same or slightly lower rate approximately 15–30 min before injection of Tc-99m-IDA, is probably adequate for this application.

CCK Pre-cholescingraphy Administration for Suspected Biliary Sphincter (Sphincter of Oddi) Dysfunction

CCK is infused at a dose of 0.02 μg/kg over 3–10 min 15 min prior to injection of IDA derivative and then study is carried out for the initial standard of 60 min [85]. If the condition is not post-cholecystectomy, longer infusion for 45–60 min is carried out after the initial cholescintigraphy study and GBEF is determined since if it is useful in predicting the outcome of sphincterotomy.

CCK Post-cholescingraphy Administration for Acalculous Biliary Syndromes

Determination of GBEF after CCK administration is important for confirmation of this group of disorders and also in predicting the outcome of surgery. The technique for administration of CCK is of the utmost importance. The degree of gallbladder emptying is dependent on the CCK dose and rate of administration, as well as on the total number of receptors in the gallbladder wall smooth muscle. Spasm of the neck of the gallbladder and decreased GBEF may occur due to unphysiologically high serum levels of sincalide following a bolus injection. This paradoxical response is attributable to the different threshold level of the CCK receptors in the body and fundus of the GB and cystic duct. The cystic duct does not contract when the dose of CCK is physiological. Therefore, this agent should not be given as a bolus. Although infusion of 20 ng/kg sincalide over 2–4 min (an average dose rate of 6.6 ng/kg/min) was once a popular technique [140–145], this dosage protocol has also been demonstrated to be unphysiological [86, 145]. Aside from frequent incomplete gallbladder emptying, infusion of 20 ng/kg over 3 min or less is often associated with such side effects as abdominal discomfort, pain, and nausea.

Comparison of various sincalide doses for a 3-min infusion technique demonstrated that 10 ng/kg (the rate of 3.3 ng/kg/min) produces maximal gallbladder emptying [86]. With further increase of the dose rate, i.e., 20 ng/kg/3 min, the GBEF actually decreases. The normal GBEF value using 10 ng/kg/3 min was established as greater than 35%. Falsely reduced GB emptying associated with a 3-min infusion of 20 ng/kg of sincalide is illustrated well in Fig. 10.30 [146]. However, Ziessman et al. showed that even the infusion at a so-called physiological rate (10 ng/kg infused over 3 min) produces an excessively variable GBEF response to establish a clinically useful and reproducible normal range compared with the same dose infused over a longer period, i.e., 10 ng/kg infused for 60 min [147]. Although the optimal dose and duration of infusion is the subject of some controversy, a long infusion seems to produce more complete gallbladder emptying and less severe side effects than a short infusion, probably due to the 2.5-min plasma half-life of sincalide. When performing and interpreting sincalide-augmented hepatobiliary imaging, it is important to adhere to a specific sincalide infusion technique and to use normal GBEF values that have been validated for that particular method. Recently, an interdisciplinary

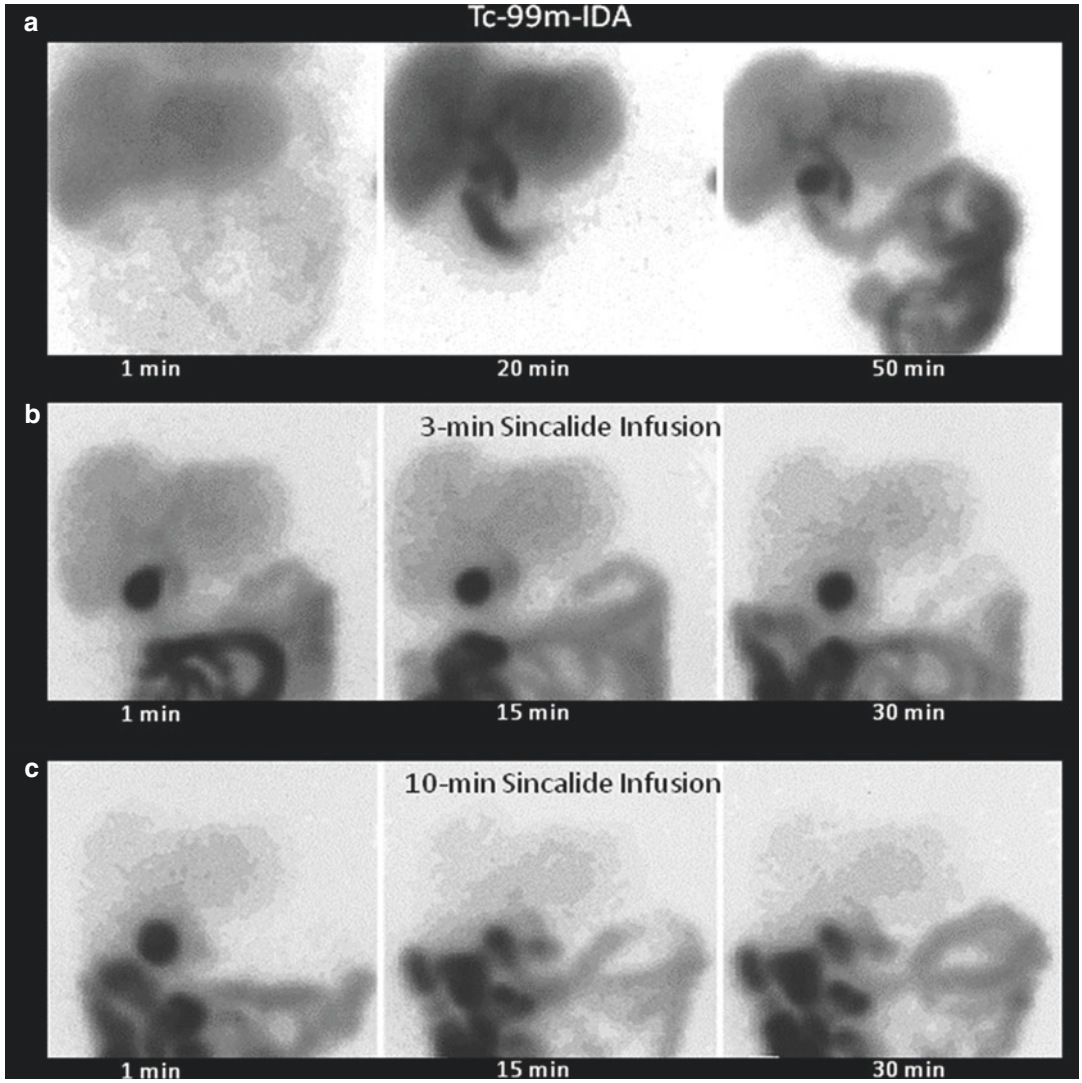

Fig. 10.30 A hepatobiliary scan using Tc-99m-IDA performed in a patient with suspected chronic acalculous biliary disease. The scan shows prompt visualization of the GB and small bowel (**a**). Following a 3-min infusion of 20 ng/kg sincalide, the GB is poorly contracted, with an EF of approximately 10% (**b**). Immediately after this, a 10-min infusion of the same dose produced a GBEF of 80% (**c**)

panel suggested that the optimal sincalide infusion method is 20 ng/kg/60 min with 38% as the lower limit of normal GBEF [148].

Various fatty meals have been evaluated as an alternative to sincalide. However, controversy exists over the use of fatty meals versus sincalide. The major disadvantage of meal stimulation is that an abnormal GB response may result from factors other than the GB, such as poor gastric emptying, pancreatic insufficiency, celiac disease, or abnormal bowel transit [149–153]. The onset of meal-induced GB emptying can also vary during different phases of the migrating motor complex at the time of ingestion [154]. The choice between fatty meal and sincalide can probably be made on the basis of the population being studied. Meal stimulation would be preferable when GB function in relation to the rest of the GI tract needs to be evaluated. However, evaluation of GB function independent of the

digestive process may be better achieved with sincalide when different patient populations are studied [155]. Nonetheless, a fatty meal can serve as an alternative in the case that sincalide is not available for clinical use. However, when used, careful attention should be paid to the fat content, texture, taste, manner of administration, and measurement time sequence, all of which need to be standardized [156]. Normal values for each center must be established when choosing a meal.

In summary, the overall data favor the use of this test for the diagnosis of chronic acalculous gallbladder and cystic duct disease. A low GBEF can probably be interpreted as indicating a high probability for symptomatic relief after surgery, and vice versa. Bayes' theorem should then be applied, especially for the group with a normal EF, to make a clinical decision according to the posttest probability from a clinical suspicion (pretest probability) and the GBEF (test probability).

10.2.5.2 Morphine Augmentation

Bile is secreted continuously from the liver into the biliary system. The proportion of bile flowing into the gallbladder or the duodenum depends on the relative resistance to flow determined mainly by the contractile state of the gallbladder and the sphincter of Oddi. The resistance of the sphincter of Oddi is considered the principal factor in the regulation of the intracholedochal pressure and of the common bile duct-gallbladder pressure gradient [157]. The administration of morphine sulfate (morphine) results in contraction of the sphincter of Oddi. This, in turn, causes an increase in the intraductal pressure and forces the bile to flow into the gallbladder if the cystic duct is patent [158–160]. A widely used protocol an alternative to delayed imaging involves the administration of 0.04 mg/kg morphine intravenously over 3 min at 1 h after the injection of radiotracer, provided that activity is seen in the bowel. Generally, morphine is not administered during the first hour because (1) the gallbladder is visualized within 1 h in the majority of patients undergoing cholescintigraphy and (2) delayed filling of the gallbladder or delayed excretion into the bowel, suggesting the presence of chronic cholecystitis or other biliary tract disease, could be missed by the early administering morphine. After morphine administration, imaging is continued for an additional 30 min. Typically, the gallbladder is visualized within 30 min if the cystic duct is patent If visualization does not occur within 30 min, the findings are interpreted as consistent with acute cholecystitis (Fig. 10.31). Therefore, the entire study can be terminated at 90 min in contrast to 4 h or more with conventional delayed imaging without morphine augmentation. Reports by Chen et al. and Kim et al. [161, 162] show that morphine administration helps to visualize the gallbladder in 32–42% of patients with gallbladder nonvisualization at up to 60–90 min despite sincalide pretreatment. These results suggest that sincalide pretreatment alone is not sufficient to detect all patent cystic ducts.

Variants Associated with CCK and Morphine Intervention

Significantly delayed tracer excretion into the bowel associated with prompt and progressive gallbladder filling can be a normal variant seen in the fasting state [163]. Morphine administered to the patient prior to the study can have the same result. This finding is well known and is now actually used in a positive way to enhance gallbladder visualization during cholescintigraphy.

In a series by Kim et al., approximately 40–50% of subjects with prompt gallbladder filling showed a markedly delayed biliary-to-bowel transit after sincalide pretreatment (Fig. 10.32) compared with only 4% of patients who did not receive sincalide [164]. Delayed biliary-to-bowel transit, when present, should not necessarily be read as abnormal, i.e., as hyperacute or partial CBD obstruction. However, a hyperacute or partial CBD obstruction may not be totally excluded in certain clinical settings, although this pattern, with intact gallbladder visualization, is not typical of CBD obstruction. In such a situation, CCK administration can help to exclude CBD obstruction by inducing gallbladder contraction and demonstrating bowel activity [164].

Oates et al. [165] and Shih et al. [166] reported that morphine administration increases the frequency and the degree of duodenogastric reflux.

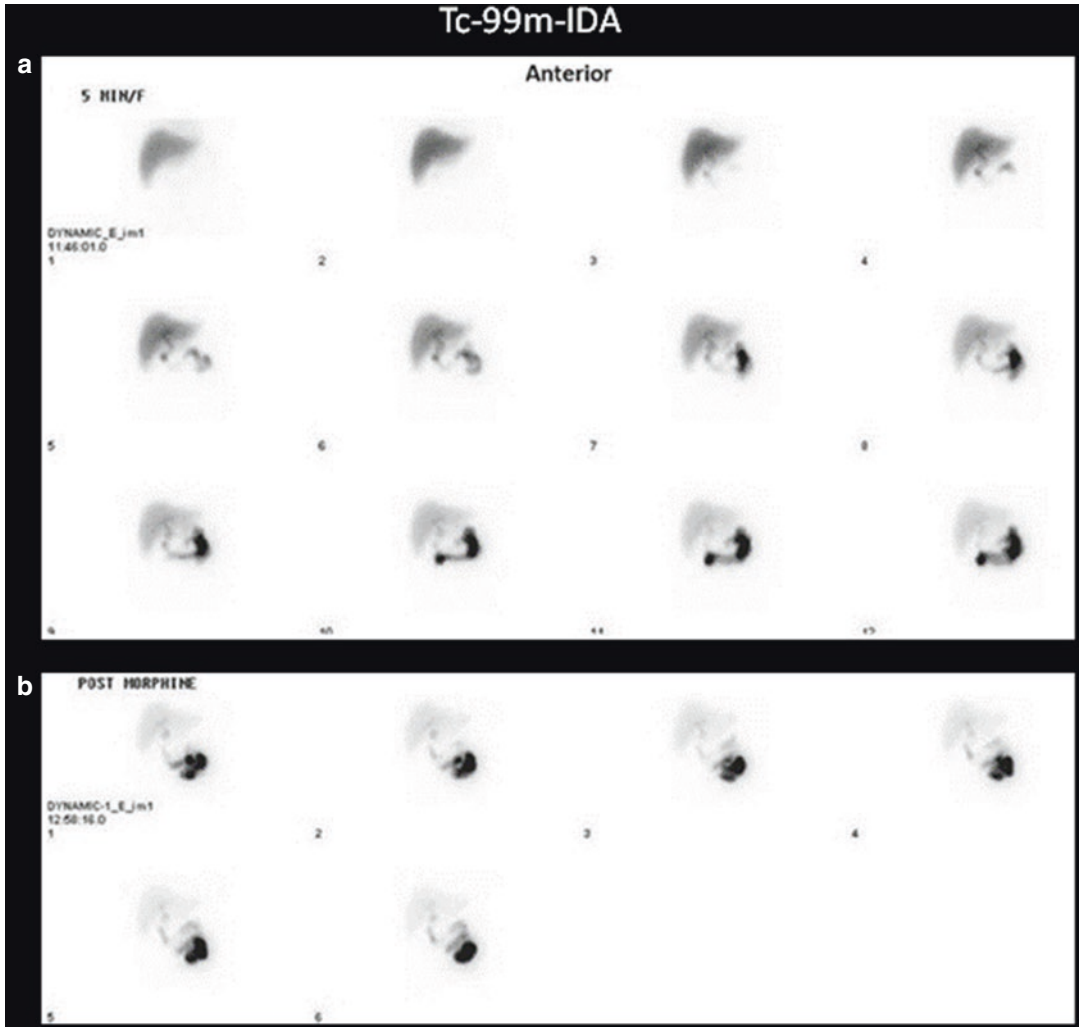

Fig. 10.31 Hepatobiliary study showing nonvisualization of gall bladder during routine study (**a**) and after low-dose morphine injection (**b**) in a patient suspected of having acute cholecystitis. The CBD and small bowel are promptly visualized but the gallbladder is not visualized up to 60 min. Following morphine administration, the gall bladder did not show filling. The finding indicates obstruction of the cystic duct which indicates acute cholecystitis in the clinical setting of this patient

In brief, in addition to its logistic advantage (shortening the imaging time), morphine augmentation provides more specific diagnosis for acute cholecystitis than does delayed imaging. Sincalide pretreatment, when administered at the physiological rate, will be helpful in conditions in which functional resistance to tracer flow into the gallbladder may be present. However, morphine augmentation will further improve the efficacy of the test even after sincalide pretreatment. The technique is therefore recommended for routine clinical use when the gallbladder is not visualized at 1 h.

10.2.6 Hyperbilirubinemia

Cholescintigraphy is often performed to differentiate surgical jaundice (CBD obstruction and biliary atresia) from medical jaundice (intrahepatic cholestasis and/or hepatocellular disease) in both adults and neonates. Alternatively, CBD obstruc-

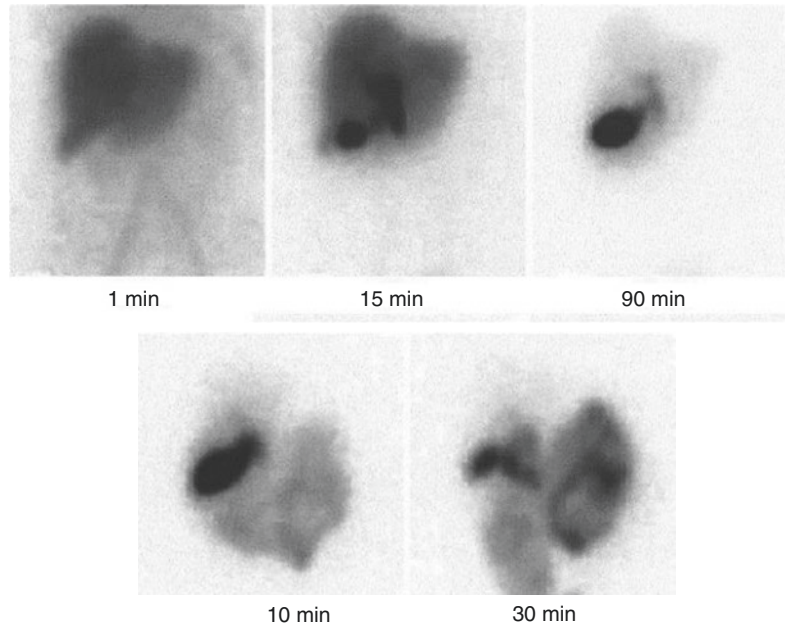

Fig. 10.32 The patient was pretreated with sincalide before receiving an injection of Tc-99m-IDA. The gallbladder filling is prompt but bowel activity is not identified until 90-min postinjection (**a**). Following administration of a second dose of sincalide (**b**), there is prompt tracer excretion into the bowel, which excludes common duct obstruction

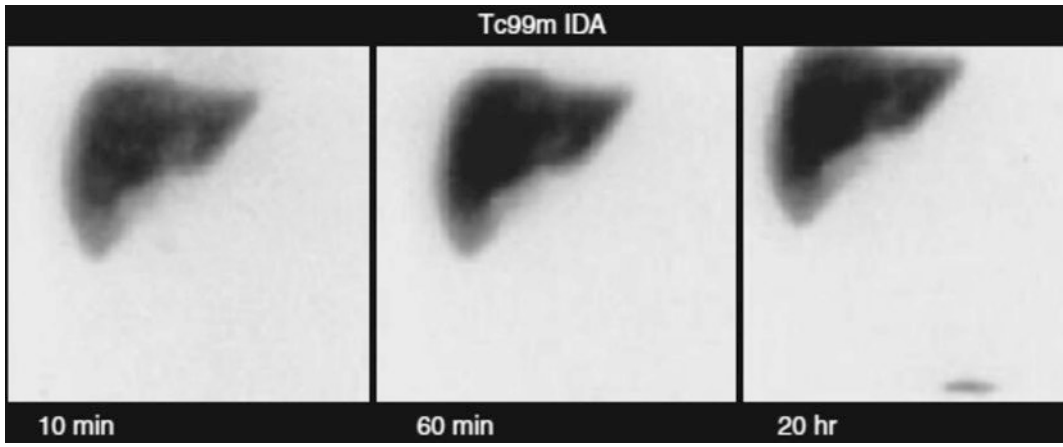

Fig. 10.33 The pattern of acute CBD obstruction imaged with Tc-99m-IDA. The initial hepatic uptake is prompt, with prolonged retention and no evidence of intestinal excretion throughout the study and on delayed image at 20 h pot injection

tion or intrahepatic cholestasis is occasionally detected incidentally on cholescintigraphy performed in patients who present with abdominal pain.

10.2.6.1 Common Bile Duct Obstruction

Cholescintigraphy is useful to diagnose biliary obstruction in patients with normal ultrasonography and who are not clearly jaundiced and only mild liver dysfunction as if serum bilirubin levels are high, bilirubin occupies the available receptors and blocks the IDA uptake since both have the same mechanism for uptake by hepatocytes. Prompt hepatic uptake of IDA that persists 2–4 h (sometimes even up to 24 h) without evidence of biliary excretion is the obstructive pattern that has been commonly described (Fig. 10.33) [167,

168]. The presence of an obvious photopenic defect in the area of the porta hepatis corresponding to dilated bile ducts or slow tracer filling of dilated bile ducts makes CBD obstruction more likely. The presence of intestinal activity without visualization of the CBD makes intrahepatic cholestasis more likely. However, without ancillary findings, the distinction between a high-grade CBD obstruction and a high-grade intrahepatic cholestasis (with relatively preserved hepatocyte function) may be difficult. Ultrasonography may play a complementary role in this situation.

In patients with partial CBD obstruction, cholescintigraphy may demonstrate absence of intestinal activity, delayed biliary-to-bowel transit, and/or a prominent ductal pattern persistent for 2 h [168]. When CBD obstruction is suspected, the patient should not be pretreated with sincalide, which may cause prompt gallbladder filling with delayed biliary-to-bowel transit, as discussed earlier. Poor hepatic uptake with persistent blood pool activity of IDA in jaundiced patients generally indicates hepatocellular disease, regardless of the presence or absence of bowel activity (Fig. 10.32).

Quantification of hepatocyte function by measuring the hepatocyte extraction fraction (HEF) of IDA agents with deconvolutional analysis was reported to be useful for the distinction between CBD obstruction and hepatocellular dysfunction [169–171]. Despite profound hyperbilirubinemia, patients with CBD obstruction typically have only slightly reduced HEF values compared with normal controls, whereas patients with hepatocellular dysfunction have markedly reduced HEF values.

10.2.6.2 Neonatal Hyperbilirubinemia

Persistent jaundice is considered to be pathological beyond 3 weeks of age in full-term babies and 4 weeks in preterm babies. Cholestasis with conjugated hyperbilirubinemia can be due to a wide variety of abnormalities including extrahepatic biliary tree abnormalities (i.e., extrahepatic biliary atresia (EHBA) and choledochal cyst) or intrahepatic diseases (i.e., interlobular bile duct paucity or neonatal hepatitis syndrome).

The cause and pathogenesis of biliary atresia remain largely unknown [172–174]. Both chronic and acute inflammatory changes have been shown histopathologically. Biliary atresia is typically a progressive panductular obliterative process. Without correction of bile flow obstruction within 2–3 months of life, irreversible hepatic damage and complete obliteration of the extrahepatic biliary tree will result. This process could be progressive even after surgical correction of the obstruction [175, 176]. The neonatal hepatitis syndrome includes various kinds of diseases such as idiopathic neonatal hepatitis, infectious hepatitis, and hepatitis from metabolic or genetic causes.

The urgency in correctly diagnosing EHBA is reflected in the surgical results following portoenterostomy (Kasai procedure). Sustained bile flow is significantly greater in infants operated on before 60 days of age (91%), compared with those operated on after 3 months (17%) [177]. The preoperative distinction of EHBA from the other disorders causing severe cholestasis is essential if the correct patients are to be selected for surgery.

Cholescintigraphy has been known to have 100% sensitivity for the diagnosis of extrahepatic biliary atresia, but low specificity [178–181]. In neonates, normal cholescintigraphy should show prompt and uniform uptake of tracer in the liver with a maximum tracer accumulation within 5 min [182, 183]. The gallbladder may be visualized as early as 10 min, but nonvisualization of the gallbladder can be a normal variant in the neonatal period. The hepatic, cystic, and common bile ducts are generally not visualized in the neonatal period even when there is normal excretion and gallbladder visualization. Bowel activity is seen usually by 30–40 min.

In general, cholescintigraphy performed in patients with biliary atresia within the first 2 months of life usually shows reasonably good hepatic uptake, nonvisualization of the gallbladder, and prolonged retention of the tracer in the liver with no biliary excretion (Fig. 10.34). In contrast, patients older than 3 months usually show evidence of decreased hepatic function with reduced hepatic extraction fraction and no biliary excretion [183].

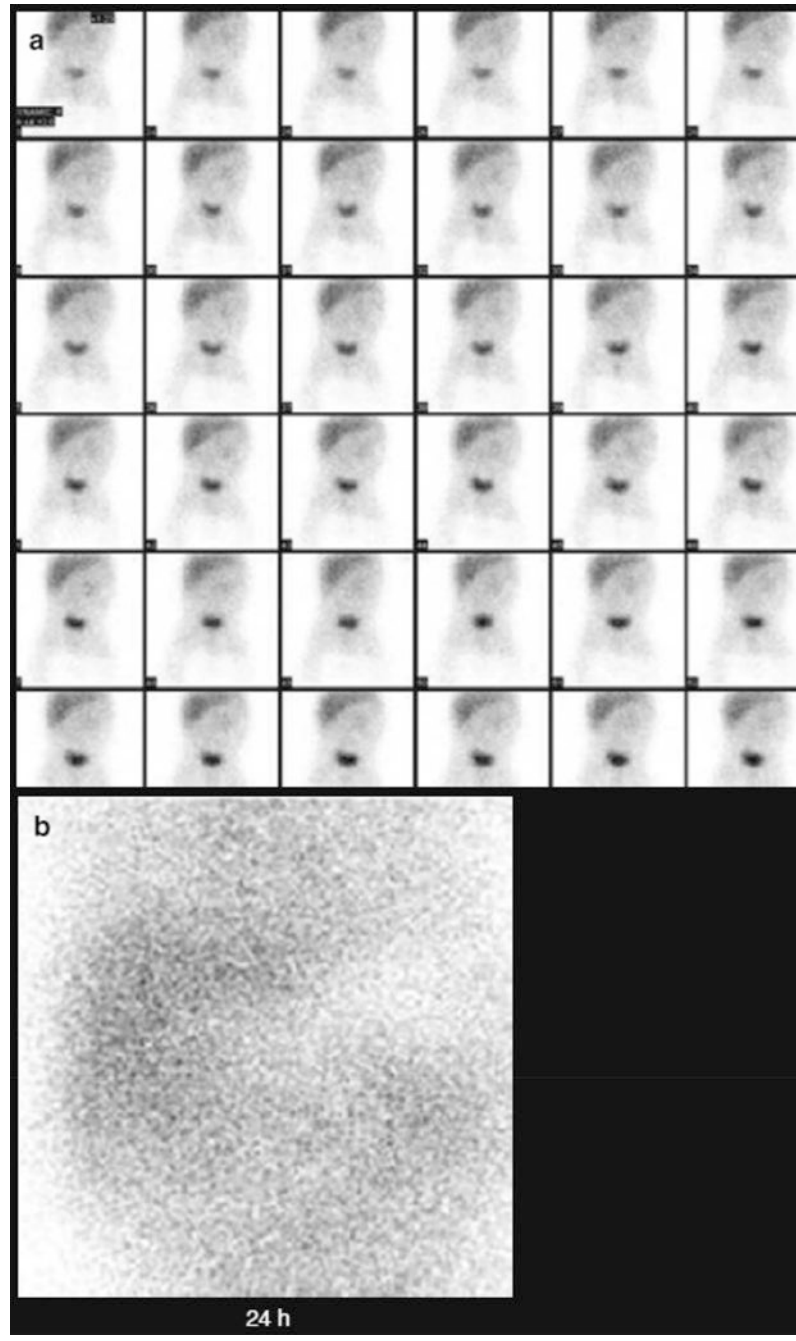

Fig. 10.34 Hepatobiliary study in a neonate carried out for 60 min (**a**) and delayed 24 h image (**b**) illustrating no secretion of activity in the intestine as well as nonvisualization of the gall bladder. Biliary atresia in such case cannot be excluded. However, since the function of the liver is adequate biliary atresia is more likely than neonatal hepatitis

If there is no excretion in an infant less than 2 months of age and the initial uptake suggests liver dysfunction, then the neonatal hepatitis syndrome should be suspected. A repeat study will show the improved function and transit as the condition resolves. In infants under 2 months who do not excrete, those with biliary atresia tend to have better liver-to-heart ratios of radioactivity at 5 min than those with the neonatal hepatitis syndrome. However, no excretion with normal or near normal hepatic uptake may be seen in some cases of severe neonatal hepatitis

syndrome [184]. Cholescintigraphy is most useful in excluding the diagnosis of biliary atresia with a sensitivity and negative predictive value of virtually 100% when intestinal and/or extrahepatic biliary activity is seen. Urine activity in the diaper or contamination of the skin of the abdomen should not be confused with intestinal activity. Acquiring delayed images after cleaning the skin and changing the diaper can prevent this from occurring. The reported specificity ranges from 43 to 90% [179–181, 184–188]. Patients are typically premedicated with phenobarbital, 5 mg/kg daily in two divided doses given for 5 days. Ursodeoxycholic acid, an additional choleretic agent, may also be given at a dose of 20 mg/kg daily in two divided doses in order to optimize bile flow prior to the study.

Phenobarbital stimulates the hepatic transport system for organic anions. This is primarily achieved by induction of hepatic microsomal enzymes, thereby increasing bilirubin conjugation and excretion. Situations.

10.2.6.3 Postoperative Evaluation

Complications After Hepatobiliary Surgery

The increase in the number of laparoscopic cholecystectomy and liver transplantations leads to increased utilization of cholescintigraphy for the evaluation of postoperative complications [189]. Bile duct complications include bile leaks, common bile/hepatic duct injuries or strictures, retained biliary calculi, and obstruction. Most investigators agree that bile leaks are best detected by cholescintigraphy rather than by other anatomical imaging modalities [190–193]. When acquiring scintigraphic images, it is often helpful to enhance image intensity for accurate assessment of the extent of extravasation (Fig. 10.35). The extent of leak is often better identified on

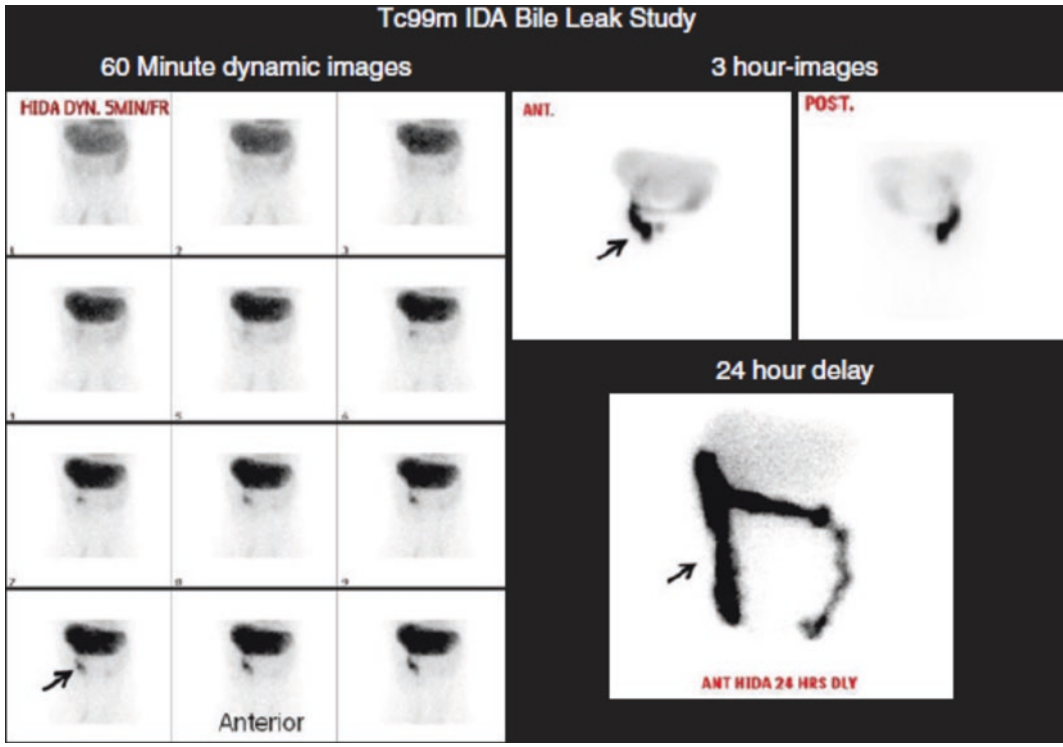

Fig. 10.35 Bile leak study of a patient who underwent liver transplantation 20 days earlier and was referred to rule out possible bile leak. The study shows bile activity early through the study which increased on later images in a linear pattern and appears to be confined within the intestines and colon with no extravasation. Accordingly the study does not show evidence of bile leak

delayed images [194]. Endoscopic retrograde cholangiopancreatography and/or percutaneous transhepatic cholangiography can be a supplement as needed for more definitive diagnosis and treatment [195, 196]. When ultrasonography or CT shows a fluid collection, cholescintigraphy can be helpful not only in confirming but also in excluding biloma [109]. The addition of SPECT/CT imaging can help in localization and improving the accuracy of the study.

The image obtained at 40 min after injection of Tc-99m-IDA reveals intense tracer accumulation, localized only in the gallbladder fossa. However, a subsequently obtained image at an increased intensity (50 min) shows that the leak is more extensive. Delayed images best delineate the extent of the leak (reprinted from Kim [109] with permission).

Clinically insignificant leaks usually heal spontaneously. However, if a major leak is present, reoperation, percutaneous transhepatic biliary drainage, or endoscopic sphincterotomy with placement of a stent or nasobiliary drainage catheter is required. The effectiveness of such interventional procedures may be assessed with cholescintigraphy if clinically indicated (Fig. 10.36).

10.2.6.4 H Miscellaneous

Patients with sclerosing cholangitis were evaluated with planar and SPECT imaging using Tc-99m-IDA [197]. Planar imaging showed beading or band-like constrictions of the biliary tract corresponding to lesions seen on cholangiography. The SPECT images demonstrated multiple focal areas of tracer retention, representing bile stasis in intrahepatic bile ducts.

In patients with cystic fibrosis, ERCP often shows changes consistent with sclerosing cholangitis, with beading and stricturing of the intrahepatic ducts [198]. While various scintigraphic findings in these patients have been described, the most common finding appears to be retention of tracer in the intrahepatic ducts [198–201]. It was suggested that cholescintigraphy is valuable for monitoring the therapeutic responses of cystic fibrosis patients with liver disease to ursodeoxycholic acid therapy [199] and in the early detection of liver involvement [201].

Cholescintigraphy was found to be a useful noninvasive screening test in HIV-positive patients with right upper quadrant pain who are suspected of having AIDS-related sclerosing cholangitis, for the purpose of determining who should be referred for ERCP [202, 203]. The response to specific antimicrobial or surgical intervention can be monitored with cholescintigraphy [203].

Cholescintigraphy is a useful noninvasive test which complements an anatomical finding on ultrasonography in the diagnosis of choledochal cyst [204, 205]. And in assessing the effectiveness of anti-enterogastric reflux procedures (e.g., Roux-en-Y diversion).

Investigators have found cholescintigraphy useful for assessing the patency of a biliary-enteric bypass [206–209]. A case was reported in which biliary stasis seen in the region of the biliary-enteric anastomosis in the supine images disappeared almost completely when the images were repeated after 30 min with the patient in an upright position [210]. We have observed a similar finding in a patient postoperatively. These cases illustrate the importance of imaging in the upright position when biliary or afferent loop stasis is seen in postoperative patients.

10.2.7 Summary

Cholescintigraphy plays a pivotal role in the evaluation of various biliary tract diseases, particularly when coupled with pharmacological intervention. The physician monitoring the study should be familiar with the most optimal technique for the pharmacological intervention and with conditions and medications that affect gallbladder contraction. It is also important to be aware of the various physiological and pharmacological effects on imaging findings, i.e., not only those findings that are normal but also the undesirable variants. Failure to recognize such effects can lead to incorrect interpretations.

Radionuclide imaging of the liver using the various tracers provides unique functional information, i.e., the functional reserve, presence or absence of hepatocytes/Kupffer's cells, and RBC

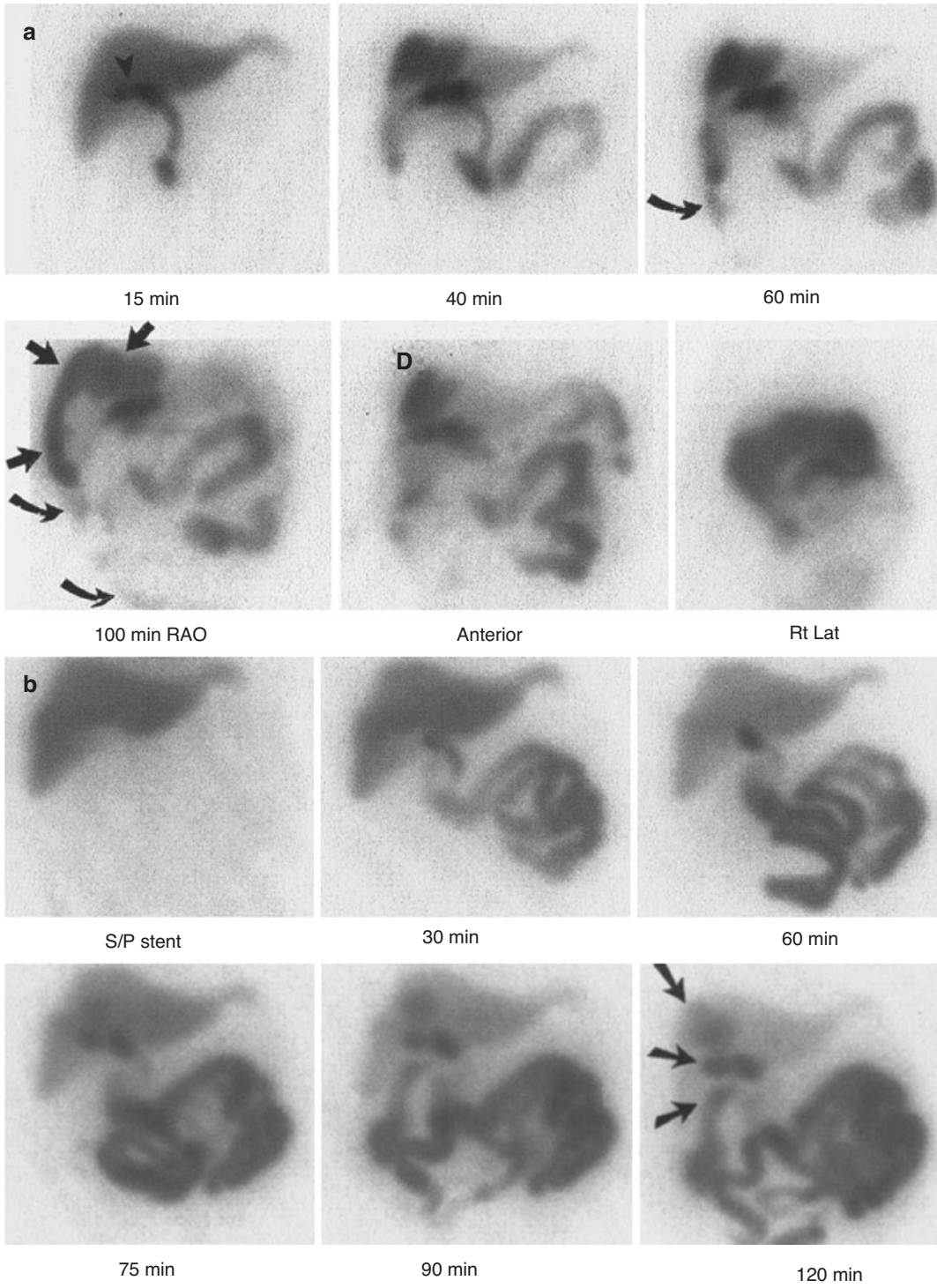

Fig. 10.36 (**a**, **b**) Post-liver transplantation Tc-99m-IDA scan. (**a**) After removal of the t-tube, a bile leak is first noted at 15 min (*arrowhead*). The anterior images show localization of extravasated activity predominantly at the dome (*D*) of the liver. The right anterior oblique (*RAO*) image better delineates extravasated activity over the superior and posterolateral surface of the liver (*straight arrows*), in addition to the right paracolic gutter (*curved arrows*). (**b**) A repeat study after CBD stent placement shows markedly improved drainage of bile into the intestine. However, a milder degree of leak is still evident on the images acquired during the second hour (*arrows*). (Reprinted from Kim [108] with permission)

pooling. This has been augmented further by the improved resolution with multi-head SPECT systems. Advances in instrumentation such as PET and development of new radiopharmaceuticals, including PET tracers specifically for the evaluation of the liver, will likely expand clinical applications further.

References

1. Kuo B, Urma D (2006) Esophagus-anatomy and development. GI Motility online
2. Mittal RK (2011) Upper esophageal sphincter. In: Mittal RK (ed) Motor function of the pharynx, esophagus and its sphincters. Morgan and Claypool Life Sciences, San Rafael. https://www.ncbi.nlm.nih.gov/books/NBK54282
3. Sama SK, Daniel EE, Waterfall WE (1977) Myogenic and neural control systems for esophageal motility. Gastroenereology 73:1345–1352
4. Richards WG, Stamler JS, Kobzik L et al (1995) Role of nitric oxide in human esophageal circular smooth muscle in vitro. J Thorac Cardiovasc Surg 110: 157–164
5. Meyer GW, Gerhardt DC, Castell DO (1981) Human esophageal response to rapid swallowing: muscle refractory period or neural inhibition? Am J Phys 241:G129–G136
6. Sidhu AS, Triadafilopoulos G (2008) Neuroregulation of lower esophageal sphincter function as treatment for gastro-esophageal reflux disease. World J Gastroenterol 14:985–990
7. Wong RKH, Waysonovitch CL (1995) Achalasia. In: Castell DO (ed) The esophagus, 3rd edn. Little Brown, Boston, pp 219–245
8. Oude Nijhuis RAB, Zaninotto G, Roman S, Boeckxstaens GE, Fockens P, Langendam MW et al (2020) European guidelines on achalasia: United European Gastroenterology and European Society of Neurogastroenterology and Motility recommendations. United European Gastroenterol J 8(1):13–33
9. Lacy BE, Weiser K (2008) Esophageal disorders: medical therapy. J Clin Gastroenterol 42:652–658
10. Penaginie R, Schoeman MN, Dent J, Tipnett MD, Holloway RH (1996) Motor events underlying gastroesophageal reflux in ambulant patient with reflux esophagitis. Neurogastroenterol Motil 8:131–141
11. Kahrilas PJ (1999) The role of hiatus hernia in GERD. Yale J Biol Med 72:101–111
12. Kahrilas PJ, Manka M, Shi G, Joehl RJ (2000) Increased frequency of transient lower esophageal sphincter relaxation induced by gastric distention in reflux patients with hiatal hernia. Gastroenterology 118:688–695
13. Galmiche JP, Janssens J (1995) The pathophysiology of gastroesophageal reflux disease: an overview. Scand J Gastroenterol Suppl 211:7–18
14. Goldstein JL, Waykins JL, Greger JA, Layden TL (1994) The esophageal mucosal resistance. J Lab Clin Med 123:653–659
15. Minami H, McCallum RW (1984) The physiology and pathophysiology of gastric emptying in humans. Gastroenterology 86:1592–1600
16. Hinder RA, Kelly KA (1977) Human gastric pacesetter potential: site of origin, spread and response to gastric transection and proximal gastric vagotomy. Am J Surg 133:29–33
17. Meyer JH, Ohashi H, Jehn D et al (1981) Size of liver particles emptied from the human stomach. Gastroenterology 80:1489–1496
18. Brener W, Hendrix TR, McHugh PR (1983) Regulation of the gastric emptying of glucose. Gastroenterology 85:76–82
19. Siegel JA, Urbain JL, Adler LP, Charkes ND, Maurer AH, Krevsky B, Knight LC, Fisher RS, Malmud LS (1988) Biphasic nature of gastric emptying. Gut 29:85–89
20. Loo FD, Palmer DW, Soergel KH, Kalbfleisch JH, Wood CM (1984) Gastric emptying in patients with diabetes mellitus. Gastroenterology 86:485–494
21. Horowitz M, Harding PE, Chatterton BE et al (1985) Acute and chronic effects of domperidone on gastric emptying in diabetic autonomic neuropathy. Dig Dis Sci 30:1–9
22. Muller-Lissner SA, Fimmel CJ, Sonnenberg A et al (1983) Novel approach to quantify duodenogastric reflux in healthy volunteers and in patients with type I gastric ulcer. Gut 24:510–518
23. Tolin RD, Malmud LS, Stelzer F et al (1979) Enterogastric reflux in normal subjects and patients with Billroth II gastroenterostomy. Gastroenterology 77:1027–1033
24. Shaffer EA, McOrmond P, Duggant T (1980) Assessment of gall bladder filling and emptying and duodenogastric reflux. Gastroenterology 79:899–906
25. Markowitz JF (1990) Duodenogastric reflux: state of the art. J Pediatr Gastroenterol 10:287–289
26. Elgazzar AH, Fernandez-Ulloa M, Ryan JR et al (1992) Scintigraphic evaluation of duodenogastric reflux: significance in the diagnosis of acute cholecystitis. Am J Physiol Imaging 3(4):239–241
27. Slavin JD, Sharzynski JJ, Spencer RP (1985) High incidence of gastric reflux during hepatobiliary imaging in pancreatitis. Clin Nucl Med 10:5–6
28. Kutchai HC (2000) Gastrointestinal system. In: Berne RM, Levy MN (eds) Principles of physiology, 3rd edn. Mosby, St. Louis, pp 366–371
29. Chandran P, Satthaporn S, Robins A, Eremin O (2003) Inflammatory bowel disease; dysfunction of GALT and gut bacterial flora (I). Surgeon 2:63–75
30. Halsted CH (2003) Absorption of water-soluble vitamins. Curr Opin Gastroenterol 19:113–117

31. Divgi CR, Lisann NM, Yeh SD, Benua RS (1995) Technetium-99m albumin scintigraphy in the diagnosis of protein-losing enteropathy. J Nucl Med 27:1710–1712
32. Bhatnagar A, Lahoti D, Singh AK et al (1995) Scintigraphic diagnosis of protein losing enteropathy using Tc-99m dextran. Clin Nucl Med 20:1070–1073
33. Bhatnagar A, Singh K (1996) Technetium-99m dextran: a promising new protein-losing enteropathy imaging agent. Eur J Nucl Med 23:572–578
34. Hatoum OA, Binion DG (2005) The vasculature and inflammatory bowel disease: contribution to pathogenesis and clinical pathology. Inflamm Bowel Dis 11:304–313
35. Rogler G, Biedermann L, Scharl M (2018) New insights into the pathophysiology of inflammatory bowel disease: microbiota, epigenetics and common signalling pathways. Swiss Med Wkly 148:w14599
36. Wen Z, Fiocchi C (2004) Inflammatory bowel disease; autoimmune or immune-mediated pathogenesis? Clin Dev Immunol 11:195–204
37. Ahmad T, Tamboli CP, Jewell D, Colombel JF (2004) Clinical relevance of advances in genetics and pharmacogenetics of IBD. Gastroenterology 126:1533–1549
38. Old JL, Dusing RW, Yap W, Dirks J (2005) Imaging for suspected appendicitis. Am Fam Physician 71: 71–78
39. Whiteford MH, Whiteford HM, Yee LF, Ogunbiyi OA, Dehdashti F, Siegel BA, Birnbaum EH, Fleshman JW, Kodner IJ, Read TE (2000) Usefulness of FDG-PET scan in the assessment of suspected metastatic or recurrent adenocarcinoma of the colon and rectum. Dis Colon Rectum 43(6):759–767; discussion 767–70
40. Aabakken L (2005) Non variceal upper gastrointestinal bleeding. Endoscopy 37:195–200
41. Carney BW, Khatri G, Shenoy-Bhangle AS (2019) The role of imaging in gastrointestinal bleed. Cardiovasc Diagn Ther 9(Suppl 1):S88
42. Strate LL, Gralnek IM (2016) Management of patients with acute lower gastrointestinal bleeding. Am J Gastroenterol 111(4):459
43. Zurkiya O, Walker TG (2015) Angiographic evaluation and management of nonvariceal gastrointestinal hemorrhage. Am J Roentgenol 205(4):753–763
44. Gerson LB, Fidler JL, Cave DR, Leighton JA (2015) ACG clinical guideline: diagnosis and management of small bowel bleeding. Am J Gastroenterol 110(9):1265–1287
45. ACR Appropriateness Criteria for LGIB 2014. https://www.acr.org/Clinical-Resources/ACR-Appropriateness-Criteria
46. Stone DN, Mancuso AA, Rice D, Hanafee WN (1981) Parotid CT sialography. Radiology 138:393–397
47. Arroyo V, Bernadi M, Epstein M (1998) Pathophysiology of ascites and functional renal failure in cirrhosis. J Hepatol 6:239
48. Bories P (1986) The treatment of refractory ascites by the Leveen shunts; a multicenter controlled trial of 57 patients. J Hepatol 3:212–218
49. Conn HO (1993) Transjugular intrahepatic portosystemic shunts: the state of the art. Hepatology 17:148–158
50. Singh A (1996) Peritoneovenous shunts: patency studies. In: Henkin RE, Bles MA, Dillehay GL, Halama JR, Karesh SM, Wagner PH, Zimmer AM (eds) Textbook of nuclear medicine. Mosby, New York, pp 1041–1052
51. Desai A, O'Connor M, Neja B, Delaney K, Camilleri M, Zinsmeister AR, Bharucha AE (2018) Reproducibility of gastric emptying assessed with scintigraphy in patients with upper GI symptoms. Neurogastroenterol Motil 30(10):e13365
52. Wang YT, Mohammed SD, Farmer AD, Wang D, Zarate N, Hobson AR et al (2015) Regional gastrointestinal transit and pH studied in 215 healthy volunteers using the wireless motility capsule: influence of age, gender, study country and testing protocol. Aliment Pharmacol Ther 42(6):761–772
53. Kostamo KL (1996) Evaluation of gastrointestinal bleeding by nuclear medicine techniques. In: Henkin RE, Bles MA, Dillehay GL, Halama JR, Karesh SM, Wagner PH, Zimmer AM (eds) Textbook of nuclear medicine. Mosby, New York, pp 1016–1022
54. Nicholson ML, Neoptlemos JP, Sharp JF et al (1989) Localization of lower gastrointestinal bleeding using in vivo technetium 99m-labeled red blood cell scintigraphy. Br J Surg 76:358–361
55. Nogueira HJV (2020) Detection of ectopic gastric mucosa using scintigraphy in pediatric patients
56. Gyorke T, Duffek L, Bratfai K et al (2000) The role of nuclear medicine in inflammatory bowel disease. A review with experiences of a specific bowel activity using immunoscintigraphy with 99mTc anti-granulocyte antibodies. Eur J Radiol 3: 183–192
57. Lantto E (1994) Investigation of suspected intra-abdominal sepsis: the contribution of nuclear medicine. Scand J Gastroenterol Suppl 203:11–14
58. Perlman SB, Hall BS, Reichelderfer M (2013) PET/CT imaging of inflammatory bowel disease. Semin Nucl Med 43:420–426
59. Saha GB (2009) Fundamentals of nuclear pharmacy, 6th edn. Springer, New York
60. Sarkady E, Sapi Z, Toth V, Kiss S (1999) Warthin-like tumor of the thyroid: a case report. Pathol Oncol Res 5:315–317
61. Loutfi I, Nair MK, Ebrahim AK (2003) Salivary gland scintigraphy: the use of semi quantitative analysis for uptake and clearance. J Nucl Med Technol 31(2): 81–85
62. Rypins EB, Evans DG, Hinrichs W et al (1997) Tc-99m-HMPAO white blood cell scan for diagnosis of acute appendicitis in patients with equivocal clinical presentation. Ann Surg 226:58–65
63. Kipper SL (1999) The role of radiolabeled leukocyte imaging in the management of patients with acute appendicitis. Q J Nucl Med 43:83–92
64. Bourgeois S, Van Den Berghe I, De Geeter F (2016) Incidental finding of silent appendicitis on F-FDG

PET/CT in a patient with small cell lung adenocarcinoma. Hell J Nucl Med 19:164–166
65. O'Connor A (2021) The Urea Breath Test for the noninvasive detection of Helicobacter pylori. In: Helicobacter pylori. Humana, New York, pp 15–20
66. Graham DY, Malaty HM, Evans DG et al (1991) Epidemiology of Helicobacter pylori in asymptomatic population in the United States. Gastroenterology 100:1495–1501
67. Peterson WL (1991) Helicobacter pylori and peptic ulcer disease. N Engl J Med 324:1043–1048
68. Parsonnet J, Friedman GD, Vandersteen DP et al (1991) Helicobacter pylori infection and the risk of gastric carcinoma. N Engl J Med 325:1127–1131
69. Logan RP, Dill S, Baner FE et al (1991) The European C13 urea breath test for the detection of Helicobacter pylori. Eur J Gastroenterol Hepatol 3:915–921
70. Philips M (1992) Breath tests in medicine. Sci Am 267:74–79
71. Ormand JE, Talley NJ, Carpenter HA et al (1990) C-14 urea breath test for diagnosis of Helicobacter pylori. Dig Dis Sci 35:879–884
72. Debongnie JC, Pauwels S, Raat A et al (1991) Quantification of Helicobacter pylori infection in gastritis and peptic ulcer disease using a simple and rapid carbon-14-urea breath test. J Nucl Med 32:1192–1198
73. Strubbs JB, Marshall BJ (1993) Radiation dose estimates for the C-14 labeled urea breath test. J Nucl Med 34:821–825
74. Sasaki Y, Lio M, Kameda H et al (1970) Measurement of C-14 lactose absorption in the diagnosis of lactase deficiency. J Lab Clin Med 76:824–835
75. Sasaki Y (1991) Breath test by CO_2 analysis: I. Progress of breath test using isotopes of carbon in Japan. Radioisotopes 40:475–484
76. Sherr HP, Sasaki Y, Newman A et al (1971) Detection of bacterial deconjugation of bile salts by a convenient breath analysis technique. N Engl J Med 285:656–661
77. Sasaki Y (1995) Carbon-14 and carbon 13 breath tests. In: Wagner HN, Buchanan JW, Szabo Z (eds) Principles of nuclear medicine, 2nd edn. Elsevier, Amsterdam, pp 958–965
78. Rassam F, Olthof PB, Richardson H, van Gulik TM, Bennink RJ (2019) Practical guidelines for the use of technetium-99m mebrofenin hepatobiliary scintigraphy in the quantitative assessment of liver function. Nucl Med Commun 40(4):297–307
79. Imura S, Shimada M, Utsunomiya T (2015) Estimation of hepatic functional reserve. Hepatol Res 45:10–19. https://doi.org/10.1111/hepr.12325
80. Katabathina VS, Zafar AM, Suri R (2015) Clinical presentation, imaging, and management of acute cholecystitis. Tech Vasc Interv Radiol 18:256–265
81. Lambie H, Cook AM, Scarsbrook AF, Lodge JPA, Robinson PJ, Chowdhury FU (2011) Tc^{99m}- hepatobiliary iminodiacetic acid (HIDA) scintigraphy in clinical practice. Clin Radiol 66:1094–1105
82. Koizumi K, Uchiyama G, Arai T et al (1992) A new liver functional study using Tc-99m DTPA-galactosyl human serum albumin: evaluation of the validity of several functional parameters. Ann Nucl Med 6: 83–87
83. Yumoto Y, Yagi T, Sato S, Nouso K, Kobayashi Y, Ohmoto M, Yumoto E, Nagaya I, Nakatsukasa H (2010) Preoperative estimation of remnant hepatic function using fusion images obtained by ^{99m}Tc-labelled galactosyl-human serum albumin liver scintigraphy and computed tomography. Br J Surg 97(6):934–944
84. Harvey E, Loberg M, Ryan J, Sikorski S, Faith W, Cooper M (1979) Hepatic clearance mechanism of Tc-99m-HIDA and its effect on quantitation of hepatobiliary function: concise communication. J Nucl Med 20:310–313
85. Tulchinsky M, Ciak BW, Debelke D, Hilsom A, Holes-Lewis KA et al (2010) SNM practice guidelines fir hepatobiliary scintigraphy 4. J Nucl Med Technol 38:210–218
86. Krishnamurthy S, Krishnamurthy GT (1988) Quantitative assessment of hepatobiliary disease with Tc-99m-IDA scintigraphy. In: Freeman LM, Weissman HS (eds) Nuclear medicine annual. Raven, New York, pp 309–330
87. Doo E, Krishnamurthy GT, Eklem MJ, Gilbert S, Brown PH (1991) Quantification of hepatobiliary function as an integral part of imaging with technetium-99m-mebrofenin in health and disease. J Nucl Med 32:48–57
88. Mitsumori A, Nagaya I, Kimoto S, Akaki S, Togami I, Takeda Y, Joja I, Hiraki Y (1998) Preoperative evaluation of hepatic functional reserve following hepatectomy by technetium-99m galactosyl human serum albumin liver scintigraphy and computed tomography. Eur J Nucl Med 25:1377–1382
89. Fujimoto H, Uchiyama G, Araki T et al (1991) Exophytic regenerating nodule of the liver: misleading appearance on iodized-oil CT. J Comput Assist Tomogr 15:495–497
90. Calvet X, Pons F, Bruix J et al (1988) Technetium-99m DISIDA hepatobiliary agent in diagnosis of hepatocellular carcinoma: relationship between detectability and tumor differentiation. J Nucl Med 29:1916–1920
91. Hasegawa Y, Nakano S, Hiyama T et al (1991) Relationship of uptake of technetium-99m(Sn)-N-pyridoxyl-5-methyltryptophan by hepatocellular carcinoma to prognosis. J Nucl Med 32:228–235
92. Boulahdour H, Cherqui D, Charlotte F et al (1993) The hot spot hepatobiliary scan in focal nodular hyperplasia. J Nucl Med 34:2105–2110
93. Kotzerke J, Schwarzrock R, Krischek O et al (1989) Technetium-99m DISIDA hepatobiliary agent in diagnosis of hepatocellular carcinoma, adenoma, and focal nodular hyperplasia (letter). J Nucl Med 30:1278–1280
94. Barwick KW, Rosai J (1996) Liver (non-neoplastic disease). In: Rosai J (ed) Ackerman's surgical pathology. Mosby-Year Book, St Louis, pp 857–942
95. Lin J, Westerhoff M (2021) Vascular neoplasms of the liver. Clin Liver Dis 17:261–266

96. Brant WE, Floyd JL, Jackson DE et al (1987) The radiological evaluation of hepatic cavernous hemangioma. JAMA 257:2471–2474
97. Kudo M, Ikekubo K, Yamamoto K et al (1989) Distinction between hemangioma of the liver and hepatocellular carcinoma: value of labeled RBC-SPECT scanning. AJR Am J Roentgenol 152:977–983
98. Ziessman HA, Silverman PM, Patterson J et al (1991) Improved detection of small cavernous hemangiomas of the liver with high-resolution three-headed SPECT. J Nucl Med 32:2086–2091
99. Langsteger W, Lind P, Eber B et al (1989) Diagnosis of hepatic hemangioma with ^{99m}Tc-labeled red cells: single photon emission computed tomography (SPECT) versus planar imaging. Liver 9:288–293
100. Farlow DC, Chapman PR, Gruenewald SM et al (1990) Investigation of focal hepatic lesions: is tomographic red blood cell imaging useful? World J Surg 14:463–467
101. Krause T, Hauenstein K, Studier-Fischer B et al (1993) Improved evaluation of technetium-99m-red blood cell SPECT in hemangioma of the liver. J Nucl Med 34:375–380
102. Bonanno N, Baldari S, Cerrito A et al (1991) Diagnosis of hepatic hemangiomas with $^{99mTc\text{-}labeled}$ red blood cell scanning: value of SPECT. J Nucl Biol Med 35:135–140
103. Moon DH, Lee MH, Yang SK et al (1992) Diagnosis of hepatic hemangioma (HH) with triple-head (3H) high-resolution SPECT. J Nucl Med 33:918(abstract)
104. Birnbaum BA, Weinreb JC, Megibow AJ et al (1990) Definitive diagnosis of hepatic hemangiomas: MR imaging versus Tc-99m-labeled red blood cell SPECT. Radiology 176:95–101
105. Jhuang J-Y, Lin L-W, Hsieh M-S (2011) Adult capillary hemangioma of the liver: case report and literature review. Kaohsiung J Med Sci 27:344–347
106. Swayne LC, Diehl WL, Brown TD et al (1991) False-positive hepatic blood pool scintigraphy in metastatic colon carcinoma. Clin Nucl Med 16: 630–632
107. Hod N, Pour MC, Juven Y, Horne T (2004) "Positive" Tc-99m red blood cell scintigraphy in a patient with hepatic lymphoma. Clin Nucl Med 29:272–274
108. Kim CK (1998) Scintigraphic evaluation of the liver and biliary tract. In: Gazelle SG, Saini S, Mueller PR (eds) Hepatobiliary and pancreatic radiology: imaging and interventions. Thieme, New York, pp 108–153
109. Zheng JG, Yao ZM, Shu CY, Zhang Y, Zhang X (2005) Role of SPECT/CT in diagnosis of hepatic hemangiomas. World J Gastroenterol 11:5336–5341
110. Schillaci O, Danieli R, Manni C, Capoccetti F, Simonetti G (2004) Technetium-99m-labelled red blood cell imaging in the diagnosis of hepatic haemangiomas: the role of SPECT/CT with a hybrid camera. Eur J Nucl Med Mol Imaging 31:1011–1015
111. Siegel A, Mazurek R (1997) Early dynamic SPECT acquisition for the imaging of hepatic hemangiomas utilizing Tc-99m-labeled red blood cells. Clin Nucl Med 22:745–748
112. Khosa F, Khan AN, Eisenberg RL (2011) Hypervascular liver lesions on MRI. AJR Am J Roentgenol 197:W204–W220
113. Kobayashi S, Maruyama H, Okugawa H, Yoshizumi H, Matsutani S, Ebara M et al (2008) Contrast-enhanced US with Levovist for the diagnosis of hepatic hemangioma: time-related changes of enhancement appearance and the hemodynamic background. Hepato-Gastroenterology 55: 1222–1228
114. Kim CK, Worsley WF, Lentle B (1998) Scintigraphic evaluation of tumors of the liver. In: Murray IPC, Ell PJ (eds) Nuclear medicine in clinical diagnosis and treatment, 2nd edn. Churchill Livingstone, London, pp 775–782
115. Tanasescu D, Brachman M, Rigby J et al (1984) Scintigraphic triad in focal nodular hyperplasia. Am J Gastroenterol 79:61–64
116. Welch TJ, Sheedy PF Jr, Johnson CM et al (1985) Focal nodular hyperplasia and hepatic adenoma: comparison of angiography, CT, US, and scintigraphy. Radiology 156:593–595
117. Salvo AF, Schiller A, Athanasoulis C et al (1977) Hepatoadenoma and focal nodular hyperplasia; pitfalls in radiocolloid imaging. Radiology 125: 451–455
118. Lubbers PR, Ros PR, Goodman ZD et al (1987) Accumulation of technetium-99m sulfur colloid by hepatocellular adenoma: scintigraphic-pathologic correlation. AJR Am J Roentgenol 148:1105–1108
119. Schein CJ (1972) Acute cholecystitis. Harper and Row, New York, p 40
120. Jivegard L, Thornell E, Svanvik J (1987) Pathophysiology of acute obstructive cholecystitis: implications for non-operative management. Br J Surg 74:1084–1086
121. Jivegard L, Thornell E, Bjorck S, Svanvik J (1985) The effects of morphine and enkephaline on gallbladder function in experimental cholecystitis. Inhibition of inflammatory gallbladder secretion. Scand J Gastroenterol 20:1049–1056
122. Greenberger NJ, Isselbacher KJ (1991) Diseases of the gallbladder and bile ducts. In: Wilson JD, Braunwald E, Isselbacher KJ et al (eds) Harrison's principles of internal medicine, 12th edn. McGraw-Hill, New York, pp 1358–1368
123. Freitas JE (1994) Cholescintigraphy. In: Murray IPC, Ell PJ (eds) Nuclear medicine in clinical diagnosis and treatment. Churchill Livingstone, London, pp 77–86
124. Ziessman HA (2014) Hepatobiliary Scintigraphy in 2014. J Nucl Med Technol 42:249–259
125. Ziessman HA (2010) Nuclear medicine hepatobiliary imaging. Clin Gastroenterol Hepatol 8:111–116
126. Kumar V, Abbas A, Aster JC (2014) Robbins and Cotzan, pathologic basis of disease, 9th edn. Saunders, Philadelphia

127. Shea JA, Berlin JA, Escarce JJ et al (1994) Revised estimates of diagnostic test sensitivity and specificity in suspected biliary tract disease. Arch Intern Med 154:2573–2581
128. Ziessman HA (2003) Acute cholecystitis, biliary obstruction and biliary leakage. Semin Nucl Med 38:279–296
129. Kiewiet JJ, Leeuwenburgh MM, Bipat S, Bossuyt PM, Stoker J, Boermeester MA (2012) A systematic review and meta-analysis of diagnostic performance of imaging in acute cholecystitis. Radiology 264:708–720
130. Colletti PM, Cirimelli KM, Radin DR et al (1989) Radionuclide angiography in suspected acute cholecystitis: further observations. Clin Nucl Med 14:867–873
131. Brachman MB, Goodman MD, Waxman AD (1993) The rim sign in acute cholecystitis. Comparison of radionuclide, surgical, and pathologic findings. Clin Nucl Med 18:863–866
132. Nahrwold DL (1991) Chronic cholecystitis and cholelithiasis. In: Sabiston DC (ed) Textbook of surgery, 14th edn. Saunders, Philadelphia, pp 1057–1063
133. Weedon D (1984) Pathology of the gallbladder. Masson, New York
134. Bolen G, Javitt NB (1982) Biliary dyskinesia: mechanisms and management. Hosp Pract 17:115–130
135. Misra DC Jr, Blossom GB, Fink-Bennett D et al (1991) Results of surgical therapy for biliary dyskinesia. Arch Surg 126:957–960
136. Hogan WJ, Geenen JE (1988) Biliarydyskinesia. Endoscopy 20:179–183
137. Coelho JC, Wiederkehr JC (1996) Motility of Oddi's sphincter: recent developments and clinical applications. Am J Surg 172:48–51
138. Sostre S, Kalloo AN, Spiegler EJ et al (1992) A noninvasive test of sphincter of Oddi dysfunction in postcholecystectomy patients: the scintigraphic score. J Nucl Med 33:1216–1222
139. Ziessman HA (1992) Atlas of cholescintigraphy: selective update. In: Ziessman HA, Van Nostrand D (eds) Selected atlas of gastrointestinal scintigraphy. Springer, Berlin, pp 1–34
140. Fink-Bennett D (1991) Augmented cholescintigraphy: its roles in detecting acute and chronic disorders of the hepatobiliary tree. Semin Nucl Med 21:128–139
141. Madacsy L, Velosy B, Lonovics J et al (1994) Differentiation between organic stenosis and functional dyskinesia of the sphincter of Oddi with amyl nitrite-augmented quantitative hepatobiliary scintigraphy. Eur J Nucl Med 21:203–208
142. Freeman LM, Sugarman LA, Weissmann HS (1981) Role of cholecystokinetic agents in ^{99m}Tc-IDA cholescintigraphy. Semin Nucl Med 11:186–193
143. Fink-Bennett D, DeRidder P, Kolozsi WZ et al (1991) Cholecystokinin cholescintigraphy: detection of abnormal gallbladder motor function in patients with chronic acalculous gallbladder disease. J Nucl Med 32:1695–1699
144. Halverson JD, Garner BA, Siegel BA et al (1992) The use of hepatobiliary scintigraphy in patients with acalculous biliary colic. Arch Intern Med 152:1305–1307
145. Reed DN Jr, Fernandez M, Hicks RD (1993) Kinevac-assisted cholescintigraphy as an accurate predictor of chronic acalculous gallbladder disease and the likelihood of symptom relief with cholecystectomy. Am Surg 5:273–277
146. Zech ER, Simmons LB, Kendrick RR et al (1991) Cholecystokinin enhanced hepatobiliary scanning with ejection fraction calculation as an indicator of disease of the gallbladder. Surg Gynecol Obstet 17:21–24
147. Ziessman HA, Fahey FH, Hixson DJ (1992) Calculation of a gallbladder ejection fraction: advantage of continuous sincalide infusion over the three-minute infusion method. J Nucl Med 33:537–541
148. Kim CK, Worsley DF, Machac J (1996) Interventions in gastrointerventional nuclear medicine. In: Freeman LM (ed) Nuclear medicine annual. Raven, New York, pp 213–257
149. Ziessman HA, Muenz LR, Agarwal AK, ZaZa AA (2001) Normal values for sincalidecholescintigraphy: comparison of two methods. Radiology 221:404–410
150. DiBaise JK, Richmond BK, Ziessman HH, Everson GT, Fanelli RD, Maurer A, Ouyang A, Shamamian P, Simons RJ, Wall LA, Weida TJ, Tulchinsky M (2011) Cholecystokinin-cholescintigraphy in adults: consensus recommendations of an interdisciplinary panel. Clin Gastroenterol Hepatol 9:376–384
151. Fisher RS, Rock E, Malmud LS (1987) Effects of meal composition on gallbladder and gastric emptying in man. Dig Dis Sci 32:337–344
152. Maton PN, Selden AC, Fitzpatrick ML, Chadwick VS (1985) Defective gallbladder emptying and cholecystokinin release in celiac disease: reversal by gluten-free diet. Gastroenterology 88:391–396
153. Masclee AAM, Jansen JBMJ, Corstens FHM, Lamers CBHW (1989) Reversible gallbladder dysfunction in severe pancreatic insufficiency. Gut 30:866–872
154. Masclee AA, Jansen JB, Driessen WM, Geuskens LM, Lamers CB (1991) Gallbladder sensitivity to cholecystokinin in coeliac disease. Correlation of gallbladder contraction with plasma cholecystokinin-like immunoreactivity during infusion of cerulein. Scand J Gastroenterol 26:1279–1284
155. Oster-Jorgensen E, Qvist N, Pedersen SA, Rasmussen L, Hovendal CP (1992) Postprandial gallbladder emptying is related to intestinal motility at the time of meal ingestion. Scand J Gastroenterol 27:699–702
156. Brugge WR (1991) Motor function of the gallbladder: measurement and clinical significance. Semin Roentgenol 16:226–231
157. Kloiber R, Molnar CP, Shaffer EA (1992) Chronic biliary-type pain in the absence of gallstones: the value of cholecystokinin cholescintigraphy. AJR Am J Roentgenol 159:509–513

158. Torsoli A, Corazziari E, Habib FI, Cicala M (1990) Pressure relationships within the human bile tract. Normal and abnormal physiology. Scand J Gastroenterol Suppl 175:52–57
159. Murphy P, Solomon J, Roseman DL (1980) Narcotic anesthetic drugs: their effect on biliary dynamics. Arch Surg 115:710–711
160. Dedrick DF, Tanner WW, Bushkin FL (1980) Common bile duct pressure during enflurane anesthesia: effects of morphine and subsequent naloxone. Arch Surg 115:820–821
161. Chen CC, Holder LE, Maunoury C et al (1997) Morphine augmentation increases gallbladder visualization in patients pretreated with cholecystokinin. J Nucl Med 38:644–647
162. Kim CK, Goyal M, San Pedro E et al (1995) The effect of CCK pretreatment on gallbladder visualization on delayed or morphine-augmented imaging (abstract). J Nucl Med 36:74
163. Klingensmith WC (1988) Hepatobiliary imaging: normal appearance and normal variations. In: Gottschalk A, Hoffer PB, Potchen J (eds) Diagnostic nuclear medicine. Williams and Wilkins, Baltimore, pp 575–581
164. Kim CK, Palestro CJ, Solomon RW et al (1990) Delayed biliary-to-bowel transit in cholescintigraphy after cholecystokinin treatment. Radiology 176:553–556
165. Oates E, Achong DM (1992) Incidence and significance of enterogastric reflux during morphine-augmented cholescintigraphy. Clin Nucl Med 17:926–928
166. Shih WJ, Lee JK, Magoun S et al (1995) Morphine-augmented cholescintigraphy enhances duodenogastric reflux. Ann Nucl Med 9:225–228
167. Zeman RK, Lee C, Jaffe MH et al (1984) Hepatobiliary scintigraphy and sonography in early biliary obstruction. Radiology 153:793–798
168. Miller DR, Egbert RM, Braunstein P (1984) Comparison of ultrasound and hepatobiliary imaging in the early detection of acute total common bile duct obstruction. Arch Surg 119:1233–1237
169. Juni JE, Reichle R (1990) Measurement of hepatocellular function with deconvolutional analysis: application in the differential diagnosis of acute jaundice. Radiology 177:171–175
170. Lieberman DA, Brown PH, Krishnamurthy GT (1990) Improved scintigraphic assessment of severe cholestasis with the hepatic extraction fraction. Dig Dis Sci 35:1385–1390
171. Balistreri WF, Grand R, Hoofnagle JH et al (1996) Biliary atresia: current concepts and research directions. Summary of a symposium. Hepatology 23:1682–1692
172. Bezerra JA, Tiao G, Ryckman FC et al (2002) Genetic induction of proinflammatory immunity in children with biliary atresia. Lancet 360(9346):1653–1659
173. Perlmutter DH, Shepherd RW (2002) Extrahepatic biliary atresia: a disease or a phenotype? Hepatology 35(6):1297–1304
174. Miyano T, Fujimoto T, Ohya T, Shimomura H (1993) Current concept of the treatment of biliary atresia. World J Surg 17:332–336
175. McEvoy CF, Suchy FJ (1996) Biliary tract disease in children. Pediatr Clin N Am 43:75–98
176. Kasai M, Suzuki K, Ohashi E et al (1978) Technique and results of operative management of biliary atresia. World J Surg 2:571–580
177. Gerhold JP, Klingensmith WC III, Kuni CC et al (1983) Diagnosis of biliary atresia with radionuclide hepatobiliary imaging. Radiology 146:499–504
178. Spivak W, Sarkar S, Winter D et al (1987) Diagnostic utility of hepatobiliary scintigraphy with 99mTc-DISIDA in neonatal cholestasis. J Pediatr 110:855–861
179. Ben-Haim S, Seabold JE, Kao SC et al (1995) Utility of Tc-99m mebrofenin scintigraphy in the assessment of infantile jaundice. Clin Nucl Med 20:153–163
180. Cox KL, Stadalnik RC, McGahan JP et al (1987) Hepatobiliary scintigraphy with technetium-99m disofenin in the evaluation of neonatal cholestasis. J Pediatr Gastroenterol Nutr 6:885–891
181. Howman-Giles R, Moase A, Gaskin K, Uren R (1993) Hepatobiliary scintigraphy in a pediatric population: determination of hepatic extraction fraction by deconvolution analysis. J Nucl Med 34: 214–221
182. Howman-Giles R, Uren R, Bernard E, Dorney S (1998) Hepatobiliary scintigraphy in infancy. J Nucl Med 39:311–319
183. Majd M, Reba RC, Altman RP (1981) Effect of phenobarbital on ^{99m}Tc-IDA scintigraphy in the evaluation of neonatal jaundice. Semin Nucl Med 11:194–204
184. Balistreri WF (1985) Neonatal cholestasis. J Pediatr 106:171–184
185. Larrosa-Haro A, Caro-Lopez AM, Coello-Ramirez P et al (2001) Duodenal tube test in the diagnosis of biliary atresia. J Pediatr Gastroenterol Nutr 32: 311–315
186. Lin WY, Lin CC, Changlai SP et al (1997) Comparison technetium of Tc-99m disofenin cholescintigraphy with ultrasonography in the differentiation of biliary atresia from other forms of neonatal jaundice. Pediatr Surg Int 12(1):30–33
187. Johnson K, Alton HM, Chapman S (1998) Evaluation of mebrofenin hepatoscintigraphy in neonatal-onset jaundice. Pediatr Radiol 28:937–941
188. Kim CK, Heyman S (1994) Scintigraphic evaluation of liver transplants. In: Murray IPC, Ell PJ (eds) Nuclear medicine in clinical diagnosis and treatment. Churchill Livingstone, London, pp 69–75
189. Rayter Z, Tonge C, Bennett C et al (1991) Ultrasound and HIDA: scanning in evaluating bile leaks after cholecystectomy. Nucl Med Commun 12: 197–202
190. Brugge WR, Rosenberg DJ, Alavi A (1994) Diagnosis of postoperative bile leaks. Am J Gastroenterol 89:2178–2183

191. Walker AT, Shapiro AW, Brooks DC et al (1992) Bile duct disruption and biloma after laparoscopic cholecystectomy: imaging evaluation. AJR Am J Roentgenol 158:785–789
192. Banzo I, Blanco I, Gutierrez-Mendiguchia C, Gomez-Barquin R, Quirce R, Carril JM (1998) Hepatobiliary scintigraphy for the diagnosis of bile leaks produced after T-tube removal in orthotopic liver transplantation. Nucl Med Commun 19:229–236
193. Worsley DF, Kim CK (1994) Hepatic and splenic trauma. In: Murray IPC, Ell PJ (eds) Nuclear medicine in clinical diagnosis and treatment. Churchill Livingstone, London, pp 63–67
194. Trerotola SO, Savader SJ, Lund GB et al (1992) Biliary tract complications following laparoscopic cholecystectomy: imaging and intervention. Radiology 184:195–200
195. Peters JH, Ollila D, Nichols KE et al (1994) Diagnosis and management of bile leaks following laparoscopic cholecystectomy. Surg Laparosc Endosc 4:163–170
196. Rodman CA, Keeffe EB, Lieberman DA et al (1987) Diagnosis of sclerosing cholangitis with technetium 99m-labeled iminodiacetic acid planar and single photon emission computed tomographic scintigraphy. Gastroenterology 92:777–785
197. O'Brien S, Keogan M, Casey M et al (1992) Biliary complications of cystic fibrosis. Gut 33:387–391
198. Colombo C, Castellani MR, Balistreri WF et al (1992) Scintigraphic documentation of an improvement in hepatobiliary excretory function after treatment with ursodeoxycholic acid in patients with cystic fibrosis and associated liver disease. Hepatology 15:677–684
199. Dogan AS, Conway JJ, Lloyd-Till JD (1994) Hepatobiliary scintigraphy in children with cystic fibrosis and liver disease. J Nucl Med 35:432–435
200. O'Connor PJ, Southern KW, Bowler IM et al (1996) The role of hepatobiliary scintigraphy in cystic fibrosis. Hepatology 23:281–287
201. Buscombe JR, Miller RF, Ell PJ (1992) Hepatobiliary scintigraphy in the diagnosis of AIDS-related sclerosing cholangitis. Nucl Med Commun 13: 154–160
202. Quinn D, Pocock N, Freund J et al (1993) Radionuclide hepatobiliary scanning in patients with AIDS-related sclerosing cholangitis. Clin Nucl Med 18:417–422
203. Kim OH, Chung HJ, Choi BG (1995) Imaging of the choledochal cyst. Radiographics 15:69–88
204. Camponovo E, Buck JL, Drane WE (1989) Scintigraphic features of choledochal cyst. J Nucl Med 30:622–628
205. Rosenthall L, Fonseca C, Arzoumanian A et al (1979) ^{99m}Tc-IDA hepatobiliary imaging following upper abdominal surgery. Radiology 130:735–739
206. Zeman RK, Lee C, Stahl RS et al (1982) Ultrasonography and hepatobiliary scintigraphy in the assessment of biliary-enteric anastomoses. Radiology 145:109–115
207. Weissmann HS, Gliedman ML, Wilk PJ et al (1982) Evaluation of the postoperative patient with 99mTc-IDA cholescintigraphy. Semin Nucl Med 12:27–52
208. Belli G, Romano G, Monaco A et al (1988) HIDA scan in the follow-up of biliary-enteric anastomoses. HPB Surg 1:29–32
209. Aigner RM, Fueger GF, Schimpl G, Sauer H, Nicoletti R (1997) Cholescintigraphy in the evaluation of bile flow after Roux-en-Y hepatico-jejunostomy and hepatico-antrostomy in infants with choledochal cysts. Pediatr Radiol 27:850–854
210. Lucas MH, Elgazzar AH, Cummings DD (1995) Positional biliary stasis: scintigraphic findings following biliary-enteric bypass surgery. J Nucl Med 36:104–106

Central Nervous System

11

James M. Mountz

11.1 Introduction

In this chapter, we present a review of the anatomy, physiology, and pathophysiology of the brain. This will lay the groundwork for a more in-depth presentation of the physiological basis for use of nuclear medicine methods in disease diagnosis and therapy management. This will be discussed in the context of radiopharmaceuticals commonly used to diagnose brain diseases. The specific patterns of radiotracer distribution as seen in nuclear scintigraphy will be correlated with the pathophysiology of the disease process. The different scintigraphic techniques will be reviewed to be followed by relevant clinical applications.

11.2 Anatomic and Physiologic Considerations

11.2.1 Anatomy

The central nervous system consists of the brain and the spinal cord. The major anatomic divisions of the brain are the cerebrum and the cerebellum, together weighing about 1400 g in the adult. Brain cells are classified as glia or neurons. About 10,000 different types of neurons totaling approximately 100 billion neurons comprise the human brain. The cerebral cortex consists of two hemispheres connected by a large mass of white matter called the corpus callosum. The surface layer of each hemisphere is folded into gyri comprising the gray matter. The brain is divided into functional areas called the frontal lobe (anterior to the central sulcus) and the parietal lobe (posterior to this sulcus). The occipital lobe lies below the parieto-occipital sulcus, and the temporal lobe is situated below the lateral sulcus (Figs. 11.1 and 11.2).

Knowledge of cross-sectional anatomy of the brain (Figs. 11.3, 11.4, and 11.5) is a prerequisite for proper interpretation of brain imaging since tomographic imaging is the rule in current functional neuroimaging. The interpretation of brain SPECT and PET studies depends on a background of neuroanatomy which with current techniques allows co-registration of MRI and CT with the functional SPECT and PET images (Figs. 11.3, 11.4, and 11.5).

11.2.2 Physiology

11.2.2.1 Perfusion

Blood flow utilization by neurons is primarily related to synaptic activity at the neuron cell body; thus, gray matter requires about four times

J. M. Mountz (✉)
Division of Nuclear Medicine, Department of Radiology, The University of Pittsburgh Medical Center, Pittsburgh, PA, USA
e-mail: mountzjm@upmc.edu

A. H. Elgazzar (ed.), *The Pathophysiologic Basis of Nuclear Medicine*,
https://doi.org/10.1007/978-3-030-96252-4_11

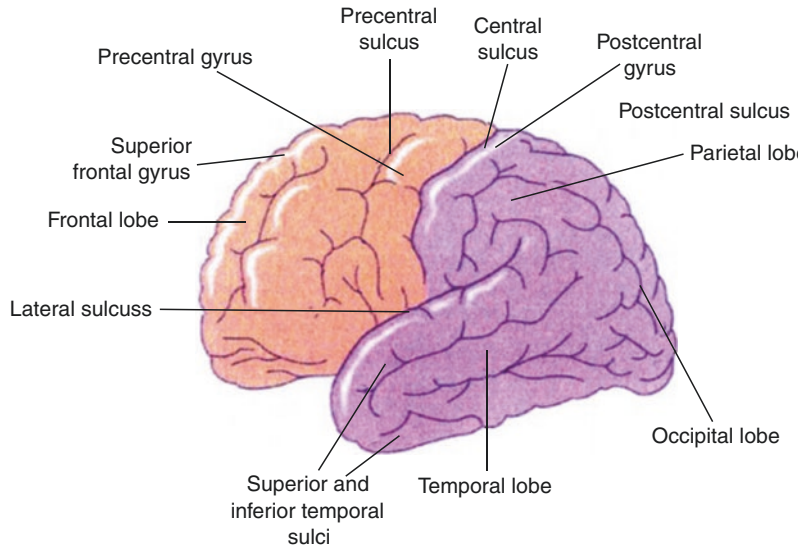

Fig. 11.1 Diagram of the lateral surface of the brain illustrating its main anatomic features

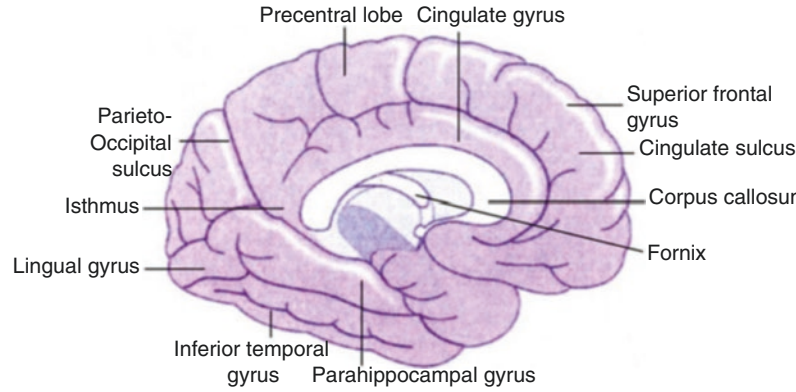

Fig. 11.2 Diagram of the brain illustrating the main internal structures

as much blood flow as white matter. In the normal brain, the overall determinant of regional cerebral blood flow (rCBF) is dependent on vascular integrity, cerebral anatomy, and cerebral function. Since diseases of the brain can disrupt one or more of these functions, for accurate diagnosis it is important to integrate these three physiological functions with the pattern of rCBF change from normal to arrive at an accurate diagnosis of disease. Perfusion changes noted with SPECT radiotracers are appreciated due to the differences in the cortical gray to white matter perfusion related to the large amount of neurons in the cortex. Coupling of perfusion and metabolism provides functional information regarding the state of the patient during tracer injection with ^{99m}Tc-HMPAO and ^{99m}Tc-ethyl cysteinate dimer (ECD).

11.2.2.2 Metabolism

In the brain, glucose metabolism provides approximately 95% of adenosine triphosphate (ATP) required for brain function. Under normal physiological conditions, glucose metabolism is tightly connected to neuronal activity. ^{18}F-FDG is an analog of glucose and is taken up by living cells via the normal glucose pathway. ^{18}F-FDG is suitable for imaging regional cerebral glucose consumption with PET since it accumulates in neuronal tissue depending on facilitated transport of glucose and hexokinase-mediated phosphorylation. The rationale behind its use as a tracer for cancer diagnosis depends on an increased glycolytic activity in neoplastic cells. The cell alterations related to neoplastic transformation are associated with functional impairments that are discernible before structural alterations occur.

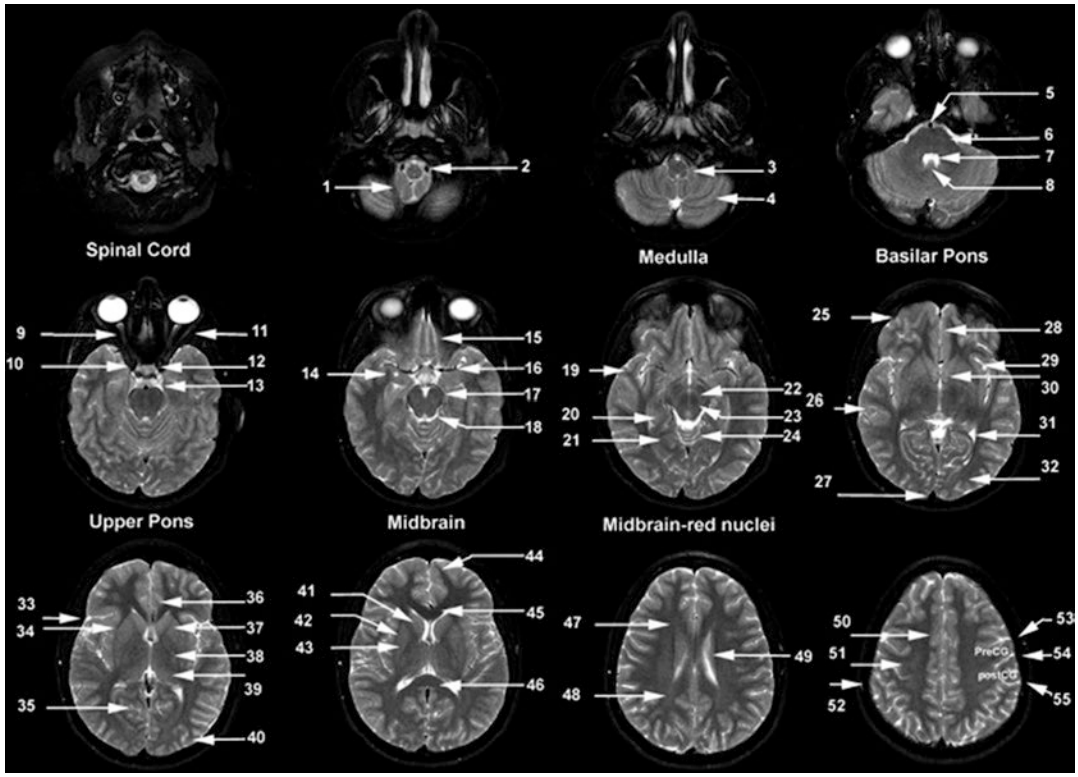

Fig. 11.3 Axial T2-weighted MR images. (*1*) Cerebellar tonsil, (*2*) vertebral artery, (*3*) medulla, (*4*) cerebellar hemisphere, (*5*) basilar artery, (*6*) pons, (*7*) 4th ventricle, (*8*) uvula, (*9*) optic nerve, (*10*) internal carotid artery siphon, (*11*) lateral rectus muscle, (*12*) pituitary gland, (*13*) ambient cistern, (*14*) amygdala, (*15*) gyrus rectus, (*16*) middle cerebral artery, (*17*) posterior cerebral artery, (*18*) mesencephalic cistern, (*19*) temporal pole, (*20*) hippocampus, (*21*) parahippocampal gyrus, (*22*) substantia nigra, (*23*) red nucleus, (*24*) cerebellar vermis, (*25*) frontal lobe, (*26*) temporal lobe, (*27*) superior sagittal sinus, (*28*) gyrus rectus, (*29*) insular cortex, (*30*) anterior commissure, (*31*) posterior horn lateral ventricle, (*32*) occipital lobe, (*33*) Sylvian fissure, (*34*) external capsule, (*35*) calcarine sulcus, (*36*) cingulate gyrus, (*37*) anterior limb of the internal capsule, (*38*) posterior limb of the internal capsule, (*39*) thalamus, (*40*) occipital lobe, (*41*) head of the caudate nucleus, (*42*) putamen, (*43*) globus pallidus, (*44*) frontal pole, (*45*) genu of the corpus callosum, (*46*) splenium of the corpus callosum, (*47*) forceps minor, (*48*) forceps major, (*49*) caudate nucleus, (*50*) cingulate gyrus, (*51*) centrum semiovale, (*52*) calvarial marrow, (*53*) precentral sulcus, (*54*) central sulcus, (*55*) postcentral sulcus. PreCG, precentral gyrus; PostCG, postcentral gyrus

Therefore, changes in neuronal activity induced by disease are reflected in an alteration of glucose metabolism.

^{18}F-FDG PET is currently the most accurate *in vivo* method for the investigation of regional human brain metabolism in health and disease states, when conventional morphologic diagnostic modalities (i.e., CT, MRI) do not yet detect any evident for lesions.

11.3 Pathophysiology of Relevant Diseases

11.3.1 Cerebrovascular Disease

Stroke is the third leading cause of death (~1 in 17 deaths) and the most expensive form of disability in the United States [1]. Disruption in blood flow usually results in transient ischemic

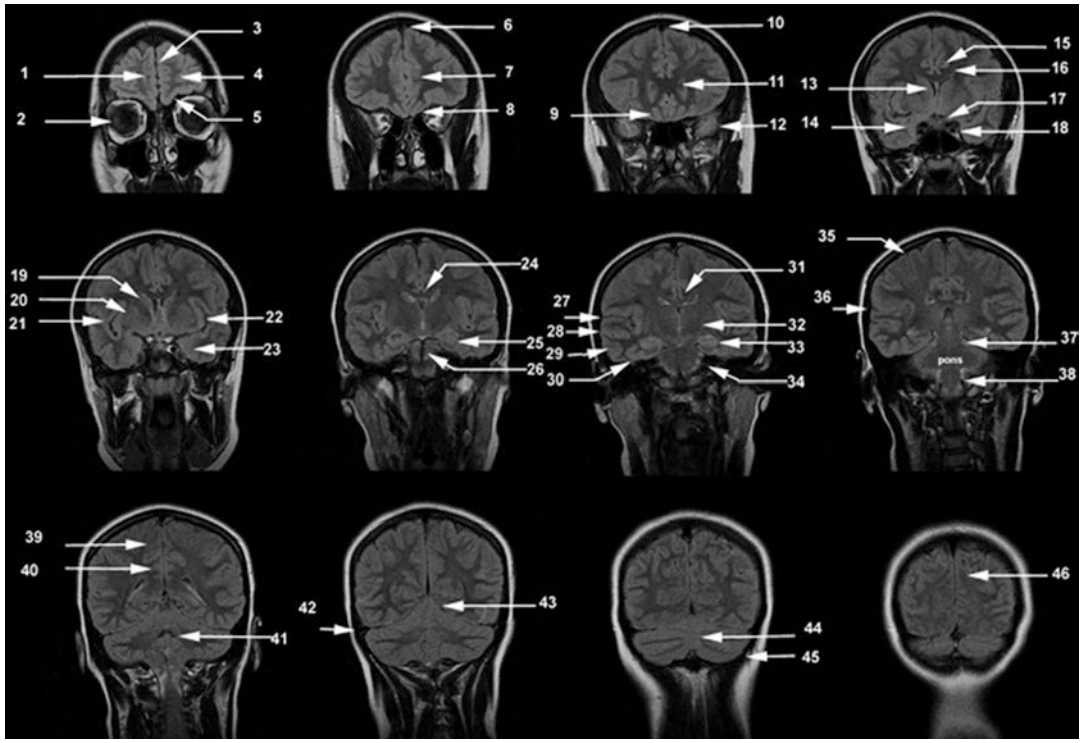

Fig. 11.4 Coronal FLAIR MR images. (*1*) Superior frontal gyrus, (*2*) orbit, (*3*) interhemispheric fissure, (*4*) frontal pole, (*5*) orbital gyrus, (*6*) superior sagittal sinus, (*7*) cingulate gyrus, (*8*, *9*) gyrus rectus, (*10*) superior sagittal sinus, (*11*) genu of the corpus callosum, (*12*) temporal pole, (*13*) anterior horn lateral ventricle, (*14*) mesial temporal lobe, (*15*) cingulate gyrus, (*16*) corpus callosum, (*17*) optic nerve, (*18*) cavernous sinus, (*19*) head of the caudate nucleus, (*20*) lenticular nucleus, (*21*) Sylvian fissure, (*22*) insular cortex, (*23*) amygdala, (*24*) corpus callosum, (*25*) hippocampus, (*26*) basilar artery, (*27*) Sylvian fissure, (*28*) superior temporal gyrus, (*29*) middle temporal gyrus, (*30*) inferior temporal gyrus, (*31*) cingulate gyrus, (*32*) thalamus, (*33*) parahippocampal gyrus, (*34*) vestibulocochlear nerve, (*35*) central sulcus, (*36*) Sylvian fissure, (*37*) mesencephalon, (*38*) medulla, (*39*) paracentral lobule, (*40*) cingulate gyrus, (*41*) 4th ventricle, (*42*) transverse sinus, (*43*), tentorium (*44*) cerebellar vermis, (*45*) cerebellar hemisphere, (*46*) cuneus

episode or a stroke. The pathologic mechanism is most often thrombotic or embolic (87%), but arterial occlusion by atheromatous disease combined with the lowering of systemic arterial blood pressure could also produce "hemodynamic" stroke; alternatively, cerebrovascular compromise results from intraparenchymal (10%) and/or subarachnoid (3%) hemorrhage with acute effects because of blood and/or elevated intracranial pressure and delayed effects because of ischemic deficits from cerebral vasospasm (CVS) [2].

Through early studies with ^{15}O-water PET [3, 4], hypoperfusion to the brain was classified into three stages: irreversible cerebral infarction occurring with cerebral blood flow (CBF) <7–12 mL/100 g/min (ischemic core), abnormally functioning but viable tissue with the potential for recovery or progression to infarction with CBF <20 mL/100 g/min but above the infarction threshold (penumbra), and mildly hypoperfused but otherwise normally functioning and not at-risk tissue with CBF >20–22 (oligemia; normal CBF is 50–55 mL/100 g/min) [5]. The infarction rCBF threshold allowed the prediction of tissue necrosis in a probabilistic way, while the fate of penumbral tissue depends on events after the scan, namely, early reperfusion or not. Viability additionally required regional metabolic rate of oxygen >1.3 mL/100 g/min [2–4]. Thus, the brain distal to a vascular occlusion could remain viable, with relatively preserved cerebral metabolic rate of oxygen ($CMRO_2$), through compensatory

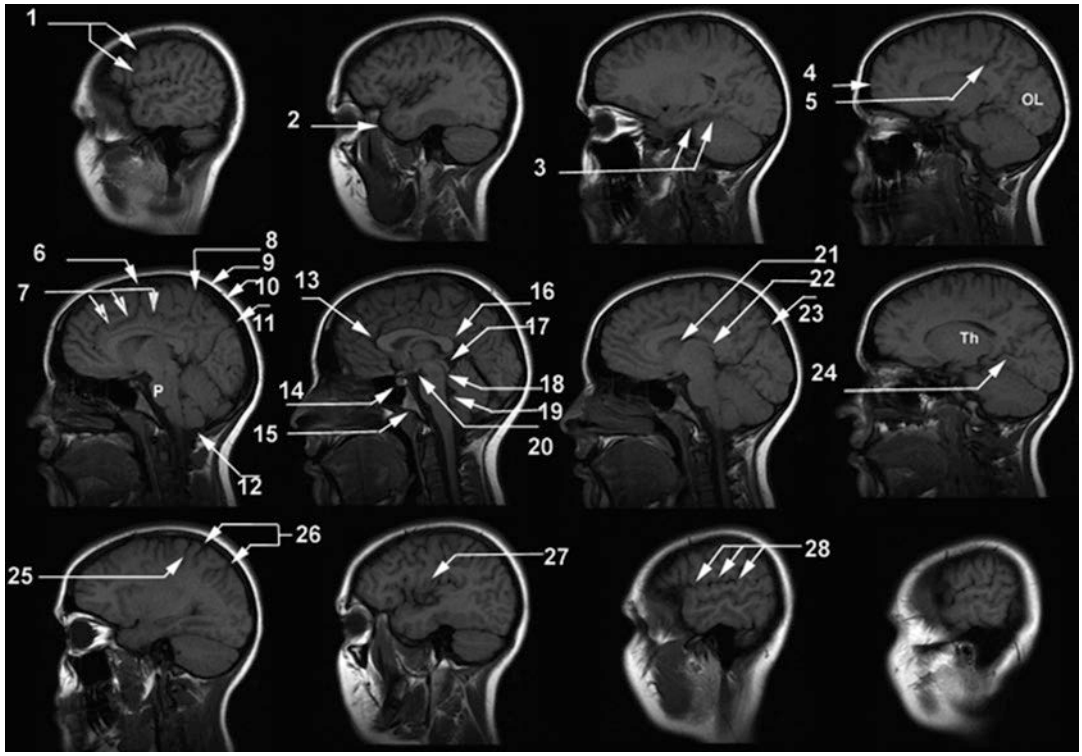

Fig. 11.5 Sagittal T1-weighted MR images. (*1*) Central sulcus, (*2*) temporal pole, (*3*) parahippocampal gyrus, (*4*) frontal pole, (*5*) ascending branch of cingulate sulcus, (*6*) paracentral sulcus, (*7*) cingulate sulcus, (*8*) ascending branch of cingulate sulcus, (*9*) scalp, (*10*) calvarium, (*11*) superior sagittal sinus, (*12*) cerebellar tonsil, (*13*) genu of the corpus callosum, (*14*) pituitary gland, (*15*) clivus, (*16*) splenium of the corpus callosum, (*17*) tectal plate, (*18*) aqueduct of the 3rd ventricle, (*19*) 4th ventricle, (*20*) mammillary body, (*21*) head of the caudate nucleus, (*22*) thalamus, (*23*) parieto-occipital sulcus, (*24*) calcarine sulcus, (*25*) central sulcus, (*26*) postcentral sulcus, (*27*) insular cortex, (*28*) Sylvian fissure. *OL* occipital lobe, *P* pons, *Th* thalamus

increase in oxygen extraction fraction (misery perfusion) [3, 4, 6, 7], or conversely, infarcted brain could demonstrate relative or absolute increase in rCBF with low oxygen extraction fraction (OEF) secondary to delayed reperfusion (luxury perfusion) [8–11].

11.3.2 Dementia

Approximately 3–4% of the adult population in the United States demonstrates significant cognitive impairment. In general, the causes of dementia include primary neurodegenerative disorders with the most prevalent being Alzheimer's disease, followed by frontotemporal dementia, Lewy body dementia, parkinsonian dementia, progressive supranuclear palsy, Pick's disease, cortical basilar degeneration, Huntington's disease, and Wilson's disease [12]. Vascular dementias are categorized as multi-infarct, Binswanger's, cerebral autosomal dominant arteriopathy with subcortical infarctions, and leukoencephalopathy. Inflammatory etiologies include multiple sclerosis and vasculitis. Infectious etiologies include syphilis, human immunodeficiency virus (HIV), Lyme disease, and other viral diseases and fungal diseases. Cancers are a rare cause of dementia which can be attributed to primary result of the disease, metastatic disease to the brain, and perineoplastic syndromes. Other causes and physical abnormalities include trauma and hydrocephalus.

The prevalence of dementia in the population increases significantly with age, with approximately 13% of the population having dementia in

the 77–84-year-old range, and almost 50% in the population 95 years and older. With the increasing age of the population of the United States, dementia is expected to be a significant healthcare problem. It has been documented [13] that approximately 80% of all dementias are attributable to Alzheimer's disease or Lewy body dementia. Vascular dementia comprises approximately 18% of the dementias, with the other dementias comprising approximately 5.5%.

11.3.2.1 Alzheimer's Disease (AD)

Alzheimer's disease (AD) is the most common cause of dementia in patients over 65 years of age. It causes approximately 50–60% of all dementias, followed by dementia with Lewy bodies (DLB) and frontotemporal dementia (FTD) [14]. Approximately 27 million individuals are diagnosed with AD worldwide, a number that is estimated to quadruple by 2050, meaning 1 in 85 people will be affected [15, 16].

Alzheimer's disease was first described by Alois Alzheimer in 1906 as an unusual disease of the cerebral cortex in a 51-year-old woman named Auguste Deter. Her symptomatology included presenile dementia with memory loss, disorientation, hallucinations, and ultimately death by the age of 55. The autopsy showed classic neuropathological changes as senile plaques and neurofibrillary tangles. He also described a granulovascular degeneration and amyloid angiopathy. The diagnosis of Alzheimer's disease has traditionally been through the NINCDS/ADRDA criteria [17]. In these clinical criteria, dementia is established by clinical examination and documented by the mini-mental test or Blessed Dementia Scale and confirmed by a neuropsychological examination. Alzheimer's dementia requires cognitive deficits in two or more areas, with progressive worsening of memory and other cognitive function. There should be no disturbances in consciousness. The age of onset is typically between the ages of 40 and 90 years, most often after 65 years. In addition, the absence of systemic disorders or other brain diseases are required as these can confound the diagnosis of Alzheimer's disease.

The two basic types of Alzheimer's disease are familial and sporadic. Familial AD (FAD) is a rare form of AD, affecting less than 10% of AD patients. All FAD is early onset, meaning the disease develops before age 65. Apolipoprotein E (APOE) epsilon4 gene dose (i.e., the number of epsilon4 alleles in a person's APOE genotype) is associated with a higher risk of AD and a younger age at dementia onset [18], and correlates with reduced regional hypometabolism in brains of patients with AD. In addition, advanced age, prior head trauma, low educational levels, and gender, with female greater than male predominance, have been associated with an increased risk for Alzheimer's disease.

Previous guidelines for the detection of AD included meeting the Diagnostic and Statistical Manual of Mental Disorders (fourth edition) criteria for dementia, which required an episodic memory disorder and impairment in >1 cognitive domain that interfered with daily life activity or social function. Beyond that, a diagnosis of "probable AD" was essentially a diagnosis of exclusion [16, 19, 20]. The Diagnostic and Statistical Manual of Mental Disorders (fifth edition), released in May 2013, replaces the term dementia with major neurocognitive disorder and mild neurocognitive disorder. For a diagnosis of AD, it requires memory problems and impairment in at least one other cognitive domain interfering with functional independence. For those with Mild Neurocognitive Disorder, AD diagnosis can only be made if the subject additionally tests positive for a mutation in an autosomal dominant AD gene or certain biomarkers. However, for the first time in 27 years, the National Institute on Aging and the Alzheimer's Association established new guidelines for the diagnosis and treatment of dementia. The new guidelines examine the biological changes underlying symptoms of dementia, whereas previous diagnosis relied primarily on neuropsychological evaluation, clinical assessment, and evaluation of family history or reports. Albert et al. [21] described three distinct phases for AD: presymptomatic, mildly symptomatic but predementia, and dementia caused by AD. Furthermore, in

conjunction with clinical evaluation, three biomarkers—cerebrospinal fluid (CSF), magnetic resonance imaging (MRI) volume, and PET—were identified to be useful for diagnosis. The presymptomatic stage marks a preclinical form of AD when biomarker changes indicate the presence of an early stage of a dementia process, but memory loss or other behavioral symptoms are not yet noticeable. At this stage, individuals could potentially benefit from vaccination approaches or other preventive strategies. The mildly symptomatic phase is marked by noticeable cognitive changes that do not necessarily interfere with daily life. The last stage is distinguished by definite memory, cognitive, and behavioral deficits that disrupt daily tasks.

11.3.3 Seizures and Epilepsy

Epilepsy is the most common serious brain disorder in children, occurring in all parts of the world and within every stratum of the population. Through its effects, it exerts a significant physical, psychological, economic, and social toll on children and their caregivers. An epileptic seizure is defined as an excessive burst of abnormally synchronized neuronal activity affecting small or large neuronal networks that results in clinical manifestations that are sudden, transient, and usually brief.

The 1981 International League Against Epilepsy classification dichotomizes seizures into generalized and partial based solely on electroclinical features [22]. Generalized seizures are those that arise from large areas of the cortex in both hemispheres and in which consciousness is invariably impaired from the onset. Generalized seizures are subdivided into multiple categories. Typical absence (petit mal) seizures comprise an abrupt loss of consciousness, often described as a vacant look, and cessation of all motor activity, classically with preservation of tone. The attack ends as abruptly as it started, and previous activity is resumed as if nothing had happened. A myoclonic seizure is a brief contraction of a muscle, muscle group, or several muscle groups due to a cortical discharge. It can be single or repetitive, varying in severity from an almost imperceptible twitch to a severe jerking. Clonic seizures are typically seen in young children and consist of clonic jerking, which is often asymmetric and irregular. Tonic seizures take the form of a tonic muscle contraction with altered consciousness, without a clonic phase. Tonic–clonic (grand mal) seizures are the classic form of epileptic seizure, with altered consciousness followed by tonic extension and then clonic convulsive movements of all four extremities. Atonic seizures may manifest as the classic drop attack, in which all postural tone is suddenly lost, or more subtle changes, such as a slight head drop or bowing at the knees.

Partial seizures are those that arise in specific, often small, loci of the cortex in one hemisphere. They are divided into simple partial seizures, which occur without alteration of consciousness and have motor, sensory, autonomic, or psychic manifestations, and complex partial seizures, in which consciousness is impaired or lost. Either type of partial seizure may evolve into a secondarily generalized seizure. Importantly, from a surgical perspective, partial seizures invariably imply focal brain pathology, although this may not always be readily apparent on investigation.

Medical treatment of a first seizure is controversial, as the recurrence risk of a subsequent seizure is approximately 50%. Antiepileptic drug therapy after the first seizure appears not to alter the long-term prognosis for developing epilepsy, but may reduce the risk for a second seizure. The risk of having a third seizure on the background of two previous events is higher, and for these reasons, most neurologists advocate institution of antiepileptic drug therapy after the second seizure. Clearly, treatment should be individualized, as the recurrence risk is affected by such patient-specific variables as etiology (structural brain abnormalities carry a higher risk), electroencephalography (EEG) findings (spike and wave discharges on the first EEG carry a higher risk), and age (younger patients are at higher risk of recurrence, likely because of the confounding effect of etiology). Other issues such as seizure type, timing, and frequency (impact of seizures on quality of life); the cognitive, behavioral, and psychoso-

cial side effects of antiepileptic drug therapy; and patient compliance with therapy must also be considered.

11.3.4 Brain Tumors

Brain tumors manifest with the subacute or chronic onset of generalized symptoms, such as confusion, headaches, seizures, and nausea or focal symptoms and signs, such as visual field deficit, loss of language, unilateral weakness, sensory neglect, or difficulty walking. There are no symptoms or signs specific to any brain tumor because the anatomic location of the tumor in the brain dictates the presentation. A tissue diagnosis through a biopsy or surgical resection is necessary to confirm the pathology, except in patients with metastatic tumors with a known primary tumor. The differential diagnosis of mass lesions in the brain includes abscess, multiple sclerosis lesions, inflammatory disease, and other infections, such as toxoplasmosis and cysticercosis.

Brain tumors share some features and challenges for diagnosis and therapy with tumors elsewhere in the body, but they also pose specific issues that are related to the unique properties of the organ they sit in. Most of the brain is separated from the blood by the blood–brain barrier (BBB) that exerts a much more restrictive control over substances that are allowed to pass (or may even be subject to facilitate transport) than most other organs.

Brain tumors are categorized as metastatic or primary. The incidence and prevalence of metastatic tumors exceed primary tumors by 4:1. Lung and breast carcinoma make up the majority of metastatic tumors, largely because of the fact of their increased prevalence in the population compared with other tumors. Melanoma is a less prevalent malignancy but has a high propensity to metastasize to the brain. Meningioma is usually a benign tumor that is found most often in the fourth through sixth decade with a female to male ratio of 2:1. Primary central nervous system lymphoma (PCNSL) is a rare tumor that usually affects patients in the sixth decade and older.

Primary brain tumors or gliomas consist of astrocytomas, oligodendrogliomas, and ependymomas in decreasing order of prevalence. It was once thought that these tumors are derived from mutations of normal glial cells, but it is increasingly recognized that gliomas are derived from brain tumor stem cells.

Histologic features of gliomas give them a grade according to the World Health Organization (WHO) system [23].

Grade I glioma (pilocytic astrocytoma) is rarely ever seen in adults. Grade II gliomas are low-grade gliomas (LGG) with subtypes astrocytoma and oligodendroglioma and usually affect patients in the third and fourth decades. They show little cellular atypia and proliferation but frequently infiltrate healthy surrounding brain and, therefore, cannot be cured by surgery or radiotherapy. Despite being lower-grade tumors, LGG are not benign. The natural history is that patients with LGG ultimately progress to HGG. LGG make up about 15% of all primary brain tumors. LGG are more likely to present with seizures than HGG.

Grade III and IV tumors are high-grade gliomas (HGG) and include tumors with gross cellular atypia and necrosis. They are made up predominantly of glioblastoma multiforme (GBM) and anaplastic astrocytoma (AA) (WHO grade III), whereas anaplastic oligodendroglioma and anaplastic ependymoma are less common. Glioblastoma (GBM) is the most malignant glioma and makes up 60–70% of all gliomas.

Symptoms and signs of brain tumor should prompt neuroimaging. Magnetic resonance imaging (MRI) has largely replaced computed tomography (CT) for evaluating brain tumors, although CT serves as a quick screening modality and must be used in patients who have contraindications to MRI. Radiographic features on MRI can predict the type of tumor, but cannot accurately confirm the pathology. MRI and CT rely on blood–brain barrier (BBB) damage (frequent in grades III and IV, absent in grade II) and morphologic appearance (e.g., presence of necrosis, vascularity) for grading. Although this is regarded as largely sufficient in untreated gliomas, it becomes unreliable in treated tumors because BBB dam-

age and necrosis also can result from formation of reactive tissue after therapy. In that situation, imaging methods that distinguish tumor from reactive nonneoplastic tissue will contribute significantly to clinical decision-making. Contrast enhancement also cannot provide proper grading in brain tumors with a constitutive lack of BBB, such as meningiomas and lymphomas. In general, functional measures related to tumor proliferation are expected to deliver more reliable information on prognosis than morphologic imaging methods.

Because of the BBB, many tracers that easily reach tumors in other parts of the body would only reach brain tumors once there is a disruption of the BBB by the brain tumor. Thus, the disruption of the BBB, which can easily be detected on contrast-enhanced magnetic resonance imaging (MRI) and computed tomography (CT), is regarded as the main diagnostic indicator for malignant gliomas, meningiomas, and brain metastases, as well as for some less frequent tumors without an intact BBB.

As a consequence of the exclusion of all radiotracers that cannot pass the BBB from the normal brain, there usually also is a good tumor-to-brain contrast for all tracers with these properties, which historically included ^{99m}Tc-pertechnetate and ^{99m}Tc-diethylene triamine pentaacetic acid and currently also fluorothymidine (^{18}F-FLT) and virtually all labeled macromolecules (although low-capacity slow-specific transfer by receptors has been observed for some). However, the excellent contrast may not indicate much more than the presence of BBB damage, which can readily be seen and even quantified by contrast-enhanced MRI. Therefore, much interest and effort has been invested into the development and evaluation of brain tumor tracers that do not depend on BBB damage, such as fluorodeoxyglucose (^{18}F-FDG) and labeled amino acids, because they are being transferred by large-capacity specific transporters across the intact BBB.

There is a large variation in the response of tumors to therapy by irradiation and cytostatic drugs within tumor types and often even in different areas of the same tumor. However, with morphologic imaging, it is difficult to determine whether a tumor is responding, and only late after completion of therapy, the outcome becomes evident. Especially with chemotherapy, monitoring of therapeutic efficacy is a major goal to modify inefficient therapy before the patient's condition worsens to a degree that reduces any further therapeutic options. Thus, molecular imaging techniques are expected to provide improved outcome parameters for therapy monitoring, which also is relevant for conducting efficient clinical trials of new therapeutics.

11.3.5 Movement Disorders

Parkinson's disease is the most common of the movement disorders, affecting approximately 1.5% of people over 65 years and 2.5% of those over the age of 80. As degeneration occurs in dopaminergic neuron in the substantia nigra, patients exhibit clinical symptoms of resting tremor, rigidity, and bradykinesia. Parkinsonian syndromes are a group of diseases that share similar cardinal signs of parkinsonism.

Although the neurodegenerative condition Parkinson's disease is the most common cause of parkinsonism, numerous other etiologies can lead to a similar set of symptoms, including multiple system atrophy, progressive supranuclear palsy, corticobasal degeneration, drug-induced parkinsonism, vascular parkinsonism, and psychogenic parkinsonism. Essential tremor typically occurs during voluntary movement rather than at rest; however, some patients with essential tremor can demonstrate resting tremor, rigidity, or other isolated parkinsonian features, mimicking other etiologies. Clinical diagnosis of parkinsonism is often straightforward, obviating additional tests in many cases. However, for incomplete syndromes, or an overlap between multiple concurrent conditions, particularly early on, an improvement in diagnostic accuracy may be possible using a test for dopamine transporter (DaT) visualization [24–26].

11.3.6 Hydrocephalus

11.3.6.1 Anatomy and Physiology of Hydrocephalus

CSF is a clear fluid similar to blood plasma. The intracranial and spinal cord structures float in CSF and are protected from jolts and blows. Principally, the choroid plexus in the lateral, third, and fourth ventricles produces the major portion of CSF. Normally, between 125 and 150 mL of CSF is circulating within the ventricles and subarachnoid space at any given time. Approximately 600 mL of CSF is produced daily. The CSF normally drains from the lateral ventricles sequentially through the interventricular foramen of Monro, the third ventricle, and the cerebral aqueduct of Sylvius into the fourth ventricle and then leaves the ventricular system through the median foramen of Magendie and two lateral foramina of Luschka. Here, the CSF enters the subarachnoid space. Along the base of the brain, this space extends into a number of lakes called cisterns. The CSF is absorbed through the pacchionian granulations of the pia-arachnoid villi into the superior sagittal sinus.

The term hydrocephalus generally refers to those conditions that produce an imbalance between the rate of production and absorption of the cerebrospinal fluid, leading to dilatation of the ventricular system. Hydrocephalus normally occurs as a result of obstruction to the flow and absorption of CSF, although there are rare cases of choroid plexus papillomas causing hydrocephalus by the overproduction of CSF.

Hydrocephalus is traditionally classified as communicating and noncommunicating, based on whether ventricular obstruction is present. In the former, the ventricular system continues to communicate with the subarachnoid spaces outside the brain through the fourth ventricular foramina of Luschka and Magendie.

Noncommunicating hydrocephalus correspondingly refers to the presence of occlusion within the ventricular system. Hydrocephalus may be either congenital or acquired. Arnold–Chiari malformation, Dandy–Walker malformations, and aqueductal stenosis/atresia are common causes of the congenital variety. In the acquired type, many pathologic conditions, including inflammatory, infectious, traumatic, and neoplastic disorders, can cause hydrocephalus [27].

11.3.6.2 Pathophysiology of Hydrocephalus

Noncommunicating hydrocephalus can be the result of intraventricular mass, aqueductal obstruction, or fourth ventricular obstruction. Communicating hydrocephalus, on the other hand, results from meningitis, meningeal carcinomatosis, or cerebral dural sinus thrombosis, or it is idiopathic in elderly patients. Normal-pressure hydrocephalus (NPH) is a communicating hydrocephalus of particular interest to nuclear medicine professionals since radionuclide cisternography is useful in its diagnosis and management. In NPH, the usual flow of CSF is impaired somewhere in the intracranial subarachnoid space, resulting in a reversal of CSF flow and dilatation of the lateral ventricles. There is free communication between the ventricular system and the subarachnoid pathways and no elevation of CSF pressure. Clinically, the entity presents as dementia, gait disturbances, and fecal and urinary incontinence. Most commonly, this condition results from subarachnoid hemorrhage or meningoencephalitis.

11.3.6.3 Cerebrospinal Fluid Leakage

Leaking of CSF may be etiologically classified into:

1. Traumatic: occurring in about 30% of basilar skull fractures. Two percent of all head injuries develop a CSF fistula. This leak is usually unilateral, scanty, seen within 48 h after trauma, and resolves in 1 week.
2. Nontraumatic: taking place in tumors (pituitary, brain, skull), skull infections, and congenital defects (encephalocele). This leak is profuse and may persist for years. Infection complicates the untreated leak in 25% of the cases. CSF rhinorrhea may occur anywhere from the frontal sinus to the temporal bone. The cribriform plate is the most susceptible to fracture and rhinorrhea. Otorrhea is much less common [28, 29].

3. Spontaneous intracranial hypotension (SIH). This is an increasingly recognized condition due to CSF leak without apparent prior cause. This condition is recognized now among causes of postural headache, which in this case is secondary to low CSF pressure [30–32].

11.4 Scintigraphic Evaluation of CNS Diseases

11.4.1 Radiopharmaceuticals

There are three main classes of radiopharmaceuticals now available for functional brain imaging in nuclear medicine (1) regional cerebral blood flow, (2) regional cerebral metabolism, and (3) central nervous system receptor binding and other molecularly targeted agents. After intravenous injection, the regional uptake and distribution of radiotracers are measured by single-photon emission computed tomography (SPECT) or positron emission tomography (PET) imaging systems. In this chapter, we describe the most important tracers routinely employed in clinical nuclear medicine practice. More comprehensive descriptions of radiopharmaceuticals for brain imaging have been provided in numerous prior reports [33–35].

SPECT radiopharmaceuticals used for measuring regional cerebral blood flow (rCBF) are lipophilic agents which are transported from the arterial vascular compartment to the normal brain tissue compartment by diffusion and are distributed proportional to regional tissue blood flow. After this first phase of transport, the tracers are essentially irreversibly trapped in the tissue compartment. The two major blood flow agents used in brain SPECT imaging are technetium-99m hexamethylpropylene amine oxime (^{99m}Tc-HMPAO) and Tc-99m ethyl cysteinate dimer (^{99m}Tc-ECD) [36, 37]. Xenon-133 (133Xe) is unique since it is freely diffusible and not trapped in the tissues. Inhaled or IV injection of 133Xe dissolved in saline can more accurately and quantitatively provide measurements of blood flow by determination of the clearance rate of this tracer from the cerebral compartment, after a brief uptake period (Lassen) [38]. The major PET radiopharmaceutical used to measure cerebral perfusion is 15O-water [39].

The second major class of radiopharmaceuticals is those that measure brain metabolism. These radiopharmaceuticals are transported to the brain tissues by regional cerebral blood flow, but subsequent regional cerebral distribution reflects the utilization rate of the tracer in a cerebral metabolic pathway. Currently, there are no SPECT tracers that specifically measure normal cerebral metabolism. However, in brain tumor imaging, where the blood–brain barrier is broken, ionic tracers such as Thallium-201(201Tl) [40] or other SPECT tracers such as ^{99m}Tc-methoxyisobutyl ^{99m}Tc-sestamibi [41] can be used to detect new, recurrent, or residual viable tumor. The PET radiopharmaceutical predominantly used is fluorine-18 2-fluoro-2-deoxy-D-glucose (^{18}F-FDG), [42]. [18F]-fluoro-3′-deoxy-3′-L-fluorothymidine (^{18}F-FLT) is a new tracer used to indicate tumor proliferation to more specifically identify new, recurrent, or residual viable brain tumor. Other tracers being used in research include amino acids and amino acid analog PET tracers like 11C-methionine (^{11}C-MET) and 3,4-dihydroxy-6-^{18}F-fluoro-L-phenylalanine (^{18}F-FDOPA).

The third class of radiotracers important in brain imaging is central nervous system receptor binding agents, which measure neuronal receptor density and binding affinity [26]. In SPECT, a tracer which has been well characterized is 123I-β-CIT. This benzamide compound has been used to image the dopaminergic (D_2) transporter system in the corpus striatum [43]. In the United States, ^{123}I-ioflupane (^{123}I-FP-CIT) SPECT radiotracer dopamine receptor imaging was approved by the Food and Drug Administration on January 2011 and is commercially available. It has now been established as a standard part of diagnostic assessment in movement disorders [44].

Numerous reviews have been published describing PET tracers that have been developed for application in brain PET imaging, primarily for brain receptor studies or metabolic incorporation into essential biochemical pathways [45,

46]. After IV injection, these tracers initially follow first-order kinetics compartmental distribution since their delivery depends on cerebral blood flow. Over time, there is clearance of nonspecific uptake, and the delayed scan reflects specific receptor binding.

11.4.1.1 ^{99m}Tc-Hexamethylpropyleneamine Oxime (^{99m}Tc-HMPAO)

To understand the uptake mechanism of ^{99m}Tc-hexamethylpropyleneamine oxime (^{99m}Tc-HMPAO), a three-compartmental analysis model can be used for analysis [47]. In this model, the first compartment is the lipophilic tracer in the blood pool of the brain, but outside of the blood–brain barrier. The second compartment is consisting of the lipophilic tracer inside of the blood–brain barrier. The third compartment is the hydrophilic form of the tracer that is retained in the brain. Transport from the first compartment to the second compartment represents efflux of lipophilic tracer from the blood compartment to the brain compartment. Back-exchange from the third compartment to the second compartment represents back-diffusion of the lipophilic form of the tracer and is essentially equal to zero since the tracer is irreversibly trapped (by intracellular reaction with glutathione) in the brain. Figure 11.6 shows a normal brain SPECT scan

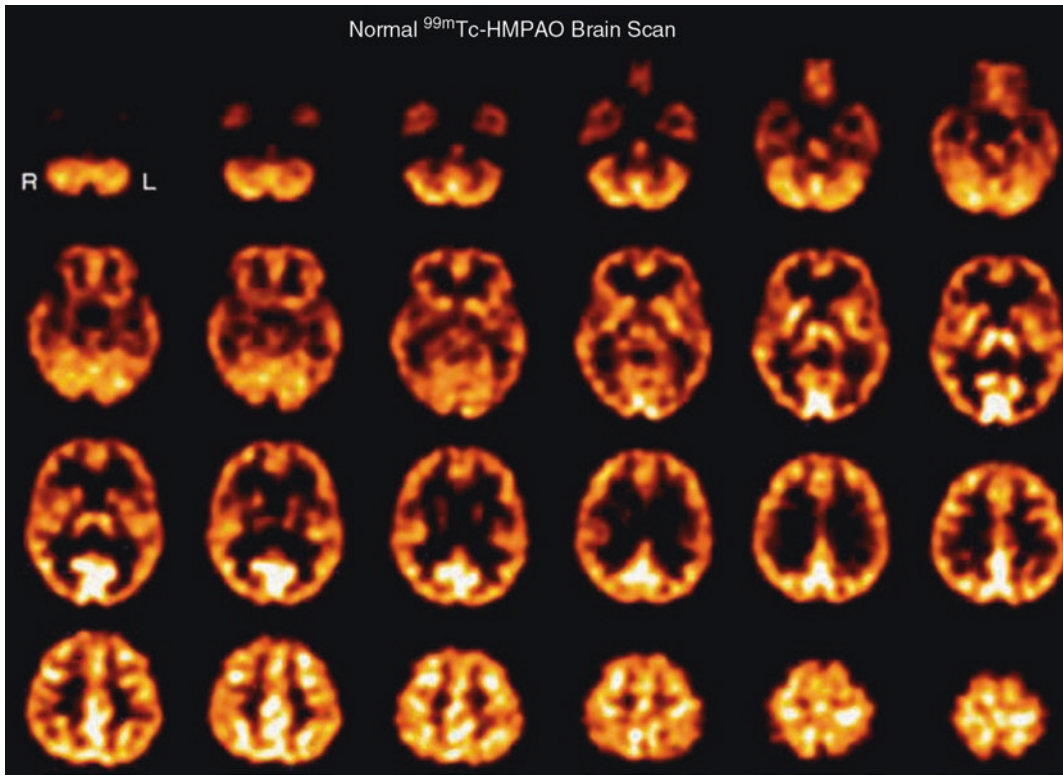

Fig. 11.6 Transverse tomographic images from a normal 42-year-old female subject after injection of 20 mCi ^{99m}Tc-HMPAO. The transverse images are arranged parallel to and sequentially above the canthomeatal line, with the cerebellum at the *top left* and the vertex of the brain at the *bottom right*. The scan slice thickness is 4 mm. The scan resolution is approximately 7-mm full width at half maximum. There is seen to be high uptake of tracer in the cerebellum (*top row*), the thalamus and basal ganglia (*2nd row from top*), and the primary visual cortex (*2nd and 3rd row from top*). There is high uptake in all cortical structures compared to white matter. This is expected since the white matter physiologically has approximately 50% lower blood flow than gray matter. The ventricles in this patient are small, and the central reduction in tracer uptake is almost completely due to lower uptake in the white matter. These differences in uptake bestow the functional scan with anatomic definition

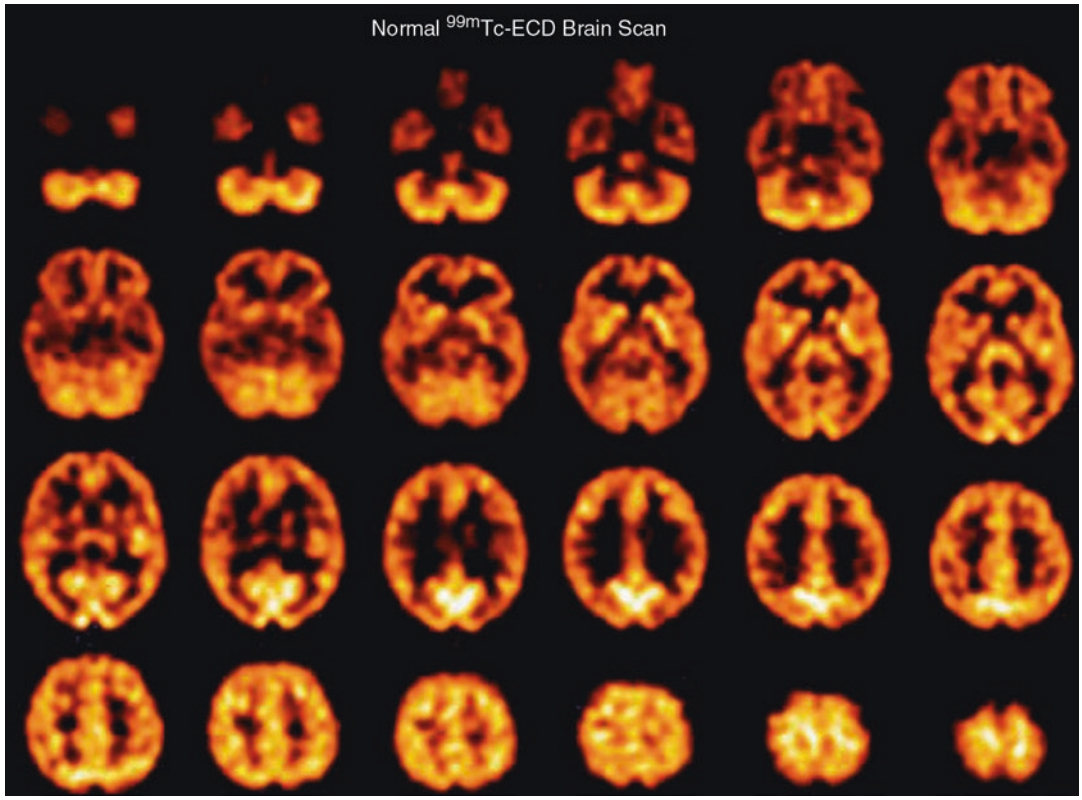

Fig. 11.7 Transverse tomographic images from a normal 41-year-old female subject after injection of 20 mCi ^{99m}Tc-ECD. The transverse images are arranged parallel to and sequentially above the canthomeatal line, with the cerebellum at the *top left* and the vertex of the brain at the *bottom right*. The scan slice thickness is 4 mm. The scan resolution is approximately 7-mm full width at half maximum. While the distribution of ^{99m}Tc-ECD is similar to^{99m}Tc-HMPAO, it is not identical, as described in the text

after injection of 20 mCi (740 MBq) IV of ^{99m}Tc-HMPAO and acquired on a triple-head Picker Prism (Picker International, Cleveland, OH). There is noted to be excellent uptake of this tracer in the gray matter of the brain, and there is clear distinction of small brain structures.

11.4.1.2 Technetium-99m Ethyl Cysteinate Dimer (^{99m}Tc-ECD)

The second tracer commonly used in brain SPECT to measure regional cerebral perfusion is ^{99m}Tc-ECD [48]. This radiopharmaceutical is lipophilic, similar to ^{99m}Tc-HMPAO, and rapidly traverses the endothelium and capillary membranes into the brain cells [49]. However, in the third compartment irreversible trapping mechanism of this tracer differs from ^{99m}Tc-HMPAO, since ^{99m}Tc-ECD is enzymatically metabolized to a polar complex, which is trapped in the brain. This tracer has been reported to demonstrate less nonspecific scalp and facial tissue background activity compared with ^{99m}Tc-HMPAO. Figure 11.7 shows a normal ^{99m}Tc-ECD scan brain SPECT scan after injection of 20 mCi (740 MBq) IV. However, it has been reported that there are differences in regional uptake of these tracers, predominantly in the thalamus and the cerebellum.

This difference in distribution is illustrated by scans from a 42-year-old female normal subject who received both tracers separated by a 48-h time period (Fig. 11.8).

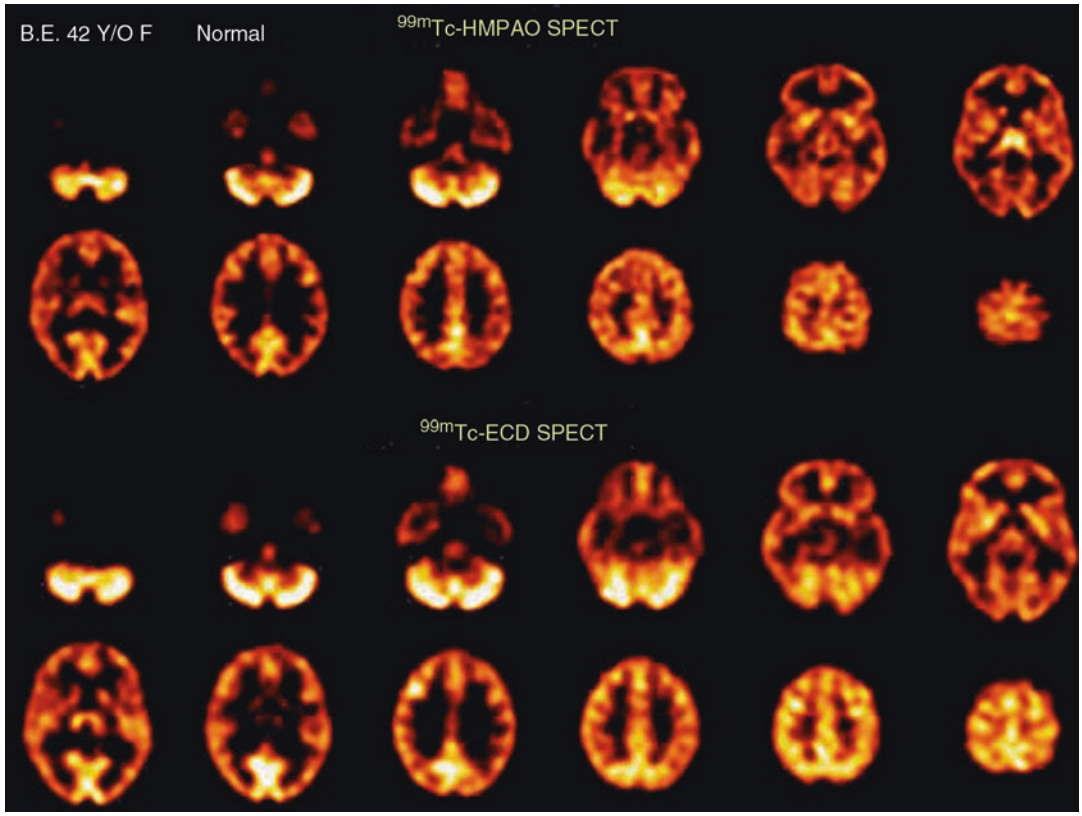

Fig. 11.8 Images of a ^{99m}Tc-HMPAO brain SPECT scan (*top*) compared with a ^{99m}Tc-ECD brain SPECT scan (*bottom*) from a 42-year-old normal female. The ^{99m}Tc-HMPAO SPECT scan was oriented parallel to and sequentially above the canthomeatal line (*rows 1 and 2*). The ^{99m}Tc-ECD brain SPECT scan from the same patient was count normalized and spatially co-registered with the ^{99m}Tc-HMPAO SPECT scan and corresponding sections are displayed in *rows 3* and *4* to facilitate comparison. Each scan section is 8 mm thick. The ^{99m}Tc-HMPAO brain SPECT scan shows increases in tracer uptake in the thalami but less uptake in the parietal and occipital regions, as compared to the ^{99m}Tc-ECD brain SPECT scan

11.4.1.3 ^{133}Xe for Quantitative Regional Cerebral Blood Flow

A recent advancement in brain SPECT imaging has been the development of special software primarily used on the Picker Prism triple-head camera system which allows dynamic scan acquisition (10 s per scan for 7 min). This acquisition results in a total of 42 scans of temporally separated individual tomographic image data sets. This allows calculation of tomographically displayed absolute quantification of regional cerebral perfusion (rCBF) in milliliters per 100 g of tissue per minute [50]. This is possible since the clearance of ^{133}Xe is linearly proportional to the rCBF, and unlike tracers such as ^{99m}Tc-HMPAO or ^{99m}Tc-ECD, ^{133}Xe does not underestimate rCBF due to the limitations on extraction fractions at high cerebral blood flow rates. In our experience, we have found that the 133Xe clearance technique is more sensitive to changes in blood flow during Diamox augmentation of rCBF in the evaluation of hemodynamically significant vascular stenosis and in cases of cortical blood flow changes in brain activation studies. One of the major limitations of 133Xe SPECT is the relatively low

energy of the emission photon resulting in a significant attenuation and loss of spatial resolution of the central structures of the brain. In addition, due to the rapid SPECT acquisition necessary to obtain accurate clearance on a pixel-by-pixel basis, the count rate is low, requiring use of a 64 × 64 matrix, resulting in reduction in spatial resolution throughout the scan.

Dynamic ^{133}Xe SPECT is excellent in assessing large territorial vascular abnormalities due to its ease of quantitation and its ability to detect large major vessel territorial reductions in regional cerebral perfusion. Its utility is exemplified in a study designed to measure cerebrovascular perfusion reserve with rest/stress SPECT brain scans in patients with cerebrovascular disease (CVD) and suffering from TIA undergoing evaluation for extracranial/intracranial (EC/IC) arterial anastomosis or superficial temporal artery (STA)/middle cerebral artery (STA/MCA) bypass to assess and to specifically identify the presence or the absence of a vascular reserve constraint, which has been previously documented to be of value using increased oxygen extraction fraction PET [51]. Figure 11.9 illustrates the imaging results of a 62-year-old female with TIA. The angiogram showed the presence of a 99% left ICA stenosis. The ^{133}Xe SPECT study confirms the presence of hemodynamic vascular reserve constraint due to a high-grade stenosis of the left internal carotid artery.

In a study on nine CVD patients, ^{99m}Tc-HMPAO SPECT was found to be a more specific indicator of hemodynamic constraint since it was asymmetric only in cases of severe ischemia [52]. 133Xe SPECT detected asymmetries, even in the mild ischemic group, and therefore is a more sensitive detector of vascular disease. Because ^{133}Xe SPECT measures absolute rCBF (ml/100 g/min), it has one major advantage (i.e., to measure absolute perfusion) and thus can establish parameters of significant ischemia independent from semi-quantitative asymmetry values.

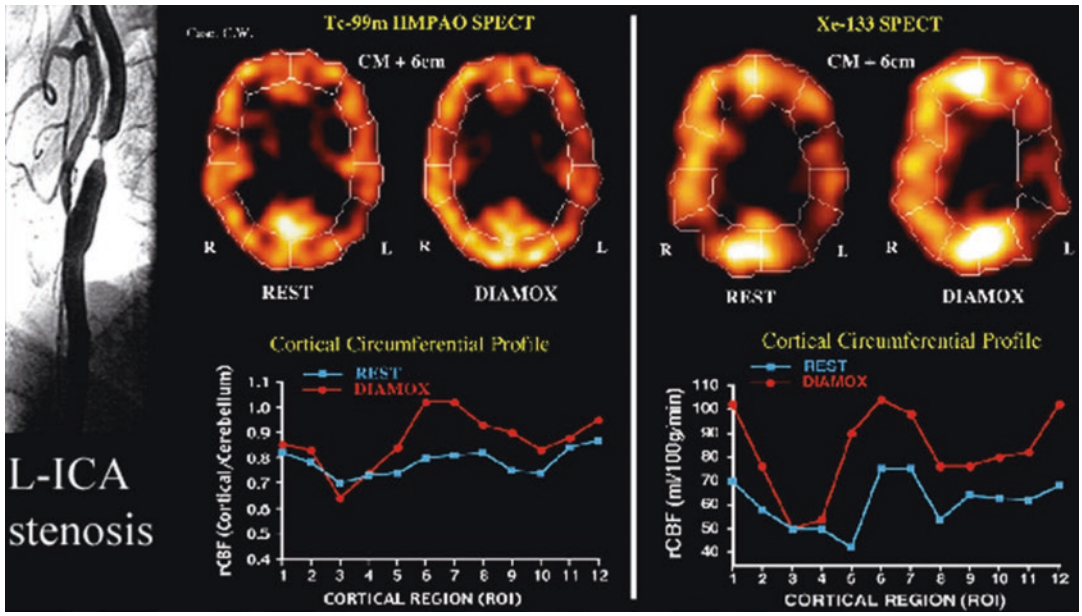

Fig. 11.9 Case of severe ischemia in a 62-year-old female with 99% stenosis of the left ICA (*left*). The resting-state ^{99m}Tc-HMPAO SPECT scan (*middle*) was normal. The post-Diamox ^{99m}Tc-HMPAO SPECT scan (*middle*) showed mild perfusion reduction in the left ICA territory (*middle*). This can be seen on the graphs of rCBF progressing clockwise around the cortex (cortical ROI progressing from 1 o'clock to 12 o'clock) the "circumferential cortical profiles" (regions 3 and 4 shown on the *red graph*). The ^{133}Xe SPECT at rest showed mild vascular compromise (*right*). The post-Diamox ^{133}Xe SPECT showed severe vascular constraint in the left ICA territory (*right*). This can be seen as a more clear reduction compared with the ^{99m}Tc-HMPAO SPECT scan (regions 3 and 4 shown on the circumferential *red graph*)

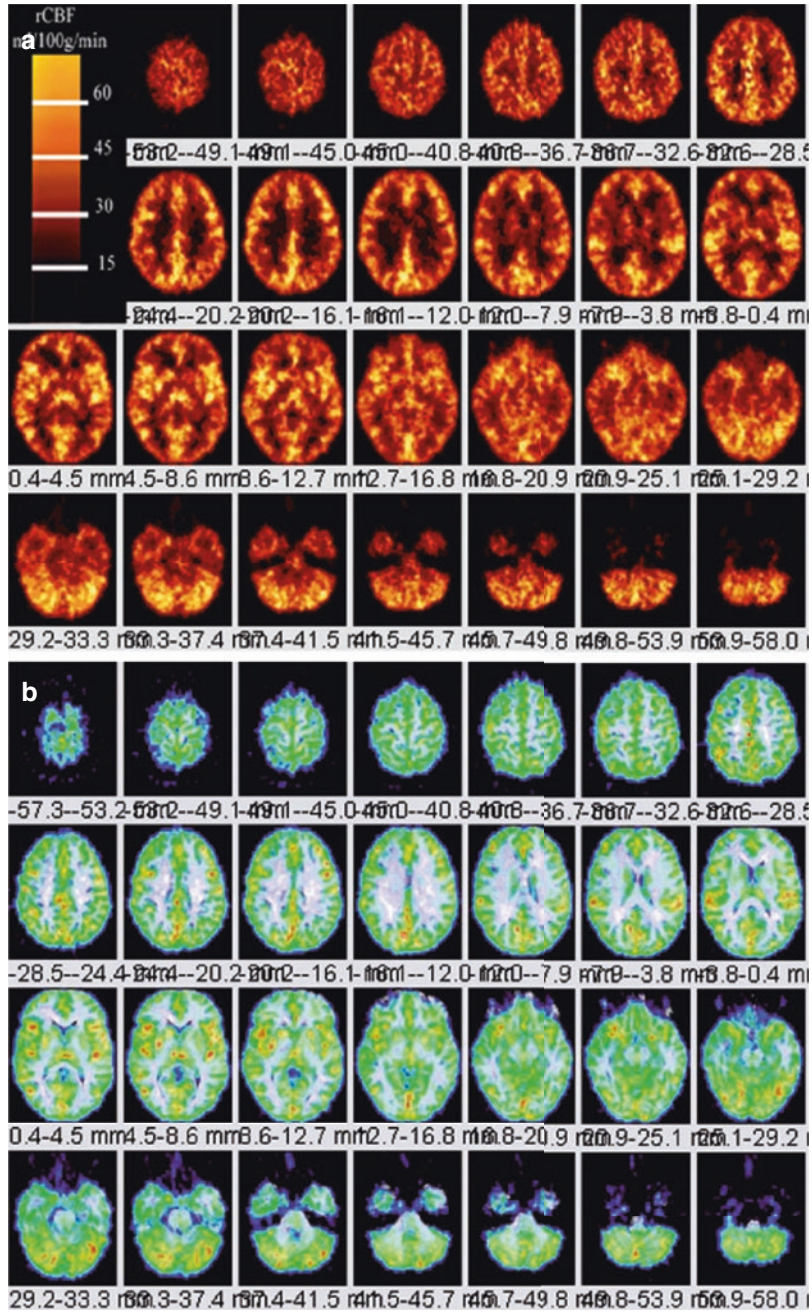

Fig. 11.10 (**a**) *Left*. Dynamic 15O-water PET scan from the top of the brain (*top left*) through the cerebellum (*bottom right*) from a 36-year-old normal female volunteer for the measurement of quantitative regional cerebral perfusion. PET scan are obtained from a Siemens CTI ECAT HR + operating in 3D mode. Regional cerebral blood flow (rCBF) quantified in units of ml/100 g/min (*color bar*). (**b**). *Right*. PET scan shown in (**a**) is co-registered using the automated image registration software onto a spoiled gradient echo (SPGR) MRI data volume (1-mm-thick MRI sections) resectioned and co-registered using the AIR routine to the 15O-water PET scan. Careful examination reveals increased blood flow localized to the gray matter regions of brain

11.4.1.4 15O-water for Quantitative Regional Cerebral Perfusion Measured by PET

Dynamic 15O-water PET scans with arterial sampling provide the ability for the quantitative assessment of regional cerebral perfusion. Each emission scan is short, approximately 3 min in duration. Data are typically analyzed using a 1-tissue-compartment model to obtain K1 (mL/min/mL), and quantification is expressed in standard units of ml/100 g/min [53].

The PET scan shown in Fig. 11.10a was acquired on a Siemens/CTI ECAT HR + scanner in 3D imaging mode (63 parallel planes); axial

field-of-view, 15.2 cm; in-plane resolution, 4.1-mm full width at half maximum; and slice width, 2.0 mm. The scanner gantry is equipped with a Neuro-insert (CTI PET Systems, Knoxville, TN) to reduce the contribution of scattered photon events. PET data was reconstructed using filtered back-projection (Fourier rebinning and 2D back-projection with Hann filter: kernel FWHM = 3 mm). Data was corrected for photon attenuation, scatter, and radioactive decay. A windowed transmission scan (10–15 min) was obtained for attenuation correction using rotating ^{68}Ge/^{68}Ga rods, and a model-based correction was applied to account for the 3D scatter fraction. The final reconstructed PET image resolution was about 6 mm (transverse and axial planes). PET–MRI fusion images shown in Fig. 11.10b are obtained from the MRI data that were transferred to the PET facility and co-registered to the dynamic 15O-water PET scans by automated image registration (AIR) software [54].

11.4.1.5 Thallium-201(^{201}Tl)

^{201}Tl in the form of thallous chloride is a cyclotron produced radiopharmaceutical shown to have affinity for brain tumors as early as the 1970s [55]. Although more commonly used as a myocardial perfusion imaging agent, thallium has high sensitivity for detection of new, recurrent, or residual viable tumor, which is difficult to differentiate from postradiation necrosis and edema on CT or MRI.

Thallium decays by electron capture with a half-life of 73 h and emits photons with a range of 0.78–167.4 keV [56]. The useful energy for imaging is at 80 keV corresponding to mercury X-rays when thallium decays to stable Hg-201. In its intravenous form, ^{201}Tl is supplied in isotonic solution at pH 4.5–7.0 and contains NaCl for isotonicity and 0.9% benzyl alcohol as a bactericidal agent [57]. The uptake of thallium in normal tissues has been hypothesized to act as a potassium analog. Both elements belong to group IIIA of the periodic table. The distribution and retention of ^{201}Tl in the normal brain and tumors is an active process related to blood flow, loss of integrity of the blood–brain barrier, tumor cell viability, tumor type, tumor cell membrane function, and the Na^+–K^+ ATPase pump activity.

Normal brain tissues show minimal to no uptake of ^{201}Tl. The normal physiological distribution in the head and neck region includes the scalp, lacrimal gland, nasopharyngeal area, salivary gland, and the pituitary gland. There is also minimal thallium uptake in the choroid plexus. Thallium is normally taken up by regions of the brain which do not have a blood–brain barrier (BBB) such as the pituitary gland and pineal gland and minimally taken up by the choroid plexus (Fig. 11.11). The evaluation of viable tumor can be performed with great accuracy using brain SPECT or brain PET imaging. Brain SPECT imaging employs the tracer ^{201}Tl to detect new, residual, or recurrent viable tumor due to the fact that there is transport of ^{201}Tl across the breakdown in the blood–brain barrier and uptake of ^{201}Tl into regions of hypermetabolism. ^{201}Tl is postulated to represent "potassium analog" with affinity for the sodium–potassium ATPase enzyme [58]. Thallium accumulates in the residual or recurrent viable tumor cells in proportion to malignant grade and total viable tumor bulk.

11.4.1.6 ^{99m}Tc-Hexakis-2-methoxy-2-isobutyl Isonitrile (^{99m}Tc-Sestamibi)

Tc-99m Hexakis-2-methoxy-2-isobutyl isonitrile is a monovalent cation complex formed by a central technetium atom surrounded by six 2-methoxy-2-isobutyl isonitrile groups. This compound is also used extensively in myocardial perfusion imaging. The normal brain tissue shows minimal uptake of ^{99m}Tc-sestamibi (MIBI). The normal physiological distribution in the head and neck region is similar to that of thallium and includes the scalp, nasopharyngeal area, salivary gland, and pituitary gland. There is notable significant choroid plexus uptake, much greater when compared to ^{201}Tl. The choroid plexus uptake may be due in part from the pertechnetate in the solution that is known to be actively taken up and secreted by the cells. This may account for secretion into the CSF and the presence of activity in the 4th ventricle which is visible on careful scrutiny of MIBI brain SPECT images (Fig. 11.12). It is postulated that after crossing the cell membrane MIBI is taken by the mitochondria in relation to negative electric potential. Normal myocardial uptake of MIBI depends on blood flow and the uptake of the mitochondria in metaboli-

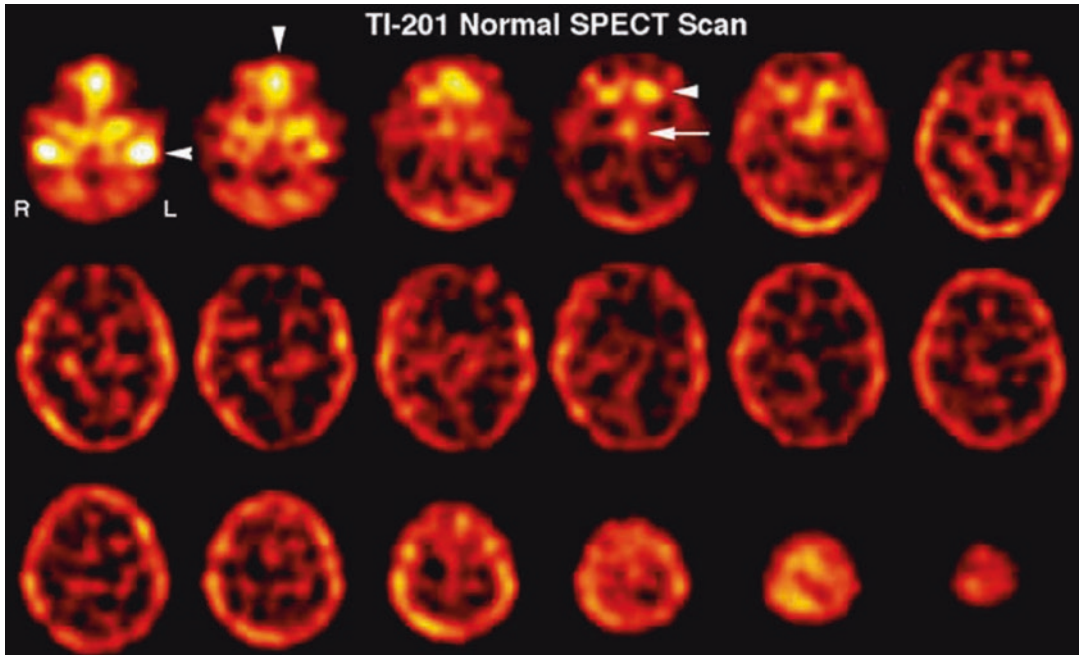

Fig. 11.11 SPECT scan of ^{201}Tl in the normal brain. Uptake of ^{201}Tl in the normal brain is very low. It is important to note that there is significant uptake by some of the structures just inferior to the cranium, which can interfere with the positive detection of tumor in the inferior frontal and inferior midportions of the brain. There is significant uptake in the jugular veins (*row one*, *image one*, *arrow*), the nasopharynx (*row one*, *image two*, *arrow*), and the salivary glands and pituitary glands (*row one*, *image four*, *arrowhead* and *arrow*, respectively)

cally active tissue. In brain tumors, the mechanism of tumor uptake is also thought to be dependent on mitochondrial activity and the presence of P-glycoprotein [59].

11.4.1.7 2-[F-18]-Fluoro-2-deoxy-D-glucose (18F-FDG)

A 36-year-old normal female volunteer underwent a fully dynamic 18F-FDG PET with arterial sampling at rest as shown in Fig. 11.13. ^{18}F-FDG PET scan image slice thickness = 2.0 mm and reconstructed in-plane image resolution = 4 mm FWHM. The 18F-FDG PET data is acquired over 90 min (34 frames) with arterial blood sampling throughout the scan period. The method of quantitative assessment of 18F-FDG PET has been well established [60–64].

18F-FDG PET has led to a more widespread capability in allowing evaluation of cerebral neoplasms and other diseases of the brain [65, 66]. In addition, due to the relatively long half-life of 18F (109 min), it can be transported regionally (within approximately 2–4-h travel time from a cyclotron production facility) enabling a centrally located production facility to supply several camera sites. For purposes of tumor diagnosis, 18F-FDG brain PET should be interpreted in conjunction with a current brain MRI scan since low-grade tumors may produce areas of reduced uptake, while high-grade brain tumors may produce areas of uptake equal to or slightly greater than gray matter.

11.4.1.8 L-[Methyl-^{11}C] methionine (11C-MET)

A PET amino acid isotope, L-[methyl-^{11}C] methionine (11C-MET) [67] has a relatively short half-life of 20 min. The tracer's use requires a nearby cyclotron. A study by Hustinx et al. explains its potential role in differentiating tumor recurrence from radiation necrosis [68]. The extent of tracer uptake is greater than the degree of contrast enhancement indicative of better delineation of tumor margins [69].

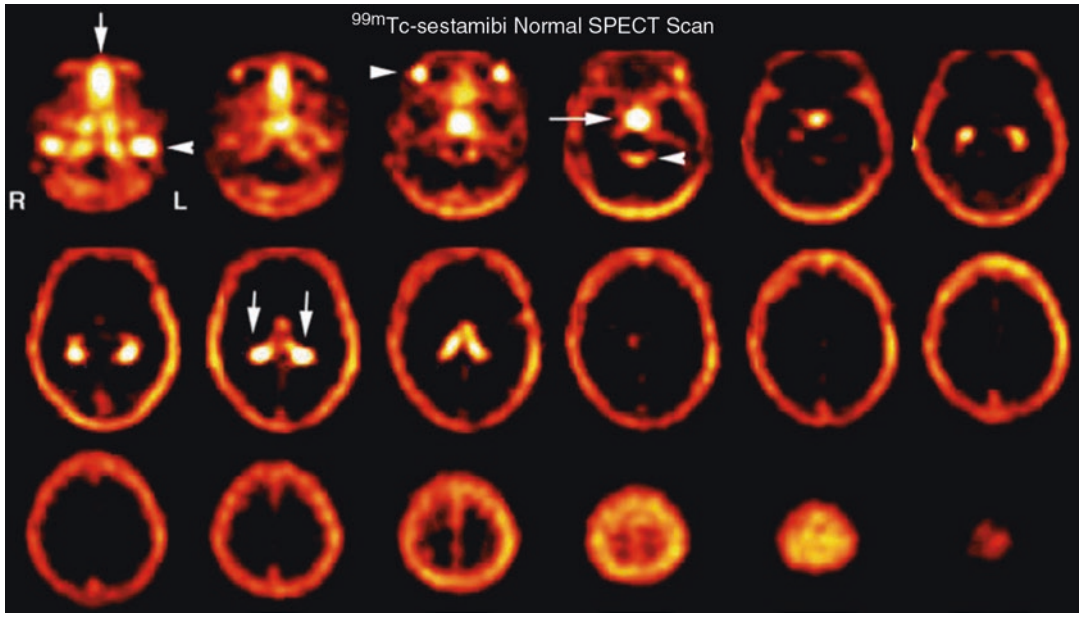

Fig. 11.12 Normal ^{99m}Tc-MIBI brain SPECT scan. The figure shows very low uptake of MIBI in the normal brain. However, similar to the thallium brain SPECT scan, there are several structures just inferior to the cranium which can interfere with accuracy of tumor recurrence identification. As seen in the normal ^{201}Tl brain SPECT scan, there is intense uptake in the jugular veins (*row one*, *image one*, *arrow*) and the nasopharynx (*row one*, *image one*, *arrow*). There is also intense uptake in the salivary glands (*row one*, *image three*, *arrow*) and the pituitary gland (*row one*, *image three*, *arrow*). In addition, there seemed to be increased uptake in the ambient cistern (*row one*, *image four*, *arrow*) due to secretion of significant ^{99m}Tc-MIBI through the choroid plexus (*row two*, *image two*, *arrows*). This secretion by the choroid plexus often significantly limits the utility of this tracer in the detection of recurrent tumor since many tumors tend to recur in the region of the basal ganglia

The tracer uptake has been shown to correlate with prognosis and survival in low-grade gliomas [70, 71], where the uptake is increased in the absence of BBB breakdown which is a significant advantage over CT, conventional MRI, and F-18 FDG PET [72, 73]. In high-grade gliomas, ^{11}C-MET uptake is greater than in low-grade tumors [74–76] establishing its potential for use in monitoring anaplastic transformation.

In a study of 21 patients with brain metastases status post stereotactic radiosurgery, the tracer accurately identified 7 of 9 recurrences and 10 of 12 radiation injuries [77]. A combined ^{18}F-FDG and ^{11}C-MET study for stereotactic biopsy of 32 unresectable glioma patients demonstrated that ^{11}C-MET generates a more sensitive signal, making it a potential single-tracer PET agent for neurosurgical intervention of gliomas [78].

A study by Ullrich et al. shows that increased ^{11}C-MET uptake during tumor growth parallels an upregulation of angiogenic markers such as vascular endothelial growth factor (VEGF) [79]. A study by Yamane et al. talks about the clinical impact of ^{11}C-MET and that the addition of ^{11}C-MET PET changed patient management [80].

11.4.1.9 O-(2-[^{18}F] fluoroethyl)-L-tyrosine (18F-FET)

O-(2-[^{18}F] fluoroethyl)-L-tyrosine (18F-FET) is a PET tracer studied for its potential role in the differentiation of radiation necrosis and residual tumor. Studies have shown the absence of ^{18}F-FET uptake in a case of radiation necrosis [81], but further systematic studies are necessary to confirm this finding. In contrast to ^{18}F-FDG, ^{18}F-FET uptake was absent from macrophages, a

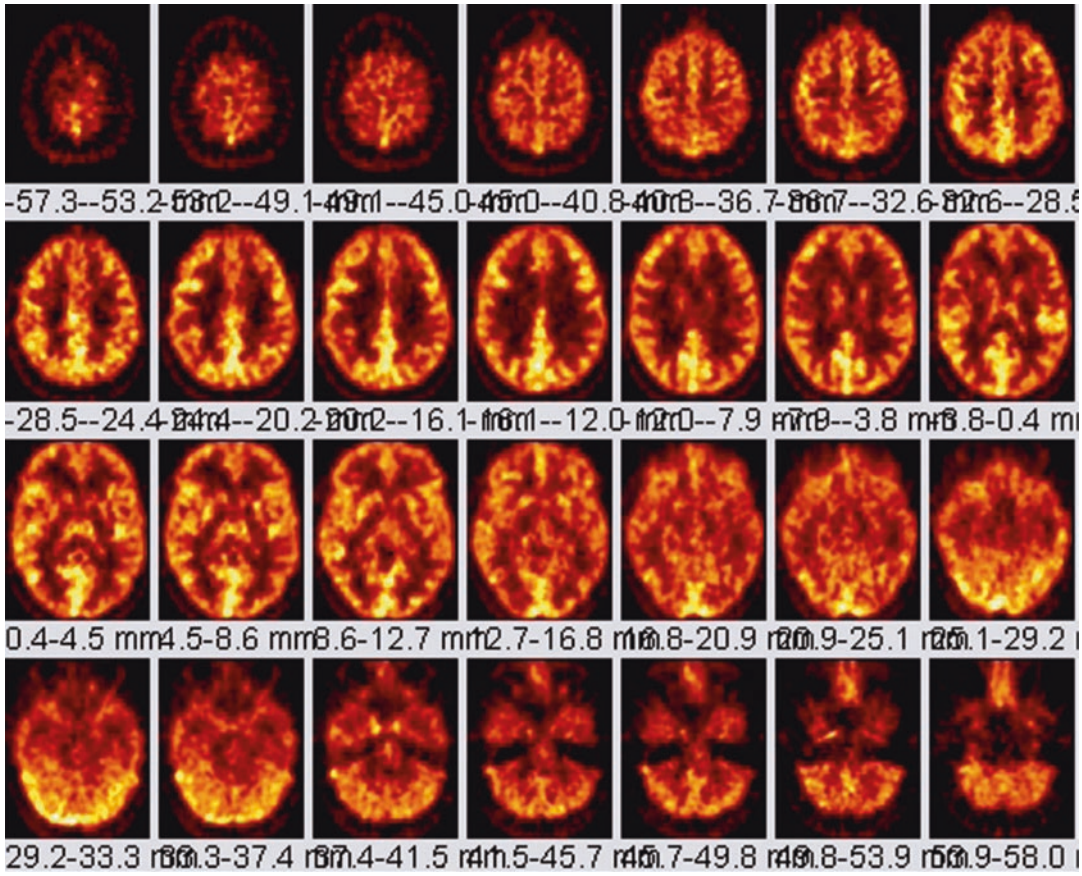

Fig. 11.13 Normal 18F-FDG PET. A 36-year-old normal female volunteer underwent fully dynamic 18F-FDG PET with arterial sampling at rest

common inflammatory mediator [82]. In another study, the ratio of ^{18}F-FET uptake in radiation necrosis to that in the normal cortex was much lower than the corresponding ratios for ^{18}F-FDG and ^{18}F-choline suggestive of its potential for differentiating radiation necrosis from tumor recurrence [83].

In the last decade, studies on combined 18F-FET and MRI have shown improved identification of tumor tissue as compared to either modality alone [84]. The specificity of distinguishing gliomas from normal tissue could be increased from 68% with the use of MRI alone to 97% with the use of MRI in conjunction with ^{18}F-FET PET and MRI spectroscopy [85].

11.4.1.10 3,4-Dihydroxy-6-^{18}F-fluoro-l-phenylalanine (^{18}F-FDOPA)

3,4-dihydroxy-6-^{18}F-fluoro-L-phenylalanine (^{18}F-FDOPA) is an amino acid tracer initially used for the evaluation of movement disorders [86, 87] but recently being studied in the imaging of brain tumors. ^{18}F-DOPA crosses the BBB in the normal brain via the neutral amino acid transporter [88]. Although increased sensitivity and specificity of ^{18}F-DOPA over ^{18}F-FDG was shown, no correlation to tumor grade or contrast enhancement was observed [83]. The same study found a tumor-to-normal-brain ratio of less than 1.6 with ^{18}F-DOPA in four cases of radiation

necrosis. A recent study showed that correlation between tracer uptake and tumor proliferation was observed only in newly diagnosed gliomas and not in recurrent gliomas [899]. When compared to ^{11}C-MET PET, no significant difference in uptake was shown in either low- or high-grade tumors [89]. Larger series of radiation necrosis cases will be needed for confirmation of these findings, however.

11.4.1.11 ^{18}F-Fluoromisonidazole (18F-FMISO)

^{18}F-Fluoromisonidazole is a nitroimidazole derivative PET agent used to image hypoxia [90], a physiological marker for tumor progression and resistance to radiotherapy [91]. Its preferential uptake in high-grade rather than low-grade gliomas [92], a significant relationship with the upregulation of angiogenic markers such as VEGF-R1 [93], and correlation to progression and survival after radiotherapy [94] suggest its potential role in monitoring response to therapy targeting hypoxic tissue.

11.4.1.12 Cell Proliferation Imaging with 18F-FLT-PET

3′-deoxy-3′-18F-fluorothymidine (18F-FLT) has been used to indicate tumor proliferation in both preclinical and clinical studies [95, 96]. Transport of ^{18}F-FLT is mediated by both passive diffusion and Na^+-dependent carriers. The tracer is subsequently phosphorylated by thymidine kinase 1 (TK_1) into ^{18}F-FLT monophosphate where TK_1 is a principal enzyme in the salvage pathway of DNA synthesis. Whereas the TK_1 activity is virtually absent in quiescent cells, its activity reaches the maximum in the late G_1 and S phases of the cell cycle in proliferating cells [97]. The phosphorylation of the tracer by TK_1 therefore makes ^{18}F-FLT a good marker for tumor proliferation.

Imaging of brain tumor proliferative activity has been performed using semiquantitative measures of standard uptake values. ^{18}F-FLT imaging can be correlated with stereotactic biopsies representing the Ki-67 proliferation index. Recurrent or residual viable tumor demonstrates increased quantitative ^{18}F-FLT utilization and can provide a useful index to separate residual or recurrent viable tumor from radiation or chemotherapy necrosis. ^{18}F-FLT is more specific for detection of viable tumor proliferation since the background activity in the normal brain is low (Fig. 11.14), unlike ^{18}F-FDG which has a high normal brain background.

Figure 11.15 demonstrates 1-year follow-up gadolinium-enhanced MRI of patient in image Fig. 11.14.

11.4.1.13 Ga-68 DOTATATE for SSTR characterization in Meningiomas

Somatostatin (SSTR) binding agents for detection and characterization of neuroendocrine tumors has been employed for over 20 years. Initial studies for detection of SSTR positive meningiomas were performed using In-111-pentetreotide scans [99].

But recently somatostatin imaging agents such as gallium 68 dotatate (^{68}Ga-DOTATATE) PET has allowed for high sensitivity as well as improved image resolution for detection of neuroendocrine tumors. Over the past few years, its role in tumor detection has also been extended to meningiomas [100].

In addition, ^{68}Ga-DOTATATE positive imaging has gained importance as a theranostic agent for detection of avidity to distinguish patients who will qualify for and benefit from peptide receptor radionuclide therapy (PRRT) using Lu-77 DOTATATE^{177}. A recent study has shown however that the ^{68}Ga-DOTATATE positive regions of tumors may not necessarily be the areas of greatest metabolism, and there is a complementary role for F-18 FDG PET combined with ^{68}Ga-DOTATATE to better select patients who may most benefit from ^{177}Lu-Lutathera PRRT therapy [101].

Figure 11.16 illustrate that a single imaging modality may not be able to provide all needed information to accurately assess the metabolic and molecular characteristics of a meningioma, in order to guide targeted therapeutic management and patient prognosis. 68Ga-DOTATATE and 18F-FDG FDG PET may provide complementary information for this purpose. In the case

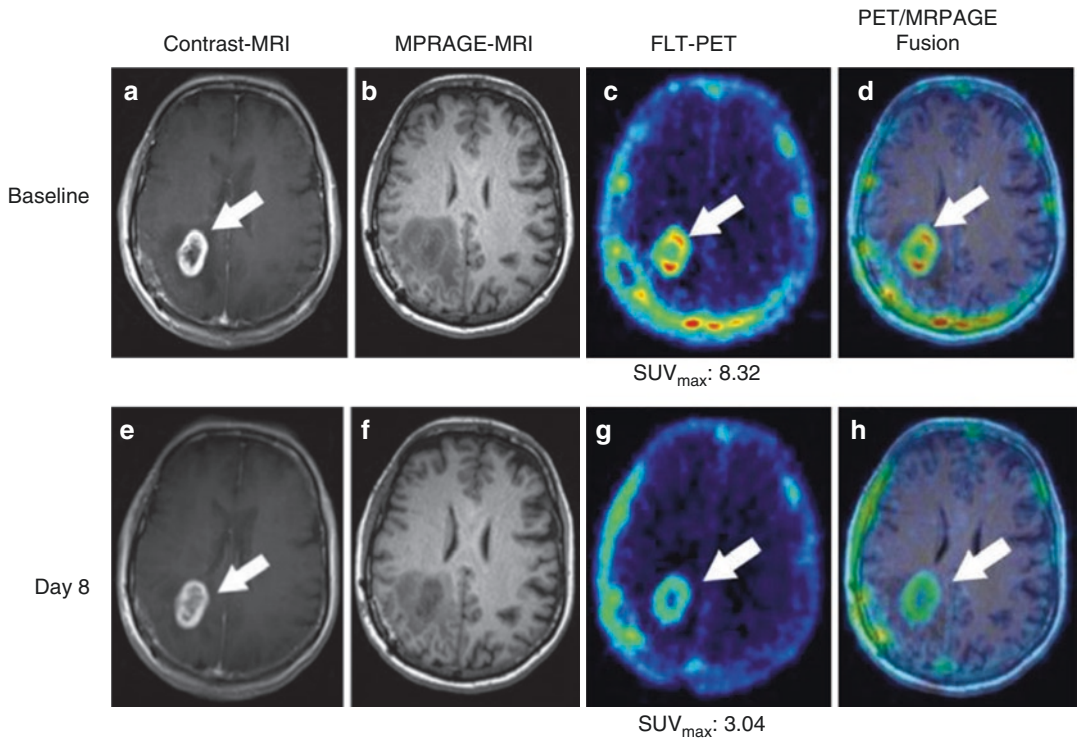

Fig. 11.14 A 64-year-old female patient diagnosed with glioblastoma multiforme of the right parietal lobe, proven by surgical biopsy. 18F-FLT-PET/CT scans was performed 40 min after injection of 185 MBq F-18 3′-deoxy-3′-^{18}F-fluorothymidine (FLT) with a 30-min acquisition, followed by gadolinium-enhanced MRI [1] (**a**) T1-weighted MR images. (**b**) Magnetization-prepared rapid acquisition with gradient echo (MP-RAGE) MR images, arrows). The baseline 18F-FLT-PET/CT scans (**c**) show high uptake with $SUV_{max} = 8.32$. (**d**) PET-MR fusion images. The patient was treated with 6 weeks of temozolomide and a total of 60-Gy radiotherapy (STUPP protocol) [2, 3]. A post-therapy T1 weighted MR (**e**), post-therapy MP-RAGE (**f**) and post-therapy ^{18}F-FLT-PET (**g**) was acquired 8 days after the initiation of temozolomide and radiotherapy combination to assess early response [4–7]. While MRI (**h**) shows no substantial change, FLT uptake was significantly decreased after first week of therapy (**g**) now with SUVmax = 3.04 [98]

above, high ^{68}Ga-DOTATATE uptake in regions of corresponding high metabolism would suggest that this patient would be a good candidate for ^{177}Lu-Lutathera therapy.

Figure 11.17b shows Ga-68 Dotatate images from a 54-year-old male s/p resection of the right temporal meningioma and subsequent Gamma knife radiosurgery. The patient now presents with a recurring anaplastic meningioma. Positive Ga-68 Dotatate uptake suggested he would be a good candidate for 177Lu-Lutathera therapy, as shown in Fig. 11.17c.

11.4.2 Scintigraphic Imaging Techniques

11.4.2.1 Image Acquisition

SPECT Image Acquisition

In single-photon emission computed tomography (SPECT) of the brain, triple-head Anger gamma cameras are now in common use and can provide very high-resolution images [approximately 7-mm full width at half maximum (FWHM) extrinsic resolution] [102]. The resolution has

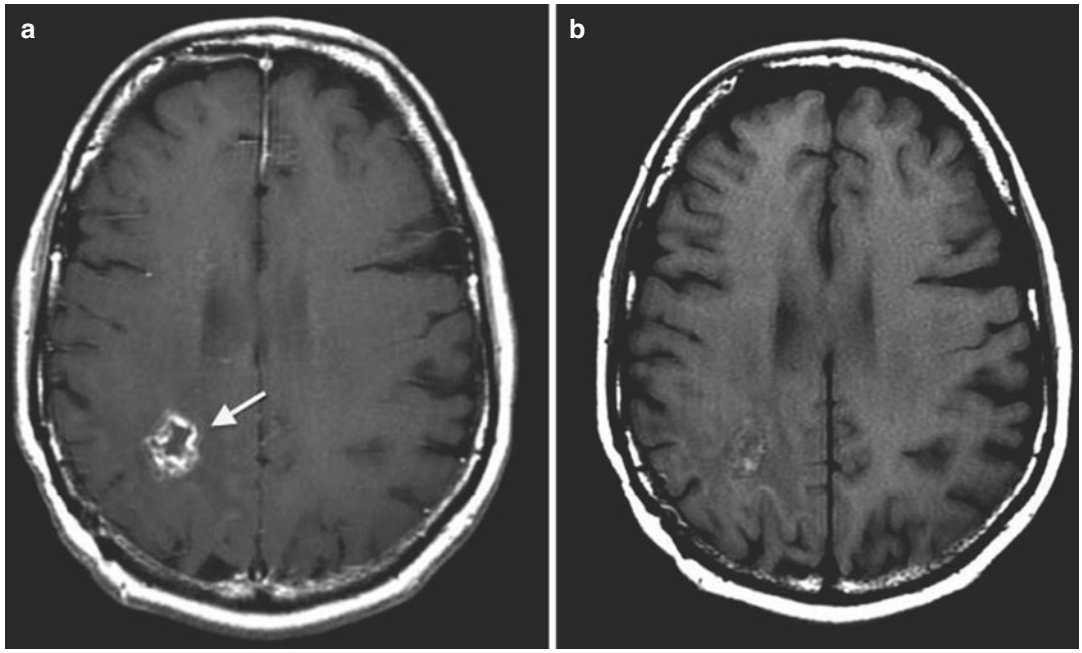

Fig. 11.15 1-year follow-up gadolinium-enhanced MRI of patient in image Fig. 11.14. MRI was repeated every 3–4 months according to European Society for Medical Oncology (ESMO) clinical guidelines. There has been no evidence of disease progression for 1 year of follow-up. The 1-year follow-up MRI shows a cavitary lesion in location of primary tumor, (**a**) gadolinium-enhanced T1-weighted MR image and (**b**) T1-weighted spin echo sequence image (*arrows*) [98]

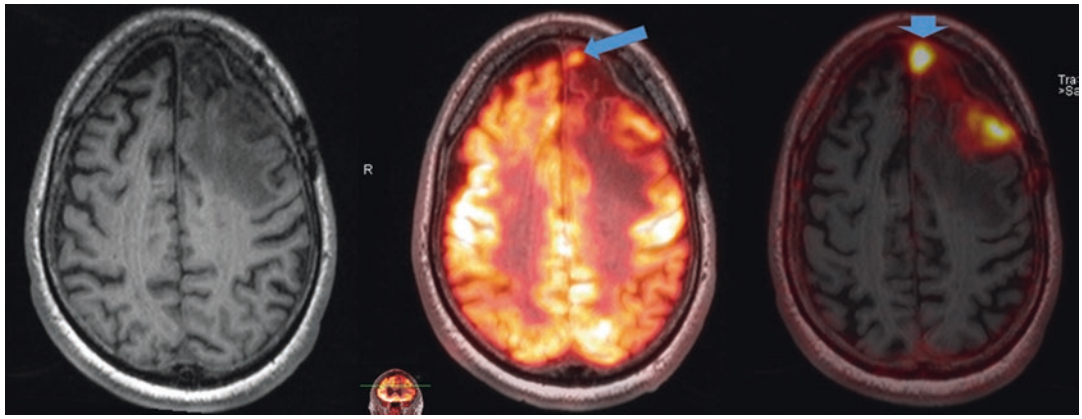

Fig. 11.16 A 67-year-old man with an intracranial WHO grade III anaplastic meningioma. He underwent tumor resection followed by intensity modulated radiation therapy (IMRT) but suffered a recurrence 25 months later. He received a ^{18}F-(FDG) and ^{68}Ga-DOTATATE PET/MR to evaluate for the presence of somatostatin receptor expression and guide subsequent treatment. (left) (MP-RAGE MRI section through tumor in the left frontal lobe). (middle) (Corresponding section from a^{18}F-(FDG) PET/MR scan showing moderately intense tumor uptake). (right) (corresponding section from a ^{68}Ga-DOTATATE PET/MR) showing very intense tumor uptake in the anterior frontal tumor (arrow) to a much greater degree than seen F-18 FDG uptake in the same location (arrow). The ratio of ^{68}Ga-DOTATATE to F-18 FDG uptake was much greater as compared to the same ratio in the more laterally positioned lesion [101]

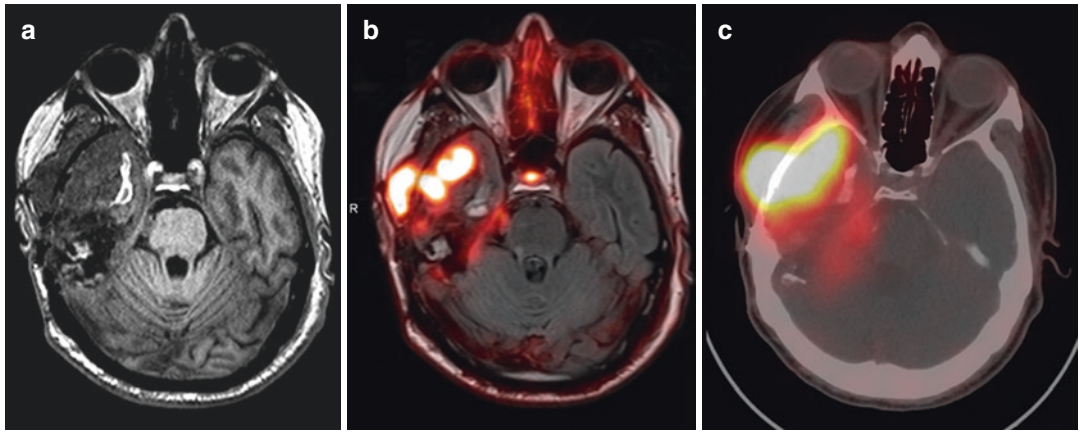

Fig. 11.17 54-year-old male with a recurring anaplastic meningioma underwent a PET/MR scan performed on the Siemens 3T PET-MR. (**a**) Shows the T1_MP-RAGE image of the multilobulated tumor in the right middle cranial fossa. (**b**) Shows there is intense Ga-68 Dotatate uptake in the tumor with max SUV equal to 17.23. The patient was deemed to be a good candidate for 177Lu-Lutathera therapy, and the resulting PET/CT immediately after IV administration of 200 mCi177Lu-Lutathera is shown in (**c**). Note the 177Lu-Lutathera uptake pattern is in the location of the Ga-68 Dotatate uptake

improved, primarily, due to the increased count detection capability of these cameras. In addition, these cameras allow faster throughput of patients since the scan time can be decreased. Scanning can be performed in temporal segments, with summation of the projection images at the end of acquisition. This enables salvaging of studies in which patient motion might occur. For example, a 30-min scan can be divided into two 15-min segments, each obtaining a 360° set of projection images. If the patient moves during the last 15-min imaging segment, the first 15-min imaging segment can be used for reconstruction of the complete set of tomographic images. If the patient does not move, both sets of projection images can be summed together to obtain a higher count rate examination. Patient motion occasionally occurs in the evaluation of severe dementia or epilepsy. Fortunately, in many of these cases, the cortical regions under investigation are relatively large, and a scan with only moderate counts or mild motion is still adequate for clinical diagnosis.

In conjunction with the advancements in radiopharmaceuticals and cameras, there have also been advances in computer software. Algorithms for SPECT reconstruction and post-processing are now simplified and more routine which reduces pre-acquisition and post-processing errors by the technologist. In addition, images are DICOM compatible [103], allowing the SPECT imaging computer to be used to store anatomic images from CT or MRI, which permits image registration methods to be routinely employed to compare anatomy and function.

PET Image Acquisition

Subject environmental conditions during the performance of 18F-FDG PET scans should be standardized whenever possible. 18F-FDG PET studies should be performed during "a resting state" (e.g., eyes open, ears un-occluded in a dark room with minimal ambient noise). Procedures to minimize head movement during scan acquisition should be implemented using well-tolerated head immobilization procedures. The use of medications and the behavioral state of patients at the time of the scan also should be carefully taken into account since they may produce changes in cerebral metabolism that could alter 18F-FDG tracer distribution.

The normal brain has high 18F-FDG uptake, and therefore administration of approximately 10 mCi 18F-FDG IV is sufficient. The PET scanner should be of the latest generation, full ring, and multislice to cover the entire brain. The 3D

acquisition mode should be used to accommodate lower dosimetery and to improve the count statistics of the data. Measured attenuation correction should be employed. The image should be reconstructed with the standard clinical reconstruction including all necessary corrections (such as for randoms, scatter, and attenuation). Quality control with calibration phantoms should be performed in order to assure qualitative accuracy (e.g., using the Hoffman brain phantom) and quantitative accuracy (e.g., using a uniform cylinder phantom) should be run periodically to assess scanner stability [104].

Hybrid SPECT-CT, PET-CT, and PET-MRI Image Acquisition

Hybrid scanners combining PET or SPECT with high-resolution multi-detector CT are becoming the standard for almost all commercially available nuclear imaging systems. In addition, the latest generation of scanners offers combination of PET with MRI. These systems allow acquisition of SPECT or PET images simultaneously with CT or MRI images.

Combined SPECT-CT or PET-CT scanners provide both functional information from SPECT or PET and structural information from CT in a single examination. CT scan can be acquired for attenuation correction/anatomic localization (AC/AL) or it can be optimized for a diagnostic CT scan. If the CT scan is obtained for AC/AL, use of a low milliampere-seconds setting is recommended to decrease the radiation dose to the patient. For an optimized diagnostic CT scan, standard CT milliampere-seconds settings are recommended to optimize the spatial resolution of the CT scan. Tube current modulation may be used to minimize radiation dose to the patient. In some cases, intravenous or oral contrast material may be used. A separate CT acquisition for a specific region of the body may be necessary to produce an optimized diagnostic CT scan.

Hybrid or integrated PET-MRI scanners provide simultaneous molecular and functional PET imaging with anatomical and functional MRI imaging. MRI when compared to CT, offers superior soft-tissue contrast and hence better anatomical visualization of soft tissue and bony structures. PET-MRI is preferable for imaging the brain, head and neck, abdominal and pelvic organs, heart and musculoskeletal system.

Multiple vendors globally provide PET-MRI imaging systems. An example is Siemens Biograph mMR PET–MRI whole-body human scanner integrates a 3-T Verio MRI and PET scanner. The mMR can acquire simultaneous MR and PET images with the quality of separate PET and MRI scanners (Fig. 11.18). The design allows simultaneous acquisition of MRI and PET data. Using the NEMA 2007 protocol, PET resolution (FWHM) was measured to be 4.0 cm (transverse, 1 cm off center).

11.4.2.2 Registration and Analysis Methods

Image Registration

The main techniques for registration of images are use of atlases (e.g., the Talairach atlas [105]) and use of a computer-based automated routine for aligning and reslicing tomographic image data using automated image registration algorithms (AIR) [54].

The Talairach et al. [105] atlas method relies on identification of the anterior (AC) and posterior (PC) commissures of the brain to define the AC–PC line. After the AC–PC line is identified, an origin (O) is defined along this line. A perpendicular line is then drawn from O to the top of the brain. This gives longitudinal and vertical dimensions. The width of the brain is defined from the scan itself. Thus, in this coordinate system, three Cartesian axes are defined, with the edges of the brain identified to yield measurable dimension. When comparing separate patients on SPECT or PET scans, these dimensions are stretched proportionally such that the dimensions of the brain along this axis are the same lengths in all patients.

Automated image registration (AIR) algorithms include computer routines for aligning and reslicing tomographic image data. The typical strategy for AIR is as follows: The brain SPECT or PET scans are converted to analyze format. These analyzed format image sets are resized (spatially co-registered) for conversion of image pixel size and x, y, and z to common units. The registration algorithms are used from a family of automated

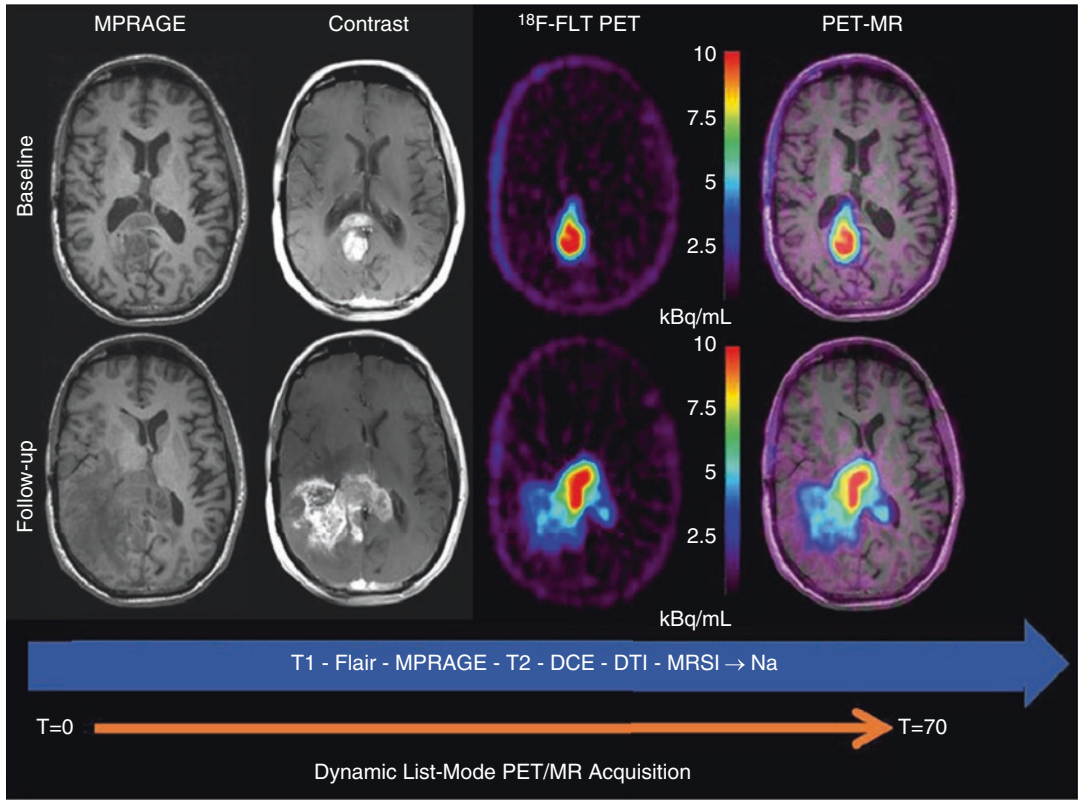

Fig. 11.18 A 42-year-old male with a GBM with baseline scan (*top row*). Treatment was started with Temodar + veliparib (ABT-888). Two-month follow-up scan (*bottom row*) shows disease progression on contrast-enhanced MRI and FLT-PET. PET and MR sequence were simultaneously acquired

image registration programs to align image data set to the same position [54]. The images can then be registered into a standardized image spaces, such as the patient's functional image space or standardized space, such as the Montreal Neurological Institute (MNI) space [106].

An example of the precision to which these techniques can provide image registration between 18F-FDG PET and MRI is illustrated by a 36-year-old normal female volunteer who underwent a resting-state fully dynamic 18F-FDG PET scan with arterial sampling at the University of Pittsburgh PET Center, as shown in Fig. 11.19. A 2-tissue-compartment model was used to analyze the data and spoiled gradient echo (SPGR) MRI volume data (1-mm-thick MR sections) were transferred to the PET facility over the electronic network from the MRI center and registered with the PET data. MR data were spatially normalized and sectioned in the patient's PET space to preserve the maximum resolution of the original PET data. ^{18}F-FDG PET scan image slice thickness = 2.0 mm with reconstructed in-plane image resolution = 4-mm FWHM. The ^{18}F-FDG PET data is acquired over 90 min (34 frames) with arterial blood sampling for each scan time period.

SPECT and PET Image Analysis

Statistical parametric mapping (SPM) refers to the construction and assessment of spatially extended statistical processes used to test hypotheses about functional imaging data. In rCBF SPECT or ^{18}F-FDG PET image data analysis, this translates to methods to test hypotheses about regionally specific effects (e.g., the probability of finding a region of increased regional cerebral perfusion or metabolism by chance). It was

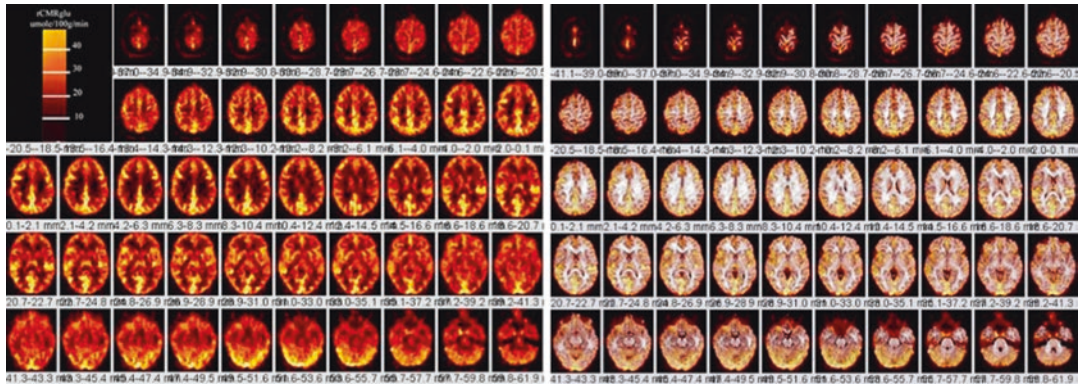

Fig. 11.19 *Left*. 18F-FDG PET scan sections through the brain (*left*) and corresponding PET–MRI co-registered fusion images (*right*). Images are from a 36-year-old normal female volunteer who underwent fully dynamic ^{18}F-FDG PET with arterial sampling at rest. Regional cerebral metabolic rates of glucose utilization expressed as rCMRglu in units of micromole/100 g/min (*color bar*). PET images are registered to a spoiled gradient echo (SPGR) MRI volume data (1-mm-thick MR sections) that were transferred to the PET facility over the electronic network and registered with the PET data. The ^{18}F-FDG PET scan image slice thickness = 2.0 mm with reconstructed in-plane image resolution = 4-mm FWHM. *Right*. MRI–PET fusion image. In general, the fusion technique is clinically helpful to assess structural versus functional changes on ^{18}F-FDG brain PET scans or regional cerebral blood flow brain SPECT scans

originally developed in the early 1980s by Friston et al. [107] for the routine statistical analysis of functional neuroimaging data from PET. When two image data sets are evaluated by SPM, all voxels contained within the scans are compared in the same space on a voxel-by-voxel basis using linear constraints to test hypotheses for specific focal effects using a univariate statistical test. The resulting statistical parameters are then assembled onto an image (i.e., the statistical parametric map). Statistical differences are interpreted as regionally specific effects, attributable to some alteration in brain function from one scan to the other. The significance of these differences is assessed using statistical tests (usually the *t* or *F* statistic). Criteria for accepting voxels (those intended to represent true changes in regional cerebral perfusion) can be set for voxel height (*p*) and extent of contiguous cluster of voxels (*k*). For visualization of the results, a pseudo-color scale can be applied to accepted significant voxels, which are then overlayed in a semitransparent fashion onto the MRI of either the normative atlas or the patient's own MRI anatomy. The most recent version of SPM (SPM2) combines the general linear model to create the statistical map and the random field theory to make statistical inference about regional effects. Although the SPM package includes most of the programs required for image processing and analysis, visualization of images and some processing or image editing and reformatting may require more dedicated biomedical image processing software.

Statistical parametric mapping was performed to compare the regional distribution of ^{99m}Tc-HMPAO brain SPECT scans with ^{99m}Tc-ECD brain SPECT scans in normal patients [108]. All patients were screened for drug use, head injury, medication status, and other psychiatric or mental illnesses. The two groups were matched for age, sex, and race, and analysis was performed on a group of 35 normal patients undergoing ^{99m}Tc-HMPAO brain SPECT scans and 55 patients undergoing ^{99m}Tc-ECD brain SPECT scans. Statistical parametric mapping was performed after the patients' data were spatially normalized to a standardized stereotactic atlas (Talairach atlas). The results showed that these tracers had differences in their regional perfusion patterns, presumably due to the differences in the pharmacokinetics of tracer extraction and trapping. Specifically, large areas of the parietal, occipital, and superior temporal cortices demonstrated

lower uptake in the ^{99m}Tc-HMPAO brain SPECT scan group as compared to the ^{99m}Tc-ECD brain SPECT scan group. There were increases in tracer uptake seen in the subcortical nuclei, thalami, and parts of the brainstem and hippocampus as well as small areas of the cerebellum in the ^{99m}Tc-HMPAO group as compared to the ^{99m}Tc-ECD group. The importance of this study is to point out that, when performing rCBF SPECT, one should be aware of the differences in the perfusion pattern. In cases of repeat studies, these data suggest that one tracer cannot be substituted for the other.

11.4.3 Clinical Applications

11.4.3.1 Cerebrovascular Disease

Nuclear medicine techniques have been used for the past 55–60 years to investigate cerebrovascular diseases and stroke mainly through tomographic applications, such as positron emission tomography (PET) and single-photon emission computed tomography (SPECT) [108]. It is ironic that tracers which directly measure regional cerebral perfusion have not assumed greater clinical application in the evaluation of cerebrovascular disease. This is partly due to the fact that, in many cases, the identification of a poststroke blood flow defect has not provided unequivocal useful clinical information beyond that offered by neurological exam combined with CT or MRI. Furthermore, the use of rCBF tracers in patients with TIA has had unclear clinical usefulness since a rest perfusion scan may not provide significant additional clinical information beyond the neurological examination.

Hemodynamic Vascular Constraint

In a recent study of 64 patients in which cerebral perfusion and vascular reactivity were assessed before and after carotid endarterectomy using Diamox-enhanced SPECT, the authors concluded that Diamox SPECT assessment of vascular reserve was of value in identification of patients at risk for stroke [109]. After carotid endarterectomy, these patients underwent repeat SPECT which confirmed improvement in vascular reactivity. Therefore, Diamox SPECT scans may provide objective evidence for the selection of patients with a high-grade asymptomatic carotid stenosis who will benefit from carotid endarterectomy [109].

The standard vasoreactive stress protocol is to first perform a resting-state ^{99m}Tc-HMPAO brain SPECT scan to assess the blood flow to the vascular territories of the brain. In many cases in patients with TIA, the blood flow is often symmetric or may show small regions of cortical hypoperfusion due to small embolic infarctions. The vasoreactive challenge SPECT is performed either by using the same dose of ^{99m}Tc-HMPAO after a 24–48-h wait or by using a much higher dose than the initial dose (the so-called low-dose/high-dose method). The main problem with this method is that, in order to comply with regulatory requirements pertaining to the total amount of injected ^{99m}Tc-HMPAO, the low-dose scan usually has relatively poor count statistics. Therefore, it is best to perform the rest–vasoreactive comparative test on 2 separate days using the same dose. After the intravenous administration of 1 g of Diamox and waiting 15 min, there is an increase in CO_2 in the brain which causes dilatation of the vasculature. There is an increase in the blood flow to the normal brain of about 30%, and areas of hemodynamic constraint can be identified since CVD patients may be at the limit of their vasoreactive reserve before Diamox and, therefore, will illustrate no increase in perfusion as compared to normal vascular territories of the brain which can accommodate a 30% increase in blood flow.

Figure 11.20 illustrates the clinical utility of vasoreactive challenge rCBF SPECT in a 58-year-old man who presented with transient ischemic attack characterized by transient neurological deficits in motor function of the right upper and right lower extremities. On angiography, there was 100% narrowing of the left internal carotid artery. The MRI scan was normal. The resting-state ^{99m}Tc-HMPAO (pre-Diamox) brain SPECT scan showed only mild decrease in perfusion. The post-Diamox vasoreactive stress scan showed a large region of decreased regional cerebral perfusion in the left frontal, temporal, and parietal lobes representing severe rCBF compro-

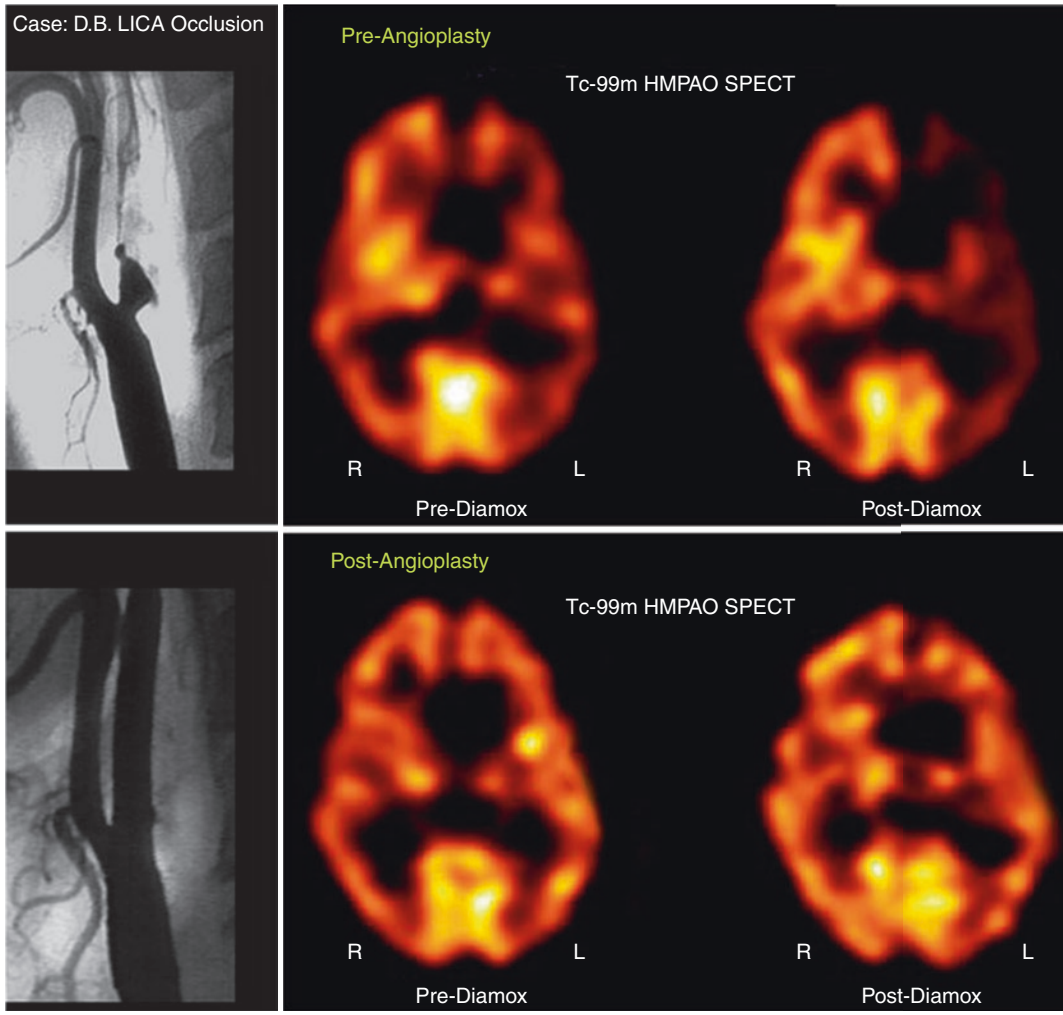

Fig. 11.20 Angiogram showing complete left ICA occlusion in a patient with transient ischemic symptoms (*top*, *left*). The resting scan (*top*, *middle*) shows slight reduction of blood flow to the left ICA distribution. The post-Diamox scan (*top*, *right*) shows significant relative reduction of rCBF to the left ICA territory as compared to the remainder of the brain. The *bottom row* of images shows the results after angioplasty. The angiogram (*bottom*, *left*) now shows a patent left internal carotid artery. The resting ^{99m}Tc-HMPAO brain SPECT scan (*bottom*, *middle*) shows a more symmetric perfusion of tracer distribution at rest. More importantly, after Diamox, there is no relative reduction in the left hemisphere as compared to the right hemisphere (*bottom*, *right*)

mise in the distribution of the left internal carotid artery. This patient subsequently underwent left ICA balloon angioplasty. A follow-up rest and vasoreactive challenge rCBF SPECT indicated that all regions of the brain increased in blood flow as a result of Diamox flow augmentation and the left internal carotid artery vascular territory was no longer constrained. It is important to diagnose areas of hemodynamic vascular constraint since patients with this degree of vascular compromise have significant risk for sudden infarction in addition to a chronic risk for selective neuronal loss and vascular dementia. Figure 11.21 shows ^{99m}Tc-HMPAO (pre- and post-Diamox) brain SPECT images of a 52-year old male with acute and chronic infarction in the region of right MCA territory. Post diamox images demonstrate a more severe constraint in the region of right frontal lobe as compared to pre diamox study. Figure 11.22 shows rest and post

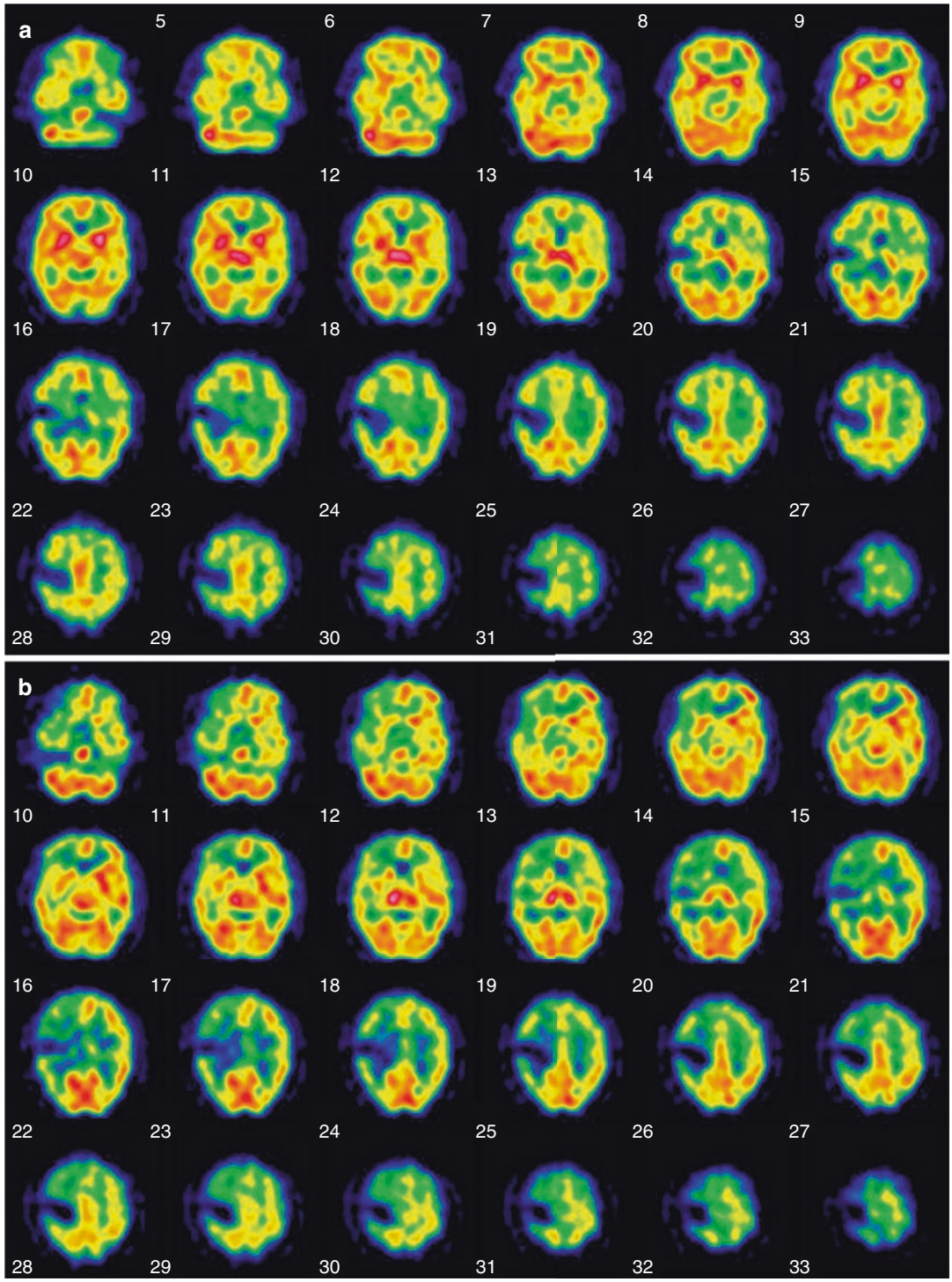
a
5
6
7
8
9
10
11
12
13
14
15
16
17
18
19
20
21
22
23
24
25
26
27
28
29
30
31
32
33
b
10
11
12
13
14
15
16
17
18
19
20
21
22
23
24
25
26
27
28
29
30
31
32
33

diamox stress ^{99m}Tc-HMPAO SPECT images, and subtraction images fused with MR of 60-year-old female with transient left-sided weakness and facial droop. There is decreased radiotracer uptake in right ICA territory on Diamox stress images. This is further demonstrated on Subtraction images.

Assessment for Carotid Artery Sacrifice: Balloon Occlusion Test (BOT)

In some instances, it may be necessary to sacrifice a carotid artery in the treatment of patients with head and neck tumors or cerebral aneurysms. It is thus necessary to evaluate whether the patient can tolerate temporary or permanent carotid occlusion and to predict the potential risk before the surgical procedures. Balloon occlusion testing (BOT) is useful for evaluating whether patients will tolerate temporary or permanent carotid occlusion and has been considered to result in a decrease in postsurgical complications after carotid occlusion [110].

Measurement of cerebral blood flow (CBF) has revealed that substantial cerebral hypoperfusion may occur when a patient does not show any neurological symptoms during BOT and may thus predict the potential risk after carotid occlusion [111]. Among several methods of CBF studies, SPECT ^{99m}Tc-HMPAO or ^{99m}Tc-ECD has been increasingly applied in conjunction with BOT, because both tracers—^{99m}Tc-HMPAO and ^{99m}Tc-ECD—rapidly distribute in the brain and the image is constant long after injection. SPECT images acquired after the completion of BOT might still reflect the CBF distribution during BOT when the tracer was injected.

However, reports have indicated that ischemic events or infarction can occur after permanent carotid occlusion in some patients considered to be tolerant of carotid occlusion by BOT with SPECT [111]. Although the cause of these ischemic events seems to be either embolic or hemodynamic, how hemodynamic change may occur after permanent carotid occlusion has not been sufficiently clarified. Figure 11.23 illustrates the value of the balloon occlusion testing (BOT), in a 55-year-old female with a skull base meningioma.

Fig. 11.21 (**a**) ^{99m}Tc-HMPAO (pre-Diamox) brain SPECT images of a 52-year-old male with acute and chronic infarction in the region of right MCA territory. Patient had mental status changes and worsening of his neurological exam. After injection of 34.7 mCi of ^{99m}Tc-HMPAO IV in a dimly lit and quiet room, a brain SPECT scan was performed 15 min post radiotracer injection to assess for blood flow during the resting state. There is a dense focal area of tracer reduction in the mid right MCA territory, at the junction of approximately the frontoparietal region on the right, consistent with the known prior infarction. Around this area of dense reduction, the uptake is mildly reduced, but almost symmetric with respect to the contralateral left hemisphere. The findings of dense reduction of tracer uptake in the mid right MCA territory, consistent with the prior known infarction. (**b**) ^{99m}Tc-HMPAO (post-Diamox) brain SPECT to assess for the degree of hemodynamic vascular constraint. The patient was injected with 1 g of Diamox dissolved in sterile water. After waiting approximately 15 min for Diamox to have its vasodilatory effect, the 33.9 mCi of technetium 99m Ceretec IV was injected. After waiting approximately another 15 min for radiotracer uptake, incorporation, and fixation in the brain, a brain SPECT scan was performed. Again seen is the area of dense reduction in the mid right MCA territory as seen on the resting-state scan. However, on this scan, there is a significant reduction in the penumbral region around the infarction extending to involve the right frontal lobe predominantly but also the right temporal lobe and the right parietal lobe regions of the brain. There is more extensive degree of reduction in radiotracer uptake after Diamox as compared to rest in the region of right frontal lobe. Findings are consistent with hemodynamic vascular constraint in the right ICA territory with the most severe constraint involving the territories involving the right frontal lobe

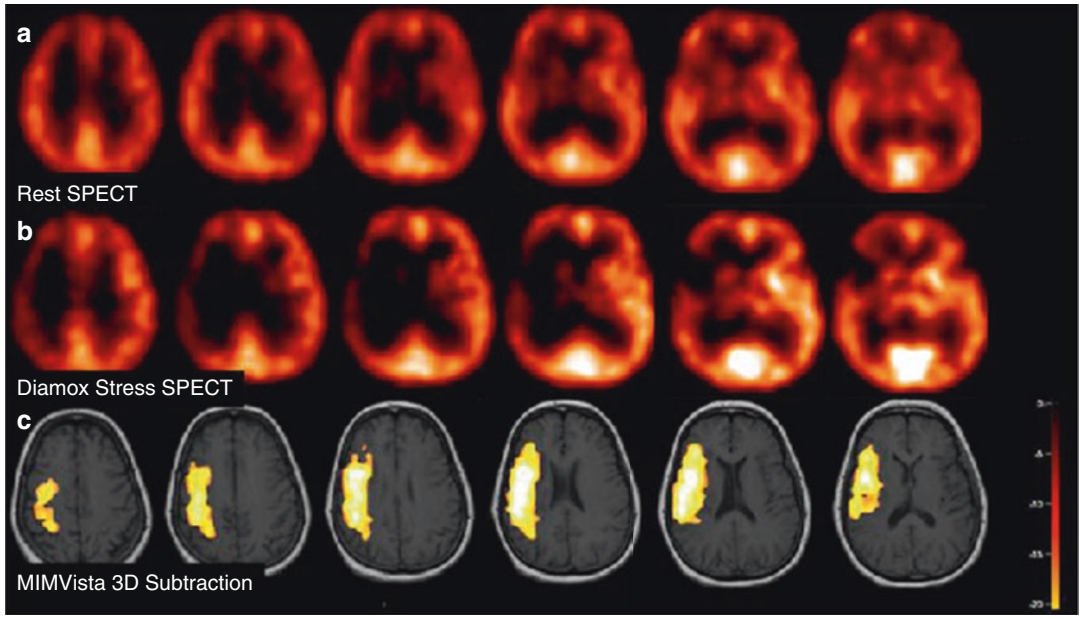

Fig. 11.22 A 60-year-old female with transient left-sided weakness and facial droop. (**a–c**) Rest, stress, and 3D subtraction SPECT demonstrate relative decreased cerebral perfusion in right ICA territory between rest and stress states

11.4.3.2 Dementia

Alzheimer's Disease

The initial rationale for imaging as a diagnostic tool for Alzheimer's disease is based on the disease-associated reduction in metabolic brain activity which can be visualized on both ^{18}F-FDG brain PET and ^{99m}Tc-HMPAO or ^{99m}Tc-ECD brain SPECT. There is a reduction of brain glucose metabolism identified on PET due to reduced neuronal metabolism and synaptic activity. A reduction in brain perfusion on regional cerebral perfusion SPECT is identified as a decrease in blood flow and reduction in neuronal and synaptic activity (proportional to the blood flow) in areas of reduced metabolism caused by amyloid deposition, a finding characteristic of Alzheimer's disease. The characteristic findings on ^{18}F-FDG brain PET and regional cerebral perfusion SPECT are as follows: (1) often bilateral involvement with asymmetry of reduction in the posterior temporoparietal cortical areas, (2) reduction of metabolism and blood flow to the posterior cingulate gyrus, (3) relatively early onset (less than 65 years) with more marked abnormalities on reduction of ^{18}F-FDG uptake and blood flow, (4) less common primary visual cortex involvement (which is more common in Lewy body dementia), and (5) coexisting micro- or macrovascular disease involvement resulting in neuronal injury and death.

Another recent and more specific rational for PET imaging of Alzheimer's disease is the utilization of amyloid radiotracers to target Aβ plaque in the brain, which is the hallmark of the disease.

SPECT Imaging of Alzheimer's Disease

Alzheimer's disease (the most common progressive degenerative dementia) is characterized by low global blood flow with accentuation of the diminution in the posterior temporoparietal lobes, relative sparing of the thalamus and corpus striatum as well as the sensorimotor cortex, and late involvement of the frontal lobes. Figure 11.24 shows a 67-year-old woman with a progressive cognitive decline. Her ^{99m}Tc-HMPAO brain SPECT scan shows significant diminution in global perfusion with accentuation of the rCBF decrease in the posterior temporoparietal regions. In the differential diagnosis of both Alzheimer's disease and vascular dementia, the cerebellum is often useful as a structure for semiquantitative

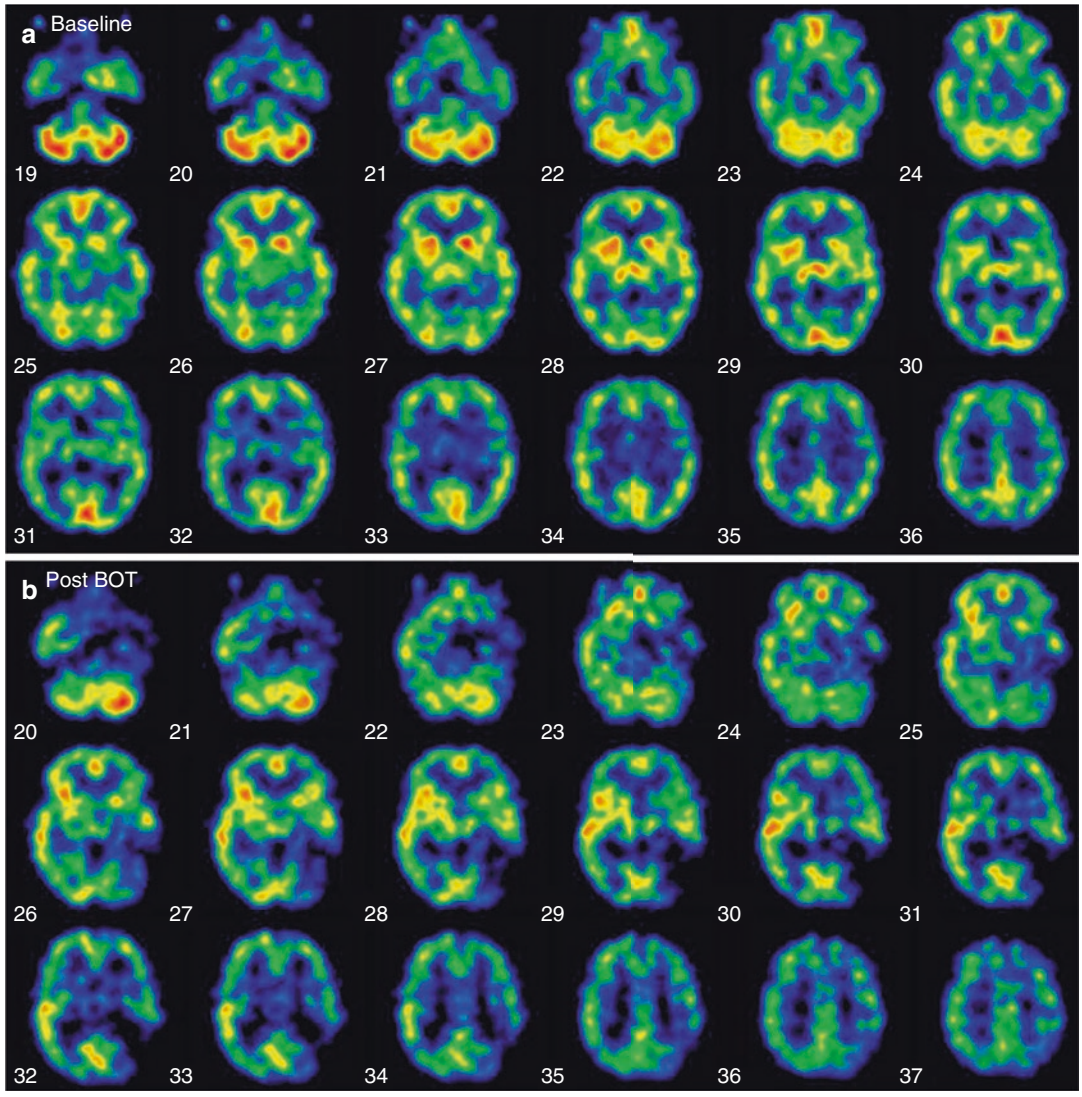

Fig. 11.23 (**a**) Pre-balloon occlusion baseline study: patient is a 55-year-old female with a skull base meningioma. The patient was injected with radiopharmaceutical (44.5 mCi of ^{99m}Tc-HMPAO IV) in a dimly lit and quiet room during the resting state. After waiting approximately 10 min for radiotracer incorporation into the brain, a brain SPECT scan was performed. SPECT images demonstrate symmetric tracer uptake in both the left and right internal carotid artery territories. This baseline study shows good filling of all vascular territories. Findings were consistent with normal baseline resting-state study, with no major vascular territorial significant reductions of blood flow. Post balloon occlusion images (**b**). In angiography suite, balloon test occlusion (*BOT*) of the left internal carotid artery was performed. During the 13 min of balloon inflation, the radiotracer (30.4 mCi of Tc-99m Ceretec) was injected intravenously. It was noted at 13 min the patient developed receptive aphasia and mild right hemiparesis, and the balloon was deflated. After patient stabilization, a brain SPECT scan was performed. There is a region of dense hypoperfusion in the left internal ICA territory. The scan shows essentially no significant blood flow to the posterior territory. There is also noted to be a right carotid cerebellar diaschisis. There is asymmetry also seen in the other areas of the left internal carotid artery distribution, most notably the basal ganglia region and hemithalamus. Subtraction images were also obtained (**c**), which also suggest areas of decreases perfusion in the region of left ICA. These findings are consistent with dense reduction of blood flow to a relatively large part of the left internal carotid artery indicating lack of collateral supply to the region

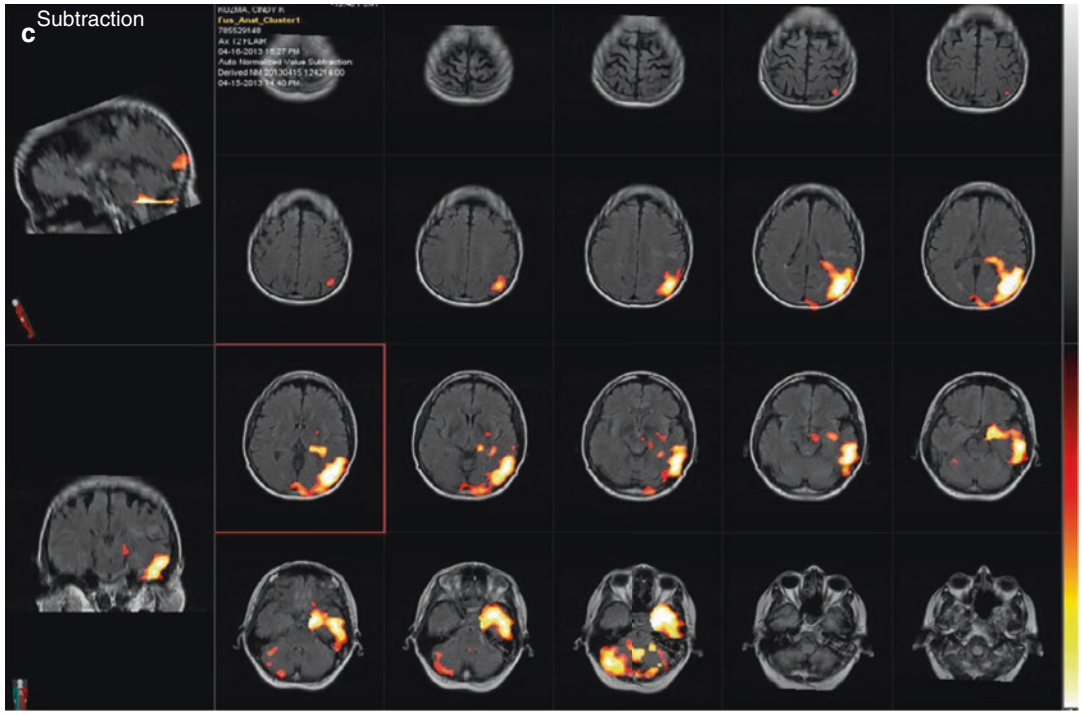

Fig. 11.23 (continued)

normalization of blood flow since it is relatively uninvolved in most cases of progressive cerebral cognitive decline.

It is important to distinguish, on a rCBF brain SPECT scan, the differences between a progressive degenerative dementia such as Alzheimer's disease and a vascular dementia, usually from hemodynamic compromise or embolic vascular disease at the internal carotid artery level, or higher. The importance of this differentiation now extends beyond the theoretical issue of clinical diagnosis and prognosis, since currently therapeutic protocols have now been established for these two causes of memory impairment [112]. Recent therapeutic advances are emerging from clinical trials of cholinomimetic drugs indicating that these drugs may improve the abnormal behavioral symptoms of Alzheimer's disease [112]. The inhibition of acetylcholinesterase (AChE) by acetylcholinesterase inhibitors reduces the enzymatic breakdown of endogenously released acetylcholine (ACh) resulting in greater synaptic concentrations of ACh at the postsynaptic ACh receptors. Inhibitors (such as donepezil) have been reported to significantly improve many manifestations of behavioral disturbance including agitation, apathy, hallucinations, and aberrant motor behavior. Cholinesterase inhibitors can be effective in slowing the memory loss in Alzheimer's disease. Figure 11.25 shows a ^{99m}Tc-HMPAO brain SPECT scan of a 66-year-old patient with early Alzheimer's disease before and after 1 year of therapy with the acetylcholinesterase inhibitor donepezil.

PET Imaging of Alzheimer's Disease

^{18}F-FDG Imaging

Accurate and early diagnosis of Alzheimer's disease (AD) is vital to ensure patients receive the proper treatment, research is targeted correctly, and prevention and cures are found. However, it can be difficult to distinguish between AD and other forms of dementia, or even from other reversible disorders. The standard tools for assessing AD include neuropsychological or cognitive evaluation, physical exam, neurological exam, laboratory testing, neuroimaging, behav-

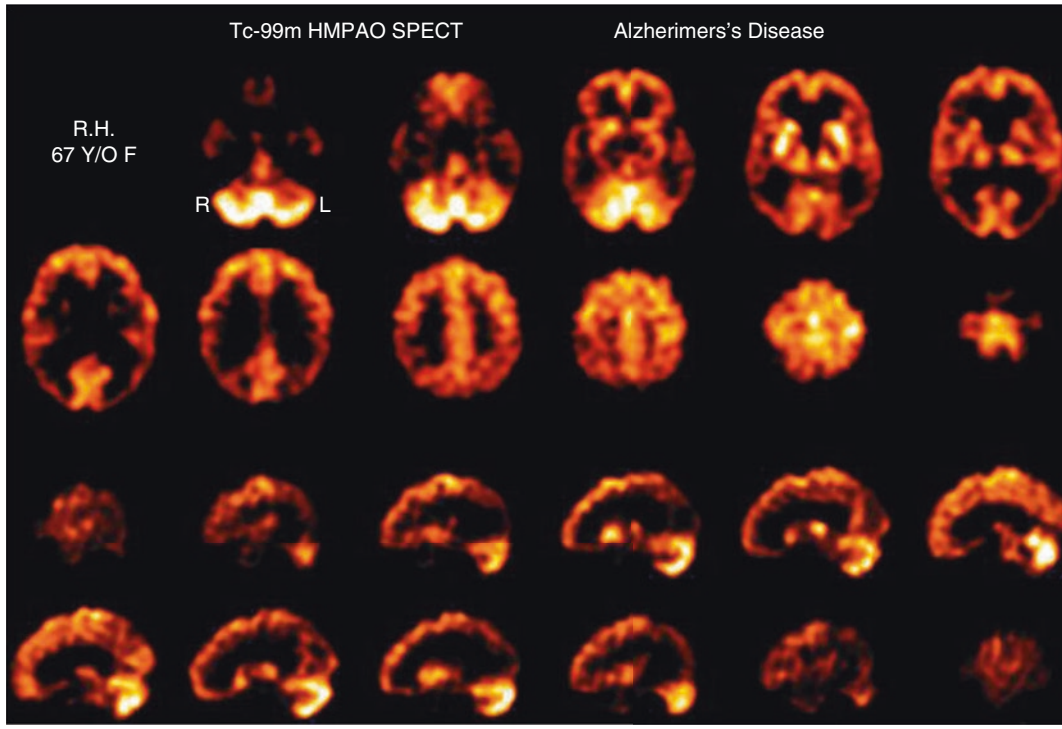

Fig. 11.24 Transverse sections (*top*) and sagittal sections (*bottom*) from a ^{99m}Tc-HMPAO brain SPECT scan of a 67-year-old female with Alzheimer's disease. The scans scan shows global decrease in blood flow to essentially all cortical structures (relative to the cerebellum) with accentuation of the decrease in the posterior temporoparietal region. There is relatively spared uptake in the cerebellum, caudate head, lentiform, and thalamus. Alzheimer's disease is characterized by globally diminished blood flow throughout the cortex, accentuation of that diminution in the posterior temporoparietal regions, and relative spearing of the basal ganglia structure and sensorimotor cortex, as well as the cerebellum. All these major features characteristic of the cerebral blood flow pattern defects seen in Alzheimer's disease are seen in this patient

ioral assessment, and patient history. ^{18}F-FDG PET imaging has been reported to have a sensitivity of 93% and a specificity of 63% [112]. Figures 11.26 and 11.27 show examples of ^{18}F-FDG PET scanning in the diagnosis of AD. In the analysis of ^{18}F-FDG uptake in these patients the three-dimensional stereotactic surface projection (3D SSP) algorithm was employed. The 3D SSP statistical map shows difference between a single subject and normal age-matched controls [112].

Figure 11.27 shows ^{18}F-FDG PET images of a 53-year-old male with symptoms of cognitive impairment and memory loss for 2 years. The patient satisfied the ADRDA criteria for probable Alzheimer's disease and had a Folstein mini-mental status score 16 out of 30. The MRI scan revealed mild diffuse atrophy. Figure 11.27 (left) shows standard PET images in transverse section illustrating reduction of ^{18}F-FDG uptake in the posterior temporoparietal regions. The patient's MRI scan showed nonspecific atrophy for age. Figure 11.27 (right) illustrates the value of analysis of ^{18}F-FDG PET statistical parametric mapping using 3D SSP. The 3D SSP statistical map shows difference between the patient and normal age-matched controls. The 3D SSP map shows significant reduction of metabolism in the temporoparietal regions bilaterally which on this image shows *Z* scores of significant reduction of ^{18}F-FDG uptake between four and six in the posterior temporoparietal regions.

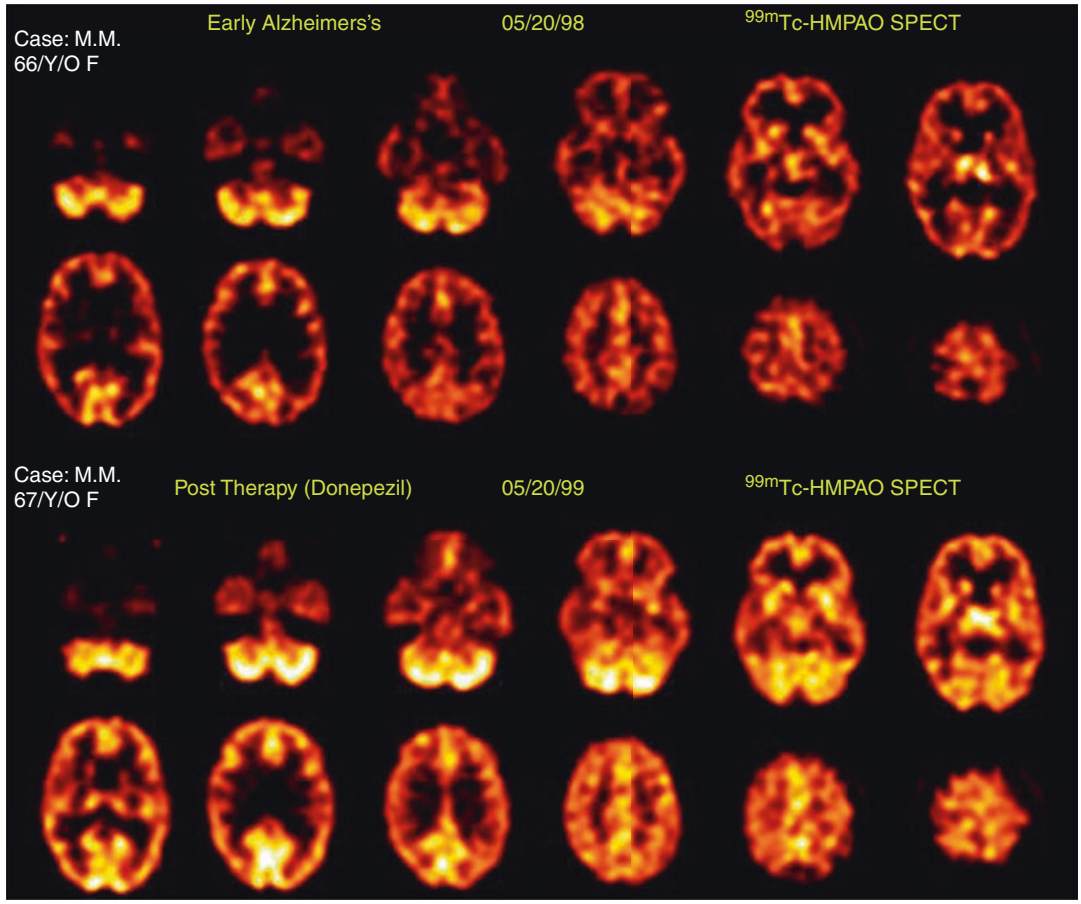

Fig. 11.25 ^{99m}Tc-HMPAO brain SPECT scan of a 66-year-old patient with early Alzheimer's disease who was treated with donepezil. The top two rows of images show sequential transverse sections from this patient's ^{99m}Tc-HMPAO scan before beginning therapy. There is diminution of rCBF to the posterior temporoparietal regions. The 1-year post-donepezil therapy (*bottom*) transverse sections show markedly increased blood flow to the frontal lobes and slightly increased blood flow to the posterior temporoparietal regions

^{18}F-Florbetapir (AMYViD or ^{18}F-AV-45) Imaging

PET amyloid-beta (Aβ) imaging detects amyloid plaque density in vivo in the human brain. Several PET imaging agents are available for Aβ imaging, including Pittsburgh compound B (^{11}C-PIB) and several F18-labeled agents (florbetapir, florbetaben, flutemetamol). The longer half-lives of the F18-labeled agents make them more practical in clinical settings.

In April 2012, the Food and Drug Administration (FDA) approved a new radiopharmaceutical agent to assist clinicians in detecting causes of cognitive impairment other than Alzheimer's disease. ^{18}F-florbetapir injection (AMYViD, Eli Lilly) is indicated for positron emission tomographic (PET) imaging of the brain in cognitively impaired adults undergoing evaluation for Alzheimer's disease and other causes of cognitive decline [112]. Florbetapir binds to amyloid aggregates in the brain, and the florbetapir PET image is used to estimate the density of β-amyloid neuritic plaque. As a component of a comprehensive diagnostic evaluation, the finding of a "negative" florbetapir scan should intensify efforts to find a non-Alzheimer's disease cause of cognitive decline. Florbetapirbrain imaging is a new type of nuclear medicine imaging, and the interpretation of the image requires special train-

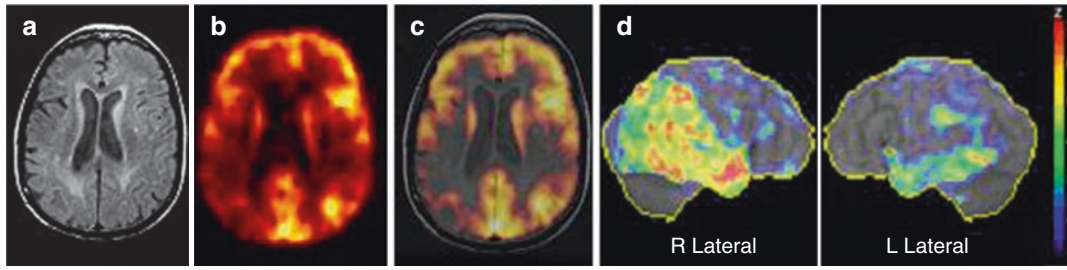

Fig. 11.26 Brain images from a 72-year-old female who was seen with concerns of cognitive decline for 6 months, but on questioning there has been memory loss beginning about 4 years prior to the ^{18}F-FDG PET scan. Her Folstein mini-mental score was 9/30 and satisfies the ADRDA criteria for probable Alzheimer's disease. (**a**) MRI scan reveals chronic small vessel ischemic changes and mild diffuse atrophy without a specific pattern which would be diagnostic for Alzheimer's disease. (**b**). ^{18}F-FDG brain PET scan section obtained from the Siemens HR + shows ^{18}F-FDG reduction involving the posterior temporal and parietal lobes bilaterally, the right more severely affected as compared to the left. (**c**) ^{18}F-FDG brain PET scan fused with the T1-weighted MRI scan. In the areas of decreased ^{18}F-FDG uptake, there is no cerebral atrophy out of proportion with other areas of the brain to indicate that the reduction of ^{18}F-FDG uptake is an atrophy effect, and therefore decreased ^{18}F-FDG uptake can be attributed to reduced neuronal metabolic activity as a result of neuronal impairment attributable to the amyloidopathy of Alzheimer's disease. (**d**) Three-dimensional stereotactic surface projection (3D SSP) results (lateral projections) of the patient's brain PET scan fused on a MRI standard brain. There is significant reduction of metabolism in the right temporoparietal region as indicated by the *color* overlay map which ranges from a *z* score difference between the patient and normal control database of two for *blue areas* of the brain and six for *red areas* of the brain. There is also reduction in the left temporal lobe with *z* scores ranging between 2 and 5. The overall constellation of findings is typical for Alzheimer's disease, slightly asymmetric, with greater impairment of the right hemisphere

ing. The unique features of the imaging information also require careful consideration when the scan results are integrated into a diagnostic evaluation.

Although the pathophysiological consequences of accumulation of β-amyloid in the brain are uncertain, neuropathological identification of amyloid plaques, typically at autopsy, has long been recognized as essential to confirming the diagnosis of Alzheimer's disease. Because β-amyloid plaques in the brain have been described as a "hallmark" of Alzheimer's disease, some clinicians may regard the florbetapir scan as a new test for the disease [112]. Figure 11.28 demonstrates ^{18}F-florbetapir (AMYViD) PET images of a 42-year-old male with cognitive decline. PET was performed to assess for amyloid plaques. Tracer uptake is less intense in the gray matter and more intense in the white matter, and none of the areas that are typically seen to be involved with Alzheimer's disease are identified as having significantly abnormal amounts of uptake relative to the cerebellar hemispheres to suggest the presence of abnormal amount of the amyloid plaque in the cortex.

Figure 11.29 illustrates AMYViD brain scan of a 55-year-old male with clinical suspicion of early onset of Alzheimer's disease. There is significantly increased tracer uptake in the gray matter, predominantly in the frontal lobes, but also to a significant degree in almost all of the other gray matter areas. There is also complete loss of distinction between white and gray matter in the frontal, temporal, and parietal lobes. This loss of distinction between white and gray matter is consistent with amyloid plaques deposition in the cortex, suggestive of Alzheimer's disease.

Imaging of Vascular Dementia with rCBF SPECT Tracers

Patients with vascular dementia may show relatively normal perfusions in areas not involved with vascular disease. These patients may benefit from a revascularization procedure before any further dementia or frank infarction occurs. A

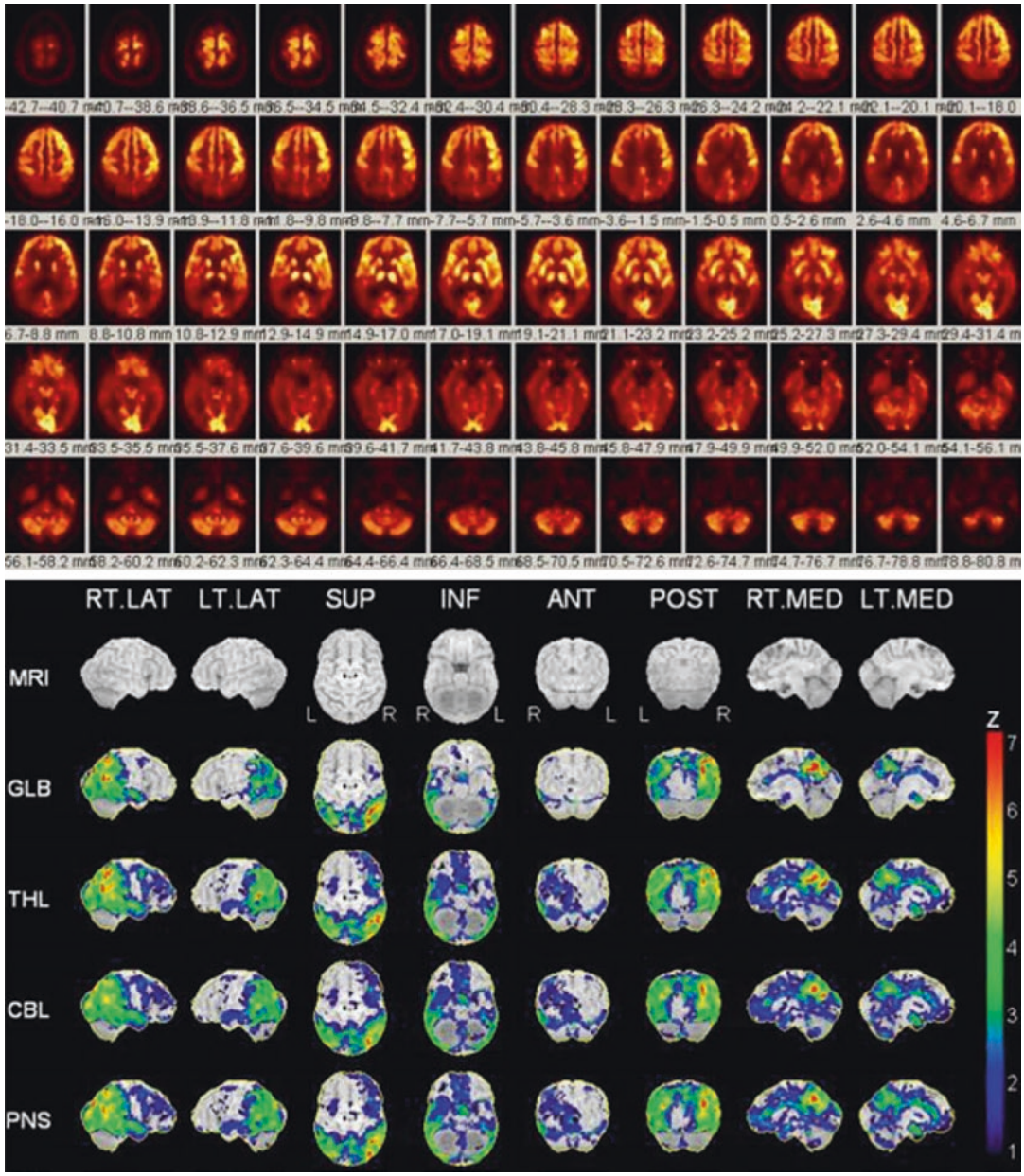

Fig. 11.27 (*Left*) ^{18}F-FDG brain PET scan in transverse section illustrating significant reduction in regional glucose metabolism in the posterior temporoparietal lobes bilaterally. The patient is a 52-year-old male with symptoms of cognitive impairment and memory loss for 2 years. The patient satisfied the ADRDA criteria for probable Alzheimer's disease with a Folstein mini-mental status measuring 16 out of 30. In addition to significant reduction of ^{18}F-FDG uptake involving the temporoparietal lobes bilaterally, there is also significant reduction in the posterior cingulate gyrus region. There is relative sparing in the sensorimotor cortical area and basal ganglia region. (*Right*) The 3D SSP map of statistically significant difference between the patient and age-matched normal controls shows significantly reduced glucose metabolism in the posterior temporoparietal lobes bilaterally, right slightly greater than left (lateral views), and posterior cingulate (medial views)

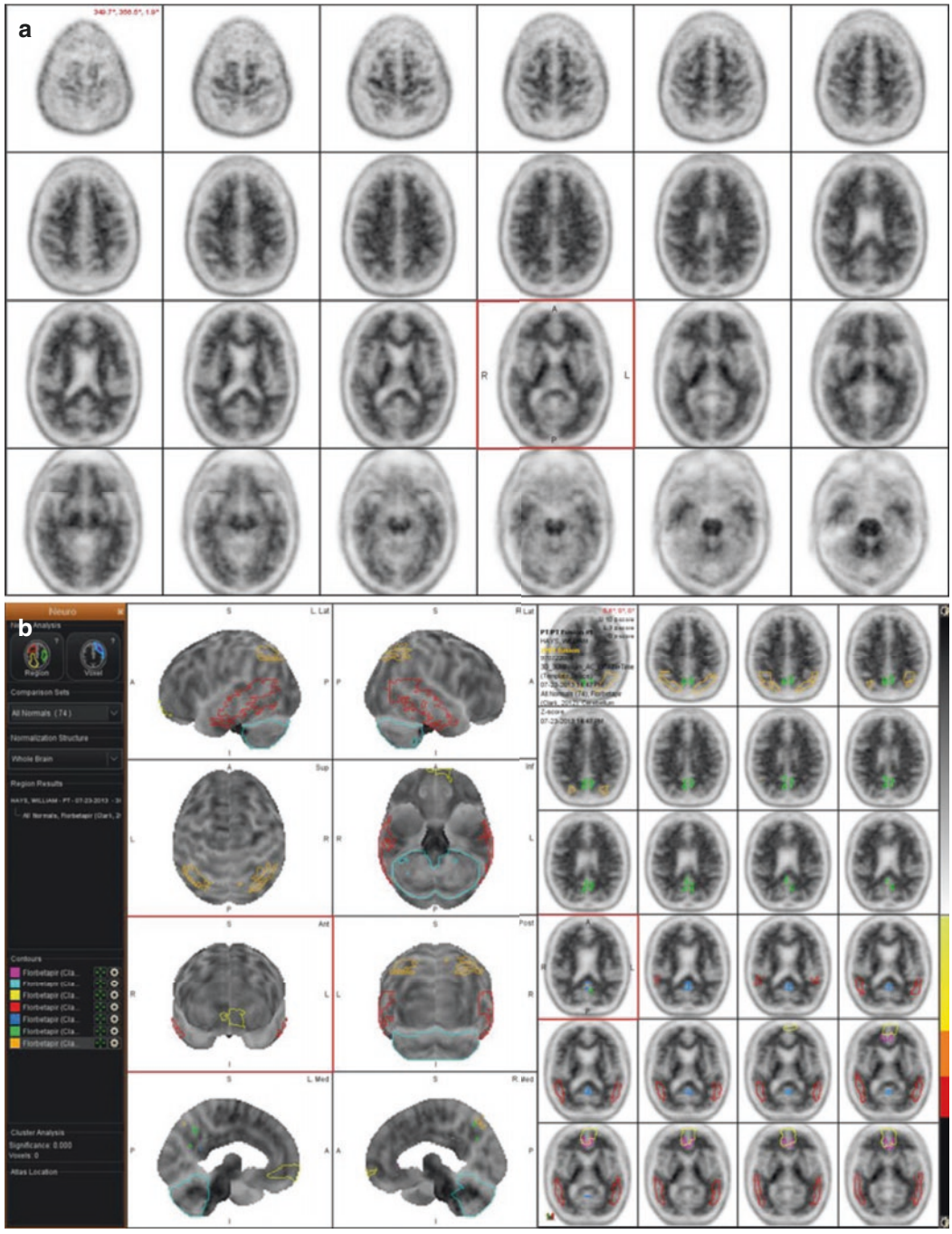

Fig. 11.28 Negative AMYViD scan: (**a**) Cross-sectional images of 42-year-old male with cognitive decline. This scan is being performed to assess for amyloid plaques. After injection of 10 mCi of AMYViD IV, a brain PET scan was performed at 30 min on the GE VCT PET/CT scanner. Visually, contrast uptake is less intense in the gray matter and more intense in the white matter, and none of the areas that are typically seen to be involved with Alzheimer's disease are identified as having statistically significantly abnormal amounts of uptake relative to the cerebellar hemispheres to suggest the presence of abnormal amount of the amyloid plaque in the cortex. Using the MIMvista quantitative algorithm (**b**), the target areas involving the superior parietal lobule, the precuneus, the posterior cingulate gyrus, the temporal lobes, the inferior frontal lobes, and the anterior cingulate gyrus do not show a statistically significant abnormal increase in tracer uptake to suggest the presence of abnormal amyloid plaque deposition

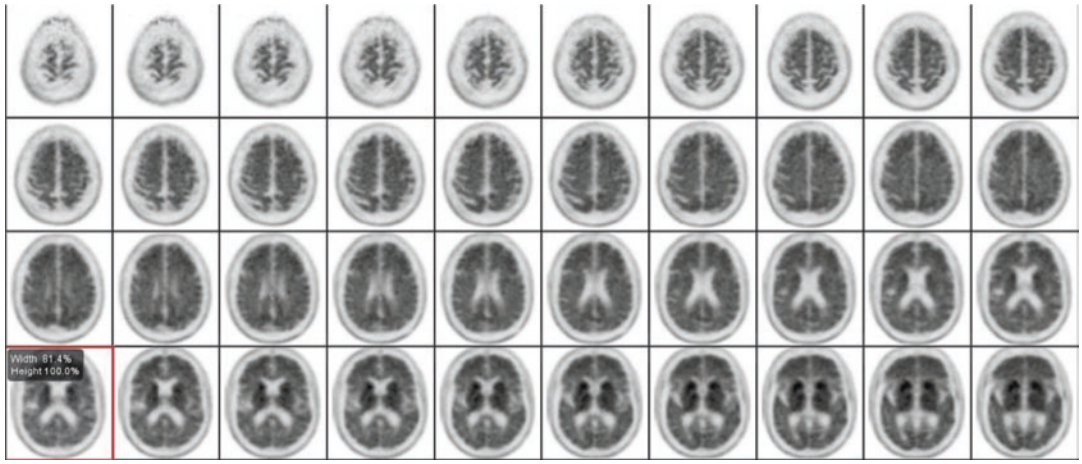

Fig. 11.29 Positive AMYViD scan: AMYViD brain scan of a 55-year-old male with clinical suspicion of early onset of Alzheimer's disease. After the injection of 10 mCi of AMYViD radiotracer in a dimly lit and quiet room, PET images were obtained at 30 min on the GE VCT PET/CT scanner. Images were reconstructed and sectioned in the transverse, sagittal, and coronal planes for interpretation. Non-contrast CT scan was also performed for attenuation correction and to obtain an assessment of brain atrophy. On visual inspection of the transverse sections, beginning inferiorly at the cerebellar hemispheres to assess white and gray matter uptake and progressing superiorly to the vertex, there is noted to be significantly increased tracer uptake in the gray matter, predominantly in the frontal lobes, but also to a significant degree in almost all of the other gray matter areas. There is noted to be a complete loss of distinction between white and gray matter in the frontal, temporal, and parietal lobes, and only the outer edge of the cortical gray matter is observed. Gray matter uptake is more similar to the white matter uptake, and the gray–white matter border is not observed. Findings of loss of distinction between white and gray matter are consistent with amyloid plaques deposition in the cortex

common form of vascular dementia is produced by small embolic events, and, therefore, small punctate cortical ribbon breaks may be observed in these patients. In addition, there tends to be more involvement of the frontal lobes as compared to the posterior regions of the brain. Finally, the subcortical structures or internal capsule region may demonstrate asymmetry in blood flow due to the presence of small embolic events in these locations. Figure 11.30 illustrates a case of vascular dementia in a 62-year-old male with bilateral MCA chronic ischemia and transient ischemic attacks. The image shows a CT scan of the patient and a corresponding section from the ^{99m}Tc-HMPAO brain SPECT scan and the CT–SPECT fusion image. The CT scan shows atrophy with areas of tissue loss characteristic of small embolic infarctions. The ^{99m}Tc-HMPAO brain SPECT shows diminution at the 2 o'clock and 4 o'clock as well as the 8 o'clock and 11 o'clock positions which is characteristic of embolic disease. There is no specific reduction of rCBF to the posterior regions of the brain as would be characteristic of Alzheimer's disease.

Imaging of Tau Deposits in Alzheimer's Disease Using [^{18}F]AV-1451

It is well established that the two primary cardinal lesions associated with Alzheimer's disease are the neurofibrillary tangles and the senile plaques. The neurofibrillary tangle consists of abnormal accumulations of abnormally phosphorylated tau within the perikaryal cytoplasm of certain neurons. Braak and Braak noted that mesial temporal neurofibrillary tangles are a common autopsy finding in subjects who died in their late 1950s to late 1970s and had few Aβ plaques [113]. This led to the hypothesis that mesial temporal tau pathology may follow independent pathways in the normal aging process separate from pathways leading to AD [114]. These questions underscore the need for a non-invasive technique capable of assessing brain tau

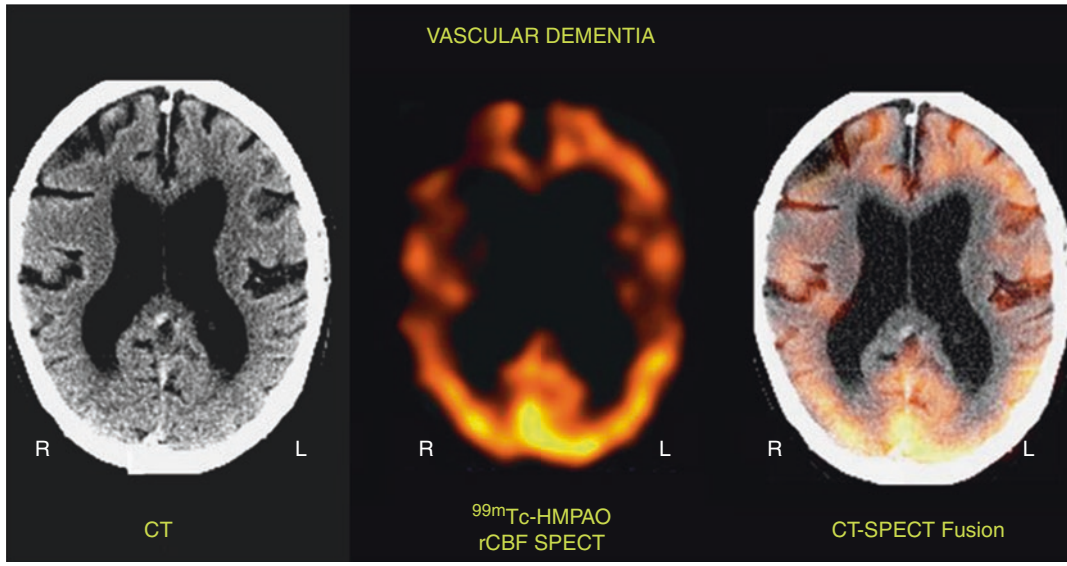

Fig. 11.30 A 62-year-old male described in the text with bilateral MCA chronic ischemia and transient ischemic attacks. The image shows a CT scan of the patient (*left*), a corresponding section from the ^{99m}Tc-HMPAO brain SPECT scan (*middle*), and the CT–SPECT fusion image (*right*). The CT scan shows atrophy with areas of tissue loss characteristic of small embolic infarctions. The ^{99m}Tc-HMPAO brain SPECT scan through the same level shows irregular uptake in the cortical structures with diminutions at the 2 o'clock and 4 o'clock as well as the 8 o'clock and 11 o'clock positions which is characteristic of embolic disease. There is no reduction of rCBF to the posterior portion of the brain as noted in the case of Alzheimer's disease

deposits analogous to the development of Aβ imaging capabilities.

[^{18}F]AV-1451 (F-18 flortaucipir) is one of the several new tau-specific imaging agents that have advanced to human studies. Preclinical investigations of AV-1451 demonstrated its selective labeling of paired helical filament tau [115]. Initial human studies of [^{18}F]AV-1451 were reported [116] in six subjects: 2 AD [mini-mental state examination score (MMSE): 21 and 7], 1 MCI (MMSE: 26), and 3 NC (MMSE > 28). Increased [^{18}F]AV-1451 retention was observed in regions associated with tau deposits in AD and MCI subjects (parietal, lateral temporal, and mesial temporal cortices), whereas no significant [^{18}F]AV-1451 retention was observed in any of the 3 NC subjects studied. These findings are consistent with neuropathological studies forming the basis for the Braak staging scheme. Figure 11.31 shown distribution of [^{18}F]AV-1451 labeled tau, as compared to FDG (metabolism) and C-11 PiB (b-amyloid) in a 60 year old male with AD.

Imaging of Other Causes of Dementia

Pick's disease is a rapidly progressing frontal lobe-type dementia. A ^{99m}Tc-HMPAO brain SPECT scan of a patient with early Pick's disease is shown in Fig. 11.32. The scan is of a 67-year-old female with rapidly progressing frontal lobe-type dementia. The CT scan shows mild atrophy in the peri-Sylvian regions but no significant frontal lobe atrophy. The ^{99m}Tc-HMPAO brain SPECT scan shows marked diminution of tracer uptake in the frontal lobes. The fusion image shows that the diminution is due to loss of regional cerebral activity, since there is no substantial cortical gray matter loss.

Primary progressive aphasia (PPA) is an uncommon type of degenerative dementia characterized by gradual impairment of language function that remains neuropsychologically focal for several years with sparing of the memory domain. Compared with other neurodegenerative disorders that initially affect cognition followed by language impairment, many patients with PPA retain their cognitive functions allowing them to

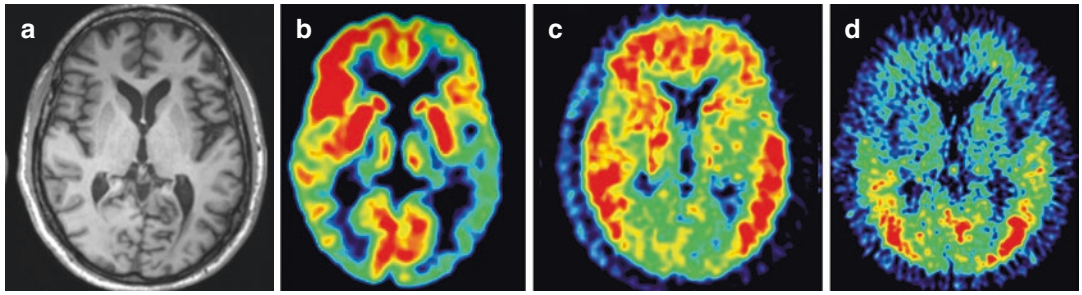

Fig. 11.31 PET images from a 60 y/o M with fatigue, difficulty concentrating, memory, and mood disorder, diagnosed with AD. (**a**) structural MRI, (**b**) [^{18}F]FDG PET, (**c**) [^{11}C]PiB PET, and (**d**) [^{18}F]AV-1451 PET. The MRI scan shows mild atrophy. The [^{18}F]FDG scan shows abnormally decreased uptake in the posterior brain regions. The degree of uptake is asymmetric, much lower in the left posterior temporoparietal brain region, also a pattern characteristic of AD. The [^{11}C]PiB PET scan demonstrates abnormally increased uptake in the temporal, parietal, and frontal lobes in a pattern characteristic of AD. The [^{18}F]AV-1451 PET scan shows broad areas of abnormal intensely increased [^{18}F]AV-1451 uptake in the bilateral parietal and occipital lobes

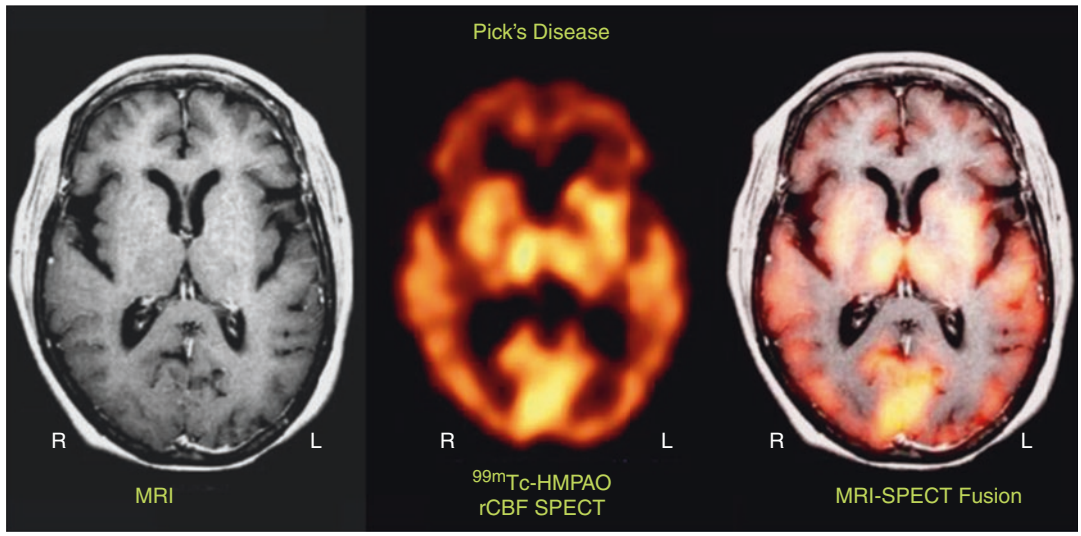

Fig. 11.32 ^{99m}Tc-HMPAO brain SPECT scan of a patient with early Pick's disease. The scan is of a 67-year-old female with a rapidly progressing frontal lobe-type dementia. The CT scan (*left*) shows mild atrophy in the Sylvian regions but no frontal lobe atrophy. The ^{99m}Tc-HMPAO brain SPECT scan shows marked diminution of tracer uptake in the frontal lobes (*middle*). The fusion image (*right*) shows that the diminution is due to loss of cortical synaptic activity (which is proportional to regional cerebral perfusion) since there is no substantial cortical gray matter loss in the region of frontal lobe hypoperfusion seen on the ^{99m}Tc-HMPAO brain SPECT scan

continue with their activities of daily living. "Word-finding" or "naming" difficulty (dysnomia) is the most common and earliest clinical presentation of PPA. Figure 11.33 shows an MRI and ^{99m}Tc-HMPAO SPECT scan of a 65-year-old woman with a mild degree of dysnomia. The subject presented with a 7-year history of "tripping" over words. Initially, she had trouble with multisyllable words but progressed to have difficulty even with single-syllable words. She complained of problems with her decreasing fluency. She claims to know what she wanted to say but is "not able to get the words out." She used to play the piano and sing with accompaniment but lately complains of loss of her interest due to her inability to get the right tune. She scored 30/30 on the

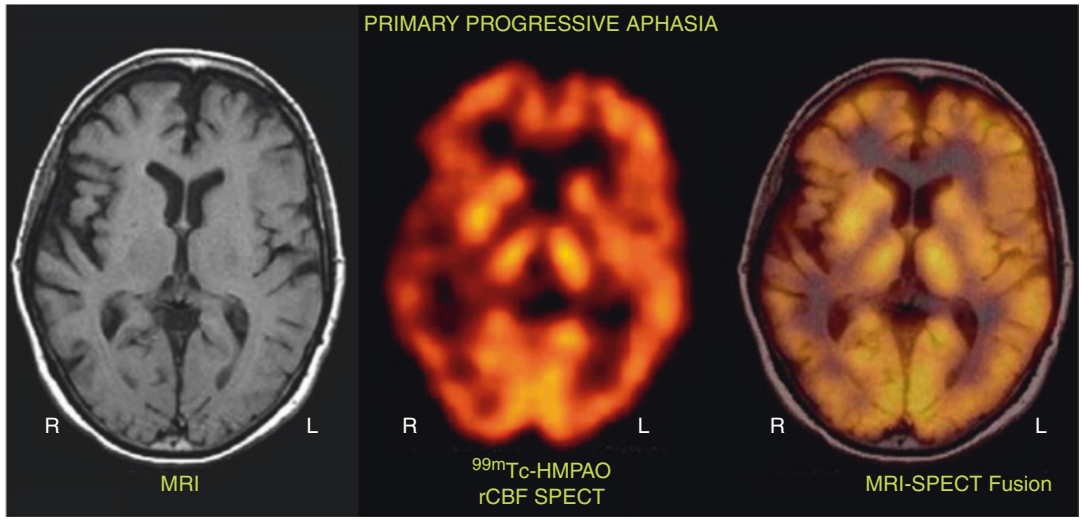

Fig. 11.33 MRI scan (*left*), ^{99m}Tc-HMPAO brain SPECT scan (*middle*), and a MRI–SPECT fusion image (*right*) of a 65-year-old female with a mild degree of dysnomia. The subject presented with a 7-year history of "tripping" over words. She initially had trouble with multisyllable words but currently has difficulty even with single-syllable words. The images show right frontotemporal atrophy on MRI. The SPECT scan, however, shows a much larger region of decreased perfusion involving the frontotemporal region as well as the posterior temporal region. This case is an unusual presentation of primary progressive aphasia since it involves the right side of the brain in a right-handed woman. The images demonstrate that there is a functional deficit extending beyond the mild degree of anatomic atrophy

mini-mental status examination (MMSE). Her right frontotemporal region shows atrophy on MRI and reduced rCBF on SPECT. There is a larger area of right frontotemporal hypoperfusion on rCBF SPECT in relation to the degree of atrophy identified on MRI.

11.4.3.3 Epilepsy: Epileptogenic Focus Localization Imaging

Regional cerebral perfusion evaluation in patients with epilepsy has proven to be of significant clinical value for identification of the epileptogenic focus location. The underlying pathophysiology concerning the advantages of using regional cerebral perfusion tracers in epilepsy is based on the clinical observation that was first reported by Sir Victor Horsley more than 100 years ago. He described (by direct observation of the brain during surgery) an increase in cortical blood flow in the area of seizure discharge. Therefore, the most valuable use of ^{99m}Tc-HMPAO evaluation of the epilepsy patient is to localize the epileptogenic focus during the ictal state.

Ictal ^{99m}Tc-HMPAO or ^{99m}Tc-ECD SPECT

In order to perform these studies, the tracer (either ^{99m}Tc-HMPAO or ^{99m}Tc-ECD) must be rapidly injected immediately after seizure onset. Because the time of an active seizure event cannot be predetermined, and occurs over a relatively short time (typically a few seconds to 1–2 min). It becomes immediately obvious that the tracer could not be ordered and prepared by the radiopharmacy and brought to the epilepsy unit in time to perform an IV injection at the time of the seizure.

Thus it is necessary to have the tracer labeled and in the epilepsy monitoring unit, near the patient, in a radiation shielding container and quickly accessible to the person performing the IV injection. However, even if the person performing the injection maintained a position at the bedside of the patient, it was still very difficult to obtain a satisfactory ictal injection during the timeframe of most seizure events given the injection delay time required to remove the tracer from the shielded case, perform for the injection and inject the venous

Fig. 11.34 (left) The epilepsy monitoring unit video EEG stations. Technologies simultaneously view the epilepsy patients Video-EEG, and when a desired seizure occurs they activate the automated injector by pushing a control button, and noting satisfactory activation by the automated injector status monitor, upper right. (right) Shows the patient as she is receiving the tracer through the automated injector system (positioned by the patient bedside). Immediately after the delivery of tracer, a second syringe within the automated injector flashes the IV line. After the injection is complete, the technologist can be seen entering the room to obtain the subjective seizure semiology from the patient, and inform the patient that they just received the injection, and they will be transported to the Department of nuclear medicine for imaging

flush of the tracer. Nevertheless, for the first decade of practice, from approximately 1990 to 2000, this was the procedure [117]. In many cases, the ictal event was missed, and it became prohibitively expensive for this operation to be continued given the cost of having a patient admitted to the hospital for several days, purchasing the tracer, and waiting for the seizures event to occur and then trying to inject the tracer in a timely fashion.

Introduction of the Automated Injector

Thus, it became necessary to invent an automated injector that could be triggered from the epilepsy monitoring unit by an epilepsy monitoring technician injector [118] as shown in Fig. 11.34.

This also requires extending approvals of radiation safety policies and establishment of guidelines for training of EEG personnel (non-nuclear medicine technologist) to ensure that the proper techniques and safeguards regarding quality control are maintained. However, once these procedures became more routine, it became possible to have a relatively high rate of tracer injections during the ictal state at the University of Pittsburgh hospitals [119].

In our initial study [118], we found significantly improvement in obtaining high-quality ictal SPECT scans. We examined ictal SPECT data from Group A (45 patients, 61 scans) before implementing the automated injector compared to Group B (15 patients, 16 scans) after implementing the automated injector (Table 11.1). In summary, there was a reduced injection time after the onset of seizure and injection (latency time), a decrease in the number of necessary repeat studies, and a lower number of days of hospitalization. There was also a reduction in radiation exposure to hospital personnel involved in the injection process (Fig. 11.35).

Table 11.1 Comparison of Parameters Between Subject Groups Before Use of the Automatic Injector (Group A) with Subject Groups After Use of the Automatic Injector (Group B)

Number of studies	Average ictal delay (s)	# of true ictal studies	# of repeat study	Extra days in hospital
Group A ($n = 61$)	19.6	37/61 (61%)	15/61 (25%)	0.6
Group B ($n = 16$)	11.5	13/16 (81%)	1/16 (6%)	0.1
p value	0.008			0.02

After injection, the patient is stabilized and transferred to the SPECT scanner within several hours to receive a brain SPECT scan which will indicate the regional cerebral perfusion at the time of ictus. This method is feasible since ^{99m}Tc-HMPAO or ^{99m}Tc-ECD is irreversibly trapped in

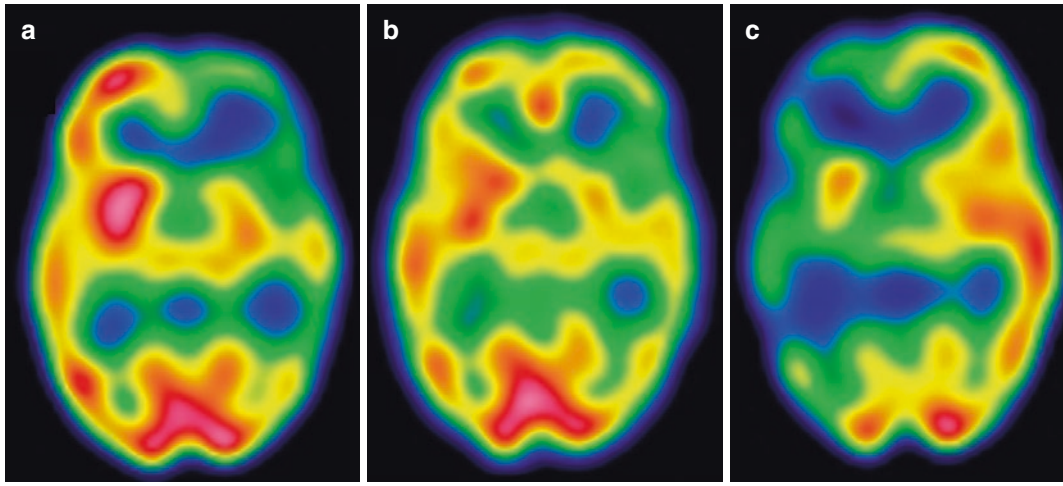

Fig. 11.35 Ictal and interictal SPECT scans with manual injection in 3-year-old male with intractable epilepsy as compared with ictal SPECT using the automated injector. (**a**) Interictal SPECT images demonstrate diffuse prominent hypoperfusion involving left frontotemporal region. (**b**) First ictal SPECT attempt. The injection was performed 40 s after onset of seizure. Seizure duration was 46 s, and therefore this late ictal SPECT scan which redemonstrated the hypoperfusion in left frontotemporal region, with similar perfusion pattern seen in interictal SPECT. (**c**) Repeated ictal SPECT using the automated injector. The injection was able to be performed 2 s after onset of seizure. This seizure duration was only 9 s. Because this was a very early ictal SPECT, the scan was able to demonstrate increased perfusion to left frontotemporal region compared with right when subtracted relative to the interictal (baseline) SPECT. Due to the identification of the probable seizure location, the patient underwent surface grid electrode placement and underwent careful resection of the epileptogenic focus which rendered the patient nearly seizure free with minimal neurological deficit

the epileptogenic hyperemic region at the time of seizure and therefore, during the period between injection and scan, there is essentially no tracer redistribution.

The subsequent scan (albeit several hours after the injection) still shows hyperemia in the region of the epileptogenic focus.

Figure 11.36 illustrates the value of ictal SPECT in a 9-year-old right-handed boy who had a 7-year history of intractable seizures. The figure shows a ^{99m}Tc-HMPAO brain SPECT scan which was performed 2 h after tracer injection. The tracer was injected at the bedside 3 s after seizure onset (the seizure lasted ~25 s).

The ictal SPECT scan shows a focal area of intense uptake in the right frontal lobe. The patient's developmental history and neurological findings on examination were normal. Computed tomographic (CT) and magnetic resonance imaging (MRI) studies carried out at our and other institutions were normal. Multiple EEG investigations were inconclusive. On referral to our institution, the patient averaged 20–30 seizures a day characterized by an aura of tingling in the mouth, followed by simultaneous extension of the legs and flexion of the right upper extremities with nonpurposeful movements of both legs lasting 20 s. Previous EEGs revealed infrequent slowing over the right hemisphere. Multiple video EEG monitoring studies performed at our and other institutions showed stereotypical seizures with no ictal scalp localization. Interictal activity revealed occasional sharp discharges involving the right frontal central parietal regions.

The ^{99m}Tc-HMPAO ictal brain SPECT scan showed a focal area of hyperperfusion in the right premotor area. The right to left asymmetry in blood flow for this region was 1.32, and the intensity of uptake in the right frontal lobe measured 1.13 (cortical to cerebellar ratio) with a range of normals = mean ± 1SD of 0.90 ± 0.07. The result of the ictal brain SPECT scan was subsequently co-registered with the MRI scan and placement of subdural grid electrodes confirmed the epilep-

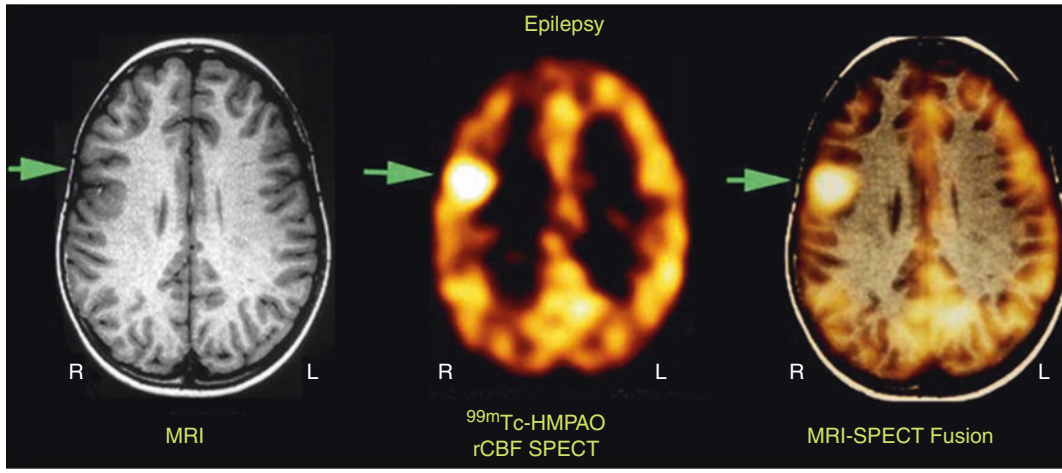

Fig. 11.36 Frontal lobe epilepsy in a 9-year-old right-handed boy. The MRI scan (*left*) is normal. The ^{99m}Tc-HMPAO brain SPECT scan (*middle*) reflects the regional cerebral perfusion at the time the tracer was injected during the epileptogenic seizure. The intense region of hyperemia is seen at the 10 o'clock position. A SPECT MRI fusion image (*right*) clearly identifies the location of the focus on the MRI scan

togenic focus location. Based on the fusion image, the anatomic location was determined, the epileptogenic focus was surgically excised, and the patient was rendered seizure-free.

It has been shown that ictal SPECT in patients with extra-temporal lobe epilepsy have superior localization capability as compared to interictal ^{18}F-FDG PET. On the other hand, if ictal SPECT is not available, identification of the epileptogenic focus during the interictal state using ^{99m}Tc-HMPAO is less sensitive compared to interictal ^{18}F-FDG PET. In cases of suspected temporal lobe epilepsy, the preferred diagnostic method is to perform interictal ^{18}F-FDG PET in addition to ictal and interictal SPECT.

Figure 11.37 shows epileptogenic focus localization in a patient with history of intractable complex partial epilepsy for 2 years. Ictal SPECT shows increased rCBF in the region of right temporal lobe, corresponding to an area of decrease uptake on interictal SPECT. MIMvista SPM subtraction shows significant right temporal rCBF on ictal SPECT.

^{18}F-FDG Brain PET Assessment in the Interictal State

Figure 11.38 illustrates concordance between abnormalities on MRI and ^{18}F-FDG PET in a 16-year-old boy with temporal lobe epilepsy and hippocampal sclerosis of the right mesial temporal lobe on MRI. The MRI shows abnormal high signal intensity in the right hippocampal region. The ^{18}F-FDG PET shows a corresponding area of focal reduction of ^{18}F-FDG uptake in the right hippocampal region. After right temporal lobectomy, the patient was rendered seizure-free.

Figure 11.39 demonstrates the significant advantage of ictal SPECT as compared to interictal ^{18}F-FDG PET. The patient, a 42-year-old female with seizure activity felt to arise from the frontal lobe regions, underwent a ^{18}F-FDG brain PET scan which was nonlocalizing. An interictal ^{99m}Tc-HMPAO brain SPECT scan also showed minimal reduction in the frontal lobe, as well as other areas of the brain. An ictal brain SPECT scan showed significant hyperemia in the right frontal lobe. The figure shows correlative images of the significant hyperemia on ictal SPECT as compared with nonspecific reduction on ^{18}F-FDG PET.

Ictal and Interictal SPECT Analysis

A subgroup of "frontal" focal cortical epilepsy involves the pericallosal gyrus. This type of epilepsy, termed "cingulate epilepsy," demonstrates variable clinical semiology and poorly localizing

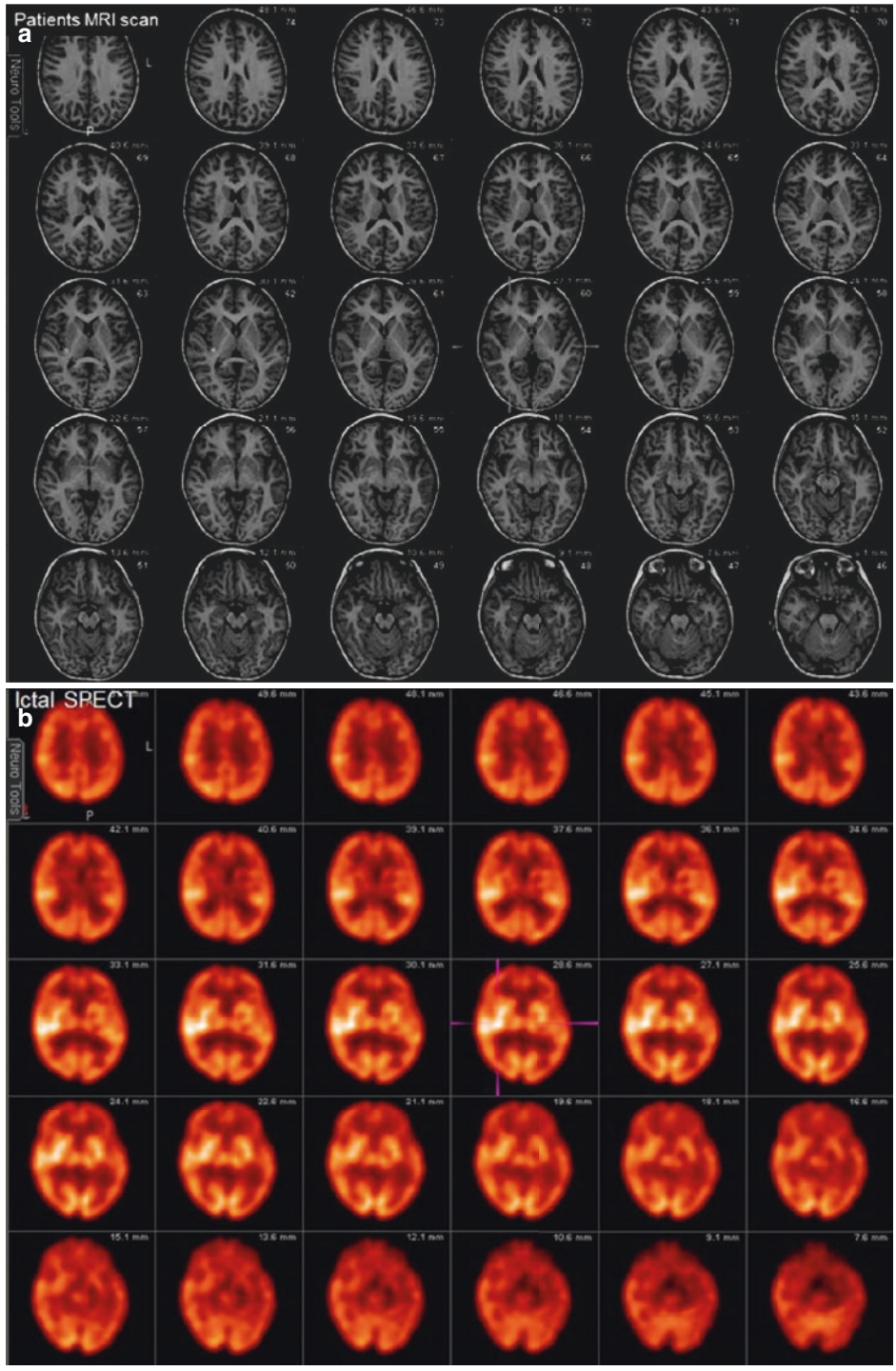

Fig. 11.37 (**a**–**e**) Patient with history of intractable complex partial epilepsy for 2 years presents for evaluation localization of epileptogenic focus. Seizure semiology reveals unusual scream during sleep appears scared and hallucinating and seeing objects. Daily nocturnal seizures average from two to up to eight per night. (**a**) MRI findings are suggestive of a possible small AVM, in the right temporal lobe. (**b**) Ictal SPECT shows increased rCBF in the region of the right temporal lobe, corresponding to an area of decrease uptake on interictal SPECT (**c**). (**d**) MIMvista SPM subtraction shows significant right temporal rCBF on ictal SPECT. (**e**) Shows pre- and postsurgery MR images

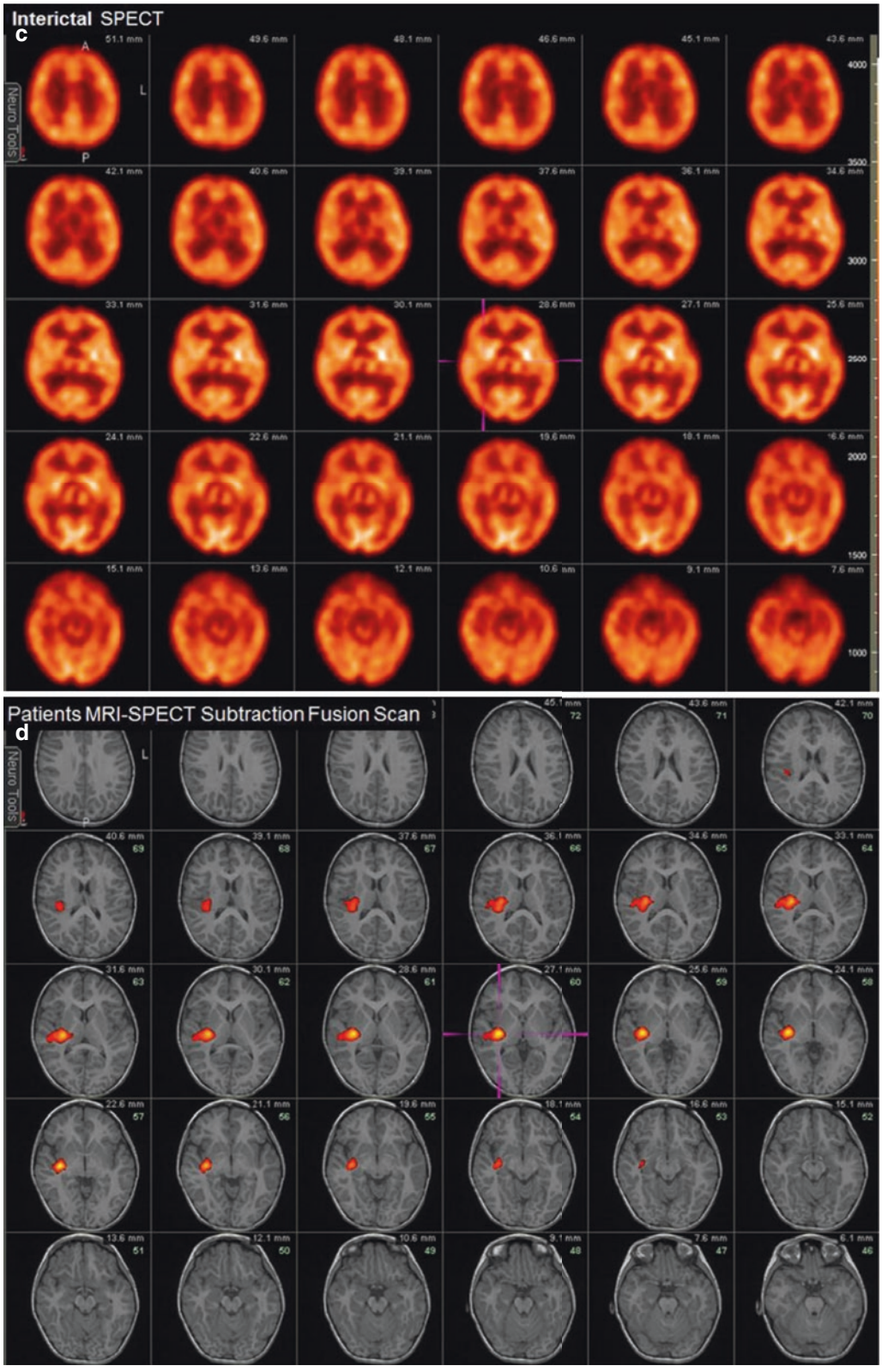

Fig. 11.37 (continued)

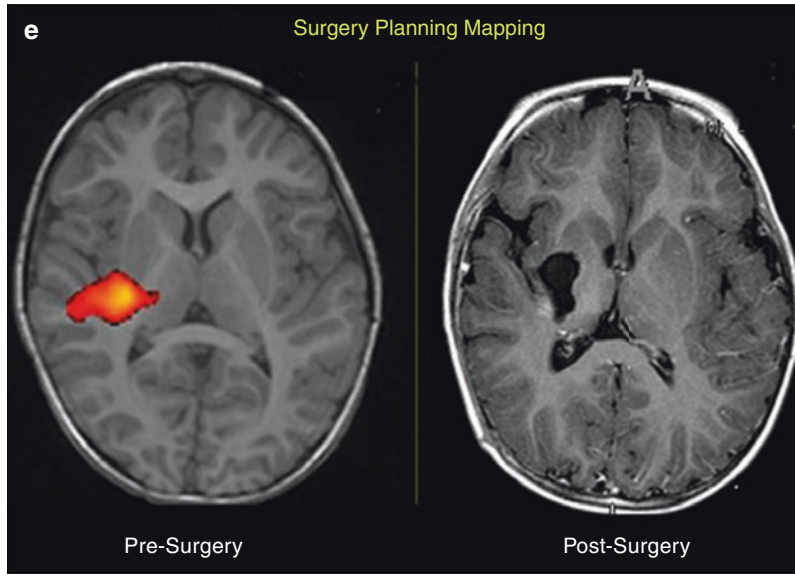

Fig. 11.37 (continued)

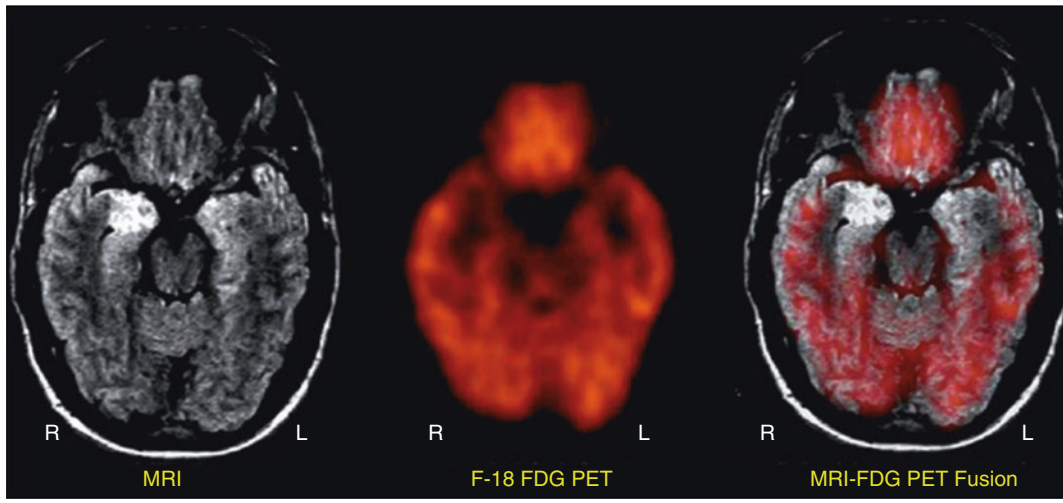

Fig. 11.38 Right mesial temporal lobe sclerosis in a 16-year-old boy. (*Left*) MRI shows abnormal high signal intensity in the right mesial temporal lobe (hippocampal region). (*Middle*) FDG PET scan shows a focal reduction of FDG uptake in the right mesial temporal lobe (hippocampal region). (*Right*) MRI–PET fusion image illustrating that the reduction in FDG corresponds to the region of MRI increase in signal intensity

scalp electroencephalography patterns [120]. Seizures in most patients consist of "pseudoabsences" often mistaken for inattention and can be confused with "absence" attacks resulting in misdiagnosis and unsuccessful seizure control. Dropping or nodding of the head is commonly observed. Head turning to the side contralateral to the involved cingulum and autonomic phenomena are observed in some patients. There is also a strong association between psychotic behavior and cingulate epilepsy. A complete clinical, neuropsychological, and neuroimaging investigation is therefore usually performed in an attempt to localize the epileptogenic focus in this

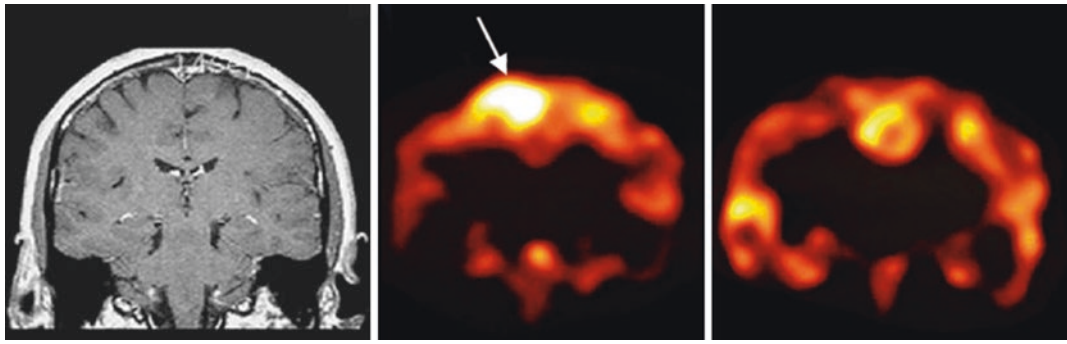

Fig. 11.39 Coronal images from MRI (*left*), ictal ^{99m}Tc-HMPAO SPECT (*middle*), and interictal ^{18}F-FDG PET scan (*right*) of a 42-year-old female with intractable seizures. (*Left*) The MRI scan is normal. *Middle*. The ictal ^{99m}Tc-HMPAO brain SPECT scan showed a focal area of significant hyperemia in the right mesial frontal lobe (*arrow*). (*Right*) There was minimal reduction of ^{18}F-FDG uptake in this location, but this was not specific for identification of the epileptogenic focus. This scan illustrates the relative nonspecificity of mild areas of reduction on ^{18}F-FDG brain PET scan in cases of frontal lobe epilepsy, and in these cases, an ictal ^{99m}Tc-HMPAO brain SPECT scan can provide greater accuracy in diagnosis

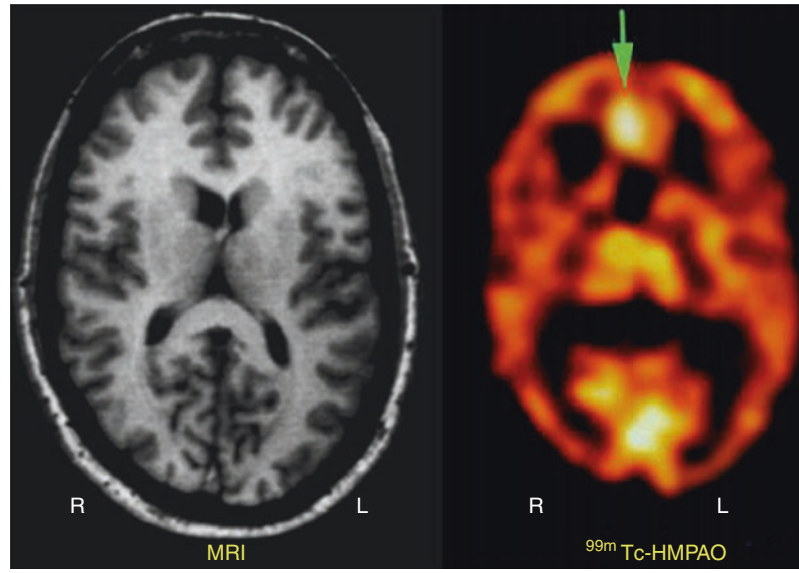

Fig. 11.40 High-resolution MRI (*left*) and ictal ^{99m}Tc-HMPAO brain SPECT scan (*right*) of a patient with cingulate gyrus epilepsy. Evaluation of the frontal lobes and cingulate region on MRI failed to reveal any structural abnormalities to suggest a possible seizure focus. The ictal SPECT scan (*right*) showed a focal region of hyperperfusion in the right anterior cingulate region (*arrow*)

subgroup of patients. Due to the difficulty in the identification of these seizure foci, we illustrate the value of comparing ictal SPECT with normal controls using statistical parametric mapping (SPM). Figure 11.40 shows a high-resolution MRI and ictal ^{99m}Tc-HMPAO brain SPECT scan of a 39-year-old man with cingulate gyrus epilepsy. Evaluation of the frontal lobes and cingulate region on MRI failed to reveal any structural abnormalities to suggest a possible seizure focus.

The ictal SPECT scan showed a focal region of hyperperfusion in the right anterior cingulate region. Count data were obtained by drawing regions of interest (ROI) around the right and left cingulate gyrus and showed that the right to left blood flow ratio was 1.3 and the right cingulate gyrus blood flow relative to cerebellar counts is 1.54 which is >4 SD above our normal control population (cingulate gyrus/cerebellum = 1.05 ± 0.12). Figure 11.41 shows

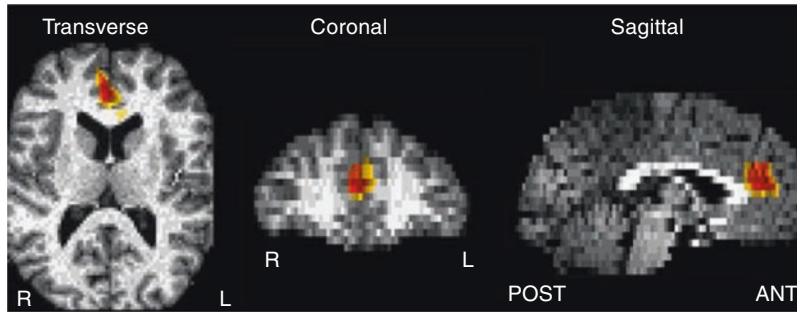

Fig. 11.41 Transverse (*left*), coronal (*middle*), and sagittal (*right*) projection of the fusion image between statistically significant increases in blood flow values (identified using statistical parametric mapping) and Talairach standard anatomic brain atlas from MEDx SPM. The highest value of statistically significant pixel values is shown in *red*. The region demonstrating maximum statistical significance was located in the right anterior cingulate gyrus; SPM coordinates (x, y, z) (mm) = (−6, +42, +24) in the transverse, coronal, and sagittal sections, respectively

the transverse, coronal, and sagittal projections of the fusion image between statistically significant increases in blood flow values and the Talairach standard anatomic brain atlas using the MEDx SPM software package (Sensor Systems, Sterling, VA).

The highest value of statistical significant pixel values is shown in red. The region demonstrating maximum statistical significance was located in the right anterior cingulate gyrus; SPM coordinates (x, y, z) (mm) = (−6, +42, +24) in the transverse, coronal, and sagittal sections, respectively.

Method and Illustration of SPM Image Analysis in Epilepsy

The use of SPM image analysis is now increasingly being applied in the clinical diagnosis of neuroimaging of numerous disorders including epilepsy. An ictal SPECT scan can be compared with the interictal SPECT scan and correlated with a normal brain SPECT atlas using SPM to identify regions of significant alterations in regional cerebral blood flow related to seizure activity and localize these regions in Montreal Neurological Atlas space. Recent studies support SPM analysis of ictal SPECT scans [121]. Blinded analysis demonstrated correct lateralization in 18 of 21 mesial temporal lobe epilepsy cases with no false lateralization compared with subtraction analysis that showed correct lateralization in 16 and false lateralization in one patient.

Figures 11.42 and 11.43 demonstrate epilepsy analysis in an 11-year-old male suffering from tonic–clonic seizures since age 7 and the application of subtraction ictal SPECT co-registered to MRI (SISCOM) [122]. MRI scan (Fig. 11.42 *left*) shows an arterial venous malformation in the right parietal lobe. ^{18}F-FDG PET scan (Fig. 11.42 *right*) also shows reduction around the AVM area. An interictal ^{99m}Tc-ECD SPECT scan (Fig. 11.43 *top*) shows reduced perfusion in the region of the arterial venous malformation, in addition to a large area around the lesion. Ictal ^{99m}Tc-ECD SPECT (Fig. 11.43 *bottom left*) showed hyperperfusion in a region anterior and inferior to the AVM, confirming the location of epileptogenesis. This is shown on a SPM analysis fusion scan correlating regional cerebral perfusion with a T1-weighted MRI scan (Fig. 11.43 *right*).

Figure 11.44 shows Ictal ^{99m}Tc-ECD as compared to interictal ^{99m}Tc-ECD SPECT in a 39-year-old right-handed male who has a 25-year history of refractory complex partial epilepsy of possible multifocal origin versus an indeterminate focal origin.

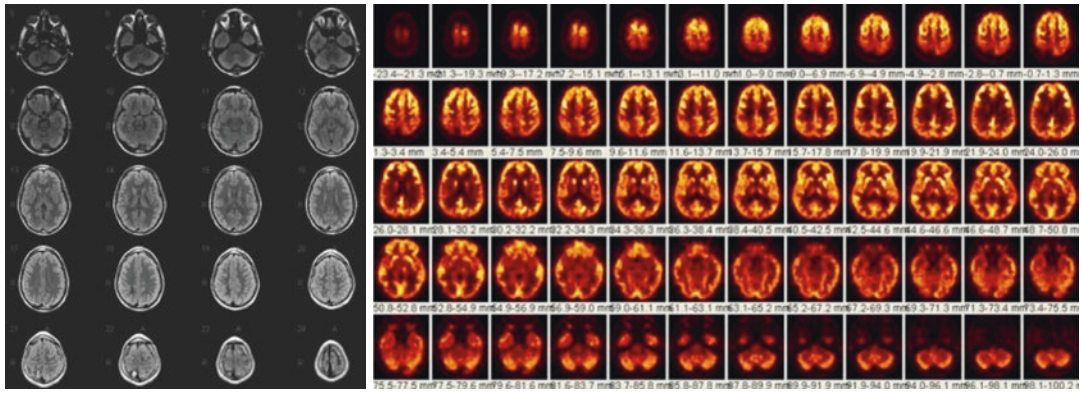

Fig. 11.42 (*Left*) MRI scan sections of an 11-year-old boy suffering from seizure disorder since age 7. The patient has tonic–clonic seizures. The MRI scan shows an arterial venous malformation in the right parietal lobe. (*Right*) The interictal brain ^{18}F-FDG PET scan shows an area of reduced metabolic activity in the right parietal lobe consistent with the location of the arterial venous malformation

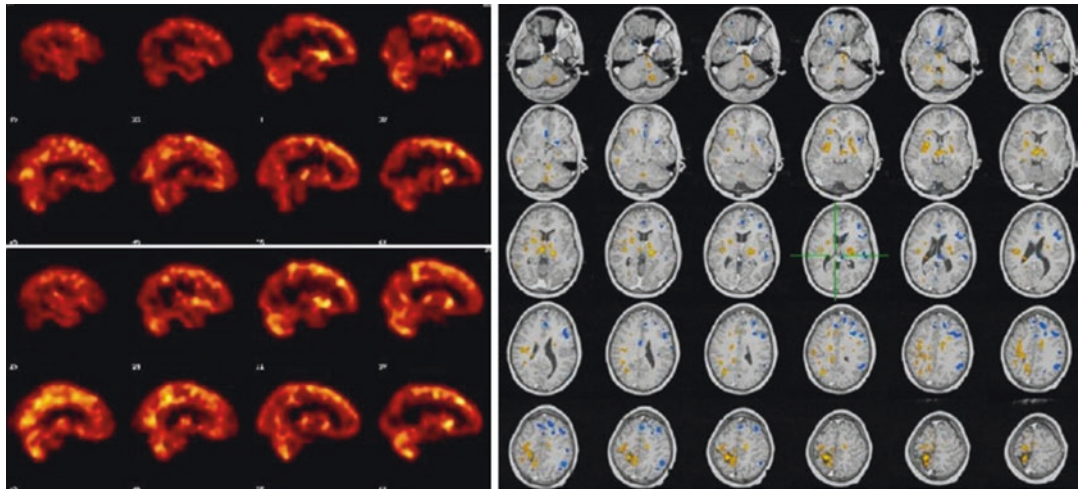

Fig. 11.43 Same patient as shown in Fig. 11.42. (*Left*) images from an interictal ^{99m}Tc-ECD brain SPECT (*top*) as compared to an ictal ^{99m}Tc-ECD brain SPECT scan (*bottom*). One can see significant hyperemia anterior and inferior to the region of the arterial venous malformation on the ictal ^{99m}Tc-ECD brain SPECT scan as compared to the interictal ^{99m}Tc-ECD brain SPECT scan. (*Right*) SISCOM analysis where the ictal and interictal SPECT are compared and statistically significant differences between the two are mapped onto the patient's MRI scan. One can see significantly increased differences in the ictal SPECT study as compared to the interictal SPECT study in the region anterior and in the location of the arterial venous malformation (*highlighted yellow areas*). The highlighted blue area shows areas of decreased uptake on the ictal scan as compared to the interictal scan, which can be seen to be positioned randomly throughout the cortex and has no clinical or localizing significance

11.4.4 Psychiatry and Learning Disabilities

The diagnostic application of rCBF SPECT brain scanning in psychiatry are limited (on an individual patient basis), since most prior studies which showed statistical significance were performed on large patient groups. For example, in one study comparing regional cerebral blood flow in patients with major depressive disorder to that of healthy subjects, there was found to be a relationship between rCBF and negative depressive symptoms [123]. The study found decreased frontal lobe rCBF (hypofrontality) in a group of

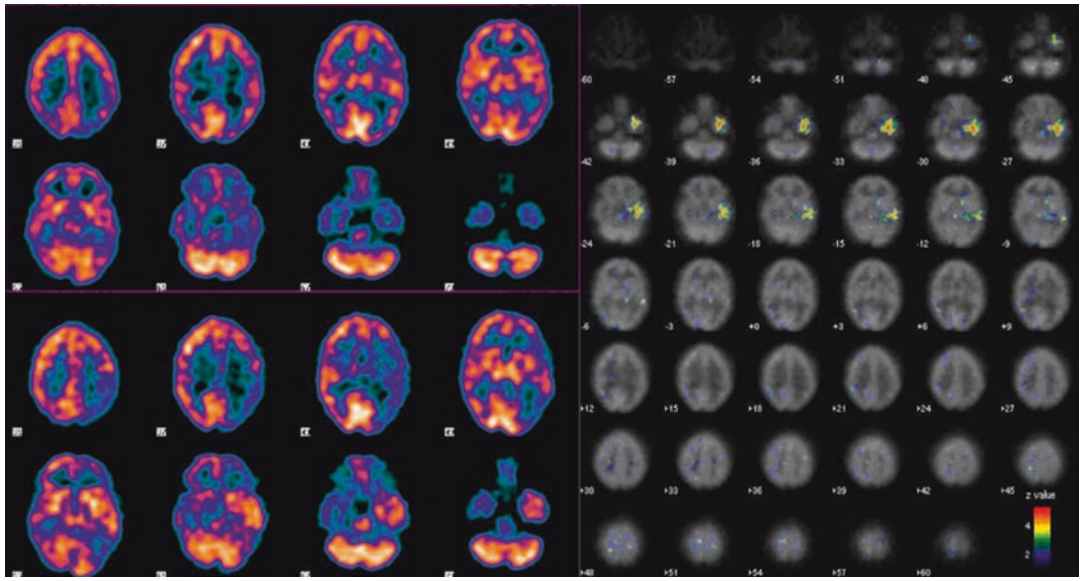

Fig. 11.44 (*Left*) An interictal ^{99m}Tc-ECD brain SPECT scan (*top*) as compared with an ictal ^{99m}Tc-ECD brain SPECT scan (*bottom*). On the ictal brain SPECT scan, one can see increased hyperemia involving the left temporal lobe. (*Right*) Using SPM statistical comparison, one can see statistically significant differences between the ictal and interictal scan involving the left temporal lobe. The test for statistical significance has *z* values between three and four (*coded color bar* on the image)

patients, with lower blood flow to the dorsolateral prefrontal cortex bilaterally, the right orbitofrontal cortex, and the cingulate gyrus. This study suggests that decreased perfusion is associated specifically with negative symptom severity. These results support the hypothesis that, in major depressive disorder, negative symptoms and symptoms of depression are distinct phenomena and underscore the importance of negative symptom evaluation in neuroimaging studies of major depressive disorder and other disorders. Figure 11.45 shows a ^{99m}Tc-HMPAO brain SPECT scan from a 42-year-old female presenting with a 6-year history of depression characterized with significant negative symptomatology. However, on an individual basis, patients with depression may have normal frontal lobe rCBF.

We have performed a study to evaluate changes in rCBF in children with autistic disorder [124]. In this study, the autistic children underwent ^{99m}Tc-HMPAO brain SPECT scans which showed significant decreases in rCBF to the temporal lobes and frontal lobes. The corresponding CT and MRI scans failed to show any abnormality. This confirmed the sensitivity of rCBF brain SPECT to assist in the diagnosis of this severe brain disorder. Figure 11.46 shows images from a 12-year-old boy with autistic disorder who had a performance IQ of 70 and an Autistic Behavior Checklist score of 80. The subject was severely autistic, with severe language deficits. The reduction of perfusion to the temporal lobes is in accord with the neuropsychological location of the abnormalities identified in this disorder.

11.4.4.1 Brain Tumors

Brain Tumor Evaluation with ^{201}Tl

Identification of viable tumor after brain tumor therapy is a significant clinical problem since distinction between necrosis and residual or recurrent viable tumor cannot be accurately evaluated by either computed tomography or magnetic resonance imaging. Functional imaging can distinguish cerebral necrosis from viable brain tumor and determine viability grade [125, 126]. Figure 11.47 illustrates an example of the clinical utility of ^{201}Tl SPECT in a

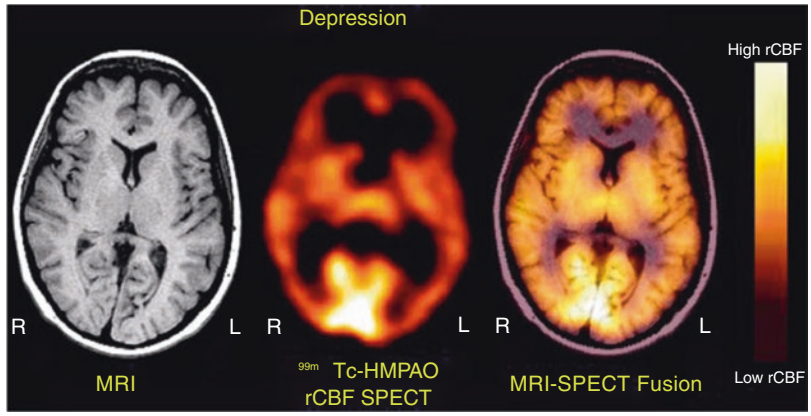

Fig. 11.45 A 42-year-old female presented with a 6-year history of depression. The patient had a normal MRI scan (left). The ^{99m}Tc-HMPAO brain SPECT scan shows significant decrease in perfusion to the frontal lobe (middle). The MRI–SPECT fusion images (right) show that the diminution of rCBF is functional since there is no corresponding anatomic atrophy to account for the low reduction in frontal lobe perfusion. In addition, there was no evidence for cerebral vascular disease. This image illustrates that patients with severe depression can show reduction in frontal blood flow due to a relative reduction in synaptic activity with resultant loss of frontal lobe function and the concomitant associated mood of depression

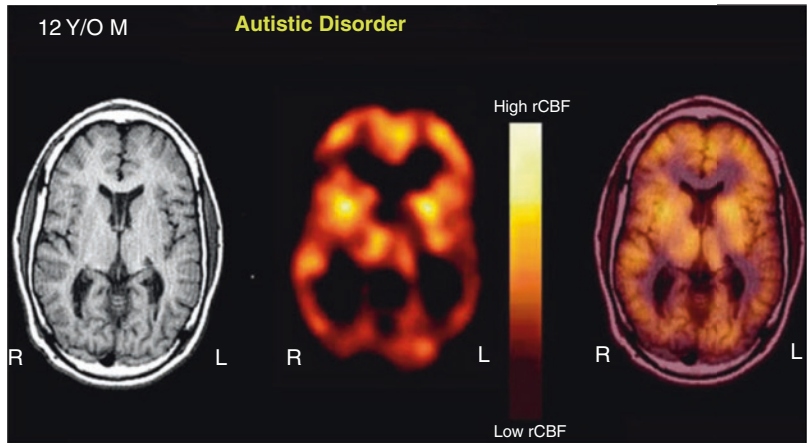

Fig. 11.46 Images from a 12-year-old boy with autistic disorder demonstrating low temporal lobe activity. The MRI scan (*left*) is normal. The co-registered ^{99m}Tc-HMPAO brain SPECT scan (*middle*) shows bilateral posterior temporal (*left*, *lower* than *right*) and bilateral occipital diminution of tracer uptake with no corresponding anatomic abnormality, as demonstrated by the MRI–SPECT fusion image (*right*)

14-year-old female with recurrent high-grade astrocytoma involving the right hemisphere of the brain. The patient was initially diagnosed 2 years prior to the scans shown in this figure and underwent two courses of chemotherapy and radiation therapy. The ^{201}Tl brain SPECT scan was performed in order to determine if there was residual or recurrent viable tumor in this patient who now presented with recurrent symptoms. It is not uncommon for patients to present with recurrent symptoms; however, the etiology of the symptoms can be due to either radiation necrosis and brain edema or recurrent viable tumor growth, and often, these cannot be differentiated by an anatomic scan such as MRI. The MRI scan, in this case, shows radiation necrosis and cystic lesions, but viability cannot be determined.

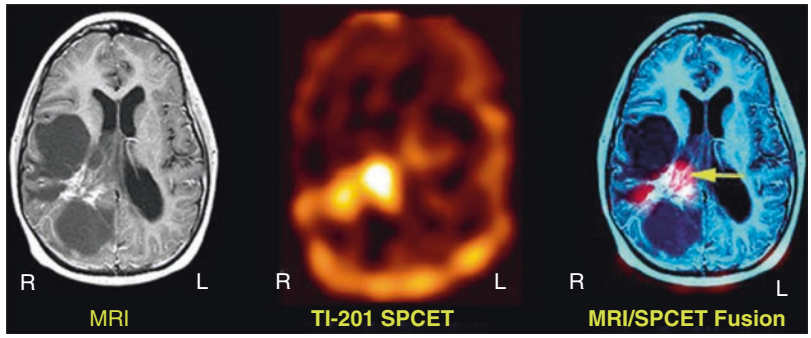

Fig. 11.47 ^{201}Tl brain SPECT scan and MR images from a 14-year-old female with recurrent high-grade astrocytoma involving the right hemisphere of the brain. The patient was diagnosed 2 years prior to the scans shown in this figure and underwent two courses of chemotherapy and radiation therapy. The MRI scan (*left*) shows radiation necrosis and cystic lesions, but residual tumor viability cannot be assessed. The ^{201}Tl brain SPECT scan (*middle*) shows a focal region of intense uptake; however, the exact location cannot be determined with certainty. Because this patient was a candidate for gamma knife surgery, it was important to correlate the functional and anatomic image to locate the region of high-grade viable tumor. The MRI–SPECT fusion image (*right*) clearly showed a localized region of intense uptake (*green arrow*). The ^{201}Tl brain SPECT scan shows a focal region of intense uptake, however, the exact location cannot be determined with certainty. Because this patient was a candidate for gamma knife surgery, it was important to correlate the functional and anatomic image to obtain specific coordinates of the region of high-grade viable tumor. Using the fiduciary reference system and fusion software described earlier, the MRI/SPECT fusion image clearly showed an area of intense uptake which was localized to the MRI scan and subsequent gamma knife surgery allowed the patient to have extremely high doses of radiation directed only to the area of viable tumor, and the patient remains free of additional symptoms one year after gamma knife surgery

The main utility of thallium in brain SPECT imaging is in the visualization of primary and metastatic CNS tumor. Blood–brain barrier (BBB) breakdown in any lesion of the brain allows the passage and localization of ^{201}Tl. After intravenous administration, the first 5 min of ^{201}Tl uptake depends on rCBF, rCBV, and BBB breakdown. Subsequently, the uptake depends on active transport by the tumor cell, tumor grade, and activity of the Na^+–K^+ ATPase pump. ^{201}Tl is therefore an extremely sensitive, but sometimes nonspecific indicator of residual recurrent viable tumor since there is nonspecific uptake in regions of blood–brain barrier breakdown not due to tumor. Figure 11.48 shows an example of this nonspecific uptake in a patient with stroke. The patient is a 65-year-old man who was originally referred to our institution to evaluate for infarction versus tumor. The ^{201}Tl scan shows slight nonspecific uptake in the right basal ganglia region. The MRI scan shows an enhancing lesion in that location. The question of tumor versus stroke remained, and an ^{18}F-FDG PET scan was performed which was entirely negative in the location of the enhancing lesion on CT and the uptake on ^{201}Tl, ruling out tumor. This case also shows that ^{18}F-FDG has greater specificity in detection of recurrent or residual viable tumor but may have decreased sensitivity since ^{18}F-FDG is also taken up by the normal brain. Therefore, early and delayed ^{201}Tl SPECT imaging with semiquantification may aid in the differentiation of specific thallium versus nonspecific BBB breakdown uptake when BBB breakdown is present in lesions which are low grade, inflammatory, or stroke.

^{99m}Tc-sestamibi (Tc-99m Hexakis-2-Methoxy-2-Isobutyl Isonitrile) and Brain Tumors

Comparison of differences in uptake of ^{201}Tl and ^{99m}Tc-MIBI is illustrated in a 47-year-old female with glioblastoma multiforme who previously underwent radiation therapy and chemotherapy (Fig. 11.49). The MRI scan shows high signal intensity in the right cerebral hemisphere. From the MR image, one cannot distinguish between residual viable tumor versus radiation necrosis and edema. The ^{201}Tl brain SPECT scan section

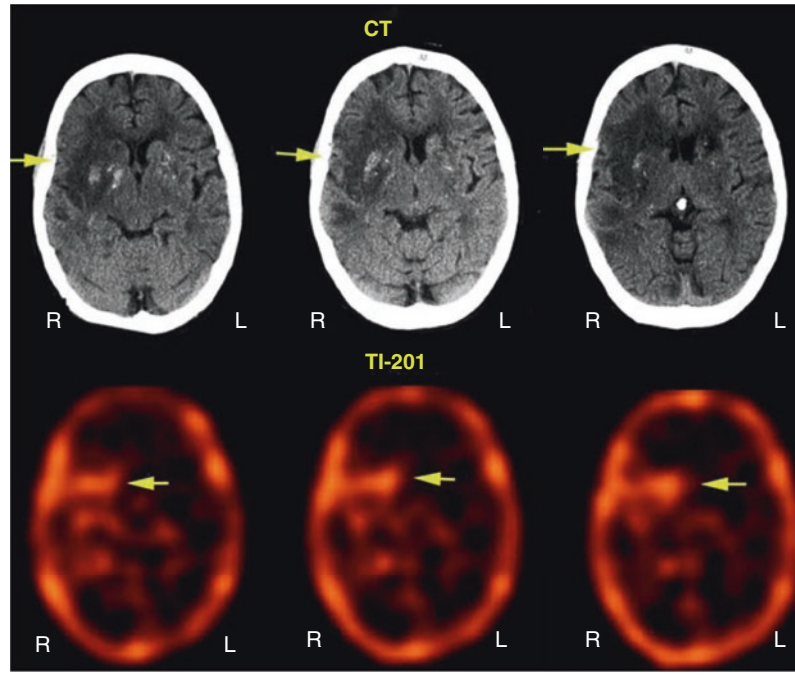

Fig. 11.48 Non-Specific uptake with ^{201}Tl. The patient is a 65-year-old man who was originally referred to our institution to evaluate for infarction versus tumor. The ^{201}Tl scan shows slight nonspecific uptake in the right basal ganglia region (*arrow*). The MRI scan shows an enhancing lesion in that location. The question of tumor versus stroke remained, and an ^{18}F-FDG PET scan was performed which was entirely negative in the location of the enhancing lesion on CT and the uptake on ^{201}Tl, ruling out tumor

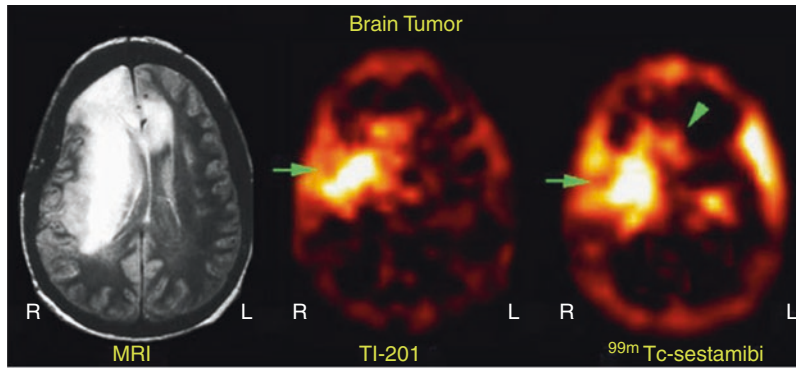

Fig. 11.49 This figure shows images from a 47-year-old female with glioblastoma multiforme who previously underwent radiation therapy and chemotherapy. The MRI scan (*left*) shows high signal intensity in the right cerebral hemisphere. From the MR image, one cannot distinguish between residual viable tumor versus radiation necrosis and edema. The ^{201}Tl brain SPECT scan section through the same level (*middle*) shows intense uptake indicating tumor recurrence (*arrow*). A ^{99m}Tc-sestamibi scan (*right*) shows intense uptake with better anatomic delineation of the tumor boundary as noted by extension of the tumor through the anterior commissure (*green arrowhead*), whereas in the same location, the thallium scan has less clear definition. Also note ^{99m}Tc-MIBI in the midportion of the left hemisphere, which is unrelated to tumor uptake but due to choroid plexus secretion of ^{99m}Tc-MIBI

through the same level shows intense uptake indicating tumor recurrence. The ^{99m}Tc-sestamibi scan shows intense uptake with better anatomic delineation of the tumor boundary as noted by extension of the tumor through the anterior commissure, whereas in the same location, the thallium scan has less clear definition.

Effect of Chemotherapy on Metabolism

It has been observed that there is greater uptake of ^{99m}Tc-MIBI in malignant gliomas compared to ^{201}Tl in patients who did not receive chemotherapy or have been remotely treated [127]. Conversely, those patients who had recent chemotherapy have low ^{99m}Tc-MIBI uptake in the tumor.

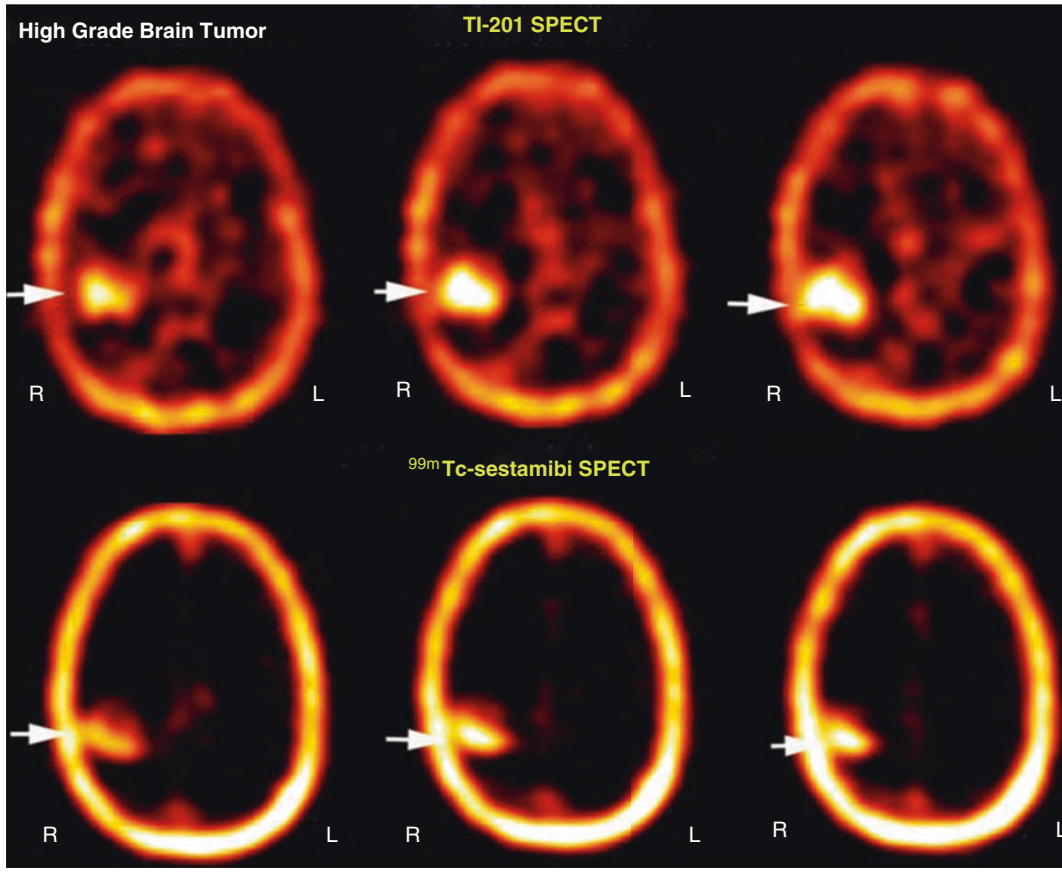

Fig. 11.50 ^{201}Tl and ^{99m}Tc-MIBI SPECT scans of a 45-year-old female with high-grade brain tumor in the right temporal lobe who had recent chemotherapy and who had low ^{99m}Tc-MIBI uptake in the tumor, compared with ^{201}Tl. This case compares the diagnostic capability of ^{201}Tl SPECT (*top row*) as compared with ^{99m}Tc-HMPAO MIBI SPECT (*bottom row*). Each of the tracers shows increased uptake in recurrent viable tumor. The reduction of MIBI immediately after chemotherapy indicates that there is DNA damage and the tumor is less able to recover from chemotherapy damage and, therefore, the patient has a better prognosis

Tissue fractionation studies have demonstrated the release of ^{99m}Tc-MIBI from the mitochondria and a decline in ^{99m}Tc-MIBI uptake in the presence of Ca^{+2} [128]. It is conceivable that irreversible tissue injury leads to the sequestration of extracellular Ca^{+2} into the cell and the mitochondria leading to cell death. Injury to brain tumor cells from radiation or chemotherapy will theoretically increase the Ca^{+2} level and alter the mitochondrial membrane potential leading to a decline in ^{99m}Tc-MIBI uptake. Early response to treatment can therefore theoretically be determined by comparing ^{99m}Tc-MIBI uptake before and after a course of radiation or chemotherapy. Decline in the ^{99m}Tc-MIBI or ^{201}Tl uptake ratio may indicate lethal injury or decreased viability of neoplastic cells and effective response to treatment.

Several studies [127] have established that in the evaluation of brain tumor, a semiquantitative method using counts from the tumor region to counts in the normal brain can be useful in the assessment of viability, tumor bulk, and chemotherapeutic efficacy.

The differential effect of tumor therapy on ^{201}Tl and ^{99m}Tc-MIBI uptake is illustrated in a 45-year-old female with high-grade brain tumor in the right temporal lobe. This case compares the diagnostic capability of ^{201}Tl SPECT as compared with ^{99m}Tc-MIBI SPECT (Fig. 11.50).

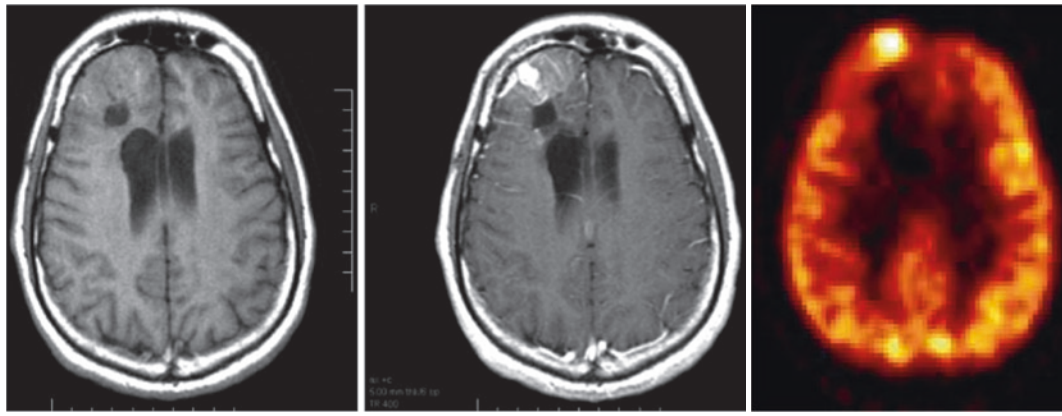

Fig. 11.51 (*Left*) Non-contrast MRI scan with abnormality involving the right frontal lobe. (*Middle*) Contrast MRI scan shows enhancement in the right frontal lobe. (*Right*) Focal area of increased ^{18}F-FDG uptake involving the right frontal lobe consistent with high-grade transformation and recurrence of tumor in the right frontal lobe 8 years after initial diagnosis, therapy, and complete remission

Each of the tracers show increased uptake in recurrent viable tumor. It has been postulated that ^{201}Tl is taken up by the sodium–potassium ATPase activity and reflects global cellular energetics. On the other hand, the uptake of ^{99m}Tc-MIBI is related to mitochondrial energetics, and high uptake of ^{99m}Tc-MIBI possibly indicates a poor prognosis since the tumor continues to have a high glycolytic rate, glucose utilization, and good repair mechanisms. The reduction of ^{99m}Tc-sestamibi immediately after chemotherapy indicates that there is DNA damage (both to the nucleus and the mitochondrial DNA) with impairment of the TCA cycle and involved glycolytic enzymes. This compromises the production of ATP and cripples the cellular reparative mechanisms such that the tumor is less able to recover from chemotherapy damage and, therefore, the patient has a better prognosis. It is suggested that the use of MIBI before and after chemotherapy treatment may be used as an indicator for the efficacy of a specific type of chemotherapy, possibly after one dose. This would permit several trials to be performed to determine the most efficacious chemotherapy before complete treatment is instituted allowing the patient to remain relatively refractory from the hematologic and other side effects of the chemotherapy.

2-[F-18] Fluoro-2-Deoxy-D-Glucose ^{18}F-FDG Imaging of Brain Tumors

^{18}F-FDG PET has allowed monitoring of therapeutic response in brain tumors with a greater specificity than CT or MRI. ^{18}F-FDG, a glucose analog, is taken up by high-glucose-using cells, including normal brain and cancer cells. FDG is actively transported across the BBB into the cell, and the ^{18}F-FDG-6-phosphate formed when ^{18}F-FDG enters the cell prevents its further metabolism. As a result, the distribution of ^{18}F-FDG is a good reflection of the distribution of glucose uptake and utilization by cells in the body.

Figure 11.51 shows a PET scan with abnormal uptake of ^{18}F-FDG in a patient with recurrent brain tumor involving the anterior frontal lobe after 8 years of remission. The MRI shows contrast enhancement. ^{18}F-FDG is a less sensitive but more specific tracer for the detection of recurrent or residual viable tumor as compared to ^{201}Tl which is a more sensitive but less specific tracer due to nonspecific BBB breakdown accumulation. The lack of sensitivity of ^{18}F-FDG is due to the fact that it is taken up by the normal brain. The lack of specificity of ^{201}Tl is due to the fact that it accumulates at the site of blood–brain barrier breakdown prior to its uptake through the Na^+–K^+ ATPase pump.

Since most cancer cells, including gliomas, demonstrate a high rate of glycolysis [129], ^{18}F-FDG helps in differentiation between tumor and normal brain tissue. It should be noted, however, that the correlation between ^{18}F-FDG uptake and glucose metabolism in tumors may differ from that in the normal tissue [130]. In untreated tumor, the degree of ^{18}F-FDG uptake has been correlated with tumor grade: high-grade tumors demonstrate increased tracer uptake, and high uptake in a previously categorized low-grade tumor confirms anaplastic transformation of the tumor [131]. Quantitatively, ratios of $^{18F\text{-}FDG}$ uptake in tumors to that of white matter (>1.5) or gray matter (>0.6) were able to distinguish low-grade (grades I and II) from high-grade tumors (grades III and IV). Based on a preliminary finding, delayed imaging at 3–8 h after injection can further distinguish tumor and normal gray matter due to the faster tracer excretion in the normal brain than in tumor [132]. However, after therapy, the degree of tracer uptake does not necessarily correlate with tumor grade in that high-grade tumors may have uptake similar to or slightly above that of white matter.

^{18}F-FDG PET also plays a role in differentiating between recurrent or residual tumor and radiation necrosis (Figs. 11.52 and 11.53). However, due to the ^{18}F-FDG uptake in the normal brain, the sensitivity of detecting recurrent or residual tumor is low. The specificity is also low in the initial few weeks post-therapy due to radiation necrosis. A study showed a sensitivity of 81–86% and a specificity of 40–94% for distinguishing between radiation necrosis and tumor. It is thus recommended that ^{18}F-FDG PET should not be performed less than 6 weeks after the completion of radiation treatment.

Recently, new issues have emerged regarding the evaluation of disease response, and also with the identification of patterns such as pseudoprogression, frequently indistinguishable from real disease progression, and pseudoresponse. The MacDonald criteria, widely used clinically as a guideline for evaluating therapeutic response in high-grade gliomas, uses contrast-enhanced CT and MRI and defines progression as greater than a 25% increase in size of enhancing tumor. The enhancement of brain tumors, however, primarily reflects a disturbed blood–brain barrier.

By definition, pseudoprogression of gliomas is a treatment-related reaction of the tumor with an increase in enhancement and/or edema on MR imaging, suggestive of tumor progression but without increased tumor activity (Fig. 11.54). Typically, the absence of true tumor progression is shown by a stabilization or decrease in size of the lesion during further follow-up and without new treatment. Pseudoprogression occurs frequently after combined chemo-irradiation with temozolomide, the current standard of care for glioblastomas [125, 126].

In an effort to identify patients likely to exhibit pseudoprogression, some studies have attempted to correlate O^6-alkylguanine DNA alkyltransferase (MGMT) promoter methylation status with pseudoprogression [126]. Studies have demonstrated that MGMT methylation status is an important biomarker for assessing primary brain tumors, as MGMT status has been shown to correlate with both therapy response and overall survival in GBM when therapy includes alkylating agents [133, 134]. However, similar studies of MGMT promoter methylation in anaplastic oligodendrogliomas were unable to find a correlation between MGMT methylation status and either response rate, time to progression, or overall survival, suggesting that MGMT promoter methylation patterns may be dependent on cell type [127].

Another phenomenon, pseudoresponse is the decrease in contrast enhancement and/or edema of brain tumors on MRI without a true antitumor effect. It occurs after treatment with agents that induce a rapid normalization of abnormally permeable blood vessels or regional cerebral blood flow [128]. Recent trials on high-grade gliomas with agents that modify the signaling pathways of vascular endothelial growth factor (VEGF), formerly also known as the vascular permeability factor [135] (e.g., bevacizumab, cediranib), have shown a rapid decrease in contrast enhancement with high response rate and 6 months progression-free survival (PFS-6), but with rather modest effects on overall survival [129].

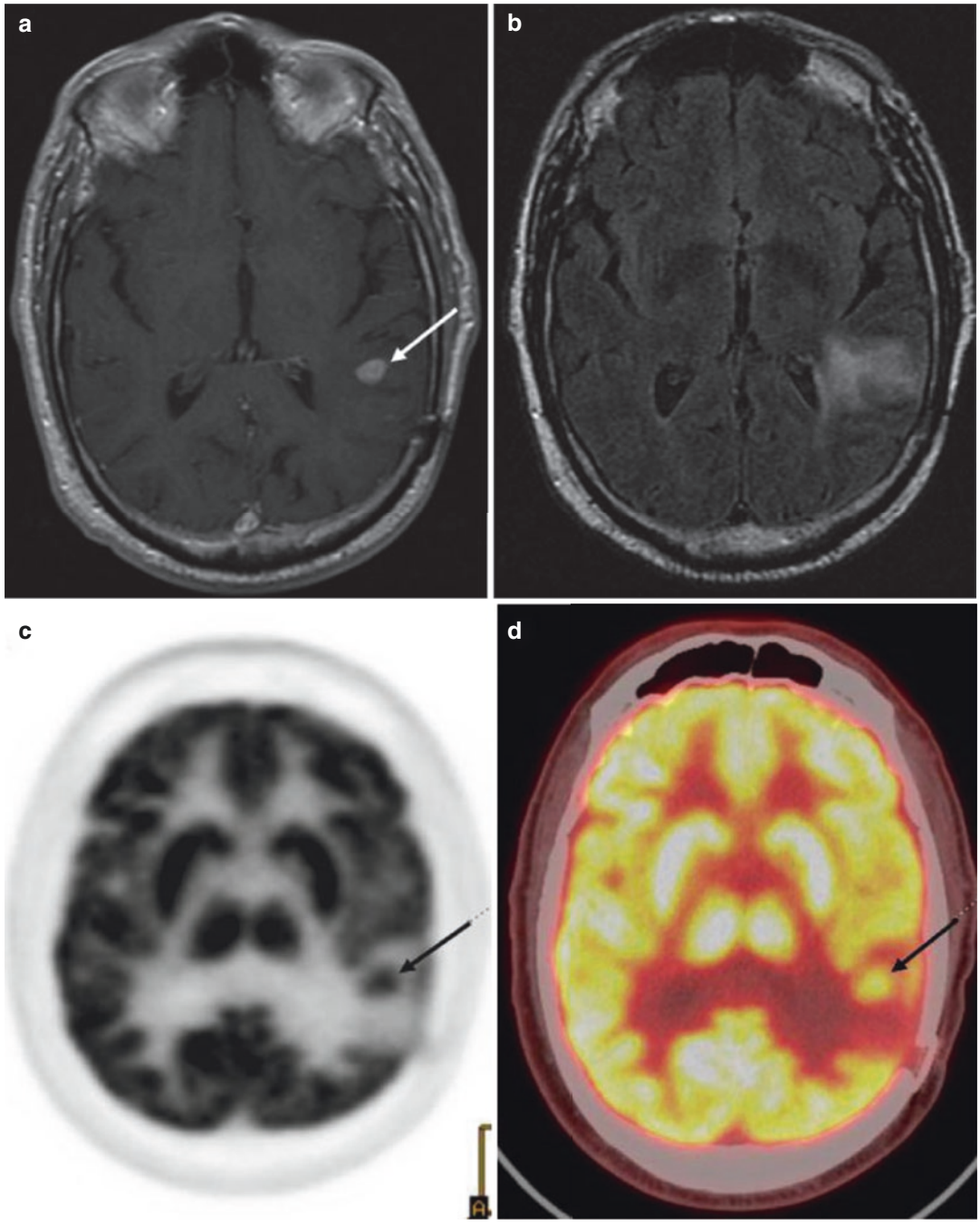

Fig. 11.52 Tumor recurrence versus radiation-induced changes: images of a 77-year-old male who was originally diagnosed with glioblastoma, treated with external beam radiation and adjuvant chemotherapy with temozolomide. Ten-month follow-up MR T1 postcontrast images (**a**) demonstrate a distinct area of enhancement (*arrow*) in the left temporoparietal lobe region, region of prior tumor. T2-weighted MR images (**b**) demonstrate hyperintense signal in the left parietal lobe extending to the left temporal lobe. This pathologic contrast enhancement is suggestive of an infiltrative mass. ^{18}F-FDG-PET only (**c**) and PET–CT fusion images (**d**) demonstrate a focus of increases FDG activity (*arrow*) corresponding to an enhanced area of uptake on postcontrast T1 images. These findings are consistent with tumor recurrence. There is also noted to be the expected decreased tracer uptake surrounding these areas consistent with vasogenic edema

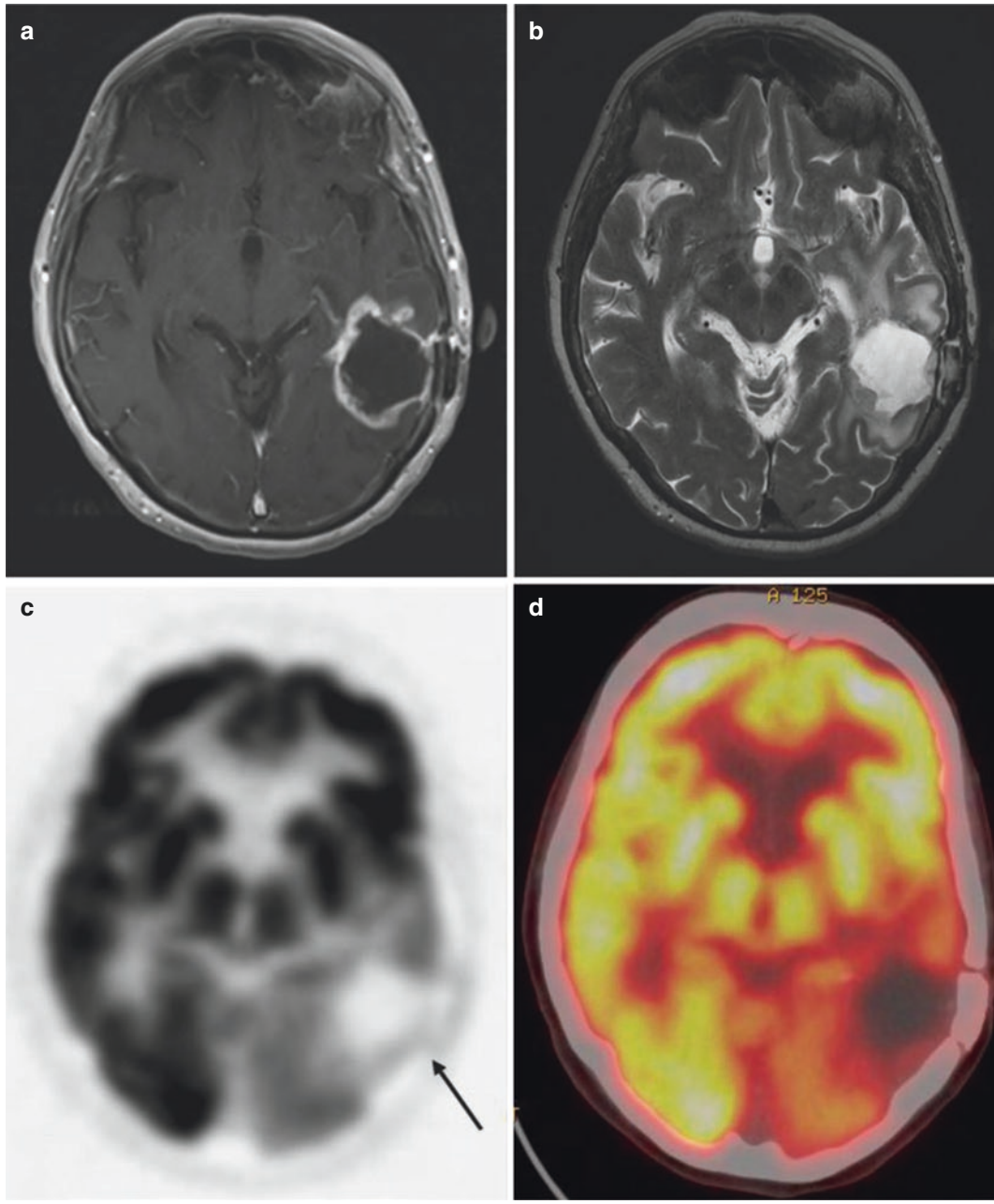

Fig. 11.53 ^{18}F-FDG PET for tumor recurrence: a 71-year-old male patient with history of glioblastoma multiforme, status post resection, presents for evaluation of recurrence. Contrast-enhanced MR T1 images (**a**) demonstrate a large cavity in the left posterotemporoparietal junction with an irregular rim of enhancement. T2-weighted images (**b**) demonstrate hyperintensity in the posterotemporal and parietal lobes. These findings are suspicious for tumor recurrence around the periphery of previous location of mass in left posterior temporoparietal region. (**c**) ^{18}F-FDG PET only and (**d**) PET–CT fusion images demonstrate a relatively large area of absent FDG uptake (*arrow* on **c**) corresponding to the cavity noted on MRI, with no area of abnormally increased FDG to suggest the presence of residual or recurrent high-grade viable tumor

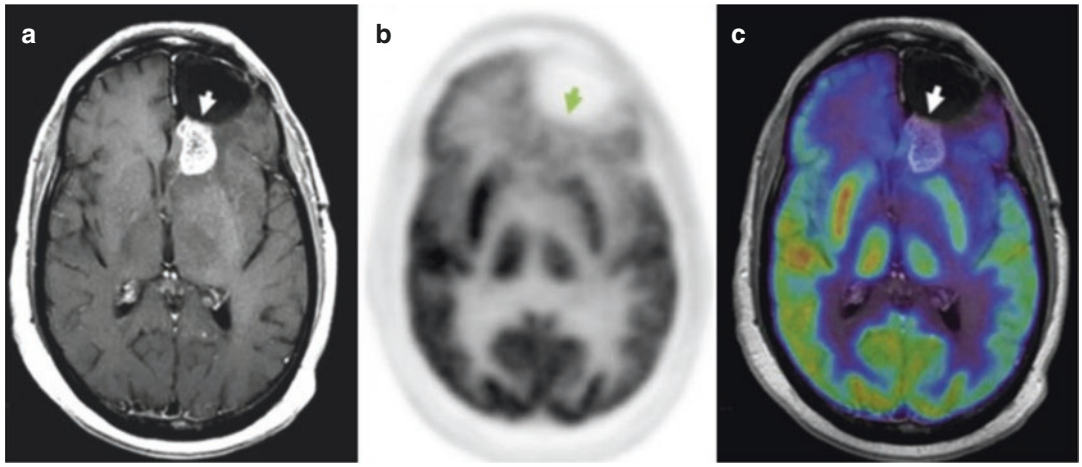

Fig. 11.54 ^{18}F-FDG PET diagnosis of pseudoprogression. Patient with a history of glioblastoma, status post resection, and after treatment with total dose of 60 Gy in 2-Gy fractions presents for a follow-up, 1 month after radiation therapy. MRI (**a**) demonstrates enhancement posterior to the prior resection cavity in the left frontal lobe (*arrowhead*). However, the patient showed clinical improvement, and therefore an ^{18}F-FDG PET scan was done to assess for tumor progression. On PET (**b**), no abnormal areas of increased ^{18}F-FDG uptake in the region of MRI contrast enhancement were identified (*green arrow*). (**c**) PET-MR fusion images show decreased uptake in region of prior resection. Thus, additional therapy was deemed not indicated; the patient was monitored on follow-up contrast-enhanced MRI scans which were negative. Thus, PET scan was helpful in differentiating pseudoprogression from true progression (from Oborski et al. [98])

These two opposing phenomena emphasize that enhancement by itself is not a measure of tumor activity, but only reflects a disturbed BBB. A recent case report by our group emphasizes the value of ^{18}F-FDG PET when pseudoprogression is strongly suspected by the referring physician [98]. Currently, ^{18}F-FDG PET is not a clinically standard method for evaluating therapeutic response in high-grade gliomas, as it is only used for initial staging and to confirm suspected recurrence observed on Gd-MRI. However, a central advantage of ^{18}F-FDG PET is that it can be used to determine the metabolic state of tumor cells in contrast to Gd-MRI, which is limited to evaluating changes in size of contrast enhancement. This is an important distinction in comparing ^{18}F-FDG PET and Gd-MRI results as changes in contrast enhancement are generally a conglomeration of many effects, such as local vascularity, changes in both normal and tumor cell density, necrosis, apoptosis, and blood–brain barrier (BBB) breakdown. All these morphologic changes are presumably preceded by changes in tumor metabolism, suggesting that, in many cases, ^{18}F-FDG PET may allow for comparatively faster discrimination of pseudoprogression from true progression and pseudoresponse from true response.

Recent efforts have focused on the coregistration of PET and MR images, which has increased sensitivity over using either modality alone [66, 130]. The simultaneous PET–MRI scan, which offers better MRI-based motion correction of PET data, is also being studied in more centers [131, 135–137].

Nucleic Acid Analog: [F-18]-Fluoro-3′-Deoxy-3′-L-Fluorothymidine (^{18}F-FLT) Imaging of Brain Tumors

Recent findings suggest that ^{18}F-FLT is a promising biomarker for differentiating between radiation necrosis and tumor recurrence [132, 138] (Figs. 11.14 and 11.15). A study by Hatakeyama et al. [138] showed its superiority over ^{11}C-MET in tumor grading. Chen et al. demonstrated FLT-PET as a promising imaging biomarker that seems to be predictive of overall survival in bevacizumab and irinotecan treatment of recurrent gliomas in which both early and later ^{18}F-FLT-PET responses were more significant predictors

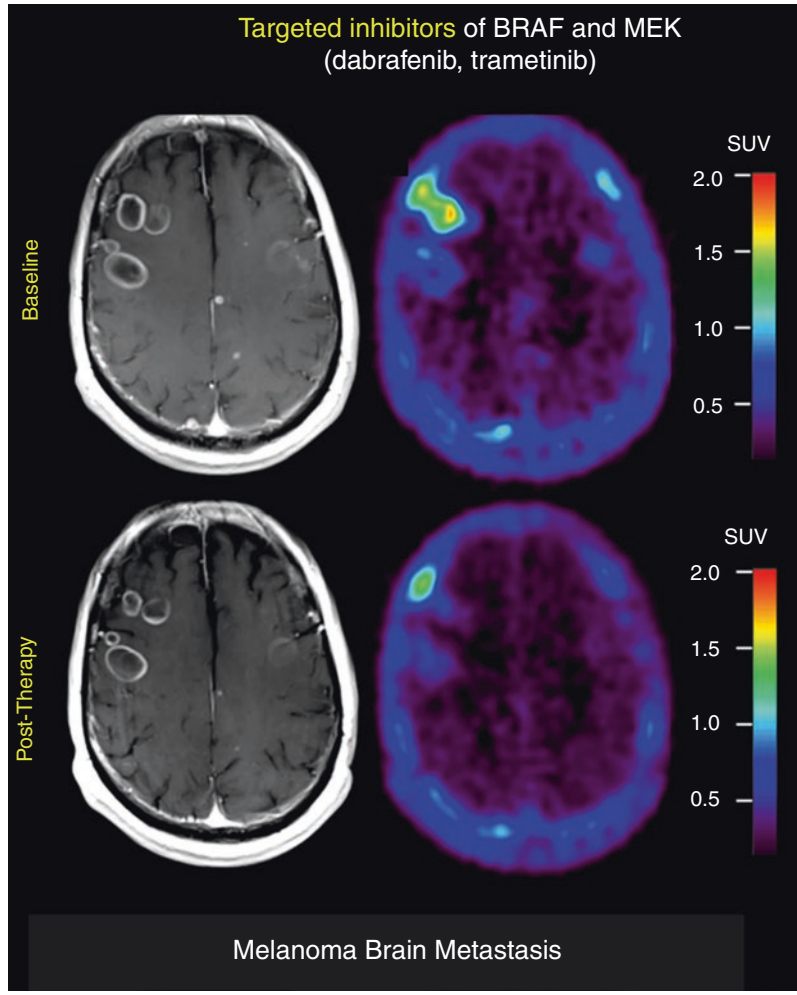

Fig. 11.55 The value of an early post-therapy assessment scan using F-18 FLT to assess proliferation change induced by chemotherapy is shown in this figure. Images are from a 55-year-old man who received targeted BRAF inhibitor and MEK inhibitor therapy with dabrafenib and trametinib [142]. The patient underwent a baseline and an early therapy response assessment scan on the Seimens 3T PET/MR system, allowing for simultaneous correlation of anatomic and proliferation change. Fused 18F-FLT-PET/MRI scan data demonstrated a significant reduction in tumor proliferative activity at three weeks of therapy (bottom) compared to baseline (top)

of overall survival compared with the MRI responses [136]. In addition, a recent prospective study by Schwarzenberg et al. [137] showed that ^{18}F-FLT uptake was highly predictive of progression-free and overall survival in patients with recurrent gliomas on bevacizumab therapy (Avastin, Genentech, a recombinant humanized monoclonal antibody targeting VEGF, a protein released by tumor cells to recruit novel blood vessels to support tumor growth [139, 140]) and that ^{18}Fv-FLT-PET seems to be more predictive than MRI for early treatment response.

Nguyen et al. [141] presents five cases of metastatic brain melanoma in order to demonstrate the benefit of hybrid FLT-PET/MRI for accurate diagnosis. In this study, the additional benefit for treatment monitoring of targeted therapy and immunotherapy is well illustrated (Fig. 11.55).

Note that as shown in Fig. 11.56, the MRI anatomic scan is essentially unchanged. This supported continuation of the current treatment regimen and that the patient would have a favorable response at the end of the therapy course. Recent studies have confirmed the value of early post-therapy molecular imaging to provide an individualize approach as a nearly prediction of cancer treatment response [143–145]. Sequential molecular assessments during therapy allow for physicians to use an adaptive therapeutic approach that evolves in response to the temporal and spatial variability of tumor microenvironment and cellular phenotype as well as therapy-induced perturbations [142].

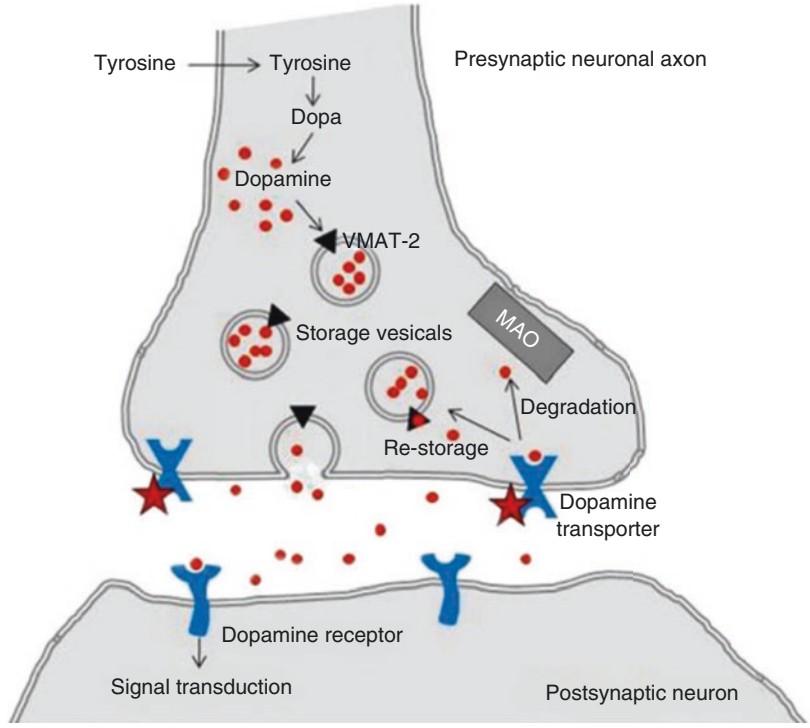

Fig. 11.56 Schematic of striatal dopaminergic synapse (*star* indicates where ^{123}I-FP-CIT binds) (From Djang et al. [44])

11.4.4.2 Parkinsonism and Dopamine Receptor Imaging

Parkinsonian syndromes are a group of diseases that share similar cardinal signs of parkinsonism, characterized by bradykinesia, rigidity, tremor at rest, and postural instability.

The dopaminergic neurotransmitter system plays a vital role in parkinsonism. The chief clinical role for imaging the degenerating dopaminergic system in Parkinson's disease (PD) has been to confirm diagnosis and thus serves as an important role in the clinical management of Parkinson's disease. Recently, there is increasing interest in identifying premotor PD patients, particularly because potential disease-modifying therapies are developed and the clinical imperative becomes early and accurate diagnosis. Typically, patients present with very subtle motor symptom like unilateral tremor or impairment of fine motor ability, and the role of the dopamine transporter scan is to assess for altered striatal dopamine terminal integrity.

The nigrostriatal dopaminergic pathway can be analyzed at the striatal level, where the nigrostriatal neurons end and connect to the postsynaptic neurons using dopamine as the neurotransmitter. Dopamine is produced in the presynaptic nerve terminals and transported into vesicles by the vesicular monoamine transporter 2 (an integral membrane protein that transports neurotransmitters such as dopamine from the cytosol into vesicles). On excitation, the dopamine from these vesicles is released into the synapse and binds to the predominantly postsynaptic dopamine receptors. On the presynaptic side, DaTs move dopamine out of the synaptic cleft and back into the nigrostriatal nerve terminals for either storage or degradation. Imaging the integrity of the nigrostriatal dopaminergic system can improve the accuracy of diagnosing movement disorders. DaT concentrations are lower in presynaptic parkinsonian syndromes, which include Parkinson's disease, multiple system atrophy, and progressive supranuclear palsy, and are also lower in dementia with Lewy bodies. In these cases, the decrease in DaT density is probably even greater than the decrease in intact synapses, due to compensatory downregulation of DaT in an attempt to increase synaptic dopamine concentrations. Conversely, DaT concentrations will

generally be normal in parkinsonism without presynaptic dopaminergic loss, which includes essential tremor, drug-induced parkinsonism, and psychogenic parkinsonism. And in contrast to dementia with Lewy bodies, DaT concentrations are usually normal in Alzheimer's disease [146, 147].

Although the initial clinical indications for dopamine transporter imaging have focused on the differential diagnosis between essential tremor and a parkinsonian syndrome or identification of dementia with Lewy bodies (LBs) in cognitively impaired patients, recent thinking has suggested additional roles for dopamine transporter imaging in the clinic. Because novel therapies for improved management of PD patients come online, especially those purported to slow down disease progression, the onus on the clinical and nuclear medicine community is to refine the diagnostic algorithms, especially in those patients at the very earliest stages of their disease. The concept of premotor PD has recently evolved, keying off the understanding that although PD and related disorders are characterized as movement disorders, many of the initial manifestations may be outside the motor spectrum. Imaging may become a larger part of clinical nuclear medicine practice in those patients who are at risk for motor disorders by virtue of membership in an at-risk cohort based on combinations of nonmotor symptoms and/or genetic factors, although these diagnostic algorithms remain to be validated.

There is now an extensive literature detailing the clinical utility, sensitivity, and specificity for distinguishing patients with movement disorders and presynaptic dopaminergic deficits, suggesting a diagnosis of parkinsonism from those with tremor or other motor signs with no dopamine transporter loss. This information informs both prognosis and treatment with dopamine replacement strategies.

Dopamine Transporter Receptor Binding Agents and Image Interpretation

Anatomic imaging is of little help when determining the integrity of dopaminergic neurotransmitter system, but both presynaptic and postsynaptic levels can be targeted by PET and SPECT tracers. There are several PET tracers (e.g., ^{18}F-dihydroxyphenylalanine for L-dihydroxyphenylalanine decarboxylase activity; ^{11}C-dihydrotetrabenazine for vesicular monoamine transporter 2), but their use is limited primarily to scientific research. For SPECT, most tracers are cocaine analogs and target DaT [148]. One such tracer is ^{123}I-iometopane (^{123}I-β-CIT), available largely for research. Similar in chemical structure, ^{123}I-ioflupane (^{123}I-FP-CIT) is a SPECT tracer, licensed by the European Medicines Agency and available in Europe since 2000. In the United States, ^{123}I-FP-CIT was approved by the Food and Drug Administration (FDA) on January 2011 and is now commercially available; it has now been established as a standard part of diagnostic assessment in movement disorders.

^{123}I-ioflupane, also abbreviated as ^{123}I-FP-CIT, is a molecular imaging agent used to demonstrate the location and concentration of dopamine transporters (DaTs) in the synapses of striatal dopaminergic neurons (Fig. 11.56). DaT SPECT study with ^{123}I-FP-CIT evaluates the integrity of nigrostriatal dopaminergic synapses by visualizing the presynaptic DaTs. This agent has shown efficacy for detecting degeneration of the dopaminergic nigrostriatal pathway, allowing better separation of patients with essential tremor from those with presynaptic parkinsonian syndromes, as well as differentiating between some causes of parkinsonism.

Before the study is performed, a brief history about symptoms, past or current drug use, history of head trauma, stroke, psychiatric illness, epilepsy or tumor, or any other neurological symptoms is obtained. Specific questions should be asked about use of cocaine, amphetamines, methylphenidate, ephedrine and phentermine, bupropion, fentanyl, and some anesthetics (ketamine, phencyclidine, and isoflurane) as these decrease ^{123}I-FP-CIT binding to DaT. Anti-parkinsonian drugs (e.g., L-dihydroxyphenylalanine, dopamine agonists, monoamine oxidase B inhibitors, *N*-methyl-D-aspartate receptor blockers, amantadine, and catechol-*O*-methyltransferase inhibitors in standard dosages) do not interfere with

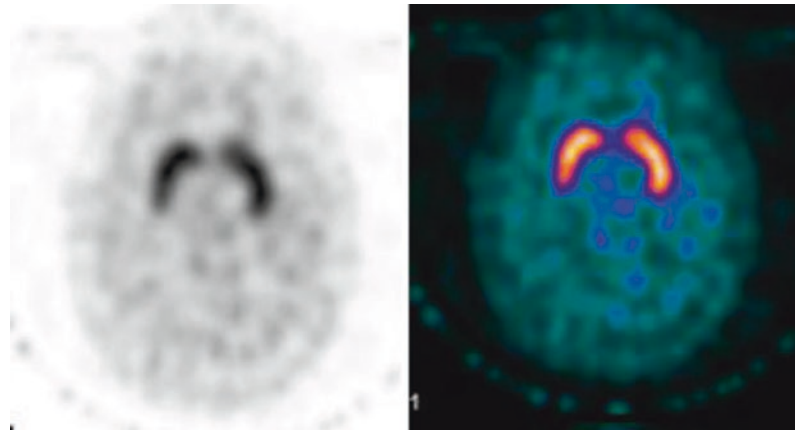

Fig. 11.57 Normal ^{183}I-FP-CIT scan. 50-year-old male with tremors presented for the evaluation of dopamine transporter status. In transaxial images, normal striatal binding is characterized by two symmetric crescent- or comma-shaped regions of activity. Distinction from surrounding brain tissue background is excellent

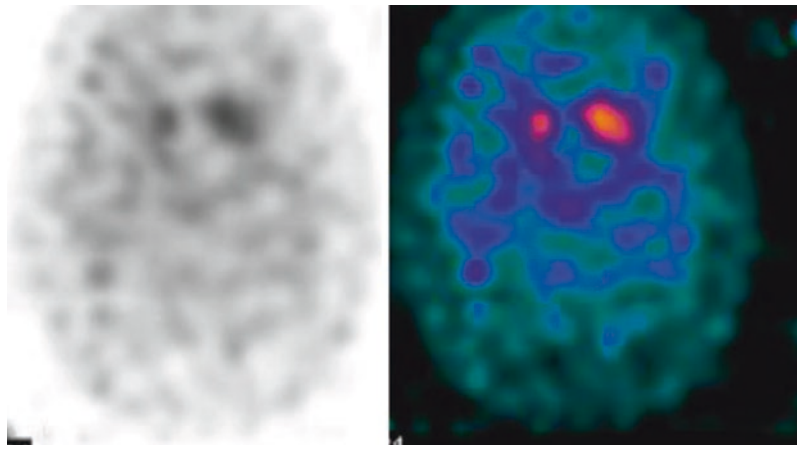

Fig. 11.58 Abnormal ^{123}I-FP-CIT SPECT: transaxial SPECT of a 60-year-old male with Parkinson's disease. In both the left and right hemispheres, there is loss of uptake in the posterior putamen. In addition, the right hemisphere shows moderately reduced uptake to the caudate head nucleus. The uptake to the left caudate head nucleus appears to be within the normal range. The overall constellation of findings is consistent with Parkinson's disease

^{123}I-FP-CIT binding to DaT to any significant degree.

To reduce exposure of the thyroid to free ^{123}I, administer a single 400-mg dose of potassium perchlorate or a single dose of potassium iodide oral solution or Lugol's solution (equivalent to 100 mg of iodide) at least 1 h before the tracer injection.

For imaging, the recommended dosage of ^{123}I-FP-CIT is 111–185 MBq (3–5 mCi), typically 185 MBq (5 mCi). It is administered as a slow intravenous injection (over approximately 20 s), followed by a saline flush. SPECT imaging is performed at 3–6 h after radiotracer injection.

Visual interpretation of the ^{123}I-FP-CIT remains the standard clinical nuclear medicine assessment. A normal scan demonstrating symmetric left and right striatal uptake with a full "kidney bean" appearance would be consistent with a non-parkinsonian syndrome like essential tremor, although an abnormal scan manifests by the left/right striatal and/or caudate–putamen asymmetry reflects one of the parkinsonian syndromes (Fig. 11.57). Figures 11.58 and 11.59 demonstrate asymmetric uptake of radiotracer, consistent with Parkinson's disease.

Visual interpretation may be challenged by patient positioning, motion, use of different color scales, and the lack of experience of the novice

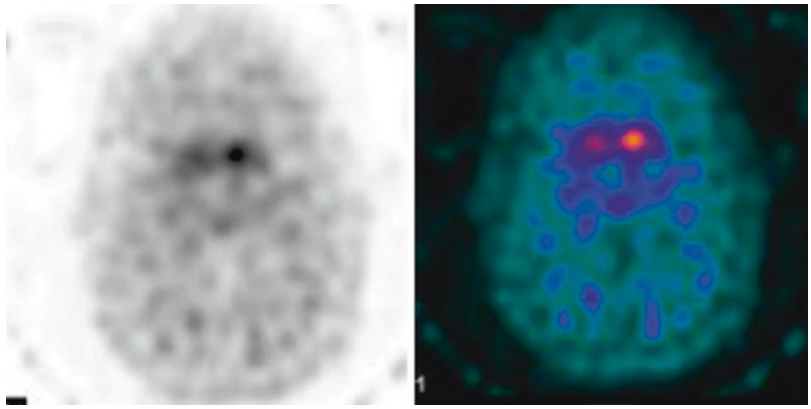

Fig. 11.59 Abnormal ^{123}I-FP-CIT SPECT. Patient is a 54-year-old female with movement disorders and Parkinson's disease. Scan being performed to assess for integrity of the nigrostriatal pathway. There is absence of uptake in the putamen both on the right and the left. There is also asymmetry of uptake in the caudate head nuclei which is slightly lower on the right inferiorly, but with some sections showing a mild decrease in the left in the midportion. The overall constellation of findings is consistent with Parkinson's disease

reader for calling subtle anatomic asymmetry as pathologic uptake. The recent Society of Nuclear Medicine practice guidelines for ^{123}I-FP-CIT provides very useful technical descriptions of the optimal injection, acquisition, reconstruction, and visual assessment approach [44].

Dopamine transporter imaging does not easily differentiate between idiopathic PD and the parkinsonian variants like progressive supranuclear palsy or multiple system atrophy [147, 149]. In many instances, patients are just started on a course of the dopamine replacement therapy to check for clinical response consistent with a diagnosis of idiopathic PD and managed over the illness course with therapeutic adjustments as the disease progresses.

I-123 labeled I-123 *N*-methyl-2 beta-carbomethoxy-3 beta-(4-iodophenyl) tropane ^{123}I-β-CIT is also used for imaging dopamine and serotonin transporters by SPECT [6, 43]. This cocaine derivative binds with high affinity to dopamine uptake sites in the striatum and can be used to visualize dopaminergic nerve terminals in vivo in the human brain with SPECT. It has been validated that the calculation of a simple ratio of specific/nonspecific binding during a period of binding equilibrium in the striatum about 2–4 h after bolus injection of the tracer gives a strong and reliable index of the binding potential of dopamine uptake sites.

Figure 11.60 shows SPECT imaging with ^{123}I-β-CIT. There is decreased tracer uptake in posterior inferior aspect of the globus pallidus. Use of this tracer in conjunction with anatomic–functional fusion imaging can be used for precision stereotactic ablation or dopamine supplementary implants. Preliminary results of these studies show excellent utility in patients with Parkinson's disease who otherwise are refractory to L-dopa therapy.

The radiotracer ^{123}I-β-CIT is a sensitive marker of dopamine uptake sites that can be used to visualize dopaminergic nerve endings in vivo in the human brain. A study reporting on ^{123}I-β-CIT single-photon emission computed tomography (SPECT) findings in a patient with DOPA-responsive dystonia [145], ^{123}I-β-CIT SPECT showed a striatal radiotracer uptake in the upper range of normal, indicating intact dopamine transporters and structural integrity of nigrostriatal neurons. This differentiates with DOPA-responsive dystonia from clinically similar cases with juvenile-onset parkinsonism with dystonia that have a poorer prognosis.

11.4.4.3 Radionuclide Cisternography

When hydrocephalus is suspected, the goal of imaging evaluation in general is to identify any abnormality of the ventricular or the subarach-

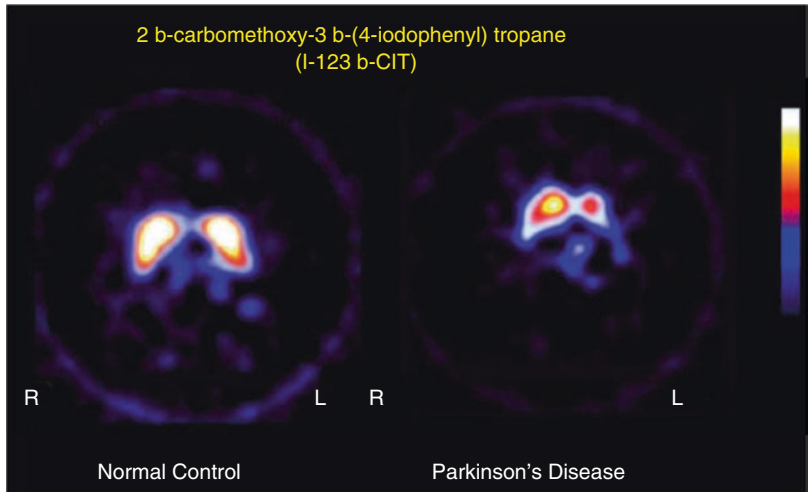

Fig. 11.60 SPECT images with ^{123}I-β-CIT. Images were obtained 4 h after the intravenous injection of five mCi of I-123-b-CIT in a 57-year-old normal control (*left*) which is compared with a 62-year-old male with Parkinson's disease (*right*). The normal control shows almost complete clearance of the tracer from all cortical and white matter regions of the brain except for the corpus striatum which appear as "bright" comma-shaped objects in the center of the brain. There is symmetry comparing the left corpus striatum to the right corpus striatum. The specificity of binding is due to the specific prevalence of dopamine uptake sights in these brain structures. The image on the left shows significant reduction of uptake, which is asymmetric and lower in the left corpus striatum. Semiquantitative analysis comparing the uptake in the corpus striatum to cerebellum shows that there is a 41% reduction in striatal binding on the left and a 30% reduction in striatal binding on the right in this patient with Parkinson's disease. This is indicative of the loss of the dopaminergic input from the substantia nigra which is the etiology of Parkinson's disease

noid space morphology and, if other unexplained ventriculomegaly is present, to demonstrate the site and nature of any impediment to the flow of the CSF. MRI is generally the best imaging method for achieving this goal. It also visualizes CSF movement and evaluates the ventricles and sulci. On T2-weighted images, the low signal intensity of CSF flowing in the cerebral aqueduct stands out in contrast to the high signal intensity of the adjacent tectum of the mesencephalon, a useful sign of aqueductal patency [27]. In children with patent anterior fontanels, the ventricular size can be assessed by ultrasound. When NPH is suspected and to assess patient's qualification for shunting surgery, several diagnostic modalities have been utilized. These include the infusion test using PMR pressure measurement of the ventricular system or the subarachnoid space on the spinal cord level, the neuropsychological evaluation, as well as the brain imaging using ^{99m}Tc-HMPAO SPECT or ^{18}F-FDG PET and radionuclide cisternography. Radionuclide cisternography has been repeatedly proven to be the most physiological method. The results of this procedure have been the most reliable criterion in the diagnosis of NPH [150, 151].

Cisternography has proven to be the most specific in differentiating patients with normal-pressure hydrocephalus (NPH) from those with other forms of degenerative brain disorder who would clearly not benefit from surgical treatment by ventricular shunting [152, 153].

In radionuclide cisternography the radiotracer (mostly ^{111}In-DTPA) is injected into the CSF system, via the lumbar subarachnoid space. Planar images are obtained immediately and at 4, 24, and 48 h post radiotracer injection. Figure 11.61 demonstrates a normal Cisternogram in a 53-year-old male with a history of severe headaches, who was originally suspected of having a CSF leak.

For patients suspected of having NPH, brain imaging is performed up to 72 h following injection of the radiopharmaceutical in the anterior, posterior, lateral, and vertical projections. Many institutions now perform SPECT imaging with

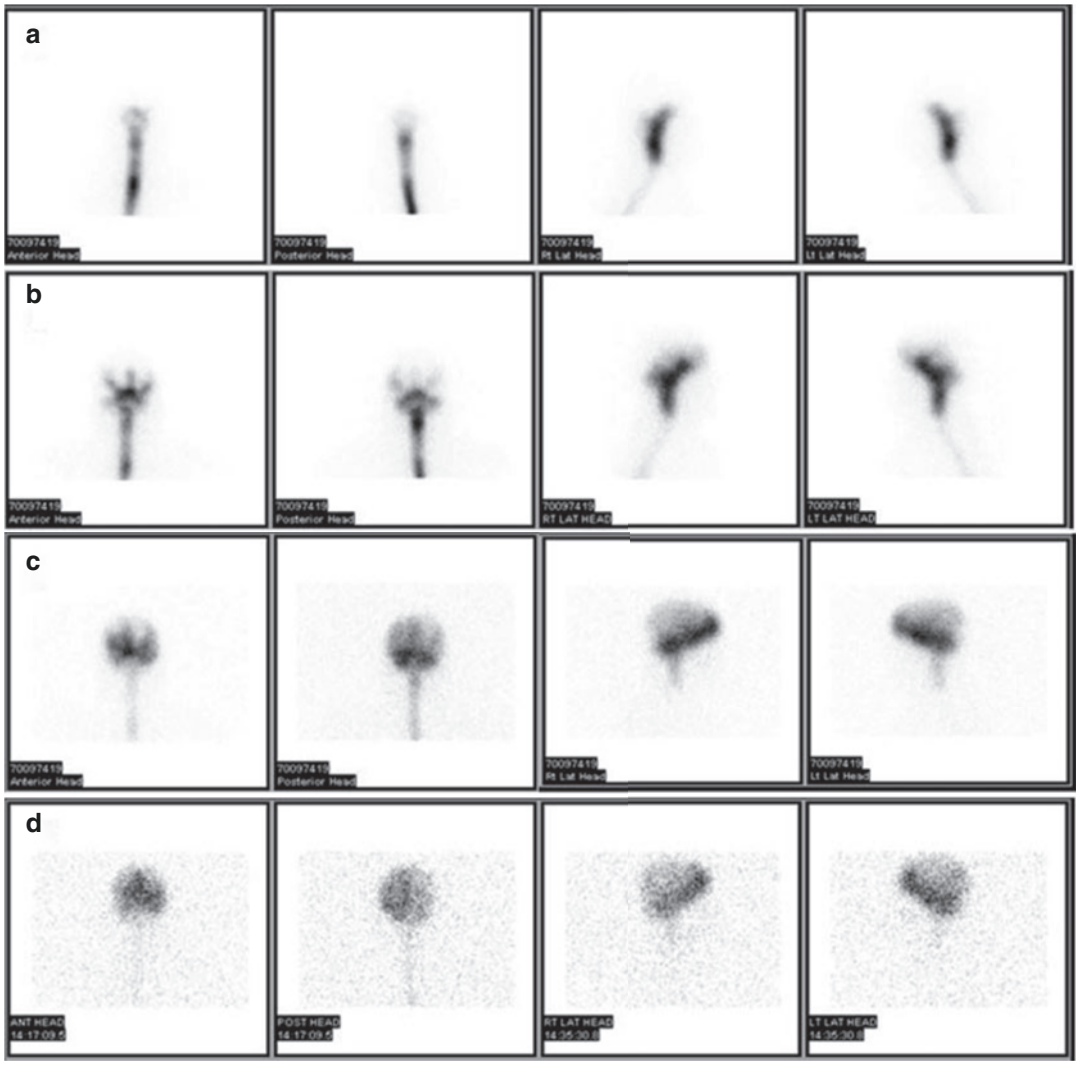

Fig. 11.61 Normal CSF Cisternogram: Planar images of brain, spinal canal of a 53-year-old male with a history of severe headaches. After administration of 1.1 mCi of ^{111}In-DTPA via lumbar puncture, planar images were obtained in the anterior posterior and lateral projections, at 0, 4, 24 and 48 h. Immediately after radiotracer injection (**a**), activity is noted in the spinal canal and at site of injection. At 4 h (**b**), expected activity is noted within the CSF spaces in the spine and within the basal cisterns. At 24 h (**c**), activity has progressed through the CSF is now over the bilateral convexities. Activity remains within the basal cisterns and spinal CSF spaces. At 48 h (**d**), there continues to be normal dynamics of CSF, with increased activity over the vertex and convexities. There is comparatively diminished uptake in the spinal column, which is expected with increased excretion and normal CSF flow

planar images. In patients with NPH 2–4-h post injection images shows radioactivity in the lateral ventricles which persists for 24–48 h (Fig. 11.62), indicating ventricular reflux. There is delayed clearance of the tracer as evidenced by minimal visualization of the convexities as late as 24–48 h.

Radionuclide studies have proven to be a sensitive and accurate method of detecting CSF leaks [28]. For CSF leaks, images are also obtained for the same duration and projections as for a cisternogram for NPH. The site of CSF leak is most likely to be identified when there is more significant CSF leak. It is also important that

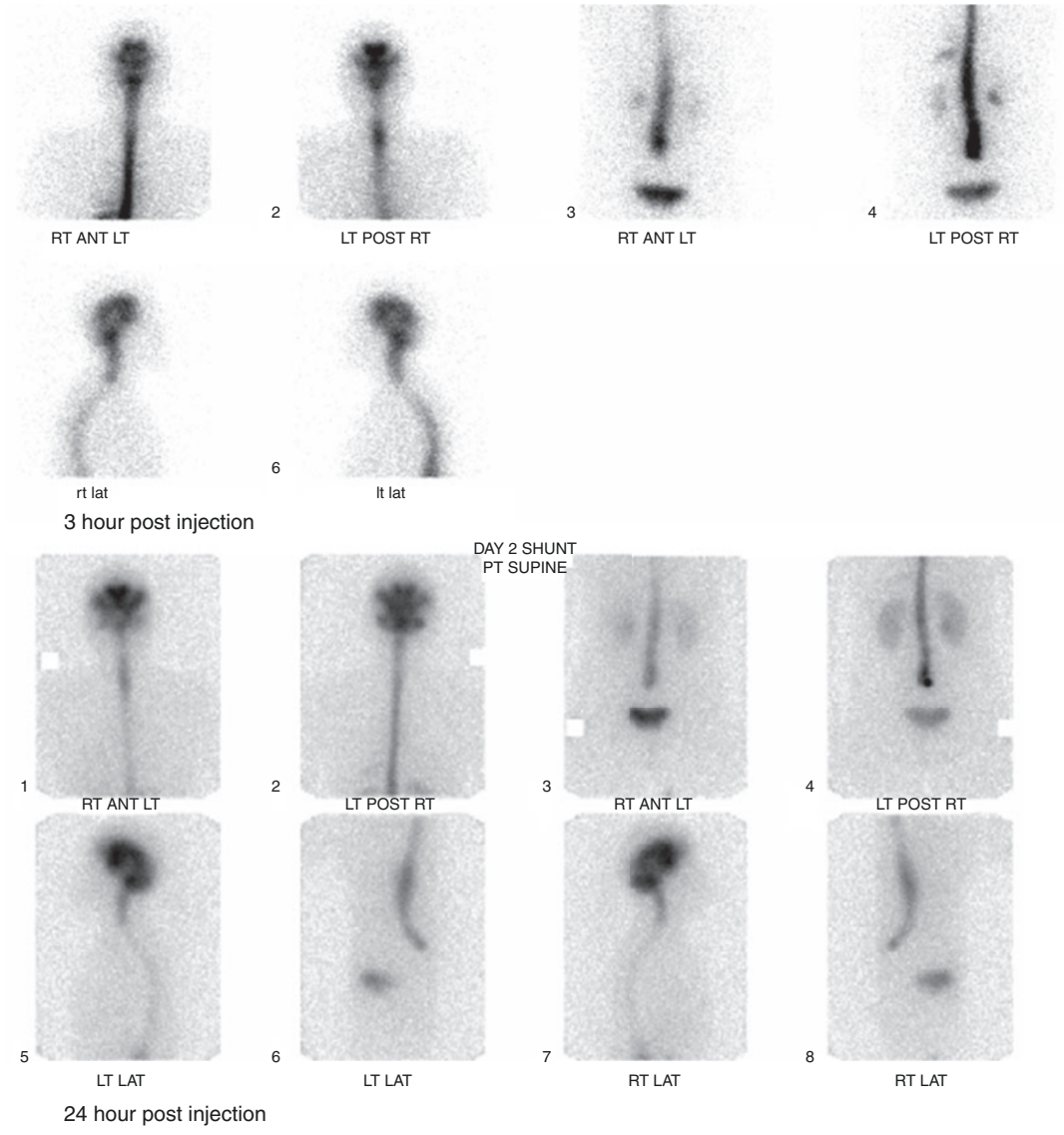

Fig. 11.62 Normal-pressure hydrocephalus (NPH) a 70-year-old female with headaches presents for evaluation of hydrocephalus. After injection of 1.0 mCi ^{111}In-DTPA into the subarachnoid space, planar images of the head and abdomen were obtained at 3 (*top 2 rows*) and 24 h (*bottom 2 rows*). Early (3 h postinjection) images show radiopharmaceutical accumulation in the ventricular system, as well as in the lumbar and basilar cistern portions of the subarachnoid space, with no tracer seen to ascend over the convexities. Repeat imaging was performed at approximately 24 h after injection, and there is again seen the tracer accumulation in the ventricles, with accumulation in the basilar cisterns, but no radiotracer is seen sent over convexities. Findings of persistent tracer in the lateral ventricles with no ascend over the convexities is consistent with normal-pressure hydrocephalus

imaging in appropriate projections is also performed; for e.g., posterior projection for otorrhea, whereas lateral and anterior projections for rhinorrhea. SPECT and quantitation are also used to detect leaks and diagnose the spontaneous intracranial hypotension due to cerebrospinal fluid (CSF) leaks and other causes of leak including postoperative. Alternatively, radioactive counts

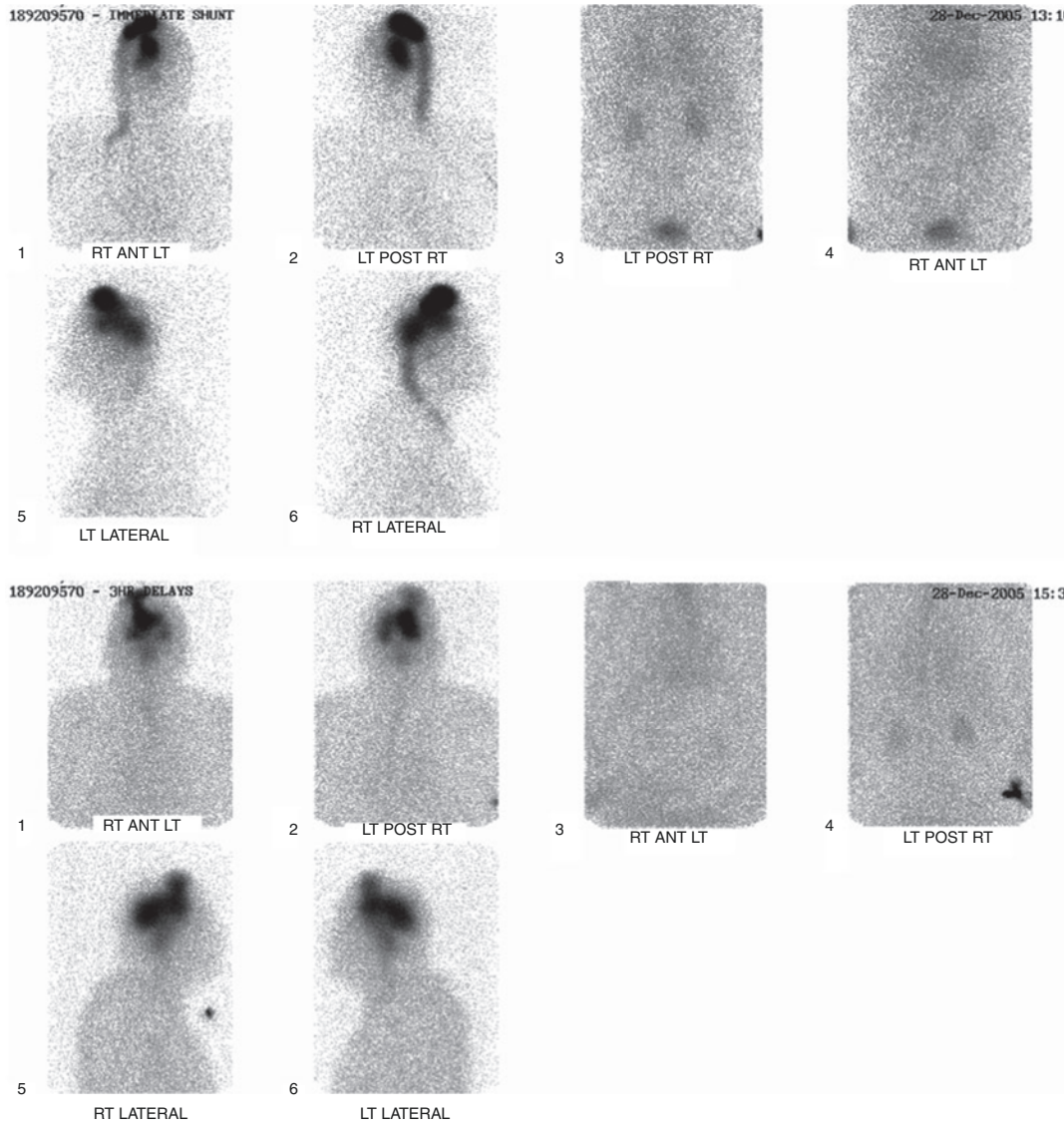

Fig. 11.63 VP shunt study: 35-year-old male patient with history of hydrocephalus and VP shunt presents for evaluation of VP shunt patency. Following administration of 1.0 mCi ^{111}In-DTPA intrathecally, scintigraphic images were obtained of the head, chest, and abdomen in the anterior and lateral projections immediately and 3 h after radiotracer injection. Radiotracer activity is seen only within the ventricular system, and none is seen within the VP shunt tubing. There was no spillage seen into the peritoneal cavity. Findings consistent with obstructed VP shunt

may be obtained from an absorbent material placed in the orifice in question to determine whether CSF is indeed leaking. Counting blood samples has also more recently been used along with pledget counting [30–32, 154].

Radionuclide CSF studies are also used in the evaluation of patency of ventricuperitoneal (VP) shunts. Figure 11.63 shows patient with history of hydrocephalus, and VP shunt presents for evaluation of VP shunt patency. Radiotracer activity is seen only within the ventricular system, and none is seen within the VP shunt tubing. There was radiotracer activity in the peritoneal cavity, to suggest a patent shunt.

11.4.4.4 Brain Death

Brain death is "the irreversible loss of function of the brain, including the brainstem" [155]. Prerequisites to diagnosing brain death based on physical examination include a sufficient mechanism of injury, lack of confounding factors such as drug intoxication or poisoning, and exclusion of complicating medical conditions that may interfere with clinical assessment, including hypothermia or severe electrolyte, acid–base, and endocrine disturbances.

Although the cardinal findings in brain death are determined on physical examination, confirmatory examinations, including imaging tests, may be called on in special situations to supplement the physical examination when specific components cannot be reliably performed or evaluated [155]. Confirmatory tests for brain death include tests of electrical activity (electroencephalography [EEG] and somatosensory evoked potentials) as well as radiologic examinations of blood flow (commonly contrast angiography, transcranial Doppler ultrasound, and radionuclide methods).

In addition to EEG and somatosensory evoked potentials, the American Academy of Neurology enumerates three confirmatory methods of evaluating blood flow: conventional contrast angiography, transcranial Doppler ultrasonography, and ^{99m}Tc-exametazime (HMPAO) radionuclide scintigraphy [155].

Radionuclide studies have been used as confirmatory tests in the determination of brain death for almost four decades [156]. Initially, radionuclide imaging was performed to evaluate cerebral blood flow using radiopharmaceuticals with rapid renal clearance (^{99m}Tc-diethylene triamine pentaacetic acid or ^{99m}Tc-glucoheptonate). Cerebral perfusion imaging is performed after radiopharmaceutical is injected intravenously, and the flow of activity within the internal cerebral artery circulation is assessed on dynamic planar scintigraphy at a rapid temporal resolution of 1 image per 1–2 s. Visualization of any activity within the anterior and middle cerebral artery territories indicates the presence of intracranial perfusion (Fig. 11.64), while the absence thereof, in the presence of an adequate common carotid bolus, indicates absent blood flow (Fig. 11.65). Static blood pool imaging of the skull, immediately after dynamic imaging, is typically performed as a component of this examination. Normally, static images portray blood pool of the intracranial venous sinuses and soft tissues of the face and skull. Nondiffusible radiopharmaceuticals do not cross the blood–brain barrier and consequently do not appear within the brain parenchyma. In the context of a brain death study, nonvisualization of the venous sinuses further confirms absent intracranial blood flow [157].

Use of nondiffusible radiopharmaceuticals for brain death studies has been largely supplanted by use of lipophilic compounds, specifically HMPAO [158, 159]. This radiopharmaceutical passively crosses the blood–brain barrier and becomes stably trapped within the brain parenchyma in proportion to regional perfusion [160]. Although the determination of brain death with lipophilic compounds has primarily been validated with HMPAO, it appears reasonable to extend the concept to a second commercially available ^{99m}Tc-labeled lipophilic radiopharmaceutical, ^{99m}Tc-bicisate (Neurolite) [161]. Cerebral uptake is quantitatively similar with these two compounds [162]. Multiple planar views of the brain are obtained to assess perfusion. Lack of localization of lipophilic compounds within the brain indicates absent blood flow. If any activity is visualized within the parenchyma of the brain or brainstem, there is incontrovertible evidence of blood flow.

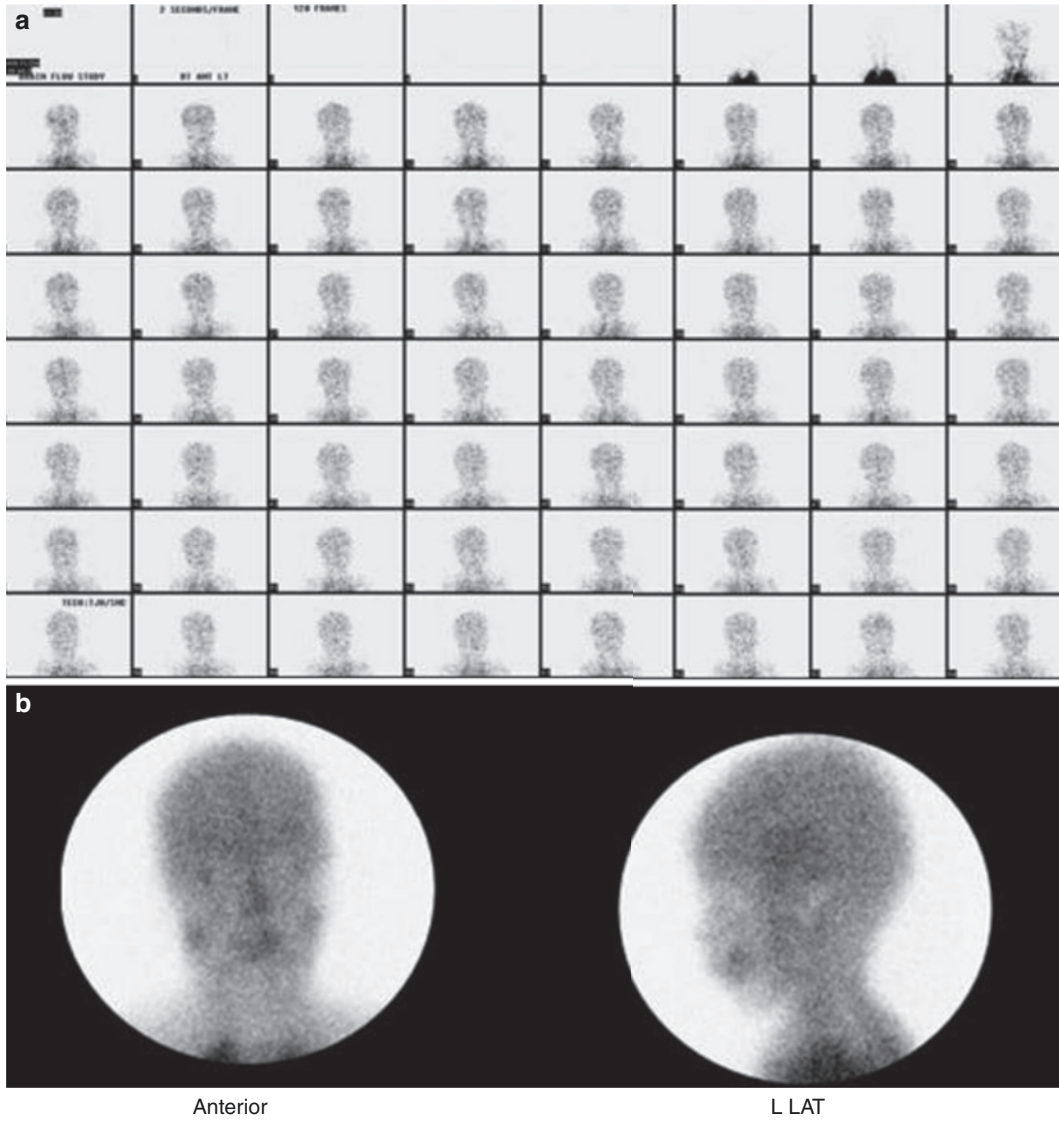

Fig. 11.64 Cerebral perfusion imaging of a 16-month-old boy after near-drowning incident. After injection 6 mCi of ^{99m}Tc-HMPAO IV, dynamic blood flow images (**a**) were obtained for 1 min in anterior projection, and then static images were obtained approximately 5 min post radiotracer injection in the anterior and lateral projections. The flow images showed flow in bilateral carotid arteries followed by perfusion of the brain. (**b**) The static images demonstrate radiotracer activity in the brain. These findings are not suggestive of brain death

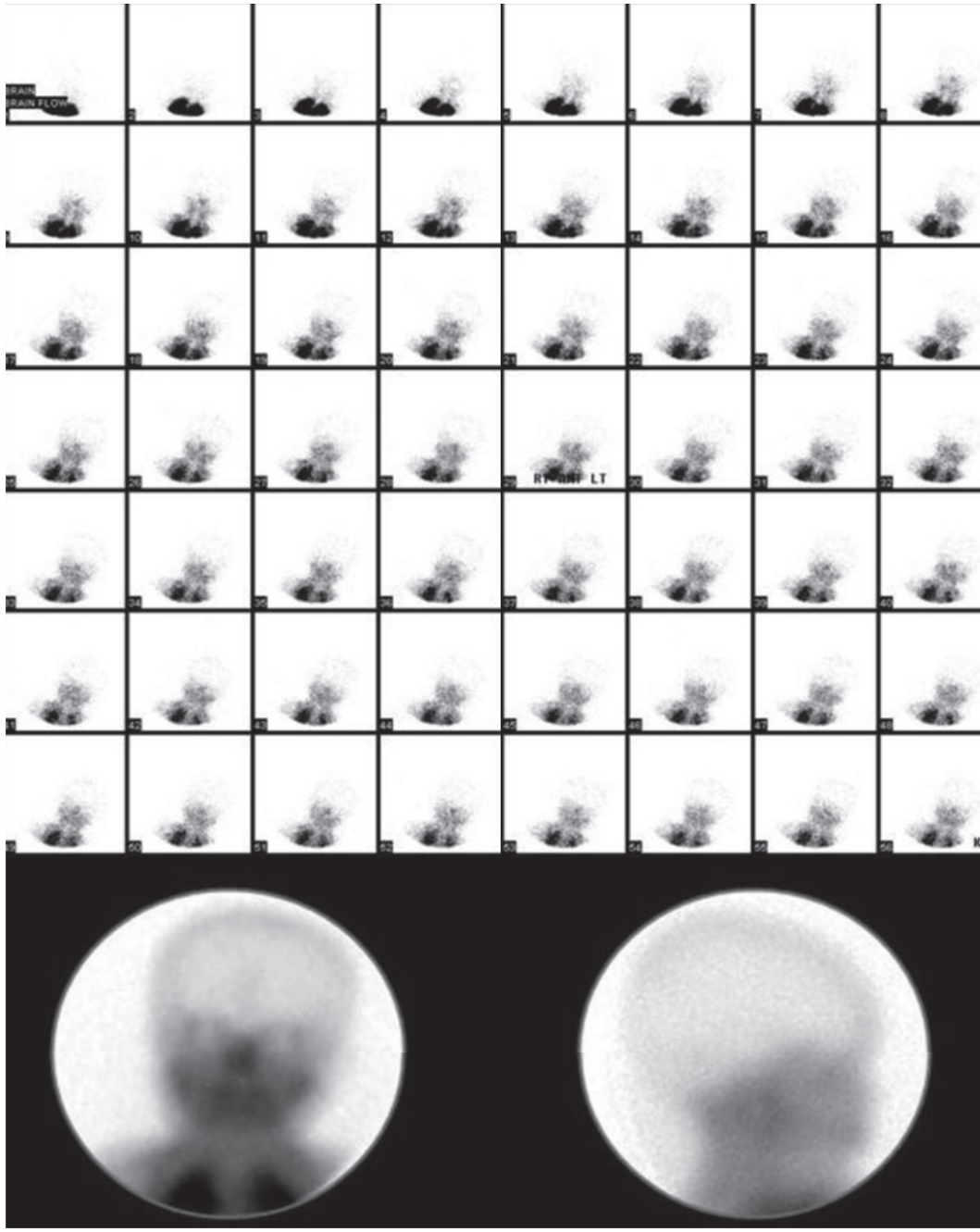

Fig. 11.65 Brain dead: a 2-year-old female with the clinical suspicion of brain death. After injection of 18.9 mCi of ^{99m}Tc-HMPAO IV, dynamic blood flow top images were obtained for 1 min in anterior projection, and then static images were obtained approximately 5 min post radiotracer injection (*bottom images*) in the anterior and lateral projections. On the blood flow/dynamic images, there is perfusion up to the level of the base of the skull and around the scalp, but no perfusion is noted intracranially. On the anterior and lateral static images, there was no perfusion identified to the supratentorial or infratentorial brain structures. The absence of blood flow is consistent with the clinical diagnosis of brain death

References

1. Lloyd-Jones D, Adams R, Carnethon M et al (2009) Heart disease and stroke statistics-2009 update a report from the American Heart Association Statistics Committee and Stroke Statistics Subcommittee. Circulation 119(3):480–486
2. Lewis DH, Toney LK, Baron JC (2012) Nuclear medicine in cerebrovascular disease. Semin Nucl Med 42(6):387–405
3. Powers WJ, Grubb RL, Raichle ME (1984) Physiological-responses to focal cerebral-ischemia in humans. Ann Neurol 16(5):546–552
4. Powers WJ, Grubb RL, Darriet D, Raichle ME (1985) Cerebral blood-flow and cerebral metabolic-rate of oxygen requirements for cerebral function and viability in humans. J Cereb Blood Flow Metab 5(4):600–608
5. Baron JC, Jones T (2012) Oxygen metabolism, oxygen extraction and positron emission tomography: historical perspective and impact on basic and clinical neuroscience. NeuroImage 61(2):492–504
6. Baron JC, Bousser MG, Comar D, Soussaline F, Castaigne P (1981) Non-invasive tomographic study of cerebral blood-flow and oxygen-metabolism in vivo – potentials, limitations, and clinical-applications in cerebral ischemic disorders. Eur Neurol 20(3):273–284
7. Baron JC, Bousser MG, Rey A, Guillard A, Comar D, Castaigne P (1981) Reversal of focal misery-perfusion syndrome by extra-intracranial arterial bypass in hemodynamic cerebral-ischemia - a case-study with O-15 positron emission tomography. Stroke 12(4):454–459
8. Heiss WD (2012) The ischemic penumbra: how does tissue injury evolve? Ann N Y Acad Sci 1268:26–34
9. Lassen NA (1966) Luxury-perfusion syndrome and its possible relation to acute metabolic acidosis localised within brain. Lancet 2(7473):1113–1115
10. Terpogossian MM, Herscovitch P (1985) Radioactive O-15 in the study of cerebral blood-flow, blood-volume, and oxygen-metabolism. Semin Nucl Med 15(4):377–394
11. Lenzi GL, Frackowiak RSJ, Jones T (1982) Cerebral oxygen-metabolism and blood-flow in human cerebral ischemic infarction. J Cereb Blood Flow Metab 2(3):321–335
12. Victor M, Ropper AH, Adams RD (2005) Adams and Victor's principles of neurology. McGraw-Hill, New York
13. von Strauss E, Viitanen M, De Ronchi D, Winblad B, Fratiglioni L (1999) Aging and the occurrence of dementia – findings from a population-based cohort with a large sample of nonagenarians. Arch Neurol 56(5):587–592
14. Gauthier S, Reisberg B, Zaudig M et al (2006) Mild cognitive impairment. Lancet 367(9518): 1262–1270
15. Brookmeyer R, Johnson E, Ziegler-Graham K, Arrighi HM (2007) Forecasting the global burden of Alzheimer's disease. Alzheimers Dement 3(3):186–191
16. Torosyan N, Silverman DHS (2012) Neuronuclear imaging in the evaluation of dementia and mild decline in cognition. Semin Nucl Med 42(6):415–422
17. McKhann G, Drachman D, Folstein M, Katzman R, Price D, Stadlan EM (1984) Clinical diagnosis of Alzheimer's disease: report of the NINCDS-ADRDA work group under the auspices of Department of Health and Human Services Task Force on Alzheimer's disease. Neurology 34(7):939–944
18. Reiman EM, Chen K, Alexander GE et al (2005) Correlations between apolipoprotein E epsilon4 gene dose and brain-imaging measurements of regional hypometabolism. Proc Natl Acad Sci U S A 102(23):8299–8302
19. Toney LK, McCue TJ, Minoshima S, Lewis DH (2011) Nuclear medicine imaging in dementia: a practical overview for hospitalists. Hosp Prac 39(3):149–160
20. Stieglitz RD (2000) Diagnostic and statistical manual of mental disorders. Z Klin Psychol Forsc 29(1):63–64
21. Albert MS, DeKosky ST, Dickson D et al (2011) The diagnosis of mild cognitive impairment due to Alzheimer's disease: recommendations from the National Institute on Aging-Alzheimer's Association workgroups on diagnostic guidelines for Alzheimer's disease. Alzheimers Dement 7(3):270–279
22. Commission on Classification and Terminology of the International League Against Epilepsy (1981) Proposal for revised clinical and electroencephalographic classification of epileptic seizures. Epilepsia 22(4):489–501
23. Kleihues P, Louis DN, Scheithauer BW et al (2002) The WHO classification of tumors of the nervous system. J Neuropathol Exp Neurol 61(3):215–225
24. Meara J, Bhowmick BK, Hobson P (1999) Accuracy of diagnosis in patients with presumed Parkinson's disease. Age Ageing 28(2):99–102
25. Hughes AJ, Ben-Shlomo Y, Daniel SE, Lees AJ (2001) What features improve the accuracy of clinical diagnosis in Parkinson's disease: a clinicopathologic study. Neurology 57(10):S34–S38
26. Marshall V, Grosset D (2003) Role of dopamine transporter imaging in routine clinical practice. Mov Disord 18(12):1415–1423
27. Bradley WG, Kortman KE, Burgoyne B (1986) Flowing cerebrospinal-fluid in normal and hydrocephalic states – appearance on MR images. Radiology 159(3):611–616
28. Kawaguchi S, Iio M, Murata H et al (1980) Comparative-study of NPH by RN cisternography and CT scan in the aged. J Nucl Med 21(6):84
29. Silberstein EB (1983) Brain scintigraphy in the diagnosis of the sequela of head trauma. Semin Nucl Med 13(2):153–167
30. Mitjavila M, Balsa MA, Penin J, Pey C (2004) Radionuclide cisternography in spontaneous intra-

cranial hypotension syndrome. Rev Esp Med Nucl 23(5):338–342
31. Takahashi M, Momose T, Kameyama M, Mizuno S, Kumakura Y, Ohtomo K (2005) Detection of cerebrospinal fluid leakage in intracranial hypotension with radionuclide cisternography and blood activity monitoring. Ann Nucl Med 19(4):339–343
32. Ozaki Y, Sumi Y, Kyogoku S, Shindoh N, Katayama H (1999) Spontaneous intracranial hypotension: characteristic findings of radionuclide cisternography using In-111 DTPA. Clin Nucl Med 24(10):823–825
33. Saha GB, MacIntyre WJ, Go RT (1994) Radiopharmaceuticals for brain imaging. Semin Nucl Med 24(4):324–349
34. Kung HF, Kung MP, Choi SR (2003) Radiopharmaceuticals for single-photon emission computed tomography brain imaging. Semin Nucl Med 33(1):2–13
35. Otte A, Halsband U (2006) Brain imaging tools in neurosciences. J Physiol Paris 99(4–6):281–292
36. Lassen NA, Blasberg RG (1988) Technetium-99m-d, l-HM-PAO, the development of a new class of 99mTc-labeled tracers: an overview. J Cereb Blood Flow Metab 8(6):S1–S3
37. Walovitch RC, Hill TC, Garrity ST et al (1989) Characterization of technetium-99m-L, L-ECD for brain perfusion imaging, part 1: pharmacology of technetium-99m ECD in nonhuman primates. J Nucl Med 30(11):1892–1901
38. Lassen NA (1985) Cerebral blood flow tomography with xenon-133. Semin Nucl Med 15(4):347–356
39. Mintun MA, Raichle ME, Martin WR, Herscovitch P (1984) Brain oxygen utilization measured with O-15 radiotracers and positron emission tomography. J Nucl Med 25(2):177–187
40. Mountz JM, Raymond PA, McKeever PE et al (1989) Specific localization of thallium 201 in human high-grade astrocytoma by microautoradiography. Cancer Res 49(14):4053–4056
41. O'Tuama LA, Treves ST, Larar JN et al (1993) Thallium-201 versus technetium-99m-MIBI SPECT in evaluation of childhood brain tumors: a within-subject comparison. J Nucl Med 34(7):1045–1051
42. Conti PS (1995) Introduction to imaging brain tumor metabolism with positron emission tomography (PET). Cancer Investig 13(2):244–259
43. Emond P, Chalon S, Garreau L et al (1997) A new iodinated tropane derivative (beta-CDIT) for in vivo dopamine transporter exploration: comparison with beta-CIT. Synapse 26(1):72–80
44. Djang DSW, Janssen MJR, Bohnen N et al (2012) SNM practice guideline for dopamine transporter imaging with I-123-ioflupane SPECT 1.0. J Nucl Med 53(1):154–163
45. Maisey MN (2002) Overview of clinical PET. Br J Radiol 75:S1–S5
46. Ell PJ, Gambhir S (2004) Nuclear medicine in clinical diagnosis and treatment. Churchill Livingstone, Edinburgh
47. Andersen AR, Friberg H, Knudsen KB et al (1988) Extraction of [99mTc]-d, l-HM-PAO across the blood-brain barrier. J Cereb Blood Flow Metab 8(6):S44–S51
48. Leveille J, Demonceau G, De Roo M et al (1989) Characterization of technetium-99m-L, L-ECD for brain perfusion imaging, part 2: biodistribution and brain imaging in humans. J Nucl Med 30(11):1902–1910
49. Jacquier-Sarlin MR, Polla BS, Slosman DO (1996) Cellular basis of ECD brain retention. J Nucl Med 37(10):1694–1697
50. Slosman DO, Chicherio C, Ludwig C et al (2001) (133)Xe SPECT cerebral blood flow study in a healthy population: determination of T-scores. J Nucl Med 42(6):864–870
51. Yamauchi H, Fukuyama H, Nagahama Y et al (1999) Significance of increased oxygen extraction fraction in five-year prognosis of major cerebral arterial occlusive diseases. J Nucl Med 40(12):1992–1998
52. Deutsch G, Mountz JM, Liu HG, SanPedro EC, Sutor RJ (1997) Xenon-133 brain SPECT provides improved sensitivity to cerebrovascular stress studies. J Nucl Med 38(5):37p
53. Price JC (2003) Principles of tracer kinetic analysis. Neuroimaging Clin N Am 13(4):689–701
54. Woods RP, Cherry SR, Mazziotta JC (1992) Rapid automated algorithm for aligning and reslicing PET images. J Comput Assist Tomogr 16(4):620–633
55. Ancri D, Basset JY, Lonchampt MF, Etavard C (1978) Diagnosis of cerebral lesions by thallium 201. Radiology 128(2):417–422
56. Nass HW (1977) New Tl-201 nuclear decay data. J Nucl Med 18(10):1047–1048
57. Saha GB (1992) Fundamentals of nuclear pharmacy, 3rd edn. Springer, New York
58. Sehweil AM, Mckillop JH, Milroy R, Wilson R, Abdeldayem HM, Omar YT (1989) Mechanism of Tl-201 uptake in tumors. Eur J Nucl Med 15(7):376–379
59. Piwnicaworms D, Kronauge JF, Lefurgey A et al (1994) Mitochondrial localization and characterization of Tc-99-sestamibi in heart-cells by electron-probe X-ray-microanalysis and Tc-99-Nmr spectroscopy. Magn Reson Imaging 12(4):641–652
60. Sokoloff L, Reivich M, Kennedy C et al (1977) Deoxyglucose-C-14 method for measurement of local cerebral glucose-utilization – theory, procedure, and normal values in conscious and anesthetized albino-rat. J Neurochem 28(5):897–916
61. Huang SC, Phelps ME, Hoffman EJ, Sideris K, Selin CJ, Kuhl DE (1980) Non-invasive determination of local cerebral metabolic-rate of glucose in man. Am J Phys 238(1):E69–E82
62. Lucignani G, Schmidt KC, Moresco RM et al (1993) Measurement of regional cerebral glucose-utilization with fluorine-18-FDG and PET in heterogeneous tissues – theoretical considerations and practical procedure. J Nucl Med 34(3):360–369

63. Patlak CS, Blasberg RG (1985) Graphical evaluation of blood-to-brain transfer constants from multiple-time uptake data - generalizations. J Cereb Blood Flow Metab 5(4):584–590
64. Sokoloff L (1997) Relation between physiological function and energy metabolism in the central nervous system. J Neurochem 29:13–26
65. Liu HG, Mountz JM (2003) F-18FDG brain positron emission tomography and tl-201 early and delayed SPECT in distinguishing atypical cerebral tumor from cerebral infarction. Clin Nucl Med 28(3):241–242
66. Chao ST, Suh JH, Raja S, Lee SY, Barnett G (2001) The sensitivity and specificity of FDG PET in distinguishing recurrent brain tumor from radionecrosis in patients treated with stereotactic radiosurgery. Int J Cancer 96(3):191–197
67. Herholz K, Holzer T, Bauer B et al (1998) 11C-methionine PET for differential diagnosis of low-grade gliomas. Neurology 50(5):1316–1322
68. Hustinx R, Pourdehnad M, Kaschten B, Alavi A (2005) PET imaging for differentiating recurrent brain tumor from radiation necrosis. Radiol Clin N Am 43(1):35–47
69. Ericson K, Lilja A, Bergstrom M et al (1985) Positron emission tomography with ([11C]methyl)-L-methionine, [11C]D-glucose, and [68Ga]EDTA in supratentorial tumors. J Comput Assist Tomogr 9(4):683–689
70. De Witte O, Goldberg I, Wikler D et al (2001) Positron emission tomography with injection of methionine as a prognostic factor in glioma. J Neurosurg 95(5):746–750
71. Ribom D, Eriksson A, Hartman M et al (2001) Positron emission tomography (11)C-methionine and survival in patients with low-grade gliomas. Cancer 92(6):1541–1549
72. Ogawa T, Inugami A, Hatazawa J et al (1996) Clinical positron emission tomography for brain tumors: comparison of fludeoxyglucose F 18 and L-methyl-11C-methionine. AJNR Am J Neuroradiol 17(2):345–353
73. Chang CC, Kuwana N, Ito S, Yokoyama T, Kanno H, Yamamoto I (2003) Cerebral haemodynamics in patients with hydrocephalus after subarachnoid haemorrhage due to ruptured aneurysm. Eur J Nucl Med Mol Imaging 30(1):123–126
74. Kaschten B, Stevenaert A, Sadzot B et al (1998) Preoperative evaluation of 54 gliomas by PET with fluorine-18-fluorodeoxyglucose and/or carbon-11-methionine. J Nucl Med 39(5):778–785
75. Sasaki M, Kuwabara Y, Yoshida T et al (1998) Carbon-11-methionine PET in focal cortical dysplasia: a comparison with fluorine-18-FDG PET and technetium-99m-ECD SPECT. J Nucl Med 39(6):974–977
76. Bustany P, Chatel M, Derlon JM et al (1986) Brain tumor protein synthesis and histological grades: a study by positron emission tomography (PET) with C11-L-Methionine. J Neuro-Oncol 3(4):397–404
77. Tsuyuguchi N, Sunada I, Iwai Y et al (2003) Methionine positron emission tomography of recurrent metastatic brain tumor and radiation necrosis after stereotactic radiosurgery: is a differential diagnosis possible? J Neurosurg 98(5):1056–1064
78. Pirotte B, Goldman S, Massager N et al (2004) Combined use of 18F-fluorodeoxyglucose and 11C-methionine in 45 positron emission tomography-guided stereotactic brain biopsies. J Neurosurg 101(3):476–483
79. Ullrich RT, Kracht L, Brunn A et al (2009) Methyl-L-11C-methionine PET as a diagnostic marker for malignant progression in patients with glioma. J Nucl Med 50(12):1962–1968
80. Yamane T, Sakamoto S, Senda M (2010) Clinical impact of (11)C-methionine PET on expected management of patients with brain neoplasm. Eur J Nucl Med Mol Imaging 37(4):685–690
81. Weber WA, Wester HJ, Grosu AL et al (2000) O-(2-[18F]fluoroethyl)-L-tyrosine and L-[methyl-11C] methionine uptake in brain tumours: initial results of a comparative study. Eur J Nucl Med 27(5):542–549
82. Spaeth N, Wyss MT, Weber B et al (2004) Uptake of 18F-fluorocholine, 18F-fluoroethyl-L-tyrosine, and 18F-FDG in acute cerebral radiation injury in the rat: implications for separation of radiation necrosis from tumor recurrence. J Nucl Med 45(11):1931–1938
83. Chen W, Silverman DH, Delaloye S et al (2006) 18F-FDOPA PET imaging of brain tumors: comparison study with 18F-FDG PET and evaluation of diagnostic accuracy. J Nucl Med 47(6):904–911
84. Pauleit D, Floeth F, Hamacher K et al (2005) O-(2-[18F]fluoroethyl)-L-tyrosine PET combined with MRI improves the diagnostic assessment of cerebral gliomas. Brain 128(Pt 3):678–687
85. Rachinger W, Goetz C, Popperl G et al (2005) Positron emission tomography with O-(2-[18F]fluoroethyl)-l-tyrosine versus magnetic resonance imaging in the diagnosis of recurrent gliomas. Neurosurgery 57(3):505–511
86. Floeth FW, Pauleit D, Wittsack HJ et al (2005) Multimodal metabolic imaging of cerebral gliomas: positron emission tomography with [18F]fluoroethyl-L-tyrosine and magnetic resonance spectroscopy. J Neurosurg 102(2):318–327
87. Garnett S, Firnau G, Nahmias C, Chirakal R (1983) Striatal dopamine metabolism in living monkeys examined by positron emission tomography. Brain Res 280(1):169–171
88. Garnett ES, Firnau G, Nahmias C (1983) Dopamine visualized in the basal ganglia of living man. Nature 305(5930):137–138
89. Yee RE, Cheng DW, Huang SC, Namavari M, Satyamurthy N, Barrio JR (2001) Blood-brain barrier and neuronal membrane transport of 6-[18F]fluoro-L-DOPA. Biochem Pharmacol 62(10):1409–1415
90. Stout DB, Huang SC, Melega WP, Raleigh MJ, Phelps ME, Barrio JR (1998) Effects of large neutral amino acid concentrations on 6-[F-18]Fluoro-L-DOPA kinetics. J Cereb Blood Flow Metab 18(1):43–51
91. Fueger BJ, Czernin J, Cloughesy T et al (2010) Correlation of 6-18F-fluoro-L-dopa PET uptake with

proliferation and tumor grade in newly diagnosed and recurrent gliomas. J Nucl Med 51(10):1532–1538
92. Becherer A, Karanikas G, Szabo M et al (2003) Brain tumour imaging with PET: a comparison between [18F]fluorodopa and [11C]methionine. Eur J Nucl Med Mol Imaging 30(11):1561–1567
93. Rasey JS, Koh WJ, Evans ML et al (1996) Quantifying regional hypoxia in human tumors with positron emission tomography of [18F]fluoromisonidazole: a pretherapy study of 37 patients. Int J Radiat Oncol Biol Phys 36(2):417–428
94. Brown JM (2001) Therapeutic targets in radiotherapy. Int J Radiat Oncol Biol Phys 49(2):319–326
95. Szeto MD, Chakraborty G, Hadley J et al (2009) Quantitative metrics of net proliferation and invasion link biological aggressiveness assessed by MRI with hypoxia assessed by FMISO-PET in newly diagnosed glioblastomas. Cancer Res 69(10):4502–4509
96. Cher LM, Murone C, Lawrentschuk N et al (2006) Correlation of hypoxic cell fraction and angiogenesis with glucose metabolic rate in gliomas using 18F-fluoromisonidazole, 18F-FDG PET, and immunohistochemical studies. J Nucl Med 47(3): 410–418
97. Spence AM, Muzi M, Swanson KR et al (2008) Regional hypoxia in glioblastoma multiforme quantified with [18F]fluoromisonidazole positron emission tomography before radiotherapy: correlation with time to progression and survival. Clin Cancer Res 14(9):2623–2630
98. Oborski MJ, Laymon CM, Lieberman FS, Mountz JM (2013) Distinguishing pseudoprogression from progression in high-grade gliomas: a brief review of current clinical practice and demonstration of the potential value of 18F-FDG PET. Clin Nucl Med 38(5):381–384
99. Barthel H, Cleij MC, Collingridge DR et al (2003) 3′-deoxy-3′-[F-18]fluorothymidine as a new marker for monitoring tumor response to antiproliferative therapy in vivo with positron emission tomography. Cancer Res 63(13):3791–3798
100. Chen W, Cloughesy T, Kamdar N et al (2005) Imaging proliferation in brain tumors with F-18-FLT PET: comparison with F-18-FDG. J Nucl Med 46(6):945–952
101. Munch-Petersen B, Cloos L, Jensen HK, Tyrsted G (1995) Human thymidine kinase 1. Regulation in normal and malignant cells. Adv Enzym Regul 35:69–89
102. d'Asseler YM, Koole M, Lemahieu I et al (1997) Recent and future evolutions in NeuroSPECT with particular emphasis on the synergistic use and fusion of imaging modalities. Acta Neurol Belg 97(3):154–162
103. Blume H, Hemminger BM (1997) Image presentation in digital radiology: perspectives on the emerging DICOM display function standard and its application. Radiographics 17(3):769–777
104. Bartenstein P, Asenbaum S, Catafau A et al (2002) European association of nuclear medicine procedure guidelines for brain imaging using[F-18]FDG. Eur J Nucl Med Mol Imaging 29(10):43–48
105. Talairach JSG, Tournoux P, Prossalentis M, Bordasferrer L, Covello L, Jacob M, Mempel E (1967) Atlas of stereotaxis anatomy of the telencephalon. Masson, Paris
106. Evans AC, Collins DL (1993) A 305-Member MRI-based stereotaxic atlas for CBF activation studies. J Nucl Med 34(5):70–71
107. Friston K, Holmes AP, Worsley KJ, Poline JP, Frith CD, Frackowiak RSJ (1995) Statistical parametric maps in functional imaging: a general approach. Hum Brain Mapp 2:189–210
108. Asenbaum S, Brucke T, Pirker W, Pietrzyk U, Podreka I (1998) Imaging of cerebral blood flow with Technetium-99m-HMPAO and Technetium-99m-ECD: a comparison. J Nucl Med 39(4):613–618
109. Abraham T, Feng J (2011) Evolution of brain imaging instrumentation. Semin Nucl Med 41(3):202–219
110. Cikrit DF, Dalsing MC, Harting PS et al (1997) Cerebral vascular reactivity assessed with acetazolamide single photon emission computer tomography scans before and after carotid endarterectomy. Am J Surg 174(2):193–197
111. Berenstein A, Ransohoff J, Kupersmith M, Flamm E, Graeb D (1984) Trans-vascular treatment of giant aneurysms of the cavernous carotid and vertebral arteries – functional investigation and embolization. Surg Neurol 21(1):3–12
112. Petersen RC, Thomas RG, Grundman M et al (2005) Vitamin E and donepezil for the treatment of mild cognitive impairment. N Engl J Med 352(23):2379–2388
113. Silverman DHS (2004) Brain F-18-FDG PET in the diagnosis of neurodegenerative dementias: comparison with perfusion SPECT and with clinical evaluations lacking nuclear imaging. J Nucl Med 45(4):594–607
114. Burdette JH, Minoshima S, Borght TV, Tran DD, Kuhl DE (1996) Alzheimer disease: improved visual interpretation of PET images by using three-dimensional stereotaxic surface projections. Radiology 198(3):837–843
115. Administration FaD. Highlights of prescribing information: Amyvid (florbetapir F18 injection). http://www.accessdata.fda.gov/drugsatfda_docs/label/2012/202008s000lbl.pdf
116. Okie S (2011) Confronting Alzheimer's disease. N Engl J Med 365(12):1069–1072
117. O'Brien TJ, O'Connor MK, Mullan BP et al (1998) Subtraction ictal SPET co-registered to MRI in partial epilepsy: description and technical validation of the method with phantom and patient studies. Nucl Med Commun 19(1):31–45
118. Galynker II, Cai J, Ongseng F, Finestone H, Dutta E, Serseni D (1998) Hypofrontality and negative symptoms in major depressive disorder. J Nucl Med 39(4):608–612
119. Mountz JM, Tolbert LC, Lill DW, Katholi CR, Liu HG (1995) Functional deficits in autistic disorder:

characterization by technetium-99m-HMPAO and SPECT. J Nucl Med 36(7):1156–1162
120. Krug DA, Arick J, Almond P (1980) Behavior checklist for identifying severely handicapped individuals with high levels of autistic behavior. J Child Psychol Psychiatry 21(3):221–229
121. Wilms G, Marchal G, Demaerel PH, Van Hecke P, Baert AL (1991) Gadolinium-enhanced MRI of intracranial lesions. A review of indications and results. Clin Imaging 15(3):153–165
122. Valk PE, Dillon WP (1991) Radiation injury of the brain. AJNR Am J Neuroradiol 12(1):45–62
123. Schwartz RB, Holman BL, Polak JF et al (1998) Dual-isotope single-photon emission computerized tomography scanning in patients with glioblastoma multiforme: association with patient survival and histopathological characteristics of tumor after high-dose radiotherapy. J Neurosurg 89(1):60–68
124. Kaplan WD, Takvorian T, Morris JH, Rumbaugh CL, Connolly BT, Atkins HL (1987) Thallium-201 brain tumor imaging: a comparative study with pathologic correlation. J Nucl Med 28(1):47–52
125. Delbeke D, Meyerowitz C, Lapidus RL et al (1995) Optimal cutoff levels of F-18 fluorodeoxyglucose uptake in the differentiation of low-grade from high-grade brain tumors with PET. Radiology 195(1):47–52
126. Wurker M, Herholz K, Voges J et al (1996) Glucose consumption and methionine uptake in low-grade gliomas after iodine-125 brachytherapy. Eur J Nucl Med 23(5):583–586
127. Langleben DD, Segall GM (2000) PET in differentiation of recurrent brain tumor from radiation injury. J Nucl Med 41(11):1861–1867
128. MacDonald DR, Cascino TL, Schold SC Jr, Cairncross JG (1990) Response criteria for phase II studies of supratentorial malignant glioma. J Clin Oncol 8(7):1277–1280
129. Taal W, Brandsma D, de Bruin HG et al (2008) Incidence of early pseudo-progression in a cohort of malignant glioma patients treated with chemoirradiation with temozolomide. Cancer 113(2): 405–410
130. Brandes AA, Franceschi E, Tosoni A et al (2008) MGMT promoter methylation status can predict the incidence and outcome of pseudoprogression after concomitant radiochemotherapy in newly diagnosed glioblastoma patients. J Clin Oncol 26(13):2192–2197
131. Esteller M, Garcia-Foncillas J, Andion E et al (2000) Inactivation of the DNA-repair gene MGMT and the clinical response of gliomas to alkylating agents. N Engl J Med 343(19):1350–1354
132. Hegi ME, Diserens AC, Gorlia T et al (2005) MGMT gene silencing and benefit from temozolomide in glioblastoma. N Engl J Med 352(10):997–1003
133. Brandes AA, Tosoni A, Cavallo G et al (2006) Correlations between O6-methylguanine DNA methyltransferase promoter methylation status, 1p and 19q deletions, and response to temozolomide in anaplastic and recurrent oligodendroglioma: a prospective GICNO study. J Clin Oncol 24(29):4746–4753
134. Clarke JL, Chang S (2009) Pseudoprogression and pseudoresponse: challenges in brain tumor imaging. Curr Neurol Neurosci Rep 9(3):241–246
135. Vredenburgh JJ, Desjardins A, Herndon JE et al (2007) Phase II trial of bevacizumab and irinotecan in recurrent malignant glioma. Clin Cancer Res 13(4):1253–1259
136. Schlemmer HP, Pichler BJ, Schmand M et al (2008) Simultaneous MR/PET imaging of the human brain: feasibility study. Radiology 248(3):1028–1035
137. Boss A, Bisdas S, Kolb A et al (2010) Hybrid PET/MRI of intracranial masses: initial experiences and comparison to PET/CT. J Nucl Med 51(8):1198–1205
138. Wang SX, Boethius J, Ericson K (2006) FDG-PET on irradiated brain tumor: ten years' summary. Acta Radiol 47(1):85–90
139. Hatakeyama T, Kawai N, Nishiyama Y et al (2008) 11C-methionine (MET) and 18F-fluorothymidine (FLT) PET in patients with newly diagnosed glioma. Eur J Nucl Med Mol Imaging 35(11):2009–2017
140. Jacobs AH, Thomas A, Kracht LW et al (2005) 18F-fluoro-L-thymidine and 11C-methylmethionine as markers of increased transport and proliferation in brain tumors. J Nucl Med 46(12):1948–1958
141. Chen W, Delaloye S, Silverman DH et al (2007) Predicting treatment response of malignant gliomas to bevacizumab and irinotecan by imaging proliferation with [18F] fluorothymidine positron emission tomography: a pilot study. J Clin Oncol 25(30):4714–4721
142. Benamer HTS, Patterson J, Grosset DG et al (2000) Accurate differentiation of parkinsonism and essential tremor using visual assessment of [I-123]-FP-CIT SPECT imaging: the [I-123]-FP-CIT Study Group. Mov Disord 15(3):503–510
143. Schwarzenberg J, Czernin J, Cloughesy TF et al (2012) 3′-deoxy-3′-18F-fluorothymidine PET and MRI for early survival predictions in patients with recurrent malignant glioma treated with bevacizumab. J Nucl Med 53(1):29–36
144. Hicklin DJ, Ellis LM (2005) Role of the vascular endothelial growth factor pathway in tumor growth and angiogenesis. J Clin Oncol 23(5):1011–1027
145. Ferrara N, Hillan KJ, Novotny W (2005) Bevacizumab (Avastin), a humanized anti-VEGF monoclonal antibody for cancer therapy. Biochem Biophys Res Commun 333(2):328–335
146. Booij J, Habraken JBA, Bergmans P et al (1998) Imaging of dopamine transporters with iodine-123-FP-CIT SPECT in healthy controls and patients with Parkinson's disease. J Nucl Med 39(11):1879–1884
147. Gunther I, Hall H, Halldin C, Swahn CG, Farde L, Sedvall G (1997) [I-125]beta-CIT-FE and [I-125] beta-CIT-FP are superior to [I-125]beta-CIT for dopamine transporter visualization: autoradiographic evaluation in the human brain. Nucl Med Biol 24(7):629–634

148. AbiDargham A, Gandelman MS, DeErausquin GA et al (1996) SPECT imaging of dopamine transporters in human brain with iodine-123-fluoroalkyl analogs of beta-CIT. J Nucl Med 37(7):1129–1133
149. Booij J, Tissingh G, Winogrodzka A et al (1997) Practical benefit of [I-123]FP-CIT SPET in the demonstration of the dopaminergic deficit in Parkinson's disease. Eur J Nucl Med 24(1):68–71
150. Booij J, Tissingh G, Boer GJ et al (1997) [123I] FP-CIT SPECT shows a pronounced decline of striatal dopamine transporter labelling in early and advanced Parkinson's disease. J Neurol Neurosurg Psychiatry 62(2):133–140
151. Marek K, Jennings D, Seibyl J (2003) Single-photon emission tomography and dopamine transporter imaging in Parkinson's disease. Adv Neurol 91:183–191
152. Tatsch K, Schwarz J, Mozley PD et al (1997) Relationship between clinical features of Parkinson's disease and presynaptic dopamine transporter binding assessed with [I-123]IPT and single-photon emission tomography. Eur J Nucl Med 24(4):415–421
153. Chmielowski K, Podgorski JK, Twarkowski P, Pietrzykowski J, Szalus N (2004) Radionuclide cisternography in the diagnosis of normal pressure hydrocephalus. Pol Merkur Lekarski 16(96): 576–580
154. Cernochova I, Lipina R (2004) Radionuclide cisternography in diagnostics of obstruction hydrocephalus in introduced ventriculoperitoneal shunt. Nucl Med Rev Cent East Eur 7(1):85–86
155. Borbely K (2004) Functional imaging of cerebrospinal fluid pathology. IdeggyogySz 57(9–10):301–312
156. The Quality Standards Subcommittee of the American Academy of Neurology (1995) Practice parameters for determining brain death in adults (summary statement). Neurology 45(5):1012–1014
157. Okizaki A, Shuke N, Aburano T, Hashizume K, Nakai H, Tanaka T (2001) Detection of cerebrospinal fluid leak by dual-isotope SPECT with In-111 DTPA and Tc-99m HMDP. Clin Nucl Med 26(7):628–629
158. Goodman JM, Mishkin FS, Dyken M (1969) Determination of brain death by isotope angiography. JAMA 209(12):1869–1872
159. Nagle CE (1980) Use of immediate static scans in combination with radionuclide cerebral angiography as a confirmatory test in the diagnosis of brain death. Clin Nucl Med 5(4):152–153
160. Roine RO, Launes J, Lindroth L, Nikkinen P (1986) 99mTc-hexamethylpropyleneamine oxime scans to confirm brain death. Lancet 2(8517):1223–1224
161. Reid RH, Gulenchyn KY, Ballinger JR (1989) Clinical use of technetium-99m HM-PAO for determination of brain death. J Nucl Med 30(10): 1621–1626
162. Sharp PF, Smith FW, Gemmell HG et al (1986) Technetium-99m HM-PAO stereoisomers as potential agents for imaging regional cerebral blood flow: human volunteer studies. J Nucl Med 27(2):171–177
163. Donohoe KJ, Frey KA, Gerbaudo VH, Mariani G, Nagel JS, Shulkin B (2003) Procedure guideline for brain death scintigraphy. J Nucl Med 44(5):846–851
164. Leveille J, Demonceau G, Walovitch RC (1992) Intrasubject comparison between technetium-99m-ECD and technetium-99m-HMPAO in healthy human subjects. J Nucl Med 33(4):480–484
165. Herholz K, Heiss WD (2004) Positron emission tomography in clinical neurology. Mol Imaging Biol 6(4):239–269
166. Nguyen NC et al (2018) Targeted therapy and immunotherapy response assessment with F-18 Fluorothymidine positron-emission tomography/ magnetic resonance imaging in melanoma brain metastasis: a pilot study. Front Oncol 8:18

Nuclear Oncology

12

Razi Muzaffar, Medhat M. Osman, Ismet Sarikaya, and Abdelhamid H. Elgazzar

12.1 Introduction

Nuclear medicine has a major role in the management of malignant tumors. With the developments toward molecular imaging and the technological advancement of scanners providing a fusion of both physiologic and anatomic imaging, it has even become a more integral part of management protocols. This role includes detection of malignant tumors, staging and restaging of the disease, early detection of recurrence, evaluation of the response to therapy, and prediction of the prognosis. Radionuclide diagnosis and therapy for tumors depend on the characteristics of tumors including increased vascularization, increased blood flow, newly proliferated capillaries with more permeable walls, increased metabolic activity of cells, increased energy demand, high density of some common antigens or several specific antigens, and several specific receptors as discussed in the previous chapter.

R. Muzaffar · M. M. Osman (✉)
Division of Nuclear Medicine, Department of Radiology, Saint Louis University, St. Louis, MO, USA
e-mail: razi.muzaffar@health.slu.edu; medhat.osman@health.slu.edu

I. Sarikaya · A. H. Elgazzar
Department of Nuclear Medicine, Kuwait University, Kuwait City, Kuwait

Understanding the cell biology of tumors and their features including the angiogenesis, cell proliferation, necrosis, apoptosis, and specific cell receptors has and will lead to development of new imaging methods to evaluate various aspects of the tumor to help improve the diagnostic and therapeutic capabilities. Furthermore, this understanding has led to the development of newer methods to treat tumors as well as development of new drugs. The pathophysiologic characteristics of tumors are utilized in several scintigraphic clinical applications effectively including diagnosis, staging, and evaluation of the response to therapy, selection of drug therapy, and prediction of prognosis.

The use of positron-emitting radionuclide imaging has revolutionized the imaging of physiologically and pathologically important molecules. It provides data at both a molecular and metabolic level needed for the evaluation and treatment for effective patient care. Positron emission tomography (PET) has continued to gain momentum in diagnosing, staging, and restaging many cancers. The technology has been in rapid evolution and dissemination and has become a standard procedure in the management of many cancer patients. The fusion of functional (PET) and anatomic (CT) imaging continues to evolve and provide valuable clinical information. PET/CT imaging has supplanted myocardial perfusion imaging as the highest volume and revenue study in many institutions. According to the

A. H. Elgazzar (ed.), *The Pathophysiologic Basis of Nuclear Medicine*,
https://doi.org/10.1007/978-3-030-96252-4_12

Academy of Molecular Imaging, there are more than 5,000 PET/CT systems installed worldwide, making it one of the fastest growing imaging modalities [1].

^{18}F-FDG has played an important and more extended role in oncology, but other F-18-labeled PET tracers have and will be available commercially similar to FDG. ^{67}Ga citrate, ^{201}Tl chloride, and ^{99m}Tc-sestamibi and similar compounds for the purpose of tumor imaging will ultimately be used only in those hospitals that have no access to a PET imaging facility (dedicated or multifunctional system). Also, in the case of pediatric imaging, ^{201}Tl chloride, ^{67}Ga citrate, and ^{99m}Tc-sestamibi in conjunction with ^{111}In-octreotide and ^{131}I- or 123- I MIBG can still play a major role in pediatric oncology [2–4]. Nevertheless, the advent of 68Ga, 64Cu, and 177Lu in conjunction with 18F in the era of theranostics appears to be the future of molecular imaging.

12.2 Principles of Tumor Pathology and Biology

12.2.1 Tumor Pathology

Tumor classification is based on histogenesis, degree of cellular differentiation (i.e., well or poorly differentiated), and biological behavior (benign versus malignant). All tumors, whether benign or malignant, have two components: (1) proliferating neoplastic cells and (2) supportive stroma. While the neoplastic cells determine the nature of the tumors, tumor growth and evolution depend on the stroma [5].

Most tumors arise from immature cells that can transform and acquire phenotypic features similar to those of one or more normal cell types. In some instances, the immature cells can undergo divergent differentiation into two cell types, as in the case of mixed tumors of the salivary gland (Fig. 12.1), or they have the capacity to differentiate into any adult cell type, as in teratoma.

The categorization of tumors into benign and malignant is an oversimplification of the wide behavioral range of neoplasms. In general, a benign tumor is composed of well-differentiated cells that resemble their normal counterpart. A tumor is considered benign when its gross and microscopic characteristics are relatively innocent, implying that it will remain localized and cannot spread to other sites.

Currently, the malignant category is restricted to tumors that have metastatic properties. Malignant neoplasms arising from epithelial cells are termed carcinomas (Figs. 12.2 and 12.3). Malignant epithelial tumors that have not extended through the underlying basement membrane are described as in situ carcinoma.

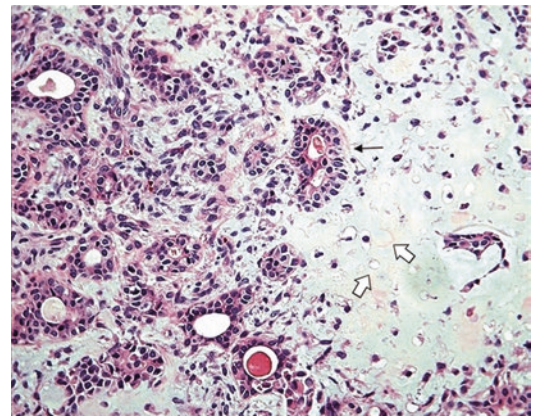

Fig. 12.1 Benign mixed tumor of the salivary gland (pleomorphic adenoma). The tumor consists of an epithelial component "glands" (*arrow*) and a mesenchymal component "cartilage" (*open arrows*)

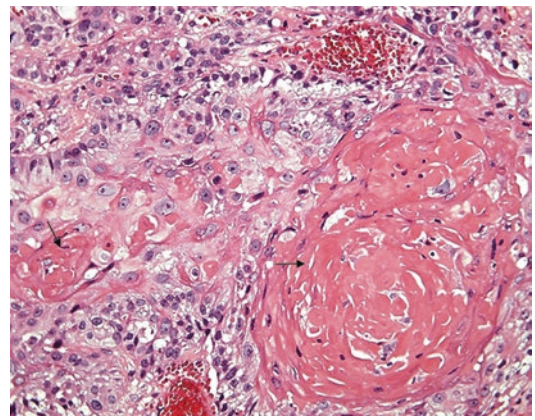

Fig. 12.2 Squamous cell carcinoma. The tumor consists of well-differentiated squamous cells forming keratin pearls (*arrow*)

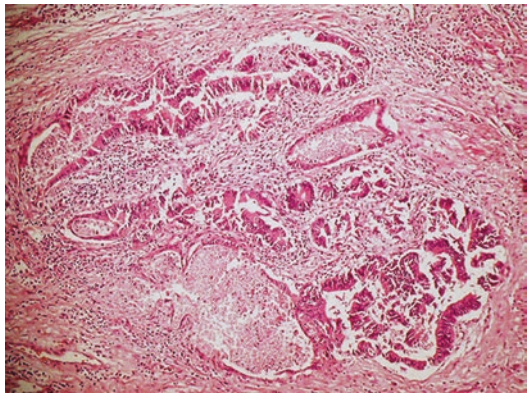

Fig. 12.3 Adenocarcinoma. Note the glandular formation of the malignant cells (*arrows*)

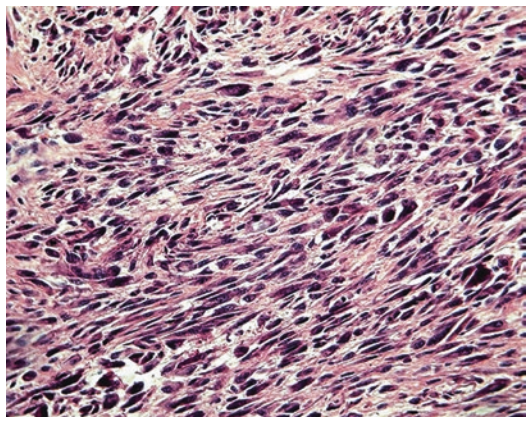

Fig. 12.4 Soft tissue sarcoma consisting of pleomorphic spindle cells, illustrating the features of malignancy as variable cell size and shapes and increased nuclear/cytoplasmic ratio

Malignant tumors arising from mesenchymal tissue are broadly designated as sarcomas (Fig. 12.4). Lymphomas are tumors of lymphatic system cells, while myelomas are those of plasma cells. There are tumors that do not follow any classification scheme, such as seminoma and melanoma. Other tumors carry eponyms, such as Hodgkin's disease and Ewing's sarcoma.

Tumors within a single organ or single type of epithelium are further subclassified into different types; each has its own characteristics, prognosis, and response to therapy. A comprehensive and detailed histological classification of tumors of various organ systems is presented in several reviews and monographs [6, 7].

Grading is a scheme that attempts to determine the degree of malignancy and is based on the evaluation of certain parameters that vary according to the system used. These broadly include the following: degree of tumor cellularity, resemblance of tumor cells to their normal forebears morphologically and functionally, cellular pleomorphism or anaplasia, mitotic activity (number and abnormality), and necrosis. In general, a three-grade system has proven to be the most reproducible; well, moderately, and poorly or undifferentiated, or grades I, II, and III, where grade III represents the least-differentiated tumor.

Staging of cancer depends on the size of the primary neoplasm, its extent to regional lymph nodes, and the presence or absence of metastasis. The TNM system has been developed by the American (American Joint Committee on Cancer, AJCC) and European (Union International Contre le Cancer, UICC) commissions on cancer to allow systematic categorization and description of cancer patients. TNM is an expression of the anatomical extent of disease and is based on the assessment of three components:

- T—the extent of primary tumor
- N—the absence or presence and extent of regional lymph node metastases
- M—the absence or presence of distant metastases

TNM clinical–diagnostic staging allows for pretreatment characterization via clinical examination and specific diagnostic studies. TNM surgical–evaluative staging is applied following a major surgical exploration or biopsy. TNM postsurgical treatment–pathological staging characterizes the extent of the cancer following thorough examination of the resected surgical specimen. TNM retreatment staging is applied in instances where the initial therapy has failed and additional treatment decisions are being considered. TNM autopsy staging is the final staging, done after the postmortem study.

The rate of growth of malignant tumors correlates in general with their level of differentiation. Rapidly growing malignant neoplasm often contains central areas of ischemic necrosis

because the tumor blood supply, derived from the host, fails to keep pace with the oxygen needs of the expanding mass of cells [5].

12.2.2 Tumor Biology

Developing cancer cells must acquire a variety of characteristics not generally found in non-transformed cells. The cancer cell represents the culmination of a complex process of developing capacity for largely unregulated growth.

The main characteristics that differentiate the cancer cell from the precancerous or noncancerous cell are capabilities of self-sufficiency in growth signals, insensitivity to antigrowth signals, evasion of apoptosis, limitless replicative potential, sustained angiogenesis, and a potential for tissue invasion and metastasis. In addition, the enabling characteristic of genetic instability was noted as a driving force for acquiring these cell characteristics.

Normal cell proliferation (also known as cell growth or cell division) is essential for tissue homeostasis in the adult body. When stimulated to divide, a normal cell progresses through a tightly regulated process known as the cell cycle. This cycle is biochemically initiated by external stimuli, modulated by both external and internal growth controls. The cell cycle has different phases. Cyclins are special proteins that activate the various phases of the cell cycle. Cyclins combine with, activate, and direct the action of special tyrosine kinases called cyclin-dependent kinases. Normal cells have mechanisms or checkpoints that detect abnormalities in DNA sequences. When DNA is damaged, a number of repair mechanisms replace damaged nucleotides with normal molecules. Normal tissue maintains a stable cell population through two distinct growth and antigrowth signaling networks that regulate the cell-cycle machinery.

Extrinsic growth or antigrowth stimuli can come from several sources outside of the cell including soluble growth factors, extracellular matrix components, or other cell-surface molecules. Cancer cells can achieve growth autonomy by internally producing abnormal amounts of their own mitogenic growth factors. This is known as autocrine stimulation. Also, cancer cells may stimulate the neighboring cells in the tumor microenvironment.

Although overexpression of growth factors is frequently involved in cancer cell proliferation, less is known about the role of antigrowth factors in the evasion of antiproliferative signals. Transforming growth factor-beta (TGF-β) is an antigrowth factor expressed by most normal epithelial cells. TGF-β functions in an autocrine fashion to inhibit proliferation and therefore may be a tumor suppressor protein.

Antigrowth signaling can be disabled or disrupted through mutations in transmembrane receptors. The mutations lead to the expression of fewer receptors or dysfunctional receptors that are less responsive to normal levels of extracellular antigrowth signals. The best known example is the TGF-β receptor. Also, insensitivity to antigrowth signals can occur when intracellular signaling pathways are disrupted and become unresponsive to TGF-β signaling or other antigrowth stimulation [8, 9].

Cell survival and proliferation is dependent on an adequate supply of oxygen and nutrients and the removal of toxic metabolites. Neovascularization is a feature of neoplasia and is initiated, maintained, and controlled by multiple molecules that are released from tumor cells, endothelial cells, and other cell types. Additionally, endothelial cells of the vessels stimulate the growth of adjacent tumor cells by secreting different factors, such as insulin-like growth factor, platelet-derived growth factor (PDGF), granulocyte–macrophage colony-stimulating factor (GM-CSF), and interleukin (IL)-1. Angiogenesis is required not only for continued tumor growth but also for metastasis [5].

Tumor-associated angiogenic factors may be produced by tumor cells or may be derived from inflammatory cells (e.g., macrophages) that infiltrate tumors. The two most important tumor-associated angiogenic factors are vascular endothelial growth factor (VEGF) and basic fibroblast growth factor. The tumor cells not only

produce angiogenic factors but also induce antiangiogenesis molecules. Hypoxia within the growing tumor favors angiogenesis by release of hypoxia-inducible factor-1 (HIF-1) [1]. Increased tumor vascularization and increased levels of angiogenic inducers are associated with increased risk of tumor metastases and shortened survival in patients with cancer [10].

The VEGF pathway has also been targeted by antiangiogenic drugs which inhibit the tyrosine kinase receptors of several angiogenic factors, through targeting the cytoplasmic portion of the receptor. These drugs block cell division and inhibit new blood vessel growth. A major advantage of antiangiogenic therapy is that it targets a cell population (endothelial cells) with relative genetic stability compared with other cancer cells [11–15].

Most human malignancies show various degrees of genetic heterogeneity even if they originate from single cells. The multistep progression model determines that cells pass through a number of distinctive intermediate stages of evolution from normalcy to full malignancy [16]. The evolved tumor cells vary significantly from their normal counterparts.

Normal cells have an ordered growth pattern and a predicted relationship with their neighboring cells, and that growth pattern is predominantly two dimensional. Further normal cell division is inhibited by contacts made with other cells; this is the phenomenon of contact inhibition13. In contrast, tumor cells exhibit loss of contact inhibition and continue to display a disordered growth pattern. Another feature that distinguishes normal growth from malignant proliferation is the reduced dependence of the latter on the presence of the known stimulatory and inhibitory growth factors [17, 18].

The immune system is also thought to play a role in the detection and elimination of malignant cells. Immune cells can identify cancer cells that express tumor-specific antigens (molecules unique to cancer cells) or tumor-associated antigens (molecules differentially expressed by cancer cells and normal cells). Tumors can induce immunosuppression through a variety of mechanisms such as expression of immunosuppressive molecules and induction of apoptosis in lymphoid cells. An example of an immunosuppressive molecule is the transforming growth factor-β (TGF-β) [19].

A relatively new approach to cancer therapy is the use of vaccines to boost antibody production or elicit T-cell responses against cancer cells.

Tumor cells exhibit a vast array of metabolic differences distinguishing them from their untransformed counterparts. Some of the most striking metabolic alterations include the utilization of anaerobic pathways and the increased utilization of glucose transport [19].

Metastasis is a multistep process in which tumor cells invade nearby tissues and colonize other parts of the body. Malignant neoplasms disseminate by one of three pathways: (1) seeding within body cavities, (2) lymphatic spread which is the preferred way of spread by carcinomas in general, or (3) hematogenous spread which is favored by sarcomas.

Carcinogenesis or oncogenesis is a process by which normal cells are transformed into cancer cells. Genes that promote autonomous cell growth in cancer cells are called oncogenes20. They are derived by mutations in proto-oncogenes and are characterized by the ability to promote cell growth in the absence of normal growth-promoting signals. Their products, called oncoproteins, resemble the normal products of proto-oncogenes except that oncoproteins are devoid of important regulatory elements, and their production in the transformed cells does not depend on growth factors or other external signals. Typically, a series of several mutations to these genes is required before a normal cell transforms into a cancer cell (Fig. 12.5).

All normal cells require stimulation by growth factors to undergo proliferation. Many cancer cells acquire growth self-sufficiency, however, by acquiring the ability to synthesize the same growth factors to which they are responsive. Such is the case with platelet-derived growth factor (PDGF) and transforming growth factor-α (TGF-α)21. There are several oncogenes that encode growth factor. Those oncogenes represent either

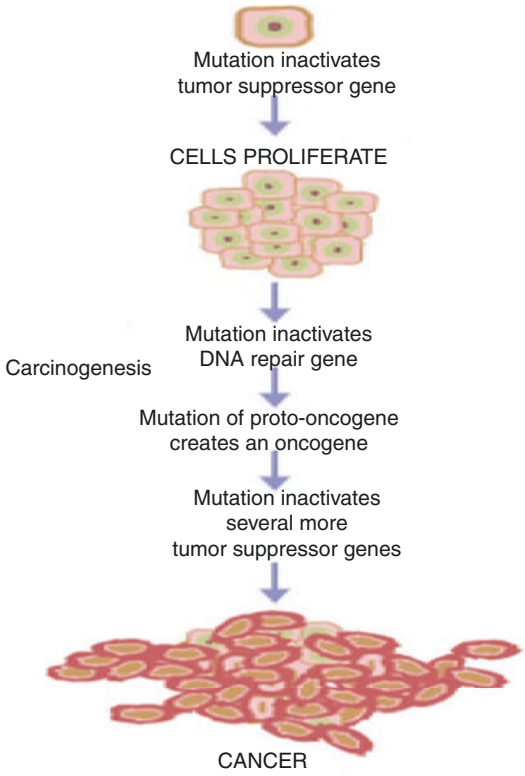

Fig. 12.5 Cancers are caused by a series of mutations. Each mutation alters somewhat the behavior of the cell (adapted from Wikipedia)

mutation or overexpression of normal forms of growth factor receptors. Overexpression can render cancer cells hyperresponsive to normal levels of the growth factor, a level that would not normally trigger proliferation. Among the examples of overexpression is the receptor called HER2 (ERBB2) [18, 19].

Mutations in genes that encode various components of the signaling pathways are a common process in cancer. These signaling molecules couple growth factor receptors to their nuclear targets. The most important members in this category are RAS and ABL. While oncogenes play a critical role in tumorigenesis, another group of genes known as tumor suppressors appears to be equally significant. The loss of wild-type tumor suppressor genes such as Rb and p53 is associated with a wide variety of human tumors.

The most commonly mutated tumor suppressor gene in human cancer is p53, with at least 50% of tumors having abnormal p53 genes [20].

The number of cells in an area of tissue is not only determined by the rate of cell proliferation but also regulated by the rate of cell death. Each day, approximately 50–70 billion cells die in the average adult because of programmed cell death. Most normal cells that acquire carcinogenic mutations are eliminated by apoptosis. By contrast, one of the key capabilities of the cancer cell is its capacity to evade apoptosis. Therefore, evasion of apoptosis is an early event in carcinogenesis that allows for the accumulation of mutations that are essential to malignant transformation [20]. Apoptosis-inducing drugs cause cells to undergo apoptosis by targeting proteins involved in deregulated apoptotic signaling. Resistance to apoptosis is a major problem for traditional chemotherapy, which causes DNA damage and is intended to induce apoptosis. For chemotherapeutic agents to be effective, the cancer cell must be capable of undergoing apoptosis. Therefore, apoptosis-inducing drugs may be most effective when used in combination with chemotherapeutic agents.

Senescence is the process by which a normal somatic cell loses the ability to divide [20, 21]. Cancer stem cells must evade senescence to extend their replicative life span. Senescence is a cellular program that blocks progression through the cell cycle via induction of cyclin-dependent kinase inhibitors. Senescent cells remain functional. Senescence can be triggered by telomere shortening or other forms of physiological stress. Many normal human cell types are capable of undergoing only 60–70 cell divisions, after which they stop growing and undergo cell-cycle arrest (replicative senescence). Unless the cell enters a senescent state, further replication involving the unprotected chromosomal ends would result in gross chromosomal abnormalities and ultimately trigger cell death.

The evidence now indicates that for many types of cancer, including the most common forms, there exists not only environmental influences but also hereditary predispositions. Inherited cancer syndromes include several well-defined cancers in which inheritance of a single mutant gene greatly increases the risk of a person to develop a tumor. Almost all the common types of cancers that occur sporadically have been reported to occur in familial forms.

Table 12.1 Biological characteristics of cancer cells

Self-sufficiency in growth signals
Loss of sensitivity to antigrowth signals
Evasion of apoptosis
Evasion of immune surveillance
Loss of capacity for senescence
Loss of contact inhibition
Sustained angiogenesis
Immortality
Genetic instability
Ability to invade neighboring tissues
Ability to form metastases at distant sites

In summary, the molecular pathogenesis of cancer is a complex process requiring the disruption of a number of regulatory pathways. There are a vast number of molecules and genes in a cell that can regulate cell growth. Defects in any of these that shift the balance toward uncontrolled growth, invasiveness, and decreased cell death and other characteristics of cancer cells (Table 12.1) lead to cancer. Recent progress during the last 20 years in understanding these pathways has been tremendous and may explain not only the molecular paradigms for the development of cancer phenotypes, but also is finally being brought to force as new cancer therapeutics. Molecular-targeted agents have already made dramatic differences in the treatment of cancers that were previously considered untreatable. The next decade will continue to see explosive growth in novel cancer diagnosis particularly molecular and in therapeutics targeting the different pathways that define a cancer cell.

12.3 Radiopharmaceuticals

12.3.1 Conventional Radiopharmaceuticals

There are numerous radiopharmaceuticals that are used for the differentiation of benign from malignant lesions including gallium-67 citrate, thallium-201 chloride, ^{99m}Tc-sestamibi, and fluorine 18 fluorodeoxyglucose (^{18}F-FDG). However, with the advent of ^{18}F-FDG as well as computed tomography (CT) and magnetic resonance imaging (MRI), many of the others are not routinely used. The most notable of which is gallium-67 (^{67}Ga) citrate. It was used as a tumor imaging agent initially for Hodgkin's lymphoma. Approximately 90% of Hodgkin's lymphomas are gallium-avid pretreatment [22]. It was later found that ^{67}Ga was also useful in other types of malignancies such as non-Hodgkin's lymphoma, melanoma, hepatocellular carcinoma, and lung cancers among others. ^{67}Ga is trapped on the transferrin or lactoferrin receptors and then passes through the cytoplasm intracellularly [1, 2, 23, 24]. Therefore, when transferrin-binding sites in the plasma are saturated by iron, gallium stays in free form in plasma; it will not bind to the transferrin and will not pass across the cell membrane. As a result in these conditions of transferrin saturation, ^{67}Ga citrate uptake will be less sensitive for detection of inflammatory and malignant disease. Background activity will be high and the quality of the scan will be poor. When indicated, these patients were given a dose of 10 mCi (370 MBq) for adults or 75–100 uCi/kg for pediatric patients. Whole body images with or without SPECT were performed initially at 48–72 h and at 5–10 days as needed [25]. ^{67}Ga citrate is still used in centers where PET service is not available, in spite of its poor physical characteristics, relatively poor sensitivity, and lack of specificity. This is due primarily to its lower cost and long half-life of 3 days, which makes it suitable for worldwide delivery. Those centers that have access to ^{18}F-FDG PET/CT imaging do not recommend ^{67}Ga citrate studies for tumor imaging, but still used for chronic infection localization.

Although predominantly a myocardial perfusion agent, thallium-201 chloride (^{201}Tl) has been used to image viable benign and malignant tumors throughout the body. It was found that ^{201}Tl was also useful in malignancies including lung, breast, thyroid, glioblastomas, and some sarcomas. However, the use of ^{201}Tl below the diaphragm is limited due to the normal uptake in the liver, spleen, kidneys, and intestines. Chemotherapy and radiation therapy do not alter the uptake of thallium as they do with gallium. ^{201}Tl chloride has a mechanism of uptake in the

cell related to the sodium pump, ATPase activity, angiogenesis, and ill-formed and well-formed new blood vessels [26–28]. The typical administered dose is 3–4 mCi (111–148 MBq). Imaging can be performed as early as 10 min postinjection since it localizes in active neoplasms such as lymphoma. Delayed imaging at 3 h can provide enhanced target-to-background ratios [29].

Technetium-99m sestamibi (^{99m}Tc) has also been found useful for a number of tumors including breast, thyroid, and CNS neoplasms. ^{99m}Tc-sestamibi uptake is related to the electrical gradient difference across the cell membrane and mitochondrial uptake. Retention of this radiopharmaceutical inside the cell, on the other hand, is thought to be inversely proportional to the multidrug resistance of its glycoprotein content and its activation in the cell [30–32]. The typical administered dose is 20–30 mCi (740–1110 MBq). Imaging can be performed at 10–20 min postinjection and as far as 2 h delayed imaging since there is little washout from malignant lesions [33, 34].

Indium-111 pentetreotide (OctreoScan) is a somatostatin analog which has been found to be useful for evaluation of neuroendocrine tumors, particularly in carcinoid tumors and gastrinomas. It has also been used to assess patients with lymphomas and granulomatous diseases [35]. Somatostatin is a 14-amino acid peptide that inhibits the release of pituitary hormones as well as the release of certain intestinal and pancreatic peptides such as insulin, glucagon, gastrin, VIP, gastric inhibitory polypeptide, secretin, motilin, and cholecystokinin. Since there is a large quantity of somatostatin receptors in neuroendocrine tumors, radiolabeled analogs are useful for imaging. The typical administered dose of In-111 pentreotide is 3.0–6.0 mCi (111–222 MBq). Imaging can be performed at 4 and 24 h with an option of 48 h imaging to confirm equivocal findings. SPECT imaging is helpful and increases the sensitivity of the examination. The normal distribution includes the blood pool, thyroid, kidneys, bladder, liver, gallbladder, spleen, and bowel.

Metaiodobenzylguanidine (MIBG) can be labeled to either Iodine-123 or Iodine-131. MIBG is a guanethidine analog and resembles norepinephrine making it useful for the detection and evaluation of pheochromocytomas and neuroblastomas [36]. MIBG can also be utilized to evaluate other tumors with a lower affinity such as carcinoid tumors, paraganliomas, and medullary thryoid carcinoma. The ability of MIBG to detect extra-adrenal tumors is integral to the proper staging. The typical administered dose of MIBG for adults is 500 uCi (18.5 MBq) for I-131 or 10–30 mCi (370–1,110 MBq) for I-123. Imaging with I-131 MIBG is performed 1 and 2 days after injection and can be repeated at day 3. Imaging with I-123 MIBG is performed between 20 and 24 h with optional delayed images at up to 48 h. When evaluating for pheochromocytomas, the sensitivity and specificity of I-123 MIBG is 88 and 84%, respectively [37]. When evaluating for neuroblastomas, the sensitivity and specificity of I-123 MIBG is 90 and 94%, respectively [38].

12.3.2 PET Radiopharmaceuticals

12.3.2.1 Glucose Metabolism Agents

Fluorine-18-2-deoxy-D-glucose (^{18}F-FDG) diagnoses, stages, and restages many cancers with an accuracy ranging from 80 to 90%. PET/CT has become a standard procedure in the management of many cancer patients [39]. ^{18}F-FDG uptake in the cell is related to several glucose transporters in the cell membrane which allow active ^{18}F-FDG passage across the membrane to the cytoplasm and trapping without further metabolism. One of the biochemical characteristics of malignant cells is an enhanced rate of glucose metabolism due to an increased number of these cell surface glucose transporter proteins (such as Glut-1 and Glut-3) and increased intracellular enzyme levels of hexokinase and phosphofructokinase which promote glycolysis [40, 41]. FDG is phosphorylated to FDG-6-phosphate which, unlike glucose-6-phosphate, cannot be metabolized further and remains trapped in the cell. Imaging needs to be performed in the fasting state in order to minimize competitive inhibition of FDG uptake by glucose [42]. It is recommended that patients fast for a minimum of 4 h prior to FDG administration. Patients

should also be well hydrated for the exam and avoid any type of exercise or strenuous work at least 24 h before scanning [43]. A serum glucose level should be obtained prior to FDG administration since image quality is significantly influenced by plasma glucose levels. A commonly used glucose cutoff level is 200 mg/dl. An elevated level will cause an increase in soft tissue uptake and lead to decreased accumulation in tumors. In addition, diabetic patients will have to adjust insulin requirements and are best imaged early in the morning prior to the first meal and insulin (or other hypoglycemia medications). Insulin will also affect image quality by increasing accumulation in skeletal muscles which will in turn decrease accumulation in tumors [44]. FDG PET imaging is performed approximately 60 min following the intravenous administration of 10–20 mCi of FDG (0.14–0.21 mCi/kg of body weight) [43]. For pediatric patients, a dose of 0.15–0.30 mCi/kg is recommended with a minimum dose of 1 mCi [45]. The most common PET acquisition is from the base of the skull to the mid thighs, but some institutions have also recommended imaging from the top of the skull to the feet in all patients as unsuspected malignancies can be found outside the typical field of view in up to 4% of patients (Fig. 12.6). In the following cases, images should be obtained from top of the head to toes: melanoma and other skin malignancies, paraneoplastic syndromes, primary unknown tumors, multiple myeloma, neuroblastoma, and extremity tumors [46].

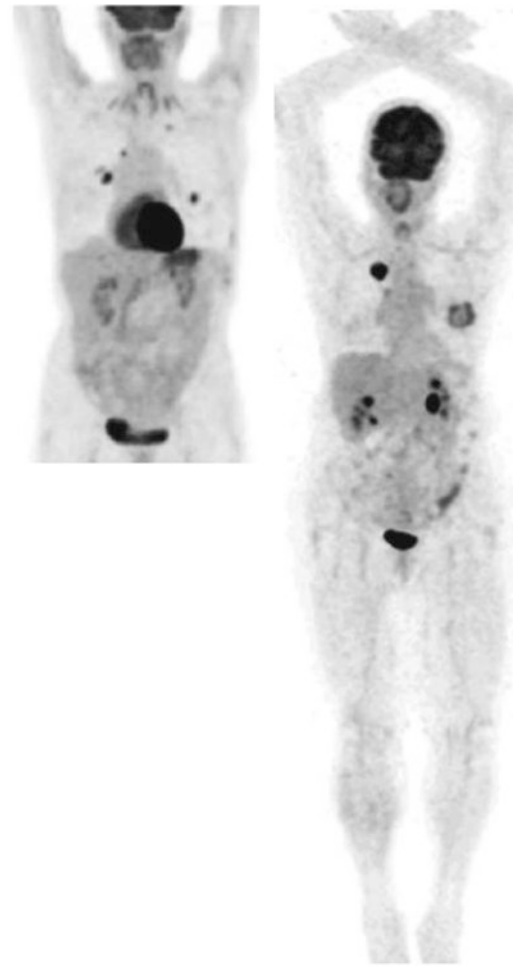

Fig. 12.6 LWB vs. TWB. Differences are the acquired field of views. The commonly used limited whole body field of view (*left*) from the base of the skull to the upper thighs compared to the true whole body field-of-view (right) on a 78 year old female with a left lower leg lesion found to be large B-cell lymphoma as the only lesion

12.3.2.2 Bone Seeking Agent

F-fluoride is a sensitive agent for detecting altered osteogenic activity with a mechanism of uptake similar to that of ^{99m}Tc-MDP (Fig. 12.7). The radiotracer accumulates in the vicinity of metastatic lesions in bone like MDP. However, 18F-fluoride has the advantage of faster blood clearance and higher bone uptake. Deposition of the radiotracer in bone is secondary to the blood flow to the bone as well as the efficiency of the bone to extract the fluorine ions from the blood which are not bound to serum proteins [47]. Given these characteristics, studies have shown that this is more accurate and sensitive for detection of bone metastasis when compared to the current gold standard bone scan as well as MRI [48]. However, one of the drawbacks to this modality is the lack of physiologic information in regard to the soft tissues. At times, both ^{18}F-FDG and 18F-fluoride studies are needed on a given patient. This is typically done as two separate studies on different days which is both inconvenient for the patient and increases radiation exposure from the CT component of both studies. Some have suggested that both ^{18}F-FDG and 18F-fluoride can be combined in a single PET/

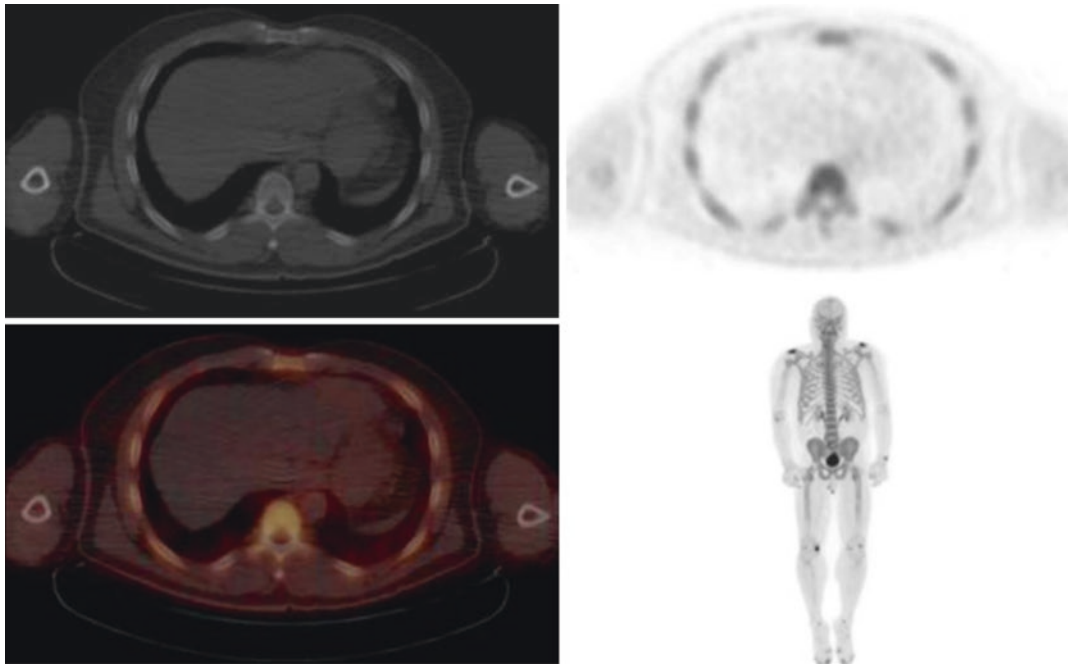

Fig. 12.7 A 57-year-old male patient with a history of prostate cancer. NaF PET/CT images demonstrate a normal radiotracer distribution throughout the skeleton with areas of focal uptake in the shoulders, wrists, knees, and feet which are consistent with degenerative arthropathy

CT scan by administering the two radiopharmaceuticals simultaneously or in sequence. Preliminary studies have shown this to increase the sensitivity for detecting bone lesions compared with ^{18}F-FDG, which only scans with the benefit of additional soft tissue evaluation [49].

12.3.2.3 Proliferation Agents

Currently, only ^{18}F-FDG is widely accepted and used in clinical practice for proliferation imaging. ^{18}F-fluorodeoxythymidine (^{18}F-FLT) is an amino acid agent labeled with ^{18}F that can be used to measure tumor cell proliferation [50, 51]. The agent is transported into the cell by the same nucleoside carrier as thymidine [52]. The agent is then phosphorylated within the cell by thymidine kinase-1 (TK_1) which is upregulated in rapidly dividing tumor cells (thymidine kinase activity is a marker of cellular proliferation) [50, 53]. Because ^{18}F-fluorodeoxythymidine is resistant to catabolism by thymidine phosphorylase, there is prolonged intracellular retention of the agent [50]. Based on ^{18}F-FLT uptake, an overall reduction in the proliferative activity of gross tumor volumes was observed across the duration of treatment. This information may be useful to monitor changes in cellular proliferation occurring during treatment, to provide valuable prognostic information, and to adapt treatment based on individual biologic response [54].

Other agents of cell growth and proliferation imaging are based on utilization of the uptake of the molecules that are needed for synthetic pathways, including labeled amino acids for measuring transport and protein synthesis, and nucleosides for DNA synthesis. An example of such an agent to track cancer cell proliferation is C-11 thymidine, which is taken up into DNA but not by RNA to map proliferation. ^{11}C-methionine is another example, which seeks amino acid transport. A higher correlation with proliferation of lung tumors was seen for (11)C-4DST than for (18)F-FDG [55]. C-11-labeled agents, however, have very short half-life. For this reason, F-18-radiolabeled tracers are preferred. This radiotracer was also used to evaluate the response

to radiation therapy in patients with lung cancer (NSCLC).

^{11}C-choline (^{11}C-CHOL) is an agent that is incorporated into tumor cells by conversion into ^{11}C-phosphorlycholine which is trapped inside the cell. This is followed by synthesis of ^{11}C-phosphatidylcholine, which constitutes a main component of cell membranes. Because tumor cells duplicate very quickly, the biosynthesis of cell membranes is also very fast, and there is increased uptake of choline and upregulation of the enzyme choline kinase [56]. Essentially, the uptake of ^{11}C-CHOL in tumors represents the rate of tumor cell proliferation [57]. ^{11}C-CHOL is very rapidly cleared from the blood, and optimal tumor-to-background contrast is reached within 5 min [56, 58].

12.3.2.4 Hypoxia Agents

It has been established that hypoxic tumor cells are more resistant than aerobic cells to ionizing radiation and chemotherapy. Hypoxic cells are more resistant to radiation therapy and therefore require additional radiation to achieve adequate cell killing, which might exceed the tolerance of the surrounding normal tissues, called the tumor bed [59, 60]. Accordingly, tumor hypoxia is an important factor in relapse-free survival. The potential importance of tumor hypoxia as a cause of treatment failure in patients treated with radiation has been recognized for a long time. Methods have been developed to add compounds to act as hypoxic cytotoxin to potentiate the effect of radiation. Accordingly, evaluation of tumor hypoxia can help in patient's management. PET/CT imaging using F-18-misonidazole (FMISO) is used in evaluating hypoxia and in evaluating prognosis in patients receiving radiation therapy and certain chemotherapy [61, 62].

^{18}F-fluoromisonidazole (^{18}F-FMISO) acts as a bioreceptor molecule and is incorporated into cell constituents under hypoxic conditions [59]. Unfortunately, there is slow cellular uptake and slow washout from non-hypoxic tissues. ^{62}Cu-ATSM is another tumor hypoxia agent, which accumulates in hypoxic tissues where it is reduced, trapped, and has the advantage of rapid clearance from non-hypoxic tissue [59, 60].

12.3.2.5 Receptor Imaging Agents

The increased expression of various types of receptors on the cell surface are a unique biomarker for specific types of cancers. For example, somatostatin receptors is a unique characteristic of neuroendocrine tumors. 68-Ga-DOTATATE and the newly approved 64-Cu-DOTATATE are radiolabeled somatostatin analogs for the diagnosis and pretreatment evaluation of neuroendocrine tumors with PET. There are five types of somatostatin receptors characterized (sst1 to sst5), but sst2 is the predominant one in neuroendocrine tumors [63]. Studies have demonstrated that the sensitivity of these agents was up to 96% with a specificity of up to 100% in the diagnosis of neuroendocrine tumors on PET. In addition, this was found to be superior to conventional somatostatin receptor scintigraphy and diagnostic CT in diagnosis, staging, and restaging [64–66]. The advent of 64-Cu-DOTATATE allows for a lower radiation-dose option with superior lesion detection rates compared to 68-Ga [67]. In addition, these radiotracers are linked to a therapy arm with Lutetium-177 for the treatment of neuroendocrine tumors. Further discussion on theranostics will be reviewed in another chapter.

Estrogen receptors (ER) are a unique biomarker of breast cancers and can be evaluated using the radiolabeled estrogen analog 18F-estradiol. The advantage of this type of imaging is the ability to assess the estrogen receptor status of tumor lesions throughout the body. The mainstay for treatment of this type of tumor is endocrine therapy, however, resistance can occur with progression. Imaging with 18F-estradiol can help clinicians predict response to therapy and select optimal treatment in the future while sparing patients from unnecessary chemotherapy. For the detection of ER+ breast cancer, 18F-estradiol imaging has a sensitivity of 84% and specificity of 98% [68].

Human epidermal growth factor receptor 2 (HER2 or erb2) is a member of the ERbBs or type 1 receptor kinase family involved in cell development, proliferation and differentiation. Tumors that overexpress HER2 show high rate of proliferation and are associated with more aggressive disease, poor prognosis and shorter overall survival. Approximately 20% of invasive ductal breast cancers are classified as HER2 positive. Zr-89 Trastuzumab is a radiolabeled monoclonal antibody which targets HER2. HER2 PET helps to noninvasively assess HER2 expression in tumors and identify patients who may benefit from HER2-targeted therapy, to monitor the change in HER2 status during therapy, and selecting cases for targeted radionuclide therapy [69].

Prostate-specific-membrane antigen (PSMA) is a cell-surface glycoprotein overexpressed on prostate cancer cells. Its expression is 100 to 1000-fold higher in prostate cancer than in other tissues and the levels increase with higher tumor stage and grade (Gleason score). 68Ga-PSMA and 18F-PSMA are analogs for the diagnosis and pretreatment of prostate cancer with PET. It has been established that PSMA PET-CT imaging has superior diagnostic accuracy than conventional imaging with CT or MRI in men with high-risk prostate cancer. 18F-PSMA has several advantages over 68-Ga such as a longer half-life (110 min vs 68 min), can be produced in larger quantities due to the cyclotron production vs generator-produced, and greater spatial resolution due to the lower positron energy. As in neuroendocrine tumors, imaging with PSMA tracers is linked to the therapy arm with Lutetium-177 for the treatment of prostate cancer [70, 71].

12.3.2.6 Tumor Stroma Agent

We are now coming to the age where we have the potential to image and treat a wide variety of malignancies using a single target. Imaging and therapy for neuroendocrine tumors and prostate cancer discussed in this chapter are dependent on unique biomarkers (DOTATATE and PSMA). The introduction of fibroblast activation protein (FAP), however, has the potential of transforming our treatment strategy. FAP is a serine proteinase which is expressed on the cell surface of activated fibroblasts during wound healing, fibrotic processes and the stroma of many malignancies. Normal fibroblasts can be differentiated from the cancer-associated fibroblasts by the expression of FAP. In cancer-associated fibroblasts, FAP promotes tumor growth and progression while being overexpressed in various types of malignancies. Approximately 90% of a tumor's mass can be attributed to these cancer-associated fibroblasts [72, 73]. Given this attribute, FAP is a potential target for theranostics with a wide variety of applications. Studies have already been performed with promising results using FAP inhibitors (FAPIs). A recent study evaluating 68Ga-FAPI PET/CT in 28 different kinds of cancer demonstrated high uptake in many prevalent cancers including breast, esophageal, lung, pancreatic, head and neck, and colorectal [74]. In addition, the therapeutic application of 90Y-FAPI has been performed on a patient with advanced breast cancer with equally encouraging results [75]. Alpha emitters have also been shown in mice to be an effective treatment in pancreatic cancer. Multiple additional studies are being performed to evaluate FAP as a viable target for theranostics but it could bring us a step closer to the development of a universal cancer therapy.

12.4 PET Imaging Interpretation

12.4.1 Normal Distribution

The normal pattern of ^{18}F-FDG uptake on PET imaging performed approximately 1 h after intravenous administration reflects glucose metabolism and includes the brain, heart, kidneys, ureters, and bladder. The prominent uptake in the urinary tract is secondary to the clearance of the tracer. The brain typically demonstrates intense uptake when compared to the remainder of the body since it is an obligate user of glucose (Fig. 12.8). There is variable uptake in the heart which is based on the type of fuel being used for metabolism. In a prolonged fasting state (typically greater than 12 h), the metabolism shifts from glucose to free fatty acids resulting in an uptake similar to background activity. The liver

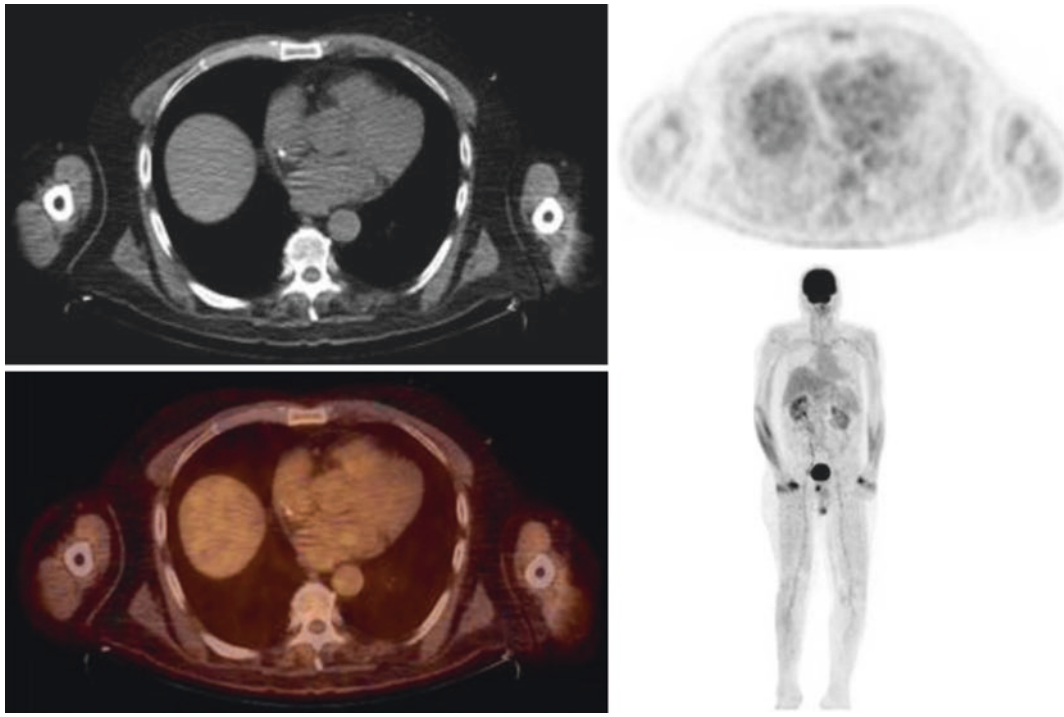

Fig. 12.8 A 64-year-old male with a history of lymphoma. PET/CT images demonstrate a normal distribution of radiotracer. Note physiologic activity in the forearm muscles and excretion of the FDG by the kidneys and urinary bladder

and spleen demonstrate variable uptake but are most often greater than background, with liver being slightly more prominent than the spleen. Bowel and stomach uptakes are seen with varying degrees and can be influenced by outside factors including medications such, as the case of intense bowel uptake in diabetic patients on metformin. Uptake in the oropharynx can be variable as well, including the salivary and parotid glands. Intense uptake is often seen in the pharyngeal and lingual tonsil. This uptake is often symmetric, but normal asymmetry is also seen [76, 77].

12.4.2 Benign Normal Variants

Skeletal muscle at rest demonstrates low FDG uptake. However, muscle uptake will increase when there is active contraction of muscles during the uptake phase or with heavy exercise within 24 h prior to the exam. Elevated insulin levels may also cause the same effect [78]. In addition, patients with labored breathing or COPD can demonstrate uptake in the diaphragm, intercostal, and scalene muscles depending on the severity (Fig. 12.9) [79]. Patients with head and neck cancers who have undergone surgery can demonstrate unilateral uptake in the vocal cord secondary to paralysis of the contralateral cord. This will also cause asymmetrical muscular uptake in the head and neck.

A common variant typically seen in colder months of the year is symmetric intense uptake in the bilateral neck which can extend to the supraclavicular, axilla, and paraspinal regions attributed to brown adipose tissue (BAT) (Fig. 12.10). These cells are characterized by multilocular lipid droplets and increased number of mitochondria, which express uncoupling protein 1 (UCP1). UCP1 is located in the inner membrane of the mitochondria and uncouples the rates of substrate oxidation and ATP production by favoring a loss of protons and thus energy release [80]. This uptake occurs due to heat generation in response to cold, ingestion of food, or increased sympa-

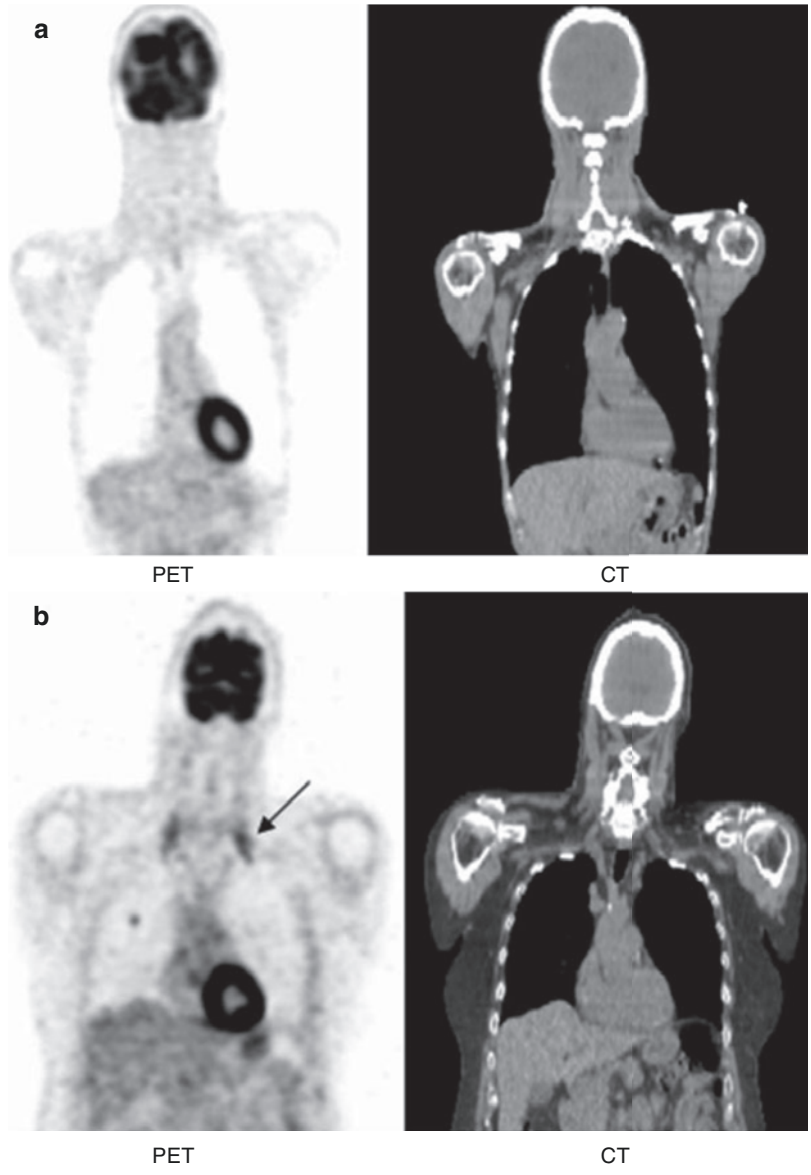

Fig. 12.9 (**a**) Patient with no COPD showing no uptake in scalene muscles. (**b**) Patient with COPD showing intense FDG uptake in scalene muscles bilaterally (*arrow*)

thetic activity in anxious patients. There is abundance of BAT in infancy and slowly declines with age. Warming patients before injection as well as during the uptake phase has shown to be effective in decreasing this uptake [81].

Other variants such as normal thymic uptake in the anterior mediastinum can be seen in children and adults up to 30 years of age. In addition, uniform FDG distribution is commonly seen in circulation. However, when the normal blood flow is interrupted by a thrombus, a region of tracer void is seen on PET. In contrast, increased FDG uptake along a vessel wall is due to inflammation [82]. Normal thyroid tissue does not demonstrate significant FDG uptake. However, diffuse uptake can be seen in cases of thyroiditis and Graves' disease. Focal uptake can be seen in benign nodules but carry a 33% risk of malignancy [83]. Normal bone marrow uptake is commonly seen as similar intensity as the liver. FDG uptake is affected when a process alters marrow distribution. For example, hematopoietic stimu-

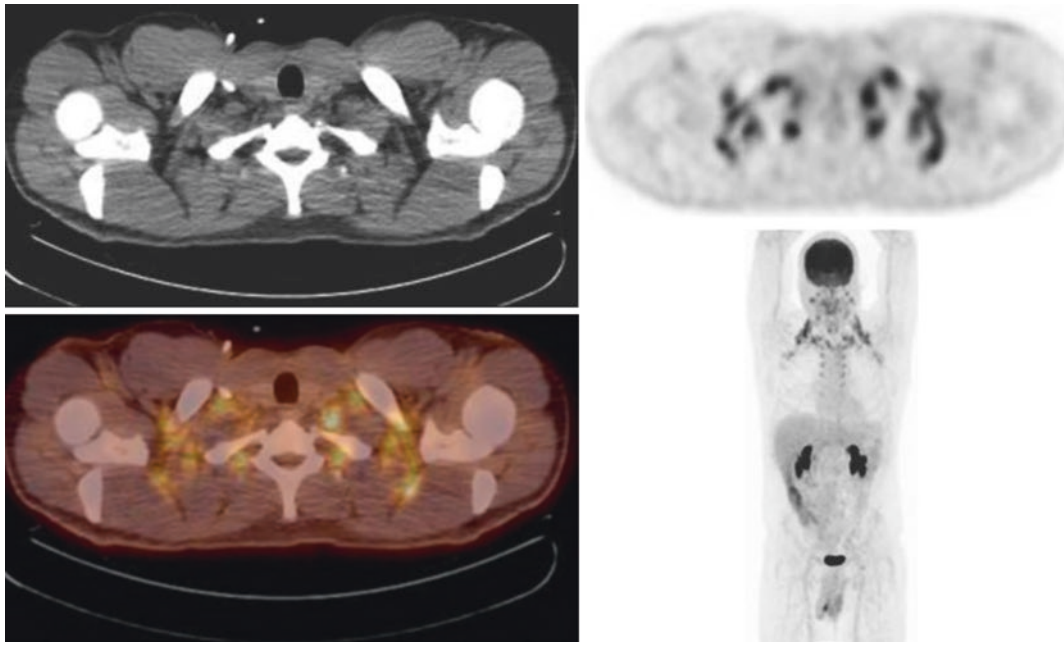

Fig. 12.10 A 34-year-old male with a history of colon cancer. PET/CT images demonstrate diffuse symmetric FDG uptake within the bilateral neck, supraclavicular, and axillary regions due to brown fat activity

lants such as colony-stimulating growth factors will increase marrow uptake as will anemia or inflammatory processes [84]. On the other hand, radiation therapy will decrease uptake in the marrow. Compression deformities or fractures can cause intense uptake in the vertebra which can lead to misinterpretation as malignancy.

Mild growth plate uptake is usually seen in children on FDG PET studies. Hypermetabolic activity in tonsils/waldeyer ring is also a common finding in children.

12.4.3 Uptake in Inflammation and Infection

^{18}F-FDG uptake is not specific for only neoplasm. The agent also demonstrates activity in areas of active infection and inflammation. This can make it difficult to differentiate infections such as pneumonia from a malignant lesion. This can also cause misinterpretation in patients with sarcoidosis and granulomatous disease. A commonly encountered pattern of uptake is seen in lung cancer patients who have undergone radiation therapy. This causes intense FDG uptake initially in the lung parenchyma following the field used for therapy. This pattern of uptake may persist for many months and delaying the PET scan is recommended to allow for reduced inflammation (Fig. 12.11) [85]. FDG PET/CT also has a role in the evaluation of musculoskeletal infection demonstrating increased uptake in osteomyelitis as well as prosthetic joint loosening and infection [86].

Although the immune response can cause a false positive finding on FDG PET/CT, there has also been some utility with the response due to the introduction of immunotherapy in patient management. Immunotherapy is a type of cancer treatment that helps the body's immune system fight cancer. For example, immune checkpoint inhibitors have contributed to a marked improvement in the outcome for patients with advanced melanoma. These drugs act by blocking the immune checkpoints which normally keep the immune responses from being too strong. By blocking them, the drugs allow immune cells to have a stronger response to cancer. However, this can also lead to systemic immune or inflammatory response in the

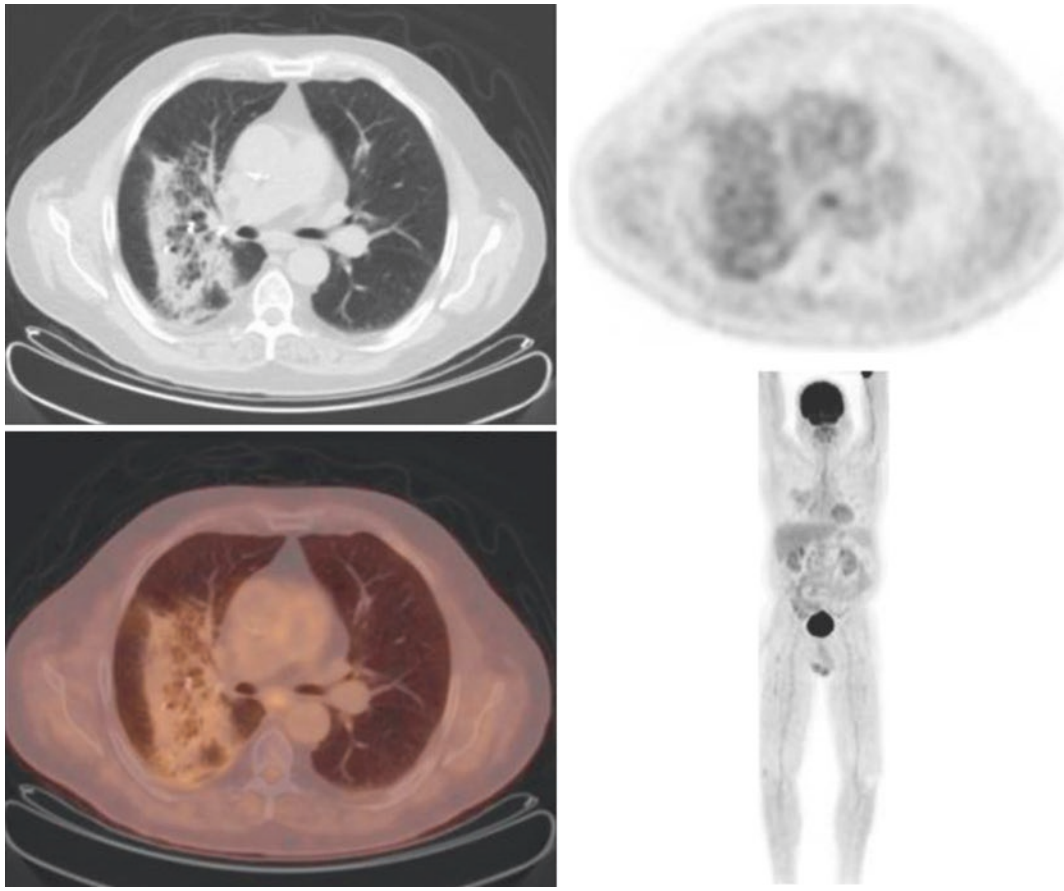

Fig. 12.11 A 68-year-old male with a history of right upper lobe adenocarcinoma. PET/CT images following cyber knife treatment showing fiducial markers at the site of a spiculated lesion surrounded by FGD avid postradiation changes

form of clinical manifestations. The utility of 18F-FDG PET/CT in these cases can show the increased inflammatory response prior to clinical manifestations which can then be treated to reduce the severity [87–89].

PET is useful to identify immune check point related adverse effects (autoimmune reaction in various tissues). Common PET findings in patients receiving immune check points inhibitors are diffuse thyroid uptake due to thyroiditis, diffuse liver uptake due to hepatitis, uptake in bilateral hilar and mediastinal lymph nodes with or without lung uptake due to sarcoid like reactions, uptake in joints and muscles due to arthritis and myositis, uptake in adrenals due to adrenalitis and uptake in pituitary gland due to hypophysitis. Uptake in various tissues due to immune related adverse effect may mimic malignancy/metastases and care should be taken when interpreting studies. Their presence also has a prognostic value (favorable prognosis) [90].

12.4.4 Artifacts

A commonly encountered pitfall of image interpretation is secondary to image acquisition and reconstruction algorithms causing artifacts. Dense objects such as metal from orthopedic hardware or iodinated contrast can produce areas of intense uptake on the attenuation-corrected PET images. Therefore, it is recommended to review the non-attenuation-corrected

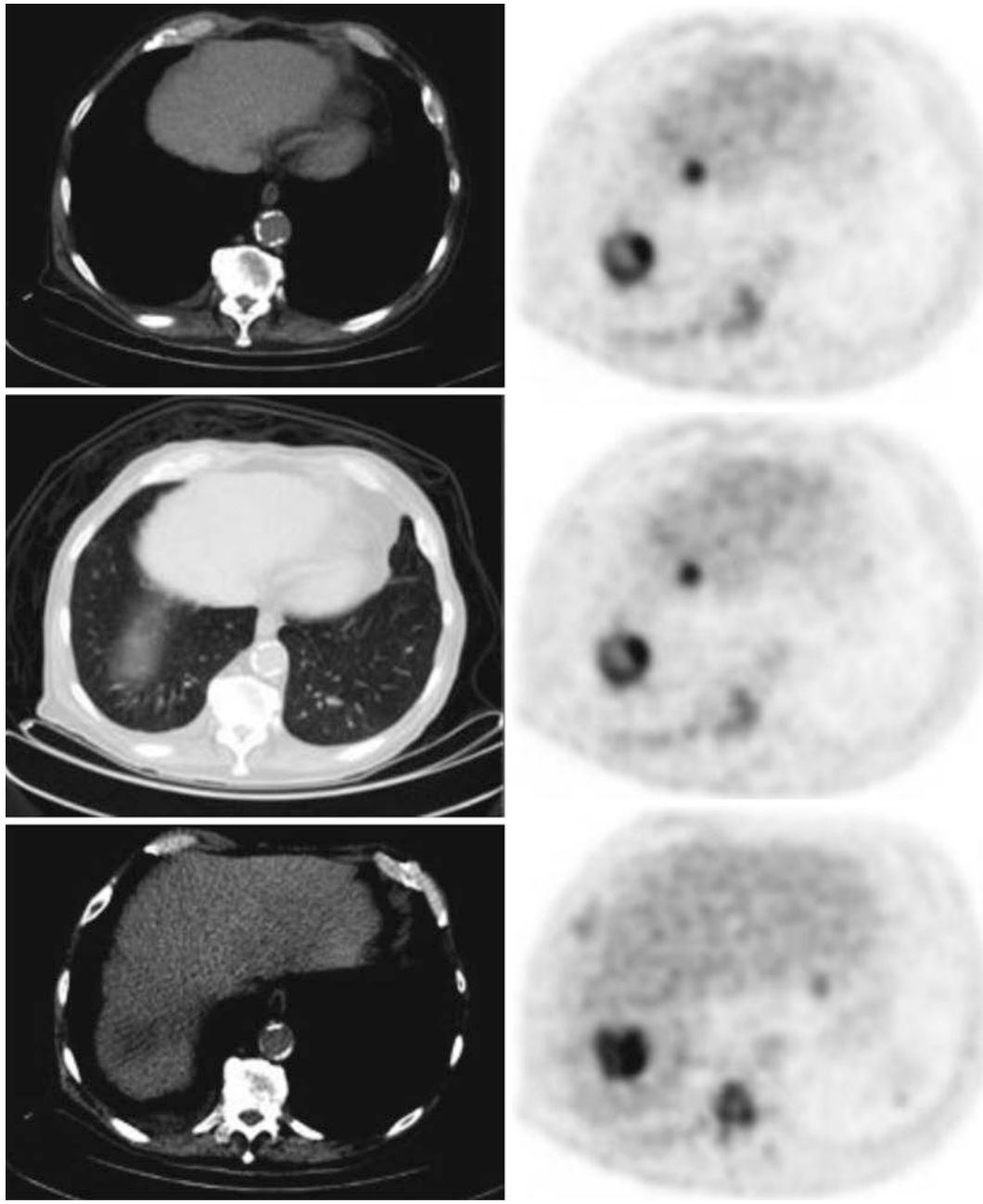

Fig. 12.12 A 71-year-old male with leukemia demonstrating respiratory motion artifact. (*Top row*) Focal FDG uptake appearing in the lung base on PET image (*right*). (*Middle row*) Lung window demonstrates no definite lung lesion. (*Bottom row*) Hypodense lesion in the dome of the liver on CT matching the PET abnormality

images for confirmation of these abnormalities. In addition, these can also cause beam hardening artifacts on CT. Respiratory motion artifact is also frequently encountered. This is due to the lung motion during normal breathing. PET/CT images are usually acquired during quiet respiration so the CT and images closely match PET. However, any deviation from this can cause abnormalities projecting in an incorrect location. This is commonly seen as a liver lesion which projects in the lung base (Fig. 12.12) [91].

Images taken in arms down position can also cause various artifacts in the area of body, particularly in obese patients, such as cold defects, beam hardening, truncation, motion artifacts, scatter artifacts, and artifacts caused by extravasation of activity [92]. Whereas images taken in arms up position cause similar artifacts in head and neck region. To eliminate these artifacts arms should be positioned up when imaging the body and down when imaging head and neck area.

12.4.5 Uptake Patterns of Malignancy

Interpretation of PET/CT imaging requires an understanding of normal and normal variant patterns of uptake. In addition, a familiarity of basic anatomy and physiology is needed to evaluate whether an area is normal or abnormal. In general, there is a higher degree of metabolism in tumors, which is represented as increased FDG accumulation. However, low levels of uptake can be seen is certain malignancies such as bronchoalveolar carcinoma, carcinoid, prostate cancer, and mucinous adenocarcinoma. Areas of necrosis can demonstrate central photopenia on PET with a rim of increased uptake. Malignant pleural effusions can show variable uptake which is likely due to the dispersion of tumor cells in the effusion. Lesion activity is most commonly quantified as the standard uptake value (SUV). It is a measure of uptake in a specific region of interest and is corrected for body mass or body surface area.

$$SUV = \frac{\text{tissue activity } (\text{mCi/ml})}{\text{injected dose } (\text{mCi}) / \text{body surface area}}$$

SUV generally accurately estimates the degree of uptake of radiopharmaceuticals in lesions and normal tissues but is affected by various patient, biologic, and technical factors that can cause over- or underestimation of the activity in lesions and tissues [93].

SUV normalized by body weight is overestimated in obese and overweight patients [94, 95]. SUV normalized by lean body mass (SUL) is recommended when comparing images. Alternatively tumor to liver or tumor to blood pool ratios can also be used when comparing studies. In pediatric patients SUV, normalized by BSA is recommended [96].

12.5 Clinical Uses of PET/CT in Soft Tissue Malignancies

12.5.1 CNS Tumors

Brain metastasis is a common complication of cancer affecting 15–40% of patients [97]. These patients have a poor prognosis, even in the absence of systemic disease, with a median survival time ranging from 9 to 18 months [98]. The most common primary cancers that metastasize to the brain in adults are lung (40%), breast, colon, renal cell carcinoma, and melanoma. In children, the most common are sarcoma and germ cell tumor. The cerebral cortex is the most common location for cerebral metastasis (80%) with multiple lesions in two-thirds of the patients [99].

On the other hand, primary CNS tumors are much more rare, with 7–19 cases per 100,000 [100]. According to the World Health Organization, there are three main types of gliomas: astrocytomas, oligodendrogliomas, and mixed oligoastrocytomas. Tumors are then graded I–IV based on the most malignant region within the tumor. Grades I and II are considered low grade and grades III and IV are considered high grade. Grading is based on the amount of mitosis, microvascular proliferation, nuclear atypia, and necrosis. There are three subtypes of low-grade gliomas, pilocytic astrocytoma (grade I), astrocytoma (grade II), and oligodendroglioma (grade II). High-grade gliomas include anaplastic tumors (grade III) and glioblastoma (grade IV). Glioblastoma is the most common glioma which also happens to be the most

malignant. It accounts for 45–50% of all gliomas [101].

The gold standard for brain imaging continues to be MRI which provides excellent anatomic details. FDG uptake within these tumors usually correlates with the grade of the tumor. Low-grade gliomas demonstrate lower metabolic activity than high-grade gliomas. In addition, high FDG uptake in a lesion that was a previously known low-grade tumor is suggestive of anaplastic transformation. Although MRI is the gold standard, there are limitations after treatment. In general, these tumors are surgically resected followed by radiation with or without chemotherapy. On follow-up imaging, MRI cannot clearly distinguish tumor recurrence from radiation necrosis. PET imaging has the upper hand in this situation. Tumor recurrence will show intense metabolic activity in the region of the lesion, whereas radiation necrosis will demonstrate reduced uptake or photopenia in the region (Fig. 12.13) [100]. The other radiotracers such as 18F-FDOPA and 18F-

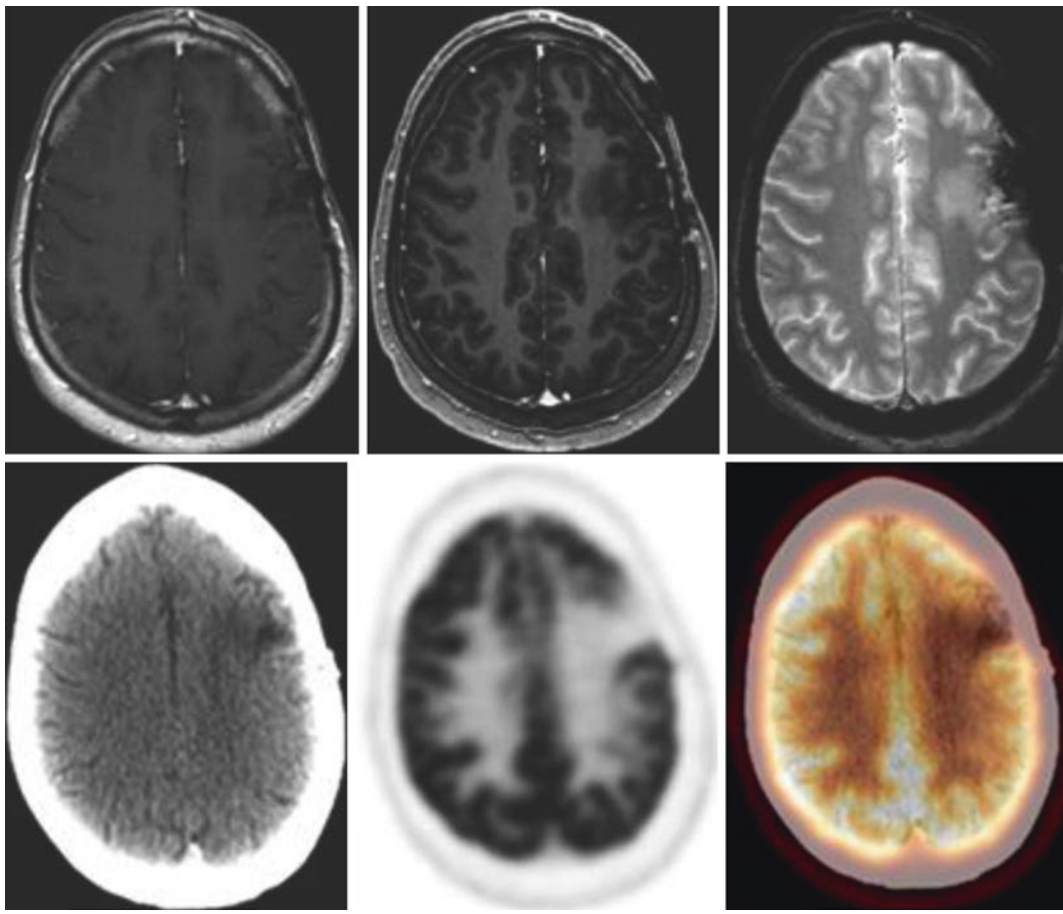

Fig. 12.13 A 41-year-old male with left frontal lobe mixed oligoastrocytoma, WHO grade 3, status post-resection and radiation therapy. (*Top row*) Axial post contrast T1WI, STIR, and T2 WI showing slightly increased T2 hyperintensity adjacent to the superior medial aspect of the resection cavity in the left frontal lobe concerning for gliosis vs. tumor recurrence. (*Bottom row*) FDG PET/CT images showing postoperative changes of left frontoparietal craniotomy with gliosis in the left frontal without evidence of focal FDG uptake in this region to represent tumor recurrence

FET (assessing amino acid transport) and 18F-fluorothymidine (assessing cellular proliferation) provide better results than FDG PET in detecting primary or recurrent gliomas. Uptake of amino acid radiotracers correlate with LAT1 (amino acid transporter) expression [102, 103]. These tracers also show low or no uptake in the brain, which is an advantage over FDG.

A commonly seen phenomenon in brain imaging is reduced uptake in the cerebellar hemisphere contralateral to a supratentorial insult and referred to as crossed cerebellar diaschisis (Fig. 12.14). This manifestation is not only seen in tumors but in any supratentorial process including trauma, demyelination, gliosis, unilateral edema, and infarction [104]. This phenomenon occurs as a result of an interruption to the corticopontocerebellar pathway from the cerebral hemispheres to the contralateral cerebral cortex [105].

12.5.2 Head and Neck Tumors

Head and neck cancers account for up to 5% of all cancers in the United States. Of these, the majority of cases are due to squamous cell carcinomas of the oral cavity, nasopharynx, oropharynx, and larynx. The overall annual mortality rate in the United States is 23% with a 5-year survival rate of 56% [59, 106]. Lymph node involvement is crucial in assessing if a patient should undergo surgical resection. The location, number, and size are all important considerations for treatment planning. It has been reported that nearly 40% of patients have localized disease, while the remaining 60% have advanced disease. FDG PET has been found to be equivalent, if not superior, to CT and MRI for the detection of nodal disease. PET has the upper hand when evaluating nodes which are normal in size by CT and MRI criteria. These tumors are often treated with surgical resection and/or radiation. PET/CT is particularly helpful in assessing for tumor recurrence in the postoperative patient. Due to the loss of symmetry and distortion of the normal anatomy, evaluation of post-therapeutic changes from recurrent or residual disease can be challenging (Fig. 12.15). False-positive findings can occur secondary to recent surgery or radiation therapy. In addition, laryngeal muscle activity, patterns of increased muscle uptake, and reactive lymph nodes can also lead to misinterpretation. However, PET has been found to have a sensitivity for diagnosing recurrence up to 100% with a specificity of 85% [107].

FDG PET is very useful in detecting/locating the primary tumor in patients with primary unknown lymph node metastasis in the neck.

12.5.3 Thyroid Cancer

Radioiodine imaging with I-131 has been the mainstay for the evaluation of thyroid cancer. The follicular cells within the thyroid gland are responsible for neoplasm and give rise to papillary, follicular, or mixed cell variants and are commonly well differentiated. These tumors are iodine avid and diagnosed and treated with I-123 or I-131. FDG does not accumulate in these cell types and is therefore not indicated for the diagnosis of thyroid cancer. Often, the diagnostic I-123 scan will underestimate the disease burden when compared to the I-131 post-treatment scans. The use of I-124 PET/CT has been shown to detect and image differentiated thyroid cancer lesions with high sensitivity and resolution. This imaging also has the ability to detect new metastaic lesions which are not visualized on the post-treatment I-131 scans. Although in its infancy, I-124 has shown promising results [108].

Tumor recurrence is not always iodine avid which is secondary to tumor dedifferentiation. When tumors have lost the ability to synthesize hormones from iodine, they have increased glucose metabolism [109]. These patients present with elevated human thyroglobulin levels with negative I-131 scans. In these patients with a high clinical suspicion for disease but negative I-131

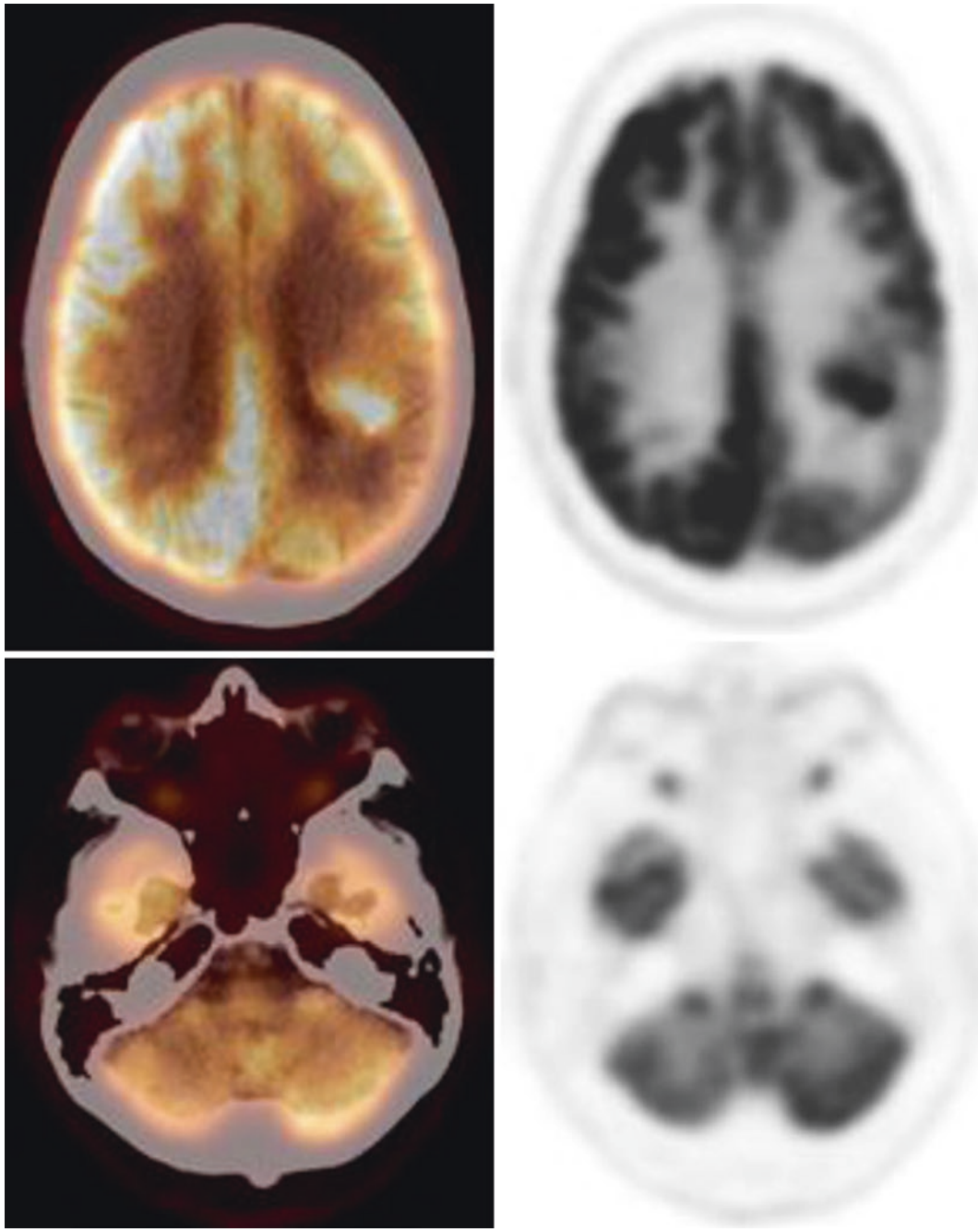

Fig. 12.14 A 61-year-old male with a history of biopsy-proven left temporal glioblastoma multiforme. PET/CT images demonstrate the left temporal lesion (*top row*). There is also decreased metabolic activity in the right cerebellum consistent with crossed cerebellar diaschisis (*bottom row*)

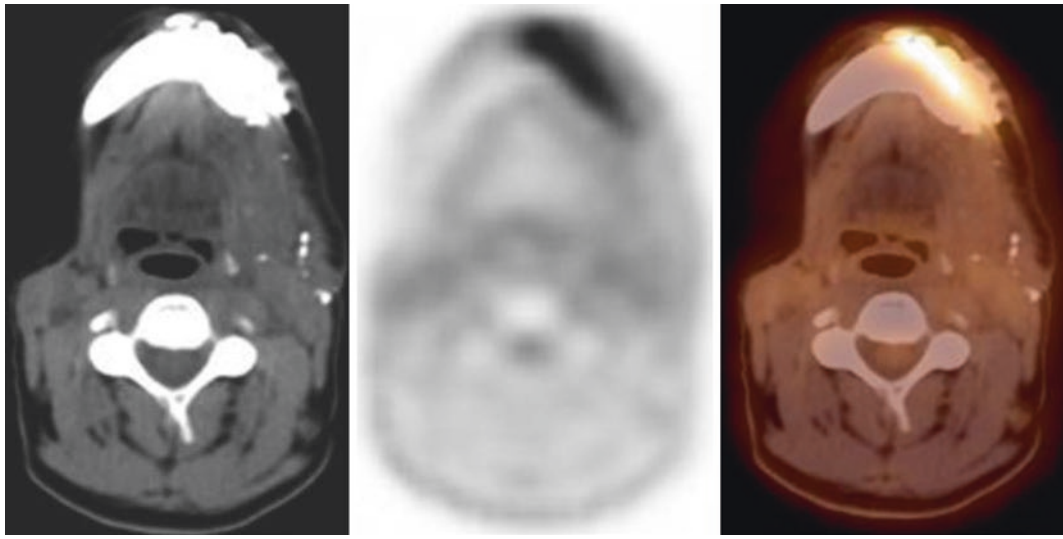

Fig. 12.15 A 49-year-old male with a history of squamous cell carcinoma of the floor of the mouth and alveolar ridge, status post left marginal mandibulectomy and bilateral supraomohyoid neck dissection. PET/CT images show multiple surgical clips at the operative bed with distorted anatomy of the floor of the mouth. There is no evidence of focal activity to suggest tumor recurrence

scan, FDG PET/CT can aid in the detection of metastatic disease (Fig. 12.16). In addition to poorly differentiated tumors, FDG has also been found to be useful for medullary thyroid carcinoma. This is a relatively rare disease which arises from the parafollicular cells and does not accumulate I-131. It accounts for 3–10% of all malignant thyroid tumors [110]. This type of cancer typically demonstrates intense FDG avidity, making PET/CT essential for proper staging and follow-up, with a sensitivity of 76–78% and specificity of 79% [109].

12.5.4 Esophageal Cancer

The esophagus is a hollow muscular tube that connects the pharynx to the stomach. The mucosal lining of the esophagus is primarily comprised of stratified squamous epithelium. Malignancy in this area is commonly due to squamous cell carcinoma, accounting for 85% of cases. The distal portion is comprised of columnar epithelium. Adenocarcinoma is commonly encountered in this area. Patients will often present with dysphagia or by endoscopic biopsy in patients with Barrett's esophagus, considered a premalignant condition which predisposes patients to the development of adenocarcinoma. Barrett's esophagus has been shown to increase the risk of developing adenocarcinoma by 30-fold when compared to the general population [111].

The normal metabolic activity in the esophagus is typically low, resembling background. Both squamous cell carcinoma and adenocarcinoma are FDG avid, and any focal areas of uptake within the esophagus should raise a suspicion for malignancy. However, focal FDG uptake can also be seen in many benign processes such as esophagitis, postprocedural inflammation, postradiation inflammation, hiatal hernia, and Barrett's esophagus (Fig. 12.17).

The most important indicators for prognosis are depth of tumor penetration and nodal involvement. The 5-year survival rate for patients without nodal involvement is 40% but then decreases to 3% when nodal disease is present [111]. Locoregional nodal metastasis is most common, but the location of nodes often depends on the level of the primary tumor. Cervical nodes are often found with more proximal esophageal

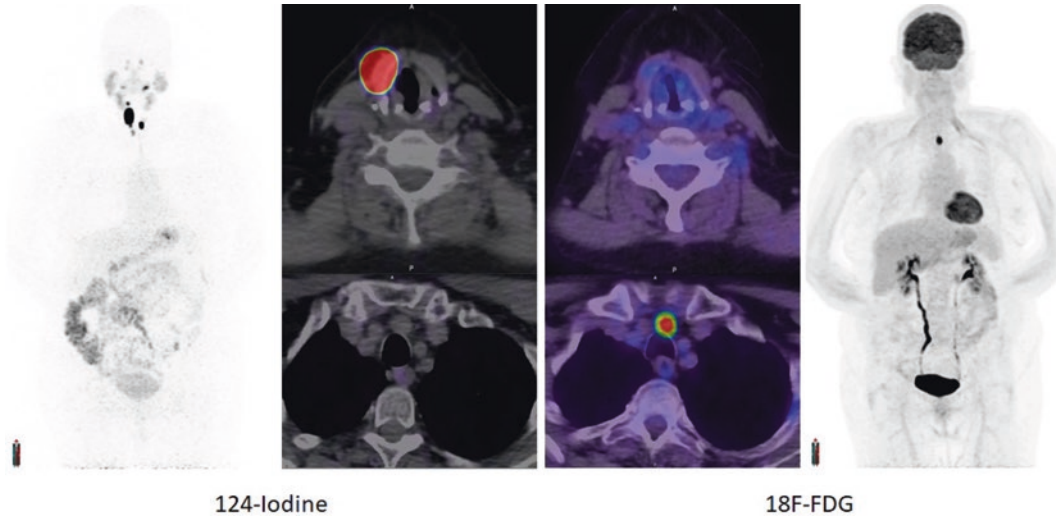

Fig. 12.16 A patient with Hurthle cell carcinoma following thyroidectomy. Stimulated (following T4 withdrawl) I-124 PET/CT (left) shows residual functioning thyroid tissue in the bilateral thyroid bed with no FDG avidity. 18F-FDG PET/CT (right) in the same patient shows intensely avid lymph node in the superior mediastinum with no iodine uptake. Image courtesy of Dr. Amir Iravani

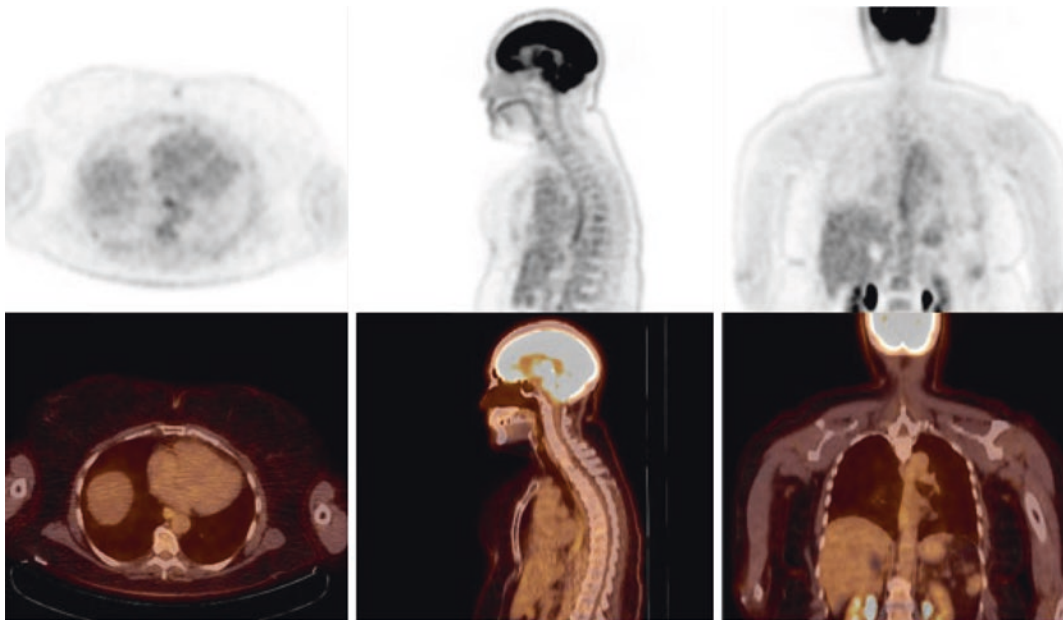

Fig. 12.17 A 63-year-old female with a history of meningioma. FDG PET/CT images show mild liner activity along the mid- and distal esophagus related to esophagitis from gastroesophageal reflux disease

lesions, and abdominal nodes are often associated with more distal lesions (Fig. 12.18). FDG PET/CT has been found to be more sensitive than CT alone for diagnosing nodal metastasis in esophageal cancer [112]. In addition, PET/CT has also been found to affect patient staging in up to 40% and change management in up to 34% of cases [113].

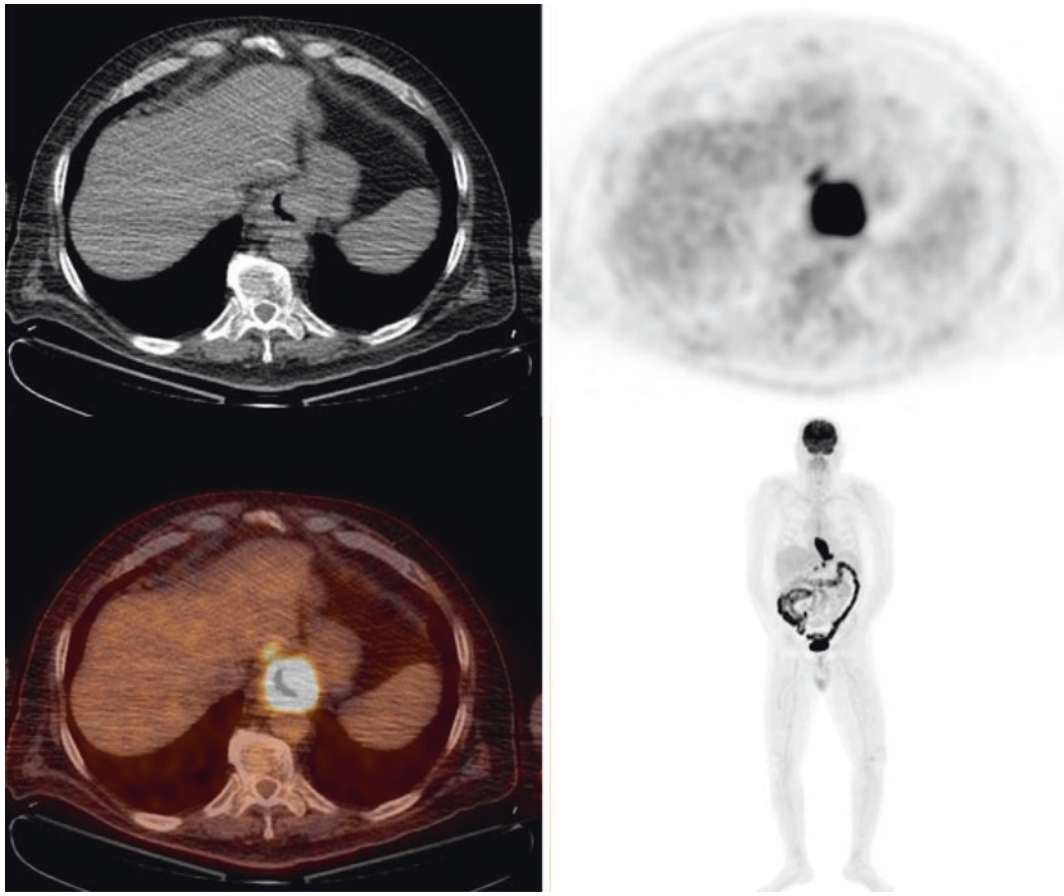

Fig. 12.18 A 69-year-old male complaining of dysphagia, odynophagia especially after solid food, and weigh loss of 35 lb over 6 months. FDG PET/CT shows an FGD avid mass in the distal esophagus extending into the gastric fundus with FDG avid metastatic gastrohepatic, perigastric, and precaval/peripancreatic lymph nodes. Biopsy revealed moderately differentiated adenocarcinoma of the gastroesophageal junction

12.5.5 Renal and Bladder Cancers

Both renal and bladder cancers are difficult to evaluate with PET/CT primarily due to the variability of FDG uptake in both entities as well as the intense urinary excretion of ^{18}F-FDG within these structures (Fig. 12.19). Renal cell carcinoma account for approximately 3.5% of all malignancies and is the most lethal. The sensitivity of PET/CT in renal cell carcinoma ranges from 31 to 94% [114]. Therefore, PET/CT tends to have a complimentary role in the diagnosis of renal cell carcinoma. It is, however, superior to conventional imaging for detecting recurrence and metastasis. Bladder cancers also tend to follow the same pattern. Diagnosis is based on cystoscopy and biopsy with transitional cell carcinoma accounting for more than 90% of all bladder cancers. PET/CT has a limited role in this setting, but it has been noted that the use of various techniques such as delayed imaging, fluid loading, diuresis, and bladder catheterization can help with disease detection [115].

Studies used 11C-acetate in renal cell carcinoma. 11C-acetate is rapidly picked-up by cells and metabolized to acetyl-CoA. In cancer cells acetyl-CoA is used to build membrane fatty acid. Due to short half-life of C-11 and challenges in synthesis of C-11 labeled tracers its use is limited.

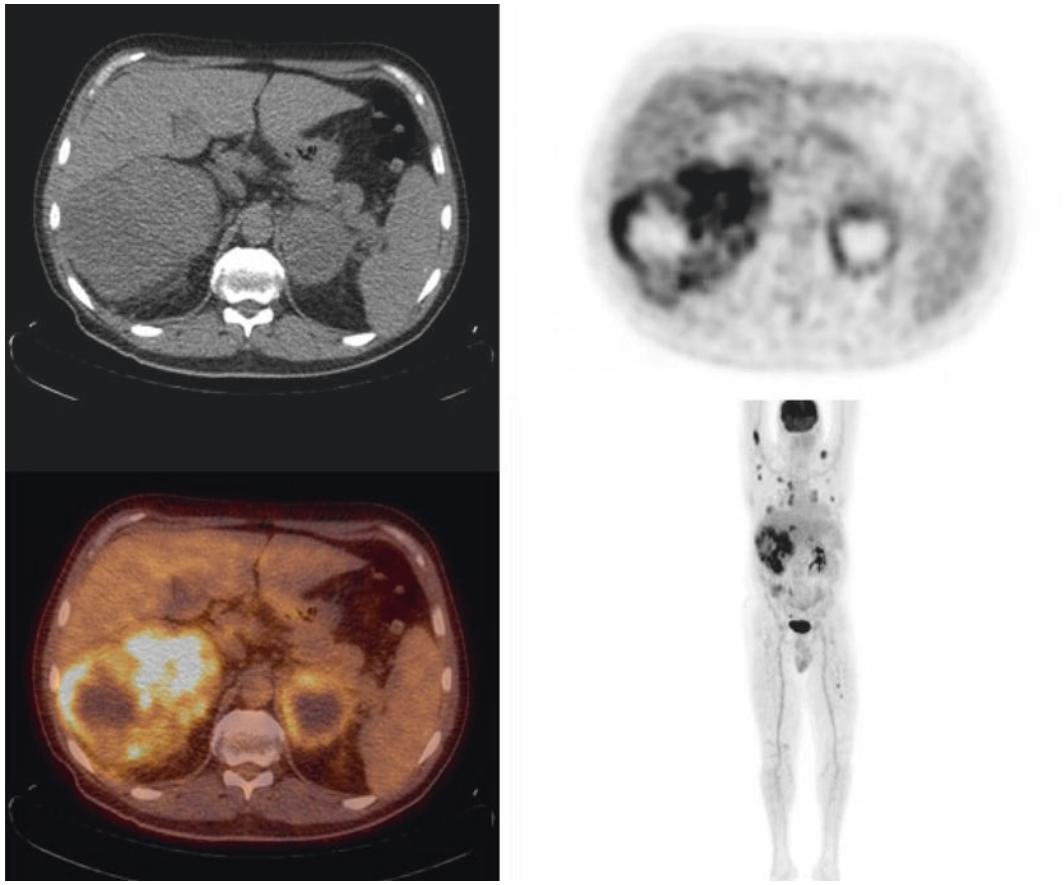

Fig. 12.19 A 54-year-old male with incidentally discovered enlarged mediastinal lymph nodes on a CT angiography of the neck/done for a bleeding cavernoma of the brain. FDG PET/CT images show a large FDG avid right renal cell carcinoma with widespread metastasis to the lungs, mediastinal lymph nodes, left adrenal gland, and multiple bones

12.5.6 Gynecologic Cancers

Cervical cancer is the most common gynecologic cancer and the second most common cancer in women [116]. It is commonly treated with surgery, but chemotherapy and radiation can be required for advanced disease. Although FDG PET/CT has limited value of staging primary tumors due to the variable uptake in nearby structures (bowel and urinary tract), it does have a role in detecting lymph node metastasis [117]. It has been shown that FDG PET can detect lymph node metastasis in these patients with a sensitivity of 91% and specificity of 100%. On the other hand, MRI had a sensitivity of 73% and specificity of 83% [118].

Ovarian carcinoma is the second most common gynecologic cancer and the leading cause of death in women with gynecologic malignancies [119]. Again, FDG PET/CT has limited value of staging primary tumors due to the nearby structures, but to further complicate matters, physiologic conditions such as ovulation and menstruation can also lead to false-positives. Many other false-positives have been reported and are due to inflammatory adnexal masses, endometriomas, corpus luteum cysts, and other benign ovarian tumors. FDG PET/CT is often

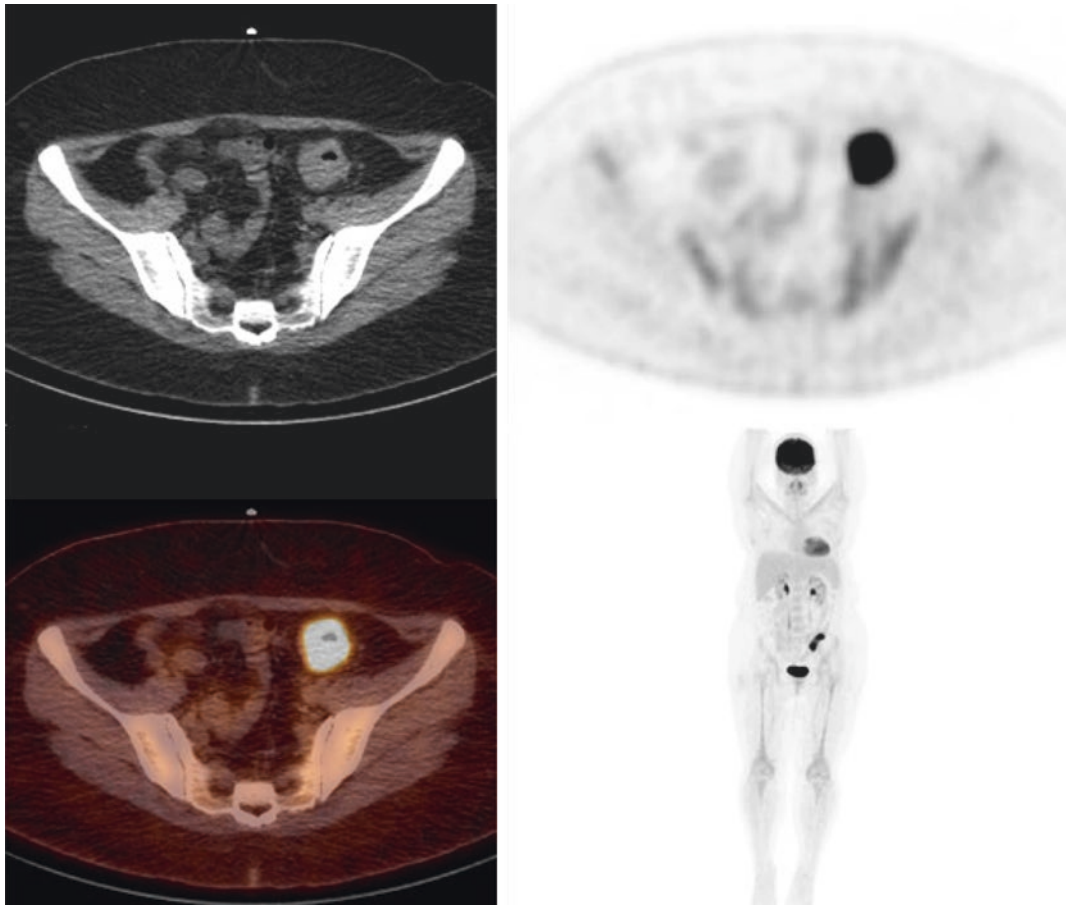

Fig. 12.20 A 45-year-old female with a adenocarcinoma of the colon. FDG PET/CT images demonstrate circumferential mural thickening of the sigmoid colon with intense FDG uptake, consistent with the patient's biopsy-proven malignancy

used for restaging and detecting metastatic disease in conjunction with serum markers (Ca-125, Ca 19-9, alpha-fetoprotein, and human chorionic gonadotropin). The sensitivity of FDG PET has been reported to be 58% with a specificity of 76% [120].

12.5.7 Colorectal Cancer

According to the American Cancer Society, colorectal carcinoma is the third most common cancer in both men and women as well as the third leading cause of death from cancer in the United States [121]. Diagnosis is largely based on direct visualization with colonoscopy as well as imaging with barium enema and CT. When diagnosed, colorectal carcinoma is localized to the primary tumor in 36% of patients, with regional lymph node metastasis in 39%, and distant metastasis in 19% [122]. Therefore, proper staging is crucial for disease management. FDG PET/CT is often used to accurately stage disease prior to surgical resection or to confirm equivocal findings prior to treatment (Fig. 12.20). One study found that FDG PET was able to detect 95% of primary tumors as compared to CT which detected only 49% [123]. It is important to note, however, that FDG PET is not sensitive for the detection of regional lymph node involvement

(sensitivity of 29%) due to the intense uptake in bulky primary lesions which can obscure smaller lymph nodes [124]. In addition, the presence of physiologic bowel activity, inflammation, and benign polyps can limit evaluation and cause false-positives. The liver is a common site for metastasis. It has been shown that up to 20% of patients present with liver metastasis and up to 70% of all patients will develop liver metastasis. Small lesions, typically less than 1 cm, can be missed on PET given the physiologic heterogeneity within the organ as well as image resolution. Some authors recommend MRI as the best modality for the evaluation of liver metastasis in a patient who has not undergone therapy [125]. After initial treatment, PET does play a significant role in the evaluation of recurrent disease. A review of PET literature demonstrated that PET had a sensitivity of 94% for detecting recurrence and specificity of 87% compared to CT with a sensitivity of 79% and specificity of 73% [126]. As in other areas of the body, PET has the ability to delineate postradiation changes from disease recurrence.

12.5.8 Lung Cancer

Lung cancer is the second most common cancer in both men and women (second to prostate and breast cancers). It is, however, the leading cause of cancer death in both men and women [127]. FDG PET/CT is useful for imaging lung cancer since the tumor cells have both an increased uptake of glucose due to a higher number of Glut-1 surface proteins as well as a higher rate of glycolysis compared to nonneoplastic cells [128].

There are two main types of lung cancer, non-small cell lung cancer (NSCLC) and small cell lung cancer, and lung carcinoid tumor. NSCLC is the most common type of lung cancer comprising of approximately 85% of all lung cancers. These include squamous cell carcinoma, adenocarcinoma, and large cell carcinoma. The remaining 10–15% comprises primarily of small cell lung cancer with a small percentage of carcinoid lung cancer.

One of the first indications for the use of FDG PET was for the evaluation of a solitary pulmonary nodule (SPN). These are usually incidentally discovered on chest X-ray or CT and measure 1–3 cm in size. When these are found in younger patients with little or no risk factors, they are often felt to be benign and followed to document stability. However, in older high-risk patients, there is a greater need to establish a diagnosis. The differential can be broad for an SPN, but there is a high risk of malignancy in these lesions. In addition, only 10–20% of patients with a malignant SPN will have positive sputum, and nearly 30% will have false-negative transthoracic needle biopsy [129]. FDG PET has proven to be an accurate method to differentiate benign from malignant nodules (Fig. 12.21). A large meta-analysis showed that FDG PET had a sensitivity and specificity of 97 and 78% with a negative predictive value of 98% [130].

FDG PET is recommended for the initial staging of lung cancer to define both local and distant metastasis, which greatly impacts patient management. Clinical staging is performed using the TNM system which required accurate tumor size (T), lymph node involvement (N), and evidence of distant metastasis (M). The proper staging is critical in assessing the prognosis and tailoring the appropriate therapy. PET/CT has been found to have better accuracy in determining the correct stage of disease than CT alone with an accuracy of 60% compared to 40% [131].

After initial therapy, tumor progression during chemotherapy can occur in approximately 30% of patients with advanced disease [132]. Therefore, it is imperative to continue to assess response to therapy in order to identify nonresponders and switch to second- or third-line treatments. Also, when surgery or other therapies distort the anatomy, PET/CT imaging can assist in differentiating between residual/recurrent disease from post-therapy changes. It is important to note, however, that radiation therapy can cause inflammatory changes in the lung parenchyma which will take up FDG and make it difficult to differentiate from recurrent tumor. The FDG uptake may be due to the cellular inflammation and macrophage response elicited by radiation-induced necrosis.

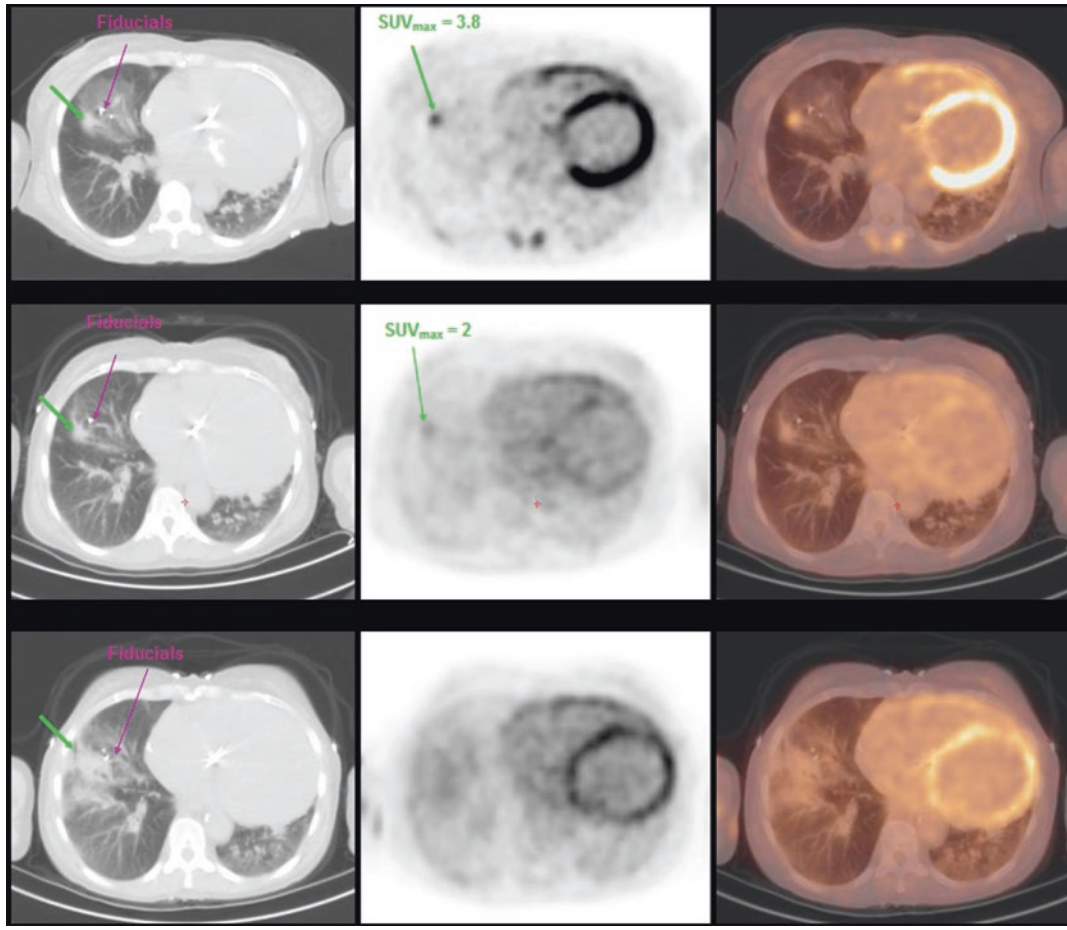

Fig. 12.21 Solitary pulmonary nodule. (*Top row*) PET/CT images of a patient with a solitary pulmonary nodule in the right upper lobe with fiducials in place. (*Middle row*) 1 month after radiation with decreased metabolic activity of the pulmonary nodule. (*Bottom row*) 5 months after radiation with diffuse opacities in the right lung with mild FDG uptake consistent with postradiation inflammation

This inflammation can last up to 6 months after therapy but slowly decreases over time (Fig. 12.6) [133]. It has been recommended to wait at least 3 months after completion of radiation therapy for reliable evaluation [134].

Small cell lung carcinoma represents approximately 18–25% of all lung cancers and is almost exclusively associated with smoking. It is a very aggressive tumor that has a rapid tumor doubling time and early development of distant metastasis. Patients are classified as having limited stage (disease in only one hemithorax) or extensive stage (outside one hemithorax) which includes distant metastasis including the contralateral lung [135]. Treatment is based on the extent of the disease with surgical resection with chemotherapy and radiation for patients with limited disease. Patients with extensive disease are often limited to chemotherapy alone. PET has been found to change management in up to 37% of patients for initial staging and up to 15% for restaging [136].

There are some limitations with FDG PET/CT in the evaluation of some types of lung cancers. For example, neoplasms with low FDG avidity such as lung carcinoid tumor, bronchoalveolar cancer, or well-differentiated adenocarcinoma have been known to demonstrate false-negative PET findings (Fig. 12.22).

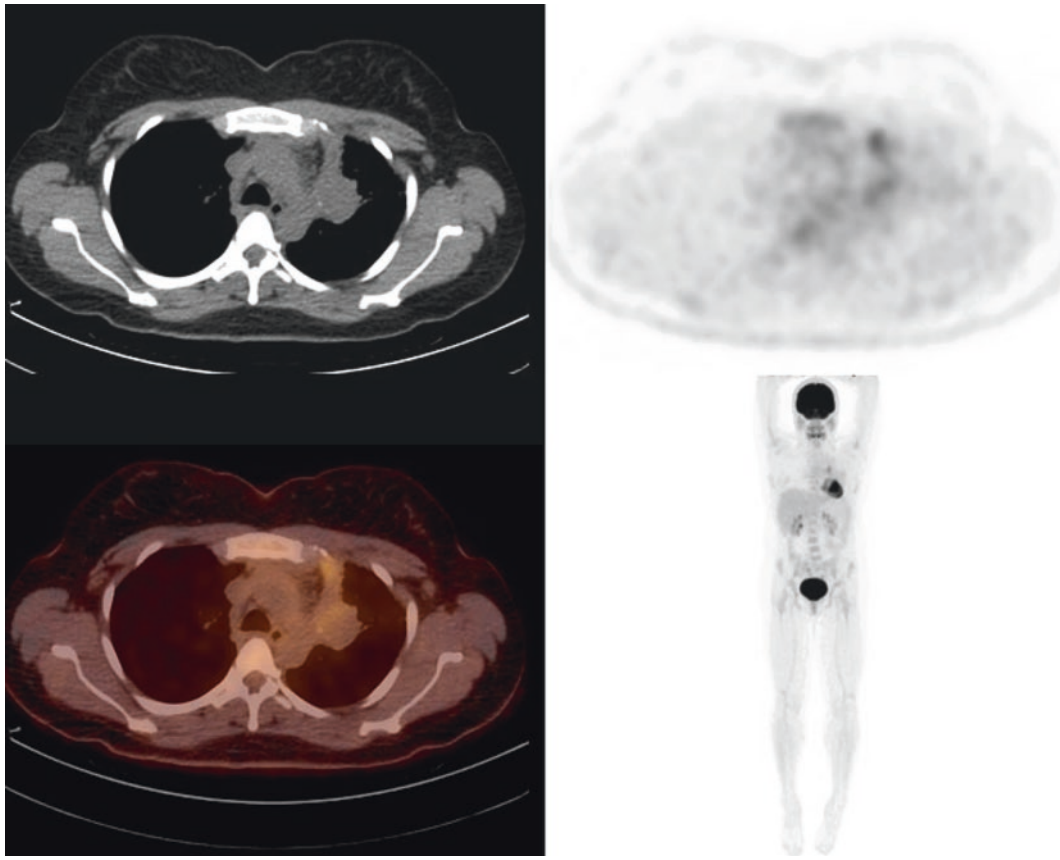

Fig. 12.22 A 37-year-old female presenting with a left lung mass. PET/CT images demonstrate a left upper lobe mass with SUV max 2.0. Subsequent biopsy of the mass revealed a well-differentiated carcinoid tumor

12.5.9 Lymphoma

Lymphoma is a type of hematologic malignancy that occurs in B or T lymphocytes undergoing uncontrolled cell growth and multiplication. Both cell types are designed to recognize and destroy abnormal cells and infections. Lymphomas are divided into two types, Hodgkin's lymphoma (HL) and non-Hodgkin's lymphoma (NHL). NHL is a common malignancy with up to 60,000 new cases each year in the United States. HL is much less common than NHL with up to 7500 new cases per year [137]. Both types of lymphoma tend to accumulate FDG, but low-grade lymphomas are not as avid as intermediate- or high-grade diseases.

NHL is further divided based on histopathology, clinical behavior, response to therapy, and clinical outcome [138]. The most common types are diffuse large B cell and follicular lymphomas which account for more than 50% of all NHLs. Others types which are not as common include marginal zone, peripheral T cell, small lymphocyte B cell, and mantle cell [139]. These lymphomas are largely grouped into low-, intermediate-, and high-grade diseases which directs treatment planning. There is a direct correlation with the amount of metabolic activity within the tumor to the grade of lymphoma. Low-grade tumors have lower FDG uptake than high-grade disease [140].

There are also different subtypes of HL with the most common form being nodular sclerosing. Others include mixed cellularity, lymphocyte predominant, and lymphocyte depleted. The most

FDG avid tends to be the nodular sclerosing subtype and the least FDG avid is the lymphocyte predominant subtype [141].

Staging is based on the Ann Arbor classification for both NHL and HL.

- *Stage I:* disease limited to a single lymph node area, single lymphoid organ, or one area of a single organ outside the lymph system
- *Stage II:* two or more noncontiguous nodal groups or the spleen on the same side of the diaphragm
- *Stage III:* two or more nodal groups or the spleen on both sides of the diaphragm
- *Stage IV:* disease in extranodal sites (bone marrow, liver, lung, bone, or other organs/tissues)

Overall, staging of both NHL and HL with FDG PET showed a sensitivity of 90.3% and specificity of 91.1% [142]. Depending on the type and stage of the disease, treatment is with chemotherapy alone or in combination with radiation therapy. It is common practice to monitor therapy response with FDG PET/CT but requires a baseline study prior to treatment initiation for proper evaluation of therapy. A follow-up study can be performed after one or two cycles of chemotherapy in certain settings (Fig. 12.23).

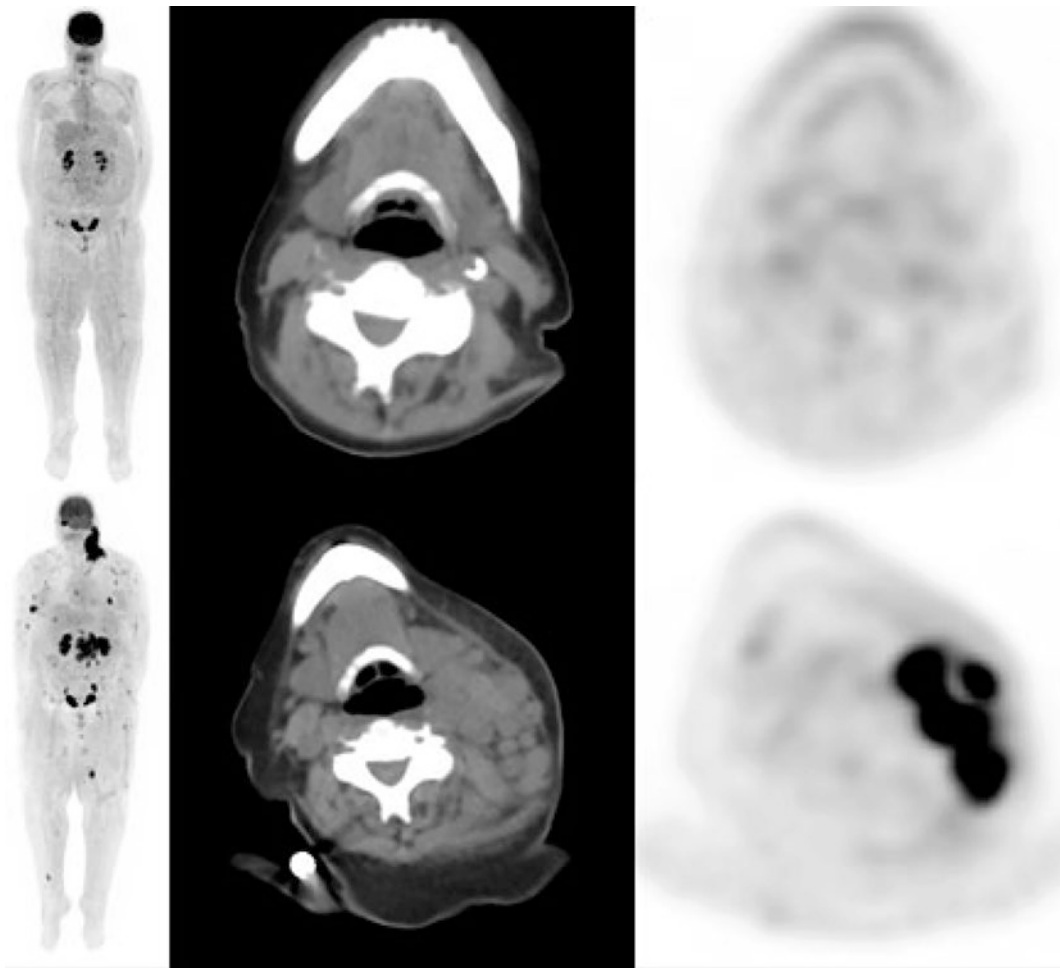

Fig. 12.23 A 58-year-old female with a history of lymphoma. FDG PET/CT images demonstrate widespread lymphoma predominantly involving the left cervical lymph nodes (*bottom row*). The patient received chemotherapy with follow-up PET/CT 1 month later showing complete response of the disease

12.5.10 Melanoma

Malignant melanoma originates from melanocytes (melanin-producing cells) and is the most aggressive form of skin cancer. Primary neoplasms are usually found in the skin, most commonly on the chest and back on men and legs in women, but can also develop in melanocytes of the eye. Factors implicated in the pathogenesis of the tumor are:

- Genetic predisposition
- Exposure to ultraviolet light
- Fair hair
- Light skin
- Steroid hormone activity
- Freckles

Early signs of melanoma are summarized by the mnemonic ABCDE:

- Asymmetry
- Borders (irregular)
- Color (variegated)
- Diameter (greater than 6 mm)
- Evolving over time

Accurate staging is important for treatment and prognosis. The most predictive factor for recurrence and prognosis is tumor thickness and is graded according to the Breslow classification [41]. Regional lymph nodes are the most frequent sites for metastasis, but prognosis is poor with nodal or distant disease. Treatment typically consists of surgical resection of the primary lesion followed by sentinel lymph node evaluation with the assistance of lymphoscintigraphy [40]. The added value of PET/CT is for patients with more advanced disease for accurate tumor staging (Fig. 12.24). In vitro and in vivo experiments

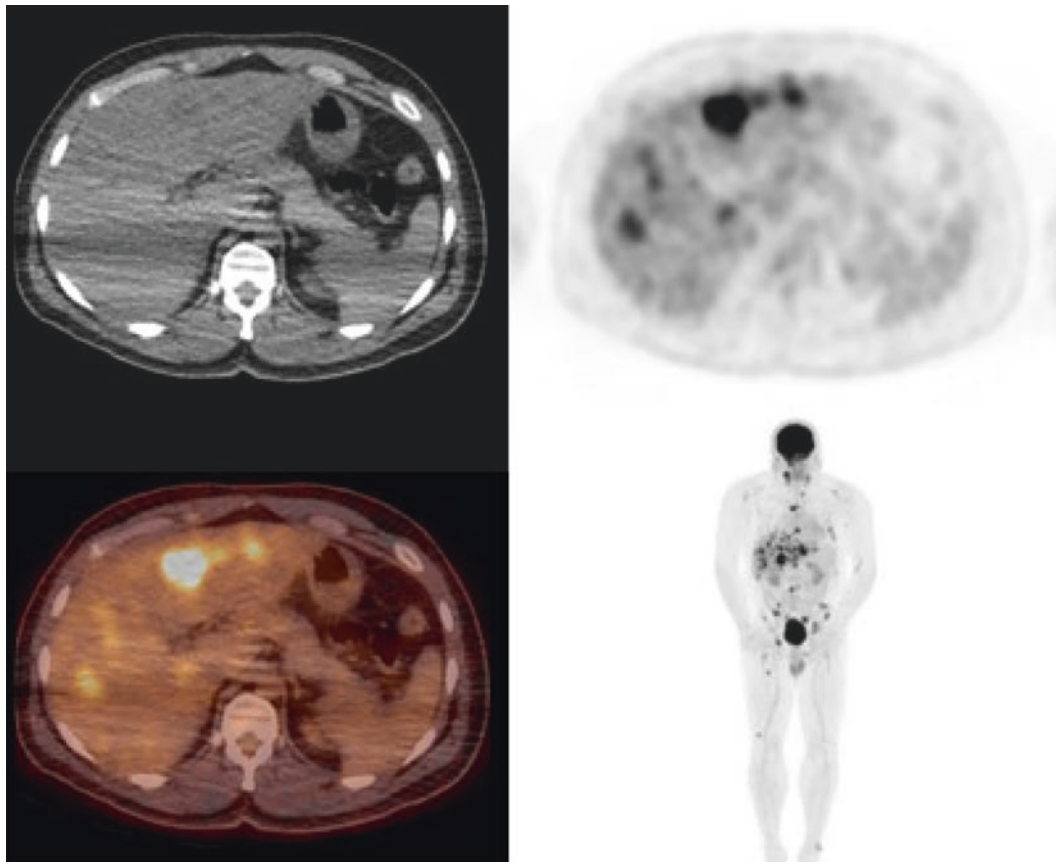

Fig. 12.24 A 33-year-old male with nasal melanoma. FDG PET/CT images demonstrate widespread metastatic disease involving the lungs, liver, cervical lymph nodes, abdominal cavity, musculoskeletal system, left thyroid gland, and skin

with tumor cells show higher FDG accumulation in melanoma than in any other tumors [143]. The advantage of PET/CT in melanoma is the unpredictable hematogenous spread of metastasis. This is the reason why whole body imaging from head to toe is commonly performed in these patients. It has been reported that the efficacy of FDG PET in the diagnosis of involved lymph nodes had a sensitivity of 95% and specificity of 84% [144]. However, micrometastasis in the sentinel node can be found in up to 38% of patients; FDG PET/CT should not replace sentinel node biopsy with lymphoscintigraphy [145].

Positron emission tomography has been and will continue to be a rapidly growing modality worldwide. FDG PET/CT has been proven to provide important information in the staging and therapy monitoring of various types of tumors. However, although PET has been synonymous with FDG, there are numerous other tracers that have been and are being developed, some of which have been discussed in this chapter. Hundreds of PET radiotracers have been developed in the last few decades, but only a few have been approved by the Food and Drug Administration (FDA) for clinical use. Not only have strides been made in oncologic imaging, but these new tracers are producing an impact in other aspects of patient care, most notably in neurology and cardiology. In addition, while beyond the scope of this chapter, the technological advancements of nuclear medicine equipment from SPECT/CT to digital PET/CT and PET/MRI have and will have a profound impact on patient management. Nuclear imaging is no longer limited to diagnosis and risk stratification of various diseases but also has a significant contribution to treatment strategy. Molecular imaging as a whole has been growing at an unparalleled rate. For these reasons, the future is promising for molecular imaging.

12.5.11 Breast Cancer

Breast cancers are predominantly screened with mammography and breast ultrasound. Mammography is highly sensitive and can identify 80–90% of patients with breast cancer. However, a positive mammogram does not always lead to malignancy. Based on histologic analysis, only between 20 and 40% of patients with abnormal mammograms are found to have breast cancer. In addition, about 10% of breast cancers cannot be identified on mammograms even when palpable [146]. The most common type of breast cancer is invasive ductal carcinoma consisting of 70–80% of cases. Invasive lobular carcinoma is relatively uncommon and consists of 5–10% of cases [139]. Although FDG PET/CT is primarily used in the evaluation of restaging, recurrence, and response to therapy, it is also useful in the evaluation of non-palpable masses in dense breast as well as when mammography is equivocal.

The estrogen receptor (ER) status of breast cancers carries important prognostic information which can guide patient management. Almost two-thirds of invasive breast cancers are ER+. The most common therapy for these tumors are endocrine therapy due to the favorable toxicity profile and efficacy. In some of these patients, disease progression can arise from gradual resistance to endocrine therapy. The transcription of ERs is regulated by epigenetic modifications, including histone deacetylases. Histone deacetylase inhibitors (HDACIs), however, can reverse endocrine resistance and has shown to increase breast cancer drug sensitivity. Clinical studies have shown promising results when combining endocrine therapy with HDACIs. The ER status of breast cancers can be reliably evaluated with PET using 18F-Fluoroestradiol. The amount of radiotracer uptake correlates well with ER expression and can predict response to endocrine therapy [147].

A major benefit of PET is that it is not affected as other modalities by dense breast tissue, prior surgery, breast augmentation, or radiation therapy. It has the ability to not only identify primary tumors but also locoregional nodes and distant metastasis (Fig. 12.25). The ability of PET/CT to localize primary lesions is related to tumor size. For lesions less than 1 cm, PET has a sensitivity of 25%, but for lesions 1–2 cm, the sensitivity can be as high as 84% [121]. In general, the amount of metabolic activity within a tumor cor-

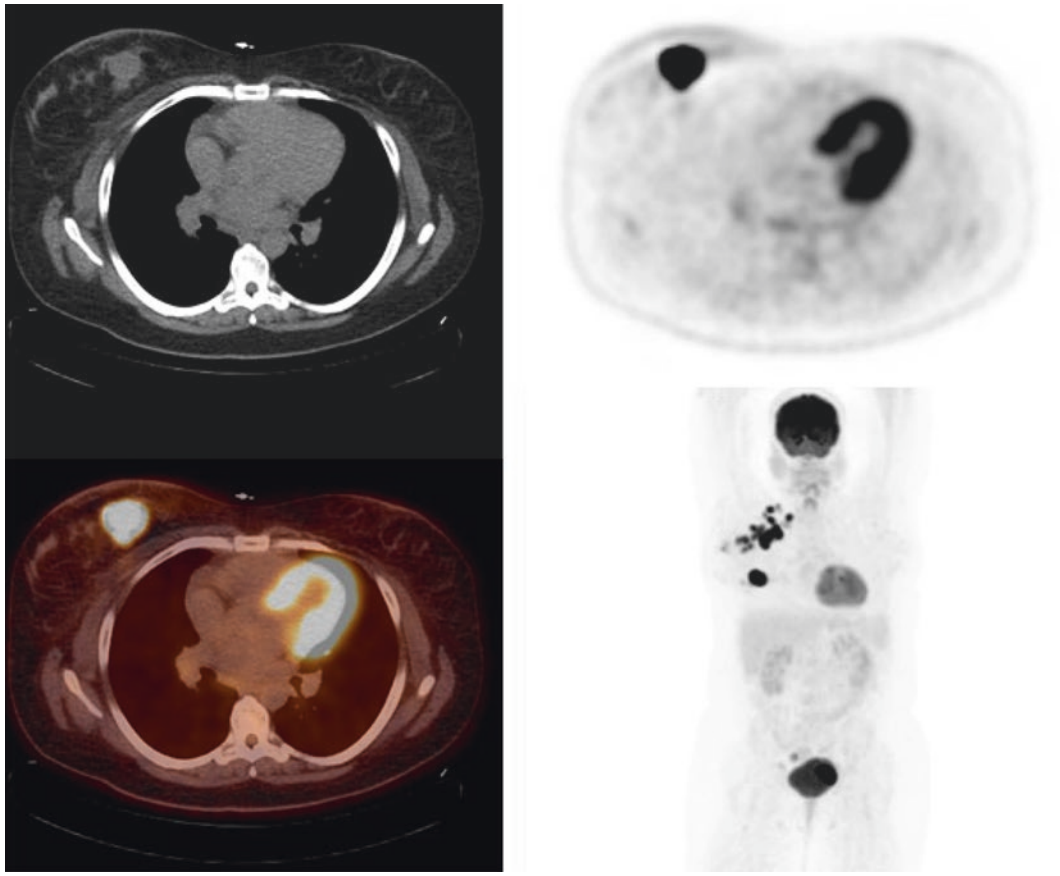

Fig. 12.25 A 34-year-old female presenting with a right breast mass. FDG PET/CT images show an intensely hypermetabolic right breast mass with multiple hypermetabolic right axillary lymph nodes. Biopsy revealed right breast invasive ductal carcinoma with metastatic right axially lymph nodes

relates with tumor grade as well as proliferation index (Ki67 expression). In addition, there is higher FDG uptake in infiltrating ductal carcinoma than in infiltrating lobular carcinoma. This may be secondary to its infiltrative properties as well as low tumor cell density [148].

Lymph node involvement is the most important variable in staging and essential in the proper therapeutic approach. The gold standard in the evaluation of axillary lymph nodes continues to be lymphoscintigraphy with ^{99m}Tc sulfur colloid. FDG PET/CT is helpful in evaluating metastasis in lymph nodes that would otherwise be normal by CT criterion. However, it has been reported that the sensitivity of detecting axillary lymph node metastasis with PET/CT rages from 44 to 67% with a specificity of 90–99%. False-negative results tend to occur in patients with small deposits of tumor in subcentimeter nodes. Nonetheless, in a noninfectious setting, increased metabolic activity in an axillary lymph node is suspicious for malignancy with a positive predictive value of up to 80% [105].

Per NCCN, FDG PET is most helpful in situations where standard staging studies are equivocal or suspicious for stage III and stage IV invasive breast cancer, and inflammatory breast cancer [149]. FDG uptake shows a correlation with the tumor grade, histological and molecular subtypes of breast cancer and various other factors. FDG uptake is higher in higher-grade tumors than lower grade tumors. FDG uptake is higher in IDC than ILC histological subtype. FDG uptake is positively correlated with the tumor size, tumor cell prolifera-

tion (Ki67 expression), nuclear atypia, mitosis counts, tumor invasive size, and lymph node metastasis. FDG uptake is negatively correlated with the hormonal receptor status of the tumor. ER-, PR-, and triple-negative subtypes show higher FDGuptake than ER+, PR+, ER+PR+HER2+, or ER+PR+HER2- subtypes [150–152].

12.5.12 Neuroendocrine Tumors

Neuroendocrine tumors (NETs) are a rare type of malignancy arising from endocrine cells which can appear in almost every organ or tissue but typically within the gastrointestinal tract and bronchopulmonary system. Although rare, the incidence has increased over 600% over the last 4 decades and is now the second most prevalent gastrointestinal cancer after colon cancer. These tumors tend to be slow growing, therefore 60–70% of patients present with metastasis due to the average time from the onset of symptoms to diagnosis being 5–7 years [153, 154]. The conventional imaging techniques using CT, MRI, and ultrasound are utilized in neuroendocrine tumors. However, the overexpression of somatotatin receptors allows for the binding of labeled somatostatin anaologs to these receptors (Fig. 12.26). The arrival of 68Ga-DOTATATE PET/CT has revolutionized imaging of NETs. Due to the greater affinity to somatostatin receptors, 68Ga has increased sensitivity, greater spatial resolution, lower radiation dose, and shorter exam time compared to In-111 pentetreotide. It has therefore become the gold standard for imaging well-differentiated NETs. Imaging the 68Ga-DOTATATE has been documented as altering diagnosis and management in one-third of patients and changing operative plans in half the patients referred for surgical intervention [154].

Additionally, the recent emergence of 64Cu-DOTATATE further improves imaging of NETs (Fig. 12.27). There are multiple advantages of 64Cu over 68Ga, including the shorter positron range resulting in improved spatial resolution, cyclotron-produced rather than generator-produced allowing for large scale production, and longer shelf life (12.7 h vs 68 min), making it more widely available [67]. Treatment is then being performed with 177Lutetium DOTATATE which will be further discussed in another chapter.

FDOPA is also a valuable tracer in detecting NETS, such as carcinoid tumor, medullary thyroid cancer and pheochromocytoma/paraganliomas with certain genetic mutations [155, 156].

12.5.13 Prostate Cancer

FDG PET/CT has limited use for the diagnosis of primary prostate cancer which is likely due to the low level of glucose metabolism. In addition, intense urine uptake particularly in the bladder can interfere with evaluation. Focal FDG uptake in the prostate can be seen in prostatitis and prostate cancer. It has been reported that the sensitivities of FDG PET in metastatic prostate cancer ranges from 18 to 65% [157]. However, the same study showed an increase in sensitivity to 72% when imaging with ^{11}C-methionine PET. Although no longer widely used, 18F-fluoride PET/CT for the assessment of bone metastasis which has found to be more sensitive than the gold standard ^{99m}Tc MDP bone scan (Fig. 12.28). It has been reported that 18F-fluoride PET/CT had a sensitivity ranging from 81 to 100% with a specificity of 93% compared to a sensitivity of 70% for the conventional bone scan [158, 159]. Increased uptake on these scans, however, is not limited to tumors and can also be seen in benign bone lesions and degenerative changes.

Unlike 18F-FDG, 18F-Fluciclovine PET/CT is approved for imaging men with suspected prostate cancer recurrence (Fig. 12.29). It can

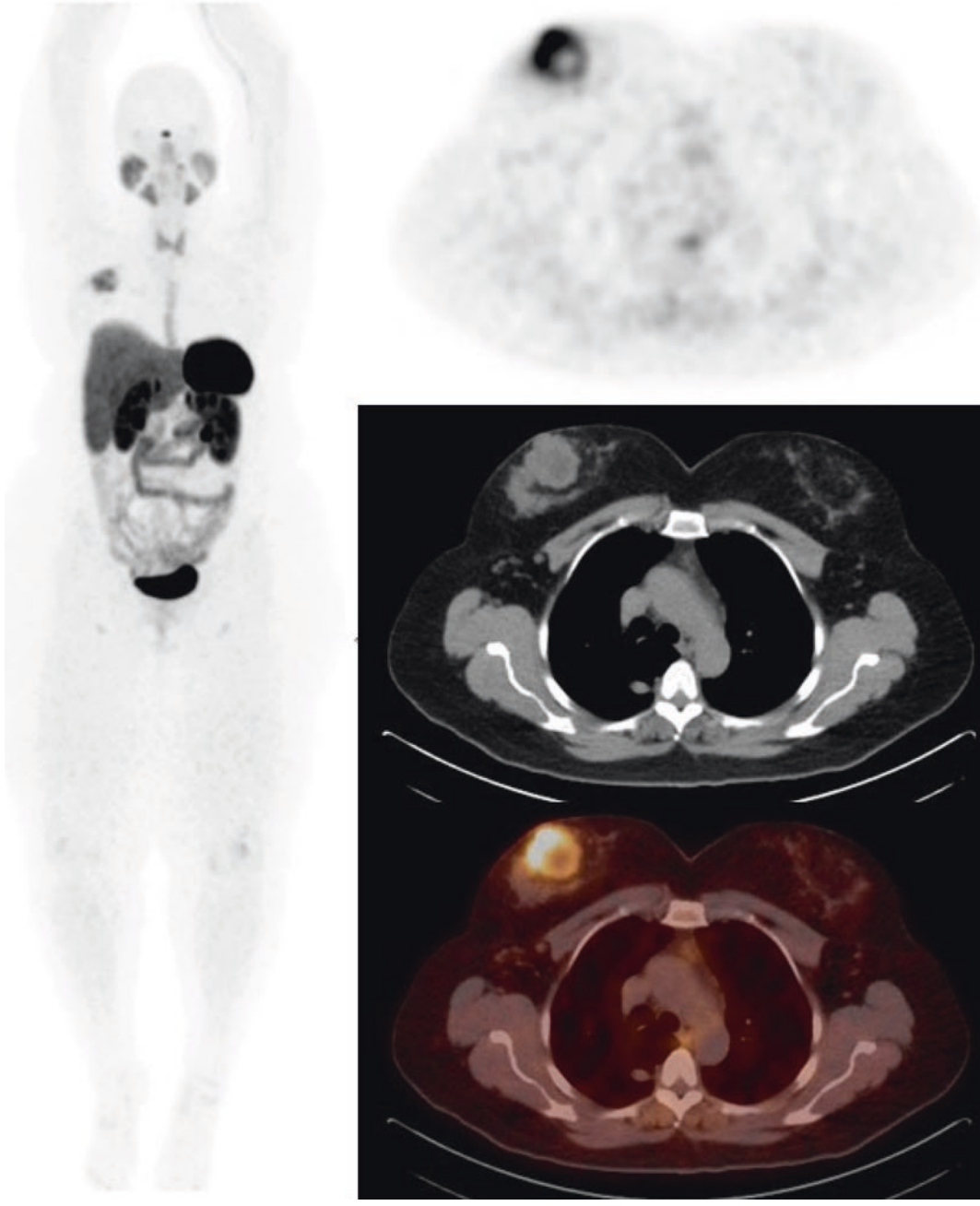

Fig. 12.26 A 56-year old female with a neuroendocrine tumor of the breast. 68Ga Dotatate PET/CT demonstrating a mass in the right breast with central necrosis with no additional lesions

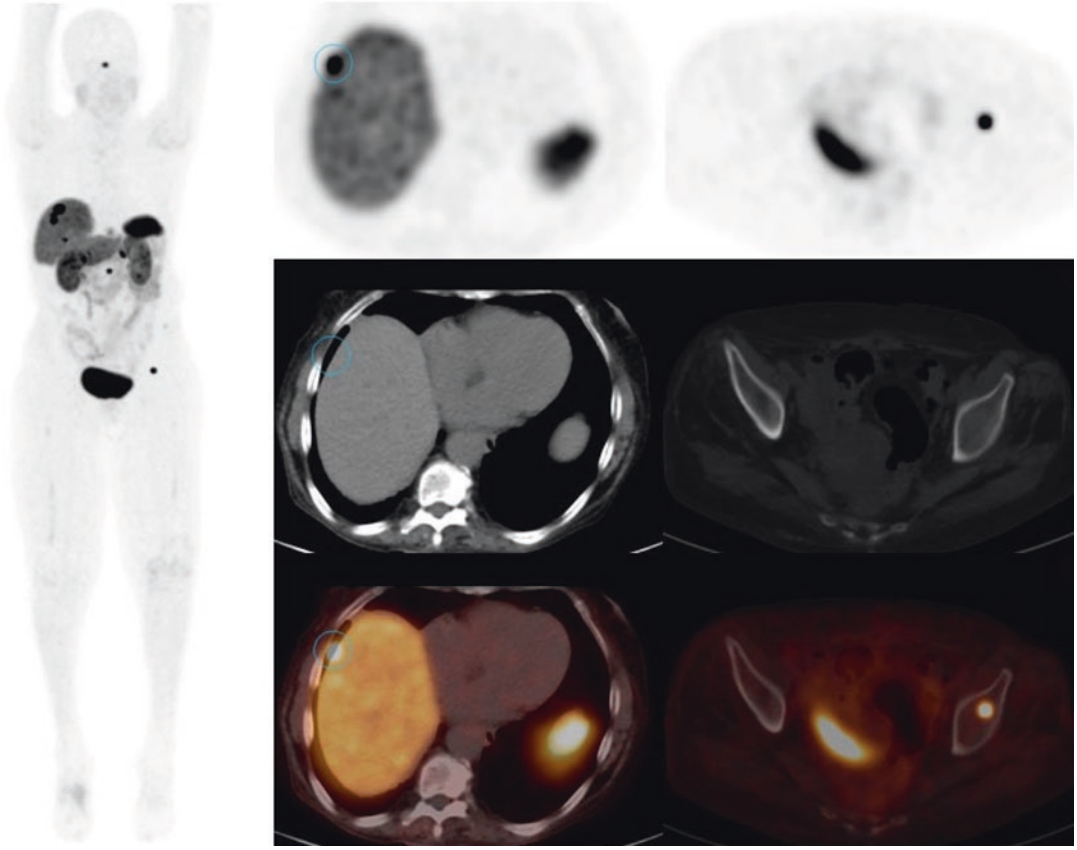

Fig. 12.27 A 70-year old female with carcinoid tumor initially diagnosed in the small bowel. 64Cu PET/CT demonstrates multiple foci of uptake in the liver (middle column), abdominal nodes, left iliac wing and left acetabulum (right column)

detect both bone and soft tissue lesions with high sensitivity notably in subcentimeter lymph nodes.

However, in the era or theranostics, the drawback to 18F-Fluciclovine is the lack of a linked therapeutic arm [160]. PSMA PET/CT is emerging as a superior replacement for both 18F-Fluciclovine and conventional imaging using CT and bone scan in prostate cancer, particularly in tumor recurrence, which been proven to change patient management. Although 68Ga-PSMA is not yet approved in the US, it has been carefully reviewed worldwide and has been used as the gold standard for restaging recurrent prostate cancer (Fig. 12.30).

Despite the advances of 68Ga-PSMA at imaging the intended target, it does have limitations in order to be routinely utilized worldwide. In order to address the limitations, there has been a shift from 68Ga to 18F-labeled PSMA targeted compounds. Limited quantities of 68Ga can be made since it is generator-produced compared to the high amounts of 18F to be produced from cyclotrons. The longer half-life of 18F makes it better for transport and distribution (110 min vs 68 min). In addition, the higher positron yield and lower positron energy decreases noise which provides images with better resolution. Treatment is then being performed with 177Lu-PSMA and is being widely seen as a major

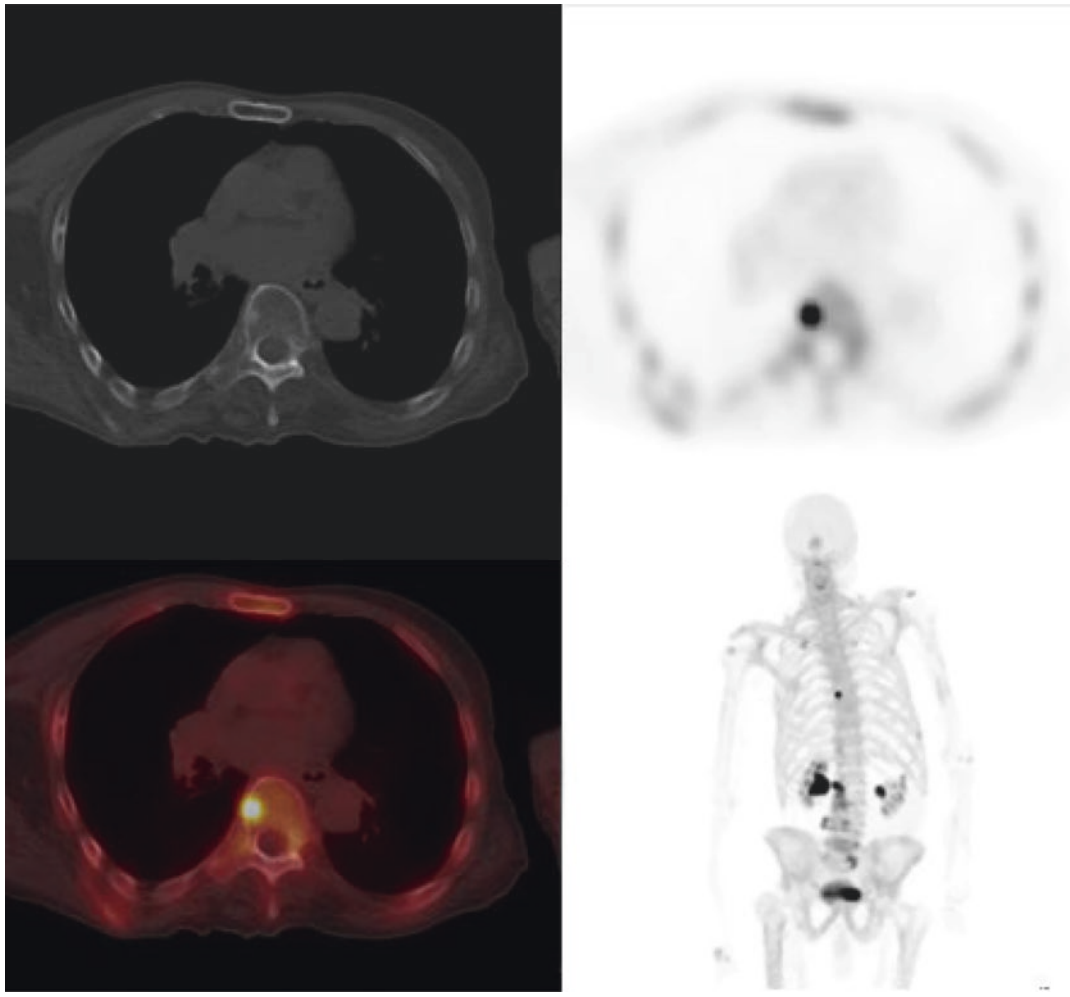

Fig. 12.28 A 67-year-old male patient with a remote history of treated adenocarcinoma of the prostate who presented with an elevated PSA of 89.4 ng/ml. Technetium-99m MDP bone scan was negative for metastatic bone disease (not shown). NaF PET/CT images demonstrated metastatic bone disease involving the skull and T8 vertebra, with degenerative changes seen at the lumbosacral spine

therapeutic option and even recommended by some urologic-oncologic guidelines even though the therapy has yet to be approved [70, 71].

Furthermore, treating prostate cancer with 177Lu-PSMA has discovered a role for 18F-FDG as an anti-theranostic agent. When patients are imaged with both 68Ga-PSMA and 18F-FDG PET/CT, the most effective treatment is with PSMA-positive disease with no sites of metastatic disease with discordant FDG-positive and PSMA-negative findings [161]. Therefore, 18F-FDG can be used in the selection of patients to allow for the greatest targeting and highest overall survival.

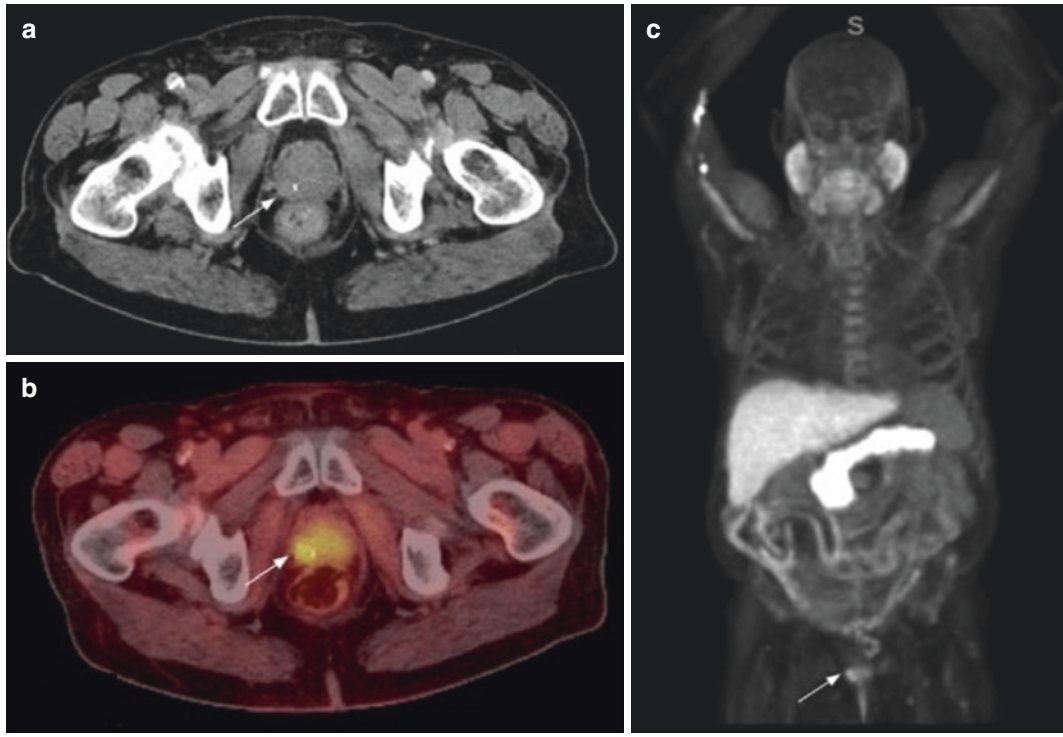

Fig. 12.29 A 65-year-old male with prior history of prostate cancer diagnosed 7 years ago (Gleason 4 + 3 = 7) status post definitive radiation therapy with rising PSA of 2.9 ng/ml. CT body scan with contrast and bone scan were negative for recurrent disease. (**a**) Radiation seeds are seen in the prostate without evidence of mass or enhancement on CT (arrow). 18F-fluciclovine PET/CT axial fused (**b**) and coronal MIP images (**c**) demonstrate localized intense radiotracer uptake in the right aspect of the prostate apex (arrow) consistent with recurrent disease

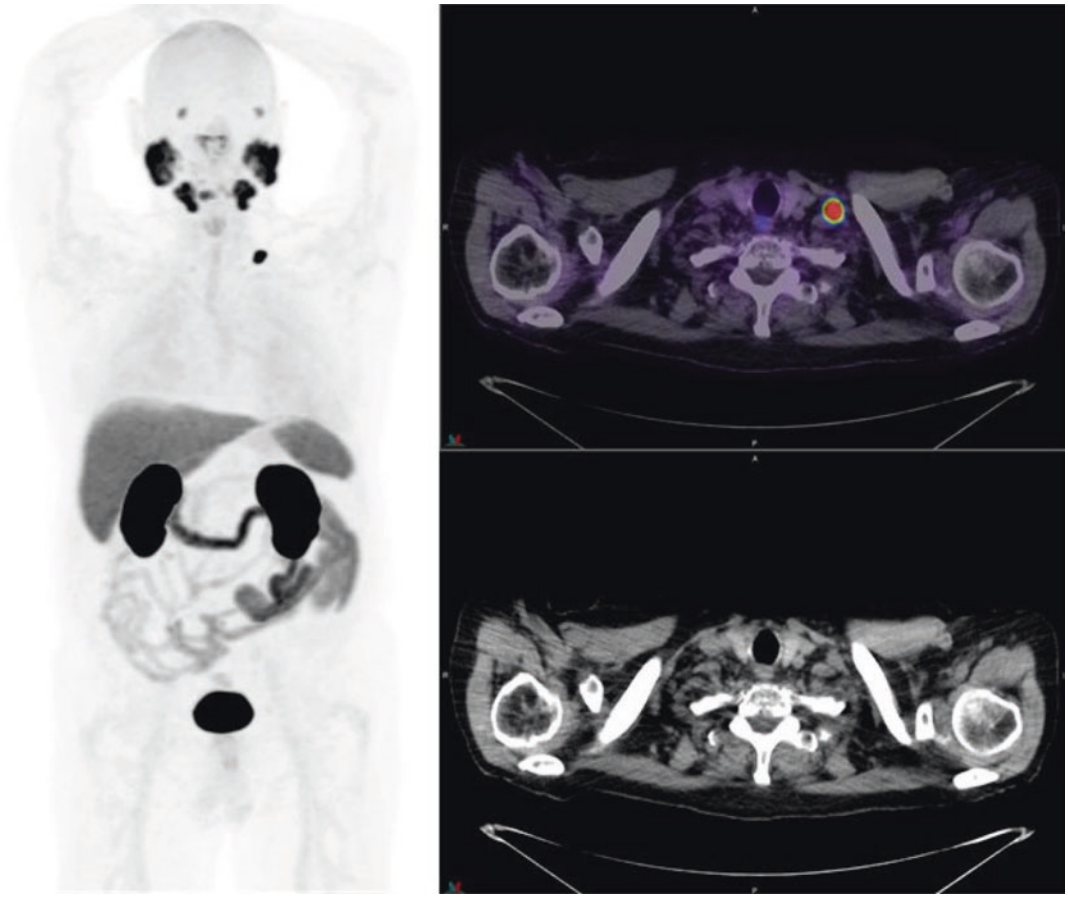

Fig. 12.30 A male patient with a history of prostate cancer presenting with biochemical recurrence with PSA of 1.49 ng/ml. 68Ga-PSMA PET/CT images demonstrate a single gallium-avid left supraclavicular lymph node which was biopsy-proven prostate cancer metastasis. Image courtesy of Dr. Amir Iravani

References

1. International Survey of PET/CT Operations and Oncology Imaging (2010) Academy of molecular imaging. http://www.ami-maging.org/index.php?option=com_content&task=view&id=181. Accessed 19 Sept 2012
2. Schuetze SM, Rubin BP, Vernon C, Hawkins DS, Bruckner JD, Conrad EU, Eary JF (2005) Use of positron emission tomography in localized extremity soft tissue sarcoma treated with neoadjuvant chemotherapy. Cancer 103:339–334
3. Yeung H, Sanches A, Squire O, Macapinlac H, Larson S, Erdi Y (2002) Standardized uptake value in pediatric patients: an investigation to determine the optimum measurement parameter. J Nucl Med 43:61–66
4. Hawkins DS, Rajendran JG, Conrad EU III, Bruckner JD, Eary JF (2002) Evaluation of chemotherapy response in pediatric bone sarcomas by [F-18]-fluorodeoxy-D-glucose positron emission tomography. Cancer 94:3277–3284
5. Kumar V, Abbas A, Aster JC (2014) Robbins and Cotzan, pathologic basis of disease, 9th edn. Saunders, Philadelphia
6. Rosai J, Sobin LH (1998) Atlas of tumor pathology, vol 3. Armed Forces Institute of Pathology American Registry of Pathology, Washington, DC
7. World Health Organization (1967) International classification of tumors, 2nd edn. WHO, Geneva
8. Lei X, Bandyopadhyay A, Le T, Sun L (2002) Autocrine TGFbeta supports growth and survival of human breast cancer MDA-MB-231 cells. Oncogene 21:7514–7523
9. Markowitz SD, Roberts AB (1996) Tumor suppressor activity of the TGF-beta pathway in human cancers. Cytokine Growth Factor Rev 7:93–102
10. Ebos JM, Lee CR, Cruz-Munoz W et al (2009) Accelerated metastasis after short-term treatment with a potent inhibitor of tumor angiogenesis. Cancer Cell 15:232–239

11. Folkman J (2006) Angiogenesis. Annu Rev Med 57:1–18
12. Herbst RS, Onn A, Sandler A (2005) Angiogenesis and lung cancer: prognostic and therapeutic implications. J Clin Oncol 23:3243–3256
13. Loges S, Mazzone M, Hohensinner P, Carmeliet P (2009) Silencing or fueling metastasis with VEGF inhibitors: antiangiogenesis revisited. Cancer Cell 15:167–170
14. Rak J, Mitsuhashi Y, Bayko L et al (1995) Mutant ras oncogenes upregulate VEGF/VPF expression: implications for induction and inhibition of tumor angiogenesis. Cancer Res 55:4575–4580
15. Foulds L (1969) Neoplastic development, vol 2. Academic, London
16. Abercrombie M, Heaysman JE (1954) Observations on the social behaviour of cells in tissue culture. II. Monolayering of fibroblasts. Exp Cell Res 6:293–306
17. Todaro GJ, Green H (1963) Quantitative studies of the growth of mouse embryo cells in culture and their development into established lines. J Cell Biol 17:299–313
18. Jakowlew SB (2006) Transforming growth factor-beta in cancer and metastasis. Cancer Metastasis Rev 25:435–457
19. Kirsch DG, Kastan MB (1998) Tumor-suppressor p53: implications for tumor development and prognosis. J Clin Oncol 16:3158–3168
20. Ben-Porath I, Weinberg RA (2004) When cells get stressed: an integrative view of cellular senescence. J Clin Invest 113:8–13
21. Lleonart ME, Artero-Castro A, Kondoh H (2009) Senescence induction; a possible cancer therapy. Mol Cancer 8:3
22. Israel O, Mekel M, Bar-Shalom R et al (2002) Bone lymphoma: 67Ga scintigraphy and CT for prediction of outcome after treatment. J Nucl Med 43:1295–1303
23. Larson SM, Rasey JS, Allen DR, Nelson NJ (1979) A transferrin-mediated uptake of gallium-67 by EMT-6 sarcoma. I. Studies in tissue culture. J Nucl Med 20:837–842
24. Berry JP, Escaig F, Poupon MF, Galle P (1983) Localization of gallium in tumor cells. Electron microscopy, electron probe microanalysis and analytical ion microscopy. Int J Nucl Med Biol 10:199–204
25. Ziessman H, O'Malley J, Thrall J (2006) Nuclear medicine: the requisites in radiology. Mosby, Philadelphia
26. Gehring PJ, Hammond PB (1967) The interrelationship between thallium-201 chloride and potassium in animals. J Pharmacol Exp Ther 155:187–201
27. Britten JS, Blank M (1968) Thallium-201 chloride-201 chloride activation of the (Na + K +) activated ATPase of rabbit kidney. Biochim Biophys Acta 159:160–166
28. Sessler MJ, Geck P, Maul FD, Hor G, Munz DL (1986) New aspects of cellular thallium-201 chloride-201 chloride uptake: Tl+-Na+-2Cl-cotransport is the central mechanism of ion uptake. Nucl Med 23:24–27
29. Abdel-Dayem HM et al (1994) Role of Tl-201 chloride and Tc-99m-sestamibi in tumor imaging. Nucl Med Annu 1994:181–234
30. Piwnica-Worms D, Holman BL (1990) Noncardiac applications of hexakis-(alkylisonitrile) technetium-99m complexes. J Nucl Med 31:1166–1167
31. Piwnica-Worms D, Chiu ML, Budding M, Kronauge JF, Kramer RA, Croop JM (1993) Functional imaging of multidrug-resistant P-glycoprotein with an organotechnetium complex. Cancer Res 53:977–984
32. Ballinger JR, Sheldon KM, Boxen I, Erlichman C, Ling V (1995) Differences between accumulation of 99mTc-MIBI and 201Tl-thallous chloride in tumour cells: role of P-glycoprotein. Q J Nucl Med 39:122–128
33. Henze M, Mohammed A, Schlemmer HP et al (2004) PET and SPECT for detection of tumor progression in irradiated low-grade astrocytoma: a receiver-operating-characteristics analysis. J Nucl Med 45:579–586
34. Taillefer R (1999) The role of 99mTc-sestamibi and other conventional radiopharmaceuticals in breast cancer diagnosis. Semin Nucl Med 29:16–40
35. Kwekkeboom D, Krenning EP, de Jong M (2000) Peptide receptor imaging and therapy. J Nucl Med 41(10):1704–1713
36. Freitas JE (1995) Adrenal cortical and medullary imaging. Semin Nucl Med 25:235–250
37. Wiseman GA, Pacak K, O'Dorisio MS et al (2009) Usefulness of 123I-MIBG scintigraphy in the evaluation of patients with known or suspected primary or metastatic pheochromocytoma or paraganglioma: results from a prospective multicenter trial. J Nucl Med 50:1448–1454
38. Shulkin BL, Shapiro B (1998) Current concepts on the diagnostic use of MIBG in children. J Nucl Med 39:679–688
39. Czernin J, Phelps ME (2002) Positron emission tomography scanning: current and future applications. Annu Rev Med 53:89–112
40. Delbeke D (1999) Oncological applications of FDG PET imaging: brain tumors, colorectal cancer, lymphoma and melanoma. J Nucl Med 40:591–603
41. Ak I, Stokkel MP, Pauwels EK (2000) Positron emission tomography with 2-[18F]fluoro-2-deoxy-D-glucose in oncology. Part II. The clinical value in detecting and staging primary tumours. J Cancer Res Clin Oncol 126:560–574
42. Lowe VJ, Naunheim KS (1998) Current role of positron emission tomography in thoracic oncology. Thorax 53:703–712
43. Shankar LK, Hoffman JM, Bacharach S et al (2006) Consensus recommendations for the use of ^{18}F-FDG PET as an indicator of therapeutic response in patients in national cancer institute trials. J Nucl Med 47:1059–1066

44. Coleman RE (1999) PET in lung cancer. J Nucl Med 40:814–820
45. Jadvar H, Alavi A, Mavi A et al (2005) PET in pediatric diseases. Radiol Clin N Am 43:135–152
46. Osman MM, Chaar BT, Muzaffar R et al (2010) 18F-FDG PET/CT of patients with cancer: comparison of whole-body and limited whole-body technique. AJR Am J Roentgenol 195:1397–1403
47. Sodium Fluoride F18 injection investigator's brochure. http://imaging.cancer.gov/images/documents/Generic-NaF_IB_Edition1_10-2009.pdf
48. Even-Sapir E, Metser U, Flusser G et al (2004) Assessment of malignant skeletal disease: initial experience with 18F-fluoride PET/CT and comparison between 18Ffluoride PET and 18F-fluoride PET/CT. J Nucl Med 45:272–278
49. Lin FI, Rao JE, Mittra ES et al (2012) Prospective comparison of combined ^{18}F-FDG and 18F-NaF PET/CT vs. ^{18}F-FDG PET/CT imaging for detection of malignancy. Eur J Nucl Med Mol Imaging 39:262–270
50. Rasey JS, Grierson JR, Wiens LW, Kolb PD, Schwartz JL (2002) Validation of FLT uptake as a measure of thymidine kinase-1 activity in A549 carcinoma cells. J Nucl Med 43:1210–1217
51. Buck AK, Halter G, Schirrmeister H, Kotzerke J, Wurziger I et al (2003) Imaging proliferation in lung tumors with PET: ^{18}F-FLT versus ^{18}F-FDG. J Nucl Med 44:1426–1431
52. Van Waarde A, Cobben DC, Suurmeijer AJ, Maas B, Vaalburg W et al (2004) Selectivity of ^{18}F-FLT and ^{18}F-FDG for differentiating tumor from inflammation in a rodent model. J Nucl Med 45:695–700
53. Cobben DC, Jager PL, Elsinga PH, Maas B, Suurmeijer AJ et al (2003) 3′-(18)F-fluoro-3′-deoxy-L-thymidine: a new tracer for staging metastatic melanoma? J Nucl Med 44:1927–1932
54. Everitt S, Hicks RJ, Ball D, Kron T, Schneider-Kolsky M et al (2009) Imaging cellular proliferation during chemo-radiotherapy: a pilot study of serial ^{18}F-FLT positron emission tomography/computed tomography imaging for non–small-cell lung cancer. Int J Radiat Oncol Biol Phys 75:1098–1104
55. Minamimoto R, Toyohara J, Seike A, Ito H, Endo H et al (2012) 4′-[Methyl-11C]-thiothymidine PET/CT for proliferation imaging in non-small cell lung cancer. J Nucl Med 53:199–206
56. Pieterman RM, Que TH, Elsinga PH, Pruim J, van Putten JW et al (2002) Comparison of (11)C-choline and (18)F-FDG PET in primary diagnosis and staging of patients with thoracic cancer. J Nucl Med 43:167–172
57. Hara T, Inagaki K, Kosaka N, Morita T (2000) Sensitive detection of mediastinal lymph node metastasis of lung cancer with 11C-choline PET. J Nucl Med 41:1507–1513
58. Torizuka T, Kanno T, Futatsubashi M, Okada H, Yoshikawa E et al (2003) Imaging gynecologic tumors: comparison of ^{11}C-choline PET with ^{18}F-FDG PET. J Nucl Med 44:1051–1056
59. Kostakoglu L, Goldsmith SJ (2004) PET in the assessment of therapy response in patients with carcinoma of the head and neck and of the esophagus. J Nucl Med 45:56–68
60. Bradley JD, Perez CA, Dehdashti F, Siegel BA (2004) Implementing biologic target volumes in radiation treatment planning for non-small cell lung cancer. J Nucl Med 45(Suppl 1):96S–101S
61. Huang T, Civelek A, Zheng H et al (2013) F-18 misonidazole PET imaging of hypoxia in micrometastases and macroscopic xenografts of human non-small cell lung cancer: a correlation with autoradiography and histopathological findings. Am J Nucl Med Mol Biol 3:142–153
62. Richin D, Hicks RJ, Fisher R et al (2006) Prognostic significance of F-18 misonidazole positron emission tomography-detected tumor hypoxia in patients with advanced head and neck cancer randomly assigned chemo-radiation with or without tirapazamine:a substudy of tasman radiation oncology group 98.2. J Clin Oncol 24:2098–2104
63. Poeppel TD, Binse I, Petersenn S et al (2011) 68Ga-DOTATOC versus 68Ga-DOTATATE PET/CT in functional imaging of neuroendocrine tumors. J Nucl Med 52:1864–1870
64. Yang J, Kan Y, Ge BH et al (2013) Diagnostic role of Gallium-68 DOTATOC and Gallium-68 DOTATATEPET in patients with neuroendocrine tumors: a meta-analysis. Acta Radiol 55:389–398
65. Sandström M, Velikyan I, Garske-Román U et al (2013) Comparative biodistribution and radiation dosimetry of 68Ga-DOTATOC and 68Ga-DOTATATE in patients with neuroendocrine tumors. J Nucl Med 54:1755–1759
66. Gabriel M, Decristoforo C, Kendler D et al (2007) 68Ga-DOTA-Tyr3-octreotide PET in neuroendocrine tumors: comparison with somatostatin receptor scintigraphy and CT. J Nucl Med 48:508–518
67. Delpassand ES, Ranganathan D, Wagh N, Shafie A, Gaber A et al (2020) 64Cu-DOTATATE PET/CT for imaging patients with known or suspected somatostatin receptor–positive neuroendocrine tumors: results of the first U.S. prospective, reader-masked clinical trial. J Nucl Med 61:890–896
68. Fowler AM, Linden HM (2017) Functional estrogen receptor imaging before neoadjuvant therapy for primary breast cancer. J Nucl Med 58:560–562
69. Bensch F, Brouwers AH, Lub-de Hooge MN et al (2018) 89Zr-trastuzumab PET supports clinical decision making in breast cancer patients, when HER2 status cannot be determined by standard work up. Eur J Nucl Med Mol Imaging 45:2300–2306
70. Lenzo NP, Meyrick D, Turner JH (2018) Review of gallium-68 PSMA PET/CT imaging in the management of prostate cancer. Diagnostics 11:8
71. Hofman MS, Lawrentschuk N, Francis RJ et al (2020) Prostate-specific membrane antigen PET-CT in patients with high-risk prostate cancer before curative-intent surgery or radiotherapy (proPSMA):

a prospective, randomised, multicentre study. Lancet 395:1208–1216
72. Langbein T, Weber WA, Eiber M (2019) Future of theranostics: an outlook on precision oncology in nuclear medicine. J Nucl Med 60:13S–19S
73. Kratochwil C, Flechsig P, Lindner T et al (2019) 68Ga-FAPI PET/CT: tracer uptake in 28 different kinds of cancer. J Nucl Med 60:801–805
74. Lindner T, Loktev A, Altmann A et al (2018) Development of quinoline-based theranostic ligands for the targeting of fibroblast activation protein. J Nucl Med 59:1415–1422
75. Yilmaz S, Ozhan M, Sager S et al (2011) Metformin-induced intense bowel uptake observed on restaging FDG PET/CT study in a patient with gastric lymphoma. Mol Imaging Radionucl Ther 20:114–116
76. Nakamoto Y, Tatsumi M, Hammoud D et al (2005) Normal FDG distribution patterns in the head and neck: PET/CT evaluation. Radiology 234:879–885
77. Roy FN, Beaulieu S, Boucher L et al (2009) Impact of intravenous insulin on ^{18}F-FDG PET in diabetic cancer patients. J Nucl Med 50:178–183
78. Osman MM, Tran IT, Parkar N, Muzaffar R et al (2011) Does 18F-FDG Uptake of respiratory muscles on PET/CT correlate with chronic obstructive pulmonary disease diagnosis? J Nucl Med Technol 39:252–257
79. Tam CS, Lecoultre V, Ravussin E (2012) Brown adipose tissue: mechanisms and potential therapeutic targets. Circulation 125(22):2782–2791
80. Cronin CG, Prakash P, Daniels GH et al (2012) Brown fat at PET/CT: correlation with patient characteristics. Radiology 263:836–842
81. Muzaffar R, Nguyen NC, Kudva G, Osman MM (2011) Incidental diagnosis of thrombus within an aneurysm in FDG PET/CT: frequency in 926 patients. J Nucl Med 52:1408–1411
82. Are C, Hsu JF, Ghossein RA, Schoder H, Shah JP, Shaha AR (2007) Histological aggressiveness of fluorodeoxyglucose positron-emission tomogram (FDG-PET)-detected incidental thyroid carcinomas. Ann Surg Oncol 14:3210–3215
83. Berthet L, Cochet A, Kanoun S et al (2013) In newly diagnosed diffuse large B-cell lymphoma, determination of bone marrow involvement with ^{18}F-FDG PET/CT provides better diagnostic performance and prognostic stratification than does biopsy. J Nucl Med 54:1244–1250
84. Zhang X, Liu H, Balter P et al (2012) Positron emission tomography for assessing local failure after stereotactic body radiotherapy for non-small-cell lung cancer. Int J Radiat Oncol Biol Phys 83:1558–1565
85. Palestro CJ (2013) FDG-PET in musculoskeletal infections. Semin Nucl Med 43:367–376
86. Iravani A, Osman MM, Weppler AM et al (2020) FDG PET/CT for tumoral and systemic immune response monitoring of advanced melanoma during first-line combination ipilimumab and nivolumab treatment. Eur J Nucl Med Mol Imaging 47:2776–2786
87. Hodi FS, Chiarion-Sileni V, Gonzalez R, Grob JJ, Rutkowski P et al (2018) Nivolumab plus ipilimumab or nivolumab alone versus ipilimumab alone in advanced melanoma (CheckMate 067): 4-year outcomes of a multicentre, randomised, phase 3 trial. Lancet Oncol 19:1480–1492
88. Larkin J, Chiarion-Sileni V, Gonzalez R, Grob JJ, Rutkowski P, Lao CD et al (2019) Five-year survival with combined nivolumab and ipilimumab in advanced melanoma. N Engl J Med 381:1535–1546
89. Postow MA, Sidlow R, Hellmann MD (2018) Immune-related adverse events associated with immune checkpoint blockade. N Engl J Med 3778:158–168
90. Prigent K, Aide N (2020) 18F-Fludeoxyglucose PET/computed tomography for assessing tumor response to immunotherapy and detecting immune-related side effects: a checklist for the PET reader. PET Clin 15:1–10
91. Blake MA, Singh A, Setty BN et al (2006) Pearls and pitfalls in interpretation of abdominal and pelvic PET-CT. Radiographics 26:1335–1353
92. Sarikaya I, Sarikaya A (2021) PET/CT image artifacts caused by the arms. J Nucl Med Technol 49:19–22
93. Sarikaya I, Sarikaya A (2020) Assessing PET parameters in oncologic ^{18}F-FDG studies. J Nucl Med Technol 48:278–282
94. Zasadny KR, Wahl RL (1993) Standardized uptake values of normal tissues at PET with2-[fluorine 18] fluoro-2-deoxy-D-glucose: variations with body weight and amethod for correction. Radiology 189:847–850
95. Sarikaya I, Albatineh A, Sarikaya A (2019) Re-visiting SUV-weight and SUV-lean body mass in FDG PET studies. J Nucl Med Technol 2020(48):163–167
96. Sugawara Y, Shulkin BL, Zasadny KR et al (2000) Standardized uptake values inpediatric patients: variations with patient characteristics and methods for correction. J Nucl Med 41:196
97. Grupta NC, Peter N, Blomfield SM (1999) FDG-PET in staging work-up of patients with suspected intracranial metastatic tumors. Ann Surg 230:202–206
98. Chidel MA, Suh JH, Greskovich JF et al (1999) Treatment outcome for patients with primary nonsmall-cell lung cancer and synchronous brain metastasis. Radiat Oncol Investig 7:313–319
99. Vecht CJ (1998) Clinical management of brain metastasis. J Neurol 245:127–131
100. Langleben DD, Segall GM (2000) PET in differentiation of recurrent brain tumor from radiation injury. J Nucl Med 41:1861–1867
101. Chen W (2007) Clinical applications of PET in brain tumors. J Nucl Med 48:1468–1481
102. Kratochwil C, Combs SE, Leotta K, Afshar-Oromieh A, Rieken S et al (2014) Intra-individual comparison of ^{18}F-FET and ^{18}F-DOPA in PET imaging of recurrent brain tumors. Neuro-Oncology 16:434–440

103. Fink JR, Muzi M, Peck M, Krohn KA (2015) Multimodality brain tumor imaging: MR imaging, PET, and PET/MR imaging. J Nucl Med 56:1554–1561
104. Patronas NJ, Bousser MG, Comar D et al (1984) Crossed cerebellar glucose metabolism in supratentorial tumors. Brain Res 291:93–101
105. Fulham MJ, Brooks RA, Hallett M et al (1995) Cerebellar diaschisis revisited: pontine hypometabolism and dentate sparing. J Neurol 142:2267–2273
106. Quon A, Fischbein NJ, McDougall IR et al (2007) Management of squamous cell carcinoma of the head and neck and thyroid carcinoma. J Nucl Med 48:585–675
107. Abgral R, Querellou S, Potard G et al (2009) Does ^{18}F-FDG PET/CT improve detection of posttreatment recurrence of head and neck squamous cell carcinoma in patients negative for disease on clinical follow-up? J Nucl Med 50:24–29
108. Santhanam P, Taieb D, Solnes L et al (2017) Utility of I-124 PET/CT in identifying radioiodine avid lesions in differentiated thyroid cancer: a systematic review and meta-analysis. Clin Endocrinol 86:645–651
109. Zhuang H, Kumar R, Mandel S et al (2004) Investigation of thyroid, head, and neck cancers with PET. Radiol Clin N Am 42:1101–1111
110. Szakall S, Esik O, Bajzik G et al (2002) 18F-FDG PET detection of lymph node metastases in medullary thyroid carcinoma. J Nucl Med 43:66–71
111. Lyer RB, Silverman PM, Tamm EP et al (2003) Diagnosis, staging, and follow-up of esophageal cancer. Am J Roentgenol 181:785–793
112. Yoon YC, Lee KS, Shim YM et al (2003) Metastasis to regional lymph nodes in patients with esophageal squamous cell carcinoma: CT versus FDG PET for presurgical detection- prospective study. Radiology 227:764–770
113. Barber TW, Duong CP, Leong T et al (2012) 18F-FDG PET/CT has a high impact on patient management and provides powerful prognostic stratification in the primary staging of esophageal cancer: a prospective study with mature survival data. J Nucl Med 53:864–871
114. Park JW, Jo MK, Lee HM (2009) Significance of 18F-fluorodeoxyglucose positron-emission tomography/computed tomography for the postoperative surveillance of advanced renal cell carcinoma. BJU Int 103:615–619
115. Anjos DA, Etchebehere EC, Ramos CD et al (2007) 18F-FDG PET/CT delayed images after diuretic for restaging invasive bladder cancer. J Nucl Med 48:764–770
116. Armstrong EP (2010) Prophylaxis of cervical cancer and related cervical disease: a review of the cost-effectiveness of vaccination against oncogenic HPV types. J Manag Care Pharm 16:217–230
117. Belhocine T, Thille A, Fridman V (2002) Contribution of whole-body 18FDG PET imaging in the management of cervical cancer. Gynecol Oncol 87:90–97
118. Reinhardt MJ, Ehritt-Braun C, Vogelgesang D et al (2001) Metastatic lymph nodes in patients with cervical cancer: detection with MR imaging and FDG PET. Radiology 218:776–782
119. Pandit-Taskar N (2005) Oncologic imaging in gynecologic malignancies. J Nucl Med 46:1842–1850
120. Fenchel S, Grab D, Nuessle K et al (2002) Asymptomatic adnexal masses: correlation of FDG PET and histopathologic findings. Radiology 223:780–788
121. American Cancer Society (2011) Colorectal cancer facts & figures 2011–2013. American Cancer Society, Atlanta
122. Willkomm P, Bender H, Bangard M et al (2000) FDG PET and immunoscintigraphy with 99mTc-labeled antibody fragments for detection of the recurrence of colorectal carcinoma. J Nucl Med 41:1657–1663
123. Kantorová I, Lipská L, Bêlohlávek O et al (2003) Routine (18)F-FDG PET preoperative staging of colorectal cancer: comparison with conventional staging and its impact on treatment decision making. J Nucl Med 44:1784–1788
124. Cascini GL, Avallone A, Delrio P et al (2006) 18F-FDG PET is an early predictor of pathologic tumor response to preoperative radiochemotherapy in locally advanced rectal cancer. J Nucl Med 47:1241–1248
125. Niekel MC, Bipat S, Stoker J (2010) Diagnostic imaging of colorectal liver metastases with CT, MR imaging, FDG PET, and/or FDG PET/CT: a meta-analysis of prospective studies including patients who have not previously undergone treatment. Radiology 257:674–684
126. Gambhir SS, Czernin J, Schwimmer J et al (2001) A tabulated summary of the FDG PET literature. J Nucl Med 42:1S–93S
127. American Cancer Society (2013) Cancer fact & figures. American Cancer Society, Atlanta
128. Higashi K, Ueda Y, Sakuma T et al (2001) Comparison of [(18)F]FDG PET and (201)Tl SPECT in evaluation of pulmonary nodules. J Nucl Med 42:1489–1496
129. Kaiser LR, Shrager JB (1995) Video-assisted thoracic surgery: the current state of the art. AJR Am J Roentgenol 165:1111–1117
130. Gould MK, Maclean CC, Kuschner WG et al (2001) Accuracy of positron emission tomography for diagnosis of pulmonary nodules and mass lesions: a meta-analysis. JAMA 285:914–924
131. Schreyögg J, Weller J, Stargardt T et al (2010) Cost-effectiveness of hybrid PET/CT for staging of non-small cell lung cancer. J Nucl Med 51:1668–1675
132. de Geus-Oei LF, van der Heijden HF, Visser EP et al (2007) Chemotherapy response evaluation with ^{18}F-FDG PET in patients with non-small cell lung cancer. J Nucl Med 48:1592–1598
133. Rohren EM, Turkington TG, Coleman RE (2004) Clinical applications of PET in oncology. Radiology 231:305–332

134. Kostakoglu L, Agress H Jr, Goldsmith SJ (2003) Clinical role of FDG PET in evaluation of cancer patients. Radiographics 23:315–340
135. Bunyaviroch T, Coleman RE (2006) PET evaluation of lung cancer. J Nucl Med 47:451–469
136. Kamel EM, Zwahlen D, Wyss MT et al (2003) Whole-body (18)F-FDG PET improves the management of patients with small cell lung cancer. J Nucl Med 44:1911–1917
137. Segall GM (2001) FDG PET, imaging in patients with lymphoma: a clinical perspective. J Nucl Med 42:609–610
138. Spaepen K, Stroobants S, Dupont P et al (2001) Prognostic value of positron emission tomography (PET) with fluorine-18 fluorodeoxyglucose ([18F]FDG) after first-line chemotherapy in non-Hodgkin's lymphoma: is [18F]FDG-PET a valid alternative to conventional diagnostic methods? J Clin Oncol 19:414–419
139. Ben-Haim S, Ell P (2009) 18F-FDG PET and PET/CT in the evaluation of cancer treatment response. J Nucl Med 50:88–99
140. Römer W, Schwaiger M (1998) Positron emission tomography in diagnosis and therapy monitoring of patients with lymphoma. Clin Positron Imaging 1:101–110
141. Paes FM, Kalkanis DG, Sideras PA et al (2010) FDG PET/CT of extranodal involvement in non-Hodgkin lymphoma and Hodgkin disease. Radiographics 30:269–291
142. Wahl RL, Hutchins GD, Buchsbaum DJ et al (1991) 18F-2-deoxy-2-fluoro-D-glucose uptake into human tumor xenografts. Feasibility studies for cancer imaging with positron-emission tomography. Cancer 67:1544–1550
143. Crippa F, Leutner M, Belli F et al (2000) Which kinds of lymph node metastases can FDG PET detect? A clinical study in melanoma. J Nucl Med 41:1491–1494
144. Rossi CR, De Salvo GL, Trifirò G et al (2006) The impact of lymphoscintigraphy technique on the outcome of sentinel node biopsy in 1,313 patients with cutaneous melanoma: an Italian Multicentric Study (SOLISM-IMI). J Nucl Med 47:234–241
145. Vallabhajosula S, Solnes L, Vallabhajosula B (2011) A broad overview of positron emission tomography radiopharmaceuticals and clinical applications: what is new? Semin Nucl Med 41:246–264
146. Avril N, Rose CA, Schelling M et al (2000) Breast imaging with positron emission tomography and fluorine-18 fluorodeoxyglucose: use and limitations. J Clin Oncol 18:3495–3502
147. Dose Schwarz J, Bader M, Jenicke L et al (2005) Early prediction of response to chemotherapy in metastatic breast cancer using sequential ^{18}F-FDG PET. J Nucl Med 46:1144–1150
148. Groheux D, Espie M, Giacchetti S et al (2013) Performance of FDG PET/CT in the clinical management of breast cancer. Radiology 266:388–405
149. NCCN Clinical Practice Guidelines in Oncology (NCCN guidelines). National Comprehensive Cancer Network. Version 4 2017-2018
150. Crippa F, Seregni E, Agresti R et al (1998) Association between [18F]fluorodeoxyglucose uptake and postoperative histopathology, hormone receptor status, thymidine labelling index and p53 in primary breast cancer: a preliminary observation. Eur J Nucl Med 25:1429–1434
151. Ueda S, Tsuda H, Asakawa H et al (2008) Clinicopathological and prognostic relevance of uptake level using 18F-fluorodeoxyglucose positron emission tomography/computed tomography fusion imaging (18F-FDG PET/CT) in primary breast cancer. Jpn J Clin Oncol 38:250–258
152. Wang CL, MacDonald LR, Rogers JV et al (2011) Positron emission mammography: correlation of estrogen receptor, progesterone receptor, and human epidermal growth factor receptor 2 status and 18F-FDG. AJR Am J Roentgenol 197:W247–W255
153. Alexandraki KI, Kaltsas G (2012) Gastroenteropancreatic neuroendocrine tumors: new insights in the diagnosis and therapy. Endocrine 41:40–52
154. Crown A, Rocha FG, Raghu P et al (2020) Impact of initial imaging with gallium-68 dotatate PET/CT on diagnosis and management of patients with neuroendocrine tumors. J Surg Oncol 121:480–485
155. Rust E, Hubele F, Marzano E, Goichot B, Pessaux P et al (2012) Nuclear medicine imaging of gastro-entero-pancreatic neuroendocrine tumors. The key role of cellular differentiation and tumor grade: from theory to clinical practice. Cancer Imaging 21(12):173–184
156. Taïeb D, Jha A, Treglia G, Pacak K (2019) Molecular imaging and radionuclide therapy of pheochromocytoma and paraganglioma in the era of genomic characterization of disease subgroups. Endocr Relat Cancer 26:R627–R652
157. Nuñez R, Macapinlac HA, Yeung HW et al (2002) Combined ^{18}F-FDG and 11C-methionine PET scans in patients with newly progressive metastatic prostate cancer. J Nucl Med 43:46–55
158. Even-Sapir E, Metser U, Mishani E et al (2006) The detection of bone metastases in patients with high-risk prostate cancer: ^{99m}Tc-MDP planar bone scintigraphy, single- and multi-field-of-view SPECT, ^{18}F-fluoride PET, and ^{18}F-fluoride PET/CT. J Nucl Med 47:287–297
159. Apolo AB, Pandit-Taskar N, Morris MJ (2008) Novel tracers and their development for the imaging of metastatic prostate cancer. J Nucl Med 49:2031–2041
160. Parent EE, Schuster DM (2018) Update on 18 F-Fluciclovine PET for prostate cancer imaging. J Nucl Med 59:733–739
161. Hofman MS, Emmett L, Sandhu S et al (2021) [177 Lu]Lu-PSMA-617 versus cabazitaxel in patients with metastatic castration-resistant prostate cancer (TheraP): a randomised, open-label, phase 2 trial. Lancet 397:797–804

13 Basis of Therapeutic Nuclear Medicine

Abdelhamid H. Elgazzar and Ismet Sarikaya

13.1 Introduction

Therapeutic applications of nuclear medicine are expanding (Table 13.1). Until 5–10 years ago, the use of radioisotopes in therapy was limited predominantly to treatment of hyperthyroidism and thyroid cancer with I-131, polycythemia rubra vera with P-32, bone metastases(palliative) with strontium-89 (Sr-89), rhenium-186 (Re-186), samarium-153 (Sm-153), tin-117m (Sn-117), liver tumor and metastases with Y-90 microspheres and neuroblastoma, pheochromocytoma, and paraganglioma with I-131 MIBG. In recent years Lu-177 and Y-90 labeled somatostatin analogs for the treatment of neuroendocrine tumors (NETs), Lu-177 labeled PSMA ligands and Ra-223 dichloride for metastatic prostate cancer have been increasingly used.

It is not the objective of this chapter to discuss different protocols and experiences in the treatment of various conditions using radioisotopes. Rather, the objective is to explore some of the pathological features of the disease processes being treated, the underlying theory behind the action of the radioisotopes that induce therapeutic effects.

A. H. Elgazzar (✉) · I. Sarikaya
Department of Nuclear Medicine, Faculty of Medicine, Kuwait University, Kuwait City, Kuwait

Generally, treatment options for cancer may be local (surgery or external beam radiation) or systemic. The role of nuclear medicine focuses on a targeted systemic approach (Fig. 13.1), whether dealing with a primary tumor or with its metastatic foci.

13.2 Treatment of Hyperthyroidism

For more than 60 years, iodine-131 has been used to treat most cases of Graves' disease and hyperfunctioning nodules. It has become the modality of choice in treating Graves' disease, with the result that surgeons are becoming less and less

Table 13.1 Therapeutic applications of nuclear medicine

Oncologic
1. Lymphomas and leukemias
2. Polycythemia rubra vera
3. Solid tumors (thyroid carcinoma, neuroblastoma, ovarian, prostate, breast, osteogenic sarcoma, others)
4. Treatment of metastasis-induced bone pain
Non-oncologic
1. Benign thyroid disease particularly hyperthyroidism
2. Radionuclide synovectomy
3. Bone marrow ablation
4. Intravascular radionuclide therapy for prevention of restenosis

A. H. Elgazzar (ed.), *The Pathophysiologic Basis of Nuclear Medicine*,
https://doi.org/10.1007/978-3-030-96252-4_13

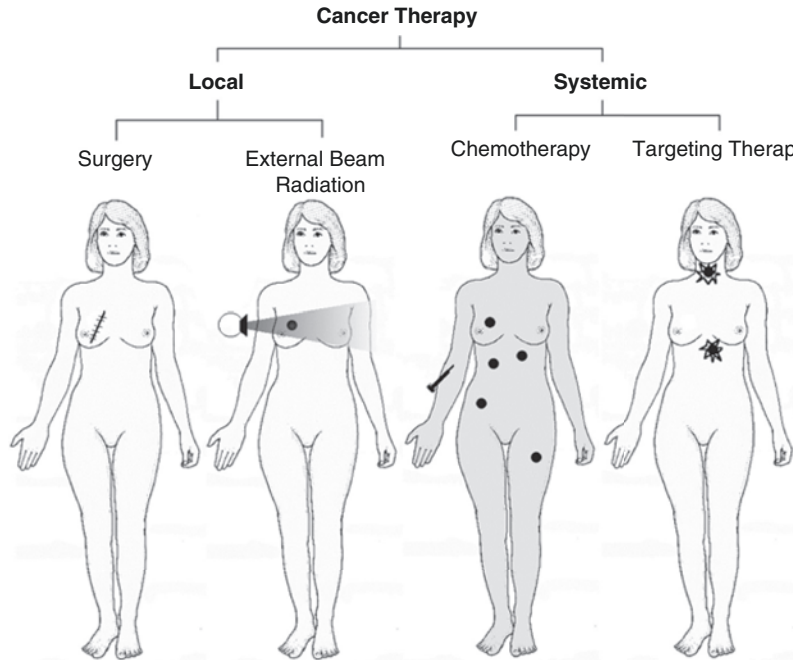

Fig. 13.1 The major types of cancer therapy. Nuclear medicine uses principally the targeting method in treating cancer and cancer metastases (modified from Prvulovich et al. [1])

experienced in thyroidectomy since the number of operations has decreased significantly. In a recent Canadian survey study, endocrinologist were found to be the most common to prescribe I-131 for malignant, while nuclear medicine physicians were the most in prescribing it for benign disease [2].

The normal thyroid gland varies in shape between individuals, and the average weight is approximately 20 g. The gland utilizes iodine for the synthesis of thyroid hormones (see Chap. 7). The cells of the gland do not differentiate between stable iodine and radioactive iodine. Accordingly, if radioactive iodine is administered, it is trapped and then organified by thyroid follicular cells exactly like nonradioactive iodine.

13.2.1 Pathophysiology

After oral administration, I-131 iodide is absorbed rapidly from the upper gastrointestinal tract, 90% within 60 min. After entering the blood stream, the iodide is distributed in the extrathyroid compartment similar to the stable iodide and leaves this compartment to be taken up by the thyroid and by renal excretion. Approximately 20% of the administered activity is taken up normally by the thyroid gland. A small amount of I-131 is also found in the salivary glands, gastric mucosa, choroid plexus, breast milk, and placenta. Up to 75% is excreted by the kidney and 10% by fecal excretion. Approximately 40% of the administered activity has an effective half-life of 0.43 days while 60% has an effective half-life of 7.6 days.

Graves' disease is the most common form of hyperthyroidism, comprising approximately 56% of all cases. It is also the major immunologically mediated form. It occurs most commonly in young women and is characterized by symptoms of hyperthyroidism with or without ophthalmopathy and dermopathy. Rarely, lymphadenopathy and splenomegaly may be present. The thyroid gland is usually diffusely enlarged but sometimes normal in size. The condition is an autoimmune process with autoantibodies directed against the TSH receptors on thyroid follicular cells which may be stimulatory and/or destructive [3]. Thyroid stimulatory antibodies include long-acting thyroid stimulator (LATS). This antibody is detected in most patients with Graves' disease and behaves like TSH, stimulating the production of thyroid hormones and consequently trapping and organifying radioiodine. The other stimulatory antibody is the LATS protector, the antibody

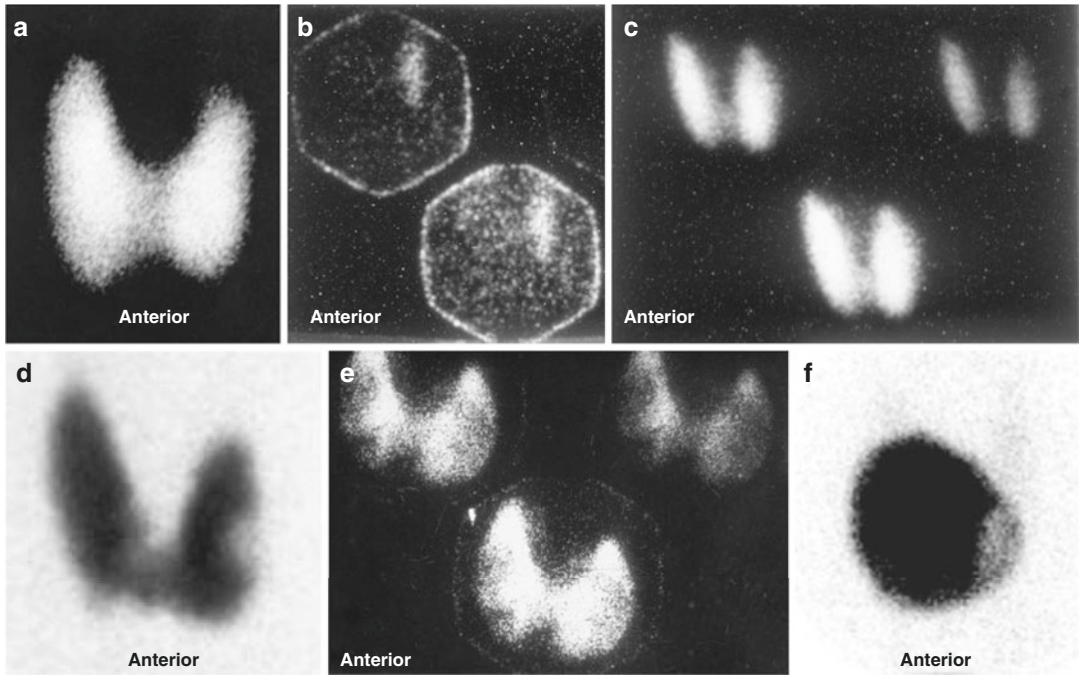

Fig. 13.2 Examples of thyroid scans of patients with hyperthyroidism illustrating patterns that affect the treatment strategy using iodine-131. (**a**) Illustrates pattern of uniform uptake in a patient with Graves' disease. Note that scans of patients during recovery phase of thyroiditis may simulate Graves' disease scintigraphically and show high uptake. Example (**b**) is of a patient with subacute thyroiditis. Scan shows decreased and nonuniform uptake with a 24-h uptake of 1%. Follow-up scan (**c**) shows uniform uptake throughout the gland with an uptake of 38%. This may be mistaken for Graves' disease if the patient is referred first during this phase. Example (**d**) shows diffusely toxic gland with significant nonuniformity and multiple cold nodules. Example (**e**) shows a scan of a patient with Graves' disease and a colloid nodule illustrating another pattern of "Marine–Lenhart" syndrome which is more resistant to iodine-131 therapy. Compare this pattern to that of multiple toxic nodules (Fig. 7.2). This pattern also needs to increase activity per gram of tissue for successful treatment. Example (**f**) is for autonomous single toxic adenoma which is treated by relatively high activity

that prevents degradation of LATS; accordingly, it helps to stimulate thyroid cells indirectly. The disease is associated with other autoimmune disorders such as pernicious anemia and myasthenia gravis.

Graves' disease is also known to be associated in Caucasians with HLA B8, DR2, and DR3 and with an inability to secrete certain glycoproteins coded for on chromosomes 6 and 19. A 50% concordance rate is seen among monozygous twins while 5% concordance is noted in dizygous twins. These facts suggest a genetic susceptibility for the disease. The observation that *Yersinia enterocolitica* and *Escherichia coli* and other gram-negative organisms contain TSH binding sites raised the possibility that the initiating event in the pathogenesis of the disease may be infectious in genetically susceptible individuals.

Histologically, there is hyperplasia of the thyroid epithelium, sometimes with papillary unfolding. Lymphocytic infiltration is present, usually less than in other forms of autoimmune diseases as postpartum thyroiditis. Little colloid storage is also seen. With time, the untreated gland will show progressive fibrosis and the end stage will lead to hypothyroidism, which may be considered part of the natural history of the disease [4, 5].

Thyroid scintigraphy shows uniform uptake throughout the gland or, less commonly, varying degrees of nonuniform uptake. This nonuniformity is related predominantly to different stages of involution of the disease with variable amounts of fibrosis based on the duration of the disease or the presence of nodules (Fig. 13.2). The presence of a TSH-dependent functioning nodule in a dif-

fusely toxic gland has been referred to as Marine–Lenhart's syndrome (Fig. 13.2). Since the function of such nodule is much less than the surrounding hyperfuctioning tissue, it appears scintigraphically cold.

Ophthalmopathy occurs in approximately 50% of patients with Graves' disease [6]. Infiltration of extraocular muscles by an inflammatory reaction consisting predominantly of lymphocytes is the main pathological feature of ophthalmopathy. These lymphocytes are believed to be sensitized to antigens common to the orbital muscles and thyroid gland. Similar inflammatory infiltrates may also be present in the dermis, causing the dermopathy or pretibial myxedema which may be present in up to 10% of patients with unclear etiology.

Single thyroid nodules can, via an autonomous function, secrete sufficient thyroid hormone to cause hyperthyroidism. These nodules are usually greater than 3 cm in diameter in order to be capable of producing this level of function [7]. Hyperfunction may also arise in a gland containing multiple nodules [8]. In this case, the secretion of thyroid hormones can be either from hyperfunctioning nodules that are assumed to be autonomous or from the internodule parenchyma, which may be an expression of Graves' disease in an otherwise nodular goiter. The nodules in the latter situation may be cold or a mixture of cold and hot, hypertrophic nodules. The term Plummer's disease, or toxic nodular goiter, has been used to designate hyperthyroidism in glands with both single and multiple toxic nodules. The term nodular toxic goiter may be reserved for a toxic gland that contains nodules that are not hyperactive. The presence of cancer in toxic nodular goiter is extremely rare and varies from 0.1 to 0.9%. The toxic nodular goiter may have a cold nodule representing a TSH-dependent adenoma. Scintigraphic imaging cannot exclude malignancy in the cold nodule that is not TSH dependent.

The therapeutic effects of I-131 sodium iodide are due to the emission of ionizing radiation from the decaying radionuclide. In benign conditions such as Graves' disease, division of some metabolically active cells is prevented by the effect of this ionizing radiation. Cell death is another mechanism activated when the cells are exposed to high levels of radiation, particularly when high doses are given to patients with toxic adenoma, where the suppressed normal thyroid tissue is essentially spared with delivery of a very high concentration to the cells of the toxic nodule. Cell death is followed by replacement with connective tissue, which may lead to hypothyroidism, depending on the number of cells destroyed and replaced by fibrous nonfunctioning tissue. Since 90% of the radiation effects of I-131 are due to beta radiation, which has a short range in tissue of 0.5 mm, the extrathyroid radiation and consequently the side effects are minimal. It has been estimated that 15% of patients treated with I-131 may show worsening of ophthalmopathy [9, 10]. Since posttreatment hypothyroidism has been associated with exacerbation of ophthalmopathy, lower-dose radioactive iodine or starting replacement hormones early (2 weeks) after therapy along with the use of prednisone 40–80 mg per day tapered over 3 months may prevent severe eye disease in up to two thirds of patients [11, 12]. It is interesting that cigarette smoking has been also implicated as a risk factor for progression of Graves' ophthalmopathy [10].

13.2.2 Factors Affecting the Dose of I-131 Used for Therapy of Hypothyroidism

Several factors affect the therapeutic dose to be administered to patients suffering from hyperthyroidism. These include some parameters related to the patient, such as age, sex, medical history, and duration of treatment with antithyroid medications, and factors related to the gland itself, particularly its size, the level of radioiodine uptake, scintigraphic findings of uniform or nonuniform uptake, and whether nodules are present. Additionally, the dose is dependent on how the therapist defines the goals of therapy. If the control of thyrotoxicosis is the most important consideration, the total dose or the dose per gram of estimated thyroid tissue weight will be higher than when the therapist is trying to avoid or delay

hypothyroidism [13]. Using empirical low-dose iodine therapy to avoid hypothyroidism has been shown to result in persisting hyperthyroidism in up to 54% of patients [14]. Additionally, it has been found that the rate of hypothyroidism is not different among those treated with low-dose and high-dose radioiodine [15].

13.3 Treatment of Differentiated Thyroid Cancer

Radioactive iodine is the mainstay of therapy for residual, recurrent, and metastatic thyroid cancer that takes up iodine and cannot be resected, for presumed disease (adjuvant therapy), and ablation of residual thyroid tissue. Radioactive iodine adjuvant therapy is routinely recommended after total thyroidectomy for high-risk differentiated thyroid cancer patients by the American Thyroid Association (ATA) [16]. Per ATA, radioactive iodine remnant ablation is not routinely recommended after lobectomy or total thyroidectomy for patients with unifocal papillary microcarcinoma, in the absence of other adverse features [16]. The tissue of normal thyroid and its tumors expresses a variety of oncogenes, growth factors, and growth factor receptors. There is increased expression of some oncogenes, namely, c-myc/c-fos and c-ras, in some epithelial and medullary thyroid carcinomas.

C-myc mRNA and c-fos mRNA are found in high levels in papillary carcinomas compared with the surrounding normal thyroid tissue. Patients with an unfavorable prognosis were twice as likely to overexpress c-myc as patients with good prognosis [17].

Ras oncogenes were found in 80% of follicular and 20% of papillary carcinomas. This high prevalence of transforming ras oncogenes in follicular carcinomas may explain its aggressive behavior in comparison to papillary carcinoma and may suggest a role of this oncogene in the metastatic phenotype of this cancer [18]. Recently a tissue-specific oncogene associated with papillary carcinoma has been identified.

Excessive growth factor and increased expression of oncogenes encoding growth factors or growth factor expression, such as the oncogene of c-ras B were identified in papillary carcinoma, adenomas, and anaplastic carcinoma.

Besides the importance of growth factors in the development of thyroid carcinoma, links have also been found to certain risk factors. The most important of these is radiation exposure. Exposure to radiation following the explosion of the atomic bombs in Japan, as well as after head and neck radiation, resulted in a 30-fold increase in the incidence of thyroid cancer [19].

About 90% or more of thyroid carcinomas are well differentiated, of the papillary, papillofollicular, follicular, and Hürthle-cell types, which take up iodine and accordingly can be successfully treated with I-131. The therapeutic effects on differentiated thyroid cancer, where larger doses of radioactive iodide are administered, are based on destruction of cells of the residual thyroid tissue and the functioning carcinoma cells by the high dose of administered radionuclide. The mortality of patients treated with subtotal thyroidectomy and limited I-131 therapy was found to be three to four times higher than that of patients treated with total thyroidectomy and I-131 therapy to ablate known foci of radioiodine uptake [20] (Fig. 13.3). Because of the larger dose of radionuclide and the lower uptake by the tissue in the case of thyroid cancer, more side effects can be seen, particularly transient sialadenitis, than in treatment of hyperthyroidism. This however does not justify using limited therapy such as 30 mCi. A recent study confirmed the high rate of efficiency of the high ablative dose of 100 mCi of I-131 particularly in patients with less than 2% neck uptake values [21]. This study confirmed also that success rate is dependent on the pre-therapy neck uptake. The success rate was 94% when pre-ablation uptake was less than 2, 80% with uptake between 2 and 5, and 60% when uptake value was more than 5% [21].

Thyroglobulin and calcitonin are the major tumor markers for thyroid cancer of the follicular epithelium and parafollicular C cells, respectively. These markers are unique, in the sense that they are not only specific for tumor tissue but are also specific components of normal thyroid tissue. Thyroglobulin is an iodinated glycoprotein

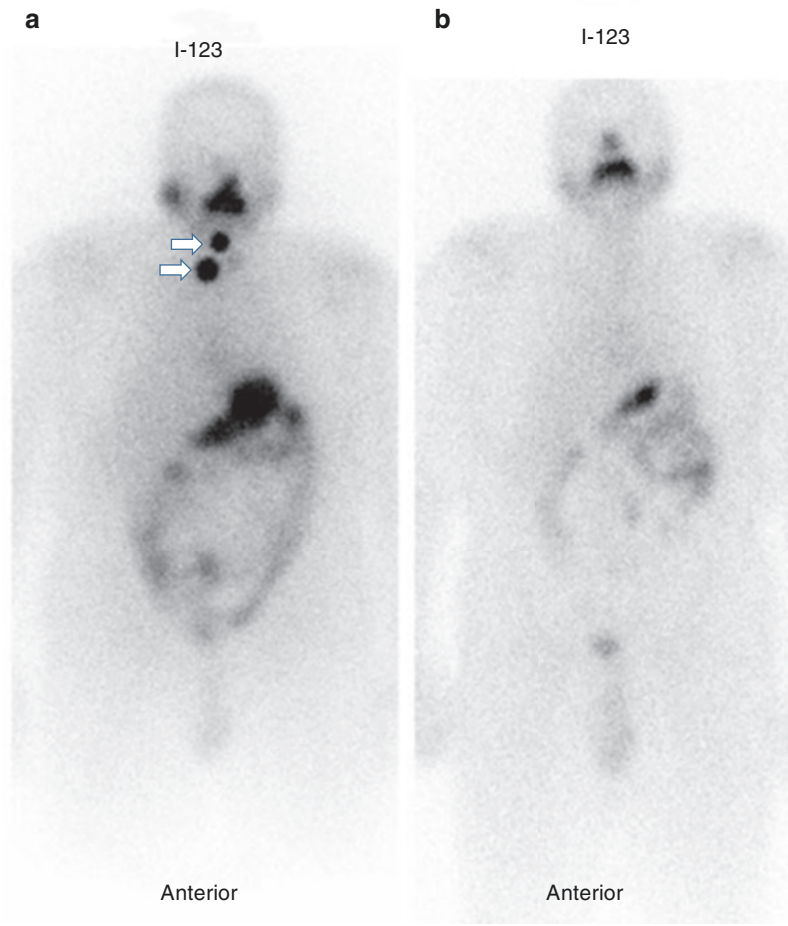

Fig 13.3 ^{123}I whole-body scan (**a**) for a patient with papillary thyroid carcinoma treated with total thyroidectomy. The scan shows neck activity (*arrows*). Follow-up scan (**b**) one year after I-131 ablation shows complete resolution

essential for synthesis and storage of thyroid hormones. Since thyroglobulin is produced exclusively by thyroid tissue, only very small amounts can be found in the blood after thyroidectomy and ablative radioiodine therapy. Accordingly, any post-therapeutic elevation of its levels indicates either remnant thyroid tissue, requiring further ablative treatment, or the presence of metastases or local recurrence. Other tumor markers used for many other tumors, such as carcinoembryonic antigen (CEA) and tissue polypeptide antigen (TPA), are not specific for thyroid cancer. TPA, which is a cytokeratin-related nonspecific proliferation marker, has a sensitivity of 40–60% for thyroid cancer. However, it has a good correlation with tumor progression or therapeutic response, with a high positive predictive value of 90%. Evaluation of ablative therapy and follow-up of patients post ablation to monitor disease recurrence has further improved and facilitated by the availability of recombinant human thyrotropin as well as the use of F-18 FDG positron emission tomography. The value of recombinant human thyrotropin (rhTSH) rests on providing the opportunity to obtain diagnostic whole-body I-131 scan under adequate TSH elevation as well as representative thyroglobulin levels while the patients receiving their thyroid hormone [22]. FDG-PET is useful in evaluating patients in instances where radioiodine imaging fails to identify known or suspected recurrent or metastatic disease [23]. Additionally, the use of Tl-201 and Tc-99m MIBI particularly when FDG-PET is not available is of value for this purpose [24].

There are many purposes to ablate postoperative normal residual thyroid tissue with I-131. Residual thyroid tissue, if large, can cause start

artifact and obscure the surrounding nodal uptake on radioiodine images. It can also take up most of the activity and leave small amount of activity for metastatic foci. It can mimic local/regional disease. It can harbor micrometastases. Residual thyroid tissue will also continue producing Tg and make Tg measurements unreliable. The usual amount of I-131 activity for ablation of the thyroid remnant is 1.11–3.7 GBq (30–100 mCi) which depends on the radioactive iodine uptake measurement and amount of residual thyroid tissue.

13.4 Treatment of Pain Secondary to Skeletal Metastases

Approximately 75% of patients with advanced cancer have pain, with a high percentage due to skeletal metastases. Bone metastases cause intractable pain, which affects the quality of life for the patient, especially if it is associated with immobility, anorexia, and anxiety, with the consequent long-term use of narcotic analgesics. The mechanism of bone pain may not be clear in many of these patients and could be due to cell-secreted pain modulators such as interleukin-1 beta, interleukin-8, and interferon [25]. Depending on the extent of bone metastases, radiation therapy or radiopharmaceuticals can be used instead of narcotics to alleviate the pain with the objective of improving the quality of life.

Radiotherapy for focal painful metastases with delivery of 2000–3000 rads induces pain relief in 60–90% of cases [26, 27]. Controlling pain of multiple metastases using external beam radiotherapy is difficult. Hemibody irradiation using 800 rads to the lower half of the body and 600 rads to the upper half has resulted in complete response in 30%, partial response in 50%, and no response in 20% of patients. Radiotherapy used for painful skeletal metastases often produces significant side effects such as nausea, vomiting, and diarrhea, as well as bone marrow toxicity in one third of patients. Vomiting and diarrhea can be severe in 10% of cases and hematological side effects can be life threatening in approximately 9% of patients [28].

Bone-seeking radiopharmaceuticals emitting beta particles have been used to deliver local radiotherapy to metastases to decrease pain at their sites. Radiopharmaceuticals which are taken up at the sites of bone metastases will cause less toxicity than external radiation therapy. These radiopharmaceuticals control pain while causing only transient bone marrow depression, which is usually mild. The uptake of these radiopharmaceuticals by metastases is several fold (up to 15–20 times) that of normal bone. These agents are absorbed to hydroxyapatite crystals at the site of active new bone, similar to Tc99m-MDP. They include phosphorus-32, strontium-89, rhenium-186 diphosphonate, and samarium-153 EDTMP. The list of radiopharmaceuticals for bone palliation has been increasing including Re-188, Lu-177, and others [29].

13.4.1 Radiopharmaceuticals

13.4.1.1 Strontium-89 Chloride (Sr-89 Chloride)

Systemic radionuclide therapy with Sr-89 chloride was first used to relieve pain from bone metastases in 1937 and regained popularity in the 1980s. It is a pure beta emitter with a relatively long half-life of 50.5 days. It is a chemical analogue of calcium, and accordingly it concentrates avidly in areas of high osteoblastic activity. After intravenous injection, strontium quickly accumulates in the mineral bone matrix where active bone formation takes place. Therefore, there is preferential uptake in and around metastatic tumor deposits which has been confirmed by external measurements using the gamma emitting radionuclide Sr-85 and by autoradiography. It was found that Sr-89 concentration is 2–20 times greater in bone metastases than normal bone [30]. The biological half-life of Sr-89 in bone lesions is about 90 days, compared to about 2 weeks in normal bone which can be explained by the immature nature of reactive bone compared to normal lamellar bone. This selective uptake and prolonged retention at sites of increased bone mineral turnover provide precise targeting of bone lesions. The radionuclide is

typically administered as a single 150 MBq (4 mCi) intravenous dose. Overall, pain relief occurs in up to 80% of patients, of whom 10–40% became effectively pain free. The mean duration of palliation is 3–4 months [31, 32]. Furthermore, 89Sr-chloride may cause slowing of metastatic progression due to inhibition of expression of cell adhesion molecules (E-selectins) that participate in the metastatic process. The significant transient decrease in serum E-selectin concentration as observed after systemic radionuclide therapy in a study on 25 men with metastatic prostate carcinoma is an indication of such an observation [33] and may provide opportunities for clinical trials.

13.4.1.2 Samarium-153 Ethylenediaminetetramethylene Phosphonate (Sm-153-EDTMP)

Samarium-153 is produced in the nuclear reactor by neutron activation of both natural Sm-203 and 98% enriched Sm-152 targets. It has a relatively short half-life of about 48 h. Coupling of the radionuclide to ethylenediaminetetramethylene phosphonate (EDTMP) leads to the high uptake of the radionuclide by bone. Gamma camera imaging is possible due to the 103 KeV gamma ray emitted during decay of Sm-153. The resulting images are similar to those obtained with Tc99m-MDP or other diphosphonates showing increased uptake at the site of metastases. The calculated lesion to normal-bone ratio was reported to be 4.0 and to soft-tissue ratio to be 6.0 [34].

Administration of 153Sm-EDTMP according to the supplier's recommendations at 37 MBq (1 mCi)/kg would deliver a bone marrow dose of 3.27–5.90 Gray (Gy) which would induce myelotoxicity as a side effect. Dosimetric calculation by urine collection and whole-body scintigraphy has been used to limit the bone marrow dose to 2 Gy by Cameron and associates [35]. This was achieved by anterior and posterior whole-body images obtained 10 min and 5 h after the intravenous injection of 740 MBq (20 mCi) of 153Sm-EDTMP with determination of bone activity by imaging and by counting urine collected for 5 h. The total administered activity of 153Sm-EDTMP predicted on a 2 Gy bone marrow dose was found to be 35–63% of the standard recommended dose of 37 MBq/kg. The authors reported pain relief in eight of the ten patients treated using this dosimetric method [35].

13.4.1.3 Rhenium-186 Ethylene Hydroxy Diphosphonate (Re-186-EHDP)

Similar to Sm-153, Re-186 has been coupled to a bone-seeking phosphonate, ethylene hydroxy diphosphonate (EHDP). This radionuclide emits beta particles with a maximum energy of 1.07 MeV and gamma photons with an energy of 137 keV which allows bone scanning. Re-186-EHDP undergoes renal excretion within 6 h after intravenous injection, as is the case with the common bone-scanning agents. At 4 days, 14% of the radioactivity remains in bone [36].

Several studies have shown encouraging clinical results of palliative therapy using 186Re-HEDP with an overall response rate of approximately 70% for painful osseous metastasis from prostate and breast cancer. Myelosuppression has been limited and reversible, which makes repetitive treatment safe [37, 38]. In a study of 31 patients with various cancers (10 prostate, 10 breast, 4 rectum, 5 lung, 2 nasopharynx) and bone metastases treated with a fixed dose of 1295 MBq (35 mCi) of Re-186 HEDP. When necessary, the same dose was repeated two to three times after an interval of 10–12 weeks. The mean response rate was 87.5% in patients with breast and prostate cancer, 75% in patients with rectal cancer, and 20% in patients with lung cancer. The overall response rate was 67.5% and the palliation period varied between 6 and 10 weeks. The maximal palliation effect was observed between the third and seventh weeks [38].

13.4.1.4 Tin-117m-Diethylenetriaminepentaacetic Acid (Sn-117m-DTPA)

Tin-117m is a reactor produced radionuclide, with a half-life of 13.6 days. Contrary to the other radionuclides mentioned above, this radionuclide emits internal conversion electrons. Tin-117m is linked to diethylenetriaminepentaacetic acid (DTPA). More than 50% of the administered

activity is absorbed by bone in patients with metastatic carcinoma with a bone to red marrow ratio of up to 9:1. Its 159 keV photon energy allows correlative imaging with a similar uptake pattern as Tc99m-MDP [39].

In a preliminary study in 10 patients by Atkins et al. [40], none of the patients who received Sn-117m-DTPA for palliation developed marrow toxicity. Another recent study on 47 patients treated with Sn-117-DTPA showed that the experimental mean absorbed dose to the femoral marrow was 0.043 cGy/KBq. In comparison to P-32-orthophosphate, Sn-117m-DTPA yielded up to an eightfold therapeutic advantage over the energetic beta emitter P-32. Accordingly, it was suggested that internal conversion electron emitter Sn-117m offers a large dosimetric advantage over the energetic beta-particle emitters allowing higher administered activity for alleviating bone pain, while minimizing marrow toxicity [41].

13.4.1.5 Phosphorus-32 Orthophosphate

This radionuclide is used uncommonly for the treatment of bone metastases. Dosimetric studies have demonstrated a relatively high dose to the bone marrow from the highly energetic beta particles of this radionuclide causing myelosuppression with pancytopenia. Increased incidence of acute leukemia has been reported although this was reported following P-32-therapy in patients with polycythemia vera.

13.4.1.6 Rhenium-188 Dimercaptosuccinic Acid Complex [Re-188(V)DMSA]

Re-188(V)DMSA, a potential therapeutic analogue of the tumor imaging agent Tc99m(V) DMSA, is selectively taken up in bone metastases. In a study by Blower et al. [42] on ten patients with metastatic prostate cancer studied by Tc99m(V)DMSA and 188Re(V)DMSA to compare their biodistribution, only minor differences between both radiopharmaceuticals were found. Accordingly, Tc99m(V)DMSA scans are predictive of 188Re(V)DMSA biodistribution and could be used to estimate tumor and renal dosimetry and assess suitability of patients for Re-186(V) DMSA treatment [42]. This advantage makes this tracer a candidate for more trials as a potentially successful agent for bone metastases palliation.

13.4.1.7 Ra-223 Dichloride

Ra-223 dichloride has both palliative and therapeutic effect approved for the treatment of castration-resistant prostate cancer with symptomatic bone metastases. This will be discussed in Metastatic Prostate Carcinoma section.

13.4.2 Mechanism of Action

Metastatic bone pain is believed to be due to mechanical factors due to local bony destruction and to humoral factors resulting from secretion of certain mediators by tumor and peri-tumoral cells (Table 13.2). Although the mechanism of action of these radiopharmaceuticals in relieving bone pain is not completely known, the therapeutic effect is thought to be achieved by delivering suf-

Table 13.2 Types of cellular damage in relation to approximate radiation dose

Dose (grays (rads))	Type of damage	Comments
0.01–0.05 (1–5)	Mutation (chromosomal aberration, gene damage)	Irreversible chromosome breaks, may repair
1 (100)	Mitotic delay, impaired cell function	Reversible
3 (300)	Permanent mitotic inhibition, impaired cell function, activation and deactivation of cellular genes and oncogenes	Certain functions may repair; one or more divisions may occur
>4–10 (>400–1000)	Interphase death	No division
500 (50,000)	Instant death	No division
		Proteins coagulate

Modified from Maxon et al. [4] with permission

ficient energy from the sites of reactive bone directly to the cells of metastases and/or to peritumor cytokine-secreting cells that may be responsible for the patient's pain. Pain relief by radiation was found to be independent of the radiosensitivity of the tumor and therefore the mechanism of action does not involve actual killing of the tumor cell. It is more likely that radiation interrupts processes that are maintained by humoral pain mediators in the microenvironment of the tumor [43]. This view is also supported by absence of a dose-response relationship [44].

13.4.3 Choice of Radiopharmaceutical

It has been demonstrated that myelosuppression is less severe using radionuclides with relatively shorter half-lives favoring the use of Sm-153, Re-186, Sn-117, and Sr-89. Other physical properties including radiolabeled conjugate biological uptake and clearance, product-specific activity, range and type of emissions, and resultant effects on tumor and normal tissue cellular survival should be all considered along with the clinical outcome to choose a radiopharmaceutical. The response rate of different radiopharmaceuticals currently in use appears not to differ significantly [45].

13.4.4 Clinical Use

Radiopharmaceutical therapy is indicated for the treatment of patients with painful widespread bone metastases. However, the patient with pain secondary to either spinal cord or peripheral nerve invasion by adjacent metastases will not benefit from such treatment. The contraindication in pregnancy is absolute, and relative contraindications include preexisting severe myelosuppression, urinary incontinence, severe insufficiency, and spinal cord compression or pathological fracture. A pre-therapy bone scan within 3 mos, neurological examination, and blood counts should be available before the patient is treated. Follow-up blood counts should be performed at least biweekly to evaluate myelotoxicity. The response to these radiopharmaceuticals is more or less similar, with an average success rate of 70–80% [46–52].

The difference in half-life of the radiopharmaceuticals and the extent of bone metastases has consequences for both the onset and the duration of pain relief. Relief rates using the newer agents are not significantly different and are comparable with those of external beam radiotherapy, but side effects are minimal and compare favorably with those of the older agent P-32.

Using radionuclide along with chemotherapy for palliation is being investigated and may proof useful. Palmedo et al. reported a case of a patient with disseminated bone metastases due to breast cancer and multifocal pain. Because of persisting pain after a first cycle of chemotherapy, 1295 MBq Re-186 HEDP was administered and pain relief was significant. Subsequently, the patient received combined chemotherapy along with Re-186 HEDP therapy and remained pain free. Follow-up Tc99m-MDP bone scan showed significant regression of osseous metastases. The authors speculated that the combination of Re-186 HEDP and chemotherapy resulted in significantly increased palliation of metastatic bone disease [53].

The side effects, which are mainly hematological, vary among the agents used, being more pronounced with P-32 than with the newer agents. Some agents have the advantage of emitting gamma energy suitable for scintigraphy such as samarium-153 EDTMD (ethylenediaminetetramethylene phosphonate). Tin-117m DTPA differs from the other radiopharmaceuticals in that it emits conversion electrons rather than beta particles. These conversion electrons have low energy and a shorter path in tissue and may then result in less marrow toxicity [50, 54].

13.5 Treatment of Neuroendocrine Tumors

Neuroendocrine tumors constitute a heterogeneous group of neoplasms originating from neuroendocrine cells that secrete biogenic amines and polypeptide hormones. Recently, the incidence of these tumors has gradually increased worldwide. The clinical behavior of neuroendocrine tumors is significantly variable; they may be hormonally active or nonfunctioning, ranging from very slow-growing tumors to highly aggressive and very malignant tumors. Surgery is currently the only available curative treatment for these tumors, but for patients who have inoperable primary, recurrent or metastatic disease, few therapeutic options are available. The goals of radionuclide therapy for neuroendocrine tumors are to control symptoms and pain, improve the quality of life, reduce medical requirements, and stabilize the disease. Additionally, in limited disease it is used to reduce tumor volume, reduce hormone secretion, and help complete remission.

Several neuroendocrine tumors are candidates for radionuclide therapy. I-131 has been used to treat neuroblastoma, pheochromocytoma, and paraganglioma. More recently octreotide and other analogues labeled with In-111, Y-90, and Lu-177 are being used [55–57] (see later).

I-131 metaiodobenzylguanidine (MIBG) is being used for the treatment of pheochromocytoma, malignant paraganglioma, neuroblastoma, medullary thyroid carcinoma, and symptomatic carcinoid tumors. The radiopharmaceutical resembles guanethidine and is concentrated by normal and abnormal sympathetic adrenergic tissue.

When I-131 MIBG is administered intravenously, it is transported by blood to be taken up by normal adrenergic tissue such as the adrenal medulla and sympathetic nervous system and by tumors of neuroectoderm-derived tissue. The uptake by these tumors is secondary to active uptake-1 mechanism and passive diffusion through the cell membrane, followed by active intracellular transport to the neurosecretory granules in the cytoplasm, where it is retained.

In normal adrenergic tissue such as the adrenal medulla, heart, and salivary glands, as well as in pheochromocytoma, 90% of MIBG is stored in the neurosecretory granules, while in neuroblastoma it was found that up to 60% is stored within the extragranular cells. The major part of the radiopharmaceutical is excreted unchanged in urine. Other than in the adrenergic tissues, uptake is normally noted in the liver, spleen, urinary bladder, bowel, lungs, nose, near the trapezium muscle in children, and in the uterus in some women [58, 59]. The radiation effect is due to emission of beta particles from the decaying I-131 with a mechanism similar to that in treating thyroid disorders. A long list of medications is known to block the uptake and/or retention of MIBG by the target tissues, while some reports have suggested that others such as calcium channel blockers may increase its uptake. The mechanism of interference of these drugs varies. Beta-blockers, for example, interfere with the uptake by inhibiting the uptake mechanism-1 and by depleting the neurosecretory granules, while reserpine exerts this action by depleting the granules and inhibiting the intracellular transport. More recently peptide therapy has been increasingly used to treat these tumors (shown later in the chapter).

13.5.1 Neuroblastoma

Therapeutic amounts of I-131 MIBG can be delivered to neuroblastoma with acceptable bone marrow toxicity [60–62]. Among patients with stages 3 and 4 neuroblastoma who had failed treatment with chemotherapy, I-131 MIBG induced partial remission in many children and complete remission in a small number of patients. The agent has also been used for early therapy at the time of diagnosis, with a success rate comparable to that of chemotherapy with fewer side effects [61]. Since some neuroblastomas express somatostatin receptors, peptide receptor radionuclide therapy particularly with 177Lu-DOTA-TATE is also beneficial.

13.5.2 Pheochromocytoma

Malignant pheochromocytoma and its metastases are known to be resistant to chemotherapy and external beam radiation therapy. I-131 MIBG has a limited role in the treatment of malignant pheochromocytoma, functioning paraganglioma, and medullary carcinoma of the thyroid. Palliative effects have been achieved in patients with pheochromocytoma [63]. Several reports from the USA and Europe have collectively shown a response of 62.5% among patients with pheochromocytoma [45]. Soft-tissue metastases responded better than skeletal metastases.

13.5.3 Carcinoid Tumor

Carcinoid liver metastases are common and rarely can be resected. Treatment for symptomatic patients with unresectable disease includes chemotherapy, interferon alpha, and the somatostatin analogue, octreotide. The response to these medical therapies is usually poor. Hepatic artery ligation and embolization are alternatives and have a better response rate. Preliminary experience also suggests that external beam radiotherapy can be useful. I-131 MIBG and radiolabeled octreotide have recently been tried. I-131 MIBG is highly concentrated by more than 60% of carcinoid metastases. Carcinoid tumor cells stain positive for chromogranin A [64]. I-131 MIBG targets the metabolically active lesions, reduces the hormonal secretion, and improves symptoms [1, 65]. Data indicate a partial response in 20% of patients and a palliative effect in more than 50% of those with end-stage disease. I-131 MIBG causes temporary myelosuppression, which makes its use favorable compared with chemotherapy. It is also preferred to interferon alpha and octreotide, which require frequent subcutaneous injections.

Pathologically, I-131 MIBG produces gross cystic changes in liver metastases which probably are due to ischemic necrosis. Surgical deroofing and aspiration of cysts can lead to regeneration of normal liver tissue [1].

13.6 Radioimmunotherapy

Monoclonal antibodies are now contributing increasingly to cancer treatment, following early disappointments. I-131 anti-CD-20 and I-131 anti-CD-22 are good examples which are used for non-Hodgkin's lymphomas. These antibodies can be used alone to kill tumor cells or conjugated with drugs, cytotoxic agents, and radionuclides to improve their effects.

Radioimmunotherapy using monoclonal antibodies conjugated with isotopes allows the delivery of radiation to tumor tissue while sparing normal tissue. This radiation can be administered as a single large dose of radiolabeled monoclonal antibodies or, more commonly, in multiple fractions [66–68].

Although the way they work is not entirely clear, generally monoclonal antibodies can kill tumor cells through the following mechanisms [69]:

1. Activation of host immune system to lyse tumor cells, e.g., complement, antibody-dependent cellular cytotoxicity (ADCC)
2. Directing biologically active agents to tumor cells (e.g., drugs, toxins, cytokines, isotopes)
3. Triggering or interfering with the function of physiologically important cell receptors
4. Inducing indirect antitumor response by triggering the formation of autoantibodies or activation of cellular responses to tumor antigens to destroy tumor cells
5. Killing tumor cells by apoptosis, which is simply an intrinsic "programmed" cell death characterized by chromatin condensation and DNA degeneration

The use of radioimmunotherapy for treating lymphoma has been expanding in the last decade. It is currently being used for recurrent and relapsed disease of low-grade B cell and follicular and transformed lymphomas. Clinical trials are being conducted for aggressive B cell, mantle cell, and non-follicular indolent B cell types as well as chronic lymphocytic leukemia. Results of a study on the long-term impact of radioimmunotherapy using yttrium-90 (^{90}Y)–ibritumomab

tiuxetan in advanced-stage follicular lymphoma in first remission showed a median duration of progression-free survival of 4.1 years after radioimmunotherapy and 1.1 years for controls [70].

13.7 Radionuclide Synovectomy

There may be a need for a definitive solution to the joint pain of many arthropathies, particularly rheumatoid arthritis, after failure of conventional medications. Therapeutic nuclear medicine offers an alternative to surgical synovectomy. Several radiopharmaceuticals can destroy the synovial membrane when injected intraarticularly (radionuclide synovectomy or radiosynoviorthesis) and the patients become pain free.

Yttrium-90 colloid, erbium-169 citrate colloid, rhenium-186 colloid, phosphorus-32 (P-32) colloid, and others are all used to treat synovial disease [71, 72]. Since these colloids vary in their physical characteristics and thus in their range of penetrability, they are used differently to achieve the therapeutic effects and avoid injuring the surrounding tissue. Accordingly, some radiopharmaceuticals are used for the knee while others are used for small joints (Table 13.3). Yttrium-90 citrate or silicate is generally used for big joints such as the knee; rhenium-186 colloid is used for the shoulder, elbow, hip, and ankle; and erbium-169 citrate for the small joints in the hands and feet (Fig. 13.4).

13.7.1 Radiopharmaceuticals for Synovectomy

13.7.1.1 Yttrium-90 Colloid (^{90}Y)

This radionuclide is used predominantly for radionuclide synoviorthesis of the knee joint. It is also for malignant pleural and peritoneal effusions. The pharmacological characteristics of the silicate and citrate forms are the same. The average range in tissue is 3.6 mm and the maximum is 11 mm. After direct intra-articular administration the colloid penetrates into the surface cells of the synovia. Small amounts of particles are transported through the lymphatics, mainly after active or passive movement of the joint, from the knee to the regional lymph nodes. The safety of this modality of management has been reported, and hence the patients' age should not be regarded as a limiting factor [73]. It is recommended that Y-90 synoviorthesis should be performed in very young patients, when the amount of synovium is still moderate. Once the degree of synovitis has become severe, the expected results of radioactive synoviorthesis are worse [74].

Table 13.3 Physical properties and main uses of major radiopharmaceuticals for synovectomy

Isotope	Mode of decay	Physical half-life (days)	Main energy	Penetration range	Main use/adult dose
^{90}Y-silicate or citrate colloid with an average particle size of 10 nm	Emission of beta particles	2.7	2.24 MeV	3–5 mm in soft tissue, 2.8 mm in cartilage, max. 11 mm in soft tissues	Knee joint; 185 MBq
^{169}Er-citrate colloid with an average particle size of 10 nm	Emission of beta particles	9.4	0.4 MeV	Max 1 mm in soft tissue and 0.7 mm in cartilage	Small joints of hand and feet; 37 MBq
^{186}Re-sulfide colloid with an average particle size of 5–10 nm	Emission of beta particles and gamma rays (92.2%); electron capture (7.8%)	3.7	Gamma 137 keV, beta 1.07 MeV	1.2 mm in soft tissues and 0.9 mm in cartilage	Shoulder, elbow and wrist joints; 74 MBq
^{32}P-colloid with an average particle size of 5–20 nm	Emission of beta particles	14	1.7 MeV	Max 7.9 mm in soft tissue	Knee, elbows and ankles; 37 MBq

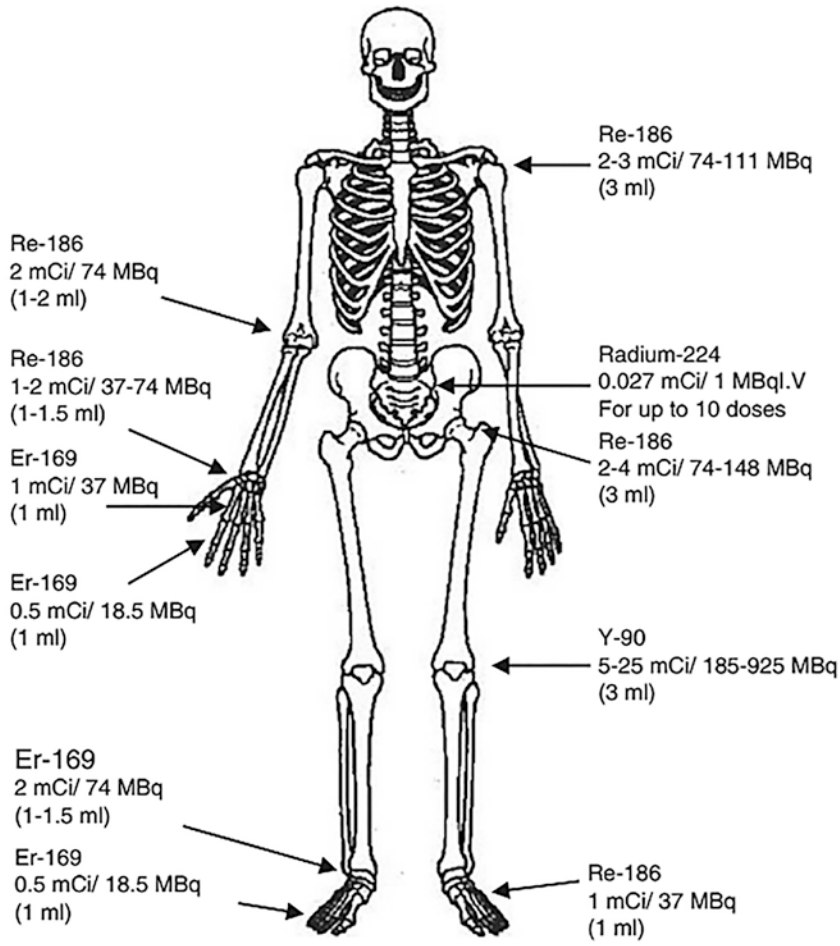

Fig. 13.4 Diagram illustrating the choice of radiopharmaceuticals for radiosynovectomy of different joints

13.7.1.2 Rhenium-186 Sulfide ([^{186}Re] Colloid)

This radiopharmaceutical is used particularly for radionuclide synoviorthesis of the hip, shoulder, elbow, wrist, or ankle joint. After intra-articular injection, it is absorbed by the superficial cells of the synovia. Beta radiation leads to coagulation necrosis and sloughing of these cells.

13.7.1.3 Erbium-169 Citrate [^{169}Er] Colloid

This is more suitable for the radionuclide synoviorthesis of metacarpophalangeal, metatarsophalangeal, and proximal interphalangeal joints. Beta radiation of the absorbed radiopharmaceutical in the synovia causes coagulation necrosis and sloughing of cells, as with other colloids used for other joints. ^{169}Er colloid has an affinity to chelates; therefore, the simultaneous administration of iodine contrast medium containing EDTA should be avoided.

Absolute contraindications for the use of the three therapeutic radiopharmaceutical colloids for synovectomy are pregnancy and continued breast feeding.

13.7.1.4 Phosphorus-32 Chromic Sulfate (P-32)

^{32}P chromic phosphate has a 14 days half-life, is several times larger than ^{90}Y silicate, Re-186, Er-169, or ^{198}Au colloids, and emits only beta radiation. Its beta radiation has a soft-tissue pen-

etration midway between them at 2–3 mm. These physical advantages have led some investigators to use it for the treatment of with rheumatoid arthritis and hemophilic arthritis [75, 76].

13.7.1.5 Radioactive Gold Au-198

Radioactive gold (Au-198) has a mean soft-tissue penetration of only 1–2 mm. It has also been used also radiosynovectomy. It has a physical half-life of 197 days and a colloid particle size ranging from 20 to 70 μm.

13.7.1.6 Rhenium-188 Colloid

Rhenium-188 is a generator-produced beta-emitting radionuclide; the importance of 188Re for radionuclide therapy is increasing rapidly. Jeong [77] prepared 188Re-colloid and compared its properties with 188Re-colloid. They found that 188Re tin colloid is more advantageous over 188Re sulfur colloid since it showed higher labeling efficiency, allowed better control of the particle size, and lower residual activity in the injection syringes [9].

13.7.1.7 Dysprosium-165 (Dy-165)

This radionuclide has a short half-life of 2.3 h, energetic beta emission with a tissue penetration of 5.7 mm, and a very large particle size. Furthermore, it has a 3.6 abundance of gamma emission that can be used by the gamma camera to detect any possible leak. It showed a response rate of 65–70% with the best results in patients with early-stage joint disease [78].

13.7.1.8 Ho-166-Ferric Hydroxide

The first experience with Ho-166 was recently reported [79]. Knee joints of 22 patients were treated with a mean activity of 1.11 GBq (mCi). Ho-166 has a maximum beta energy of 1.85 MeV with a mean penetration in inflamed synovial layer of 2.2 mm and a maximum of 8.7 mm. Its particle size is 1.2–12 nm.

13.7.2 Mechanism of Action

Although the mechanism of action cannot be totally explained, the current belief is that after intra-articular administration the radioactive particles are absorbed by superficial cells of the synovium. Beta radiation leads to coagulation necrosis and sloughing of these cells.

13.7.3 Choice of Radiopharmaceutical

The choice of radiopharmaceutical depends on the physical characteristics and the size of the joint to be treated as well as the disease status. The therapeutic agents are particulate in nature and labeled with beta-emitting radionuclides. Radiation tissue penetration is proportional to the energy of the beta particles. For example, yttrium-90, with its highly energetic beta, has a mean soft-tissue penetration of 3–4 mm, while rhenium-186 has a mean penetration of 1–2 mm, the beta of phosphorus-32 has a soft-tissue penetration midway between them at 2–3 mm, and both radioactive gold and Re-186 have a mean soft-tissue penetration of only 1–2 mm. Radiopharmaceuticals with shallow depth of penetration are not optimal for large joints such as the knee or for patients with extensively thickened synovium as cases with rheumatoid arthritis and pigmented villonodular synovitis. Since the rate of exposure to the radiation is proportional to the severity of the post therapy inflammatory reaction, a radionuclide with a moderately long half-life of days may be preferred to that with a half-life of a few hours. It appears that there is an inverse relationship between the size of radioactive particle used and the tendency for the radiocolloid to leak from the joint space which, in general, makes the choice of a relatively large radiocolloid more appropriate. A radionuclide that emits only beta radiation would have more advantages than those which emit both beta and gamma radiation in order to minimize whole-body radiation.

13.7.4 Clinical Use

Hemophiliac patients with chronic synovitis and hemarthropathy, rheumatoid arthritis, pigmented villonodular synovitis, psoriatic arthritis, ankylosing spondylitis, and collagenosis are candi-

dates for this treatment modality. Furthermore, persistent effusion after joint prosthesis is a relative indication [80].

The absolute contraindications for the use of the therapeutic radiopharmaceutical colloids for synovectomy are pregnancy and continued breast feeding. Fresh fracture, serious liver disease, myelosuppression, and acute infections are other contraindications. Relative contraindications include children or young adults, in which case therapy should only be administered if the estimated benefit outweighs the potential risks [81]. The presence of a Baker cyst in the knee joint is considered by some workers in the field as a contraindication. Ultrasonography is particularly important for the knee joint to exclude the presence of a Baker cyst which is an evagination of the medial dorsal part of the joint capsule in communication with the main joint. If there is inflammation in the knee joint, the effusion can be pumped into Baker cyst by enhanced motion. If a valve mechanism exists in the connection duct, this could have a deleterious effect after radiosynovectomy. The increased pressure in the cyst might lead to its rupture and the radioactive fluid getting into the surrounding tissue of the joint. The consequence could be possible necrosis of the muscles, nerves, and blood vessels. Radiosynovectomy should be delayed for 4–6 weeks after arthroscopy [81].

Two or three phase bone scan should be obtained before planning therapy to assess the degree of inflammation of the joint and soft tissue and in order to be able to decide if radiosynovectomy is possible and if the patient would benefit from this therapy. Scintigraphy is particularly important to evaluate the extent of abnormalities in the joint being treated and quantitation methods could be used before and after therapy. History of arthroscopy must be checked. Ultrasound or MRI is also helpful to assess the amount of effusion, joint space, and the status of the synovium to ensure homogenous distribution of the radiopharmaceutical. Complete blood cell count must be obtained before therapy as well as pregnancy test for women of child-bearing age. Injection should be done using aseptic technique. Radiosynovectomy can generally be repeated in 6 months.

The largest number of treated patients are those with rheumatoid arthritis and hemophilia. Good results are generally obtained from among those patients as well as those with psoriatic arthropathy. On the other hand, in osteoarthritis with recurrent joint effusion, radiosynovectomy has not been as successful in relieving the symptoms. Good response is reported in 40–70% of patients [82]. In patients with advanced cartilage destruction or bone-on-bone interaction, the synovial membrane is likely to be practically nonexistent. Accordingly, patients with less radiological damage generally show better results than those with more severe damage. If there is initially a poor response or a relapse, more than half the patients may benefit from a reinjection [71, 83]; 2190 joints were treated with radiosynovectomy with a minimum of 1 year follow-up but without specifying the radiopharmaceutical used and the overall success rate was 73%. For rheumatoid arthritis it was 67%, whereas it was 56% for osteoarthritis, 91% for hemophilia and Willebrand's disease, and 77% for pigmented villonodular synovitis [83].

13.8 Treatment of Primary and Secondary Liver Malignancies

Blood supply to the normal liver depends on portal vein and to a much lesser extent on hepatic artery. Tumors on the other hand depend on their blood supply on arterial supply and are additionally hypervascular. This forms the basis of selective internal radiotherapy (SIRT) for hepatocellular carcinomas and metastases. This approach is considered a combination of embolization and radiation. Microscopic radioactive spheres of approximately 35 μm in size are administered through a catheter in the hepatic artery. These occlude the small branches of the hepatic artery, which reduces the blood supply to the metastatic tissue. Ho-166 microspheres, Re-188 microspheres, Re-188 lipiodol, and Y-90 microspheres are all being used [84–87]. This therapy is used as an adjunct therapy before and after surgery and it may be curative. It is recom-

mended as an option of palliative therapy for large or multifocal hepatocellular carcinomas without major portal vein invasion or extrahepatic spread. It can also be used for recurrent unresectable HCC, as a bridging therapy before liver transplantation, as a tumor downstaging treatment, and as a curative treatment for patients with associated comorbidities who are not candidates for surgery. Combined I-131 lipiodol and chemotherapy is also being studied [85].

Currently, microspheres are labeled either with pure beta emitters (e.g., yttrium-90: Y-90) or with combined beta/gamma emitters such as rhenium-188. The decay of the radionuclide results in prolonged radiation of the tumor tissue, with a dosage of approximately 150–200 Gy. Because the radionuclides used are beta emitters, the energy is deposited only in a few millimeters around the microsphere; e.g., 90% of the energy is deposited within 5.3 mm in the case of Y-90 with preservation of the normal liver tissue [86, 87].

13.9 Peptide Receptor Radionuclide Therapy

Since cells express on their plasma membranes receptor proteins with high affinity for regulatory peptides such as somatostatin, peptide analogues are used to image and treat receptor positive tumors. The amount of these receptors changes with diseases. Overexpression of such receptors is the pathophysiologic basis of visualization and treatment of receptor positive tumors [88]. Peptide receptor radionuclide therapy (PRRNT) is a molecularly targeted radiation therapy using systemic administration of a radiolabeled peptide designed to target with high affinity and specificity receptors overexpressed on tumors.

High level of expression of somatostatin receptors on several tumor cells is the molecular basis of the utilization of radiolabeled somatostatin analogues in diagnostic and therapeutic nuclear oncology. Several radiolabeled somatostatin analogues therapeutic radiopharmaceuticals (Table 13.4) have been used to treat patients with NETs in the recent years. Since peptides can be produced easily and have rapid clearance, rapid tissue penetration, and low antigenicity, several labeled peptides have been developed over the last few years. These include somatostatin, cholecystokinin (CCK), gastrin, vasoactive intestinal peptide (VIP), bombesin, substance P, and neuropeptide Y (NPY) analogues [57, 89].

Table 13.4 Radiolabeled somatostatin analogues for treatment of neuroendocrine tumors

111In-DTPAOC (111indium-DTPAO] octreotide)
111In-DOTA-TATE (111indium-DOTA-TYR3-octreotate)
90Y-DOTATOC (90yttrium-DOTA-TYR3-octreotide)
90Y-DOTA-TATE (90yttrium-DOTA-TYR3-octreotate)
177Lu-DOTATOC (177lutetium-DOTA-TYR3-octreotide)
177Lu-DOTA-TATE (177lutetium-DOTA-TYR3-octreotate)

Candidate patients for PRRNT using radiolabeled somatostatin analogues are mainly those with sstr2-expressing NET of the gastroenteropancreatic and bronchial tracts but may also include patients with phaeochromocytoma, paraganglioma, neuroblastoma [57], or medullary thyroid carcinoma. Iodine-negative metastases of differentiated thyroid cancer may express somatostatin receptors and could benefit from Y-90 DOTA octreotide or lanreotide [82]. Detection of somatostatin-positive metastases before considering this treatment should be done using diagnostic sstr imaging with Ga-68 labeled somatostatin analogs or In-111 labeled octreotide or lanreotide. Some metastases respond to octreotide while others respond to lanreotide, and there is no apparent explanation. Combination of I-131 and Y-90 DOTA octreotide or lanreotide is being considered.

NETs have proven to be ideal neoplasms for PRRNT, as the majority of these malignancies overexpress somatostatin receptors. Appropriate candidates for PRRNT are patients presenting with well-differentiated or moderately differentiated neuroendocrine carcinomas, defined as NETs of grade 1 or 2 according to the WHO classification of 2010 [90–93]. A study (82) has shown that In-111 DTPA octreotide effect is dependent on tumor size in animal model bearing

somatostatin pancreatic tumor expressing somatostatin receptor type2 (sst_2). Complete response was seen in 50% of tumors of 1 cm or less in diameter while the response was less pronounced with increasing tumor size. This study indicates that this therapy may be preferred to start as early as possible when tumors are small.

Combined [^{90}Y]DOTA-TATE and [^{177}Lu]DOTA-TATE therapy has been found feasible and effective therapeutic option in NET refractory to conventional therapy. In a study of 26 patients with metastatic neuroendocrine tumors treated with four therapeutic cycles of alternating [^{177}Lu]DOTA-TATE (5.55 GBq) and [^{90}Y]DOTA-TATE (2.6 GBq), a median progression-free survival longer than 24 months was achieved. Among patients with pretreatment carcinoid syndrome, 90% showed a symptomatic response or a reduction in tumor-associated pain [94]. Peptide receptor radionuclide therapy for somatostatin-positive neuroendocrine tumors has resulted in improved symptoms, prolonged survival, and an enhanced quality of life.

13.10 Treatment of Malignant Effusions

Radiopharmaceuticals can also be used in the treatment of malignant effusions. After intrapleural or intraperitoneal administration, Y-90 colloid is distributed in the effusion and penetrates the surface cells of tumors. The radionuclide destroys free tumor cells in malignant effusions and may have an additional radiation effect on metastases and mesothelioma by tumor penetrational intratumoral distribution.

13.11 Other Therapeutic Procedures

13.11.1 Treatment of Bone Tumors

13.11.1.1 Osteogenic Sarcoma

Targeted radionuclide therapy using 153Sm-EDTMP was reported to give substantial palliative effect in a case of relapsed primary osteogenic sarcoma in the first lumbar vertebra with progressive back pain after conventional treatment modalities had failed. The patient was bedridden and developed paraparesis and impaired bladder function. On a diagnostic bone scan, intense radioactivity was localized in the tumor. The patient was treated with 153Sm-EDTMP treatment twice, 8 weeks apart using 35 and 32 MBq/kg body weight, respectively. After a few days the pain was significantly relieved and by the second radionuclide treatment the paresis subsided. For 6 months he was able to be up and about without any neurological signs or detectable metastases. Eventually, however, the patient redeveloped local pain and paraparesis, was reoperated, and died 4 months later. The investigators recommended further exploration using 153Sm-EDTMP as a boost technique, supplementary to conventional external radiotherapy given dramatic transient improvement observed in this case [95].

Another case was also reported which illustrated high-activity Sm-153-EDTMP therapy within a multimodal therapy concept to improve local control of an unresectable osteosarcoma with poor response to initial polychemotherapy. A 21-year-old woman with an extended, unresectable pelvic osteosarcoma and multiple pulmonary metastases was treated with high activity of Sm-153-EDTMP. Subsequently, external radiotherapy of the primary tumor site was performed and polychemotherapy continued, followed by autologous peripheral blood stem cell reinfusion. Within 48 h after Sm-153-EDTMP treatment, the patient had complete pain relief. Three weeks later the response was documented by 3-phase Tc99m-MDP bone scan which showed a decrease in tracer uptake in the primary tumor and metastases. Whole-body F-18 FDG-PET also demonstrated an interval decrease of uptake. Further evaluation of feasibility and efficacy of this multimodal therapy combination of high-activity Sm-153-EDTMP therapy, external radiation, polychemotherapy, and stem cell support for unresectable osteosarcomas is warranted [96].

An animal study was conducted on fifteen dogs with spontaneous osteogenic sarcoma and local pain. They were treated with Sm-153-

EDTMP. The tumors were located in the extremities, scapula, maxilla, and the frontal bone. The dogs were injected intravenously one to four times with 153Sm-EDTMP; 36–57 MBq/kg body weight. Three dogs had surgery in addition to the radionuclide treatment. Platelet and WBC counts showed a moderate and transient decrease with no other toxicity observed. The average tumor doses after a single injection were approximately 20 Gy. Seven dogs had metastases on autopsies. Even though none of the dogs was cured, nine of the dogs had obvious pain relief, and five of them seemed pain free: one for 13 months and one for 48 months [97].

13.11.1.2 Multiple Myeloma

Recent use of high-dose Ho-166-DOTMP (Ho-166-1, 4, 7, 10-tetraazcyclododecane-1, 4, 7, 10-tetramethylene-phosphonic acid) in patients with multiple myeloma has been reported [86]. Thirty-two patients were treated with 581–3987 mCi with an average of 2007 mCi (74.3GBq). Ho-166 has a half-life of 26.8 h and a beta emission of 1.85 MeV (51%) and 177 MeV (48%) as well as an 80.6 KeV (6.6%) gamma emission suitable for a gamma camera imaging. The beta particles have a mean range of 4 mm in soft tissue and can deliver high levels of radiation to the marrow and trabecular bone [98]. This radiopharmaceutical has selective bone uptake and rapid urinary excretion of the remaining activity. However, due to the high doses used, catheterization and continuous irrigation of the urinary bladder after therapy has to be used to reduce radiation dose to bladder mucosa. This agent has a potential to treat patients with resistant multiple myeloma. However clinical studies with emphasis on the outcome in comparison with the currently used high dose of chemoradiotherapy with or without stem cell rescue are warranted to evaluate the impact on the poor survival of patients affected by the tumor. Also more studies are needed to compare the adverse effects of this agent to the high incidence of systemic toxicities of the currently available radiopharmaceuticals [99–102]. Holmium-166 tetraphosphate (Ho-166 DOTMP), a high-energy beta emitter, is now used in treating bone and bone marrow-based tumors such as multiple myeloma [103]. The mechanism of action is through cell death by beta particles.

13.11.1.3 Metastatic Prostate Carcinoma

A study was conducted to explore the effects of Re-186-HEDP treatment on the progression of lumbar skeletal metastasis in an animal model using the Copenhagen rat model and to correlate the eventual treatment efficacy with the radionuclide tissue distribution. The 186Re-HEDP administration, given either 1 day or 8 days after surgical induction of lumbar metastasis was found to significantly increase the symptom-free survival of the animals. These results were confirmed by a significant decrease in the presence of histologically detectable tumor tissue. Biodistribution studies demonstrated the uptake of the major part of the radionuclide within bone tissue. The uptake of radioactivity within the lumbar vertebrae on a microscopic scale, as shown by phosphor screen autoradiography, was concentrated in areas of bone formation and turnover. These results show that radionuclide treatment with Re-186-HEDP is a potentially efficacious treatment option in prostate cancer disseminated to the skeleton [104]. A clinical trial on selected patients with advanced, androgen-independent, prostate carcinoma who received consolidation bone-targeted therapy comprised of Sr-89 with weekly doxorubicin after induction chemotherapy had a longer survival compared with patients who did not receive the bone-targeted therapy [105]. More recently Ra = 223 dichloride and Lu-177 PSMA are used.

The FDG-PET therapy response assessments in men with osseous metastatic prostate cancer are not always in agreement with composite clinical designations of response, stable disease, or progression [106]. Uptake and sensitivity vary in the same tumor type, for example, prostatic cancer. Generally, the FDG avidity is low in treatment naïve prostate cancer, increased in CRPC, and almost always present in docetaxel-refractory prostate cancer [107, 108]. All this indicate that

the FDG is not ideal for response assessment of prostate cancer osseous metastases especially in earlier disease states.

Ra-223 Dichloride Treatment

Ra-223 dichloride is a bone-seeking calcium analogue, an alpha-emitter, approved for the treatment of castration-resistant prostate cancer with symptomatic bone metastases. It has both therapeutic and palliative effects. Ra-223 has alpha, beta and gamma emissions with total decay energy of 28 MeV (mean 5.78 MeV). Ra-223 is produced from an actinium-227 (Ac-227) generator. Half-life of Ra-223 is 11.43 days. Its range in tissue is 0.04–0.05 mm with a highly localized effect and minimal detrimental effects on healthy tissues near tumor. Maximum α-energies of 223Ra are 5.78, 6.88, 7.53 MeV. Maximum β-energies are 450 keV and 490 keV. Gamma energy peaks of Ra-223 are 82, 154, 269, 351, and 402 keV. Ra-223 dicholoride selectively accumulates in the bone, specifically in areas of high bone turnover through forming complexes with the mineral hydroxyapatite [109]. The high linear energy transfer of the alpha radiation results in a high probability of DNA double-strand breaks in the adjacent cells [109]. Radionuclide therapy with Ra-223 is given as single or repeated intravenous administration. The treatment is usually given on an outpatient basis with respect to national legislation and regulations. Hospitalization is recommended in cases of fecal incontinence or seriously ill patients. Contraindications are listed in EANM guidelines [109]. Patients should have bone metastases seen on recent bone scan (not older than 3 mos) and no known visceral metastatic disease. Supplementation of calcium, phosphates, or vitamin D should be paused about 4 days before and after each injection of radium-223. The dose is 55 kBq/kg, given at 4-week intervals for six injections [109]. Ra-223 localization in the bone/bone metastases is around 44–77% at 4 h. Fecal excretion is the major elimination route which is approximately 60–75% of the administered activity and 5% is excreted in the urinary tract. Instructions are given for 7–10 days. The most common side effects are diarrhea, nausea, vomiting, and thrombocytopenia. Risk of hematological adverse reactions increases if patients received chemotherapy or external beam radiotherapy or if patients have advanced diffuse metastases in the bones. Pain relief is rapid but not expected in every patient. The ALSYMPCA study (ALpharadin in SYMPtomatic Prostate CAncer) is an international clinical study to evaluate the efficacy and safety of Ra-223 [110–112]. The ALSYMPCA study showed an overall survival benefit with ^{223}Ra treatment (in over 900 patients). Also, the frequency of skeletal-related events was reduced with Ra-223 treatment. Improved survival with ^{223}Ra was accompanied by significant quality-of-life benefits, including a higher percentage of patients with meaningful quality-of-life improvements and a slower decline in quality-of-life over time.

Lu-177 PSMA Ligand Treatment

Luteium-177 (Lu-177) PSMA ligand therapies have demonstrated promising results in a significant proportion of men with metastatic prostate cancer who have failed other therapies. Treatment with Lu-177 PSMA ligands is currently undergoing clinical validation. Lu-177 is a radiometal produced in reactor. Lu-177 is a medium-energy beta emitter (490 keV) with a maximal tissue penetration of <2 mm which provides better irradiation of small tumors. It also emits low-energy gamma rays, 208 and 113 keV which allows for ex vivo imaging after treatment. Lu-177 has a physical half-life of 6.73 days. Current clinical knowledge is predominantly based on two low molecular weight PSMA ligands: PSMA-617 and PSMA-I&T [113]. Patients should have adequate uptake of PSMA ligands on pre-therapy imaging. Dose calculations are based on disease burden, patient weight and renal function. Injected doses range from 3.7 to 9.3 GBq (100–250 mCi) per single injections with up to six injections, generally at a minimum 6-week intervals [113]. Contraindications to this treatment are described in detail at EANM guidelines [113]. For kidney protection (to decrease reabsorption of radiotracer via the proximal renal tubules and thereby decrease the radiation dose to the kidneys some institutes give IV amino acid infusion (lysine and arginine) over 4 h, starting 30 min

prior to the treatment. Lu-177 PSMA is given as outpatient treatment in some countries and inpatient in other countries with respect to national legislation and regulations. Lu-177 PSMA is excreted via kidneys in the first 48 h following injection. Prospective clinical trial confirmed a high response rates, low toxicity and reduction of pain in metastatic castration-resistant prostate cancer. In 30–70% of men treated with Lu-177 PSMA, there was a >50% reduction in serum PSA levels [114]. In another study, 80% of all men had a PSA response to PSMA therapy [115].

13.12 Combined Therapeutic Approach

The use of radionuclide therapy has been used alone. Recently, several trials have used a combined approach combining radionuclide with other treatment modalities [116, 117]. Sr89 in combination with doxorubicin has been used for bone metastases. This combination was found to be associated with longer time interval to disease progression and longer overall survival when compared to those who only received doxorubicin [117, 118]. Combining low-dose cisplatin to the standard dose of Sr-89 chloride was found to improve pain palliation significantly [119].

CHOP was also used in combination with I-131 tositumomab and Y-90–ibritumomab and Rituxan–CHOP combinations for untreated non-Hodgkin's lymphoma [120, 121].

Combining I-131 MIBG and chemotherapy or myeloablative chemotherapy has been also used in a limited number of patients [122, 123]. In a pilot study, Y-90 biotin was used as an adjunct to surgery and radiation therapy for malignant glioma [124]. The disease-free interval and overall survival was significantly longer among patients with this adjunct therapy than in control group. External beam radiotherapy has been used in combination with and I-131 MIBG for neuroblastoma, and paraganglioma and with I-131 for a large thyroid metastasis. This combined method takes into consideration the nonuniform dose distribution on the basis of tumor function and the radionuclide therapy dose delivered [125]. Combined chemotherapy and I-131 lipiodol for the treatment of hepatocellular carcinoma is being studied as mentioned earlier.

13.13 Summary

Radionuclide therapy is effective, safe, and cost effective and deserves consideration earlier in the management of cancer patients rather than being left as a terminal choice. Several radiopharmaceuticals are being used with varying degrees of success in treating several benign and malignant disease processes. The mechanisms of action are not entirely clear for all of them. Table 13.5 summarizes the probable mechanisms of action of the major radiopharmaceutical tracers currently used. More choices in radionuclide therapy are now available to the

Table 13.5 Effects and mechanisms of action of therapeutic radiopharmaceuticals

Therapeutic procedure/target	Probable mechanism
Hyperthyroid	Cell injury/death to reduce or ablate the thyroid gland
Thyroid cancer	Cell death to ablate residual thyroid tissue, tumor, and metastases
Synovectomy	Phagocytosis of radiolabeled colloid by synoviocytes which are distributed uniformly on the surface of the synovium, with subsequent destruction of the synovium by the beta particles
Radioimmunotherapy	Destruction of tumor cells through multiple mechanisms including cell lysis, formation of autoantibodies, and/or apoptosis
Painful bone metastases	Uptake of the radiopharmaceutical by metastases and/or surrounding bone, with radiation injury or death to the tumor cells or the surrounding cytokine-secreting cells
Peptide therapy	High expression of peptide receptor such as somatostatin and cholecystokinin by cells of specific tumors

physicians for local and systemic uses to palliation and definitive therapy. Clinical acceptance is expected to increase as oncologists accept more the limitations of the curative and palliative role of chemotherapy and external radiation. The areas of research in the field of therapeutic nuclear medicine are wide open for developing new therapeutic radiopharmaceuticals and clinical applications.

References

1. Prvulovich EM, Stein RC, Bomanji JB et al (1998) Iodine-131 MIBG therapy of a patient with carcinoid liver metastases. J Nucl Med 39:1743–1745
2. Demeter S, Leslie WD, Levin DP (2005) Radioactive iodine therapy for malignant and benign thyroid disease: a Canadian national survey of physician practice. Nucl Med Commun 26:613–621
3. McKenzie JM, Zakrija M, Sato A (1978) Humoral immunity in Graves' disease. Clin Endocrinol Metab 7:31
4. Maxon HR, Thomas SR, Saenger EL et al (1977) Ionizing irradiation and induction of clinically significant disease in human thyroid. Am J Med 63:967
5. Sofa AM, Skillern PG (1975) Treatment of hyperthyroidism with a large initial dose of sodium iodide I-131. Arch Intern Med 135:673
6. Woeber KA (2000) Update on the management of hyperthyroidism and hypothyroidism. Arch Intern Med 160:1067–1071
7. Hamburger JI (1980) Evaluation of toxicity in solitary nontoxic autonomously functioning thyroid nodules. J Clin Endocrinol Metab 50:1089–1093
8. Peter HJ, Studer H, Forster T, Herber H (1982) The pathogenesis of "hot" and "cold" follicle in multinodular goiters. J Clin Endocrinol Metab 55:941–946
9. Ginsberg J (2003) Diagnosis and management of Grave's disease. CMAJ 168:575–585
10. Bartalena L, Marcocci C, Bogazzi F, Manetti L, Tanda ML, Dell'Unto E et al (1998) Relation between therapy for hyperthyroidism and the course of Grave's ophthalmopathy. N Engl J Med 338:73–78
11. Reid JR, Wheeler SF (2005) Hyperthyroidism: diagnosis and treatment. Am Fam Physician 72:623–630
12. Perros P, Kendall-taylor P, Neoh C, Frewin S, Dickinson J (2005) A prospective study of the effects of radioiodine therapy for hyperthyroidism in patients with minimally active Grave's ophthalmopathy. J Clin Endocrinol Metab 90:5321–5532
13. Maxon HR, Thomas SR, Chen IW (1981) The role of nuclear medicine in the treatment of hyperthyroidism and well differentiated thyroid adenocarcinoma. Clin Nucl Med 6:87–98
14. Sankar R, Sekhri T, Sripathy G, Walia RP, Jain SK (2005) Radioactive iodine therapy in Grave's hyperthyroidism: a prospective study from a tertiary referral center in North India. J Assoc Physicians India 53:603–606
15. Allahabadia A, Daykin J, Sheppard MC, Gough SC, Franklyn JA (2001) Radioiodine treatment of hyperthyroidism. Prognostic factors for outcome. J Clin Endocrinol Metab 86:3611–3617
16. Haugen BR, Alexander EK, Bible KC, Doherty GM, Mandel SJ et al (2016) 2015 American Thyroid Association management guidelines for adult patients with thyroid nodules and differentiated thyroid cancer: the American Thyroid Association guidelines task force on thyroid nodules and differentiated thyroid cancer. Thyroid 26:1–13
17. Terrier P, Sheng ZM, Schlumberger M et al (1988) Structure and expression of c-myc and c-fos protooncogenes in thyroid carcinomas. Oncogene 2:403
18. Lemoine NR, Mayall ES, Wyllie FS et al (1988) Activated ras oncogenes in human the thyroid cancers. Cancer Res 48:44–59
19. Atay-Rosenthal S (1999) Controversies on treatment of well-differentiated thyroid carcinoma and factors influencing prognosis. In: Freeman L (ed) Nuclear medicine annual. Lippincott/Williams and Wilkins, Philadelphia, pp 303–334
20. Beierwaltes WH (1978) The treatment of thyroid carcinoma with radioiodine. Semin Nucl Med 8:79
21. Rosario PW, Barroso AL, Rezende LI, Padrao EL, Fagundes TA, Reis JS, Purisch S (2005) Outcome of ablation of thyroid remnants with 100 mCi (3.7 GBq) iodine -131 in patients with thyroid cancer. Ann Nucl Med 19:247–250
22. Kolfuerest S, Igerc I, Lind P (2005) Recombinant human thyrotropin is helpful in the follow up and I-131 therapy of patients with thyroid cancer: a report of the results and benefits using recombinant thyrotropin in clinical routine. Thyroid 15:371–376
23. Intenzo CM, Jabbour S, Dam HQ, Capuzzi DM (2005) Changing concepts in the management of differentiated thyroid cancer. Semin Nucl Med 35:257–265
24. Fujie S, Okumura Y, Sato S, Akaki S, Katsui K, Himei K, Takemoto M, Kanazawa S (2005) Diagnostic capabilities of I-131, Tl-201, and Tc99m MIBI scintigraphy for metastatic differentiated thyroid carcinoma after total thyroidectomy. Acta Med Okayama 59:99–107
25. Ferreira SH, Lorenzethi BB, Bristow AF et al (1988) Interleukin-1 beta as a potent hyperalgesic agent antagonized by a tripeptide analogue. Nature 334:698–700
26. Poulson HS, Nielsen OS, Klee M et al (1989) Palliative irradiation of bone metastases. Cancer Treat Rev 16:41–48

27. Tong D, Gillick L, Hendrickson FR (1982) Palliation of symptomatic osseous metastases. Cancer 50:893–899
28. Salazar OM, Rubin P, Hendrickson FR et al (1986) Single-dose half-body irradiation for palliation of multiple bone metastases from solid tumors. Final Radiation Therapy Oncology Group report. Cancer 58:29–36
29. Bauman G, Charette M, Reid R, Sathya J (2005) Radiopharmaceuticals for the palliation of painful bone metastasis-a systemic review. Radiother Oncol 75:258–270
30. Pauwels EKJ, Stokkel MPM (2001) Radiopharmaceuticals for bone lesions imaging and therapy in clinical practice. Q J Nucl Med 45:18–26
31. Giammarile F, Mognetti T, Resche I (2001) Bone pain palliation with strontium-89 in cancer patients with bone metastases. Q J Nucl Med 45:78–83
32. Patel BR, Flowers WM Jr (1997) Systemic radionuclide therapy with strontium chloride Sr 89 for painful skeletal metastases in prostate and breast cancer. South Med J 90:506–508
33. Papatheofanis FJ (2000) Decreased serum E-selectin concentration after 89Sr-chloride therapy for metastatic prostate cancer bone pain. J Nucl Med 41:1021–1024
34. Ramamoorthy N, Saraswathy P, Das MK, Mehra KS, Ananthakrishnan M (2002) Production logistics and radionuclidic purity aspects of 153Sm for radionuclide therapy. Nucl Med Commun 23:83–89
35. Cameron PJ, Klemp PF, Martindale AA, Turner JH (1999) Prospective 153Sm-EDTMP therapy dosimetry by whole-body scintigraphy. Nucl Med Commun 20:609–615
36. Maxon HR, Thomas S, Hertzberg VS, Schroder LE, Englaro EE, Samaratunga R et al (1992) Rhenium-186 hydroxyethylidene diphosphonate for the treatment of painful osseous metastases. Semin Nucl Med 22:33–40
37. Han SH, De Klerk JM, Zonnenberg BA, Tan S, Van Rijk PP (2001) 186Re-etidronate. Efficacy of palliative radionuclide therapy for painful bone metastases. Q J Nucl Med 45:84–90
38. Kucuk NO, Ibis E, Aras G, Baltaci S, Ozalp G, Beduk Y, Canakci N, Soylu A (2000) Palliative analgesic effect of Re-186 HEDP in various cancer patients with bone metastases. Ann Nucl Med 14:239–245
39. Atkins HL, Mausner LF, Srivastava SC, Meinken GE, Cabahug CJ, D'Alessandro T (1995) Tin-117 m (4+)-DTPA for palliation of pain from osseous metastases: a pilot study. J Nucl Med 36:725–929
40. Atkins HL, Mausner LF, Srivastava SC, Meinken GE, Straub RF, Cabahug CJ et al (1993) Biodistribution of Sn-117 m DTPA for palliative therapy of painful osseous metastases. Radiology 186:279–283
41. Bishayee A, Rao DV, Srivastava SC, Bouchet LG, Bolch WE, Howell RW (2000) Marrow-sparing effects of 117mSndiethylenetriaminepentaacetic acid for radionuclide therapy of bone cancer. J Nucl Med 41:2043–2050
42. Blower PJ, Kettle AG, O'Doherty MJ, Coakley AJ, Knapp FF Jr (2000) 99mTc(V)DMSA quantitatively predicts 188Re(V)DMSA distribution in patients with prostate cancer metastatic to bone. Eur J Nucl Med 27:1405–1409
43. Krishnamurthy GT, Krishnamurthy S (2000) Radionuclides for metastatic bone pain palliation: a need for rational re-evaluation in the new millennium [comment]. J Nucl Med 41:688–691
44. Hoskin PJ, Ford HT, Harmer CL (1989) Hemibody irradiation (HBI) for metastatic bone pain in two histologically distinct groups of patients. Clin Oncol 1:67–69
45. Fischer M (1998) I-131 therapy of neural crest tumors. Nucl Med Newslett 5:9–10
46. Quilty PM, Kirk D, Bolger JJ et al (1994) A comparison of the palliative effects of strontium-89 and external beam radiotherapy in metastatic prostate cancer. Radiother Oncol 31:33–40
47. Silberstein EB, Elgazzar AH, Kapilivsky A (1992) Phosphorus-32 radiopharmaceuticals for the treatment of painful osseous metastases. Semin Nucl Med 17:17–27
48. Maxon HR, Thomas SR, Hertzberg VS et al (1982) Rhenium-186 hydroxyethylidene diphosphonate for the treatment of painful osseous metastases. Semin Nucl Med 22:30–40
49. Elgazzar AH, Maxon HR (1993) Radioisotope therapy for cancer related bone pain. Imaging Insights 2:1–6
50. Windsor PM (2001) Predictors of response to strontium-89 (Metastron) in skeletal metastases from prostate cancer: report of a single centre's 10-year experience. Clin Oncol 13:219–227
51. Sideras PA, Stavraka A, Gouliamos A, Limouris GS (2013) Radionuclide therapy of painful bone metastases – a comparative study between consecutive radionuclide infusions, combination with chemotherapy, and radionuclide infusions alone: an in vivo comparison of their effectiveness. Am J Hosp Palliat Care 30:745–751
52. Dickie GJ, MacFarlane D (1999) Strontium and samarium therapy for bone metastases from prostate carcinoma. Australas Radiol 43:476–479
53. Sciuto R, Festa A, Pasqualoni R, Semprebene A, Rea S, Bergomi S, Maini CL (2001) Metastatic bone pain palliation with 89-Sr and 186-Re-HEDP in breast cancer patients. Breast Cancer Res Treat 66:101–109
54. Kvinnsland Y, Skretting A, Bruland OS (2001) Radionuclide therapy with bone- seeking compounds: Monte Carlo calculations of dose-volume histograms for bone marrow in trabecular bone. Phys Med Biol 46:1149–1161
55. Spetz J, Dalmo J, Nilsson O, Wängberg B, Ahlman H, Forssell-Aronsson E (2012) Specific binding and uptake of 131I-MIBG and 111In-octreotide in metastatic paraganglioma–tools for choice of radionuclide therapy. Horm Metab Res 44:400–404
56. Bomanji JB, Papathanasiou ND (2012) 111In-DTPA0-octreotide (Octreoscan), ^{131}I-MIBG

and other agents for radionuclide therapy of NETs. Eur J Nucl Med Mol Imaging 39(1):S113–S125
57. Zaknun JJ, Bodei L, Mueller-Brand J, Pavel ME, Baum RP, Hörsch D, O'Dorisio MS, O'Dorisiol TM, Howe JR, Cremonesi M, Kwekkeboom DJ (2013) The joint IAEA, EANM, and SNMMI practical guidance on peptide receptor radionuclide therapy (PRRNT) in neuroendocrine tumours. Eur J Nucl Med Mol Imaging 40:800–816E
58. Gelfand MJ, Elgazzar AH, Kriss VM et al (1994) Iodine-123 MIBG SPECT versus planar imaging in children with neural crest tumors. J Nucl Med 35:1753–1757
59. Paltiel HJ, Gelfand MJ, Elgazzar AH, Washburn LC et al (1994) Neural crest tumors: I-123 MIBG imaging. Radiology 190:117–121
60. Hoefnagel CA, deKraner J, Voute PA, Valdes Olmos RA (1991) Preoperative I-131 MIBG therapy in the management of neuroblastoma (abstract). J Nucl Med 32:921
61. Hoefnagel CA, deKraner J, Valdes Olmos RA, Voute PA (1994) I-131 MIBG as a first time treatment in high risk neuroblastoma patients. J Nucl Med 15:712–717
62. Mastrangelo R, Lasorell A, Troncone L et al (1991) I-131 metaiodobenzylguanidine in neuroblastoma patients. J Nucl Med 35:248–251
63. Sisson JC, Shapiro B, Beirwaltes WH et al (1984) Radiopharmaceutical treatment of malignant pheochromocytoma. J Nucl Med 25: 197–206
64. Hoefnagel CA (1991) Radionuclide therapy revisited. Eur J Nucl Med 18:408–431
65. Taal BG, Hoefnagel CA, Vables Olmos RA, Boot H, Beijen JK (1996) Palliative effect of metaiodobenzylguanidine in metastatic carcinoid tumors. J Clin Oncol 14:1829–1839
66. Press OW, Eary JF, Applelbaum FR, Martin PJ, Badger CC, Nelp WB, Glenn S, Buchko GM, Fisher LD, Porter B et al (1993) Radiolabeled-antibody therapy of B-cell lymphoma with autologous bone marrow support. N Engl J Med 329:1219–1224
67. Press OW, Eary JF, Applbaum FR, Martin PJ, Nelp WB, Glenn S, Fisher DR et al (1995) Phase II trial of I-131-B1 (anti-CD20) antibody therapy with autologous stem cell transplantation for relapsed B cell lymphomas. Lancet 346:336–340
68. De Nardo GL, De Nardo SJ, O'Grady LF, Levy NB, Adams GP, Mills SL (1990) Fractionated radioimmunotherapy of B-cell malignancies with I-131-Lym-1. Cancer Res 50:1014–1016
69. DeNardo GL, O'Donnell RT, Oldham RK, DeNardo SJ (1998) A revolution in the treatment of non-Hodgkin's lymphoma. Cancer Biother Radiopharm 13:213–223
70. Morschhauser F, Radford J, Van Hoof A et al (2013) 90Yttrium-Ibritumomab Tiuxetan consolidation of first remission in advanced-stage follicular non-Hodgkin lymphoma: updated results after a median follow-up of 7.3 years from the international, randomized, phase III first-line indolent trial. J Clin Oncol 31:1977–1983
71. Deutsch E, Brodack JW, Deutsch KF (1993) Radiation synovectomy revisited. Eur J Nucl Med 20:1113–1127
72. Gschwend N (1989) Synovectomy. In: Kelly WN, Harris ED, Ruddy S et al (eds) Textbook of rheumatology. Saunders, Philadelphia, pp 1934–1961
73. Heim M, Goshen E, Amit Y, Martinowitz U (2001) Synoviorthesis with radioactive Yttrium in haemophilia: Israel experience. Haemophilia 7(Suppl 2):36–39
74. Rodriguez-Merchan EC, Jimenez-Yuste V, Villar A, Quintana M, Lopez-Cabarcos C, Hernandez-Navarro F (2001) Yttrium-90 synoviorthesis for chronic haemophilic synovitis: Madrid experience. Haemophilia 7(Suppl 2):34–35
75. Onetti CM, Guyierrez F, Hiba E et al (1982) Synoviorthesis with P-32 colloid chromic phosphate in rheumatoid arthritis and hemophilia, clinical, histopathological and arthographic changes. J Rheumatol 9:229–238
76. Rivard GE, Givard M, Belanger R et al (1994) Synoviorthesis with colloidal P-32 chromic phosphate for the treatment of hemophilic arthropathy. J Bone Joint Surg Am 76:482–487
77. Jeong JM, Lee YJ, Kim YJ, Chang YS, Lee DS, Chung JK, Song YW, Lee MC (2000) Preparation of rhenium-188-tin colloid as a radiation synovectomy agent and comparison with rhenium-188-sulfur colloid. Appl Radiat Isot 52:851–855
78. Siegel ME, Siegel HJ, Luck JV Jr (1997) Radiosynovectomy's clinical applications and cost effectiveness: a review. Semin Nucl Med 28:364–371
79. Ofluoglu S, Schwameis E, Zehetagruber I, Havlic E, Wanivenhaus A, Schweeger I, Weiss K et al (2002) Radiation synovectomy with Ho-166-Ferric hydroxide: a first experience. J Nucl Med 43:1489–1494
80. Fischer M, Modder G (2002) Radionuclide therapy of inflammatory joint disease. Nucl Med Commun 23:829–831
81. Hauss F (1992) Radiosynoviorthese in der orthopadie. Aktule Rheumatol 17:64–66
82. Asavatanabodee P et al (1997) Yttrium-90 radiochemical synovectomy in chronic knee synovitis: a one year retrospective review of 133 treatment interventions. J Rheumatol 24:639–642
83. Kresnik E, Mikososch P, Gallowitsch HJ, Jesenko R, Just H, Kogler D, Gasser J, Heinisch M, Unterweger O, Kumnig G, Gomez I, Lind P (2002) Clinical outcome of radiosynoviorthesis: a meta-analysis including 2190 treated joints. Nucl Med Commun 23:683–688
84. Sundram FX, Jiomg JM, Zanzonico P, Bernal P, Chau T, Onkhuudai P, Divgi C, Knapp FF Jr, Padhy AK (2002) Trans-arterial rhenium-188 lipiodol in the treatment of inoperable hepatocellular carcinoma – results of a multi-centre phase-1 study. World J Nucl Med 1:5–11

85. Uccelli L, Pasquali M, Boschi A, Giganti M, Duatti A (2011) Automated preparation of Re-188 lipiodol for the treatment of hepatocellular carcinoma. Nucl Med Biol 38:207–213
86. Nijsen JF, van het Schip AD, Hennink WE, Rook DW, van Rijk PP, deKlerk JM (2002) Advances in nuclear oncology: microspheres for internal radionuclide therapy of liver tumours. Curr Med Chem 9:73–82
87. Van de Wiele C, Maes A, Brugman E, D'Asseler Y, De Spiegeleer B, Mees G, Stellamans K (2012) SIRT of liver metastases: physiological and pathophysiological considerations. Eur J Nucl Med Mol Imaging 39(10):1646–1655
88. Jong M, Kwekkeboom D, Volkema R, Krenning ER (2003) Radiolabelled peptides for tumor therapy: current status and future directions. Eur J Nucl Med 30:463–469
89. Rindi G (2010) The ENETS guidelines: the new TNM classification system. Tumori 96:806–809
90. Gulenchyn KY, Yaoy X, Asa SL, Singh S, Lawjj C (2012) Radionuclide therapy in neuroendocrine tumours: a systematic review. Clin Oncol 24:294–308
91. Sansovini M, Severi S, Ambrosetti A, Monti M, Nanni O et al (2013) Treatment with the radiolabelled somatostatin analog 177Lu-DOTATATE for advanced pancreatic neuroendocrine tumors. Neuroendocrinology 97:347–354
92. Pfeifer AK, Gregersen T, Grønbæk H, Hansen CP, Müller-Brand J et al (2011) Peptide receptor radionuclide therapy with 90 Y-DOTATOC and 177 Lu-DOTATOC in advanced neuroendocrine tumors: results from a Danish cohort treated in Switzerland. Neuroendocrinology 93: 189–196
93. Kwekkeboom DJ, Krenning EP, Lebtahi R et al (2009) ENETS consensus guidelines for the standards of care in neuroendocrine tumours: peptide receptor radionuclide therapy with radiolabeled somatostatin analogs. Neuroendocrinology 90:220–226
94. Seregni E, Maccauro M, Chiesa C, Mariani L, Pascali C, Mazzaferro V, De Braud F, Buzzoni R, Milione M, Lorenzoni A, Bogni A, Coliva A, Vullo SL, Bombardieri E (2014) Treatment with tandem [90Y]DOTA-TATE and [177Lu]DOTA-TATE of neuroendocrine tumours refractory to conventional therapy. Eur J Nucl Med Mol Imaging 41:223–230
95. Bruland OS, Skretting A, Solheim OP, Aas M (1996) Targeted radiotherapy of osteosarcoma using 153 Sm-EDTMP. A new promising approach. Acta Oncol 35:381–384
96. Franzius C, Bielack S, Sciuk J, Vollet B, Jurgens H, Schober O (1999) High-activity samarium-153-EDTMP therapy in unresectable osteosarcoma. Nucl Med 38:337–340
97. Aas M, Moe L, Gamlem H, Skretting A, Ottesen N, Bruland OS (1999) Internal radionuclide therapy of primary osteosarcoma in dogs, using 153Sm-ethylene-diamino-tetramethylene-phosphonate (EDTMP). Clin Cancer Res 5(10 Suppl):3148s–3152s
98. Boyouth Je Macey DJ, Kasi LP et al (1995) Pharmacokinetics, dosimetry and toxicity of holmium-166 DOTMP for bone marrow ablation multiple myeloma. J Nucl Med 36:730–737
99. Rajendran JG, Eary JF, Bensinger W, Durack LD, Vernon C, Fritzberg A (2002) High-dose 166Ho-DOTMP in myeloablative treatment of multiple myeloma: pharmacokinetics, biodistribution, and absorbed dose estimation. J Nucl Med 43:1383–1390
100. Alexanan R, Dimopoulos M (1994) The treatment of multiple myeloma. N Engl J Med 330:484–489
101. Barlogie B, Alexanian R, Dick KA et al (1987) High dose chemotherapy and autologous bone marrow transplantation for resistant myeloma. Blood 70:869–872
102. Hoefnagel CA (1988) Radionuclide cancer therapy. Ann Nucl Med 12:61–70
103. Srivastava S, Dadachova E (2001) Recent advances in radionuclide therapy. Semin Nucl Med 31:330–341
104. Geldof AA, van den Tillaar PL, Newling DW, Teule GJ (1997) Radionuclide therapy for prostate cancer lumbar metastasis prolongs symptom-free survival in a rat model. Urology 49:795–801
105. Logothetis C, Tu SM, Navone M (2003) Targeting prostate cancer bone metastases. Cancer 97:785–788
106. Yu EY, Muzi M, Hackenbracht JA et al (2011) C11-acetate and F-18 FDG PET for men with prostate cancer bone metastases: relative findings and response to therapy. Clin Nucl Med 36:192–198
107. Jadvar H (2013) Imaging evaluation of prostate cancer with 18 F- fluorodeoxyglucose PET/CT: utility and limitations. Eur J Nucl Med Mol Imaging 40(Suppl 1):S5–S10
108. Meirelles GS, Schoder H, Ravizzini GC et al (2010) Prognostic value of baseline [18F] fluorodeoxyglucose positron emission tomography and 99mTc-MDP bone scan in progressing metastatic prostate cancer. Clin Cancer Res 16:6093–6099
109. Poeppel TD, Handkiewicz-Junak D, Andreeff M, Becherer A, Bockisch A et al (2018) EANM guideline for radionuclide therapy with radium-223 of metastatic castration-resistant prostate cancer. Eur J Nucl Med Mol Imaging 45:824–845
110. Sartor O, Hoskin P, Coleman RE, Nilsson S, Vogelzang NJ et al (2016) Chemotherapy following radium-223dichloride treatment in ALSYMPCA. Prostate 76:905–916
111. Hoskin P, Sartor O, O'Sullivan JM, Johannessen DC, Helle SI, Logue J et al (2014) Efficacy and safety of radium-223 dichloride inpatients with castration-resistant prostate cancer and symptomaticbone metastases, with or without previous docetaxel use: prespecified subgroup analysis from the randomised, double-blind, phase 3 ALSYMPCA trial. Lancet Oncol 15:1397–1406
112. Sartor O, Coleman RE, Nilsson S, Heinrich D, Helle SI, O'Sullivan JM et al (2017) An exploratory analy-

sis of alkaline phosphatase, lactate dehydrogenase, and prostate-specific antigen dynamics in the phase 3 ALSYMPCA trial with radium-223. Ann Oncol 2017(28):1090–1097
113. Kratochwil C, Fendler WP, Eiber M, Baum R, Bozkurt MF et al (2019) EANM procedure guidelines for radionuclide therapy with ^{177}Lu-labelled PSMA-ligands (^{177}Lu-PSMA-RLT). Eur J Nucl Med Mol Imaging 46:2536–2544
114. Baum RP, Kulkarni HR, Schuchardt C et al (2016) 177Lu-labeled prostate-specific membrane antigen radioligand therapy of metastatic castration-resistant prostate cancer: Safety and efficacy. J Nucl Med 57:1006–1013
115. Oudard S (2011) Phase III trial of cabazitaxel for the treatment of metastatic castration-resistant prostate cancer. Future Oncol 7:497–506
116. Valdes Olmos RA, Hoefnagel CA (2004) Radionuclide therapy in oncology: the drawing of its concomitant use with other modalities? Eur J Nucl Med Mol Imaging 31: 929–931
117. Bodey RK, Flux GD, Evans PM (2003) Combining dosimetry for targeted radionuclide and external beam therapies using the biologically effective dose. Cancer Biother Radiopharam 18:89–97
118. Logothetis C, Tu S, Navone N (2003) Targeting prostate cancer bone metastases. Cancer 07:758–788
119. Sciuto R, Festa A, Rea S et al (2002) Effects of low dose cisplatin on Sr-89 therapy for painful bone metastases from prostate cancer: a randomized clinical trial. J Nucl Med 43:79–86
120. Horning SJ (2003) Future directions in radioimmunotherapy for B-cell lymphoma. Semin Oncol 30(17):29–34
121. Press OW, Unger JM, Braziel RM et al (2003) A phase 2 trial of CHOP chemotherapy followed by tositumomab/iodine I-131 tositumomab for previously untreated non Hodgkin's lymphoma: Southwest Oncology Group Protocol S9911. Blood 102:1606–1612
122. Mastrangelo S, Tornesello A, Diociaiuti L et al (2001) treatment of advanced neuroblastoma; feasibility and therapeutic potential chemotherapeutic potential of a novel approach combining I-131-MIBG and multiple drug chemotherapy. Br J Cancer 84:460–464
123. Yanik GA, Levine JE, Matthay KK et al (2002) Pilot study of iodine-131-metaiodobenzylguanidine in combination with myeloablative chemotherapy and autologous stem-cell support for the treatment of neuroblastoma. J Clin Oncol 20:2142–2149
124. Grana C, Chinol M, Robertson C et al (2002) Pretargeted adjunct radioimmunotherapy with yttrium-90-biotin in malignant glioma patients: a pilot study. Br J Cancer 86:207–212
125. Bodey RK, Evans PM, Flux GD (2005) Targeted radionuclide therapy. Spatial aspects of combined modality radiotherapy. Radiother Oncol 77:301–309

Glossary

Abscess A collection of pus in tissues, organs, or confined spaces, usually caused by bacterial infection.

Absorbed dose Amount of energy absorbed per unit mass of target material.

Acquired immunity A defense system responding to exposure to various antigens building immunity against that specific antigen.

ALARA "As low as reasonably achievable." A concept recommended by the US National Regulatory Commission for safe radiation practice.

Amplitude image A computer-generated image representing analysis of a process whereby each pixel in the heart is evaluated with respect to movement changes over time. The amplitude image shows the magnitude of blood ejected from each pixel within the ventricular chamber.

Angiogenesis Angiogenesis or neovascularization describes formation of new vessels. It occurs in several pathologies particularly neoplasia. Tumor angiogenesis is initiated, maintained, and controlled by multiple molecules that are released from tumor cells, endothelial cells, and other cell types.

Anion Negatively charged ion.

Ankylosing spondylitis The most common type of spondyloarthropathy with chronic inflammatory changes leading to stiffening and fusion (ankylosis) of the spine and sacroiliac joints with a strong genetic predisposition associated with HLA B27. Other joints such as hips, knees, and shoulders are involved in approximately 30% of patients.

Antibody A protein formed by the body to defend it against infection and other diseases.

Antisense oligonucleotides Synthetic single-strand DNA (or RNA) molecules designed to bind with high affinity to the complementary sequences of mRNA. Several antisense oligodeoxynucleotide pharmaceuticals have been developed as therapeutic agents that act to block protein synthesis by inactivating mRNA. This is the basis of antisense imaging.

Apophysis An accessory secondary ossification center that develops late and forms a protrusion from the growing bone where tendons and ligaments insert or originate.

Apoptosis A type (programmed) of cell death implicated in both normal and pathological tissue, designed to eliminate unwanted host cells in an active process of cellular self-destruction effected by a dedicated set of gene products.

Atrophy A decrease in size and function of the cell.

Attenuation The reduction of radiation intensity during its passage through matter due to absorption, scatter, or both.

Avulsion Complete separation of tendons or ligaments, with or without a portion of bone and/or cartilage.

Behçet's syndrome An uncommon disorder characterized by recurrent oral and genital ulceration, uveitis, or retinal vasculitis, cutaneous pustules or erythema nodosum or cutaneous pathergy and synovitis. The disease is more common in Mediterranean countries and Japan than in the USA.

A. H. Elgazzar (ed.), *The Pathophysiologic Basis of Nuclear Medicine*,
https://doi.org/10.1007/978-3-030-96252-4

Biologic half-life Time required for half of the radioactivity to be eliminated from the body or an organ.

Brodie's abscess An intraosseous abscess in the cortex that becomes walled off by reactive bone.

Bronchial circulation Part of the high-pressure systemic circulation that supplies oxygenated blood to the lung tissue itself.

Budd-Chiari syndrome An uncommon condition usually caused by thrombosis of the hepatic veins such as associated with polycythemia vera, following oral contraceptive use or renal cell carcinoma with tumor involving veins. Sulfur colloid liver scan typically shows decreased uptake in the right lobe with increased uptake in the caudate lobe representing hypertrophy of that lobe.

Bystander effect The directly irradiated cells communicate with adjacent cells and spread the effect of radiation to a larger number of cells.

Calcinosis cutis A term used to describe a group of disorders in which calcium deposits form in the skin, subcutaneous tissue, and connective tissue sheaths around the muscles but not within the muscles.

Calciphylaxis A condition of soft tissue calcification affecting mainly patients with chronic renal failure. The calcification involves the media of small- and medium-sized cutaneous arterioles with extensive intimal hyperplasia and fibrosis. There is also subcutaneous calcification and necrosis which may lead to sepsis, the main cause of morbidity which may be significant.

Carcinogenesis Carcinogenesis or oncogenesis is a process by which normal cells are transformed into cancer cells.

Cation Positively charged ion.

Cell adhesion molecules Protein molecules responsible for connection of cells to each other and to basal membranes and are behind tissue structural organization. They include integrins, selectin (endothelial cell adhesion), and IgG superfamily (nervous system cell adhesion).

Chemotaxis Directional migration of leukocytes at varying rates of speed in interstitial tissue towards a chemotactic stimulus in the inflammatory focus. Through chemoreceptors at multiple locations on their plasma membranes, the cells are able to detect where the highest concentrations are of chemotactic factors and to migrate in their direction.

Costochondritis (Tietze's syndrome) This is a common painful condition affecting the costochondral junction usually in young patients and is self-limited. The etiology remains unknown although trauma and infection are proposed. It can affect any rib but the first and second ribs are most commonly involved.

Chronic obstructive airway disease Chronic bronchitis, emphysema, and bronchial asthma are collectively known as obstructive airway disease.

Colloid A substance that will not easily diffuse through membranes when dissolved in a liquid.

Complex regional pain syndrome type I (reflex sympathetic dystrophy) A pain syndrome that usually develops after an initiating noxious event with no identifiable major nerve injury, is not limited to the distribution of a single peripheral nerve, and is disproportional to the inciting event or expected healing response.

Connective tissue Body tissue that provides and maintains form in the body. It serves to connect and bind the cells and organs and gives support to the body. Unlike the other tissue types of the body that are formed mainly by cells, the major constituent of connective tissue is its extracellular matrix, composed of protein fibers, an amorphous ground substance, and tissue fluid in addition to cells such as fibroblasts, fat cells, and bone cells.

Conn's syndrome Primary aldosteronism with increased production of aldosterone by abnormal zona glomerulosa (adenoma or hyperplasia) leading to hypertension through the increased reabsorption of sodium and water from the distal tubules. A benign adenoma accounts for 75 % of cases of this syndrome.

CPPD Calcium pyrophosphate dihydrate deposition disease, also called pseudogout and chondrocalcinosis, a type of crystal deposition arthropathy with such crystals deposited in cartilage, synovium, tendons, and ligaments.

Cushing's syndrome A disease caused by abnormal stimulation of zona fasciculata of adrenal gland leading to excessive secretion of cortisol. The stimulation of the zona fasciculata may be stimulated by excess ACTH from the pituitary gland, or less commonly the ectopic production of ACTH (as in small cell lung cancer and neural crest tumors) or corticotropin-releasing factor (CRF) (as in bronchial carcinoid and prostate cancer). The disease may also be due to autonomous adrenal cortisol production due to adrenal adenoma or hyperfunctioning adrenal carcinoma.

Detector sensitivity The ratio between the output and the input variable being measured.

Dose rate Dose rate expresses the time for which dose is administered.

Dosimetry A process of calculating the level of radiation exposure from a radioactive source.

Dysplasia Abnormality of the growth or development resulting in alteration in size, shape, and organization of adult cells or organs. In dysplasia, cell maturation and differentiation are delayed, in contrast to metaplasia, in which cells of one mature differentiated type are replaced by another mature cell.

Dystrophic calcification A type of soft tissue calcification that occurs in the setting of normal serum calcium and phosphate levels and occurs in damaged, inflamed, neoplastic, or necrotic tissue.

Ectopic hyperparathyroidism Parathyroid disease due to abnormalities in ectopically located glands.

Effective half-life Time required to reduce radioactivity by half by a combination of physical and biologic elimination processes.

Endochondral ossification Most of the skeleton forms by this type of ossification where a preexisting cartilage forms first and then undergoes ossification.

Enteropathic arthropathies Arthropathies associated with inflammatory bowel diseases including ulcerative colitis, Crohn's disease, Whipple's disease, intestinal bypass surgery, and celiac disease.

Entheses The sites of insertion of tendons, ligaments, and articular capsule to bone.

Enthesopathies A pathologic process affecting entheses particularly trauma and or inflammation resulting in regional periosteal reaction with osteoblastic bone activity.

Epididymis A comma-shaped structure lying on the testicle on its posterolateral surface.

Epididymitis An inflammatory condition affecting the epididymis usually in adults secondary to infection or following trauma. Bacteria usually reach the epididymis from the prostate, seminal vesicles, urethra, or uncommonly hematogenously.

Erythropoiesis The formation of mature red blood cells in the bone marrow starting with the first stem cell progeny committed to erythroid differentiation and ending with the release of red cells into the circulation.

Eutopic hyperparathyroidism Parathyroid disease with typical location of glands.

Exudate An inflammatory extravascular fluid with a high protein content, much cellular debris, and a specific gravity above 1.020. This is the hallmark of acute inflammation, which may also be called exudative inflammation. It indicates significant alteration in the normal permeability of small blood vessels in the region of injury.

Fibrous dysplasia A benign bone disorder characterized by the presence of the fibrous tissue in lesions of trabeculae of nonlamellar bone (woven bone), which remains essentially unchanged.

First-pass radionuclide angiography Examination of the initial transit of a radionuclide bolus through the different major vascular compartments can provide information about the function of each chamber.

Flare pattern on bone scan An initial apparent deterioration of primary or some or all metastatic lesions on the bone scan, followed by improvement usually accompanying successful treatment.

Fracture delayed union Fracture union is delayed beyond the expected time (usually 9 months).

Fracture nonunion Complete cessation of repair process of a fracture.

Fracture A break in the continuity of a bone.

Ganglioneuroma A benign tumor found in older children and young adults that is most commonly present in the adrenal medulla and the posterior mediastinum. The tumor consists

of mature ganglion cells and is well encapsulated; it is frequently calcified and rarely hormone active.

Gas exchange airways Consists of the more distal bronchioles (respiratory) and the alveoli that are lined by nonciliated mucus membrane.

Gene therapy A method designed to manipulate the expression of genes in order to inhibit tumor growth.

Gout A metabolic disorder that results in hyperuricemia and leads to deposition of monosodium urate monohydrate crystals in various sites in the body, especially joint cartilage.

Heterotopic ossification A specific type of soft tissue calcification that may or may not follow trauma and is due to a complex pathogenetic mechanism believed to be due to transformation of certain primitive cells of mesenchymal origin in the connective tissue septa within muscles, into bone forming cells.

Hibernated myocardium Hibernation occurs in myocardium that has undergone a downregulation of contractile function, thus reducing cellular demand for energy, in response to chronic ischemia. It requires the restoration of blood flow in order to improve function.

Homeostasis The term describing maintenance of static, or constant, conditions in the internal environment by means of positive and negative feedback of information.

Hydrocephalus Conditions that produce imbalance between the rate of production and absorption of the cerebrospinal fluid, leading to dilatation of the ventricular system. They may result from obstruction to the flow and absorption of CSF or rarely from overproduction of CSF.

Hyperplasia An increase in cell number.

Hypertrophic cardiomyopathy An idiopathic process that affects mainly the LV myocardium, but the right ventricle may also be involved. Other causes of myocardial hypertrophy such as systemic hypertension and aortic valve stenosis must first be excluded.

Hypertrophic osteoarthropathy A form of periostitis that may be painful and may be associated with clubbing of fingers and toes, sweating, and thickening of skin. It may be primary or follow a variety of pathologic conditions predominantly intrathoracic and is characterized by periosteal new bone formation.

Hypertrophy An increase in cell size which can lead to enlargement of an organ or part of it.

Hungry bone syndrome Severe and prolonged hypocalcemia after parathyroidectomy.

Immigrant cells The cells that travel transiently through blood or lymph and enter connective tissue as needed. These cells include erythrocytes (red blood cells), granulocytes, monocytes, lymphocytes, plasma cells, and platelets.

Impingement syndromes A group of painful conditions caused by friction of joint tissue which include bone impingement, soft tissue impingement, and entrapment neuropathy depending on the type of tissue involved.

Inflammation A complex nonspecific tissue reaction to injury by living agents such as bacteria and viruses leading to infection, or nonliving agents including chemical, physical, immunologic, or radiation injurious agents.

Inflammatory bowel disease (IBD) An idiopathic disease, probably involving an immune reaction of the body to its own intestinal tract. The two major types of IBD are ulcerative colitis and Crohn's disease.

Information density The count number per square centimeter within an image.

Intensity A term describing the energy or number of particles passing through an area unit per unit of time.

Intramembranous ossification Occurs through the transformation of mesenchymal cells into osteoblasts seen in flat bones of the skull, part of the mandible and part of the clavicle.

Involucrum A layer of new bone formation around the site of skeletal infection formed secondary to the body response to infection.

Ionizing radiation A radiation that causes ionization (production of ion pair) when passing through a material.

Isotope dilution Diluting a radiotracer (or tracer) of known activity (or mass) in an unknown volume. By measuring the degree to which the radiotracer was diluted by the unknown volume, one can determine the total volume (or mass) of the unknown volume.

Jodbasedow The condition of iodine-induced hyperthyroidism, which characteristically

occurs in persons with nodular thyroid glands after iodine supplementation in endemic goiter areas. Iodine-containing medical products, including amiodarone, radiographic dyes, and kelp, may also cause jodbasedow.

Juxtaglomerular apparatus The afferent arteriole has specialized smooth muscle cells called juxtaglomerular (JG) cells that form this system and store renin and stretch receptors which respond to changes in arteriolar pressure. The system releases renin when stimulated.

Lactase deficiency A common cause of malabsorption that is found in 15% of Caucasian, 50% of blacks, and about 90% of Asians. Often, patients may have partial lactase deficiency that causes symptoms but not full-blown malabsorption syndrome. Treatment is to avoid lactose-containing dairy products (milk, ice cream, and cheese) and use lactose enzymes to aid in digestion.

Lisfranc injury Fracture or fracture dislocation of tarsometatarsal joints.

List mode An acquisition method for cardiac blood pool studies in patients with arrhythmias. Following acquisition of cardiac gated blood pool study, each individual beat can be reviewed to eliminate atrial or ventricular premature beats that exceed a determined R-R interval duration (arrhythmia rejection). The acceptable beats can then be framed in the most appropriate timing interval for the type of analysis needed.

Lower respiratory airways Trachea, bronchi, bronchioles, and alveolar ducts connected by the larynx.

Maffucci syndrome A nonhereditary disorder characterized by multiple enchondromas and multiple bony hemangiomas.

Malunion Healing of a bone in a nonanatomic orientation.

Marine-Lenhart syndrome Graves' disease with incidentally functioning nodule(s) which are responsive to thyroid-stimulating hormone. It is not responsive to thyroid-stimulating immunoglobulins. It appears as cold, but after successful treatment with radioiodine, it will show uptake on follow-up thyroid scan since TSH level starts to rise.

Mast cells The secretory cells that mediate immediate hypersensitivity reactions. These cells are distributed along blood vessels in connective tissue. Stimulation of these cells by a variety of stimuli such as mechanical trauma, heat, X-rays, and toxins induces secretion of their granule contents, mainly histamine.

Megaloblastosis A morphological abnormality that occurs predominantly in the erythroid precursor cells in the bone marrow and in other replicating cells in human subjects due to deficiency of vitamin B12 and folate or metabolic abnormalities involving these vitamins.

MEN (multiple endocrine neoplasia) An autosomal dominant syndrome that involves hyperfunctioning of two or more endocrine organs. Primary hyperparathyroidism, pancreatic endocrine tumors, and anterior pituitary gland neoplasms characterize type 1 MEN. Medullary thyroid carcinoma, pheochromocytoma, and hyperparathyroidism caused by parathyroid gland hyperplasia characterize type MEN 2A. MEN 2B is defined by medullary thyroid tumor and pheochromocytoma.

Metachondromatosis A hereditary (autosomal dominant) disorder characterized by the presence of multiple enchondromas and osteochondromas.

Metaplasia An alteration of cell differentiation.

Metastatic calcification The type of soft tissue calcification that involves viable undamaged normal tissue as a result of hypercalcemia and/or hyperphosphatemia associated with increased calcium phosphate product locally or systematically.

Monoclonal antibody An antibody derived from a single clone of cells and hence binds only to one unique epitope.

Moyamoya disease A noninflammatory, nonatherosclerotic, nonamyloid vasculopathy characterized by chronic progressive stenosis or occlusion of the terminal internal carotid arteries. It occurs mainly under the age of 10 with a smaller peak during the fourth decade. It presents with transient ischemic attacks and occasionally headache and seizures. Intracranial hemorrhage is the serious complication.

Murine antibody An antibody produced by mouse.

Mutation Any inherited change in the genetic material involving irreversible alterations in the sequence of DNA nucleotides.

Myositis ossificans progressive The congenital and rare form of heterotopic ossification.

Necrosis Cellular death resulting from the progressive degradative action of enzymes on the lethally injured cells, ultimately leading to the processes of cellular swelling, dissolution, and rupture. The morphological appearance of necrosis is the result of denaturation of proteins and enzymatic digestion (autolysis or heterolysis) of the cell.

Nephron The functional unit of the kidney. It consists of a glomerulus and a tubule. Urine is formed as a result of glomerular filtration, tubular reabsorption, and tubular secretion.

Neuroblastoma A malignant tumor of the sympathetic nervous system of childhood. It accounts for up to 10% of childhood cancers and 15% of cancer deaths among children. Seventy-five percent of neuroblastoma patients are younger than 4 years. The tumor has the potential to mature into pheochromocytoma or ganglioneuroma.

Nonuniformity A term describing variations of intensity of an image.

Ollier disease A nonhereditary disorder characterized by multiple enchondromas with a predilection for unilateral distribution.

Oncogenesis See carcinogenesis.

Osteochondritis dissecans Transchondral fracture with fragmentation and separation of portions of cartilage or cartilage and bone which is most prevalent in adolescents.

Osteomalacia Abnormal mineralization of bone with a decrease in bone density secondary to lack of both calcium and phosphorus with no decrease in the amount of osteoid (bone formation).

Osteomyelitis A term applied to skeletal infection when it involves the bone marrow.

Osteopetrosis A rare inherited metabolic bone disease characterized by a generalized increase in skeletal mass due to a congenital defect in the development or function of the osteoclasts leading to defective bone resorption.

Osteoporosis Reduction of bone tissue amount increasing the likelihood of fractures.

Oxalosis Deposition of calcium oxalate crystals that leads to arthropathy.

Pair production When a photon with energy greater than 1.02 MeV is converted into an electron and a positron the process is called pair production. It occurs when the high energetic photon passes through a strong electric field.

Pandemic A worldwide epidemic.

Paraganglioma Pheochromocytoma arising at sites other than adrenal medulla (extra-adrenal).

Parkinson's disease A neurologic disorder characterized by tremor, rigidity, akinesia, bradykinesia, and postural instability.

Passive immunity Passive immunity is due to antibodies entering the body but are formed in another body other than the person's own body. Examples include vaccinations with antibodies such as against tetanus or hepatitis virus and infant antibodies transferred from mother through the placenta. This immunity provides immediate protection against antigen but does not last long.

Pathologic fracture A fracture at a site of preexisting abnormalities that weakens bone.

Pathophysiology Pathophysiology is a convergence of pathology and physiology. It deals with the disruption of normal mechanical, physical, and biochemical functions, either caused by a disease, or resulting from a disease or abnormal syndrome or condition that may not qualify to be called a disease and now includes the molecular mechanisms of disease.

Phase image A computer-generated image representing evaluation of each pixel in the heart with respect to count changes over time. This helps identify abnormal timing of ventricular contraction.

Pheochromocytoma A rare tumor arising from chromaffin cells of the adrenal medulla. It commonly produces excessive amounts of norepinephrine, attributable to autonomous functioning of the tumor, although large tumors secrete both norepinephrine and epinephrine and in some cases also dopamine.

Releasing the catecholamine into the circulation causes hypertension and other signs.

Physical half-life Time required for half of a radioactivity to decay.

Plantar fasciitis (calcaneal periosteitis) An inflammatory condition that can occur as an isolated entity such as secondary to occupation, degenerative, or it may accompany spondyloarthropathies. *Pneumocystis carinii* (*jiroveci*) An opportunistic pathogen currently classified as a fungus. It causes an infection leading to significant morbidity and mortality in human immunodeficiency virus and nonhuman immunodeficiency virus-associated immunosuppressed patients although it also occurs in nonimmunocompromised patients.

Podagra A term describing affection of the metatarsophalangeal joint of the great toe in gout and the most typical finding of gouty arthritis.

Primary hyperparathyroidism Hyperparathyroidism caused by neoplastic or hyperplastic parathyroid glands or when nonparathyroid tumors such as bronchogenic or renal cell carcinomas secrete ectopically parathyroid hormone or a biologically similar product.

Pseudoarthrosis A gap between the fracture bone ends containing a space filled with fluid. Also termed false joint.

Pulmonary circulation A low-pressure, low-resistance system through which oxygen enters and carbon dioxide is removed.

Pyrogens Pyrogens are mostly endotoxins which are lipopolysaccharides produced by bacteria mainly gram negative and they are the reason behind fever in infections.

Radiolabeling The process of attaching radioactive isotope.

Reactive arthritis (Reiter's disease) A syndrome characterized by a combination of nongonococcal urethritis, arthritis, and conjunctivitis.

Renal osteodystrophy A metabolic condition of bone associated with chronic renal failure.

Resolution Ability to separate or discriminate very close quantities by a detector.

Rheumatoid arthritis An autoimmune disease causing inflammation of connective tissue mainly in the joints with synovial inflammatory response triggered by immune complexes in the blood and synovial tissue through activation of plasma protein complement. This inflammation spreads from the synovial membrane to the articular cartilage, joint capsule, and the surrounding tendons and ligaments leading to pain, loss of function, and joint deformity.

SAPHO syndrome A syndrome characterized by synovitis, acne, palmoplantar pustulosis, hyperostosis, and osteitis. The small and large joints of the feet, ankles, knees, hips, sacroiliac joints, and shoulders are affected by the synovitis.

Sarcoidosis A multisystem granulomatous disorder, occurring most commonly in young adults, more commonly in blacks and in temperate areas with an unknown etiology, but it is believed to be due to exaggerated cellular immune response on the part of helper/inducer T lymphocytes to exogenous or autoantigens.

Scattered radiation This term describes radiation that during its passage through a substance deviates in direction with possible loss of energy.

Secondary hyperparathyroidism Hyperparathyroidism due to compensatory hyperplasia of parathyroids in response to hypocalcemia.

Septic tenosynovitis An inflammatory condition affecting generally the flexor tendons of the hands and feet of diabetic patients and resulting from penetrating injuries or spread of infection from a contiguous focus of infection.

Sequestrum Segmental bone necrosis that develops when normal blood supply to the bone is interrupted by the edema and ischemia produced by the inflammation.

Shin splints Periosteal elevation with reactive bone formation secondary to extreme tension on muscles or muscle groups inserting on bones.

Slipped capital femoral epiphysis Displacement of the proximal femoral epiphysis or simply femoral head from the femoral neck at the site of the growth plate during the growth condition.

Spondyloarthropathies A group of seronegative arthropathies formerly called rheumatoid variants that share common clinical and radiographic features with characteristic involvement of the sacroiliac joints, spine, and to

various degrees the peripheral joints, which are linked to HLA B27 histocompatibility antigen and include ankylosing spondylitis, psoriatic arthritis, reactive arthritis (Reiter's disease), and enteropathic spondylitis.

Spondylolysis A loss of continuity of bone of the neuroarch of the vertebra due to stress or trauma.

Spondylolisthesis Forward movement of one vertebra on another usually as a result of fracture of the neuroarch.

Spontaneous intracranial hypotension (SIH) An increasingly recognized condition due to CSF leak without apparent prior cause. It can cause postural headache, which in this case is secondary to low CSF pressure.

Sprains Tears to tendons.

Stem cells Undifferentiated cells in adults known also as pluripotent cells, precursor cells that are not totally committed to a specific function.

Strains Tears to ligaments.

Stress fracture A pathologic condition of bone due to repeated episodes of stress; each is less forceful than that needed to cause acute fracture of the bony cortex.

Stunned myocardium Continued dysfunction due to ischemia-induced oxidative stress.

Synovial joints Specialized joints found mainly in the appendicular skeleton and which allow free motion.

Tertiary hyperparathyroidism The condition of patients who develop hypercalcemia following long-standing secondary hyperparathyroidism due to the development of autonomous parathyroid hyperplasia, which may not regress after correction of the underlying condition, as with renal transplantation.

Theranostics A new field of medicine which provides specific targeted therapy based on specific targeted diagnostic tests. The specific diagnostic test shows a particular molecular target on a tumor, allowing a therapy agent to specifically target that receptor on the tumor, rather than more broadly.

Thyrotropin-releasing hormone (TRH) A tripeptide originating from the hypothalamic median eminence, which stimulates the secretion and synthesis of thyroid-stimulating hormone from anterior pituitary.

Toddler's fracture Fracture in preschool children which is typically a nondisplaced spiral fracture of the mid tibia but also involves other fractures including the fibula, calcaneus, talus, metatarsal, and cuboid bones in this age group.

Transient synovitis A joint inflammation of unknown origin and self-limited course affecting most frequently boys between 5 and 10 years of age. It was known as toxic synovitis and affects preferentially the hip or knee and subsides without antibiotics.

***T*-score** A parameter used to express bone mineral density by relating an individual's bone density to the mean BMD of healthy young adults, matched for gender and ethnic group.

Tumor grading Grading is a scheme that attempts to determine the degree of malignancy and is based on the evaluation of certain parameters such as degree of tumor cellularity, resemblance of tumor cells to their normal forebears morphologically and functionally, cellular pleomorphism or anaplasia, mitotic activity (number and abnormality), and necrosis.

Tumoral calcinosis A type of soft tissue calcification characterized by large, calcified, periarticular soft tissue masses of calcium phosphate near the large joints such as the hip, the shoulder, and the elbow, in addition to the wrist, feet, and hands.

Uniformity correction Addition or subtraction of counts to the image in order to correct for flood field irregularities.

Upper respiratory airways Nasopharynx and oropharynx.

Urinary tract infection, complicated Infection in patients with risk factors such as extremes of age, diabetes, failed course of antibiotics, or extended symptoms

Urinary tract infection, uncomplicated Infection in otherwise healthy patient with structurally and functionally normal urinary tract

Ventilation The process by which air flows in and out of the gas exchange airways.

Ventricular ejection fraction The stroke volume divided by the end-diastolic volume.

Whipple's disease A systemic bacterial illness usually affecting middle-aged men causing

malabsorption and presenting diarrhea, arthritis, fever, weight loss, swollen lymph nodes, and skin pigmentation. It is diagnosed mainly by a small bowel biopsy through an endoscope, and the treatment is antibiotics for 1 year or longer.

Wolff-Chaikoff effect An intrathyroid autoregulatory mechanism other than the hypothalamus-pituitary-thyroid axis mechanism. When intrathyroid iodine concentrations are significantly increased, the rate of thyroid hormone synthesis is decreased, with a reduction in iodothyronine synthesis and a decrease in the DIT/MIT ratio.

Woven bone Immature nonlamellar bone that is later normally converted to lamellar bone.

***Z*-score** A parameter used to express bone mineral density by comparing the bone density value of an individual to the mean value expected for his/her age-matched peer.